ERAD2018

10th European Conference on Radar in Meteorology & Hydrology



1 July - 6 July 2018, Ede-Wageningen, The Netherlands

WAGENINGEN
UNIVERSITY & RESEARCH

Royal Netherlands
Meteorological Institute

10th European Conference on Radar in Meteorology and Hydrology (ERAD 2018)

Royal Netherlands Meteorological Institute (KNMI)
Wageningen University
1 - 6 July 2018
De Reehorst Hotel and Conference Centre, Ede-Wageningen
The Netherlands

Editors: Lotte de Vos, Hidde Leijnse and Remko Uijlenhoet
Lay-out: Bingyu Zhang

Royal Netherlands Meteorological Institute
P.O. Box 201, 3730 AE De Bilt, The Netherlands

Hydrology and Quantitative Water Management Group, Wageningen University
P.O. Box 47, 6700 AA Wageningen, The Netherlands

Quotation from or reference to any part of this book should be made with full reference to the above data

DOI: 10.18174/454537

Sponsors


LEONARDO
Meteorological
TECHNOLOGY INTERNATIONAL
METEK
Meteorologische Messtechnik GmbH
Germany
EMS
VAISALA
RST
BARON
Critical Weather Intelligence
ELDES
RADAR SYSTEMS FOR METEOROLOGY AND DEFENCE
gamic
EEC
PROTECTING PEOPLE AND ASSETS™
FURUNO

Welcome

Dear ERAD 2018 participant,

On behalf of the Royal Netherlands Meteorological Institute (KNMI) and Wageningen University & Research (WUR), welcome to the Netherlands, welcome to the Reehorst Conference Centre in Ede-Wageningen, and welcome to the 10^{th} European Conference on Radar in Meteorology and Hydrology!

Every other year, ERAD is held to promote the exchange of knowledge between students, research scientists, radar engineers and operators, and end users of weather radar. ERAD provides a platform to transfer knowledge from research into operational use (and vice versa) of weather radar. Beginning with the establishment of the conference series in Locarno, Switzerland, in 1998 and the first conference held in 2000 in Bologna, Italy, the series has been an important forum that brings together meteorologists, hydrologists, radar engineers and practitioners, whose research and daily work involves weather radar.

Results presented and discussed at the ten previous meetings have been published in numerous refereed journal articles and are often widely cited. In addition, the ERAD conference series has been instrumental in promoting applications of weather radar in meteorology, hydrology, water management and many other fields, in Europe and beyond. Over the years, the scope of ERAD has also broadened into related developments in fields such as spaceborne radar and other emerging technologies.

This anniversary edition of ERAD is organised jointly by the Royal Netherlands Meteorological Institute (KNMI) and Wageningen University & Research (WUR). The general setup of ERAD2018 is a five-day scientific conference with one plenary oral session with three keynotes each morning from 8:30 to 10:00 AM, while during the rest of the day there will be two parallel oral sessions intertwined with one single poster session. Our aim is that, in this manner, we achieve maximum exposure of all participants to each other's work. We hope, once the conference is over, you will be able to look back on a fruitful meeting and conclude that this goal has been achieved. The conference is preceded by a full day of five short courses, which together have attracted more than 100 participants! On Wednesday afternoon there will be a one-hour session celebrating the career of our colleague and friend Isztar Zawadzki, followed by an excursion and conference dinner at Ouwehands Zoo in the nearby town of Rhenen.

As venue for the conference we have chosen the Reehorst Hotel and Conference Centre, conveniently located within a three-minute walking distance from the Ede-Wageningen railway station, with direct train connections to Amsterdam Airport

Schiphol (∼1 hour) and other destinations in the Netherlands, such as the cities of Utrecht (∼25 min) and Amsterdam (∼55 min). A regular bus service (line 84/88 from the Ede-Wageningen railway station or line 86 directly from the conference centre) will bring you to the campus of Wageningen University & Research Centre in less than 15 min and to the city centre of college town Wageningen in ∼20 min. For those of you who have a (rental) car, the conference centre is within 1 km from exit 24 of (inter)national highway A12/E35 (UtrechtArnhem). National Park "De Hoge Veluwe" and the Kröller-Müller Museum are only a ∼30 min bus ride (line 108) from Ede-Wageningen railway station. By the way, 2018 is a fitting year to visit the area, as Wageningen University & Research is celebrating its 100^{th} anniversary.

As Organizing Committee, we thank you very much for keeping the spirit of the ERAD conference series alive by submitting nearly 400 abstracts! The Program Committee was impressed by the general quality of the abstracts, which made it easier for them to assemble an attractive conference program, with 15 keynote lectures, 120 oral presentations, as well as a poster session with 218 posters.

Finally, we would like to thank our sponsors: the Royal Netherlands Meteorological Institute (KNMI), Wageningen University & Research (WUR), LEONARDO / SELEX, BARON, EEC, ELDES, the European Meteorological Society (EMS), FURUNO, GAMIC, METEK, Meteorological Technology International, RST, and VAISALA. Their support has been instrumental in organizing ERAD2018.

We wish you a fruitful conference in a friendly environment!

Remko Uijlenhoet
Hidde Leijnse

Organizing committee

Hidde Leijnse - KNMI, Netherlands - co-chair ERAD 2018

Remko Uijlenhoet - WUR, Netherlands - co-chair ERAD 2018

Lotte de Vos - KNMI, Netherlands

Hedy Wessels-van Blijenburgh - WUR, Netherlands

Renée Logtenberg - WUR, Netherlands

Tamara Schalkx - WUR, Netherlands

Petra van den Broek - WUR, Netherlands

Program committee

Ali Tokay - NASA/UMBC, USA - co-chair ERAD 2016 and chair AMS Radar Committee

Kurtuluş Öztürk - TSMS, Turkey - co-chair ERAD 2016

Martin Hagen - DLR, Germany - co-chair ERAD 2014

Aurora Bell - BOM, Australia - chair ERAD 2010

Daniel Sempere Torres - CRAHI-UPC, Spain - chair ERAD 2006

Daniel Michelson - Environment and Climate Change Canada - chair ERAD 2004

Elena Saltikoff - FMI, Finland

Alexis Berne - EPFL, Switzerland

Scott Collis - Argonne National Laboratories, USA - co-chair AMS Radar Conference 2017

Luca Baldini - ISAC-CNR, Italy

Frank Marzano - University L'Aquila, Italy

Urs Germann - MeteoSwiss, Switzerland

Contents

Welcome **3**

Session 1. Microphysical studies **35**

Keynote presentation . . . 36

1.1 DENSITY OF SNOWFLAKES BASED ON SURFACE OBSERVATIONS (*A. VON LERBER, D. MOISSEEV , J. TIIRA , D. ORI*) . . . 36

Oral presentation . . . 38

1.2 ICE MICROPHYSICAL RETRIEVALS USING POLARIMETRIC RADAR DATA (*A.RYZHKOV, A.MURPHY , G.MCFARQUHAR*) . . . 38

1.3 AN INVERSE PROBLEM APPROACH TO RETRIEVE FIELDS OF DROP SIZE DISTRIBUTION PARAMETERS FROM XBAND POLARIMETRIC RADAR VARIABLES (*M. ALCOBA, M. GOSSET, H. ANDRIEU*) . . . 39

1.4 MULTI-INSTRUMENT RAINFALL RATE ESTIMATION IN THE PERUVIAN CENTRAL ANDES (12.0°S) (*D. SCIPION, J. VALDIVIA, F. SILVA, M. MILLA*) . . . 40

1.5 RAINDROP SIZE DISTRIBUTION IN COASTAL RAINFALL SYSTEMS IN SOUTH EAST AUSTRALIA: EFFECT ON Z-R RELATIONSHIPS AND ATTENUATION (*A. GUYOT, J. PUDASHINE, V. PAUWELS, A. PROTAT, A. SEED, R. UIJLENHOET, M. PRAKASH, J.P. WALKER*) . . . 41

1.6 RECONSTRUCTION OF THE DRIZZLE MODE OF THE RAINDROP SIZE DISTRIBUTION: AN APPROACH USING DOUBLE-MOMENT NORMALISATION (*T. H. RAUPACH, M. THURAI, V. N. BRINGI, A. BERNE*) . . . 42

1.7 POLARIMETRIC RADAR RETRIEVALS OF LOWER ORDER DSD MOMENTS: CASE STUDIES USING CSU-CHILL RADAR (*V. N. BRINGI, T. RAUPACH, M. THURAI, P. C. KENNEDY, A. BERNE*) . . . 43

1.8 VERTICAL VARIABILTIY RAIN DROP SIZE DISTRIBUTION FROM DISDROMETER AND MICRO RAIN RADAR MEASUREMENTS (*E. ADIROSI , A. TOKAY , N. ROBERTO, E. GORGUCCI, M. MONTOPOLI, L. BALDINI*) . . . 44

1.9 IMPACT EVALUATION OF VERTICAL AIR VELOCITY ON THE MICROPHYSICAL RETRIEVALS BY K BAND RADAR PROFILERS USING COMBINED UHF AND S BAND PRODUCTS (*M. MONTOPOLI , E. ADIROSI, N. ROBERTO, L. BALDINI*) . . . 46

1.10 A MICROPHYSICAL RETRIEVAL FOR THE DUAL-FREQUENCY PRECIPITATION RADAR (*K. MROZ, A. BATTAGLIA*) . . . 48

1.11 CHARACTERIZATION OF THE VERTICAL PROFILES OF DUAL-POLARIZATION RADAR OBSERVATIONS IN AND ABOVE THE BRIGHT BAND AT S, C AND X-BANDS (*CLOTILDE AUGROS, GUY DELRIEU, NAN YU, NICOLAS GAUSSIAT*) . . . 49

1.12 VERTICAL PROFILE OF REFLECTIVITY FROM K-BAND RADAR OBSERVATIONS IN EAST ANTARCTICA (*C. DURAN-ALARCON, A. BERNE, B. BOUDEVILLAIN, C. GENTHON, N. SOUVERIJNS, N.P.M. VAN LIPZIG*) 50
1.13 INVESTIGATION OF ICE MICROPHYSICS USING SIMULTANEOUS MEASUREMENTS AT C- AND KA-BAND (*M. HAGEN, F. EWALD, S. GROSS, Q. LI,B. MAYER, T. ZINNER*) . 51
1.14 FINGERPRINTS OF PRECIPITATION PROCESSES REVEALED BY UNSUPERVISED CLASSIFICATION OF PROFILES OF POLARIMETRIC RADAR VARIABLES (*J. TIIRA, D.N. MOISSEEV*) 52
1.15 CHARACTERISATION OF THE MELTING LAYER VARIABILITY IN THE SWISS ALPS USING POLARIMETRIC X-BAND RADARS (*F. VAN DEN HEUVEL, M. GABELLA, A. BERNE*) 53
1.16 IMPACT OF RIMED AND UNRIMED SNOW ON SNOWFALL RETRIEVALS AT X, KA AND W BAND (*M. T. FALCONI, A. VON LERBER, D. ORI, F.S. MARZANO, D. MOISSEEV*) 54
1.17 A PROBABILISTIC POLARIMETRIC RADAR FORWARD MODEL FOR SMALL ICE PARTICLES (*ROBERT S. SCHROM, MATTHEW R. KUMJIAN*) 56
1.18 WHY THE GENERALIZED GAMMA? - AN ANSWER BASED ON MEASUREMENTS WITH METEOROLOGICAL PARTICLE SPECTROMETER AND 2D VIDEO DISDROMETER (*M. THURAI, V. N. BRINGI, P. N. GATLIN, W. A. PETERSEN, M. WINGO*) 58
1.19 MULTI-FREQUENCY RADAR RETRIEVAL OF SNOWFALL MICROPHYSICS (*J. LEINONEN, M. D. LEBSOCK, O. O. SY, S. TANELLI, B. DOLAN, R. J. CHASE, J. A. FINLON, D. MOISSEEV, A. VON LERBER*) 60

Poster presentation 61

1.20 A POLARIMETRIC ANALYSIS OF ICE MICROPHYSICAL PROCESSES IN MELTING LAYERS OF WINTER STORMS, USING QUASI-VERTICAL PROFILES (*E. M. GRIFFIN, T. J. SCHUUR, A. V. RYZHKOV*) 61
1.21 ICE MICROPHYSICS DURING OLYMPEX: COMPARISON BETWEEN REMOTE SENSING AND AIRBORNE IN SITU OBSERVATIONS (*F. TRIDON, A. BATTAGLIA, R. CHASE, K. MROZ, J. TURK, S. TANELLI, S. NESBITT, J. LEINONEN, S. KNEIFEL*) 62
1.22 A FOUR YEAR LAGRANGIAN STUDY OF ISOLATED CONVECTION IN HOUSTON, TEXAS: USING PUBLIC DATA AND OPEN SOURCE CODE TO DESIGN A FIELD CAMPAIGN (*S. COLLIS, R. JACKSON, M. PICEL, M VAN LIER-WALQUI, A. FRIDLIND*) 63
1.23 LEVERAGING RADAR OBSERVATIONS TO PROBABILISTICALLY INFORM NEW CLASSES OF MICROPHYSICAL PARAMETERIZATION SCHEMES (*M. VAN LIER-WALQUI, M. KUMJIAN, H. MORRISON,O. PRAT, J. TURK, K. RIEMEL, J. HARRINGTON , A. JENSEN, R. SCHROM*) 64
1.24 ESTIMATION OF OBSERVATIONAL AND FORWARD-SIMULATOR UNCERTAINTIES IN THE CONTEXT OF MICROPHYSICAL STUDIES USING DOPPLER SPECTRA AND POLARIMETRIC RADAR OBSERVATIONS (*M. VAN LIER-WALQUI, D. POSSELT, J. REMILLARD, M. KUMJIAN, H. MORRISON, O. PRAT, K. REIMEL, S. COLLIS, J. HARRINGTON, A. JENSEN, R. SCHROM*) 65
1.25 AUTOMATIC DETECTION OF THE MELTING LAYER USING POLARIMETRIC RADAR PROFILER (*M.T. BERNDSEN, C.M.H. UNAL, H.W.J. RUSSCHENBERG*) 66
1.26 THE HYMID PROJECT HYDROMETEORCLASSIFICATION IN THE ALPS (*L. TCHLER, V. MEYER, R. KALTENBÖCK*) 67

1.27 A STUDY OF HEAVY AND PERSISTENT PRECIPITATION IN SW ENGLAND (*A. BLYTH, Y. HUANG, L. BENNETT, D. DUFTON*) 68
1.28 HYDROMETEOR CLASSIFICATION BY PORTABLE X-BAND POLARIMETRIC RADAR OF KOCHI UNIVERSITY (*KOJI SASSA, KOTARO YOSHIMURA*) 69
1.29 MODELING CLOUDS AND PRECIPITATION IN ADÉLIE LAND, ANTARCTICA: POLAR-WRF SIMULATIONS VERSUS IN-SITU AND RADAR OBSERVATIONS (*ETIENNE VIGNON, CHRISTOPHE PRAZ, JOSUÉ GEHRING, NIKOLA BESIC, ALEXIS BERNE*) . . . 70
1.30 LONG-TERM ANALYSIS OF REFLECTIVITY-RAINFALL RATE RELATIONSHIPS USING DISDROMETER DATA (*DANIEL SANCHEZ-RIVAS, M. A. RICO-RAMIREZ*) 71
1.31 TEMPORAL EVOLUTION OF PRECIPITATION RELATED MICROPHYSICAL PROCESSES BASED ON DUAL-POL DATA OF S-, X-, AND C-BAND DOPPLER RADARS (*M. LUKACH, R. R. NEELY III, D. DUFTON*) 72
1.32 SIMULATIONS OF THE RADAR VARIABLES DURING VAPOR DEPOSITION AND RIMING IN ARCTIC MIXED-PHASE CLOUDS (*ROBERT S. SCHROM, MATTHEW R. KUMJIAN, JERRY Y. HARRINGTON*) 73
1.33 AUTOMATIC IDENTIFICATION OF MELTING LAYER BASED ON FUZZY LOGIC AT OPERATIONAL S-BAND DUAL POLARIZATION RADAR (*HYE-YOUNG HAN, SUNG-HWA JUNG, GYUWON LEE, DONG-JIN KIM, SUN-KI LEE*) 75
1.34 PRELIMINARY RESULT OF ICE-POP 2018: SNOW MICROPHYSICAL CHARACTERISTICS BY DIFFERENT TYPES OF SNOW HABIT (*KWONIL KIM, WONBAE BANG, CHOENG-LYONG LEE, DAEHYUNG LEE, DAEJIN YEOM, SU-JEONG CHO, KWANG-DEUK AHN, NAMWON KIM, CHRISTOPHE PRAZ, ALEXIS BERNE, WALTER PETERSEN, STELLA MELO, WEI-YU CHANG, FRANCISCO TAPIADOR,GYUWON LEE*) 76
1.35 LINKING SNOWFALL MICROPHYSICAL PROPERTIES AND WATER CONTENT USING A MASC, A 2DVD AND A PLUVIO (*A. REVERDIN, C. PRAZ, T. RAUPACH, A. BERNE*) 77
1.36 PRELIMINARY RESULTS ON MICROPHYSICAL CHARACTERIZATION OF PRECIPITATION OVER ANTARCTICA COAST (*N.ROBERTOL. BALDINI, A. BRACCI, M.MONTOPOLI, E. ADIROSI, E.GORGUCCI, C. SCARCHILLI, P. GRIGIONI, V. CIARDINI, F.PORCU'*) 78
1.37 PAIRED DISTROMETRIC MEASUREMENTS IN SOUTH BRAZIL: WIND EFFECTS AND SAMPLING UNCERTAINTIES (*R.V. CALHEIROS, C.BENETI*) 80
1.38 STUDY OF THE MONSOON VARIABILITY BY THE CLOUD RADARS ESTIMATED MICROPHYSICAL PROFILES (*M.C.R KALAPUREDDY, SUKANYA PATRA, VIPUL DHAVALE*) 82
1.39 FIELD OBSERVATION FOR INVESTIGATING THE MICROPHYSICAL CHARACTERISTICS OF PRECIPITATION SYSTEM IN KOREA (*DONG-IN LEE, MI-YOUNG KANG, HYEON-JOON KIM, SUNG-HO SUH*) 83
1.40 A RADAR BASED AUTOMATED DETECTION ALGORITHM FOR REFREEZING LAYER AND ITS IMPLEMENTATION INTO A FUZZY LOGIC HYDROMETER CLASSIFICATION SCHEME (*BRANDON HICKMAN, SILKE TRÖMEL, ALEXANDER RYZHKOV, CLEMENS SIMMER*) 84
1.41 TOPOGRAPHIC INFLUENCE ON SNOWFALL: A RADAR BASED SPATIO-TEMPORAL ANALYSIS (*N. BESIC, F. GERBER, D. NERINI, L. FORESTI, J. FIGUERAS I VENTURA, M. GABELLA, U. GERMANN, M. LEHNING, A. BERNE*) 85

1.42POLARIMETRIC RADAR CHARACTERISTICS OF THE ASYMMETRIC EYEWALL OF HURRICANE HARVEY (2017) (*YA-CHIEN FENG, MICHAEL M. BELL*) 86
1.43 SNOWFALL FORMATION AND ENHANCEMENT PROCESSES IN TWO CONTRASTED MOUNTAIN RANGES: THE ALPS AND THE TAEBAEK MOUNTAINS (*J. E. GEHRING, N. BESIC, C. PRAZ, A. BERNE*) 87
1.44 SIMULTANEOUS OBSERVATIONS OF KA BAND PROFILER AND GPM DUAL-FREQUENCY PRECIPITATION RADAR OVER TROPICAL CENTRAL ANDES (12.0° S) (*J. VALDIVIA, S. KUMAR, Y. SILVA, D. SCIPION*) 88
1.45 CLOUD ELECTRIFICATION MODEL IN THE COSMO NUMERICAL WEATHER PREDICTION MODEL (*Z. SOKOL, J. MINAROVA*) 89
1.46 AN X-BAND STUDY OF KDP AND RAINFALL OVER SOUTHERN ENGLAND DURING WINTER 2018 (*J. M. HAMPTON, R. R. NEELY III, A. M. BLYTH*) 90
1.47 CORRECTION OF DROP SIZE DISTRIBUTIONS FROM DIFFERENT DISDROMETERS USING GENERALIZED NORMALIZATION PARAMETERS DURING ICE-POP 2018 PROJECT (*WONBAE BANG, KWONIL KIM, SU-JEONG CHO, DAEJIN YEOM, CHOENGLYONG LEE, DAEHYUNG LEE, SEUNGWOO BAEK, GYUWON LEE*) 91
1.48 POLARIMETRIC DOPPLER OBSERVATIONS OF ICE PARTICLES WITH SCANNING 94 GHZ CLOUD RADAR (*A.MYAGKOV, T. ROSE*) 92
1.49 MICROPHYSICAL CHARACTERISTICS OF ORGANIZED CONVECTION OBSERVED BY POLARIMETRIC RADAR IN EASTERN CHINA (*KUN ZHAO, GANG CHEN, GUIFU ZHANG, WEN-CHAU LEE*) 93
1.50 INVESTIGATION OF THE SPECTRAL DIFFERENTIAL PHASE IN THE CASE OF A S-BAND RADAR PROFILER (*C. UNAL*) 94
1.51 VARIATIONS IN RADAR RAINFALL ESTIMATORS WITH GENERAL WEATHER TYPES AND LOCATION IN BAVARIA (*W. GHADA, ANNETTE MENZEL*) 95
1.52 A HYDROMETEOR CLASSIFICATION ALGORITHM FOR THE UK C-BAND WEATHER RADAR NETWORK (*S.R. BEST, D.L. HARRISON*) 96

Session 2. Mesoscale and severe weather **97**

Keynote presentation 98
2.1 PERFORMANCE OF A NEW ALGORITHM FOR NOWCASTING ANOMALOUS TRAJECTORIES (*A. DEL MORAL, T. RIGO, M.C. LLASAT*) 98
Oral presentation 99
2.2 IMPACT OF MULTIPLE RADAR REFLECTIVITY DATA ASSIMILATION ON THE NUMERICAL SIMULATION OF A FLASH FLOOD EVENT DURING THE HyMeX CAMPAIGN (*I. MAIELLO, S. GENTILE, R. FERRETTI, L. BALDINI, N. ROBERTO, E. PICCIOTTI, P.P. ALBERONI, F.S. MARZANO*) 99
2.3 THE ROLE OF SMALL-SCALE VORTICES IN ENHANCING SURFACE WINDS AND DAMAGE IN HURRICANE HARVEY (*JOSHUA WURMAN, KAREN KOSIBA*) 100
2.4 THE TWIRL PROJECT: FINE-SCALE MOBILE RADAR AND IN SUTU OBSERVATIONS OF TORNADO STRUCTURE (*KAREN A. KOSIBA, JOSH WURMAN, HOWARD BLUESTEIN*) 101
2.5 FRESH WATER FLUX ESTIMATED BY SHIPBOARD C-BAND POLARIMETRIC RADAR AND ITS POSSIBLE IMPACT TO THE OCEANIC STRATIFICATION OBSERVED IN THE MARITIME CONTINENT (*M. KATSUMATA, B. GENG, S. YOKOI, S. MORI, R. SHIROOKA, I. UEKI*) 103

2.6 RAPID SCAN EXPERIMENT OF DOPPLER WEATHER RADAR FOR MONITORING RAINSTORMS AND TROPICAL CYCLONES IN HONG KONG (*W. KONG*) 104
2.7 CHARACTERISTICS OF CONVECTIVE AGGREGATION IN MID-LATITUDES IDENTIFIED IN A DOPPLER C-BAND RADAR NETWORK (*I. PSCHEIDT, S. TRÖMEL*) 105
2.8 EVALUATING THE DEVELOPMENT STAGE OF THUNDERSTORMS BY USE OF 4D RADAR DATA-PARAMETERS (*MALTE NEUPER, JAN HANDWERKER*) 106
2.9 DUAL-POLARIZATION RADAR OBSERVATIONS OF DEEP CONVECTION OVER THE LAKE VICTORIA BASIN IN EAST AFRICA (*P. WANIHA, A. KIJAZI, R. ROBERTS, J. WILSON*) 108
2.10 WEATHER RADAR DERIVED RAIN CELL SIZE STATISTICS FOR LOWER AUSTRIA (*R. TESCHL, F. TESCHL, S. TANI, H. PAULITSCH*) 109
2.11 EARLY DETECTION OF DEEP CONVECTION USING NWCSAF RDT PRODUCT AND NATIONAL RADAR MOSAIC IN ITALY (*R. CREMONINI, M. CELANO, P.P. ALBERONI, R. BECHINI, V. CAMPANA, G. VULPIANI, P. GIORDANO*) 110
2.12 DOPPLER RADAR OBSERVATIONS OF TWO TORNADIC THUNDERSTORM CASES IN THE WESTERN MEDITERRANEAN REGION (*J. BECH, O. RODRIGUEZ, P. ALTUBE, T. RIGO, N. PINEDA, S. CASTÁN, J. ARÚS, J. MONTANYÀ*) 111
2.13 CONVECTIVE CLOUD TOP HEIGHTS IN NORTHERN AUSTRALIA IN DIFFERING WET SEASON REGIMES (*R. JACKSON, S. COLLIS, A PROTAT, V LOUF, W LIN, A. VOGELMANN, S. ENDO*) 112
Poster presentation 113
2.14 UNDERSTANDING AND PREDICTION OF RAINFALL ASSOCIATED WITH LANDFALLING TROPICAL CYCLONES (UPDRAFT) (*YUAN WANG*) 113
2.15 DUAL-DOPPLER AND POLARIMETRIC RADAR ANALYSIS OF CONVECTIVE SYSTEMS IN WEST GERMANY (*RAQUEL EVARISTO, SILKE TRÖMEL, CLEMENS SIMMER*) . 114
2.16 IT'S TIME FOR COLOR VISION DEFICIENCY FRIENDLY COLOR MAPS IN THE RADAR COMMUNITY (*S. COLLIS, R. JACKSON, Z. SHERMAN, C HOMEYER, K. MHLBAUER, R. CHASE, S. NESBITT, T. LANG, D. STECHMAN*) 115
2.17 DIURNAL CYCLE OF PRECIPITATION AND WINDS IN CENTRAL PERUVIAN ANDES, USING CLOUD AND WIND PROFILING RADARS (*Y. SILVA, S. CHAVEZ*) 116
2.18 MULTIFRACTAL ANALYSIS OF TROPICAL CYLCONE RADAR DATA: REMOVING MISSING DATA BIASES AND CONSEQUENCES FOR MESO-SCALE MODELLING (*D.SCHERTZER, J. LEE, D.I. LEE, I. TCHIGUIRINSKAIA*) 117
2.19 IMPLEMENTATION OF A DYNAMIC EQUATION CONSTRAINT BASED ON THE STEADY STATE MOMENTUM EQUATIONS WITHIN THE WRF HYBRID ENSEMBLE-3DVAR DATA ASSIMILATION SYSTEM AND TEST WITH RADAR T-TREC WIND ASSIMILATION FOR TROPICAL CYCLONE CHANTHU (2010) (*JIE MING, XIN LI , MING XUE , YUAN WANG, KUN ZHAO*) 118
2.20 INTEGRATION OF RESEARCH WEATHER RADARS INTO ATMOSPHERIC SCIENCE EDUCATION AT PURDUE UNIVERSITY, USA (*R. TANAMACHI*) 119
2.21 SINGLE- AND DUAL- POLARIZATION RADAR HAIL DETECTION AT THE BOHEMIA HAILSTORMS ON 23 MAY 2016 (*K. SKRIPNIKOVA, D. REZACOVA*) 120
2.22 IMPROVING RADAR HAIL ALGORITHMS FOR THE SWISS HAIL CLIMATOLOGY PROJECT FIRST SENSITIVITY STUDIES (*S. TREFALT, A. HERING, L. NISI, C. SCHWIERZ, U. GERMANN*) 121

2.23 USING EUSKALMET RADAR FOR ANALYSIS OF INTENSE AND PERSISTENCE PRECIPITATION EVENT IN BASQUE COUNTRY DURING WINTER: THE 11 JANUARY 2018 CASE. (*J. EGAÑA, S. GAZTELUMENDI, O. PRINCIPE, V. PALACIO, M. MARURI*) 122
2.24 USING EUSKALMET RADAR FOR ANALYSIS OF A HEAVY STORMS EVENT IN BASQUE COUNTRY DURING SUMMER: THE 30 AUGUST 2017 CASE (*J. EGAÑA, S. GAZTELUMENDI, M. CELANO, O. PRINCIPE, M. CELANO, V. PALACIO, M. CELANO, M. MARURI*) 123
2.25 LONG-TERM CHARACTERISTICS OF WEATHER RADAR PRODUCTS DERIVED FROM 15-YR DATASET OF VOLUMETRIC MEASUREMETS (*P. NOVK, H. KYZNAROV*) . . 124
2.26 POLARIMETRIC SIGNATURES IN SEVERE STORMS: OBSERVATIONS BY THE FRENCH RADAR NETWORK VS. FORECASTS FROM THE AROME CONVECTIVE-SCALE NWP SYSTEM (*M. MONTANGON, O. CAUMONT, C. AUGROS*) 125
2.27 STORM CELL CHARACTERISTICS DERIVED BY CELL-TRACKING ALGORITHM CELLTRACK - EVALUATION AND OPERATIONAL VISUALIZATION (*H. KYZNAROVÁ, P. N-OVÁK*) 126
2.28 USE OF POLARIMETRIC DATA FOR BETTER ANALYSES OF CONVECTIVE STORM CHARACTERISTICS (*DAVID RÝVA*) 127
2.29 AN OVERVIEW OF THE SHONAI AREA RAILROAD WEATHER PROJECT (*K. KUSUNOKI, T. ADACHI, H. Y. INOUE, K. ARAI, N. ISHITSU, S. ONOMURA, C. FUJIWARA, H. SUZUKI*) 128
2.30 ANALYSIS OF HAIL EVENT IN FIELD OF REFLECTIVITY AND DIFFERENTIAL REFLECTIVITY (*S.STEVANOVIĆ, S.BILJIĆ, M.VASIĆ, G.BOGUNOVIĆ*) 129
2.31 CONVECTIVE CLOUDS OBSERVATIONS AND ANALYSIS WITH POLARIMETRIC RADAR IN THE QINGHAI-XIZANG PLATEAU (*M. YAO, Z. HU, X. HUANG*) 130
2.32 TORMIC: RADAR-BASED DETECTION AND FORECASTING TORNADOES AND MICROBURST OVER NORWAY (*SEVIM M.-GULBRANDSEN, LAILA FODNES SIDSELRUD, CRISTIAN LUSSANA*) 131
2.33 IRMA - IMPLEMENTATION OF A HIGH RESOLUTION 3D RADAR MOSAIC FOR AVIATION WITHIN SESAR (*L. DONOHUE, M. SIMPSON, R. SCOVELL, M. MOTT, B. BECKMANN, N. GAUSSIAT*) 132
2.34 MESOCYCLONE DETECTION AT MÉTÉO-FRANCE (*CLOTILDE AUGROS, JEAN IMBERT, NICOLAS GAUSSIAT, MICKAEL KREITZ, TONY LE BASTARD, MAUD MARTET*) . . 133
2.35 MESOSCALE FACTORS IMPACTING STORM INITIATION OVER THE TORINO METROPOLITAN AREA, ITALY (*ENRICO SOLAZZO, ROBERTO CREMONINI, RENZO BECHINI, CLAUDIO CASSARDO, ALESSANDRO PEZZOLI*) 135
2.36 RADAR CHARACTERISTICS OF DEEP CONVECTION OCCURRED IN THE LAST DECADE ON THE TERRITORY OF SERBIA (*MAJA RABRENOVIC*) 136
2.37 USING A FOUR-DIMENSIONAL VARIATIONAL RADAR AND SURFACE DATA ASSIMILATION SYSTEM TO INVESTIGATE THE PROCESS LEADING TO A HEAVY PRECIPITATING EVENT OVER COMPLEX TERRAIN: A CASE STUDY IN NORTHERN TAIWAN (*Y.-J. WU, Y.-C. LIOU, S.-L. TAI, J. SUN*) 137
2.38 EXTREME RAINFALL ANALYSIS AND ESTIMATION OF INTENSITY-DURATION-FREQUENCY CURVES USING DUAL POLARIZATION WEATHER RADAR DATA OF ESTONIA AND ITALY (*T. VOORMANSIK, R. CREMONINI, D. MOISSEEV, P. POST*) 138

Session 3. Radar networking **140**

Keynote presentation 141

3.1 A RENDEZVOUS OF RESEARCH AND OPERATIONS THE NEW SWISS RADAR GENERATION (*U. GERMANN, M. GABELLA, H. BARRAS[1], Y. BARTON[1], N. BESIC[1], M. BOSCACCI, L. CLEMENTI, J. FIGUERAS, L. FORESTI, J. GRAZIOLI, U. HAMANN, A. HERING, D. NERINI[1], L. NISI, L. PANZIERA, M. SARTORI, I. SIDERIS, S. TREFALT[1], F. VAN DEN HEUVEL[1], B. CALPINI*) 141

3.2 OPERA PAST, PRESENT AND FUTURE (*E.SALTIKOFF, G.HAASE, P.NOVÁK, H.LEIJNSE, L.DELOBBE*) 143

Oral presentation 145

3.3 MULTI-RADAR MULTI-SENSOR QPE SYSTEM: OVERVIEW AND FUTURE (*K. HOWARD, J. ZHANG, L. TANG[1], S. COCKS[1],S. MARTINAITIS[1], C. LANGSTON[1],K. COOPER[1], J. GOURLEY, A. ARTHUR[1]*) 145

3.4 NEW OPERATION STRATEGIES FOR NATIONWIDE WEATHER RADAR NETWORK IN KOREA (*SUNG-HWA JUNG, JONG-SEONG KIM, YOUN CHOI, SUN-KI LEE, DONG-JIN KIM, JEONG-WHAN LEE*) 146

3.5 LONG-TERM ANALYSIS OF GAUGE-ADJUSTED PAN-EUROPEAN RADAR RAINFALL ACCUMULATION (*SHINJU PARK, MARC BERENGUER, DANIEL SEMPERE-TORRES*) . 147

3.6 THE CASA DALLAS-FORT WORTH URBAN DEMONSTRATION NETWORK AFTER 5 YEARS OPERATION: ACCOMPLISHMENTS AND CHALLENGES FROM A UNIQUE PLATFORM OF COLLABORATIVE PARTNERSHIP BETWEEN LOCAL, REGIONAL AND NATIONAL ENTITIES (*V. CHANDRASEKAR, HAONAN CHEN, BRENDA PHILIPS, FRANCESC JUNYENT, ERIC LYONS, APOORVA BAJAJ*) 148

3.7 PROSPECT OF IMPLEMENTING THE ADVANCED RADAR REFRACTIVITY TECHNIQUE ON OPERATIONAL RADARS (*YA-CHIEN FENG, FREDERIC FABRY, MICAHEL M. BELL*) 150

3.8 MULTI-RADAR DATA FUSION FOR HIGH-RESOLUTION QPE IN URBAN AREA (*BRANDON HICKMAN, JUSSI TIIRA, ROBERTO CREMONINI, DMITRI MOISSEEV*) 151

3.9 CHARACTERISTIC SPATIAL EXTENSION OF RAIN EVENTS IN GERMANY FROM A RADAR BASED PRECIPITATION CLIMATOLOGY (*K. LENGFELD, M. HAFER, T.JUNGHÄNEL, E. WEIGL, T. WINTERRATH, A. BECKER*) 152

3.10 ENGAGING THE RADAR COMMUNITY THROUGH OPEN SOURCE SOFTWARE (*Z. SHERMAN, S. COLLIS, R. JACKSON*) 153

Poster presentation 154

3.11 POTENTIAL FOR USE OF RADAR DATA FOR CLIMATE MONITORING (*E.SALTIKOFF, A.BECKER, R.HOLLMANN, B.URBAN, K.FRIEDRICH, C.TASSONE*) 154

3.12 SEVERE WEATHER AND HAIL DETECTION USING THE X BAND WEATHER RADAR TUSCANY NETWORK (*A. ANTONINI, S. MELANI[1], A.ORTOLANI[1], A. TELLESCHI, A. LOMBARDI, I. GIANNINI, B.GOZZINI[1]*) 156

3.13 ENHANCING WEATHER SURVEILLANCE WITH EECS 3.5GHZ HIGH FREQUENCY DUAL-POL S-BAND WEATHER RADAR SYSTEMS (*DR. QING CAO, R. STEDRONSKY, M. KNIGHT*) 157

3.14 NETWORK OF WEATHER RADARS IN REPUBLIC OF SRPSKA, BOSNIA, HERZEGOVINA (*T. DEJANOVIC, V. VRANIC, Z. VUCINIC*) 158

3.15 IMPLEMENTATION AND OPERATIONAL USE OF A HETEROGENEOUS RADAR NETWORK IN THE COMPLEX OROGRAPHY OF ABRUZZO REGION (*E. PICCIOTTI, S. DI FABIO, M. MONTOPOLI, S. BARBIERI, R. ZAURI, A. CIPOLLONE, F.L. ROSSI, F.S. MARZANO*) . . . 159
3.16 A FIRST ANALYSIS OF THE VALLIRANA RADAR DATA QUALITY AND ITS CONTRIBUTION TO THE RADAR NETWORK OF THE METEOROLOGICAL SERVICE OF CATALONIA (XRAD) (*O. ARGEMÍ, P. ALTUBE, T. RIGO*) . . . 160
3.17 REPLACEMENT OF THE CANADIAN WEATHER RADAR NETWORK (*P.LEIBIUK, Q.LI, J.M.C.YOUNG*) . . . 161
3.18 RADAR NETWORK, PRODUCTS AND PERSPECTIVES AT DEUTSCHER WETTERDIENST (*K. HELMERT, T. HENGSTEBECK, M. MOTT, N. RATHMANN, J. STEINERT, P. TRACKSDORF, K. WAPLER, M. WERNER*) . . . 162
3.19 NETWORKS OF UHF WIND PROFILERS WITH S-BAND DOPPLER RADARS (*PARKSA KIM, BERNARD CAMPISTROM, KWANG-HO KIM, MIN-SEONG KIM, BYUNG HYUK KWON*) . . . 163
3.20 KMA DUAL-POLARIZATION RADAR NETWORK AND OBSERVATION DATA QUALITY (*BONGJAE KUK, JONGSUNG KIM, WEONIL SOHN, WOOSUK KIM, HYE-YOUNG HAN, DONG-JIN KIM, SUN-KI LEE*) . . . 164
3.21 SERVAL: A NEW CENTRALIZED PROCESSING SYSTEM FOR THE FRENCH RADAR NETWORK (*V. VOGT, N. GAUSSIAT, M. MARTET, S. CHAUMONT, J. MILLET, I. PFAFFENZELLER, B. FARDON*) . . . 165
3.22 FROM PULSE TO PRODUCT UPDATE OF THE DUTCH WRN (*T.MATHIJSSEN, H. BEEKHUIS*) . . . 166
3.23 HYDRO-METEOROLOGICAL OBSERVATORY OF CORDOBA, ARGENTINA (*IGNACIO-A. MONTAMAT, GIORGIO M. CARANTI, RAÚL A. COMES, ANDRÉS RODRÍGUEZ, PABLO SONNA, DENIS A. POFFO, RICARDO INGARAMO, JORGE SAFFE, AGUSTÍN MARTINA, SANTIAGO A. RODRIGUEZ GONZALEZ*) . . . 167
3.24 REAL-TIME IMPLEMENTATION OF VARIATIONAL 3-D WIND SYNTHESIS TECHNIQUE (WISSDOM) USING WEATHER RADAR NETWORK OF KMA (*KWANG-HO KIM, YU-CHIENG LIOU, HAE-LIM KIM, SUNG-HWA JUNG, SUN-KI LEE*) . . . 169

Session 4. Hydrological Studies Using Weather Radar **170**

Keynote presentation . . . 171
4.1 DESERT PRECIPITATION CHARACTERISTICS AND FLASH FLOOD RESPONSE STUDIED USING WEATHER RADAR DATA (*E. MORIN, M. ARMON, I. BELACHSEN, F. MARRA, N. PELEG, J. SMITH, Y. ENZEL*) . . . 171
Oral presentation . . . 172
4.2 TOWARD IMPROVED FLASH FLOOD WARNINGS BASED ON HIGH-RESOLUTION PRECIPITATION NOWCASTS (*J. DEMARGNE, P. JAVELLE, D. ORGANDE, J.-A. FINE, C. FOUCHIER, L. GARANDEAU*) . . . 172
4.3 A NEW MULTIPLICATIVE RANDOM CASCADE MODEL FOR DOWNSCALING INTERMITTENT RAINFALL FIELDS (*M. SCHLEISS*) . . . 174
4.4 OPERATIONAL HYDROLOGICAL MODELLING OF SMALL WATERSHED USING QPE FROM DUAL-POL RADAR IN BRAZIL (*C. BENETI, R. V. CALHEIROS, M. SORRIBAS, C. OLIVEIRA, L. CALVETTI, J. RUVIARO, R. NEUNDORF*) . . . 175

4.5 USING RADAR DATA FOR THE ANALYSIS AND DESIGN OF EXTREMAL EPISODES (*M. SCHEIBEL*) . . . 176
4.6 HOW ERRORS IN RAINGAUGE, RADAR AND MICROWAVE LINK DATA PROPAGATE THROUGH HYDROLOGICAL MODELS (*C.C. BRAUER, A. OVEREEM, H. LEIJNSE, R. UIJLENHOET*) . . . 177
4.7 FLASH FLOOD EARLY WARNINGS BASED ON RADAR: COMPARISON OF THE ERICHA FLASH FLOOD INDICATOR WITH A CONTINUOUS DISTRIBUTED HYDROLOGICAL MODEL IN THE FLASH FLOOD CASES OF AUTUMN 2014 IN LIGURIA (ITALY) (*D. SEMPERE-TORRES, C. CORRAL, M. BERENGUER, L. POLETTI, F. SILVESTRO, N. REBORA*) . . . 178
4.8 INVESTIGATING THE SENSITIVITY OF HYDROLOGICAL RESPONSE MODELLING TO CRITICAL RAINFALL AND CATCHMENT SCALES IN THE (SEMI-)URBANISED CHARLOTTE AREA (*E. CRISTIANO, M-C. TEN VELDHUIS, D. B. WRIGHT, J. A. SMITH, N. C. VAN DE GIESEN*) . . . 180
4.9 DEVELOPMENT OF A DETECTION SYSTEM OF HEAVY RAINFALL USING X-BAND PHASED-ARRAY WEATER RADAR (*K. YOSHIMI, F. MIZUTANI, N. TAKAHASHI, T. USHIO*) . . . 181

Poster presentation . . . 182

4.10 INTENSIFICATION OF CONVECTIVE RAIN CELLS AT WARMER TEMPERATURES OBSERVED FROM WEATHER RADAR OVER MEDITERRANEAN TO SEMIARID CLIMATES (*N. PELEG, F. MARRA, S. FATICHI, P. MOLNAR, E. MORIN, A. SHARMA, P. BURLANDO*) . . . 182
4.11 SPATIAL PROPERTIES OF PRECIPITATION EXTREMES USING RADAR AND PLUVIOMETERS (*GEOFF PEGRAM, ANDRAS BARDOSSY*) . . . 183
4.12 SHIPBORNE POLARIMETRIC RADAR OBSERVATION OF THE MODULATION OF THE DIURNAL VARIATION OF OROGRAPHIC PRECIPITATION ALONG THE WESTERN COAST OF SUMATRA ISLAND BY SYNOPTIC-SCALE DISTURBANCES (*B. GENG, M. KATSUMATA*) . . . 184
4.13 TOWARDS A COMMON PROCEDURE FOR THE EVALUATION OF DAMAGE-PRODUCING EVENTS (*T. EINFALT, S. HINSKEN, M. SCHEIBEL*) . . . 185
4.14 AN ANALYSIS OF X-BAND POLARIMETRIC RADAR RAINFALL OBSERVATIONS FROM VARIOUS COMPLEX TERRAIN SITES (*M. ANAGNOSTOU, D. YAGMUR, J. KALOGIROS, E. ANAGNOSTOU*) . . . 187
4.15 REGIONAL FREQUENCY ANALYSIS OF RADAR RAINFALL IN BELGIUM (*E. GOUDENHOOFDT, L. DELOBBE, P. WILLEMS*) . . . 188
4.16 OPERATIONAL HYDROLOGICAL NOWCASTING: CHAIN COMPARISON APPLIED ON MEDITERRANEAN SMALL CATCHMENTS (*M.L. POLETTI, M. BERENGUER, F. SILVESTRO, N. REBORA, C. CORRAL, D. SEMPERE-TORRES*) . . . 189
4.17 EXPLORING THE SPATIAL VARIABILITY OF EXTREME RAINFALL INTENSITIES AT RADAR SUBPIXEL SCALE USING A HIGH-RESOLUTION STOCHASTIC RAINFALL GENERATOR (*N. PELEG, F. MARRA, S. FATICHI, A. PASCHALIS, P. MOLNAR, P. BURLANDO*) . . . 190
4.18 SNOW-LEVEL ESTIMATES FROM POLARIMETRIC OPERATIONAL WEATHER RADAR MEASUREMENTS (*S. MATROSOV, D. GOTTAS, A. WHITE*) . . . 191

4.19 MEAN-FIELD-BIAS CORRECTION OF RADAR FORECASTS BY USING BACKWARD TRACKING METHOD (*W. NA, M. KANG, C. YOO*) . . . 192
4.20 METHODS AND STATISTICAL TOOLING FOR DETERMINING RAINFALL EVENTS IN RADAR DATASETS (*M. A. A. ALDERLIESTE, T. EINFALT, T. MORDELT, A. PFISTER, H. PLAGGENMARS, M. SCHEIBEL, A. TREIS*) . . . 193
4.21 SPATIAL RESOLUTIONS IN AREAL RAINFALL ESTIMATION AND THEIR IMPACT ON HYDROLOGICAL SIMULATIONS OF A LOWLAND CATCHMENT (*W. TERINK, H. LEIJNSE, G.A.P.H. VAN DEN EERTWEGH, R. UIJLENHOET*) . . . 195
4.22 SPATIAL AND TEMPORAL AUTOCORRELATION STRUCTURE OF CONVECTIVE RAINFALL IN SEMIARID-ARID CLIMATE: IMPLICATIONS FOR REMOTE SENSING ESTIMATION (*F. MARRA, E. MORIN*) . . . 197
4.23 HYDROLOGICAL APPLICATION OF RADAR RAINFALL NOWCASTING IN THE NETHERLANDS (*D. HEUVELINK, C.C. BRAUER, M. BERENGUER, D. SEMPERE, R. UIJLENHOET*) . . . 198
4.24 RAINFREQ: RAINFALL FREQUENCY ANALYSIS FROM REMOTE SENSING RAINFALL ESTIMATES (*F. MARRA, N. PELEG, E.I. ANAGNOSTOU, E. MORIN*) . . . 199
4.25 AN APPROACH FOR CLASSIFICATION OF HYDROMETEORS BY K-MEANS CLUSTERING (*O. GOKDERE*) . . . 200
4.26 OPTIMIZATION OF RAIN GAUGE SAMPLING DENSITY FOR DISCHARGE PREDICTION USING BAYESIAN CALIBRATION (*ALEXANDRE M.J-C. WADOUX, REMKO UIJLENHOET, SYTZE DE BRUIN, GERARD B.M. HEUVELINK*) . . . 201

Session 5. Use of Weather Radar Data in NWP Models 202

Keynote presentation . . . 203
5.1 A MOMENT-BASED POLARIMETRIC RADAR FORWARD OPERATOR FOR RAIN MICROPHYSICS (*M. R. KUMJIAN, C. P. MARTINKUS, O. P. PRAT, S. COLLIS, H. C. MORRISON, M. VAN LIER-WALQUI*) . . . 203
Oral presentation . . . 204
5.2 ASSIMILATION OF AIRBORNE DOPPLER W-BAND RADAR DATA IN THE KILOMETRE-SCALE NWP MODEL AROME (*M. BORDERIES, O. CAUMONT, J. DELANOË, V. DUCROCQ*) . . . 204
5.3 ASSIMILATION OF WEATHER RADAR DATA FOR THE SIMULATION OF A HEAVY RAINFALL CASE IN CENTRAL ITALY: A COMPARISON BETWEEN 3D-VAR AND 4D-VAR TECHNIQUES (*VINCENZO MAZZARELLA, IDA MAIELLO, VINCENZO CAPOZZI, GIORGIO BUDILLON, ROSSELLA FERRETTI*) . . . 206
5.4 CONTINENTAL-SCALE WEATHER RADAR DATA ASSIMILATION USING NORTH AMERICAN DATA (*D. MICHELSON, D. JACQUES, B. HANSEN, J-F. CARON, L. FILLION*) . . . 208
5.5 X-NET BASED RADAR DATA ASSIMILATION STUDY OVER SEOUL METROPOLITAN AREA (*K.-H. MIN, Y. LEE, G. LEE, Y. KIM*) . . . 209
5.6 DATA ASSIMILATION OF RADAR REFLECTIVITY VOLUMES IN A LETKF SCHEME (*V. POLI, T. GASTALDO, C. MARSIGLI, P.P. ALBERONI, T. PACCAGNELLA*) . . . 210
5.7 RADAR DATA ASSIMILATION AT GERMAN METEOROLOGICAL SERVICE OPERATIONAL APPLICATIONS AND PRE-OPERATIONAL RESEACH (*K. STEPHAN, U. BLAHAK, E. BAUERNSCHUBERT, A. DE LOZAR, A. SEIFERT, C. WELZBACHER*) . . . 211

5.8 USING WEATHER RADAR OBSERVATIONS FOR DATA ASSIMILATION TO MODEL THE AMSTERDAM URBAN CLIMATE (*SYTSE KOOPMANS, RONALD VAN HAREN, GERT-JAN STEENEVELD, NATALIE THEEUWES, REINDER RONDA, REMKO UIJLENHOET, ALBERT A.M. HOLTSLAG*) 212

5.9 ASSIMILATION OF DIFFERENT RADAR DATA FOR A BETTER FORECASTING OF SEVERE WEATHER PHENOMENA (*L. ROVAI, A. ANTONINI, S. MELANI, V. CAPECCHI, R. BENEDETTI, L. FIBBI, B.GOZZINI, G. MESSERI, A.ORTOLANI F.PASI*) . . 214

Poster presentation 215

5.10 INFORMATION SPARSENESS, A KEY OBSTACLE TO RADAR DATA ASSIMILATION IN CONVECTION (*F. FABRY*) 215

5.11 QUALITY CONTROL OF SEA CLUTTER AND CONSTANT POWER FUNCTION ARTIFACTS FOR OPERATIONAL U.S. NAVY SHIPBOARD RADAR DATA ASSIMILATION (*PAUL R. HARASTI*) 216

5.12 IF INSECTS ARE THE PASSIVE TRACERS WE WANT THEM TO BE TO ESTIMATE WINDS, WHY ARE THEY GENERALLY ALIGNED? (*F. FABRY, V. MEUNIER, R. KRISHNAMOORTHY, A. KILAMBI*) 218

5.13 A HYDROMETEORLOGICAL ANALYSIS OF AN EXTREME FLASH FLOOD EVENT IN THE URBAN AREA OF WEST ATTICA, GREECE (*M. ANAGNOSTOU, VARLAS G., J. KALOGIROS, P. KATSAFADOS, A. PAPADOPOULOS, E. BALTAS, E. ANAGNOSTOU*) 219

5.14 REAL-TIME RADAR DATA QUALITY FOR DATA ASSIMILATION (*S. ELLIS, D. ALBO, J. SUN, T. WECKWERTH, J. HUBBERT*) 220

5.15 ASSIMILATION OF ZDR COLUMNS FOR IMPROVING THE SPINUP AND FORECAST OF CONVECTIVE STORMS IN STORM-SCALE MODELS (*J. CARLIN, J. GAO, J. SNYDER, A. RYZHKOV*) 221

5.16 ENSEMBLE KALMAN FILTER ASSIMILATION OF SIMULATED POLARIMETRIC RADAR DATA FOR A TWO-MOMENT BULK MICROPHYSICS SCHEME: OSS EXPERIMENTS (*KEFENG ZHU, MING XUE, KUN ZHAO*) 222

5.17 IMPACT OF THE ASSIMILATION OF THE DUAL-POLARIZATION DOPPLER RADAR DATA FOR A CONVECTION SYSTEM USING THE 4DVAR ALGORITHM ON QUANTITATIVE PRECIPITATION NOWCASTING (*SHAO-FAN CHANG, YU-CHIENG LIOU, WEI-YU CHANG, JUANZHEN SUN*) 223

5.18 QUANTIFYING ERRORS ASSOCIATED WITH POLARIMETRIC RADAR FORWARD OPERATORS (*JEFFREY C. SNYDER, ALEXANDER RYZHKOV, ALEXANDER KHAIN*) 224

5.19THE IMPORTANCE OF ASSIMILATING THERMODYNAMIC FIELDS WITH RADAR OBSERVATIONS IN CONVECTIVE-SCALE WEATHER SYSTEMS (*CHING-YIN KE, KAO-SHEN CHUNG*) 225

5.20 COMPARISON OF EXTREME PRECIPITATION EVENTS SIMULATED BY THE NWP MODEL COSMO WITH ADJUSTED WEATHER RADAR DATA IN A HIGH TEMPORAL RESOLUTION (*V. BLIŽŇÁK, P. ZACHAROV, M. KAŠPAR, M. MÜLLER*) 226

5.21 SOLAR ENERGY PERSPECTIVE ON THE DATA ASSIMILATION OF RADAR REFLECTIVITY IN A LIMITED AREA NWP MODEL (*TUULI PERTTULA, SAMI NIEMELÄ, ANDERS LINDFORS, ELENA SALTIKOFF*) 227

5.22 EVALUATION OF HEAVY RAINFALL EVENTS IN THE PERUVIAN ANDES USING WRF MODEL AND WEATHER RADAR (*Y. SAAVEDRA, Y. SILVA, A. MOYA*) 229

Session 6. Radar calibration and monitoring **230**

Keynote presentation . . . 231

6.1 MODELING DIFFERENTIAL REFLECTIVITY BIAS DUE TO ANTENNA TOPOLOGY AND OPERATING FREQUENCY (*J. HUBBERT, C. CAPPELLIN, U. ROMATSCHKE, R. JØRGENSEN, M. DIXON*) . . . 231

Oral presentation . . . 232

6.2 MONITORING OF THE NEXRAD NETWORK USING SOLAR SIGNALS (*I. HOLLEMAN, A. HUUSKONEN*) . . . 232

6.3 MONITORING DOPPLER DUAL-POLARIZATION RADAR USING AN INDIVIDUAL AND SINGULAR GROUND CLUTTER CELL (*M. GABELLA, F. VAN DEN HEUVEL*) . . . 233

6.4 OPERATIONAL SOLAR MONITORING FOR IMPROVING THE HOMOGENEITY OF THE EUROPEAN RADAR NETWORK (*A.HUUSKONEN, G. HAASE, D. MICHELSON, H. LEIJNSE, I. HOLLEMAN, M. PROBERT, R. GILL, M. FRECH, M. KURRI, H. HOHTI*) . . . 234

6.5 THE STATISTICAL DISTRIBUTION OF ZDR IN DRY SNOW, WITH IMPLICATIONS FOR ZDR CALIBRATION (*M.J. DIXON, J.C. HUBBERT, G. MEYMARIS*) . . . 235

6.6 ASSESSING ZDR VARIABILTY USING DEDICATED SOLAR BOX SCANS AND OPERATIONAL ZDR MONITORING RESULTS (*MICHAEL FRECH, J.C. HUBBERT*) . . . 236

6.7 WEATHER RADARS AND RADIO FREQUENCY INTERFERENCES (*M. VACCARONO, V. CHANDRASEKAR, R. BECHINI, R. CREMONINI*) . . . 237

6.8 THE OPERATIONAL REALITY OF WEATHER RADARS WORLDWIDE A TRAVEL REPORT (*H. AL SAKKA, J. DIDSZUN, A. WEIPERT*) . . . 239

6.9 WIND TURBINES SEEN IN RADAR DATA WITH THE BIG DIFFERENCE METHOD (*WILLI SCHMID, STEFAN MÜLLER*) . . . 240

6.10 ENHANCING THE CONSISTENCY OF SPACEBORNE AND GROUND-BASED RADAR COMPARISONS BY USING QUALITY FILTERS (*I. CRISOLOGO, R. WARREN, K. MÜHLBAUER, M. HEISTERMANN*) . . . 241

6.11 IMPACT OF A WET RADOME ON A DUAL-POLARIZED S-BAND WEATHER RADAR PERFORMANCE (*Alessio Mancini, Jorge L. Salazar*) . . . 242

6.12 UAV-AIDED WEATHER RADAR CALIBRATION (*J.YIN, F.VAN DER ZWAN, E.OUDEJANS, P.HOOGEBOOM, C.UNAL, H.RUSSCHENBERG*) . . . 243

6.13 CENTER FOR CLOUD REMOTE SENSING: DOPPLER CLOUD RADAR CALIBRATION CAMPAIGN (*F. TOLEDO, J. YIN, J. DELANOË, J-C. DUPONT, M. HAEFFELIN, H. RUSSCHENBERG*) . . . 244

Poster presentation . . . 246

6.14 COMBINING WEATHER RADAR SYSTEMS TO IMPROVE REAL TIME RAINFALL ESTIMATION FOR URBAN FLOOD MONITORING AND PREDICTION (*GEOFF AUSTIN, LUKE SUTHERLAND-STACEY, JOHN NICOL, ANDREW COFFIN, KEN WILLIAMS*) . 246

6.15 EVOLUTION OF THE CONFIGURATION OF THE LIGHTNING PROTECTION SYSTEM OF THE KAPILDUI WEATHER RADAR INSTALLATION (*M. MARURI, J.A. ARANDA*) . . . 248

6.16 MONITORING THE ONGOING UPGRADE OF THE SWEDISH WEATHER RADAR NETWORK (*D. DUFTON, G. HAASE, D. JOHNSON, G. VULPIANI*) . . . 249

6.17 ON THE CAPABILITIES OF THE GPM CORE OBSERVATORY OVER GREAT BRITAIN AND IRELAND (*D. WATTERS, A. BATTAGLIA, K. MROZ, F. TRIDON*) . . . 251

6.18 EVALUATION OF REFLECTIVITY/POLARIMETRY/RADIOMETRY-BASED C-BAND ATTENUATION CORRECTION SCHEME USING NEIGHBOURING RADARS (*N. HUSNOO, T. DARLINGTON, R. THOMPSON, A. ILLINGWORTH*) . . . 252
6.19DIRECT COMPARISONS OF POLARIMETRIC C-BAND AND S-BAND MOMENTS IN SNOW (*B.M. TAYLOR*) . . . 253
6.20 CALIBRATION OF RADAR REFLECTIVITY AND DIFFERENTIAL REFLECTIVITY FOR OPERATIONAL DUAL-POLARIZATION WEATHER RADAR NETWORK (*JEONG-EUN LEE, HAE-LIM KIM, SUNG-HWA JUNG, SUN-KI LEE*) . . . 254
6.21 STANDARD OPERATION PROCEDURES (SOP) FOR WEATHER RADARS OPERATION, MONITORING, MAINTENANCE AND CALIBRATION (*L. LIMAN, T.POSIO, M.KURRI*) 255
6.22 CALIBRATION OF THE NCAR AIRBORNE W-BAND RADAR USING OCEAN SURFACE BACKSCATTERING DATA (*U. ROMATSCHKE, J. VIVEKANANDAN, R. RILLING, P.-S. TSAI, S. M. ELLIS*) . . . 256
6.23 MONITORING OF CALIBRATION HOMOGENITY OF HUNGARIAN WEATHER RADAR NETWORK (*MARIANNA HADVÁRI, PETER NEMETH, ROLAND STEIB*) . . . 257
6.24 RADOME EFFECTS ON THE POLARIMETRIC VARIABLES OF A MOBILE X-BAND RADAR (*J. FIGUERAS I VENTURA, Z. SCHAUWECKER, E. SULMONI, J. GRAZIOLI*) . . . 258
6.25 OPERATIONAL MONITORING OF TR-LIMITER DEGRADATION BASED ON CLOSE RANGE GROUND CLUTTER (*T.MATHIJSSEN, S. BROERE, H. BEEKHUIS, H. LEIJNSE*) . . . 259
6.26 IMPROVED COLLOCATION TECHNIQUES BETWEEN RADAR AND AIRCRAFT (*F.LUMB, R.NEELY, A.BLYTH, G.NOTT, A.WELLPOTT, C.WALDEN, J.CROSIER, C.WESTBROOK, S.ABEL, S.BEST, J.DORSEY, M.FORTESCUE, D. HARRISON, D.LADD, S.O'SHEA, C.REED*) . . . 260
6.27 OPERATIVE CORRECTION OF DUAL-PRF VELOCITY OUTLIERS (*P. ALTUBE, T. RIGO, O. ARGEMÍ, N. PINEDA, J. BECH, S. COLLIS, J. HELMUS*) . . . 261

Session 7. Synergetic Use of Weather Radars and Other Sensors 262

Keynote presentation . . . 263
7.1 WEATHER RADAR AND SUPERCONDUCTING GRAVIMETER FOR ESTIMATING HEAVY RAINFALL (*L. DELOBBE, S. WILFERT, A. WATLET, M. VAN CAMP*) . . . 263
Oral presentation . . . 264
7.2 OBSERVATIONS OF THE ATMOSPHERIC BOUNDARY LAYER FROM A VERTICALLY POINTING, S-BAND, FMCW RADAR IN NORTHERN ALABAMA, U.S.A. DURING VORTEX-SOUTHEAST (2016-2017) (*R. TANAMACHI, S. J. FRASIER, J. WALDINGER, A. T. LAFLEUR, F. ROCADENBOSCH*) . . . 264
7.3 REAL-TIME RAINFALL FROM A COUNTRY-WIDE NETWORK OF COMMERCIAL MICROWAVE LINKS IN GERMANY (*C. CHWALA, G. SMIATEK, H. KUNSTMANN*) . . . 265
7.4 WHEN IS RADAR DATA CALIBRATION BY IN-SITU NETWORKS MISLEADING? (*I.TCHIGUIRINSKAIA, A. ICHIBA, I. PAZ, E. SKOURI-PLAKALI, A. GIRES, D. SCHERTZER*) . . . 266
7.5 RAIN-RATE ESTIMATION FROM CEILOMETER MEASUREMENTS: A COMPARATIVE CASE STUDY USING S-BAND RADAR AND DISDROMETER RETRIEVALS (*RUBEN-BARRAGAN, FRANCESC ROCADENBOSCH, JOSEPH WALDINGER, STEPHEN J. FRASIER, DAVID D. TURNER, ROBIN TANAMACHI, DANIEL DAWSON*) . . . 267

7.6 REAL TIME DETECTION OF LIGHTNING ACTIVITY USING A LOW-COST AND PORTABLE X-BAND RADAR AND A CLUSTER ANALYSIS APPROACH (*V. CAPOZZI, M. MONTOPOLI, V. MAZZARELLA, A.C. MARRA, N. ROBERTO, G. PANEGROSSI, S. DIETRICH, G. BUDILLON*) . . . 269
7.7 EVALUATION OF MULTIPLE DOPPLER RETRIEVALS OF CONVECTION IN DARWIN (*R. JACKSON, S. COLLIS, P. KOLLIAS, M. OUE, S. ENDO, A. VOGELMANN, W. LIN, T. LANG, C. POTVIN*) . . . 270

Poster presentation . . . 271

7.8 STRUCTURAL CHARACTERISTICS OF PRECIPITATING CLOUDS MEASURED BY TRMM PR AND IGRA (*Y. FU, R. WANG, J. XIA, L. SUN, M. WANG*) . . . 271
7.9 ASSESSMENT OF PROPAGATION EFFECTS AND RADAR DATA QUALITY WITH A DUAL-POL TARGET SIMULATOR DURING THE OLYMPIC WINTER GAMES (*M. SCHNEEBELI, A. LEUENBERGER, J. GEHRING, G. LEE, K.D. AHN, F. TAPIADOR, A. BERNE*) . . . 272
7.10 HAIL EVENT ANALYSIS AND DAMAGE ASSESSMENT BASED ON MULTI-DATA APPROACH (*S.TANI, H.PAULITSCH, B.SÜSSER-RECHBERGER, R. TESCHL*) . . . 273
7.11 STUDIES OF THE MELTING LAYER OF PRECIPITATIVE SYSTEMS USING X-BAND DUAL POLARIZATION WEATHER RADAR AND SMARTLNB NETWORK (*S. MELANI, A. ANTONINI, A.ORTOLANI, L. BALDINI,, E. ADIROSI,, L. FACHERIS,, F. GIANNETTI, A. PETROLINO*) . . . 274
7.12 INTRA- AND INTER-EVENT VARIABILITY OF DROP SIZE DISTRIBUTION IN MEDITERRANEAN REGIONS (*B. BOUDEVILLAIN, S. HACHANI, G. DELRIEU, Z. BARGAOUI*) . . . 276
7.13 PRODUCING CONVECTION DAILY MAPS BASED ON OPERA COMPOSITE AND EUCLID LIGHTNING DATA (*D. R. POELMAN, L. DELOBBE*) . . . 277
7.14 RESULTS OF THE MONITORING TASKS AND CO-CREATION ACTIVITIES OF THE PRECIPITATION PRODUCTS OF KAPILDUI WEATHER RADAR (*M. MARURI, S. GAZTELUMENDI, K. OTXOA DE ALDA, R. HERNANDEZ, C. STOCKER J. SALAZAR, I. EGUIARA, J.A. ARANDA*) . . . 278
7.15 SYNERGY OF GPM AND GROUND-BASED RADAR OBSERVATIONS FOR PRECIPITATION ESTIMATION AND DETECTION OF MICROPHYSICAL PROCESSES (*V. PEJCIC, S. TRÖMEL , K. MÜHLBAUER, P. SAAVEDRA , J. BEER , C. SIMMER*) . . . 279
7.16 NOWCASTING OF THUNDERSTORM AND HAIL EVENTS USING GROUND BASED REMOTE SENSING DATA (*T. BÖEHME, C. HEROLD, A. LEYSER, T. HENGSTEBECK*) . . . 280
7.17 WEATHER RADAR DATA DRIVEN NEAR-GROUND PRECIPITATION TYPE ESTIMATION AT DEUTSCHER WETTERDIENST (*J. STEINERT*) . . . 281
7.18 X-BAND RADAR PARMETERS FROM PARSIVEL2 DATA USING PYDSD (*E. SULMONI, J. FIGUERAS I VENTURA, J. GRAZIOLI*) . . . 282
7.19 ARM AERIAL FACILITY AND RADAR CLOUD OBSERVATIONS FROM THE ACE-ENA FIELD CAMPAIGN (*A. MATTHEWS, J. HARDIN, B. ISOM, F. MEI, L. GOLDBERGER, S. GIANGRANDE, R. WOOD, N. BHARADWAJ*) . . . 283
7.20 ON THE USE OF COMMERCIAL MICROWAVE LINKS FOR RAINFALL ESTIMATION IN SEMI-ARID AREAS (*R. RAICH, P. ALPERT, H. MESSER*) . . . 284

7.21 PERFORMANCES OF GROUND RADAR AND INFRARED SATELLITE NEW COMBINED ALGORITHM FOR THE ITALIAN PENINSULA (*LEO PIO DADDERIO, GIANFRANCO VULPIANI, SILVIA PUCA, GIULIA PANEGROSSI, PAOLO SANO', ANNA CINZIA MARRA, STEFANO DIETRICH*) 285
7.22 RAINFALL MAPS FROM COMMERCIAL MICROWAVE LINKS (CMLS) AND URBAN FLOOD PREDICTION: PILOT TESTS IN SEVERAL AFRICAN CITIES (*M. ALCOBA, M. GOSSET, F. CAZENAVE, N. CHAHINIAN, C. BOUVIER, M. TURKO, A. YAPI*) 286
7.23 A COMPARISON OF TOTAL LIGHTNING REFLECTIVITY PROXIES AND WEATHER RADAR DATA IN SOUTHERN BRAZIL FOR HIGH IMPACT WEATHER MONITORING AND NOWCASTING (*W. F. COELHO, L. CALVETTI, C. BENETI, N. A. ROZIN*) . . . 287
7.24 MULTISOURCE DATA VERIFICATION OF A WEATHER RADAR SURFACE PRECIPITATION TYPE PRODUCT (*E. CASELLAS', J. BECH, R. VECIANA, N. PINEDA, T. RIGO, J. MORÉ*) 288

Session 8. New and Emerging Radar Technologies 290

Keynote presentation 291
8.1 POLARIMETRIC VARIABLES ON THE PLANAR PHASED ARRAY RADAR: APPROXIMATE COMPUTATIONS (*D. ZRNIC*) 291
Oral presentation 292
8.2 OSAKA URBAN PHASED ARRAY RADAR NETWORK EXPERIMENT (*TOMOO USHIO', H. KIKUCHI, T. MEGA, F. MIZUTANI, M. WADA, N. TAKAHASHI, S. SATOH*) 292
8.3 THE ADVANCED TECHNOLOGY DEMONSTRATOR AT THE NATIONAL SEVERE STORMS LABORATORY (*S. TORRES', K. HONDL*) 293
8.4 DIFFERENTIAL PHASE UPON TRANSMISSION AS A NEW RADAR PARAMETER (*VALERY-MELNIKOV*) 294
8.5 AN ALL-DIGITAL POLARIMETRIC PHASED ARRAY RADAR FOR COMBINED WEATHER AND AIRCRAFT SURVEILLANCE (*ROBERT PALMER', CALEB FULTON', JORGE SALAZAR', HJALTI SIGMARSSON', MARK YEARY'*) 295
8.6 WEATHER OBSERVATIONS WITH A PHASED ARRAY RADAR (*L. BOROWSKA, D. ZRNIC, Y. ZHANG, G. ZHANG*) 297
8.7 X-BAND PHASED-ARRAY POLARIMETRIC RADAR TESTBED: STATUS AND INITIAL RESULTS (*S. J. FRASIER, W. HEBERLING, C. WOLSIEFFER, M. ADAM*) 298
8.8 BISTATIC SCATTERING FROM BRAGG TURBULENCE AT X-BAND: A POTENTIAL MECHANISM FOR CLEAR AIR SENSING USING CASA-TYPE RADAR NETWORKS (*DAVID J.-MCLAUGHLIN*) 299
8.9 THE CITY OF SÃO PAULO (BRAZIL) AS A TESTBED OF RAINFALL ESTIMATES FROM COMMERCIAL MICROWAVE LINK NETWORKS (*M.F. RIOS GAONA, A. OVEREEM', H. LEIJNSE, T. RAUPACH, R. UIJLENHOET*) 300
Poster presentation 301
8.10 NEW C-BAND, 1-DEGREE, DUAL-FREQUENCY, DUAL-POLARIZATION, FAST-SCANNING 2X 1MW, MOBILE RADAR (*JOSHUA WURMAN, KAREN KOSIBA*) 301
8.11 THE CSU SEA-POL SHIP-BOARD RADAR: SALIENT FEATURES AND FIRST RESULTS (*J. GEORGE, V. CHANDRASEKAR, S. RUTLEDGE (F. JUNYENT, P. KENNEDY)*) . . 302
8.12 ON THE USE OF HORN ANTENNA TO CALIBRATE THE MPAR ADVANCED TECHNOLOGY DEMONSTRATOR (*IGOR R. IVIĆ'*) 303

8.13 THE LIDAR RADAR OPEN SOFTWARE ENVIRONMENT (LROSE) "BLAZE" RELEASE (*MICHAEL M. BELL, MICHAEL J. DIXON, WEN-CHAU LEE*) 304
8.14 VERTICAL WIND PROFILE MEASUREMENTS ON THE OPERATIONAL WEATHER RADAR IN "WIND PROFILER" MODE (*Yu.B. PAVLYUKOV, A.V. TRAVOV, N.A. EROSHKINA*) 305
8.15 USING THE SPARC SIMULATOR TO REFINE AND JUSTIFY SENSR WEATHER SURVEILLANCE REQUIREMENTS (*F. NAI, C. CURTIS, F. NAI, D. SCHVARTZMAN, J. BOETTCHER, S. TORRES*) 306
8.16 CHARACTERIZATION OF WIND TURBINE CLUTTER ON THE RADAR NETWORK AT THE SOUTHERN GREAT PLAINS ARM SITE (*B. ISOM, I. LINDENMAIER1*) 307
8.17 THE GAMIC WAVE SENSING RADAR AND THE GD-APS FUTUREWAVES WAVE AND VESSEL MOTION FORECASTING SYSTEM (*S. GERHARDS, J. KUSTERS, J. MERTENS, M. TOUSSAINT, D. VEERKAMP*) 308
8.18 PROGRESS IN THE PROGRAM FOR EARLY DETECTION OF TORRENTIAL RAINFALL BY USING MULTI-PARAMETER PHASED ARRAY WEATHER RADAR IN JAPAN (*N. TAKAHASHI, K. IWANAMI, M. KAWASAKI*) 309
8.19 A SYSTEM FOR SYNCHRONIZED MULTI-RADAR SCANNING FOR METEOROLOGICAL REMOTE SENSING (*C. J. WALDEN, M. FORTESCUE, M. L. TRETHEWEY, D. N. LADD, A. DOO*) 310
8.20 CALIBRATION OF THE POLARIMETRIC PHASED ARRAY WEATHER RADAR USING THE COMPUTATIONAL ELECTROMAGNETICS APROACH THE DIFFERNTIAL PHASE (*DJORDJE MIRKOVIC, D.S. ZRNIC*) 311
8.21 ARE SENSRS TEMPORAL RESOLUTION REQUIREMENTS FOR THE WEATHER FUNCTION FEASIBLE USING ADAPTIVE SCANNING? (*D. SCHVARTZMAN, S. TORRES*) 312
8.22 WATER VAPOR ESTIMATION USING REFLECTED WAVE OF DIGITAL TERRESTRIAL BROADCASTING WAVE (*T. KOUKETSU, S. KAWAMURA, H. HANADO, H. OHTA*) . . 313

Session 9. Nowcasting and Blending Techniques **314**

Keynote presentation 315
9.1 STATISTICAL LEARNING OF OROGRAPHIC PRECIPITATION GROWTH AND DECAY PATTERNS FROM A 10-YEAR RADAR ARCHIVE IN THE SWISS ALPS (*L. FORESTI, I.V. SIDERIS, L. BEUSCH, D. NERINI, U. GERMANN*) 315
Oral presentation 316
9.2 THE NOWCASTING POTENTIAL OF LIGHTNING-JUMPS IN CONVECTIVE CELLS TRACKED BY RADAR IN COMPLEX OROGRAPHY (*ALESSANDRO HERING, LUCA NISI, ULRICH HAMANN, URS GERMANN*) 316
9.3 NOWPRECIP: AN ALGORITHM FOR LOCALIZED PROBABILISTIC PRECIPITATION NOWCASTING IN THE COMPLEX TERRAIN OF SWITZERLAND (*I.V. SIDERIS, L. FORESTI, U. GERMANN, D. NERINI*) 318
9.4 DERIVING AND COMPOSITING MOTION FIELDS SPEED AND QUALITY CHALLENGES (*M. PEURA, H. HOHTI, T. PERTTULA*) 319
9.5 LOCALIZED VARIATIONAL BLENDING FROM INCA AND AROME-RUC (*A. ATENCIA, A. KANN, Y. WANG, F. MEIER*) 320
9.6 IMPROVED RAINFALL NOWCASTING BY NON-STATIONARY MOTION VECTOR FROM BURGERS EQUATION (*GYUWON LEE, SOOROK RYU, GEUNSU LYU, HONG-MOK PARK*) 321

9.7 FROM QUALITATIVE TO QUANTITATIVE HAIL NOWCASTING (*A. BELL, E. MORGAN, A.SEED, M.CURTIS, R.BUNN*) . . . 322
9.8 A BAYESIAN COMBINATION OF RADAR-BASED NOWCASTS WITH COSMO-E PRECIPITATION FORECASTS (*D. NERINI, U. GERMANN, L. FORESTI*) . . . 323
9.9 BLENDING FIELD-BASED AND CELL TRACKING METHODS FOR IMPROVED PRECIPITATION NOWCASTING (*S. PULKKINEN, V. CHANDRASEKAR*) . . . 324

Poster presentation . . . 325

9.10 USING WEATHER RADAR AND A NEW ICE MASS ESTIMATOR TO FORECAST LIGHTNING (*EVAN RUZANSKI, V. CHANDRASEKAR*) . . . 325
9.11 OPTICAL FLOW MODELS BENCHMARKING FOR RADAR-BASED PRECIPITATION NOWCASTING (*G. AYZEL, M. HEISTERMANN, T. WINTERRATH*) . . . 326
9.12 RADAR RAINFALL COMPOSITING: COMPARISON OF DIFFERENT METHODS (*A. JURCZYK, J. SZTURC, K. OŚRÓDKA*) . . . 328
9.13 STOCHASTIC ENSEMBLE PRECIPITATION NOWCASTING IN WINTER CONDITIONS (*S. PULKKINEN, E. SALTIKOFF, P. KARSISTO, A. VON LERBER*) . . . 329
9.14 DEVELOPMENT OF A NEW SEAMLESS PREDICTION SYSTEM FOR VERY SHORT RANGE CONVECTIVE-SCALE FORECASTING AT DEUTSCHER WETTERDIENST (*ULRICH BLAHAK, KATHRIN WAPLER, MARCUS PAULAT, ROLAND POTTHAST, AXEL SEIFERT, LISELOTTE BACH, ELISABETH BAUERNSCHUBERT, ROBERT FEGER, KATHRIN FEIGE, MICHAEL HOFF, MARKUS JUNK, ALBERTO DE LOZAR, LISA NEEF, RAFAEL POSADA, MARTIN REMPEL, MARKUS SCHULTZE, CHRISTIAN WELZBACHER, MANUEL WERNER*) . . . 330
9.15 OPTICAL FLOW BASED NOWCASTING AT DWD (*M. WERNER*) . . . 331
9.16 DEVELOPMENT OF A PROBABILISTIC PRECIPITATION-NOWCASTING APPROACH (*M. SCHULTZE, R. FEGER, R. POSADA, M. REMPEL, M. WERNER, K. WAPLER, U. BLAHAK*) . . . 332
9.17 RADAR NETWORK-BASED MESOCYCLONE DETECTION (*T. HENGSTEBECK, K. WAPLER, D. HEIZENREDER, P. JOE*) . . . 334
9.18 BLENDING HIGH-FREQUENCY NWP PRECIPITATION FORECASTS IN AN ENSEMBLE NOWCASTING SYSTEM: STEPS-ALARO (*L. DE CRUZ, M. REYNIERS, L. DELOBBE, L. FORESTI*) . . . 335
9.19 EVALUATING THE ACCURACY OF OPTICAL FLOW TECHNIQUES ON NOWCASTING (*ARTHUR C. T. DE SOUZA, MAIK HEISTERMANN, GEORGY AYZEL*) . . . 336
9.20 NOWCASTING THE FREEZING RAINFALL IN THE AUTOMATED SYSTEM “METEOTRASSA” (*IGOR ZAMORIN, TATIANA BAZLOVA, NIKOLAY BOCHARNIKOV, MARK VINOGRADOV*) . . . 337
9.21 SEVERE HAIL DETECTION: HYDROMETEOR CLASSIFICATION FOR POLARIMETRIC C-BAND RADARS USING FUZZY-LOGIC AND T-MATRIX SCATTERING SIMULATIONS (*M. SCHMIDT, S. TRÖMEL, A. V. RYZHKOV, C. SIMMER*) . . . 338
9.22 A K-NN METHOD FOR NOWCASTING RAINFALL INTENSITIES AT FINE TEMPORAL AND SPATIAL SCALES (*B.SHEHU, U. HABERLANDT*) . . . 339
9.23 RADAR REFLECTIVITY ADVECTION ESTIMATION VIA PROXY CIRCLE IMAGES (*A.C.P. OUDE NIJHUIS, Y. DUFOURNET, T. OTTO, I. STEPANOV*) . . . 340
9.24 COMBINATION OF OBJECT-BASED PROBABILISTIC NOWCASTING AND OBJECT-BASED NWP ENSEMBLE (*R. POSADA, R. FEGER, M. SCHULTZE, K. WAPLER, M. WERNER*) 341

9.25 DEVELOPMENT OF TRAIN OPERATION CONTROL METHOD AGAINST GUST USING DOPPLER RADAR (*C. FUJIWARA, K. KUSUNOKI, H. INOUE, N.ISHITSU, K. ARAI, H.SUZUKI*) . . . 342

Session 10. Airborne and Spaceborne Radars **343**

Keynote presentation . . . 344

10.1 GPMS DUAL-FREQUENCY PRECIPITATION RADAR (DPR) ALGORITHM AND MEASUREMENT OF ICE PRECIPITATION (*T. IGUCHI, R. OKI, N. KAWAMOTO*) . . . 344

Oral presentation . . . 345

10.2 VERIFICATION OF CLOUDSAT INSTANTANEOUS SNOWFALL RATE RETRIEVALS WITH GROUND-BASED RADAR MEASUREMENTS (*S. MATROSOV, J. HARDIN, G. DE BOER*) . . . 345

10.3 A RADAR-BASED EVALUATION OF GPM RETRIEVALS OF THE RAIN DROP SIZE DISTRIBUTION (*WALTER A. PETERSEN, PATRICK N. GATLIN, DAVID B. WOLFF, ALI TOKAY, MIRCEA GRECU*) . . . 346

10.4 AIRBORNE IMPLEMENTATION OF PDPP TECHNIQUE ON THE NRC W-BAND RADAR (*C. NGUYEN, A. BATTAGLIA, M. WOLDE, A. PAZMANY, A. ILLINGWORTH*) . . . 348

10.5 COMPARISON OF THE GPM DPR SINGLEAND DOUBLE-FREQUENCY PRODUCTS OVER THE MEDITERRANEAN AREA (*LEO PIO D'ADDERIO, FEDERICO PORCÙ, GIULIA PANEGROSSI, PAOLO SANO', ANNA CINZIA MARRA, STEFANO DIETRICH*) . . . 349

Poster presentation . . . 350

10.6 COMPARISON OF PRECIPITATION TYPE ALGORITHMS (*A. TOKAY, B. SWICK, P. KIRSTETTER. D. MARKS, J. PIPPITT, W. A. PETERSEN, D. B. WOLFF*) . . . 350

10.7 EVALUATIONS OF RAIN MICROPHYSICS RETRIEVAL USING GPM DPR THROUGH COMPARISON WITH A SELF-CONSISTENT NUMERICAL METHOD (*E. GORGUCCI, L. BALDINI*) . . . 352

10.8 WIVERN, A PROPOSED SATELLITE TO PROVIDE GLOBAL IN-CLOUD WINDS, ICE WATER CONTENT AND RAINFALL (*A. J. ILLINGWORTH, A. BATTAGLIA*) . . . 353

10.9 A METHOD FOR ESTIMATE OF RANGE VARIATION OF ATTENUATION FROM DUAL FREQUENCY RADAR AND DUAL POLARIZATION RADAR (*TAKAHISA KOBAYASHI, SOICHIRO SUGIMOTO ,MITSUHARU NOMURA, AHORO ADACHI, NOBUHIRO NAGUMO, HIROMARU HIRAKUCHI*) . . . 354

10.10 PRELIMINARY DESIGN STUDY OF AIRBORNE PHASED ARRAY WEATHER RADAR TARGETING THE TYPHOON OBSERVATION (*N. TAKAHASHI*) . . . 355

10.11 VERIFICATION OF PRECIPITATION CHARACTERISTICS FOR WARM AND COLD SEASON USING GPM AND GROUND INSTRUMENTS IN KOREAN PENINSULA (*CHOENGLYONG LEE, GYUWON LEE, GEUNHYEOK RYU*) . . . 356

10.12 DUAL-POLARIZATION FOR CIVIL AIRCRAFT RADAR: EXPERIMENTS WITH A PROTOTYPAL SYSTEM IN THE NETHERLANDS AND IN ITALY (*L. BALDINIF. BERIZZI, A. COCCIA, F. CUCCOLI, M. D'AMICO, S. LISCHI, A. LUPIDI, F. MILANI*) . . . 357

10.13 COMPARING THE GLOBAL PRECIPITATION MEASUREMENT MISSION WITH RADAR NETWORKS (*P. KIRSTETTER, W. PETERSEN, D. FAURE, N. GAUSSIAT, D. WOLFF*) 358

Session 11. Advances in signal processing **359**

Keynote presentation . . . 360
11.1 REJUVENATING REFRACTIVITY PROCESSING TO IMPROVE RETRIEVAL QUALITY WHILE REDUCING LABOR-INTENSIVE MAINTENANCE NEEDS (*F. FABRY, D. W. HOGG, Y.-C. FENG*) . . . 360
Oral presentation . . . 361
11.2 ATMOSPHERIC BOUNDARY-LAYER HEIGHT TRACKING FROM S-BAND RADAR RETURNS WITH AN EXTENDED KALMAN FILTER: APPLICATION TO VORTEX-SE (*FRANCESC ROCADENBOSCH, ROBIN TANAMACHI, STEPHEN J. FRASIER*) . . . 361
11.3 COMPARISON OF CLUTTER DETECTION SCHEMES FOR NON-DOPPLER, NON-POLARIMETRIC X BAND RADARS (*S. MELANI, A. ANTONINI, F. CAPARRINI, A. TELLESCHI, A. LOMBARDI, A. MAZZA, A.ORTOLANI*) . . . 363
11.4 PRINCIPLE AND REAL-DATA APPLICATION RESULTS OF MMSE DOPPLER SPECTRAL PROCESSING (*EIICHI YOSHIKAWA, NAOYA TAKIZAWA, HIROSHI KIKUCHI, TOMOAKI MEGA, TOMOO USHIO*) . . . 364
11.5 FILCOH, A METHOD TO ELIMINATE GROUND ECHOES FOR WEATHER RADARS OPERATING IN MULTIPLE PRT MODE BY USING THE AVAILABLE AUTOCORRELATION COEFFICIENTS (*M. TAHANOUT, J. PARENT DU CHATELET*) . . . 365
Poster presentation . . . 366
11.6 EXTENDING DOPPLER VELOCITY COVERAGE FOR DATA ASSIMILATION (*F. FABRY, A. KILAMBI*) . . . 366
11.7 ALTERNATIVE DATA PROCESSING FOR MICRO RAIN RADAR (MRR) OBSERVATIONS (*ALBERT GARCIA-BENADÍ, JOAN BECH, SERGI GONZÁLEZ , JOAQUIN DEL RIO FERNANDEZ*) . . . 367
11.8 AUTOMATED IDENTIFICATION OF GROUND CLUTTER CONTAMINATION FOR POLARIMETRIC DOPPLER WEATHER RADARS (*DAVID A. WARDE, SEBASTIAN M. TORRES*) . . . 369
11.9 DUAL PRF PROCESSING WITHIN THE BARON PROCESSOR SUITE (*B. MRINAL, C. DARRIN, L. JAMES*) . . . 370
11.1 UNCERTAINTY QUANNTIFICATION FOR ARM CLOUD RADARS (*N. BHARADWAJ, B. ISOM*) . . . 371
11.11 DROPLET FALLING VELOCITIES, WINDSPEEDS, AND KA-BAND ATTENUATION DEDUCED FROM PPI AND RHI SCANS (*MATTHIAS RICHARD BAUER-PFUNDSTEIN*) . . . 372
11.12 SPECTRAL POLARIMETRIC FILTERS DESIGN FOR BROAD-BAND WEATHER CLUTTER MITIGATION (*J.YIN, C.UNAL, H.RUSSCHENBERG*) . . . 373
11.13 DEEP LEARNING FRAMEWORK FOR PRECIPITATION RETRIEVALS FROM COMMUNICATION SATELLITES (*AHMAD GHARANJIK, KUMAR VIJAY MISHRA, M. R. BHAVANI SHANKAR, BJÖRN OTTERSTEN*) . . . 374
11.14 A MONOTONIC ALGORITHM FOR ESTIMATION OF THE SPECIFIC DIFFERENTIAL PHASE (*NAN.YU, NICOLAS.GAUSSIAT*) . . . 375
Session 12. Millimeter wavelength radars **376**
Keynote presentation . . . 377

12.1 AN OVERVIEW OF MILLIMETER WAVE CLOUD RADAR OBSERVATIONS AT THE DOE-ARM OLIKTOK POINT SITE (*JOSEPH C. HARDIN, ROBERT A. HOUZE, MATTHEW SHUPE, SCOTT GIANGRANDE, TODD HOUCHENS, CHRIS WILLIAMS, NITIN BHARADWAJ*) . . . 377

Oral presentation . . . 378

12.2 USING TRIPLE-FREQUENCY RADAR DOPPLER SPECTRA TO CONSTRAIN SNOW PARTICLE SCATTERING MODELS (*S. KNEIFEL, PAVLOS KOLLIAS, ALESSANDRO BATTAGLIA*) . . . 378

12.3 VERTICAL AIR MOTION IN PRECIPITATING CLOUDS FROM AN AIRBORNE MILLIMETER WAVELENGTH RADAR (*E. JUNG, G.-W LEE*) . . . 379

12.4 A STUDY ON RADAR FIRST ECHOES OVER THE WESTERN GHATS WITH AN INSIGHT INTO UNDERSTANDING THE AEROSOL-CLOUD-PRECIPITATION INTERACTION AT A HIGH ALTITUDE SITE IN WESTERN GHATS (*AMBUJ KUMAR JHA, SACHIN M DESHPANDE, G PANDITHURAI*) . . . 380

12.5 HOW MUCH ATTENUATION AT W AND KA BANDS IS CAUSED BY MELTING LAYER? AN ANSWER FROM MULTI-FREQUENCY RADAR DOPPLER SPECTRA (*HAORAN LI, DMITRI MOISSEEV*) . . . 381

Poster presentation . . . 382

12.6 HOW ACCURATE IS THE DISCRETE DIPOLE APPROXIMATION FOR MODELING THE SINGLE SCATTERING PROPERTIES OF PARTIALLY MELTED SNOWFLAKES (*D. ORI, S. KNEIFEL*) . . . 382

12.7 CHARACTERISTICS OF CLOUD VERTICAL STRUCTURE DURING DIFFERENT PHASES OF INDIAN SUMMER MONSOON: CLOUD RADAR PERSPECTIVE (*SUKANYA PATRA , M.C.R KALAPUREDDY*) . . . 384

12.8 PARAMETRIZATION OF FALLING SNOW MICROPHYSICS AND ITS APPLICATION TO DUAL-FREQUENCY RADAR RETRIEVALS (*D. MOISSEEV, A. VON LERBER, J. LEINONEN, J. TYYNELÄ*) . . . 385

12.9 ARM CLOUD RADARS AT THE EASTERN NORTH ATLANTIC SITE: AN UPDATE (*B. ISOM, N. BHARADWAJ*) . . . 386

12.10 OCCURRENCE AND VERTICAL DISTRIBUTION OF CLOUDS IN KOREAN PENINSULA FROM GROUND-BASED KA-BAND CLOUD RADAR OBSERVATIONS (*BO-YOUNG YE, GYUWON LEE, SANGWON JOO*) . . . 387

Session 13. Quantitative precipitation estimation **388**

Keynote presentation . . . 389

13.1 PROBABILISTIC QUANTITATIVE PRECIPITATION ESTIMATES WITH GROUND- AND SPACE-BASED RADARS (*P. KIRSTETTER, J.J GOURLEY, J. ZHANG*) . . . 389

13.2 ANYWHERE NEAR THE SEVEN-YEAR ITCH? ON THE STATE OF WRADLIB UPON THE RELEASE OF V1.0 (*K. MÜHLBAUER M. HEISTERMANN*) . . . 390

Oral presentation . . . 391

13.3 COMMERCIAL MICROWAVE LINKS FOR RAINFALL MONITORING: A NATION-WIDE VALIDATION STUDY IN THE NETHERLANDS (*L.W. DE VOS, A. OVEREEM, H. LEIJNSE, R. UIJLENHOET*) . . . 391

13.4 HOW TO BENEFIT FROM HIGH-RESOLUTION DIGITAL ELEVATION MODELS TO SIMULATE PARTIAL BEAM BLOCKAGE? (*K. MÜHLBAUER, M. HEISTERMANN*) . . . 392

13.5 RADAR-RAINFALL ESTIMATION USING SPECIFIC ATTENUATION: IMPROVEMENTS AND CHALLENGES (*B.-C. SEO, W. F. KRAJEWSKI, A. RYZHKOV*) 393
13.6 INVESTIGATION INTO USING A NEURAL NETWORK TO SELECT BETWEEN USING FILTERED OR ALOFT MEASUREMENTS TO IMPROVE QPE IN CLUTTER CONTAMINATED REGIONS (*S. LYONS, T. DARLINGTON, S. TORRES, D. WARDE*) 394
13.7 THE DEVELOPMENT OF A CANADIAN OPERATIONAL DUAL-POLARIZATION RAINFALL ESTIMATION ALGORITHM (*S. BOODOO, D. HUDAK, N. DONALDSON, J. REID, D. MICHELSON, M. COUTURE, P. RODRIGUEZ, V. STOJANOVIC*) 395
13.8 A SIMULATION-BASED AND EXPERIMENTAL APPROACH TO INVESTIGATE THE IMPACT OF SKYSCRAPERS AND WIND TURBINE FARMS ON WEATHER RADAR DATA (*KURTULU ÖZTÜRK, ALPER ÇUBUK, OSMAN KARABAYIR, ELİF UÇURUM*) . . . 397
13.9 A DUAL-POL RADAR SYNTHETIC QPE FOR OPERATIONS (*J. ZHANG, L. TANG, S. COCKS, P. ZHANG, A. RYZHKOV, K. HOWARD*) 398
13.10 INCLUDING THE TIME DIMENSION IN RADAR-RAINGAUGE BLENDING (*MARC BERENGUER, DANIEL SEMPERE-TORRES, EDUARDO CASSIRAGA, JAIME GÓMEZ-HERNÁNDEZ*) 399
13.11 RADAR REMOTE SENSING FOR RAIN/SNOW ESTIMATION IN AN ALPINE CONTEXT: THE GRENOBLE EXPERIMENT (*G.DELRIEU, F. CAZENAVE, N. YU, D. FAURE, B. BOUDEVILLAIN, A. KHANAL, C. AUGROS, N. LE BASTARD, N. GAUSSIAT*) 400
13.12 X-BAND RADAR ATTENUATION STATISTICS: HOW OFTEN DO WE LOSE THE SIGNAL? (*H. LEIJNSE*) 401
13.13 ON THE USE OF NWP MODEL OUTPUTS TO PRODUCE RADAR VPR CORRECTIONS (*T. LE BASTARD, O. CAUMONT, N. GAUSSIAT, F. KARBOU*) 402
13.14 QUALITY-BASED RADAR DATA PROCESSING AND QPE AT THE SLOVAK HYDROMETEOROLOGICAL INSTITUTE (*L. MÉRI, M. JURAŠEK, L. OKON, J. KAŇÁK*) . . . 405
13.15 RADAR-DERIVED QUANTITATIVE PRECIPITATION ESTIMATION BASED ON VERTICAL-RAINCLOUD TRAJECTORY PROFILES (*HANGGAR G MAWANDHA, SATORU OISHI*) 406
13.16 POLARIMETRIC RADAR AND MACHINE LEARNING: FROM THE SOLID PHASE HYDROMETEOR STATISTICS TO THE PRECIPITATION INTENSITY AT THE GROUND (*Y. CHEVALLEY, N. BESIC, J. GEHRING, L. FORESTI, I.V. SIDERIS, M. GABELLA, U. GERMANN, A. BERNE*) 407
13.17 QUANTIFICATION OF MEASUREMENT ERROR OF POLARIMETRIC X-BAND RADARS IN MOUNTAINOUS REGIONS (*NAN.YU, NICOLAS.GAUSSIAT*) 408
13.18 RAINFALL RATE ESTIMATION USING HYDRO-ESTIMADOR (GOES) AND DUAL POLARIMETRIC RADAR IN A COASTAL TROPICAL BASIN OF PERU (*J. VALDIVIA, M. SAAVEDRA, D. SCIPION, Y. SILVA, J. PRADO, B. L. CHEONG*) 409
13.19 CLOUD RADAR SPECTRAL POLARIMETRY FOR QUANTITATIVE PRECIPITATION ESTIMATION (*A.MYAGKOV, T. ROSE*) 410
13.20 PRECIPITATION VARIABILITY BETWEEN AFTERNOON MIXED LAYER AND FREE ATMOSPHERE CLOUDS IN SEMI-ARID SOUTHEAST ARIZONA (*PIETER HAZENBERG, MAX MITCHELL, ERIKA CROPP, DAVE GOODRICH, ELEONORA DEMARIA, MARK KAUTZ, WALTER PETERSEN*) 411

Poster presentation 412

13.21 THE EUROPEAN CLIMATOLOGICAL HIGH-RESOLUTION GAUGE-ADJUSTED RADAR RAINFALL DATASET: (*A. OVEREEM, G. VAN DER SCHRIER, E.V. VAN DER PLAS, G. LENDERINK, H. LEIJNSE, J.F. MEIRINK, S. PARK, M. BERENGUER, D. SEMPERE-TORRES*) . . . 412
13.22 SEVERE HAIL DETECTION: HYDROMETEOR CLASSIFICATION FOR POLARIMETRIC C-BAND RADARS USING FUZZY-LOGIC AND T-MATRIX SCATTERING SIMULATIONS (*M. SCHMIDT, S. TRÖMEL, A. V. RYZHKOV, C. SIMMER*) . . . 414
13.23 PRECIPITATION MEASUREMENTS BY RADAR DURING DACCIWA (*JAN HANDWERKER, NORBERT KALTHOFF, THE KITCUBE TEAM*) . . . 415
13.24 REGIME-DEPENDENT RADAR REFLECTIVITYRAIN RATE RELATIONSHIPS AND THEIR POTENTIAL TO IMPROVE RADAR RAINFALL ESTIMATES (*B. KIRSCH, F. AMENT, M. CLEMENS*) . . . 416
13.25 SIMPLE YET ADJUSTABLE RADAR DATA VIEWER (*C.FENNIG, T.EINFALT, I.FRERK*) . . . 417
13.26 DIFFERENTIAL PHASE PROCESSING AT X-BAND FREQUENCY TO IMPROVE THE ESTIMATION OF THE SPECIFIC ATTENUATION AND BACKSCATTER DIFFERENTIAL PHASE (*R. REINOSO-RONDINEL, C. UNAL, H. RUSSCHENBERG*) . . . 419
13.27 LONG-TERM ANALYSIS OF RADAR RAINFALL MEASUREMENTS IN THE UK FOR HYDROLOGICAL APPLICATIONS (*M. A. RICO-RAMIREZ*) . . . 420
13.28 ACCURATE MONITORING OF PARTIAL BEAM BLOCKING USING EMISSION AND SHORT-RANGE VERTICAL REFLECTIVITY CONSISTENCY (*R. J. THOMPSON, A. J. ILLINGWORTH*) . . . 421
13.29 GROUND ECHO REMOVAL EMPLOYING DUAL-POL C-BAND RADARS IN THE NETHERLANDS: (*A. OVEREEM, R. UIJLENHOET, H. LEIJNSE*) . . . 422
13.30 DUAL-POLARIZATION RADAR RAINFALL ESTIMATION USING A DATABASE OF SIMULATED RAINDROP SIZE DISTRIBUTIONS (*BIN PEI, FIRAT Y. TESTIK*) . . . 423
13.31 PARAMETER ESTIMATION OF Z-R RELATIONSHIP FOR FLASH FLOOD WARNING SYSTEM (*M. KANG, W. NA, C. YOO*) . . . 425
13.32 IMPROVEMENTS TO POLARIMETRIC RADAR RETRIEVALS DURING HURRICANE HARVEY (*D. B. WOLFF, W. A. PETERSEN, A. TOKAY, D. A. MARKS, J. L. PIPPITT, P. KIRSTETTER*) . . . 426
13.33 IMPROVEMENT OF RADAR DATA QUALITY CONTROL WITHIN RADVOL-QC SYSTEM (*K. OŚRÓDKA, J. SZTURC, A. JURCZYK*) . . . 427
13.34 PAN-EUROPEAN MULTI-INSTRUMENTAL RAINFALL COMPOSITE (PERC) (*H. SINISALO, S. PULKKINEN, A. VON LERBER, J. KOISTINEN*) . . . 428
13.35 IMPROVEMENT OF THE ADJUSTMENT PROCEDURE ON A LONG- TERM RADAR DATA SET (*M.JESSEN, T.EINFALT, I.FRERK*) . . . 429
13.36 THE ROLE OF METEOROLOGICAL RADAR STATION IN THE SYSTEM OF EFFECTIVE MANAGEMENT AND PREDICTION OF HAIL (*VARDUHI MARGARYAN*) . . . 431
13.37 IMPACT OF THE VERTICAL GRADIENTS OF PRECIPITATION ON THE RADAR QPE BIAS IN THE FRENCH ALPS (*D. FAURE, N. GAUSSIAT, G. DELRIEU*) . . . 434
13.38 RADAR QPE FOR AN EXTREME PRECIPITATION EVENT IN SOUTHERN BRAZIL: JANUARY 2018 FLASH FLOOD - 409MM IN 48H (*L. CALVETTI, C. BENETI, W. F. COELHO, C. CARDOSO, T. SILVA, M. QUADRO, D. HERDIES*) . . . 436

13.39 RADAR-BASED QUANTITATIVE PRECIPITATION ESTIMATION (QPE) USING CONCEPTS FROM INFORMATION THEORY: ANALYSING THE POTENTIAL OF DATA-BASED, DYNAMIC Z-R RELATIONS, AND INVESTIGATING INFORMATION LOSSES FROM CLOUD TO GROUND (*MALTE NEUPER, UWE EHRET, HANS-STEFAN BAUER, VOLKER WULFMEYER*) 437
13.40 RAINFALL ESTIMATION IN HIGH SPATIOTEMPORAL RESOLUTION USING X-BAND DUAL-POL RADARS IN SEOUL METROPOLITAN AREA (*DAEHYUNG LEE, GEUNSU LYU, HONG-MOK PARK, WONBAE BANG, ALEXANDER RYZHKOV, GYUWON LEE*) 438
13.41 OPEN SOURCE POLARIMETRIC RADAR AND WEATHER STATION DATA USING PYTHON (*REMCO VAN DE BEEK*) 439
13.42 COMPARISON BETWEEN DIFFERENT QPE BASED ON: MICROWAVE LINKS, RADAR ADJUSTED AND GAUGES (*P.P. ALBERONI, A. FORNASIERO, G. ROVERSI, S. PASETTI, M. FOLEGANI, F. PORCÙ*) 440
13.43 TESTING OF CONVENTIONAL ATTENUATION ESTIMATION ALGORITHMS WITH OPERATIONAL RADARS IN DIFFERENT BANDS (*ALEKSANDR LIALIUSHKIN, ALEXANDER SOLONIN, NIKOLAY BOCHARNIKOV, TATIANA BAZLOVA, NADEZHDA YAKIMAINEN, VASILIY OLENEV*) 442
13.44 EVALUATION OF PRECIPITATION TYPE CLASSIFICATION METHODS FOR GROUND-BASED AND GPM DPR SATELLITE RADAR DATA (*SOICHIRO SUGIMOTO, MITSUHARU NOMURA, TAKAHISA KOBAYASHI*) 443
13.45 USING MICROWAVE LINK SIGNAL FLUCTUATIONS FOR RETRIEVAL OF RAINFALL RATES (*E. SEAGER, J. FRANK, R. UIJLENHOET, H. LEIJNSE*) 444
13.46 RAINFALL SPATIO-TEMPORAL CORRELATION STRUCTURE IN DUTCH CLIMATE FROM SUB-PIXEL TO MESOSCALE (*T. C. VAN LETH, H. LEIJNSE, A. OVEREEM, R. UIJLENHOET*) 445
13.47 AN EVALUATION OF RAIN RADAR ADJUSTMENT PROCEDURES (*MICHA SILVER, ARNON KARNIELI, ERICK FREDJ*) 446
13.48 EFFECT OF URBAN ENVIRONMENT ON SUMMER PRECIPITATION IN STUTTGART (*YAOYAO ZHENG, JAN HANDWERKER, NORBERT KALTHOFF*) 447
13.49 GEOSTATISTICAL MERGING OF X-BAND WEATHER RADAR AND A SPARSE RAIN GAUGE NETWORK OVER AN URBAN CATCHMENT (*I. SECK, J. VAN BAELEN*) . . 448
13.50 CHARACTERIZING THE APPARENT MULTIFREQUENCY REFLECTIVITY SIGNATURES OF OROGRAPHIC PRECIPITATION USING A COUPLED RAINSHAFT MICROPHYSICS-RADIATIVE TRANSFER MODEL AND OBSERVATIONS (*MALARVIZHI ARULRAJ, P. BARROS*) 449
13.51 ENHANCEMENT OF RADAR RAINFALL ESTIMATES FOR ESTONIAN TERRITORY THROUGH OPTICAL FLOW TEMPORAL INTERPOLATION (*J.RAHU, T. VOORMANSIK, P. POST*) 450
13.52 PARAMETERIZING RAINDROP SIZE DISTRIBUTIONS USING MICROWAVE LINKS (*T. C. VAN LETH, H. LEIJNSE, A. OVEREEM, R. UIJLENHOET*) 451
13.53 IMPROVEMENT OF PRECIPITATION ESTIMATES FROM CHUVAONLINE X-BAND RADARS THROUGH THE IMPLEMENTATION OF A NEW ATTENUATION CORRECTION TECHNIQUE (*KEYLA M. MORA NAVARRO, CARLOS AUGUSTO MORALES*) 452
13.54 QUANTITATIVE PRECIPITATION ESTIMATION BY X-BAND POLARIMETRIC RADAR NETWORK OF KOCHI UNIVERSITY (*AKIRA NISHII, KOJI SASSA*) 453

13.55 VERIFICATION OF RADAR HYDROMETEOR CLASSIFICATION ALGORITHMS FOR THE UK C-BAND NETWORK (*B. PICKERING, R. NEELY III, D. HARRISON, S. BEST, ALAN BLYTH*) . . . 454
13.56 MELTING LAYER CLIMATOLOGY IN THE GENOBLE VALLEY USING MULTI-FREQUENCY, MULTI-PARAMETER, MULTI-ANGLE RADAR MEASUREMENTS (*A. KHANAL, G. DELRIEU, S.KREMER, F. CAZENAVE*) . . . 455
13.57 SHORT TIME PRECIPITATION ESTIMATION USING WEATHER RADAR AND SURFACE OBSERVATIONS: WITH WIND DRIFT INTEGRATED USING A STOCHASTIC METHOD (*JIERU YAN, ANDRÁS BÁRDOSSY*) . . . 456
13.58 GEOSTATISTICAL APPROACH TO RAINFALL MAPPING FROM COMMERCIAL MICROWAVE LINKS (*W. WOLFF, A. OVEREEM, R. UIJLENHOET*) . . . 457
13.59 HYBRID SURFACE RAINFALL ESTIMATION FOR OPERATIONAL APPLICATION USING DUAL POLARIZATION RADAR NETWORK IN KOREA (*YOUNG-A OH, MI-KYUNG SUK, SUNG-HWA JUNG, SUN-KI LEE*) . . . 458

Session 14. Non-meteorological use of weather radar **459**

Oral presentation . . . 460
14.1 RETRIEVING VOLCANIC MASS ERUPTION RATE FROM GROUNDBASED X-BAND AND L-BAND MICROWAVE RADARS DURING MT. ETNA EXPLOSIVE ERUPTION (*F.S. MARZANO, L. MEREU, S. DI FABIO, M. MONTOPOLI, E. PICCIOTTI, S. SCOLLO, C. BONADONNA*) . . . 460
14.2 EUROPE-WIDE PATTERNS OF NOCTURNAL AVIAN MIGRATION FROM WEATHER RADAR DATA (*CECILIA NILSSON, ADRIAAN DOKTER, LIESBETH VERLINDEN, JUDY SHAMOUN-BARANES, BAPTISTE SCHMID, PETER DESMET, SILKE BAUER, JASON CHAPMAN, JOSE ALVES, PHIL STEPANIAN, NIR SAPIR, CHARLOTTE WAINWRIGHT, MATHIEU BOOS, ANNA GÓRSKA, MYLES MENZ, PEDRO RODRIGUEZ, HIDDE LEIJNSE, PAVEL ZEHTINDJIEV, ROBIN BRABANT, GÜNTHER HAASE, NADJA WEISSHAUPT, MICHA CIACH, FELIX LIECHTI*) . . . 462

Poster presentation . . . 463
14.3 TRACKING OF SMALL UNMANNED AERIAL VEHICLES USING WEATHER RADAR (*K. ORZEŁ, D. PEPYNE, S. TURNER, J. VILARDELL-SANCHEZ, A. BAJAJ, M. ZINK, S. FRASIER*) . . . 463
14.4 TIME-SERIES BASED APPROACH TO IDENTIFY AND PROCESS BIOLOGICAL TARGETS IN RADAR WIND PROFILER DATA FOR CROSS DISCIPLINARY PURPOSES (*N. WEISSHAUPT, V. LEHMANN, A. HAEFELE, M. MARURI*) . . . 465
14.5 COMPARISON OF ONSHORE AND OFFSHORE BIRD MIGRATION BY DIFFERENT RADAR SYSTEMS NEAR THE BELGIAN COAST (*M. REYNIERS, R. BRABANT,M. LUKACH, B. SCHMID, M. BOOS*) . . . 466
14.6 RAIN ATTENUATION STATISTICS AT KA-BAND ESTIMATED FROM WEATHER RADAR OBSERVATIONS (*M. LUKACH, L. QUIBUS, D. VANHOENACKER, L. DELOBBE*) . . . 467

Extended Abstracts **468**

1 RADAR REFLECTIVITY ADVECTION ESTIMATION VIA PROXY CIRCLE IMAGES (*A.C.-P. OUDE NIJHUIS, Y. DUFOURNET, T. OTTO, I. STEPANOV*) . . . 469

2 USING A FOUR-DIMENSIONAL VARIATIONAL RADAR AND SURFACE DATA ASSIMILATION SYSTEM TO INVESTIGATE THE PROCESS LEADING TO A HEAVY PRECIPITATING EVENT OVER COMPLEX TERRAIN: A CASE STUDY IN NORTHERN TAIWAN (*WU, Y.-J., Y.-C. LIOU, S.-L. TAI, J. SUN*) . . . 473
3 DEEP LEARNING FRAMEWORK FOR PRECIPITATION RETRIEVALS FROM COMMUNICATION SATELLITES (*KUMAR VIJAY MISHRA, AHMAD GHARANJIK, M. R. BHAVANI SHANKAR, AND BJÖRN OTTERSTEN*) . . . 477
4 POTENTIAL FOR USE OF RADAR DATA FOR CLIMATE MONITORING (*ELENA SALTIKOFF, ANDREAS BECKER, BERNARD URBAN, KATJA FRIEDRICH, RAINER HOLLMANN, JOSHUA SODERHOLM, CATERINA TASSONE*) . . . 486
5 OPERA PAST, PRESENT AND FUTURE (*ELENA SALTIKOFF, GÜNTHER HAASE, HIDDE LEIJNSE, PETR NOVÁK, LAURENT DELOBBE*) . . . 491
6 ICE MICROPHYSICAL RETRIEVALS USING POLARIMETRIC RADAR DATA (*A. RYZHKOV, P. BUKOVCIC, A. MURPHY, P. ZHANG, AND G. MCFARQUHAR*) . . . 494
7 A HYDROMETEOR CLASSIFICATION ALGORITHM FOR THE UK C-BAND WEATHER RADAR NETWORK (*STEVEN BEST, DAWN HARRISON*) . . . 505
8 OBSERVATIONS OF THE ATMOSPHERIC BOUNDARY LAYER FROM A VERTICALLY POINTING, S-BAND, FMCW RADAR IN NORTHERN ALABAMA, U.S.A. DURING VORTEX-SOUTHEAST (*ROBIN L. TANAMACHI, S. J. FRASIER, J. WALDINGER, A. T. LAFLEUR, AND F. ROCADENBOSCH*) . . . 514
9 WHY THE GENERALIZED GAMMA? - AN ANSWER BASED ON MEASUREMENTS WITH METEOROLOGICAL PARTICLE SPECTROMETER AND 2D VIDEO DISDROMETER (*MERHALA THURAI, V.N. BRINGI, PATRICK GATLIN, WALTER PETERSEN AND MATT WINGO*) . . . 524
10 QUANTITATIVE PRECIPITATION ESTIMATION BY X-BAND POLARIMETRIC RADAR NETWORK OF KOCHI UNIVERSITY (*AKIRA NISHII, KOJI SASSA*) . . . 534
11 STANDARD OPERATION PROCEDURES (SOP) FOR WEATHER RADARS OPERATION, MONITORING, MAINTENANCE AND CALIBRATION. (*LJUBOV LIMAN,TIMO POSIO, MIKKO KURRI*) . . . 542
12 USING EUSKALMET RADAR FOR ANALYSIS OF INTENSE AND PERSISTENCE PRECIPITATION EVENT IN BASQUE COUNTRY DURING WINTER: THE 11 JANUARY 2018 CASE (*JOSEBA EGAÑA, SANTIAGO GAZTELUMENDI, OLATZ PRINCIPE, VIRGINIA PALACIO AND MERCEDES MARURI*) . . . 545
13 USING EUSKALMET RADAR FOR ANALYSIS OF A HEAVY STORMS EVENT IN BASQUE COUNTRY DURING SUMMER: THE 30 AUGUST 2017 CASE (*JOSEBA EGAÑA, SANTIAGO GAZTELUMENDI, OLATZ PRINCIPE, VIRGINIA PALACIO AND MERCEDES MARURI*) . . . 552
14 RESULTS OF THE MONITORING TASKS AND CO-CREATION ACTIVITIES OF THE PRECIPITATION PRODUCTS OF KAPILDUI WEATHER RADAR (*M. MARURI, S. GAZTELUMENDI, K. OTXOA DE ALDA, R. HERNANDEZ, C. STOCKER. J. SALAZAR, I. EGUIARA, J.A.. ARANDA*) . . . 558
15 EVOLUTION OF THE CONFIGURATION OF THE LIGHTNING PROTECTION SYSTEM OF THE KAPILDUI WEATHER RADAR INSTALLATION (*M. MARURI, J.A. ARANDA*) . 566

16 SEVERE HAIL DETECTION: HYDROMETEOR CLASSIFICATION FOR POLARIMETRIC C-BAND RADARS USING FUZZY-LOGIC AND T-MATRIX SCATTERING SIMULATIONS (*MARI L. SCHMIDT, SILKE TRÖMEL, ALEXANDER V. RYZHKOV, AND CLEMENS SIMMER*) 574
17 EFFECT OF URBAN ENVIRONMENT ON SUMMER PRECIPITATION IN STUTTGART (*YAOYAO ZHENG, JAN HANDWERKER, AND NORBERT KALTHOFF*) 579
18 MULTI-FREQUENCY RADAR RETRIEVAL OF SNOWFALL MICROPHYSICS (*JUSSI LEINONEN, MATTHEW D. LEBSOCK, OUSMANE O. SY, SIMONE TANELLI, BRENDA DOLAN, RANDY J. CHASE, JOSEPH A. FINLON, DMITRI MOISSEEV, AND ANNAKAISA VON LERBER*) 586
19 OPERATIONAL SOLAR MONITORING FOR IMPROVING THE HOMOGENEITY OF THE EUROPEAN RADAR NETWORK (*ASKO HUUSKONEN, GÜNTHER HAASE, DANIEL MICHELSON, HIDDE LEIJNSE, IWAN HOLLEMAN, MATT PROBERT, RASHPAL GILL, MICHAEL FRECH, MIKKO KURRI, AND HARRI HOHTI*) 594
20 NETWORK OF WEATHER RADARS IN REPUBLIC OF SRPSKA, BOSNIA AND HERZEGOVINA (*TIHOMIR DEJANOVIC, VELIMIR VRANIC AND ZORAN VUCINIC*) 601
21 MONITORING THE ONGOING UPGRADE OF THE SWEDISH WEATHER RADAR NETWORK (*DAVID DUFTON, GÜNTHER HAASE, DANIEL JOHNSON, AND GIANFRANCO VULPIANI*) 605
22 ASSIMILATION OF DIFFERENT RADAR DATA FOR A BETTER FORECASTING OF SEVERE WEATHER PHENOMENA (*LUCA ROVAI, ANDREA ANTONINI, SAMANTHA MELANI, VALERIO CAPECCHI, RICCARDO BENEDETTI, LUCA FIBBI, BERNARDO GOZZINI, GIANNI MESSERI, ALBERTO ORTOLANI, AND FRANCESCO PASI*) 615
23 TIME-SERIES BASED APPROACH TO IDENTIFY AND PROCESS BIOLOGICAL TARGETS IN RADAR WIND PROFILER DATA FOR CROSS DISCIPLINARY PURPOSES (*NADJA WEISSHAUPT, VOLKER LEHMANN, ALEXANDER HAEFELE, MERCEDES MARURI*) 620
24 DIFFERENTIAL PHASE UPON TRANSMISSION AS A NEW RADAR PARAMETER (*VALERY MELNIKOV*) 627
25 GEOSTATISTICAL MERGING OF X-BAND WEATHER RADAR AND A SPARSE RAIN GAUGE NETWORK OVER AN URBAN CATCHMENT (*I.SECK, J. VAN BAELEN*) . . . 633
26 DEVELOPMENT OF A DETECTION SYSTEM OF HEAVY RAINFALL USING X-BAND PHASED-ARRAY WEATHER RADAR (*KAZUHIRO YOSHIMI, FUMIHIKO MIZUTANI, NOBUHIRO TAKAHASHI, TOMOO USHIO*) 640
27 SOLAR ENERGY PERSPECTIVE ON THE DATA ASSIMILATION OF RADAR REFLECTIVITY DATA IN A LIMITED AREA NWP MODEL (*TUULI PERTTULA, SAMI NIEMELÄ, ANDERS V. LINDFORS AND ELENA SALTIKOFF*) 646
28 IMPLEMENTATION AND OPERATIONAL USE OF A HETEROGENEOUS RADAR NETWORK IN THE COMPLEX OROGRAPHY OF ABRUZZO REGION (*ERRICO PICCIOTTI, SAVERIO DI FABIO, STEFANO BARBIERI, MARIO MONTOPOLI, RENATO ZAURI*) . 654
29 ANALYSIS OF HAIL EVENT IN FIELD OF REFLECIVITY AND DIFFERENTIAL REFLECIVITY (*S.STEVANOVIĆ, S.BILJIĆ, M.VASIĆ, G.BOGUNOVIĆ*) 662
30 QUALITY-BASED RADAR DATA PROCESSING AND QPE AT THE SLOVAK HYDROMETEOROLOGICAL INSTITUTE (*LADISLAV MÉRI, MARIÁN JURAŠEK, JÁN KAŇÁK, L'UBOSLAV OKON*) 672

31 MULTI-RADAR DATA FUSION FOR HIGH-RESOLUTION QPE IN URBAN AREA (*BRANDON HICKMAN, JUSSI TIIRA , ROBERTO CREMONI, DMITRI MOISSEEV*) 681
32 OPERATIVE CORRECTION OF DUAL-PRF OUTLIERS (*PATRICIA ALTUBE, TOMEU RIGO, ORIOLARGEMÍ, NICOLAU PINEDA, JOAN BECH, SCOTT COLLIS, JONATHAN HELMUS*) 687
33 PERFORMANCE OF A NEW ALGORITHM FOR NOWCASTING ANOMALOUS TRAJECTORIES (*ANNA DEL MONRAL, TOMEU RIGO AND MARIA CARMEN LLASAT*) . . . 695
34 INFORMATION SPARSENESS, A KEY OBSTACLE TO RADAR DATA ASSIMILATION IN CONVECTION (*FRÉDÉRIC FABRY*) 704
35 WIND TURBINES SEEN IN RADAR DATA WITH THE BIG DIFFERENCE METHOD (*WILLI SCHMID, STEFAN C. MÜLLER*) 713
36 RAPID SCAN EXPERIMENT OF DOPPLER WEATHER RADAR FOR MONITORING RAINSTORMS AND TROPICAL CYCLONES IN HONG KONG (*WAI KONG, YING-WA CHAN*) 722
37 RADAR-DERIVED QUANTITATIVE PRECIPITATION ESTIMATION BASED ON VERTICAL-RAINCLOUD TRAJECTORY PROFILES (*HANGGAR G MAWANDHA, SATORU OISHI*) . 733
38 NOWPRECIP: AN ALGORITHM FOR LOCALIZED PROBABILISTIC PRECIPITATION NOWCASTING IN THE COMPLEX TERRAIN OF SWITZERLAND (*I.V. SIDERIS, L. FORESTI, D. NERINI, AND U. GERMANN*) 738
39 CONTINENTAL-SCALE WEATHER RADAR DATA ASSIMILATION USING NORTH AMERICAN DATA (*DOMINIK JACQUES, DANIEL MICHELSON, BJARNE HANSEN, JEAN-FRANOIS CARON, AND LUC FILLION*) 747
40 FILCOH, A METHOD TO ELIMINATE GROUND ECHOES FOR WEATHER RADAR OPERATING IN MULTIPLE PRT MODE BY USING THE AVAILABLE AUTOCORRELATION COEFFICIENTS (*MOHAMMED TAHANOUT, JACQUES PARENT DU CHATELET*) . . . 756
41 IMPACT OF THE VERTICAL GRADIENTS OF PRECIPITATION ON THE RADAR QPE BIAS IN THE FRENCH ALPS (*DOMINIQUE FAURE, NICOLAS GAUSSIAT, AND GUY DELRIEU*) 765
42 DERIVING AND COMPOSITING MOTION FIELDS SPEED AND QUALITY CHALLENGES (*MARKUS PEURA, TUULI PERTTULA, AND HARRI HOHTI*) 772
43 CHARACTERISATION OF THE MELTING LAYER VARIABILITY IN THE SWISS ALPS USING POLARIMETRIC X-BAND RADARS (*FLOOR VAN DEN HEUVEL, MARCO GABELLA, AND ALEXIS BERNE*) 780
44 ALTERNATIVE DATA PROCESSING FOR MICRO RAIN RADAR (MRR) OBSERVATIONS (*ALBERT GARCIA-BENADÍ, JOAN BECH, SERGI GONZALEZ, AND JOAQUIN DEL RIO FERNANDEZ*) 786
45 BLENDING FIELD-BASED AND CELL TRACKING METHODS FOR IMPROVED PRECIPITATION NOWCASTING (*SEPPO PULKKINEN, V. CHANDRASEKAR*) 797
46 A PROBABILISTIC RADAR FORWARD MODEL FOR SMALL ICE PARTICLES (*ROBERT-S. SCHROM, MATTHEW R. KUMJIAN*) 804
47 RADAR QPE FOR AN EXTREME PRECIPITATION EVENT IN SOUTHERN BRAZIL: JANUARY 2018 FLASH FLOOD 409 MM IN 48H (*LEONARDO CALVETTI, CESAR BENETI, WILLIAM COELHO, CAMILA CARDOSO, TULIPA SILVA, MARIO QUADRO, DIRCEU HERDIES AND ROBERTO CALHEI-ROS*) 810

48 A COMPARISON OF TOTAL LIGHTNING REFLECTIVITY PROXIES AND WEATHER RADAR DATA IN SOUTHERN BRAZIL FOR HIGH IMPACT WEATHER MONITORING AND NOWCASTING (*WILLIAM F. COELHO, LEONARDO CALVETTI, CESAR A. A. BENETI AND NICOLE A. ROZIN*) 817
49 THE DEVELOPMENT OF A CANADIAN OPERATIONAL DUAL-POLARIZATION RAINFALL ESTIMATION ALGORITHM (*S. BOODOO, D. HUDAK, N. DONALDSON, J. REID, D. MICHELSON, P. RODRIGUEZ, M. COUTURE, V. STOJANOVIC*) 822
50 A HYDROMETEORLOGICAL ANALYSIS OF AN EXTREME FLASH FLOOD EVENT IN THE URBAN AREA OF WEST ATTICA, GREECE (*MARIOS N. ANAGNOSTOU, GEORGE VARLAS, JOHN KALOGIROS, PETROS KATSAFADOS, A. PAPADOPOULOS, E. BALTAS, AND E. ANAGNOSTOU*) 830
51 A METHOD FOR ESTIMATE OF RANGE VARIATION OF ATTENUATION FROM DUAL FREQUENCY AND DUAL POLARIZATION RADAR -VALIDATION USING SCATTERING DATABASE OF SNOW- (*TAKAHISA KOBAYASHI, MISTUHARU NOMURA, SOICHIRO SUGIMOTO, AHORO ADACHI, NOBUHIRO NAGUMO AND HIROMARU HIRAKUCHI*) . 837
52 VERTICAL WIND PROFILE MEASUREMENTS ON THE OPERATIONAL WEATHER RADAR IN "WIND PROFILER" MODE (*YURI PAVLYUKOV, ALEX TRAVOV, NADJA EROSHKINA*) 846
53 COMPARISON BETWEEN DIFFERENT QPE BASED ON: MICROWAVE LINKS, RADAR ADJUSTED AND GAUGES (*PIER PAOLO ALBERONI, ANNA FORNASIERO, GIACOMO. ROVERSI, STEFANIA PASETTI, MARCO FOLEGANI, FEDERICO PORCÙ*) 851
54 IMPACT OF RIMED AND UNRIMED SNOW ON SNOWFALL RETRIEVALS AT X, KA, AND W BAND (*M. T. FALCONI, A. VON LERBER, D. ORI, F. S. MARZANO, AND D.MOISSEEV*) 861
55 HOW MUCH ATTENUATION AT W AND KA BANDS IS CAUSED BY MELTING LAYER? AN ANSWER FROM MULTI-FREQUENCY RADAR DOPPLER SPECTRA (*HAORAN LI, DMITRI MOISSEEV*) 864
56 TESTING OF CONVENTIONAL ATTENUATION ESTIMATION ALGORITHMS WITH OPERATIONAL RADARS IN DIFFERENT BANDS (*ALEKSANDR LIALIUSHKIN, ALEKSANDR SOLONIN, NIKOLAY BOCHARNIKOV, TATIANA BAZLOVA, NADEZHDA YAKIMAINEN1 AND VASILIY OLENEV*) 870
57 THE IMPORTANCE OF ASSIMILATING THERMODYNAMIC FIELDS WITH RADAR OBSERVATIONS IN CONVECTIVE-SCALE WEATHER SYSTEMS (*CHING-YIN KE, KAO-SHEN CHUNG*) 875
58 DATA ASSIMILATION OF RADAR REFLECTIVITY VOLUMES IN A LETKF SCHEME (*VIRGINIA POLI, THOMAS GASTALDO, CHIARA MARSIGLI, PIER PAOLO ALBERONI, AND TIZIANA PACCAGNELLA*) 883
59 SEVERE WEATHER AND HAIL DETECTION USING THE X BAND WEATHER RADAR TUSCANY NETWORK (*ANDREA ANTONINI, SAMANTHA MELANI, ALBERTO ORTOLANI, ANDREA TELLESCHI, ANDREA LOMBARDI, IRENE GIANNINI, BERNARDO GOZZINI*) 889
60 MULTISOURCE DATA VERIFICATION OF A WEATHER RADAR SURFACE PRECIPITATION TYPE PRODUCT (*E. CASELLAS, J. BECH, R. VECIANA, N. PINEDA, T. RIGO, J. MORÉ, S. GONZÁLEZ, A. PACI*) 897

61 COMPARISON OF CLUTTER DETECTION SCHEMES FOR NON-DOPPLER, NON-POLARIMETRIC X BAND RADARS (*SAMANTHA MELANI, ANDREA ANTONINI, FRANCESCA CAPARRINI, ANDREA TELLESCHI, ANDREA LOMBARDI, ALESSANDRO MAZZA AND ALBERTO ORTOLANI*) . . . 906
62 OPERATIONAL HYDROLOGICAL MODELLING OF SMALL WATERSHED USING QPE FROM DUAL-POL RADAR IN BRAZIL (*CESAR BENETI, ROBERTO V. CALHEIROS, MINO SORRIBAS, CAMILA OLIVEIRA, LEONARDO CALVETTI, JORGE RUVIARO, AND REVERTON NEUNDORF*) . . . 915
63 PAIRED DISTROMETRIC MEASUREMENTS IN THE SOUTH OF BRAZIL: WIND EFFECTS AND SAMPLING UNCERTAINTIES (*ROBERTO V. CALHEIROS, CESAR BENETI, CAMILA OLIVEIRA, AND LEONARDO CALVETTI*) . . . 923
64 TRACKING SMALL UNMANNED AERIAL VEHICLES USING WEATHER RADAR (*KRZYSZTOF ORZEŁ, DAVID PEPYNE, SEAN TURNER, JEZABEL VILARDELL SANCHEZ, APOORVA BAJAJ, MICHAEL ZINK, AND STEPHEN FRASIER*) . . . 932
65 AIRBORNE IMPLEMENTATION OF PDPP TECHNIQUE ON THE NRC W-BAND RADAR (*CUONG NGUYEN, ALESSANDRO BATTAGLIA, MENGISTU WOLDE, ANDREW PAZMANY AND ANTHONY ILLINGWORTH*) . . . 937
66 BISTATIC SCATTERING FROM BRAGG TURBULENCE AT X-BAND: A POTENTIAL MECHANISM FOR CLEAR AIR SENSING USING CASA-TYPE RADAR NETWORKS (*DAVID J. MCLAUGHLIN*) . . . 946
67 OPERATIONAL MONITORING OF T/R-LIMITER DEGRADATION BASED ON CLOSE RANGE GROUND CLUTTER (*TIEMO MATHIJSSEN, STAN BROERE, HANS BEEKHUIS, AND HIDDE LEIJNSE*) . . . 956
68 FROM PULSE TO PRODUCT, HIGHLIGHTS OF THE UPGRADE PROJECT OF THE DUTCH NATIONAL WEATHER RADAR NETWORK (*HANS BEEKHUIS, TIEMO MATHIJSSEN*) . . . 960

Republication of Zawadzki, I. (1984) 966

1 REPUBLICATION OF ZAWADZKI, I. (1984). FACTORS AFFECTING THE PRECISION OF RADAR MEASUREMENTS OF RAIN . . . 967

Author Index 973

Session 1. Microphysical studies



Keynote presentation

1.1 DENSITY OF SNOWFLAKES BASED ON SURFACE OBSERVATIONS

A. VON LERBER[1], D. MOISSEEV [1,2], J. TIIRA [2], D. ORI [3]

[1] Radar Science, Finnish Meteorological Institute, Finland
[2]Institute for Atmospheric and Earth System Research, University ofHelsinki, Finland
[3]Institute for Geophysics and Meteorology, University of Cologne, Germany
annakaisa.von.lerber@fmi.fi

Irregular structure and different sizes of snowflakes present in Nature are challenging for microphysical parametrization and thereby also introduce uncertainty in remote sensing retrievals. Nowadays surface-based data are gathered mostly by automatic optical imagers. A typical limitation of automatic observations, however, is that only a subset of needed parameters is directly measured and the observations are limited by the viewing projection. Although, microphysical properties of snow particles are not independent, for example fall velocity can be computed from particle mass and shape equalizing gravitational attraction and aerodynamic drag, the remaining degrees of freedom are rather numerous. Typically mass or density of snow particles are either retrieved from combined observations of disdrometer and other instrument or utilizing the general hydrodynamic theory.

We have implemented two methods to retrieve the density of snowflakes with combined measurements of optical disdrometer (Particle Imaging Package, PIP) and precipitation gauge. The first method retrieves the ensemble mean density, i.e. the volume-flux weighted snow density, as function of median volume diameter. One of the biggest uncertainties with this method is the estimated volume-equivalent diameter. We have assumed that snowflakes are spheroids with axis ratios of 0.6 and given this assumption, a conversion factor relating volume equivalent and disc equivalent diameters observed from a single projection was defined.

The second method utilizes the hydrodynamic theory, where mass of single particle is computed from the observed dimension, fall velocity and area ratio of a snow particle. PIP observes falling particles from the side, whereas the particle dimensions projected to the flow are needed for the hydrodynamic calculations. The errors associated with the observation geometry and the measured particle size distribution were addressed by devising a simple correction procedure; the value of the correction was chosen for each snow event by comparing the estimated accumulated precipitation to gauge measurements. With the retrieved masses of snowflakes the ensemble densities with various definitions can be determined and compared.

Various definitions may yield significantly different results. We have processed snowfall cases over winters 2014-2017 and studied the changes of the microphysical properties corresponding to environmental conditions. Preliminary results indicate that the ensemble mean snow density and the volume-flux weighted snow density calculated from the retrieved masses of the second method are corresponding well, although comparison is sensitive to the assumption of the conversion factor relating volume equivalent and disc equivalent diameters.

In our study, we present a comparison of density definitions based on observations relative to the microphysical properties of snow particles and link the differences to uncertainties in parametrization. For example, the volume flux weighted snow density is expected to be lower in values than the velocity-weighted snow density, although the difference is not generally prominent especially with low-density aggregates, whose velocity is weekly dependent on snowflake size. The magnitude of differences are assumed to be determined by the exponential term of power-law expression of snow particle mass-dimensional relation.

1.2 ICE MICROPHYSICAL RETRIEVALS USING POLARIMETRIC RADAR DATA

A.RYZHKOV[1], A.MURPHY [1], G.MCFARQUHAR [1]

[1] Cooperative Institute for Mesoscale Meteorological Studies,
University of Oklahoma, USA
alexander.ryzhkov@noaa.gov

A novel polarimetric radar method for size distribution retrievals of ice and estimation of ice water content (IWC) has been developed. The technique is based on the combination of three radar variables: radar reflectivity Z, differential reflectivity Z_{DR} (or reflectivity difference Z_{DP}), and specific differential phase K_{DP}. The latter plays a particularly important role because it is proportional to the first moment of size distribution in ice and, therefore, is very sensitive to ice particles of small sizes. It is demonstrated that the estimates of the mean volume diameter D_m, total concentration N_t, and IWC of ice particles obtained from Z and the ratio of Z_{DP} and K_{DP} are robust with respect to the diversity of ice habits, their shapes, orientations, density, and size distributions.

It is instrumental to use new methodologies for processing and displaying polarimetric radar data such as quasi-vertical profiles (QVP) and columnar vertical profiles (CVP) to ensure appropriate quality of the K_{DP} and Z_{DP} measurements for reliable retrievals.

Preliminary testing of the suggested technique using the WSR-88D radar data collected in hurricanes Irene, Harvey, and Irma reveals extreme concentrations of very small ice with significant IWC that is almost an order of magnitude higher than the one estimated from conventional Z IWC relations. Comparisons of the radar-retrieved size distribution parameters of ice with their in situ aircraft measurements in a midlatitude MCS show good agreement between the two.

1.3 AN INVERSE PROBLEM APPROACH TO RETRIEVE FIELDS OF DROP SIZE DISTRIBUTION PARAMETERS FROM XBAND POLARIMETRIC RADAR VARIABLES

M. ALCOBA[1], M. GOSSET[1,2], H. ANDRIEU[3]
[1]GET-OMP/World Bank, Toulouse France
[2]GET-OMP/IRD, Toulouse France
[3]IFSTTAR, Nantes France
matias.alcoba@get.omp.eu

Polarimetric radars use indirect information on raindrops′ oblateness at falling to provide more information about the drop size distribution than conventional radars. Many studies have used empirical relationships between polarimetric radar variables and physical parameters of rainfall (and snow) to retrieve rain rate and DSD fields from radars. Another common approach is to use relationship based on modeling polarimetric variables through the T-matrix scattering calculations for oblate scatters [Mitchenko 1996] and DSD information. At attenuating frequency like in the X-band, a two-step approach is usually taken with first attenuation correction and second DSD retrieval. Here an inverse method approach is applied to derive DSD parameters at each radar gate over a radial before any attenuation correction.

We will discuss this radial based inversion method deriving fields of DSD parameters from fields of uncorrected polarimetric radar variables. Comparing retrieved DSD parameters to in situ disdrometer measurements performs the method validation. The method shows convincing agreement with observed DSD. Its main asset is to use all the independent information available per gate (Z_{dr}, Z_h, K_{dp}) and their respective uncertainty to find a compromise solution between observed variables and an "a priori" solution. Another important asset of the method is that no previous attenuation correction is made: the correction of attenuation is handled by the inversion procedure.

1.4 MULTI-INSTRUMENT RAINFALL RATE ESTIMATION IN THE PERUVIAN CENTRAL ANDES (12.0°S)

D. SCIPION[1], J. VALDIVIA[2], F. SILVA[2], M. MILLA[3]

[1] Instituto Geofísico del Perú, Lima, Perú

[2] Subdirección de Ciencias de Atmósfera e Hidrósfera, Instituto Geofísico del Perú, Lima, Perú

[3] Radio Observatorio de Jicamarca, Instituto Geofísico del Perú, Lima, Perú

dscipion@igp.gob.pe

Agriculture is one of the main economic activities in the Peruvian Andes, where most of the vegetables of the whole country are produced. Rain water alone irrigates more than 80% of the fields for agriculture purposes. However, the cloud and rain generation mechanisms in the Andes still remain mostly unknown.

In early 2014, The Instituto Geofísico del Perú (IGP) decided to intensify studies in the central Andes in order to better understand cloud microphysics, and the Atmospheric Microphysics And Radiation Laboratory (LAMAR) was finally founded in 2015 in the Huancayo Observatory (12°02′18″S, 75°19′22″W) at 3330 m.a.s.l.

As part of LAMAR, a Ka-band cloud profiler (MIRA-35C) was installed in late 2015, for cloud and rainfall estimation, along with a disdrometer (PARSIVEL2) and a few rain gauges. LAMAR also served as a testbed for UHF wind profiler (CLear-Air and Rainfall Estimation CLAIRE) radar also developed at IGP′s Radio Observatorio de Jicamarca. CLAIRE was designed to operate at 445 MHz, which makes it sensitive to turbulence and precipitation.

In this work, we will present a combination of precipitation observations at LAMAR by the two radar systems, showing their similarities and differences due to the operational frequencies and scattering mechanisms. Doppler spectra vertical velocity are used to estimate the dropsize distribution, and in turn to estimate the rainfall rate. These radar-based estimates will also be validated by the disdrometer and rain gauges. Causes for over/under-estimation of the rainfall estimated will also be discussed in the paper.

1.5 RAINDROP SIZE DISTRIBUTION IN COASTAL RAINFALL SYSTEMS IN SOUTH EAST AUSTRALIA: EFFECT ON Z-R RELATIONSHIPS AND ATTENUATION

A. GUYOT[1], J. PUDASHINE[1], V. PAUWELS[1], A. PROTAT[2], A. SEED[2], R. UIJLENHOET[3], M. PRAKASH[4], J.P. WALKER[1]

[1]Monash University, Department of Civil Engineering, Victoria, Australia
[2]Australian Bureau of Meteorology, Victoria, Australia
[3]Wageningen University, The Netherlands
[4]Data 61, Commonwealth Scientific and Industrial Research Organisation, Victoria, Australia
adrien.guyot@monash.edu

This study presents for the first time an analysis of raindrop size distributions (DSD) for a coastal environment in southeast Australia, an area prone to maritime and continental rainfall influences. DSD were collected using collocated laser optical disdrometers (2 OTT Parsivel and 3 Clima Thiess) over three years (2014-2017) in Melbourne, Australia. Quality checks were performed based on particle velocities and a collocated pluviometer, and discrepencies between collocated instruments were analysed. Characteristics of the DSD for a range of rain rates, rainfall types (stratiform, convective) and rainfall origin (continental, maritime) were studied. Gamma distributions were fitted to the different rainfall types and DSD parameters (N_0 and shape μ, slope Λ and μ, and N_W and D_m) were derived. Reflectivity rainfall rate (Z-RR) relationships were estimated from regression of scatter plots both using T-matrix and moment approaches for deriving radar moments. Attenuation is modelled for a range of weather radar and Commercial Microwave Links (CML) frequencies. Finally, 3D reflectivity data collected by operational C- and S-Band radars were observed concomitantly and compared to the DSD-derived reflectivities.

This study fills an important gap of knowledge for this region and will help improve operational weather radar-derived quantitative precipitation estimates. A better characterization of rainfall-attenuation relationships will also provide a baseline for leveraging the development of rainfall rates retrievals at improved temporal and spatial resolutions using CML.

1.6 RECONSTRUCTION OF THE DRIZZLE MODE OF THE RAINDROP SIZE DISTRIBUTION: AN APPROACH USING DOUBLE-MOMENT NORMALISATION

T. H. RAUPACH[1], M. THURAI[2], V. N. BRINGI[2], A. BERNE[1]

[1]École Polytechnique Fédérale de Lausanne, Switzerland
[2]Colorado State University, Fort Collins, CO, USA
tim.raupach@epfl.ch

The raindrop size distribution (DSD) describes the microstructure of liquid precipitation. Bulk rainfall variables of interest can be derived as weighted moments of the DSD, and the DSD is thus fundamental to studies of rainfall microphysics, as well as processes that occur on larger scales such as radar retrieval of rainfall properties.

It is well known that commonly used disdrometers do not measure well the small-drop end of the DSD spectrum, meaning that most disdrometer measurements are inaccurate or missing below a minimum drop size of about 0.5 mm. Recent work by Thurai et al. (*J. App. Met. and Clim., 56, 2017*) used collocated measurements from 2D-video-disdrometer (2DVD) and an optical array probe (Meteorological Particle Spectrometer, MPS) to measure a more complete DSD down to a minimum drop size of 0.05 mm. The spectra measured using this technique exhibited peaks of small drops in a "drizzle mode" for diameters less than about 0.7 mm, often separated from the rest of the DSD by a "shoulder" region. The drizzle mode and shoulder region are not well captured by often-used disdrometers, yet influence important rainfall parameters such as the total drop concentration and shape parameters of DSD models.

In this study we investigate whether the drizzle mode and shoulder region of the DSD can be "reconstructed" from truncated DSD measurements made using ordinary disdrometers. To do so we use the double-moment normalisation technique of Lee et al. (*J. App. Met., 2004*), in which the DSD is represented as a combination of two of its statistical moments and a shape function that is assumed to be invariant. We determine which two DSD moments are best measured by "incomplete", truncated DSDs. We fit a generalised gamma model to the shape function, using "complete" DSDs made up of combined 2DVD and MPS measurements. Using this shape function and moments measured by an ordinary disdrometer, this technique shows promising potential to reconstruct the drizzle mode of the DSD even when it is outside the measurement range of a given instrument. The effects of the reconstruction on bulk rainfall variables are examined.

1.7 POLARIMETRIC RADAR RETRIEVALS OF LOWER ORDER DSD MOMENTS: CASE STUDIES USING CSU-CHILL RADAR

V. N. BRINGI[1], T. RAUPACH[2], M. THURAI[1], P. C. KENNEDY[1], A. BERNE[2]
[1]Colorado State University, Fort Collins, CO, USA
[2]École Polytechnique Fédérale de Lausanne, Switzerland
bringi@colostate.edu

Polarimetric radar-based retrieval of rain rate which is proportional approximately to the 3.67^{th} moment of the DSD ($M_{3.67}$) has now reached a mature stage with many operational systems at S-, C- , and X-bands. The retrieval of lower order moments (M_0-M_3) which are important in numerical modeling of collisional, break-up and evaporation processes has largely been neglected by the radar community as the radar observables are strongly dependent on the higher order moments ($M_{4.5}$-M_6). Most algorithms are based on the gamma DSD model with the shape parameter set a priori at $\mu \approx 3$ or empirical (μ-Λ) polynomials based on disdrometer data (Parsivel, 2DVD or Joss) which due to resolution or sensitivity issues cannot measure the concentration of the small drops (D<0.5-0.7 mm) which control the lower order moments. Thus, the basis for comparing or evaluating microphysical schemes that predict M0 and M3 with radar retrievals needs more research, leading the way to data assimilation in numerical models in the future.

In this study we use and extend the approach of Raupach and Berne (Atmos. Meas. Tech., 10, 2017) to retrieve the lower order moments. The method developed at X-band uses the double-moment normalization of the DSD using two reference moments [M_3 and M_6] along with the intrinsic shape h(x) where $x=D/(M_{63})^{1/3}$ and $M_{63}=M_6/M_3$. The h(x) is assumed to be generalized gamma (GG) with two shape parameters (μ,c). The M6 is retrieved using radar Zh whereas M3 is retrieved using [Zdr, Kdp] with (μ,c) based on average h(x) assumed to be "stable". Essentially, the DSD variability with rain rate for example, is attributed mostly to variability in [M_3,M_6] and much less due to h(x) deviating from its stable shape. The caveat is that h(x) be measured over the entire size range from drizzle sizes (0.1-0.7 mm) to maximum drop sizes (<8 mm) which cannot be done with a single disdrometer. Once [M_3,M_6] are retrieved the lower order moments are derived as power laws of [M_3,M_6] with (μ,c) based on theoretical GG DSD model.

We use the CSU-CHILL radar which is a dual-band system (S/X) and collocated high resolution (50 microns) Meteorological Particle Spectrometer and moderate resolution (170 microns) 2D-video disdrometer located at 13 km range. This combination of disdrometers accurately measures both the small and large drop ends as well as the frequently-observed plateau region in between. We propose to use the X-band measured [Z_h,Z_{dr},Kdp], as well as S-band [Z_h,Z_{dr}] and X-band [K_{dp}] with the dual-band method chosen to avoid attenuation-correction uncertainties, especially for two convective events chosen as case-studies (23 May 2015 multi-cell storm with >55 dBZ echoes and 19 August 2015 which was a combination of stratiform rain and rain showers).

1.8 VERTICAL VARIABILTIY RAIN DROP SIZE DISTRIBUTION FROM DISDROMETER AND MICRO RAIN RADAR MEASUREMENTS

E. ADIROSI[1,2], A. TOKAY[3,4], N. ROBERTO[2], E. GORGUCCI[2], M. MONTOPOLI[2], L. BALDINI[2]

[1]Consorzio Nazionale Interuniversitario per le Telecomunicazioni (CNIT), Italy
[2]CNR - Institute of Atmospheric Sciences and Climate, Rome, Italy
[3]Joint Center for Earth Systems Technology, University of Maryland Baltimore County, Baltimore, MD
[4]NASA Goddard Space Flight Center, Greenbelt, Maryland
elisa.adirosi@artov.isac.cnr.it

Vertical variability of rain drop size distribution (DSD) affects in many ways the accuracy of radar quantitative rainfall obtained by radar. For conventional scanning weather radar, rain estimation is obtained at a certain altitude that depends on the radar elevation angle and on the distance from the radar. If rain at ground is the measurement of interest, radar rainfall estimate suffers from the time-height ambiguity between the altitude of radar measurement and rainfall at the ground. Although gauge adjustment is often used to mitigate this issue, the knowledge of the vertical variability of the precipitation between the height of the radar measurements and ground is a key factor to address this issue. Moreover, variability of DSD within the radar resolution volume (typically more extended along the vertical than along the range) affects in different ways dual-polarization measurements that are associated to a radar sampling volume and, in a non-trivial way, the rain estimates obtained from them. As the distance from the radar increases, the radar sampling volume increases and assuming homogeneous beam filling becomes likely incorrect. This condition is known as non uniform beam filling (NUBF). For satellite borne radar, such as the GPM Dual Frequency Precipitation Radar, the impact of NUBF within the footprint has recently been addressed. However, assessing NUBF along the vertical is also needed, being a potential source of uncertainty.

To investigate vertical variability of rain, vertically pointing radars are a valuable tool, being able both to support investigations of the variability of precipitation within the radar sampling volume, and to fill the gap between the ground level and the first available radar elevation. Among these systems, the Micro Rain Radar (MRR), 24 GHz system using the continuous-wave frequency-modulated scheme, has become popular both for fixed installations and for the use in field campaigns where it is often co-located with disdrometers. A Doppler velocity based method for determining vertical profiles of drop size distributions and, consequently, DSD moments taking advantage from the availability of collocateddisdrometer measurements have been developed. Data collected by MRRs and co-located disdrometers are available from different field campaigns. For the GPM Ground Validation Iowa Flood Studies (IFloodS) field experiment an interesting and unique set up was adopted: in three different sites, clusters of co-located Parsivel2, 2D Video Disdrometer and MRR (with 35 m vertical resolution) were almost aligned along a radial at different distances from the NASA NPOL radar. This set-up has been used first to evaluate MRR drop size distribution estimates closer to the ground with respect to available disdrometers. Then MRR data, resampled onto the NPOL resolution volumes are

used to evaluate the uncertainties of the different dual-polarization measurements along the vertical. The vertical variability of DSD and integral rainfall parameters within the MRR coverage is finally investigated to provide some insight on the variability of the rainfall microphysical characteristics within about 1 km above the ground in the different precipitation regimes.

1.9 IMPACT EVALUATION OF VERTICAL AIR VELOCITY ON THE MICROPHYSICAL RETRIEVALS BY K BAND RADAR PROFILERS USING COMBINED UHF AND S BAND PRODUCTS

M. MONTOPOLI[1,2], E. ADIROSI[13], N. ROBERTO[1], L. BALDINI[1]

[1]Institute of Atmospheric Sciences and Climate (ISAC)- CNR Rome, Italy
[2]Center of Excellence in Telesensing of Environment and Model Prediction of Severe Events, University of LAquila, Italy
[3]RaSS-CNIT, Galleria G.B. Gerace 18, Pisa, Italy
m.montopoli@isac.cnr.it

Doppler microwave radar profilers are recognised as key tool because they give new insights on microphysical precipitation processes. The backscattered power signal returned by these systems when they observe falling particles, is distributed in a Doppler velocity domain (Doppler spectrum), which covers the set of velocities of the falling particles. The amplitude of the Doppler spectrum in each Doppler bin depends by the particles size, composition and orientation. Thanks to the relationship between diameter and particle velocity, Doppler spectrum brings information of the falling particle size distribution (PSD). In still air, the retrieved PSD can suffer by system calibration, beam broadening and, eventually, radome attenuation. In the presence of turbulence effects and vertical air motion Doppler spectrum broadening and shifting drastically compromises the final PSD retrieval.

In [1], a first quantification of the impact of updrafts on estimated concentration of raindrops, was given. Few more recent studies proposed solutions for compensating of Doppler widening and shift contamination. Recently, [2] exploited the differences in the retrieved characteristic fall velocity closest the surface from K-band (24.24 GHz) radar and that from a collocated ground disdrometer to compensate for Doppler shift due to vertical air velocity and assuming a constant propagation of that velocity shift along the vertical column. Instead, [3] uses a multi-frequency approach at Ka and W band (35-94 GHz) for retrieving rain PSD simultaneously with the vertical wind speed, the air density, and the air broadening caused by turbulence and wind shear.

However, as far as the authors have been able to ascertain, none of the previous studies used collocated air velocity measurements from wind profilers to support their conclusions. In this work, we want to verify the impact of vertical air motion based on measurements collected by a K-band vertically pointing Doppler radar and microphysical estimation obtained from them by using air velocity from a product that combine measurements from UHF (449 MHZ) wind profiler and S band (2.835 GHz) radar profiler. Numerical simulations at K-band will be also used to corroborate our findings. The mid-latitude continental convective clouds experiment (MC3E) which took place in Oklahoma, during April-June 2011 [4], gave us the unprecedented opportunity to analyse simultaneous measurements from NASA K-band Micro Rain Radar [6], Parsivel disdrometer and NOAA S-band, UHF radar profilers [5], which were installed in Southern Great Plains Central Facility.

References

[1] Atlas, D. et al., (1973) Doppler radar characteristics of precipitation at vertical incidence, Rev. Geophys., 11.

[2] Adirosi E. et al.(2016) Improvement of vertical profiles of raindrop size distribution from micro rain radar using 2D video disdrometer measurements , Atmo. Res. 169

[3] Tridon, F. et al. (2015) Dual-frequency radar Doppler spectral retrieval of rain drop size distributions and entangled dynamics variables, J. Geophys. Res. Atmos., 120

[4] Jensen M. P. et al. (2016) The midlatitude continental convective clouds experiment (MC3E), BAMS

[5] Williams, C. R.(2012) Vertical air motion retrieved from dual-frequency profiler observations, J Atmos OceanTech. 29

[6] Petersen W. A. et al. (2012) GPM ground validation NASA micro rain radar.

1.10 A MICROPHYSICAL RETRIEVAL FOR THE DUAL-FREQUENCY PRECIPITATION RADAR

K. MROZ[1], A. BATTAGLIA[1]

[1]National Centre for Earth Observation, UK
[2]University of Leicester, UK
kamil.mroz@le.ac.uk

The representation of microphysical processes in ice clouds is a longstanding problem for a modelling community. Remote sensing techniques can help in better constrain parametrization of ice microphysics in models. This paper presents a microphysical retrieval for stratiform regions suited for the Dual-frequency Precipitation Radar (DPR) on board of the Global Precipitation Measurement mission core satellite. The DPR is well suited for the retrieval of bulk properties of hydrometeors thanks to its dual-frequency capabilities. Moreover, low spatial variability of stratiform rain regions minimizes the problem of non-uniform beam filling. The algorithm accounts for the large degree of uncertainty in ice particle scattering properties and utilizes the measurements at both DPR channels accompanied by their corresponding path integrated attenuation estimates for producing a physically consistent three-dimensional structure of storms. The retrieved parameters include the mean mass weighted volume diameter and the water content of both rain and ice particles. Uncertainties in the retrieval are greatly reduced by incorporating statistical relationships between rain parameters gathered during GPM ground validation campaigns. By exploiting the flux preservation constraint, the information on liquid particles is transferred above the melting level. The radiometric consistency of the retrieval has been tested against the GPM Microwave Imager measurements. The performance of the retrieval is presented with a number of case studies.

1.11 CHARACTERIZATION OF THE VERTICAL PROFILES OF DUAL-POLARIZATION RADAR OBSERVATIONS IN AND ABOVE THE BRIGHT BAND AT S, C AND X-BANDS

CLOTILDE AUGROS[1], GUY DELRIEU[2], NAN YU[1], NICOLAS GAUSSIAT[1]

[1]Météo France, Centre Météorologique Radar, Toulouse, France
[2]Institut des Géosciences et de l'Environnement (IGE), Grenoble, France
clotilde.augros@meteo.fr

In this study, the vertical evolution of dual-polarization radar variables in and above the bright band is examined for a number of cases at S, C and X-bands, using the Meteo France operational radars. The behaviours of the mean profiles of reflectivity at horizontal polarization Z_h, differential reflectivity Z_{dr}, copolar cross-correlation coefficient hv, and specific differential phase shift K_{dp} are interpreted by considering the microphysics of precipitation.

In particular, the profiles are analysed as a function of hydrometeor fall speed estimated using the Doppler radial velocity at 90° elevation angle (measured by the same or by neighbouring radars). The hydrometeor fall speed is a good indicator of the occurrence of riming: unrimed crystals or aggregates rarely fall faster than 1.5 m/s while rimed particles usually fall at speeds from 1.5 to 2.5 m/s (e.g. Vogel et al, 2017).

To complement the radar observations, Micro Rain Radar (MRR) observations of vertical velocity available from the IGE MRR deployed in Grenoble, close to the Moucherotte X-band radar, are used. In-situ aircraft observations (liquid water content, median drop diameter and temperature) close to the Plabennec C-band radar are also examined, to help infer the presence of supercooled liquid water.

For all the cases, the performance of the Meteo France Hydrometeor Classification Algorithm (HCA: Al Sakka et al, 2013) will be evaluated and improvements to this algorithm for stratiform precipitation cases will be considered, taking into account the vertical distribution of the radar variables.

References

Al-Sakka, H., A. Boumahmoud, B. Fradon, S.J. Frasier, and P. Tabary, 2013: A New Fuzzy Logic Hydrometeor Classification Scheme Applied to the French X-, C-, and S-Band Polarimetric Radars. J. Appl. Meteor. Climatol., 52, 2328-2344, https://doi.org/10.1175/JAMC-D-12-0236.1

Vogel, J.M. and F. Fabry, 2017: Contrasting polarimetric observations of stratiform riming and non-riming events. J. Appl. Meteor. Climatol., https://doi.org/10.1175/JAMC-D-16-

1.12 VERTICAL PROFILE OF REFLECTIVITY FROM K-BAND RADAR OBSERVATIONS IN EAST ANTARCTICA

C. DURAN-ALARCON[1], A. BERNE[2], B. BOUDEVILLAIN[1], C. GENTHON[1], N. SOUVERIJNS[3], N.P.M. VAN LIPZIG[3]

[1]Institut des Géosciences de l′Environnement, Universié Grenoble Alpes, Saint-Martin d′Hères, France

[2] Laboratoire de Télédétection Environnementale, École Polytechnique Fédérale de Lausanne, Lausanne, Switzerland

[3]Afdeling Geografie en Toerisme, Katholieke Universiteit Leuven, Leuven, Belgium

claudio.duran-alaron@univ-grenoble-alpes.fr

K-band micro rain radar (MRR) systems have been deployed to monitor precipitation in east Antarctica, at the Dumont d′Urville station (DDU), Adélie Land, and at the Princess Elizabeth (PE) station in Queen Maud Land. At DDU, two such MRRs are complemented with a precipitation weighing gauge, disdrometers and LIDAR observations. In November 2015, a first MRR (MRR1) was installed inside of a radome with a vertical resolution of configuration of 100 m. A second MRR (MRR2) was deployed in January 2017, outside of the radome and it was configured with the same parameters than MRR1 to evaluate the radome attenuation. Afterwards, the vertical resolution of MRR2 was changed to 15 m to increase the resolution of observation near to the surface. At PE, a MRR is deployed since January 2012, later complemented by a disdrometer and a ceilometer. Equivalent reflectivity factor (Ze), fall speed (W) and Doppler spectrum width (σ) were obtained using the method proposed by Maahn and Kollias (2012). The post-processing method was adapted to filter remaining noise that is recurrent in these type of equipment, based on the frequency of observations and on the Doppler spectrum. Results show that sublimation of the snowfall particles near the surface has an important impact on the structure of the VPR. The maximum Ze occurs within the first 1.5 km near to the surface and often shows a decrease due to the effect of the sublimation induced by the dry katabatic winds. This effect is stronger at DDU than PE. At the same time, strong katabatic winds produce blowing snow events that are frequent in winter and can be observed only using MRR2 that covers the first 450 m with high resolution, since both MRRs present a blind zone within the two lower height bins.

1.13 INVESTIGATION OF ICE MICROPHYSICS USING SIMULTANEOUS MEASUREMENTS AT C- AND KA-BAND

M. HAGEN[1], F. EWALD[1], S. GROSS[1], Q. LI[1],B. MAYER[2], T. ZINNER[2]

[1]Deutsches Zentrum für Luft- und Raumfahrt, Institut für Physik der Atmosphäre, Oberpfaffenhofen, Germany

[2] Meteorologisches Institut München, Ludwig-Maximilians-Universität München, Münich, Germany

martin.hagen@dlr.de

The synergy of radars with different wavelength provides additional information on the physics of clouds and precipitation. While C-band weather radars are not sensitive enough to detect small ice and water particles, almost no attenuation is observed for weak to medium precipitation. On the other hand, Ka-band cloud radars are sensitive to detect small ice and water particles. However, attenuation limits the ability to perform measurements in rain.

Synchronous RHI scans are being performed with DLRs dual-polarization C-band radar POLDIRAD and a Mira-36 Ka-band cloud radar operated at the University of Munich. The two radars are separated by a distance of about 23 km and have an overlapping measurement range of about 30 km. Both reflectivity measurements agree quite well in the reflectivity range between -10 to 10 dBz. For lower reflectivity values the measurements with the C-band radar are limited to short ranges. At reflectivity values above 15 dBz attenuation effects at Ka-band are visible. Interestingly in ice clouds the overlapping region of both radars is quite large and the C-band radar has a high detection efficiency in ice clouds. This gives evidence on the presence of larger ice particles were the backscatter is sufficient high enough due to the D^6 dependence.

The high sensitivity on ice particles in the combination of both frequencies allows for the investigation of the initiation of precipitation through the ice phase - the cold rain process. The dual-wavelength measurements will provide an enhanced hydrometeor classification and enable for the retrieval of ice microphysics parameters like effective radius and ice water content IWC. Other processes observable will be drizzle formation, cloud glaciation, distinction between depositional growth of small ice particles and onset of quicker ice particle growth into precipitation sized particles by aggregation, and initiation of first precipitation at the surface.

1.14 FINGERPRINTS OF PRECIPITATION PROCESSES REVEALED BY UNSUPERVISED CLASSIFICATION OF PROFILES OF POLARIMETRIC RADAR VARIABLES

J. TIIRA[1], D.N. MOISSEEV[1,2]

[1] Institute for Atmospheric and Earth System Research / Physics, University of Helsinki, Finland

[2] Finnish Meteorological Institute, Helsinki, Finland

jussi.tiira@helsinki.fi

The broad spectrum of snow particle types with different microphysical properties pose a challenge to radar retrievals of e.g. precipitation rate. Due to the typical sparsity of radar networks, often a large fraction of observations of precipitation particles originate from above the melting layer even with low elevation angles. The ability to automatically deduce snow particle types or the growth processes that generate them would have a great potential in improving such retrievals. In this study we develop an unsupervised classification method of dual-polarization radar profiles to facilitate the detection of growth processes along a vertical column.

The size, shape and degree of riming of a growing snow particle depend mainly on ambient temperature, supersaturation and presence of liquid water. As these ambient conditions are not constant through a vertical column, the significance of different growth processes vary along the paths of growing snow particles. Although, with remote sensing techniques we cannot directly measure which growth processes are taking place in a vertical column, dual polarization radar measurements of vertical columns can be viewed as containing fingerprints of these processes. Currently there are studies of individual features in the profiles, e.g. enhanced values of specific differential phase (K_{dp}) or differential reflectivity (Z_{dr}), but no attempts have been made so far to create objective documentation of such profiles.

In the present study, an automated classification method for vertical profiles of dual polarization radar observations is developed using profiles derived from RHI scans in southern Finland. The proposed method is based on k-means clustering of dimensionally reduced combination of vertical profiles of equivalent reflectivity factor (Z_e), Z_{dr} and K_{dp}. Since snow growth processes are of the main interest, separate approaches are taken for the profile classification in rain and snow. In rain, only the parts of the profiles that are above melting layer are used as input to the classification process. In case of snowfall, the whole profiles are used and ground temperature is included as an extra classification parameter.

We look at vertical profiles over Hyytiälä forestry station in Juupajoki, Finland using Ikaalinen weather radar which is located 64 km west from the station. Measurements have been performed during the Biogenic Aerosols Effects on Clouds and Climate field campaign in early 2014, and the winter of 2014/2015. Preliminary results show that the method can be used for producing profile classification schemes with distinct, physically meaningful classes many of which represent characteristic precipitation properties such as liquid water equivalent (LWE) precipitation rate, prefactor of Z_e-snowrate power-law relation and degree of riming. In this investigation we link the classification results and class characteristics to precipitation properties and show how this can be used for identifying snow growth processes.

1.15 CHARACTERISATION OF THE MELTING LAYER VARIABILITY IN THE SWISS ALPS USING POLARIMETRIC X-BAND RADARS

F. VAN DEN HEUVEL[1,2], M. GABELLA[2], A. BERNE[1]

[1]EPFL, Lausanne, Switzerland

[2]MeteoSwiss, Locarno Monti, Switzerland

floortje.vandenheuvel@epfl.ch

The melting layer (ML) is a typical feature in radar observations of the vertical structure of stratiform precipitation and designates the transition region from solid to liquid precipitation. The well-known signature in the (polarimetric) radar variables which characterises the ML, with a notable increase in the horizontal reflectivity factor (ZH) and a reduction of the copolar correlation coefficient (Rhohv), facilitates its identification with automatic detection algorithms. The ML is often assumed spatially and temporally homogeneous by algorithms for quantitative precipitation estimation (QPE) and vertical profile of reflectivity (VPR) correction. However as the VPR shape is dependent on both microphysical processes and the vertical profile of temperature, this assumption may not be accurate for wintertime precipitation in an orographic context. As yet, the spatial variability of the ML remains poorly documented, and this work presents a method based on the Fourier transform for the quantification of the variability of the ML at various spatial and temporal scales. The proposed method can accurately and concisely describe the the spatial variability of the ML and can therefore also be used as a tool for comparison of variability between datasets. In the context of this research the method has been applied to datasets from two measurement campaigns with the same radar; one in the Spring of 2014 on the densely populated Swiss plateau and a second one in the Winter of 2016-2017 in the main valley of the Swiss Alps. A melting layer detection algorithm was first applied to the range-height indicator (RHI) scans of the two campaigns and approximately 2000 scans with sufficiently long melting layers were retained for further analysis with the Fourier transform method. Consistent with previous studies, the statistical distributions of the values of the polarimetric variables within and around the ML showed very little differences between the datasets. The Fourier analysis on the other hand, indicated a higher relative importance of variability at the smaller spatial scales in the case of the Alpine dataset. The same method was also applied on the vertical scans of the radar in order to study the temporal variability of the ML and to assess the spatio-temporal coherence of the ML variability.

1.16 IMPACT OF RIMED AND UNRIMED SNOW ON SNOWFALL RETRIEVALS AT X, KA AND W BAND

M. T. FALCONI[1], A. VON LERBER[2], D. ORI[3], F.S. MARZANO[1], D. MOISSEEV[2,4]

[1]Department of Information Engineering, Sapienza University of Rome, Italy and CETEMPS, LAquila, Italy
[2]Radar Science, Finnish Meteorological Institute, Finland
[3]Institute for Geophysics and Meteorology, University of Cologne, Cologne, Germany
[4]Department of Physics, University of Helsinki, Finland
martatecla.falconi@uniroma1.it

The correlation between the snowfall rate S and the radar equivalent reflectivity factor Z_e is challenging due to their dependence on the microphysical properties of snowfall. The variability of the Z_e-S and S-Z_e relations at millimetre and centimetre wavelengths is largely affected by microphysical snow growth processes. When a Ze-S power-law relation is assumed, its coefficients depend on different parameters such as the snow type, degree of riming and aggregation, density and terminal velocity (e.g., Von Lerber et al., 2017). The Z_e-S relation is also strongly dependent on radar frequency since various electromagnetic wavelength are more sensitive to different parts of the particle size distribution (PSD).

The radar-based snowfall intensity retrieval at X, K_a and W band has been investigated in previous works (e.g., Falconi et al., 2018) in terms of Z_e-S relation using data from four snowfall events, recorded during the Biogenic Aerosols Effects on Clouds and Climate (BAECC) campaign in Finland. The dataset was divided in rimed and unrimed snow on a daily basis using the total liquid water equivalent (LWE) and the minimum and maximum temperature for each event as an indicator of riming occurence. This classification highlighted two different Z_e-S relations for rimed and unrimed snow on temporal scales larger than few minutes.

In this work, the four case studies of the 2014 winter from BAECC are used to illustrate the impact of the microphysical processes on the snowfall retrieval every 5 minutes. This time-window is selected to average data in order to avoid spurious results and detect changes in the prevailing particle habit or type. Here, we firstly apply a more accurate snowfall classification based on quantification of the riming effect using the retrieval of the rimed mass fraction (FR), as in Moisseev et al., 2017. A particle video imager, the NASA Particle Imaging Package (PIP) is used to compute the particle volume flux to retrieve the FR. An independent evaluation of the proposed approach is obtained by estimating particle-effective liquid water paths (ELWP) and comparing these to microwave radiometer (MWR) observations. The two-channel MWR is located on the BAECC site 20 m away from PIP.

Based on the new classification approach, the estimation of Z_e-S coefficients is carried out by dividing the 5-minute periods to rimed and unrimed snow. The reflectivity Z_e is measured by the AtmosphericRadiation Measurement (ARM) vertically-pointing cloud radars operating at X, K_a and W frequency bands, collocated with the other measuring instruments. S is derived from PIP using the measured mass, velocity, particle size distribution and liquid water density. To improve the estimation of S, the Z_e-S relation is compared with a direct S-Z_e regressive relation. Defining the error as the difference between S estimated from radars and observed

from PIP, the uncertainty of the two approaches is evaluated in terms of the root mean square error (RMSE) and normalized RMSE. Improvements in the snowfall retrieval and classification at multi-frequency are discussed proposing two sets of coefficients for rimed and unrimed snow for both Z_e-S and S-Z_e relations.

1.17 A PROBABILISTIC POLARIMETRIC RADAR FORWARD MODEL FOR SMALL ICE PARTICLES

ROBERT S. SCHROM[1], MATTHEW R. KUMJIAN[2]

[1]The Pennsylvania State University, United States
[2]The Pennsylvania State University, United States
rss5116@psu.edu

Polarimetric radar observations provide information about the physical properties of ice particles; this information is valuable for better understanding cloud and precipitation systems, as well as evaluating microphysical model simulations of such systems. Comparisons of polarimetric radar observations and microphysical model output require a forward model to convert the physical properties simulated within the microphysical model to the polarimetric radar observables.

In the most detailed microphysical models, ice particles are characterized with a maximum dimension, an aspect ratio, and a bulk effective density; these properties must also be used to determine the scattering properties of the ice crystals. Frequently, scattering of these ice crystals is represented by homogeneous, bulk-density spheroids, with the assumption that the ice particle mass is evenly distributed throughout its volume. The scattering is then calculated (for particles small relative to the radar wavelength) using the Rayleigh approximation with an effective dielectric constant that approximates a mixture of ice and air.

However, this method often underestimates the values of the polarimetric radar quantities. For example, errors in differential reflectivity (ZDR) can be up to 4.5 dB for low-density, and low-aspect-ratio branched planar ice crystals. Calculations with numerical techniques such as the Discrete Dipole Approximation (DDA) accurately capture the scattering of ice crystals with detailed shapes but require relatively large computational resources, and provide no estimate of the uncertainty in scattering due to the uncertainty in the assumed shape.

To address these issues, an analytical forward model for the polarimetric radar variables is developed that also provides estimates of the uncertainty in the radar variables due to the ambiguity in ice crystal structure for a given effective density. This forward model was generated using several thousand DDA calculations for a variety of realistic ice crystal shapes, sizes, and aspect ratios. The scattering of each realistic ice crystal was then assumed to be represented by an equivalent solid-ice spheroid. This mapping from model-predicted ice particle properties to solid-ice spheroids is performed analytically using fits of the changes in maximum dimension and thickness as functions of effective density and aspect ratio. The scattering properties are then calculated for the equivalent solid-ice spheroids using the Rayleigh approximation. The variability in the equivalent solid-ice spheroids for a given maximum dimension, aspect ratio, and effective density is then used to estimate uncertainty in each of the radar variables due to the natural variability in ice particle structure.

Comparisons of the radar variables calculated with DDA and with the analytical forward model show negligible biases in the backscatter cross-section, Z_{DR}, and specific differential phase. Forward simulations of the radar variables from microphysical model output are more consistent with radar observations than the

Rayleigh approximation for homogeneous, reduced-density spheroids, where low biases in these variables occur. These improvements in realistically capturing the scattering of natural branched planar ice crystals and estimates of the uncertainty in the radar variables due to structural variability will allow for retrievals of the physical properties of ice particles from radar observations.

1.18 WHY THE GENERALIZED GAMMA? - AN ANSWER BASED ON MEASUREMENTS WITH METEOROLOGICAL PARTICLE SPECTROMETER AND 2D VIDEO DISDROMETER

M. THURAI[1], V. N. BRINGI[1], P. N. GATLIN[2], W. A. PETERSEN[2], M. WINGO[3]
[1]Colorado State University, Fort Collins, CO, USA
[2]NASA Marshall Space Flight Center, Huntsville, AL, USA
[3]University of Alabama Huntsville, Huntsville, AL, USA
merhala@colostate.edu

The generalized gamma (GG) formulation for representing rain and ice particle size distributions has been considered by several researchers in the past 15 years. From theory the GG form is mathematically sound and has the following desired properties: (a) it reduces to standard gamma, exponential, and Weibull forms (which are special cases) and as a limiting case to the log-normal form, (b) any power law of drop diameter (D) such as mass or mass flux also falls in the GG form and (c) it maximizes relative entropy under moment constraints (Wu and McFarquhar, private communication). The DSD formulation used herein is based on double-moment normalization using the 3^{rd} and 4^{rd} moments as the reference moments (M_3,M_4) and the intrinsic shape of the normalized distribution h(x) where x=D/D_{43} is the scaled diameter and D_{43} (i.e., mass-weighted mean volume diameter, Dm′) is the ratio of M_4 to M_3. The h(x;μ,c) is chosen of the gamma form with two shape parameters (μ,c). Thus, N(D) is expressed in compact form as N(D)=M_3/D_{43}^4 h(x; μ,c)=N_0'h(x; μ,c). This form has the advantage that any moment of the DSD can be expressed as power laws of the two reference moments and (μ,c); in particular the lower order moments (M_0-M_2) which are involved in modeling microphysical processes such as coalescence and break-up which control the DSD shape at the small drop and large drop ends as well as the plateau region in between. Most currently available disdrometers cannot accurately measure the small drop end (D< 0.5-0.7 mm) due to poor resolution and sensitivity issues.

In this study, we consider measurements of rain drop size distributions (DSD) using collocated high resolution (50 microns) Meteorological Particle Spectrometer and moderate resolution (170 microns) 2D-video disdrometer from two different rain climatologies (Greeley, Colorado, and Huntsville, Alabama, USA). The combination of the two instruments yields what we term as the "full" DSD spectra, e.g. over 1-minute, covering the size range from 100 microns to large rain drops whose shape cannot generally be represented by the standard gamma (SG) model, but requires the additional flexibility of the GG model, with the two abovementioned shape parameters (μ,c). With (M_3,M_4) as reference moments, the SG value of c=1 was not reached for majority of the cases, even when considering 0.6<c<1.4. This finding also highlights a problem with DSD assumptions in the rainfall retrieval algorithm employed for the Global Precipitation Measurement mission Core satellite.

Examples of events will include light precipitation, stratiform rain and convective rain events as well as outer bands of hurricane Irma and tropical storm Nate. The latter two are special cases, which fortuitously had crossed our instrumentation site. Evidence for equilibrium-shaped DSDs will also be discussed by comparing

measurements with numerically modeled DSDs under the condition of balance between coalescence and break-up processes. We demonstrate that most of the DSD variability, for example with rain rate can be attributed to variability in N'_0 and D'_{43} allowing for identification of number-controlled or size-controlled DSDs.

1.19 MULTI-FREQUENCY RADAR RETRIEVAL OF SNOWFALL MICROPHYSICS

J. LEINONEN[1,2], M. D. LEBSOCK[1], O. O. SY[1], S. TANELLI[1], B. DOLAN[3], R. J. CHASE[4], J. A. FINLON[4], D. MOISSEEV[5,6], A. VON LERBER[6]

[1]Jet Propulsion Laboratory, California Institute of Technology, Pasadena, California, USA

[2]Joint Institute for Earth System Science and Engineering, University of California, Los Angeles, California, USA

[3]Department of Atmospheric Science, Colorado State University, Fort Collins, Colorado, USA

[4]Department of Atmospheric Sciences, University of Illinois at Urbana-Champaign, Urbana, Illinois, USA

[5]Department of Physics, University of Helsinki, Helsinki, Finland

[6]Radar Science, Finnish Meteorological Institute, Helsinki, Finland

jussi.s.leinonen@jpl.nasa.gov

We have developed a method for retrieving the microphysical properties of falling snow from multi-frequency radar measurements. The method uses recent advances in simulating the radar reflectivity of snowflakes as the basis of its forward model. The microphysical properties are retrieved using a Bayesian approach that does not require the use of iterative algorithms; this enables the retrieval to be performed quickly and robustly. An exponential particle size distribution and a power-law mass-dimensional relationship are assumed. The attenuation correction scheme takes advantage of the availability of multiple frequencies, allowing stable correction of reflectivity at frequencies affected by attenuation.

Plentiful test data with collocated multi-frequency radar measurements is available from recent field campaigns. We tested the algorithm using triple-frequency radar data available from the OLYMPEX/RADEX field campaign. This dataset contains collocated airborne radar measurements collected by the NASA APR-3 radar at Ku band (13.4 GHz), Ka band (35.6 GHz) and W band (94 GHz). We compared the results to hydrometeor identification using the NPOL radar, which was also present at the campaign, and was often overflown by the DC-8 aircraft carrying the APR-3. We also assessed the retrieval performance using the in situ data collected by the University of North Dakota Citation aircraft. Using these data, we examined the sensitivity of the algorithm to the a priori assumptions and to the number of available radar frequencies.

The results show that multi-frequency radars have a substantial advantage over single-frequency radars for constraining snowfall microphysics, especially the size of snowflakes. The benefits of a third frequency are more limited, but three-frequency radars can be used to detect occurrences of graupel, which has a particularly high density. Among the three frequencies, there does not seem to be any single one that would be preferable from an information content perspective, nor is any of the dual-frequency combinations particularly better than any other. Even with the triple-frequency configuration, the retrieval results are somewhat sensitive to the prior assumptions; this emphasizes the importance of accurate climatological statistics for the microphysical parameters.

1.20 A POLARIMETRIC ANALYSIS OF ICE MICROPHYSICAL PROCESSES IN MELTING LAYERS OF WINTER STORMS, USING QUASI-VERTICAL PROFILES

E. M. GRIFFIN[1,2,3], T. J. SCHUUR[1,2], A. V. RYZHKOV[1,2]

[1]University of Oklahoma/Cooperative Institute for Mesoscale Meteorological Studies, Norman, Oklahoma, USA

[2]NOAA/OAR National Severe Storms Laboratory, Norman, Oklahoma, USA

[3]University of Oklahoma, School of Meteorology, Norman, Oklahoma, USA

erica.griffin@noaa.gov

Quasi-vertical profiles (QVPs) obtained from a large-scale database of U.S. WSR-88D radar data are used to document the polarimetric characteristics of the melting layer (ML) in cold-season storms with high vertical resolution and accuracy. A polarimetric technique to define the top and bottom of the ML is first introduced. Using the QVPs, statistical relationships are then developed to gain insight into the evolution of microphysical processes above, within, and below the ML, leading to a statistical polarimetric model of the ML that reveals characteristics that reflectivity data alone are not able to provide, particularly in regions of weak Z_H. Results reveal strong positive correlation between Z_H in rain (i.e., 0.3 km below ML) and Z_H in snow (i.e., 0.3 km above ML) and between maximum Z_{DR} in the ML and Z_{DR} in rain. Strong positive correlation is also observed between maximum K_{DP} and maximum Z_H in the ML; these are the first QVP observations of K_{DP} in MLs documented at S band. Strong negative correlation occurs between maximum Z_{DR} and minimum hv in the ML and between minimum hv in the ML and the corresponding enhancement of Z_H (i.e., $\triangle Z = Z_{Hmax}$ ZH_{rain}). Quantifying the Z(min(ρhv)) dependence is crucial for implementation of a polarimetric vertical profiles of rain (PVPR) technique designed to mitigate the impact of the ML contamination on QPE. The evidence of very large Z_{DR} (up to 4 dB) associated with lower Z_H (-10 to 20 dBZ) in the ML is documented in the situations when pristine, nonaggregated ice falls through it. Strong microphysically-driven connection between polarimetric signatures in the ML and aloft in the dendritic growth layer (DGL, between -10 and -20°C) and the temperature at the top of the cloud has been found. For example, "sagging" of the ML typically occurs during the periods of enhanced KDP in the DGL.

1.21 ICE MICROPHYSICS DURING OLYMPEX: COMPARISON BETWEEN REMOTE SENSING AND AIRBORNE IN SITU OBSERVATIONS

F. TRIDON[1], A. BATTAGLIA[1,2], R. CHASE[3], K. MROZ[2], J. TURK[4], S. TANELLI[4], S. NESBITT[3], J. LEINONEN[4], S. KNEIFEL[5]

[1]Department of Physics and Astronomy, University of Leicester, UK [2]National Center Earth Observation, University of Leicester, Leicester, UK

[3]Department of Atmospheric Sciences, University of Illinois at UrbanaChampaign, Urbana, Illinois

[4]Jet Propulsion Laboratory, California Institute of Technology, Pasadena, CA, USA

[5]Institute for Geophysics and Meteorology, University of Cologne, Cologne, Germany

ft57@le.ac.uk

While the majority of rainfall is generated via the ice phase over the mid-latitude, the microphysical characterisation of ice is still a challenge. Large uncertainties arise from the difficulty in directly measuring various critical microphysical parameters associated with ice particles, such as particle size distribution (PSD), particle mass-size and fall speedsize relationships, and particle habit and orientation. Riming strongly alters these properties and is known to be correlated with snow accumulation in mountainous areas.

Several recent studies have shown the ability of a triple-frequency radar combination to distinguish between rimed and fluffy aggregates. Such triple-frequency signatures can be reproduced by scattering models (e.g. Discrete Dipole Approximation or Rayleigh-Gans approximation) which take into account the non-homogeneous internal structure of snowflakes. Using one of these state-of-the-art scattering models, triple-frequency radar observations can be optimally matched for retrieving quantitative properties of ice (such as the mean mass diameter, D_m, and Ice Water Content, IWC), yet large uncertainties remain in the scattering properties.

The Olympic Mountains Experiment (OLYMPEX) which took place in Washington State (USA) during the winter 2015-2016 provides an unprecedented dataset for narrowing down this challenge, with coordinated flight transects of triple frequency radar and in situ measurements. Firstly, images of ice particles are used to qualitatively confirm the type of ice retrieved by the radar retrieval. Secondly, consistency between triple frequency signatures and ice properties derived from total mass and PSD in situ measurements is investigated. Finally, radar retrieved and in situ derived Dm and IWC are compared.

1.22 A FOUR YEAR LAGRANGIAN STUDY OF ISOLATED CONVECTION IN HOUSTON, TEXAS: USING PUBLIC DATA AND OPEN SOURCE CODE TO DESIGN A FIELD CAMPAIGN

S. COLLIS[1], R. JACKSON[1], M. PICEL[1], M VAN LIER-WALQUI[2], A. FRIDLIND[2]

[1]Argonne National Laboratory, USA
[2]NASA Goddard Institute of Space Studies, USA
scollis@anl.gov

Due to the role aerosols play in droplet and ice nucleation, to understand and accurately simulate wet convective processes in weather and climate models, aerosol cloud processes need to be understood. Similar to cloud seeding research, the greatest challenge in obtaining statistically meaningful data sets is the natural variability in non-aerosol related forcings. To overcome this, members of the Aerosol, Cloud, Precipitation, and Climate Working Group are proposing a deployment of radar and aerosol instrumentation to Houston, Texas. The Houston region is attractive for aerosol cloud studies as there is a natural variation of aerosol content due to the Houston metroplex and a constant flow of isolated towering cumulus systems that are weakly externally forced and therefore relatively more susceptible to aerosol variation. Radars are attractive owing to their ability to rapidly scan a large number of storm cells. In designing an experiment there are several questions that need to be answered: What is the best time of year to deploy to maximize observed cells? What are the prevailing propagation paths of isolated cells? How many cells can we observe over their full lifecycle (initiation to dissipation) as a function of maximum unambiguous range of a radar?

To answer this a four year study of data from the Houston NEXRAD radar (KHGX) was performed. The open source TINT (TINT Is NOT TITAN) package was used to calculate cell tracks and the Python ARM Radar Toolkit was used to retrieve cell statistics including the spatial properties of specific differential phase (K_{dp}) structures above the freezing level. This reduces a data set of several terabytes to several hundred megabytes allowing for quick statistical analysis. This presentation will showcase the processing and cell tracking techniques and present a full statistical picture of the nature of convection propagating off the Gulf of Mexico into the Houston region. Issues of NEXRAD samping and the impact on the spatial structure of K_{dp} will also be addressed.

1.23 LEVERAGING RADAR OBSERVATIONS TO PROBABILISTICALLY INFORM NEW CLASSES OF MICROPHYSICAL PARAMETERIZATION SCHEMES

M. VAN LIER-WALQUI[1], M. KUMJIAN[2], H. MORRISON[3],O. PRAT[4], J. TURK[4], K. RIEMEL[2], J. HARRINGTON[2] , A. JENSEN[3], R. SCHROM[2]

[1]CCSR Columbia University & NASA/GISS, USA
[2]Pennsylvania State University, USA
[3]National Center for Atmospheric Research, USA
[4]JNorth Carolina State University, USA
mv2525@columbia.edu

We present work on using profiling radar Doppler spectra and polarimetric radar to develop and constrain new classes of microphysical parameterization schemes, using Bayesian parameter estimation methodologies to robustly quantify scheme uncertainties. We are motivated by clear and persistent biases in existing microphysics schemes, as well as by the richness of profiling and polarimetric radar data. In one case, we develop a liquid (i.e. rain and cloud) microphysics scheme designed such that both its parameters and its structural complexity are capable of being constrained by observations. We present how such a constraint is implemented in an idealized framework, and will discuss opportunities and challenges with using real radar observations to inform the scheme's structure and sensitivities. We also show initial results from work combining polarimetric and profiling radar data to constrain ice microphysical processes of a particle property predicting ice microphysics scheme. We consider vapor growth, riming, and aggregation, and simulate observed cases where individual processes are considered the dominant source of hydrometeor property and size distribution evolution. Our model is coupled to a detailed ice scattering database capable of modeling the polarimetric radar signatures of combinations of diverse crystal habits. In all cases observational uncertainties are fed into the Markov Chain Monte Carlo parameter estimation framework that simultaneously constrains our model parameters and estimates their respective uncertainties.

1.24 ESTIMATION OF OBSERVATIONAL AND FORWARD-SIMULATOR UNCERTAINTIES IN THE CONTEXT OF MICROPHYSICAL STUDIES USING DOPPLER SPECTRA AND POLARIMETRIC RADAR OBSERVATIONS

M. VAN LIER-WALQUI[1], D. POSSELT[5], J. REMILLARD[6], M. KUMJIAN[2], H. MORRISON[3], O. PRAT[4], K. REIMEL[2], S. COLLIS[7], J. HARRINGTON[2], A. JENSEN[3], R. SCHROM[2]

[1]CCSR Columbia University & NASA/GISS, USA
[2]Pennsylvania State University, USA
[3]National Center for Atmospheric Research, USA
[4]North Carolina State University, USA
[5]NASA Jet Propulsion Laboratory, USA
[6]Stonybrook University, USA
[7]Argonne National Laboratory, USA
mv2525@columbia.edu

Use of polarimetric radar observations to improve our understanding of cloud microphysics is often best accomplished with the help of a dynamical model that accounts for the dynamic and thermodynamic evolution of the cloud system. However, such efforts are hampered by an inability to account for uncertainties associated with the comparison of simulated weather to that observed by radars or in situ observations. These uncertainties include, but are not limited to, initial and boundary condition uncertainties, inaccuracies in model numerical integration, and approximations in microphysics scheme. Here we focus primarily on the first and third sources of uncertainty. In the case of the first, we quantify uncertainties associated with the assumption of a steady-state in radar observations of the atmosphere — a common assumption in comparisons between observed quantities and idealized 1D or 2D atmospheric simulations. In the case of the third source, we consider the uncertainties that arise from: (a) the assumption of a particular functional form for the hydrometeor particle size distribution (e.g. gamma or exponential distribution) and, (b) the assumption of complex crystal shape for ice hydrometeors in the common case where the microphysics scheme assumes a simplified form (e.g. spheroids). We use large disdrometer databases of liquid drop size distributions, as well as extensive ice scattering libraries to perform these tasks. Quantification of these uncertainties is the first step in preventing the problem of over-fitting when estimating model microphysical quantities from radar observations.

1.25 AUTOMATIC DETECTION OF THE MELTING LAYER USING POLARIMETRIC RADAR PROFILER

M.T. BERNDSEN[1], C.M.H. UNAL[1], H.W.J. RUSSCHENBERG[1]

[1]Delft University of Technology, The Netherlands
m.t.berndsen@student.tudelft.n

On the one hand the melting layer (ML) is an unwanted effect in radar rainfall estimation. To counter this effect, several ML detection algorithms have been developed. On the other hand, for scientific purposes, it is interesting to better understand the characteristics of the melting layer. The current ML detection algorithms are primarily based on specific radar observable thresholds and are not always well suited for application with all radar types under all climatologic conditions. Some observables have a distinct signature with a horizontally oriented radar, while others are more pronounced with a vertically oriented radar. Some radars do not have the ability to measure the linear depolarisation ratio (LDR), while others do. These differences make it difficult to develop an algorithm which can be used more universally.

In this research work, such an algorithm is being investigated. The data of the Doppler polarimetric radar, TARA (Transportable Atmospheric RAdar), are used. Two elevations are considered, 90° and 45°. At first a thorough analysis of the radar observables under different circumstances using the ACCEPT (Analysis of the Composition of Clouds with Extended Polarization Techniques) campaign is being made. Then, a choice is made on the radar observables which are best suited for ML detection. Next, an algorithm is developed using the characteristics of the radar to optimally select the best suited observables. Finally, an entirely different approach on ML detection is made. Some first steps will be set in using image processing techniques to identify the ML or to improve the detection probability of the previously mentioned methods.

After the algorithms are developed, a measure of detection quality will be investigated to be able to analyse the detection performance of the algorithms.

1.26 THE HYMID PROJECT HYDROMETEORCLASSIFICATION IN THE ALPS

L. TCHLER[1], V. MEYER[1], R. KALTENBÖCK[2]
[1]Zentralanstalt für Meteorologie und Geodynamik (ZAMG), Austria
[2]Austro Control GmbH, Austria
lukas.tuechler@zamg.ac.at

In the last years, the weather radar network in Austria was upgraded to C-band dual-pol technology. On the basis of the dual-pol information, a hydrometeor classification will be developed to determine the precipitation type within the measuring volume. Special attention is given to (a) the detection of hail and the estimation of hail size, and (b) the estimation of the precipitation type which finally reaches ground level. The mostly alpine conditions in Austria, which complicate radar measurements on one side and frequently lead to substantial distances between the lowest radar beam and the surface on the other side, hereby pose an additional challenge.

The results shall finally improve the data quality as well as enable the generation of new radar products which improve downstream applications like weather warnings, weather forecasts and the analysis of precipitation amounts.

NWP data will be used to estimate the surface precipitation type from the measurements aloft. The benefit of Mode-S data to adjust NWP temperature profiles will be tested. Station data, spotter reports, insurance data and Mode-S data will provide comparative data to evaluate the results.

This work will be done within the three-year FFG project HYMID and is supported by the Austrian radar data provider Austro Control and the insurance companies Oberösterreichische Versicherung and österreichische Hagelversicherung.

An overview of the project with emphasis on the hail size estimation, the vertical hydrometeor type adaption, and the verification approach of the results will be presented.

1.27 A STUDY OF HEAVY AND PERSISTENT PRECIPITATION IN SW ENGLAND

A. BLYTH[12], Y. HUANG[2], L. BENNETT[12], D. DUFTON[3]

[1] National Centre for Atmospheric Science, UK
[2]School of Earth and Environment, University of Leeds, UK
[3]Swedish Meteorological and Hydrological Institute, Sweden
alan.blyth@ncas.ac.uk

Observations were made with three aircraft, a ground-based X-band radar (NXPol) and several other ground-based instruments during the COnvective Precipitation Experiment (COPE) in the southwest peninsula of England during the summer of 2013. Convergence lines form in the region as a result of colliding sea-breeze fronts. Convective clouds often develop along the lines sometimes resulting in flash flooding. The most infamous recent example occurred in Boscastle in August 2004. The flash floods and convergence lines have been studied using models and the UK Met Office (MO) network radars and rain gauges, but observations of the microphysics and dynamics of the systems had never been made until COPE.

Modelling results and observations of a quasi-stationary convective system on 3 August 2013 will be presented. Heavy precipitation persisted for several hours in a fairly localised region, although a flash flood did not occur. The measurements on this day were made with two research aircraft (University of Wyoming King Air and UK BAe 146), the NXPol radar, the MO network of radars and ground-based aerosol instruments. NXPol made PPIs with a volume return time of about 5 mins. The WRF model run at 400-m resolution and a detailed microphysics model were used to help interpret the observations. The interplay of the warm rain process, freezing of supercooled raindrops, growth and then melting of graupel particles and cloud-scale dynamics (multiple thermals) appears to be key to the intensity and persistence of the precipitation.

1.28 HYDROMETEOR CLASSIFICATION BY PORTABLE X-BAND POLARIMETRIC RADAR OF KOCHI UNIVERSITY

KOJI SASSA[1], KOTARO YOSHIMURA[2]
[1]Kochi University, Kochi, Japan
[2]Railtec Co., LTD, Osaka, Japan
sassa@kochi-u.ac.jp

Kochi prefecture faces on Pacific Ocean where the Kuroshio Current flows and its north boundary is Shikoku Mountains of more than 1500m. Then, many heavy rain events occur. Many heavy rain events are accompanied by lightning but sometimes without lightning. Some thunderstorms have many positive cloud-to-ground lightning events even in summer season. Therefore we need to clarify the structures of hydrometeor distribution in various kinds of thunderstorms. As the first step of our work to solve such problem, the present study aims to verify the availability of hydrometeor classification algorism for the portable Xband polarimetric radar in Kochi University.

We identified hydroclass type using hydrometeor classification method based on fuzzy logic (Kouketsu et al. 2015). In this method, raw data; received power (dBm),ϕ_{dp} (deg.) and ρ_{hv}, observed by PPI scans up to 16deg. in elevation angle are used for attenuation correction of polarimetric parameters, Z_h, Z_{dr}, K_{dp} and ρ_{hv}. Then we compared these values and their beta function in order to identify hydrometeor. We also used background temperature obtained from mesoscale model initial value provided from Japan Meteorological Agency. The data of hydrometeor classification were compared with the data obtained by a disdrometer and visual observation.

As the preliminary results, we identified snow and graupel in relatively low cloud of less than 5 km in top heights in snow day, 10 February 2017. The data obtained by the disdrometer also show the existence of same particles. We also observed dry graupel upper the level of -10 degrees Celsius in the developing stage of thunderstorm when the lightning was active. On the other hand, there are wet snow and wet graupel in the melting layer of the decaying thunderstorm.

1.29 MODELING CLOUDS AND PRECIPITATION IN ADÉLIE LAND, ANTARCTICA: POLAR-WRF SIMULATIONS VERSUS IN-SITU AND RADAR OBSERVATIONS

ETIENNE VIGNON[1], CHRISTOPHE PRAZ[1], JOSUÉ GEHRING[1], NIKOLA BESIC[1], ALEXIS BERNE[1]

[1] Environmental Remote Sensing Laboratory (LTE), École Polytechnique Fédérale de Lausanne (EPFL), Lausanne, Switzerland
etienne.vignon@epfl.ch

Despite recent satellite-based estimations, the amount of precipitation reaching the Antarctic surface and its contribution to the surface mass balance of the ice-sheet remain poorly constrained. In the austral summer 2015-2016, an intensive campaign of observation took place at Dumont d′Urville station, Adélie Land, to provide a better quantification of precipitation and insights into the microphysics of clouds and precipitating hydrometeors in this remote region. The campaign included in particular the deployment of a micro-rain radar (MRR) and an X-band polarimetric radar (MXPol).

The obtained dataset has already evidenced that riming is an active process even at those latitudes and that a significant part of the precipitation is sublimated by katabatic winds before reaching the ground surface.

In this poster, we aim to go a step further in the understanding of cloud and precipitation processes in the Antarctic periphery using numerical simulations carried out with the Polar-WRF atmospheric model. The model is first evaluated against the extensive observational dataset at Dumont d′Urville station. Sensitivity tests to microphysical parameterizations, external forcings and resolution are performed and the simulations can be directly compared with radar data by using the CR-SIM radar operator. This evaluation paves the way to a further usage of the model to figure out how the regional scale dynamics constrains and affects the microphysics and the amount of precipitation over Adélie Land.

1.30 LONG-TERM ANALYSIS OF REFLECTIVITY-RAINFALL RATE RELATIONSHIPS USING DISDROMETER DATA

DANIEL SANCHEZ-RIVAS[1], M. A. RICO-RAMIREZ[1]

[1] Department of Civil Engineering, University of Bristol, Bristol, United Kingdom
ds17589@bristol.ac.uk

Accurate precipitation rates constitute an essential input data for many hydrometeorological applications as a hydrological model based on precise rainfall estimation will reduce the uncertainty in the simulations of hydrological processes. There are different instruments available to measure precipitation; the rain gauge is the most worldwide used device as, despite the relative simplicity of this instrument, a description of the temporal distribution of rainfall (a very important characteristic) especially for large periods of time can be obtained. The advances in optical and electronic technologies have allowed the development of a variety of instruments based on different principles which can measure some other precipitation characteristics. In particular, the disdrometers can describe (among other variables) the size, shape, and fall velocity of precipitation particles, and in particular they measure the drop size distribution (DSD), which can be used to calibrate the Z-R relationship used to estimate rainfall rates (R) from radar reflectivity measurements (Z). In this work, long-term records of disdrometer measurements are analysed to examine the relation between the rainfall rate (R) and the reflectivity (Z). Up to ten years of data from two impact-type JossWaldvogel disdrometers located in the Chilbolton Facility in the UK were processed and then validated using rain gauges. The rainfall rate and the reflectivity were derived using the information available from disdrometers in order to determine parameters (a and b) of the power-law relationship $Z=aR^b$. Specific criteria were applied to the data as low-values of rainfall rate may affect the power-law regression. Four different settings in the calculation of power-law model parameters were applied to analyse the variability of the estimated values, allowing to assess the reliability of the linear and least-squares regression methods. As the Z-R relationships can be influenced by local weather, affecting the estimated-radar precipitation, the seasonal variability of the Z-R relationships is also analysed. The results indicate that the selection of the regression method has an impact in the estimated parameters of the Z-R equation.

1.31 TEMPORAL EVOLUTION OF PRECIPITATION RELATED MICROPHYSICAL PROCESSES BASED ON DUAL-POL DATA OF S-, X-, AND C-BAND DOPPLER RADARS

M. LUKACH[1,2], R. R. NEELY III[1,2], D. DUFTON[3]

[1] School of Earth and Environment, University of Leeds, UK
[2] National Centre for Atmospheric Science, University of Leeds, UK
[3] Swedish Meteorological and Hydrological Institute, Sweden
maryna.lukach@ncas.ac.uk

The aim of the work is to improve our understanding of high-impact extratropical winter-precipitation events by analysing polarised Doppler radar data from S-, X- and C-band radars. Correct interpretation of radar observations requires an accurate understanding of microphysical processes and well-developed techniques that automatise their recognition in both the spatial and temporal dimensions of the data.

This can be achieved by tracking the temporal evolution of precipitation-related microphysical processes in the radar observations. Temporal dynamics from QuasiVertical Profiles (QVPs)are analysed, where QVP's are retrieved from the polarised radar observations at multiple frequencies simultaneously and compared to available ground-based and airborne in-situ measurements.

This technique will be extended through the analysis of the temporal evolution of volume data, which may include a data-driven clustering algorithm. This algorithm will label main clusters in the data and allow for their temporal evolution to be tracked within precipitation events.

1.32 SIMULATIONS OF THE RADAR VARIABLES DURING VAPOR DEPOSITION AND RIMING IN ARCTIC MIXED-PHASE CLOUDS

ROBERT S. SCHROM[1], MATTHEW R. KUMJIAN[1], JERRY Y. HARRINGTON[1]

[1] The Pennsylvania State University, United States
rss5116@psu.edu

Arctic mixed-phase clouds develop and persist through complex interactions between radiative cooling, turbulence, surface energy fluxes, and ice microphysical processes. These systems may maintain themselves for several days and thus have important impacts on the radiative budget of the Arctic. In order to better understand ice particle growth in Arctic mixed-phase clouds, microphysical model simulations were performed for cases primarily of vapor depositional growth and riming, and the radar variables were simulated for each case and compared to the observations.

These simulations were performed using a microphysical model with adaptive habit microphysics, where the ice particle properties of maximum dimension, aspect ratio, and effective density evolve continuously based on the temperature, supersaturation, and liquid water content of the environment. In order to more realistically simulate the effective density evolution of branched planar crystals during vapor depositional growth, a parameterization for the density as a function of size was implemented in the adaptive habit model. This parametrization is based on the shapes of naturally observed branched planar crystals and therefore provides a more consistent representation of these particles in the model. The simulated ice particle properties were then used to calculate the radar variables with a forward model for the polarimetric radar variables that captures the scattering of realistic rimed and unrimed branched planar ice crystals.

The simulated radar variables for the vapor deposition case correspond well to the reflectivity (Z_H) and differential reflectivity (Z_{DR}) observations taken at the Atmospheric Radiation Measurement (ARM) site in Barrow, AK, United States by the X-band Scanning ARM Precipitation Radar (XSAPR). Both the model-simulated and observed radar variables show generally increasing Z_H and slightly decreasing Z_{DR} towards the ground. Based on the model-simulated ice particle properties, Z_{DR} was found to decrease during vapor depositional growth due to decreasing density of the branched planar crystals.

The simulated radar variables for the riming case are also relatively consistent with the XSAPR observations from Barrow, AK, United States, with Z_H increasing towards the ground and Z_{DR} decreasing towards the ground. Both Z_H and Z_{DR} changed more substantially in magnitude during the riming case than during the vapor deposition case. Additional simulations of light riming, where the liquid cloud drops were confined to a thinner layer in the model environment, produced similar radar signatures to those found for cases of vapor deposition. This similarity suggests that light riming of branched planar crystals may be difficult to distinguish from pure vapor depositional growth using polarimetric radar observations. In addition to the thickness of the liquid layer, the simulated radar variables were also found to

be sensitive to the slope of the effective density function and the assumed density of the mass added during riming. This sensitivity suggests that polarimetric radar variables may help constrain these variables, and thus reduce the uncertainty in the vapor deposition and riming processes occurring within Arctic mixed-phase clouds.

1.33 AUTOMATIC IDENTIFICATION OF MELTING LAYER BASED ON FUZZY LOGIC AT OPERATIONAL S-BAND DUAL POLARIZATION RADAR

HYE-YOUNG HAN[1,2], SUNG-HWA JUNG[1], GYUWON LEE[2], DONG-JIN KIM[1], SUN-KI LEE[1]

[1]Weather Radar Center, Korea Meteorological Administration, Republic of Korea
[2]Dept. of Astronomy and Atmospheric Sciences, Kyungpook National University, Republic of Korea
hyhan98@korea.kr

The accurate identification of melting layer (ML) and the study on ML characteristics are important for radar QPE, rain and snow microphysics, and hydrometeor classification. For sing-polarization radar, ML was usually identified using vertical profile of reflectivity. Dual-polarization capability allows to more robust and accurate identification than single-polarization radar. Specially, linear depolarization ratio (LDR) shows extraordinaire performance to identification of ML. However, use of LDR for identification of ML is extremely limited for operational polarization weather radar because most of operational polarimetric weather radar operated at STAR mode cannot provide LDR with other polarimetric observations simultaneously. Most of studies on ML detection has been conducted based on RHI mode, not for PPI mode of operational polarimetric radar. In this study, we proposed automatic fuzzy logic algorithm for real-time identification of ML at every PPI mode of operational S-band dual-polarization radar.

S-band dual-polarization radar were utilized for fifteen rainy cases from April 2015 to September 2016. The top, bottom, and peak of bright band (BB) were identified by the combination of the suggestion of Rico-Ramirez and Cluckie (2007) and Quasi-Vertical Profile (QVP) of polarimetric observations. The seven feature parameters and their weights were then computed at BB and non-BB region: 1) radial smoothed Z_H, 2) radial smoothed Z_{DR}, 3) radial smoothed P_{hv}, azimuthal textures of 4) Z_{DR}, 5) Φ_{DP}, 6) P_{hv}, and 7) height. The membership functions (MFs) are then determined from the normalized frequency distributions (NFD) of feature parameters over BB and non-BB region. The identification of ML at PPI mode was done by fuzzy logic classifier consisting of the predetermined MFs and their weights. If total membership values obtained from the classifier would be greater than threshold, the radar gate will be identified as BB. By comparing to traditional ML identification based on vertical profile of polarimetric observation, the identification performance was evaluated using skill scores such as POD, FAR, and CSI. To determine optimal value of threshold, we developed the additional technique based on vertical profile of membership values.

Acknowledgements
The research is supported by "Development and application of cross governmental dual-pol radar harmonization (WRC-2013-A-1)" project of the Weather Radar Center, Korea Meteorological Administration.

1.34 PRELIMINARY RESULT OF ICE-POP 2018: SNOW MICROPHYSICAL CHARACTERISTICS BY DIFFERENT TYPES OF SNOW HABIT

KWONIL KIM[1], WONBAE BANG[2], CHOENG-LYONG LEE[1], DAEHYUNG LEE[1], DAEJIN YEOM[1], SU-JEONG CHO[2], KWANG-DEUK AHN[3], NAMWON KIM[3], CHRISTOPHE PRAZ[4], ALEXIS BERNE[4], WALTER PETERSEN[5], STELLA MELO[6], WEI-YU CHANG[7], FRANCISCO TAPIADOR[8],GYUWON LEE[1,2]

[1]Department of Astronomy and Atmospheric Sciences, Kyungpook National University, Daegu, South Korea

[2]Center for Atmospheric REmote sensing, Kyungpook National University, Daegu, South Korea

[3]Numerical Modeling Center, Korea Meteorological Administration, Seoul, South Korea

[4]Environmental Remote Sensing Laboratory, École Polytechnique Fédérale de Lausanne, Lausanne, Switzerland

[5]NASA Marshall Space Flight Center, Alabama, United State

[6]Environment and Climate Change Canada, Ontario, Canada

[7] Department of Atmospheric Science, Chinese Culture University, Taipei, Taiwan

[8] Institute of Environmental Sciences, University of Castilla-La Mancha, Toledo, Spain

gyuwon@knu.ac.kr

The ICE-POP 2018 (International Collaborative Experiments for Pyeongchang 2018 Olympic & Paralympic winter games) project was held from November 2017 to March 2018. The project is aimed at understanding the winter precipitation process over complex terrain at Pyeongchang region using intensive observational networks. Various snow microphysical instruments from USA, Switzerland, Spain, Taiwan, and so on were installed at 19 sites around Pyeongchang region.

In particular, 2DVD (2D-Video distrometer), MASC (Multi-Angle Snowflake Camera), PARSIVEL (PARtical Size VELocity), Pluvio, Geonor, POSS (Precipitation Occurrence Sensor System), VertiX (Vertically pointing X-band radar), WProf (W-band Profiler radar), MRR (Micro Rain Radar), Doppler Lidar and other instruments were installed in the main supersite of this project, MayHills Supersite (MHS). 2DVD, MASC, PARSIVEL and Pluvio were inside Double Fence Intercomparison Reference to improve the accuracy of snow measurement. MASC provides full information about snow habit, and distrometers give snow microphysical characteristics such as particle size distribution and its moments at ground. High-resolution profiling radars show detailed feature of vertical structure.

In this study, we will focus on snow habit linked with vertical structure of precipitation using the dataset from MHS site. We will present different snow habits determined by MASC (Praz et al., 2017) in terms of microphysical properties of snowflake at ground and vertical structure.

1.35 LINKING SNOWFALL MICROPHYSICAL PROPERTIES AND WATER CONTENT USING A MASC, A 2DVD AND A PLUVIO

A. REVERDIN[1], C. PRAZ[1], T. RAUPACH[1], A. BERNE[1]

[1] Environmental Remote Sensing Laboratory (LTE), École Polytechnique Fédérale de Lausanne (EPFL), Lausanne, Switzerland
(audrey.reverdin@epfl.ch)

The quantification of solid precipitation is known to be a challenging task for the meteorological community. The variety of snowflake types and related physical properties (rimed, wet, dry) lead to different densities and the link between the physical properties and water content remains poorly known. In this context, a field campaign involving three collocated instruments was conducted at a mountainous site near Davos, Switzerland: a Multi-Angle Snowflake Camera (MASC), a 2D Video-Disdrometer (2DVD) and an OTT Pluvio2 weighing gauge were installed within a WMO Double Fence International Reference (DFIR). This study takes advantage of this unique instrumental set-up. The MASC and the 2DVD both take images of falling snowflakes, which provides information on the microstructural properties of the particles (i.e. size and fall velocity), while the Pluvio2 gives a direct measurement of the snowfall liquid water equivalent. In addition, an algorithm developed for MASC images gives crucial additional information on snowflake types and their degree of riming. As a first step, the similarity between the particle size distribution (PSD) from the MASC and the 2DVD is evaluated. For this purpose, and because the two sensors are different and have both encountered operational issues, the data were thoroughly checked and cleaned using different methods and sensitivity tests to provide comprehensive and reliable datasets in order to compare their PSD in the best conditions. Results derived over 35 snow events show that the PSD of MASC and 2DVD instruments are in good agreement. The 2DVD has a bigger measurement area than the MASC, allowing for a largeer particle sample.

The next step is the analysis of the links between liquid water equivalent precipitation rate measured by the Pluvio2 and the PSD measured by the 2DVD conditional on the hydrometeor types and riming degree estimated from MASC images, in order to better characterize solid precipitation.

1.36 PRELIMINARY RESULTS ON MICROPHYSICAL CHARACTERIZATION OF PRECIPITATION OVER ANTARCTICA COAST

N.ROBERTO[1],L. BALDINI[1], A. BRACCI[1,2], M.MONTOPOLI[1], E. ADIROSI[1], E.GORGUCCI[1], C. SCARCHILLI[3], P. GRIGIONI[3], V. CIARDINI[3], F.PORCÙ[2]

[1]Institute of Atmospheric Sciences and Climate (ISAC)- CNR Rome, Italy
[2] University of Bologna, dept. of Physics and Astronomy, Italy [3] ENEA, Italy
n.roberto@isac.cnr.it

Knowledge of the snowfall spatial and temporal variability in Antarctica is essential to define the impact of the ice sheet on sea level rise. To date, the main source of precipitation evaluation is indirectly through snow accumulation measurements but during recent years satellite observation seems to give promising result.

However, satellite measurements and related products need for calibration and validation with observations from ground sensors. In spite of its key role, available measurements of precipitation at ground are scarce in Antarctica and not appropriate to give an adequate representation of specific microphysical characteristic of precipitations especially in terms of scattering and absorption properties of ice particles.

Recently, different stations in Antarctica (Princess Elizabeth, McMurdo, Mario Zucchelli, and Dumont d'Urville) have been equipping with observatories for cloud and precipitation. The setup of a long term experiment at the Italian Station Mario Zucchelli (MZ, Latitude 74° 41' 42" S; Longitude 164° 07' 23E"), in the Terranova Bay area, plans to integrate the current instrumentation for weather measurements with other instruments specific for precipitation observations, in particular, a 24-GHz vertical pointing radars such as the Micro Rain Radar (MRR), and optical disdrometers. The synergetic use of MRR and disdrometers allows for characterizing precipitation and studying properties of Antarctic precipitation such as dimension, shapes, fall behavior, density of particles as well as particles size distribution, particles terminal velocity, reflectivity factor including some information on their vertical extent.

During last Italian Antarctic expedition an OTT Parsivel disdrometer and an MRR were installed on the roof of a logistic container (at 6 m of height) of the MZ station . The disdrometer measures size and fall velocity of particles, passing through a laser matrix from which the Particle Size Distribution (PSD) is obtained. The OTT Parsivel manufacturer software assumes spherical shape to compute the size and the fall velocity of ice particles. In the case of solid precipitation, this assumption can be unrealistic, but, averaging over a long time the influence of irregular shape of the particles can be reduced. Despite this known limitation, such instrument has been used in several studies to measure falling snow. In this work, some preliminary measurements from OTT Parsivel at MSZ during summer season are presented. In particular, the PSD collected during summer seasons 2016-2017 and 2017-2018 are analyzed in order to infer microphysical characteristics of snows in Antarctica. A specific methodology to estimate the snow rate from snow size spectra collected by Parsivel is investigated. In order to understand the relation between ice particles microphysical properties and the vertical pointing 24 GHz backscattering

cross section, some numerical simulations are also performed by using the particle size distribution provided by the in-situ disdrometers. Simulations are driven by a pre-computed discrete dipole approximation (DDA) database for complex shape particles and carried out by the T-matrix model for spheroids with different aspect ratios, density and falling behavior. The results of this work will be of practical interest giving an important contribution toward a more accurate quantification of snow deposit in the Antarctica region.

1.37 PAIRED DISTROMETRIC MEASUREMENTS IN SOUTH BRAZIL: WIND EFFECTS AND SAMPLING UNCERTAINTIES

R.V. CALHEIROS[1], C.BENETI[1]

[1]SIMEPAR - Parana Meteorological Service, Brazil
[2]UFPR Parana Federal University, Brazil
[3]UFPel Federal University of Pelotas, Brazil
rv_calheiros@hotmail.com

Drop size distribution (DSD) is basic for the analysis of the microstructure of rainfall, which is of primary importance for the remote sensing of precipitation. As well, DSD plays an important role e.g. in precipitation physics, numerical weather and hydrological modeling, telecommunications, and agricultural and soil sciences. Reliable measurements of DSD are of primary importance for the understanding of the microstructure of rainfall at a more advanced level of analysis. Measurements of DSD are usually performed at ground level using distrometers; the OTT Parsivel instrument is one of the distrometers most widely used in validation and comparisons of weather radars. Inherent to the measurement of a physical process uncertainties affect the DSD measurements, and results from both the natural variability of rainfall and sampling fluctuations. At a more advanced level of analysis, these uncertainties must be considered quantitatively. This paper is directed to weather radar remote sensing, following the approach of Jaffrain and Berne (2011) to characterize and quantify the sampling uncertainty in rain due to the the limited sampling area of the Parsivel. OTT Parsivel distrometers were installed in the state of Paran, southern Brazil, in association with two long-range S-band radars (TXS: -25.5053, -50.3613, and CAS: -25.5053, -53.5293) covering regions of high socio-economical relevance with outstanding agro-industrial activities and energy production. These radars survey a region where more than 33% of the hydro-power energy in the country is generated. In a previous work, distrometer based R and Z were compared with those from gages and radars. In the present work, approximately 6 months of data from paired OTT Parsivel at CAS, disposed in the N-S and E-W directions and wind data from a collocated anemometer are used to: a) correlate corresponding measurements from both distrometers, b) correlate the differences between corresponding measurements from the distrometers with wind speed and direction, c) generate the DSDs, d) generate the time evolution of rainfall accumulation along the 6-month period, e) generate the time evolution of the difference between measurements f) compute the relative sampling uncertainty of rainfall measurements, for different classes of rainfall throughout the full range of values, as a function of time resolution. The negligible correlation coefficients obtained in b) (0.01 for speed; 0.03 for direction) indicates that, in general, wind effects are not significant. Notwithstanding, events with significant differences between the distrometers, in special one case of extreme rain rate with a large value of the difference and the presence of associated wind shift and gusts, were identified and will be investigated. First uncertainty results in f) show values in the 0.17 to 0.34 range. So far, results are compatible with the findings of Jafrain and Berne (2011), before mentioned. Their work was based in a data set comprising only light-to-moderate rainfall, in a region of temperate climate while the work in this paper uses data from a different climate

with typical occurrence of heavy rainfall. Continuing work includes computation of the sampling uncertainty for reflectivity and polarimetric variables.

1.38 STUDY OF THE MONSOON VARIABILITY BY THE CLOUD RADARS ESTIMATED MICROPHYSICAL PROFILES

M.C.R KALAPUREDDY[1], SUKANYA PATRA[1], VIPUL DHAVALE[2]

[1]Indian Institute of Tropical Meteorology,India
[2] Savitribai Phule Pune University,India
kalapureddymcr@gmail.com

To understand rapid variation of cloud microphysical process, and hence for the comprehensive cloud characterization, fine resolution cloud profiling is indispensable. Advanced cloud radar technology is capable us for making such fine resolution cloud measurements. High spatial and temporal resolution cloud measurements are allowing us in the investigation of both the cloud macro- and micro-physical aspects. Jonson′s three level convective cloud inferred the importance of diverse tropical monsoon cloud systems. Temperature variation with altitude changes the phase of the cloud particles which can be indicated by CVS. Therefore CVS act as a versatile parameter for deciphering the contrasting cloud character associated with Indian Summer Monsoon (ISM) through its different phases(warm, mixed and ice). The present work mainly contains the retrieval of fine resolution cloud microphysical profiles from the quality controlled cloud radar measurements over Western Ghats region of India. The cloud radar reflectivity and retrieved Cloud Ice and Water Content (IWC and LWC) measurements are cross validated with Cloud Profiling Radar (CPR) onboard CLOUDSAT. A Good agreement has been found out between the two radar profiles. Wide coverage of CPR is explored for extending the point measurements from Western Ghats to the central India to establish a large scale CVS confining on ISM. Two cases on cloud microphysical studies associated with ice clouds clearly demonstrated that entrainment process at the cloud top boundary increases the ice growth process just lying below it. Weaker or calm turbulence activity regions at the base of cirrus clouds are found to be much favorable for the rapid growth of IWC. On the other hand, strong shear at the mid portion of cloud inducing K-H instability reduces the IWC. Such microphysical characteristics seen during ISM are distinct and those results will be discussed in the forth coming ERAD conference.

1.39 FIELD OBSERVATION FOR INVESTIGATING THE MICROPHYSICAL CHARACTERISTICS OF PRECIPITATION SYSTEM IN KOREA

DONG-IN LEE[1], MI-YOUNG KANG[1], HYEON-JOON KIM[1], SUNG-HO SUH[1]

[1]Division of Earth Environmental System Sciences, Pukyong National University, Busan, Korea

leedi@pknu.ac.kr

In order to examine the microphysical characteristics of precipitation system and improve the accuracy of radar rainfall estimation in Korea, the field observation equipped with three PARSIVEL (PARticle SIze and VELocity) disdrometers, two S-band polarimetric radars, and rain gages has been done at the southern part of Korea since 2015. The three disdrometers and rain gages were installed along the line connecting two radars with same distance. The remote surveillance system was also deployed to monitor the status of instruments and collect data. For analyzing snowfall system, a routine observation network composed of 2 DVD, PARSIVEL, rain gage, and test-bed radar of KMA was used because there was no chance to catch snow in southern part of Korea.

First, the PARSIVEL data were processed for data quality control using the 60% terminal velocity threshold of each drop diameter. The truncated gamma model was employed to calculate DSD variables like as normalized intercept parameter (N_w) and mass-weighted diameter (D_m). To investigate the microphysical characteristics with respect to rainfall types, convective and stratiform, 1.5 mmh^{-1} of standard deviation of rainrate for 5 minutes were adopted. For snowfall case, the classification of dry and wet snow was examined by using terminal velocity observed by 2DVD and QVP (Quasi Vertical Profile) method was firstly applied to the snowfall system observed by Korean polarimetric radar to understand the dendrite growth zone. The microphysical properties of snowfall obtained from 2DVD and the vertical microphysical characteristics using dual polarization radar parameters were compared and analyzed. The fall velocity was determined by the classified types of snow particles based on their shapes and densities in this work. Application of density parameter to hydrometeor classification for snow particles were suggested and evaluated.

1.40 A RADAR BASED AUTOMATED DETECTION ALGORITHM FOR REFREEZING LAYER AND ITS IMPLEMENTATION INTO A FUZZY LOGIC HYDROMETER CLASSIFICATION SCHEME

BRANDON HICKMAN[1], SILKE TRÖMEL[1], ALEXANDER RYZHKOV[2], CLEMENS SIMMER[1]

[1] University of Bonn, Meteorological Institute, Germany
[2]Cooperative Institute for Mesoscale Meteorological Studies, University of Oklahoma, Norman, Oklahoma, and NOAA/OAR/National Severe Storms Laboratory, Norman, Oklahoma
bhickman@uni-bonn.de

Winter time near-surface hydrometeor classification is highly reliant on the detection of changing temperatures aloft, because melting and refreezing layers can shift the phase of the hydrometeors from solid to liquid or vice-versa at the surface. The detection of these layers can be problematic during winter, when the upper melting layer is usually already quite close to the surface. Weather radar observations often lack the necessary spatial resolution for their accurate detection, or even overshoot these layers. Moreover, a potential refreezing layer below the melting layer is hard to detect with traditional plane position indicator (PPI) scans. These layers are relatively rare, but important for distinguishing freezing rain from ice pellets. While many operational melting layer detection algorithms exist already, refreezing layer detection methods have yet to be developed for operational use. We present a new hybrid phase transition detection algorithm, which exploits Quasi-Vertical Profiles (QVPs) of reflectivity, differential reflectivity, and co-polar correlation derived from azimuthally averaged PPIs at high elevation angles. QVPs offer the opportunity to observe small changes of polarimetric properties often overlooked in PPI scans, where short dwell times often produce large errors. The presentation of QVPs as time-height graphs allows for an easy detection of temporal trends. The method was tested on several cases in United States and Germany, including known freezing rain, ice pellets and wet snow events. The methodology was further developed in order to detect refreezing layers characterized by small bumps in Z_{DR} and dips in Z_H and ρ_{HV} . The algorithm outputs a refreezing factor that can be implemented into fuzzy logic algorithms for real-time hydrometeor classification, that can be used in conjunction with thermodynamic profiles for further output refinement. Surface observations and model reanalysis data were used for the evaluation of the ice pellet detection scheme. The presented hybrid phase transition algorithm identifies both melting and refreezing layers, which - when used in tandem with ordinary hydrometeor typing algorithms - increases the accuracy and likelihood of the detection of multiple phase changes aloft and constitutes an important step towards an operational freezing rain warning scheme.

1.41 TOPOGRAPHIC INFLUENCE ON SNOWFALL: A RADAR BASED SPATIO-TEMPORAL ANALYSIS

N. BESIC[1,2], F. GERBER[3,4], D. NERINI[2], L. FORESTI[2], J. FIGUERAS I VENTURA[2], M. GABELLA[2], U. GERMANN[2], M. LEHNING[3,4], A. BERNE[1]

[1] Environmental Remote Sensing Laboratory (LTE), EPFL, Lausanne, CH
[2] Radar, Satellite and Nowcasting Dept., MeteoSwiss, Locarno-Monti, CH
[3] Laboratory of Cryospheric Sciences (CRYOS), EPFL, Lausanne, CH [4] WSL Institute for Snow and Avalanche Research (SLF), Davos, CH
nikola.besic@epfl.ch

In this contribution we analyze the topographic influence on snow precipitation, in terms of variability and microphysics, by interpreting polarimetric radar data. The former is related to the dynamics i.e. growth and decay analysis of the snowfall precipitation field, obtained by re-sampling high resolution radar observations (83m in range). The latter is related to the 3D hydrometeor classification of precipitation, supplemented by the hydrometeor de-mixing approach. The analysis focuses on the region around the Weissfluhgipfel (WFG) radar, in the vicinity of Davos, in the Eastern Swiss Alps.

The growth and decay analysis is based on the advection (semi-Lagrangian scheme) of the snowfall field and the comparison with the following actual measurement. Basically, we shift the precipitation field without incorporating the impact of the local topography and then compare it with the measurement which obviously accounts for the micro-scale influence. The growth and decay maps are obtained by averaging the instantaneous estimates over several different time periods, allowing us to conduct analysis at various temporal resolutions.

The applied hydrometeor classification is a semi-supervised approach, adapted to the technical specificities of a radar, capable of distinguishing between 9 different hydrometeor classes, among which rimed ice particles, aggregates (AG), crystals (CR) and vertically aligned ice. The hydrometeor de-mixing allows to estimate, beside the primary hydrometeor type, the proportions of secondary hydrometeor types present in radar sampling volumes, which proves to be very relevant for such a spatially concentrated study.

Links of both variability (snowfall growth) and microphysics (intense riming + AG/CR co-occurrence) observation to the local topography are assessed through multi-scale spatial wavelet analysis. Also, the analysis shows an interesting correspondence between the zones of snowfall growth on one side and the zones of relatively more intense riming and AG/CR co-occurrence on other side.

1.42POLARIMETRIC RADAR CHARACTERISTICS OF THE ASYMMETRIC EYEWALL OF HURRICANE HARVEY (2017)

YA-CHIEN FENG[1], MICHAEL M. BELL[1]

[1]Department of Atmospheric Sciences, Colorado State University, Fort Collins, USA
ya-chien.feng@colostate.edu

In this study, we explore the microphysical characteristics of Hurricane Harvey (2017) during its peak intensity stage. Asymmetric structures of the hurricane eyewall are associated with the hurricane intensity change and have been widely studied from the dynamic perspective. Yet, few studies discuss the microphysical structure of the asymmetric eyewall due to limited observations. Here, data collected from NEXRAD WSR-88D polarimetric radars and airborne radars are analyzed to document the microphysical and kinematic structures of the Harveys asymmetric eyewall.

The reflectivity field of the hurricane eyewall shows a wavenumber-1 asymmetric pattern for more than six hours during its peak intensity period. A higher reflectivity value of the eyewall was consistently found to the left of the vertical wind shear vector. Differential reflectivity (Z_{DR}) and specific differential phase shift (K_{DP}) also displayed similar asymmetric wavenumber-1 patterns, but both fields were shifted azimuthally with respect to the reflectivity pattern. A Z_{DR} column was found upstream of the reflectivity maximum, but higher values of KZ_{DP} were observed downstream of the reflectivity maximum. Potential causes of this unique structure due to microphysical, advective, and size sorting processes will be discussed.

1.43 SNOWFALL FORMATION AND ENHANCEMENT PROCESSES IN TWO CONTRASTED MOUNTAIN RANGES: THE ALPS AND THE TAEBAEK MOUNTAINS

J. E. GEHRING[1], N. BESIC[1,2] C. PRAZ[1], A. BERNE[1]

[1] Environmental Remote Sensing Laboratory (LTE), École Polytechnique Fédérale de Lausanne (EPFL), Lausanne, Switzerland

[2]Radar, Satellite and Nowcasting Department, MeteoSwiss, Locarno-Monti, Switzerland

josue.gehring@epfl.ch

Understanding snowfall formation and enhancement processes in the atmosphere is crucial to correctly forecast the precipitation intensity. Particularly in mountainous regions, the interaction between the large-scale atmospheric flow and the topography can lead to snowfall enhancement or even to local-scale snow formation. To understand the microphysical processes at play, a synergistic use of remote-sensing and in-situ measurements is needed. Moreover, to contrast the processes in two different mountain ranges, a similar instrumental setup is required. Past field campaigns in the Alps and in the Cascade mountains allowed to understand how similar baroclinic systems interplay with a mountain barrier. Here we analyse the measurements from two field campaigns where the meteorological conditions were very contrasted. The Valais2016 campaign took place in the Swiss Alps from Nov. 2016 to May 2017. An X-band polarisation scanning radar was deployed at a low altitude, while a W-band cloud profiler and a Multi-Angle Snowflake Camera (MASC) were installed higher up in the mountains. The ICE-POP 2018 campaign is an international experiment, which took place in the Taebaek Mountains to support the PyeongChang2018 Olympic and Paralympic Winter Games. A similar configuration as during Valais2016 was deployed, while multiple remote-sensing and in-situ instruments from international research groups completed the setup. Our analysis shows that in the Alps precipitation systems interact with the topography and snowfall is enhanced by aggregation and riming. In the Taebaek mountains, winter are dry, windy and cold and we did not observe much large-scale precipitation systems during the winter months. However, snowfall can form locally in shallow orographic clouds and is hence more challenging to forecast. In particular, the availability of supercooled liquid water can be decisive and lead to graupel showers. A detailed analysis of the contrasted polarimetric and Doppler radar signatures in both environments will be presented

1.44 SIMULTANEOUS OBSERVATIONS OF KA BAND PROFILER AND GPM DUAL-FREQUENCY PRECIPITATION RADAR OVER TROPICAL CENTRAL ANDES (12.0° S)

J. VALDIVIA[1], S. KUMAR[1], Y. SILVA[1], D. SCIPION[1]

[1]Instituto Geofísico del Perú, Lima, Perú
jvaldivia@igp.gob.pe

Peru is a vulnerable country to natural hazards from hydrometeorological origin with great social and economic impact, such as the intense rainfall in the northern and central coast during the "El Niño Costero 2017" phenomenon. The complex topography of the Andes, which covers much of the Peruvian territory, makes the precipitation obtained by satellite be underestimated. On the other hand, the atmospheric models are not able to adequately represent the rains, because the physical and microphysical processes of clouds and precipitation in the Andes are not well known.

In order to obtain atmospheric data to study the physical processes associated with water and energy balance; in 2015 the Instituto Geofísico del Perú implemented the Atmospheric Microphysics And Radiation Laboratory (LAMAR), Huancayo Observatory (12.0°S, 75.3°W, 3313 m asl). As part of LAMAR, a Ka-band cloud profiler (MIRA-35C) was installed in late 2015, for cloud and rainfall estimation, along with a disdrometer (PARSIVEL2) and a few rain gauges.

In this work, we will present some case of study of simultaneous observations between MIRA-35C and Dual-Frequency Precipitation Radar (DPR) onboard the GPM. We will analyse the vertical profiles of reflectivity, rainfall rate, and drop size distribution with focus in the fixed shape factor of the gamma distribution. Some uncertainties derived from complex topography will be discussed.

1.45 CLOUD ELECTRIFICATION MODEL IN THE COSMO NUMERICAL WEATHER PREDICTION MODEL

Z. SOKOL [1], J. MINAROVA [1]

[1] Institute of Atmospheric Physics CAS, Czech Republic
sokol@ufa.cas.cz

In this contribution, we implemented the Cloud Electrification Model (CEM) in the COSMO non-hydrostatic numerical weather prediction model. CEM computes with 2-moment cloud microphysics and consists of both the inductive and non-inductive charging mechanisms with the last the dominant. CEM explicitly describes the concentration of ions and the ion interaction with six kinds of hydrometeors to which the concentration of charge is bounded.

CEM models the advection of charges bounded to hydrometeors, changes in charge concentration in cloud microphysical scheme, ion equation, separation and transfer of charge related to collisions of hydrometeors, and lightning. Lightning scheme is based on bidirectional concept of the flash leader and the propagation of the flash is given by probabilistic branching (dielectric breakdown concept).

The results of simulations show that CEM enables to capture the typical thundercloud tripole charge structure with two positive layers separated by a negative layer. The negative layer is related to high concentration of graupel, ice and snow hydrometeors which are the hydrometeors the most participating in the charge transfer due to their collisions. In more detail, CEM also simulates the charge distributed following the updrafting and downdrafting motion, similar to that given in literature.

1.46 AN X-BAND STUDY OF KDP AND RAINFALL OVER SOUTHERN ENGLAND DURING WINTER 2018

J. M. HAMPTON[1,2], R. R. NEELY III[1,2], A. M. BLYTH[1,2]

[1] School of Earth and Environment, University of Leeds, UK [2] National Centre for Atmospheric Science, University of Leeds, UK
joshua.hampton@ncas.ac.uk

This study investigates the link between KDP throughout the cloud depth, and rainfall experienced at the surface, using data collected during a field campaign over southern England using radar measurements and in-situ observations from aircraft.

During Winter 2018, a number of flights took place over south west England to make observations of ice within clouds, with three frequencies of polarimetric Doppler radar being used at the same time to make ground based measurements from Chilbolton, UK. Here we focus on the observations made by NCAS mobile X-band dual-polarisation Doppler radar (NXPol), to study KDP measurements at temperatures throughout the cloud layer. Continuing from previous studies (mainly at S- and C- band), this work looks at the idea of increased values of KDP at temperatures around -15°C resulting in higher rainfall rates at the surface. This is done by looking at correlations between KDP measured close to the radar at different temperatures and rainfall rates as measured by drop count rain gauges located about 100 metres from the radar. As well as instantaneous correlations, correlations with rainfall lagged in time are also considered, as a stronger time-lagged correlation would prove more useful in nowcasting rainfall from operational radar observations. A stronger link between KDP aloft and rainfall at the surface in stratiform than in convective regimes has also been observed previously, so an attempt is made here to distinguish between the two to observe and verify this change in correlation strength.

1.47 CORRECTION OF DROP SIZE DISTRIBUTIONS FROM DIFFERENT DISDROMETERS USING GENERALIZED NORMALIZATION PARAMETERS DURING ICE-POP 2018 PROJECT

WONBAE BANG[1], KWONIL KIM[2], SU-JEONG CHO[1], DAEJIN YEOM[2], CHOENG-LYONG LEE[1], DAEHYUNG LEE[2], SEUNGWOO BAEK[1], GYUWON LEE[1,2]

[1]Center for Atmospheric REmote sensing, Kyungpook National University, Daegu, South Korea

[2] Research and Training Team for Future Creative Astrophysics and Cosmologists, Department of Astronomy and Atmospheric Sciences, Kyungpook National University, Daegu, South Korea

gyuwon@knu.ac.kr

The drop size distribution (DSD) can be measured by various disdrometers such as 2D-Video Disdrometer (2DVD), PARticle Size VELocity (PARSIVEL) and Precipitation Occurrence Sensor System (POSS). These disdrometers were installed in Pyeongchang area for ICE-POP 2018 (International Collaborative Experiments for Pyeongchang 2018 Olympic & Paralympic winter games) project. Their observation principles are different. For example, 2DVD is optical disdrometer using two optical cameras and PARSIVEL is laser optical disdrometer. POSS is based on radar principle. The measured DSD can be influenced by these discrepancy and various sources of errors. Therefore, the development of correction technique of DSD is required.

In this study, correction of the disdrometers was performed by using generalized normalization parameters such as N0 (Generalized characteristics number concentration) and Dm′ (Generalized characteristics diameter) with 2DVD as a reference. To perform inter-comparison of the disdrometers, one 2DVD, 13 PARISVELs and 5 POSSs were installed at the same site, Daegwallyeong Weather office (DGW), in the summer of 2017. About 2000 1-minute DSDs were collected during the inter-comparison experiment. The comparison of generalized normalization parameters between 2DVD and the others were performed. We define that bias of N0 is concentration correction factor and bias of Dm is diameter correction factor. DSD were corrected by these two factors. Single moments (0th to 6th) and rainfall rate (R) were compared between original DSD and corrected DSD to evaluate our correction technique of DSD. The moments and R of corrected DSD are relatively closer to these of 2DVD than original DSD. Corrected averaged DSDs also have very similar shape with that of 2DVD. The value of two factors obtained in this study can be used to correct the disdrometer data observed during ICE-POP 2018 project.

1.48 POLARIMETRIC DOPPLER OBSERVATIONS OF ICE PARTICLES WITH SCANNING 94 GHZ CLOUD RADAR

A.MYAGKOV[1], T. ROSE[1]

[1]Radiometer Physics GmbH, Meckenheim, Germany
alexander.myagkov@radiometer-physics.de

Cloud radars are one of the main tools for remote-sensing of the atmosphere, and ice particles in particular. These radars operate at millimeter wavelengths and have a great potential for investigations of cloud particle formation and development. (1) Having high sensitivity and dynamic range up to 80 dB, cloud radars can observe a wide spectrum of particle sizes. (2) Cloud particles have distinct sizes, shapes, and orientations, and, therefore have different terminal velocities. Therefore, radar Doppler spectra measured with the resolution down to few cm/s allow for characterization of different particle populations in the same resolution volume. (3) Cloud radars often have polarimetric capabilities used for a classification of cloud scatterers and efficient clutter removing.

In this study we show the first observations of ice particles with a newly developed polarimetric scanning 94 GHz cloud radar. The radar allows for measurements of a set of spectrally resolved polarimetric parameters, including differential reflectivity, correlation coefficient, depolarization ratio, and differential phase. Results of preliminary analysis of the polarimetric parameters and their relation to ice microphysical properties are shown.

1.49 MICROPHYSICAL CHARACTERISTICS OF ORGANIZED CONVECTION OBSERVED BY POLARIMETRIC RADAR IN EASTERN CHINA

KUN ZHAO[1], GANG CHEN[1], GUIFU ZHANG[2], WEN-CHAU LEE[3]

[1] Key Laboratory for Mesoscale Severe Weather/MOE and School of Atmospheric Science, Nanjing University, Nanjing, China

[2] School of Meteorology and Advanced Radar Research Center, University of Oklahoma, Norman, Oklahoma, USA

[3] National Center for Atmospheric Research, Boulder, Colorado, USA

zhaokun@nju.edu.cn

Polarimetric radar and disdrometer data obtained during the 2014 Observation, Prediction and Analysis of Severe Convection of China (OPACC) field campaign are used in the study to investigate the microphysical characteristics over three different organized convection systems (meiyu rainband, typhoon rainband and squall line) with intense rainfall in eastern China. Drop size distributions (DSDs) and vertical distribution of hydrometeors are derived from the Nanjing University C-band polarimetric radar and compared with surface DSDs measured from a disdrometer. All three systems possess deep moist environment below the freezing level, favorable for warm rain processes. Convection is tallest in the squall line where abundant ice-phase processes generated large amount of rimed particles (graupel and hail) above freezing level and possesses the largest raindrops among these three systems at the surface. The lower storm tops in the typhoon rainband and meiyu systems composed of less active ice processes above the freezing level and hold equally high medium to small raindrop concentration causing high rainfall rates. The precipitation is more intense in the typhoon rainband, it is found that higher coalescence efficiency in the typhoon rainband enhances the rainfall rate. A conceptual model is proposed to describe microphysical processes over different environment conditions and illustrate the relative importance of the ice-phased and warm-rain processes to the heavy rainfall.

1.50 INVESTIGATION OF THE SPECTRAL DIFFERENTIAL PHASE IN THE CASE OF A S-BAND RADAR PROFILER

C. UNAL[1]

[1] Delft University of Technology, The Netherlands
c.m.h.unal@tudelft.nl

The differential phase (Ψ_{dp}) is a radar observable, which consists of the differential propagation phase (Φ_{dp}) and the backscattering differential phase (δ_{co}). The slope of the differential propagation phase, specific differential phase (K_{dp}), is extensively used to estimate the rainfall rate at radar low elevations. Kdp is as well analysed for ice crystals in ice/mixed-phased clouds in the RHI mode.

The question asked in this work is: what is the potentiality of the spectral differential phase ($s\Psi_{dp}$)? This question is examined at S-band, using the Transportable Atmospheric Radar (TARA) at Cabauw (The Netherlands). To study relations between Doppler measurements containing size information and polarimetric measurements containing shape and density information, it is necessary to profile to an intermediate elevation between 0 and 90 deg. It is why TARA profiles at 45 deg. elevation.

Theoretically, we do not expect a size dependency for the spectral differential propagation phase ($s\phi_{dp}$). Consequently the spectral differential phase should vary versus range, but not versus Doppler velocity in the range-Doppler spectrogram. Unless there is a contribution of the spectral backscattering differential phase ($s\delta_{co}$). This contribution is not straightforward to be investigated at low frequency radars, like S-band. However this component may appear in case of unremoved clutter and in the melting layer.

After a small review of the potentiality of the spectral differential phase for clutter suppression, Doppler de-aliasing in the case of the polarimetric alternate mode, the purpose is to investigate whether spectral differential phase signatures, size dependent, are present at S-band.

1.51 VARIATIONS IN RADAR RAINFALL ESTIMATORS WITH GENERAL WEATHER TYPES AND LOCATION IN BAVARIA

W. GHADA[1], ANNETTE MENZEL[1,2]

[1] Professorship of Ecoclimatology, Technical University of Munich, Hans-Carl-von-Carlowitz-Platz 2, D-85354 Freising

[2] Institute for Advanced Study, Technical University of Munich, Lichtenbergstrae 2a, D-85748 Garching, Germany

ghada@wzw.tum.de

Accurate estimation of rain intensity is vital for many environmental and hydrological applications. Radar estimation of rain intensity is based on the equation $Z=AR^b$, where the parameters A and b are linked to local and temporal features in rain microstructure as well as to other factors such as rain type (convective - stratiform). However, general weather types exhibit a number of properties which might influence rain microstructure, including cyclonity, wind direction and humidity in upper levels. This research inspects the variation of rain properties with each of these factors, and explores the possibility of improving radar estimation of rain intensity by accounting for them.

The raw output of 11 disdrometers in southern Bavaria with a temporal resolution of one minute from June, 2013 through June, 2017 was combined with daily records of objective weather types as classified by the German Meteorological Service DWD. The disdrometers′ raw output was used to extract the main properties of rain in each interval: rain intensity R [$mm.h^{-1}$], total concentration N [m^{-3}] and mass weighted rain drop diameter D_m [mm]. Each interval was classified by rain type into convective or stratiform. Z-R parameters were determined for each rain type (general model) and then for each combination of rain type and general weather type (weather type model). The accuracy of both models in determining rain intensity was evaluated.

The preliminary results suggest significant differences in R, N and D_m values between weather types in both convective and stratiform rain. Consequently, the general model is expected to perform better than the weather type model. Wind direction in upper levels might provide a plausible explanation for the variation in rain microstructure indicators particularly in stratiform rain.

1.52 A HYDROMETEOR CLASSIFICATION ALGORITHM FOR THE UK C-BAND WEATHER RADAR NETWORK

S.R. BEST[1], D.L. HARRISON[1]

[1] Observations R&D, Met Office, Fitzroy Road, Exeter, EX1 3PB, UK
steven.best@metoffice.gov.uk

The UK Met Office completed the upgrade of its C-band weather radar network to dual-polarisation capability in early 2018. Ongoing improvements to the in-house processing software, Radarnet IV, have recently included new algorithms designed to extract the benefit from the supply of polarimetric data. The latest of these developments is a hydrometeor classification algorithm, currently designed to distinguish between seven different classes of hydrometeor: rain, drizzle, wet snow, dry snow, hail, graupel, and ice crystals.

The core of the algorithm is a fuzzy logic scheme, which combines the likelihood of a given hydrometeor type based on both the polarimetric variable signatures and the atmospheric temperature profile (though a classification can also be made using either of these data sources individually). The likelihoods associated with the polarimetric data are calculated using bivariate membership functions many of which are borrowed from the operational Météo France algorithm (Al-Sakka et al., 2013). The temperature-based likelihoods are calculated using NWP model wet-bulb freezing level (WBFL) information to define a bright band region – here the radar beam power profile is integrated to determine the fractional power returned from each region associated with the bright band. A novel approach is also introduced here by allowing the WBFL to be perturbed in order to account for errors in the model, or small scale fluctuations from the model in the observed data. The polarimetric- and temperature-based membership values are combined multiplicatively to calculate the final likelihood for each hydrometeor type, and a tier-based method is employed to ensure the maximum number of classifications is made by using likelihood values based on reduced variable sets where the full variable set returns values of zero.

Case studies are presented which highlight the strengths and current limitations based on subjective qualitative analysis - of the algorithm in a variety of meteorological situations, and using both Plan Position Indicator (PPI) and Range-Height Indicator (RHI) type-datasets. Possible improvements, verification methods, as well as future requirements of the algorithm are also discussed prior to its scheduled operational release later in 2018.

Session 2. Mesoscale and severe weather



Keynote presentation

2.1 PERFORMANCE OF A NEW ALGORITHM FOR NOWCASTING ANOMALOUS TRAJECTORIES

A. DEL MORAL[1,3], T. RIGO[2], M.C. LLASAT[1,3]

[1] University of Barcelona, Spain
[2] Meteorological Service of Catalonia, Spain
[3] Water Research Institute of the University of Barcelona, Spain
adelmoral@meteo.ub.edu

Severe weather is commonly associated with thunderstorms that have anomalous trajectories. We define as anomalous trajectory the one that doesn′t follow a linearly constant path (split, merge, sudden change of direction, etc.). In this sense, the authors propose a new technique that optimizes the better identification of the convective cells, their tracking, and the identification of any key feature associated with an anomalous movement.

In order to test the performance of the new algorithm, several cases of severe weather (large hail, downburst, tornadoes and heavy rainfalls that produce flash floods) have been analysed. The set of events has been chosen from the database of the Meteorological Service of Catalonia (SMC) and the INUNGAMA database, and the selection has been made considering the following aspects: the season of the year, the area affected, the time of the day, the degree of organization of the convection, the duration, among others.

The first step of the evaluation has consisted in the application of the technique to the radar imagery of the SMC. The first results show how in different cases, it is observed changes at high levels within the convective cells structure, which cause also changes at low levels before the cell finally splits or merge. The results have been compared with the obtained from the current nowcasting tool of the weather service, in order to detect those issues that make the new algorithm more appropriate in those cases.

2.2 IMPACT OF MULTIPLE RADAR REFLECTIVITY DATA ASSIMILATION ON THE NUMERICAL SIMULATION OF A FLASH FLOOD EVENT DURING THE HyMeX CAMPAIGN

I. MAIELLO[1,2], S. GENTILE[2,3], R. FERRETTI[2], L. BALDINI[4], N. ROBERTO[4], E. PICCIOTTI[2,5], P.P. ALBERONI[6], F.S. MARZANO[1,2]

[1] Department of Information Engineering, Electronics and Telecommunications, Sapienza University of Rome,Rome, Italy

[2] CETEMPS, Department of Physical and Chemical Sciences, University of L′Aquila, L′Aquila, Italy

[3] Institute of Methodologies for Environmental Analysis, CNR IMAA, Potenza, Italy

[4] Institute of Atmospheric Sciences and Climate, CNR ISAC, Rome, Italy

[5] Himet s.r.l., L′Aquila, Italy

[6] Arpae Emilia Romagna, Servizio Idro-Meteo-Clima, Bologna, Italy

ida.maiello@aquila.infn.it

An analysis to assess the impact of multiple radar reflectivity data with a three-dimensional variational (3D-Var) assimilation system on a heavy precipitation event is presented. The main goal is to build a regionally tuned numerical prediction model and a decision-support system for environmental civil protection services and demonstrate its validity in the central Italian regions. Moreover, an investigation on which type of observations, conventional and not (or a combination of them), is more effective in improving the accuracy of the forecasted rainfall is also carried out. In that respect, during the first special observation period (SOP1) of HyMeX (Hydrological cycle in the Mediterranean Experiment) campaign several intensive observing periods (IOPs) were launched and nine of which occurred in Italy. Among them, IOP4 is chosen for this study because of its low predictability regarding the exact location and amount of precipitation. This event hit central Italy on 14 September 2012 producing heavy precipitation and causing several cases of damage to buildings, infrastructure, and roads. Reflectivity data taken from three C-band Doppler radars running operationally during the event are assimilated using the 3D-Var technique to improve high-resolution initial conditions. In order to evaluate the impact of the assimilation procedure at different horizontal resolutions and to assess the impact of assimilating reflectivity data from multiple radars, several experiments using the Weather Research and Forecasting (WRF) model are performed. Finally, traditional verification scores such as accuracy, equitable threat score, false alarm ratio, and frequency bias interpreted by analysing their uncertainty through bootstrap confidence intervals (CIs) are used to objectively compare the experiments, using rain gauge data as a benchmark.

2.3 THE ROLE OF SMALL-SCALE VORTICES IN ENHANCING SURFACE WINDS AND DAMAGE IN HURRICANE HARVEY

JOSHUA WURMAN[1], KAREN KOSIBA[1]

[1] Center for Severe Weather Research, USA

jwurman@cswr.org

Small-scale structures have been observed in the landfalling hurricane / tropical cyclone boundary layer, including boundary layer rolls and streaks, and mesovortices. Roll structures have been linked to variations in the surface wind field observationally and through modeling. Damage mapping in Hurricane Andrew revealed small, coherent regions of enhanced damage.

To explore the relationship between small-scale wind field features and damage, Doppler On Wheels (DOW) mobile radars were deployed near the landfalls of hurricanes Harvey and Irma during the summer of 2017. Intense and complex mesovortices were observed from inside the eye of Harvey. In addition, much smaller, $\sim$1 km tornado-scale, vortices were documented in the eyewall, as well as the ubiquitous boundary layer rolls. A DOW-mounted anemometer at 8 m AGL measured 1-second winds of 65 m/s during the eyewall passage. 300 m upstream, two vehicles were lofted and a building destroyed. Anemometer data illustrate the contributions of mesovortices and tornado-scale vortices to the surface wind field.

We will present an analysis of the evolution of the eyewall mesovortices and tornado-scale vortices and how these may relate to regions of documented enhanced damage.

2.4 THE TWIRL PROJECT: FINE-SCALE MOBILE RADAR AND IN SUTU OBSERVATIONS OF TORNADO STRUCTURE

KAREN A. KOSIBA[1], JOSH WURMAN[1], HOWARD BLUESTEIN[2]

[1]Center for Severe Weather Research, USA

[2] University of Oklahoma, USA

kakosiba@cswr.org

During the spring of 2016, The Center for Severe Weather Research (CSWR) fielded three Doppler on Wheels (DOW) mobile radars, three mobile mesonets, and 15 rapidly deployable Tornado Pods to quantify the wind structure in and around tornadoes. DOWs 6 and 7 have gating resolution of 12.5 m, and the Rapid-Scan DOW has resolution of 11.2 m. The Rapid-Scan DOW has a 0.8x-0.9-degree beam width and 7-second volumetric resolution, permitting matched fine-scale 4D resolution of small and quickly evolving sub-tornadic features.

On 09 May 2016 the University of Oklahoma RAXPOL and CSWR DOW7 mobile radars deployed near and in front of a large and intense tornado in southern Oklahoma, establishing an unprecedentedly short 3.5 km dual-Doppler baseline. The tornado, exhibiting a complex wind field structure, moved through the dual-Doppler lobes of the radars and crossed between them at a range of < 2 km to each radar. Sweep update rates are 2 s for RAXPOL and 7 s for DOW7, resulting in the shortest time-scale dual-Doppler observations ever in a tornado. Gating is 12.5 m in DOW7 and 75 m for RAXPOL, with $\sim$1 -degree beam widths. The result is 4D temporal-spatial resolution of 2 s (7 s) x 27 m x 27 m x 75 (12.5) m = 109,000 (64,000) m^3s for RAXPOL (DOW7) at the tornado's closest approach.

Dual-Doppler analysis with volumetric gridding as small as $\sim$60 m x 60 m x 60 m, at 7-second intervals, capable of revealing the vector-wind structure of sub-tornadic structures, is possible for the first time. Rotational space-time conversion will be implemented to accurately retrieve features spinning about the tornado. RAXPOL and DOW7 are both dual-polarimetric, DOW7 with two independent dual-polarimetric systems, providing unique fine-scale and intercomparable ZDR and rho-HV observations of tornadic debris lofted by the tornado and its sub-vortices.

RAXPOL and DOW data revealed a large tornado with a core flow diameter of $\sim$500 m, exhibiting a complex and rapidly evolving structure including intense sub-vortices. Preliminary dual-Doppler vector wind syntheses, dual-polarimetric analysis will be presented, documenting the evolution of the near-ground wind field and debris structure in this tornado.

Additionally, on 09 May 2016, a tornado pod was deployed in the tornado path just north of the core flow region – well within the subsequent damage swath – and measured peak winds of about 45 m/s. DOW7, which was < 2 km range, observed winds at 20 m AGL, over the tornado pod. Peak DOW winds during this tornado were 97 m/s. Combined DOW-damage analyses indicated that the strongest winds and greatest damage occurred in association with multiple vortices. Then, on 24 May 2016, two tornado pods, with contemporaneous DOW data at 40 m AGL, sampled the core region of a tornado in southwest Kansas. The peak DOW-measured winds during this event exceeded 80 m/s. Observations from both the 09

May and 24 May indicated that the 1-meter AGL wind speeds were ∼60%-70% of the DOW-measured winds at 20-40 m AGL. The wind-height-damage relationship as a function of tornado structure will be discussed on the context of these and past DOW-in situ observations.

2.5 FRESH WATER FLUX ESTIMATED BY SHIPBOARD C-BAND POLARIMETRIC RADAR AND ITS POSSIBLE IMPACT TO THE OCEANIC STRATIFICATION OBSERVED IN THE MARITIME CONTINENT

M. KATSUMATA[1], B. GENG[1], S. YOKOI[1], S. MORI[1], R. SHIROOKA[1], I. UEKI[1]

[1] Japan Agency for Marine-Earth Science and Technology (JAMSTEC), Japan
katsu@jamstec.go.jp

To investigate the air-land-sea interaction in the Maritime Continent (the world's largest archipelago bridging tropical Indian Ocean and tropical western Pacific), we deployed our research vessel "Mirai" which equipped C-band polarimetric radar as a part of the project "Years of the Maritime Continent (YMC)". Two field campaigns in YMC had carried out in boreal winter in 2015 and 2017. During each field campaign, "Mirai" stayed one station near the west coast of Sumatra Island to obtain time series.

The data from polarimetric radar is converted to the rainrate (i.e. fresh water flux) by utilizing the data from land-based and shipboard disdrometers. The estimated fresh water flux is compared to the oceanic parameters such as salinity and temperature which is observed at "Mirai" and unmanned platforms (surface mooring and wave glider) to discuss possible impact of the fresh water flux to the near-surface oceanic stratification.

2.6 RAPID SCAN EXPERIMENT OF DOPPLER WEATHER RADAR FOR MONITORING RAINSTORMS AND TROPICAL CYCLONES IN HONG KONG

W. KONG[1]

[1] Hong Kong Observatory, Hong Kong
wkong@hko.gov.hk

The Hong Kong Observatory (HKO) carried out a rapid scan experiment using an S-band Doppler weather radar at Tai Mo Shan in 2017. Low-elevation scan at 0 degree was performed once every minute for more intensive monitoring of severe weather. The one-minute rapid scan enabled reception of radar data 5 to 10 minutes earlier as well as 6 times higher update frequency of radar imageries compared with the conventional 6-minute volume scan. The rapid scan provided better continuity in observing the evolution of rainstorms and tropical cyclones which would be useful for weather diagnosis, nowcasting and numerical weather prediction.

This paper introduces the radar scanning strategy adopted in the experiment and describes the rapid scan observations of several rainstorm cases and tropical cyclone Hato in 2017. The operational applications of rapid scan radar data are also discussed. Preliminary analysis shows that 1-minute rapid scan data are more effective in revealing the formation and dissipation of various small-scale and short-lived weather systems such as downburst, mesocyclone and low-level convergence, etc., thereby enhancing the understanding of rainstorms' precipitation mechanisms. In the case of Hato, rapid scan imageries depict more clearly variation of the rotation speed of its spiral rainbands around the eye, allowing a better diagnosis of Hato's rapid intensification.

2.7 CHARACTERISTICS OF CONVECTIVE AGGREGATION IN MID-LATITUDES IDENTIFIED IN A DOPPLER C-BAND RADAR NETWORK

I. PSCHEIDT[1], S. TRÖMEL[1]

[1] Meteorological Institute, University of Bonn, Auf dem Hgel 20, 53121 Bonn, Germany
pscheidt@uni-bonn.de

Cloud-resolving models have shown that convective aggregation can spontaneously emerge in homogeneously forced simulations and affect the mean state of the atmosphere. Aggregated convection leads to drier free atmosphere and thus, to more outgoing longwave radiation. This phenomenon might have possible implications for climate and climate change. A better knowledge of the physical processes that favour convective clouds to aggregate, their characteristics and impact on the environmet is fundamental to improve climate prediction. Renewed attention has been given to the understanding of convective aggregation, specially over the tropical region. In this study we proposed to characterize convective aggregations in the mid-latitudes. We aim at answering the questions: i) how aggregated is convection outside the tropical region, ii) what is the frequency of occurrence and iii) what are the common characteristics. For this purpose we focused on the region of Germany and used radar reflectivities from the Doppler C-band radar network operated by the German Weather Service (DWD). The period of interest comprehended the months from April to September of 2014 and of 2015. Signatures of convective clouds were identified on the radar fields by means of a segmentation algorithm. Organization indices were applied to the segmented objects to determine their characteristics, namely the spatial arrangements (random, regular or aggregated), the degree of aggregation, the number of objects, the geometrical distances, the dominat shape of the objects and the amount of rainfall that they produced. In approximately 98% of the time convective clouds were aggregated emphasizing their importance for the German summer. The degree of aggregation was dependent on the distance between all possible pairs of clouds, however, it did not present significant relationship with the amount of rainfall, the shape and the number of clouds. Random and regular arrangements were identified in 1.5% and 0.5% of the time, respectively. These arrangements showed to be associated with fewer convective clouds than in aggregations. In an effort to understand more the differences and similarities in convective aggregations in the tropical and in the mid-latitude regions, the current results will be compared with the results obtained with a Doppler S-band radar located in Barbados.

2.8 EVALUATING THE DEVELOPMENT STAGE OF THUNDERSTORMS BY USE OF 4D RADAR DATA-PARAMETERS

MALTE NEUPER[1], JAN HANDWERKER[2]

[1]Institute of Water and River Basin Management - Chair of Hydrology, Karlsruhe Institute of Technology KIT, Karlsruhe, Germany

[2]Institute of Meteorology and Climatology, Karlsruhe Institute of Technology KIT, Karlsruhe, Germany

malte.neuper@metteam.de

Thunderstorms undergo several development stages (cumulus stage, mature stage and decaying stage, c.f. Byers and Braham Jr, 1948) which are in a specific case more or less pronounced and/or extended. Whether a location is affected by severe weather or not depends on the stage and on the development of the stage.

In this study we carried on the examination of the development of thunderstorms using single pol radar volume data. We used TRACE3D (Handwerker, 2002) to identify and track individual thunderstorms, applying a constant reflectivity threshold of 40 dBZ. For each thunderstorm we calculated bulk and specific descriptors which are supposed to describe the stage of maturation or to be indicators of different external and internal processes which occur during a life cycle.

Next to "often" used properties - like the total volume, the maximum reflectivity, the velocity of a storms reference point and others the calculated parameters include a "reflectivity mass" as a reflectivity weighted volume, the height of the centre of gravity of the thunderstorms volume and reflectivity mass and some special ratios. These last parameters are also evaluated in relation to some specific, the convective environment representing heights like the level of free convection, the 0°C and the -10°C level, which were extracted from data of operational upper air rawind soundings.

For a further evaluation we then compared the evolution of these parameters and their physical meanings with the current conceptual models of the thunderstorm development.

Special emphasis was laid on the updraft strength, which is an integral part of the thunderstorms development. In addition, we tried to obtain an evaluation of the severity of internal processes, which in turn gives information about the organization of the thunderstorm.

We investigated the temporal evolution of the storms center of gravity with respect to the different convective levels in order to evaluate whether the storm is still top heavy (and capable of a further development) or whether the storm is already foot heavy and in the decaying stage of at least the actual life cycle) .

Our results fit quite well with the conceptual models of the different storm types. One can discover a meaning and a pattern behind the development of the parameters and maybe also infer a short term forecast value for the further development of the cell.

Next to the evolution and differences of the characteristics of single cell, multicell and supercell storms, we will also present a case of an unusual split. The derived parameters early suggested, that the "left" daughter cell would undergo a stronger further development, whereas the "right" daughter exhibited no strong potential of

further development, although the wind field pattern supported according to the classical conceptional models - a dominant “right” daughter.

2.9 DUAL-POLARIZATION RADAR OBSERVATIONS OF DEEP CONVECTION OVER THE LAKE VICTORIA BASIN IN EAST AFRICA

P. WANIHA[1], A. KIJAZI[1], R. ROBERTS[2], J. WILSON[2]

[1] Tanzania Meteorological Agency, Tanzania

[2] National Center for Atmospheric Research, U.S.A.

pascal.waniha@meteo.go.tz

Lake Victoria in East Africa supports the livelihood of thousands of fisherman and it is estimated that 5000 deaths occur per year over the lake. It is believed that these fatalities are due to localized, severe winds produced by intense thunderstorms over the lake during the rainy season and larger scale, intense winds over the lake during the dry season. The intense winds are causing rough state of the lake (Big wave heights) that cause fishermen boats to capsize.

The Tanzania Meteorological Agency operates an S-band polarimetric radar in Mwanza, Tanzania, along the south shore of Lake Victoria. Observations show that there is a pronounced diurnal cycle of storm formation in the Lake Victoria Basin region. During the daytime, storms develop and intensify over the higher terrain surrounding the lake. This pattern is reversed at night with storm formation over the lake. The nocturnal thunderstorms are well observed by the Mwanza radar and are strongly forced by sea breezes, land breezes and gust fronts. Unexpected is the detection of clear air echo (backscattering by insects) to ranges >100 km over the lake that makes it possible to observe clear air winds, gust fronts and other convergence lines over the lake. Tracking the movement of thunderstorms and these low level convergence lines provide the opportunity to nowcasts intense winds and also subsequent thunderstorm development.

We will present examples of these radar features and discuss efforts that are currently underway at the Tanzania Meteorological Agency to use the radar observations to verify and to improve the performance of numerical weather prediction fields.

2.10 WEATHER RADAR DERIVED RAIN CELL SIZE STATISTICS FOR LOWER AUSTRIA

R. TESCHL[1], F. TESCHL[2], S. TANI[1], H. PAULITSCH[1]

[1] Graz University of Technology, Institute of Microwave and Photonic Engineering, Austria

[2] Graz University of Technology, Institute of Communication Networks and Satellite Communications, Austria

reinhard.teschl@tugraz.at

Knowledge about the dimensions of intense rain cells and their frequency of occurrence in a region can be of relevance to several areas of research. Besides meteorological fields of study, such statistics can be interesting for hydrological purposes e.g. urban hydrology. At the same time such information is useful to model tropospheric effects in satellite communications links, especially for site diversity considerations, where signal fading due to an intense rain cell along the signal path to one ground station is compensated by one or more ground stations that are located a sufficient distance apart.

Rain cell size statistics can be based on in-situ measurements like rain gauges or remote sensing systems. Apart from a few exceptions, most rain gauge networks are too coarse to properly capture the spatial variability of rain cells. Thus, rain cell size studies are usually based on weather radar measurements. The three-dimensional data provide additional information on the vertical structure of the rain cells. But due to the working principle and effects like clutter and shielding, the radar exhibits also limitations. Thus, caution is advised when using radar data to deduce rain cell statistics, especially when comparing data from radar stations that differ in frequency and in the applied attenuation and clutter correction procedure.

That is why the Study Group on Wave Propagation of the International Telecommunication Union (ITU) provided with the objective of establishing a global rain cell size database recommendations on the methods to be used when extracting rain cell characteristics from weather radar data for modelling the attenuation of radio waves propagating through the troposphere.

The present study is an extension of a former investigation that addressed the question of automatically generated rain cell size statistics deduced by weather radar data. Starting in 2009, several precipitation periods during the summer seasons in the surrounding areas of Vienna, Austria were included. The measurements of the C-Band weather radar from Rauchenwarth were analysed. The data are available in a Cartesian format as volume elements (voxels) with a grid size of 1 km 1 km 1 km. Based on the applied definition of the rain cell as a contiguous volume in which the radar reflectivity is throughout equal to or higher than a specified threshold (minimum 34.2 dBZ), a MATLAB program identifies connected voxels in the clutter filtered archive data and derives the dimensions.

So far thousands of cells were identified. Besides the horizontal extent of the rain cells in different altitude levels, also the vertical spread and the height of the cell center was collected. It was observed that intense rain cells with vertical and horizontal dimensions higher than 5 km are rare.

2.11 EARLY DETECTION OF DEEP CONVECTION USING NWCSAF RDT PRODUCT AND NATIONAL RADAR MOSAIC IN ITALY

R. CREMONINI[1], M. CELANO[2], P.P. ALBERONI[2], R. BECHINI[2], V. CAMPANA[2], G. VULPIANI[3], P. GIORDANO[3]

[1] Arpa Piemonte, Dipartimento Sistemi Previsionali, Torino, Italy
[2] Arpae Emilia-Romagna, Servizio Idro-Meteo-Clima, Bologna, Italy
[3] Dipartimento Nazionale della Protezione Civile, Roma, Italy

Due to the rapid development of convection and potential effects that severe storms may have locally, an early identification of deep convective clouds is essential to improve nowcasting and warning operational procedures. To this purpose, a synergy between radar and satellite information can provide a crucial contribution.

The Rapid Development Thunderstorm (RDT) of NWCSAF, a satellite application facility of Eumetsat, provides information on clouds related to significant convective systems from meso-alpha scale (200 to 2,000 km) down to smaller scales (several kilometres).

In this work, co-located observations of RDT and C-band radar data, obtained from the Italian mosaic managed by the National Civil Protection Agency, are investigated in several convective case studies, with the aim of improving early detection of severe convection and short-term forecasting (0-2 h).

2.12 DOPPLER RADAR OBSERVATIONS OF TWO TORNADIC THUNDERSTORM CASES IN THE WESTERN MEDITERRANEAN REGION

J. BECH[1], O. RODRIGUEZ[1], P. ALTUBE[2], T. RIGO[2], N. PINEDA[2], S. CASTÁN[3], J. ARÚS[4], J. MONTANYÀ[5]

[1] Department of Applied Physics Meteorology, University of Barcelona, Spain
[2] Meteorological Service of Catalonia, Barcelona, Spain
[3] Agencia Pericial, Cornell de Llobregat, Spain
[4] Agencia Estatal de Meteorologa, Barcelona, Spain
[5] Department of Electrical Engineering, Universitat Politcnica de Catalunya, Spain
joan.bech@ub.edu

Severe thunderstorms producing large hail, heavy rainfall and strong winds from convective origin, occur frequently in southern Europe and near the Mediterranean coastal regions in particular, mostly during late summer and early autumn. For example over the period 2000 to 2016 a yearly average of 5 tornadoes, mostly weak (<EF2) were reported in Catalonia (NE Spain) - see Rodriguez and Bech (2017). This study, which benefits from the improved processing of dual-PRF Doppler radial velocity field proposed in Altube et al (2017), describes two recent cases of tornadic storms that took place on 18 October 2017 and 7 January 2018. The first event affected the city of Valls (S Catalonia), causing several injuries, and damaging more than 250 trees and over 100 traffic signal and lamp posts. A damage survey indicated a linear 6.2 km long path with EF1 estimated damage in the Fujita scale. The passage of a well organised mesoscale convective system moving NE with a leading convective line and trailing stratiform region spawned the tornado responsible of the damage. The second event, characterised by a surface southeast flow affected central and NE Catalonia. Convection was organised in precipitation bands and embedded intense thunderstorms, two of which spawned tornadoes with associated EF2 Fujita damage intensities and path lengths of 9 and 19 km respectively. This second event, unlike most documented EF2 previous cases in the region, was particularly remarkable due to the date (early January) and timing (night and dawn) of occurrence.

References

Altube P, Bech J, ArgemÍ O, Rigo T, Pineda N, Collis S, Helmus J, 2017: Correction of dual-PRF Doppler velocity outliers in the presence of aliasing. Journal of Atmospheric and Oceanic Technology, 34, 15291543. DOI:10.1175/JTECH-D-16-0065.1

Rodriguez O, Bech J, 2017: Sounding-derived parameters associated with tornadic storms in Catalonia. International Journal of Climatology, (in press). DOI:10.1002/joc.5343

2.13 CONVECTIVE CLOUD TOP HEIGHTS IN NORTHERN AUSTRALIA IN DIFFERING WET SEASON REGIMES

R. JACKSON[1], S. COLLIS[1], A PROTAT[2], V LOUF[2], W LIN[3], A. VOGELMANN[3], S. ENDO[3]

[1] Argonne National Laboratory, USA
[2] Bureau of Meteorology, Australia
[3] Brookhaven National Laboratory, USA
rjackson@anl.gov

General circulation models (GCMs) have difficulty representing the hydrological cycle owing, in part, to the parameterization of convective systems. Furthermore, mechanisms coupling large scale forcing and convective organization are not well represented, leading to a poor representation of the macrophysical properties of convection. The U.S. Department of Energy (DOE) Energy Exascale Earth System Model (E3SM) aims to run at a regionally refined resolution of 12 km. At this scale mesoscale motions are partially resolved but how they interact with the convective parameterization is unknown. This prompts the need for observational datasets to validate the macrophysical characteristics, including cloud top heights, of convection in simulations and guide model development in E3SM in several regions of the globe. This presentation will showcase a radar based study of convective systems observed at the Tropical Western Pacific (TWP) ARM site in Darwin, Australia and the surrounding maritime continent. In Darwin clear forcing regimes occur during the wet season from November to April with the onset and break of the Northern Australian Monsoon and the phase of the Madden-Julian Oscillation (MJO) which can alter the characteristics of convection over the region. The echo top heights (ETHs) are derived using a novel technique based on reflectivity and velocity texture from fifteen years of continuous plan position indicator scans from the C-band POLarimetric (CPOL) radar. ETHs in convective regions are 2 to 3 km lower than those retrieved by the Multifunctional Transport Satellites over Darwin at ETHs greater than 10 km, suggesting that the radar underestimates the vertical extent of deep convection. Bimodal distributions of convective echo top heights have been observed at heights of 5 to 7 km and at 12 to 13 km during break conditions. More unimodal ETH distributions are observed when the convective mode of the MJO is over Australia. A stable layer present at 4 km can likely explain the bimodality seen in break conditions. During the daytime, the spatial distribution of ETHs are more consistent with the presence of Hector and seabreeze convergence lines during break conditions. At night and during monsoon conditions, the spatial distributions are consistent with more widespread mesoscale convective systems.

2.14 UNDERSTANDING AND PREDICTION OF RAINFALL ASSOCIATED WITH LANDFALLING TROPICAL CYCLONES (UPDRAFT)

YUAN WANG[1]

[1] Nanjing University, School of Atmospheric Sciences, Nanjing, China
yuanasm@nju.edu.cn

The western North Pacific and East Asian regions are affected the most by tropical cyclones (TCs) in the world. In particular, landfalling TCs can bring heavy precipitation to coastal areas, which is of limited predictability. Inorder to improve the forecast of rainfall associated with landfalling TCs, we propose to establish a WMO/WWRP Research and Development Project (RDP) to advance the understanding and prediction of rainfall associated with landfalling TCs. This RDP will promote research on multi-scale dynamical and physical processes that govern rainfall intensity and distribution in landfalling TCs. The ability of both state-of-the art research and operational NWP models in forecasting rainfall associated with landfalling TCs will be systematically evaluated first. A prototype of optimized configuration of research and operational NWP models for the forecast of landfalling TCs will be established. New forecast techniques based on ensemble of multiple NWP model outputs will be exploited. The proposed RDP will be coordinated and collaborated with the on-going WMO Typhoon Landfall Forecast Demonstration Project (TLFDP) and the Forecast Demonstration Project in Southeast Asia (SWFDP). The establishment of this RDP is expected to help significantly reduce the risk of landfalling TCs to the affected coastal regions by achieving improved rainfall forecast, and also contribute to improved understanding of the fine-scale structure and processes in landfalling TCs.

2.15 DUAL-DOPPLER AND POLARIMETRIC RADAR ANALYSIS OF CONVECTIVE SYSTEMS IN WEST GERMANY

RAQUEL EVARISTO[1], SILKE TRÖMEL[1], CLEMENS SIMMER[1]

[1] Meteorological Institute, University of Bonn, Bonn, Germany
revarist@uni-bonn.de

The interaction between dynamics and microphysics in convective systems is complex, and not yet fully understood. Doppler and Polarimetric weather radars have the ability to look simultaneously into the microphysics and dynamics of precipitation systems and thus provide insight in their interaction, helping in better understanding their development and ultimately improve nowcasting of severe weather.

The Meteorological Institute at the University of Bonn owns and maintains an X-band polarimetric Doppler radar (BoXPol), installed in the city of Bonn. A similar radar (JuXPol) located about 50 km to the west-northwest of the Bonn radar at is owned by the Forschungszentrum Jülich. Using the data from both radars and performing a Dual Doppler analysis the 3D wind field may be retrieved. Simultaneously, the polarimetric capability of the radars allows the retrieval of hydrometeor types and microphysical processes. Therefore, we are able to identify the processes through which precipitation systems evolve by revealing the interdependence between storm dynamics and microphysics. One prominent example of such interactions is the development of so-called Zdr columns, that are associated with storm updrafts, and consequent freezing and potential hail formation.

The retrieval of the wind fields was successfully applied to two distinct events where large hail was observed at the surface. Strong mid-level updrafts (over 15m/s) are observed near the Zdr columns, and the regions where hail was reported. One of the events presented a well defined bounded weak echo region (BWER) which was also closely located to a maximum in the updraft.

The temporal evolution of some derived parameters (updraft strength, updraft volume and volume of the Zdr column) were analyzed. It was observed that the updraft peaks in volume first, then in intensity, and lastly the Zdr column reaches its maximum. This is however still very preliminary because it was only performed for one case. In the future we plan to investigate a larger number of systems. This will help in understanding how each of these parameters relate to the others and can help interpret how convective storms develop, intensify, and dissipate.

2.16 IT'S TIME FOR COLOR VISION DEFICIENCY FRIENDLY COLOR MAPS IN THE RADAR COMMUNITY

S. COLLIS[1], R. JACKSON[1], Z. SHERMAN[1], C HOMEYER[2], K. MHLBAUER[3], R. CHASE[4], S. NESBITT[4], T. LANG[5], D. STECHMAN[4]

[1] Argonne National Laboratory, USA
[2] University of Oklahoma, USA
[3] University of Bonn, Germany
[4] University of Illinois, USA
[5] NASA Marshall Space Flight Center, USA
scollis@anl.gov

Color blindness, or color vision deficiency (CVD), impacts 1 in 12 men and 1 in 200 women. There are numerous examples in the atmospheric sciences and in radar meteorology in particular of CVD. The radar community is particular when it comes to the choice of colors used to represent numerical values (ie color maps) with the choice of color map often being an institutional choice. Some color maps, such as those used by the USA National Weather Service for reflectivity as well as other variables, are particularly unaccommodating with numerous perceptual duplications when viewed by those with CVD. The challenge is to build a colormap that has a monotonically increasing, decreasing, or diverging luminosity while remaining visually pleasing and able to convey scientific meaning. For presentation purposes these colormaps also need to be perceptually uniform, in order to remain meaningful when printed in greyscale.This presentation will showcase several examples of existing colormaps in the Python ARM Radar Toolkit (Py-ART) as seen by CVD individuals illustrating this issue, and demonstrate the improvements in data interpretation using CVD friendly versions. By using an online survey this presentation aims to collect the views of the radar community and provide a recommended set of color maps that make displays, presentations, and publications accessible to a wider audience.

2.17 DIURNAL CYCLE OF PRECIPITATION AND WINDS IN CENTRAL PERUVIAN ANDES, USING CLOUD AND WIND PROFILING RADARS

Y. SILVA[1], S. CHAVEZ[1,2]

[1] Instituto Geofísico del Perú (IGP), Lima, Perú

[2] Duke University, USA

fsilva@igp.gob.pe

The diurnal cycle in the central Andes of Peru is strong, at elevations above 3500 m almost all the rainfall is observed in the afternoon and early night and it is associated to convective clouds that extend in the vertical until 13000 masl. Also, at that time the echo-top heights in the Andes are higher than in the Amazon. Nevertheless, according to 15 years of TRMM PR observations the convective clouds do not become organized into larger systems, the precipitation systems observed in the central Andes of Peru are small and medium size in term of their horizontal extension (25 km^2 24700 km^2). During the night, the vertical profiles of reflectivity and winds measured by radars show that convective profiles turns into profiles with a bright band typical of stratiform precipitation and the vertical updrafts turn into downward winds. Also, the drop size distribution show less large drops at that time. This continues during early morning when according to the TRMM PR almost all the rainfall is stratiform and the echo-top height reach lower altitudes compared to the afternoon and lower altitudes than in the Amazon. On average, based in the TRMM PR observations, in the Mantaro Valley, 60% of daily rainfall is stratiform, and 40% is convective.

2.18 MULTIFRACTAL ANALYSIS OF TROPICAL CYLCONE RADAR DATA: REMOVING MISSING DATA BIASES AND CONSEQUENCES FOR MESO-SCALE MODELLING

D.SCHERTZER[1], J. LEE[1,2], D.I. LEE[2], I. TCHIGUIRINSKAIA[1]

[1] 1 HM&Co, École des Ponts, Marne-la-Vallée, France

[2] Pukyong National University, Busan, Republic of Korea

daniel.schertzer@enpc.fr

The tropical cyclone Bolaven struck hard South Korea in August 2012, after passing through Jeju island. We analysed in details the structure and mechanisms of Bolaven across scales, with the help of a universal multifractal (UM) analysis. Surprisingly, there had not been so many multifractal studies of typhoons (see however, Chygyrynskaia et al., 1995; Lazarev et al, 1995 on 1D multifractal analysis of the wind field) in spite of the inherent capacity of multifractals to deal with extreme multiscale phenomena like typhoons and the increased availability of higher quality data.

We used the rain rate estimates from AWS (Automatic Weather System) and a S-band radar in Jeju island, both operated by KMA (Korea Meteorological Administration), as well as from simulations of the mesoscale CReSS model. This large amount of space time data was analyzed to quantify the mean intermittency with the help of its fractal co-dimension C1 and its multifractality index , which measures how fast the intermittency evolves for higher order statistics.

We discuss in detail the biases due to missing radar data, unfortunately reported as zero values, as well as how to analytically remove them. At the lowest altitudes, they are due to the minimum radar beam elevation angle of 0.5 degrees that does not affect the estimates α=1.42 and C_1=0.114 at 5 km altitude. The empirical and semi-theoretical scaling moment functions put clearly on evidence the existence of a critical order of divergence of statistical moments $q_D = 3$. This extreme behavior is unfortunately missed by the current CReSS outputs that are furthermore limited to an average over the altitude.

2.19 IMPLEMENTATION OF A DYNAMIC EQUATION CONSTRAINT BASED ON THE STEADY STATE MOMENTUM EQUATIONS WITHIN THE WRF HYBRID ENSEMBLE-3DVAR DATA ASSIMILATION SYSTEM AND TEST WITH RADAR T-TREC WIND ASSIMILATION FOR TROPICAL CYCLONE CHANTHU (2010)

JIE MING[1], XIN LI[1,2], MING XUE[1 3], YUAN WANG[1], KUN ZHAO[1]

[1] Key Laboratory of Mesoscale Severe Weather/MOE and School of Atmospheric Sciences, Nanjing University, China

[2] Jiangsu Research Institute of Meteorological Sciences, China

[3] Center for Analysis and Prediction of Storms, and School of Meteorology, University of Oklahoma, USA

jming@nju.edu.cn

Proper dynamic equation constraints in data assimilation (DA) systems can help improve balance of analyzed atmospheric state. The formulation of ensemble-variational DA algorithms allows for easy incorporation of such constraints but their impacts within such DA systems have been little studied. A dynamic constraint based on the steady momentum equations is incorporated into the WRF (Weather Research and Forecasting) hybrid ensemble-3DVar (En3DVar) DA system as a weak constraint. The constraint aims at improving the coupling and balance among wind and thermodynamic state variables, especially when few state variables are directly observed. The scheme is applied to the assimilation of radar T-TREC (Typhoon-Tracking Radar Echo by Correlation) winds at a convection-allowing resolution, for landfalling typhoon, Chanthu (2010), when it was within the range of a coastal radar. Parallel experiments using the 3DVar and En3DVar with and without the dynamic constraint are run to examine the impact of the constraint. The flow-dependent ensemble covariance used in En3DVar helps to update unobserved pressure and temperature fields in a dynamically more consistent way compared to the static covariance; the added dynamic constraint produces more accurate pressure within the typhoon. The pressure field improved by the dynamic constraint also leads to better temperature and moisture analyses within the variational minimization through flow-dependent cross-covariance. En3DVar analysis with the dynamic constraint produces the best intensity forecast for the typhoon, in terms of the minimum sea level pressure and maximum surface wind speed. Additional sensitivity experiments examine the impact of the weight of the dynamic constraint.

2.20 INTEGRATION OF RESEARCH WEATHER RADARS INTO ATMOSPHERIC SCIENCE EDUCATION AT PURDUE UNIVERSITY, USA

R. TANAMACHI[1]

[1] Department of Earth, Atmospheric, and Planetary Sciences, Purdue University, West Lafayette, Indiana, USA
rtanamachi@purdue.edu

Since 2015, the Department of Earth, Atmospheric, and Planetary Sciences at Purdue University has actively integrated research-grade weather radars into its atmospheric science education curriculum in order to enhance student learning and research. This presentation will detail the following activities:

- Installation of Purdues own X-band, polarimetric weather radar (the XTRRA). This installation was achieved at a modest cost (US$600K) owing to use of existing infrastructure and a competitively priced radar model. The XTRRA serves as a unique source of radar observations in the region, enhancing knowledge of the local atmospheric conditions and augmenting student and faculty research projects across a wide variety of disciplines.

- Revision of the existing Radar Meteorology course to include hands-on activities such as field trips to operational radar sites, the use of mobile radars (e.g., DOW) in lab exercises, and the use of open source radar software (e.g., Py-ART).

- Creation of a new course, Severe Storms Field Work, in which students collect data using mobile radar (among other instruments) in the context of a small severe storm observation field campaign. A novel polarimetric mobile radar was field-tested in this setting during 2018. Survey results are presented showing that the course design, which includes training on and operation of research-grade instrumentation, enhances student learning.

- Participation of undergraduate and graduate students in radar data collection and analysis during larger field projects such as VORTEX-Southeast.

These activities are grounded in an experiential learning framework, and set Purdue University apart from its regional competitors.

2.21 SINGLE- AND DUAL- POLARIZATION RADAR HAIL DETECTION AT THE BOHEMIA HAILSTORMS ON 23 MAY 2016

K. SKRIPNIKOVA[1], D. REZACOVA[1]

[1] Institute of Atmospheric Physics Czech Academy of Sciences, Bocni II/1401, Prague 4, Czech Republic
skripka@ufa.cas.cz

Comparative analysis of radar based hail detection methods is presented which uses C-band polarimetric radar data from a stormy day in 2016. Hail detection results obtained by using single and dual polarization radar data are compared.

Severe hailstorms occurred on 23 May 2016 and produced damaging hail at several Czech locations including Prague. The hailstorm cells were propagating through the region of Bohemia from the south to the north. Several ground truth records from the hailstorms were accepted in the ESWD. They confirm the occurrence of large hailstones, and thick hailstone layers at several locations.

Former hail detection algorithms using single polarization radar reflectivity and atmospheric sounding data were computed for the area of hailstorms occurrence. At present, there are two dual-polarization radars operated by the Czech Hydrometeorological Institute in Czechia since the year 2015. Polarimetric radar measurements give more possibilities in hydrometeor type identification. Therefore, the performance of former hail detection was compared with the hydrometeor classification using dual polarimetric radar data. Hail size reports on the ground are related to the polarimetric radar signatures. Finally the contribution of dual-polarimetric data to the detection is discussed.

2.22 IMPROVING RADAR HAIL ALGORITHMS FOR THE SWISS HAIL CLIMATOLOGY PROJECT FIRST SENSITIVITY STUDIES

S. TREFALT[1], A. HERING[1], L. NISI[2], C. SCHWIERZ[3], U. GERMANN[1]

[1] MeteoSwiss, Division for Radar, Satellite and Nowcasting, Switzerland
[2] MeteoSwiss, Division for Analysis and Forecasting, Switzerland
[3] MeteoSwiss, Division for Climatology, Switzerland
simona.trefalt@meteoswiss.ch

In regions surrounding the Swiss Alps, hail causes substantial damage almost on a yearly basis. A new Swiss Hail Climatology Project has recently started to compile spatial and temporal hail distributions to the benefit of insurance companies, agricultural stakeholders, private and public sectors. The outcome of this project will flow directly into damage prevention, risk assessment, and additional applied uses. Within this project, we will develop statistical methods to estimate the return period of severe hail events, as well as tools to straightforwardly update the hail climatology of Switzerland on a yearly basis in the years to come.

A direct spatially inclusive and comprehensive observation of hail is difficult because of its high variability in space and time. This is why, alternative indirect observation methods were developed already several decades ago, based mainly on weather radar data. Well-known methods for the estimation of hail occurrence and size are based on empirical relations among hail (size) observations at the ground, radar echo top heights (ET), and the freezing level height (H_o), available today from numerical weather prediction (NWP) models. For the Swiss radar network, we operationally compute the "Probability Of Hail" (POH) and the "Maximum Expected Severe Hail Size" (MESHS) at the ground since 2002. These products can be verified with other more recent hail datasets at MeteoSwiss, such as hail sensor data, available from a pilot network since 2015, crowd-sourced hail reports from the MeteoSwiss App, also available since 2015, and dual-pol radar data, available since 2012, and derived products (e.g. hydrometeor classification).

The two hail products POH and MESHS need to be homogeneous over the full 16 years they are available, to be employed for the Swiss Hail Climatology Project. However, the NWP models operational at MeteoSwiss have changed several times since 2002, due in particular to improved spatial resolution. This influenced the computation of H_o. The POH and MESHS products, both calculated with H_o, are, hence, not necessarily homogeneous throughout this period. Furthermore, ET, the second measure required to compute POH and MESHS, depends on the chosen spatial interpolation and compositing techniques of the radar network, especially at long range. This is because the spatial resolution of the radar volume decreases with range, and in some regions the vertical distance between radar scans exceeds the desired ET intervals.

The aim of this paper is to present first results of the Swiss Hail Climatology Project related to the single-pol radar-based hail products. These will include sensitivity studies showing the dependence of POH and MESHS products on specific methods employed to determine both the H_o and ET.

2.23 USING EUSKALMET RADAR FOR ANALYSIS OF INTENSE AND PERSISTENCE PRECIPITATION EVENT IN BASQUE COUNTRY DURING WINTER: THE 11 JANUARY 2018 CASE.

J. EGAÑA[1,2], S. GAZTELUMENDI[1,2], O. PRINCIPE[1,2], V. PALACIO[1,2], M. MARURI[2]

[1] Basque Meteorology Agency, Basque Country, Spain.

[2] Meteorology Area, Energy and Environmet Division,Tecnalia R&I, Basque Country, Spain.

joseba.egana@tecnalia.com

In this work a study of a severe weather episode (11 January 2018) is performed focusing on synoptic, mesoscale and local aspects based on different data available in the studied area including Radar products provided by Basque Meteorology Agency (Euskalmet). Euskalmet radar is sited in Kapildui Mountain (1174 m) near the capital of Basque Country, is a METEOR 1500 Doppler Weather Radar with Dual polarization capabilities. This radar is based on a Klystron transmitter system and operates in C-band frequency.

A depression initially located on Brittany descends rapidly towards the south, losing strength. The occluded front associated with that low affects especially the Basque Country (CAV) during the afternoon of the 11 January 2018. At the 500hPa level a relatively cold air mass (-30°C) favors certain convection and the formation of storms accompanied by hail.

The local pressure field configuration in the Basque Country region generates a surface convergence zone in the area of Gernika where two different air masses join, one warmer that is situated towards the west and another cold stagnated at the east, this causes a special activation of the front in the affected area.

The persistence of precipitation throughout all day, leaves more than 70 mm in 24 hours in different parts of the territory, with hourly intensities greater than 25 mm and ten minutes intensities greater than 8 mm. Those quantities are unusual in our territory in winter season cases. In the different radar products we can see the location of the convergence zone and the areas of maximum activity.

In different municipalities in Bizkaia, water accumulations on streets, the overflow of several rivers, local floods and numerous problems on roads are produced. The most affected area is the surroundings of Gernika, where material damage occurs and the Firemen had to rescue several people from cars trapped by water.

2.24 USING EUSKALMET RADAR FOR ANALYSIS OF A HEAVY STORMS EVENT IN BASQUE COUNTRY DURING SUMMER: THE 30 AUGUST 2017 CASE

J. EGAÑA[1,2], S. GAZTELUMENDI[1], M. CELANO[2], O. PRINCIPE[1], M. CELANO[2], V. PALACIO[1], M. CELANO[2], M. MARURI[2]

[1] Basque Meteorology Agency, Basque Country, Spain.

[2] Meteorology Area, Energy and Environmet Division,Tecnalia R&I, Basque Country, Spain.

joseba.egana@tecnalia.com

In this work a study of a very heavy showers summer episode (30 August 2017) is performed focusing on synoptic, mesoscale and local aspects based on different data available in the studied area including Radar products provided by Basque Meteorology Agency (Euskalmet). Euskalmet radar is sited in Kapildui Mountain (1174 m) near the capital of Basque Country (CAV), is a METEOR 1500 Doppler Weather Radar with Dual polarization capabilities. This radar is based on a Klystron transmitter system and operates in C-band frequency.

During the study day, the synoptic configuration is marked by a deep trough of Atlantic origin and a surface anticyclonic wedge situation. During the day a front sweeps the Cantabrian coast, causing stormy showers in the CAV. The storms begin to affect the territory in the west (Bizkaia), extending later to the East (Gipuzkoa) of the CAV. In Gipuzkoa showers are longer and more intense than those that occurred in Bizkaia.

The highest amount of rain is recorded in the east of the Gipuzkoa coast with accumulations greater than 30 mm in an hour; in the neighbourhood of Ereozu (Hernani) 47.5 mm in an hour are reached. The amount of rain during study day evening leaves a lot of incidents throughout the territory, particularly in Gipuzkoa, fortunately without personal injuries. In San Sebastian heavy showers affect the city around six in the afternoon, leaving large puddles throughout the city, especially in the centre and in the old town.

This type of event, in spite of its severity, is not atypical in the region and usually occurs recurrently once or twice during summer season, affecting different points of the territory. In the different radar products and other data analysed, the vertical development of the different convective cells, their displacement and the areas with high probability of hail can be appreciated.

2.25 LONG-TERM CHARACTERISTICS OF WEATHER RADAR PRODUCTS DERIVED FROM 15-YR DATASET OF VOLUMETRIC MEASUREMETS

P. NOVK[1], H. KYZNAROV[1]

[1] Czech Hydrometeorological Institute, Czech Republic
petr.novak@chmi.cz

Since the 90's, the Czech Hydrometeorological Institute (CHMI) has been operating digital Czech weather radar network (CZRAD) covering whole area of the Czech Republic and its neighbourhood. Additionally CHMI has been utilizing lightning data from the Central European Lightning Detection Network (CELDN) over the same domain. Both types of data are operationally used in CHMI meteorological and hydrological forecast offices and they proved to be very useful for operational detection, monitoring and nowcasting of convective storms.

Archive of both datasets (volumetric CZRAD measurements and CELDN lightning detections) is available in CHMI. Data from fifteen-year period 2002-2016 have roughly the same quality, therefore this time period was used to calculate long-term spatial and temporal characteristics of various weather radar and lightning products. These long-term characteristics show many quality issues of weather radar products and are also very useful for definition of decision thresholds of convective storms severity in automatic nowcasting applications.

The presentation will present these long-term characteristics and their utilization. It will discuss relation between radar and lightning characteristics and will present also long-term characteristics of convective storms identified by the cell-oriented nowcasting algorithm CELLTRACK.

2.26 POLARIMETRIC SIGNATURES IN SEVERE STORMS: OBSERVATIONS BY THE FRENCH RADAR NETWORK VS. FORECASTS FROM THE AROME CONVECTIVE-SCALE NWP SYSTEM

M. MONTANGON[1,2,3], O. CAUMONT[2], C. AUGROS[3]

[1] ISAE-SUPAERO, Toulouse, France
[2] CNRM, Météo-France and CNRS, Toulouse, France
[3] Centre for Radar Meteorology, Météo-France, Toulouse, France
olivier.caumont@meteo.fr

In the last years, substantial efforts have been devoted world-wide to upgrade operational weather radar networks with dual-polarization capabilities. Besides measuring the intensity and the displacement of precipitation, dual-polarization radars provide additional information about the characteristics of hydrometeors within the observed volume. In particular, it has been shown that specific signatures could be observed in distinctive parts of severe thunderstorms (e.g., K_{DP} columns and Z_{DR} arcs and columns).

Concurrently, a new generation of Numerical Weather Prediction (NWP) models with kilometre-scale horizontal resolutions and advanced representations of microphysics is making it possible to represent atmospheric processes at the convective scale with improved realism.

The joint use of dual-polarization radars and high-resolution NWP models opens a new area of investigation with potential breakthroughs in terms of knowledge of the microphysics and dynamics of thunderstorms, as well as improvements in the nowcasting and short-term prediction of these hazardous weather systems. Indeed, the simulation of realistic radar observations might shed light on the unobserved processes that drive the evolution of thunderstorms. Besides, such simulations could be useful to create diagnostics of severe convection for nowcasting applications or to assimilate dual-polarization radar observations in NWP systems.

Here, the concurrent availability of operational dual-polarization data and of state-of-the-art numerical modelling tools is leveraged with the aim of improving the knowledge and short-term prediction of thunderstorms. More specifically, dual-polarization radar observations from the French weather service are analysed for severe convection cases. The dual-polarization signatures of thunderstorms are characterized for each stage of their life cycles and related to their severity. For the same cases, short-range forecasts from the French operational convective-scale NWP system AROME are compared with the dual-polarization observations. Such comparisons allow to determine to which extent AROME and its microphysical scheme are able to reproduce dual-polarization signatures observed in thunderstorms.

2.27 STORM CELL CHARACTERISTICS DERIVED BY CELL-TRACKING ALGORITHM CELLTRACK - EVALUATION AND OPERATIONAL VISUALIZATION

H. KYZNAROVÁ[1], P. NOVÁK[1]

[1] Czech Hydrometeorological Institute, Czech Republic
kyznarova@chmi.cz

A cell-tracking algorithm CELLTRACK was developed in the Czech Hydrometeorological Institute (CHMI) in the past. It is one of many cell-tracking algorithms developed to identify and track radar reflectivity cores representing fairly well convective storm cells. Primarily, CELLTRACK determines and tracks storm cell characteristics derived from various radar products, but characteristics derived from other sources (e.g. lightning detection data) can also be used. CELLTRACK has been running routinely for several years in the CHMI. CELLTRACK results are available to forecasters and other users but their presentation is currently not suitable for routine use. The development of a suitable tool for processing and displaying of radar reflectivity cores and their characteristics is under way.

The contribution describes evaluation of various radar-based storm cell characteristics identified by CELLTRACK in order to find suitable characteristics or their combination for identification of potentially severe storm cells. Storm cell characteristics connected with occurrence of hail (POH index based on Waldvogel criterium, POSH and MEHS based on HDA algorithm described by Witt, and also hail identification by polarimetric radar measurements) were verified against ground truth. The contribution also shows examples of advanced CELLTRACK visualization in a new development version of a web-based application JSMeteoView for operational displaying of radar data in the CHMI.

2.28 USE OF POLARIMETRIC DATA FOR BETTER ANALYSES OF CONVECTIVE STORM CHARACTERISTICS

DAVID RÝVA[1]

[1] Czech Hydrometeorological Institute [2] Charles University, Prague, Czech Republic
david.ryva@chmi.cz

In 2015 the Czech weather radar network (CZRAD), consisting of two radar sites, was significantly modernized by the new dual-polarization C-band radars. This fact allows us to use polarimetric radar data for many purposes including a better correction for attenuation which can give us a better data of precipitation estimations, better erasing of ground clutters and WLAN interferences or a better detection of hailstorms. Use of polarimetric data also should allow us to identify updrafts of convective storm cells based on the detection of so called ZDR-columns. These are column-like features with positive ZDR values which can reach altitudes up to a few kilometers above the freezing level because of presence of liquid water droplets in the warmer updraft air and also their ability to stay in supercooled state for some time in a rapidly rising air parcel. This study sets the starting point in investigation of potencial of polarimetric data use for a better estimation of storm cores behaviour, especially their tendency to get stronger or weaker in the next 5 to 15 minutes based on the detection of ZDR-columns. Such knowledge could notably help to forecasters with issuing of the severe weather warnings, especially in cases of flash floods and severe hailstorms. In the present analysis we focused on several selected situations with isolated hail producing supercells, heavy rain producing multicellular systems and also derecho producing MCS′s which occurred during the storm seasons of 2016 and 2017. We studied the ability of data from ZDR-column detection (its area, vertical development, integrated spatial volume and also their temporal variations) to predict intensity of the convective storm and its accompanied phenomena in the next tens of minutes.

2.29 AN OVERVIEW OF THE SHONAI AREA RAILROAD WEATHER PROJECT

K. KUSUNOKI[1], T. ADACHI[1], H. Y. INOUE[1], K. ARAI[1], N. ISHITSU[1], S. ONOMURA[1], C. FUJIWARA[2], H. SUZUKI[2]

[1] Meteorological Research Institute, Tsukuba, Japan
[2] East Japan Railway Company, Saitama, Japan
kkusunok@mri-jma.go.jp

On Japan railroads, wind conditions affect operating efficiency, infrastructure, and safe passage of people and freight. For instance, strong and gusty winds cause regional delays or shutdowns, and especially hazardous crosswinds may lead to overturn of railcars. Since propeller-vane/cup anemometers densely cover on the railroads for operations through some wind speed thresholds (e.g., winds in excess of 25 ms^{-1}), small-scale but strong gusty winds are difficult to detect with the present system. The Shonai area railroad weather project will investigate fine-scale structure of wind gust dynamics and kinetics such as tornadoes, downbursts, and gustfronts.

The goal of the project is to develop an automatic strong gust detection system for railroads, which the decision to warn is generally based upon information from a single-Doppler radar at low elevation angles. In this presentation, we will introduce an overview of the project as well as highlights from the our recent results will be presented.

2.30 ANALYSIS OF HAIL EVENT IN FIELD OF REFLECTIVITY AND DIFFERENTIAL REFLECTIVITY

S.STEVANOVIĆ[1], S.BILJIĆ[1], M.VASIĆ[1], G.BOGUNOVIĆ[1]

[1] Republic Hydrometeorological Service of Serbia, Kneza Viseslava 66, 11030 Belgrade, Serbia

svetlana.stevanovic@hidmet.gov.rs

The aim of the analysis is to detect spatial characteristics and intensity in the field of reflectivity and differential reflectivity, their comparison with the occurrences of small hail and hail, as well as the potential of the storm to produce the hail. The reason for the resulting analysis is stormy weather on the territory of two radar centers in Central Serbia, which are close to the position of Dualpol Doppler radar Jastrebac. Hail and small hail, as well as damage from individual storms, were recorded. During the analysis products MAX, CAPPI Z, ZDR, CC (RohHV), KDP and ZHAIL, were used. Product analysis is dictated by the values of reflectivity, the probability of occurrence of hail and temperature conditions.

2.31 CONVECTIVE CLOUDS OBSERVATIONS AND ANALYSIS WITH POLARIMETRIC RADAR IN THE QINGHAI-XIZANG PLATEAU

M. YAO[1,2], Z. HU[1], X. HUANG[2]

[1] State Key Laboratory of Severe Weather, Chinese Academy of Meteorological Sciences Beijing, China

[2] Collaborative Innovation Center on Forecast and Evaluation of Meteorological DisastersNanjing University of Information Science & Technology, Nanjing, China
huzq@cma.gov.cn

Based on the data on July 30 and August 5, 2014 in Naqu region, Tibet, detected with the mobile C-band dual polarimetric radar (C-POL) and Chinese new generation weather radar in Naqu (CINRAD CD), two cases of hailstorm cell and its dynamical, microphysical and thermal characteristics are detailed demonstrated by means of dual Doppler radar wind field retrieval and dual polarization radar hydrometeor class identification technique. The convective cells mostly appear in the afternoon in the plateau region. Although the cells horizontal and vertical scales are small, they are frequent occurrence and rapid evolution, which generally last for dozens of minutes. In the RHI (range height indicator) images of ZH, ZDR and Class, the whole dynamic and microphysical process can be obviously seen in where the hydrometeor particles raise and grow up following the zero line and accompanying the echo intensity increase, then form a hail wall dropping down in the other side of main updraft after overtaking it. From the successive three RHI scan, the phases of particle change from wet snow to hailstorm during the evolution process in one convective cell. The height of the echo is lower and its intensity is very weak when the cell is just triggered. However, when a large amount of wet snows appear in region above the melting level, it always hints that the updraft is so strong that the wet snows are brought back to high levels while they has not completely melted in the air below the melting level. Through physical processes such as condensation, rime, and attachment, the wet snow can rapidly grow into hailstones in just over 10 minutes. During the re-condensation of wet snows, the unstable structures are promoted and the updraft and downdraft are strengthened further because of latent heat releasing. Therefore, if numerous wet snows appear in a newly generated weak echo region above the melting level, it usually indicates that the region occurs strong updraft and will develop rapidly to a strong cell. The configuration of wind field in different height levels obtained by 3D wind field inversion shows that the existence of wind shear not only provides horizontal rotation, but also accelerates the vertical circulation. This is conducive to the conversion of unstable energy to kinetic energy, and cells can develop rapidly.

2.32 TORMIC: RADAR-BASED DETECTION AND FORECASTING TORNADOES AND MICROBURST OVER NORWAY

SEVIM M.-GULBRANDSEN[1], LAILA FODNES SIDSELRUD[1], CRISTIAN LUSSANA[1]

[1] Norwegian Meteorological Institute, Norway
smg@met.no

Core objectives of the Norwegian Meteorological Institute (MET Norway) are providing weather forecasting and warnings to ensure that the public and stakeholders are best able to protect life and property, have reliable information for planning and environmental protection. Forecasting extreme wind and precipitation events are a high priority task. Tornadoes and microbursts have a high impact on safety and decision making. The occurrence of tornadoes and microburst in Norway are infrequent and are mainly concentrated in the southern regions. Climate changes imply that the amount of these events will increase with time. The project "TorMic - (radar-based) forecasting of tornadoes and microbursts over Norway" is investigating how to set up warnings of these phenomena.

Tornadoes and microbursts are convective phenomena. The convection on a synoptic scale can be forecasted in advance by state-of-the-art numerical weather prediction (NWP) models on the basis of the available data a day or two before. However, convection on a local scale of few kilometers is characterized by a limited predictability in time. Thus frequent data assimilation cycles, every one hour or so, would be needed to properly represent thunderstorms within NWP. A radar-based method and nowcasts are widely used to monitor the evolution of heavy precipitation events over the next few (1-2) hours and can be used to detect the occurrence of hail and mesocyclonic rotation. In this context, the TorMic-project aims at implementing a mesocyclone and tornado detection algorithm based on radar observations. For this we will try to adapt existing mesocyclone and tornado detection algorithms to fit the Norwegian environmental conditions. The method will be evaluated over selected case studies extracted from the archived radar observations, moreover a dedicated scan on a mobile X-band radar placed at the Oslo airport will be operated during the summer of 2018 to test the best radar setup targeted to our purposes. TorMic is a part of a local project at MET-Norway, that aims to give new methods in forecasting of extreme weather events. The project focus on Norwegian meteorological and environmental conditions, nonetheless we believe that the outcomes would be relevant also for other countries with a similar climate.

2.33 IRMA - IMPLEMENTATION OF A HIGH RESOLUTION 3D RADAR MOSAIC FOR AVIATION WITHIN SESAR

L. DONOHUE[1], M. SIMPSON[1], R. SCOVELL[1], M. MOTT[2], B. BECKMANN[2], N. GAUSSIAT[3]

[1] Met Office, United Kingdom
[2] DWD, Germany
[3] Météo France, France
lauren.donohue@metoffice.gov.uk

Three dimensional mosaics produced from radar volume data at high spatial and temporal resolution (1 km, 5 min) are an enrichment for air traffic controllers as well as for operational forecasters. Provision of derived 2D products from 3D mosaics such as maximum reflectivity, echo top or vertical integrated liquid water, offer a focused and consistent view of precipitation and convection at a glance for users.

As part of SESAR1 Work Package (WP 11.2), a prototype code for generating hi-resolution 3D mosaics in real-time was developed and tested on two Terminal Manoeuvring Areas (400km x 400km horizontal at 2km resolution, 12km vertical on 24 levels) centred on Charles de Gaulle Airport in Paris and Heathrow Airport in London (Scovell and Al-Sakka, 2016).

Within SESAR Deployment Manager, a project to implement many SESAR1 initiatives has been undertaken. A new tool called "hI Resolution Mosaic for Aviation" (IRMA) will take weather radar observations from across Europe (via the OPERA hub) to produce 3D Radar products that can supply the aviation community, including air traffic controllers, with services via the MET-GATE. To achieve this, a set of preconditions must be fulfilled. This paper shows the cooperation with other projects as well as the requirements of the 3D mosaic such as data format, quality tolerance and pre-processing. In addition, the production environment is discussed and the data flow is presented in terms of the failover solution and archive.

References

Scovell, R and H. Al-Sakka, 2016: A Point Cloud Method for Retrieval of High-Resolution 3D Gridded Reflectivity from Weather Radar Networks for Air Traffic Management. Journal of Atmospheric and Oceanic Technology 33 461-479

2.34 MESOCYCLONE DETECTION AT MÉTÉO-FRANCE

CLOTILDE AUGROS[1], JEAN IMBERT[2], NICOLAS GAUSSIAT[1], MICKAEL KREITZ[2], TONY LE BASTARD[1], MAUD MARTET[1]

[1] Météo France, École Nationale de la Météorologie, Toulouse, France
[2] Météo France, Centre Météorologique Radar, Toulouse, France
clotilde.augros@meteo.fr

Supercells are particularly long-lived thunderstorms known for their capacity to produce damaging weather phenomena such as large hail, heavy rain, severe wind gusts or tornadoes. They are characterized by the presence of a deep and persistent rotating updraft called mesocyclone, whose diameter ranges from 2 to 10 km. The rotation can be seen as a symetric dipole of inbound/outbound velocities in the radial storm-relative velocity field of Doppler weather radars. Several mesocyclone algorithms have been developed in the past (e.g. Zrnic 1985, Stumpf et al 1998, Entsgebeck et al 2017) for operational nowcasting.

At Meteo-France, the Doppler information from the radar network is used to produce a wind-shear mosaic (Augros et al, 2013) that provides to forecasters an estimation of the maximum horizontal wind shear detected in low levels (between 0 and 2 km AGL). This product is suited for the detection of gust fronts, or strong convergence areas inside thunderstorms but is not well adapted for the detection of azimuthal shear that characterizes the mesocyclones in radial velocity images.

The aim of the study presented in this paper is to develop and evaluate a dedicated mesocyclone algorithm for the Meteo France radar network. Following the "pattern vector approach" from Zrnic et al (1985) and applied by Entsgebeck et al (2017), the algorithm looks for sequences of azimuthal shear grouped in one-dimensional "pattern vectors", which are combined to two-dimensional "features". Adjacent "features" in consecutive elevation angles are then merged into 3D mesocyclone objects. The adaptation of the algorithm to the specificity of the 3-PRT scheme used at Meteo France to measure Doppler velocities unambiguously at maximum range will be presented and discussed. A few case studies will be shown to illustrate the performance of the algorithm.

References

Augros, C., P. Tabary, A. Anquez, J. Moisselin, P. Brovelli, and O. Bousquet, 2013: Development of a Nationwide, Low-Level Wind Shear Mosaic in France. Wea. Forecasting, 28, 12411260.

Hengstebeck, T., K. Wapler, D. Heizenreder, and P. Joe, 2018: Radar NetworkBased Detection of Mesocyclones at the German Weather Service. J. Atmos. Oceanic Technol., 35, 299321, https://doi.org/10.1175/JTECH-D-16-0230.1

Stumpf, G. J., A. Witt, E. D. Mitchell, P. L. Spencer, J. T. Johnson, M. D. Eilts, K. W. Thomas, and D. W. Burgess, 1998: The National Severe Storms Laboratory mesocyclone detection algorithm for the WSR-88D. Wea. Forecasting, 13, 304326.

Zrnić, D. S., Burgess, D. W., & Hennington, L. D. (1985). Automatic detection of mesocyclonic shear with Doppler radar. Journal of Atmospheric and Oceanic

2.35 MESOSCALE FACTORS IMPACTING STORM INITIATION OVER THE TORINO METROPOLITAN AREA, ITALY

ENRICO SOLAZZO[1], ROBERTO CREMONINI[2,3], RENZO BECHINI[2], CLAUDIO CASSARDO[3], ALESSANDRO PEZZOLI[1]

[1] DIST, Politecnico di Torino & University of Torino, Italy
[2] ARPA Piemonte, Italy
[3] Department of Physics, University of Torino, Italy
enrico.solazzo@hotmail.it

The importance of mesoscale and local factors, like orography, land cover, insolation, and local winds in thunderstorms development is an active topic of research. Over the metropolitan area of Torino severe storms can be dangerous due to the inadequate fine-scale predictability and the potential impact in a highly urbanized area. The interaction between atmospheric flows and the hill surrounding the city on the east side (700 meters above mean seal level, i.e. ∼400 meters above the city center) is one of the main factors influencing convective initiation over the metropolitan area.

This research investigates the distribution of thunderstorms in the study area, using the operational Bric della Croce weather radar, ground observations, and numerical weather prediction models (NWPs), considering eight years of observations (2010-2017). The work focuses in particular on the role of the Froude number. Fifty-nine ordinary thunderstorms, which developed between 2 pm and 6 pm local time, have been analyzed according to different values of the Froude number derived from Milano radiosounding at 925 hPa and 850 hPa pressure levels. A detailed analysis of the initial stage of the thunderstorms formed over the metropolitan area of Torino is carried out.

The study confirms the impact of the Torino hill on the storms development and it shows how different atmospheric flows, respect to the hill, determine different areas for storm initiation. In particular, when the Froude number is less than one (between 0.10 and 0.8) for both pressure levels, storm cells are most likely to occur around the hill (on the southern and western side), with low-level winds from the plains splitting around the orographic obstacle. When the Froude is higher than one (between 1.10 and 1.8), storm cells are found to develop downwind of the hill, while Froude number near unity at both pressure levels are associated with storm cells occurring on the ridge of the hill. It is argued that the operational use of the Froude number may improve the predictability of the storm initiation, helping to anticipate the location of the convective activity across the Torino metropolitan region.

2.36 RADAR CHARACTERISTICS OF DEEP CONVECTION OCCURRED IN THE LAST DECADE ON THE TERRITORY OF SERBIA

MAJA RABRENOVIC[1]

[1] Republic Hydrometeorlogical Service, Serbia
maja.rabrenovic@hidmet.gov.rs

Summer period in Serbia is characterized by high thunderstorm activities and frequent severe weather followed by occurrence of large hail, severe winds and flesh floods, that makes damage to crops and sometimes even public infrastructure. This paper gives an analysis of different convective modes (supercells, squall lines, etc) occurred in the last decade on the territory of Serbia using radar and satellite images of the Republic Hydrometeorological Service of Serbia and in the final part recommendations will be given for the improved forecasting of these severe weather events.

2.37 USING A FOUR-DIMENSIONAL VARIATIONAL RADAR AND SURFACE DATA ASSIMILATION SYSTEM TO INVESTIGATE THE PROCESS LEADING TO A HEAVY PRECIPITATING EVENT OVER COMPLEX TERRAIN: A CASE STUDY IN NORTHERN TAIWAN

Y.-J. WU[1], Y.-C[1]. LIOU, S.-L. TAI[2], J. SUN[3]

[1] Dept. of Atmospheric Sciences, National Central University, Taiwan
[2] Pacific Northwest National Laboratory, USA
[3] National Center for Atmospheric Research, USA
wu890355@gmail.com

The complex terrain in Taiwan area makes it challenging to forecast convection initiation, propagation and intensification. In this research, a heavy rainfall event occurred on 19 August, 2014 in northern Taiwan is selected. We use a newly-developed four-dimensional Variational Doppler radar assimilation system (IBM_-VDRAS), which is capable of simulating the topographic effect by adopting the so-called Immersed Boundary Method, and assimilating radar observations and surface station data. The products of IBM_VDRAS are a series of frequently-updated three-dimensional analyses fields over the complex terrain. In this case study a total of eight analysis fields are generated with a temporal interval of 17.5 min over a period of 2.5 hours.

From the surface observations and the high temporal/spatial resolution analysis fields generated by IBM_VDRAS, it is found that the rainfall process starts from the initiation of individual convective cells. The outflow of one of the convective cells merges with another convective system, and helps to intensify the latter. The intensified major convective cell moves into the Taipei metropolitan, and produces 80 mm of heavy precipitation within 2 hours. The role played by the topographic forcing on the development of the convective system is investigated. A series of experiments are also designed by taking into account the surface heat and moisture flux to examine IBM_VDRAS′ performance in short-term rainfall forecast.

2.38 EXTREME RAINFALL ANALYSIS AND ESTIMATION OF INTENSITY-DURATION-FREQUENCY CURVES USING DUAL POLARIZATION WEATHER RADAR DATA OF ESTONIA AND ITALY

T. VOORMANSIK[1,2], R. CREMONINI[3], D. MOISSEEV[4], P. POST[2]

[1] Estonian Weather Service, Estonian Environment Agency, Tallinn, Estonia
[2] Institute of Physics, University of Tartu, Estonia [3] Department of Forecasting Systems, Regional Agency for Environmental Protection of Piemonte, Torino, Italy
[4] Department of Physics, University of Helsinki, Finland
tanel.voormansik@ut.ee

Intensity-duration-frequency (IDF) curves are widely used to quantify the probability of occurrence of extreme rainfall events. These data are commonly taken into account when designing storm water management systems. Rain gauge data have often been used to estimate the rainfall intensity for a given return period. However, the main issue of using rain gauges for this purpose is their low spatial and temporal resolution. Here, weather radar data have obvious advantage with their higher spatial and temporal resolution.

Past studies used horizontal reflectivity (Zh) based rainfall estimates, but they come with a great caveat while proven reliable on low rainfall rates they are subject to major errors in extreme rainfall and convective cases. It is widely known that especially shorter wavelength X-band and C-band weather radars underestimate precipitation intensity due to attenuation and overestimate due to hail contamination.

This study attempts to circumvent these shortcomings by using specific differential phase (KDP) data from dual polarization radars which is immune to attenuation and hail contamination issues. The aim of this study is to derive and analyze IDF curves from polarimetric weather radar data using KDP based quantitative precipitation estimations (QPEs). Furthermore, these parameters were also calculated from legacy Zh based radar rainfall and rain gauge data and they were included in the comparative analysis. Weather observations from Italy and Estonia, hence in two different climate regimes, were used to study the performance of the method in different climate conditions and radar hardware setups.

Data from warm period of the year were used as most of the extreme precipitation events take place at this time. Limiting the dataset to this period also helps to ensure that radar reflectivities are only from liquid precipitation which is required for reliable rainfall intensity estimation by KDP. For Estonia the warm period was defined as months from April to October and for Italy from March to November.

Single radar site data was used both from Estonia and Italy. From Italy radar data from Bric della Croce dual-polarization Doppler C-band radar located in Turin, northern Italy, were used. It was available with 5 minutes temporal resolution and from years 2012-2016. From Estonia radar data from Estonian Weather Service operated Srgavere dual-polarization Doppler C-band radar located in central Estonia in Viljandi county were used. It was available with 15 minute temporal resolution and from years 2010-2016. The lowest Plan Position Indicator (PPI) scan was used to derive radar Zh and KDP based QPEs.

Rain gauge observations were used for the reference IDF curves calculation. From Italy 1-minute tipping bucket rainfall data were available from 1988 to 2016. From Estonia 10-minute gauge data were available from 2011 to 2016, while for the period 2003-2010 rain gauge data were available with 1 hour resolution.

Session 3. Radar networking



Keynote presentation

3.1 A RENDEZVOUS OF RESEARCH AND OPERATIONS THE NEW SWISS RADAR GENERATION

U. GERMANN[1], M. GABELLA[1], H. BARRAS[1,2], Y. BARTON[1,2], N. BESIC[1,3], M. BOSCACCI[1], L. CLEMENTI[1], J. FIGUERAS[1], L. FORESTI[1], J. GRAZIOLI[1], U. HAMANN[1], A. HERING[1], D. NERINI[1,4], L. NISI[1], L. PANZIERA[1], M. SARTORI[1], I. SIDERIS[1], S. TREFALT[1,2], F. VAN DEN HEUVEL[1,3], B. CALPINI[1]

[1] MeteoSwiss, Locarno-Monti, Switzerland
[2] University of Bern, Mobiliar Lab for Natural Risks, Switzerland
[3] Environmental Remote Sensing Lab, EPFL, Lausanne, Switzerland
[4] Institute for Atmospheric and Climate Science, ETH, Zurich, Switzerland
urs.germann@meteoswiss.ch

The renewal and extension of the operational Swiss radar network is completed. The design was driven by the needs of air traffic control, civil protection and hydrology requiring high stability, availability and accuracy. The complex terrain in the Swiss Alps and the demands for new and customized products also require adapted data processing and flexibility for continuous improvements. Furthermore, two new radar stations are located on mountain tops close to 3000 meters above sea level, a challenge for installation, operation and data processing. The system combines fully-digital dual-polarization Doppler receiver-over-elevation technology and has triggered an avalanche of innovation and research. The paper presents the design and performance of the network and discusses recent achievements and ongoing research.

More than 350 system parameters are monitored and submitted from each radar to the central server after completion of every single sweep, that is 20 times in five minutes. The parameters are crucial for the surveillance of unmanned stations on remote mountain tops and are automatically checked for anomalies and archived for diagnostic analyses.

Dual-polarisation capability has proved its practical usefulness in short time. The incorporation of polarimetric moments in the clutter suppression substantially improved the distinction between mountain returns and weather, especially in regions with Doppler velocity close to zero. A semi-supervised polarimetric hydrometeor classification was developed and implemented. The usage of dual-polarisation for attenuation correction and QPE is under investigation. The QPE processing chain is currently being re-designed with the aim to incorporate dual-polarization and hydrometeor-specific processing and to replace the VPR correction operational since 2001 with a novel approach for vertical extrapolation.

The operational space-time kriging-with-external-drift technique for real-time integration of radar and rain-gauge data has recently been upgraded to 5-minute resolution. This was possible thanks to the development of new algorithms for

automatic identification of outliers and proper treatment of representativeness errors of gauge data in convective rain.

For seamless blending of QPE, Lagrangian nowcasts and NWP forecasts we are currently testing flow-dependent methods using local anisotropic correlated noise and a Kalman-ensemble filter. Furthermore, we are exploring the added value of machine learning techniques trained on 10+ years of radar imagery to predict flow-dependent growth and decay as precipitation moves over the orography. The QPE archive has also been used to derive a radar-based study of extreme rainfall over Switzerland.

For the nowcasting of convective storms radar cell tracking is integrated with satellite and lightning data and the operational nowcasting systems TRT and COALITION are continuously being improved. In addition to the existing single-polarization hail algorithms hail is identified operationally in 3D using dual-polarization moments. In order to verify and re-calibrate radar hail algorithms hail information from three independent sources is combined: crowd sourced reports from users of the MeteoSwiss weather app, insurance damage claims, and kinetic energy and diameter of hail stones observed by a new network of 80 automatic hail sensors currently under construction. The combination builds the basis for automatic hail nowcasts and a new hail climatology over Switzerland.

3.2 OPERA PAST, PRESENT AND FUTURE

E.SALTIKOFF[1], G.HAASE[2], P.NOVÁK[3], H.LEIJNSE[4], L.DELOBBE[5]
[1] Finnish Meteorological Institute, Finland
[2] SMHI, Sweden
[3] CHMI, Czech republic
[4] KNMI, The Netherlands
[5] RMI, Belgium
elena.saltikoff@fmi.fi

The EUMETNET Radar project OPERA is transiting from one programme phase (2013-2018) to next one (2019-2023). So what has been achieved?

A visible difference can be seen in the Pan-European composites produced by the OPERA operational data center (Odyssey). First, the area covered by the composite has been substantially increased by the progressive incorporation of new radars. The quality and the homogeneity of the composite have increased as well. During the first year, the homogenization was mainly due to improvements in incoming data, but from late 2015 the central processing has been cancelling more unwanted echoes than before through non-meteorological echo detection algorithms and the application of a satellite-based cloud mask. This increase in quality has been confirmed with quantitative studies. The negative bias in the northern areas is also obvious, and applications for VPR and different ZR for snow have been developed but not yet applied operationally.

OPERA has defined and maintains the OPERA Data Information Model (ODIM), which is used for description of weather radar data in HDF5 or BUFR format. This format has became the standard for radar data exchange over the Europe. It is vital for running of Odyssey and it has also accelerated bilateral exchange of radar (volume) data between meteorological services.

OPERA has also executed several surveys and studies. Results from a survey about maintenance shows large differences in national maintenance policies, and reveals that the primary causes of missing data are not with the radar itself but are related to issues with the electricity supplies or telecommunications. A survey about application priorities shows that the most important uses of radar data are aviation and severe weather warnings. Importance of other applications such as hydrological applications, NWP assimilation and verification, television and web have a large variability across Europe. These differences of priorities of national meteorological services is the main reason of the wide variability in measurement schedules observed over Europe.

The use of polarimetric radar variables in Europe was also subject of a survey. Currently the largest benefit of dual-polarization radars is in the quality improvement of other data (reflectivity and Doppler), especially in removal of unwanted echoes such as radio interference and wind turbines. Only a limited number of OPERA members are testing dual-pol attenuation correction, and even less have started using this operationally.

In the next programme phase, OPERA is focusing even harder on the needs of users outside the radar community. We have identified several different user types, and discuss splitting the production lines accordingly. What will certainly continue

is the exchange of knowledge, information and experiences between European radar experts, which has been the heart of OPERA for 20 years.

3.3 MULTI-RADAR MULTI-SENSOR QPE SYSTEM: OVERVIEW AND FUTURE

K. HOWARD[1], J. ZHANG[1], L. TANG[1,2], S. COCKS[1,2],S. MARTINAITIS[1,2], C. LANGSTON[1,2],K. COOPER[1,2], J. GOURLEY[1], A. ARTHUR[1,2]

[1] National Severe Storms Lab, USA

[2] University of Oklahoma/CIMMS, USA

kennth.howard@noaa.gov

Over the last two decades there has been a rapid expansion of weather radar and surface networks worldwide. These networks have provided meteorologists and hydrologist critical information for situational awareness for extreme weather and flash floods. Radar observations alone provided hydrologists with precipitation information at a much higher spatial and temporal resolution than the traditional gauge observations. Along with the deployment of radar and surface networks, advances in computational speed and expanding communications bandwidth has facilitated the movement of base data from individual radar sites into regional and national centers for processing and product generation that is unprecedented. The Multi-Radar Multi-Sensor (MRMS, Zhang et al. 2016) system implemented at the United States National Center for Environmental Prediction (NCEP) demonstrates such capabilities by integrating ∼180 operational weather radars from conterminous United States and Canada into a seamless national 3-D radar mosaic with very high spatial (1 km) and temporal (2 min) resolution. The radar network data was integrated with high-resolution numerical weather prediction model data, satellite data, model analysis and rain gauge observations to generate a suite of severe weather and quantitative precipitation estimation (QPE) products.

A unique feature of MRMS is a standalone research system that runs in real-time at the National Severe Storms Laboratory (NSSL), which includes a real-time web-based verification and product assessment system for QPE and QPF. The MRMS verification system provides statistical tools and screening procedures for viewing and analyzing real time operational, experimental and historical products in addition to MRMS QPE products. Operational forecasters from US National Weather Service Forecast Offices and River Forecast Centers have used the web-based verification system and provided invaluable feedback that guided MRMS research and development. The real-time MRMS research system serves as a national testbed for advanced radar applications and can facilitate rapid and seamless research to operations transitions for new radar QPE technologies.

The talk will provide an overview of the current and near future capabilities of the MRMS systems.

References

Zhang, J., K Howard, C. Langston, B. Kaney, Y. Qi, L. Tang, H. Grams, Y. Wang, S. Cocks, S. Martinaitis, A. Arthur, K. Cooper, J. Brogden, D. Kitzmiller, 2016: Multi-Radar Multi-Sensor (MRMS) Quantitative Precipitation Estimation: Initial Operating Capabilities. Bull. Amer. Met. Soc., 97, 621-638.

3.4 NEW OPERATION STRATEGIES FOR NATIONWIDE WEATHER RADAR NETWORK IN KOREA

SUNG-HWA JUNG[1], JONG-SEONG KIM[1], YOUN CHOI[1], SUN-KI LEE[1], DONG-JIN KIM[1], JEONG-WHAN LEE[1]

[1] Weather Radar Center, Korea Meteorological Administration, Seoul, Republic of Korea
shjung95@korea.kr

Operational efficiency of nationwide weather radar network depends on the design of radar operation strategy that involves a combination of various radar scanning strategies and an efficient data processing. Over the last decades, Korea Meteorological Administration (KMA) has employed two fixed scanning strategies with 10 minutes update cycle, which is composed of the volumetric scan (∼240 km) with 10∼12 elevation angles and long-range scan (∼480km) of single elevation angle. The elevation angles in the conventional scan strategies were subjectively designed by human experiences. These scanning strategies shows the weakness such as failing to detect a shallow convection or an initiation of convective system that occurred at low altitude below 1km above the ground while they provide three-dimensional structure of deeply developed weather system successfully. In addition, the existing data processing chain is also not suitable for providing an early monitoring of rapidly developing convective system because they start processing a radar data after completion of volumetric scan over all elevation angles. For more effective operation of radar network, we evaluated the current scanning strategies and proposed new scan strategies that are objectively determined based on radar beam propagation simulation. The existing scanning strategies can only cover 24% area below 1km above ground while the coverage of new strategies occupied 47%. New strategies employed more rapid update cycle of 5 minutes and negative elevation angles for more effective monitoring of low level convection. For removal of second trip echo and calibration of system biases in reflectivity and differential reflectivity, we employed an efficient combination of long-, short-range, and vertical pointing observation, and we set up suitable sampling number, quality parameters, and dual-PRF at each elevation angle. The data processing procedure is also changed into fast processing chain based on single sweep in volume scan instead of full volumetric scan. First accessible time of final radar product such as nationwide mosaic was reduced from 20 minutes to 5 minutes after beginning time of radar observation. Furthermore, to increase low level coverage over Seoul metropolitan area, three X-band radar networks have been installed. By combination of S- and X-band radar network, the low coverage of radar network below 1km above ground would be increase from 22% into 94%.

Acknowledgements
The research is supported by "Development and application of cross governmental dual-pol radar harmonization (WRC-2013-A-1)" project of the Weather Radar Center, Korea Meteorological Administration.

3.5 LONG-TERM ANALYSIS OF GAUGE-ADJUSTED PAN-EUROPEAN RADAR RAINFALL ACCUMULATION

SHINJU PARK[1], MARC BERENGUER[2], DANIEL SEMPERE-TORRES[3]

[1] Universitat Politcnica de Catalunya, Center of Applied Research in Hydrometeorology (UPC-CRAHI), Barcelona, Spain

[2] Universitat Politcnica de Catalunya, Center of Applied Research in Hydrometeorology (UPC-CRAHI), Barcelona, Spain

[3] Universitat Politcnica de Catalunya, Center of Applied Research in Hydrometeorology (UPC-CRAHI), Barcelona, Spain

shinju.park@crahi.upc.edu

High-resolution pan-European radar composites (2 km, 15 min) have been produced operationally by EUMETNET OPERA (Operational Programme for the Exchange of weather RAdar) data center ODYSSEY since 2012. In the framework of a number of European projects (e.g., H2020-ANYWHERE, EC-SMUFF) on flash flood hazard assessment and nowcasting, CRAHI-UPC has been producing near real-time radar rainfall accumulations from the OPERA rainrate composites accounting for the effect of the precipitation motion.

Because the quality of the input rainfall accumulation is critical to the flash flood hazards assessment, the pan-European radar accumulation products are adjusted in real-time using a spatially-variable factor. This adjustment factor is calculated based on the long-term comparison (up to 6 months) of daily radar rainfall accumulations with those calculated from SYNOP-gauge records at European scale.

We present the analyses of OPERA rainfall accumulations with and without the gauge adjustment during the period of 2015-2017 showing the status of radar QPE and the impact of the QPE to the flash flood identification.

3.6 THE CASA DALLAS-FORT WORTH URBAN DEMONSTRATION NETWORK AFTER 5 YEARS OPERATION: ACCOMPLISHMENTS AND CHALLENGES FROM A UNIQUE PLATFORM OF COLLABORATIVE PARTNERSHIP BETWEEN LOCAL, REGIONAL AND NATIONAL ENTITIES

V. CHANDRASEKAR[1], HAONAN CHEN[1], BRENDA PHILIPS[2], FRANCESC JUNYENT[1], ERIC LYONS[2], APOORVA BAJAJ[2]

[1]Colorado State University, Fort Collins, USA
[2] University of Massachusetts Amherst, Amherst, USA
haonan.chen@colostate.edu

Since the establishment of the center for Collaborative Adaptive Sensing of the Atmosphere (CASA) dedicated to innovative sensing of the lower atmosphere, the X-band radar system has been an emerging tool for severe weather warning and decision making. Typical examples include the dense X-band radar networks planned or already deployed in big cities such as Dallas-Fort Worth (DFW), Beijing, Tokyo, and the RainGain project in Leuven-London-Paris-Rotterdam. These X band radar networks are developing their own operational domain for urban weather disaster detection and mitigation. CASA has been operating a Research-to-Operations (R2O) radar network in DFW metroplex for over five years. During the five years operation, CASA has developed a real-time end-to-end weather warning system that includes sensors, software architecture, products, data dissemination and visualization, and user decision making. This innovative system is a partnership of academic institutions, National Weather Service, local government agencies, and business user community.

A number of real-time product sub-systems have been developed for sever weather detection and quantification in a live environment for DFW area. Over 1000 public safety officials and 300 residents are using the CASA mobile app for receiving context-aware alerts derived from these products. The local Weather Forecast Office is using the real-time data and products operationally when issuing weather watches and warnings. At the same time, local stakeholders and weather stations are also providing live data into the network to demonstrate how a regional approach to a heterogeneous Network of Networks can help provide a more complete picture of the lowest parts of the atmosphere. For example, in-situ measurements of hail and wind by Understorys network of over 140 sensors in the DFW area are ingested into the CASA data stream in real-time, which can be used to combine with radar data and alert users in emergency management to dangerous wind and hail conditions in their area. Customers from across economic sectors are partnering with CASA to evaluate how high resolution radar data can help with improved decision making when bad weather occurs.

This paper presents the accomplishments and lessons learned from the five years operation of the CASA DFW dense urban radar network. Various application products in the presence of hails, tornadoes, floods, and high-winds will be detailed. The product performance is demonstrated through cross-comparison with ground weather reports and in-situ observations. This paper will also discuss our findings

related to user needs for weather information, challenges in creating and delivering products, and user feedback on the value proposition from both scientific, engineering and economic perspectives.

3.7 PROSPECT OF IMPLEMENTING THE ADVANCED RADAR REFRACTIVITY TECHNIQUE ON OPERATIONAL RADARS

YA-CHIEN FENG[1], FREDERIC FABRY[2], MICAHEL M. BELL[3]

[1] Colorado State University, Fort Collins, USA

[2] McGill University, Canada

ya-chien.feng@colostate.edu

Radar refractivity is a proxy for two-dimensional near-surface moisture fields. This technique is based on the temporal phase variation from ground targets as an indication of the refractivity change along the radar beam path. High temporal and spatial resolution refractivity maps have been used to study the spatial variation of near-surface moisture associated with convection evolution and boundary layer processes, as well as for assimilation in numerical weather prediction models to improve quantitative precipitation forecasting skills.

In this study, we introduce the recent progress in the radar refractivity retrieval technique and how these improvements benefit the future implement on operational radars. With the improved algorithm, the three-dimensional refractivity information is provided, consisting of a horizontal map at a given height above the terrain and the averaged refractivity profile over the data coverage. Newly obtained knowledge on the ground targets also improve the ground target section at the calibration stage and the quantification of observation errors. The related preparation, such as scanning strategy, will be suggested. In the second part, new prospects on how to use the refractivity fields will be introduced with examples, e.g. heat island effect.

3.8 MULTI-RADAR DATA FUSION FOR HIGH-RESOLUTION QPE IN URBAN AREA

BRANDON HICKMAN[1,2], JUSSI TIIRA[2], ROBERTO CREMONINI[2,3], DMITRI MOISSEEV[2,4]

[1] University of Bonn, Germany
[2] Institute for Atmospheric and Earth System Research / Physics, University of Helsinki, Finland
[3] ARPA-Piemonte, Turin, Italy
[4] Finnish Meteorological Institute, Helsinki, Finland
bhickman@uni-bonn.de

Urban areas are the most sensitive areas to extremes in precipitation, but also offer a slew of problems. Observations of precipitation in urban areas requires high-quality data with accurate temporal-spatial resolution in order for accurate understanding, analysis, and forecast. The Helsinki weather radar network, which consists of three dual-polarized C-band weather radars, is presented. To enable use of the radar network for quantitative precipitation estimation and urban hydrological applications a quality-based data compositing method is developed. Given the urban location of the radars and the objective of observing precipitation at relatively close ranges a number of data quality issues have to be addressed including ground clutter, beam and radome attenuation, beam blockage, and beam broadening and overshooting. The urban location produces a rather challenging environment for ground clutter and beam blockage and the application of even advanced ground clutter filters could cause data loss in regions of interest. Quantitatively precipitation estimations (QPE) especially close to a radar imply that wet radome attenuation as well needs to be accounted for. A self-consistency method was implemented for calibration of reflectivity for the individual radars, as well as being implemented as a filter for spurious specific different phase measurements. It is shown that most of the listed and additional data quality problems can be resolved by using the proposed quality-controlled compositing method. In order to increase the temporal resolution of the composite and to match observations from radars that are operating on non-synchronized scan strategies, an minutely interpolation is performed over the QPE output. A blended dual-polarization rainfall algorithm, that uses a combination of R(ZH) and R(Kdp) relations, is implemented to illustrate an application of the quality controlled composite to QPE. Comparisons to local urban rain gauges shows considerable improvement over the individual radars.

3.9 CHARACTERISTIC SPATIAL EXTENSION OF RAIN EVENTS IN GERMANY FROM A RADAR BASED PRECIPITATION CLIMATOLOGY

K. LENGFELD[1], M. HAFER[1], T.JUNGHÄNEL[1], E. WEIGL[1], T. WINTERRATH[1], A. BECKER[1]

[1] Deutscher Wetterdienst, Offenbach am Main, Germany
katharina.lengfeld@dwd.de

Precipitation is highly variable in space and time. In contrast to in-situ observations with rain gauges, weather radars provide reliable information also on the spatial variability and the extent of precipitation. Since 2001 the Deutscher Wetterdienst (DWD) operates a nationwide network of C-band weather radar systems. A climatology for Germany has been generated from this 16-year radar-based precipitation dataset permitting the analysis of extreme rainfall for different durations D and return periods T as well as their spatial distribution and extension on a 1 km x 1 km grid.

The spatial distribution for rare events with long durations (e.g., T=20 a, D=24 h) obtained from the radar climatology is clearly influenced by the orography and coincides well with those obtained from interpolated rain gauge data. However, in case of short duration (D=1 h) the spatial distribution and structure differs significantly between radar and rain gauge based climatologies, because these are mainly based on local events with sizes too small to be sufficiently captured by the rain gauge network. The radar based climatology indicates that strong short term events can occur everywhere regardless of the orography.

The correlation between the time series of all grid points allows for an estimation of the spatial extension of rain events with different durations. The correlation length (drop in correlation to 1-1/e) indicates that typical extensions are approximately ten times smaller for D=1 h than for D=24 h in case of T=20 a. Additionally, the field of correlation coefficients reveals regions of similar characteristics of rain events, e.g., mountainous regions in South-West and Central Germany.

We will give a brief overview of the methods used to compute the radar climatology and a comparison of radar- and gauge-based precipitation maps for selected durations and return periods. Furthermore, the characteristic spatial extension of rain events with certain durations and return periods will be investigated.

3.10 ENGAGING THE RADAR COMMUNITY THROUGH OPEN SOURCE SOFTWARE

Z. SHERMAN[1], S. COLLIS[1], R. JACKSON[1]

[1] Argonne National Laboratory, USA
zsherman@anl.gov

Hosted on GitHub and implemented in the Python programming language, the Python Atmospheric Radiation Measurement (ARM) Radar Toolkit (Py-ART) is an instrumental component in radar workflows at many institutions. Py-ART is used for reading, plotting and analyzing radar data and has a rich input/output suite making it applicable to many platforms. The package also has a variety of correction and retrieval algorithms that allow for the user to quality control their data, such as attenuation corrected reflectivity and velocity dealiasing. Py-ART can create plots from different scan types, and can also be used to create Cartesian grids from data from one or more radars. Py-ART has grown over the years, and this is due to the open source community. Partly due to the use of good software engineering practices (self documenting code, modularity and unit testing), Py-ART is particularly amenable to accepting contributions from the community. With 25 contributors, Py-ART has become a platform for collaboration in the radar community. This presentation will describe Py-ART as a project, provide some specific examples of how the community came together to make radar code better and introduce the Py-ART roadmap, a five year plan leading to a fully featured open source architecture: Py-ART 2.0.

3.11 POTENTIAL FOR USE OF RADAR DATA FOR CLIMATE MONITORING

E.SALTIKOFF[1], A.BECKER[2], R.HOLLMANN[2], B.URBAN[3], K.FRIEDRICH[4], C.TASSONE[5]

[1] Finnish Meteorological Institute, Finland
[2] Deutscher Wetterdienst, Germany
[3] Meteo France, France
[4] University of Colorado, United States
[5] World Meteorological Organization, Switzerland
elena.saltikoff@fmi.fi

Many NMHSes have now archives of over 10 years of radar data, and there is growing need to use this data also for climate monitoring. This implies an additional archival and documentation requirement on top of those that had been addressed for the canonical use of radar systems for real-time purposes like warning.

Through WMO and GCOS a Task Team has been initiated leading discussions between climate researchers and radar experts, and preparing recommendations for mandatory and suitable data and metadata to be archived for climate monitoring purposes. This serves the baseline information to develop accepted guidelines and standards, with a view on the rather limited lifetimes of radar systems being shorter than those of stations and the characteristic climate time scale of 30yrs. Therefore it is essential to keep not only the metadata describing the latest hardware and processing, but also a history of important hardware changes such as from non-Doppler to Doppler radars to allow for a full retrieval of the essential information also decades after the measurements had been taken and to avoid false interpretations of apparent trends which come from changes in equipment, not changes in climate.

The phenomena to be monitored with weather radars include in addition to precipitation also severe mesoscale phenomena such as hailstorms and tornadoes e.g., Becker 2013, Brimelow 2004,Chen 2012, Grams 2012, Lukach 2017, Nisi 2015, Punge 2016

The central parameter is horizontal reflectivity, ZH, which is basis of precipitation estimates. The other key parameters have importance for improving the quality of precipitation estimates and as independent variables for process and climate studies. As for the extreme precipitation, radar systems are the only instruments that can claim to fully resolve and fetch the scale of such meteorological events giving their unique capacity to study their developments during the first decades where climate change impacts the hydrometeorology.

The team is proposing a recommendation to save the Level 2 data (dBZ, not mm, and volumes, not images) to allow later reprocessing with more advanced methods. For this, the team prepared also example tables for metadata parameters.

References

Becker, A, 2013: Review of the climate requirements for Weather Radar data. CBS Workshop on radar data exchange, CBS/OPAG-IOS/WxR_EXCHANGE/2.4

Brimelow et al,2004: A radar-based methodology for preparing a severe thunderstorm climatology in central Alberta. Atmosphere-Ocean.

Chen et al 2012: Diurnal variations in convective storm activity over contiguous North China during the warm season based on radar mosaic climatology. JGR

Grams et al, 2012: A Climatology and Comparison of Parameters for Significant Tornado Events in the United States. Wea.Forec.

Lukach, M., L. Foresti, O. Giot and L. Delobbe (2017): Estimating Occurrence and Severity of Hail Based on 10-years Observations From Weather Radar in Belgium. Meteor. Appl.

Nisi et al, 2015: Spatial and temporal distribution of hailstorms in the Alpine region: a long-term, high resolution, radar-based analysis. QJRMS

Punge et Kunz, 2016 Hail observations and hailstorm characteristics in Europe: A review. Atm.Res.

3.12 SEVERE WEATHER AND HAIL DETECTION USING THE X BAND WEATHER RADAR TUSCANY NETWORK

A. ANTONINI[1], S. MELANI[1,2], A.ORTOLANI[1,2], A. TELLESCHI[3], A. LOMBARDI[3], I. GIANNINI[3], B.GOZZINI[1,2]

[1] LaMMA Consortium, Italy
[2] CNR-IBIMET, Italy
[3] ELDES s.r.l, Italy
antonini@lamma.rete.toscana.it

In the last years, an occurrence increment of the weather patterns generating severe thunderstorms was observed for the Mediterranean area. This aspect has been particularly relevant in Tuscany (central Italy) where several heavy rains events leaded to river floods and landslides, especially in coastal areas. Indeed, the synergy of high sea surface temperatures and moist air-masses combined with deep troughs can produce very unstable environments that are favourable to the occurrence of such events.

For a better characterization of these phenomena and for limiting the related risks, a regional X-band weather radar network has been implemented in the Tuscany coastal areas. Three single-polarization weather radars, located in Livorno, Castiglione della Pescaia and Cima di Monte (Elba island), compose the regional network.

Firstly, this work describes the performances of such a network in the monitoring of some precipitation events, particularly intense. The radar composite has been compared with some ancillary data as satellites, raingauges, lightning observations and other radar systems operating in different frequencies (C and S band).

Severe weather systems are sometimes characterized by the presence of hail. Because of its spatial and temporal variability, an accurate detection of hail from ground measurements is very difficult, but an operational hail detection system could be useful for several objectives, from supporting risk management at urban scales to the assessment of damages in agriculture.

Few methods exist for automatic hail detection using single polarization radars, mainly based on the analysis of the vertical structure of reflectivity. Some methods use ancillary data, as the freezing level and the ground temperature, for a better characterization of the microphysics of the maximum vertical reflectivity cell, and consequently the presence of hail.

Two different algorithms, based on the Waldvogel approach and on the Vertically-Integrated Liquid Density (VIL-Density) product, have been tested and compared to assess the capability of such radar network in hail detection with the aim of developing a POH (Probability-of-Hail) index.

Some hail case studies, identified by the Tuscany meteorological office reports, have been analysed and preliminary results concerning the performances of these methods are shown.

3.13 ENHANCING WEATHER SURVEILLANCE WITH EECS 3.5GHZ HIGH FREQUENCY DUAL-POL S-BAND WEATHER RADAR SYSTEMS

DR. QING CAO[1], R. STEDRONSKY[2], M. KNIGHT[3]

[1] First Author's affiliation and country: Enterprise Electronics Corporation (EEC), Norman, Oklahoma, USA

[2] Second Author's affiliation and country: Enterprise Electronics Corporation (EEC), Fort Worth, Texas, USA

[3] Third Author's affiliation and country: Enterprise Electronics Corporation (EEC), Enterprise, Alabama, USA

qing.cao@eecweathertech.com

Weather radar systems typically operate in one of three frequency bands: S-band, C-band, or X-band. In general, S-band weather radars have the longest surveillance range, the least Doppler velocity ambiguity, and the best performance in observing severe weather (hail, tornado, hurricane, etc.). Therefore, the National Weather Service (NWS) in the United States (US) has chosen the S-band frequency range (2.7-3.0 GHz) for its nationwide Next-Generation Weather Radar (NEXRAD) network. A major disadvantage for S-band radars is the large antenna required to achieve a comparable angular resolution as compared with C-band/X-band radar. The NEXRAD systems typically use a ∼8.5 m (28-foot) dish, achieving a beam width of 0.96°@2.7 GHz and 0.88°@3.0 GHz. Given such a large antenna, the system complexity and cost, both up-front and life-cycle, are considerably higher than comparable C-band and X-band systems.

Recently, Enterprise Electronics Corporation (EEC) in Alabama, United States, developed a new type of "high-frequency" (3.5-3.6 GHz) S-band weather radarthe Defender SK1000H series. Compared to NEXRAD systems, EEC's "high-frequency" system applies a much smaller antenna (6.096m or 20-feet), while maintain a similar beam width (0.95°) to that of more traditions S-band radars with a 8.5m dish. Therefore, its size, cost, and complexity are effectively reduced. In addition, due to the frequency increase (from 2.7-3GHz to 3.5-3.6GHz), the radar performance is improved for radar sensitivity, measurement accuracy, and clutter filtering. It is noted that the attenuation @3.5 GHz is only slightly increased and does not affect data quality.

EEC's "high-frequency" Defender SK1000H systems have been delivered to several television (TV) station customers across the US to provide local weather analysis. These systems are generally operated with a very high spatial-temporal resolution configurations (0.25 degree and 125 meters azimuth-range resolution, updating every 0.5-1 minute). Compared to NEXRAD data (0.5-1 degree, 250-1000 meters, updating roughly every 5 minutes), the high-resolution Defender SK1000H data presents surprisingly in-depth details of storm features and evolution. With EEC's advanced radar analysis software, EDGE, the local TV stations can provide high quality weather services, such as quantitative precipitation estimation, flash flood forecasts & warning, and severe weather detection, nowcasting, & alerts. This study presents several cases of high-quality weather surveillance taken from operational EEC Defender SK1000H "high-frequency" S-band radar systems, including several tornadoes and hailstorms in the southern plains of US.

3.14 NETWORK OF WEATHER RADARS IN REPUBLIC OF SRPSKA, BOSNIA, HERZEGOVINA

T. DEJANOVIC[1], V. VRANIC[2], Z. VUCINIC[3]

[1] JP "Protivgradna preventiva RS" a.d., Republic of Srpska, Bosnia and Herzegovina
[2] "Protivgradna preventiva RS" a.d., Republic of Srpska, Bosnia and Herzegovina
[3] Republic hydrometeorological service of Serbia, Serbia
tihomirdej@gmail.com

This paper will present a new weather radar network in the region of the Western Balkans. This new radar network will very well fit into the existing radar networks in Croatia and Serbia, so that by establishing it, most of the Western Balkan region will be covered by high quality radar data.

During July 2017, JP "Protivgradna preventiva RS" a.d. has installed the EEC DWSR-3501C SDP Doppler Weather Radar at the location of Borje, Republic of Srpska, Bosnia and Herzegovina. The location of the new radar is Lat 44.58326400N, Long 17.60608900E and height 1075 m. From this location in the range of 200 km, most of the territory of Bosnia and Herzegovina, as well as parts of the territory of Croatia, are covered.

By the end of 2018 or at the beginning of 2019, it is planned to set up another EEC DWSR-3501C SDP Doppler Weather Radar at Jahorina, Republic of Srpska, Bosnia and Herzegovina. Location of the planned radar is Lat 43.72019944N, Long 18.56186110E and height 1911.5 m. In this way, in the 200km range, both radars would cover the entire territory of the Republic of Srpska, Bosnia and Herzegovina, parts of the territory of Croatia, Serbia and almost the entire territory of Montenegro.

Coverage of the territory of the new radar network and its integration into existing radar networks in Croatia and Serbia will be shown. Also, the connection of a new radar network in Republic of Srpska, Bosnia and Herzegovina to European and regional radar networks is planned, especially in the OPERA program.

3.15 IMPLEMENTATION AND OPERATIONAL USE OF A HETEROGENEOUS RADAR NETWORK IN THE COMPLEX OROGRAPHY OF ABRUZZO REGION

E. PICCIOTTI[1], S. DI FABIO[1], M. MONTOPOLI[2], S. BARBIERI[1], R. ZAURI[3], A. CIPOLLONE[3], F.L. ROSSI[3], F.S. MARZANO[1,4]

[1] CETEMPS, University of L'Aquila (Italy)
[2] CNR, Institute of Atmospheric Sciences and Climate of Rome (Italy)
[3] CFA, Functional Centre of Abruzzo Region Civil Protection (Italy)
[4] DIET, University of Rome (Italy)
errico.picciotti@aquila.infn.it

This work shows recent advancements in terms of structure, processing and mosaicking methods specifically implemented for the local radar network covering the Abruzzo region, in central Italy. The Abruzzo radar network (ARAD) design was driven by the needs of the Functional Centre of Abruzzo Region (CFA) for the detection and warning of severe weather and related hydrological risks, which requires high redundancy, availability and accuracy of radar data.

The hydrological risks are further enhanced by the complex topography of Abruzzo region, which is characterized by high mountainous, relatively small catchments, river basins and Adriatic sea side. Complex orographic environment introduces additional difficulties in the matching of observations of the same phenomenon from different radars during the mosaicking.

The ARAD is constituted by two single-polarization radars at C- and X-band, respectively and by two dual-polarization X-band radars jointly operated by the CFA and CETEMPS, respectively. Moreover in the south part of Abruzzo region, a dual-polarization C-band radar managed by the Italian Department of Civil Protection, is operative.

As known, any fruitful usage of network radar data either for quantitative precipitation estimation or just for operational monitoring, must deal with a careful check of data quality. This aspect is particularly critical for networks with heterogeneity radar having different system features. In this respect, a dedicated algorithmic chain, able to process raw data, enhance their quality, extract from them accurate and useful hydro-meteorological products have been developed and customized for the different installations.

Acknowledgements
This work is partly supported by EU co-financing and the Interreg Italy-Croatia CBC Programme through the AdriaMORE project.

3.16 A FIRST ANALYSIS OF THE VALLIRANA RADAR DATA QUALITY AND ITS CONTRIBUTION TO THE RADAR NETWORK OF THE METEOROLOGICAL SERVICE OF CATALONIA (XRAD)

O. ARGEMÍ[1], P. ALTUBE[1], T. RIGO[1]
[1] Servei Meteorològic de Catalunya, Barcelona
oargemi@meteo.cat

In 2012, the Vallirana radar (PBE) had a critical leveling pointing problem, among other issues, that arose because the antenna system was outdated and the tower was too old. From January 2013 to September 2016, the operation of this radar was interrupted, the old inappropriate tower was replaced for a new, reinforced one and the antenna-pedestal system was upgraded to the "standard" XRAD module, Orbit AL-1017-1E, in order to match the specifications of the rest of the XRAD radars. With these changes and the corresponding reception chain configuration, the PBE data has been included in the XRAD composite, improving the reflectivity data field coverage over Catalonia, especially over the Metropolitan Area of Barcelona (MAB), which is one of the most populated areas of South Europe, also with high precipitation rates and frequently affected by floods and severe weather.

The reception chain configuration included: (1) the receiver calibration measurements, (2) the tuning of the processing algorithms already implemented in the RVP8 signal processor and (3) the configuration tasks. One of the main problems, while configuring the PBE reception chain, was to deal with the high electromagnetic noise produced by the significant telecommunication activity in the surroundings of the radar site, which degrades the signal-to-noise (SNR) figure. On one hand, this random noise affects negatively the threshold values of the static quality filters applied: SNR (LOG), Clutter-to-Signal Ratio (CSR) and Signal Quality Index (SQI). On the other hand, the random noise in combination with the ground clutter produces false echoes, holes and speckles in the weather echoes registered by the radar. In this case, due to the noisier environment, the clutter filter which better minimizes these non-desired effects is the Gaussian Model Adaptive Processing technique (GMAP, Siggia and Passarelli 2004), while the common option in the XRAD is the use of a filter with fixed or variable window in the frequency domain. In this work, this issue is described and briefly discussed by comparing different reflectivity outputs depending on the configuration.

In the present work, a description of the PBE receiver calibration and antenna operation is presented. In addition, a XRAD coverage study over the MAB is carried on, comparing the situation with and without PBE. The incorporation of this radar to the XRAD improves notably the quality of the reflectivity field over this region, lowering the beam height relative to the terrain surface, increasing the registration time rate and filling the pixels that present beam blockage for the other XRAD radars.

Finally, in order to show the relevance of the PBE contribution to the XRAD composite, different rainfall episodes that took place at the beginning of 2018 have been analysed, comparing the outputs with and without the radar. The results of the evaluation of several derived reflectivity products, individual or composite, exemplify the data quality enhancement over the studied area.

3.17 REPLACEMENT OF THE CANADIAN WEATHER RADAR NETWORK

P.LEIBIUK[1], Q.LI[1], J.M.C.YOUNG[1]

[1] Meteorological Service of Canada
peter.leibiuk@canada.ca

On February 28th, 2017 Canada's Minister of the Environment and Climate change announced investments to modernize Canadas weather-forecasting infrastructure. As part of this initiative, an $83-million contract was awarded to Selex ES GmbH for 20 new weather radars that are to be built across the country by 2023, the first installation having been completed this past fall.

This exciting multi-year infrastructure project aims to replace the existing mixed national network of aging and obsolete single-polarized radars with new, modern, dual-polarized systems. Canadas existing network consists of 31 weather radars, including two radars operated in partnership with the Department of Defence and one owned by McGill University. One additional radar site will be added to provide new coverage in the Lower Athabasca region of Alberta. The contract also includes options to replace up to 13 additional existing radars in the network, within the same timeframe.

Accurate weather information is critical to the health, safety and economic prosperity of Canadians; as well as to security, defence, emergency management, and search and rescue. A new, modernized, sustainable, and reliable weather radar network is a central element of Environment and Climate Change Canada's monitoring infrastructure.

The approach used in designing this network modernization involved many factors, such as climatology, qualitative and quantitative user requirements, and lessons learned from over 30 years of operating and supporting the existing network.

A procurement strategy that included early consultations with industry was used to ensure the competitive solicitation balanced the desired system performance and features against was available from the industry in a field proven "turn-key" weather radar system.

In sharing the effective strategies and lessons learned during the planning, procurement, and early implementation stages of this project, the Meteorological Service of Canada aims to provide the radar community with information that can be leveraged by other services, and industry, to inform future large scale national weather radar network installations.

3.18 RADAR NETWORK, PRODUCTS AND PERSPECTIVES AT DEUTSCHER WETTERDIENST

K. HELMERT[1], T. HENGSTEBECK[1], M. MOTT[1], N. RATHMANN[1], J. STEINERT[1], P. TRACKSDORF[1], K. WAPLER[1], M. WERNER[1]

[1] Deutscher Wetterdienst, Germany
kathleen.helmert@dwd.de

Radar data and derived products play an important role in weather forecast and warn management. From 2011 to 2015 DWD has replaced the radar network with modern dual-polarization systems successively. Currently DWD operates a network of 16 C-Band dual polarimetric Doppler radars and one single polarimetric Doppler radar evenly distributed over Germany. The actual scan strategy enables spatial and temporal resolved 3D measurements every 5 min.

A comprehensive process chain in the software framework POLARA includes diverse algorithms for quality control, composite generation, creation of different products and offers the possibility for new developments or extension of existing algorithms. The dual-polarization measurements allow the derivation of new products like hydrometeor classification or an improved quantitative precipitation estimation. Several algorithms are used, which detect convective precipitation cells in 2D (e.g., KONRAD) and 3D radar data, such as a mesocyclone detection algorithm and the 3D cell detection (KONRAD3D, currently under development). The shift of radar products is realised on the basis of motion vectors derived from the motion in previous data.

The main focus in further development is an improved nowcasting for both convective and winter events. Especially the temporal development in precipitation events is taken into account. The complex three dimensional structure of precipitating clouds requires the use of parameters which best describe the cloud characteristics. New possibilities arise with 3D volume scans with 5-min intervals and the dual-polarisation technology as well as the combination with data from other sensors like satellites, lightning etc.

The presentation gives an overview about the actual status of the radar network, the algorithms and products as well as perspectives in further development.

3.19 NETWORKS OF UHF WIND PROFILERS WITH S-BAND DOPPLER RADARS

PARKSA KIM[1], BERNARD CAMPISTROM[2], KWANG-HO KIM[3], MIN-SEONG KIM[1], BYUNG HYUK KWON[4]

[1] Geo Sciences Institute, Korea
[2] Centre de Recherches Atmospheriques, France
[3] Weather Radar Center, Korea
[4] Pukyong National University, Korea
nhkwon@pknu.ac.kr

The Korean peninsula extends between 33°N and 40°N. It is bordered by the Yellow Sea to the west and the East Sea to the east. The Chinese mainland and the southernmost Siberian form its northern limit. This geographical environment induces a climate described as humid subtropical with well-marked and contrasting seasons. Spring and autumn are mild and temperate periods. During the summer a hot and humid monsoon regime is established. Under the continental influence, winter is generally cold and snowy. The weather events are very often violent, sudden and destructive: typhoons and torrential rains during the hot months, blizzard and winter snow storms blocking human activities in a very mountainous country. In these conditions, the weather forecasting is a perilous exercise of which the improvement need to implement powerful numerical models supported by dense networks of observation and measurement. This study focuses on the networks of wind profilers and weather radars that have been operated over the past ten years. The peninsula is covered by 10 UHF profilers and 11 Doppler weather radars (8 in the S-band and 3 in the C band). The spacing of these instruments is on average 150 km, which is particularly interesting resolution because it allows the restitution of wind field in 3D at atmospheric boundary layer as well as mesoscale, and the direct comparison with the meteorological models. These networks also make possible the experimental restitution of second-order parameters of the divergence and rotation type, which are often tainted by error in digital applications. The evaluation of these networks is the objective of this study.

3.20 KMA DUAL-POLARIZATION RADAR NETWORK AND OBSERVATION DATA QUALITY

BONGJAE KUK[1], JONGSUNG KIM[1], WEONIL SOHN[1], WOOSUK KIM[1], HYE-YOUNG HAN[1], DONG-JIN KIM[1], SUN-KI LEE[1]

[1] Weather Radar Center, Korea Meteorological Administration, Republic of Korea
bjkuk@korea.kr

There were many issues related with weather radar operation in and outside of Korea Meteorological Administration (KMA) at the stage of establishment of Weather Radar Center (WRC). Outside of KMA, since the other different governmental agencies had been operating their own weather radars, it was needed to collaborate on radar operations among agencies and manage it more efficiently, and lead the entire weather radar operations to incorporate eventually as one in South Korea. Meanwhile inside of KMA, the organization had a self-modernization plan to improve service quality to satisfy in response to gradually increasing needs on public weather service. Eventually, in order to come up to their expectations, WRC was established April, 2010.

As a part of improvement plan on service quality, WRC/KMA determined to install 10 operational radars and 1 Radar Test Bed (RTB) for dual-polarization as one model from the same manufacturer. In the year of 2012, with the beginning of RTB installation at Yong-In, a total of 8 dual-polarization radars were replaced, and 2 radars are being replaced this year. The entire installation of the weather radars will be done in year of 2019 at Gangneung site.

The observation data quality has been evaluating by two methods during site acceptance test: Texture analysis and Point-mode analysis. In order to perform texture analysis, firstly it needs to smooth values of the gates in radial direction. If there are bad data, then those gates should be taken out when calculating. Secondly, calculate the subtraction between raw data and smoothed data, and then calculate standard deviation estimation. In addition, it is needed to extract values on a radar moment by using SNR, cross relation coefficient, and spectrum width. Lastly, calculate median from the standard deviation values. All steps for calculation can be done on every radar moments such as reflectivity, differential reflectivity, correlation coefficient, differential phase, radial velocity and spectrum width. However, texture analysis has cons such as overestimation of measurement errors from non-uniform rainfall, rainfall attenuation and boundary effect. Compared texture analysis, point-mode analysis can discriminate "system-induced error" from "sampling-induced error". Therefore, KMA has been applying both texture mode and point mode analysis methods to evaluating radar observation data quality since 2017.

Acknowledgements
The research is supported by "Development and application of cross governmental dual-pol radar harmonization (WRC-2013-A-1)" project of the Weather Radar Center, Korea Meteorological Administration.

3.21 SERVAL: A NEW CENTRALIZED PROCESSING SYSTEM FOR THE FRENCH RADAR NETWORK

V. VOGT[1], N. GAUSSIAT[1], M. MARTET[1], S. CHAUMONT[1], J. MILLET[1], I. PFAFFENZELLER[1], B. FARDON[1]

[1] Radar Meteorology Centre, Météo-France, France
valerie.vogt@meteo.fr

With the increasing number of radars and products and the increasing complexity of the processing chain, Météo France was led to develop a centralized radar processing system called SERVAL (Système d'Élaboration des produits Radar et de VisALisation). The new system is hosted on Météo France mainframe processing platform called SOPRANO in Toulouse and is designed to be flexible and easily extensible to facilitate the integration of new algorithms and the deployment of the system to larger networks.

SERVAL ingests raw data in polar form, which represents the best compromise between native measurement made by the sensor and capabilities of dissemination and archiving. The system offers supervision facilities throughout the whole processing chain thanks to a friendly configurable web interface that delivers information on the radar network state and enables the visualization of intermediate and final products. A configurable replay facility is included to facilitate the reprocessing of archived raw data and to trial new products more easily.

A particular advantage of SERVAL is to facilitate the integration of new ideas into the operational production software by offering object-oriented and a standardized framework for common actions such as decoding, encoding, logging or images visualization. Thus, any new developer, whether engineer or scientist, benefits from the experience of former developments to add its contribution. An integration procedure allows the deployment of the latest version of the code as soon as it is available on a Linux server on which a continuous data processing is scheduled using real time data.

In this paper we will give an overview of SERVAL, present the supervision and describe how SERVAL can be used both as an operational platform and a research and development tool.

3.22 FROM PULSE TO PRODUCT UPDATE OF THE DUTCH WRN

T.MATHIJSSEN[1], H. BEEKHUIS[1]

[1] Royal Netherlands Meterological Institute (KNMI), Utrechtseweg 297, 3731 GA, De Bilt, The Netherlands
t.mathijssen@knmi.nl

KNMI has updated his Weather Radar Network (WRN) in the years 2015-2016 during a European tender. As part of the tender process KNMI has reflected on what innovations could be requested from the industry, without running into major development costs.

As a result KNMI radars run nowadays the radars in an innovative scanning strategy called Constant Duty Cycle Scan. This scanning strategy provides an optimal probing of the atmospheric volume, enhancing at the same time the frequency stability of magnetron driven transmitters.

Other enhancements provided are in the area of calibration and monitoring of the Radars. Automated reports, containing a great amount of detail, are generated in order to have a clear view on the network calibration and performance.

This presentation will cover the operational setup of the Dutch Weather Radar Network, starting with the pulsed Magnetron driven transmitter, showing consecutive processing steps, finally resulting in the radar products KNMI disseminates to its professional users and the general public.

3.23 HYDRO-METEOROLOGICAL OBSERVATORY OF CORDOBA, ARGENTINA

IGNACIO A. MONTAMAT[1], GIORGIO M. CARANTI[1], RAÚL A. COMES[1], ANDRÉS RODRÍGUEZ[1], PABLO SONNA[1], DENIS A. POFFO[1], RICARDO INGARAMO[1], JORGE SAFFE[1], AGUSTÍN MARTINA[1], SANTIAGO A. RODRIGUEZ GONZALEZ[1]

[1] National Weather Radar Network of Argentina (SiNaRaMe)
nachomontamat@gmail.com

Very few countries in Latin America have Weather Radars in operation and even less have managed to integrate them as a network along with some other remote sensing instruments for hydrometeorological monitoring. More developed countries around the globe have already recognized its importance decades ago, as these systems are crucial for everyday nowcasting and, more importantly, for decision making over large regions of intense storm generation as the central region of Argentina. This region arguably has among the most intense convective systems in the world with respect to the frequency of large hail, height of storm tops and extreme lightning activity[1].

In the wake of these facts, Argentina's National Government started a radarization programme called SiNaRaMe (Sistema Nacional de Radares Meteorologicos) in 2010. Its main purpose consists in providing weather radar coverage for the Argentine territory by integrating and upgrading existing infrastructure[2] and more importantly, by fully manufacturing twelve new generation weather radar systems (the RMA series). In parallel to this ambitious goal, is the need for specialized human resources. Engineers, scientists and technicians capable of exploiting a weather radar network full potential. In order to create valuable human resources, among several training courses -both locals and internationals-, a MSc. career in Radar Systems and Instrumentation was created in Cordoba province in 2012. This important milestone was possible thanks to the joined efforts between two recognized Universities: the National University of Cordoba (UNC) and "Instituto Universitario Aeronáutico (IUA)".

Since 2015, Cordoba's State Government in particular has made important efforts to implement a central region dedicated organism, focused on preventing hydrometeorological catastrophes by remote sensor data analysis, both real-time and forecasted or modeled. This organism is the Hydro-meteorological Observatory of Cordoba. This entity is being developed with a measure of success and it is expected to be fully operational by the end of this year.

Even though radar and other remote sensing technologies are incipient in Argentina, a lot has been achieved in a relatively short lapse and a lot of know-how has been capitalized. Nevertheless, much more is yet to be done as a very challenging goal approaches for Argentina: its remote sensing network calibration process!

References

[1] RELAMPAGO (Remote Sensing of Electrification, Lightning and Mesoscale/micr oscale Processes with Adaptive Ground Observations) white paper, 2016, https://pub lish.illinois.edu/relampago/.

[2] Meaning many other remote sensing instruments for hydrometeorological monitoring e.g. weather stations, disdrometers, limnimeters, lightning-strike detectors, etc.

3.24 REAL-TIME IMPLEMENTATION OF VARIATIONAL 3-D WIND SYNTHESIS TECHNIQUE (WISSDOM) USING WEATHER RADAR NETWORK OF KMA

KWANG-HO KIM[1], YU-CHIENG LIOU[2], HAE-LIM KIM[1], SUNG-HWA JUNG[1], SUN-KI LEE[1]

[1] Weather Radar Center, Korea Meteorological Administration, Republic of Korea
[2] National Central University, Tao-Yuan, Taiwan
khkim777@korea.kr

Three-dimensional wind fields in high spatiotemporal resolution is essential to enhance an understanding of dynamic evolution of weather phenomena. For last decade, advanced technologies have been proposed to retrieve three-dimensional wind fields based on variational approach which find an optimal wind vector with minimum error between analysed and observation terms by using dynamic constraints such as an anelastic continuity equation, a vertical vorticity equation, a smoothness filter. The WISSDOM, WInd Synthesis System DOppler Measurement, is one of leading techniques for retrieval of 3-D wind fields. The WISSDOM showed significant advantages comparing to conventional wind synthesis method using of multiple-Doppler radar. WISSDOM has a flexibility to select top and bottom boundary conditions for wind fields, and it even yields 3-D wind fields using single radar and along baseline between two radars, as well as over complex terrain by adopting the Immersed Boundary Method. However, WISSDOM has not been utilized for operational weather forecast or monitoring of severe weather over nationwide radar network with rapid update cycle of 5 ∼10 minutes in real time, mainly due to its requirement of huge computational resource for finding an optimal solution among complex equations. For providing a 3-D wind field during PyeongChang 2018 Olympic and Paralympic Winter Games, we have conducted the modularization and optimization tasks for real-time implementation of WISSDOM. On the domain (151 x 151, 20 layers) of the Olympic and Paralympic Games, the computational time of WISSDOM decreases from 71 minutes to 27 minutes after the modulization task and then was dramatically reduced up to 6 minutes by the implementation on supercomputer system of KMA. We are also planning to reduce the computation time by additional code parallelization by the end of this year. Its accuracy was evaluated by comparing to wind information from radiosonde and wind profiler, and wind report from commercial aircraft (AMDAR).

Acknowledgements
The research is supported by "Development and application of cross governmental dual-pol radar harmonization (WRC-2013-A-1)" project of the Weather Radar Center, Korea Meteorological Administration.

Session 4. Hydrological Studies Using Weather Radar



Keynote presentation

4.1 DESERT PRECIPITATION CHARACTERISTICS AND FLASH FLOOD RESPONSE STUDIED USING WEATHER RADAR DATA

E. MORIN[1], M. ARMON[1], I. BELACHSEN[1], F. MARRA[1], N. PELEG[2], J. SMITH[3], Y. ENZEL[1]

[1] Institute of Earth Sciences, Hebrew University of Jerusalem, Israel
[2] Institute of Environmental Engineering, ETH Zurich, Switzerland
[3] Department of Civil and Environmental Engineering, Princeton University, USA
efrat.morin@mail.huji.ac.il

Precipitation in the desert is scarce, but under distinct conditions can lead to high-magnitude flash floods. In a series of studies focused on the Levant deserts, we aim on: (i) characterizing precipitation space-time patterns, (ii) quantifying their extremes, (iii) identifying precipitation patterns leading to large floods, and, (iv) linking these distinct patterns with meteorological forcing and flooding patterns. Data from weather radar systems are most appropriate for characterizing precipitation, especially in desert regions, due to their typical high space-time resolution matching the high variance and local nature of desert precipitation. Our database includes 24 years of corrected and gauge-adjusted precipitation estimates from a C-band radar used for event-based and climatological analyses.

We analysed case studies from three synoptic patterns: Mediterranean cyclone (MC), active Red Sea trough (ARST) and subtropical jetstream disturbances, also termed tropical plumes (TPs). Significant differences in space-time precipitation patterns and hydrometeorological conditions were identified between these flood-producing synoptic systems: MC storms draw moisture from the Mediterranean and generate moderate rain intensities in the northern and wetter part of the region. ARST and TP storms transfer large amounts of moisture from the south, which is converted to rainfall in the hyperarid southernmost parts of the Levant. ARST rainfall is local and intense, whereas TP rainfall is widespread and prolonged due to high precipitation efficiency and large-scale forcing. Consequently, TP rainfall can generate high-magnitude floods in the largest catchments.

Climatological analysis of precipitation cores ("convective rain cells") has shown that ARST systems produce shorter rain events composed of rain cells with higher rain intensities, longer lifetime, smaller area and lower velocities, compared to MC systems. It was also found that rain cell area is positively correlated with topographic height while cell number is negatively correlated with distance from shoreline. Surprisingly, rain cell intensity is negatively correlated with mean annual precipitation. It was further shown that flash-flood-related events are dominated by rain cells of large size, low velocity, and long lifetime that move downstream with the main axis of the catchments.

4.2 TOWARD IMPROVED FLASH FLOOD WARNINGS BASED ON HIGH-RESOLUTION PRECIPITATION NOWCASTS

J. DEMARGNE[1], P. JAVELLE[2], D. ORGANDE[1], J.-A. FINE[1], C. FOUCHIER[2], L. GARANDEAU[3]

[1] HYDRIS Hydrologie, France
[2] IRSTEA, RECOVER group, France
[3] SCHAPI, Operational Hydrologic Modelling group, France
julie.demargne@hydris-hydrologie.fr

Flash flood events, which are typically triggered by intense precipitation and efficient runoff production, are difficult to monitor and predict due to large hydrometeorological uncertainties. The French national service in charge of flood forecasting (SCHAPI) has developed, in collaboration with Irstea and Météo-France, a national warning system, Vigicrues Flash, to provide flash flood warnings at ungauged locations based on high-resolution radar-gauge rainfall products. Operational since March 2017 for about 10,000 municipalities, this system complements flood warnings produced by the Vigicrues procedure for French monitored rivers. Compared to Météo-France APIC warnings for heavy precipitation events, Vigicrues Flash includes a simplified distributed rainfall-runoff model to forecast the basin response to rainfall inputs.

Vigicrues Flash is based on a discharge-threshold flood warning method called AIGA (Javelle et al. 2014) to characterize flood hazard in real time at any point along the river network. The operational radar-gauge Quantitative Precipitation Estimate (QPE) grids from Météo-France at a 1-km^2 resolution are ingested into the hourly distributed hydrologic model to produce real-time peak discharge estimates on any river cell. Every 15 minutes, these discharges are compared to reference flood quantiles, which were derived from long-term streamflow simulations. The automated system determines rivers exceeding the high flood and very high flood thresholds, as well as their associated municipalities. These flood hazard maps are published on a web platform and warning messages are automatically sent to registered users who might be impacted to help them mitigate flood damages.

The flash flood warning system is being enhanced to ingest high-resolution precipitation nowcasts from the AROME convection-permitting numerical weather prediction model and account for the input and hydrological uncertainties. Météo-France's AROME-NWC precipitation nowcasts are provided at a 1.3-km resolution for a 6-hr forecast horizon, and hourly updated (Auger et al. 2015). The deterministic AROME-NWC forecasts are ingested as time-lagged ensembles and combined with multiple sets of hydrological regionalized parameters. The resulting flow ensembles lead to define probabilistic flood warnings. The evaluation was carried out with hindcasting experiments for significant events from September 2014 to June 2017 for 750 French basins. Results indicate significant improvements in terms of flash flood event detection and effective warning lead time, compared to warnings from the current setup (without any future precipitation) and warnings based on

single-valued persistency benchmarks. We also discuss the impact of the QPE products used to derive hydrological model states and flow forecasts and the need to account for QPE uncertainty.

Planned enhancements include running the hydrologic model at a sub-hourly time step, accounting for and reducing hydrologic uncertainties via data assimilation, developing a comprehensive post-event damage database and characterizing flood vulnerability.

References

Auger, L., Dupont, O., Hagelin, S., Brousseau, P., Brovelli, P., 2015. AROMENWC: a new nowcasting tool based on an operational mesoscale forecasting system. Quarterly Journal of the Royal Meteorological Society, 141: 16031611, doi:10.1002/qj.2463

Javelle, P., Demargne, J., Defrance, D., Arnaud, P., 2014. Evaluating flash flood warnings at ungauged locations using post-event surveys: a case study with the AIGA warning system. Hydrological Sciences Journal. doi: 10.1080/02626667.2014.92397

4.3 A NEW MULTIPLICATIVE RANDOM CASCADE MODEL FOR DOWNSCALING INTERMITTENT RAINFALL FIELDS

M. SCHLEISS[1]

[1] Geoscience & Remote Sensing, Delft University of Technology, The Netherlands
m.a.schleiss@tudelft.nl

Stochastic rainfall downscaling algorithms are statistical methods designed to artificially enhance the resolution of rainfall measurements. Many of them are built on the notion of multiplicative random cascades. They assume that the spatial organization of precipitation is the consequence of a process during which water is redistributed over smaller and smaller grid boxes. One of the most controversial aspect of such an approach is the way zero-rainfall values are produced during the cascade. Lots of efforts have gone into solving this issue but so far downscaled fields still exhibit rather unrealistic spatial structures and intermittency. To overcome these issues, I explore a new way of downscaling rainfall using a combination of random cascades and adaptive sampling. The cascade works by prescribing a maximum bucket capacity b>0 to each grid box in the original domain. As long as the total volume of water in a grid box exceeds this maximum capacity, the box is split in two smaller sub-regions with equal amounts of water (i.e., half that of the parent grid box). However the areas over which these equal amounts of water get redistributed can be vastly different. The underlying probability distribution governing how redistribution takes place is modelled by a logit-normal distribution with zero mean and variable standard deviation. The cascade ends when the amount of water in all grid boxes is less than the maximum bucket capacity. The result is an irregular grid with grid boxes of various sizes and shapes depending on the local rainfall intensity. The latter is then re-sampled over a regular grid, which gives rise to intermittency without the need for any arbitrary thresholding. To help you understand how the technique works, I show two examples of downscaled radar rainfall fields over the Netherlands. The first represents a stratiform event with moderate intensities and the other is a strongly convective event with large amounts of intermittency. The fraction of zero-rainfall values and the variograms of the downscaled occurrence/intensity fields are used to assess the performance of the downscaling algorithm and outline some of the advantages and limitations of this new way of downscaling rainfall using adaptive grid box sizes.

4.4 OPERATIONAL HYDROLOGICAL MODELLING OF SMALL WATERSHED USING QPE FROM DUAL-POL RADAR IN BRAZIL

C. BENETI[1], R. V. CALHEIROS[1], M. SORRIBAS[1], C. OLIVEIRA[1,2], L. CALVETTI[3], J. RUVIARO[1,2], R. NEUNDORF[1,2]

[1] SIMEPAR - Parana Meteorological Service, Brazil
[2] UFPR Parana Federal University, Brazil
[3] UFPel Federal University of Pelotas, Brazil
cesar.beneti@simepar.br

Among other applications, radar-rainfall (RR) and QPE (Quantitative Precipitation Estimation) based on radar reflectivity, dual polarization variables and multi sensor information, provide important information for land surface hydrology, such as flood forecasting. The Marrecas River watershed (335 km2) is a headwater catchment of the Iguazu river, located at southwest of Parana state, in southern Brazil. The watershed is predominantly covered by agriculture land, but it was severely channelized close to Francisco Beltrao City where significant flash floods occur during rainfall periods. Historical records indicate that once a year Francisco Beltrao has a flash flood after 5-6 hours of extreme rainfall. Therefore, SIMEPAR (Parana Meteorological Service) developed a flood alert system using rainfall-runoff model forced with RR and QPE, and tipping-bucket observations to forecast river water levels (using rating-curves). In this study, we used hourly dataset from a S-Band dual polarimetric radar with two tropical R(Z) relations based on climatology and distrometer data, a polarimetric R(Z,ZDR) algorithm from the literature and a multi-sensor approach using radar, satellite and rain gauge. Two hydrological models (Sacramento Soil Moisture Accounting, SAC-SMA; IPH-II model) were used and calibrated with the Shuffle Complex Evolution (SCE-UA) using observed discharge time-series. Although our previous studies indicated accurate RR-based simulations, in some cases small floods were not detected when using catchment-lumped rainfall derived from multi-sensor QPE. In this study we advance further in this subject using improved R(Z,ZDR) relations and QPE for the period of 2016-2017, but also different approaches for the rainfall-runoff calibration. In a first step, we evaluate model optimization for high flows thresholds and flood events. The Marrecas River has two tributaries in the upper reaches and a major contribution from the Quatorze River in the lower reaches, but all these catchments are ungauged. Hence, the development (and timing) of floods in the Marrecas River can be complex and strongly related to storms spatio-temporal distribution. To explore this aspect, we also perform a first analysis in using RR in rainfall-runoff model calibration with a semi-distributed catchment discretization, which will be presented in this conference.

4.5 USING RADAR DATA FOR THE ANALYSIS AND DESIGN OF EXTREMAL EPISODES

M. SCHEIBEL[1]

[1]Wupperverband, Wuppertal, Germany
schei@wupperverband.de

There are two possible concepts for hydrological and hydraulic modelling: one is to use continuous time series as an input the other to extract design situations from known or possible extremal episodes. Both concepts have pros and cons. Continuous simulations represent all appeared combinations of initial conditions and system load. The events are experienced and recorded. It is also possible to find the frequency of occurrence and probability of the effect means the discharge without looking at and discussing necessarily the return periods or influential time intervals of the input means the climatology data. The precondition for the assumption that the output is representative, is a long time series. Different climate periods must be included to cover significant events and to be able to find a proper probability distribution to extrapolate values for higher return periods. With design situations exaggerated from known extremal episodes it is possible to find thinkable (physically possible) situations which just not have occurred during the recorded time period or even not at the examined location. One important precondition for that concept is to know, which factors and parameters have to be used to randomly generate design storms. That means to analyse the sensitivity and relevance to describe the interested impact.

The advantage of rainfall radar data is the more detailed information about e.g. cell sizes, cell velocities and spatial distribution. The presented studies shows which parameters are more relevant to describe and understand storm events. Therefore the continuous data base of 15 years of radar data is analysed for extremal episodes and compared to the reaction of the hydrological system. To rank the rather short - time period into the local climatology conditions, nearly hundred years of point measurement and modelled discharge (with a calibrated model) are taken for comparison.

Certain characteristic values and indices are more stable for comparing different sets of date including various measurement types. Relatively frequencies and trends are more significant than to compare absolute values. Design events have to deal with uncertainties of prediction anyway. Therefore the uncertainties are analysed on their effect of the investigated discharge to give them the accurate meaning.

Both mentioned concepts are used to design measures or to find thresholds for flood forecasting. But a combination of experienced and thinkable events, like different initial conditions or more intense or longer rainfall, extract the knowledge of impact and related outcome. Therefore the local hydrological regime is more understandable and a better preparation to handle extreme episodes is possible and to improve forecast systems.

4.6 HOW ERRORS IN RAINGAUGE, RADAR AND MICROWAVE LINK DATA PROPAGATE THROUGH HYDROLOGICAL MODELS

C.C. BRAUER[1], A. OVEREEM[2], H. LEIJNSE[2], R. UIJLENHOET[1]

[1] Hydrology and Quantitative Water Management Group, Wageningen University, The Netherlands

[2] R&D Observations & Data Technology, Royal Netherlands Meteorological Institute, The Netherlands

claudia.brauer@wur.nl

Several rainfall measurement techniques are available for hydrological applications, each with its own spatial and temporal resolution and errors. When using these rainfall datasets as input for hydrological models, their errors and uncertainties propagate through the hydrological system. The aim of this study is to investigate the effect of differences between rainfall measurement techniques on groundwater and discharge simulations in a lowland catchment, the 6.5-km^2 Hupsel Brook experimental catchment.

We used five distinct rainfall data sources: two automatic raingauges (one in the catchment and another one 30 km away), operational (real-time and unadjusted) and gauge-adjusted ground-based C-band weather radar datasets and finally a novel source of rainfall information for hydrological purposes, namely, microwave link data from a cellular telecommunication network. We used these data as input for a recently developed rainfall-runoff model for lowland catchments, and intercompared the five simulated discharges time series and groundwater time series for a heavy rainfall event and a full year. Three types of rainfall errors were found to play an important role in the hydrological simulations, namely: (1) Biases, found in the unadjusted radar dataset, are amplified when propagated through the hydrological system; (2) Timing errors, found in the nearest automatic raingauge outside the catchment, are attenuated when propagated through the hydrological system; (3) Seasonally varying errors, found in the microwave link data, affect the dynamics of the simulated catchment water balance. We conclude that the hydrological potential of novel rainfall observation techniques should be assessed over a long period, preferably a full year or longer, rather than on an event basis, as is often done.

4.7 FLASH FLOOD EARLY WARNINGS BASED ON RADAR: COMPARISON OF THE ERICHA FLASH FLOOD INDICATOR WITH A CONTINUOUS DISTRIBUTED HYDROLOGICAL MODEL IN THE FLASH FLOOD CASES OF AUTUMN 2014 IN LIGURIA (ITALY)

D. SEMPERE-TORRES[1], C. CORRAL[1], M. BERENGUER[1], L. POLETTI[2], F. SILVESTRO[2], N. REBORA[2]

[1] Centre de Recerca Aplicada en Hidrometeorologia. Universitat Politcnica de Catalunya (CRAHI-UPC). Barcelona. Spain. [2] CIMA Research Foundation. Savona. Italy
sempere@crahi.upc.edu

The anticipation of flash flood events is crucial to issue warnings to mitigate their impact. They usually affect steep and small to medium catchments (up to few hundreds of square kilometres), and are typically induced by heavy rainfalls in the upstream area. The response time between the rainfall (the cause) and that the flash flood takes place (the effect) depends primarily on the features of the catchment, ranging from the order of tens of minutes to a few hours in the larger basins. In this context, the capacity of the meteorological radars to provide high resolution QPEs and QPFs are of crucial interest for any Flash Flood Early Warning System. In the last ten years, several developments have been made to transform radar-based QPEs and QPFs into indicators able to anticipate flash flood occurrence. From the FF-EWS concept first proposed by CRAHI and operationally implemented in Catalonia in 2006, to the ERICHA system running over the OPERA radar data composite (operationally integrated in the European Flood Awareness System, EFAS, since March 2017), many promising advancements have been made.

In the framework of the H2020 Innovation Action ANYWHERE (www.anywhere-h2020.eu) a comparison of two early warning systems for real-time flash flood hazard assessment and forecasting at regional scale is presented: the ERICHA FF-EWS (directly using the concept of basin-aggregated rainfall as indicator) and the Continuum rainfall runoff model developed by CIMA, a continuous distributed hydrological model computing river flows based on a geomorphological approach. These two systems are based on a gridded drainage network and they use the same meteorological radar QPE inputs to assess the flash flood hazard level in different points of the study area, considering the probability of the event (expressed in years of return period) as a good indicator to assess the flash flood hazard. The essential difference between the systems is that one is a rainfall-based system, only using the upstream basin-aggregated rainfall as the variable to determine the flash flood hazard level, while the other simulates streamflows with a distributed rainfall-runoff model. The comparison has been done for three rainfall events in the autumn of 2014 that resulted in severe flooding, over 100-year return period in the event of 9 October 2014, in the Liguria region (Northwest of Italy).

The results obtained by the two systems show many similarities, particularly for catchments over 50 km2 and for large return periods (extreme floods). They allow the verification of the usefulness of the ERICHA indicator for the anticipation of flash floods over 20-year return period, and its suitability to be combined with vulnerability and exposure cartographies to provide Flash Flood Impact forecasting to

support decision making during emergencies in the framework of the ANYWHERE Innovation Action.

4.8 INVESTIGATING THE SENSITIVITY OF HYDROLOGICAL RESPONSE MODELLING TO CRITICAL RAINFALL AND CATCHMENT SCALES IN THE (SEMI-)URBANISED CHARLOTTE AREA

E. CRISTIANO[1], M-C. TEN VELDHUIS[1], D. B. WRIGHT[2], J. A. SMITH[3], N. C. VAN DE GIESEN[1]

[1] Department of Water Management, Delft University of Technology, Delft, The Netherlands

[2] Civil and Environmental Engineering, University of Wisconsin-Madison, Madison, WI 53706, USA

[3] Department of Civil and Environmental Engineering, Princeton University, Princeton, New Jersey, USA

e.cristiano@tudelft.nl

Hydrological response is mainly influenced by the interactions between rainfall variability in space and time and catchment characteristics. These aspects are relevant especially in urban areas, where runoff generation is fast, due to the high degree of imperviousness. For this reason, it is necessary to use high resolution rainfall data to investigate and predict the hydrological response of an urban system. In the last decades, new technologies and instruments have been developed and improved to capture the rainfall variability in space and time at a high resolution. This has led to an increased use of rainfall data derived from weather radars for urban hydrological applications. At the same time, many studies focused on the development of distributed models, that can represent the system with high resolution. However, the interactions between rainfall and catchment scale and their influence on the sensitivity of hydrological response to small-scale variability remain poorly understood. In this study, we aim to identify critical scales of rainfall variability in time and space and catchment characteristics that determine the sensitivity of hydrological response for the Charlotte metropolitan area (North Carolina, USA). The watershed of Little Sugar Creek (111km2) was chosen as study case and a physically-based distributed model was used to predict the hydrological response of the system. Twenty-five storm events were selected from a 15-year (2001 2015) high-resolution (15 min, 1 km^2) radar data set, measured from the National Weather Service (NWS) Next Generation Radar network (NEXRAD). To investigate hydrological response sensitivity to different combinations of spatial and temporal rainfall resolutions, rainfall events were aggregated in space (3 km^2 and 6 km^2) and time (30 min and 60 min). The selected rainfall events were used as input for the hydrological model and the simulated flow at the output of the catchment was compared with local measurements. To classify the rainfall events, we analysed the variability in space and time of the storm core. A cluster classification was applied, identifying the main storm core dimension above selected thresholds at each time step and evaluating the variability of the main cluster during the rainfall event. In a previous synthetic study, three dimensionless parameters were introduced to define the interaction between rainfall and basin scale and their effects on the urban hydrological response sensitivity. The applicability of these parameters to different catchment scale was investigated and validated with the use of local flow measurements. Preliminary results suggest that cluster classification can be a valid instrument to characterize rainfall variability.

4.9 DEVELOPMENT OF A DETECTION SYSTEM OF HEAVY RAINFALL USING X-BAND PHASED-ARRAY WEATER RADAR

K. YOSHIMI[1], F. MIZUTANI[1], N. TAKAHASHI[2], T. USHIO[3,4]

[1] Toshiba Infrastructure Systems and Solutions Corp., Japan
[2] National Institute of Information and Communications Technology (NICT), Japan
[3] Osaka University, Osaka, Japan
[4] Tokyo Metropolitan University, Tokyo, Japan
kazuhiro1.yoshimi@toshiba.co.jp

Toshiba has been developing a detection system of heavy rainfall using observation data of X-band Phased-Array Weather Radar (PAWR) which already installed in Osaka University, Japan under a grant of NICT. The information distributed from the system can be expected to be applied for river or drainage management. The mainly characteristics of the system are as follows:
i) the data of the weather radar which achieved precise 3 dimensional observation of cumulonimbus can be used.
ii) it is available to notify the alarm about localized heavy rainfalls. For the first time in Japan, we asked Osaka local governments to use the system for disaster-prevention activities and conducted demonstration experiments with them for 3 years between 2015 and 2017. In the experiments, we defined the disaster-prevention activities as a protocol in advance in case of alarm notification. The Osaka local government conducted the disaster-prevention activities in accordance with the protocol during the experiments. Specifically, when an alarm was received, preparation for pump operation in sewage-treatment plant, evacuation guidance for the park users and monitoring the point of risk of inundation were carried out, and the application of the weather radar data was confirmed through the system.

As a result of this experiments, we obtained many cases that the alarm notification succeeded immediately before localized heavy rainfalls. Moreover, we were able to accumulate a lot of cases that disaster-prevention activities of local government proceed smoothly. Finally, it is showing that three dimensional rainfall data observed by PAWR is critically useful for disaster-prevention work of Osaka local government.

Moreover, we succeeded in developing a latest dual-polarization phase-array weather radar which is possible to observe with a high degree of accuracy and we started trial observation from Feb. 2018. In this presentation, the outline of this newly developed radar and system are presented.

4.10 INTENSIFICATION OF CONVECTIVE RAIN CELLS AT WARMER TEMPERATURES OBSERVED FROM WEATHER RADAR OVER MEDITERRANEAN TO SEMIARID CLIMATES

N. PELEG[1], F. MARRA[2], S. FATICHI[1], P. MOLNAR[1], E. MORIN[2], A. SHARMA[3], P. BURLANDO[1]

[1] Institute of Environmental Engineering, Hydrology and Water Resources Management, ETH Zurich, Zurich, Switzerland

[2] Institute of Earth Sciences, Hebrew University of Jerusalem, Jerusalem, Israel

[3] School of Civil and Environmental Engineering, University of New South Wales, Sydney, New South Wales, Australia

nadav.peleg@sccer-soe.ethz.ch

Air temperature influences extreme rainfall intensity due to the increased water vapor-holding capacity of warmer air that follows the well-known Clausius-Clapeyron (CC) relation. The possible intensification of extreme rainfall intensity in a warmer climate has stimulated many studies, most have focused on the scaling of extreme rainfall intensity with temperature, defined as the relative change of rainfall intensity in high quantiles per degree of increase in the air temperature. In this study we explored the relationship between air temperature and convective rainfall by analyzing the characteristics of rainfall at the storm-scale and at the scale of scattered convective features, more specifically, individual convective rain cells. The study is focused on Mediterranean and semiarid climates, where convective rainfall largely contributes to the total annual rainfall and is associated with triggering of high-magnitude flash floods, especially in small- to medium-size catchments. Rainfall estimates from a C-band weather radar (1-km, 5-min, 24-year) were coupled with near-surface air temperature over Mediterranean and semiarid regions in the eastern Mediterranean Sea. The peak intensity of individual convective rain cells was found to increase with temperature (for the examined temperature range of 5 to 25°C), but at lower rate than the 7% $^{\circ}C^{-1}$ scaling expected from the CC relation, while the area of the individual convective rain cells slightly decrease or, at most, remains unchanged. At the storm-scale, the areal convective rainfall was found to increase with warmer temperatures, whereas the areal non-convective rainfall and the storm-wide area decrease. This suggests an enhanced moisture convergence from the storm-wide extent towards the convective rain cells. Results indicate a reduction in the total rainfall amounts and an increased heterogeneity of the spatial structure of the storm rainfall for temperatures increasing up to 25 °C. Thermodynamic conditions, analyzed using convective available potential energy (CAPE), were determined to be similar between Mediterranean and semiarid regions. Limitation in the atmospheric moisture availability when shifting from Mediterranean to semiarid climates was detected and explains the suppression of the intensity of the convective rain cells when moving towards drier regions.

4.11 SPATIAL PROPERTIES OF PRECIPITATION EXTREMES USING RADAR AND PLUVIOMETERS

GEOFF PEGRAM[1], ANDRAS BARDOSSY[2]

[1] University of KwaZulu-Natal, South Africa
[2] University of Stuttgart, Germany
pegram@ukzn.ac.za

Records of precipitation extremes are essential for hydrological design. Intensity duration frequency curves (IDFs) are typically used for urban hydrology. They are usually estimated from gauge observation records. These observations can be continuous in time but have no spatial extent. The areal component is then typically determined by the use of duration-dependent area reduction factors (ARFs). These however are based on speculations, as there are seldom any spatially continuous observations available.

In this contribution we investigate the problems: (i) to what extent are point observations representative for point extremes (as the real extremes are most likely to occur elsewhere than at the measurement points, (ii) how are the extremes occurring somewhere in a selected area related to extremes observed at a fixed location and (iii) what are the statistical properties of extreme areal precipitations occurring in subareas of a large domain?

The investigations are carried out using (i) a dense precipitation network in Germany, (ii) radar observations available for the same area and (iii) with simulated radar precipitation, based on 8 years of data from the Bethlehem radar station in South Africa, obtained using the String of Beads model.

Our research shows that extremes measured at a single location may lead to considerable underestimation of the risks. Furthermore, an example using a non-Gaussian simulation shows that the structure of the spatial dependence of extreme events plays an essential role for determining their space-time risk of occurrence.

4.12 SHIPBORNE POLARIMETRIC RADAR OBSERVATION OF THE MODULATION OF THE DIURNAL VARIATION OF OROGRAPHIC PRECIPITATION ALONG THE WESTERN COAST OF SUMATRA ISLAND BY SYNOPTIC-SCALE DISTURBANCES

B. GENG[1], M. KATSUMATA[1]

[1] Japan Agency for Marine-Earth Science and Technology (JAMSTEC), Japan
bgeng@jamstec.go.jp

This study analysed the spatial and temporal variations of local precipitation along the western coast of Sumatra Island. The study utilized the data collected from the polarimetric radar on board the research vessel Mirai, which conducted an intensive observation at 4.067°S and 101.9°E from 23 November to 17 December 2015. Results show the dominance of the diurnal cycle of orographic precipitation, developing during the afternoon along the western coast of Sumatra Island, then propagating westward over the sea during the night. The topography-induced precipitation was significantly modulated by the passages of synoptic-scale disturbances, which could be associated with tropical mixed Rossby-gravity waves and induced the periodical changes of local circulations. Orographic precipitating systems triggered along the western coast of Sumatra Island became more intense and organized accompanying the passages of the troughs of synoptic-scale disturbances. In addition, the offshore enhancement and strong propagation of orographic precipitation over the sea at night occurred during disturbed periods. Furthermore, orographic precipitating systems during disturbed periods featured greater vertical development and more enhanced polarimetric radar signatures above the melting level than during nondisturbed times. It appears that the modification of local environmental conditions by synoptic-scale disturbances makes a great impact on the diurnal variability of orographic precipitation along the western coast of Sumatra Island, whose processes are discussed according to the observational results.

4.13 TOWARDS A COMMON PROCEDURE FOR THE EVALUATION OF DAMAGE-PRODUCING EVENTS

T. EINFALT[1], S. HINSKEN[2], M. SCHEIBEL[3]
[1] hydro & meteo GmbH & Co. KG, Lübeck, Germany
[2] City of Dsseldorf, Germany
[3] Wupperverband, Wuppertal, Germany
einfalt@hydrometeo.de

There is a growing number of requests for an analysis of damage producing events and its classification as "normal" (within the limitations of design standards and should be therefore handled by existing structures) or "exceptional" (known as force majeure) for liability purposes. Since this classification is crucial for the decision who is liable for occurred damage, a standard procedure is required for transparent decisions processes on compensation, which is also accepted by courts and can be a basis for accords or even verdicts.

Damage sites regarding convective events - may be very local and therefore, the rainfall data need to have a high spatial resolution 1 x 1 km or better). Also, flow paths or the whole hydrological catchment must be considered since a damage site may differ from the location of the highest precipitation observed.

A suitable procedure should include the following minimum standards:

- Initial conditions must be known (soil wetness, current capacity of the sewer system etc.).
- The basic data for the event analysis should span the entire event, including at least 24 hours before damage occurrence in order to include a potential time of water accumulation on the ground and possible basin retention times.
- Radar data are required with a time step of 5 or 6 minutes or less so that statistical assessments can be performed.
- Radar data must be quality controlled according to the state of the art of radar data processing. This includes corrections for clutter, blockage, attenuation, hail, bright band (if applicable), temporal interpolation and second trip.
- Rain gauges must be used as ground reference for radar adjustment when reflectivity data are used. Adjustment has to be performed according to national and international regulations. If available, stations close to the damage site of all operators shall be included. Because adjustment procedures are sensitive to rain gauge data, the measurements from rain gauges must be quality controlled as well. If the gauge network density is less than 1 gauge per 10 km^2, a sensitivity analysis of the result is required, giving the 90%-percentile of the adjustment procedure.
- For the classification, a extreme value statistics / design storms of locally representative stations (point or grid) are preferable to the official statistics grid (like KOSTRA in Germany). The classification is then performed for the highest value for each relevant pixel for different selected integration periods,

ranging from 5 minutes to 24 hours. A relevant pixel is defined as a pixel above the damage site and upstream of the damage site. For events with strong winds, upwind pixels also have to be included.

This procedure allows the intercomparison of events, based on a similar data quality standard. Further work needs to formulate the detailed minimum requirements of this procedure as an internationally acknowledged guideline.

4.14 AN ANALYSIS OF X-BAND POLARIMETRIC RADAR RAINFALL OBSERVATIONS FROM VARIOUS COMPLEX TERRAIN SITES

M. ANAGNOSTOU[1], D. YAGMUR[3], J. KALOGIROS[1], E. ANAGNOSTOU[3]

[1] IERSD, National Observatory of Athens, Athens, Greece

[2] Department of Water Resources and Environmental Engineering, School of Civil Engineering, National Technical University of Athens, Greece

[3] Department of Civil and Environmental Engineering, School of Engineering, University of Connecticut

sifneos@live.com

Precipitation estimation in mountainous regions remains a challenging task due to the complex interaction of physical processes like orographic enhancement taking place at small spatial scales and the associated observational difficulties posed on measurement networks. Precipitation estimates based on raingauge networks are usually associated with low coverage density, particularly at high altitudes. On the other hand, operational weather radar networks may provide valuable information of precipitation at these regimes but reliability of their estimates is often limited due to retrieval (variability in the reflectivity-to-rainfall relationship) and observational constrains (blockage issues, overshooting effects). As a result, currently there is lack accurate precipitation estimates over complex terrain areas, which essentially means that there is lack of accurate knowledge of the triggering meteorological factor for a number of hydrological hazards like flash floods and debris flows/landslides occurring in those areas. A potential solution to overcome observational limitations and retrieval uncertainty of current observational radar networks is the use of locally deployed low-power dual-polarization X-band radars as complement to raingauges and gap-filling to long range operational, lower frequency (C-band or S-band) weather radars.

This study evaluates rainfall estimates collected from high spatial and temporal resolution dual-polarization observations from different X-band radars during various field experiments in US (Appalachian and Olympic Mountains), Europe (Alps and South Mediterranean region) and South Korea. The study conducts an independent error analysis of an X-band dual-polarization retrieval algorithm (called here SCOP-ME), consistently applied in all radar observations, using independent in situ rainfall observations from a dense network of raingauges and disdrometers. In addition, the study will use operational C-band and S-band weather radar rainfall observations in the evaluation analysis. Results reveal that in contrast with the other two rainfall sources (in situ and C-band/S-band radar), X-band radar rainfall estimates offer an improved representation of the local precipitation variability and magnitude due to orographic enhancement, which in turn has significant impact on the simulation of peak flows associated with these events.

4.15 REGIONAL FREQUENCY ANALYSIS OF RADAR RAINFALL IN BELGIUM

E. GOUDENHOOFDT[1], L. DELOBBE[1], P. WILLEMS[2]

[1] The Royal Meteorological Institute of Belgium, Belgium
[2] University of Leuven, Belgium
edouard.goudenhoofdt@meteo.be

In Belgium, only rain gauge time series have been used so far to study extreme rainfall at a given location. In this study, the potential of a 12-year quantitative precipitation estimation (QPE) from a single weather radar is evaluated. The peak intensities are fitted to the exponential distribution using regression in Q-Q plots with a threshold rank which minimises the mean squared error. Compared to automatic rain gauges on a 2005-2016 period, the basic radar product exhibits unrealistic high extremes for 1h accumulation. The radar QPE needs a bias correction for 24h accumulations. Differences between radar and gauge rainfall values are caused by radar signal attenuation, spatial and temporal sampling, gauge underestimations and other remaining radar errors. Nonetheless, the fit to the QPE data is within the confidence interval of the gauge fit, which remains large due to the short study period. A regional frequency analysis for 1h duration is performed at the locations of four gauges with 1965-2008 records using the spatially independent QPE data in a circle of 20km. The confidence interval of the radar fit, which is small due to the sample size, contains the gauge fit for the two closest stations from the radar. In Brussels, the radar extremes are significantly higher than the gauge rainfall extremes, but similar to those observed by an automatic gauge during the same period. The extreme statistics exhibit slight variations related to topography. The radar-based extreme value analysis can be extended to different area sizes.

4.16 OPERATIONAL HYDROLOGICAL NOWCASTING: CHAIN COMPARISON APPLIED ON MEDITERRANEAN SMALL CATCHMENTS

M.L. POLETTI[1], M. BERENGUER[2], F. SILVESTRO[1], N. REBORA[1], C. CORRAL[2], D. SEMPERE-TORRES[2]

[1] CIMA Research Foundation, Savona, Italy

[2] Center of Applied Research in Hydrometeorology, Universitat Politcnica de Catalunya, Barcelona, Spain

laura.poletti@cimafoundation.org

The exposure of the urban areas to flash-floods is particularly significant in Mediterranean coastal cities, generally densely populated. Along the last century severe rainfall events, often associated with intense and organized thunderstorms, produced flash-floods and landslides causing serious damages to urban areas and, in the worst events, also human losses.

The temporal scale of these events is strictly linked to the size of the catchments involved: in the Mediterranean area a great number of catchments that pass through coastal cities have a small drainage area (less than 100 km^2), corresponding to very short hydrologic response (in the order of few hours). Meteorological forecasting systems are unable to predict precipitation at the space and time scales of these events, of the order of few km and few hours. Nowcasting techniques generate precipitation forecasts to complement the time series of observations and, thus, extend the predictability limits of the forecasting models in support of real-time flood alert system operations.

The coupling of a precipitation nowcasts with a hydrological model aims to build an operational nowcasting chain that, in real time, can be used as a support to decision for Civil Protection actions. In this work, a comparison between two different nowcasting techniques is carried on. The first one, PhaSt, is operational at the Hydro-Meteorological Monitoring Centre of the Liguria Region, and second, SBMcast, is based on the statistical model String of Beads. At each time step, both generate ensembles of equiprobable future precipitation scenarios on time horizons up to 3 h starting from the most recent radar observations.

The precipitation nowcasting ensembles produced by the two techniques are connected with the hydrological model Continuum and then the comparison is performed on the output of entire hydrological nowcasting chain for some well-known events that affected the Liguria region during 2014 and caused flash-floods and significant losses.

4.17 EXPLORING THE SPATIAL VARIABILITY OF EXTREME RAINFALL INTENSITIES AT RADAR SUBPIXEL SCALE USING A HIGH-RESOLUTION STOCHASTIC RAINFALL GENERATOR

N. PELEG[1], F. MARRA[2], S. FATICHI[1], A. PASCHALIS[3], P. MOLNAR[1], P. BURLANDO[1]

[1] Institute of Environmental Engineering, Hydrology and Water Resources Management, ETH Zurich, Zurich, Switzerland

[2] Institute of Earth Sciences, Hebrew University of Jerusalem, Jerusalem, Israel

[3] Institute Faculty of Engineering, Department of Civil and Environmental Engineering, Imperial College London, London, United Kingdom

nadav.peleg@sccer-soe.ethz.ch

Extreme rainfall intensities are often quantified using IntensityDurationFrequency curves (IDF) that are traditionally derived from rain-gauges and more recently also from remote sensing instruments, such as weather radars and satellites. These instruments measure rainfall at different spatial scales: rain-gauge samples rainfall at the point scale while remote sensing devices averages precipitation on a relatively large area. As a result, a remotely sensed derived IDF curve is representative of the mean areal rainfall over a given grid cell and neglects the within-grid cell rainfall variability. In this study, we quantify the variability of extreme rainfall intensity over a common C-band weather radar grid cell (of 1 km^2). We have used a high resolution space-time rainfall generator that downscales the rainfall intensities in space to a 10 m by 10 m resolution. The study was conducted using a unique radar data record (23 years) and a very dense rain-gauge network in the Eastern Mediterranean area (northern Israel). RadarIDF curves, together with an ensemble of point-based IDF curves representing the radar subpixel extreme rainfall variability, were developed fitting Generalized Extreme Value distributions to annual rainfall maxima. It was found that the mean areal extreme rainfall derived from the radar underestimate most of the extreme values computed for point locations within the radar pixel (on average, 70%). The subpixel variability of rainfall extreme was found to increase with longer return periods and shorter durations (e.g. from a maximum variability of 10% for a return period of 2 years and a duration of 4 h to 30% for 50 years return period and 20 min duration). For the longer return periods, a considerable enhancement of extreme rainfall variability was found when stochastic (natural) climate variability was taken into account. Bounding the range of the subpixel extreme rainfall derived from radarIDF can be of major importance for different applications that require very local estimates of rainfall extremes.

4.18 SNOW-LEVEL ESTIMATES FROM POLARIMETRIC OPERATIONAL WEATHER RADAR MEASUREMENTS

S. MATROSOV[1], D. GOTTAS[2], A. WHITE[2]

[1] Cooperative Institute for Research in Environmental Sciences, University of Colorado and NOAA Earth System Research Laboratory, Boulder, USA

[2] NOAA Earth System Research Laboratory, Boulder, USA

sergey.matrosov@noaa.gov

Information on snow-level (SL) heights (i.e., the heights in the atmosphere where precipitation type transitions from snow to rain) is important for hydrometeorological forecasts. Operational weather radars provide a convenient tool for estimating SL heights based on polarimetric measurements. The operational melting layer products derived from US National Weather Service next generation radar (NEXRAD) network for slant viewing are used to retrieve SL heights in the vertical atmospheric column. The quality and representativeness of the NEXRAD-based SL heights for the areas around the ground-based radar sites is evaluated by comparing these heights with robust results from several dedicated vertically pointing radars which are deployed at different locations in the Western United States. It is shown that for close radar ranges (∼15 km) the NEXRAD-based SL heights are relatively unbiased and the uncertainty of the retrievals is around 170 m. At longer distances from operational radar sites uncertainty in SL heights increases, though results typically do not significantly degrade up to distances of about 50 km. The use of different polarimetric radar variables for retrieving SL heights is discussed.

4.19 MEAN-FIELD-BIAS CORRECTION OF RADAR FORECASTS BY USING BACKWARD TRACKING METHOD

W. NA[1], M. KANG[2], C. YOO[3]

[1] School of Civil, Environmental & Architectural of Engineering, Korea University, Seoul, Republic of Korea

[2] School of Civil, Environmental & Architectural of Engineering, Korea University, Seoul, Republic of Korea

[3] School of Civil, Environmental & Architectural of Engineering, Korea University, Seoul, Republic of Korea

uoo92@hanmail.net

The very-short-range-forecast (VSRF) model is an indispensable component of a flash flood warning system (FFWS). Two problems arise when the rainfall forecast is used for the FFWS. The first problem is the accuracy of the rainfall forecast itself. Unfortunately, the accuracy of rainfall forecast is not good enough to be used for the FFWS. To overcome this problem in Korea, a simple mean-field-bias-correction procedure is introduced to correct the rainfall forecast before applying to the FFWS. The G/R ratio (ground rain gauge rain rate/radar rain rate) is generally used for this purpose, as it is easily applicable. The second problem is related with the size of the storm. Especially, the G/R ratio, estimated by the conventional method by comparing the radar rain rate and the rain gauge rain rate over the given domain, could be inappropriate. That is, the G/R ratio may not be properly estimated for a localized storm. In this study, a backward storm tracking is introduced to locate the storm which will arrive at the area of interest in short time. The G/R ratio is estimated where the storm is located at present. The estimated G/R ratio will then be applied to correct the rainfall forecast, which is assumed to arrive at the area of interest in short time. This method of correcting the rainfall forecast has been applied to several locations in Korea with some storm events. As a result, it was found that the proposed method is more reliable and stable than the conventional method of estimating the G/R ratio.

4.20 METHODS AND STATISTICAL TOOLING FOR DETERMINING RAINFALL EVENTS IN RADAR DATASETS

M. A. A. ALDERLIESTE[1], T. EINFALT[2], T. MORDELT[3], A. PFISTER[4], H. PLAGGENMARS[1], M. SCHEIBEL[5], A. TREIS[4]

[1] HydroLogic BV, The Netherlands
[2] hydro & meteo GmbH & Co. KG, Germany
[3] Niersverband, Germany
[4] Emschergenossenschaft / Lippeverband, Germany
[5] Wupperverband, Germany
marcel.alderlieste@hydrologic.com

With the large number of heavy precipitation events in recent years, the demand for data and tools to post-process and analyse precipitation data has increased steadily. Therefore, the accuracy and high-resolution availability of weather radar data makes it an ideal source for detailed analyses of extreme precipitation events and the subsequent influence on the water system.

The reconstruction of flood events and the evaluation of a water system for flood resilience, are typically performed using hydro-dynamic or hydrologic models. These models can be fed with detailed precipitation information. However, as the radar data sets continually grow, it can be very difficult to extract the relevant data for further use in models and for further analysis.

An online system has been developed in which the user can search for precipitation events with defined characteristic qualities. The system holds a database of 13 years of radar data (5 minute time step, 1 km2 resolution, 19 000 km2 area). The data have been corrected and composited from three radars of the German Weather Service DWD in a conjoint project of 10 water boards in North-Rhine-Westphalia using SCOUT software. Accessible through the HydroNET online platform (www.hydronet.com), a user can choose periods, areas, duration (time intervals) and thresholds of precipitation amount depending on the related questions. The system will then determine the unique rainfall events which match these criteria.

To determine unique events, the system evaluates each grid cell which exceeds a given amount of rainfall of a specified duration. If a neighbouring grid cell also exceeds this threshold within a given time-frame, the cells are assumed to have a joined rainfall event. This process is repeated automatically until no further exceedances are found in the data set. The result is a list with all precipitation events per predefined duration which match the specified search criteria.

The application allows the preparation of time series for hydrological simulation, the shift of an event to another location and preparation of data for simulation, the statistical analysis of extreme events and their spatial extent and variation, as well as a comparison to extreme value statistics of rain gauge station series. This could subsequently be done using external time series management systems. The user can browse through the list of all events, each event can be viewed geographically, the maximum pixel or all pixels of the search area can be downloaded as time-series or grid data for further usage e.g. in GIS. Additionally to downloading the grids, the user can re-locate a given event to another place. The latter can be useful to

investigate What-If scenarios regarding how a water system reacts to a known event from another location.

By that, the system helps to find and analyse relevant storm events and get a better knowledge of the impacts on the hydrological cycle.

4.21 SPATIAL RESOLUTIONS IN AREAL RAINFALL ESTIMATION AND THEIR IMPACT ON HYDROLOGICAL SIMULATIONS OF A LOWLAND CATCHMENT

W. TERINK[1], H. LEIJNSE[2], G.A.P.H. VAN DEN EERTWEGH[3], R. UIJLENHOET[4]

[1] Environment Canterbury Regional Council, New Zealand
[2] KNMI, R&D Observations and Data Technology, The Netherlands
[3] KnowH2O, The Netherlands
[4] Wageningen University & Research, Hydrology and Quantitative Water Management Group, The Netherlands
terinkw@gmail.com

Many studies suggest that high-density rain gauge networks are required to capture the rainfall heterogeneities necessary to accurately describe the components of the hydrological cycle. However, equipping and maintaining a high-density rain gauge network will also involve high costs. Although many studies provided useful insights on the required accuracy of rainfall estimates to accurately describe the components of the hydrological cycle, most of these studies focused on streamflow simulations, large river basins or urban environments. The objective of this study is therefore to evaluate the impact of areal rainfall, estimated at several spatial resolutions, on hydrological simulations of a small 6.5 km2 rural lowland catchment. The approach followed in this study is to force a calibrated spatially-distributed hydrological model (SPHY) with rainfall retrieved from an X-band radar and various synthetic rainfall products, calculated using bootstrap samples of a varying number of radar pixels, treated as virtual rain gauge locations within the catchment. This enables us to determine the most appropriate resolution of rainfall data to accurately describe the hydrology of a small rural lowland catchment. The novelty of this study is the combined approach of a spatially distributed model forced with bootstrapped rainfall fields from an X-band radar with ultra-high spatial (120 m range; 1.875 degrees in azimuth) and temporal (16 s) resolutions, which is unique in the sense that the majority of weather radars used in other studies have much coarser spatial and temporal resolutions. We found that the use of one rain gauge to estimate the catchment's areal rainfall may lead to a potential error of 0.56 mm/h. This may lead to uncertainties in simulated discharge that approach 60% of the average hourly discharge. More than 40 rain gauges are required to reduce the potential error in areal rainfall estimation to values <0.1 mm/h. The associated uncertainty in discharge simulations is 20% if 10 rain gauges are used, and 10% if 40 rain gauges are used. The simulation of soil moisture contents and evapotranspiration rates are hardly affected by the number of rain gauges used to estimate the areal rainfall, which is due to the high saturated hydraulic conductivities of the top-soil. Approximately 2/3 of the radar pixels need to be covered with rain gauges in order to capture the spatial rainfall variation that is present in radar rainfall estimates. Analysis of an individual 18-hour rainfall event revealed that the uncertainty in peak areal rainfall estimated using one rain gauge may range between 100% and +600%. The associated uncertainty in simulated discharge for this event ranges between 67 and

+233%. With 25 rain gauges the uncertainty in simulated discharge is still in the range of 17 to +33%.

4.22 SPATIAL AND TEMPORAL AUTOCORRELATION STRUCTURE OF CONVECTIVE RAINFALL IN SEMIARID-ARID CLIMATE: IMPLICATIONS FOR REMOTE SENSING ESTIMATION

F. MARRA[1], E. MORIN[1]

[1] Institute of Earth Sciences, Hebrew University of Jerusalem, Israel
f.marra@mail.huji.ac.il

Small scale rainfall variability is a key factor driving runoff response, particularly in fast responding systems, such as mountainous, urban and arid catchments and needs to be taken into account when interpreting and using rainfall estimates from rain gauges or remote sensing instruments. We derive the spatial and temporal autocorrelation structure of convective rainfall for 11 storms occurred between 2014-2016 in a semiarid-arid region in the eastern Mediterranean, exploiting the extremely high resolution (60 m, 1 min) of an X-Band weather radar. We present results on the 2-dimensional spatial autocorrelation as well as on the temporal autocorrelation of point-wise and distributed rainfall fields. The autocorrelation structures highlight extremely large rainfall variability, with spatial anisotropies, correlation distances rarely exceeding 5 km (mostly ∼1.52.8 km), and time-correlation distances rarely exceeding 10 min (mostly ∼1.86.4 min). We discuss the impact of such observations on rainfall estimation by means of rain gauges and remote sensing instruments such as coarser-resolution weather radars, satellites, and commercial microwave links.

4.23 HYDROLOGICAL APPLICATION OF RADAR RAINFALL NOWCASTING IN THE NETHERLANDS

D. HEUVELINK[1], C.C. BRAUER[1], M. BERENGUER[2], D. SEMPERE[2], R. UIJLENHOET[1]

[1] Hydrology and Quantitative Water Management Group, Wageningen University, The Netherlands

[2] Centre de Recerca Aplicada en Hidrometeorologia, Universitat Politcnica de Catalunya (CRAHI-UPC), Barcelona, Spain

danny.heuvelink@wur.nl

The high temporal and spatial variability of rainfall fields make that they are difficult to predict. Good predictions of rainfall for the first hours can be very useful in operational flood forecasting. To make such predictions of rainfall, radar rainfall nowcasting techniques can be used.

This study applied radar rainfall nowcasting for discharge predictions for several lowland catchments. Deterministic (Lagrangian persistence) and probabilistic (SBMcast) techniques were used to produce rainfall forecasts based on radar imagery. These rainfall forecasts were used as input for the hydrological model WALRUS.

In terms of rainfall, the forecasts got worse with increasing forecasting time, with most often an underestimation of rainfall. The results showed that the discharge could be forecasted between 25 and 170 minutes earlier than without rainfall nowcasting, with the best performance for the largest catchment. With respect to the catchment response time, the best performance was found for the smallest catchment, but that was also the most variable. The probabilistic nowcasting effectively showed the uncertainty of the rainfall and discharge predictions. The uncertainty in rainfall predictions was shown to be largest for smaller catchments. Moreover, the ensemble forecasts effectively showed the uncertainty in how much earlier the discharge could be forecasted. This uncertainty ranged between 15 and 50 minutes.

To apply radar rainfall nowcasting in operational flood forecasting better real-time radar products need to be developed to overcome the rainfall bias and the performance of the nowcasting techniques has to be tested for more events and catchments.

4.24 RAINFREQ: RAINFALL FREQUENCY ANALYSIS FROM REMOTE SENSING RAINFALL ESTIMATES

F. MARRA[1], N. PELEG[2], E.I. ANAGNOSTOU[3], E. MORIN[1]

[1] Institute of Earth Sciences, Hebrew University of Jerusalem, Israel

[2] Institute of Environmental Engineering, Hydrology and Water Resources Management, ETH Zurich, Switzerland

[3] Department of Civil and Environmental Engineering, University of Connecticut, Storrs, CT, USA

f.marra@mail.huji.ac.il

IntensityDurationFrequency (IDF) curves are used to provide a direct link between the characteristics of a rainfall event and the probability of its occurrence, and have wide applications in hydrological design and flood risk management. The standard approach relies on rain gauge data and applies to point rainfall, raising two issues: (i) usual applications require catchment-scale information; (ii) no data is available for ungauged areas or regions where rain gauges have been deployed only recently, moreover rain gauge representativeness decreases with distance, especially in presence of climatological gradients. A number of contributions aimed to issue (i), but generally relying on rain gauge records and, as such, making the second issue even more important.

Crucial objective of present-day research is to address issue (ii) by means of remote sensing rainfall estimates. This would allow exploring the spatial distribution of rainfall extremes with increased detail over wide areas, providing new perspectives for studying precipitation regimes, and promising theoretical and practical implications. Research on the topic, so far, used concepts and techniques developed for rain gauge data (i.e. point or multiple-point) and have been validated against gauge-derived analyses. These procedures add further sources of uncertainty and prevent from isolating between data and methodological uncertainties and from fully exploiting the available information. Aim of this project is to advance knowledge on the use of remote sensing rainfall estimates for rainfall frequency analysis stepping out of gauge-centred concept and identifying new methods for improved estimates of high quantiles from short data records. We present results from this project placing them in the context of present-day research on the topic. Specific results include: (a) derivation of IDF curves for the eastern Mediterranean area from the longest weather radar record worldwide; (b) quantification of the impact of small-scale variability of rainfall extremes on the estimation of IDF curves from rain gauges and remote sensing estimates; and (c) direct comparison of IDF curves from weather radar and satellite based products on corresponding spatial and temporal scales.

4.25 AN APPROACH FOR CLASSIFICATION OF HYDROMETEORS BY K-MEANS CLUSTERING

O. GOKDERE[1]

[1] RST Teknoloji, Turkey
ogokdere@rstteknoloji.com.tr

Weather radar base moments including especially polarimetric moments are used for classification of hydrometeors. Some of hydrometeor classes have values in approximately same intervals, i.e. have intersecting regions. In general, melting layer phenomenon or temperature information is used in order to distinguish ambiguity. These information could be manually provided or automatically obtained by some another algorithms. Aim of this study is to acquire melting layer position information and hydrometeor classes with a single clustering study such as k-means clustering.

4.26 OPTIMIZATION OF RAIN GAUGE SAMPLING DENSITY FOR DISCHARGE PREDICTION USING BAYESIAN CALIBRATION

ALEXANDRE M.J-C. WADOUX[1], REMKO UIJLENHOET[2], SYTZE DE BRUIN[3], GERARD B.M. HEUVELINK[1]

[1] Soil Geography and Landscape group, Wageningen University & Research, Netherlands.
[2] Hydrology and Quantitative Water Management Group, Wageningen University & Research, Netherlands.
[3] Laboratory of Geo-Information Science and Remote Sensing, Wageningen University & Research, Netherlands.
alexandre.wadoux@wur.nl

Stream discharges are often predicted based on a calibrated rainfall-runoff model. The major sources of uncertainty, namely input, parameter and model structure uncertainty must all be taken into account to obtain realistic estimates of the accuracy of discharge predictions. Over the past years, Bayesian calibration has emerged as a valuable method to quantify uncertainty in model parameters and model structure, where the latter is usually simplistically modelled by an additive or multiplicative stochastic term. Much work has also recently been done on including input uncertainty in the Bayesian framework. However, studies that included rainfall input uncertainty did not employ geostatistical methods to characterize the prior distribution of the overall catchment rainfall and did not consider how an increase or decrease of the rain gauge network density influences the discharge prediction accuracy. In this presentation we integrate geostatistics and Bayesian calibration to analyse the effect of rain-gauge density on discharge prediction accuracy. We calibrated the well-known HBV hydrological model while accounting for input, initial state, model parameter and model structure uncertainty, while also taking uncertainties in the discharge measurements into account. Results for the Thur catchment in Switzerland show that (i) an increase of the rain gauge density leads to a decrease of input uncertainty, but (ii) further increase of the rain-gauge density (larger than 1 gauges/170 km^2) does not lead to improvement of the total error. We also show that a low rain-gauge density does not necessarily lead to biased predictions, provided that the major sources of uncertainty are explicitly accounted for and that large input uncertainty can be safely lumped into parameter uncertainty.

Session 5. Use of Weather Radar Data in NWP Models



Keynote presentation

5.1 A MOMENT-BASED POLARIMETRIC RADAR FORWARD OPERATOR FOR RAIN MICROPHYSICS

M. R. KUMJIAN[1], C. P. MARTINKUS[1], O. P. PRAT[2], S. COLLIS[3], H. C. MORRISON[4], M. VAN LIER-WALQUI[5]

[1] Department of Meteorology and Atmospheric Science, The Pennsylvania State University, University Park, PA, USA

[2] North Carolina Institute for Climate Studies, North Carolina State University, Asheville, NC, USA

[3] Argonne National Laboratory, Chicago, IL, USA

[4] National Center for Atmospheric Research, Boulder, CO, USA

[5] NASA Goddard Institute for Space Studies and Center for Climate Systems Research, Columbia University, New York, NY, USA

kumjian@psu.edu

Polarimetric radars have often been used to provide information about the hydrometeor distribution within storms (e.g., via hydrometeor classification algorithms). Of greater use to the modeling community are studies exploring polarimetric radar "fingerprints" of individual microphysical processes observed in precipitation. Numerical models are useful for this purpose, but typically employ microphysical parameterization schemes with poorly constrained and ill-defined structural and parameter-value uncertainties and biases. A new parameterization approach that explicitly quantifies these uncertainties is in development (BOSS), and differs from most traditional schemes in that it does not impose a functional form for the drop size distribution (DSD). This presents challenges for the forward-simulation of radar quantities from model prognostic DSD moments (typically the 0th and/or 3rd and/or 6th moments for traditional one-, two-, and three-moment microphysics schemes), because such forward simulation requires discretizing a DSD using a priori knowledge of the DSD functional form (e.g. exponential, gamma, etc.). What is required for the new probabilistic approach is a moment-based polarimetric radar forward operator with no fundamental restrictions on the DSD form. We present the development and initial testing of such an operator. To capture the large parameter space of "realistic" DSDs, we use (i) 1D bin microphysical rain shaft simulations, and (ii) surface disdrometer measurements from around the world. The resulting dataset includes nearly 200 million DSDs, allowing for a robust statistical assessment of forward operator uncertainty. To our knowledge, such a forward operator is unique in relating polarimetric radar observables (ZH, ZDR, and KDP) to integrated DSD moments. Comparison of "truth" and forward-simulated vertical profiles of the polarimetric radar variables are shown for bin simulations, including an assessment of error statistics.

5.2 ASSIMILATION OF AIRBORNE DOPPLER W-BAND RADAR DATA IN THE KILOMETRE-SCALE NWP MODEL AROME

M. BORDERIES[1], O. CAUMONT[1], J. DELANOË[2], V. DUCROCQ[1]
[1] CNRM UMR 3589 (Météo-France/CNRS), Toulouse, France
[2] LATMOS, Guyancourt, France
mary.borderies@umr-cnrm.fr

Because of their high sensitivity to cloud microphysical and dynamical properties, Doppler W-band radars are very complementary to the traditional sensors whose measurements are commonly used in data assimilation. Currently, these data are not used to initialise kilometre-scale NWP models such as the AROME model from Météo-France (Seity et al. 2011).

This study investigates the potential of Doppler W-band radar to improve the quality of analyses and short-term forecasts of heavy precipitation events in the Mediterranean area. Here, we take advantage of the data collected in various conditions by the airborne Doppler W-band radar RASTA (Radar Airborne System Tool for Atmosphere, Delanoë et al. 2013) over the Western Mediterranean during the HyMeX SOP1 field campaign dedicated to intense rainfall. This unique instrument allows the documentation of the microphysical properties and the three components of the wind field in the vertical at a high resolution of 60 m and quasi-continuously in time during the flights.

First, several data assimilation experiments were conducted over the two-month field campaign period to assess the impact of RASTA horizontal wind data. They are directly assimilated in the AROME 3D-Var assimilation system every 3 hours when they are available. The positive impact of the assimilation of RASTA wind data is first evidenced in a case of strong convection. More generally, the scores show that the assimilation of RASTA wind data improves the 6, 9 and 12-hour precipitation forecasts greater than 30 mm.

Next, the assimilation of the W-band radar reflectivity is also investigated by employing the 1D+3D-Var assimilation method that is operationally used to assimilate the radar reflectivity in AROME (Caumont et al. 2010, Wattrelot et al. 2014). This method requires the simulation of vertical profiles of reflectivity, which is done here through the use of the observation operator of Borderies et al. (2018). Vertical profiles of relative humidity are first retrieved from observed and simulated vertical profiles of reflectivity via a 1D Bayesian retrieval, and then used as pseudo-observations in the 3D-Var assimilation system of AROME. A validation of the 1D Bayesian retrieval with in-situ measurement of humidity will be presented. Finally, the respective impacts of the W-band reflectivity and Doppler velocity data assimilation will be discussed.

References

Borderies, M., O. Caumont, C. Augros, É. Bresson, J. Delanoë, V. Ducrocq, N. Fourrié, T. Le Bastard, M. Nuret (2018). Simulation of W-band radar reflectivity

for model validation and data assimilation. Quarterly Journal of the Royal Meteorological Society, DOI: 10.1002/qj.3210.

Caumont O., Ducrocq V., Wattrelot É., Jaubert G., Pradier-Vabre S. (2010). 1D+ 3DVar assimilation of radar reflectivity data: a proof of concept. Tellus A, 62(2), 173-187.

Delanoë, J., Protat, A., Jourdan, O., Pelon, J., Papazzoni, M., Dupuy, R., ... & Jouan, C. (2013). Comparison of airborne in situ, airborne radarlidar, and spaceborne radarlidar retrievals of polar ice cloud properties sampled during the POLARCAT campaign. Journal of Atmospheric and Oceanic Technology, 30(1), 57-73.

Seity, Y., Brousseau, P., Malardel, S., Hello, G., Bnard, P., Bouttier, F., Lac, C., and Masson, V. (2011). The AROME-France Convective-Scale Operational Model. Monthly Weather Review, 139(3):976991.

Wattrelot, E., Caumont, O., and Mahfouf, J.-F. (2014). Operational Implementation of the 1D+3D-Var Assimilation Method of Radar Reflectivity Data in the AROME Model. Monthly Weather Review, 142(5):18521873.

5.3 ASSIMILATION OF WEATHER RADAR DATA FOR THE SIMULATION OF A HEAVY RAINFALL CASE IN CENTRAL ITALY: A COMPARISON BETWEEN 3D-VAR AND 4D-VAR TECHNIQUES

VINCENZO MAZZARELLA[1,2], IDA MAIELLO[2,3], VINCENZO CAPOZZI[1], GIORGIO BUDILLON[1], ROSSELLA FERRETTI[2]

[1] Department of Science and Technology, University of Naples "Parthenope", Naples, Italy

[2] Centre of Excellence CETEMPS, Department of Physical and Chemical Sciences - University of L'Aquila, L'Aquila, Italy

[3] Department of Information Engineering, Electronics and Telecommunications - Sapienza University of Rome, Rome, Italy

vincenzo.mazzarella@uniparthenope.it

The Italian territory, characterized by densely urbanized watersheds with steep slopes, is particularly exposed to hydraulic and hydrological risk. Therefore, persistent heavy rainfall events are a highly relevant problem for damages and numerous victims caused every year. In this respect, data assimilation plays a key role in improving initial conditions and, consequently, forecast accuracy. The assimilation of a dense network of conventional observations and local measurements with a high spatial and temporal resolution, such as radar data, may produce more accurate rainfall forecasts and a better estimation of the localization of the precipitation cells.

The goal of this study is to provide a comparison/evaluation between 3D-VAR and 4D-VAR assimilation systems of the Weather Research and Forecasting (WRF) model to forecast a heavy precipitation event in a complex orography region, such as the central Italy. Radar radial velocity and reflectivity data, acquired by Mt. Midia and St. Pietro Capofiume C-band radar, and conventional observations (SYNOP and TEMP) have been assimilated into the model to estimate the precipitations occurred on 14 September 2012. The case study, used in this work, is the IOP4 of the HYdrological cycle in the Mediterranean EXperiment (HyMeX) campaign. The meteorological scenario was characterized by a cut-off low over the Southern Tyrrhenian Sea, which produced heavy and persistent precipitation along the Adriatic coast of central Italy.

The performance of 3D-VAR and 4D-VAR experiments has been evaluated using two different statistical methodologies: point to point (or traditional approach) and neighborhood. The first method compares the rainfall data, recorded by rain gauges, and the precipitation forecast in the exact location. In this respect, critical success index (CSI) and equitable threat score (ETS), have been evaluated for several threshold values. The other method applies a smoothing filter to the predicted and observed precipitation fields and then matches both fields using a neighborhood approach. In this context, the fraction skill score (FSS) index has been calculated. Finally, a sensitivity study on warm start initialization has been performed with the aim to reduce the model spin-up time and evaluate the role of data assimilation in the first hour of simulation.

The results show that radar data have a relevant contribution in the estimation of precipitation both with 3D-VAR and 4D-VAR. Furthermore, the experiments with

4D-VAR produce an improvement of statistical scores, pointing out the positive impact of this method. However, the performance concerning the high threshold values decreases outside the assimilation window, highlighting the weakness of tangent linear model (TM).

5.4 CONTINENTAL-SCALE WEATHER RADAR DATA ASSIMILATION USING NORTH AMERICAN DATA

D. MICHELSON[1], D. JACQUES[1], B. HANSEN[1], J-F. CARON[1], L. FILLION[1]

[1] Environment and Climate Change Canada, Canada
daniel.michelson@canada.ca

Determining the impact of assimilating weather-radar data in numerical weather prediction models at continental scales is still relatively uncommon. This is partly due to data availability, but also due to data quality issues when data are available. As Environment and Climate Change Canada (ECCC) starts replacing its weather radar network, C-band radars are being replaced with S-band systems, and ECCC is preparing for a new generation of quantitative applications based on the new data. Weather radar data assimilation is being introduced to ECCC, and the initial focus is on weather radar quality control and impact studies using a large model domain with the Canadian Regional Deterministic Prediction System (RDPS) covering North America and surrounding waters.

Archived weather-radar data from the Canadian and American networks, around 180 radars, have been used in this study for the summers of 2014 and 2016. Canadian C-band data require significant quality control, mostly to address clutter but also attenuation and metrics designed to characterize data quality in various ways. NEXRAD Level II data and McGill University data, both at S band, do not require the same processing for clutter, but are subject to the other quality controls. The BALTRAD Toolbox is used to quality control all radar data, and generate continental composites at 2.5 km horizontal resolution containing both corrected and uncorrected reflectivity data and associated quality fields. Radar data quality monitoring functionality has been established that utilizes hourly surface observations of precipitation occurrence.

At continental scales, latent heat nudging (LHN) is deemed a suitable first technique for exploiting the radar data. The system developed for the RDPS is intended to provide a low-cost benchmark against which to compare more advanced assimilation techniques in the future. For this impact study, forecast skill with and without LHN will be discussed. When validated against radar composites, LHN improves precipitation forecasts for approximately three hours. Verification against aircraft measurements indicates small but significant improvements of temperature and winds throughout the atmospheric column for lead times up to 36 hours. A comparison against precipitation forecasts by the McGill algorithm for precipitation nowcasting by Lagrangian extrapolation (MAPLE) will also be made.

5.5 X-NET BASED RADAR DATA ASSIMILATION STUDY OVER SEOUL METROPOLITAN AREA

K.-H. MIN[1], Y. LEE[1], G. LEE[1], Y. KIM[2]

[1] School of Earth System Sciences, Kyungpook National University, South Korea
[2] Department of Statistics, Kyungpook National University, South Korea
kmin@knu.ac.kr

The ability of a high resolution (500 m) Weather Research and Forecasting (WRF) model in simulating a convective precipitation case with X-band radar network (X-Net) data over Seoul metropolitan area is studied. To understand the convective storm initiation process over the urban area, we performed sensitivity tests using different initial condition (IC) times. Despite simulating the same case, the quantitative precipitation forecast (QPF) varied widely among the experiments, depending on the timing of the ICs. The difference in timing of convective rainfall among the experiments are related to the atmospheric boundary layer (ABL) growth. Rapid growth of the ABL enabled moist convection to occur early in the presence of outflow, resulting in less rainfall amount. An overestimated maximum ABL height by the model also led to earlier collapse of the ABL compared to observations, which contributed to a reduction of convective available potential energy over the urban area in late afternoon. The sensitivity tests showed the importance of accurate simulation of ABL growth for reasonable prediction of timing and intensity of convective precipitation. When assimilation of surface observations and radar data was performed, the simulation reproduced the location and amount of rainfall reasonably well within the first 6 hours. This shows that high resolution WRF model with data assimilation can predict convective storm initiation in the first few hours and improve precipitation forecast skill in the very short-term forecasting range.

5.6 DATA ASSIMILATION OF RADAR REFLECTIVITY VOLUMES IN A LETKF SCHEME

V. POLI[1], T. GASTALDO[1,2], C. MARSIGLI[1], P.P. ALBERONI[1], T. PACCAGNELLA[1]

[1] ARPAE Emilia Romagna - SIMC, Italy

[2] Department of Physics and Astronomy - University of Bologna, Italy

vpoli@arpae.it

At Arpae, the HydroMeteorological Service of Emilia-Romagna Region (Italy), it is operational an ensemble data assimilation system at the convection permitting scale (KENDA), based on a LETKF scheme. The system has been been developed for the Consortium for Small scale Modeling (COSMO) model and, currently, it is used to assimilate only conventional observations.

The main issue of the presented work is to produce the most accurate analysis to initialize deterministic and ensemble forecast runs. For rapidly evolving systems, such as summer thunderstorms, this involves the assimilation of dense and frequent observations. For this reason in the experimental KENDA set-up, reflectivity volumes from the Italian radar network are assimilated by means of the COSMO Radar Forward Operator (EMVORADO).

The quality of the analysis depends on various factors, but the observational error plays a crucial role. This is influenced by three sources: instrumental error, representativity error and errors derived from observation operator. Since none of these are known and their effects are not distinguishable, the choice of its value is not straightforward. To estimate this error a diagnostic based on statistical averages of observation-minus-background and observation-minus-analysis residual is used. This is performed separately for each radar since the Italian radar network is inhomogeneous both in the acquisition strategy and from an instrumental point of view.

Results, both in the assimilation and in the forecast cycle, are presented by means of a statistical analysis and the verification of forecasted fields.

5.7 RADAR DATA ASSIMILATION AT GERMAN METEOROLOGICAL SERVICE OPERATIONAL APPLICATIONS AND PRE-OPERATIONAL RESEACH

K. STEPHAN[1], U. BLAHAK[1], E. BAUERNSCHUBERT[1], A. DE LOZAR[1], A. SEIFERT[1], C. WELZBACHER[1]

[1] German Meteorological Service (DWD), Germany
klaus.stephan@dwd.de

Radar data contains very valuable information on the current structure of the atmosphere. The very high resolution in space and time provided by radar measurements is expected to narrow the large gap NWP is facing when trying to initialize the high dimensional numerical weather prediction models. Especially the improvement of the very short range NWP with respect to high impact weather is a main goal. Application of radar observation in the process of data assimilation is a very challenging task and has to consider a lot of issues, concerning observation, model and assimilation techniques.

At DWD radar observation is assimilated operationally since 2006 by applying a very simple technique, called latent heat nudging (LHN). This more indirect method of assimilation, using a 2D composite of derived precipitation rates, has proven to be beneficial not only on precipitation forecasting but also shows positive impact on surface parameters. However, as 3d volume data at a European scale become available more easily, the hope is to get even more benefits on the three dimensional structure of the model atmosphere by assimilating this amazing data source applying the operational LETKF scheme.

The presentation will give an overview of the state of the current radar data assimilation done at DWD. The focus will be more on the research part, and may address important issues of treating such data within a LETKF frame (localization, influence on spread, representation of observation errors, possibilities to make model background and observations more comparable). At the time of the conference it is expected, that 3D radial wind observations are assimilated operationally, at least for measurements of German radar sites. Be curious!

5.8 USING WEATHER RADAR OBSERVATIONS FOR DATA ASSIMILATION TO MODEL THE AMSTERDAM URBAN CLIMATE

SYTSE KOOPMANS[1], RONALD VAN HAREN[2], GERT-JAN STEENEVELD[1], NATALIE THEEUWES[3], REINDER RONDA[4], REMKO UIJLENHOET[1], ALBERT A.M. HOLTSLAG[1]

[1] Wageningen University and Research, the Netherlands
[2] Netherlands eScience Center, the Netherlands
[3] University of Reading, United Kingdom
[4] Royal Netherlands Meteorological Institute (KNMI), the Netherlands
sytse.koopmans@wur.nl

Ongoing world-wide climate change and urbanization illustrate the need to understand urban hydrometeorology and its implications for human thermal comfort and water management. Weather forecasting and climate models can assist to understand these issues, as they progress increasingly towards finer scales. With high model resolutions (grid spacing of 100m), effective representation of cities becomes crucial. The complex structures of cities, configuration of buildings, streets and scattered vegetation, require a different modelling approach than the homogeneous rural surroundings. The current urban canopy-layer schemes account for these city specific characteristics, but differ substantially amongst each other due to uncertainty in land use parameters and incomplete physical understanding. Therefore, meteorological forecasting and hindcasting of the urban environment requires improvement. In this study we create a 15-year high resolution climatological urban re-analysis data archive of (hydro)meteorological variables for Amsterdam. The rest of the Netherlands will be archived on a slightly lower resolution. This will enable us to trace trends in thermal comfort and extreme precipitation.

Model simulations are performed with the WRF (Weather Research and Forecasting) mesoscale model, which uses nested domains to bridge the resolution of ECMWF re-analysis data on the boundaries towards the finer resolutions in the inner domain. We attempt to improve the WRF (Weather Research and Forecasting) mesoscale model performance by incorporating observations of a variety of sources using data assimilation and nudging techniques. Data assimilation aims to accurately describe the most probable atmospheric state by steering the model fields in the direction of the observations. Data assimilation has been conducted every 2 hours and consists of WMO synoptic weather observations, volume radar data and urban weather observations recorded by hobby meteorologists.

The volume radar data is retrieved from one of the C-Band Doppler weather radar from the Royal Netherlands Meteorological Institute (KNMI). We use both the reflectivity and radial wind from the elevation scans. The reflectivity is converted to rain water mixing ratio before assimilation takes place. This leads to a lower conversion error compared to direct assimilation of reflectivity. For our study this is crucial to get an improved analysis field.

Different data assimilation methods are evaluated for hindcasts of July 2014 for the Netherlands. That month is characterized by both a warm dry period and two days with extreme precipitation (more than 100mm in two days). The largest improvement is made by assimilating the air temperature, dew point temperature and

pressure from WMO synoptic stations. Applying additional radar data assimilation, slightly improves the location of the precipitation indicated by the fraction skill score. The data assimilation of urban weather stations, lastly, reduces the cold biases within the canopy which appeared in WRF.

5.9 ASSIMILATION OF DIFFERENT RADAR DATA FOR A BETTER FORECASTING OF SEVERE WEATHER PHENOMENA

L. ROVAI[1], A. ANTONINI[2], S. MELANI[1,2], V. CAPECCHI[2], R. BENEDETTI[2], L. FIBBI[1,2], B.GOZZINI[2], G. MESSERI[1,2], A.ORTOLANI[1,2] F.PASI[1,2]

[1] CNR-IBIMET, ITALY

[2] LAMMA CONSORTIUM, ITALY

rovai@lamma.rete.toscana.it

One aspect of climate change is the modification in frequency and characteristics of severe weather phenomena, which makes them less predictable in occurrence and effects. In order to address this issue, meteorological centers in charge of regional forecasts are investing to upgrade their capability of nowcasting and short-term forecasting of such events. When dealing with fast, intense and very localized phenomena the integration of proper, often heterogeneous, real-time measurements with high-resolution model simulation is at the moment the most promising mean to catch and follow the evolution of critical events.

In this context, for a few cases of severe weather in Tuscany, we show the results of assimilating local data in a limited area model configured for operational forecasts of central Italy. The main focus is on the impact of radar observations from different systems operating in different bands and their added value with respect to assimilating data from available ground-stations and radiosoundings. The adopted local area model (LAM) is based on the WRF code, with the WRF-DA assimilation scheme in a 3DVar configuration and an architecture that allows a rapid refresh of the model (every 3h) with the assimilation of new observations, in order to provide high-resolution forecasts, in view of operational nowcasting of intense precipitation events. In-situ data are from the regional sensor networks (about 800 stations), while radar data are from different systems, namely a S-band radar in Corse, three X-band radars in Tuscany and the C-band composite of the Italian radar network. The different impacts on the model simulations are analysed for the data coming from different types of radars and their combination.

The preliminary results show a significant impact from the assimilation of local ground weather stations and radar data in correcting the space and time localization of the precipitation, and its rate, with respect to the non-assimilated simulations. We also investigate on which extent the heterogeneity of the available data, specifically of the radar systems operating at different frequencies, can bring complementary information on the precipitation phenomenology and its horizontal and vertical distribution, supporting a better reconstruction of the rainfall event.

5.10 INFORMATION SPARSENESS, A KEY OBSTACLE TO RADAR DATA ASSIMILATION IN CONVECTION

F. FABRY[1]

[1] McGill University, Canada
frederic.fabry@mcgill.ca

Radar is our best instrument to monitor storms; data assimilation is our best method to merge information; numerical forecasting is our best forecasting tool. So why are a) simple nowcasting approaches beating numerical forecasting for a couple of hours, b) the skill of numerical forecasting aided by radar data assimilation dropping so rapidly in the first forecast hour, and c) assimilated radar data showing positive effect for much shorter periods (e.g., about two hours) than other instruments (e.g., six hours for surface observations)?

In an attempt to answer these questions, we tried to understand what made the assimilation of radar data assimilation more challenging and limiting than that of other data sources. The rapid drop in the skill of radar data assimilation with forecast time suggests that radar data assimilation has difficulties affecting the fields that will shape storm development in the future. Reasons why this arises include:

- Over 90+% of the troposphere, the only information available from radar is no precipitation, largely limiting new information to a few areas where either the analysis or the observations have precipitation;

- The air feeding the storms and controlling their environment in a few hours largely come from regions of no precipitation; hence its properties are largely unconstrained directly by radar. Any innovation must hence come from distant correlations with precipitation areas;

- Though there is significant correlation between overall storm intensity and thermodynamic properties, the correlations computed at the scale of model grid points are limited because the field of precipitation and its errors have much more energy at smaller unpredictable scales compared to other fields. Limited ensemble sizes and localization then prevent such weak long-distance correlations to be fully utilized. And as model resolution increases, this problem becomes worse.

In the end, it appears that it is the sparseness of the radar information, and the inability of many assimilation approach to deal with this sparseness, that currently limits the usefulness of radar data assimilation.

5.11 QUALITY CONTROL OF SEA CLUTTER AND CONSTANT POWER FUNCTION ARTIFACTS FOR OPERATIONAL U.S. NAVY SHIPBOARD RADAR DATA ASSIMILATION

PAUL R. HARASTI[1]

[1] Marine Meteorology Division, U.S. Naval Research Laboratory, Monterey, California, U.S.A.

paul.harasti@nrlmry.navy.mil

The Marine Meteorology Division of the U.S. Naval Research Laboratory (NRL) has developed and transitioned a three-dimensional variational (3DVAR) reflectivity data assimilation (DA) system to Fleet Numerical Meteorology and Oceanography Center (FNMOC), located in Monterey, California. The system assimilates hourly, volumetric, radar reflectivity data into the Coupled Ocean/Atmosphere Mesoscale Prediction System (COAMPS®)[2] high-resolution NWP model within the ship-following COAMPS On demand System (COAMPS-OS®)[2]. Both land-based Next-Generation Radar (NEXRAD) and U.S. Navy shipboard SPS-48/Hazardous Weather Detection and Display Capability (HWDDC) radar data are assimilated depending on the radars available within the COAMPS® domain. The SPS-48/HWDD C units are installed on eighteen U.S. Navy aircraft carriers and amphibious assault ships, and when underway on a mission, the available units automatically transmit compressed, radar data files to FNMOC near the top of the hour. Through previously reported NRL and FNMOC demonstrations, and more recent operationally testing at FNMOC, the COAMPS-OS® radar DA system's nowcasting products have demonstrated their ability to provide improved predictions of precipitation events out to at least 6 hour forecasts compared to 3DVAR conventional DA into COAMPS® alone. Shipboard SPS-48/HWDDC radar data and their assimilation into COAMPS-OS at FNMOC provide critical environmental awareness in the data sparse oceanic regions of the world that the Navy warfighter encounters.

The SPS-48 radar is a S-band, phased-array, air-search radar that rotates azimuthally and scans electronically in elevation. The HWDDC passively taps into the SPS-48 radar system to generate ship-motion-compensated volume scan files with angular resolution, range and elevation specifications similar to NEXRAD. Doppler velocity data are produced at the lowest three elevation scans whereas reflectivity data are produced for all elevation scans. The volume scan data are archived in Universal Format and compressed before dissemination to FNMOC. Owing to the limited HWDDC Doppler velocity data both in range ($\sim$0.25 the range of reflectivity) and elevation, reflectivity data quality control is particularly challenging. New algorithms have been developed to handle sea clutter and constant power function artifacts, such as bullseyes and sun strobes. There are two algorithms for sea clutter; the first one deals with evaporation duct sea clutter, and the second one deals with the more widespread and distant sea clutter due to surface, surface-based, and elevated electromagnetic ducts resulting from trapped moist air under temperature inversions often encountered off the coasts of California and the Arabian Gulf region. The algorithms are currently undergoing operational testing at FNMOC within the ship-following COAMPS-OS® radar DA system. An overview of the algorithms and

examples of their applications to SPS-48/HWDDC data will be presented.

Acknowledgements
[2]COAMPS and COAMPS-OS are registered trademarks of the Naval Research Laboratory

5.12 IF INSECTS ARE THE PASSIVE TRACERS WE WANT THEM TO BE TO ESTIMATE WINDS, WHY ARE THEY GENERALLY ALIGNED?

F. FABRY[1], V. MEUNIER[1], R. KRISHNAMOORTHY[1], A. KILAMBI[1]

[1] McGill University, Canada

frederic.fabry@mcgill.ca

Outside of the storm itself, the information provided by radar is generally limited to Doppler velocity from insect echoes. Past work have suggested that insects, particularly smaller ones, can be generally considered as passive tracers; as such, one can use their Doppler velocity as if it was a measurement of the wind.

We have just added dual-polarization capability to one of our vertically pointing radars, and one of the measurements we make is the differential reflectivity between the wave polarized in the east-west direction and that polarized in the north-south direction ("H" and "V" do not make sense when pointing vertically). While precipitation echoes are unaligned, most biological echoes in summer show a net alignment that varies with time and does not correspond with the direction of the wind. This suggests that, at least in Montreal in early August, most insects try to fly in a specific direction, and hence probably have net air speeds. If this finding is generalizable, the Doppler velocity obtained from such insects would then a biased estimate of the wind, affecting our ability to assimilate this data correctly.

5.13 A HYDROMETEORLOGICAL ANALYSIS OF AN EXTREME FLASH FLOOD EVENT IN THE URBAN AREA OF WEST ATTICA, GREECE

M. ANAGNOSTOU[1,2,5], VARLAS G.[2], J. KALOGIROS[1], P. KATSAFADOS[2], A. PAPADOPOULOS[3], E. BALTAS[4], E. ANAGNOSTOU[5]

[1] IERSD, National Observatory of Athens, Athens, Greece

[2] Department of Geography, Harokopio University of Athens, Greece

[3] Institute of Marine Biological Resources and Inland Waters, Hellenic Centre for Marine Research, Greece

[4] Department of Water Resources and Environmental Engineering, School of Civil Engineering, National Technical University of Athens, Greece

[5] Department of Civil and Environmental Engineering, School of Engineering, University of Connecticut

sifneos@live.com

Urban areas often experience high precipitation rates and heights associated with extreme flash food events. Numerical models are employed to predict these adverse phenomena. Nevertheless, flood prediction in urban areas is still an open scientific issue and remains a challenge. A sophisticated approach is the combination of atmospheric-hydrological modeling methods with surface precipitation observations. This approach is becoming more attractive to the scientific community since they are fully coupled in a single advanced observation-modelling system. This study aims to provide a hydrometeorological analysis to an extreme flash flood event took place in the sub-urban area of Mandra, Attica, Greece. A three-day (14 - 16 November 2017) wave of hazardous weather with intense precipitation rates persisted around the Mt. Pateras in the sub-urban town of Mandra, resulting to tremendous flooding with landslides, extensive damages and a total of 23 fatalities. The area is highly urbanized with complex terrain effect. This case study has been simulated by the non-hydrostatic WRF-ARW atmospheric model coupled with an advanced hydrological module (WRF-Hydro) able to offer improved simulation of land surface hydrology and energy states and fluxes at a fairly high spatial resolution using a variety of physics-based and conceptual approaches. The WRF-Hydro simulated this case study under three different precipitation forcings. The first was based on WRF-ARW hindcasts (WRF-Hydro), the second one was based on XPOL and C-Band radar estimates (XPOL-Hydro) and the third on core GMP/IMERG estimated precipitation rates (GMP/IMERG-Hydro). The initial precipitation forcings are evaluated against surface raingauge and disdrometer observations close to the area of interest. Preliminary results indicate that XPOL-Hydro outperforms the WRF-Hydro and the GMP/IMERG-Hydro in terms of water level and surface runoff estimations.

5.14 REAL-TIME RADAR DATA QUALITY FOR DATA ASSIMILATION

S. ELLIS[1], D. ALBO[1], J. SUN[1], T. WECKWERTH[1], J. HUBBERT[1]

[1] National Center for Atmospheric Research, USA

sellis@ucar.edu

A system for real-time quality control of ground-based scanning weather radars has been developed and tested. The goals for the system are real-time editing of contaminated radar data and estimation of the measurement variance, with the results being suitable for use in numerical weather prediction models without further processing. Version 1 of the Radar Quality Control System (RQCS) has been completed. The RQCS currently operates on reflectivity (Ze) and radial velocity (Vr) with plans to expand to spectrum width and the dual-polarization variables in the future.

For editing radar data, the system uses a number of different quality control indices based on parameters determined to be good indicators of data quality, e.g. signal-to-noise ratio, Ze gradients etc. The system provides edited Ze and Vr data in near real-time. The QC indices and thresholds can all be customized for different radar systems and different thresholding needs.

The measurement variance is estimated directly from the data. The first step is to remove the natural gradients in the radar data that might otherwise contribute to a spatial variance estimate. This is accomplished by subtracting a smoothed version of the data from the original data, leaving just the measurement variance in the detrended data. The filter used is a finite impulse response (FIR) filter with a designed response that removes the gate-to-gate variations. The measurement variance can then be computed from the detrended data over the user-defined spatial resolution. The results are consistent with the theoretical values of measurement variance. An advantage of this method is that, since it comes directly from the data, it accounts for all sources of variance.

These methods have been demonstrated on the NCAR S-Pol radar and several NWS NEXRAD radars using VDRAS. Improvements were shown compared to the previous VDRAS radar QC system. The methods will be described and results presented.

5.15 ASSIMILATION OF ZDR COLUMNS FOR IMPROVING THE SPINUP AND FORECAST OF CONVECTIVE STORMS IN STORM-SCALE MODELS

J. CARLIN[1,2], J. GAO[3], J. SNYDER[3], A. RYZHKOV[2]

[1] School of Meteorology, University of Oklahoma, Norman, Oklahoma, USA

[2] Cooperative Institute for Mesoscale Meteorological Studies, University of Oklahoma, Norman, Oklahoma, USA

[3] NOAA/OAR/National Severe Storms Laboratory, Norman, Oklahoma, USA

jacob.carlin@noaa.gov

A primary motivation for assimilating radar reflectivity data is the reduction of spin-up time for modeled convection. Cloud analysis techniques, which seek to induce and sustain convective updrafts by inserting temperature and moisture increments and hydrometeor mixing ratios into the model analysis from simple relations with reflectivity, are commonly used to assimilate radar into storm-scale models. Polarimetric radar data provide additional insight into the microphysical and dynamic structure of convection beyond that of reflectivity alone. Many distinct polarimetric signatures have been discovered. In particular, the radar meteorology community has known for decades that convective updrafts cause, and are typically co-located with, differential reflectivity (ZDR) columns – vertical protrusions of enhanced ZDR above the environmental 0°C level. Despite these benefits, limited work has been done thus far to assimilate dual-polarization radar data into numerical weather prediction model.

This study performs proof-of-concept experiments that explore the utility of assimilating ZDR columns to improve storm-scale model analyses and forecasts of convection for real data cases. Using the Advanced Regional Prediction System (ARPS), we modify the existing cloud analysis routine to adjust model temperature and moisture state variables in regions of detected ZDR columns as proxies for convective updrafts, and compare the resultant cycled analyses and forecasts with those from the original reflectivity-based cloud analysis formulation. Results indicate both qualitative and quantitative improvements from assimilating ZDR columns. These improvements include more coherent and fewer spurious updrafts, forecast updraft helicity swaths that better match radar-derived rotation tracks, more realistic forecast reflectivity fields, and improved equitable threat scores and reduced bias. These findings support the use of dual-polarization radar signatures to improve storm-scale model analyses and forecasts and warrant further study.

5.16 ENSEMBLE KALMAN FILTER ASSIMILATION OF SIMULATED POLARIMETRIC RADAR DATA FOR A TWO-MOMENT BULK MICROPHYSICS SCHEME: OSS EXPERIMENTS

KEFENG ZHU[1], MING XUE[1,2], KUN ZHAO[1]

[1] Key Laboratory of Mesoscale Severe Weather/Ministry of Education and School of Atmospheric Sciences, Nanjing University, Nanjing, 210093, China

[2] Center for Analysis and Prediction of Storms and School of Meteorology, University of Oklahoma 73072, United States

kefeng@nju.edu.cn

Dual polarization radar observations is the only observation that could provide three dimensional in-cloud information. The United States has already upgraded all the Doppler radar to polarimetric radar. In China, Doppler radar will also be upgraded to dual polarimetric propriety in the 13^{th} Five-Year planning. How to effectively use the dual Doppler radar data are very important to the future use of dual Doppler radar observations in the operational forecast application.

In this study, the impact of polarmetric variables including Z_{dr} and K_{dp} are examined within Advanced Regional Prediction System Ensemble Kalmar Filter (ARPSEnKF) package for a ideal super storm case. The horizontal grid spacing is 1 km. The microphysical processes are parameterized using double-moment scheme of Milbrandt and Yau. It was found that the optimal horizontal and vertical radius were 4 km and 2 km for both Z_{dr} and K_{dp}. The optimal assimilation threshold of Z_{dr} is 0.3 dB while 0.6 for K_{dp}. Both Z_{dr} and K_{dp} assimilation have reduced analysis and forecast error. The experiment with Z_{dr} assimilation performs better than that of K_{dp}. A series of experiments have also been carried out for the selection of analysis variables for Zdr and Kdp assimilation. It was found the optimal combination of analysis variables for Z_{dr} are the vertical velocity, potential temperature, water vapor, hail mixing ratio and number concentration of all species. To our surprise, the adjustment of rain mixing ratio (q_r) does not improve the forecast as expected. In turn, the upgradation of qr make the forecast worse. For K_{dp}, the upgration of all analysis variables are the best. Finally, for the assimilation of both Z_{dr} and K_{dp}, experiment with optimal analysis variables combination performs better than experiment without the selection of analysis variables.

5.17 IMPACT OF THE ASSIMILATION OF THE DUAL-POLARIZATION DOPPLER RADAR DATA FOR A CONVECTION SYSTEM USING THE 4DVAR ALGORITHM ON QUANTITATIVE PRECIPITATION NOWCASTING

SHAO-FAN CHANG[1], YU-CHIENG LIOU[1], WEI-YU CHANG[2], JUANZHEN SUN[3]

[1] Department of Atmospheric Sciences, National Central University, Taiwan
[2] Department of Atmospheric Sciences, Chinese Culture University, Taiwan
[3] National Center for Atmospheric Research, USA
shaofan.chang@gmail.com

The dual-polarization Doppler radar can provide the more accurate precipitation estimation compared with the traditional Doppler radar. In this study, the horizontal reflectivity (Z_H), specific differential phase (K_{DP}), and radial velocity (V_r) collected by two Taiwan Central Weather Bureau (CWB) operational S-band traditional Doppler radars and the S-band dual-polarization Doppler radar (S-Pol) of the National Center for Atmospheric Research (NCAR) are assimilated for a frontal convection system observed during intensive operation periods (IOP) 8 of the 2008 Southwest Monsoon Experiment (SoWMEX). The warm-rain radar forward operator for K_{DP} data assimilation is based on the observational relationship between KDP and water content from the data collected by all disdrometers during the entire period of 2008 SoWMEX. The four-dimensional Variational Doppler Radar Analysis System (VDRAS) and its 4DVAR data assimilation algorithm are used in this study. The impact of assimilating polarization data on the quantitative precipitation nowcasting (QPN) is demonstrated. The experimental results show that Z_H and K_{DP} data assimilation provides better QPN performance compared with the original Z_H-only data assimilation.

5.18 QUANTIFYING ERRORS ASSOCIATED WITH POLARIMETRIC RADAR FORWARD OPERATORS

JEFFREY C. SNYDER[1], ALEXANDER RYZHKOV[1,2], ALEXANDER KHAIN[3]

[1] NOAA/OAR National Severe Storms Laboratory: U.S.A.

[2] University of Oklahoma, Norman: U.S.A.

[3] Hebrew University of Jerusalem: Israel

jeffrey.snyder@noaa.gov

Several polarimetric radar forward operators have been developed in the past decade; these forward operators have allowed for more thorough comparisons between observations from polarimetric weather radars and output from numerical weather models. Such comparisons can facilitate the assessment of microphysics schemes and are likely to prove useful for improving data assimilation and, subsequently, model analyses and forecasts. However, current microphysics schemes do not provide the full array of information needed to accurately calculate commonly used polarimetric radar quantities (e.g., differential reflectivity and co-polar correlation coefficient), requiring that those who use the forward operator to select a priori relations or make assumptions to obtain everything necessary to calculate the radar variables. This work examines the impacts of several of the most important assumptions that must be made including hydrometeor fall behavior (e.g., canting angle distributions), water distribution in mixed-phased hydrometeors, lookup table granularity, and effective dielectric constant models in an effort to provide more robust guidance and elucidate expected errors to users of these forward operators.

5.19THE IMPORTANCE OF ASSIMILATING THERMODYNAMIC FIELDS WITH RADAR OBSERVATIONS IN CONVECTIVE-SCALE WEATHER SYSTEMS

CHING-YIN KE[1], KAO-SHEN CHUNG[1]

[1] Department of Atmospheric Sciences, National Central University, Zhongli, Taiwan
cyke812@g.ncu.edu.tw

At convective scale, the evolution of severe weather is rapid and nonlinear. Radar observations have been assimilated to improve the quantitative precipitation forecast at the convective scale, and many studies have shown the positive impact of it. By using the Ensemble Kalman filter system and conducting observing system simulation experiments (OSSEs), this study investigates the importance of assimilating three dimensional thermodynamic variables with radar data. A case study of frontal system with extremely heavy rainfall on 11 June 2012 is selected. The results show that: 1) assimilating temperature and humidity fields are more important in the stratiform area than in the convective region; 2) with less cycling process, the position error of precipitation can be corrected, and extend the performance of the short-term forecast.

5.20 COMPARISON OF EXTREME PRECIPITATION EVENTS SIMULATED BY THE NWP MODEL COSMO WITH ADJUSTED WEATHER RADAR DATA IN A HIGH TEMPORAL RESOLUTION

V. BLIŽŇÁK[1], P. ZACHAROV[1], M. KAŠPAR[1], M. MÜLLER[1,2]

[1] Institute of Atmospheric Physics CAS, Department of Meteorology, Prague, Czech Republic

[2] Charles University in Prague, Faculty of Science, Department of Physical Geography and Geoecology, Prague, Czech Republic

bliznak@ufa.cas.cz

Extreme precipitation events (EPEs) belong to the most studied natural hazards because of their extra high impacts on the human society. However, quantitative precipitation estimates based on weather radar data with a high temporal and spatial resolution along with a sufficient level of accuracy is available for the last several years only and is completely missing for historical EPEs. On the other hand, quantitative precipitation forecast produced by high-resolution numerical weather prediction (NWP) models can be considered as a competitive tool to obtain information about temporal course of historical EPEs. Nevertheless, their main disadvantage is a limited accuracy of generated forecasts coming from initial and boundary conditions as well as due to the large spatial and temporal variability of precipitation systems. The contribution will present a new correction procedure that improves an accuracy of raw NWP model forecasts in a 10-min temporal step. The procedure first adjusts model precipitation sum by daily rain gauge measurements and then correct a localization of 10-min precipitation totals based on the highest correlation coefficient between the model and observed precipitation sums. The selected EPEs that occurred over the Czech Republic between 2002 and 2013 will be simulated by the non-hydrostatic NWP model COSMO with a spatial resolution of 2.8 km and temporal step of 10-minutes. A corrected and raw precipitation forecasts will be compared and objectively verified with adjusted weather radar data. The adjustment procedure combines radar reflectivity at 2 km (CAPPI 2 km) interpolated from two adjacent radar beams and daily rain gauge measurements collected from the whole territory of the Czech Republic. The verification will be performed using classical (e.g., correlation coefficient) as well as spatial (e.g., Fractions Skill Score) verification scores.

5.21 SOLAR ENERGY PERSPECTIVE ON THE DATA ASSIMILATION OF RADAR REFLECTIVITY IN A LIMITED AREA NWP MODEL

TUULI PERTTULA[1], SAMI NIEMELÄ[1], ANDERS LINDFORS[1], ELENA SALTIKOFF[1]

[1] Finnish Meteorological Institute, Finland
tuuli.perttula@fmi.fi

Traditionally radar reflectivity observations have been used for getting information about precipitation. Thus, in the context of renewable energy the main users of radar reflectivity data have been water power companies. However, as the data assimilation of radar reflectivity data has an impact on cloudiness inside the NWP model through the humidity information, it also affects the forecast solar radiation and therefore might be of interest also for the solar energy sector.

In our work the radar reflectivity data was assimilated into the HARMONIE (ALADIN-HIRLAM) limited area numerical weather prediction (NWP) model to study its impact on solar radiation forecasts. The Harmonie-AROME configuration of the model was used (Bengtsson et al. 2017). Radar reflectivities were assimilated using indirect 1D+3D-Var assimilation method (Wattrelot et al. 2014) in which vertical humidity profiles are first retrieved using 1D Bayesian method and are then assimilated inside the 3D-Var data assimilation system.

Our HARMONIE model domain covers Finland, Scandinavia and the Baltic countries. The assimilated radar data were quality-controlled full-volume scans of radar reflectivity from Finland, Sweden, Norway and Denmark. We ran two one-month-long HARMONIE model experiments for July 2016 to study the impact of assimilation of radar reflectivity data: one experiment in which both radar reflectivity data and in-situ observations were assimilated and a control run with only in-situ observations assimilated. Verification scores against SYNOP and radiosonde observations were calculated and studied for both experiments. Assimilated radar reflectivity observations and their impact on the analysis were also monitored. Additionally, to study the impact of radar reflectivity assimilation specifically from the point of view of solar energy we compared the forecast global radiation against observations from 26 stations of the Finnish solar radiation monitoring network.

Verification against radiosonde observations showed that the radar reflectivity data had a slightly positive impact on the specific humidity between 300 hPa and 700 hPa. There was a slight negative impact on temperature between 200 hPa and 700 hPa. Other studied parameters in verification against SYNOP and radiosonde observations showed mainly neutral impact from data assimilation of radar reflectivity observations. These results are in line with earlier studies.

Comparison against global radiation observations showed positive impact from data assimilation of radar reflectivity at some stations, which looks promising. However, at some stations the impact was negative. We would next like to look more into reasons on why global radiation is sometimes well forecast and sometimes not and why the impact of radar reflectivity assimilation varies.

References

Bengtsson, L., and Coauthors, 2017: The HARMONIEAROME model configuration in the ALADINHIRLAM NWP system. Mon. Wea. Rev., 145, 19191935.

Wattrelot, E., O. Caumont, and J.-F. Mahfouf, 2014: Operational Implementation of the 1D+3D-Var Assimilation Method of Radar Reflectivity in the AROME Model. Monthly Weather Review. Vol. 142. 1852-1873.

5.22 EVALUATION OF HEAVY RAINFALL EVENTS IN THE PERUVIAN ANDES USING WRF MODEL AND WEATHER RADAR

Y. SAAVEDRA[1], Y. SILVA[1], A. MOYA[1]

[1] Instituto Geofísico del Perú (IGP), Lima, Perú

fsilva@igp.gob.pe

The Weather Research and Forecast model (WRF) was implemented in the Geophysical Institute of Peru in operational mode in order to evaluate its capacity to predict heavy rainfall events in the Peruvian Andes. The study is focused in the Rimac river basin, one of the more important basin for water resources for Lima, the city capital, as well as for the risk management related to landslides and avalanche during the rainy season.

The WRF was run in 3 domains (18, 6 and 2 km). In this paper we present the event occurred February 15 and 16, 2018. To validate the model, precipitation data of eight surface stations was used, as well as precipitation data obtained from PX1000 polarimetric weather radar and the band-14 from GOES 16 images were used. Statistical parameters (RSME, BIAS and correlation coefficient) and a qualitative comparison for the spatial distribution of precipitation were used.

Preliminary analysis showed that the WRF′s peak of precipitation occurred three three hours early than observed. The best correlation is observed in the middle part of the basin. Precipitation is overestimated with a bias of 0.10 mm / h and an RSME of 1.34 mm / h in average. The model has a good performance to predict the event achieved the spatial distribution similar then observed by the weather radar and GOES, reproducing the main characteristics of the precipitation in the middle part of the basin, near the city of Lima.

Session 6. Radar calibration and monitoring



Keynote presentation

6.1 MODELING DIFFERENTIAL REFLECTIVITY BIAS DUE TO ANTENNA TOPOLOGY AND OPERATING FREQUENCY

J. HUBBERT[1], C. CAPPELLIN[2], U. ROMATSCHKE[1], R. JØRGENSEN[2], M.J. DIXON[1]

[1] National Center for Atmospheric Research, Boulder, CO
[2] TICRA Corp. Copenhagen, Denmark
hubbert@ucar.edu

Differential reflectivity (Z_{dr}) calibration for weather radars is an ongoing area of research. An accurate estimation of the Z_{dr} bias is important for both quantitative and qualitative interpretation of Z_{dr}. It has recently been shown that the Z_{dr} bias is a function of the ambient temperature at the radar site (Hubbert, 2017, JTECH), and data shows that it is due to the antenna system. The specific nature of the temperature dependent bias is not well understood. Numerical modeling of the NCAR's S-Pol (S-band Dual Polarimetric Radar) is carried out in an attempt to better understand of the factors affecting Z_{dr} bias such as the antenna support struts, waveguide attached to the support struts, frequency of operation and location of the phase center of the feed horn. TICRA's GRASP software is used to model the antenna. Modeling results and experimental data are presented to illustrate the concepts.

6.2 MONITORING OF THE NEXRAD NETWORK USING SOLAR SIGNALS

I. HOLLEMAN[1], A. HUUSKONEN[2]

[1] Radboud University, Faculty of Science, Nijmegen, Netherlands
[2] Finnish Meteorological Institute, Helsinki, Finland
iwan.holleman@ru.nl

During the past decade we have developed and characterized a method for using solar signals for monitoring operational weather radars and networks thereof. The method relies on signals resulting from occasional solar interferences in the radar antenna during operational scanning. There is no need for dedicated radar scans or interruption of the operational scanning. In a series of publications we have shown that the solar method can reliably be used to determine the antenna pointing, identify signal processor issues, keep track of receiver chain stability and calibration, and monitor the balance between horizontal and vertical polarization receiver chains. The solar method has already been taken into use by numerous national weather services in Europe, Canada, Australia and South Africa, and its operational use has proven to be highly effective in reducing radar downtimes, in focussing maintenance activities, and in keeping radars calibrated.

NEXRAD is the homogenous network of 160 high-resolution S-band weather radars operated by the National Weather Service in the USA. Volumetric data (level II) from this network are available online and this makes NEXRAD ideal for demonstrating the application of our solar method on a continental-scale radar network. The level-II data contain for each radial a noise power estimate and when a scanning radar antenna hits the sun the observed noise power will be higher. Our decoding software extracts the radial-based noise power estimates for the horizontal and vertical receiver channels (converted to solar flux units) and relevant metadata, such as the azimuth, elevation, observation time and radar location. Furthermore, we have optimized our solar modelling method for analysing the NEXRAD noise power data.

Here we present the first results from the application of our solar method on a continental-scale radar network. The results demonstrate that the solar method can provide great benefits for monitoring and harmonizing national and transnational operational radar networks.

6.3 MONITORING DOPPLER DUAL-POLARIZATION RADAR USING AN INDIVIDUAL AND SINGULAR GROUND CLUTTER CELL

M. GABELLA[1], F. VAN DEN HEUVEL[1,2]

[1] MeteoSwiss, Locarno Monti, Switzerland

[2] École Polytechnique Fédérale de Lausanne, Switzerland

marco.gabella@meteoswiss.ch

"Bright" scatterer are useful for monitoring modern Doppler and dual-polarization weather radars: in order to be "Bright", a target should have a large radar cross section, be located in the radar near range and hit by the antenna beam axis. In this note, a statistical analysis based on data of seven clear sky days (2016 samples with spatial resolution of $1^\circ \times 1^\circ \times$ 83.33 m) of one of the "Bright" scatterers in Switzerland is presented. It is a metallic tower located at Cimetta, at 18 km range and the same altitude as the Monte Lema radar. Its spectral (Doppler) and polarimetric signatures are impressive: the 2nd Doppler moment (spectrum width) is perfectly stable (always the same, lowest-allowed, Digital Number). The 1st Doppler moment (mean radial velocity) is very stable: only two Digital Numbers, out of 255 possible values, are found within the $314 \times 314 \times 83.33$ m^3 radar cell that contains the bright scatterer; as expected, one value corresponds to zero radial velocity (the other value corresponds to quasi zero velocity). The 0th Doppler moment (radar reflectivity) is also quite stable, with vertical (V) polarization being more variable (the Log-transformed ratio between the 90th percentile and the mean, $90\xi\mu$, is typically $\sim$1.5 dB) than the horizontal (H) polarization ($90\xi\mu \sim$1 dB). Regarding the polarimetric information, the daily average of the differential reflectivity is positive (slightly larger than +1 dB) and also stable (standard deviation smaller than 1 dB). The co-polar correlation coefficient between H and V is remarkably large (0.9963, on average) and stable: the (MAX) min daily difference between the 90 percentile and the mean is as small as (0.0030) 0.0010. The daily standard deviation of the differential phase shift is typically 5° (910 Digital Numbers out of 65536). In addition to characterizing the polarimetric properties of this monitoring-oriented, target using classical descriptive statistics, we are currently investigating them using Fourier analysis and the power spectrum. Detailed results will be presented at the conference; as an example, the H and V reflectivity values are found to follow the variability of Fractional Brownian Motion signals: they are characterized by a slope of the power spectrum exponent $\beta \approx 1.4(\pm 0.3)$, which would correspond to a fractal dimension of 1.8. It is then argued that these peculiar and stable ground clutter signals can be used to monitor and check the quality of operational dual-polarization weather radars.

6.4 OPERATIONAL SOLAR MONITORING FOR IMPROVING THE HOMOGENEITY OF THE EUROPEAN RADAR NETWORK

A.HUUSKONEN[1], G. HAASE[2], D. MICHELSON[3], H. LEIJNSE[4], I. HOLLEMAN[5], M. PROBERT[6], R. GILL[7], M. FRECH[8], M. KURRI[1], H. HOHTI[1]

[1] Finnish Meteorological Institute, Finland
[2] Swedish Meteorological and Hydrological Institute, Sweden
[3] Environment and Climate Change Canada, Canada
[4] Royal Netherlands Meteorological Institute, Netherlands
[5] Radboud University, Faculty of Science, Nijmegen, Netherlands
[6] UK Met. Office, United Kingdom
[7] Danish Meteorological Institute, Denmark
[8] German Meteorological Service, Germany
asko.huuskonen@fmi.fi

Online solar monitoring is an efficient method for monitoring antenna pointing, receiver stability, the balance between the polarization channels and several other properties of a weather radar. The method uses solar interferences observed during operational radar measurements and hence requires neither stopping of measurements nor dedicated measurement tasks. The solar method has already been taken into use by numerous national weather services in Europe, Canada, Australia and South Africa, and its operational use has proven to be highly effective in reducing radar downtimes, in focussing maintenance activities, and in keeping radars calibrated.

Since 2017 OPERA, the weather radar project of Eumetnet, has provided solar monitoring services to its members. The solar hit detection is done at the Eumetnet OPERA Data Centre, Odyssey, which collects volume data from 160 radars and produces a European wide composite at every 15 minutes. During the pre-processing of data, solar hits are detected and stored to files. Analysis of the solar hit files is performed at the Finnish Meteorological Institute, at present on a monthly basis.

The OPERA radar network is not homogeneous; the radar types, properties, and operation modes vary a lot. Hence the amount of solar hits detected daily varies from a few hits to about 100 solar hits daily. Some radars provide sufficient number of observations for a daily analysis and we obtain a full set of results (solar flux, antenna biases, and widths); in some cases solar hits need to be collected for up to one month before results are obtained and we only can provide an estimate for the antenna pointing biases. At present, we are able to get monthly pointing results from close to 90 radars, and results on pointing and solar flux from about 60 radars. In some cases the solar fluxes are still on an arbitrary scale, because all required metadata (e.g. radar constant, receiver band width) are not supplied with the data.

Here we show results of the work and discuss the benefits of the monitoring for improving homogeneity of the network and the quality of the continental scale composites.

6.5 THE STATISTICAL DISTRIBUTION OF ZDR IN DRY SNOW, WITH IMPLICATIONS FOR ZDR CALIBRATION

M.J. DIXON[1], J.C. HUBBERT[1], G. MEYMARIS[1]

[1] National Center for Atmospheric Research, Boulder, Colorado, USA
dixon@ucar.edu

Z_{DR} is an important quantity for the identification of hydrometeor type, and for the estimation of precipitation rate. For these purposes it is important that Z_{DR} be accurate, i.e. that the radar be well calibrated with respect to Z_{DR}. Prior work has shown that the statistical distribution of Z_{DR} in dry snow varies with meteorological regime, showing differences between mid-latitude continental situations and tropical maritime regimes. Furthermore, prior work and theory indicate that Z_{DR}, as measured by the radar, varies with elevation angle because the shape of the particle as seen by the radar varies. We study Z_{DR} in dry snow, using S-band radars, to investigate the statistical properties of the Z_{DR} distribution. This allows for a quantitative approach not only with respect to the mean of Z_{DR}, but the spread and skewness of the distribution as well. Using this approach we can summarize the Z_{DR} properties in snow for different regimes and elevation angles. This quantitative description of the Z_{DR} distribution is interesting on its own, but will also allow for improvements in the use of observations in the routine monitoring of Z_{DR} calibration for operational radars.

6.6 ASSESSING ZDR VARIABILTY USING DEDICATED SOLAR BOX SCANS AND OPERATIONAL ZDR MONITORING RESULTS

MICHAEL FRECH[1], J.C. HUBBERT[2]

[1] German Meteorological Service, Germany
[2] National Center for Atmospheric Research, USA
michal.frech@dwd.de

The calibration of differential reflectivity Z_{DR} with a target accuracy of 0.2 dB is a challenging task especially for operational weather radar networks. In recent years, end-to-end methods have been developed and implemented to monitor and adjust automatically Z_{DR} within the DWD (German Meteorological Service) polarimetric weather radar network. Monitoring and adjustment of ZDR is based on a combination of sources that characterize the differential imbalance of the transmit and receive path. At DWD, the primary source of the diurnal calibration of Z_{DR} is the birdbath scan. In addition, solar hits extracted from operational scanning are used to monitor the Z_{DR} of the receive path and the positioning accuracy of the radar system. On average this approach appears to capture most of the Z_{DR} variability. However, we have observed a dependency of Z_{DR} on temperature which has not been fully understood. A comprehensive investigation using NCAR's S-Pol research radar suggests that the observed temperature dependence may be related to thermal expansion of the antenna assembly. There, solar box scans proved to be one effective source to systematically separate out the sources of ZDR variability (Hubbert, 2017). DWD polarimetric radar systems (EEC DWSR5001SDP/CE)) up to now do not have the same capabilities as the research system at NCAR. However, using DWD's Hohenpeienberg research radar (which is identical to the radars in the network), we systematically employ solar box scans in order to better understand the observed variability within the DWD radar network. To this end over 800 solar box scans have been carried in 2017/18. Typically, consecutive solar box scans were carried throughout the day every 5 minutes. The resulting pseudo ZDR antenna patterns match very well with antenna pattern taken during the site acceptance in 2011. The peak power solar beams are about 30 dB above noise. Contrary to S-Pol, our system has an air-conditioned (AC) radome. Thus the AC was used to control the temperature environment for the antenna receiver assembly. We find up 0.2 dB variation in Z_{DR} over a temperature range of 20 K. With those measurements we show that the azimuthal Z_{DR} variability introduced by the radome appears negligible (the radome manufacturer claimed $<$0.005 dB, which is a number based on simulations). Also, using the solar box scans, we demonstrate a Z_{DR} 0.1 dB bias introduced by lightning protection. The solar box scans are compared to the operational Z_{DR} monitoring measurements from the operational solar hit analysis and the birdbath scan. These measurements are also effective for assessing the attitude of the pedestal / antenna assembly. Furthermore, those measurements can be used to assess the azimuth bias as a function solar azimuth angle, which directly relates to the condition of the azimuth drive.

6.7 WEATHER RADARS AND RADIO FREQUENCY INTERFERENCES

M. VACCARONO[1,2], V. CHANDRASEKAR[1], R. BECHINI[3], R. CREMONINI[3]

[1] Colorado State University, Fort Collins, USA

[2] Arpa Piemonte, Dipartimento Tematico Radiazioni, Via Jervis 13, Ivrea

[3] Arpa Piemonte, Dipartimento Sistemi Previsionali, Via Pio VII 9, Torino

mvaccar@colostate.edu

Radio frequency interferences are affecting weather radars around the world and this problem is becoming increasingly more frequent. In Europe, the major radar networks are in the C band and they share the frequency band with other telecommunication systems such as Radio Local Area Network and Hyper-LAN access points for broadband internet communications. Through collaborative experiments and identifying the SSIDs we were able to determine the source of the interference as Hyper-LAN access points. This paper will present the results from these experiments.

It appears that the coexistence of weather radars and telecommunication systems is increasingly causing more cross contamination, not only by frequency-sharing radio sources but also by antennas working in frequency bands far from the radar operating frequency. This is especially true for the case of X-band weather radars. In fact, since a couple of years, the X-band radar managed by Arpa Piemonte is experiencing increasing occurrence of interferences, which is starting to impact on the radar measurements. Therefore, we have made that into a pilot study platform for interferences.

The analysis of the interferences received during the month of October 2017 showed a daily pattern, with interferences detected mostly between 7am and midnight local time. This typical pattern seems related to out-of-band emissions of some transmitting towers, since no other civil communications are allowed in the X-band. In particular, the analysis focused on a possible relation with the 4G mobile communications working in the 1.8GHz band, which could give out-of-band emissions exactly at the X-band radar operating frequency (9.37 GHz). Comparing the transmitting towers locations available in the regional database of electromagnetic sources managed by Arpa Piemonte with the directions of the interferences received by the X-band radar, it is likely that the radio frequency interferences are caused by mobile telecommunication transmitting towers. Furthermore, those transmitting tower do not operate the 1.8 GHz 4G systems from midnight to 6am to reduce power consumption unless the other 4G carriers, such as 0.8GHz and 2.6GHz, cannot handle the mobile communications in the coverage area. This hypothesis is currently being verified with in-field measurement, to assess a possible relation with the 4G mobile communications working in the 1.8GHz band. Given the increasing number of X-band radars deployed in Europe, Asia and the United States, such as the Dallas Fort Worth X-band radar network, the coexistence of the these smaller radars with telecommunications system is an important task and is the main focus of this work.

In addition, Arpa Piemonte and Colorado State University are developing techniques to identify the radio frequency interferences sources, using the regional database of electromagnetic sources, and with in-field measurements. Based on this we are in the process of developing mitigating solutions. This paper will present quantitative

analysis of the interference strength direction and long-term variability. A map of the 1.8 GHz band towers along with simple models for interference zones will be presented. In addition, preliminary results for cooperative experiments to positively identify the major source of interference at X band will also be presented.

6.8 THE OPERATIONAL REALITY OF WEATHER RADARS WORLDWIDE A TRAVEL REPORT

H. AL SAKKA[1], J. DIDSZUN[1], A. WEIPERT[1]

[1] Meteorological Information Systems Department, Selex ES GmbH, Neuss Germany
h.alsakka@selex-es-gmbh.com

Weather radar has become an essential tool for meteorological real time monitoring and studying, nowcasting, forecasting and modeling. However, a discrepancy exists between the detailed ongoing research in this area and the operational reality of weather radar data processing and usage world-wide.

The paper presents a résumé and sharing experience after three years of traveling between six continents, training and working with local users on weather radars (operators, forecasters, hydrologists, and scientists). It is a collection of the main usage and problems of the end users′ daily work. It wraps up their current and future needs and uses from their perspective.

Despite major enhancements in the radar technology and data processing chain, there are still some gaps between research and development and the final operational usage of the weather radar data. Different problems persist: attenuation, quality control standards, interference (between radars or from other devices like Wifi, data links, etc.), anomalous propagation, the type and the quantification of the precipitation, compositing (especially with heterogeneous radars), and other hardware and software problems. Although most of these problems are tackled by research in one or other way, for some problems practical solutions are still rare and some are not reflected in research as it should be regarding their effect on the operational data quality.

In other words, this paper reflects the reality of the usage of weather radars worldwide, it shows the advantages, the inconveniences, the limitations of the weather radars, and what the end users are expecting from the scientific community.

6.9 WIND TURBINES SEEN IN RADAR DATA WITH THE BIG DIFFERENCE METHOD

WILLI SCHMID[1], STEFAN MÜLLER[2]

[1] meteoradar gmbh, Rbacher 4, 8143 Stallikon, Switzerland
[2] Meteotest AG, Fabrikstrasse 14, 3012 Bern, Switzerland
schmid@meteoradar.ch

Erroneous radar measurements due to wind turbines are easily seen by eye in radar images. In order to identify these errors quantitatively, we evaluate the differences between two plan position indicator (PPI) scans taken at two adjacent elevation angles. Big differences ("BD" hereafter) in radar reflectivity (dBZ) and Doppler velocity (m/s) are attributed to wind turbines, affecting the radar data on either one or both elevation angles. The range of radar reflectivity considered for this study starts at 5 dBZ, hence neglecting the highly random behaviour of weaker reflectivities. The BD-method works best close to the radar (when the vertical distance between the neighboring elevation angles is small), well below the melting layer (when the radar values remain quasi-constant in the vertical), and when the advection effects caused by fast echo motions and large horizontal gradients in the radar patterns are negligible.

The BD-method is used to assess the size of the volumes around wind turbines that may contain erroneous radar data. We evaluate a 9-hour data set of the DWD-radar at Trkheim, Germany. The data passed the filtering by the radar processor, but did not pass any post-processing to correct erroneous data. The data cover a period with dry weather and heavy thunderstorms followed by stratiform precipitation. The size of the radar pixels is 1 km in range and 1 degree in azimuth. We investigate three wind parks which are in a distance of 2.5, 5 and 7 km from the radar. We define an "influencing volume" ("IV") and a "neighboring volume" ("NV" hereafter). The IV of a single wind turbine is composed of two radar pixels in range, and three radar pixels in azimuthal direction. The NV is composed of two adjacent rows of pixels on the left, back and right side of the IV, seen from the radar site.

We found that the effects of the wind turbines producing BD are restricted to the IV of the wind parks at 5 and 7 km distance from the radar. In the NV, the number of the BD is almost zero, as also far away from the wind parks. Some few BD are still present in the NV of the closest wind park (2.5 km distance to the radar). Inside the IV, the number of the BD decreases with increasing average rainfall intensity. These properties of the BD facilitate the identification and correction of the radar data affected by wind turbines.

6.10 ENHANCING THE CONSISTENCY OF SPACEBORNE AND GROUND-BASED RADAR COMPARISONS BY USING QUALITY FILTERS

I. CRISOLOGO[1], R. WARREN[2], K. MÜHLBAUER[3], M. HEISTERMANN[1]

[1] Institute of Earth and Environmental Sciences, University of Potsdam, Germany
[2] School of Earth, Atmosphere and Environment, Monash University, Australia
[3] Meteorological Institute, University of Bonn, Germany
crisologo@uni-potsdam.de

Coinciding monsoon and typhoon seasons in the Philippines cause torrential rainfall, and associated hazards such as flooding and landslides. While early warning systems require accurate radar-based rainfall estimates, low-density rain gauge networks in the Philippines make it challenging to monitor the calibration of the ground-based radars (GRs). As an alternative, we explore the potential of spaceborne radar (SR) observations from the Ku-band precipitation radars on board the TRMM and GPM satellites as a reference to quantify the calibration bias of an S-band GR in the Philippines. To this end, the 3-D volume-matching algorithm proposed by Schwaller and Morris (2009) is implemented and applied to five years (2012-2016) of observations. We further extend the procedure by a framework to take into account the data quality of each ground radar bin. Through these methods, we are able to assign a quality index to each matching SR-GR volume, and thus compute the GR calibration bias as a quality-weighted average of reflectivity differences in any sample of matching GR-SR volumes. We exemplify the idea of quality-weighted averaging by using the beam blockage fraction as a basis of a quality index. As a result, we can increase the consistency of SR and GR observations, and thus the precision of calibration bias estimates. The remaining scatter between GR and SR reflectivity, as well as the variability of bias estimates between overpass events indicate, however, that other error sources are not yet fully addressed. Still, our study provides a framework to introduce any other quality variables that are considered relevant in a specific context.

6.11 IMPACT OF A WET RADOME ON A DUAL-POLARIZED S-BAND WEATHER RADAR PERFORMANCE

Alessio Mancini[1,2], Jorge L. Salazar[1,2]
[1] Advanced Radar Research Center (ARRC)
[2] University of Oklahoma, United States
amancini@ou.edu

This paper presents a new test procedure to characterize and asset the impact of a wet radome in S-band on the performance of a dualpolarized weather radar system. An analytical model was developed to evaluate the water distribution under various formations (droplets, rivulets or continuous film). For the scenario where water distributes as droplets, the model computes the drop-size distribution (DSD) on a flat radome, at different tilting angles, at various rain rates. Based on the hydrophobic property of the outer skin of the radome and tilting angle, different droplet distributions occur. Based on these configurations, the level of absorption, attenuation, and depolarization introduced by the droplets formation was calculated. As a second part, laboratory experiments were performed to characterize, both in dry and wet conditions, a panel of an S-band radome to validate the model created. The characterization was based on a new method to measure the reflections generated at the radome-air interface by using a single probe connected to mono-port reflectometer. The Time Domain Gating (TDG) algorithm, implemented in the reflectometer, was imperative to minimize the amount of reflections generated from the rest of the environment and therefore, improve the measurement quality. The attenuation of the dry radome can be computed indirectly from the measurement of the reflections. This is possible because the absorption of a dry radome is negligible. In case of a wet radome, the level of absorption is estimated as a function of the rain rate, with the algorithm earlier described. Once that the absorption is known, the attenuation of the wet radome is obtained. Measured results show good agreement both with the results derived analytically and numerical simulations, proving the validity of the model and the approach proposed.

6.12 UAV-AIDED WEATHER RADAR CALIBRATION

J.YIN[1], F.VAN DER ZWAN[1], E.OUDEJANS[1], P.HOOGEBOOM[1], C.UNAL[1], H.RUSSCHENBERG[1]

[1] Delft University of Technology, the Netherlands
j.yin@tudelft.nl

Weather radar is well recognized as an effective sensor for obtaining the microphysical and dynamical properties of precipitation at high spatial and temporal resolution. Radar calibration is one of the most important prerequisites for achieving accurate observations. Current calibration methods either use a metal sphere hanging underneath a tethered balloon or a trihedral corner reflector locating on the top of a tower or mast. However, there are some problems with these methods: (1) They are location bound. The calibrator should be placed in the far-field, which seems impossible for some radars located on the top of high buildings or towers. (2) It is relatively costly for tower setup or helium balloon purchase. (3) It is not easy to repeat the calibration process for mobile radars, especially for some fieldwork campaigns in complex terrain. (4) For vertically pointing cloud radars, the current methods cannot be used to calibrate them. Therefore we propose a portable, cost-effective and repeatable solution to replace the current calibration techniques.

An industrial-grade UAV serves as the stable aerial platform carrying a metal sphere, flying over the radar illumination areas to complete the calibration process. The flying routine of the UAV can be pre-programmed, thus the antenna pattern may be obtained. To retrieve the position of the sphere, the real-time single-frequency Precise Point Positioning (PPP) type GNSS solution is developed. Both receiver, microcontroller and antenna are mounted inside one GPS box which is placed underneath the metal sphere. With the GPS coordinates obtained from the UAV and GPS box, the position of the sphere is derived. Note that the connecting lines between the UAV and metal sphere and between the metal sphere and GPS box should be long enough to separate each other backscattering. The radar constant is calculated in the range-Doppler domain, and only the data where metal sphere separates from the clutter and other objects are selected. In addition, the spectral-polarimetric features are studied to further verify the recognition of metal sphere. The S-band polarimetric Doppler Transportable Atmospheric Radar (TARA) is used in the calibration campaign. The results demonstrate the following results: 1) alignment calibration can be completed; 2) antenna pattern can be retrieved and weather radar equation can be more accurately defined; 3) differential reflectivity can also be calibrated.

6.13 CENTER FOR CLOUD REMOTE SENSING: DOPPLER CLOUD RADAR CALIBRATION CAMPAIGN

F. TOLEDO[1], J. YIN[2], J. DELANOË[3], J-C. DUPONT[4], M. HAEFFELIN[5], H. RUSSCHENBERG[2]

[1] Laboratoire deétéorologie Dynamique/IPSL, École Polytechnique, Université Paris-Saclay, 91128 Palaiseau, France

[2] Delft University of Technology, The Netherlands

[3] Laboratoire Atmosphères, Milieux, Observations Spatiales/UVSQ/CNRS/UPMC, 78280 Guyancourt, France

[4] Institut Pierre-Simon Laplace, École Polytechnique, UVSQ, Université Paris-Saclay, 91128 Palaiseau, France

[5] Institut Pierre-Simon Laplace, École Polytechnique, CNRS, Université Paris-Saclay, 91128 Palaiseau, France

ftoledo@lmd.polytechnique.fr

Doppler Cloud Radars (DCR) have proven to be very useful tools for cloud research, enabling remote retrieval of internal properties and structure of clouds, fog and rain, as well as wind speed. However, up to now, replicable and reliable DCR calibration methods are not commonly available or implemented. Several solutions have been proposed, but they are difficult to generalize due to the particularities of the operating fields. The wide range of DCR hardware, including microwave technologies, antenna types and operating frequency is an important contributor to this complexity. However, scientific applications of these instruments for fog and cloud studies require a reliable calibration method with a well-characterized uncertainty, to ensure the quality and consistency of data between different DCRs. This is a critical issue, as already more than 15 DCRs are currently operating at ACTRIS atmospheric observatories, in Europe alone, a number that is likely to grow.

Research calibration campaigns are performed periodically at the SIRTA atmospheric observatory, located in Palaiseau, France, with the objective of developing a set of standards for DCR calibration. These standard calibration methods will then be implemented by the Center for Cloud REmote Sensing (CCRES) of the ACTRIS research infrastructure. The objectives of the CCRES is to improve the measurement quality of the Cloud remote sensing observatories in Europe, guaranteeing homogeneity to boost meteorological research.

In this work we present the campaign carried out at SIRTA in November of 2017. It consisted of experiments using calibration targets either fixed on the top of a mast or flown by an unmanned aerial vehicle (UAV), following a new method proposed by the Atmospheric Remote Sensing Group of TU-Delft, who is also part of the CCRES. Additionally, calibration transfer using natural targets (such as clouds) was studied using two 95 GHz DCRs: a vertically pointing fixed BASTA radar and a BASTA-Mini, with scanning capabilities and easy mobility.

We will present calibration methods that can be used for DCRs with scanning capabilities, and methods adapted for fixed zenith pointing DCRs. Calibration values, and their distributions, derived from the different methods will be presented. The following topics will be discussed: (1) impact of atmospheric conditions on calibration; (2) repeatability of the different methods under various meteorological

conditions; (3) advantages and disadvantages of target calibration on fixed mast; (4) advantages and disadvantages of targets flown on a UAV and proposed further developments; (5) applicability of the methods to DCR networks. Future calibration experiments to improve calibration methods will also be presented.

6.14 COMBINING WEATHER RADAR SYSTEMS TO IMPROVE REAL TIME RAINFALL ESTIMATION FOR URBAN FLOOD MONITORING AND PREDICTION

GEOFF AUSTIN[1,3], LUKE SUTHERLAND-STACEY[1], JOHN NICOL[1], ANDREW COFFIN[1], KEN WILLIAMS[2]

[1] Weatherradar.co.nz, New Zealand
[2] Auckland Council, New Zealand
[3] University of Auckland, New Zealand
geoff@weatherradar.co.nz

Weather radar base moments including especially polarimetric moments are used for classification The occurrence of high rainfall in Auckland, New Zealand sometimes leads to urban flooding events and waste water treatment problems. Auckland is a challenging city from a stormwater management perspective, as the urban area is rather large but sparsely developed, having a population of some 1.5million spread over 1000 km^2. Our research is directed to improving the real-time estimation of rainfall over cities and to produce immediate Average Return Interval (ARI) maps and forecasts using radar nowcasting in support of Auckland City's stormwater and wastewater management.

The existing national C-band radar network, operated by the NZMet Service, is currently processed operationally for Auckland Council to generate accumulation maps using a fixed Z-R relationship. The nearest radar the central business district of Auckland City is some 70 km distant and partly beam blocked, adversely contributing to the quality of the real time rainfall data. Gauge calibration, while effective at generating unbiased accumulation maps, has proved problematic in real-time as some of the gauge data can take longer than 1 hour to be available and sometimes fails to be reported completely. The gauge adjusted radar data is therefore not useful for understanding unfolding urban flooding, or indeed as input to nowcasting.

To address this situation, the city has tested using a vertically pointing Doppler radar (MRR-2 Metek GmbH), calibrated with tipping bucket rain gauge(s) setup and maintained to WMO standards, at a location 30 km from the C-band radar (in the direction of the City). From the 1+ year dataset we determined that the Auckland C-band radar has a bias of -3.1dBZ and identified a climatological of Z-R relationship of Z=250R1.4, rather than the operational 200R1.6 assumed in the network. We also found that using the VPR in real time we could successfully diagnose significant C Band radar radome wetting attenuation events.

Applying the experimentally determined Z-R climatology or real-time Z-R, along with correcting for the reflectivity biases, resulted in operationally useful skill, with negligible lag, for detection and alarming of short-duration, high intensity events exceeding 5, 10 and 20 year ARI thresholds over the northern and central parts of the city. The well know range related limitations of C-band radars tend to negate improvements at longer range over the southern part of the region.

Even with the careful calibration of the C-band radar, range effects degrade results in South Auckland. For some time we have been using two small X band

radars to give high space time resolution rainfall information in regions not well served by the C band system. We have reported on these results earlier but we are now attempting to combine all three radar systems to give a better real time estimate of the operationally significant urban rainfall events in Auckland.

The real-time VPR corrected accumulation maps will be ingested into the STEPS nowcasting model. For the real-time rainfall estimation and nowcasting of extreme events we have found that the well-calibrated combined radar measurement available immediately is far more useful operationally than the gauge corrected product available too late.

6.15 EVOLUTION OF THE CONFIGURATION OF THE LIGHTNING PROTECTION SYSTEM OF THE KAPILDUI WEATHER RADAR INSTALLATION

M. MARURI[1,2,3], J.A. ARANDA[1,4]

[1] Basque Meteorology Agency, Basque Country, Spain

[2] Meteorology Area, Energy and Environmet Division, Tecnalia R&I, Basque Country, Spain

[3] University of the Basque Country UPV/EHU, Spain

[4] Emergencies and Meteorology Directorate, Security Department, Basque Country, Spain

mercedes.maruri@tecnalia.com

The Basque Country has a complex topography and flash flooding events due to the morphology of the basins. This was the main reason to install new weather radar, the second in the region, in 2005. But to find the best place, many factors was taking into account, meteorological, accessibility, blocking effects between others. The final decision was inland in the Kapildui Mountain, although the system was built according to the lightning protection system of the installation project; the site has a high electrical activity.

The present work is a description of the evolution of the lightning protection system until to find the current solution. After more than 10 years, in octuber 2014 was installed the last design and since then neither lightning strike impact has been detected in the radome. At this moment the Kapildui weather radar is working with its third radome and there are three periods associated to each radome in which a new protection system was probed based on the previous studies of the performance under different meteorological conditions to try to find the final solution. Results based on the experience along the years are presented in this paper.

The methodology connects the electrical activity with the protection system and the performance based on the radome impacts detected after a meteorological event. The main conclusion is that the protection system installed must be 100% efficient, any impact in the radome structure changes the properties of the radome and it is a weakness to future severe weather events, therefore it is important to find the best solution to the site for operational systems.

6.16 MONITORING THE ONGOING UPGRADE OF THE SWEDISH WEATHER RADAR NETWORK

D. DUFTON[1], G. HAASE[1], D. JOHNSON[1], G. VULPIANI[1,2]
[1] Swedish Meteorological and Hydrological Institute, Sweden
[2] Department of Civil Protection, Presidency of the Council of Ministers, Italy
david.dufton@smhi.se

The upgrade of the Swedish weather radar network to dual polarisation began in 2014 and is expected to finish in 2019 with 7 of the 12 radars in the network currently upgraded. The introduction of new components into the network and a constant refinement of the network during the upgrade have increased the need to constantly monitor the stability of the radars in the network. This is compounded by the increased monitoring requirements of dual polarisation radars with the need to maintain consistent calibration of differential reflectivity particularly important. Dual polarisation also provides increased opportunities for monitoring the reflectivity through the application of self-consistent calibration techniques.

To meet these enhanced requirements SMHI has implemented several complementary monitoring techniques, including but not limited to monthly statistical analyses, the Relative Calibration Adjustment (RCA) technique (Silberstein et al, 2008), online solar monitoring techniques (Holleman et al, 2010), the commonly used birdbath calibration technique (Bringi and Chandrasekar, 2001) and self-consistent calibration techniques (Gorgucci et al, 1992).

It has been necessary to adapt these methods to the Swedish network, particularly considering ice phase precipitation is dominant during several months of the year in Sweden and the majority of the Swedish radars are located in rural environments with variable clutter targets. We present our adaptations and results from the monitoring techniques, showing how they complement one another in monitoring the upgraded network. We also present examples of how these techniques have identified radar malfunctions during the upgrade process and how they are now developing into an automated monitoring system that alerts us to any unexpected changes in the network.

References

Bringi, V. N., and V. Chandrasekar. 2001. Polarimetric Doppler Weather Radar: Principles and Applications. Cambridge University Press.

Gorgucci, E., G. Scarchilli, and V. Chandrasekar. 1992. “Calibration of Radars Using Polarimetric Techniques.” IEEE Transactions on Geoscience and Remote Sensing 30 (5): 85358. https://doi.org/10.1109/36.175319.

Holleman, Iwan, Asko Huuskonen, Mikko Kurri, and Hans Beekhuis. 2010. “Operati onal Monitoring of Weather Radar Receiving Chain Using the Sun.” Journal of Atmospheric and Oceanic Technology 27 (1): 15966. https://doi.org/10.1175/2009JTECHA1213.1.

Silberstein, David S., David B. Wolff, David A. Marks, David Atlas, and Jason L. Pippitt. 2008. “Ground Clutter as a Monitor of Radar Stability at Kwa-

jalein, RMI." Journal of Atmospheric and Oceanic Technology 25 (11): 203745. https://doi.org/10.1175/2008JTECHA1063.1.

6.17 ON THE CAPABILITIES OF THE GPM CORE OBSERVATORY OVER GREAT BRITAIN AND IRELAND

D. WATTERS[1], A. BATTAGLIA[1,2], K. MROZ[2], F. TRIDON[1]

[1] EARTH OBSERVATION SCIENCE GROUP, DEPARTMENT OF PHYSICS AND ASTRONOMY, UNIVERSITY OF LEICESTER, LEICESTER, UNITED KINGDOM

[2] NATIONAL CENTRE FOR EARTH OBSERVATION, UNIVERSITY OF LEICESTER, LEICESTER, UNITED KINGDOM

dcw17@leicester.ac.uk

The capabilities of the Global Precipitation Measurement Mission Core Observatory (GPM-CO) to measure surface rain rates with its dual-frequency precipitation radar (DPR) and GPM microwave imager (GMI) over Great Britain and Ireland are considered in comparison to the UK Met Office's (UKMO) ground-based radar network. Assessment is performed by comparing the GPM Version-5 DPR and CMB products to the UKMO Radarnet 4 composite product from May 2014 April 2017. The natively 1 km Radarnet product is collocated temporally and spatially to the GPM products' 5 km resolution, with quality-controlled and masked measurements used for a fair comparison. In particular, this study considers the comparison results and the impact of non-uniform beam filling upon them. Considering measurements within 75 km range of a ground-based radar, the DPR (CMB) product is found to underestimate the Radarnet product by 19% (6%) with a standard deviation and correlation of 108% (110%) and 0.56 (0.60) respectively. The large deviations are found to be partially due to the DPR (CMB) product overestimating surface rain rates below 0.8 mm h^{-1} (1.4 mm h^{-1}) and underestimating them above this rain intensity. Furthermore, the CMB product is also found to over-predict highly variable rain events though the DPR is not subject to this. The underestimations by GPM products in comparison to the Radarnet product may be due to poor clutter flagging within the algorithms.

6.18 EVALUATION OF REFLECTIVITY/POLARIMETRY/RADIOMETRY-BASED C-BAND ATTENUATION CORRECTION SCHEME USING NEIGHBOURING RADARS

N. HUSNOO[1], T. DARLINGTON[1], R. THOMPSON[2], A. ILLINGWORTH[2]
[1] Met Office, UK
[2] University of Reading, UK
nawal.husnoo@metoffice.gov.uk

A C-band weather radar beam can be attenuated by several dBs in heavy rainfall, leading to a severe underestimation of the rainfall.

This is traditionally corrected by using a gate-by-gate correction scheme, which is strongly sensitive to the reflectivity calibration of the radar, and can occasionally be unstable, yielding unphysically large corrections. If a dual polarisation radar is available, the differential phase change in rainfall can be measured. This is proportional to the specific attenuation, but unfortunately, the proportionality "constant" in this case can vary by a factor of about two.

A more recent technique is based on the principle that absorbers in thermal equilibrium will also emit electromagnetic radiation. This can be measured as an increase in the noise level at long range, which can then be converted into a path integrated attenuation An operational scheme was released in 2016 to produce improved attenuation corrections using this extra information. We present an evaluation of the benefits of the new scheme, using reflectivity measurements of overlapping radar volumes from neighbouring radars.

6.19DIRECT COMPARISONS OF POLARIMETRIC C-BAND AND S-BAND MOMENTS IN SNOW

B.M. TAYLOR[1]

[1] York University - Toronto, Canada
brandontaylor42@gmail.com

The Canadian Weather Radar Network is currently undergoing an upgrade to polarimetric, S-Band radar systems. Forecasting experiences in Canada with the legacy C-Band radars lends to the idea that the narrow beamwidth of C-Band systems is preferential for nowcasting the typical shallow lake-effect snow event. This idea is tested by comparing moments from King City radar, just north of Toronto, to the neighboring Buffalo, NY WSR-88D. By transforming the radar data from spherical coordinates to the Cartesian coordinate system, the two radars can be compared directly. Objective analysis indicates that the spatial patterns of reflectivity are very similiar, with King maintaining the obvious advantage in resolving fine scale features of lake-effect snow bands through a narrow physical beamwidth. Also, it is shown that comparatively, the reflectivity values obtained through this method are within 1 dB. In regards to differential reflectivity, a case by case comparison is performed to determine any event biases from the King City radar. This is achieved by subtracting out the bias of KBUF; this value comes from estimates made using the NEXRAD external target bias estimation techniques. It is shown that differential reflectivities at King City can become positively biased with snow on the radome in synoptic snowfalls, with an average value near +0.25 dB. Without snow on the radome, the differential reflectivity bias as measured in comparison with KBUF remains within +-0.0625 dB.

6.20 CALIBRATION OF RADAR REFLECTIVITY AND DIFFERENTIAL REFLECTIVITY FOR OPERATIONAL DUAL-POLARIZATION WEATHER RADAR NETWORK

JEONG-EUN LEE[1] HAE-LIM KIM[1], SUNG-HWA JUNG[1], SUN-KI LEE[1]

[1] Weather Radar Center, Korea Meteorological Administration, Republic of Korea
wjddms4634@korea.kr

Stability of radar system leads to significant uncertainty in radar-based quantitative precipitation estimation (QPE). Particularly, mis-calibration of the system results in considerable discrepancies in radar measurements over nationwide radar network. Thus, the accurate estimation of biases in reflectivity (Z_H) and differential reflectivity (Z_{DR}) is the primary requisite to improve an accuracy of rainfall estimation and to mitigate the discrepancies in hydrometeor classification based on radar network. However, it remains as a challengeable issue to estimate the accurate biases using operational dual-polarization weather radar in real time. We aim to calculate the calibration biases of Z_H and Z_{DR} for operational S-band dual polarization radar network.

Z_H bias was calculated based on self-consistency principle between Z_H and specific differential phase shift (K_{DP}). The method is suitable for the large spatial extent and moderate precipitation, but not for convective systems. Therefore, we proposed the total span K_{DP} algorithm to exclude the ray contaminated by hail or convective cells. Total span K_{DP} was defined as total differential phase shift divided by total path length along the ray. This method provides more stable calibration bias in time.

Z_{DR} bias was determined by using vertical pointing method. To obtain stable Z_{DR} biases in real time, we developed automated quality control algorithm for vertical pointing measurements, which is composed of four steps following as: 1) Removal of Z_{DR} above the top of bright band using vertical reflectivity profile, 2) Filter out an invalid radar measurement using thresholds for Z_H (<0 dBZ), Z_{DR} (<-2.0 dB or >6 dB), and ρ_{HV} (<0.95) below bright band, 3) Elimination of an invalid layer using the count threshold of valid measurements along azimuthal direction at a given radar range, and 4) Discarding of an invalid layer by the continuity check. Finally, Z_{DR} bias was estimated as averaged Z_{DR} value in linear space. The calibration bias of Z_{DR} was expected to be within 0.2 dB.

Acknowledgements
The research is supported by "Development and application of cross governmental dual-pol radar harmonization (WRC-2013-A-1)" project of the Weather Radar Center, Korea Meteorological Administration.

6.21 STANDARD OPERATION PROCEDURES (SOP) FOR WEATHER RADARS OPERATION, MONITORING, MAINTENANCE AND CALIBRATION

L. LIMAN[1], T.POSIO[1], M.KURRI[1]

[1] Finnish Meteorological Institute, Finland
ljubov.liman@fmi.fi

A standard operating procedure, or SOP, is a set of step-by-step instructions compiled by an organization to help workers carry out complex routine operations. SOPs aim to achieve efficiency, quality output and uniformity of performance, while reducing miscommunication and failure to comply regulations. The information collected in to SOP will help the present maintenance personnel in their work as well as the new maintenance personnel familiarizing themselves with operation, monitoring, maintenance and calibration procedures of radars.

This document was prepared as an example of a SOP document and is written in generic way enabling it to be used independently of the radar manufacturer or radar type. With the help of this SOP, the maintenance personnel can monitor, maintain and calibrate the weather radars and make sure that all operations and tasks are made and taken care of. These procedures are to be followed to minimize variation, reduce errors, and ensure accuracy in measurement of meteorological radar parameters.

Procedures provide a description of who does what, and when. An SOP characterizes relationships and control measures. It defines the roles and responsibilities to help workers "find themselves" in the process. Procedures clarify different decision points and provide the necessary guidance on criteria to make a decision.

The SOP is prepared based on FMI radar team experience, Timo Posio's engineering degree thesis "Functions, maintenance and calibration of the WRM200 weather radar" and an article "MAINTENANCE KEEPS RADARS RUNNING", BAMS 2017, Saltikoff et.al.

6.22 CALIBRATION OF THE NCAR AIRBORNE W-BAND RADAR USING OCEAN SURFACE BACKSCATTERING DATA

U. ROMATSCHKE[1], J. VIVEKANANDAN[1], R. RILLING[1], P.-S. TSAI[1], S. M. ELLIS[1]

[1] National Center for Atmospheric Research, Boulder, Colorado, United States of America
romatsch@ucar.edu

The HIAPER Cloud Radar (HCR) is a 94 GHz scanning W-band system which has been deployed in several field campaigns mounted in an underwing pod on the NSF/NCAR HIAPER aircraft. Because of the radars exposure to extreme environmental changes, monitoring of radar system calibration is of great importance. Utilizing the backscattering properties of the ocean surface as a calibration reference for airborne and spaceborne sensors is well established for microwaves and has recently gained popularity in the millimeter wave frequencies. Since first ocean scan data collected by HCR during the Cloud Systems Evolution in the Trades (CSET) experiment (2015) showed great promise as a calibration resource, ocean scan data were collected on a regular basis and coordinated with atmospheric profiling through the release of dropsondes in the recent Southern Ocean Clouds, Radiation, Aerosol Transport Experimental Study (SOCRATES).

We will present a comparison of these two data sets which shows a large but fairly constant bias in HCR reflectivity calibration with somewhat higher values for SOCRATES than for CSET data. However, the radar system is stable within 1 dB over the course of all flights of one field experiment. We further compare the ocean scan calibration results with other calibration methods that make use of known maximum thresholds of reflectivities observed in light rain, within the bright band, and in the ice phase of clouds. A preliminary analysis shows consistency between the different methods, underlining the potential of using the ocean surface as a calibration target.

6.23 MONITORING OF CALIBRATION HOMOGENITY OF HUNGARIAN WEATHER RADAR NETWORK

MARIANNA HADVÁRI[1], PETER NEMETH[1], ROLAND STEIB[1]

[1] Hungarian Meteorological Service, Hungary
hadvari.m@met.hu

Hungarian weather radar network consists of four dual-polarized C band radars measuring up to 240 km distance, covering the whole area of Hungary. Three old radars were upgraded from alternate polarization method to simultaneous method in the last few years. A new radar site was established and the new radar using simultaneous method was also installed in 2014.

In order to analyze the homogenity of calibration level in the network a comparison was conducted for horizontal reflectivity measured above the overlapped area. Reflectivity is scanned in operativ manner in every 5 minutes on 10 different elevation angles. The measured values are interpolated into a 16 vertical level 3D grid, with 1 km horizontal and vertical resolution.

The comparison is made for the suitable vertical levels where the difference of cross-section area of the bins is sufficiently small, neither ground clutter nor partial beam blockage exist.

6.24 RADOME EFFECTS ON THE POLARIMETRIC VARIABLES OF A MOBILE X-BAND RADAR

J. FIGUERAS I VENTURA[1], Z. SCHAUWECKER[1], E. SULMONI[1], J. GRAZIOLI[1]

[1] MeoteoSwiss, Locarno-Monti, Switzerland
jordi.figuerasiventura@meteoswiss.ch

In this submission we will analyse the effects of the radome of a mobile X-band Doppler polarimetric radar on the polarimetric data, focusing in particular on the differential reflectivity (Z_{DR}), the co-polar correlation coefficient (P_{HV}) and the system differential phase offset (Φ_{DP0}). MeteoSwiss operates this radar system for specific measurement campaigns. Usually it is operated with the radome on but in the course of a measurement campaign in Meiringen, Switzerland, we had the opportunity to remove the radome for a short period of time (from 4 to 7 September 2017), which allowed us to compare the behaviour of the polarimetric echoes of precipitation with and without radome.

The lower part of the MeteoSwiss radar radome has a cylindrical shape of 2.55 m diameter and 1.1 m height while on top there is a 2.55 m diameter semi-sphere. The entire radome has a height of 2.375 m. The radome shell has an A-sandwich structure of fiberglass skins with a polyurethane foam core. It is composed by four panels lap-joined by metallic threaded unions. There are 3 main lateral panels and a small circular panel on top of the radome. The 3 unions of the lateral panels start at the base of the radome and reach the top forming an helical shape.

In the past, our data quality monitoring measurements, performed with the radome on, have always exhibited a sinusoidal-like pattern in azimuth, visible at all elevations and for all the variables controlled (Z_{DR}, P_{HV} and Φ_{DP0}). In addition, the 80-percentile value of P_{HV} in rain had unusually low values, on the order of 0.988 instead of the typical values of 0.995 expected. We had always suspected that a possible cause were the metallic threaded unions distorting the antenna diagrams of both the horizontally and vertically polarized channels. Indeed, data collected during a rain event on 4 September (without radome), do not exhibit the sinusoidal-like behaviour and the P_{HV} in rain increased to a value of 0.992. Once the radome was put back in place, the usual pattern reappeared. A more detailed data analysis will be provided during the conference.

It is therefore recommended to operate a system with similar characteristics without the radome whenever possible to perform quantitative measurements or alternatively to develop methodologies to compensate for the radome effects.

6.25 OPERATIONAL MONITORING OF TR-LIMITER DEGRADATION BASED ON CLOSE RANGE GROUND CLUTTER

T.MATHIJSSEN[1], S. BROERE[1], H. BEEKHUIS[1], H. LEIJNSE[1]

[1] Royal Netherlands Meterologic Institute (KNMI), Utrechtseweg 297, 3731 GA, De Bilt, The Netherlands
tiemo.mathijssen@knmi.nl

TR limiters are widely employed as receiver protection equipment in operational weather radars. Typically the lifespan of a weather radar exceeds that of such limiters, resulting in a need to replace them. When replaced on a corrective basis, the radar downtime can occur at inconvenient moments during severe weather. Also the radioactive substances often present in these limiters poses strict regulation and administration of these components, which can be a nuisance during unscheduled repair. Moreover, TR limiter failure is usually preceded by degradation, which can affect data from an extended time before the failure. Preventive replacement is undesired, due to the very large variation in lifespan these components. Ideally, a warning message is generating specifying that component degradation has commenced.

TR limiters typically show an increased recovery time before failing, which can be exploited to monitor component degradation. Large recovery times will show up in produced data by reduced ground clutter at close range to the radar site. Monitoring the close-range ground clutter could give an indication of the state of the limiter.

This study presents preliminary results to which extent monitoring of ground clutter can be used to identify TR limiter degradation and prediction of failure.

6.26 IMPROVED COLLOCATION TECHNIQUES BETWEEN RADAR AND AIRCRAFT

F.LUMB[1], R.NEELY[1], A.BLYTH[1], G.NOTT[2], A.WELLPOTT[2], C.WALDEN[3], J.CROSIER[4], C.WESTBROOK[5], S.ABEL[6], S.BEST[6], J.DORSEY[4], M.FORTESCUE[3], D. HARRISON[6], D.LADD[3], S.O'SHEA[4], C.REED[2]

[1] University of Leeds, UK

[2] Facility for Airborne Atmospheric Measurements (FAAM), UK

[3] Chilbolton Observatory, STFC (Science and Technology Facilities Council), UK

[4] University of Manchester, UK

[5] University of Reading, UK

[6] Met Office, UK

freya.lumb@ncas.ac.uk

Here we present the application of geodesty to the collocation of observations made with atmospheric research aircraft and meteorological radars.

For the validation and calibration of geophysical retrievals, such as ice water content (IWC), in situ observations made by the aircraft need to be within the radar beam in order to achieve accurate collocation through precision. Previous methods have relied on statistics to make up for observations which are not collocated, which give way to other uncertainties. This analysis is applied to observations made during Parameterising Ice Clouds using Airborne obServationS and triple-frequency dOppler radar (PICASSO) campaign January and April 2018.

6.27 OPERATIVE CORRECTION OF DUAL-PRF VELOCITY OUTLIERS

P. ALTUBE[1], T. RIGO[1], O. ARGEMÍ[1], N. PINEDA[1], J. BECH[2], S. COLLIS[3], J. HELMUS[4]

[1] Servei Meteorològic de Catalunya, Barcelona
[2] Universitat de Barcelona, Barcelona
[3] Argonne National Laboratory, Argonne, Illinois
[4] Anaconda Inc., Austin, Texas
paltube@meteo.cat

Weather radar velocity images obtained using the dual-PRF technique present characteristic unfolding errors. These errors result from the violation of the assumptions involved in the procedure and appear as remarkable outliers in the velocity field. This phenomenon is frequently observed in the imagery of the weather radar network of the Meteorological Service of Catalonia, the XRAD, especially in cases of strong winds (either linear or tornadic).

Recently, a new methodology to correct these characteristic outliers has been developed and validated (Altube et al., 2017). The technique is particularly robust in the correction of clustered outliers and can be applied when extended aliasing is present.

The correction methodology has been operatively implemented for the XRAD since the beginning of 2018. The operative module outputs files that contain the corrected velocity volume data in IRIS RAW format (VAISALA). This module has been developed using the Python ARM Radar Toolkit (Py-ART) as base. The corrected files are re-ingested, in real-time, back to the processing chain of the IRIS software for visualization and generation of downstream products.

The present work collects examples of outlier correction for a series of real-case severe weather events that have taken place in Catalonia during the last 4 years. These include tornadoes, downbursts, gust fronts and a waterspout. Some of these cases took place recently, on the 7th of January 2018, with the operative correction of the dual-PRF velocity already running. This allowed the detection of the path of two tornadoes and a downburst that affected the region. For the rest of the cases, the methodology has been retroactively applied.

The examples presented show how the corrected velocity fields display a remarkably higher quality. These are, in contrast with the primary fields, well-suited for their use in automated severe weather detection algorithms and for assimilation in nowcasting systems and models.

Session 7. Synergetic Use of Weather Radars and Other Sensors



Keynote presentation

7.1 WEATHER RADAR AND SUPERCONDUCTING GRAVIMETER FOR ESTIMATING HEAVY RAINFALL

L. DELOBBE[1], S. WILFERT[2], A. WATLET[3], M. VAN CAMP[3]

[1] Royal Meteorological Institute of Belgium, Belgium
[2] Institute of Geography, University of Augsburg, Germany
[3] Royal Observatory of Belgium, Belgium
laurent.delobbe@meteo.be

The radar-based estimation of intense precipitation produced by convective storms is a challenging task and the verification through comparison with gauges is questionable due to the very high spatial variability of such type of precipitation. In this study, we explore the potential benefit of using a superconducting gravimeter for improving and verifying radar-based precipitation estimates.

The underground superconducting gravimeter used in this study is installed in Membach (BE) at 85 km distance from a C-band weather radar located in Wideumont (BE). The 15-year observation record 2003-2017 is available for both gravimeter and radar with 1-min and 5-min time steps, respectively. The gravimeter integrates soil water in a radius of about 200 m around the instrument. This allows measuring rainfall at larger spatial scale than traditional rain gauges. The precision of the gravimeter is a few nm/s^2; 1 nm/s^2 corresponding to 2.6 mm of water.

The comparison of reflectivity and gravity time series for severe rainfall events shows that high reflectivity peaks are associated with a rapid decrease of the underground measured gravity. The precipitation amounts derived from gravity measurements and from radar observations are further compared for the whole 15-year period. In order to reduce the influence of non-meteorological factors on gravity changes, the focus is given on rain and hail fall events producing large precipitation amounts over short durations. The results are analysed and the added value of the superconducting gravimeter is discussed.

7.2 OBSERVATIONS OF THE ATMOSPHERIC BOUNDARY LAYER FROM A VERTICALLY POINTING, S-BAND, FMCW RADAR IN NORTHERN ALABAMA, U.S.A. DURING VORTEX-SOUTHEAST (2016-2017)

R. TANAMACHI[1], S. J. FRASIER[2], J. WALDINGER[2], A. T. LAFLEUR[1], F. ROCADENBOSCH[3]

[1] Department of Earth, Atmospheric, and Planetary Sciences, Purdue University, West Lafayette, Indiana, U.S.A.

[2] Microwave Remote Sensing Laboratory, University of Massachusetts, Amherst, Massachusetts, U.S.A.

[3] CommSensLab, Department of Signal Theory and Communications, Universitat Politcnica de Catalunya (UPC), Barcelona, Spain

rtanamachi@purdue.edu

During spring 2016 and spring 2017, a vertically pointing, S-band FMCW radar (UMass FMCW) was deployed in northern Alabama during the Verification of the Origins of Rotation in Tornadoes Experiment (VORTEX) Southeast. The principal objective of these deployments was to characterize the boundary layer evolution near the VORTEX-Southeast domain. In total, 14 weeks worth of data were collected, in conditions ranging from quiescent clear skies to severe thunderstorms. Examples will be shown of boundary layer features observed during these two extended deployments, such as enhanced Bragg scatter at the top of the mixing layer, horizontal convective rolls, bioscatterer activity, and undular bores. In precipitation, the melting layer is easily identified, and abrupt transitions in its height are documented.

In 2017, UMass FMCW was upgraded with a solid state amplifier, replacing the traveling wave tube amplifier used in 2016 and prior seasons. Examples of data collected before and after this upgrade will be shown.

Additionally, we present results of application of three algorithms to these data: (1) a simple-but-flexible echo classification scheme to separate precipitation from non-precipitation, (2) a bright band identification algorithm, and (3) an extended Kalman filter-based boundary layer height detection algorithm. The latter technique will be discussed in greater detail in a separate presentation at this conference.

7.3 REAL-TIME RAINFALL FROM A COUNTRY-WIDE NETWORK OF COMMERCIAL MICROWAVE LINKS IN GERMANY

C. CHWALA[1], G. SMIATEK[1], H. KUNSTMANN[12]

[1] Institute of Meteorology and Climate Research (IMK-IFU), Karlsruhe Institute of Technology, Garmisch-Partenkirchen, Germany

[2] Institute for Geography, Regional Climate and Hydrology, University of Augsburg, Augsburg, Germany

christian.chwala@kit.edu

Many cell phone base stations are interconnected using a network of commercial microwave links (CMLs). At the typical frequencies of these CMLs (between 15 GHz and 40 GHz) rainfall considerably attenuates the transmitted signal along the CML paths. Therefore, the measured attenuation can be used to derive path averaged rain rates. Retrospective analyses of CML data have already shown that this technique can provide valuable rainfall information. However, applications for rainfall data, e.g. using it as input for short-term flood warning system, require timely data availability.

We now process more than 4000 CMLs all over Germany in real-time. Our CML data is based on instantaneous attenuation measurements which we acquire every minute. This data is available within seconds and is immediately fed into our processing pipeline. The processing includes outlier detection, wet/dry classification, compensation for wet antenna attenuation and temporal aggregation. The resulting rainfall information for the individual CMLs is then interpolated to rainfall fields every five minutes.

We describe our data acquisition and management system, elaborate on the processing challenges and our processing methods and show a validation of CML-derived rainfall information for Germany using RADOLAN, the rain gauge adjusted radar product of DWD. Finally, we will do a live demonstration of our web-based visualization of the CML real-time rainfall fields.

7.4 WHEN IS RADAR DATA CALIBRATION BY IN-SITU NETWORKS MISLEADING?

I.TCHIGUIRINSKAIA[1], A. ICHIBA[1], I. PAZ[1], E. SKOURI-PLAKALI[1], A. GIRES[1], D. SCHERTZER[1]

[1] Hydrology Meteorology and Complexity Lab, École des Ponts ParisTech 6-8 avenue B. Pascal, Cité Descartes, 77455 Marne-la-Vallée cedex 02 France
ioulia.tchiguirinskaia@enpc.fr

In the framework of the EU project RainGain, a dual-polarization X-band radar has been installed on the site of École des Ponts ParisTech (ENPC). With respect to the C-band radar data of Météo-France of Trappes, it gives access to the complex patterns of precipitation at much finer scales. This has enabled us to test and compare different algorithms using single and/or double polarization and their comparison in the context of different studies. These studies have furthermore shown that adjustment of radar measures on in-situ networks does not necessarily play a positive role. Considering that precipitation fields are extremely variable over a wide range of space-time scales, we use the Universal Multifractal (UM) framework to confront the highly non-Gaussian statistics of space-time structures of precipitation measured by the radars with that partial information captured by the in-situ measurement networks. A criterion for a compatibility of these measures is based on the intersection theorem between two multifractal fields. More specifically, we first evaluate the fractal dimension of the in-situ network, as well as the UM parameters (□lfa and C1) of the precipitation measured by the radar. Then the semi-theoretical results suggest that a conditioning by the in-situ network could be rather counter-productive for rainfall events with C1/□lfa -1) being weaker than the co-dimension of the fractal in-situ network. Indeed, in this case the in-situ network only introduces a bias in the rainfall estimates instead of allowing to refine them.

7.5 RAIN-RATE ESTIMATION FROM CEILOMETER MEASUREMENTS: A COMPARATIVE CASE STUDY USING S-BAND RADAR AND DISDROMETER RETRIEVALS

RUBEN BARRAGAN[1], FRANCESC ROCADENBOSCH[1], JOSEPH WALDINGER[2], STEPHEN J. FRASIER[2], DAVID D. TURNER[3], ROBIN TANAMACHI[4], DANIEL DAWSON[4]

[1] CommSensLab, Department of Signal Theory and Communications, Universitat Politcnica de Catalunya (UPC), Barcelona, Spain

[2] Microwave Remote Sensing Laboratory, University of Massachusetts, Amherst (USA)

[3] NOAA Environmental System Research Laboratory, Global Systems Division, Boulder, CO (USA)

[4] Dept. of Earth, Atmospheric, and Planetary Sciences, Purdue University, West Lafayette, IN (USA)

roca@tsc.upc.edu

Rain-rate (RR) estimation from ceilometer measurements is becoming a significant area of interest (Lewandowski et al. 2009). Ceilometers are low-cost, low-energy-aperture-product lidar (laser-radar) instruments relying on optical radiation. When compared to microwave radars, key distinctive features are that ceilometers have a much narrower field of view, on the order of fractions of a degree, and that the lidar signal is largely attenuated by rain.

We address RR estimation from vertical-configuration ceilometer measurements (Vaisala CL-31) and its limitations in comparison with co-located S-band Frequency-Modulated Continuous-Wave (FMCW) radar and disdrometer RR measurements. A modified form of the well-known slope-method (Kunz & de Leeuw 1993), (Rocadenbosch et al. 2000) is used to derive the rain optical extinction coefficient from the backscattered lidar signal. A collocated Doppler wind lidar provides complementary observations.

The methodological part addresses the foundations of the RR retrieval procedures from both the ceilometer and the radar as well as the derivation of RR-to-extinction models for both the ceilometer-radar and ceilometer-disdrometer combinations. As a proxy of calibration, RR retrievals from the collocated radar and portable disdrometer are fitted against ceilometer extinction estimates in order to derive the RR-to-extinction correlation models that would allow us to estimate the RR from ceilometer measurements without need to permanently deploy the radar or the disdrometer in similar scenarios.

A 1.5-h-long rain episode is presented in the context of the Verification of the Origins of Rotation in Tornadoes EXperiment-Southeast (VORTEX-SE), which occurred during spring 2016 in Huntsville, AL environs (Tanamachi et al. 2016).

Acknowledgements

This work was supported by NOAA under contracts NA1501R4590232 and NA16OA R4590209 and by the Purdue University Dept. of Earth, Atmospheric, and Planetary Sciences. CommSensLab (Mara de Maeztu Unit of Excellence funded by the Agencia Estatal de Investigacin (National Science Foundation), Spain) collaborated

via Spanish Gov. - European Regional Development Funds TEC2015-63832-P project.

References

Kunz, G.J. & de Leeuw, G., 1993. Inversion of lidar signals with the slope method. Applied Optics, 32(18), pp.32493256.

Lewandowski, P.A., Eichinger, W.E., Kruger, A., and Krajewski, W.F., 2009. Lidar-based estimation of small-scale rainfall: Empirical evidence. Journal of Atmospheric and Oceanic Technology, 26(3), pp.656664.

Rocadenbosch, F., Comern, A., and Albiol, L., 2000. Statistics of the slope-method estimator. Applied Optics, 39(33), pp. 604957. Available at: http://www.ncbi.nlm.nih.gov/pubmed/18354610.

Tanamachi, R., Frasier, S.J., Heberling, W., Waldinger, J., Seedorf, M., Bozell, J., 2016. Purdue-UMass Mobile Radar Observations Collected during VORTEX-Southeast 2016. In "Results from the VORTEX-SE Field Program", Session 3 in 28th Conference on Severe Local Storms. Portland: American Meteorological Society, p. Paper 3.6. Available at: https://ams.confex.com/ams/28SLS/webprogram/Paper301419.html.

7.6 REAL TIME DETECTION OF LIGHTNING ACTIVITY USING A LOW-COST AND PORTABLE X-BAND RADAR AND A CLUSTER ANALYSIS APPROACH

V. CAPOZZI[1,3], M. MONTOPOLI[2,3], V. MAZZARELLA[1,3], A.C. MARRA[2], N. ROBERTO[2], G. PANEGROSSI[2], S. DIETRICH[2], G. BUDILLON[1]

[1] Department of Science and Technology, University of Naples "Parthenope, Italy (10-point type, centered)

[2] Institute of Atmospheric Sciences and Climate, National Research Council, Italy

[3] Centre of Excellence CETEMPS, Department of Physical and Chemical Sciences - University of L'Aquila, Italy

vincenzo.capozzi@uniparthenope.it

This work proposes a multi-parameter method for the detection of cloud-to-ground (CG) lightning activity, using a low-cost and portable single-polarization X-band weather radar. With respect to previous works on the same topic, in this study various lightning proxy parameters are extracted for each rain cell seen by the radar and are jointly considered to produce an estimation of the expected stroke activity for each rain cell.

The developed methodology foresees two main steps: i) a rain cell identification based on a modified Storm Cell and Identification Tracking method for the convective cell identification and ii) on a cluster analysis, which is aimed at combining the selected lightning proxy parameters into a single label indicating the most likely category of Cloud to Ground (CG) activity that is flash rate equal or greater than zero, respectively.

Three lightning radar based proxy parameters have been selected after a correlative analysis, which considered a large number of predictors. The three radar based lightning proxy parameters selected are: i) the altitude thickness between the iso-reflectivity at Z=40-dBZ and the T=-20°C isotherm ($\triangle_{HZ}$,T); ii) the rain cell area contoured by iso-reflectivity at Z=40-dBZ found at T=-10°C isotherm ($A_{Z,T}$) and iii) the vertical integral of ice equivalent water (VII).

In order to train and test our procedure, a dataset collected in the pilot study area of Naples metropolitan environment and consisting of 1575 radar reflectivity volumes acquired from April 2012 to March 2016, LINET lighting network of cloud-to-ground (CG) and intra-cloud (IC) strokes and meteorological in-situ data has been used. Radar data have been accurately processed, in order to remove clutter and partially compensate for attenuation effects.

Results will be discussed in terms of detection scores showing as the developed techniques, although with some limitations, outperforms those that make use of single lightning proxy parameters. Overall, the main results are fairly reasonable compared with other studies and more advanced radar systems, showing a Proportion Correct (PC) detection of 0.60, a Probability of Detection (POD) of 0.67, a False Alarm Ratio (FAR) of 0.29, a Critical Success Index (CSI) of 0.52 and a Heidke Skill Score (HSS) of 0.47.

7.7 EVALUATION OF MULTIPLE DOPPLER RETRIEVALS OF CONVECTION IN DARWIN

R. JACKSON[1], S. COLLIS[1], P. KOLLIAS[2], M. OUE[2], S. ENDO[3], A. VOGELMANN[3], W. LIN[3], T. LANG[4], C. POTVIN[5]

[1] Argonne National Laboratory, USA
[2] Stony Brook University, USA
[3] Brookhaven National Laboratory, USA
[4] NASA Marshall Space Flight Center, USA
[5] Cooperative Institute for Mesoscale Meteorological Studies/NSSL, USA
rjackson@anl.gov

Wind retrievals from multiple scanning Doppler radars have numerous uncertainties related to factors such as the vertical and temporal sampling of the scanning radar data, the assumptions made in the wind retrieval regarding the mass continuity equation and particle fall speeds, as well as being only applicable where there is enough returned power from scatterers, which can potentially cause the retrieval miss important features of the convective core such as upper level divergence and weak echo regions. Few studies that have attempted to quantify such uncertainties. However, packages such as the Cloud Resolving Model Radar Simulator (CR-SIM) applied to Weather Research and Forecasting (WRF) model simulations to emulate radar data provides a methodology for quantifying the uncertainty in multiple doppler retrievals.

In this study, CR-SIM is used on WRF simulations of monsoonal convection over the Tropical Western Pacific Atmospheric Radiation Measurement Climate Research Facility site in Darwin. CR-SIM provides simulated velocities over the C-band POLarization Radar (CPOL) and Berrimah radars. Multidop, a Python package that uses the three dimensional variational wind retrieval technique to retrieve winds, is executed on the simulated velocities. The resulting vertical velocities in deep convective cores from the Multidop retrieval is then compared against those from the original WRF simulations. The results show that the vertical velocity w in updraft cores from those retrieved by Multidop are biased low compared to the original WRF data. The framework of using simulated radar measurement will be used to improve the retrieval framework by configuring the retrieval parameters to minimize such biases.

7.8 STRUCTURAL CHARACTERISTICS OF PRECIPITATING CLOUDS MEASURED BY TRMM PR AND IGRA

Y. FU[1], R. WANG[1], J. XIA[1], L. SUN[1], M. WANG[1]

[1] Laboratory of Atmospheric Observation and Water Cycle, School of Earth and Space Sciences, University of Science and Technology of China, Hefei, China
fyf@ustc.edu.cn

The temperature and humidity structure of precipitating cloud can be obtained by combining detections of ground-based radar or space-based radar with the reanalysis data, but this structure is different from the real one. The structure in a limited area can also be obtained through measurements by instruments onboard aircraft, but such flight has some dangerous and costly. To reveal the nature of the vertical structure of temperature and humidity inside precipitating clouds, a quasi-spatiotemporal synchronization dataset of temperature and humidity profiles collocated with precipitation profiles is generated in this study by merging the Integrated Global Radiosonde Archive (IGRA) and Tropical Rainfall Measuring Mission (TRMM) Precipitation Radar (PR) from 1998 to 2012. Based on this data, the vertical characteristics of precipitation, temperature, humidity and convective available potential energy (CAPE) in East Asian Summer Monsoon (EASM) region and Indian Summer Monsoon (ISM) region are investigated.

Results indicate that the height of storm tops can reach 17 km and 12 km for convective and stratiform precipitation, respectively, in EASM region. Usually, the height of storm tops in the ISM is 1 km lower than that in EASM region. The significant difference of temperature for the precipitation scenario between EASM region and ISM region appears near the surface, i.e. about 4C higher in ISM region than in EASM region. Generally, relative dryer air occurs inside convective precipitating clouds in ISM region, and there is a larger CAPE precipitation scenario in ISM region than in EASM region. In EASM region, the results show that the height of storm tops for convective precipitation are higher than that for stratiform precipitation, which causes by more unstable atmospheric movements in convective precipitation. The height of storm tops is higher at 1200 UTC (evening at local time) than at 0000 UTC (morning at local time) over land for both convective and stratiform precipitation, and vice versa over ocean. Additionally, temperature anomaly patterns inside convective and stratiform precipitating clouds show a negative anomaly of about 2 K, which results in cooling effects in the lower troposphere. This cooling is more obvious at 1200 UTC for stratiform precipitation. The positive anomaly that appears in the middle troposphere is more than 2 K, with the strongest warming at 300 hPa. Relative humidity anomaly patterns show a positive anomaly in the middle troposphere (700500 hPa) prior to the two types of precipitation, and the increase in moisture is evident for stratiform precipitation.

7.9 ASSESSMENT OF PROPAGATION EFFECTS AND RADAR DATA QUALITY WITH A DUAL-POL TARGET SIMULATOR DURING THE OLYMPIC WINTER GAMES

M. SCHNEEBELI[1], A. LEUENBERGER[1], J. GEHRING[2], G. LEE[3], K.D. AHN[4], F. TAPIADOR[5], A. BERNE[2]

[1] Palindrome Remote Sensing GmbH, Switzerland
[2] EPFL LTE, Switzerland
[3] Kyungpook National University, South Korea
[4] Korean Meteorological Administration, South Korea
[5] University of Castilla-La Mancha, Spain
marc.schneebeli@palindrome-rs.ch

A target simulator is an instrument that receives radar pulses and retransmits them with a pre-defined amplitude, time delay and Doppler shift in order generate a virtual radar target. By accurately controlling the properties of the pulse that is sent back to the radar, the generated target can be used as a calibration reference for a wealth of radar parameters, such as the radar constant and the differential reflectivity offset. During the Olympic Winter Games in PyeongChang, the worlds first dual-polarization X-band radar target simulator has been employed for seperate experiments with two different dual-polarization radars. First, the differential and absolute calibration of a Gematronik 60DX radar has been evaluated by generating a virtual radar target at 90 km distance to the radar. This target was repeatedly scanned with a sector scan and subsequently the measured radar reflectivity was compared to the pre-defined target properties. It could be shown that the horizontal radar channel was accurately calibrated within an estimated accuracy of 1 dB. The vertical channel however suffered from a hardware defect and hence could not be assessed.

For a second experiment, the target simulator was installed for several weeks in 13 km distance to EPFL's MXPOL radar. While the EPFL radar was located at an altitude close to sea level, the target simulator's altitude was approximately 700 m above. This set-up made not only possible the long-term assessment of the MXPOL's transmitter and receiver stability by evaluating clear-sky measurements, it also allowed the measurement of hydrometeor induced signal attenuation between the two instruments during precipitation events. Of special interest were cases, in which the melting layer was located between the altitudes of the two instruments in order to directly measure the attenuation of the melting layer.

Since Palindrome's target simulator is also capable to measure the phase of the incoming radar pulses, it became feasible to directly study precipitation induced phase changes on propagation which in return opened the possibility to discriminate between backscatter and propagation induced differential phase changes. Recent research shows that such unprecedented measurements are of special interest for melting layer studies.

7.10 HAIL EVENT ANALYSIS AND DAMAGE ASSESSMENT BASED ON MULTI-DATA APPROACH

S.TANI[1], H.PAULITSCH[1], B.SÜSSER-RECHBERGER[1], R. TESCHL[1]

[1] Graz University of Technology, Institute of Microwave and Photonic Engineering, Austria

satyanarayana.tani@tugraz.at

The main focus of our study is to combine the analysis of hail signature information from radar, lightning and ground measurements for the hail event analysis and crop hail damage assessment. The hailstorm days were assigned to examine the relation between radar-derived products and damages caused by hail in Styria, Austria during 2015. 3D single polarization C-band weather radar data and radiosonde freezing level data were used to indicate occurrence of hail and to derive hail kinetic energy. The spatial distribution maps of total hail kinetic energy were developed to capture the swath and intensity of the hail storms to identify potential hail damage areas. Hail events from ESWD (European Severe Weather Database) and crop damage reports from the Austrian Hail Insurance were used for validation. The hail signature information from radar was further compared with lighting trajectories. In total 16 days with high crop hail damage claims were considered for the investigation. The results show that in most cases radar-based hail signature information well correspond to the areas where hail events and damage footprints were reported.

7.11 STUDIES OF THE MELTING LAYER OF PRECIPITATIVE SYSTEMS USING X-BAND DUAL POLARIZATION WEATHER RADAR AND SMARTLNB NETWORK

S. MELANI[1], A. ANTONINI[2], A.ORTOLANI[1], L. BALDINI[3],[4], E. ADIROSI[3],[4], L. FACHERIS[4],[5], F. GIANNETTI[6], A. PETROLINO[7]

[1] CNR-IBIMET, Italy, [2] LaMMA Consortium, Italy, [3] CNR-ISAC, Italy, [4] CNIT, Italy, [5] University of Florence, Italy, [6] University of Pisa, Italy, [7] MBI srl, Italy
s.melani@ibimet.cnr.it

The characterization of the melting layer (ML) is an important task for operational radar meteorology. Melting layer identication may be used to establish distances at which radar rainfall estimates become affected by melting hydrometeors, with benets for operational hydrometeor classication, as snowfall, freezing rain and liquid precipitation. Consequently, this yields a significant performance improvement in radar-based quantitative precipitation estimation (QPE) on ground. Furthermore, knowledge of the ML location is also important for microphysical cloud characterization and the evaluation of icing potential.

Several studies and algorithms exist in literature for characterizing ML through radar measurement signature, the most popular being the increase in the radar reflectivity factor known as bright. For dual polarization radar, ML detection can be pursued using specific signatures of dual polarization measurements, such as differential reflectivity Z_{DR}, co-polar correlation coefficient ρ_{HV} , specific differential phase K_{DP}, and linear depolarization ratio LDR that exhibit well-pronounced ML signatures both in stratiform and even in convective situations.

Moreover, ML and rainfall have a strong influence on satellite links signals, as they are attenuated due to the presence of hydrometeors along the propagation path. In stratiform precipitation systems, the ML is the upper limit of the rainfall column height that is responsible of the attenuation of radio signals. Therefore, ML climatology is proficiently used for designing satellites links relative to a specific area.

Very recently, a new X-band Doppler, dual-polarization weather radar system has been installed in Florence funded by the Tuscany Region Government within the NEFOCAST project. The latter investigates a new concept system that aims at providing real time precipitation maps trough the attenuation measurements collected by a dense population of new-generation interactive satellite terminals (called SmartLNB, Smart Low-Noise Block converter). A number of SmartLNB has been deployed in the Tuscany region and a test bed has been established in cooperation with the schools of the Florence Metropolitan city.

In the present study, the potential of the new weather radar system is investigated for characterizing the ML in terms of height and thickness under different meteorological conditions and cloud systems. Measurements collected in the RangeHeight Indicator (RHI) scan mode along the direction to the Eutelsat 10A satellite (used for the experimental campaign of the NEFOCAST project) have been analysed with the simultaneous attenuation estimation obtained by the SmartLNBs with radar coverage during selected precipitative events. Statistical analyses have been performed

based on both weather radar and SmartLNB measurements, supplemented by ancillary observations from some raingauges (both impact and tipping-bucket types) co-located with SmartLNBs. In addition, a C-band radar system (Polar 55C) located in Rome has also been used for this work. Polar 55C dual polarization measurements have been analysed with respect to co-located SmartLNBs and laser disdrometer.

The results of this analysis highlight the effects of ML on radio signal attenuation, as the total attenuation of signal increases also with the increase of ML vertical thickness. Therefore, the characterization of the vertical profile of precipitation is mandatory for implementing accurate QPE on ground, both from radars and satellite links.

7.12 INTRA- AND INTER-EVENT VARIABILITY OF DROP SIZE DISTRIBUTION IN MEDITERRANEAN REGIONS

B. BOUDEVILLAIN[1], S. HACHANI[12], G. DELRIEU[1], Z. BARGAOUI[2]

[1] Université Grenoble Alpes, CNRS, IRD, IGE, 38000 Grenoble, France

[2] Universit Tunis El Manar, Ecole Nationale des Ingénieurs de Tunis (ENIT), BP 37, 1002 Tunis le Belvédère, Tunisia

brice.boudevillain@univ-grenoble-alpes.fr

Drop Size Distribution (DSD) is a key element for studying rainfall processes and their hydrological impacts. DSD observation is necessary both for the understanding of factors modifying rainfall properties (e.g. orographic influences) and for development and/or validation of microphysical schemes in meteorological models. DSD observation is also useful for understanding issues in radar-based estimates of rainfall rates and kinetic energy fluxes.

A DSD observation network has been set up throughout the HyMeX′s Long Observation Period and in the framework of the Cvennes-Vivarais Mediterranean Hydrometeorological Observatory (OHM-CV) both at small (Hpiconet, Auzon catchment) and meso scales (Cvennes-Vivarais). Thus, a climatology of rainfall properties at the ground has been established over 5 years (2012-2016). The inuence of several factors were analyzed: locations (distance from the sea, orographic environment), seasons, daily synoptic weather situations (derived from geopotential heights, at 700 and 1000 hPa), rainfall types (analyzed from 5 min radar data), as well as some combinations of these factors.

The aims of this communication are: 1) to present the main results of the climatological study finalized recently (Hachani et al., 2017); 2) to extend it in several Mediterranean contexts thanks to observations available on South-Alps, Corsica and Tunisian sites; 3) to go further on intra-event variability through the analysis of the shape of normalized DSDs and of radars observations.

References

Hachani, S., Boudevillain, B., Delrieu, G., Bargaoui, Z.: Drop Size Distribution climatology in Cvennes-Vivarais region, France. Atmos., 8, 233, 2017.

7.13 PRODUCING CONVECTION DAILY MAPS BASED ON OPERA COMPOSITE AND EUCLID LIGHTNING DATA

D. R. POELMAN[1], L. DELOBBE[1]

[1] Royal Meteorological Institute of Belgium, Belgium
dieter.poelman@meteo.be

Hazardous weather, such as extreme rainfall, hail, and other dangerous phenomena associated with severe convective storms, can be clearly identified in radar observations. Those events may affect public safety, cause property damage, and/or induce economic losses. Therefore, a daily overview of all areas in Europe affected by severe convective phenomena could be of interest to many stakeholders.

Pan-European weather radar composites are available through the EUMETNET Operational Programme for the Exchange of Weather Radar Information (OPERA). As such, daily pan-European maps can be produced based on the aggregation or accumulation of the 15 minute maximum reflectivity and rainfall OPERA products. However, the most hazardous convective storms are generally producing lightning activity. For identifying such storms, it is useful to complement radar data with lightning data. A thunderstorm daily map using data from the European-wide lightning detection network EUCLID (European Cooperation for Lightning Detection) is used in this study to improve the mapping of convective precipitation over Europe. Lightning and radar data are combined for a selection of convective episodes simultaneously affecting several countries in Europe. The benefits of combining the two sources of observations are explored.

7.14 RESULTS OF THE MONITORING TASKS AND CO-CREATION ACTIVITIES OF THE PRECIPITATION PRODUCTS OF KAPILDUI WEATHER RADAR

M. MARURI[1,2], S. GAZTELUMENDI[1,2], K. OTXOA DE ALDA[1,2], R. HERNANDEZ[1,2], C. STOCKER[3] J. SALAZAR[3], I. EGUIARA[4], J.A. ARANDA[1,5]

[1] Basque Meteorology Agency, Basque Country, Spain

[2] Meteorology Area, Energy and Environmet Division,Tecnalia R&I, Basque Country, Spain

[3] Basque Water Agency, Basque Country, Spain

[4] Traffic Directorate, Security Department, Basque Country, Spain

[5] Emergencies and Meteorology Directorate, Security Department, Basque Country, Spain

mercedes.maruri@tecnalia.com

The Directorate of Emergencies and Meteorology has weather radar that its main objective is to monitor the evolution of the precipitation field and give information to other users (public, hydrological, traffic and emergency departments between others) for different meteorological applications. To achieve that purpose there are two lines of work that interact continuously; the study of the best product that describe the surface precipitation field and evaluate the quality of the current products in critical situations during a monitoring process in a severe episode. The critical situations are the most requested for our users, before-during-after, therefore quality and usefulness of the product is demanded to the regional meteorological service.

The methodology considers an evaluation of the user requirements with the current operational products in different meteorological conditions. The input data is the Kapildui weather radar and rain gauges of a dense network of automatic surface stations in addition other sources such as the information available from Jata weather radar are included. The results are presented in a table in which is easy to identify what we need and what we have, taking into account the different measurements of precipitation. Special attention is made in the integration of the rain gauges and the weather radar in a complex topography.

The conclusion will serve to improve the current products according to a co-creation activity in which users, meteorological service and evaluation of impacts are analyzed together.

7.15 SYNERGY OF GPM AND GROUND-BASED RADAR OBSERVATIONS FOR PRECIPITATION ESTIMATION AND DETECTION OF MICROPHYSICAL PROCESSES

V. PEJCIC[1], S. TRÖMEL[1] , K. MÜHLBAUER[1], P. SAAVEDRA[1] , J. BEER[1] , C. SIMMER[1]

[1] University of Bonn, Bonn, Germany
velibor@uni-bonn.de

As successor to the TRMM mission the Global Precipitation Measurement core satellite (GPM) operates with a Ka-band and Ku-band Dual-frequency Precipitation Radar (DPR). This is the first spaceborne DPR and allows important global insights into three-dimensional precipitation structures from space. The polarimetric X-band research radar in Bonn (BoXPol), Germany, is part of an international network for ground validation of the GPM satellite. The nationwide German C-band radar composit of the German Weather Service (RADOLAN) and a vertically pointing micro rain radar (MRR) are used to evaluate the satellite based precipitation estimates, rain type and phase partitioning (solid, liquid, mixed phase). Three years of comparison (2014-2017) between GPM DPR derived near surface rain rates and the ground-based estimates from RADOLAN show high correlations. The near surface rain rates and reflectivities from the single and dual-frequency satellite products reveal robust correlations in summer but higher variability in winter. This can be attributed to reduced DPR performance for solid precipitation estimates which directly depends on the melting layer detection. Consequently, GPM-based vertical products like the bright band height and thickness used for phase partitioning require an in-depth evaluation. The measurements of the twin polarimetric X-band radars in Bonn and Jlich (JuXPol) allow a more reliable and robust detection of the bright band which is compared with GPM-based results. The use of the temporal evolution of quasi vertical profiles (QVP) sustain the polarimetric information and offer an optimal detection of phase partitioning and the melting layer during the development of precipitation systems. Furthermore, the matching method of open source software wradlib is used to obtain a direct and qualitative statement about the measurement inaccuracies between the different resolutions of both observation systems.

7.16 NOWCASTING OF THUNDERSTORM AND HAIL EVENTS USING GROUND BASED REMOTE SENSING DATA

T. BÖEHME[1], C. HEROLD[1], A. LEYSER[1], T. HENGSTEBECK[1]

[1] Deutscher Wetterdienst, Frankfurter Str. 135, 63067 Offenbach, Germany
tim.boehme@dwd.de

Ground-based remote sensing data are essential for the nowcasting of severe weather, such as thunderstorm and hail events. For this, not only the detection of mature thunderstorms is necessary, but also the identification of the preceding phase which shows the convective growth including attendant phenomena such as hail formation.

Within this contribution, radar and lightning data analyses are shown in combination with NWP and synoptic data. Modern radar data products can help to recognise hazardous weather situations. Products derived from 3D volume radar data by vertical integration, i.e., vertically integrated liquid (VIL) and vertically integrated ice (VII), have proven to be good indicators for thunderstorm development and hail formation.

This contribution will demonstrate in case studies and by means of statistical analysis how the different radar and lightning parameters are related and how their combined use can help to extract crucial information, so that warning lead time can be increased. Statistical analysis reveals that VIL is a good indicator for cell development and that VII can be utilised to estimate hail size and lightning activity. The case studies confirm that sudden increases in lightning activity are often linked with the occurrence of hail events. In some cases, a clear extension of the warning lead time is visible. For these cases, atmospheric environmental conditions extracted from NWP data are additionally presented.

7.17 WEATHER RADAR DATA DRIVEN NEAR-GROUND PRECIPITATION TYPE ESTIMATION AT DEUTSCHER WETTERDIENST

J. STEINERT[1]

[1] Deutscher Wetterdienst, Germany
joerg.steinert@dwd.de

The Deutscher Wetterdienst (DWD) operates a C-band weather radar network that is mainly equipped with dual-polarisation capability. The weather radar systems are well-established devices to analyse precipitation particles in the troposphere and therefore are taken to realise a hydrometeor classification based on the measured radar observables. But beside the advantage of an extensive coverage, the measurement geometry of weather radar, especially the antenna elevation angle and antenna beam shape, results in information that has a more or less distinct height difference to the surface in relation to the distance from the radar site. This means, those meteorological related values that are estimated with dual-polarisation weather radar measurements may differ in comparison to the meteorological condition near the ground. Nevertheless, the weather forecasting and warn management of the DWD as national weather service is strongly connected to surface based measurements and observations. For instance, the correct differentiation between snow and rain in the cold season is an important task. Because of this, the users requested a near-ground precipitation type estimation that ought to be driven by weather radar data based hydrometeor classification. To treat this issue, forecasted vertical profiles of temperature, humidity and pressure are taken from numerical weather prediction model which serve additional input.

In this study, a rough overview to the possibilities for an extrapolation of the hydrometeor classes from the height of the radar measurement to the precipitation type at 2 m above the ground is given. Hereby, the focus is laid on the transition from snow to rain as a typical application for the cold season. First impressions will be presented by case studies from last winter in Germany. So far, the presented results encourages for further development in this topic.

7.18 X-BAND RADAR PARMETERS FROM PARSIVEL2 DATA USING PYDSD

E. SULMONI[1], J. FIGUERAS I VENTURA[1], J. GRAZIOLI[1]

[1] MeteoSwiss, Locarno-Monti, Switzerland
eric.sulmoni@meteoswiss.ch

Disdrometers are fundamental instruments to study the microphysics of precipitation. They can be used to estimate the drop size distribution of rain, as a rain gauge to estimate rainfall rate and, additionally, various polarimetric radar parameters can be computed from the data they provide. This study focuses on the vertical profile of drop size distribution (DSD) comparing retrievals from radar with disdrometer data.

In this contribution, Parsivel^2 data is being processed using and extending a software repository (PyDSD) to compare it to the radar parameters of an X-Band weather radar. PyDSD is an open-source Python-based repository on github created by Joseph Hardin. It makes use of the pytmatrix package (also on github) to compute several polarimetric radar parameters, such as horizontal reflectivity (Z_H) differential reflectivity (Z_{DR}), co-polar correlation coefficient (ϕ_{dp}) and specific differential phase (K_{DP}). In addition to the radar parameters, PyDSD computes physical quantities such as rain rate, RR, median diameter, m_0, and liquid water content, LWC. The disdrometer provides internally computed values for RR and ZH. This allows an additional comparison with the repository's output. In order to process Parsivel2's raw data, a reader was developed and added to PyDSD.

The measurement setup for the comparison between radar and disdrometer data consists of 3 Parsivels. One is placed 10 m away from an X-band Doppler polarimetric radar located at a small airport in a valley in Ticino, Switzerland. The other two are placed on a mountain slope at different elevations but roughly at the same azimuth direction from the radar.

During the conference, the consistency between the PyDSD estimates and the Parsivel^2 output will be discussed and an analysis of the vertical profile of DSD, retrieved both by radar and disdrometer will be shown.

Preliminary results of the comparison between PyDSD data processing and internal Parsivel^2 show a difference in Z_H which seems to be larger at higher RR (PyDSD $>$ Parsivel^2). Furthermore, the difference in RR tend to be larger at cold temperatures with the PyDSD output being larger. The most likely reason for that is the assumption in the repository that all precipitation is liquid. Hence, the Parsivel^2 has a filter for solid precipitation. Furthermore, the method to calculate the rain rate in PyDSD from the Disdrometer raw data was adapted to estimate the maximum considered diameter of hydrometeors by the Parsivel^2's internal algorithm when solid precipitation is present as it filters hydrometeors above a diameter of approximately 1.2 mm.

7.19 ARM AERIAL FACILITY AND RADAR CLOUD OBSERVATIONS FROM THE ACE-ENA FIELD CAMPAIGN

A. MATTHEWS[1], J. HARDIN[1], B. ISOM[1], F. MEI[1], L. GOLDBERGER, S. GIANGRANDE[2], R. WOOD[3], N. BHARADWAJ[1]

[1] Pacific Northwest National Laboratory, USA
[2] Brookhaven National Laboratory, USA
[3] University of Washington, USA
alyssa.matthews@pnnl.gov

The ARM Aerosol and Cloud Experiments in the Eastern North Atlantic (ACE-ENA) campaign occurred June July, 2017 and January February, 2018 to study low clouds that are poorly represented in global climate models. The ARM Aerial Facility Gulfstream-1 (AAF G1) was deployed during ACE-ENA and flew over the Azores ARM ENA fixed site to provide details on the vertical structures and variabilities in and around these low clouds. This deployment provided an opportunity to compare ground and aircraft based observations. For this study, the KAZR zenith pointing millimeter radar and XSAPR2 scanning X-band precipitation radar located at the ENA site as well as the Two-Dimensional Stereo Probe (2DS) flown on the AAF G1 were used to analyze the clouds and drizzle. PyDSD, an open-source python software, was used to calculate radar reflectivity values based on the drop size distributions observed by the 2DS so that the aircraft data may be directly compared to the KAZR and XSAPR2 data. The AAF G1 flew over the radar site multiple times during the four-hour flights at various altitudes, allowing for comparisons below, in, and above the clouds. Patterns flown directly over the site also allow for validation of the scattering method used, so that analysis may be trusted at points further from the radar. This study will analyze the radar and cloud probe data from drizzle cases during the summer and early spring periods and discuss results for inter-cloud, event, and seasonal variability.

7.20 ON THE USE OF COMMERCIAL MICROWAVE LINKS FOR RAINFALL ESTIMATION IN SEMI-ARID AREAS

R. RAICH[1], P. ALPERT[2], H. MESSER[3]

[1] School of Electrical Engineering, Tel Aviv University, Israel
[2] Department of Geosciences, Tel Aviv University, Israel
[3] School of Electrical Engineering, Tel Aviv University, Israel
roiraich@gmail.com

The common practice for precipitation estimation involves the usage of rain gauges and weather radars. Rain gauges have been proven as good and trustworthy for liquid precipitation (i.e. rainfall) monitoring, while radar systems, on the other hand, can detect other types of precipitation as well. However, radar systems are known for accuracy issues when measuring near-ground precipitation in the distance. In addition, when monitoring rain rates in semi-arid regions and when measuring precipitation at an arid region, precipitation particles, rain, or snow flakes, may evaporate before reaching the ground. This rain and the associated evaporation are therefore entitled the Virga phenomenon and is occurring naturally when the air below the cloud is relatively dry. The virga may continue until humidity below the base of the cloud is high enough to decrease the evaporation and then, the precipitation will reach the ground. A novel method, suggested by Messer et al. in 2006, involves existing Commercial Microwave Links (CMLs) used in the backhaul communication links, for the sake of precipitation monitoring. The rain-induced-attenuation over CMLs has been the source of many studies over the past decade, and is part of an ongoing research of precipitation estimation based on the Received Signal Level (RSL) measurements. We suggest, for the first time, a method for profiling the vertical rain-rates in arid areas using a combination of several radar beams, which observe at different heights above ground along with the CMLs in order to achieve more accurate Above Ground Level (AGL) rain-rates where the Virga may affect the radar measurements of rain. This is done by estimating the cloud base level and the rain rate at the cloud base level. In addition, we suggest an approach for quantitating the Virga phenomenon, employing CMLs data in conjunction with the radar measurements. The proposed methods were validated by testing it on storm events in a semi-arid location in south-eastern Israel. Our method showed highest correlations between the estimated near ground rain intensities and the ground truth observed by the rain gauges, when compared to using weather radar or CMLs alone. This method, of measuring near ground rain rates more accurately by using measurements of both weather radar and CMLs, can assist in flash flood warnings systems for semi-arid regions, and in further expanding the study of weather phenomena in arid and semi-arid regions.

7.21 PERFORMANCES OF GROUND RADAR AND INFRARED SATELLITE NEW COMBINED ALGORITHM FOR THE ITALIAN PENINSULA

LEO PIO DADDERIO[1], GIANFRANCO VULPIANI[2], SILVIA PUCA[2], GIULIA PANEGROSSI[1], PAOLO SANO′[1], ANNA CINZIA MARRA[1], STEFANO DIETRICH[1]

[1] Institute of Atmospheric Sciences and Climate, National Research Council, Rome, Italy
[2]Department of Civil Protection, Presidency of the Council of Ministers, Rome, Italy
leopio.dadderio@artov.isac.cnr.it

The Italian radar network is currently composed by 20 C-band and 2 X-band systems, managed by 11 administrations, able to cover most of the country. The product generation at national level is carried out by the Department of Civil Protection (DPC) that currently manages 7 C-band and 2 X-band systems, all with dual-polarization capability. The national mosaic provides an estimation of the precipitation intensity with a ten minutes time resolution over a equally-spaced 1 km grid. A Quality Index (QI) map is associated to the rainfall rate map, taking into account the radar artifacts, the partial beam blockage, the height of measurements with respect to the freezing layer, the beam broadening and the rain path attenuation.

The geostationary Meteosat Second Generation (MSG) Spinning Enhanced Visible and Infrared Imager (SEVIRI) provides high-quality measurements across twelve visible (VIS) and infrared spectral (IR) bands. Several techniques have been developed exploiting VIS or IR observations (individually or in a combined way) to relate the cloud features to the surface precipitation. One of them is the blending Rapid Update (RU) technique combining IR observations with precipitation estimates obtained from spaceborne passive microwave radiometers, and used operationally within the EUMETSAT H SAF program.

Within the collaborative agreement between DPC and the Institute of Atmospheric Sciences and Climate (ISAC) of the National Research Council (CNR) a new blended algorithm has been developed that combines the ground radar precipitation estimates and the IR observations from SEVIRI to provide a precipitation map over the whole Italian territory with SEVIRI spatial-temporal resolution. The satellite-based product can integrate the low QI ground radar measurements. The algorithm estimates the rain intensity (R) from the SEVIRI brightness temperature (TB) measurements on the basis of regression curves built from a training dataset from coincident IR and high QI radar observations. At the same time, a map of the probability of precipitation (POP) is generated. The two maps are combined to give the final product. The preliminary results show a greater reliability of both R-TB and POP-TB relationships during warm months (mainly characterized by convective precipitation) with respect to cold months. Furthermore, the results also show that the blended algorithm can help to individuate and remove radar-based false alarm due to interferences, radar malfunction, etc.

The assessment of the quality of the algorithm is carried out through a comparative study with the Italian rain gauge network, analyzing seasonal behavior over different geographical areas.

7.22 RAINFALL MAPS FROM COMMERCIAL MICROWAVE LINKS (CMLS) AND URBAN FLOOD PREDICTION: PILOT TESTS IN SEVERAL AFRICAN CITIES

M. ALCOBA[1], M. GOSSET[2], F. CAZENAVE[3], N. CHAHINIAN[4], C. BOUVIER[4], M. TURKO[2], A. YAPI[5]

[1] GET-OMP/World Bank, Toulouse France
[2] GET-OMP/IRD, Toulouse France
[3] IGE/IRD, Grenoble France
[4] HSM/IRD Montpellier France
[5] LAPA, Abidjan, Ivory Coast
matias.alcoba@get.omp.eu

Demographic pressure, land use changes and possible increase in extreme events intensify the vulnerability to floods in African cities. In this context access to information on rainfall extremes and rainfall patterns is essential to understand and possibly predict urban flooding in West Africa. The lack of weather radar information and the sparsity of the gauges network in these regions make rainfall estimation through Commercial Microwave links (CML) an attractive solution. Rainfall estimation based on measuring the attenuation of microwave signal between mobile network antennas was illustrated by many studies in Europe and Israel. Our team and partners already demonstrated in Burkina Faso that CML could provide effective QPE on heavy convective rainfall as encountered in West Africa. Following these early success several pilot sites were set up in Central and West Africa to test CML base estimation for urban flood analysis and prediction. The quantitative evaluation of these QPE will be presented. We will also compare several interpolation methods used to derive the rainfall maps from the CML network. We will discuss the propagation of the CML based QPE uncertainty in the hydrological urban model used in these studies.

7.23 A COMPARISON OF TOTAL LIGHTNING REFLECTIVITY PROXIES AND WEATHER RADAR DATA IN SOUTHERN BRAZIL FOR HIGH IMPACT WEATHER MONITORING AND NOWCASTING

W. F. COELHO[1], L. CALVETTI[2], C. BENETI[3], N. A. ROZIN[3]

[1] Master Degree in Meteorology, Federal University of Pelotas (PGMET/UFPEL), Pelotas, Brazil

[2] Center for Meteorological Research and Forecasting, Federal University of Pelotas (CPMET/UFPEL), Pelotas, Brazil

[3] Parana Meteorological Service (SIMEPAR), Curitiba, Brazil

williamufpel@gmail.com

A comparison between total lightning-based reflectivity proxies (PulseRad, from Earth Networks) and S-band Weather Radar was yield for convective events in western Parana State, Brazil. PulseRad uses, as reflectivity proxies, total lightning data which includes both intra-cloud (IC) and cloud-to-ground (CG) flashes from the Earth Networks Total Lightning Network (ENTLN) with sensors installed in Brazil. The lightning proxies were compared and evaluated with reflectivity data from a dual-polarization S-Band Weather Radar of the Simepar (Meteorological System of Parana) located in Cascavel City in western Parana State, southern Brazil. Usually, the convection in this area is triggered by heat and moisture advection from South America low-level jet as well as when occur an alignment with cold fronts. It was chosen four convective events: a typical cold front; a summer ordinary cell convection and two Mesoscale Convective Systems (MCS), one during spring 2016 triggered by a high level trough and another during fall 2017 associated with an interaction between a cold front and the South America low-level jets. The comparisons indicate a very well agreement in the identification of convective cells during all events, although PulseRad could not capture mesoscale patterns as well as the weather radar data. The shape and values of reflectivity for convective areas of all the meteorological systems, such as the MCS, cold front and ordinary convection, were very well detected by PulseRad, while for stratiform region (in this study, represented by reflectivity < 35 dBZ) the reflectivity pattern was undetected or underestimated. In this study, it was not found significative delays between total lightning reflectivity proxies and the weather radar data, as established by the correct positioning of convective cells and the MCS cores. Finally, it was found an encouraging outlook to use the PulseRad as reflectivity proxies in areas without weather radar coverage for convection monitoring and nowcasting, but it is not clear its efficiency for QPE, which will be pursued in the near future.

7.24 MULTISOURCE DATA VERIFICATION OF A WEATHER RADAR SURFACE PRECIPITATION TYPE PRODUCT

E. CASELLAS[1,2], J. BECH[2], R. VECIANA[1], N. PINEDA[1], T. RIGO[1], J. MORÉ[1]

[1] Meteorological Service of Catalonia, Barcelona, Spain

[2] Department of Applied Physics - Meteorology, University of Barcelona, Spain

enric.casellas@meteo.ub.edu

Snowfall at low altitudes, despite it is a relatively rare phenomenon in southern Europe and the Mediterranean coastal regions, can cause major problems of road safety and transport during the cold season. For this reason, the Meteorological Service of Catalonia (SMC) implemented in 2006 a weather radar derived surface precipitation type product (SPT) in order to provide valuable information to decision-makers in surveillance tasks (Bech et al. 2014).

Four C-band single-polarization Doppler weather radars and a dense network of 185 automated surface observation stations cover the complex topography of Catalonia (NE Spain) and feeds the diagnostic system that discriminates precipitation type into snow, sleet and rain. The methodology is based on the original scheme described by Koistinnen and Saltikoff (1998) implemented in Finland and later adapted to the complex orography of Norway (Gjertsen and Odegaard, 2005). An empirical formula, dependant on surface temperature and relative humidity, is used to provide a conditional probability field of precipitation type. Then, this field is combined with the precipitation field obtained from quality-controlled radar data which results in a real-time estimation of surface precipitation type. The aim of this study is to provide a verification of the SMC SPT product to test its applicability particularly for events where snow and rain may be present concurrently.

Different sources of precipitation type observations are available for this verification study. Firstly, a meteorological observers network and a surveillance network, both formed by volunteer citizen-scientists supported by the SMC. Secondly, a nivometeorological manned station network, mainly located in mountain areas, and a small number of METAR and SYNOP observations. Thirdly, inputs from social networks. Fourthly, disdrometric and Micro Rain Radar (MRR) data for a specific location in the Pyrenees mountain massif. Additionally, for specific snow episodes, diagnostic data from the Local Analysis and Prediction System (LAPS) is also considered. Altogether these sources provide valuable information to verify the SPT product between 2010 and 2017 and to adjust and improve the operational version of the SPT product implemented at the SMC. This study was partly supported by projects CGL2015-65627-C3-2-R (MINECO/FEDER), CGL2016-81828-REDT (MINECO) and DI065/2017 (Industrial Doctorate Programme of the Regional Government of Catalonia).

References

Bech J, Vidal V, Ortiz JA, Pineda N, Veciana R. 2014: Real-time estimation of surface precipitation type merging radar and automated station observations. 17th International Road Weather Conference SIRWEC. La Massana, Andorra, Proceed. (8 pp).

Gjertsen U, Odegaard V. 2005. The water phase of precipitationa comparison between observed, estimated and predicted values. Atmospheric Research, 77(1-4), 218-231.

Koistinen J, Saltikoff E. 1998. Experience of customer products of accumulated snow, sleet and rain. In: Advanced Weather Radar System, COST 75, 397-406. EUR 18567.

Session 8. New and Emerging Radar Technologies



Keynote presentation

8.1 POLARIMETRIC VARIABLES ON THE PLANAR PHASED ARRAY RADAR: APPROXIMATE COMPUTATIONS

D. ZRNIC[1]
[1] NOAA/NSSL, USA
dusan.zrnic@noaa.gov

Considered is the Polarimetric Planar Phased Array Radar (PPPAR) that has micro strip patch radiating elements. The elements have two ports. Port one excites intended horizontal polarization and port two excites intended vertical polarization. The intended polarizations coincide with the actual polarizations if the plane of the antenna is vertical and the pointing direction is broadside. The intended polarizations are orthogonal if the pointing direction is in the principal planes of the antenna. In the vertical principal plane the intended vertical polarization is not vertical with respect to earth but is accepted for computing the polarimetric variables as in the case of a parabolic dish antenna. Out of the principal planes the intended polarizations are not orthogonal and to compute the polarimetric variables the returns need to be adjusted. One method of exact computation requires solving a set of at least three coupled linear equations. Although simple in principle it requires precise knowledge of the coefficients of these equations. This is quite challenging because the absolute values in the analogue part of the radar system are hard to measure or estimate. An approximation for computing the polarimetric variables is suggested. It can be applied to the alternate mode of polarization change whereby the H and V polarizations are transmitted sequentially but both are received simultaneously. It can also be applied to the simultaneous mode of transmission and reception if the transmitted polarizations are phase coded from pulse to pulse. Adjustment suggested here computes the powers and correlations of the returned signals from ports 1 and 2 and combines these into a ratio to obtain the differential reflectivity. The one absolute value needed is the angle between the intended vertically polarized field and the actual field. The field of view (azimuth versus elevation) over which the approximation holds is plotted. In the region close to the principal planes the approximation may break down therefore it is suggested that computations valid for the principal planes be extrapolated to the nearby region.

8.2 OSAKA URBAN PHASED ARRAY RADAR NETWORK EXPERIMENT

TOMOO USHIO[1,2], H. KIKUCHI[2], T. MEGA[2], F. MIZUTANI[3], M. WADA[3], N. TAKAHASHI[4], S. SATOH[4]

[1] Osaka University, Osaka, Japan
[2] Tokyo Metropolitan University, Tokyo, Japan
[3] Toshiba Corporation, Kawasaki, Japan
[4] National Institute of Information and Communications Technology (NICT), Japan
tomooushio@gmail.com

Recent progress of information and communication technologies has been enabling us to realize a rapid scanning radar system. In 2012, Toshiba Corporation and Osaka University succeeded in developing a new type of Phased Array Radar (PAR) system (Yoshikawa et al. 2013, Ushio et al. 2015) under a grant of National Institute of Communication and Information Technology (NICT), and installed in Suita Campus, Osaka University. This PAR system can scan the whole sky within 30 seconds up to 60 km in radius over 100 elevation angles with digital beam forming technique, and the initial observation results demonstrate the unique capability of the new PAR system. After its installation, a new clutter mitigation algorithm from adaptive beam forming technique was developed and tested with the PAR system, and succeeded in suppressing not only the ground clutter but also ghost echo from strong precipitation echo nearby more than 20dB. And also the adaptive algorithm was applied to supress the range sidelobe and showed the sidelobe level of -60dB.

Upon this success, a new experiment started in 2015 under a grant of SIP (Strategic Innovation Promotion Program) to create the Osaka Urban Phased Array Radar Demonstration Network. The main sensor of the Osaka Network is a 2-node Phased Array Radar Network and lightning location system. In this experiment, data products including reflectivities, VIL (Vertically Integrated Liquid water content), precipitation rates and others are transferred to Osaka Local Government in real time to prevent water related natural hazards. In this presentation, system architecture and some results are presented.

8.3 THE ADVANCED TECHNOLOGY DEMONSTRATOR AT THE NATIONAL SEVERE STORMS LABORATORY

S. TORRES[1,2], K. HONDL[2]

[1] Cooperative Institute for Mesoscale Meteorological Studies, The University of Oklahoma

[2] NOAA/OAR National Severe Storms Laboratory, USA

sebastian.torres@noaa.gov

The National Oceanic and Atmospheric Administration (NOAA) has identified evolutionary radar mission capabilities aimed at addressing current and future mission needs to support National Weather Service warning operations. Important requirements driving the next generation of weather surveillance radars include improvements in data quality, access to rapid-update volumetric data, and the ability to perform focused and tailored weather observations. Systems based on phased array antennas are promising solutions, and significant R&D investments over the last two decades have contributed to a growing understanding of this technology and to reduce risk associated with Phased Array Radar (PAR) technologies. Whereas many unique capabilities of PAR technology have been studied and even demonstrated, three main challenges remain: affordability, multifunction operation, and dual-polarization weather observations. As a major milestone in this quest, NOAA partnered with the Federal Aviation Administration (FAA) to develop the Advanced Technology Demonstrator (ATD). The ATD is a mid-scale, dual-polarized, multifunction, active, electronically scanned PAR that will be installed at the National Weather Radar Testbed in Norman, OK (USA). The ATD leverages several prior investments to provide a flexible and affordable radar system with which to evaluate performance and identify residual risk areas. The ATD proof-of-concept system is expected to provide important information about PAR polarimetric performance (including calibration), the maturity of this technology and its suitability to meet NWS mission-critical requirements, and the feasibility of having a single system supporting multiple missions. In this presentation we will provide an overview of the planned capabilities of the ATD, an update on progress to date, and a roadmap for engineering and meteorological research that will help prepare NOAA for the next generation of weather-surveillance radars.

8.4 DIFFERENTIAL PHASE UPON TRANSMISSION AS A NEW RADAR PARAMETER

VALERY MELNIKOV[1]

[1] National Severe Storms Laboratory, USA
valery.melnikov@noaa.gov

The main radar parameters are the wavelength, pulse repetition frequency, beamwidth, minimal detectable signal, and polarization configuration. These parameters are determined by the radar transmitter, receiver, antenna, and waveform of the radar pulse (e.g., pulse compression). The majority of polarization configurations are employed simultaneous transmission and reception of orthogonally polarized waves (STAR configuration). Typically, the differential phase between the transmitted waves is not controlled in STAR radars. The total system differential phase is the sum of the differential phases upon transmission and reception and is measured as a differential phase in the closest to radar edge of a radar echo.

It is shown that differential reflectivity (Z_{DR}), the differential phase (ϕ_{DP}), and correlation coefficient (ρ_{HV}) measured with STAR radars depend not only on the size, shape, and orientation of scatterers, but on the radar differential phase upon transmission as well. This is illustrated on data collected with two radars having different differential phases upon transmission (ϕ_t). Some "paradoxes" in radar data such as decreasing ϕ_{DP} values in areas of increasing Z_{DR}, the increase of ϕ_{DP} values with the antenna elevation angle, and different ϕ_{DP} range profiles measured with different radars are demonstrated and explained by the difference in ϕ_t. It is shown that a variable t allows obtaining new information about scattering media such as the shapes and axis ratios of ice cloud particles and the parameters of hailstones. These opportunities make the ϕ_t a new radar parameter.

Possible implementations of the variable ϕ_t with STAR weather radars having dish antennas and phased array antennas are discussed. It is shown that the variable ϕ_t in phased array radar allows obtaining the full set of elements of the scattering matrix.

8.5 AN ALL-DIGITAL POLARIMETRIC PHASED ARRAY RADAR FOR COMBINED WEATHER AND AIRCRAFT SURVEILLANCE

ROBERT PALMER[1,2], CALEB FULTON[1,3], JORGE SALAZAR[1,3], HJALTI SIGMARSSON[1,3], MARK YEARY[1,3]

[1]Advanced Radar Research Center (ARRC), University of Oklahoma, USA
[2]School of Meteorology, University of Oklahoma, USA
[3]School of Electrical and Computer Engineering, University of Oklahoma, USA
rpalmer@ou.edu

Currently, radars for weather observation and aircraft surveillance are specifically designed for their missions and, therefore, have quite different architectures. Modern weather radars are dual-polarization, use mechanically scanned dish antennas with pencils beams, and provide volumetric coverage with update times on the order of a few minutes. Aircraft surveillance radars are usually not dual-polarization and use a fan beam with a rapidly spinning positioner. Although high-fidelity height information is normally not provided, aircraft azimuth positions are updated every few seconds. If these two distinct mission requirements could be met with a single radar, significant reduction in lifecycle costs could be realized. The challenge is to design such a multi-mission radar at reasonable cost while continuing to provide high-quality weather observations and air traffic management capabilities. The Advanced Radar Research Center (ARRC) at the University of Oklahoma (OU) in the USA is working with NOAA's National Severe Storms Laboratory (NSSL) on this concept, which will likely leverage phased array radar technology. This goal has presented many challenges, especially regarding meeting mission requirements within the desired update time and the necessity of combining high-quality polarimetry with phased arrays. Many of these challenges can be met with a fully digital polarimetric phased array radar. The so-called Horus project is currently being undertaken by the ARRC and NSSL and will result in an all-digital, S-band, polarimetric phased array radar. The Horus radar will have 1024 dual-pol channels and will be capable of extreme flexibility in terms array segmentation, channel-independent waveforms, adaptive beamforming, etc. Given the importance of radar polarimetry to the weather community, its most-important feature will be the capability of performing real-time and frequent calibration as a routine part of the Horus scanning strategy. By exploiting mutual coupling between individual radiating elements that make up the array and the waveform independence of an all-digital array, the ARRC is currently developing automatic algorithms for array/polarimetric calibration. Finally, the all-digital design of the Horus radar will serve as an ideal testbed for evaluation of the level of digitization (e.g., subarrays versus all-digital) needed to meet multi-mission requirements. The system will be based on a slat/brick design for the majority of the electronics including the RF front-ends, commercial-off-the-shelf (COTS) transceivers, and on-board FPGA processing. This functionality will be combined into a single so-called Octoblade composed of 16 highly compact and functional channels. The Octoblade will also include liquid cooling and will be line replaceable for simplification of routine maintenance. The dual-polarization antenna has extremely high polarimetric isolation (better than -40 dB), which is enhanced further by the design of the RF channels. Although the system is extremely flexible,

if desired to reduce data size, partial systolic beamforming will be possible with the on-board FPGAs. Data transfer will be handled with a high-speed RapidIO network. The overall system concept and rationale for various design decisions will be presented along with the current status of the project.

8.6 WEATHER OBSERVATIONS WITH A PHASED ARRAY RADAR

L. BOROWSKA[1], D. ZRNIC[2], Y. ZHANG[2], G. ZHANG[3]

[1] The Advanced Radar Research Center (ARRC) and the School of Electrical and Computer Engineering, University of Oklahoma, Norman, OK, 73019 USA

[2] The National Severe Storms Laboratory, National Oceanic and Atmospheric Administration, Norman, OK 73072 USA

[3] The School of Meteorology, School of Electrical and Computer Engineering, and the Advanced Radar Research Center, University of Oklahoma, Norman, OK 73019 USA

lesya.borowska-1@ou.edu

The authors evaluate suitability of Phased Array Radar (PAR) for weather observations. The evaluation is based on actual data obtained with a couple of PARs in the USA. One of these has single polarization and its beam steering in azimuth is achieved by commutating the beam positions. The stability of the receivers was tested in pure noise region. The fields of reflectivity, Doppler velocity, and spectrum width were analyzed and compared with the nearby WSR-88D. After examination of these fields, we concluded that this particular PAR can be used for quantitative weather observation. The other PAR has dual polarization capability and its beam is steered by changing the phase of the radiating elements. As of this writing the polarimetric variables are being evaluated. Calibration of these is a challenge and we are evaluating pulse to pulse corrections and corrections of the second temporal moments of the horizontally polarized and vertically polarized components (i.e., powers and correlations of the time series data).

8.7 X-BAND PHASED-ARRAY POLARIMETRIC RADAR TESTBED: STATUS AND INITIAL RESULTS

S. J. FRASIER[1], W. HEBERLING[1], C. WOLSIEFFER[1], M. ADAM[1]

[1] Microwave Remote Sensing Laboratory, University of Massachusetts, Amherst, USA
frasier@umass.edu

An X-band, dual-polarized, phased-array radar developed by Raytheon has been adapted for weather observation by the Microwave Remote Sensing Laboratory (MIRSL) at UMass. The radar, called the Low Power Radar (LPR), operates at 9.6 GHz with a peak transmitting power of approximately 100W. The phased array consists of 2560 elements (arranged in a 64 x 40 grid), each with individual amplitude, phase, and polarization control on both transmit and receive. Each element transmits nominally 40 mW and employs a custom monolithic microwave integrated circuit chip for element control. The radar has been configured to accommodate various pulsing modes, such as single and dual-prf, and dual-prt, in various polarization transmit/receive modes such as single (HH or VV), alternating (HH,VV), fully polarimetric (HH,HV,VV,VH). Pulse compression is implemented to achieve adequate sensitivity at long ranges. We present an overview of the radar system, observations from initial deployments from a mobile platform, and outline future research plans.

The highly programmable phased-array architecture permits not only rapid scanning of extended volumes, but also element-based control of polarization. One research objective with the radar is to investigate in detail the polarimetric properties with scan angle to better understand potential biases in polarimetric products. To this end, side-by-side operations with a reference radar employing a conventional parabolic dish are planned. The flexible programmable aperture offers the possibility to mitigate these biases through polarization synthesis.

8.8 BISTATIC SCATTERING FROM BRAGG TURBULENCE AT X-BAND: A POTENTIAL MECHANISM FOR CLEAR AIR SENSING USING CASA-TYPE RADAR NETWORKS

DAVID J. MCLAUGHLIN[1]

[1] Department of Electrical and Computer Engineering, University of Massachusetts, Amherst, MA
dmclaugh@umass.edu

Dense networks of low-power, short-range (a few 10's of km) X-band radars are an emerging technology with the potential for superior spatial resolution and lower-altitude observations compared to long-range C and S band weather radars. Absent precipitation, and potentially insect echoes, there is concern about the ability of these networks to perform weather surveillance in clear-air conditions. It is well known that clear-air echoes from Bragg-scale turbulence can be used for atmospheric sensing at long micro wavelengths (eg, S band, L band, and lower frequencies) but this is not a reliable scattering mechanism at X-band, where the Bragg-resonant wavelength is below the inertial sub-range. In this presentation, we consider the problem of Bragg scattering from atmospheric turbulence in an X-band bistatic geometry. In such a geometry, where the radar transmitter and receiver are separated from each other by tens of km, the Bragg resonant wavelength can be substantially larger than the wavelength of an X-band radar. Theoretical calculations show that, when the atmospheric structure parameter is high enough, the volume reflectivity can be large enough to allow low-power X-band radars to perform clear-air weather surveillance. The theory is not new here. However, when it is applied in the context of a network of low-power phased array radars which allow practical weather surveillance in a bistatic mode it could result in a new capability to sense low-level winds in clear air at X-band. That would be a game changer.

8.9 THE CITY OF SÃO PAULO (BRAZIL) AS A TESTBED OF RAINFALL ESTIMATES FROM COMMERCIAL MICROWAVE LINK NETWORKS

M.F. RIOS GAONA[1], A. OVEREEM[1,2], H. LEIJNSE[2], T. RAUPACH[3], R. UIJLENHOET[1]

[1] Hydrology and Quantitative Water Management Group, Wageningen University, the Netherlands

[1] R&D Observations & Data Technology, Royal Netherlands Meteorological Institute, the Netherlands

[3] École Polytechnique Fédérale de Lausanne EPFL, Lausanne, Switzerland

feliperios@gmail.com

Rainfall estimates from commercial microwave link (CML) networks are path-averaged retrievals from the attenuation of the electromagnetic signals that propagate between cell phone towers. This alternative technique of rainfall estimation has gained attention from the hydrometeorological community, given its higher spatiotemporal resolution with regard to more standard sensors such as gauge networks and satellites, for instance. Accurate and high-resolution rainfall estimates are valuable in several hydrological applications as they offer a better understanding of short-lasted and heavy rainfall responsible for flash floods, for instance, which can exert a tremendous impact on society′s welfare.

This study evaluates CML rainfall estimates for a subtropical climate, namely, for the city of São Paulo (Brazil). First, we use the open-source R package RAINLINK (https://github.com/overeem11/RAINLINK) to retrieve rainfall rates from attenuation measurements of ∼200 CMLs located in the metropolitan area of São Paulo. Then, we evaluate the CML rainfall estimates against a dense automatic gauge network (∼100 gauges), for ∼3 months (October 2014 to January 2015).

The evaluation of (individual) CML estimates against collocated gauge observations yields promising results, as rainfall retrievals from ∼20 CMLs (∼1/10 of the CML network) showed a correlation larger than 0.6 and a relative bias smaller than 25 %. Rainfall estimation for a subtropical climate is highly relevant, given that many countries with few rainfall observations are located in this climate zone.

8.10 NEW C-BAND, 1-DEGREE, DUAL-FREQUENCY, DUAL-POLARIZATION, FAST-SCANNING 2X 1MW, MOBILE RADAR

JOSHUA WURMAN[1], KAREN KOSIBA[1]

[1] Center for Severe Weather Research, USA
jwurman@cswr.org

We are constructing a new quickly-deployable self-assembling dual-polarization, dual-frequency C-band Radar On Wheels (COW) which uses innovative design to achieve quick targetability and good penetration ability into intense precipitation, combined uniquely with fine spatial-and-temporal resolution, narrow-beamwidth , and fast volumetric scanning.

The COW mobile radar employs an innovative design enabling compromises inherent to existing mobile/deployable radars to be circumvented, with an only minor loss in "nimbleness".

Key aspects of the COW are:

- C-band for moderate precipitation penetation
- 1-degree beamwidth, similar to DOWs, for fine-spatial scale observations, using 3.8 m antenna
- Dual-frequency fast-scanning (2x independent samples) of rapidly evolving severe weather
- Dual-polarization with dual-frequency (45 and H/V modes configurable)
- 2x 1 megawatt transmitters for clear-air sensitivity to great range

The COW achieves 1-degree beamwith, transportabilility and fast deployment capability, through an innovate design including a integrated crane used to quickly self-assemble its 3.8 m diameter antenna.

The COW will be completed in Summer 2018. We hope/plan to deploy the COW in a variety of projects including RELAMPAGO (maybe), and future proposed projects such as PRECIP (typhoons), RadFire (wildfires). COWs unique capabilities can be used in future tornado, QLCS, MCS, and winter studies.

8.11 THE CSU SEA-POL SHIP-BOARD RADAR: SALIENT FEATURES AND FIRST RESULTS

J. GEORGE[1], V. CHANDRASEKAR[2], S. RUTLEDGE[3] (F. JUNYENT, P. KENNEDY)

[1] CSU-CHILL Radar, Colorado State University
[2] Electrical and Computer Engineering, Colorado State University
[3] Atmospheric Science, Colorado State University
jgeorge@colostate.edu

Sea-Pol is ship- and land-deployable dual-polarization meterological radar system developed at Colorado State University. It is designed for operation aboard Global-class research ships operated by the US oceanographic community. The radar operates at C-band (5.65 GHz) and has a 4.3 meter stabilized antenna system. An inertial navigation unit (INU) is used to measure and compensate for ship platform motion. The radar can operate in simultaneous-transmit, simultaneous-receive (STSR) mode, as well as horizontal-transmit, simultaneous-receive mode. The radar uses a 250 kW coaxial magnetron transmitter capable of a variety of pulse widths and PRFs within a 0.12% duty cycle limit. The radar has a sensitivity of -7 dBZ at 100 km range. The radar is designed to be easily transported by virtue of being packaged in standard ISO-668 1C containers. Special care was taken to make Sea-Pol rapidly deployable and able to withstand the harsh environmental conditions aboard research ships on the open ocean.

The radar completed its first deployment cruise aboard the R/V Revelle in the Inter-tropical Convergence Zone (ITCZ) in Pacific Ocean between October and November 2017. This was part of the SPURS-2 campaign, designed to study the fate of freshwater rain puddles on the upper ocean. Sea-Pol provided rainfall rate estimation over a 150 km range around the ship.

The paper presents an engineering overview of the radar, including its salient features that make it a world-class instrument. The dynamic stabilization system performance is shown. We then present example cases of data recorded during the SPURS-2 campaign. Data was recorded during various regimes, including rare thunderstorm activity over the open oceans and stratiform precipitation.

In summary, the Sea-Pol radar was developed and successfully deployed in a marine environment. Measurements taken while at sea demonstrated very good dual-polarization performance, and showed that the platform stabilization system suppressed platform motion to within 0.1°.

8.12 ON THE USE OF HORN ANTENNA TO CALIBRATE THE MPAR ADVANCED TECHNOLOGY DEMONSTRATOR

IGOR R. IVIĆ[1,2]

[1] Cooperative Institute for Mesoscale Meteorological Studies, University of Oklahoma
[2] NOAA/OAR National Severe Storms Laboratory, Norman, Oklahoma, USA
igor.rade.ivic@gmail.com

The goal of a Spectrum Efficient National Surveillance Radar (SENSR) initiative in the U.S. is to explore solutions for vacating the 1.3-1.35 GHz radio frequency band (currently occupied by the FAA/DoD/DHS systems) so that it can be auctioned to the private sector. One option is the Multifunction Phased Array Radar (MPAR) which seeks to combine the aircraft detection and tracking as well as weather surveillance into a single polarimetric PAR system. While the functionality of PAR technology for point targets is well-established, accurate polarimetric measurements of distributed targets using this technology have not yet been demonstrated. Currently, the cylindrical and planar architectures are being assessed for MPAR. The latter provides greater flexibility to perform point target and weather functions but (at least in theory) presents a greater challenge to achieve sufficient accuracy for polarimetric weather measurements. To evaluate the performance of a planar polarimetric PAR for weather surveillance, MPAR Advanced Technology Demonstrator (ATD) is being constructed by the MIT Lincoln Laboratory and will be installed in Norman, OK. To perform calibration functions, a tower with the horn antenna will be installed near the ATD site. It will be used to measure the peaks of the ATD antenna patterns on transmit and receive. To account for the system induced errors, these measurements will be used to correct the power measurements from the horizontal and vertical channels, as well as the cross-correlation estimates. But, the limited accuracy of beam peak measurements will affect the correction quality. Herein, an assessment of the beam peak measurement errors as well as their effects on the accuracy of polarimetric variable estimates is presented.

8.13 THE LIDAR RADAR OPEN SOFTWARE ENVIRONMENT (LROSE) "BLAZE" RELEASE

MICHAEL M. BELL[1], MICHAEL J. DIXON[2], WEN-CHAU LEE[2]
[1] Colorado State University, USA
[2] National Center for Atmospheric Research, USA
mmbell@colostate.edu

The Lidar Radar Open Software Environment (LROSE) is being developed to meet the challenges of complex lidar and radar processing needs and help address the "big data" problem faced by users in the research and education communities. Through support from the National Science Foundation, the LROSE project is developing a "Virtual Toolbox" stocked with core algorithm modules for those typical processing steps that are well understood and documented in the peer-reviewed literature. The first formal release of LROSE is called "Blaze" (a climbing rose) and focuses on key software building blocks for data processing: Convert, Display, Quality Control, Grid, Echo, and Wind. The Blaze release consists a suite of well-documented software modules for performing radar and lidar analysis with tutorials and starter kits aimed at facilitating community development and enhancement. By combining the open source approach with recent developments in virtual machines and cloud computing, we are developing a system that is both highly capable and easy to run on virtually any hardware, without the complexity of a compilation environment. The Blaze release of LROSE will be presented, along with a roadmap for future software releases.

8.14 VERTICAL WIND PROFILE MEASUREMENTS ON THE OPERATIONAL WEATHER RADAR IN "WIND PROFILER" MODE

Yu.B. PAVLYUKOV[1], A.V. TRAVOV[1], N.A. EROSHKINA[1]

[1] Central Aerological Observatory, Russia

yupav@orm.mipt.ru

The report presents the preliminary results of the experiments started in 2017 on the measurement of the vertical wind profile by operational weather radar in a special "wind profiler" (VWP) observation mode.

Radar observations were made in Dolgoprudny Moscow region by DMRL-C, Russian C-band dual-polarization doppler weather radar with pulse compression. 34 DMRL-C radars are in operational use on Russian territory now.

Radar observations in VWP mode are carried out every 10 minutes at a single scanning angle after the end of the routine radar survey. 10-μs pulses with step-phase-modulation at PRF 3,3 KHz are used for observations.

A special feature of our VWP measurement method is the use of Discrete Fourier Transformation (DFT) to process Doppler data at each range bin by a special module for digital signal processing based on the NVIDIA CUDA platform with a sampling rate of 10 MHz that provides Doppler radar measurement resolution with 15m on distance and 0.5° on the azimuth.

VAD-method application provides wind speed components calculation with height resolution of 15m $*$sin (el), where el is the radar scanning angle. Our experiments were carried out with 30° and 60° elevation angles.

The results of radar observations under different weather conditions were analyzed: from "clear sky" weather to a thunderstorm.

The radar measurements were compared with high-resolution upper-air sounding data of GRUAN 27612 ≪Dolgoprudny≫ station, that is located at the same point.

The good agreement of wind data on the speed and direction up to the upper boundary of the radio-echo is revealed.

8.15 USING THE SPARC SIMULATOR TO REFINE AND JUSTIFY SENSR WEATHER SURVEILLANCE REQUIREMENTS

F. NAI[1,2] C. CURTIS[1,2], F. NAI[1,2] D. SCHVARTZMAN[1,2], J. BOETTCHER[1,2] S. TORRES[1,2]

[1] Cooperative Institute for Mesoscale Meteorological Studies
[2] The University of Oklahoma, and NOAA/OAR National Severe Storms Laboratory, Norman, Oklahoma, USA
chris.curtis@noaa.gov

The Spectrum Efficient National Surveillance Radar (SENSR) program seeks to replace the weather and aircraft surveillance capabilities of current, USA-government-owned, ground-based radar networks to enable 30 MHz of spectrum in the L band to be auctioned in 2024. A multi-agency study is being conducted to assess the feasibility of reallocating the capabilities of current L-band radars while addressing cross-agency mission needs. The Signal Processing and Radar Characteristics (SPARC) simulator is being utilized to help refine and justify, in terms of National Weather Service mission benefit, the SENSR weather radar surveillance requirements that will be provided to industry. The SPARC simulator ingests archived moment WSR-88D radar data fields to produce realistic time-series simulations that present a wide variety of weather events as if they were observed by radar systems with similar or inferior performance characteristics. SENSR requirements that are being studied include antenna and range sidelobe levels, azimuthal sampling, dwell time, and sensitivity. Weather events with mission-critical features are being gathered so that time-series data can be simulated to show the expected performance of radar systems with different characteristics. The radar data fields obtained from the simulated time-series data are then analyzed quantitatively and qualitatively to explore the impacts of relaxing some of the cost-driving requirements. This analysis includes looking at the effects of using a phased array antenna, since one possible candidate for meeting the demanding SENSR requirements is a multifunction phased-array radar (MPAR).

8.16 CHARACTERIZATION OF WIND TURBINE CLUTTER ON THE RADAR NETWORK AT THE SOUTHERN GREAT PLAINS ARM SITE

B. ISOM[1], I. LINDENMAIER1[1]

[1] Pacific Northwest National Laboratory, USA
bisom@pnnl.gov

The Atmospheric Radiation Measurement (ARM) research facility deploys and operates a wide variety of instrumentation at strategic locations around the globe to better understand and represent the Earths atmosphere. Radar systems are a valuable component of the ARM instrumentation suite because of their ability to observe cloud and precipitation particles over a broad region at a high temporal and spatial resolution. The ARM radar group operates several scanning, polarimetric radars at multiple frequencies across the globe that are designed to observe clouds and precipitation in marine, continental, and arctic environments at both fixed and mobile sites. One of the oldest and most extensive fixed sites is the northern Oklahoma Southern Great Plains site (SGP). In recent years, the area has seen a tremendous increase in the number of wind turbines around the site, which has a positive impact on the environment, but can have negative impacts on the radar data.

Wind turbine clutter (WTC) is a form of interference caused by wind turbines that can appear on radars and is very difficult to mitigate. The dynamic nature of the clutter means it occupies the same Doppler/frequency domain as is typical with atmospheric returns, and normal ground clutter filtering techniques do not apply. Given the present situation, coupled with the potential for additional wind turbines, discussions within ARM regarding current and future impacts are occurring. A study involving multiple radars at multiple frequencies is underway and focuses on the characterization and identification of WTC. This work will describe the impact of the wind turbines on the ARM radar data, characterize the signals, and discuss opportunities for identification and masking WTC.

8.17 THE GAMIC WAVE SENSING RADAR AND THE GD-APS FUTUREWAVES WAVE AND VESSEL MOTION FORECASTING SYSTEM

S. GERHARDS[1], J. KUSTERS[2], J. MERTENS[3], M. TOUSSAINT[4], D. VEERKAMP[5]

[1] GAMIC mbH, Germany, [2] GD-APS, USA, [3] GAMIC mbH, Germany, [4] GAMIC mbH, Germany, [5] GAMIC mbH, Germany
gerhards@gamic.com

The GAMIC Wave Sensing RADAR (GWSR) is a new sensor designed to measure the characteristics of oceanic waves. It is used in the "FutureWaves" wave and vessel motion forecasting system developed by GD-APS.

The RADAR system is technically derived from the GMWR-25-SP weather radar. It uses a 25 kW X-Band magnetron and a slot antenna rotating at up to 24 rpm. In order to provide a high spatial resolution of 7.5 m, a pulse length of 50 ns is utilized. At the same time a new GAMIC intermediate frequency digitizer (IFD), with a 500 MHz sampling rate, in combination with a proven STALO from the GMWR range of weather radars, ensures a high Doppler resolution. The signal processor is based on the technology and on the algorithmic experience that makes up the ENIGMA IV Signal Processor.

The GD-APS FutureWaves^{TM} system leverages the capabilities of the GWSR in order to get high quality data as an input to a phase-resolved oceanic wave forecasting model. The output of this wave model drives a real-time vessel-motion model to provide precise timing and magnitude of vessel motions for minutes before they actually occur.

The poster will present the two systems in detail and an overview of the scientific principles employed. We will also provide a short synopsis of possible applications of the system.

8.18 PROGRESS IN THE PROGRAM FOR EARLY DETECTION OF TORRENTIAL RAINFALL BY USING MULTI-PARAMETER PHASED ARRAY WEATHER RADAR IN JAPAN

N. TAKAHASHI[1], K. IWANAMI[2], M. KAWASAKI[3]

[1] Institute for Space-Earth Environmental Research, Nagoya University
[2] National Institute for Earth Sciences and Disaster Prevention
[3] National Institute for Land and Infrastructure Management
ntaka@nagoya-u.jp

The project named "Development of multi-parameter phased array weather radar (MP-PAWR) and the early detection/mitigation of torrential rainfall and tornado risks", was started in 2014 as a part of the Cross-ministerial Strategic Innovation Promotion Program (SIP) under the Council for Science, Technology and Innovation of Japanese government, and its overview is introduced in previous ERAD in Antalya, Turkey.

In this report, recent progresses of this project will be presented. The MP-PAWR was developed in 2017 and installed at Saitama University located about 30 km north of down town Tokyo. Until the MP-PAWR was completed, the project was weighted on the study how to provide information of the early detection of torrential rainfall as users requires. We have defined six major product regarding the disaster relating to the torrential rainfall, 1) early detection of torrential rainfall, 2) inundation prediction and nowcasting, 3) high wind and tornado warning, 4) river water level prediction, 5) sediment disaster prediction and 6) railway disaster mitigation system. Currently, the target users are disaster prevention section of local government and citizens. Even in the disaster prevention section, the requirements for lead time, spatial resolution and accuracy are different for the purposes such as sewerage management, park management and prevention of underpass inundation. We have refined our product by co-working with the users. For example, we have worked with the Osaka prefecture government to provide the early detection information of torrential rainfall using Phased Array Weather Radar (PAWR) which is single polarization radar. In this case, we provided warning system consists of warning light and PC to each local office. When the PAWR detect the torrential rainfall, it is notified the local office immediately, and the local officer takes an action based on the agreed procedure. Another example is the social experiment of a torrential rainfall warning system targeting about 2000 citizens. In this experiment, users get the warning of torrential rainfall of the registered location on their smart phone.

In the summer 2018, we are going to have experiment using MP-PAWR over Tokyo metropolitan area and demonstrate the effect of the MP-PAWR and its utilization of disaster mitigation.

8.19 A SYSTEM FOR SYNCHRONIZED MULTI-RADAR SCANNING FOR METEOROLOGICAL REMOTE SENSING

C. J. WALDEN[1], M. FORTESCUE[2], M. L. TRETHEWEY[2], D. N. LADD[1], A. DOO[1]

[1] STFC Chilbolton Observatory, U.K.
[2] Control Loop Concepts Ltd., U.K.
chris.walden@stfc.ac.uk

We report on new developments at Chilbolton Observatory in the UK that enable coordinated scanning of multiple radars, and their initial application in support of the PICASSO (Parameterizing ice clouds using airborne observations and triple-frequency Doppler radar data) campaign. The inter-radar communication and control protocols were originally devised as part of a programme of work to track space hardware (orbiting satellites and debris). This is their first use in atmospheric science, and follows a need to coordinate multiple wavelength radar observations with in-situ aircraft measurements from the FAAM (Facility for Airborne Atmospheric Measurements) aircraft. The observations involved automated steering of the radar antennas using position data streamed from the aircraft via satellite communications links. The architecture has been designed to be extensible, and may be readily applied to cases where the radars are geographically separated.

8.20 CALIBRATION OF THE POLARIMETRIC PHASED ARRAY WEATHER RADAR USING THE COMPUTATIONAL ELECTROMAGNETICS APROACH THE DIFFERNTIAL PHASE

DJORDJE MIRKOVIC[1,2], D.S. ZRNIC[2]

[1] The Cooperative Institute for Mesoscale Meteorological Studies (OU), USA
[2] The National Severe Storms Laboratory (NOAA), USA
djordje.mirkovic@noaa.gov

The polarimetric weather observations with planar phased array radar (PPAR), require radar′s calibration at each pointing direction. Preliminary polarimetric data collection at the NSSL, using the Ten Panel PPAR demonstrator (TPD), in light rain with the radar antenna pointing at the zenith, reviled some of the issues traced to the radar hardware. Measurements of the differential reflectivity indicated inconsistency of the broadside bias and concavity. The differential phase behaviour in measurements remained consistent between scans. The concave differential phase change with the pointing direction differs in the maximum swing it reaches depending on the radome conditions. Issues with the radome were caused by the structure support that created a tub in which rain water collected if antenna pointed at zenith.

The computational electromagnetic (CEM) model of the TPD antenna panel has been developed. Some ensuing patterns are compared withthe measurements provingaccurate co-polar and cross-polar radiation characteristics., Water coating 3mm thick is added to the radome to mimic the physical conditions at vertical incidence. For computing expediency this model considers only a single 8x8 element panel. The radome increases the differential phase as the beam is steered in the principal plane and the radome condition (either dry or wet) cause significant differential reflectivity bias compared to the one from the antenna without the radome. Nevertheless, the simulated increase of differential phase bias, due to radome setup, is not as significant as bias observed in measurements. To further study this issue we examine the effects using a 5x5 array of patch radiators and chose two location of the reference phase element.

In one the reference element is placed on the edge of the 5 by 5 array of patch radiators, and in the other the reference is in the center of the array. The beam is steered in the E-plane of the H polarization for angles of -45° to +45° away from broadside. Simulation results indicate an unexpected change of the differential phase bias ϕ_{DPbias} between the cases. The array with the reference element on the corner exhibites steady increase of the ϕ_{DPbias}, while the array with the reference element in the center of the array has minimal deviation of the ϕ_{DPbias} that remains close the zero.

8.21 ARE SENSRS TEMPORAL RESOLUTION REQUIREMENTS FOR THE WEATHER FUNCTION FEASIBLE USING ADAPTIVE SCANNING?

D. SCHVARTZMAN[1], S. TORRES[2]

[1] Cooperative Institute for Mesoscale Meteorological Studies, University of Oklahoma
[2] NOAA/OAR/National Severe Storms Laboratory, USA
david.schvartzman@noaa.gov

Collaboration between several U.S. government agencies initiated the Spectrum Efficient National Surveillance Radar (SENSR) program in 2016, which aims to replace the weather and aircraft surveillance capabilities current operational U.S. radar networks, to reallocate 30 MHz of spectrum in the L band to be auctioned in 2024. Whereas there are no restrictions specified in SENSR′s "Preliminary Performance Requirements" document regarding the type or types of systems that would be required, one possibility involves consolidating several operational radar networks into one multi-function phased-array radar (MPAR) network. These competing functions could share the MPAR time to meet SENSR requirements. Due to the limited radar occupancy allocated per function, load-shedding algorithms would have to be developed to efficiently use the radar time while meeting the stringent requirements or achieving the best compromise in terms of meeting the mission needs of the different agencies. For the weather surveillance function, one way to address this is by developing adaptive scanning strategies that exploit MPARs beam agility to surveil the atmosphere using focused and tailored observations. Adaptive scanning involves navigating a complex space of trade-offs on which the spatial sampling, temporal resolution, and data quality are tightly coupled. Improving one of these invariable deteriorates the others, thus, developing a strategy able to provide weather surveillance that meets the demanding requirements within the radar occupancy assigned can be challenging. In this paper, we explore the use of adaptive scanning strategies to meet SENSRs requirements for the weather function using a realistic radar simulator. Through realistic simulations, we can quickly and inexpensively explore the complex space of tradeoffs using different adaptive scanning techniques, and analyze the impact on meeting the mission-critical requirements. The simulator takes archived WSR-88D base data as input and produces two-dimensional, dual-polarization time series data that results in realistic fields of radar variable estimates after processing. Through a closed command-and-control loop, simulated scans are ingested by an adaptive scanning algorithm which defines the strategy for the subsequent scan. Results of this work are expected to contribute to NOAAs initial SENSR feasibility study by providing a qualitative assessment of different tradeoffs on radar requirements that results in no or minimum impact on the weather surveillance mission.

8.22 WATER VAPOR ESTIMATION USING REFLECTED WAVE OF DIGITAL TERRESTRIAL BROADCASTING WAVE

T. KOUKETSU[1], S. KAWAMURA[1], H. HANADO[1], H. OHTA[1]

[1] National Institute of Information and Communications Technology, Koganei, Tokyo, Japan

kouketsu@nict.go.jp

The number of flood disasters brought by rapid-diveloping cumulonimbi in urban areas is increasing. For disaster prevention, it is necessary to detect such cumulonimbi, which rapidly develop in localized area, as soon as possible. Weather radar can detect them only after hydrometeors are formed from water vapor. For early detection of sign of cumulonimbus generation from the stage of water vapor, it is important to measure the spatial distribution of water vapor.

It has become well-known that precise information of spatial distribution of water vapor is necessary for the precise quantitative precipitation forecast (QPF) using high resolution numerical model. However, the measurements of water vapor are still sparse and lacking for precise QPF, although estimation of precipitable water vapor (PWV) with Global Navigation Satellite System (GNSS) have been realized.

The authors have been developing a method of water vapor measurements near the surface with propagation delay of digital terrestrial broadcasting wave due to water vapor (Kawamura et al., 2017). The basic idea of using propagation delay is the same as that of retrieving PWV using GNSS. We estimate water vapor amount near the surface from the horizontal propagation delay of digital terrestrial broadcasting waves.

The propagation delay is quite small and masked by phase fluctuations of local oscillators of transmitter and receiver of broadcasting waves. To cancel these phase fluctuations, we used the phase difference of direct wave from a broadcasting tower and reflected wave from some reflector(s), such as building or transmission line tower, opposite direction of the broadcasting tower. This gives us a pure propagation delay and the information of pass integrated water vapor amount between the receiving point and the reflector(s).

For the utilization of the integrated water vapor amount for the input of numerical model, it is necessary to identify the reflector with its range and direction, which determine the pass of propagation delay by water vapor. For this purpose, we have tried estimation of angle of arrival (AOA) of reflected wave. For the measurement of water vapor in this study, we used commercially available antennas for receiving digital terrestrial broadcasting wave. Such antennas have large beam width (several tens degrees for half-value width) and not enough for AOA.

To overcome this problem, we used plural receiving antennas to detect the path length differences and calculate the AOA geometrically.

In the presentation, we will introduce our results of water vapor measurements.

References

Kawamura, S., et al. (2017), Water vapor estimation using digital terrestrial broadcasting waves, Radio Sci., 52, 367377, doi:10.1002/2016RS006191.

Session 9. Nowcasting and Blending Techniques



Keynote presentation

9.1 STATISTICAL LEARNING OF OROGRAPHIC PRECIPITATION GROWTH AND DECAY PATTERNS FROM A 10-YEAR RADAR ARCHIVE IN THE SWISS ALPS

L. FORESTI[1], I.V. SIDERIS[1], L. BEUSCH[1,2], D. NERINI[1,2], U. GERMANN[1]

[1] Swiss Federal Office of Meteorology and Climatology, MeteoSwiss, Switzerland
[2] Institute for Atmospheric and Climate Science, ETH, Zürich, Switzerland
loris.foresti@meteoswiss.ch

Meteorological data archives are becoming more and more important for data-driven research. Useful information can be extracted from the data archives to improve the forecasting of weather in real-time, for example by using statistical post-processing techniques or by retrieving a set of similar analogue situations from the past.

Machine learning provides an algorithmic approach to solve classical statistical learning problems, which allows finding robust solutions to non-linear classification and regression problems in high dimensional spaces. Machine learning algorithms (MLA) are designed specifically to maximize the predictive performance without making strong assumptions about the data distribution (e.g. gaussianity), and thus they have a great potential to enhance the skill of weather forecasting models. This study employs MLA to derive orographic precipitation growth and decay patterns from a 10-year archive of composite radar images in the Swiss Alps. More precisely, the precipitation growth and decay is predicted for one hour lead time using as predictors the geographical location, the direction and speed of the mesoscale flows, and the freezing level height. This knowledge is used in a predictive framework to improve real-time nowcasting based on the Lagrangian persistence of radar precipitation echoes to account for the influence of orography.

9.2 THE NOWCASTING POTENTIAL OF LIGHTNING-JUMPS IN CONVECTIVE CELLS TRACKED BY RADAR IN COMPLEX OROGRAPHY

ALESSANDRO HERING[1], LUCA NISI[1], ULRICH HAMANN[1], URS GERMANN[1]

[1] Federal Office of Climatology and Meteorology MeteoSwiss, Via ai Monti 146, 6605 Locarno-Monti, Switzerland
alessandro.hering@meteoswiss.ch

The developing phase of intense convective storms is often correlated with a sudden increase in the total lightning rate within thunderstorm cells. This abrupt increase, a so-called lightning jump, can occur from few minutes to some tenth of minutes before the onset of severe convective weather characterized by hail, wind gusts and heavy rainfall. Several studies suggest that lightning jumps can be used as predictors of severe weather, with the potential to increase the lead-time of real-time thunderstorm warnings, in combination with other parameters.

In recent years, a few algorithms have been developed to exploit the lightning jump potential for nowcasting severe thunderstorms. Ground-based total lightning detection networks and space-based detectors have been used. These algorithms were first applied on ground-based data over flat or hilly terrain, and later on the data measured by the new GOES-R Geostationary Lightning Mapper. A study on how lightning jumps behave in storms over the complex orography of the Alps was until now missing. A robust, 5-year statistical analysis of thunderstorm cells and total lightning data was performed to fill this gap. About 8400 hail storms were automatically detected and tracked by the Thunderstorms Radar Tracking (TRT) algorithm based on volumetric radar data from the MeteoSwiss network, and compared to more than 50,000 non-severe convective storms. The total lightning rate (CG and IC) from an operational ground-based lightning detector network was used. Results show an average lead-time of the lightning jumps to hail initiation inside the storm cells of about 20 minutes. However, only approximately 32% of hail storms produce a lightning jump before hail initiation.

Based on these findings, for nowcasting and warning purposes, MeteoSwiss has developed a real-time prototype algorithm for the automatic lightning jump identification and display. It uses the total lightning rate from the operational network to identify the occurrence of lightning jumps based on the classical 2-sigma threshold. In addition for each cell the continuous value of the sigma-level, a metric of lightning jump strength, is also computed automatically and visualized for the forecasters in real-time. To this purpose the total lightning rate is computed inside each convective cell identified automatically by the tracking algorithm of the TRT nowcasting system. To fully exploit the high temporal availability of the lightning data, the temporal resolution has been increased to 2.5 minutes. The new algorithm is going to be integrated in the convection nowcasting and warning systems already in use at MeteoSwiss such as TRT, COALITION, NowPAL and INCA.

In this paper the nowcasting potential of lightning jumps is analyzed and discussed based on a 5-year statistical study, and a first real-time prototype for the use in the complex Alpine orography is presented. An outlook on future operational applications is also provided.

9.3 NOWPRECIP: AN ALGORITHM FOR LOCALIZED PROBABILISTIC PRECIPITATION NOWCASTING IN THE COMPLEX TERRAIN OF SWITZERLAND

I.V. SIDERIS[1], L. FORESTI[1], U. GERMANN[1], D. NERINI[1,2]

[1] Swiss Federal Office of Meteorology and Climatology, MeteoSwiss, Switzerland
[2] Institute for Atmospheric and Climate Science, ETH, Zrich, Switzerland
ioannis.sideris@meteoswiss.ch

This presentation describes the new precipitation nowcasting system "NowPrecip" which has been developed in MeteoSwiss. The new algorithm is area-tracking, fully probabilistic, and capable of producing multi-member ensembles of possible evolutions. It follows the seamless forecasting approach: evolution starts from the last radar observation and merges smoothly into the numerical weather prediction ensemble members.

The algorithm introduces five new ideas. (a) A geostatistics-based optical flow algorithm. This approach is spatiotemporally coherent and minimizes artefacts on zero-precipitation areas where the motion field may be difficult to determine. (b) A localized approach of the nowcasting problem, as opposed to the typical one which operates on the entire-domain. The localized philosophy has been motivated by the need to deal with situations where different rainfall patterns characterize different parts of the domain (for example stratiform precipitation in the north, convective precipitation in the south). This is relevant for Switzerland, but it can also be relevant for single areal nowcasting operating in large countries or extensive regions. (c) A straightforward technique to compute and include systematic growth and decay typically associated with the underlying topography, mainly the orographic effects. (d) The ability to use machine-learning inputs as a replacement or a complement to the typical Lagrangian persistence ones. This relies on the aforementioned localized design and suggests a full methodology for employing state-of-the-art machine learning algorithms into nowcasting. Proper implementation of such algorithms could capture growth and decay patterns which are by-design ignored in Lagrangian persistence schemes. (e) Capabilities to incorporate and micro-control individual precipitation cells into the evolution. This technique is used to generate and control the evolution of cells, in terms of size, intensity and shape, directly and seamlessly into the precipitation domain. W We essentially attempt to broaden the links between an area-tracking process and object-tracking or satellite-based convection initiation procedures and amplify the benefit an area-tracking algorithm can get from such connections.

9.4 DERIVING AND COMPOSITING MOTION FIELDS SPEED AND QUALITY CHALLENGES

M. PEURA[1], H. HOHTI[1], T. PERTTULA[1]

[1] Finnish Meteorological Institute, Helsinki, Finland
markus.peura@fmi.fi

In weather radar data, atmospheric motion vectors (AMV's) can be extracted using two alternative approaches: by using Doppler measurements directly, when operationally available, and by detecting apparent, visual motion in consecutive images of reflectivity. Both approaches involve challenges. Doppler measurement is beam-directional, hence principally one-dimensional, and further subject to ambiguity problem caused by aliasing (wrapping, folding) around the Nyquist velocity range. Detection of visual motion depends critically on applied window scale and level of detail in image frames. In addition, there are challenges shared by both approaches, like essentially three-dimensional structure of original velocities and definition of prevailing motion field in the presence of local phenomena like convection.

Aiming at renewing the current radar-based short-time precipitation forecast scheme "Tuliset" in the Finnish Meteorological Institute, we have tested optical flow based methods for deriving motion field. Two requirements have proven central at this stage. Firstly, computational complexity of any algorithm candidate should be analysed and fitted to operational (five-minute) production cycle. Secondly, quality control should be applied for both in preprocessing input and in the actual computation to ensure smooth, reliable vector fields. The performance of the end products precipitation forecasts depends directly on the quality of the vector input.

In this paper, we present how two-dimensional atmospheric motion fields generated from Doppler data and optical flow algorithm can be combined smoothly using quality information. That information is obtained by combining input quality fields and mathematical uncertainty of the motion vector computation. While these motion fields are somewhat different by nature motion of hydrometeors vs. motion of precipitation area the key assumption is that these fields complete each other when combined appropriately. We demonstrate the performance of the suggested methods in variable types of precipitation.

9.5 LOCALIZED VARIATIONAL BLENDING FROM INCA AND AROME-RUC

A. ATENCIA[1], A. KANN[1], Y. WANG[1], F. MEIER[1]

[1] ZAMG-Zentralanstalt für Meteorologie und Geodynamik, Wien, Austria
aitor.atencia@zamg.ac.at

Data assimilation (AROME-Rapid Update Cycle) has been proved to help solving some problems of the numerical weather prediction models such as the spin-up time and the disagreement with high resolution observations. However, these computational expensive techniques do not provide quantitative precipitation forecast able to beat the observation based lagrangian extrapolation nowcasting (INCA) of fields such as precipitation for the first hours.

These two sources of forecast do not tend to agree in the overlapping forecasting period (6 hours for nowcasting). To solve this problem, they are usually blended by adding one forecast to the other one multiplied previously by a weight, which depends on the quality of each source of forecast. In this paper, a new blending technique, most complex than a regular global weight, is developed. The technique takes advantage of variational techniques to merge both forecasts in a location dependence framework while keeping the spatial structure of the rainfall field.

The final blended nowcasting is verified for two different periods; July 2016 and January 2017, against the original nowcasting from INCA and AROME-RUC, and also against a global weighted blended nowcasting. Some statistical properties such as the variance of the field and the power spectrum for different scales are compared with the observed field in order to highlight the advantages of this variational technique.

9.6 IMPROVED RAINFALL NOWCASTING BY NON-STATIONARY MOTION VECTOR FROM BURGERS EQUATION

GYUWON LEE[1,2], SOOROK RYU[1], GEUNSU LYU[2], HONG-MOK PARK[2]

[1] Department of Astronomy and Atmospheric Sciences, Kyungpook National University, Daegu, South Korea

[2] Center for Atmospheric REmote sensing, Kyungpook National University, Daegu, South Korea

gyuwon@knu.ac.kr

Major limitations in radar-based rainfall nowcasting are 1) growth/decay and 2) non-stationarity of advection. In this work, we propose an advection diffusion equation to smooth forecast field for different lead time. Motion vectors are updated at each time by solving a system of two dimensional (2D) Burgers′ equations to take into account non-stationarity of motion vectors to improve advection of rainfield. The initial motion vector field is first derived by variational echo tracking (VET) algorithm. The time dependent advection or advection diffusion equation is solved alone or with 2D Burgers′ equation. Forecasts are then generated at each time step by solving these equations. Finally, these new forecasts are compared with the Lagrangian extrapolation scheme (MAPLE). The high-resolution forecasts are generated every 2.5 min up to 3 h for 6 rainfall events over 250 x 250 km area in southeastern Korea. To examine the effects of diffusion term and non-stationary motion vectors (obtained from Burgers′ equation), we generated four types of forecasts: advection equation (Type 1), advection equation with Burgers′ equation (Type 2), advection diffusion equation (Type 3), and advection diffusion equation with Burgers′ equation (Type 4). The forecasts from the Type 1 method was very similar as the ones of MAPLE. The other models (Type 2-4) clearly have better skill scores and correlations compared with MAPLE up to lead time of 3h on average. In addition, the non-stationary motion vectors significantly improve the forecast skill.

9.7 FROM QUALITATIVE TO QUANTITATIVE HAIL NOWCASTING

A. BELL[1], E. MORGAN[1], A.SEED[1], M.CURTIS[1], R.BUNN[1]

[1] Bureau of Meteorology, Australia

aurora.bell@bom.gov.au

The current state of the art in hail nowcasting is based on semi-quantitative products because the science is not yet ready to deliver the quantitative products that the customers need. The Bureau has developed Rainfields3 to perform radar data quality control and rainfall estimation, which will be used to deliver semi-quantitative hail products. The solution was to use proven algorithms immediately, and work with the end-users so they can make optimum use of these products.

The paper will present the Bureau's road map for enhancing hail nowcasting through the use of dual-pol S-Band radars. Major mile-stones are:

- Upgrade of the 4 S-Band radars that serve the major Australian cities to dual-polarimetry.
- Improve the single-pol hail service. The Bureau developed gridded products of probability of hail of specific size based on reflectivity (single-pol) and integrated them in Rainfields3
- Adopt the NCAR Particle ID algorithm for Dual-Pol data and integrate it in Rainfields3
- Tune the two types of algorithms (dual-pol and single-pol) for consistency using case-studies and workshops with end-users
- Develop training and evaluate the changes.

The "6^{th} element" is to motivate the science community to improve the current state of the art.

9.8 A BAYESIAN COMBINATION OF RADAR-BASED NOWCASTS WITH COSMO-E PRECIPITATION FORECASTS

D. NERINI[1,2], U. GERMANN[1], L. FORESTI[1]

[1] Federal Office of Meteorology and Climatology MeteoSwiss, Switzerland
[2] Institute for Atmospheric and Climate Science, ETH Zurich, Switzerland
daniele.nerini@meteoswiss.ch

The radar-based nowcasting of precipitation employs real-time data from a network of weather radars to produce an extrapolation forecast for the coming few hours. The main assumption relates to the persistence of observed precipitation echoes in moving coordinates, which eventually determines the predictability and uncertainty of the nowcast. One important task of nowcasting is thus to correctly quantify such uncertainty and use that information to optimally blend the radar extrapolation with the forecast from a numerical weather prediction (NPW) model.

Typically, nowcasting systems have based their blending schemes on empirical rules using fixed linear weights pre-calculated with some long-term forecast error statistics. More sophisticated systems have tried to assess in real-time the relative skill of nowcast and NWP forecast in order to introduce some flow-dependency in the merging of the two.

In this study, we propose a nowcasting blending scheme based on the ensemble Kalman filter approach. The prediction step of the filter is implemented as a standard radar extrapolation technique, while the update step uses the spread of the NWP ensemble (COSMO-E, in this study) to integrate the radar nowcast with the NWP forecast in a Bayesian fashion.

Results for several precipitation events over the Swiss Alps are presented, while a number of implementation issues are discussed. In particular, we propose to perform the update step of the ensemble Kalman filter in the Principal Component subspace in order to simplify the task of computing and inverting the error covariance matrices with high-resolution precipitation fields.

9.9 BLENDING FIELD-BASED AND CELL TRACKING METHODS FOR IMPROVED PRECIPITATION NOWCASTING

S. PULKKINEN[1], V. CHANDRASEKAR[2]
[1] Finnish Meteorological Institute, Finland
[2] Colorado State University, United States
seppo.pulkkinen@fmi.fi

The present radar-based precipitation nowcasting methods can be broadly divided into two categories: 1) field-based advection extrapolation and 2) cell-based methods that identify and track the motion of high-intensity areas as separate entities. Both can be extended to produce probabilistic nowcasts by adding stochastic perturbations.

The assumptions of field-based methods include 1) logarithm of precipitation intensities follows the normal distribution 2) predictability is proportional to spatial scale and 3) the spatiotemporal structure of precipitation can be modeled as a Gaussian random field. While mostly valid, these assumptions fail to hold for intense convective precipitation having different spatiotemporal structure from the remaining precipitation field. Consequently, the stochastically generated nowcast ensembles are unable to reproduce such features.

On the other hand, cell-based methods are ideally suited for nowcasting convective precipitation. However, such methods discard information about low-intensity areas that are relevant for hydrological applications, where precipitation accumulations are of interest.

In order to address the above limitations, a statistical methodology for seamless blending of field- and cell-based nowcasts is proposed.

The field-based method used in this study is the Short-Term Ensemble Prediction System (STEPS). The basic principle is to use an advection-based nowcast, where ensembles are generated by adding stochastic perturbations to the precipitation intensity and advection fields. The intensity field is decomposed into multiple spatial scales, and the weights between the deterministic nowcast and the stochastic perturbation field are determined by predictability on each spatial scale.

The cell tracking is done by identifying and matching cells between consecutive time frames. Advection-based temporal interpolation is applied in order to improve the reliability of the matching. Additionally, a set of decision rules is applied to detect merging and splitting of cells. Estimation of the probability distributions of cell positions and velocities, from which ensembles are generated, is done by using a Kalman filter model.

Finally, the merging is done as a weighted average of the two nowcast ensembles. The weights are determined by a predictability measure that combines the critical success index (CSI) and autocorrelation for areas containing precipitation. It is shown that compared to the original STEPS, this approach leads to improved reliability of nowcasts for intense precipitation, which is relevant for risk management and providing early warning. The data used in the study is obtained from two different sources: the country-wide C-band radar network operated by the Finnish meteorological institute, and the dense high-resolution X-band radar network deployed in the Dallas Fort-Worth area on a small-scale urban environment.

9.10 USING WEATHER RADAR AND A NEW ICE MASS ESTIMATOR TO FORECAST LIGHTNING

EVAN RUZANSKI[1], V. CHANDRASEKAR[2]
[1] Vaisala, Inc., United States
[2] Colorado State University, United States
evan.ruzanski@vaisala.com

Short-term automated forecasts (nowcasts) of lightning are important for a number of applications to help save lives and resources. The presence of ice aloft is known to be a key component in the atmospheric electrification process. The measurement range, resolution, and volumetric nature of weather radar observations provide valuable data which are inherently different from those provided by currently operational lightning detection networks. Weather radar observations can be used to estimate ice mass aloft and are thus favourable for nowcasting lightning.

This paper describes a new model for estimating ice mass aloft using weather radar data. Previously, a simplified bulk microphysical model with fixed parameters was used to estimate ice mass aloft. The new weather radar-based ice mass estimator uses a novel numerical optimization approach to dynamically update the parameters of this bulk microphysical model to improve lightning nowcasts.

This paper also introduces a new approach to nowcasting lightning activity using weather radar data. Previous methodology used a cell-based approach to lightning nowcasting and verification, where storm cells were first identified, lightning activity was associated with a particular cell, but lead times and lightning locations were not specified in the nowcast. The new method described in this paper employs a grid-based approach to lightning nowcasting and verification. This approach leverages spatial correlations and potentially complex interactions between storm cells and atmospheric scales. It also makes specific nowcasts and verifications in space and time.

A novel verification approach is described and used to assess this first-flash lightning nowcasting performance. Preliminary results show that using the new ice mass model significantly improves nowcasts versus using the traditional weather radar-based ice mass estimator or lightning flash-rate density directly for nowcasting first-flash lightning occurrences. The radar data used for this study were collected by the KFWS Weather Service Radar-1988 Doppler radar located near Fort Worth, Texas, during a severe convective storm event occurring on 03 Apr 2014 from 000335 to 235741 UTC. The lightning data used for this study were collected by processing detections of lightning discharges from multiple Vaisala remote lightning sensors part of the National Lightning Detection Network within approximately 1000 km of the KFWS radar during the same time period. The Dynamic Adaptive Radar Tracking of Storms method was used to generate the radar reflectivity nowcasts which were converted to lightning nowcasts using the numerically optimized ice mass model.

9.11 OPTICAL FLOW MODELS BENCHMARKING FOR RADAR-BASED PRECIPITATION NOWCASTING

G. AYZEL[1], M. HEISTERMANN[1], T. WINTERRATH[2]

[1] Institute for Earth and Environmental Sciences, University of Potsdam, Potsdam, Germany

[2] Deutscher Wetterdienst, Department of Hydrometeorology, Offenbach, Germany

ayzel@uni-potsdam.de

Precipitation nowcasting is crucial for early warning of hazardous events at small spatiotemporal scales (tens of kilometers, lead times of a few hours). It has been shown that nowcasting systems, if operationalized, are both efficient and effective in reducing economic and human losses caused by heavy rainfall.

We have developed and benchmarked two classes of parsimonious precipitation nowcasting models based on gridded radar data and optical flow algorithms. The Python implementation of these algorithms is entirely based on open source software libraries, notably OpenCV, NumPy, SciPy, Scikit-learn, Scikit-image, and wradlib.

The first class ("sparse" optical flow) employs a continuous stack of feature detection, tracking, and extrapolation techniques followed by a spatial transformation routine based on image warping. The second class (dense optical flow) derives a full velocity field which is then used to compute the precipitation field displacement. Each model class consists of several variants with regard to the treatment of extrapolation and field displacement. We used the German Weather Services (DWD) RY radar composite product which provides estimates of instantaneous rainfall intensity at 5 minute intervals on a 1 km regular grid for a 900 km by 900 km domain.

For our benchmarking experiment, we used the following set up:

- nowcast lead time: one hour at 5 min intervals
- 11 events during summer periods of 2016 and 2017, that cover different durations, spatial coverage, precipitation intensities, and convection types
- two "sparse" optical flow model modifications that differ with regard to the temporal extrapolation of detected features
- two dense optical flow model modifications that differ with regard to the advection technique
- primitive benchmark model based on the Eulerian persistence
- DWD operational nowcasting model (RADVOR), namely the RV product, as advanced benchmark (5 minute intervals, 1 km resolution, 2 hours lead time)
- mean absolute error (MAE) and critical success index (CSI) with different thresholds for forecast verification

Results show that the use of standard optical flow techniques for extracting relevant information about precipitation field movement provides a firm basis for radar-based precipitation nowcasting. All models show significant skill over persistence. The dense optical flow model class shows comparable results with the

RADVOR operational model baseline. Nevertheless, heavy rainfall nowcasting for the lead times longer than 30 minutes is still the most challenging task for every model.

The computational time for one forecast at one hour lead time varies from 20 sec to 150 sec on a standard office computer for a “sparse” and dense optical flow model classes respectively. The overall performance in combination with the open source implementation allows for immediate application in different contexts, and a reliable baseline for developing more advanced models.

9.12 RADAR RAINFALL COMPOSITING: COMPARISON OF DIFFERENT METHODS

A. JURCZYK[1], J. SZTURC[1], K. OŚRÓDKA[1]

[1] Institute of Meteorology and Water Management National Research Institute, Poland
anna.jurczyk@imgw.pl

Most often employed technique for compositing of weather radar rainfall data is a maximum rainfall approach, however its disadvantage is that spurious echoes from all overlapping radar data are collected. The alternative solution is to use quality information (in form of quality index, QI) as a criterion for the data merging, which can be performed by taking: (i) data of maximum QI value, (ii) QI-weighted mean, (iii) QI-weighted mean from a limited number of data with the highest QIs. A main disadvantage of the QI-weighted mean version, which is underestimation of rainfall due to impact of data from far ranges, is partially minimised, although not completely, in the version with a limited number of data. The method proposed here employs, apart from the QI value, the distance from the radar site as the parameter which describes range-related errors as a key factor in underestimation of radar estimates at far ranges. Such merging is more efficient considering different aspects, especially such as weakening of non-meteorological echoes and smoothing borders between particular radars (which are visible applying the maximum QI version). The examples of different situations are presented to depict pro and contra of different QI-based approaches.

9.13 STOCHASTIC ENSEMBLE PRECIPITATION NOWCASTING IN WINTER CONDITIONS

S. PULKKINEN[1], E. SALTIKOFF[1], P. KARSISTO[1], A. VON LERBER[1]

[1] Finnish Meteorological Institute, Finland
seppo.pulkkinen@fmi.fi

Applying the conventional radar-based precipitation nowcasting methods in winter conditions poses unique challenges. In particular, snowfall at land-sea boundaries exhibits complex growth and decay, quasi- stationary and band-like patterns that are beyond the capabilities of the present methods.

The basic principle of radar-based probabilistic nowcasting is advection-based extrapolation, from which ensembles are generated by adding stochastic perturbations. Such techniques are based on several assumptions on the spatiotemporal structure of precipitation. These involve the distribution of precipitation intensities, power spectrum, scale-dependence of precipitation lifetime and spatial homogeneity of the precipitation process. The validity of the assumptions in winter conditions and the differences compared to summertime precipitation are discussed with examples.

This study is the first attempt to evaluate the feasibility of the Stochastic Ensemble Precipitation System (STEPS) in winter conditions. An enhanced version of STEPS has been implemented for this purpose in the Finnish Meteorological Institute (FMI). In summary, STEPS uses an optical flow technique and advection-based extrapolation, and nowcast ensembles are generated by adding stochastic perturbations to the precipitation intensity and advection fields. Precipitation features on small scales that have low predictability, are gradually filtered by an autoregressive model and replaced with stochastic noise to simulate the forecast uncertainties.

A thorough evaluation of STEPS in winter conditions is carried out using a wide range of deterministic and probabilistic verification metrics. These include Critical Success Index (CSI), Mean Absolute Error (MAE), reliability diagram, Relative Operating Characteristic (ROC), rank histogram and spread-RMSE ratio. The added value of scale filtering and probabilistic nowcasts compared to deterministic advection-based nowcasts is demonstrated.

The verification study is carried out by analyzing a representative selection of snowfall events during 2014-2018 under different synoptic conditions, including difficult cases with lake-effect snowfall. The data consists of pseudo-CAPPI reflectivity mosaics gathered from the countrywide C-band radar network operated by FMI.

Providing airport decision makers accurate point nowcasts of snowfall rates is an important practical application of the study. For verification of the point nowcasts, we use data from the Vantaa and Luosto radars that are located near the Helsinki-Vantaa and Rovaniemi airports, respectively. We demonstrate by examples that STEPS is able to produce accurate point nowcasts with reliable uncertainty estimates, which is not possible by using a simple advection-based methods.

This research has been supported by the EU-funded PNOWWA project. The project aims at improved nowcasting of snowfall to enhance the decision making and promoting the use of probabilistic nowcasts for aviation purposes.

9.14 DEVELOPMENT OF A NEW SEAMLESS PREDICTION SYSTEM FOR VERY SHORT RANGE CONVECTIVE-SCALE FORECASTING AT DEUTSCHER WETTERDIENST

ULRICH BLAHAK[1], KATHRIN WAPLER[1], MARCUS PAULAT[1], ROLAND POTTHAST, AXEL SEIFERT[1], LISELOTTE BACH[1], ELISABETH BAUERNSCHUBERT[1], ROBERT FEGER[1], KATHRIN FEIGE[1], MICHAEL HOFF[1], MARKUS JUNK[1], ALBERTO DE LOZAR[1], LISA NEEF[1], RAFAEL POSADA[1], MARTIN REMPEL[1], MARKUS SCHULTZE[1], CHRISTIAN WELZBACHER[1], MANUEL WERNER[1]

[1] Deutscher Wetterdienst, Germany
ulrich.blahak@dwd.de

At Deutscher Wetterdienst (DWD) a pilot project has been set up to start the development of its future Seamless INtegrated FOrecastiNg sYstem SINFONY. The aim is to develop a system for ensemble-based storm-scale forecasting from observation time up to +6 h / +12 h forecasts, which integrates nowcasting techniques with numerical model prediction (NWP) in a more or less seamless way. The focus of the pilot project is on severe summertime convective events.

For the first 2 h the storm-scale forecasting and warning relies mostly on observation-based nowcasting products with frequent updates (typically with 5-min intervals) that are available within a few minutes. New NWP forecasts are started only every 3 h after a rather long cut-off time to wait for incoming observational data and are available to the forecaster after a longer computation time. Convection-allowing ensemble NWP is only able to reach/outperform the quality of nowcasting at later forecasting times.

Nowcasting and ensemble NWP are typically treated as two separate and independent methods, and there are few common products available for the forecasters.

The goal of SINFONY is to provide new products from observation time up to +6 h / +12 h for our forecasters combining nowcasting and NWP. To enable the development of these new combined products the currently deterministic nowcasting will be expanded to an ensemble approach and will consider life-cycle information compared to a classical pure advection approach. A further prerequisite to define the best combination of both systems is a thorough comparative verification of nowcasting ensemble and NWP ensemble.

To narrow down the differences between nowcasting and NWP concerning forecast quality and methodology, efforts are undertaken on the one hand by enhancements to both nowcasting and NWP separately and on the other hand by mutual information exchange and combination, to further enhance the quality of both. One component is the assimilation of further high-resolution observational data including 3D-radar-data, Meteosat SEVIRI satellite data and lightning densities. In this context, a Rapid Update Cycle ensemble on the km-scale with hourly updates and advanced model physics is envisaged for the ensemble NWP.

9.15 OPTICAL FLOW BASED NOWCASTING AT DWD

M. WERNER[1]

[1] German Weather Service, Germany
manuel.werner@dwd.de

Automated nowcasting of radar reflectivity, rain rates, or other meteorological quantities in many applications is essentially based on two-dimensional motion extrapolation techniques. Here, a core task is to compute motion vectors for each pixel in a two-dimensional data set, given only the data set and its predecessor from the previous time step. This problem can be solved by applying so-called $OpticalFlow$ algorithms from the field of computer vision. In the past 35 years a huge amount of different approaches has been published in this research area. By now, well-performing and fast implementations exist and are accessible through open source software libraries. By using multi-scale methodologies and techniques to balance between smoothness of the calculated vector field and local exactness, these schemes can be well tailored to the requirements of, e.g., precipitation nowcasting. To some extent, motion of large-scale and small-scale precipitation signatures can be simultaneously recognized and weighted together.

Recently, Deutscher Wetterdienst (DWD) has implemented novel schemes for precipitation and radar reflectivity nowcasting based on the Dual TV-L1 $OpticalFlow$ method realized in the OPENCV (Open Source Computer Vision) software library. Nowcasts up to two hours forecast time in steps of five minutes, updated every five minutes, are produced. Whereas the performance for large-scale stratiform precipitation fields is good, convective situations with left or right moving or stationary cells and rapid developments are still difficult to handle. Although it is possible to configure the Dual TV-L1 $OpticalFlow$ method in such a way that the motion of rather small-scale convective cells is emphasized, doing so may cause artefacts in a two-hour extrapolation because of more irregular motion fields.

In this work, the basic functionality of DWDs $opticalflow$ nowcasting methods is described, verification results are presented, and example cases are discussed. Furthermore, it is depicted how $opticalflow$ nowcasting is linked with DWDs object-based convective cell tracking scheme KONRAD3D in order to deal with the mentioned challenge of nowcasting convective events.

9.16 DEVELOPMENT OF A PROBABILISTIC PRECIPITATION-NOWCASTING APPROACH

M. SCHULTZE[1], R. FEGER[1], R. POSADA[1], M. REMPEL[1], M. WERNER[1], K. WAPLER[1], U. BLAHAK[1]

[1] Deutscher Wetterdienst, Germany
markus.schultze@dwd.de

At Deutscher Wetterdienst (DWD) a pilot project has been set up to start the development of its future Seamless INtegrated FOrecastiNg sYstem (SINFONY). The aim of the project is a novel combination of probabilistic nowcasting techniques and numerical weather prediction (NWP) ensembles to achieve improved and seamless forecasts of hazardous summerly deep convective events from observation time up to +6h/+12h. Up to now both methods are mostly treated independently of each other.

The operational radar-based precipitation nowcasting at DWD employs the so-called optical flow technique. It uses composites of terrain-following low elevation radar reflectivity measurements. With this approach the motion vector of individual reflectivity pixel in the composite is estimated from previous observations and linearly extrapolated into the future. Deterministic predictions are provided in time steps of 5 minutes with forecast periods of 2 hours. The forecasts are updated every 5 minutes according to new radar measurements.

To account for the limited predictability of precipitation, especially in convective situations, a transition from deterministic to probabilistic nowcast is necessary. To enable probabilistic precipitation nowcasting, the aforementioned algorithm is extended to an ensemble approach.

The precipitation prediction depends on the choice of various parameters within the algorithm; the most important are the following: (a) the weighting of the motion of individual pixels in comparison to the large-scale motion, (b) the length of the considered history of the track, (c) the spatial smoothness of the predicted precipitation field. These none-analytical algorithm parameters are subject to a wide uncertainty range. Consequently, as a first step, a nowcasting ensemble can be generated by varying the parameters in their valid ranges. This is comparable to the method of varying parameters in physical parametrizations within NWP ensemble prediction systems. An additional way of estimating nowcasting uncertainty is the use of NWP ensemble simulations. Assuming that the NWP ensemble simulates a realistic variance of the wind vectors within the nowcasting range, these can be used for the nowcasting ensemble generation.

In addition to the described pure-advective approach, an estimation of the likelihood for strengthening and weakening of precipitation during the forecast time is desired. This can be addressed by different approaches: One possibility is the incorporation of statistical information on the life-cycle of convective cells. Another option is the consideration of environmental conditions similar to the ingredients-based method applied in operational forecasting. It uses atmospheric stability, moisture content, lifting and vertical wind shear to estimate the likelihood and strength of convection. To consider environmental conditions in the nowcasting ensemble the relevant parameters could be taken form NWP simulations.

Considering the use of NWP results to improve nowcasting ensemble (both for information of wind vectors and environmental conditions) relies on the experience that the synoptic-scale structures are much better captured in NWP simulations compared to precipitation itself.

Results of case studies during May and June 2016 are presented. Also, conceptual ideas for a multi-modal approach and a blending of nowcast ensemble and NWP ensemble for a seamless probabilistic prediction across different forecast times will be discussed.

9.17 RADAR NETWORK-BASED MESOCYCLONE DETECTION

T. HENGSTEBECK[1], K. WAPLER[1], D. HEIZENREDER[1], P. JOE[2]

[1] Deutscher Wetterdienst, Offenbach, Germany

[2] Environment and Climate Change Canada, Toronto, Ontario, Canada

thomas.hengstebeck@dwd.de

The weather radar network of the German Weather Service (Deutscher Wetterdienst, DWD) consists of 17 individual radar sites located at a mean nearest-neighbor distance of approx. 140 km. A ten-elevation 3D-volume scan, with a maximum unambiguous range of 180 km in its lowest elevations, is recorded by each radar site with a 5 min update cycle.

The dense radar network supports a multi-radar algorithm approach for the detection of severe weather features which processes the elevation scan data of all radars simultaneously. It particularly benefits from the data in overlap areas (as opposed to single-site algorithms running independently for each radar site).

In this contribution, the performance of the network version is compared to the single-site version through detailed case studies and statistical analyses. Its use is combined with vertically integrated liquid (VIL) and rotation track multi-radar products, which further help to identify damaging storms.

9.18 BLENDING HIGH-FREQUENCY NWP PRECIPITATION FORECASTS IN AN ENSEMBLE NOWCASTING SYSTEM: STEPS-ALARO

L. DE CRUZ[1], M. REYNIERS[1], L. DELOBBE[1], L. FORESTI[2]

[1] Royal Meteorological Institute of Belgium

[2] MeteoSwiss, Switzerland

lesley.decruz@meteo.be

Since its development by the UK Met Office and the Australian Bureau of Meteorology in 2006, the ShortTerm Ensemble Prediction System (STEPS) has seen many local adaptations around the world. The success of this system lies in its accurate assessment of the uncertainty of radar-based nowcasts, that is obtained by generating an ensemble of radar extrapolation nowcasts which are perturbed by spatially and temporally correlated stochastic noise. To account for the scale dependence of the predictability of precipitation, the precipitation fields are decomposed into an 8-level multiplicative cascade, where the large-scale features evolve slowly compared with the small-scale features. Our local implementation of STEPS uses the weather radar composite of Belgium (STEPS-BE; Foresti et al., 2016). The verification of STEPS-BE in Belgium shows that the predictability of large areas of rain is lost after roughly 2 hours, while that of small convective showers is already lost after half an hour. To improve the skill of the extrapolation nowcast, blending with a forecast from numerical weather prediction (NWP) is required.

We have implemented the blending of the extrapolation-based nowcasts with precipitation fields from the NWP model ALARO. This model is run operationally at the Royal Meteorological Institute of Belgium, at a horizontal resolution of 1.3 km. ALARO uses a multi-scale package for microphysics and convection (3MT, Gerard et al. 2009). It has been adapted to produce precipitation output with a frequency of 5 minutes, the same as the radar images. In our nowcasting system, coined STEPS-ALARO, the blending of the cascade is performed level-by-level, meaning that the weight of the NWP contribution can differ between larger and smaller scales. The scale-dependent weights of the extrapolation and NWP forecasts are computed from the recent skill of the respective forecasts, and converge to a climatological value.

9.19 EVALUATING THE ACCURACY OF OPTICAL FLOW TECHNIQUES ON NOWCASTING

ARTHUR C. T. DE SOUZA[1], MAIK HEISTERMANN[1], GEORGY AYZEL[1]

[1] University of Potsdam, Germany
costatomazde@uni-potsdam.de

Optical flow (OF) techniques estimate the motion of objects or fields from a sequence of images. Such methods have been applied in the context of precipitation nowcasting for some while, using the weather radar reflectivity field or rainfall intensity as input, and have shown skill for lead times up to several hours.

In this study, we analyze the behaviour of the Sparse OF technique according to the Lucas-Kanade method implemented in the OpenCV library. Specifically, we benchmark different implementations of an intermediate step in the entire nowcasting procedure, namely the prediction of detected feature locations.

For that purpose, we detect trackable features (corners) in subsequent images, and then extrapolate their movement from forecast time t(0) until lead time t(n). The predicted feature location at t(n) is than compared to the true feature location at t(n). With "true", we refer to the feature location as detected and tracked in the observed radar images from t(0) until t(n). The error of the predicted feature location will be expressed as the Euclidean distance between the true and the predicted feature location.

In our benchmark experiment, we will analyse the predictive skill at various lead times, based on different methodological variants that differ with regard to the maximum number of detected features, the neighbourhood of a predicted feature, the number of radar images considered before t(0), and statistical extrapolation approaches of various complexity.

The experiment will be based on weather radar data from the German Weather Service, namely the the RY product, which represents a rainfall intensity composite for the whole of Germany at 5 minute intervals and a spatial resolution of $1km^2$, covering 900 x 900 km. The workflow is put together entirely based on open source Python libraries, namely NumPy, SciPy, OpenCV, matplotlib, and wradlib.

9.20 NOWCASTING THE FREEZING RAINFALL IN THE AUTOMATED SYSTEM "METEOTRASSA"

IGOR ZAMORIN[1], TATIANA BAZLOVA[1], NIKOLAY BOCHARNIKOV[1], MARK VINOGRADOV[1]

[1] Institute of Radar Meteorology (IRAM), Russia
zis@iram.ru

The "MeteoTrassa" is an automated system of measuring, collecting, processing and dissemination of the specialized meteorological information for support of technological decisions on the maintenance of highways and runways. It includes meteorological and road sensors providing measurements of air temperature and humidity, wind parameters, rainfall intensity, temperatures of surface and of soil at a depth of 40 cm and present weather detectors. The system integrates weather radar information. Dual polarization radar data is used to obtain operational information about precipitation zones, their movement and phase state. The "MeteoTrassa" provides users with current weather information and forecasts with 4 hour ahead, including forecasts of freezing rainfall onset. The forecast of freezing rainfall is based on the following information: road or runway surface temperature, air temperature at a surface layer and at the AT-850 level; information on precipitation including its phase state, parameters of cloudiness movement.

Prognostic position of the cloudiness is estimated using relevant information on wind parameters. The regression analysis in which the current predictive values of wind speed and direction act as predictors is applied for calculation of speed and direction of cloudiness field. Forecasts are run automatically every 10 minutes. Prognostic values of air and surface temperature are based on the numerical model of atmosphere boundary layer, which is a part of the system. After the complex analysis of relevant meteorological information, the "MeteoTrassa" generates forecasts of the freezing rainfall with advance time up to 4 hours. This information allows users to take measures for prevention of a negative impact of the freezing rainfall on their technological processes of maintenance of highways or runways. The "MeteoTrassa" provides on-line validation of freezing rainfall nowcasting.

Results of verification of freezing rainfall nowcasts for 2 years of the "Meteotrassa" operation at the airport of Saint-Petersburg are presented.

9.21 SEVERE HAIL DETECTION: HYDROMETEOR CLASSIFICATION FOR POLARIMETRIC C-BAND RADARS USING FUZZY-LOGIC AND T-MATRIX SCATTERING SIMULATIONS

M. SCHMIDT[1], S. TRÖMEL[1], A. V. RYZHKOV[2], C. SIMMER[1]

[1] Institute of Meteorology/Univ. of Bonn, Bonn, Germany
[2] CIMMS/Univ. of Oklahoma, Norman, Oklahoma, USA
mschmid6@uni-bonn.de

Large hail is a frequently occurring and sometimes devastating phenomenon, especially during summertime convective events. Many occasions of hail stones with diameters above 5 cm up to 14 cm have been reported and confirmed in the last years in central Europe. Concepts and algorithms to detect and distinguish large hail from small hail or rain with polarimetric radars at S band exist. However, most weather radars in Europe operate at C band. Here we present the usability of operational hydrometeor classification algorithms, like the fuzzy-logic based algorithm in Park et al. (2009), at C band and the necessity of wavelength-specific, simulated parameters for these algorithms. We emphasize that specific attenuation Ah is a major factor in identifying and discriminating hail at C band. Simulating value ranges of polarimetric variables at C band and including Ah are vital key factors for hydrometeor classification at C band. Additionally, we provide an approach to obtain parameters to distinguish between rain and small, large and giant hail at C band with fuzzy-logic. The resulting fuzzy-logic based algorithm can be used for nowcasting as it enables real-time operational hail detection and size discrimination.

9.22 A K-NN METHOD FOR NOWCASTING RAINFALL INTENSITIES AT FINE TEMPORAL AND SPATIAL SCALES

B.SHEHU[1], U. HABERLANDT[1]

[1] Institute of hydrology and water resources, Hannover Germany
boshehu90@gmail.com

The short term forecast of rainfall intensities for fine temporal and spatial resolutions, has always been challenging due to the unpredictable nature of rainfall. Commonly at such scales, radar data are employed to track and extrapolate rainfall storms in the future. Studies have shown that for short lead times (up to 30 min) linear extrapolation of rainfall storms produces reliable results, however for higher lead times (up to 2 hours) the error of linear motion increases considerably. Therefore, the aim of this study, is to include the non-linear motion and transformation of rainfall storms, by developing a K-NN method based on historical radar data that will predict rainfall intensities for lead times from 5min up to 2 hours.

For this purpose, several storms are selected from the period 2006-2012 from the Hannover radar station, in order to train and validate the forecast method (by split sampling). Based on the training set, several predictors have been extracted and tested for their importance by different methods (linear correlation, sobol indices and partial information correlation). The best predictor set with the respective weights is used to find the optimal number of neighbors, which is then used to test the method performance on the validation set. In order to reveal the advantage of including non-linear transformations, a linear extrapolation forecast method (HyRaTrac) was employed as well and tested for the validation set. Special attention is given to the quality of the radar input by comparing raw radar data versus merged radar with station data (80 stations included). The performance is assessed by computing the relative error of forecasted field from the observed radar field, for three types of events: stratiform, convective and mixed.

The results of this study emphasize the importance of including non-linear transformation for forecasting rainfall intensities at lead times higher than 15 min for different types of events. Moreover, the impact of merged radar data on the forecast itself for very short lead times (up to 15 min) is discussed.

9.23 RADAR REFLECTIVITY ADVECTION ESTIMATION VIA PROXY CIRCLE IMAGES

A.C.P. OUDE NIJHUIS[1], Y. DUFOURNET[1], T. OTTO[1], I. STEPANOV[1]

[1] Institute of Atmospheric Physics CAS, Czech Republic
sky-echo, the netherlands

Nowcasting of rainfall rates at high spatial (100 m x 100 m) and temporal resolution (1 minute) is becoming more and more relevant for urban applications. It is not only relevant for the pleasure of citizens or tourists, but also for water management, traffic management, and harbor and airport operations.

A problem with the nowcasting of high-resolution measurements is that the data stream becomes rather large so that is it difficult to process them in realtime applications. Either large computational resources or fast and efficient algorithms are necessary to be able to process them. Nowcasting of rainfall rates can be divided in two parts: (1) the localization of the rain cells, and (2) the growth or dissipation of the rain cells. In this presentation, the focus is on the first, which is the fast estimation of advection from pairs of radar reflectivity measurements. To this end, we would like to apply existing efficient image processing techniques for the estimation of the advection. There is however a problem: efficient image processing techniques, e.g. image translation registration by cross-correlation, can not be applied directly to estimate the image displacement for a pair of two radar images. Next to the displacement of the image (due to advection), the images are mostly not very identical in the details (due to the radar measurement principles and natural variability).

As a solution, proxy circle images are made from the radar reflectivity images to be able to apply existing fast image processing techniques. In the proxy circle image, a filled circle is placed at the weighted location of each rain cell with the same area. From two proxy circle images the image translation can then be estimated via subpixel image translation registration by cross-correlation (this is an efficient image processing technique to estimate image displacement). Finally, the advection of radar reflectivity patterns can be efficiently estimated from radar reflectivity image pairs. The estimation can then be further enhanced by combining estimates from multiple pairs, which also provides an error estimate of the advection estimate.

In the presentation, the advection estimation algorithm is applied to X-band radars in the Netherlands, which are going to be used for realtime nowcasting applications. The algorithm is validated by applying it to radar archive data, and comparing the predictions with measurements.

9.24 COMBINATION OF OBJECT-BASED PROBABILISTIC NOWCASTING AND OBJECT-BASED NWP ENSEMBLE

R. POSADA[1], R. FEGER[1], M. SCHULTZE[1], K. WAPLER[1], M. WERNER[1]

[1] Deutscher Wetterdienst, Germany

rafael.posada-navia-osorio@dwd.de

A pilot project has been set up at Deutscher Wetterdienst (DWD) to develop a Seamless INtegrated FOrecastiNg sYstem (SINFONY) that aims to integrate nowcasting techniques with numerical weather prediction (NWP) to create a seamless forecast from observation time up to, at least, +6 h. The pilot project focuses on severe summertime convective events.

Currently, for the first 1-2 h, the storm-scale forecasting relies mostly on observation-based nowcasting products, whereas convection-allowing ensemble NWP (COSMO-DE-EPS) is only able to reach/outperform the quality of nowcasting at later times. Furthermore, nowcasting and NWP have been treated as two separate and independent methods, which lead to a limited number of combined products that are available for the forecasters. The goal of SINFONY is to fill this gap by enhancing both nowcasting and NWP separately and by exchanging information between both techniques to later provide more reliable combined products.

The current nowcasting system used at DWD a deterministic 2h-forecast based on radar observations that are updated every 5 minutes will be extended to provide a probabilistic forecast. The current NWP-Ensemble will be replaced by a Rapid Update Cycle (RUC) ensemble with hourly updates.

Regarding the combined products, SINFONY will provide a probabilistic forecast of convective events based on the combination of cells detected in probabilistic nowcasting and NWP-Ensemble. The detection of these cells in nowcasting is carried out with KONRAD3D, a method developed at DWD as part of the nowcasting system to detect, trace and forecast the trajectory and evolution of convective cells based on observed radar reflectivity. The NWP provides simulated radar data with the same structure and time resolution as the actual radar observations (each 5 minutes) thanks to an efficient Modular VOlume scanning RADar Operator (EMVORADO) that is coupled to the COSMO model framework. This allows the use of KONRAD3D also to detect the cells simulated by the NWP-Ensemble. The use of the same method for object identification facilitates the comparison and further analysis of the identified objects in both nowcasting and NWP.

As a first approach, a comparison of the cells identified in both datasets during the selected summertime events has been carried out. The first results of this comparison are presented here.

9.25 DEVELOPMENT OF TRAIN OPERATION CONTROL METHOD AGAINST GUST USING DOPPLER RADAR

C. FUJIWARA[1], K. KUSUNOKI[2], H. INOUE[2], N.ISHITSU[2], K. ARAI[2], H.SUZUKI[1]

[1] East Japan Railway company, Japan
[2] Meteorological Research Institute, Janan
chusei-fujiwara@jreast.co.jp

On Japan railroads, wind conditions affect operating efficiency, infrastructure, and safe passage of people and freight. Strong and gusty winds cause regional delays or shutdowns, and particularly hazardous crosswinds may lead to overturn of railcars. Therefore, cup anemometers densely cover along the railroads for operations through some thresholds of wind speed (e.g., winds in excess of 25 m s^{-1} or 30 m s^{-1}). However, small-scale localized but strong gusty winds such as tornadoes, downbursts, and gustfronts are difficult to detect with the present system.

In order to detect those hazardous wind phenomena, Doppler radars that observe wind movement in a large area can be used. The East Japan Railway Company installed a X-band Doppler radar on the rooftop of the building of the Amarume Station (Yamagata Pref., Japan), located in the regions along the side of the Sea of Japan where strong gusty wind associated with severe storms occur frequently in winter season. The observation has been conducted since March 2007 to develop a gust detection method using the radar data, and the applicability of that to train operation decisions has been assessed.

Based on the obtained data, we proposed a method suitable for detecting gust using Doppler radar and developed a train operation control method against gusts. By this method, Doppler radar automatically detects and tracks vortex. If the sum of tangential speed and the movement of the vortex exceed 33 ms^{-1} (lower limit of F1 by Fujita scale) and the predicted route of vortex approaches or passes through a railway within 10 minutes, the system issues a warning for the inter-station section to stop train.

This method was put to practical use on the Uetsu Line in the Shonai area from December 2017. Practical use of such train operation control method against gusts using Doppler radar is the first time in the world.

Session 10. Airborne and Spaceborne Radars



Keynote presentation

10.1 GPMS DUAL-FREQUENCY PRECIPITATION RADAR (DPR) ALGORITHM AND MEASUREMENT OF ICE PRECIPITATION

T. IGUCHI[1], R. OKI[2], N. KAWAMOTO[3]

[1] National Institute of Information and Communications Technology, Japan
[2] Japan Aerospace Exploration Agency, Japan
[3] Remote Sensing Technology Center of Japan, Japan
iguchi@nict.go.jp

The Dual-Frequency Precipitation Radar (DPR) onboard the GPM's core satellite is the first spaceborne precipitation radar that uses matched beams of two frequencies to retrieve precipitation profiles. The DPR consists of Ku-band and Ka-band radars whose scattering volumes are matched. But it does not have polarimetric or Doppler capability. The measurable parameters are the profiles of radar reflectivity factors at two frequencies only. The presentation will describe how the backscattered signals at two frequencies are used to correct for the attenuation and to estimate the rainfall rate in the latest standard algorithm.

While accurate estimation of precipitation rates with the DPR is one of the major objectives of the GPM mission, detection of ice precipitation with the DPR is also an important objective. After the satellite launch, distiguishing ice precipitation echoes from water precipitation echoes in convective storms turned out to be much more difficult than we originally anticipated before launch. The difficulty originates from several factors that include the non-uniform beam filling of precipitation, many possible kinds of ice particles, and uncertain temperature profiles. The presentation will mention the current status of algorithm development for detection of ice preciptation and quantification of its parameters.

10.2 VERIFICATION OF CLOUDSAT INSTANTANEOUS SNOWFALL RATE RETRIEVALS WITH GROUND-BASED RADAR MEASUREMENTS

S. MATROSOV[1], J. HARDIN[2], G. DE BOER[1]

[1] Cooperative Institute for Research in Environmental Sciences, University of Colorado and NOAA Earth System Research Laboratory, Boulder, CO, USA

[2] Pacific Northwest National Laboratory, Richland, WA, USA

sergey.matrosov@noaa.gov

Instantaneous liquid equivalent snowfall rates retrieved from spaceborne CloudSat W-band radar reflectivity measurements are compared to snowfall estimates from ground-based operational and research radars. The comparisons are performed for closely collocated in time and 3D space interpolated products, so uncertainties associated with deriving near surface snowfall parameters from measurements aloft are largely avoided. This allows for evaluation of the retrieval algorithm performance. Although typical uncertainties of both ground-based and spaceborne snowfall rate retrieval approaches are quite high, the results from the standard optimal estimation CloudSat 2C-SNOW-PROFILE algorithm are shown to be on average in good agreement with the US weather service operational S-band radar default snowfall algorithm results with correlation coefficients being around 0.8-0.85. The CloudSat standard optimal estimation snowfall rate products are also shown to be in satisfactory agreement with retrievals from several simple W-band Ze-S relations suggested earlier. Snowfall rate and snow/ice water content (IWC) parameters from the CloudSat 2C-SNOW-PROFILE algorithm are highly interdependent. A tight relation between S and IWC is also evident in other W-band snowfall rate retrieval algorithms. It is introduced in retrievals through an assumption about the ice particle fall velocity which is made in the reflectivity based algorithms. This suggests that ice sedimentation rate estimates can be deduced from applications of numerous IWC- reflectivity relations derived previously for different cloud conditions. Intercomparisons between different CloudSat snow/ice water content products indicated significant discrepancies in IWC values from different retrieval algorithms. Intercomparisons of collocated CloudSat and US Department of Energys cloud radar measurements taken at the Oliktok Point Atmospheric Radiation Measurement (ARM) programs Mobile Facility 3 (AMF3) will be also presented.

10.3 A RADAR-BASED EVALUATION OF GPM RETRIEVALS OF THE RAIN DROP SIZE DISTRIBUTION

WALTER A. PETERSEN[1], PATRICK N. GATLIN[1], DAVID B. WOLFF[2], ALI TOKAY[3], MIRCEA GRECU[4]

[1] NASA Marshall Space Flight Center, Huntsville, AL., USA
[2] NASA GSFC/Wallops Flight Facility, Wallops Island, VA., USA
[3] University of Maryland Baltimore County/GSFC, Greenbelt, MD., USA
[4] Morgan State University/GSFC Greenbelt, MD., USA
walt.petersen@nasa.gov

The NASA-JAXA Global Precipitation Measurement (GPM) mission makes satellite-based dual-frequency precipitation radar (e.g., DPR) estimates of the drop size distribution (DSD) in the course of estimating rain rates. Two key DSD parameters estimated include the mass-mean diameter (D_m) and the normalized intercept (N_w) of a three-parameter gamma size distribution (in DPR algorithms, mu=3). To better understand the character of the DSD and to statistically evaluate DSD retrievals by the DPR, GPM ground-validation (GV) DSD datasets build upward in scale to DPR fields of view. This scale extension relies on point measurements from disdrometers made in myriad rainfall regimes that are subsequently used to construct dual-pol radar-based retrievals of the DSD. The GV radar DSD retrievals are then applied at continental scales using 65 Validation Network (VN) WSR-88D S-band dual-pol radars and geometrically matching DPR rays and bins to WSR-88D rays and gates at DPR footprint scales.

Specific GPM science requirements mandate the retrieval of D_m to within +/- 0.5 mm of GV with no specific requirement set for N_w. Comparisons of the 2ADPR normal and matched scan version-5 (V5) products to VN-retrieved D_m values for non-partitioned precipitation types suggest the presence of a positive DPR retrieval bias relative to the VN of ∼0.2 mm with perhaps another 0.2 mm of random error. Hence, DPR D_m estimates meet the mission requirement. This is especially the case when the DPR DSD sample is considered independent of DPR algorithm-partitioning into convective (C) or stratiform (S) components. However, the satisfaction of the L1 requirement is really driven by the much larger occurrence of S-precipitation. A larger positive bias with pronounced secondary modes of disagreement is noted in C-precipitation at large DPR D_m (>2-2.5 mm; especially for Ku-only retrievals) and these biases impact the relative bias observed between the DPR and VN-based rain rate estimates.

Similar comparisons between DPR and GV N_w are noisier than those of D_m. DPR V5 LOG10(N_w) estimates cluster around values of ∼3.0 - 3.5 in S-rain, but exhibit more dynamic range and covariance with GV in C-precipitation. The behavior of DPR-retrieved D_m vs. N_w in C and S rain is broadly consistent with DSD-based C-S partitions in the literature, though not necessarily reflective of the full range of possible DSD precipitation values/regimes detected using disdrometers. In parallel comparisons to the GPM V5 combined radar-radiometer retrieval algorithm, the overall D_m bias behavior, not partitioned by C/S type is similar to that observed with the DPR. However, trends between combined-algorithm and GV retrievals in D_m N_w joint probability distribution space are considerably different

for both C and S precipitation relative to the GV and the DPR behavior. More recent testing of improved Nw parameterizations in the combined-algorithm suggest that better agreement will be attained in the next version of the algorithm. It is expected that improved methods of estimating the DSD for both ground and satellite-based radar retrieval algorithm approaches will result in even stronger convergence between ground and space-based estimates of the DSD and by extension, global rainfall.

10.4 AIRBORNE IMPLEMENTATION OF PDPP TECHNIQUE ON THE NRC W-BAND RADAR

C. NGUYEN[1], A. BATTAGLIA[2], M. WOLDE[1], A. PAZMANY[3], A. ILLINGWORTH[4]

[1] National Research Council Canada
[2] University of Leicester, UK
[3] ProSensing Inc., Amherst, Massachusetts
[4] University of Reading, UK
cuong.nguyen@nrc-cnrc.gc.ca

As part of an ESA Doppler Wind Radar Demonstrator Project, the NRC Airborne W-band (NAW) radar was recently upgraded with a new power supply modulator and a radar control card that allow operating the NAW radar in Polarization Diversity Pulse Pair (PDPP) mode. Although the PDPP technique was demonstrated successfully in ground based systems, the NAW radar is the first airborne system with successful implementation of the PDPP mode. The NAW radar antennae sub-system consists of three fixed Gaussian Optics Lens antennae and a two-axis reflector housed in an external radome. For the PDPP demonstration, the NAW dual-polarization side-looking antenna and combination of the dual-polarization aft-looking antenna and a reflector are used. With a careful selection of aircraft maneuvers, extensive PDPP dataset was collected in 2016-2017 over a diverse weather and surface conditions.

For the NAW PDPP upgrade, a hybrid PDPP and conventional pulse-pair operating mode was implemented using the previously available NAW PP10 pulsing mode. In this new PDPP mode, sequence of H/V and V/H polarization diversity pulse-pairs are transmitted interleaved with conventional staggered PRT H/H and V/V pulse-pairs. The radar control board (RCB) does not trigger the data system at the second PDPP pulses, so the data system real-time processes the measured data using the currently available PP8 algorithm. The main NAW upgraded features include, the ability to transmit double pulsing with short spacing as low as 5 μs and recording of the raw IQ radar data in PDPP mode. The PDPP mode is also tested at 6, 12, 20 and 40 μs separations.

In this paper, we present summaries of our fight data that provides unique observations of radar cross-section of various surfaces up to 80 degrees incidence angle and measured Doppler velocity exceeding 100 m/s from a moving platform for the first time.

10.5 COMPARISON OF THE GPM DPR SINGLEAND DOUBLE-FREQUENCY PRODUCTS OVER THE MEDITERRANEAN AREA

LEO PIO D'ADDERIO[1], FEDERICO PORCÙ[2], GIULIA PANEGROSSI[1], PAOLO SANO'[1], ANNA CINZIA MARRA[1], STEFANO DIETRICH[1]

[1] Institute of Atmospheric Sciences and Climate, National Research Council, Roma, Italy
[2] Department of Physics and Astronomy, University of Bologna, Bologna, Italy
leopio.dadderio@artov.isac.cnr.it

The NASA/JAXA Global Precipitation Measurement (GPM) Core Observatory (CO) carries, for the first time, a dual-frequency Precipitation Radar (DPR). The DPR provides insights into the three-dimensional structure of precipitating clouds and intensity and is currently considered the main calibration instrument for radiometer derived global precipitation estimates. The DPR employs three scanning modes: Matched Scan (MS), Normal Scan (NS) and High Sensitivity scan (HS). The Ka- and Ku-band radar (MS) footprints of the inner swath consist of 25 angle bins with a vertical resolution of 125 m while the Ku-band radar (NS) covers the full swath with 49 angle bins with the same vertical resolution. The HS Ka-band radar footprints are interlaced with matched Ku/Ka-band footprints and consist of 24 angle bins with range sampling at 250 m. The swath widths of Ka- and Ku-band radars are 120 km and 245 km, respectively, while the diameter of both Ka- and Ku-band footprints at nadir is 5 km about. While the precipitation retrieval algorithms of the Ka- and Ku-band radar MS footprints provide a double-frequency based output (DPR products), the Ku-band NS and Ka-band HS precipitation estimates for same footprints, are single-frequency based. At the same time, for the MS footprints output based on Ka-only and Ku-only measurements is also provided.

The goal of the present works is to carry out an intercomparison of the single- and double-frequency DPR algorithms by considering the respective outputs over the Mediterranean area during rain events. A number of DPR related variables have been considered (i.e. measured and corrected reflectivity, surface rainfall rate, mean mass diameter, normalized intercept parameter, liquid and ice water content vertical profiles) to perform the analysis. The data have been categorized for surface type (land and sea) and precipitation type (stratiform and convective). The results show a more marked difference between the DPR and Ka-only products with respect to DPR and Ku-only products comparison. The feature is confirmed by the vertical profiles of the single- and double-frequency based retrieved parameters both for stratiform and convective precipitation.

A specific study will be dedicated to analyze the situation describing a mismatch in rain detection between Ka- and Ku-band measurements, with a particular focus on the vertical profiles of both measured and corrected reflectivities.

10.6 COMPARISON OF PRECIPITATION TYPE ALGORITHMS

A. TOKAY[1], B. SWICK[2], P. KIRSTETTER[3]. D. MARKS[4], J. PIPPITT[4], W. A. PETERSEN[5], D. B. WOLFF[6]

[1] University of Maryland Baltimore County and NASA Goddard Space Flight Center, Greenbelt, MD, USA

[2] St.Cloud State University, St.Cloud, MN, USA

[3] University of Oklahoma, Norman, OK, USA

[4] Science Systems and Applications Inc and NASA Goddard Space Flight Center, Greenbelt, MD, USA

[5] Marshall Space Flight Center, Huntsville, AL, USA

[6] NASA GSFC Wallops Flight Facility, Wallops Island, VA, USA

tokay@umbc.edu

A Level One requirement as specified by the National Aeronautics and Space Administration (NASA) Global Precipitation Measurement (GPM) program is to detect falling snow at an effective resolution of five km for the dual frequency precipitation radar (DPR) and 15 km for the GPM microwave imager. An S-band dual-polarized radar-based precipitation type algorithm, referred to as Hydrometeor Identification (HID) is considered a validation tool for GPM DPR precipitation type algorithms over the continental United States. The HID algorithm initially classifies the precipitation type at each radar pixel based on ten possible categories with temporal resolution of five or ten minutes based on scanning protocol. The DPR algorithm classifies precipitation type as either rain or snow, so for the comparative studies, the HID algorithm has been simplified to rain, snow, and mixed precipitation.

This study uses the Automated Surface Observing System (ASOS) present weather sensor to evaluate the performance of HID. The ASOS precipitation sensor is a light-emitting diode weather identifier (LEDWI), and works on the principle of optical phenomenon scintillation. Outside of missing data unidentified and no precipitation, the LEDWI reports rain and snow at light, moderate, and heavy intensities.

ASOS reports present weather, surface temperature, and several other observables at one-minute resolution. For this study, the database consisted of 11 ASOS stations covered by ten radar sites from the winter of 2014-2015. A total of 172 days were identified as snow, cold rain, or a mixed precipitation event. Qualitative and quantitative assessments were performed taking into account the freezing level and the radar sampling height. For the qualitative assessment, event based diagrams were made to compare each product at its native resolution. For the quantitative assessment, comparisons were made at radar resolution.

Considering LEDWI precipitation type as a reference, comparative studies have been also done through other methods and in-situ instrumentation adjacent to the ASOS site. The National Severe Storm Laboratory Multi Radar Multi Sensor (MRMS) product uses a deterministic approach to determine the precipitation type as rain or snow at its radar pixel. The approach is based on the Rapid Refresh model output temperature (T) and wet-bulb temperature (WB) thresholds. The

ASOS measured T and calculated WB is used to regenerate an MRMS like product. A probabilistic MRMS precipitation type algorithm where probability of snow has been determined based on T and WB has also been under development and is included in the comparative study. Look-up tables of frozen precipitation were also presented based on T and WB over land and ocean by Sims and Liu (2015). Performance of probabilistic methods is evaluated through the Brier score.

One of sites, NASA Wallops Flight Facility, is also equipped with three different type optical disdrometers including the OTT Parsivel2 disdrometer, that has built in synoptic code as present weather sensor. A cross comparison of ASOS and Parsivel2 precipitation type is included in the presentation.

10.7 EVALUATIONS OF RAIN MICROPHYSICS RETRIEVAL USING GPM DPR THROUGH COMPARISON WITH A SELF-CONSISTENT NUMERICAL METHOD

E. GORGUCCI[1], L. BALDINI[1]

[1] CNR - Institute of Atmospheric Sciences and Climate, Rome, Italy
e.gorgucci@artov.isac.cnr.it

The NASA/JAXA Global Precipitation Measurement (GPM) mission aims at providing 4-D measurements of precipitation at a global scale to support efforts in understanding the governing mechanisms underlying the formation of precipitation. Its Core Observatory (CO) has been equipped with a dual-frequency precipitation radar (DPR) based on two weather radars operating at two frequencies of Ku (13.6 GHz) and Ka band (35.5 GHz), respectively. In the beam-matching mode, the two radars are operated to sample the same precipitation volume, in order to fully exploit dual-frequency observation capability. One of the goal of DPR is to achieve, from space, more accurate information on microphysical properties of precipitation with respect to the single Ku band frequency radar of the predecessor NASA/JAXA Tropical Rainfall Measuring Mission. The primary objective of the study is to evaluate the accuracy of rain drop size distribution retrievals using the DPR. Direct comparison with measurements provided by ground based instrumentation might answer the question, but, unfortunately, this is task is not easy and can result in largely unmeasurable uncertainty. In this study, a self-consistent numerical method (SNM) was used to estimate microphysical parameters along rain profiles from DPR measurements. It has been preliminarily evaluated using known rain and radar profiles. Such profiles were obtained from the D3R measurements. In particular, by choosing the reflectivity measurements collected in RHI mode, the Ku-band differential phase shift was used to evaluate the corresponding specific attenuation of reflectivity from which to obtain the specific attenuation at Ka band. The correction procedure utilized algorithms found by simulation using as input a large dataset of measurements from the 2DVDs deployed for the IFloodS GPM Ground Validation campaign. Under fixed conditions, vertical reflectivity profiles were obtained by the composition of reconstructed radar cells from RHIs at Ku and Ka band, each 450 m wide and 75 m high. The SNM was applied to these profiles to estimate the corresponding profiles of microphysical parameters. The good SNM performance, characterized in the presence of a fixed μ (μ=3) and measurement errors, was pointed out by a normalized standard error in the order of 10% and 15% for D_m and $\log_{10}\mathrm{N}_w$, respectively. Subsequently, the SNM was applied to the data collected by the DPR and its results compared to thoseobtained by GPM algorithms. The entire version 4 of the GPM DPR precipitation products obtained with data collected from September 1, 2014, to February 28, 2017 was used. In the presence of bright-band features, the rain region of matched scans, was employed to retrieve DSD parameters with SNM and GPM algorithms. In particular, the comparison between the microphysical parameters showed a difference in terms of normalized standard error, while a negative sign of normalized bias indicates that both D_m and dBN_w computed with SNM are underestimated with respect to the corresponding values obtained with DPR algorithms.

10.8 WIVERN, A PROPOSED SATELLITE TO PROVIDE GLOBAL IN-CLOUD WINDS, ICE WATER CONTENT AND RAINFALL

A. J. ILLINGWORTH[1], A. BATTAGLIA[2]
[1] University of Reading, UK
[2] University of Leicester
a.j.illingworth@reading.ac.uk

In response to ESA′s call for Earth Explorer-10 Mission ideas we propose WIVERN, (a WInd VElocity Radar Nephoscope), a conically scanning space-borne broad-swath Dopplerised dual-polarisation 94GHz radar to provide global measurements of in-cloud winds, rainfall and cloud ice water content using the returns from cloud and precipitation particles. The observations will have ∼60 km horizontal and 1 km vertical resolution with visits every day at European latitudes and an accuracy of 2 m/s for clouds with a reflectivity above -20 dBZ when averaged over a distance of 20 km. This satisfies the WMO requirements for horizontal winds for global NWP. Windstorms are the single most damaging meteorological phenomenon in Europe. Data assimilation studies by weather forecasting centres demonstrate that winds are the second most important class of observations in reducing forecast errors after IR and microwave humidity and temperature sounders and suggest that wind observations from WIVERN should improve forecast skill further, leading to better predictions of timing and location of windstorms so that mitigation activities can be better focused. The in-cloud winds from WIVERN should complement the predominantly clear-air winds to be measured by the Aeolus satellite when it is launched in 2018.

The 94 GHz (3 mm) frequency is needed to achieve a 1 km vertical resolution as the 500 m pulse approaches the earth′s surface at angles around 41°. The 3 by 2.28 m elliptical antenna rotates once every eight seconds sweeping out a circular ground track that advances 60 km for each revolution. The radar transmitter will be based on the one that has operated on Cloudsat since its launch in 2006. Observing Doppler winds from a moving space platform is challenging. Doppler velocities will be derived using the returns from cloud particles from a pair of pulses separated by 20μsec (3 km slant path) polarized in the horizontal (H) and vertical (V) so that the folding velocity is 40 m/s and high wind speeds can be measured. The H and V pulses must propagate, scatter and be received independently. ESA and UKSA funded ground-based and aircraft 94 GHz indicate that problems due to cross-talk between the H and V returns can be recognised and corrected of flagged, as can be biases in velocity due to non-uniform beam filling, or the biases due to wind shear in the presence of reflectivity gradients and that wind observations should be possible down to 1 km above the ocean surface and 2 km over land. From the climatology of the vertical profiles of radar reflectivity obtained from CloudSat, we expect WIVERN to observe about one million winds a day with an accuracy of 2 m/s for 20 km long in-cloud samples accompanied by quantified errors. Such winds should be representative of the large scale winds and suitable for data assimilation. The reflectivity profiles will provide continuity to those provided by CloudSat since 2006, and continued until ∼2025 by EarthCARE; the CloudSat data set has provided the best available global climatology of ice water content, light rainfall and snowfall.

10.9 A METHOD FOR ESTIMATE OF RANGE VARIATION OF ATTENUATION FROM DUAL FREQUENCY RADAR AND DUAL POLARIZATION RADAR

TAKAHISA KOBAYASHI[1], SOICHIRO SUGIMOTO[1] ,MITSUHARU NOMURA[1], AHORO ADACHI[2], NOBUHIRO NAGUMO[2], HIROMARU HIRAKUCHI[1]

[1] Central Research Institute of Electric Power Industry, Japan
[2] Meteorological Research Institute, Japan
kobay@mri-jma.go.jp

Attenuations of precipitation are closely related to microphysical properties of precipitation. Attenuations, however, has been rarely used for retrieval of precipitation properties. The attenuation of Dry snow is generally small. While for rain, large attenuations appear. We can, therefore, classify rain and snow from attenuation properties.

We have developed a method to estimate the range variation of the attenuation from the dual-frequency precipitation radar (DPR) equipped on the Global Precipitation Mission (MAD). We have also developed a similar method to estimate the range variation of the attenuation from a dual polarization radar (MAP).

In the method of MAD, we used the dual frequency ratio (DFR) which is defined as a ratio of the equivalent radar reflectivity at Ku-band and at Ka-band. The DFR monotonically increases with radar range for rain because of the difference in attenuation between Ku and Ka-band. While for dry snow, the DFR should be constant for homogeneous snow range region because of less attenuation of snow. Thus, we can estimate attenuation from degree to which the DFR varies with radar range.

In the method of MAP, we used Ze and Kdp. The values of Ze affected by attenuation. While the values of Kdp do not affected by attenuation. From the range variation of Ze and Kdp, we can estimate the range variation of attenuation.

The both method have been applied to the ground-based radar observations operated at Ka and c-band. Results show that the both methods were in good agreement. The radar reflectivity and Kdp for snow, however, are still unclear because of its complicated shapes. To make clear of the effects of shape of snow on the methods, we made radar simulations for snow of realistic shape by using the scattering data base and examined the above two methods.

10.10 PRELIMINARY DESIGN STUDY OF AIRBORNE PHASED ARRAY WEATHER RADAR TARGETING THE TYPHOON OBSERVATION

N. TAKAHASHI[1]

[1] Institute for Space-Earth Environmental Research, Nagoya University
ntaka@nagoya-u.jp

In this report, preliminary study of airborne phased array weather radar assumed to be installed in mid- to small-size jet aircraft (e.g. Mitsubishi Regional Jet, Gulf streamII, etc.) aiming for typhoon observation is shown. Airborne measurement has great advantages for typhoon observation because it is generated and developed over the ocean, and it is usually observed further than the range of ground-based radar observation. In the study, we first set requirements such as 3-D observation and wind observation in typhoon and constraint conditions from the aircraft set-up, then the feasibility to meet the requirements are examined.

Considering the size of typhoons, the observation range is set several tens of kilometres to several hundreds of kilometres in horizontal direction and near the ground to an altitude of more than ten kilometres in height. In the case of typhoons, it is required to observe the wall cloud surrounding the eye. Also, due to the performance of the aircraft, the flight altitude is confined about 12-13 km at the maximum, sometimes it is necessary to fly avoiding wall clouds reaching more than 15 km. Also, since the horizontal wind speed is the maximum in the low altitude near the wall cloud, the aircraft should observe from the high altitude outside the wall cloud. Furthermore, since the size of the antenna is limited due to attachment to the aircraft, it is about several tens of centimetres when it is attached to a pod, for example, or about 1 m when attaching it to the fuselage of the aircraft.

Based on these conditions and the maturity of radar technology, the basic specification was defined as follows: frequency is X-band or Ku-band, observation range is 30 km to 60 km, transmission power is about 400 W, and dual polarization is used. Although the radar can measure the velocity in the line of sight direction using the Doppler effect, movement of the aircraft is utilized to measure the wind field with the forward and backward beams. From the demands of 3-D observation and wind speed observation, it is necessary that the scanning angle is at least $\pm$ 20 degrees.

Considering the efficient observation taking the advantages of phased array technology, it is possible to observe two Doppler velocities with one antenna by switching beams between forward and backward direction. The beam direction is $\pm$ 30 degrees with respect to the direction orthogonal to the nose direction in this study.

Antenna scanning is also necessary for 3-D observations. For example, when conducting 3-D observation below the altitude of an aircraft, it is necessary to direct the antenna downward by 45 degrees and perform scanning of $\pm$ 45 degrees. Assuming that the pulse repetition frequency (PRF) of the radar is 2000 to 4000 Hz based on the observation range (30 to 60 km) and the number of pulse integration is 32, 0.9 seconds is required to cover the scanning range of 90 degrees assuming the elevation interval corresponds to the beam width.

10.11 VERIFICATION OF PRECIPITATION CHARACTERISTICS FOR WARM AND COLD SEASON USING GPM AND GROUND INSTRUMENTS IN KOREAN PENINSULA

CHOENG-LYONG LEE[1,2] GYUWON LEE[1,2], GEUNHYEOK RYU[3]

[1] Research and Training Team for Future Creative Astrophysics and Cosmologists, Department of Astronomy and Atmospheric Sciences, Kyungpook National University, Daegu, South Korea

[2] Center for Atmospheric Remote Sensing, Kyungpook National University, Daegu, South Korea

[3] National Meteorological Satellite Center, Korea Meteorological Administration, Chungcheongbuk-do, South Korea

gyuwon@knu.ac.kr

The GPM (Global Precipitation Measurements) DPR (Dual-frequency precipitation radars) and GPM Microwave imager (GMI) can observe the precipitation system of mid- and high-latitude regions continuously. These measurements enable the property analysis of seasonal precipitation including rainfall and snowfall in the whole area of Korean peninsula. Besides, the dense ground radars (GRs) and gage networks (GNs) are operated by various institutions to generate the precipitation maps suitable for Korea. The ground validation of GPM is essential and is still challenging issue for different types of precipitation. In this study, we investigate the statistical properties of GPM validation in rain and snowfall cases based on these observation databases.

The time synchronization is first carried out using the central observation time of the GPM passing through the observation domain of Korean peninsula. The databases such as estimated precipitation intensity of GPM are then interpolated into digital forecast system (DFS) coordinates for direct comparison to those of GRs. For GRs, the Hybrid Surface Rainfall (HSR) and constant altitude plan position indicator (CAPPI) method is used to analyse precipitation intensity and vertical structure of systems. To convert the rainfall and snowfall intensity from calibrated reflectivity, we used the Z-R (or S) relationship $Z=219R^{1.36}$ and $Z=75S^{2.0}$. The comparison process between GPM instruments and GNs is also performed considering the spatiotemporal scales. Finally, we conduct the verification using statistical indices consisting of mean bias, root mean square errors (RMSE) and correlation coefficient (CORR).

For most of rainfall cases, the reflectivity measurements of GPM DPR are 3∼5 dB higher than GRs. The uncertainties of statistic indices for precipitation are reduced in the large spatiotemporal scales. Snowfall observations based on reflectivity of GPM are underestimated than those of GR at snowfall intensity above 1 $mmhr^{-1}$.

10.12 DUAL-POLARIZATION FOR CIVIL AIRCRAFT RADAR: EXPERIMENTS WITH A PROTOTYPAL SYSTEM IN THE NETHERLANDS AND IN ITALY

L. BALDINI[12] F. BERIZZI[1], A. COCCIA[3], F. CUCCOLI[1], M. D'AMICO[4], S. LISCHI[1], A. LUPIDI[1], F. MILANI[5]

[1] Consorzio Nazionale Interuniversitario per le Telecomunicazioni (CNIT), Italy
[2] CNR - Institute of Atmospheric Sciences and Climate, Rome, Italy
[3] METASENSING BV, Noordwijk, The Netherlands
[4] DEIB, Politecnico di Milano, Milano, Italy
[5] IDS, Ingegneria Dei Sistemi, Pisa, Italy
l.baldini@isac.cnr.it

Both civil aviation and military transport aircrafts are usually equipped with a radar mounted in the nose. Its task is to scan ahead of the aircraft for detecting the presence of dangerous meteorological phenomena along the route. In this way they support pilots to change the route to mitigate risks related to weather. For this reason, these devices are sometimes named weather avoidance radar. They operate typically at X-band with a coarse angular resolution to keep the physical size of antenna small enough to be compatible with mounting. Such systems can have Doppler capabilities, providing also forward looking windshear and turbulence detection within some limited ranges. Measurements of reflectivity are displayed according to few levels: their meteorological interpretation is left to pilot′s experience. Polarimetry has not been adopted in commercially available weather radars and its potential advantages for civil aviation aircraft are still mostly unexplored.

However, the success of ground-based dual-polarization weather radar has demonstrated several advantages that can be of interest also for avionic application. In particular, the reliable correction of X-band attenuation and a meaningful classification of the precipitation type (rain vs. hail vs. snow).

The European Commission initiative CleanSky launched several projects aimed at improving flight route planning in the presence of unforeseen events, such as the presence of rapidly evolving thunderstorms along the route. Objectives are to increase the safety and comfort of flight and to keep emissions as low as possible. In this perspective potential improvements to aircraft weather radar related to the use of dual polarization technology were investigated along such projects. In particular, specific radar signal simulators to support design phase, architecture of the data processing system, including a Support Vector Machine based hydrometeor classification system, and trajectory optimization tools to be implemented in an Electronic Flight Bag. The X-WALD project was funded with the main objective of planning and performing ad-hoc experimental airborne polarimetric radar measurements. The availability of real data is of great importance to test the quality of the simulator as well as the capability of the processing algorithms. Two measurement campaigns were conducted in 2015 and 2016 in the Netherlands and in Central Italy, respectively, using a low-power X-band radar mounted on two different aircrafts. Moreover, these measurement campaigns were the first of this kind performed in Europe. Measurements from these campaigns and their comparison with radar data collected by ground-based systems are presented and discussed.

10.13 COMPARING THE GLOBAL PRECIPITATION MEASUREMENT MISSION WITH RADAR NETWORKS

P. KIRSTETTER[1], W. PETERSEN[2], D. FAURE[3], N. GAUSSIAT[3], D. WOLFF[4]

[1] University of Oklahoma, Norman, OK, USA
[2] Marshall Space Flight Center, Huntsville, AL, USA
[3] Meteo France DSO/CMR, France
[4] NASA GSFC Wallops Flight Facility, Wallops Island, VA, USA
pierre.kirstetter@noaa.gov

Characterization of space-borne precipitation accuracy and uncertainties is critical for applications at the global scale including water budget studies or monitoring natural hazards caused by extreme rainfall events. An adequate ground reference is needed to document the consistency of the Global Precipitation Measurement (GPM) level-2 and level-3 estimates. Over the U.S., GPM products are compared to a ground reference derived from NOAA/NSSL′s Multi-Radar/Multi-Sensor (MRMS) platform involving dual-polarized radar and gauge networks. Gauge adjustment and quality controls and filtering procedures are necessary to derive a reference 1) accurate with known uncertainty bounds and 2) measured at a resolution below the pixel sizes of the GPM sensors and gridded products. An application of this framework to the French ARAMIS radar network is presented to contrast GPM regional performances. Comparisons have been carried out at fine scale within a framework developed to examine the consistency of the ground and space-based sensors in term of precipitation detection, characterization (e.g. convective, stratiform) and quantification. Perspectives will be presented such as comparison with French overseas radars of La Reunion, an area known to receive each year one the world highest annual rainfall accumulation.

Session 11. Advances in signal processing



Keynote presentation

11.1 REJUVENATING REFRACTIVITY PROCESSING TO IMPROVE RETRIEVAL QUALITY WHILE REDUCING LABOR-INTENSIVE MAINTENANCE NEEDS

F. FABRY[1], D. W. HOGG[1], Y.-C. FENG[2]

[1] McGill University, Canada

[2] Colorado State University, USA

frederic.fabry@mcgill.ca

Doppler radars have the potential to use ground targets to estimate the refractive index of air near the surface. Few forecasters can use that information directly, and enthusiasm for that new measurement has been low (mea culpa!) primarily because of 1) the complexity of the processing needed to obtain refractivity information up to a limited range and especially 2) the labor-intensive work required to obtain reliable measurements. Yet in the context of data assimilation, refractivity can provide a key constraint on humidity for convective but also mesoscale models if the data from many radars are combined.

To help resolve this problem, the 20-year old processing approach used to estimate refractivity by radar was rejuvenated:

- The flat Earth approximation of the original algorithm was replaced by an approach where varying topography and target heights are specifically taken into account in an attempt to retrieve refractivity at a specific level above the surface;

- The retrieval approach is now based on a variational approach that uses past retrievals as first guess for the initial retrieval and takes target phase, not its range derivative, as measurement constraints. A new approach to handle the aliasing of phase is implemented that does not try to dealias phases but instead considers all possible solutions by weighting them based on their probability of occurrence;

- The task of target selection and tuning and that of meteorological calibration have been automated so as not to require human decision-making. Instead of relying on two one-time process, target selection and tuning becomes a continuing process in an attempt to account for changes in targets on the ground; calibration can also be made a continuing process and now relies on longer-term comparisons between surface data and radar retrieval instead of hoping for a “perfect” situation of uniform N.

11.2 ATMOSPHERIC BOUNDARY-LAYER HEIGHT TRACKING FROM S-BAND RADAR RETURNS WITH AN EXTENDED KALMAN FILTER: APPLICATION TO VORTEX-SE

FRANCESC ROCADENBOSCH[1], ROBIN TANAMACHI[2], STEPHEN J. FRASIER[3]

[1] CommSensLab, Department of Signal Theory and Communications, Universitat Politècnica de Catalunya (UPC), Barcelona, Spain

[2] Dept. of Earth, Atmospheric, and Planetary Sciences, Purdue University, West Lafayette, IN (USA)

[3] Microwave Remote Sensing Laboratory, University of Massachusetts, Amherst (USA)

roca@tsc.upc.edu

The application of the extended Kalman filter to Atmospheric Boundary Layer Height (ABLH) estimation in the convective boundary layer from radar and lidar returns has previously been shown by (Lange et al. 2015) departing from earlier works of (Rocadenbosch et al. 1999). Validation of the lidar counterpart has been carried out using different ABL parametrizations in the Weather Research and Forecasting (WRF) numerical model under different synoptic conditions in Barcelona, Spain, and Athens, Greece (Banks et al. 2015).

In the present work, we revisit its application to S-band radar reflectivity measurements in the context of the Verification of the Origins of Rotation in Tornadoes EXperiment-Southeast (VORTEX-SE). A selected case example is presented, from data collected during spring 2016 in Huntsville, AL environs (Tanamachi et al. 2016).

The ABLH estimator is composed of a basic pre-processing filter (threshold median filter to get rid of bioscatterers) and an enhanced Kalman filter. The implementation of the latter is in the form of an Extended Kalman Filter (EKF) with adaptive boundary parameters that define reference height intervals and reflectivity levels in the mixing layer (ML) and the free troposphere (FT) as well as the ML-to-FT interface. Focus is given to appropriate selection of key guiding parameters of the EKF, namely, the ABLH initial guess and intensity factors related to the a priori information passed to the filter (i.e., state-noise and error covariance matrices).

A convenient Signal-to-Noise Ratio (SNR) estimator enables us to estimate the height dependency of the SNR and to use observation-noise information such as the presence of Travelling-Wave-Tube (TWT) spurs, which are to be rejected. Filter limitations are also outlined.

Acknowledgements

This work has been funded by European-Union H2020 project ACTRIS-2 (GA-654169), Spanish Government - European Regional Development Funds TEC2015-63832-P project, and Catalan Government grant 2014 SGR 583. CommSensLab is a "María de Maeztu" Unit of Excellence funded by the Agencia Estatal de Investigacin, Spain. VORTEX-SE was supported by NOAA under contracts NA1501R4590232

and NA16OAR4590209 and by the Purdue University Dept. of Earth, Atmospheric, and Planetary Sciences.

References

Banks, R.F., Tiana-Alsina, J., Rocadenbosch, F., Baldasano, J.M., 2015. Performance Evaluation of the Boundary-Layer Height from Lidar and the Weather Research and Forecasting Model at an Urban Coastal Site in the North-East Iberian Peninsula. Boundary-Layer Meteorology, 157(2), pp.265292.

Lange, D., Rocadenbosch, F., Tiana-Alsina, J., Frasier, S., 2015. Atmospheric boundary-layer height estimation using a Kalman filter and a frequency-modulated continuous-wave radar. IEEE Transactions on Geoscience and Remote Sensing, 53(6), pp.33383349. Available at: http://ieeexplore.ieee.org/xpls/abs_all.jsp?arnumber=6998066&tag=1 .

Rocadenbosch, F., Soriano, C., Comern, A., Baldasano, J.M., 1999. Lidar inversion of atmospheric backscatter and extinction-to-backscatter ratios by use of a Kalman filter. Applied Optics, 38(15), pp.31753189.

Tanamachi, R., Frasier, S.J., Heberling, W., Waldinger, J., Seedorf, M., Bozell, J., 2016. Purdue-UMass Mobile Radar Observations Collected during VORTEX-Southeast 2016. In Results from the VORTEX-SE Field Program, Session 3 in 28th Conference on Severe Local Storms. Portland: American Meteorological Society, p. Paper 3.6. Available at: https://ams.confex.com/ams/28SLS/webprogram/Paper301419.html .

11.3 COMPARISON OF CLUTTER DETECTION SCHEMES FOR NON-DOPPLER, NON-POLARIMETRIC X BAND RADARS

S. MELANI[1], A. ANTONINI[2], F. CAPARRINI[1], A. TELLESCHI[3], A. LOMBARDI[3], A. MAZZA[1], A.ORTOLANI[1]

[1] CNR-IBIMET, ITALY
[2] LAMMA CONSORTIUM, ITALY
[3] ELDES S.R.L, ITALY
s.melani@ibimet.cnr.it

Weather radars are the key instruments to be used for early detection of rainfall fields. C and S-band radar systems require high installation and maintenance costs and sometimes they need impressive infrastructures that limit their use in complex orography and urban areas. For the X-band weather radars, both costs and the installation complexity decrease, especially for non-coherent systems, which are very compact.

Among the main error sources, clutter echoes can seriously limit the observational capability of a radar system; thus, a proper signal processing has to be implemented to minimize the effects of clutter without reducing the echoes from desired targets.

This work presents some studies performed on a non-coherent X-band radar (WR10X-ELDES) for implementing a signal processing scheme for ground and sea clutter removal. Ground clutter and weather signals have different statistical properties, as the stability of reflectivity echoes relative to very close volumetric cells is much higher in case of clutter than of weather signals. More complex is the identification of the sea clutter because it changes very fast in the horizontal direction, and present a radial attenuation as the distance from the radar increases. In addition, sea clutter values decrease as a function of height, so vertical gradient signatures can be used in the clutter identification process.

Starting from a literature analysis, different algorithms (statistical and not) have been tested and compared, introducing also some empirical adaptations.

The performances of the clutter removal algorithms have been discussed for a number of case studies, under different meteorological conditions. Results show that the analysed algorithms are strongly dependent on the radar site and must be necessarily customized to each radar location, because the ground and sea clutter signatures are strongly dependent on the height above and proximity to the sea, surrounding orography etc.

11.4 PRINCIPLE AND REAL-DATA APPLICATION RESULTS OF MMSE DOPPLER SPECTRAL PROCESSING

EIICHI YOSHIKAWA[1], NAOYA TAKIZAWA[2], HIROSHI KIKUCHI[2], TOMOAKI MEGA[2], TOMOO USHIO[2]

[1] Japan Aerospace Exploration Agency, Japan
[2] Tokyo Metropolitan University, Japan
yoshikawa.eiichi@jaxa.jp

Our previous research presented that excellent sidelobe reduction capability in phased array digital beam forming is realized by minimum mean square error (MMSE) approach (Yoshikawa et al., 2013). This work applied the MMSE approach to Doppler spectral processing that is governed by the same equation as phased array digital beam forming. The representative approach for adaptive spectral processing is the Capon method (Capon et al., 1969), and the MMSE approach can be understood as one of modified Capon methods. Most of adaptive spectral processing approaches including the Capon method need multiple independent sequences of an analysing signal. In contrast, a remarkable feature of the MMSE approach is that it works with just one sequence of an analysing signal. Since weather radars do not afford to obtain redundant sequences of a received signal for one direction, the MMSE approach is effective to the Doppler spectral processing in weather radars. The MMSE approach was applied to signals actually received by a very fast-scanning phased array weather radar which was developed by our research group. Compared with the normal FFT spectral processing that output ground-clutter contaminated Doppler spectrum, the MMSE approach reduced sidelobes of the ground clutter by 2030 dB, narrowed mainlobe width of the ground clutter to roughly its half size, and revealed precipitation signal buried by the ground-clutter sidelobes. It was, furthermore, shown that the narrowed and sidelobe-reduced ground-clutter signal can be easily removed by a typical Doppler spectral based ground clutter rejection method, and 3D precipitation profile with almost no ground clutter can be retrieved.

References

E. Yoshikawa, T. Ushio, Z. Kawasaki, S. Yoshida, T. Morimoto, F. Mizutani, M. wada, "MMSE Beam Forming on Fast-Scanning Phased Array Weather Radar", IEEE Trans. Geosci. Remote Sens., vol. 51, no. 5, pp. 30773088, May, 2013.

J. Capon, "High-resolution frequency-wavenumber spectrum analysis", Proc. IEEE, vol. 57, no. 8, pp. 1408-1418, Aug. 1969.

11.5 FILCOH, A METHOD TO ELIMINATE GROUND ECHOES FOR WEATHER RADARS OPERATING IN MULTIPLE PRT MODE BY USING THE AVAILABLE AUTOCORRELATION COEFFICIENTS

M. TAHANOUT[1], J. PARENT DU CHATELET[2]

[1] University Mouloud Mammeri of Tizi-Ouzou, Algeria

[2] Météo-France, France

mtahanout@gmail.com

This work presents a novel technique to eliminate ground clutter echoes for a weather radar operating in multiple PRT mode. The technique, named FILCOH, takes advantage of the differences in correlation time to separate rain and ground echoes. Basically, the longest time-lag coefficients of the autocorrelation function are used to estimate the ground clutter contribution which is then subtracted from the shortest coefficients before extraction of the geophysical parameters using the classical pulse pair method. Simulation results are presented for 2-and 3-PRT time series achieved in the S, C and X bands, and application results are also presented for real data obtained with i) a single PRT Degreane Horizon wind profiler radar, and ii) an X band weather radar operating in 3PRT mode in Nice (France, Aramis radar network). The application of FILCOH shows a significant improvement in radar reflectivity and radial velocity estimates, particularly for 3-PRT radar data characterized by large ground echoes.

11.6 EXTENDING DOPPLER VELOCITY COVERAGE FOR DATA ASSIMILATION

F. FABRY[1], A. KILAMBI[1]
[1] McGill University, Canada
frederic.fabry@mcgill.ca

One way to improve radar data assimilation is to increase the coverage of radar data, primarily by trying to detect weaker echoes. This can be achieve by more aggressive processing and better thresholding of good data, as well as taking advantage of the expected properties of weak targets.

Improved signal processing did not yield noteworthy results: So far, the best way to detect weak echoes we have found is to use Doppler spectra and compute power only on spectral components that are expected to have echoes. The challenge then becomes determining the spectral components of interest. At high resolution, some small gains can be made by replacing the traditional NCP or SQI thresholding by a more holistic test combining NCP/SQI with copolar correlation and expected differential phase.

A more promising has been to compute Doppler velocities over large areas. The basis for that approach is that weak signals generally occur in benign weather where winds are not expected to be very variable in space as a result of which echoes would be concentrated in a few spectral components. That process worked, but it also enhanced contamination by clutter and second-trip echoes, as well as promoted the spreading of point contamination. Using dual-polarization data in the process, we are able to better detect spectral components containing weather echoes as they also show higher correlation and expected values of differential phase. Finally, using continuity in range, we have been able to extend low-resolution Doppler coverage by close to 10 dB while filtering out most sources of contamination.

11.7 ALTERNATIVE DATA PROCESSING FOR MICRO RAIN RADAR (MRR) OBSERVATIONS

ALBERT GARCIA-BENADÍ[1], JOAN BECH[2], SERGI GONZÁLEZ[2,3], JOAQUIN DEL RIO FERNANDEZ[1]

[1] Universitat Politècnica de Catalunya (UPC) 08800 Vilanova i la Geltrú (Spain)
[2] Department of Applied Physics - Meteorology, University of Barcelona, Spain
[3] AEMET, Barcelona, Spain
albert.gracia-benadi@upc.edu

The most common function of weather radars is to provide a description of the precipitation field, typically in four dimensions: temporal evolution of a 3D field, including characteristics of precipitation and rainfall intensity. Some radars, as the one used in this study, are designed to observe only vertical profiles. The radar used in this work is a Frequency Modulated Continuous Wave Radar (FMCW) (Strauch et al, 1976) radar, unlike traditional pulsed radar systems. The main difference is that FMCW systems transmit continuously and can change their frequency modulation to change the vertical resolution while the pulsed radar emits a great power in short time a pulse. Pulsed transmitters are typically used in weather radars systems working at mid and long ranges while FMCW systems are used in low power transmitters often for short-range applications. The MRR manufacturer offers the equipment with its own software of analysis, but some researchers (for example Maahn and Kollias (2012), Adirosi et al (2016) among others) have proposed other approaches. The premise of the software is to consider that the raindrop is falling at terminal velocity, which is usually valid for stratiform precipitation, but not for convective storms. Another hypothesis is that the hydrometeors always are in liquid phase, but in numerous occasions, this is not the case. The shape of ice crystals or snowflakes is completely different from water drops, also the terminal velocity, and the complex refractive index. The aim of this study is to propose a new technique to process data for the raw MRR′s files to achieve a better active and configurable noise detection. The technique is related to that described by Maahn and Kollias (2012) but under the assumption of hydrometer fall terminal speed, thus Mie scattering is used. The different parameters analysed include: Signal detection, Active noise level determination, Spectrum average, Dealiasing processing (Velocity unfolding), Drop size distribution, Path Integrated rain attenuation and Reflectivity calculation. The presentation will compare and discuss results obtained with the new methodology and other existing approaches. This study was partly supported by projects CGL2015-65627-C3-2-R (MINECO/FEDER) and CGL2016-81828-REDT (MINECO).

References

Adirosi E, Baldini L, Roberto, N; Gatlin P, Tokay A, 2016: Improvement of vertical profiles of raindrop size distribution from micro rain radar using 2D video disdrometer measurements. Atmospheric Research, 169, Part B:404-415

Maahn M, Kollias P, 2012: Improved Micro Rain Radar snow measurements using Doppler spectra post-processing. Atmospheric Measurement Techniques, 5:2661-

2673

Strauch R, Campbell W, Chadwick R, Moran K, 1976: Microwave FM-CW Doppler radar for boundary layer probing. Geophysical Research Letters, 3:193-196

11.8 AUTOMATED IDENTIFICATION OF GROUND CLUTTER CONTAMINATION FOR POLARIMETRIC DOPPLER WEATHER RADARS

DAVID A. WARDE[1], SEBASTIAN M. TORRES[1]

[1] Cooperative Institute for Mesoscale Meteorological Studies, The University of Oklahoma and NOAA/OAR National Severe Storms Laboratory, United States
dwarde@ou.edu

Ground clutter contamination is still a major limitation in obtaining unbiased measurements from Polarimetric Doppler weather radars. Ground clutter contamination is characterized as having near-zero Doppler velocity with a narrow spectrum width, and removing it in the signal processor prior to obtaining the radar variables involves the use of a ground clutter filter (GCF). A GCF is typically a high-pass filter that removes near-zero Doppler velocities. However, the GCF itself can negatively affect weather signals, especially when returns from hydrometeors have similar characteristics as those from ground clutter. Accordingly, it is crucial to identify clutter contamination when it occurs. Often, this identification is done by measuring the spatial variability (e.g., gate-to-gate, azimuth-to-azimuth, or both) of both the filtered and unfiltered radar variables. However, this adds significant processing and implementation complexity, given that most signal processors operate on a single range gate at a time. Thus, features that do not require the use of data from multiple range gates (e.g., in sample time) are preferable because they can help identify the presence of clutter contamination and immediately trigger the application of the clutter filter before the radar variables are calculated. In this work, we investigate the use of single-range-gate parameters to enhance the identification of clutter contamination, including directional statistics of the autocorrelation and cross-correlation. Using WSR-88D time-series data, we train a feedforward neural network with these parameters and gage their relative skill in identification of ground clutter. We then add the trained neural network into our signal processing chain and qualitatively assess its performance to mitigate ground clutter using additional archived WSR-88D data. We compare the level II radar data obtained from the neural network processing with other processes that use spatially derived parameters for ground clutter recognition. We provide these results and recommendations for future work.

11.9 DUAL PRF PROCESSING WITHIN THE BARON PROCESSOR SUITE

B. MRINAL[1], C. DARRIN[1], L. JAMES[1]

[1] Baron Services Inc., USA

mrinal.balaji@baronweather.com

The world of weather forecasting is rapidly changing driven by exponential advances in radar signal and data processing technologies. Recent years have seen the development of the Baron Services Processor Suite which introduced new ways of collecting, storing, manipulating and transmitting radar data in addition to radically transforming the way we conduct and organize weather science. This paper will illustrate how the processor suite combats the doppler dilemna challenge by employing novel hybrid architectural concepts and effectively blending traditional signal dual PRF processing techniques with innovative technologies like CLEAN-APTM for superior data quality (CLEAN-AP^{TM} ©2009 Board of Regents of the University of Oklahoma). A brief description of the implemented algorithm followed by a performance discussion of data cases under a variety of weather conditions will be presented.

11.1 UNCERTAINTY QUANNTIFICATION FOR ARM CLOUD RADARS

N. BHARADWAJ[1], B. ISOM[1]

[1] Pacific Northwest National Laboratory, USA
nitin@pnnl.gov

The ARM climate research facility has deployed scanning cloud radars in a variety of regimes around the world to study cloud properties. Cloud properties are essential for the treatment and representation of clouds in models. Cloud radars operate at millimeter wavelengths to observe smaller cloud particles when compared to the traditional weather radars operating at centimeter wavelengths. These cloud radars are able to operate with complex waveforms. This paper presents the uncertainties in spectral moments and polarimetric variables estimated with these complex waveforms. The uncertainties are presented for spectral processing as well as auto-correlation based estimators for uniform, staggered pulsing, and frequency-hopping pulsing.

11.11 DROPLET FALLING VELOCITIES, WINDSPEEDS, AND KA-BAND ATTENUATION DEDUCED FROM PPI AND RHI SCANS

MATTHIAS RICHARD BAUER-PFUNDSTEIN[1]

[1] METEK GmbH, Elmshorn, Germany
bauer@metek.de

The droplet falling velocity can be deduced easiest in vertical stare mode. But if the radar is running dome scans as frequently done in case of cloud radars there is often not much time for vertical stare mode. Detecting the droplet falling velocities is important for distinguishing between fog and drizzling shallow low clouds. The drizzle or fog is often within the blind spot of the radar when the beam is pointing vertically. For this reason, an algorithm for deducing the droplet falling velocities from RHI scans was developed.

The algorithm first splits all range gates and time steps of a complete RHI scan into height slices. Assuming a homogeneous distribution of the vertical component w and the horizontal component u of the wind parallel to the RHI plane the two parameters w and u are fitted to all radial velocities measured in the height slice. Compared to measuring the droplet falling speeds in vertical stare mode this algorithm has the advantage of averaging over a larger volume and therefore turbulent variations of the vertical wind are cancelled out.

The same algorithm with minor modifications was also used for the Doppler broadening (= peak width). The drop size distribution DSD contributes to the peak width most in the vertical beam whereas turbulence contributes at all elevations and the wind shear contributes depending on the dimensions of the radar volume and therefore on range and elevation. Therefore, it is possible to separate the DSD contribution to the peak width from the others.

With another modifications the algorithm was applied to the reflectivity. In case of very stratiform clouds or fog it is often observed that the reflectivity in one height slice goes down at both sides of the RHI scan were the radiation must propagate a longer way due to the lower elevation and therefore experiences more attenuation. The accuracy of the method for deducing the attenuation of the Ka-band waves in presence of high LWC is not very good. But when looking at larger statistics it may help to validate Z-LWC relations.

11.12 SPECTRAL POLARIMETRIC FILTERS DESIGN FOR BROAD-BAND WEATHER CLUTTER MITIGATION

J.YIN[1], C.UNAL[1], H.RUSSCHENBERG[1]

[1] Delft University of Technology, the Netherlands
j.yin@tudelft.nl

In this work, spectral polarimetric filters (SPFs) are put forward to mitigate wind turbine clutter (WTC) and radio frequency interference (RFI) which are severe broad-band clutter for weather radar, deteriorating its performance significantly. The SPFs contain the moving double spectral linear depolarization ratio (MDsLDR) filter and the object-orientated spectral polarimetric (OBSpol) filter, which have been proposed to mitigate narrow-band clutter (i.e., ground clutter and moving artifacts) for full-polarimetric radar and dual-polarization radar, respectively. These filters are extended to remove the broad-band clutter (i.e., WTC and RFI). Based on the spectral polarimetric feature and range-Doppler continuity of precipitation and clutter, the SPFs are implemented in the range-Doppler spectrogram to generate one filtering mask to keep the precipitation and remove the clutter. Data collected by a polarimetric Doppler weather radar known as the IRCTR Drizzle Radar (IDRA) are used to validate the performance of the proposed algorithms. Mounted on the top of a 213 m tower in Cabauw Experimental Site for Atmospheric Research, the Netherlands, the X-band research radar is still affected by wind turbines which are 120 m in height and 3400 m far away. Additionally, the simulated RFI which is becoming a growing concern on weather radar is added to the raw PPI as another form of broad-band clutter. Different case studies demonstrate the good performance of the filters in wind turbine and radio frequency signal suppression. In addition, SPFs are proved to be effective with different Doppler velocity resolutions. Moreover, these techniques can be applied in real-time due to their low computation complexity.

11.13 DEEP LEARNING FRAMEWORK FOR PRECIPITATION RETRIEVALS FROM COMMUNICATION SATELLITES

AHMAD GHARANJIK[1], KUMAR VIJAY MISHRA[2], M. R. BHAVANI SHANKAR[1], BJÖRN OTTERSTEN[1]

[1] Interdisciplinary Centre for Security, Reliability and Trust (SnT), University of Luxembourg, Luxembourg

[2] IIHR Hydroscience & Engineering, The University of Iowa, Iowa City, USA

ahmad.gharanjik@ext.uni.lu

Opportunistic use of communication satellite links has been shown to provide valuable precipitation information in the regions that are beyond the coverage of conventional ground-based weather radars. Deployment of additional weather radars is expensive while there are overwhelmingly many ground satellite terminals spread across the world. The link conditions of these terminals are available at a central location (gateway station) in real-time making the entire setup usable in practice. The operation of satellites at Ka-band implies strong attenuation of link signals in the rain medium. The carrier-to-noise-ratio (C/N) measurements of the link are directly related to the specific attenuation A so that rain rate R can be computed using a nearly linear R-A relationship at Ka-band during moderate and heavy rain storms.

Nonetheless, this approach cannot be directly exploited for the satellite link primarily because, in the absence of measurements such as reflectivity, Doppler velocity and dual-polarimetric variables, the link cannot differentiate between storm types and intensities. Our previous work [Gharanjik et al. 2018. Centralized rainfall estimation using carrier-to-noise of satellite communication links, IEEE Journal on Selected Areas in Communications, in press] has shown that machine learning (ML) methods help in overcoming such disadvantages by recognizing wet and dry link conditions when trained with the rain gauge data.

In this work, we investigate deep learning (DL) in the specific context of rainfall estimation using the data from single-polarized passive receivers of ground terminals. Our goal is to show that advanced DL networks can learn to recognize rain intensities (no/dry/moderate/heavy) and storm types (stratiform/convective). This information is highly beneficial to correctly apply the R-A algorithm. We compare our results with the observations from the rain gauges and the nearest German weather service Deutscher Wetterdienst (DWD) radars. To the best of our knowledge, this is the first work that employs advanced learning techniques for the passive satellite links to generate rainfall estimates.

11.14 A MONOTONIC ALGORITHM FOR ESTIMATION OF THE SPECIFIC DIFFERENTIAL PHASE

NAN.YU[1], NICOLAS.GAUSSIAT[1]

[1] Radar Meteorology Centre, Météo-France, France
nan.yu@meteo.fr

The specific differential phase (KDP) is defined as the slope of range profile of the phase difference (ϕ_{dp}) between horizontally and vertically polarised pulses. It is an appealing measurement immune to attenuation, radar calibration and partial beam blocking for the quantitative precipitation estimation (QPE). However, the derivation of KDP needs a smoothing filter to remove fluctuations, including the variability affected by the reflectivity gradient within a radar pulse volume (non-uniform beam filling effect) and the interference of differential backscattering phase (δ effect). In operational application of radars, contamination of non-meteorological echo may further increase the fluctuation in the ϕ_{dp} observation. The heterogeneous variance induced by different error source hinders the conventional filter technique, in which the errors are generally assumed to be homogeneous.

In this study, a new filter that constrains a monotonic increasing of ϕ_{dp} is presented. Two monotonic functions of ϕ_{dp} are constructed: the function follows ϕ_{dp} positive gradients from the first gate of the radar to the last one and the second function follows ϕ_{dp} negative gradients from the last gate to first one. The gap between the two functions at each radar gate reflects the local uncertainty of ϕ_{dp} measurement. An iterative process removes the most extreme gradients one by one to minimize the gap between the two functions until a criterion (e.g. less than 5°) is reached. Then a Kalman filter conditioned by the self-consistent relationship between KDP and reflectivity factor (ZH) is used to determine the derivative of the ϕ_{dp} observations with a stable variance depending on the criterion. A case study illustrates the benefice of this new filter to estimate KDP in the presence of ground clutter contamination and δ effect.

Session 12. Millimeter wavelength radars



Keynote presentation

12.1 AN OVERVIEW OF MILLIMETER WAVE CLOUD RADAR OBSERVATIONS AT THE DOE-ARM OLIKTOK POINT SITE

JOSEPH C. HARDIN[1], ROBERT A. HOUZE[1,2], MATTHEW SHUPE[3], SCOTT GIANGRANDE[4], TODD HOUCHENS[5], CHRIS WILLIAMS[6], NITIN BHARADWAJ[1]

[1] Pacific Northwest National Laboratory, USA
[2] University of Washington, USA
[3] NOAA/CIRES, USA
[4] Brookhaven National Laboratory, USA
[5] Sandia National Laboratory, USA
[6] Smead Aerospace Engineering Sciences Department, University of Colorado Boulder, USA
joseph.hardin@pnnl.gov

The US Department of Energy (DOE) Atmospheric Radiation Measurement (ARM) program operates a mobile field site on the north slope of Alaska, above the Arctic circle at Oliktok Point to study high latitude clouds and radiative processes. Among the many instruments at the site, ARM operates two multi-frequency millimeter wave cloud radars; a scanning K_a/W band fully polarimetric radar, and a vertical pointing polarimetric K_a-band radar. These radars have high sensitivity and small beam width, providing for high-resolution observations of cloud processes. The combination of high sensitivity and unique location has provided a new look at the internal structure of arctic clouds. There are more than two years of collocated data by the two radars, as well as a longer dataset with just the vertically pointing radar, so patterns and statistics of cloud structures are beginning to emerge. This presentation will show some of the more interesting and surprising examples of arctic cloud structure and dynamics. Ongoing future activities to collect and analyse these data will be discussed.

12.2 USING TRIPLE-FREQUENCY RADAR DOPPLER SPECTRA TO CONSTRAIN SNOW PARTICLE SCATTERING MODELS

S. KNEIFEL[1], PAVLOS KOLLIAS[2], ALESSANDRO BATTAGLIA[3]

[1] Institute for Geophysics and Meteorology, University of Cologne, Cologne, Germany
[2] Stony Brook University, USA
[3] University of Leicester, Leicester, UK
skneifel@meteo.uni-koeln.de

During the last years, an increasing number of scattering databases for single particles, complex aggregates and even rimed and melting aggregates became available. While these developments are in general a great step forward, their evaluation with observations is a very necessary but also challenging task. Recently available multi-frequency radar observations which cover the Rayleigh up to the Mie scattering regime revealed characteristic signatures of rimed and unrimed aggregated particles. However, the observed signatures are still affected by both, the particle size distribution (PSD) and the single scattering properties of the particles which makes a clear evaluation of one or the other challenging.

In this contribution, we present a new approach which uses the radar Doppler spectra at three frequencies (X, Ka, and W-band) collected during a recent winter field campaign in Finland. We analysed a snowfall event which includes rimed and unrimed snow aggregates. A large selection of spectra obtained from low-turbulence regions within the cloud reveals distinctly different signatures of the derived Doppler spectral ratios. Due to the third frequency, a characteristic curve can be derived which is almost independent of the underlying particle size distribution and velocity-size relation. The characteristics of the curves obtained for rimed and unrimed are distinctly different. The observed signatures were compared with scattering calculations obtained with discrete dipole approximation (DDA), self-similar Rayleigh-Gans approximation (SSRG), and with the classical soft spheroid (T-Matrix) method. While the DDA calculations of unrimed and rimed aggregates fit the observed signatures well, the T-Matrix results lie far outside the observed range. The SSRG approximations was found to be principally able to recover the main features after an adjustment of the previously published coefficients.

12.3 VERTICAL AIR MOTION IN PRECIPITATING CLOUDS FROM AN AIRBORNE MILLIMETER WAVELENGTH RADAR

E. JUNG[1], G.-W LEE[2]

[1] School of Constructional Disaster Prevention and Environmental Engineering, Kyungpook National University, Korea (ROK)

[2] Department of Astronomy and Atmospheric Sciences, Natural Science College, Kyungpook National University, Korea (ROK)

eunsil.jung@gmail.com

Measurements of vertical air motion and microphysics are essential for improving our understanding on the interaction of dynamics and microphysics in clouds. At the radar wavelength of 3.2 mm (W-band), the raindrop backscatter cross section oscillates between successive maxima and minima as a function of the raindrop diameter (D) that is described by Mie theory. The location of the first minimum, which occurs at D $\sim$1.65 mm, has been used successfully in ground-based cloud radars to retrieve the vertical air motion. Here, this technique is applied to the data from a vertically pointing (W-band) airborne Doppler radar to retrieve vertical air velocities in warm precipitating cumulus clouds over the eastern Caribbean Sea. The vertical air motion is formulated by considering the first order corrections to the vertical components of the Doppler velocity, which are contaminated by the aircraft motions and attitude such as pitch angle, speed of aircraft and the aircrafts physical up and down motions.

The air velocity retrieved using the Mie technique agrees well with air velocity obtained from the cloud droplets in a shallow precipitating clouds: velocity difference within 0.1-0.2 m s^{-1} and a correlation between them is about 0.995.

12.4 A STUDY ON RADAR FIRST ECHOES OVER THE WESTERN GHATS WITH AN INSIGHT INTO UNDERSTANDING THE AEROSOL-CLOUD-PRECIPITATION INTERACTION AT A HIGH ALTITUDE SITE IN WESTERN GHATS

AMBUJ KUMAR JHA[1], SACHIN M DESHPANDE[1], G PANDITHURAI[1]

[1] INDIAN INSTITUTE OF TROPICAL METEOROLOGY, PUNE, INDIA (411008)
ambuj0947@gmail.com

The weather radar "first-echoes" have been a subject of study since the beginning of radar meteorology. Numerous studies have been done on radar first-echoes to understand the process of onset of precipitation, both warm and cold. The temperature at which first echoes appear likely reflects the primary precipitation formation mechanism which is crucial in the cloud microphysical schemes used in the Numerical Weather Prediction (NWP) and climate models.

The study examines radar first-echo in convective clouds identified in the Western Ghats (WG), India. Out of entire radar scans, we identified suitable cases for the purpose of this study. The first-echo top heights, the seasonal variation of the first-echo heights and their distributions over the topography of WG region have been probed. Further, in a quest to understand the aerosol-cloud-precipitation interaction processes, we analyse radar first echoes and various cloud and aerosol parameters, CCN concentration and dynamics at a High Altitude Cloud Physics Laboratory set up at Mahabaleshwar (17.56°N, 73.4°E), India. The current analysis is underway and would be potentially helpful in establishing the precipitation initiation process over the WG with an insight into the aerosol-cloud interaction processes at the high altitude site in WG. This could play a great role in solving the problem of precipitation initiation in clouds which is still one of the classical unsolved problems of cloud physics.

12.5 HOW MUCH ATTENUATION AT W AND KA BANDS IS CAUSED BY MELTING LAYER? AN ANSWER FROM MULTI-FREQUENCY RADAR DOPPLER SPECTRA

HAORAN LI[1], DMITRI MOISSEEV[1,2]

[1] Institute for Atmospheric and Earth System Research / Physics, Faculty of Science, University of Helsinki, Finland

[2] Finnish Meteorological Institute, Helsinki, Finland

haoran.li@helsinki.fi

Our knowledge of radar signal attenuation in melting layer at millimeter-wavelengths, i.e. 35 and 94 GHz, is uncertain. This uncertainty hinders retrievals of cloud properties, above the melting layer, using observations from ground-based millimeter-wave radars. Furthermore, it affects quantitative interpretation of precipitation measurements by space-borne cloud and precipitation radars. The prediction of melting layer attenuation is also demanded for Earth-space communications link which is expanding to higher frequency bands.

Model predictions of melting layer attenuation are highly uncertain. One of the main sources of uncertainty is the scattering properties of melting ice particles. In the recent studies it is shown that even for dry snowflakes the connection between scattering and physical properties is ambiguous at mm-waves. Therefore, the current melting layer models cannot be used for the prediction of the attenuation.

To quantify melting layer attenuation from ground-based observations, one can use multi-frequency radar observations, where observations at one frequency are not affected by attenuation. However, for the higher frequency observations attenuations due to radome, gaseous and rain should be taken into account. The wet radome attenuation especially at mm-waves (i.e. 35 and 94 GHz) is significant and difficult to characterize.

In this study, multi-frequency, 10, 35 and 94 GHz, Doppler spectra measurements are used to quantify melting layer attenuation for millimeter wave radar measurements. The attenuation estimation consists of two parts. Below the melting layer, the W/Ka band signal attenuation profile is derived by identifying parts of Doppler spectra that are in Rayleigh scattering regime for all the frequencies. From the spectral dual wavelength ratio measurements differential attenuations due to radome and rain are computed. Above the melting layer, the signal attenuation profile could also be calculated in the same way. In addition, pristine ice crystals at the top of the precipitating clouds are good Rayleigh scatters even at W band, and the dual wavelength reflectivity ratio is used to calculate the differential attenuation between Ka/X and W band in the melting layer. In this procedure we use X-band radar measurements as the reference and the melting layer attenuation at Ka and W bands are computed with respect to X-band observations. The melting layer attenuation at X band is relatively small. It is in the order of 0.3 to 0.8 dB.

12.6 HOW ACCURATE IS THE DISCRETE DIPOLE APPROXIMATION FOR MODELING THE SINGLE SCATTERING PROPERTIES OF PARTIALLY MELTED SNOWFLAKES

D. ORI[1], S. KNEIFEL[1]

[1] University of Cologne, Germany
dori@uni-koeln.de

As a consequence of the expanding availability of computing resources, the modeling of hydrometeors single scattering properties using increasingly detailed and complex shape models becomes more and more popular within the radar science community. The Discrete Dipole Approximation (DDA) has proven to be a reliable numerical tool to calculate scattering properties of realistically shaped pristine ice crystals, snow aggregates and rimed particles.

Only a few DDA calculations for partially melted particles have been performed due to the demands of modelling the melting process and the increased computational cost of calculating single scattering properties of heterogeneous targets. However, the importance of melting particles for simulating radar polarimetry and attenuation properties of the melting layer makes these melting particles the next logical "target" for DDA calculations.

The computation of snowflake single scattering properties using DDA is of great importance considering the increasing deployment of ground-based and space-borne millimeter-wavelength radars for which simplified models like homogeneous sphere and spheroids have been proven to not adequately represent snow scattering signatures. Moreover, those simplified models rely on the usage of effective-medium approximations (EMA) which are known to give inaccurate results in case of three or more components in the dielectric mixture.

The accuracy of the DDA method in case of melting ice particles has been debated. DDA is known to give less accurate results in case of larger refractive index values. Moreover the liquid component in the melting snowflake is expected to be distributed as small and sparse droplets whose shape would be difficult to approximate using a regular grid.

In this study, the accuracy of the DDA technique for representing scattering properties of melting particles has been investigated in the special case of layered spheres for which an analytical solution of the scattering problem exists. In order to separate the distinct sources of modeling error, namely the geometric (shape) representation of the particle and the resolution error with respect to the electromagnetic wavelength, tests with increased volumetric resolution have been performed. The accuracy of the DDA algorithm has been tested for different particle sizes (up to 20 mm) and frequencies (from 9.6 to 220 GHz). An in-depth analysis has been carried out by comparing internal electric fields in cases where largest discrepancies in the simulated radiative properties have been observed.

As expected, largest errors are found when the outer water layer is thinnest and the DDA resolution becomes coarser. Results suggest that the numerical error

introduced by DDA in the computation of the scattering properties of melting ice particles can be kept within acceptable values if the grid resolution assumed in the DDA computations is fine enough. The ultimate goal of this study is to provide guidelines for future melting snowflake scattering computations in order to assure sufficiently accurate results.

12.7 CHARACTERISTICS OF CLOUD VERTICAL STRUCTURE DURING DIFFERENT PHASES OF INDIAN SUMMER MONSOON: CLOUD RADAR PERSPECTIVE

SUKANYA PATRA [1], M.C.R KALAPUREDDY[1]

[1] Indian Institute of Tropical Meteorology,India
kalapureddymcr@gmail.com

The intra seasonal oscillation (ISO) of time scales of 1020 and 3060 days comprises of the active and break phases of Indian summer monsoon (ISM). Active (break) phases of ISM correspond to the high (deficient or no) rainfall over tropical Indian regions .Here, Cloud Vertical Structure (CVS) consists of mainly three types of convective clouds. It is proposed CVS is the potent parameter to reveal the contrasting features of ISM phases in terms of cloud macro-physical as well as microphysical properties. High resolution and vertical looking cloud radar measurements of IITM over the Western Ghats serves the purpose, with the added benefit of being quality controlled. Vertical Profile of Radar Reflectivity (VPRR) can be used to infer cloud macro physical properties (e.g. cloud depth, cloud occurrence frequency, cloud particle sizes and shape information) as well as microphysical properties (e.g. liquid and ice water contents). From the present study it was observed that the CVS during active monsoon phase was favorable for clouds to transform into rain. Strikingly, owing to mid-tropospheric dryness during break, the reflectivity structure in vertical is broken between a low level shallow cloud and a thin cirrus cloud. During this period, cloud top heights in the warm regions were limited below 2-3 km (maximum 6km) signifying the fact that their generation was limited to local convection. Thus, compared to active spells, break period lacks the ingredients (updraft intensity, humidity) required for the growth and sustenance of deep clouds. Whereas, during active days, intensity of frequent convergence (besides the local boundary layer convection) is highly evident which helps cloud tops reach even up to 10-14km AMSL. The effect of diurnal heating on convection and consequent initiation of precipitation have resulted in a late afternoon and early morning maxima in the diurnal evolution of radar retrieved liquid water content. Cirrus clouds were found to dominate the occurrence frequency during both monsoon phases compared to mixed phase cloud. This study also showed the variations in the ice water content, thickness, etc of cirrus clouds are the key factors to depict the contrast between the two phases of monsoon. Despite being a point observation, the uniqueness of this study is that it captured the associated large scale monsoon features over the site in terms of radar observed variables. Further analysis is carried out on the macro and microphysical aspects of monsoon clouds using radar measurements and they are attempted to be related to the large scale state of the atmosphere. Analysis of such type and more shall be further elucidated in the conference.

12.8 PARAMETRIZATION OF FALLING SNOW MICROPHYSICS AND ITS APPLICATION TO DUAL-FREQUENCY RADAR RETRIEVALS

D. MOISSEEV[1,2], A. VON LERBER[2], J. LEINONEN[3], J. TYYNELÄ[2]

[1] Institute for Atmospheric and Earth System Research / Physics, University of Helsinki, Finland

[2] Finnish Meteorological Institute, Helsinki, Finland

[3] Jet Propulsion Laboratory, California Institute of Technology, Pasadena, California, USA

dmitri.moisseev@helsinki.fi

Since the launch of NASA Global Precipitation Mission and continuous proliferation of cloud profiling sites equipped with multi-frequency radars, operated by e.g. DOE ARM or the European Research Infrastructure for the observation of Aerosol, Clouds, and Trace gases (ACTRIS), there is a renewed interest in deriving ice cloud and precipitation properties from multi-frequency radar observations. To develop a robust retrieval method, snow microphysical properties, such as particle size distribution and mass-dimensional relations, need to be parametrized. Additionally, these properties have to be linked to radar observables. Both steps present a challenge.

To improve our knowledge of snow microphysics and to derive parametrization characteristic to high-latitude snowfall, comprehensive snow measurements at the SMEAR-II research station of University of Helsinki located in Hyytiala, Finland are being carried out since January 2014. Using observations of precipitation accumulation, PSD and particle fall velocity snowflake masses are derived using the general hydrodynamic theory. There are several ways to describe the PSD of ice particles, in this study we have adopted the normalized PSD approach and expressed the PSD as a function of the melted equivalent particle diameter, which provides an unambiguous measure of particle dimension. From the analysis of more than 40 snowfall cases, we have observed that generalized Gamma distribution provides a better fit to the data than the standard Gamma PSD used in many studies. Additionally, we have found that the observed snowflakes are typically larger and heavier than in the currently used parameterizations.

To link these findings to multi-frequency radar observations, forward modelling study is performed. To model scattering properties of snowflakes we have used both "soft-spheroid" particle approximation and complex ice particle models. Scattering properties of "soft-spheroid" models were computed using T-matrix method, while single scattering properties of complex ice particles were taken from the existing scattering databases. It was found that the difference between two methods is not as big as was previously expected. Furthermore, it is found that snowfall rate retrievals can be greatly constrained by using dual-frequency radar observations. The parameters of the normalized PSD represented in the generalized Gamma form most suitable for dual-frequency radar analysis were also derived.

12.9 ARM CLOUD RADARS AT THE EASTERN NORTH ATLANTIC SITE: AN UPDATE

B. ISOM[1], N. BHARADWAJ[1]

[1] Pacific Northwest National Laboratory, USA
bisom@pnnl.gov

The Atmospheric Radiation Measurement (ARM) research facility strategically deploys and operates a wide variety of instrumentation around the world to better understand atmospheric processes. As a part of the instrument suite, radar systems provide the ability to observe cloud and precipitation particles over a broad region at a high temporal and spatial resolution. The ARM radar group operates several scanning and vertically pointing polarimetric radars at multiple frequencies across the globe that are designed to observe clouds and precipitation in marine, continental, and arctic environments at fixed and mobile sites. Graciosa Island in the Azores is home to one of the fixed and is designated Eastern North Atlantic site (ENA). Observations of marine clouds and precipitation events are a primary focus of the radar instrumentation there.

A significant effort has gone into the development, characterization, and calibration of the scanning and vertically pointing cloud radars at the site. Recently, ENA was the focus of an extensive field campaign that included both ground-based and aircraft-base instruments: Aerosol and Cloud Experiments in the Eastern North Atlantic (ACE-ENA). This work will summarize the system cloud radar characterization and calibration efforts at the site, discuss the ACE-ENA campaign, and showcase recent data collected with the cloud radar systems.

12.10 OCCURRENCE AND VERTICAL DISTRIBUTION OF CLOUDS IN KOREAN PENINSULA FROM GROUND-BASED KA-BAND CLOUD RADAR OBSERVATIONS

BO-YOUNG YE[1], GYUWON LEE[1,2], SANGWON JOO[3]

[1] Center for Atmospheric REmote sensing, Kyungpook National University, Daegu, South Korea

[2] Department of Astronomy and Atmospheric Sciences, Kyungpook National University, Daegu, South Korea

[3] National Institute of Meteorological Sciences, Korea Meteorological Administration, Jeju, South Korea

gyuwon@knu.ac.kr

The cloud observations from ground-based millimeter wavelength radar provide vertical distribution of cloud layers with good accuracy and high vertical resolution and can be utilized to produce cloud type climatologies. We examine statistical cloud properties according to the cloud types using Ka-band cloud radar (KCR) observations that are operated by National Institute of Meteorological Sciences (NIMS) of Korea Meteorological Administration (KMA) since 2013.

For stable and accurate statistics of cloud information, system biases in measurements from KCR were adapted and strong echoes from insects in the boundary layers were removed. We, thus, conducted the calibration of system biases in reflectivity in KCR by using observations from collocated external instrument. The system biases were corrected by direct comparison with reflectivity from vertically pointing X-band radar (VertiX) and Micro Rain Radar (MRR) that are pre-calibrated by using drop size distributions from two-dimensional video disdrometer (2DVD) and Particle Size Velocity (PARSIVEL) disdrometer for rain events. Furthermore, strong echoes from insects and noise in the boundary layers were then removed using linear depolarization ratio and reflectivity thresholds.

Cloud properties (i.e., cloud occurrence, top and base heights of the cloud, and cloud thickness) were examined according to the cloud types that were objectively classified with their altitude, presence of precipitation, and vertical extents in vertical profiles of reflectivity. First, clouds were categorized into high, middle and low clouds based on height of cloud base. The low clouds were then divided into “rain” and “non-rain” based on presence of precipitation. The “rain” clouds were classified into deep and shallow clouds by their vertical extents. Preliminary analysis shows that the cloud occurrences of high and deep rain clouds are dominant in comparison with other cloud types during summer season (JJA). On the other hand, the occurrence of middle and low rain clouds are dominant during winter season (DJF).

Session 13. Quantitative precipitation estimation



Keynote presentation

13.1 PROBABILISTIC QUANTITATIVE PRECIPITATION ESTIMATES WITH GROUND- AND SPACE-BASED RADARS

P. KIRSTETTER[1], J.J GOURLEY[2], J. ZHANG[2]

[1] University of Oklahoma, Norman, OK, USA

[2] NOAA National Severe Storms Laboratory, OK, USA

pierre.kirstetter@noaa.gov

The uncertainty structure of ground- and space-based radar quantitative precipitation estimation (QPE) is largely unknown at fine spatiotemporal scales near the radar measurement scale (e.g. 1-km/5-min for ground-based radars, 5-km/instantaneous for space-based radars). Applications such as hydrological modeling, storm prediction, and flash flood monitoring require more than just one deterministic "best estimate" to adequately cope with the intermittent, highly skewed distribution that characterizes precipitation. To advance the use of uncertainty as an integral part of QPE for ground-based and space-borne sensors, an investigation has been carried out across the conterminous US on the NOAA/NSSL Multi-Radar/Multi-Sensor and on the NASA/JAXA TRMM and GPM space-based radars. Extension to satellite-based infrared passive sensors is demonstrated. Probability distributions of precipitation rates are computed instead of deterministic values using models quantifying the relation between radar reflectivity and the corresponding "true" precipitation. This approach conditions probabilistic quantitative precipitation estimates (PQPE) on factors such as the precipitation rate and typology. It preserves the fine space/time sampling properties of the sensor and integrates sources of error in QPE and the impacts of algorithms assumptions. Precipitation probability maps compare favorably to the deterministic QPE. The PQPE approach is shown to mitigate systematic biases from deterministic retrievals, quantify uncertainty, and advance the monitoring of precipitation extremes. It provides the basis for precipitation probability maps, radar and satellite precipitation ensembles needed for multisensor merging of precipitation, early warning and mitigation of hydrometeorological hazards, and hydrological modeling.

13.2 ANYWHERE NEAR THE SEVEN-YEAR ITCH? ON THE STATE OF WRADLIB UPON THE RELEASE OF V1.0

K. MÜHLBAUER[1] M. HEISTERMANN[2]

[1] University of Bonn, Germany

[2] University of Potsdam, Germany

heisterm@uni-potsdam.de

The free and open source software communities tend to release early and often. Initial versions are numbered like 0.x in order to convey that the software is a work in progress. Version 1.0 is used as a major milestone, indicating that the software is "complete", that it has all major features, and is considered reliable enough for general release.

Seven years ago, wradlib (http://wradlib.org) was born, and soon released as v0.1: an open source Python library for weather radar data processing, analysis and visualisation. Since then, wradlib has grown and matured, and, as of today, serves a large user community from all around the world, rooted in academia, government agencies, and the private sector. wradlib supports the essential steps of weather radar data processing which include: reading a range of weather radar data formats; geo-referencing observations from spherical coordinates to spatial reference systems; detection and correction of errors (e.g. beam blockage, attenuation, clutter); phase processing; quantitative precipitation estimation; quality control; integration with other sensors (gauges, space-borne platforms); compositing; matching retrievals to hydrological application scales; and, last but not least, rich visualisation options along different dimensions. The overall development paradigm was and still is a flat data model, allowing for minimal entry thresholds and maximum flexibility in building applications.

In 2018, we will finally release wradlib v1.0, and thus commit to the maturity, stability and reliability of the services it delivers. Here, we review and discuss the past seven years in terms of key developments, lessons learned, but also with regard to some promises yet to be kept. Some of these developments and issues can be considered as representative for many scientific software packages in the past decade: e.g. how GitHub and its integrated services (management of issues, pull requests, and Continuous Integration) have boosted the standards of collaborative scientific software development; how self-sustained tutorials in combination with jupyter notebooks have revolutionized package documentation; how deployment via conda-forge has finally eliminated the vast majority of issues with dependencies as complex but vital as gdal. And finally (and somewhat interesting for researchers) how the main development workload has shifted dramatically from rapid prototyping of scientific algorithms to maintenance and support of usability and reliability, which is why we can gladly release v1.0.

13.3 COMMERCIAL MICROWAVE LINKS FOR RAINFALL MONITORING: A NATION-WIDE VALIDATION STUDY IN THE NETHERLANDS

L.W. DE VOS[1,2], A. OVEREEM[1], H. LEIJNSE[1], R. UIJLENHOET[2]

[1] Royal Netherlands Meteorological Institute, The Netherlands
[2] Wageningen University, The Netherlands
lotte.devos@wur.nl

Commercial microwave links are installed and maintained for the purpose of telecommunication. Hydrometeors between transmitting and receiving antennas cause the microwave signal to be attenuated. From signal attenuation, the path averaged rainfall intensity can be calculated. A dataset of instantaneously logged signal power in almost 2000 unique links in The Netherlands over 7 months was analyzed. Rainfall intensities were calculated with the RAINLINK-package with an additional pre-processing module, enabling the package to be applied on instantaneously logged data. Validation was done by comparing rainfall intensities per link with the path averaged rainfall intensity according to a gauge-adjusted radar product. Polarization, signal frequency and link location were shown not to be relevant factors for the error in link rainfall observation. The performance of the links was better during periods of heavy rainfall and improvedfor longer aggregation intervals. Errors were largest for path lengths shorter than 2 km, observations during the late night and early morning, and observations during colder months (when solid precipitation could occur). This validation study helps determine the accuracy of a rainfall observation from instantaneously logged commercial microwave links based on known factors of the observation, such as path length, time of measurement and rainfall type.

13.4 HOW TO BENEFIT FROM HIGH-RESOLUTION DIGITAL ELEVATION MODELS TO SIMULATE PARTIAL BEAM BLOCKAGE?

K. MÜHLBAUER[1], M. HEISTERMANN[2]

[1] University of Bonn, Germany

[2] University of Potsdam, Germany

kai.muehlbauer@uni-bonn.de

In complex terrain, partial beam blockage (PBB) is among the prime sources of uncertainty in radar-based quantitative precipitation estimation. While polarimetry offers strategies to mitigate the issue (as e.g. KDP is considered rather immune to PBB), the quantification of PBB remains important (e.g. for single-pol data processing, or for exploring suitable locations to set up new radar devices).

A common procedure to quantify partial beam blockage is to simulate beam propagation through the atmosphere, and to quantify interference with the terrain surface as represented by a digital elevation model. A couple of authors (e.g. Bech et al. 2007) have suggested to interpolate (or resample) the terrain altitude to each radar range bin location. As a consequence, beam blockage would be computed based on some "average" terrain altitude in the radar bin. This may produce errors in areas with rapid terrain variations. As long as the spatial resolution of the DEM is low (e.g. 1 km in GTOPPO30), the additional error introduced by interpolation and averaging might be negligible. However, modern DEMs provide resolutions of up to 1 meter - just resampling terrain altitude to the radar bin location is an unnecessary loss of information. Instead, we should consider all terrain values inside any radar bin.

In this study, we present a new algorithm based on the open source software wradlib, that reprojects high-resolution terrain altitude directly into the spherical coordinate reference system of the weather radar. That way, we explicitly represent the terrain cross section as seen by the radar, or, in other words, the variation of topography "inside" each radar bin. We then convolve, for each radar bin, the high-resolution terrain cross-section with a Gaussian power distribution of the radar beam in order to simulate the beam blockage fraction. We will systematically evaluate the effects of our technique on cumulative beam blockage along the beam propagation path, in comparison to the simple resampling approach: for different DEM resolutions, radar set-ups and terrain surfaces. Preliminary analysis suggests that the resulting changes in simulated beam blockage can be dramatic (> 50 %).

References

Bech, J., U. Gjertsen, G. Haase (2007): Modelling weather radar beam propagation and topographical blockage at northern high latitudes, Q. J. R. Meteorol. Soc. 133, 1191-1204.

13.5 RADAR-RAINFALL ESTIMATION USING SPECIFIC ATTENUATION: IMPROVEMENTS AND CHALLENGES

B.-C. SEO[1], W. F. KRAJEWSKI[1], A. RYZHKOV[2]

[1] IIHRHydroscience & Engineering, The University of Iowa, USA

[2] Cooperative Institute for Mesoscale Meteorological Studies, University of Oklahoma, USA

bongchul-seo@uiowa.edu

The Iowa Flood Center (IFC) has been generating a real-time radar-based rain rate product with time and space resolutions of five minutes and approximately 0.5 km. This QPE product is a composite of seven NEXRAD radars that cover Iowa and drives a distributed hydrologic model called the IFC Hillslope Link Model (HLM) for state-wide streamflow prediction. The main QPE challenges the IFC is currently facing are: (1) relative biases among different radars that occasionally result in a distinctive border at the overlapping areas (e.g., because radar calibration is not synchronized among radars in the network); and (2) significant rainfall underestimation in a region covered by one of the radars (e.g., KFSD in Sioux Falls, Iowa) due to the partial beam blockage. To resolve these issues, the IFC has recently tested a rainfall estimation algorithm using specific attenuation that is immune to partial beam blockage and radar miscalibration and is less sensitive to variations in drop size distribution. Therefore, this study presents the IFCs test results regarding how well the specific attenuation method addresses the current difficulties shown in the IFC QPE product. The evaluation of the new method is based on ground reference (e.g., rain gauges) data for selected rainfall events. Since the algorithm can be applied only to the region below the melting layer, the authors discuss rainfall estimation over the melting layer. They retrieve vertical profiles of radar reflectivity and polarimetric observables and characterize their features observed over the melting layer. The study also addresses how the vertical profiles are used to improve rainfall estimation over the melting layer, complementing the specific attenuation method for the regions below the melting layer.

13.6 INVESTIGATION INTO USING A NEURAL NETWORK TO SELECT BETWEEN USING FILTERED OR ALOFT MEASUREMENTS TO IMPROVE QPE IN CLUTTER CONTAMINATED REGIONS

S. LYONS[1], T. DARLINGTON[1], S. TORRES[2], D. WARDE[2]

[1] UK MET Office, United Kingdom

[2] Cooperative Institute for Mesoscale Meteorological Studies, The University of Oklahoma and NOAA/OAR National Severe Storms Laboratory, Norman, OK 73072, United States

sam.lyons@metoffice.gov.uk

A major source of errors in quantitative precipitation estimation (QPE) comes from the fact that radar measurements are made aloft, whereas rainfall estimates at ground level are the quantity of interest. While the Met Office makes corrections for the vertical profile of reflectivity (VPR) in order to better estimate surface precipitation rates, it is known that the errors associated with this correction increase with altitude.

The application of ground clutter filters allows the use of more low elevation data than would be possible otherwise. However, it is known that in some meteorological conditions, ground clutter filtering can bias the reflectivity measurements. This can particularly be an issue when dealing with the low maximum unambiguous velocities associated with C-band rain-rate optimised pulse repetition frequencies (PRF).

As part of the collaboration between the Met Office Radar Systems team and the National Severe Storms Laboratory (NSSL) Advanced Radar Techniques team, the Clutter Environment Analysis using Adaptive Processing (CLEAN-AP^{TM}) [Torres and Warde 2014] and Weather Environment Thresholding (WET) algorithms have been implemented as the ground clutter mitigation solution on the Met Office Cyclops-D signal-processing system.

In this work we develop and evaluate a classifier to increase the accuracy of QPE by selecting radar data from CLEAN-AP/WET filtered low elevation scans, or higher elevation scans with a larger less accurate VPR correction. Supervised training of the classifier is carried out using a large dataset of synthesized volumetric tiles corresponding to a wide range of weather and clutter signal parameters. It is important that each tile preserves local spatial structure of the radar data fields, as well as contains data from each scan elevation. Each tile is generated by superposing I&Q data from un-contaminated weather echoes and clutter-only echoes. Using this method, for each tile, a VPR-corrected surface QPE can be computed from the un-contaminated, un-filtered superposed and filtered superposed data at each scan elevation. A ground-truth surface QPE is computed from the un-contaminated low elevation radar data. This allows the training set to be labeled with the elevation and filter selection that results in the minimum QPE error. A multi-layer perceptron network is trained using back propagation to allow a near-optimal selection to be made when the ground-truth is unknown; this results in an improved surface QPE.

13.7 THE DEVELOPMENT OF A CANADIAN OPERATIONAL DUAL-POLARIZATION RAINFALL ESTIMATION ALGORITHM

S. BOODOO[1], D. HUDAK[1], N. DONALDSON[1], J. REID[1], D. MICHELSON[1], M. COUTURE[1], P. RODRIGUEZ[1], V. STOJANOVIC[1]

[1] Environment and Climate Change Canada (ECCC), Canada
sudesh.boodoo@canada.ca

Environment and Climate Change Canada embarked on its weather radar replacement program in 2016. The network will be completed in 2023 and be comprised of up to 32 S-band dual-polarized weather radars covering the most populous regions of the country. In the interim the network will be a hybrid one comprised of dual polarized S bands and Doppler C bands, two of which are dual polarized. Data from the dual-polarized C-bands collected at regular 10-minute frequency are being used to develop operational quantitative precipitation estimation (QPE) algorithms with a methodology which will later be adapted to the national radar network. A significant part of the methodology is assessing the data quality of the polarimetric measurements and the removal of non-precipitation echoes prior to applying rainfall retrieval algorithms. The quality assessment used to separate precipitating from non-precipitating echoes relies on measurements of cross correlation coefficient (ρ_{HV}), signal quality index (SQI) and gradients of differential phase (ϕ_{dp}) to determine rainfall regions in the radar scans at 0.5° elevation. Since the hydrometeor classification algorithm (HCA) has not been fully implemented and tested operationally at different frequencies, removal of ground clutter contamination is handled by Doppler filters in the signal processor and applied to the polarimetric measurements in addition to low signal to noise correction of ρ_{HV} and differential reflectivity (Z_{DR}). SQI thresholding was effective at removing contamination of radio interference radials and second trip echoes but care in the choice of value was required in some rain storm situations with directional shear. The broad range of velocity (V) in the beam produced abnormally low SQI and removed valid horizontal reflectivity (Z_H) pixels in the precipitation field. Systematic Z_{DR} biases are monitored by sun calibration and vertically pointing measurements. However, radome wetting complicated Z_{DR} measurements and introduced dynamic positive mean variations in Z_{DR} that are accounted for before applying attenuation corrections to Z_H and Z_{DR} and subsequently the rainfall retrieval algorithms. A method of monitoring and quantifying these Z_{DR} deviations in rain has been implemented.

Rainfall retrieval algorithms $R(Z_H)$, $R(Z_H,Z_{DR})$, $R(K_{DP})$, $R(K_{DP},Z_{DR})$ and $R(A_H)$, where K_{DP} and A_H are specific differential phase and specific attenuation, were applied after pre-processing with standard C-band coefficients. The 10-minute retrievals were summed to produce hourly and 24 hour accumulations to evaluate against a network of tipping-bucket and automated rainfall gauges within 100 km of the radar′s location. Each relationship was applied independently of rainfall intensity, hail contamination and radome wetting effects to evaluate against the gauge accumulations. $R(K_{DP})$ and $R(A_H)$ algorithms performed better in pure heavy rain, rain hail mixtures and wet radome situations but were very noisy at lower rain intensities. R(ZH) were better at lower intensities, provided that radome attenuation

and path attenuation effects were minimal. R(Z_H,Z_{DR}) showed slightly improved performance than R(Z_H) in these conditions. The individual retrieval relationships were not sufficient to capture the large variability of rainfall rates and accumulations in time and space. A combination of algorithms demonstrated better unbiased rainfall estimate in an operational environment.

13.8 A SIMULATION-BASED AND EXPERIMENTAL APPROACH TO INVESTIGATE THE IMPACT OF SKYSCRAPERS AND WIND TURBINE FARMS ON WEATHER RADAR DATA

KURTULU ÖZTÜRK[1], ALPER ÇUBUK[1], OSMAN KARABAYIR[2], ELİF UÇURUM[2]

[1] Turkish State Meteorological Service (TSMS), Turkey
[2] The Scientific and Technological Research Council of Turkey (ÖZTÜRK, RAPSİM-BİLGEM), Turkey
kozturk@mgm.gov.tr

As a result of the increasing needs for renewable energy and smart-multiple floor tall buildings in crowded metropolitans, the number of wind turbines and skyscrapers is rapidly increasing within the last decade. In this study, the impact of wind turbine farms and skyscrapers built after the installation of Istanbul weather radar are investigated through simulation-based analyses and actual radar outputs. It is seen that the single polarization Doppler radar in Istanbul can filter the clutter echoes caused by the targets such as skyscrapers and mountains; however, it may not completely remove the clutter from wind turbines due to their rotating blades. Partial Beam Blockage (PBB) due to wind turbine- or skyscraper-based beam shielding is the other error source. PBB diagrams, beam blockage fractions and Radar Quality Index (RQI) are derived by using 30 m resolution digital elevation database and modified open source wradlib code. Since the digital elevation databases do not include skyscrapers and wind turbines, their effects are not seen in PBB and RQI fields. This study shows that radar quantitative precipitation estimates (QPE) are also adversely affected by these error sources, resulting in under or over-estimation of precipitation. Simulation results and experimental analyses verify the adverse effects of the wind turbine- or skyscraper. Additionally, it is stated that super refraction can occur due to the low-level inversion; hence the radar beam may bend more even if it is not seen in theoretical PBB diagrams where the standard atmospheric refraction applies. This study presents visual examples including radar products, Google maps and PBB diagrams to support the statements.

13.9 A DUAL-POL RADAR SYNTHETIC QPE FOR OPERATIONS

J. ZHANG[1], L. TANG[1,2], S. COCKS[1,2], P. ZHANG[1,2], A. RYZHKOV[1,2], K. HOWARD[1]

[1] National Severe Storms Lab, USA
[2] University of Oklahoma/CIMMS, USA
jian.zhang@noaa.gov

The dual-polarization (DP) upgrade of the United States NEXRAD network was completed in 2013. As a result, a near surface hydrometeor classification and a DP radar quantitative precipitation estimation (QPE) were implemented at each radar site. The hydrometeor classification provided a much improved identification of non-hydrometeor echoes over the single-polarization (SP) radar techniques, and the DP QPE had much less contamination from anomalous propagation clutter and biological scatterers. The DP QPE, based on reflectivity (Z), differential reflectivity (Zdr) and specific differential phase (Kdp), provided improved precipitation estimates over the previous SP QPE in some warm season events where the freezing level was high. However, it had relatively large random errors due to its sensitivity to errors in Zdr observations, which can be significant at times. The DP QPE also suffered from discontinuities and some biases near the melting layer. Based on these initial assessments, a new DP radar synthetic QPE was developed within the Multi-Radar Multi-Sensor (MRMS) system.

The MRMS DP QPE calculates precipitation rates (R) based on a combination of specific attenuation (A), Kdp, and Z. The R(A) relationship was based on Ryzhkov et al. (2014) with some modifications based on a large number of case studies and real-time evaluations. The R(A) relationship has advantages of being immune to calibration errors in Z and Zdr and is insensitive to partial beam blockages. It is more linearly related to the liquid water content in the radar beam path than other radar variables. However, there are no well defined R(A) relationships in areas containing ice due to complex properties of hydrometeors in the mixed and ice phases. Therefore, the MRMS DP QPE applies R(A) relationship in areas where radar is observing pure rain, R(Kdp) in regions potentially containing hail. A vertical profile corrected R(Z) is applied elsewhere. The vertical profile correction is to account for the vertical reflectivity variations in and above the melting layer.

The MRMS DP QPE has been tested in real-time over CONUS since April 2017. It′s performance during the warm season of 2017 will be presented at the conference.

References

Ryzhkov et al. 2014: Potential Utilization of Specific Attenuation for Rainfall Estimation, Mitigation of Partial Beam Blockage, and Radar Networking. JTECH, 599-619.

13.10 INCLUDING THE TIME DIMENSION IN RADAR-RAINGAUGE BLENDING

MARC BERENGUER[1], DANIEL SEMPERE-TORRES[1], EDUARDO CASSIRAGA[2], JAIME GÓMEZ-HERNÁNDEZ[2]

[1] Center of Applied Research in Hydrometeorology, Universitat Politcnica de Catalunya, Barcelona, Spain

[2] Institute for Water and Environmental Engineering, Universitat Politcnica de Valncia, Valencia, Spain

marc.berenguer@crahi.upc.edu

The aim of he geostatistical methods to combine rainfall measurements by meteorological radars and rain gauge networks for improved rainfall estimation is to benefit from the direct rainfall observations at ground from rain gauges, and the detailed description of the space-time variability of the rainfall field captured by radar measurements (with typical resolutions of 1 km and 5-10 minutes).

Velasco-Forero et al. (2009) proposed to use Kriging with external drift (KED) with non-parametric variograms. The method uses the radar rainfall estimates as the drift to interpolate raingauge observations, and considers the anisotropy of the rainfall field thanks to the use of two-dimensional variograms, which are updated every time new (radar and gauges) rainfall observations are available. The work presented here explores the extension of that technique to include the time dimension in the blending process, so that rainfall estimates are based, not only on current observations, but also on past observations. This extension accounts for the correlation in time, and implicitly imposes some coherence between consecutive QPE maps.

The technique has been evaluated for several rainfall events in the area of Barcelona (NE Spain), analysing the effect on the results of factors such as the rain gauge density or the accumulation window.

13.11 RADAR REMOTE SENSING FOR RAIN/SNOW ESTIMATION IN AN ALPINE CONTEXT: THE GRENOBLE EXPERIMENT

G.DELRIEU[1], F. CAZENAVE[1], N. YU[2], D. FAURE[2], B. BOUDEVILLAIN[2], A. KHANAL[1], C. AUGROS[2], N. LE BASTARD[2], N. GAUSSIAT[2]

[1] Institut des Géosciences de l′Environnement, Grenoble, France

[2] Centre de Météorologė Radar, Météo France, Toulouse, France

guy.delrieu@univ-grenoble-alpes.fr

The experiment aims at developing advanced methods for rain and snow estimation using weather radar remote sensing techniques in high mountain regions for improved water resource assessment and hydrological risk mitigation. Since 2016, a unique observation system composed of a Météo France operated X-band radar (volumetric, Doppler, polarimetric) on top of Mt. Moucherotte (1913m), a X-band XPORT radar (volumetric, Doppler, polarimetric), a K-band micro rain radar (MRR, Doppler, vertically pointing) and in situ sensors (rain gauges, disdrometers), latter three operated by IGE on Universit Grenoble Alpes campus (210 m asl), has been deployed in Grenoble (France) region. The first aim of the Grenoble experiment is to characterize the 3-dimensional structure of precipitation and its time variability within the Grenoble intermountain basin using the high-resolution, multi-angle, multi-frequency, multi-parameter measurements of the three weather radar systems available, as well as the in-situ sensors. As a critical aspect, the melting layer development below the 0°C isotherm altitude is receiving particular attention, since (i) it determines the rain/snow occurrence at ground level, (ii) it creates several radar artefacts (bright band, attenuation) affecting rain/snow radar estimation. An algorithm for the automatic detection of the melting layer characteristics is used to establish a climatology of the melting layer (top and bottom altitudes, peak values of the various polarimetric and Doppler parameters). In the next step, an inversion model will be developed to derive hydro-meteorological variables of interest (hydrometeor types, concentration and size distribution, falling speed distribution, intensity) from the radar and in-situ observables. Such a high-resolution information about the space-time structure of precipitation within a region of several hundreds of km^2, in rugged topography, is critical for the assessment / improvement of numerical weather prediction models (e.g. MesoNH, MAR) and satellite precipitation estimation techniques implemented within the Global Precipitation Measurement mission (GPM, NASA). The second aim is the development and quantitative assessment of the rain/snow estimation techniques using the ground-based radars. Several aspects are being studied, including (i) the capability of the Moucherotte radar to detect summer convective heavy rain events and to quantify heavy and more regular rainfall at the regional scale as a function of the 0°C isotherm altitude and other factors (topography, weather types), (ii) the added value of the XPORT radar for rain/snow estimation in the Grenoble intermount basin and more generally for improving high-elevation radars′performance.

13.12 X-BAND RADAR ATTENUATION STATISTICS: HOW OFTEN DO WE LOSE THE SIGNAL?

H. LEIJNSE[1]

[1] Royal Netherlands Meteorological Institute, De Bilt the Netherlands
hidde.leijnse@knmi.nl

X-band radars are becoming increasingly popular for urban hydrology. Their relatively small size and low cost makes them ideal for such applications. Furthermore, because they are generally only used for quantitative precipitation estimation at short ranges, the spatial resolution of derived precipitation products is generally high, and measurements are close to the ground. The well-known challenge with X-band radars is signal attenuation. This can partly be compensated by using polarimetry, but this will only be able to provide rainfall estimates if the signal-to-noise ratio is sufficiently high. It is therefore highly relevant to know how often conditions occur in which the signal attenuation is so strong that this is no longer the case.

The rate of exceedance of different levels of X-band radar attenuation at different ranges is investigated. From this it is possible to derive how often an X-band radar is no longer able to provide any precipitation estimate due to attenuation, given its characteristics (transmit power, antenna gain, noise floor, etc.) and the rate of the rain that should still be detectable. The same can be done for virtual networks of X-band radars, where it is expected that a second radar will fill in if the first radar is too strongly attenuated. The influence of wet-radome attenuation is also investigated in this framework.

A 10-year radar-rain gauge product (1-km, 5-min resolution) over the Netherlands is used to simulate X-band attenuation, assuming a known relation between specific X-band attenuation and rainfall intensity. For a given virtual X-band radar location, attenuation is computed for every 5-minute interval and for all ranges and azimuths of the X-band radar by integrating the specific X-band attenuation fields over range. Rates of exceedance of attenuation levels are then computed as a function of radar range.

The rate of signal loss (i.e., signal-to-noise ratio less than 1) is investigated for several common types of radars for given minimum detectable rain rates. This rate is typically on the order of several minutes to hours per year for a minimum detectable rain rate of 1 mm/h, depending on the radar type.

13.13 ON THE USE OF NWP MODEL OUTPUTS TO PRODUCE RADAR VPR CORRECTIONS

T. LE BASTARD[1], O. CAUMONT[2], N. GAUSSIAT[1], F. KARBOU[4]

[1] Météo France (DSO/CMR), Toulouse, France
[2] Météo France (CNRM/GMME), Toulouse, France
[2] Météo France (CNRM/CEN), Grenoble, France
tony.lebastard@meteo.fr

Radar and gauge networks offer nowadays complementary means for measuring precipitation. Rain gauge networks provide a precise but often sparse measure of the rainfall while radar networks can sample precipitation at high resolution over broad areas but with large estimation errors. Combining hourly radar rain gauge accumulations is one of the solution considered at Météo-France for producing a better QPE product (Laurantin, 2008). However, there is a strong need to produce more accurate radar precipitation estimations for situations where gauge networks cannot represent well enough precipitation field: over short accumulation periods, in convective situations or in mountainous areas. One of the most important limitation for estimating precipitation at the ground with radars is the height of the radar beam that increases with the range from the radar and the elevation considered. The estimation becomes particularly difficult when the lowest radar elevation scan is blocked by mountains and higher elevation beams are used to estimate the precipitation behind.

In many operational weather services, a Vertical Profile of Reflectivity (VPR) correction (Kitchen et al., 1994; Andrieu and Creutin, 1995; Vignal et al., 1999; Borga et al., 2000; Seo et al., 2000; Germann and Joss, 2002; Tabary, 2007; Kirstetter et al., 2010) is calculated and used to estimate the reflectivity at the ground. However, to derive this correction, radar data are generally aggregated over large parts of the radar domain and the correction can hardly take into account the true temporal and spatial variability of the VPR. Ideally, the VPR should be estimated in each point of the radar domain.

Equipped with a radar forward operator (Caumont et al. 2006; Augros et al, 2016), the French operational high-resolution NWP model AROME (Brousseau et al., 2016) can produce realistic yet possibly shifted VPRs every hour with a horizontal resolution up to 1.3 x 1.3 km^2. The new method developed in this study relies on the potential of AROME forecasts for retrieving local VPRs. Through a Bayesian method (Kummerow et al., 1996, 2001; Caumont et al. 2010), the closest simulated VPR profile to the apparent one (observation) in terms of reflectivity is searched and then applied to estimate the rain rate a the ground.

This new method has been evaluated on several precipitating events. The VPRs retrieved by the method and the current operational algorithm are compared to VPRs produced by the vertically oriented scans of the neighbouring radars, showing the greater consistency of the new VPRs. The hourly radar accumulations obtained by using this new method are in better agreement with rain gauges accumulations than the current operational ones, the RMSE is reduced by about 10%, with most of the improvements at long range.

The computational time obtained suggest that the method is compatible with a real-time use and could be implemented operationally. This first result gives inter-

esting perspectives on how to improve radar QPEs at long range and over complex terrain.

References

Andrieu, H., & Creutin, J. D. (1995). Identification of vertical profiles of radar reflectivity for hydrological applications using an inverse method. Part I: Formulation. Journal of Applied Meteorology, 34(1), 225-239.

Augros, C., Caumont, O., Ducrocq, V., Gaussiat, N., & Tabary, P. (2016). Comparisons between S, Cand Xband polarimetric radar observations and convectivescale simulations of the HyMeX first special observing period. Quarterly Journal of the Royal Meteorological Society, 142(S1), 347-362.

Borga, M., Anagnostou, E. N., & Frank, E. (2000). On the use of real-time radar rainfall estimates for flood prediction in mountainous basins. Journal of Geophysical Research: Atmospheres, 105(D2), 2269-2280.

Brousseau, P., Seity, Y., Ricard, D., & Léger, J. (2016). Improvement of the forecast of convective activity from the AROMEFrance system. Quarterly Journal of the Royal Meteorological Society, 142(699), 2231-2243.

Caumont, O., Ducrocq, V., Delrieu, G., Gosset, M., Pinty, J. P., Parent du Chtelet, J., ... & Scialom, G. (2006). A radar simulator for high-resolution nonhydrostatic models. Journal of Atmospheric and Oceanic Technology, 23(8), 1049-1067.

Caumont, O., Ducrocq, V., Wattrelot, ., Jaubert, G., & Pradier-Vabre, S. (2010). 1D+ 3DVar assimilation of radar reflectivity data: a proof of concept. Tellus A, 62(2), 173-187.

Germann, U., & Joss, J. (2002). Mesobeta profiles to extrapolate radar precipitation measurements above the Alps to the ground level. Journal of Applied Meteorology, 41(5), 542-557. Joss, J., & Lee, R. (1995). The application of radargauge comparisons to operational precipitation profile corrections. Journal of Applied Meteorology, 34(12), 2612-2630.

Kirstetter, P. E., Andrieu, H., Delrieu, G., & Boudevillain, B. (2010). Identification of vertical profiles of reflectivity for correction of volumetric radar data using rainfall classification. Journal of Applied Meteorology and Climatology, 49(10), 2167-2180.

Kitchen, M., Brown, R., & Davies, A. G. (1994). Real-time correction of weather radar data for the effects of bright band, range and orographic growth in widespread precipitation. Quarterly Journal of the Royal Meteorological Society, 120(519), 1231-1254.

Kummerow, C., Olson, W. S., and Giglio, L. (1996): A simplified scheme for obtaining precipitation and vertical hydrometer profiles from passive microwave sensors.

IEEE Trans. Geosci. Remote Sens., 34, 12131232.

Laurantin O . ANTILOPE: Hourly rainfall analysis merging radar and rain gauge data. Proceedings of the International Symposium on Weather Radar and Hydrology, Grenoble. 2008; France, 1012 March 2008. 28.

Seo, D. J., Breidenbach, J., Fulton, R., Miller, D., & O′Bannon, T. (2000). Real-time adjustment of range-dependent biases in WSR-88D rainfall estimates due to nonuniform vertical profile of reflectivity. Journal of Hydrometeorology, 1(3), 222-240.

Tabary, P. (2007). The new French operational radar rainfall product. Part I: Methodology. Weather and forecasting, 22(3), 393-408.

Vignal, B., Andrieu, H., & Creutin, J. D. (1999). Identification of vertical profiles of reflectivity from volume scan radar data. Journal of Applied Meteorology, 38(8), 1214-1228.

13.14 QUALITY-BASED RADAR DATA PROCESSING AND QPE AT THE SLOVAK HYDROMETEOROLOGICAL INSTITUTE

L. MÉRI[1], M. JURAŠEK[1], L. OKON[1], J. KAŇÁK[1]

[1] Slovak Hydrometeorological Institute (SHMÚ), Bratislava, Slovakia
ladislav.meri@shmu.sk

Some long lasting radar and rain-gauge data quality issues especially in the mountainy terrain of Slovakia led to the development of the qRad radar data processing and the qPrec precipitation estimating software at the SHMÚ.

The qRad software estimates the actual quality of the radar volume data by various quality indexes and tries to correct some undesirable effect on the measurement (e.g. beam-blockage, attenuation, interference). The corrected volume data are then directly processed to composite radar product and quality maps. The resulting radar products are used by the forecasters and for QPE, and are used for validation of the EUMETSAT H-SAF precipitation products. The software was installed also at the Hungarian Meteorological Service to support the H-SAF validation efforts.

The qPrec package uses estimation theory and probabilistic approach to estimate the rainfall intensity as accurate as possible based on heterogeneous input data (rain-gauges, radars, satellites, lightning detection). The calibrated input data fields are combined according to their precision and actual quality. The resulting precipitation estimates are regularly validated by the climatological rainfall amounts and by hydrological model runs. The first results are showing dramatic improvement of the precipitation estimation compared to the methods used previously at the institute.

13.15 RADAR-DERIVED QUANTITATIVE PRECIPITATION ESTIMATION BASED ON VERTICAL-RAINCLOUD TRAJECTORY PROFILES

HANGGAR G MAWANDHA[1], SATORU OISHI[2]

[1] Graduate School of Engineering, Kobe University, Japan

[2] Professor, Research Center for Urban Safety and Security, Kobe University, Japan

mawandha@stu.kobe-u.ac.jp

Utilization of radar polarimetric variables such as reflectivity (Zh), differential reflectivity (Zdr), and specific differential phase (Kdp), has revealed to produce robust Quantitative Precipitation Estimation (QPE). However, relationships of such factors known as growth or evaporate of drops, signal enhancement in a bright-band, and strong updrafts or downdrafts in convective rain are rarely considered for generating the QPE model. These are then assuming as causes bias between radar and raingauge measurements. Furthermore, the wind-induced factor, updraft as well as downdraft during cloud developing and dissipating process, evidently trigger some distortions in point rainfall measurement. This study is intended to assess the factor of inter-space bias between radar bins and raingauges to generate better QPE algorithm using vertical profile of raincloud. A four dimensional window including spatial (x and y axes) distribution, vertical profile, and time of occurrence, is statistically assigned.

Through the vertical profile, a trajectory pattern of raincloud's movement containing updraft and/or downdraft at the upper raingauge position could be depicted in a form of rainfall amount. The spatial correlations in vertical dimension among the trajectory fields are used to estimate the descending speed and the horizontal movement of raincloud, correspondingly. Through this process, non-parametric density estimators could be generated from the selected raingauges representing various distances from the radar site. Non-parametric estimators have no fixed structure and depend upon all the data points to get an estimate. After all variable values obtained, the empirical weighted ratio is distributed over the entire of radar grids for updating the QPE. For checking a consistency of the spatial variance over the radar coverage area, all available raingauges are utilized to validate the result. This model performs more compatible QPE model to be used for various types of rainfall, as convective and stratiform, since it is tracking a real-time profile of raincloud trajectory while such factors causing distortion toward point rainfall measurement are taken into account. Moreover, it gives better understanding particularly dealing with physical parameter during raincloud formation stages.

13.16 POLARIMETRIC RADAR AND MACHINE LEARNING: FROM THE SOLID PHASE HYDROMETEOR STATISTICS TO THE PRECIPITATION INTENSITY AT THE GROUND

Y. CHEVALLEY[1], N. BESIC[1,2], J. GEHRING[1], L. FORESTI[2], I.V. SIDERIS[2], M. GABELLA[2], U. GERMANN[2], A. BERNE[1]

[1] Environmental Remote Sensing Laboratory (LTE), EPFL, Lausanne, CH
[2] Radar, Satellite and Nowcasting Dept., MeteoSwiss, Locarno-Monti, CH
nikola.besic@epfl.ch

The relationship between the dominant microphysical processes in the ice phase (e.g. aggregation and riming) and the quantity of liquid precipitation at the ground level has not been extensively studied. In fact, it is often assumed that the local variations of liquid precipitation at the ground level are mostly influenced by warm rain processes (e.g. breakup, coalescence). In this contribution we explore and make use of the links between the respective proportions of solid hydrometeors aloft and the estimated liquid precipitation at the ground level.

The solid-phase hydrometeor statistics are obtained by applying a semi-supervised classification on the dual-pol radar datasets acquired by the MeteoSwiss C-band Monte Lema radar. These datasets relate to a dozen events of intense precipitation with significant hydrological response, over the valley of the Maggia river, Ticino, Switzerland. The precipitation intensity data come from the operational product merging radar estimated liquid precipitation with the corresponding rain gauge measurements.

In the first part of this study (analysis) we focus on the evaluation of the relationship between the precipitation intensity and the respective proportions of crystals (%CR), aggregates (%AG) and rimed particles (%RP) in the vertical column above the corresponding ground level pixel (1 km2). Various regression approaches indicate a relevant relationship between the solid-phase hydrometeor proportions and the intensity of liquid precipitation at the ground. This relationship is rather non-linear and therefore non-linear functions are fitted to the data: %CR-QPE, %AG-QPE and %RP-QPE.

The next step (synthesis) is to use machine learning to automatically estimate the liquid precipitation at the ground level from the proportions of solid hydrometeors. Namely, a neural network with one hidden layer, has as input %CR, %AG and %RP as well as the non-independent descriptors derived from these three (e.g. lower resolution, entropy, anisotropy), and provides liquid precipitation at the ground level as output. The neural network is trained and tested by means of cross validation, using the datasets analyzed in the first part. The prospective of exploiting the spatial correlation of observations is studied by involving the convolutional layers i.e. by introducing Convolutional Neural Networks (CNN) into the synthesis part.

The presented machine learning based approach, characterized by a high reliability due to the weaker clutter contamination of the solid phase measurements, provides complementary information to conventional QPE methods. This can be very relevant in the case of complex terrain.

13.17 QUANTIFICATION OF MEASUREMENT ERROR OF POLARIMETRIC X-BAND RADARS IN MOUNTAINOUS REGIONS

NAN.YU[1], NICOLAS.GAUSSIAT[1]

[1] Radar Meteorology Centre, Météo-France, France
nan.yu@meteo.fr

Four X-band dual-polarization radars were deployed in the French Alps between 2011 and 2015 and more recently have been incorporated formally into the radar network of Météo-France.

In this mountainous region, the radars′ beam shielding by the complex terrain, the very different altitudes of the radars, the significant attenuation at X-band and the low density of rain gauges have made the integration of these radars into the operational service a challenging exercise. In this study, a framework used to evaluate the corrections applied to the volume data produced by the radars is presented. The residual errors related to the partial beam blockages, the attenuation by rain, the wet radome, and the melting layer are carefully studied and disentangled. The results of the analysis suggest that: 1) the beam blockage correction requires the use of a much higher resolution digital elevation models (DEM) in mountainous regions than the 250 m resolution DEM currently used, 2) the dual-pol reflectivity (Z_h) attenuation correction used at Météo-France performs well in the rain but the differential attenuation on Z_{dr} is overestimated, 3) the attenuation of wet snow is underestimated and a mean error of 2 dB is induced by the melting layer in spring and autumn, 4) the wet radome, as well as producing significant attenuation on Z_h, induces differential attenuation on Z_{dr}.

The attenuation in the melting layer is further investigated taking advantage of the height difference between the radars sites. A new specific attenuation coefficient for wet snow is suggested and it is shown to reduce the seasonal bias on three particular events observed in spring and autumn.

13.18 RAINFALL RATE ESTIMATION USING HYDRO-ESTIMADOR (GOES) AND DUAL POLARIMETRIC RADAR IN A COASTAL TROPICAL BASIN OF PERU

J. VALDIVIA[1], M. SAAVEDRA[1], D. SCIPION[1], Y. SILVA[1], J. PRADO[1], B. L. CHEONG[2]

[1] Instituto Geofísico del Perú, Lima, Perú
[2] Advanced Radar Research Center, University of Oklahoma, EEUU
jvaldivia@igp.gob.pe

Peru is a vulnerable country to natural hazards from hydrometeorological origin with great social and economic impact, such as the intense rainfall in the northern and central coast during the "El Niño Costero 2017" phenomenon. Usual Peruvian conditions in the coast are very dry and observations of meteorological events are scare. Due to the wide and complex topography, rain gauges are not representative of the area, which represent a limitation for hydro-meteorological studies.

In early 2018, the Instituto Geofísico del Perú and the Advanced Radar Research Center of the University of Oklahoma, installed a Dual-polarimetric X-band radar (PX-1000) in middle basin of Rimac (12.0°S, 76.5°N, 2900 m asl) for a better understanding of meteorological events and spatial quantification of rainfall.

In this work, we will evaluate the Hydro-Estimador from NOAA′s Geostationary Operational Environmental Satellites (GOES) and rainfall rate estimations based on polarimetric measurements obtained from PX-1000. Uncertainties derived from stratiform and convective rain and possible applications for operational use will be discussed.

13.19 CLOUD RADAR SPECTRAL POLARIMETRY FOR QUANTITATIVE PRECIPITATION ESTIMATION

A.MYAGKOV[1], T. ROSE[1]

[1] Radiometer Physics GmbH, Meckenheim, Germany
alexander.myagkov@radiometer-physics.de

Since decades polarimetric weather radars have been widely used by national weather services for monitoring clouds and precipitation. Beside the detection and ranging of atmospheric scatterers, modern weather radars provide a detailed classification of precipitation and estimate its intensity. Such retrievals are based on a set of polarimetric variables including backscattering parameters (e.g. differential reflectivity and correlation coefficient) and propagation parameters (e.g. specific differential phase shift). In general, rain rate retrievals that include propagation properties have superior accuracy due to their proportionality to the amount of liquid water in a volume. Nevertheless, the estimation of propagation parameters from the radar signal is often problematic, especially at low signal-to-noise ratios. Relatively low accuracy of the quantitative retrievals based only on backscattering parameters is mostly related to an assumed particle size distribution. Operational weather radars usually perform fast azimuthal scans at low elevation in order to cover large areas and achieve high temporal resolution. Such regimes often limit an application of advanced techniques based on the Doppler processing.

Polarimetric cloud radars, which become more and more available nowadays, have a great potential to overcome the problems of weather radars in improving the accuracy of precipitation intensity estimations. Having Doppler capabilities, polarimetric cloud radars can measure spectra of polarimetric variables with the resolution down to a few cm/s. At millimeter wavelengths, scattering of the radar signal by raindrops larger than 1 mm in size is in the Mie regime. Detection of Mie effects in a power spectrum is a challenging task. In contrast, Mie effects are clearly seen in the spectral differential reflectivity and the spectral differential phase as consecutive peaks and lows. A deep analysis of the Mie effects in the polarimetric spectra can be a base for a development of advanced retrieval algorithms.

In this talk we present first spectral polarimetric observations in rain at W-band. The measurements are obtained with a newly developed scanning FMCW cloud radar with the hybrid polarimetric configuration. We show that (1) polarimetric spectra can be used for a relatively simple separation of backscattering and propagation effects and (2) polarimetric spectra can be used for particle size distribution retrievals.

13.20 PRECIPITATION VARIABILITY BETWEEN AFTERNOON MIXED LAYER AND FREE ATMOSPHERE CLOUDS IN SEMI-ARID SOUTHEAST ARIZONA

PIETER HAZENBERG[1], MAX MITCHELL[1], ERIKA CROPP[1], DAVE GOODRICH[2], ELEONORA DEMARIA[2], MARK KAUTZ[2], WALTER PETERSEN[3]

[1] Department of Hydrology and Atmospheric Sciences, University of Arizona, Tucson, AZ, USA

[2] USDA Agricultural Research Services, Southwest Watershed Research Center, Tucson, AZ, USA

[3] NASA Marshall Space Flight Center, Huntsville, Al, USA

hazenberg@email.arizona.edu

Precipitation in semi-arid regions is highly variable in space and time, and is subject to significant inter-annual variability, fluctuating at multi-decadal time scales due to oceanic sea surface temperature (SST) variations (e.g. ENSO). For the southwest US, the majority of precipitation results from convectively generated high-intensity rainfall that occurs during the warm season as part of the North American Monsoon (NAM).

The current work focuses on NAM precipitation variability observed within the $\sim$149 km^2 Walnut Gulch Experimental Watershed (WGEW) in southeast Arizona. Within WGEW, detailed high-resolution precipitation observations have been performed since the mid-1950's. For the summer of 2017, additional information of on spatial variations of precipitation and rain drop size variations was investigated by installing an additional ceilometer, two vertically pointing radars, multiple disdrometers and gps-met observations.

The current work will present some detailed analyses of these observations. We will focus specifically on afternoon precipitation events, distinguishing between those events originating from clouds formed on top of the mixed boundary layer and those within the free atmosphere above. Between both types of clouds, a clear distinction in surface precipitation and rain drop size characteristics was observed, with the most intense rainfall intensities originating from mixed layer clouds. However, for both types of precipitation, the reflectivity profile, as observed by vertically pointing radar, shows similar reflectivity profile characteristics. The elevated terrain of the southwest US is known to pose a challenge for operational weather radar, where for many locations, observations are taken at higher elevation. In case information on the original cloud generating mechanisms would be known, potentially improved surface precipitation estimates can be obtained.

13.21 THE EUROPEAN CLIMATOLOGICAL HIGH-RESOLUTION GAUGE-ADJUSTED RADAR RAINFALL DATASET:

A. OVEREEM[1], G. VAN DER SCHRIER[1], E.V. VAN DER PLAS[1], G. LENDERINK[1], H. LEIJNSE[1], J.F. MEIRINK[1], S. PARK[2], M. BERENGUER[2], D. SEMPERE-TORRES[2]

[1] Royal Netherlands Meteorological Institute, the Netherlands
[2] Centre de Recerca Aplicada en Hidrometeorologia, Universitat Politècnica de Catalunya (CRAHI-UPC), Barcelona, Spain
overeem@knmi.nl

The pan-European trend toward more frequent extreme precipitation is unequivocal. Nevertheless, an accurate (sub-) daily rainfall product covering Europe at the km scale is currently lacking. This internally funded project, in the framework of KNMI′s Multiannual Strategic Research Program, addresses this gap by deriving a climatological dataset of 1-h and daily rainfall depths at a 2-km grid covering a large part of Europe for 2012 to present. The archive of EUMETNET-OPERA radar composites will be employed as a starting point. First, remaining ground clutter is removed employing satellite products. Next, it is merged with a pan-European rain gauge dataset in order to substantially improve its quality.

Collaboration is established with the Center of Applied Research in Hydrometeorology of the Universitat Politcnica de Catalunya (CRAHI-UPC). In the context of the European Projects ERICHA (www.ericha.eu) and ANYWHERE (www.anywhere-h2020.eu), CRAHI-UPC has been producing in real time gauge-adjusted rainfall accumulations from the EUMETNET-OPERA composites using the rain gauge records of the SYNOP network at European scale. This product will be used as a basis for an evaluation of the KNMI outputs. The proposed dataset opens the possibility to derive reliable rainfall climatologies. We focus on the seasonal & diurnal cycle and the occurrence of extreme rainfall across Europe. The high spatial resolution allows to investigate the clustering and spatial extent of rain showers over Europe, which is a hot topic in climate research and of utmost importance from a climate impact perspective. The areal extent of extreme rainfall events is related to dew point temperature observations and atmospheric circulation.

Subsequently, the climatological rainfall dataset is utilised to validate satellite precipitation products (like the gridded IMERG product from the Global Precipitation Measurement (GPM) mission, and Meteosat Second Generation precipitation products). Hence, the quality of satellite-based quantitative precipitation estimates is assessed for a variety of European climates.

The gridded rainfall dataset will become available to the scientific community, which would boost the research on short-duration, small-scale extreme precipitation events to which the European society is vulnerable. We expect improved satellite rainfall retrieval algorithms, (validation of) weather forecasts, as well as attribution of extremes. It may also contribute to a better (near) real-time rainfall product, i.e. connect to the operational OPERA composite. In the end, this dataset will help to reduce the vulnerability to extreme weather events.

We will present an overview of the project, which is expected to start January 2019.

13.22 SEVERE HAIL DETECTION: HYDROMETEOR CLASSIFICATION FOR POLARIMETRIC C-BAND RADARS USING FUZZY-LOGIC AND T-MATRIX SCATTERING SIMULATIONS

M. SCHMIDT[1], S. TRÖMEL[1], A. V. RYZHKOV[2], C. SIMMER[1]

[1] Institute of Meteorology/Univ. of Bonn, Bonn, Germany
[2] CIMMS/Univ. of Oklahoma, Norman, Oklahoma, USA
mschmid6@uni-bonn.de

Large hail is a frequently occurring and sometimes devastating phenomenon, especially during summertime convective events. Many occasions of hail stones with diameters above 5 cm up to 14 cm have been reported and confirmed in the last years in central Europe. Concepts and algorithms to detect and distinguish large hail from small hail or rain with polarimetric radars at S band exist. However, most weather radars in Europe operate at C band. Here we present the usability of operational hydrometeor classification algorithms, like the fuzzy-logic based algorithm in Park et al. (2009), at C band and the necessity of wavelength-specific, simulated parameters for these algorithms. We emphasize that specific attenuation Ah is a major factor in identifying and discriminating hail at C band. Simulating value ranges of polarimetric variables at C band and including Ah are vital key factors for hydrometeor classification at C band. Additionally, we provide an approach to obtain parameters to distinguish between rain and small, large and giant hail at C band with fuzzy-logic. The resulting fuzzy-logic based algorithm can be used for nowcasting as it enables real-time operational hail detection and size discrimination.

13.23 PRECIPITATION MEASUREMENTS BY RADAR DURING DACCIWA

JAN HANDWERKER[1], NORBERT KALTHOFF[1], THE KITCUBE TEAM[1]

[1] Karlsruhe Institute of Technology, Institute of Meteorology and Climate Research, Department Troposphere Research, Karlsruhe, Germany
jan.handwerker@kit.edu

As part of the DACCIWA (Dynamics-aerosol-chemistry-cloud interactions in West Africa) measuring campaign, the KITcube was installed close to Sav, Benin, nearly 200 km north of the capital Cotonou at the Atlantic ocean. X-band radar measurements were performed from mid June to end of July 2016, covering the onset of the summer monsoon season. The X-band radar measured at a temporal resolution of 5 minutes up to a range of 100 km.

With this contribution we will present an overview of our measurements: spatial rain distribution, categorization of convective and stratiform events as well as

13.24 REGIME-DEPENDENT RADAR REFLECTIVITYRAIN RATE RELATIONSHIPS AND THEIR POTENTIAL TO IMPROVE RADAR RAINFALL ESTIMATES

B. KIRSCH[1], F. AMENT[1], M. CLEMENS[1]

[1] Meteorological Institute, University of Hamburg, Bundesstrasse 55, 20146 Hamburg, Germany
bastian.kirsch@uni-hamburg.de

Quantitative estimates of current rainfall fields are of central importance for hydrological processes and commonly obtained from weather radar measurements. Large parts of the uncertainty in this estimation can be assigned to the variability of the drop size distribution (DSD) that determines the relationship between radar reflectivity and rain rate (ZR relationship). Since the classical stratiform/convective classification is related to characteristic properties of the DSD, the use of different ZR relationships for the respective type provides a feasible technique to account for the inherent microphysical variability of rainfall.

In order to quantify the potential of double ZR relationships to improve radar rainfall estimates, high resolution observation data of micro rain radars in Northern Germany are analyzed. The stratiform and convective rainfall regimes are separated with the help of two methods, establishing threshold definitions for the rain rate-dependent mean drop size and the prefactor of the power-law ZR relationship. For reference, the double ZR relationships adjusted for the two separation methods are tested against a standard MarshallPalmer and a single adjusted ZR relationship.

The comparison of the DSD-based and reflectivity-derived rain rates shows that applying two different ZR relationships roughly halves the long-term estimation error of the rainfall accumulation compared to a single ZR relationship. The correlation coefficient between the instantaneous rain rates increases by around 20% while the root mean square error reduces by between 15 and 25%, dependent on the separation method.

According to the presented results, the use of separate ZR relationships for stratiform and convective rainfall is a simple and promising technique to improve radar rainfall estimates. Especially in operational and hydrological applications this approach avoids potentially dangerous underestimations of local rainfall intensities by single ZR relationships.

13.25 SIMPLE YET ADJUSTABLE RADAR DATA VIEWER

C.FENNIG[1], T.EINFALT[1], I.FRERK[1]

[1] hydro & meteo GmbH & Co. KG, Luebeck, Germany
c.fennig@hydrometeo.de

For monitoring and studying weather radar data it is important to have a good and simple tool. Therefore, the radar data viewer ScoutView2 has been developed. This visualisation software is mainly used for radar data (as single image or time series), but can also be applied to wind or satellite data. Data formats supported already comprise:

- DX, IR, PF, RQ, RW, RZ, RADOLAN, COSMO-DE etc. (German Weather Service/DWD)
- GRIB
- Rainbow (South African Weather Service/SAWS and Royal Rainmaking Department Thailand/RRD)
- HDF5 (Royal Netherlands Meteorological Institute/KNMI, ODIM, VOLTAIRE)

The radar data display can be adjusted to the user′s needs for an easy analysis of radar data as well as direct comparisons to rain gauge data. ScoutView2 offers a choice of additional data to be displayed such as OpenStreetmap, Microsoft Satellite images, user defined overlay layers (shp or gen format), cluttermaps or rain gauge locations. The colour scale either adapts automatically to the radar data or can be adjusted manually.

Radar data types range from single radar images over composites with many radars to ensembles or precipitation sums. It can be switched between different ensemble or forecast runs to visually analyse the data. HDF5 volume data can be viewed step by step through the elevations or in one elevation through time. This plays an important role when detecting and correcting height-related radar problems (e.g. bright band). Moreover, accumulated precipitation of catchment areas can be displayed by ScoutView2, which is essential for hydrologists.

Another advantage of this simple radar data viewer is its applicability in both offline mode (for detailed data analysis) and online mode (for current weather observations or forecasts).

Some technical functionalities of ScoutView2 are:

- image export (jpg, gif or png) of single radar images or an entire time interval
- customization of image animation with arrow buttons and animation speed settings
- mouse zoom, pan or rectangle selection on the map surface
- save zoom settings for a later comparison with modified data
- display of pixel values and coordinates while mouse moving

- rain sum calculation for animated time interval

ScoutView2 enormously simplifies the work with cluttermaps for quality control algorithms: It displays the cluttermap as adjustable layer over the radar image and allows to add or remove pixels in the cluttermap by mouse click.

13.26 DIFFERENTIAL PHASE PROCESSING AT X-BAND FREQUENCY TO IMPROVE THE ESTIMATION OF THE SPECIFIC ATTENUATION AND BACKSCATTER DIFFERENTIAL PHASE

R. REINOSO-RONDINEL[1], C. UNAL[1], H. RUSSCHENBERG[1]

[1] Department of Geoscience and Remote Sensing, Delft University of Technology, The Netherlands

r.r.reinosorondinel@tudelft.nl

One of the benefits of polarimetric radars is given by the measurements of the differential phase ψ_{DP} because it carries polarimetric information related to the number and shape of hydrometeors, independently of radar calibration and signal attenuation. At C- and X-band frequencies, ψ_{DP} consists of two processes: one that occurs in the same direction of wave propagation (propagation differential phase ϕ_{DP}) and another in the opposite direction (backscatter differential phase δhv). While ψ_{DP} is commonly used for attenuation correction (i.e., estimation of the specific attenuation), recent studies have demonstrated that δhv can provide information concerning the dominant size of raindrops. However, the estimation of both ϕ_{DP} and δhv profiles is not straightforward given their coupled nature and the noisy behavior of ψ_{DP} profiles, especially over short paths. Often, is estimated by the Z_ϕ method which uses, among other parameters, the total span of a given ϕ_{DP} profile and assumes a predefined value of the required parameter . Yet, it is known that is sensitive to temperature and drop size distribution variability. In order to avoid such sensitivity, the extended version of the ZPHI method includes an optimization step to estimate , using ϕ_{DP} as a reference. In consequence, the estimation of can become challenging if ϕ_{DP} is not carefully estimated from ψ_{DP}.

In this work, the impacts of estimated ϕ_{DP} profiles on the estimation of the specific attenuation , using the extended version of the Z_ϕ method, are examined. Special attention is given to the optimization of the parameter in rain. In addition, an improved technique to compute δhv is proposed to depict the spatial-variability of dominant raindrop size in convective storms. These approaches were examined using diverse storm events observed by a polarimetric X-band radar in the Netherlands, with a maximum-range of 15 km and spatial-resolution of 0.03 km.

A detailed analysis showed that the minimum errors associated with the optimization of depend on the accuracy of estimating ϕ_{DP} profiles. An adaptive and high-resolution (AHR) method that estimates ϕ_{DP} profiles at range resolution scales, led to stable values of and that were consistent with the expected variability of raindrop size distribution in the observed storms. It was also noticed that estimated δhv fields were consistent with the dominant raindrop size. By following the presented study, the reader can consider the AHR approach to obtain an accurate estimation of ϕ_{DP} and thereby enhanced estimation of A and δhv in rain, addressing the challenge of processing ψ_{DP} over short paths ($\sim$5 - 10 km) at X-band frequency.

13.27 LONG-TERM ANALYSIS OF RADAR RAINFALL MEASUREMENTS IN THE UK FOR HYDROLOGICAL APPLICATIONS

M. A. RICO-RAMIREZ[1]

[1] Department of Civil Engineering, University of Bristol, Bristol, BS8 1TR, UK
m.a.rico-ramirez@bristol.ac.uk

Weather radars can provide precipitation measurements with high spatial and temporal resolutions. However, rainfall estimation using weather radars can be subject to different sources of errors such as radar echoes due non-meteorological origin, radar calibration, variations of the drop size distribution affecting the reflectivity-rainfall (Z-R) equation, radar signal attenuation, variation of the vertical profile of reflectivity, radar beam broadening with range, partial beam blocking, radar beam overshooting the shallow precipitation, etc. (Collier, 1996; Villarini and Krajewski, 2010). Different correction techniques are applied routinely by the national meteorological offices to minimise these errors so that the radar rainfall measurements agree with rainfall observations provided by rain gauge networks (Harrison et al., 2012). However, in order to use long-term spatial radar rainfall measurements for hydrological studies is necessary to ensure that the radar rainfall product has the best possible quality and there are no gaps in the rainfall records. In this paper, we analyse the quality of the weather radar rainfall measurements for the last 10 years (2006-2015) in the UK at 1km/1h spatial/temporal resolutions. We looked at some of the challenges to interpolate missing time periods as well as some of the techniques to improve the quality of the radar rainfall by using quality-controlled daily rain gauge observations.

This work has been completed as part of the Marie Curie Initial Training Network QUICS. This project has received funding from the European Unions Seventh Framework Programme for research, technological development and demonstration under Grant agreement No 607000.

13.28 ACCURATE MONITORING OF PARTIAL BEAM BLOCKING USING EMISSION AND SHORT-RANGE VERTICAL REFLECTIVITY CONSISTENCY

R. J. THOMPSON[1], A. J. ILLINGWORTH[1]

[1] University of Reading, UK
robert.thompson@reading.ac.uk

Blocking of the radar beam is a common problem for operational weather radars, where the beam is partially blocked by trees, masts, pylons or other man-made structures, usually within a few km of the radar. The effects of partial beam blocking are immediately obvious from accumulations of the reflectivity or derived rainfall over the course of a month, with partially blocked rays appearing as "spokes". Corrections of up to a factor of two or three are applied operationally to correct for partial beam-blocking, usually based on the observed horizon or interpolation across the partially blocked beams, but these corrections are not necessarily accurate, cannot be used for high blocking fractions nor can they respond to changes in the blocking with the season or to new blocking features.

We propose a correction for partial blocking based on two different techniques, the first using vertical consistency of reflectivity at short range and the second by monitoring the increased noise from the beam blocking.

1. Comparison of the reflectivity at each gate over short ranges (inside 25km) at two different elevations when both beams are sampling widespread rain below the melting layer, followed by very careful elimination of ground clutter, reveals the amount of blocking in the lower beam. Once this blocking fraction is known, then it can then be used to correct the lower beam at longer ranges, where the upper beam would often be sampling the ice or melting layer. In practice, suitably widespread rainfall for estimating beam blocking occur on average every six weeks or so, with a tendency for fewer blocking calibrations in the winter time because of a lower bright band.

2. By measuring the radar noise levels for each ray we can also get an estimate of the degree of blocking. Objects blocking the beam will radiate at the radar frequency lead to increased noise being detected at the radar receive, with the increase depending upon the degree of blocking. If the noise level is monitored continuously each day for each azimuth and every scan, then the blocking can be estimated in dry weather, so that the degree of blocking can be interpolated between calibrations using the short range vertical consistency in the rain itself.

We will present results from the UK C-band weather radar network operated by the Met Office, in particular from the Chenies radar, located to the North-West of London. We find that day-to-day changes in blocking are generally small, but we are able to detect large seasonal changes in the blocking, as well as identifying abrupt changes to the pattern.

13.29 GROUND ECHO REMOVAL EMPLOYING DUAL-POL C-BAND RADARS IN THE NETHERLANDS:

A. OVEREEM[1,2], R. UIJLENHOET[2], H. LEIJNSE[1]

[1] R&D Observations & Data Technology, Royal Netherlands Meteorological Institute, the Netherlands

[2] Hydrology and Quantitative Water Management Group, Wageningen University, the Netherlands

overeem@knmi.nl

Since January 2017, the Royal Netherlands Meteorological Institute (KNMI) operates two new dual-polarization C-band weather radars in STAR mode. Data from these radars are composited to obtain operational 2-D rainfall products for the Netherlands. These products are extensively used for e.g. nowcasting, water management, and climatological purposes.

Despite the application of Doppler filtering, remaining ground echoes due to anomalous propagation still pose a problem. Moreover, remaining sea echoes can be abundant. This calls for additional filtering algorithms.

The polarimetric radars offer new opportunities for ground clutter removal. Here we explore the use of the correlation coefficient to discriminate weather from non-weather echoes by simply applying a threshold value. In addition, we employ an existing method to estimate the depolarization ratio from the correlation coefficient and the differential reflectivity. Since high depolarization points to non-weather echoes, depolarization ratios above a certain threshold value will be filtered, resulting in zero precipitation estimates. For both methods a sensitivity analysis will be carried out to find optimal threshold values for these C-band radars in a temperate climate.

The verification will focus on the presence of remaining ground echoes for at least a few case studies with severe ground clutter, not only including non-rainy cases. This is achieved by mapping the number of exceedances of radar reflectivity factors for given thresholds. Moreover, accumulated rainfall maps will be obtained to detect radar pixels with unrealistically large rainfall depths. The results from both methods will be compared, and also contrasted to the results for which no method has been applied.

13.30 DUAL-POLARIZATION RADAR RAINFALL ESTIMATION USING A DATABASE OF SIMULATED RAINDROP SIZE DISTRIBUTIONS

BIN PEI[1], FIRAT Y. TESTIK[2]

[1] Impact Forecasting, Aon Benfield, Chicago, IL, USA

[2] Civil and Environmental Engineering Department, University of Texas at San Antonio, San Antonio, TX, USA

firat.testik@utsa.edu

A new radar rainfall retrieval algorithm (Rainfall Estimation using Simulated Raindrop Size Distributions RESID) for dual-polarization radars was developed. There are two types of algorithms typically used by the dual-polarization radars to perform liquid rainfall estimations. The first type of algorithms uses the rain rate estimators as functions of the dual-polarization radar observables (i.e. horizontal reflectivity Z_h, differential reflectivity Z_{dr}, and specific differential phase K_{dp}). The second type of algorithms uses the theoretical rain rate computation equation and the retrieved raindrop size distributions (DSDs). Both types of algorithms typically include parameterizations developed using regression analyses, and as such, they may suffer from the regression uncertainties in the parameterizations. The RESID takes advantage of both types of algorithms and does not utilize a regression analysis. Therefore, the RESID is not subject to regression uncertainties. Moreover, by using a set of carefully selected cost functions, the RESID aims to reduce the effect of the radar measurement noise.

In developing the RESID algorithm, a large database of gamma DSDs was first constructed by varying the values of the normalized gamma DSD parameters (i.e. D0 - median volume diameter, Nw - normalized intercept parameter, and - shape parameter of the gamma distribution) within certain ranges. The corresponding dual-polarization radar observables were simulated using the T-matrix method. Then, the rain rate associated with each of the DSDs was computed using the theoretical rain rate computation equation. A set of cost functions was developed using both the simulated and the measured dual-polarization radar observables to select the representative DSDs from the simulated DSD database. For given values of the measured triplet of radar observables (i.e. Z_h, Z_{dr} and K_{dp}), a cost function was selected following an optimization scheme that was intended for maximizing the performance of the algorithm. Finally, the rain rate for the given triplet of radar observables was estimated by averaging the rain rates calculated from the selected representative DSDs.

The performance of the RESID algorithm was evaluated by comparisons with a benchmark algorithm, WSR-88D QPE (Weather Surveillance Radar 1988 Doppler Quantitative Precipitation Estimation), in liquid rainfall estimations. In these comparisons, the radar and rain gauge measurements from the Mid-latitude Continental Convective Clouds Experiment (MC3E) were utilized. The RESID was found to outperform the benchmark algorithm in terms of estimating the hourly rainfall accumulations. The favourable performance of RESID was attributed to the lack of regression analysis in algorithm development and the optimization scheme in cost function selection. This material is based upon work supported by the National Sci-

ence Foundation under Grants No. AGS-1612681 and AGS-1144846 to the second author (FYT).

13.31 PARAMETER ESTIMATION OF Z-R RELATIONSHIP FOR FLASH FLOOD WARNING SYSTEM

M. KANG[1], W. NA[2], C. YOO[3]

[1] School of Civil, Environmental and Architectural Engineering, College of Engineering, Korea University, Seoul, Korea
minseok0517@hanmail.net

In this study, a new method for estimating the parameters of Z-R relationship was proposed aiming at the application to the Flash Flood Warning System (FFWS). Generally, the parameters are estimated to minimize the mean square error between the radar rain rate and the observed rain rate on ground, which has the highest accuracy around the mean rain rate value. It is also well known that the radar rain rate based on this Z-R relationship provides somewhat over-estimated values in the small rain rate zone, but rather under-estimated values in the high rain rate zone. As the FFWS targets a very high rain rate (i.e., flash flood guidance), the radar rain rate based on the Z-R relationship cannot show a good accuracy. To overcome this problem, this study proposed a new method to estimate the parameters of the Z-R relationship aiming at the target high rain rate value. This method is based on the re-analysis of the drop size distribution (DSD) and the parameters of the Z-R relationship. Exponential and gamma distribution were considered in this re-analysis. Also, as an application example, this study analyzed the data from Biseulsan radar in Korea. As a result, it could be shown that the newly estimated Z-R relationship has a higher accuracy at the target rain rate zone than that estimated by the conventional method.

13.32 IMPROVEMENTS TO POLARIMETRIC RADAR RETRIEVALS DURING HURRICANE HARVEY

D. B. WOLFF[1], W. A. PETERSEN[2], A. TOKAY[3], D. A. MARKS[14], J. L. PIPPITT[34], P. KIRSTETTER[5]

[1] NASA Wallops Flight Facility, Wallops Island, Virginia USA
[2] NASA Marshall Space Flight Center, Huntsville, AL USA
[3] NASA Goddard Space Flight Center, Greenbelt, MD USA
[1] National Severe Storms Laboratory, Norman, OK USA
david.b.wolff@nasa.gov

Hurricane Harvey hit the Texas Gulf Coast as a major hurricane on August 25, 2017 before exiting the state as a tropical storm on September 1, 2017. In its wake, it left a flood of historic proportions, with some areas measuring 60 inches of rain over a five-day period. Although the storm center stayed west of the immediate Houston metropolitan area, training bands of precipitation being fed by the Gulf of Mexico impacted the Greater Houston area for five days. The National Weather Service (NWS) WSR88D dual-polarimetric radar (KHGX), located southeast of Houston, maintained operations for the entirety of the event. The Harris County Flood Warning System (HCFWS) had 150 rain gauges deployed in its network and seven NWS Automated Surface Observing Systems (ASOS) rain gauges are also located in the area.

In this study, we used the full radar data set to retrieve daily and event-total precipitation estimates within 120 km of the KHGX radar for the period August 25-29, 2017. These estimates were then compared to the HCFWS and ASOS gauges. Three different polarimetric hybrid rainfall retrievals were used: Cifelli et al. 2011; Bringi et al. 2004; and, Chen et al. 2017. Each of these hybrid retrievals have demonstrated robust performance in the past; however, both daily and event-total comparisons from each of these retrievals compared to those of HCFWS and ASOS rain gauge networks resulted in significant underestimates. Following Tokay et al. 2008 and others, we propose that the reason for these underestimations was due to the presence of a large number of small drops, commonly seen in tropical cyclone rain bands. The DP estimators mentioned above work quite well for continental convection, but do not perform well in these tropical systems. Following suggestions by other researchers (Cocks et al. 2017), we derive and apply another rain rate estimator using DP-based specific attenuation, which has been shown to increase with increasing concentration of small rain drops.

13.33 IMPROVEMENT OF RADAR DATA QUALITY CONTROL WITHIN RADVOL-QC SYSTEM

K. OŚRÓDKA[1], J. SZTURC[1], A. JURCZYK[1]

[1] Institute of Meteorology and Water Management National Research Institute, Poland
katarzyna.osrodka@imgw.pl

The RADVOL-QC is a system developed at Institute of Meteorology and Water Management National Research Institute (IMGW-PIB) to process 3-D weather radar data aiming at quality control: the data corrections and quality characterization. The system was described in paper published in "Meteorological Application" (Ośródka et al., 2014), however more efficient approaches have been implemented since that time in terms of removal of non-meteorological echoes among others, especially ones caused by RLAN signals, which are extremely difficult to remove in the case of many interfering signals. The proposed technique is to classify different kinds of the spurious echoes and employ dedicated sub-algorithms, which are mainly based on geometrical analysis of spatial pattern of the signal across and along the radar beam. Another problem is created by windmill farms, which are not detected by Doppler filtering. The efficient solution is to use long-term statistic maps from radar reflectivity data, e.g. monthly accumulations, and interpolate from vicinity of the farm mask. In order to minimise effects of interaction of radar beam with ground on the lowest elevation, transferring of data from the neighbouring higher one is employed in areas close to the radar site. The RADVOL-QC is operationally implemented in Polish weather radar network POLRAD.

13.34 PAN-EUROPEAN MULTI-INSTRUMENTAL RAINFALL COMPOSITE (PERC)

H. SINISALO[12], S. PULKKINEN[1], A. VON LERBER[1], J. KOISTINEN[1]

[1] Radar Science, Finnish Meteorological Institute, Finland

[2] Institute for Atmospheric and Earth System Research, University of Helsinki, Finland

annakaisa.von.lerber@fmi.fi

This study utilizes space-based rainfall estimation of EUMETSAT product Convective Rainfall Rate (CRR) to improve the European rainfall composite map.

The hazards of intense rainfall and severe storms, such as flash floods, urban floods and landslides, are one the largest and growing risk associated with weather phenomena. EUMETNET OPERA radar network is providing key observations for fine-scale precipitation analysis and nowcasting. Ground clutter and beam blocking, radio-frequency interferences, wind farms, occasional malfunction of the radars and simply the areas without radar-coverage introduce uncertainty to the rainfall estimation, and especially, in strong convective rainfall events mis-interpretations or underestimation can be severe. Hence there is a need to quality-controlled OPERA mosaics and to extend the domain of the OPERA precipitation products covering the whole Europe.

To this end we are utilizing the integrated precipitation estimates based on lightning strike density obtained from the Vaisala GLD 360 network and the operational CRR combined with OPERA radar data. The rainfall events during summer months of 2015-2017 are studied covering the Pan-European area. Both the detection skill and quantified estimation of 1h-rainfall accumulation of CRR are compared with the gauge-adjusted radar-based accumulation, and the integrated product is compared to a dense gauge network to provide independent verification.

This study is part of an EU Civil Protection and Prevention project, SMUFF (Seamless probabilistic multi-source forecasting of heavy rainfall hazards for European flood awareness), where the PERC is acting as the initial precipitation field for nowcasting. The objective of SMUFF is to develop improved tools for assessing and forecasting the hazards and risks induced by intense rainfall and severe storms. This is achieved by blending probabilistic multi-instrument precipitation nowcasts based on PERC with the numerical ensemble predictions of ECMWF creating seamless high-resolution hazard and risk tools for lead times from 15 minutes to 5 days.

13.35 IMPROVEMENT OF THE ADJUSTMENT PROCEDURE ON A LONG- TERM RADAR DATA SET

M.JESSEN[1], T.EINFALT[1], I.FRERK[1]

[1] hydro & meteo GmbH & Co.KG, Breite Str. 6-8, D-23552 Lübeck, Germany
m.jessen@hydrometeo.de

For the environmental state agency and several water authorities in North Rhine-Westphalia, Germany, a unique data set was created. It comprises continuous rainfall time series based on rain gauge and weather radar data covering an area of approximately 40000 km^2 with a spatial resolution of 1 x 1 km and time period of 16 years with a temporal resolution 5 minutes. For the analysis, polar data of four weather radar locations and precipitation data of 1300 continuous and 300 daily measuring rain gauge stations were available.

Preparation of radar and rain gauge data

To get reliable precipitation information, a careful preparation of the uncorrected radar and rain gauge data is essential. The quality of each five-minute polar radar data set was enhanced by data quality control algorithms for ground clutter, beam blockage, attenuation and temporal interpolation. Based on these data sets a radar composite product with a resolution of 1 x 1 km was prepared. Rain gauge time series were checked with neighbouring stations and corresponding radar time series, and periods of suspect values were eliminated.

Adjustment procedure

In a first step the radar and rain gauge data were combined in an adjustment procedure based on a daily generated factor field. Adjustment factors were calculated at the rain gauge locations based on minimum daily precipitation sums and then interpolated by using the IDW (Inverse Distance Weighting) method and the factors of the nearest four stations.

Adjustment evaluation was based on a comparison of daily and yearly values and the statistical behaviour of rain gauge and adjusted radar data.

The adjustment generally produced good results when comparing rain gauge and radar data sums on a daily basis (calibration and validation stations). But in parts of the investigated area the yearly precipitation sums of adjusted radar data overestimate rain gauge sums by more than 5%.

The evaluation of the daily adjustment results using the statistical behaviour between rain gauge and adjusted radar time series with intervals less than 60 minutes showed an underestimation in the adjusted radar data for some time intervals and radar ranges.

Further quality improvement could be achieved by changing the parameter settings and a modification of the adjustment procedure. Depending on the data set characteristics (density of rain gauge network, spatial and temporal resolution of the radar data etc.) the following approaches and parameters show an important impact:

- Additional use of an adjustment field based on differences between rain gauge and radar data for low daily precipitation rates
- Inclusion of a time shift between radar and rain gauge data
- Selection of rain gauge-radar factors depending on direction, distance and precipitation amount for the IDW method

- Distance-weighting parameter of the IDW method
- Z-R relationship

The results will be included in the radar event data base of North Rhine-Westphalia.

13.36 THE ROLE OF METEOROLOGICAL RADAR STATION IN THE SYSTEM OF EFFECTIVE MANAGEMENT AND PREDICTION OF HAIL

VARDUHI MARGARYAN[1,2]

[1] Yerevan State University, Department of Physical Geography
[2] Hydrometeorology, Yerevan, Armenia
vmargaryan@ysu.am

The territory of the Republic of Armenia periodically exposed to various sorts of natural disasters. The most common hazard for agriculture. It is the phenomena caused the most damage and because of it every year rural population suffers great damage. Over the last decade greatly increased intensity and frequency of natural disasters, the number of human fatalities and material losses.

So, the discovering of spatiotemporal distribution regularities of natural disasters, risk assessment and productive management, reliable forecast and warning in time, prevention and neutralization, development of rapid response, as well as alert the population and increase the level of education are one of the important prerequisites of public safety, stable development of republic.

So, the goal of this work is to discover and analysis the regularities of spatiotemporal distribution of hail in the territory of the republic of Armenia, to discuss some tasks of productive management of sphere, to evaluate the risk and vulnerability. For solving these problems theoretical base are relevant studies, decisions of government of the republic of Armenia, report of relevant services. Information base for this work are actual observations of the Ministry of Emergency Situations of the Republic of Armenia "Service for Hydrometeorology and active influence on atmospheric phenomena" and the data of the RA National Statistical Service have been used. During the research are used general scientific, characteristics, situation, systematic, statistic, mathematic, comparison and analysis, correlation methods.

So, the studies revealed, almost the entire the territory of the republic is in danger of hail, just in mountainous areas caused by hail damage or nonexistent or negligible.

The number of days with hail both of in the same and in close areas varies quite wide limits. With the height of increase in the number of days with hail.

In the territory of the republic mainly observes a tendency of decrease of number days with hail, which does not means reducing the damage caused by hail. So, is necessary to pay special attention to the intensity and duration as well as to the size of hail.

The meteorological radar MRL-5 is used to receive and process operational information about the radio location of hazardous weather phenomena (cloudiness, precipitation, thunderstorms, hail, storm), transmitting data in real time to distant users of the Grisis Management national Center of the MES of RA, as well as the regional anti-hail centers.

In Ministry of Emergency Situations of the Republic of Armenia "Service for Hydrometeorology and Active Impact on Atmospheric Phenomena" two radar stations MRL-5 are operate, one of which is in the territory of the Dsegh community of Lori marz of Armenia, the other is in the Aragatsotn marz, where radar observations

are made. On the basis of the data obtained, a decision is made on the action of anti-hail stations.

Meteorological high-potential radar MRL-5 is a specialized radar of storm warning and hail protection, designed to solve the following problems

- detection and location of thunderstorms, hail and rainfall in a radius of 300 km,
- determination of the horizontal and vertical extent of meteorological formation, the direction and speed of their movement,
- determination of the upper and lower boundaries of clouds of any form,
- measurement of average radio-echo power for meteorological purposes,
- selection of radio-echo of meteoobjects against the background of disturbing signals reflected from local objects,
- provision of hail protection, that is the detection and localization of hail foci in the clouds (measuring their coordinates and determining their physical characteristics).

Thus, the use of such an information system makes it possible to improve the level of accuracy of forecasts of hazardous meteorological phenomena. With the help of a meteorological radar MRL-5 we can determine the geometric dimensions of the hail-threatening foci (the heights of the lower and upper surfaces, in some cases also the zones and the latitude of the extent), the zones of their involvement, intensity and character of movement. All of these parameters are displayed in their color separations on the corresponding map. Use of such a system of satellite information in the hydromet service makes it possible to improve the degree of accuracy of meteorological forecasts.
Is necessary:

- Expansion of the meteorological radar network;
- To create and develop the system of monitoring and forecasting of hail and other natural disasters;
- Formation of statistical database of threatening danger to specific municipality;
- Detailed and systematic study and evaluation of damage, dynamics change, of frequency of hail with various intensity and size;
- To work out short-time reliable methods of forecast of hail for areas as small as possible;
- To work out and use more alternative productive methods with hail control;
- Increase of productivity with hail control, great investments;

- Organization of activity with hail prevention and liquidation of effects;
- To work out new methods of warning about expected hail;
- Increasing of human education in productive activity of risk management and dependence of population from natural disasters;
- To work out and invest the mechanisms of agricultural insurance.

13.37 IMPACT OF THE VERTICAL GRADIENTS OF PRECIPITATION ON THE RADAR QPE BIAS IN THE FRENCH ALPS

D. FAURE[1] , N. GAUSSIAT[1], G. DELRIEU[2]

[1] Centre de Météorologie Radar, Météo-France, Toulouse, France

[2] Insitute of Geosciences and Environment, University Grenoble Alpes, Grenoble, France

dominique.faure@meteo.fr

In the French Alps region, the quality of the radar Quantitative Precipitation Estimation (QPE) provided by the French weather radar network, can be locally limited due to radar beam blockages, the distance to the radars, and the altitude of measurement: distant C band radars, or local X band radars installed in the mountain chain between 1740 m and 2580 m of altitude, scan the atmosphere above the mountain ranges and cannot sample precipitation into the valleys. A study realised in 2017 on data of the entire year 2016 in all the French Alps (Faure et al, 2017), has shown a general bias between values of the national radar QPE mosaic and the raingauges measurement: a radar QPE over-estimation for raingauges at low altitude, and an increasing underestimation for raingauges at high altitudes (up to 2100 m). This trend has been linked to altitudinal gradients of precipitation observed at ground level in the Alps, and not taken into account by the current radar data processing.

An analysis of these gradients is presented for a subset of 23 daily raingauges around Grenoble, the greatest French Alps conurbation situated at the confluence of three valleys. The raingauges are located at the bottom of the valleys (around 220 m a.s.l.) and on the slopes and top of the three massifs surrounding the conurbation (from 220 to 1730 m a.s.l.). A radar of the national network (Moucherotte X band radar, 1910 m a.s.l) is located inside the studied area at the top of the Vercors massif, which guarantees a good radar coverage. Since November 2016, it is also possible to use the volume scans of the XPORT research radar of IGE, installed in the Grenoble Alpes University campus, at the bottom of the valley (227 m a.s.l.). The XPORT high elevation angles of measurement (15°, 25°, 45°) allow to complete the bottom (below 2000 m of altitude) of the vertical profiles of precipitation estimated by the operational Moucherotte radar.

The analysis focuses on the vertical gradients of precipitation observed at ground level for different temporal accumulations (yearly, three months periods, daily) and for different spatial integrations (the all area, by slope). The corresponding values of the radar QPE mosaic are also presented, in order to explain the impact of the vertical gradients of precipitation on the bias between radar QPEs and raingauges measurements. The results for the subset are as well compared to the widespread results obtained for 430 raingauges at the scale of the entire French Alps and the all year 2016.

References

Faure D., Gaussiat N., Dupuy P., Delrieu G., Yu N., Sarter F., 2017, Quality analysis of the 2016 quantitative precipitation estimates in the French Alps, 38th Conference on radar meteorology, AMS, Chicago, IL, USA (https://ams.confex.com/ams/38RAD

AR/meetingapp.cgi/Paper/320389 or https://www.researchgate.net/publication/319457229)

13.38 RADAR QPE FOR AN EXTREME PRECIPITATION EVENT IN SOUTHERN BRAZIL: JANUARY 2018 FLASH FLOOD - 409MM IN 48H

L. CALVETTI[1], C. BENETI[2], W. F. COELHO[3], C. CARDOSO[4], T. SILVA[2], M. QUADRO[5], D. HERDIES[5]

[1] Center for Meteorological Research and Forecasting, Federal University of Pelotas (CPMET/UFPEL), Pelotas, Brazil

[2] Parana Meteorological Service (SIMEPAR), Curitiba, Brazil

[3] Master Degree in Meteorology, Federal University of Pelotas (PGMET/UFPEL), Pelotas, Brazil

[4] Meteorology Department of Federal Institute of Santa Catarina (IFSC), Florianopolis, Brazil

[5] Center for Weather Forecasting and Climate Studies (CPTEC/INPE), Cachoeira Paulista, Brazil

lcalvetti@ufpel.edu.br

An extreme, multi day rainfall event over eastern Santa Catarina State, Brazil, during 10-12 January 2018 caused a record flooding during a beach tourism season. An unusual synoptic weather pattern induced a record precipitation of 409 mm in three days, registered by the rain gauge network. During all three days, a continuous stratiform rain ranging from 1 to 8 mmh^{-1} was predominant. At the end of 10th January and early 11th January a development of severe convective storms over Florianopolis City, Capital of the Santa Catarina State was observed. At the rain gauge network were recorded values of 31.4 mmh^{-1}, 25.8 mmh^{-1} and a historical record of 31.2 mm in 10 minutes, what generate severe damages due to flash flooding. For the analysis of rainfall spatial distribution we used Quantitative Precipitation Estimate (QPE) fields obtained by Z-R relationships from a new Dual Polarization S-Band Weather Radar located at Lontras City, about 70 km distance from Florianopolis. It was compared six Z-R relationships: traditional Marshall-Palmer (a=200, b=1.6), Joss (a=500, b=1.5), two other Z-R relationships based in studies developed in Brazil, Calheiros (a=236, b=1.5) and Santos (a=52, b=2.7), and two polarimetric Z-R relationships including reflectivity (Z), differential reflectivity (Z_{DR}) and specific differential phase (K_{DP}). A discussion about the efficiency of the QPE for the historically observed rainfall events was lead in a sense of predicted flash foods in urban areas. The tradicional Marshall-Palmer Z-R relationship show good results for the stratiform pattern of all events, but overestimated all convective cells. Using $_{DP}$ and Z_{DR} variables, it was possible to detect the rainfall peaks, but not exactly as observed in rain gauges. However, these polarimetric relationships could be useful for hydrometeorological purposes with a good skill. The persistent northeastern maritime influx of moisture in the area lead to a stratiform pattern during the three days. The precipitation peaks were generated by strong convection triggered during a zonal propagation of a mid-level shortwave trough over the coast. Therefore, these two distinct atmospheric regimes with a mix of maritime and continental hydrometeors content led thinking about the use of two type of the Z-R relationship according the precipitation regimen, which will be presented in this conference.

13.39 RADAR-BASED QUANTITATIVE PRECIPITATION ESTIMATION (QPE) USING CONCEPTS FROM INFORMATION THEORY: ANALYSING THE POTENTIAL OF DATA-BASED, DYNAMIC Z-R RELATIONS, AND INVESTIGATING INFORMATION LOSSES FROM CLOUD TO GROUND

MALTE NEUPER[1], UWE EHRET[1], HANS-STEFAN BAUER[2], VOLKER WULFMEYER[2]

[1] Institute of Water and River Basin Management - Chair of Hydrology, Karlsruhe Institute of Technology KIT, Karlsruhe, Germany

[2] Institute of Physics and Meteorology, University of Hohenheim, Hohenheim, Germany

malte.neuper@metteam.de

High-quality and high-resolution quantitative estimates of ground precipitation (QPE) are an important prerequisite of hydrological simulation and prediction. Weather radar data have a large potential to contribute to QPE due to their high space-time resolution. However, due to the strongly non-linear and time-variant relation of observed radar reflectivity factor Z, typically measured at height, and the ground rainfall rate of interest R, this potential is not straightforwardly exploited.

Applying a data-based approach in an information-theoretic framework, the work presented here has three major aspects: Firstly, the potential of applying a purely data-based and probabilistic Z-R relation instead of the standard functional form of a power-law relation is analyzed. Applying a probabilistic relation has the benefit to provide joint estimates of R and the related estimation uncertainty. Secondly, we test the potential of various operationally available observables such as the large-scale Circulation Pattern, convective and other meteorological indices like the convective available potential energy (CAPE), ground and upper air meteorological variables (relative humidity, air temperature, wind speed and direction) and season indicators to distinguish typical time-variant Z-R relationships. The idea here is to improve QPE by applying specific Z-R relationships conditional on the current hydro-meteorological situation expressed by the predictors. Thirdly, we use a comprehensive data set from four years of 1-h data available from a C-band weather radar, two vertical micro rain radars (MRR), six disdrometers and six rain gauges set up in the 250 km^2 catchment of the Attert, Luxembourg to evaluate the amount and losses of information about ground rainfall along the pathway of precipitation observation: We start with Z measured by radar at height, continue with Z measured by MRR along a vertical profile in the atmosphere and end with Z observed by disdrometer measured directly at the ground. Knowing where along this path the main losses of information occur can help to design better observation strategies in the future.

13.40 RAINFALL ESTIMATION IN HIGH SPATIOTEMPORAL RESOLUTION USING X-BAND DUAL-POL RADARS IN SEOUL METROPOLITAN AREA

DAEHYUNG LEE[1], GEUNSU LYU[2], HONG-MOK PARK[2], WONBAE BANG[2], ALEXANDER RYZHKOV[3], GYUWON LEE[1,2]

[1] Research and Training Team for Future Creative Astrophysics and Cosmologists, Department of Astronomy and Atmospheric Sciences, Kyungpook National University, Daegu, South Korea

[2] Center for Atmospheric REmote Sensing, Kyungpook National University, Daegu, South Korea

[3] Cooperative Institute for Mesoscale Meteorological Studies, University of Oklahoma, and NOAA/OAR/National Severe Storms Laboratory, Norman, Oklahoma, USA

gyuwon@knu.ac.kr

We have developed a monitoring and forecasting system of flash flood in the Seoul metropolitan area. Dual-polarized (dual-pol) X-band radars are newly installed in the Seoul metropolitan area on Feb. 2017, to overcome blind zone of S-band radar network by collecting high spatiotemporal resolution radar data.

In this study, rainfall estimation is performed using two X-band radars (XKOU, XYOU) in Seoul area. Heavy rainfall cases of X-band radar data of 2017 are used. Quality control, attenuation and system bias corrections of X-band radar data are performed using polarimetric variables. Climatological equations (A_H-K_{DP}, A_{DP}-K_{DP}, Z-Z_{DR}, R(Z), R(Z, Z_{DR}), R(K_{DP}), R(A_H)) are also defined using drop size distributions from two-dimensional video disdrometer (2DVD) and T-matrix scattering simulation (Thurai et al., 2007). Hybrid surface Rainfall technique (HSR) is adapted to avoid partial beam blockage of terrain effect and composite of HSR fields from XKOU and XYOU is generated. Rain gauge and S-band rainfall estimation results are used for comparative validation of various rainfall products.

Acknowledgements

This research was supported by a grant (18AWMP-B079625-05) from Water Management Research Program sponsored by Ministry of Land, Infrastructure and Transport of Korean government.

13.41 OPEN SOURCE POLARIMETRIC RADAR AND WEATHER STATION DATA USING PYTHON

REMCO VAN DE BEEK[1,2]
[1] WeatherFocus, The Netherlands
[2] SMHI, Sweden
remcovdbeek@gmail.com

Precipitation measurements with polarimetric radar have become very popular over the last decade with many countries moving from traditional Doppler radars to these new radar systems. Polarimetric weather radar offers a wealth of additional information that was not available before. Many countries also make the measured data freely available in open data projects. This makes progress in research much easier.

A logical problem when comparing different techniques is often that research is performed using local data. This means that data can be gathered with different types of radar and in different climates. What is presented here is the goal of setting up a more universal code and dataset(s) using open source data, where researchers can contribute to by adding their own code for processing their own local radar and weather data. This can then be added to an larger dataset. This should make research both easier to set up as well as compare to work of others.

The initial setup of the code is based on data gathered by the polarimetric weather radars operated by KNMI, The Netherlands, that have been fully operational since 2017. The radar data as wel as many other measurements and model data are available as open data provided by KNMI at data.knmi.nl.

The dataset that is created in the first stage will contain simple point data at measurement locations. While the inclusion of the full radar scans can provide very useful and interesting additional information the goal is also to keep the dataset simple and small. The code used to create the dataset will be made available to make it easy to include additional data if desired.

While there many weather stations in the Netherlands they do not all report the same amount weather elements. Of these stations 25 have been selected that also report present weather (SYNOP ww-code). Radar data at and near the location of the weather stations will be included in the dataset.

The usefulness of the dataset will be demonstrated by using several neural network variants to derive precipitation type and clutter from the data. The sensitivity of the neural networks to different inputs will be tested. Future plans include the addition of weather data from other countries that provide open data and extending the Dutch part of the dataset with a longer time period, as well as additional sources like model data and Meteosat based products.

Code written to extract and process the data from KNMI as well as the code to estimate precipitation type using a neural network are written in Python. The data and code will be made available in Github, so that researchers and students can easily test the source and contribute.

13.42 COMPARISON BETWEEN DIFFERENT QPE BASED ON: MICROWAVE LINKS, RADAR ADJUSTED AND GAUGES

P.P. ALBERONI[1], A. FORNASIERO[1], G. ROVERSI[2,3] S. PASETTI[2], M. FOLEGANI[2], F. PORCÙ[3]

[1] ARPAE Emilia Romagna, Italy
[2] MEEO S.r.l., Italy
[3] Department of Physics and Astronomy - University of Bologna, Italy
palberoni@arpae.it

Currently the most used tools to estimate quantitative precipitation are rain gauges and weather radars, both with relative merits and defects. Raingauges measurements are not reliable in case of intense precipitation event and have poor spatial representativeness due to high spatial and temporal variability of rainfall field. Weather radars monitor rainfall over large areas with high spatial resolution, but through indirect measurements and affected by various sources of error. A complementary approach is represented by a technology, that has not yet been tested in Italy, that consists in the extrapolation of rainfall intensity data from cellular communication infrastructures (i.e. in the identification of rain-induced attenuation of microwave links), usually called Microwave link (MWL) networks or Commercial Microwave links (CML).

A validation activity of these different QPE Quantitative Precipitation Estimates technologies was done over the Bologna province area (Italy) on the period February 20^{th} - June 30^{th} 2016 in the framework of the RainBO project LIFE15/CCA /IT/000035.

Validation exercise was carried out comparing microwave links QPE and radar adjusted QPE using as reference field a Raingauges spatial analysis (ERG5, a modified Shepard interpolation). Qualitative analysis, mainly based on daily accumulation maps, and quantitative analysis, mainly using statistical indexes, has been carried out. As a first step a visual inspection of rainfall fields in the datasets has been done in order to understand the general behaviour and to identify, if possible, problems or drawbacks in the data. A synoptic comparison was conducted plotting together the rainfall estimates obtained by remote sensing tools (i.e. Microwave links and radar) with the reference field. Statistical indicators and continuous verification methods based on contingency table were calculated.

Moreover single event analysis was conducted in cases of false precipitation detection by gauges and ERG5, detection of abnormal attenuation by MWL due to the presence of snow or mixed-phase precipitation, undersampling of precipitation in convective season.

The agreement between MWL QPE and the other estimates is quite promising even if it requires a tuning activity in order to make the technology used in real-time or near real-time. The qualitative analysis shows that the performance of the MWL estimate seems to increase in the second half of the analysed period, mainly characterised by convective storms, even embedded in frontal structures, where showers and heavy rain play an important role.

This behaviour is confirmed by the quantitative analysis done by using statistical indicators, that improve in case of rainfall estimation from MWL data during Sum-

mer and Spring seasons. The validation has pointed out that Microwave estimation slightly underestimate precipitation occurrence both in spatial coverage and point amount, while Adjusted radar have a complementary features.

Spatial coverage of link network is an important point which should be addressed to enlarge coverage in future in order to increase the quality of the retrieved field. Further quality control procedures should be applied to reduce the impact of false signal which was used in the validation exercise. Two main topic should be tackled: identification of false signal due to structural deformation and snow-melting data.

13.43 TESTING OF CONVENTIONAL ATTENUATION ESTIMATION ALGORITHMS WITH OPERATIONAL RADARS IN DIFFERENT BANDS

ALEKSANDR LIALIUSHKIN[1], ALEXANDER SOLONIN[1], NIKOLAY BOCHARNIKOV[1], TATIANA BAZLOVA[1], NADEZHDA YAKIMAINEN[1], VASILIY OLENEV[1]

[1] Institute of Radar Meteorology (IRAM), Russia
las@iram.ru

Quantitative precipitation estimation and severe weather detection require accurate measurements of radar reflectivity and polarimetric features. Intense precipitations might cause significant path attenuation in C-band, and especially in X-band, leading to underestimations in end-user radar products. Several single- and dual-polarization methods are commonly used for attenuation correction with the choice on which one to apply typically made by comparing resultant radar quantities against disdrometer or rain gauge data.

The paper presents a performance analysis of these rain attenuation estimation algorithms. Two operational weather radars, one C-band and the other X-band, with 16 km distance between them, are used for validating the estimates. The C-band radar data after correction was regarded as a ground truth being less prone to the attenuation effects. Disdrometer data was used as well for absolute calibration of the radars.

13.44 EVALUATION OF PRECIPITATION TYPE CLASSIFICATION METHODS FOR GROUND-BASED AND GPM DPR SATELLITE RADAR DATA

SOICHIRO SUGIMOTO[1], MITSUHARU NOMURA[1], TAKAHISA KOBAYASHI[1]

[1] Central Research Institute of Electric Power Industry, JAPAN
soichiro@criepi.denken.or.jp

Dual-frequency precipitation radar (DPR) onboard the Global Precipitation Measurement (GPM) core satellite has promise for the measurement of the vertical profile of precipitation rate with accuracy. The precipitation type classification between rain and solid particles, however, is still a challenge. We have explore a method for discriminating between rain and dry snow for DPR data, using a numerical radar data simulator based on the scattering theory. The ratio of dual frequency ratio (DFR) to the reflectivity from Ku-band radar is a key parameter for discrimination. We have also proposed a new index using the reflectivity and the specific differential phase Kdp for polarimetric radar data using simulation-based findings.

We will evaluate these two methods by a cross-validation using real observation data. First, the performance of our method for ground-based polarimetric radar data is evaluated using data from videosonde observations and a two-dimensional video disdrometer (2DVD). A videosonde is a ballon-borne instrument system, and a movie recorded by a camera onboard the system can sample the number concentration of each precipitation type. The precipitation type of a particle can be also identified from the shape of a shadow and the vertical fallspeed from 2DVD data. Next, our method for dual-frequency satellite radar data is evaluated with reference to the precipitation type identified by the above method using ground-based radar data. The applicability of two methods will be discussed in this communication.

13.45 USING MICROWAVE LINK SIGNAL FLUCTUATIONS FOR RETRIEVAL OF RAINFALL RATES

E. SEAGER[1,2], J. FRANK[2], R. UIJLENHOET[3], H. LEIJNSE[1]

[1] Royal Netherlands Meteorological Institute, De Bilt the Netherlands
[2] University of Utrecht, Utrecht, the Netherlands
[3] Wageningen University, Wageningen, the Netherlands
emily.seager@knmi.nl

It has recently been shown that microwave links can be used to measure rainfall by using the signal attenuation caused by the raindrops on the path between the link antennas. This is particularly promising as these links are abundant throughout the world as part of the infrastructure used for cellular communication. However, there are some known issues with this method of rainfall measurement such as attenuation caused by wet antennas, and proper determination of the signal level in dry weather. We present a method of rainfall retrieval from these links that is in principle insensitive to these issues, and could ultimately lead to much improved rainfall retrievals.

Instead of using existing rainfall retrieval techniques, we use high-frequency microwave link signal fluctuations for rainfall estimation. We use the fact that raindrops fall through the first Fresnel zone of the microwave link, and hence cause signal fluctuations. Because issues like base-line fluctuations and wetting of antennas occur at very low frequencies, their effect on resulting rainfall estimates are negligible.

We derive expressions for signal fluctuations as a function of link characteristics (length and frequency) and the raindrop size distribution. These relations are tested against data from an experiment with a 26-GHz microwave link carried out at the Chilbolton Observatory.

13.46 RAINFALL SPATIO-TEMPORAL CORRELATION STRUCTURE IN DUTCH CLIMATE FROM SUB-PIXEL TO MESOSCALE

T. C. VAN LETH[1], H. LEIJNSE[2], A. OVEREEM[1,2], R. UIJLENHOET[1]

[1] Wageningen University, The Netherlands

[2] Royal Netherlands Meteorological Institute (KNMI), The Netherlands

tommy.vanleth@wur.nl

We investigate the spatio-temporal structure of rainfall variability at spatial scales from 7 m to over 200 km. We used data from two networks of laser disdrometers with complementary interstation distances in two Dutch cities and a Dutch nationwide network of automated rain gauges. The smallest aggregation interval collected by the disdrometers was 30 s, while the automated rain gauges provided 10 minute rainfall sums. This study aims to supplement other sub-pixel investigations with new data, while characterizing the correlation structure at an extended range of scales. To quantify the variability, we employ a modified-exponential model fitted to the spatial correlograms and characterize the parameters of the model as a function of the temporal aggregation interval. This common method allows for meaningful comparison with other studies. We also separately analyzed the intermittency of the rainfall observations. We show that a single parameterisation can coherently describe the variability across a wide range of scales. Limiting the range of scales to those typically found in sub-pixel variability studies skews the parameterization and reduces its applicability to other scales.

13.47 AN EVALUATION OF RAIN RADAR ADJUSTMENT PROCEDURES

MICHA SILVER[1], ARNON KARNIELI[1], ERICK FREDJ[2]

[1] Ben Gurion University, Sde Boker Campus, Israel

[2] Lev Academic institute, Israel

silverm@post.bgu.ac.il

Several adjustment procedures that merge rain radar grids with observed precipitation rates from point locations have been developed over the past two decades, providing improved rainfall grids. Point observations of precipitation rates typically come from rain gauges, but can also include data derived from signal attenuation between commercial microwave link (CML) antennas. Past research has validated the various adjustment procedures under specific conditions, including a given density of observation points, a certain storm event, and a known error level of radar grids and sensors. However, to the best of the authors knowledge, no generic evaluation process has been demonstated that can address the wide variety of conditions that must be taken into account in choosing the most suitable adjustment procedure for any given situation.

This research evaluates several of the accepted adjustment algorithms under a variety of scenarios. Each scenario is composed of a particular type of storm, a density of sensors (gauges and CML derived rain rates), and an assumed error level applied to the CML based precipitation rates. The evaluation simulates a scenario by creating a set of synthetic data: storm grids, radar grids and sensor locations. This simulation is run repeatedly for each scenario with varying random number seeds, and the different adjustment algorithms are applied to each run. Then average correlations between each of the adjusted rain grids and the initial true storm grid are calculated using non-parametric tests.

Comparison of these average correlations for different adjustment procedures under different scenarios indicates the following preliminary results. Rain radar from stratiform storm fronts is not well adjusted by any of the adjustment procedures. The multiplicative and mixed (additive with multiplicative) adjustment procedures show moderate success with this type of storm when density of the sensors is high, independent of the sensor error levels. Adjustment of radar from convective type storms attains high correlation when applying either a mixed (additive and multiplicative) or conditional merge adjustment algorithm. Both of these methods perform optimally when density of the sensors is high, regardless of the sensor error levels. The mean field bias adjustment shows only moderate correlation, and only when both density of sensors is high and error levels are low.

13.48 EFFECT OF URBAN ENVIRONMENT ON SUMMER PRECIPITATION IN STUTTGART

YAOYAO ZHENG[1], JAN HANDWERKER[1], NORBERT KALTHOFF[1]

[1] Karlsruhe Institute of Technology, Institute of Meteorology and Climate Research, Department Troposphere Research, Karlsruhe, Germany
yaoyao.zheng@kit.edu

Analogous to the orographic effect, urban environment is perceived to engender a complicated influence on the precipitation occurring within or surrounding the city. The issue regarding how the urban environment modifies the precipitation is still in debate, and thus our study is intended to fathom the foregoing questions in regards to the impact of urban environment on the precipitation, for instance, to investigate the mechanism that the existence of urban environment would inhibit or encourage the initiation and development of precipitation systems.

Accordingly, high-resolution X-band measurements were performed from May-October 2017 in Stuttgart, the sixth largest city in Germany, with 10-minute interval repetitions of three 75-meter resolution low-elevation scans and one 250-meter resolution volume scan. Interlacing of two types of scan can provide both very high resolution and comprehensive inspection of the precipitation. The acknowledged and unique topographic features of Stuttgart render our study more challenging, but it might also bring about chances to investigate the interaction of urban effect and topographic effect.

Besides the highly resolved X-band radar measurements, additional instruments including automatic rain gauges "Pluvius" and a Micro-Rain Radar (MRR) can provide supplementary information of precipitation measurements at the ground (from "Pluvius") and the vertical profile (from MRR). One-site comparison from MRR and Pluvius with X-band radar measurement can improve our effective use of X-band radar measurement, further contributing to the better characterization of precipitation in the urban environment.

13.49 GEOSTATISTICAL MERGING OF X-BAND WEATHER RADAR AND A SPARSE RAIN GAUGE NETWORK OVER AN URBAN CATCHMENT

I. SECK[1], J. VAN BAELEN[1]

[1] Laboratoire de Météorologie Physique, UMR6016, CNRS - Université Clermont Auvergne, Clermont Ferrand, France
i.seck@opgc.univ-bpclermont.fr

Optimal Quantitative Precipitation Estimation (QPE) of rainfall have been proven to be crucial to the accuracy of hydrological models, especially over urban catchments. Small to medium-size towns are usually equipped with a sparse rain gauge network that struggle to catch the variability of rainfall with adequate spatial and temporal resolution. For these purposes, X-band Local Area Weather Radars (LAWRs) can provide a cost effective solution to meet this challenge.

In this study, we examine two geostatistical methods to merge X-band weather radar data with the combination of rain gauges from the network of the city of Clermont-Ferrand (13 local gauges with a 5 minutes temporal resolution) and regional Meteo France stations (7 gauges with a 6 mintes temporal resolution): Conditional merging and Kriging with an external drift (following Velasco-Forero et al., 2009). A simple method to expand the rain gauge network was introduced, using the X-band radar data to build artificial gauges to complement the already existing network and produce a new expanded network that is denser and spread over the entire study area. The effects of this expansion were found to greatly improve the retrieved QPE despite being dependant on the quality of the weather radar data.

The interpolation performance of both geostatistical blending techniques was investigated using both the ordinary kriged rainfall actual and expanded networks using a continuous time series of six months representing the summer of 2013, while further work on longer data sets is ongoing. To the contrary of previous studies using C-band radars: the modified kriging with an external drift technique performed noticeably better in our study than the conditional merging one for both the whole data set and for a subset of gauges selected through three quality control filters. Hence, this illustrates the benefits of using an X-band weather radar despite its limitations, to produce quality QPE products and support realistic QPF developments as currently investigated.

13.50 CHARACTERIZING THE APPARENT MULTIFREQUENCY REFLECTIVITY SIGNATURES OF OROGRAPHIC PRECIPITATION USING A COUPLED RAINSHAFT MICROPHYSICS-RADIATIVE TRANSFER MODEL AND OBSERVATIONS

MALARVIZHI ARULRAJ[1], P. BARROS[1]

[1] Duke University, Pratt School of Engineering, Durham, NC, United States
malarvizhi.arulraj@duke.edu

Quantitative Precipitation Estimation (QPE) in mountainous regions is especially challenging due to the high spatial and temporal variability of orographic precipitation processes modulated by landform and regional circulation patterns, and the challenges posed to radar operations in complex topography (e.g. geometry and ground-clutter artifacts). Radar measurements at different frequencies provide distinct and complementary information of the impact of the vertical structure of precipitation on the radiative properties of the lower troposphere, which can be combined to better constrain QPE algorithms. Over the last twenty years, multiple satellite-based instruments profiling the vertical distribution of precipitation from space at different operating frequencies have been launched including the CloudSat-CPR (94 GHz), the GPM-Ka PR (35 GHz), and the TRMM-PR and GPM-Ku PR (13 GHz). There are also several centimeter and millimeter ground-based radars such as the S- (2 GHz), K- (24 GHz), Ku- (13 GHz), Ka- (35 GHz) and W- (95 GHZ) band radars observing precipitation from the ground, though generally only at sparse locations. The objective of this work is to characterize the apparent reflectivity signature of the vertical structure of orographic precipitation processes at multiple frequencies, which can be used as microphysical markers to improve QPE from remotely sensed reflectivity profiles.

First, a coupled rainshaft microphysics-radiative transfer model is used to generate a very large population of space-based multi-frequency apparent reflectivity profiles (ZaPs) representative of orographic precipitation regimes identified from ground-based observations of precipitation events in mountainous regions. The ZaPs are subsequently measured, classified and clustered vis-à-vis rainfall physical regimes using ground-based observations to constrain the analysis. Finally, a Bayesian model is derived that maps reflectivity profile metrics to orographic precipitation regime, rainfall microstructure and rainfall intensity.

13.51 ENHANCEMENT OF RADAR RAINFALL ESTIMATES FOR ESTONIAN TERRITORY THROUGH OPTICAL FLOW TEMPORAL INTERPOLATION

J.RAHU[1], T. VOORMANSIK[1,2], P. POST[1]

[1] Institute of Physics, University of Tartu, Tartu, Estonia

[2] Estonian Weather Service, Estonian Environment Agency, Tallinn, Estonia

jormav@ut.ee

Accurate and reliable precipitation maps are very important in the fields of hydrology, climatology and meteorology. For Estonias territory, high spatial and temporal resolution precipitation data is obtained by dual-polarization weather radars. Rainfall products derived from radar data have multiple applications for nowcasting over urban areas, warning systems for airports and agriculture.

Although weather radars have good measurement properties it is still method of remote-sensing and getting reliable data is not straightforward. Various sources of errors are inherent to radar data and also calculations from reflectivity to actual rain rate are done via empirical relations. Therefore, accurate precipitation estimations through radar data requires verification. Quantitative Precipitation Estimation (QPE) concept is used where rain gauges and radar data are compared.

Estonias radar network consists of two dual-polarization C-band weather radars with one located near the north coast in Harku and the other in the middle of the country in Srgavere.

The problem with radar data can be that with current 15-minute interval measurement strategy, precipitation fields can pass gauge locations introducing bias to radar and gauge data comparison. Therefore, specific interest in this work is at radar data temporal resolution enhancement to make two different datasets more comparable with each other. This problem is addressed with digital signal processing method of optical flow.

Optical flow is a widely used image processing method which extracts apparent motion from 2D image sequence. This motion information can be used to infer real 3D movements, detect motion, execute object segmentation and a lot more, but for this work optical flow is used to interpolate more timesteps between two radar image frames. Also, it could be used to extrapolate radar data into near future (nowcasting application). There are plenty of different optical flow methods with very different mathematical approaches including differential methods, region-based matching or frequency-based methods (energy-based or phase-based) where every method depends highly on the specific applicational needs. Choosing optimal method (reasonably good results with reasonable computational difficulty) and implementing it for the weather radar-oriented application is intended with this work. As there is not much to compare the results to, an error estimation is also needed to ensure measure of confidence and accuracy in used method of optical flow.

13.52 PARAMETERIZING RAINDROP SIZE DISTRIBUTIONS USING MICROWAVE LINKS

T. C. VAN LETH[1], H. LEIJNSE[2], A. OVEREEM[1,2], R. UIJLENHOET[1]

[1] Wageningen University, The Netherlands

[2] Royal Dutch Meteorological Institute (KNMI), The Netherlands

tommy.vanleth@wur.nl

We present a novel method of using three collocated microwave link instruments to estimate the three parameters of a raindrop size distribution (DSD) model. This allows path-average DSD measurements over a path-length of several kilometers as opposed to the point measurements of conventional disdrometers. Our model is validated in a round-trip manner using a simulated DSD field as well as an array of laser disdrometers aligned along a path. Different potential link configurations are investigated. We also present results from the application of this method to an experimental setup of collocated microwave links measuring at 26 GHz and 38 GHz along a 2.2 km path.

13.53 IMPROVEMENT OF PRECIPITATION ESTIMATES FROM CHUVAONLINE X-BAND RADARS THROUGH THE IMPLEMENTATION OF A NEW ATTENUATION CORRECTION TECHNIQUE

KEYLA M. MORA NAVARRO[1], CARLOS AUGUSTO MORALES[1]

[1] Department of Atmospheric Science, University of São Paulo
keyla.mora@iag.usp.br

The University of São Paulo (USP) implemented the Chuva Online project in response to the state of São Paulo requirements to improve the weather forecasting and rain warning systems. This project is composed by a weather radar network that has two X-band single polarized mini-radars from ELDES and a polarimetric X-band weather radar from NOVIMET

The aim of this research is to improve the precipitation estimation at higher spacial and temporal resolution through the implementation of an attenuation correction technique for the weather radars of Chuva Online project. To correct for attenuation, a new attenuation correction technique is applied to the X-band single polarized radars measurements.

The attenuation correction technique developed is a hybrid between Hitschfeld-Bordan (HB) method and a Surface reference technique (SRT), which uses the measured reflectivity and an un-attenuated S-band reference signal. The reference signal is from a dual polarization S-band Doppler weather radar located at Salesópolis, Brazil, around 60 km from the X-band radars network. This technique has been implemented in real time and statistical results of the performance will be presented.

To validate this method, results will be analysed in post-processing and will be compared with the application of others well-established attenuation correction methods. Subsequently, the estimated corrected data will be compared with the S-band reflectivity in order to identify the algorithm is estimating properly the corrected reflectivity.

Finally, for the polarimetric X-band weather radar, a simple attenuation correction technique based on differential propagation phase is used to estimate the corrected reflectivity. The results obtained will be validated by comparing and quantifying the error related with the S-band radar reflectivity.

This radar improvement data would allow to implement reliable preventions plans and early detection of natural disasters in the state of São Paulo.

13.54 QUANTITATIVE PRECIPITATION ESTIMATION BY X-BAND POLARIMETRIC RADAR NETWORK OF KOCHI UNIVERSITY

AKIRA NISHII[1], KOJI SASSA[2]

[1] Graduate school of Kochi University, Kochi, Japan
[2] Kochi University, Kochi, Japan
nhi169.kuc.hotaka3190@gmail.com

Kochi prefecture is known to be the area where the heavy rains more than 50 mm/h in precipitation intensity and tornadoes frequently occur. Mean annual precipitation of Kochi city is 2500 mm. Though the X-band polarimetric radar network so called as XRAIN is constructed by the Ministry of Land, Infrastructure and Transport in order to observe heavy rain in Japan, it does not cover Kochi prefecture. So, we constructed Xband radar network in Kochi to complement XRAIN. At this time, we have 3 X-band polarimetric radars located at Asakura, Monobe and Aki. More two radars will be settled at Suzaki and Tosashimizu by the end of March 2018. We developed the Quantitative Precipitation Estimation (QPE) algorithm for the radar network and achieved quasi-real time QPE with 150 m special resolution. But the accuracy of the QPE for each radars seemed to be slightly different. The present study aims to evaluate the precipitation intensity observed by these radars.

We compared the hourly precipitation and the ten minutes precipitation observed by the radars with the data obtained by 12 rain gauges of Japan Meteorological Agency and our 13 rain gauges. The evaluation period is from November 2016 to October 2017. We used the data when the rainfall of 20 mm/h in intensity was observed from more than one rain gauge. For QPE, we employed K_{DP}-R relationship for heavy rain (ZH $\geq$ 30 dBZ and $K_{DP} \geq$ 0.3 deg./km) and Z-R relationship for weak rain. K_{DP} was eliminated if hv <0.6, and ZH was corrected for attenuation by K_{DP}.

The preliminary results showed that all radars underestimated precipitation intensity. The slopes of regression lines were less than 0.9. Especially, the Z-R relationship underestimated more than the K_{DP}-R relationship. This fact may be caused by the local characteristics of drop size distributions. The correlation coefficient between the radar data and the rain gauge data was low; 0.63 for Asakura, 0.75 for Monobe and 0.68 for Aki due to mountain clutter and rain attenuation, though we employed the moving target indication and the attenuation correction with polarimetric parameters.

We will remove mountain clutter by mapping and redefine Z-R relationship by employing drop size distribution at Kochi. And we will also made complementation with each other radars in our radar network.

13.55 VERIFICATION OF RADAR HYDROMETEOR CLASSIFICATION ALGORITHMS FOR THE UK C-BAND NETWORK

B. PICKERING[1,2], R. NEELY III[1,2], D. HARRISON[3], S. BEST[3], ALAN BLYTH[1,2]

[1] School of Earth and Environment, University of Leeds, England
[2] National Centre for Atmospheric Science, University of Leeds, England
[3] United Kingdom Meteorological Office, Exeter, England
ben.pickering@ncas.ac.uk

Knowledge of precipitation type in near-real-time has many applications in both operational and research meteorology. Operational uses include flood forecasting, aviation and transportation. For research, cloud microphysics and NWP assimilation are ongoing topics that will benefit from 3D precipitation type data. Hydrometeor classification using weather radar is particularly desirable, due to radars high temporal and spatial resolution. Over the past 5 years the UK Met Office network of C-band Doppler weather radars have been upgraded to dual-polarisation allowing characteristics of hydrometeor phase, shape, and orientation to be determined. This information is being used in classification algorithms to determine the most likely hydrometeor type within the observed volume. Despite such algorithms being used operationally for over a decade worldwide (notably the USA), there is limited rigorous verification in the literature. Verification of hydrometeor classification skill is a particular challenge because both the classifier and the verification data are discreet. In addition, the majority of precipitation observations are made on the ground, which creates additional sources of uncertainty as the particles fall from radar-height to the surface.

This study aims to build a rigorous framework by which to verify radar hydrometeor classifiers, enabling multiple algorithms to be compared with a wide array of data sources that have various levels of certainty and representation. Using these novel methods, the improvement in hydrometeor classification using dual-polarisation radar data compared to what was previously possible with single polarisation radar will be demonstrated. To aid this process a network of 14 laser disdrometers across the UK (DiVeN) have been established for this project. These instruments can measure the fall speed and diameter of particles that fall through the instrument′s laser beam and thus precipitation type can be empirically deduced. Initial hydrometeor class verification results using the disdrometer and other sources of observation are presented here. Focus will be placed on the development of the verification methods.

13.56 MELTING LAYER CLIMATOLOGY IN THE GENOBLE VALLEY USING MULTI-FREQUENCY, MULTI-PARAMETER, MULTI-ANGLE RADAR MEASUREMENTS

A. KHANAL[1], G. DELRIEU[1], S.KREMER[1], F. CAZENAVE[1]

[1] Institut des Géosciences de l'Environnement, Grenoble, France
anil-kumar.khanal@grenoble-inp.org

The Grenoble experiment aims at developing advanced methods for rain and snow estimation using weather radar remote sensing techniques in high mountain regions for improved water resource assessment and hydrological risk mitigation. A unique observation system has been deployed since 2016 in the Grenoble (France) region. It is composed of a Météo France operated X-band radar (volumetric, Doppler and polarimetric) on top of the Mt Moucherotte (1970 m asl), a X-band XPORT radar (volumetric, Doppler, polarimetric), a K-band micro rain radar (MRR, Doppler, vertically pointing) and in situ sensors (rain gauges, disdrometers), latter three operated by Institut des Gosciences de l'Environnement (IGE) on the Grenoble campus (210 m asl).

An algorithm for the automatic detection of the melting layer (ML) characteristics has been developed based on the use of the higher elevation angles (15°, 25° and 45°) XPORT measurements and the vertically pointing MRR data. It allows the detection of the ML, along with vertical profiles of hydrometeors reflectivity parameters (Zh, Zv, Zdr and ρ_{hv}) from XPORT measurements and vertical profile of hydrometeors apparent falling velocities from MRR measurements. In these vertical profiles the ML is characterized by the peaks and inflection points. The algorithm is applied to a series of 40 events with significant rainfall in the Grenoble valley (typically above 10 mm/day), corresponding to a large variety of weather types and vertical structures of the atmosphere. Typical signatures of the various profiles are evidenced supporting some speculations about the micro-physical processes at work in various cases.

At the moment of this abstract submission, the project is at the stage of identification of periods of homogeneous precipitation at the scale of the volume sampled by the radars. The next steps concern the establishment of statistics between various radar observables and ground-based observations (e.g. rainfall intensity and temperature) as well as with the variables predicted by the Modèle Atmosphérique Régional (MAR) of IGE (e.g. 0°C isotherm altitude, water and ice contents, rain and snowfall rates) for the Grenoble 10 x 10 km^2 mesh.

13.57 SHORT TIME PRECIPITATION ESTIMATION USING WEATHER RADAR AND SURFACE OBSERVATIONS: WITH WIND DRIFT INTEGRATED USING A STOCHASTIC METHOD

JIERU YAN[1], ANDRÁS BÁRDOSSY[1]

[1] Institute of Modeling Hydraulic and Environmental Systems, Department of Hydrology and Geohydrology, University of Stuttgart, Stuttgart, Germany
jieru.yan@iws.uni-stuttgart.de

C-band radar, which is widely used in Europe, measures instantaneous precipitation rate every 5 minutes, and the rainfall is accumulated based on the 5-min spaced radar maps. It is a frequently seen phenomenon that two consecutive radar maps have horizontal displacement in the pattern due to the horizontal component of the wind. In this paper a method of downscaling radar rainfall accumulation is proposed, where the horizontal displacement of the wind is integrated using a stochastic method, and the radar rainfall is downscaled spatially and temporally. Estimation of short time precipitation with reasonable accuracy is essential in flash flood now-casting. Weather radar, with its virtue of giving the spatial distribution of the rainfall, is combined with rain-gauge observations, which are considered as "ground truth", interspersed within the area of interest. It is common practice to compare gauge data with the collocated radar data directly, by assuming the vertical descending of the hydrometeors, which is not true in many cases. Hydrometeors are very likely to be displaced by wind during the descending from the radar measurement height and the Earths surface, i.e. the effect of wind drift. In this paper, the effect of wind drift is investigated and integrated in the radar-gauge combination scheme in a stochastic manner. The proposed combination method is powerful in giving short time precipitation estimation, which honors both the spatial distribution of the rainfall indicated by weather radar and the "ground truth" given by the rain-gauge observations. Examples are given to show the applicability and the robustness of the method.

13.58 GEOSTATISTICAL APPROACH TO RAINFALL MAPPING FROM COMMERCIAL MICROWAVE LINKS

W. WOLFF[1], A. OVEREEM[2,3], R. UIJLENHOET[3]

[1] "Luiz de Queiroz" College of Agriculture, Biosystems Department, University of São Paulo, Brazil

[2] R&D Observations & Data Technology, Royal Netherlands Meteorological Institute, the Netherlands

[3] Hydrology and Quantitative Water Management Group, Wageningen University, the Netherlands

wwolff@usp.br

In the last decade, rainfall monitoring by using rain-induced attenuation measurements from commercial microwave links (CML) became an alternative way to estimate rainfall for large areas. For this kind of monitoring, the mean rainfall is measured along a link between two cellular antennas (transmitter and receiver). That topology needs to be considered for rainfall mapping. For instance, in the sections where the links intercept each other oversampled locations are present. Due to the temporal dynamics, both of the CML network topology and of the rainfall itself, each event has a specific spatio-temporal behaviour. Thus, a geostatistical approach based on models allows estimating parameters and capturing the spatial variability for each time interval, in a straightforward way and computationally efficient. The aim of this work is to propose a method for rainfall mapping capable of dealing with crossing links, real-time parameter estimation, and large- area prediction.

Using approximately 2,600 links, the study was carried out in the Netherlands ($\sim$35,500 km^2). The R package RAINLINK was used for retrieving rainfall based on attenuation data available from 10-09-2010 18:30 until 11-09-2010 08:00 with a 15 minute temporal resolution. Since it is reasonable to consider that the rainfall spatial variability along the links can be neglected, the path-average rainfall mean can be assumed representative for any link section. Therefore, for the link intersection coordinates, basically, the mean of the links overlaid was sampled. On the other hand, for the non-overlaid links, the centroid coordinates were obtained. Using the method of restricted maximum likelihood (REML), the geostatistical model parameters were estimated. Thus, the ordinary kriging (OK) algorithm was used for rainfall mapping. Here, we call this method REML. For validating REML, a gauge-adjusted radar data set provided by the Royal Netherlands Meteorological Institute (KNMI) was used. Moreover, we compared REML with regular interpolation methods made available in RAINLINK, being OK with fixed parameters for each time interval and inverse distance squared weighted (ID2). The spatial efficiency metric (SPAEF) was employed for measuring the goodness of fit between observed (gauge-adjusted radar) and estimated rainfall maps (REML, OK, and ID2).

The results highlight a few improvements as indicated by a SPAEF value equal to 0.62 compared with 0.60 and -0.02 for OK and ID2, respectively. Moreover, REML is not constrained by crossing links and computationally efficient for large areas. This last characteristic is an advantage of REML with respect to tomography methods, which can deal with crossed links but are computationally impractical for large areas.

13.59 HYBRID SURFACE RAINFALL ESTIMATION FOR OPERATIONAL APPLICATION USING DUAL POLARIZATION RADAR NETWORK IN KOREA

YOUNG-A OH[1], MI-KYUNG SUK[1], SUNG-HWA JUNG[1], SUN-KI LEE[1]

[1] Radar Analysis Division, Weather Radar Center, Korea Meteorological Administration, Yeouidaebang-ro 16-gil, Dongjack-gu, Seoul, 07062
younga0321@gmail.com

Dual-polarization capability of weather radar led to significant improvements in radar-based rainfall estimation as well as the quality control of radar data. Radar observations usually suffer from various error sources such as ground clutter, beam blockage, anomalous propagation, sea clutter, attenuation, and so on. Recently, to mitigate the influences of complex terrain in radar-based rainfall estimation, hybrid surface rainfall (HSR) technique based on polarimetric observation has been employed as an operational radar-based QPE in KMA. HSR yields the rainfall estimation at the lowest-observable elevation surface (so called hybrid surface) that immunes to ground clutter, radar beam blockage and other non-meteorological echoes. However, in the case of hail and convective core, the accuracy of HSR decreases significantly due to mis-identification of precipitation echo by unnatural reduction of cross correlation coefficient (hv) and strong attenuation in reflectivity(ZH) and differential reflectivity(ZDR). For more stable routine operation of polarimetric rainfall estimation, we aim to develop HSR technique that is less affected by the strong contamination in polarimetric observation. The ground clutter was identified by combination of radial texutre and difference between raw and filtered reflectivity by IIR. We developed the new quality parameters such as the ratio between Z and ZDR, reflectivity-weighted hv for more reasonable classification of non-meteorological echo. The beam blockage simulation was also updated by using digital terrain with horizontal resolution of 1 arc second instead of 3 arc second. Beam shielding area and non-meteorological echo were more effectively classified comparing to existing technique. Specially, the precipitation echoes over abnormal reduction area of polarimetric observation was succefully preserved and its intensity was also corrected. In comparison to rain gauge data, the accuracy of HSR increases up to 75% with the normalized bias error less than -5%.

Acknowledgements
The research is supported by “Development and application of cross governmental dual-pol radar harmonization (WRC-2013-A-1)” project of WRC, KMA

Session 14. Non-meteorological use of weather radar



14.1 RETRIEVING VOLCANIC MASS ERUPTION RATE FROM GROUNDBASED X-BAND AND L-BAND MICROWAVE RADARS DURING MT. ETNA EXPLOSIVE ERUPTION

F.S. MARZANO[1,2], L. MEREU[1], S. DI FABIO[2], M. MONTOPOLI[3], E. PICCIOTTI[2], S. SCOLLO[4], C. BONADONNA[5]

[1] Sapienza University of Rome, Rome, Italy
[2] CETEMPS, University of L′Aquila, L′Aquila, Italy
[3] ISAC, CNR, Rome, Italy
[4] INGV, Catania, Italy
[5] University of Geneva, Geneva, Switzlerland
frank.marzano@uniroma1.it

Mt. Etna, one of the most active volcanoes in Europe, is located on the east coast of Sicily (Italy). Lava fountains are one of the most distinctive characters of Mt. Etna, relevant for the large amount of ash discharge rate. Within the INGV experimental site near the Mt. Etna volcano, a large set of instrumentation is installed, including seismic sensors, an optical lidar, a microwave radar, an infrasound array, a video camera. In the morning of 23 November 2013 an explosive lava fountain erupted from the New Southeast Crater (NSEC), lasting for about 1 hour. The lava fountain was clearly observed from two ground-based radars, an X-band polarimetric microwave weather radar (Marzano et al., 2013) and an Lband Doppler radar named Voldorad (Donnadieu, 2012) as well as from a video thermal-infrared camera.

The capability of the ground-based radars to probe the lava fountain and to estimate the volcanic mass eruption rate, a crucial parameter to describe the volcanic eruption intensity and to initialize ash dispersion numerical models, is still under discussion (e.g., Marzano et al., 2016). From the L-band Voldorad both radial velocities and the power backscattered by tephra particles can be derived, whereas from X-band microwave weather-radar polarimetric observables, by extending the VARR (Volcanic Ash Radar Retrieval) methodology, we can identify the lava fountain altitude and derive the tephra mass eruption rate (MER). The latter can be estimated from 3 main techniques: 1) the surface-flux approach (SFA), physically relating MER to the tephra exit velocity and density as well as the vent geometry; 2) top-plume approach (TPA), using semi-empirical parametric models ingesting the top plume altitude and eruption geophysical parameters; 3) mass-continuity approach (MCA), based on the mass continuity equation solved within the erupted plume volume including the volcano vent as surface boundary condition.

In this work we show how SFA, TPA and MCA retrieval techniques can be formulated within VARR and how the mass eruption rate can be retrieved from both X-band weather radar and L-band Voldorad data. This intercomparison shows that there is a consistency between these approaches when applied to both X-band and L-band data, once most of the uncertainties are taken into account and model parametrizations are constrained. Moreover, the radar-based estimates well compare

with total erupted mass estimates derived from field campaigns aimed at sampling ash loadings at ground after 23 November 2013. The analysis of this case study indicate that ground-based polarimetric microwave weather radars can be exploited to provide a self-consistent monitoring of the timevarying activity of explosive volcanic eruptions.

References

Marzano F.S., E. Picciotti, G. Vulpiani, M. Montopoli, "Inside Volcanic Clouds: Remote Sensing of Ash Plumes Using Microwave Weather Radars", BAMS, 1567-1586, 2013.

Donnadieu, F., "Volcanological applications of Doppler radars: A review and examples from a transportable pulse radar in L-band", Bech and Chau, Eds., InTech, 409446, 2012.

Marzano F.S. et al., "Near-Real-Time Detection of Tephra Eruption Onset and Mass Flow Rate Using Microwave Weather Radar and Infrasonic Arrays", TGRS, 54, 6292-6306, 2016.

14.2 EUROPE-WIDE PATTERNS OF NOCTURNAL AVIAN MIGRATION FROM WEATHER RADAR DATA

CECILIA NILSSON[1], ADRIAAN DOKTER, LIESBETH VERLINDEN, JUDY SHAMOUN-BARANES, BAPTISTE SCHMID, PETER DESMET, SILKE BAUER, JASON CHAPMAN, JOSE ALVES, PHIL STEPANIAN, NIR SAPIR, CHARLOTTE WAINWRIGHT, MATHIEU BOOS, ANNA GÓRSKA, MYLES MENZ, PEDRO RODRIGUEZ, HIDDE LEIJNSE, PAVEL ZEHTINDJIEV, ROBIN BRABANT, GÜNTHER HAASE, NADJA WEISSHAUPT, MICHA CIACH, FELIX LIECHTI

cecilila.nilsson@cornell.edu

Reliable quantification of bird migration systems is inherently difficult as much migration goes undetected, at night or high altitude, but also because of the sheer number of animals involved and the large spatial scales over which migration occurs. Within the framework of COST action ENRAM (European Network for the Radar surveillance of Animal Movement), we used the network of European weather radars to investigate nocturnal bird movements. For the first time we mapped migration at the scale of the entire European flyway. By extracting biological information from 70 weather radar stations from northern Scandinavia to Portugal, we provide a continental view of nocturnal bird migration during the autumn migration season of 2016. We map the major migration directions and show the intensity of movement as birds migrate along the West European flyway. We quantify migration intensity through different parts of Western Europe, and show how blocking weather conditions can aggregate migration into cumulative waves moving through Europe from the north to the south. By studying migration at the novel scale of synoptic weather systems, the structuring effect of continental wind patterns on the general flux of migration is revealed. This first continental-scale study using the European network of weather radars demonstrates the wealth of information available and its potential for investigating large-scale bird movements over Europe, with consequences for agriculture, domesticated animal and human health and civil and military aerial transportation.

14.3 TRACKING OF SMALL UNMANNED AERIAL VEHICLES USING WEATHER RADAR

K. ORZEŁ[1], D. PEPYNE[1], S. TURNER[1], J. VILARDELL-SANCHEZ[1], A. BAJAJ[1], M. ZINK[1], S. FRASIER[1]

[1] University of Massachusetts at Amherst, USA
korzel@umass.edu

The Federal Aviation Administration (FAA) estimates that, by 2021, as many as six million small Unmanned Aerial Vehicles (sUAVs) or micro-drones could be in U.S. skies. This trend has been driven by the ease of regulations, availability of low-cost micro-drones, capabilities such as aerial reconnaissance and maneuverability, innovative uses of these systems, such as inspections of pipelines and utility lines, law enforcement and package delivery. At the same time, however, micro-drones increasingly have been creating problems that jeopardize public safety, business continuity and privacy concerns. Drone safety incidents, including flying improperly, or getting too close to other aircraft, now average about 250 a month. A counter-drone industry has developed around drone surveillance, or the monitoring and tracking of non-cooperative sUAVs.

The Center for Collaborative Adaptive Sensing of the Atmosphere (CASA) at the University of Massachusetts. Amherst has pioneered the innovative use of Xband dual polarization weather radar to detect, classify and track sUAVs. Since most sUAV parts are made of carbon fiber, plastic and styrofoam, this class of drones is characterised by a very small radar cross section (RCS) between -30dBsm and -10dBsm. SUAVs exhibit a characteristic micro-Doppler signature that can be used for detection and for discrimination avian targets (birds) [Orzel et al., 2017]. Tracking drones or birds, either in software or visually on a display, also requires a very fast update rate on order of 5 seconds. This necessitates the use of next generation phased array radar.

The radar being used in this project is a Phase Spin Weather Radar (PSWR) [Orzel & Frasier, 2018]. In weather radar surveillance mode, PSWR performs a full 360 degree mechanical scan in the azimuth, while performing electronically RHI scans. This significantly limits the site revisit time. Furthermore, it is possible that drone will be located only in few range cells during the entire mission due to the fact that a weather radar range resolution is on order of 50-150 meters and many flights are limited to the visual line of sight (VLOS). Results from different drone flight scenarios will be presented and the result of a tracking algorithm will be verified using the information obtained by the UAV onboard GPS unit.

This work is supported through a U.S. National Science Foundation innovation grant.

References

K.Orzel and S.Frasier, "Weather Observation by an Electronically Scanned Dual-Polarization Phase-Tilt Radar", IEEE Transactions on Geoscience and Remote Sensing, Volume: 56 Issue: 3, March 2018.

K. Orzel, S. Govindasamy, A. Bennett, D. Pepyne, and S. Frasier, "Detection and identification of the Remotely Piloted Aircraft System using a weather radar", in AMS 38th Conference on Radar Meteorology, September 2017.

14.4 TIME-SERIES BASED APPROACH TO IDENTIFY AND PROCESS BIOLOGICAL TARGETS IN RADAR WIND PROFILER DATA FOR CROSS DISCIPLINARY PURPOSES

N. WEISSHAUPT[1], V. LEHMANN[2], A. HAEFELE[3], M. MARURI[1,4,5]

[1] University of the Basque Country UPV/EHU, Spain
[2] Meteorologisches Observatorium Lindenberg, Germany
[3] Federal Office of Meteorology and Climatology, MeteoSwiss, Payerne, Switzerland
[4] Basque Meteorology Agency (EUSKALMET), Spain
[5] Meteorology Area-TECNALIA R&I, Spain
nw@nweisshaupt.net

Operational radar wind profilers used in meteorology have been known to register biological targets, such as birds. Migrating birds seriously affect the quality of meteorological data, i.e. wind measurements. Existing signal processing approaches have contributed to improved data quality, in particular the Gabor frame based clutter filtering, so that the data products are suitable for operational meteorological purposes. However, there is still a potential for further refinement. The non-meteorological data content and its potential use in related areas, such as biology or even risk assessment studies, is still poorly understood. These radars accumulate a great treasure of data based on their continuous operation mode and widespread use in networks worldwide. In regard to today's budget constraints, it would be reasonable to make use of the large data pool and share its information with other disciplines.

Previous analyses have shown that time series data (and derived Gabor spectrograms) is the only appropriate level to deal with biological data content, both for meteorological and biological purposes, as it is the only level permitting unambiguous separation of atmospheric vs. non-atmospheric targets. In order to verify the utility of the developed manual methodology, data from three additional radar wind profilers (different specifications, different manufacturers etc.) were studied in regard to signal characteristics and system specifications.

The current results show that the methodology to identify biological targets is applicable to radar wind profilers with different system specifications. Biological echoes can be distinguished from atmospheric ones, and migration intensity and height distribution could be calculated for data from RWPs with different system specifications and of different manufacturers.

Even though the approach had originally an ornithological motivation, the findings are also valuable for the meteorological community, as the information on the biological signal characteristics provides novel insights potentially valuable for the improvement of wind data quality and related services. It also helps understand the interactions between meteorology and biology as well as the effect and limitations of filter mechanisms and their impact on the data output. Additionally, as the methodology allows the calculation of the height distribution and intensity of bird migration, radar wind profiler data offers a valuable source for flight safety and collision hazard evaluation in impact assessments, e.g. for wind parks.

14.5 COMPARISON OF ONSHORE AND OFFSHORE BIRD MIGRATION BY DIFFERENT RADAR SYSTEMS NEAR THE BELGIAN COAST

M. REYNIERS[1], R. BRABANT[2],M. LUKACH[34], B. SCHMID[5], M. BOOS[6]

[1] Royal Meteorological Institute of Belgium, Belgium
[2] Royal Belgian Institute of Natural Sciences, Belgium
[3] School of Earth and Environment, University of Leeds, UK
[4] National Centre for Atmospheric Science, University of Leeds, UK
[5] Swiss Ornithological Institute, Switzerland
[6] NaturaConst@, France
maarten.reyniers@meteo.be

The research program RAVen (RAdar registrations of bird migration Validation through an interdisciplinary approach) is a collaboration between the Royal Belgian Institute of Natural Sciences (RBINS) and the Royal Meteorological Institute of Belgium (RMIB) to study bird migration along the western flyway using different radar systems. RBINS owns and operates a Merlin bird radar located on an offshore platform at the Thorntonbank, a major wind farm 30 km (19 mi) off the Belgian coast. This radar is installed with the purpose of studying the impact of offshore wind farms on the behaviour of birds and bird migration. The Jabbeke weather radar operated by the RMIB is located at 10km of the Belgian coast and 40km from the Merlin radar. Additionally, a third bird radar was operated by NaturaConst@ near the French-Belgian border during the autumn migration of 2016, at 50km from the weather radar. This unique configuration was used to cross-validate the three radar systems for bird detection, and it offers also the rare opportunity to investigate onshore vs offshore migration of the same migratory events.

In this contribution we present the methodology and the first results of this intercomparison. In particular, we focus on the seasonal and diurnal patterns as seen by the three radar systems. Some additional information regarding insect contamination is obtained from the dual-pol moments of the weather radar. Furthermore, we present a preliminary analysis of vertical bird density distributions obtained by the RMIB weather radar and the RBINS offshore bird radar.

14.6 RAIN ATTENUATION STATISTICS AT KA-BAND ESTIMATED FROM WEATHER RADAR OBSERVATIONS

M. LUKACH[1,2,3], L. QUIBUS[4], D. VANHOENACKER[4], L. DELOBBE[1]

[1] Royal Meteorological Institute of Belgium, Brussels, Belgium
[2] School of Earth and Environment, University of Leeds, UK
[3] National Centre for Atmospheric Science, University of Leeds, UK
[4] ICTEAM, Universit catholique de Louvain, Belgium
maryna.lukach@ncas.ac.uk

This paper presents rain attenuation statistics for satellite-ground transmission links at Ka-band based on 10-year reflectivity observations from a C-band weather radar. The ground receiving station and the radar are both located in Belgium. Only precipitation under the freezing level is considered and the attenuation produced by hail is removed by applying a reflectivity threshold. The radar-derived attenuations are analyzed to investigate the influence of elevation and azimuthal angles on the attenuation statistics. It is shown that the azimuthal dependence is extremely low. In contrast, the exceedance probability for a given attenuation threshold strongly increases with decreasing elevation angles. The total rain attenuations exceeded with 0.1% probability increases from 3 dB at 75° elevation to 12 dB at 10° elevation. Some sensitivity tests have been performed. We show that the sensitivity to the hail reflectivity threshold is very limited. In contrast, our results show that reliable attenuation statistics cannot be obtained without taking carefully into account the height of the freezing level. Monthly averages of the freezing levels allow producing satisfactory results but it is recommended to incorporate freezing level heights with high temporal and spatial resolutions.

Extended Abstracts



Radar reflectivity advection estimation via proxy circle images

A.C.P. Oude nijhuis[1], Y. Dufournet[1], T. Otto[1], and I. Stepanov[1]

[1]*Sky-Echo, the Netherlands*
(Dated: 22 June 2018)


A.C.P. Oude nijhuis

1. Introduction

Nowcasting of rainfall rates at high spatial (100 m x 100 m) and temporal resolution (1 minute) is becoming more and more relevant for urban applications. It is not only relevant for the pleasure of citizens or tourists, but also for water management, traffic management, harbor and airport operations. A problem with the nowcasting of high-resolution measurements is that the data stream becomes rather large so that is it difficult to process them in realtime applications. Either large computational resources or fast and efficient algorithms are necessary to be able to process them.

Nowcasting of rainfall rates can be divided in two parts: (1) the advection of the rain cells, and (2) the growth or dissipation of the rain cells. Here the focus is on the first part, which is the fast estimation of advection from pairs of radar reflectivity measurements. To this end, we apply existing efficient image processing techniques for the estimation of the advection. There is, however, a problem: efficient image processing techniques are not optimized for radar images, and they can not be applied directly to estimate the image displacement for a pair of two radar images. Next to the displacement of the image (due to advection), the radar images are mostly not very identical in the details (due to the radar measurement principles and natural variability).

As a solution, proxy circle images - or otherwise so-called filtered images - are made from the radar reflectivity images to be able to apply existing fast image processing techniques. In the proxy circle image, a conical kernel is used to smooth the image. From two proxy circle images the image translation can then be estimated via subpixel image translation registration by cross-correlation (this is an efficient image processing technique to estimate image displacement). Finally, the advection of radar reflectivity patterns can be efficiently estimated from radar reflectivity image pairs. The estimation can then be further enhanced by combining estimates from multiple pairs, which also provides an error estimate of the advection estimate. In the presentation, the advection estimation algorithm is applied to X-band radars in the Netherlands, which are going to be used for realtime nowcasting applications. The algorithm is validated by applying it to radar archive data, and comparing the predictions with measurements.

2. Assessment of different techniques for radar advection estimation for high-resolution nowcasting products

Considering a high-resolution X-band radar system that is going to be used for nowcasting, there are several options to estimate the advection with a high resolution. Here we qualitatively assess the following options, which are a numerical weather prediction model (NWP), an advection field derived from radar Doppler velocities, and the estimation of advection by estimating the motion from image pairs. For a more detailed overview of nowcasting software, we refer to Sun et al. (2013) and (Wilson et al., 2004). Both these references give an intercomparison of oftenly used nowcasting software, and discuss their differences and challenges.

The NWP seems a logical choice to be used as source for the estimation of advection of rain cells, as it integrates many measurements. However, the resolved spatial scale and temporal scale of the NWP are much coarses than the desired resolution of a high-resolution nowcasting product (100 m spatial resolution and 1 min time resolution). For example, the highest spatial resolution of a NWP that is continuously running in the Netherlands is 2.5 km (de Rooy et al., 2016), for which output is generated every 6 hours, with a temporal resolution of 1 hour. Therefore, the NWPs are not a first choice, and others options have to be considered.

The second choice would be to use the radar Doppler velocities. Although the radar Doppler velocities only measure the radial component of the wind vector, they can be converted into a field of 3D wind velocities (e.g. Oude Nijhuis et al., 2014, 2016). The retrieved wind vectors are then at the same spatial and temporal resolution as the measurements of the rain intensity, so a descrepancy in resolution is not an issue anymore. There is, however, another problem. The radar Doppler velocities are approximately equal to the line-of-sight velocities of rain drops in the radar measurement cells, and the derived wind field is thus representative for the lower altitudes. The rain cells are - on the contrary - moving with the precipitating clouds, which are located at much higher altitudes. As rain is most often produced by vertical shear (Holton, 2001), and the wind vectors are thus changing with altitude, the advection field of the rain is rather different from the wind field that is derived from radar Doppler velocities. Therefore, the radar Doppler velocities are not suitable for estimating the advection of rain fields. This difficulty

might be resolved by using radar Doppler velocities at the cloud base (where the precipitaiton is originating from), but such an approach requires more research, which includes a more dedicated radar configuration.

A third option is to estimate the advection from a pair (or a series) of radar images, where the motion of the rain cells is estimated from the translation of them in the images. With this technique, there are some common problems (see also the nowcasting software references mentioned above). One problem is that the software to estimate the advection can be rather slow. For example, using 4D-Var to estimate the advection via a least squares fit approach (Oude Nijhuis et al., 2016) can easily take 10-20 minutes of processing time on a regular CPU, as the simultaneous fitting of motion and a reflectivity pattern is a non-linear problem. Another problem is that radar image pairs contain a lot of varibility, due to the natural evolution of the rainfield and the radar measurement principles, and common image processing techniques can not be applied directly. If these problems can somehow be resolved, and the advection field can be accurately estimated for a rainfield, it is expected that the nowcasting products can be significantly improved.

3. Assessment of image processing techniques to estimate translation for images with some variability

Here we propose to use fast image processing techniques, to estimate the advection field from pairs of radar images. We consider some of the image processing functions in the *scikit-image* Python module (van der Walt et al., 2014). These algorithms for image processing are highly optimized for a wide variety of image processing applications, for example the recognition of coins in photos, or the restoration of distorted images. Here we are mainly interested in the geometrical registration functions, as they can be used to estimate the advection from a pair of radar images.

A common manner to register the geometrical transformation from a source image to destination image, is to find interesting points, and consequently use a matching algorithm. Such interesting points can for example be based on an edge detection algorithm, and they can be matched to the point in a second image by a RMS error comparison of pixel values for a small area surrounding the point. This results then in a list of points that go from location A to B. The geometrical transformation parameters, that are associated with these point pairs, can then be estimated with a least squares fit. The problem with applying such a technique to radar image pairs, is that radar images do not consist solely of a geometrical transformation. They also contain varibility of the rain itself, which make the point matching algorithm unstable. And without a stable algorithm to find interesting points, these techniques don't work.

Another way to estimate is to use cross-correlation to identify the relative shift between two similar images (Guizar-Sicairos et al., 2008). This method gives a single translation vector of the image translation from one image to another. A single translation vector should not be an issue, as with radar images, such a method can be applied to smaller subdomains of the full radar image, and thus estimate an advection field by combining the results from several subdomains. The large advantage of this technique is that it isn't depending on a point-to-point matching algorithm (which is tricky for radar images because of its varibility). The performance of this technique also relies on similarity of the two images. For radar images, this can be solved by using some sort of filtering. So this technique can be quite interesting to estimate an advection field, but it also creates some new challenges. These challenges are how to choose the subdomains, and how do the filtering of radar images. We will focus now solely on using this technique, with the desire to obtain a field of advection vectors.

4. Proxy circle images

A proxy circle image is essentially a filtered rainfall rate image, where a conical kernel has been applied to smooth the image. This kernel can be applied via a convolution, and is shown in Fig. 1. The result of applying such a kernel is shown in Fig. 2, where it can be seen that the kernel smoothes the image. It can be seen that the shape of the filtered images are much more similar than the images that were not filtered. Such a smoothening filter is thus successfull in removing some of the variability in a series of radar images.

In Fig. 2, next to the images themselve, also the cross-correlation is shown for the image pairs. The place (x-offset and y-offset) where cross-correlation is maximal indicates the relative shift between the two images. This estimation of this offset can be further enhanced with efficient subpixel image registration algorithms (Guizar-Sicairos et al., 2008). In the background of the images in the second column of Fig. 2, the translated radar image of 5 minutes before is shown in gray colors. For this translation, the translation parameters were obtained with the cross-correlation technique. It can be seen that both for the filtered and non-filtered images, the radar images are well-aligned, and thus shows that this image processing technique has potential to be used for advection estimation. It is expected that in the case when there is more variability in the images, the estimated translation parameters from the filtered radar images will be more stable.

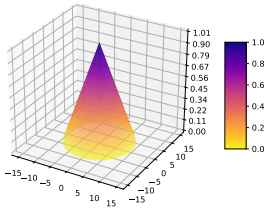
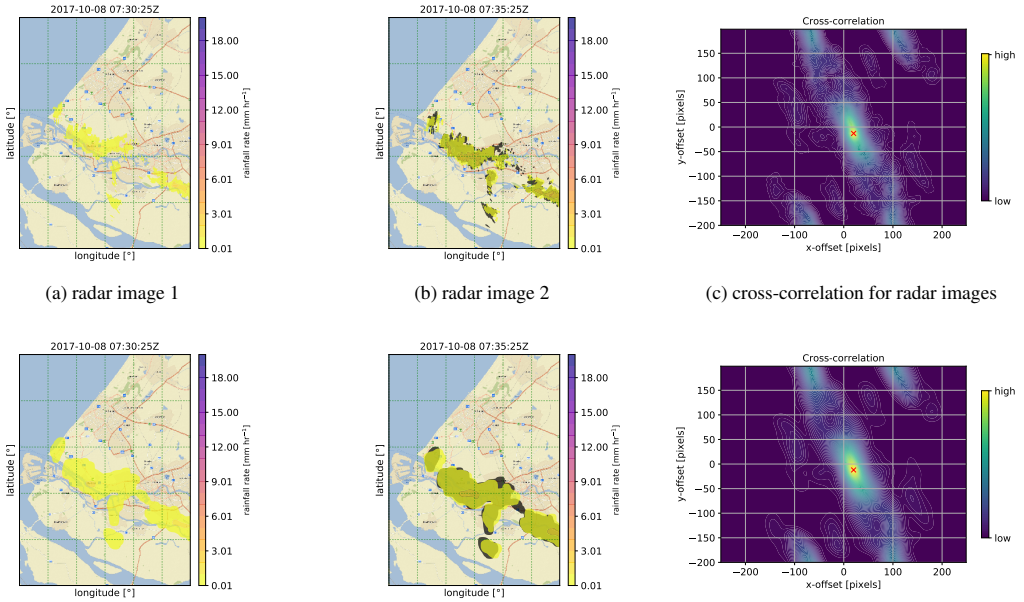


Figure 1: Conical 2D kernel for image filtering.



(a) radar image 1 (b) radar image 2 (c) cross-correlation for radar images

(d) filtered radar image 1 (e) filtered radar image 2 (f) cross-correlation for filtered radar images

Figure 2: Two images of rainfall rate that were obtained with the Rijnmond radar (left and middle). A conical filter is applied to remove noise and smooth out the measurements, which result in the filtered images (lower row). In the second rainfall rate image, also the translated first rainfall rate image is shown in the background. The cross-correlation is shown for both image pairs (right images).

5. Estimation of the advection field

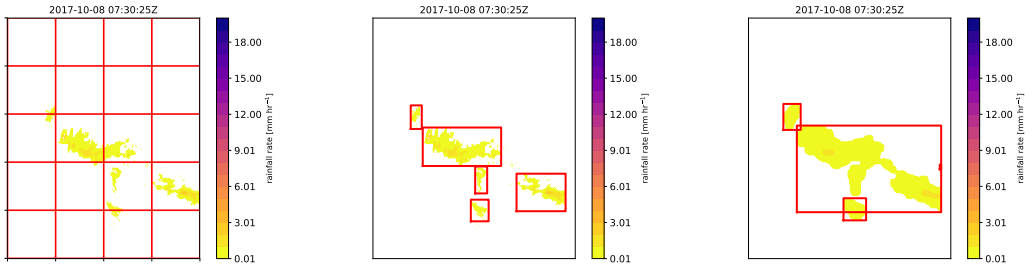
The next step is to estimate a field of advection vectors. There are several paths that can be taken, which differ in how the subdomains are selected, and how the resulting advection vectors are combined to an advection field in the end. In Fig. 3 different manners how to select subdomains are demonstrated, which we will discuss.

One option is to use windowing. In that case, for each window, the cross-correlation technique is applied, and an advection vector is estimated. A drawback of windowing is that the number of windows can get large, considering that it should be applied at different scales, and different offsets. As a result, the algorithm for advection estimation then becomes slow, which is not desired. Another drawback is that the circumference of a raincell is not matched with the subdomain. The consequene of this can is that the translation estimation performs poorly, as the translation estimation predominantly relies on the motion of the circumference.

Another option is to use regions of interest (ROIs) (van der Walt et al., 2014). This solves a few of the problems with windowing, as the circumference of the raincell will be in the subdomain where the cross-correlation technique will be applied. A drawback of the ROIs method is that it is hard to tell whether such a technique will perform for a wide variety of rainfields. In Fig. 3, the largest ROIs are shown for both the radar image and the filtered radar image. In both cases, the selected subdomains seem to be representing the raincells, with the minor note that it can be somewhat vague where a raincell start and stops.

So in the end, a combination of windowing and ROIs might be needed, to have both a stable algorithm, and localized advection vectors that are specific for the motion of tracked rain cells. In the end, the results from different subdomains

and different pairs of radar images can be combined by using a weighted averaging method to obtain an optimal solution. The weighting of such a method should then depend on the estimated uncertainty of the estimated advection vector for the subdomain.



(a) image 1, windowing (b) image 1, region of interests (ROIs) (c) filtered image 1, region of interests (ROIs)

Figure 3: Demonstration of how subdomains can be selected from a radar image: with windowing (left), with regions of interest ROIs, or with ROIs of the filtered image. Further details of image 1 are in Fig. 2.

6. Outlook

Here we showed that it is possible to efficiently estimate the advection field for radar images from the radar images themselves via commonly used fast image processing techniques that are available in *Python* in *scikit-image* (van der Walt et al., 2014). It remains to be seen whether this approach will work under a variety of rainfields. In addition, the growth and dissipation has to be developed in this nowcasting system, for which the S-PROG algorithm will be used as a first starting point (Seed, 2003). To further assess and improve this algorithm, the root-mean-square error (RMSE) of predicted images versus measured images, forecast skill and the execution time are considered.

Acknowledgement

Hereby we would like to thank all contributors to this work. In particular we would like to thank TU Delft and the municipality of Rotterdam for using the data from the Rijnmond radar. Further we would like to thank the SkyEcho company for supporting this work including grants from WBSO and CityLab010.

References

W. de Rooy, H. de Vries, C. van Dalum, S. de Haan, Meirink J, G. Lenderink, G. van Marseille, and R. Scheele, "Hirlam Scientific report: Harmonie verification and evaluation," Tech. Rep. 70, 2016.

M. Guizar-Sicairos, S. T. Thurman, and J. R. Fienup, "Efficient subpixel image registration algorithms," *Opt. Lett.*, vol. 33, no. 2, pp. 156–158, 2008.

J. R. Holton, *An introduction to dynamic meteorology*, 2001.

A. C. P. Oude Nijhuis, O. K. Krasnov, C. M. H. Unal, H. W. J. Russchenberg, and A. Yarovoy, "Outlook for a new wind field retrieval technique: The 4D-Var wind retrieval," in *2014 Int. Radar Conf.*, 2014, pp. 1–6.

A. Oude Nijhuis, O. Krasnov, A. Yarovoy, C. Unal, and H. Russchenberg, "Implementation of wind vector and turbulence intensity retrievals: Application to fast scanning X-band radar," in *2016 IEEE Metrol. Aerosp.*, Florence, 2016, pp. 113–117.

A. W. Seed, "A Dynamic and Spatial Scaling Approach to Advection Forecasting," *J. Appl. Meteorol.*, vol. 42, no. 3, pp. 381–388, 2003.

J. Sun, M. Xue, J. W. Wilson, I. Zawadzki, S. P. Ballard, J. Onvlee-Hooimeyer, P. Joe, D. M. Barker, P.-W. Li, B. Golding, M. Xu, and J. Pinto, "Use of NWP for Nowcasting Convective Precipitation: Recent Progress and Challenges," *Bull. Am. Meteorol. Soc.*, vol. 95, no. 3, pp. 409–426, 2013.

S. van der Walt, J. L. Schönberger, J. Nunez-Iglesias, F. Boulogne, J. D. Warner, N. Yager, E. Gouillart, and T. Yu, "scikit-image: image processing in Python," *PeerJ*, vol. 2, p. e453, 2014.

J. W. Wilson, E. E. Ebert, T. R. Saxen, R. D. Roberts, C. K. Mueller, M. Sleigh, C. E. Pierce, and A. Seed, "Sydney 2000 Forecast Demonstration Project: Convective Storm Nowcasting," *Wea. Forecasting*, vol. 19, no. 1, pp. 131–150, 2004.

Using a four-dimensional variational radar and surface data assimilation system to investigate the process leading to a heavy precipitating event over complex terrain: A case study in Northern Taiwan



Ying Jhang,Wu

[1]Wu, Y.-J. (wu890355@gmail.com), [1]Y.-C. Liou

[2]S.-L. Tai, [3]J. Sun

[1]Dept. of Atmospheric Sciences, National Central University, Taiwan

[2]Pacific Northwest National Laboratory, USA

[3]National Center for Atmospheric Research, USA

1 Introduction

The complex terrain in Taiwan area makes it challenging to forecast convection initiation, propagation and intensification. In this research, we use surface data and a newly-designed 4DVAR radar data assimilation system to study the structure and mechanisms leading to a heavy rainfall event occurred on 19 August, 2014 in northern Taiwan.

2 Domain setting and Methodology

✓ **Domain setting**

Lat : 24.8 N~ 25.4 N

Lon : 121E ~ 122 E

Landscape:

1. Linkou high land(200m)
2. Taipei Basin
3. Snow Mountain Range(1400m)

(see red dashed lines in Fig. 1)

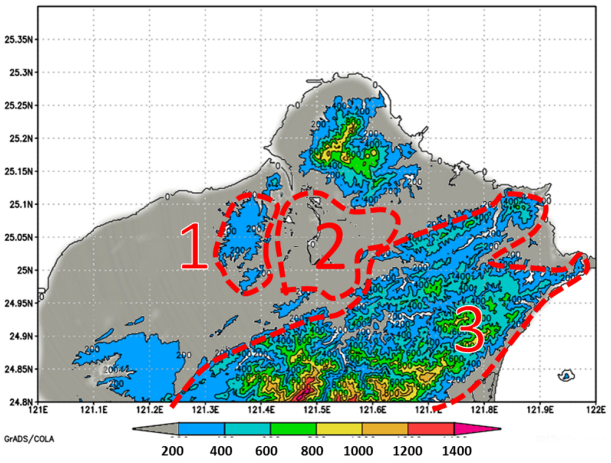


Figure 1:Terrain height(m) in northern Taiwan

✓ **Methodology**

1. Surface station data analyses

   Data: wind, temperature, precipitation

2. IBM_VDRAS: A 4DVAR data assimilation system with terrain-resolving capability, **can provide high resolution 3D meteorological fields.** (Tai et al. 2017).

   Assimilation window: 12.5mins

   IBM_VDRAS analysis update rate: 17.5 mins

   Domain resolution : dx=1 km, dy=1 km, dz=250m

   Assimilated data: radar (ZH, VR), surface station (wind, temperature, RH)

3 Surface station data analyses

A. Temperature (shaded;℃) & wind (vector)

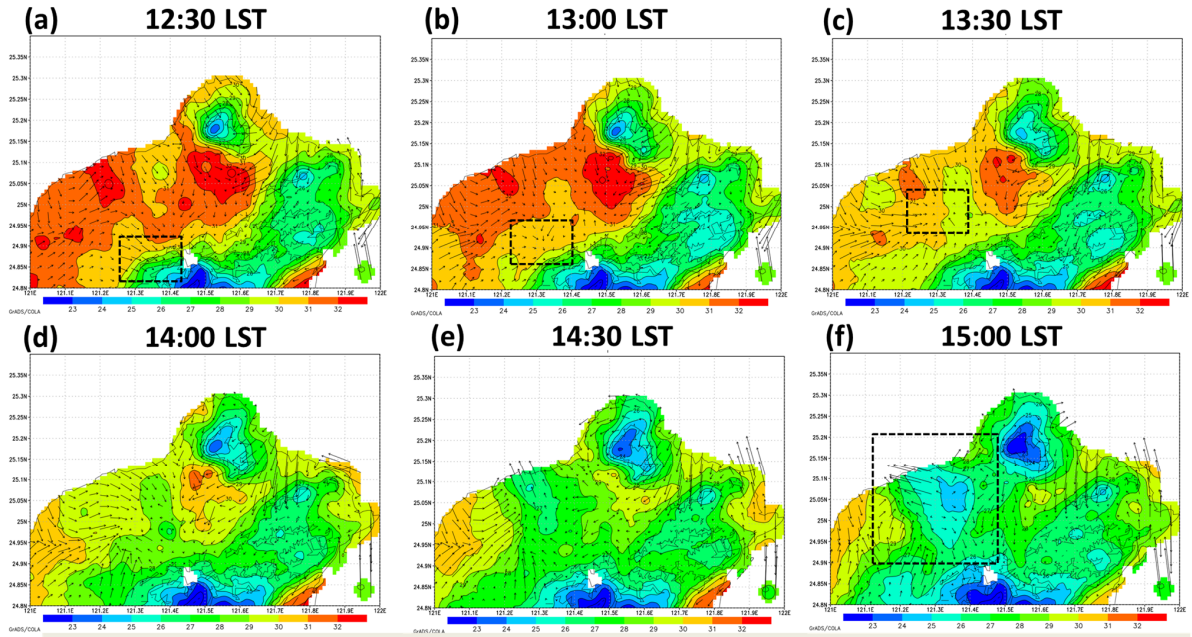


Fig 2. Surface station temperature(shaded; ℃) and wind(vector) at (a) 12:30 LST (b) 13:00 LST (c)13:30 LST (d)12:00 LST (e)14:30 LST (f) 15:00 LST

From the surface station data, the wind convergence zone propagates from foothill to plain (see black box in Figs. 2a-2c). Figures 2c-2e show that from foothill to plain, the temperature drops with time, representing a cold pool transition. Later, the convection cell reaches mature stage. The outflow from convection on the Linkou high land is obvious (see black box in Fig. 2f).

B. Precipitation (accumulated from 14:22 LST)

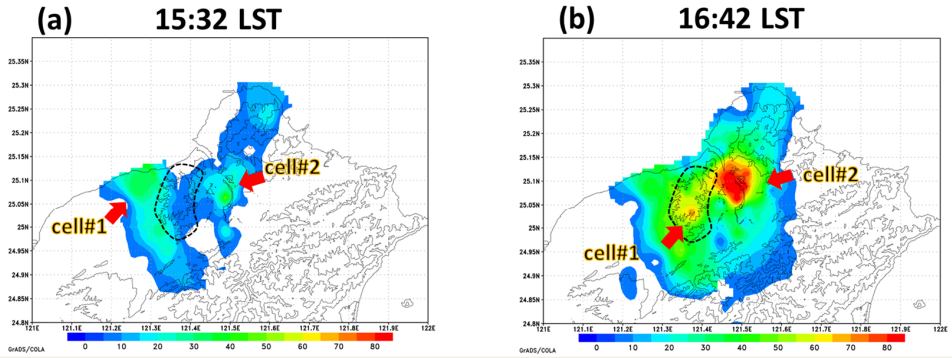


Fig 3. Surface station rain accumulation(shaded; mm) from 14:22 LST to (a) 15:32 LST (b) 16:42 LST . The maximum accumulate precipitation positions are labeled in red arrows. The black line indicates the boundary of Linko heigh land.

Two distinct rainfall maxima are separated by Linkou high land (see Fig. 3 cell #1 on the west, cell #2 on the east). At 16:42 LST, rainfall in cell#2 area has accumulated over 80 mm, due to the long lasting (1.5hr) precipitation.

*Cell position is determined by maximum accumulated precipitation location.

4 IBM_VDRAS analyses

A. Temperature perturbation (shaded;℃) & wind(vector) at lowest height

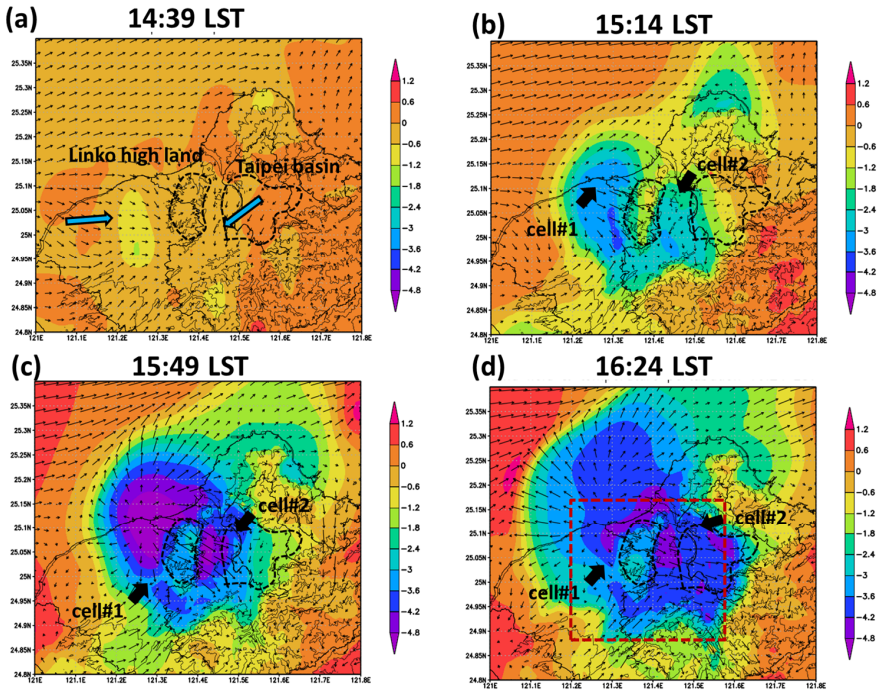


Fig 4. IBM_VDRAS analyses at (a) 14:39 LST (b) 15:14 LST (c)15:49 LST (d)16:24 LST. The shaded color is perturbation temperature(°C) and vector is (u,v) wind at lowest height. Cell positions are labeled in black arrows. The black dash line indicates the boundary of Linkou high land and Taipei basin. The dark-red square line in Fig 4d is zoom-in area for next figure.

Figure 4a shows that north-easterly wind exists in Taipei basin and westerly wind occurs on the western side of Linkou high land (see blue arrow), causing significant convergence. In Fig. 4b, precipitation cooling takes place at both cells. Westerly wind produced by the cell#1 outflow flows over the Linkou high land. From Figs. 4c and 4d, it can be seen that the cell#1 outflow intensifies, and flows over and around the Linkou high land to the eastern side of Linkou where cell#2 resides. The outflow from cell #1 merges with cell#2. The latter is thus intensified, with its duration significantly prolonged, leading to a heavy rainfall event in Taipei basin.

B. Surface convergence (shaded; m $s^{-1}km^{-1}$) & RH>95%(patch) at lowest height

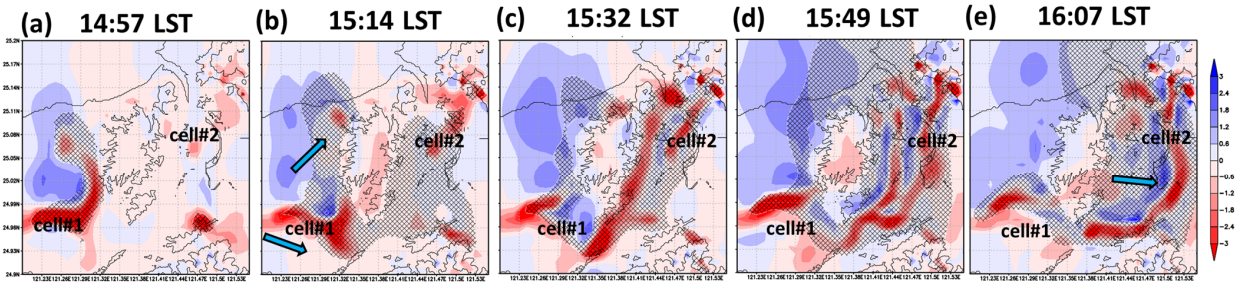


Fig 5. IBM_VDRAS zoom-in area at (a) 14:57 LST (b) 15:14 LST (c)15:32 LST (d) 15:49 LST (e) 16:07 LST . The shaded color is surface convergence ($m\ s^{-1}km^{-1}$) and patch area is near surface relative humidity greater then 95%. Cell positions are labeled in (a).

Figure 5a shows that the strong convergence (red area) in cell#1 is blocked by the Linkou high land, and splits into two branches as shown by the blue arrows in Fig. 5b. In Figs. 5b-d, the area with relative humidity greater than 95% expands dramatically. The convergence zone originated from cell#1 reaches the eastern side of Linkou high land and extends to a NE-SW-oriented line structure. Air with high humidity is transported to cell#2 area. At the final stage, convergence zones from both cells merge (see the blue arrow in Fig. 5e) and intensify the convection, causing the heavy rainfall of this event.

This series of graphs in Fig. 5 demonstrates that persistent convergence zone occurs in the Taipei basin area (labeled in Fig. 5a "cell#2"). The eastward outflow generated by cell#1 provides additional convergence and humidity, which produce a favorable condition for heavy rainfall.

5 Results

1. Based on the surface stations wind and temperature data, it is shown that cell#1 on the western side of Linkou highland propagates from foothill to plain and matures in plain area.
2. Two cells are separated by Linkou high land, and cell#2 on the eastern side of Linkou leads to heavy rainfall (80mm/2 hr) in Taipei basin.
3. From IBM_VDRAS analyses, the outflow from cell #1 is able to flow over and around Linkou high land, merges with cell#2, and provides additional convergence and high humidity to cell#2,. The latter is thus significantly intensified and prolonged, leading to a heavy rainfall event in Taipei.

6 Reference

Tai S.-L., Y.-C Liou, J. Sum and S.-F. Chang,,2017:The Development of a Terrain-Resolving Scheme for the Forward Model and Its Adjoint in the Four-Dimensional Variational Doppler Radar Analysis System (VDRAS). Mon. Wea. Rev., 145, 289-306

Sun, J., and N. A. Crook, 1997: Dynamical and microphysical retrieval from Doppler radar observations using a cloud model and its adjoint. Part I: Model development and simulated data experiments. J. Atmos. Sci., 54, 1642–1661

Chang, S.-F., Y.-C. Liou, J. Sun, and S.-L. Tai, 2016: The implementation of the ice phase microphysical process into a four-dimensional Variational Doppler Radar Analysis System (VDRAS) and its impact on parameter retrieval and quantitative precipitation nowcasting. J. Atmos. Sci., 73, 1015–1038

Deep Learning Framework for Precipitation Retrievals from Communication Satellites


Kumar Vijay Mishra

Kumar Vijay Mishra[1,2], Ahmad Gharanjik[1], M. R. Bhavani Shankar[1], and Björn Ottersten[1]

[1]*Interdisciplinary Centre for Security, Reliability and Trust (SnT), University of Luxembourg, Luxembourg*
[2]*IIHR - Hydroscience & Engineering, The University of Iowa, Iowa City, USA*
(Dated: 27 June 2018)

1. Introduction

It is well known that estimation of rainfall, while taking into account its spatio-temporal variability, is essential for several applications in earth sciences (Krajewski and Smith, 2002; Mishra et al., 2016). There is a rich heritage of research in analyzing multiple aspects of rainfall measurement and estimation using sensors such as rain gauges, disdrometers, weather radars and space-borne instruments (Testik and Gebremichael, 2013; Thurai et al., 2017). Over the past few decades, rainfall estimates based on weather radar measurements at low frequencies such as S-, C-, and X-bands have greatly enhanced our understanding of the precipitation structure. However, significantly large parts of the world, especially developing countries, remain uncovered from ground-based weather radar networks. Further, although radar-based precipitation estimates are increasingly used for quantitative precipitation estimation and forecast, it is also well established that these products suffer from large uncertainties (Mishra et al., 2013; Seo et al., 2015; Villarini and Krajewski, 2010). In regions where weather radars have been deployed, their large size and cost restricts the density of individual radar units to yield rainfall retrievals at high spatio-temporal resolutions (e.g. popular U.S. National Weather Service rainfall estimates are available at $\sim$ 1-4 km^2 resolution for a 14-minute volume scan) (Mishra et al., 2016; Thurai et al., 2017).

Recently, opportunistic use of communication satellite links to obtain valuable precipitation information in the regions that are beyond the coverage of conventional ground-based weather radars has garnered considerable research interest (Barthès and Mallet, 2013; Gharanjik et al., 2018a,b; Mugnai et al., 2015). Deployment of additional weather radars is expensive while there are overwhelmingly many ground satellite terminals spread across the world. The terminal link conditions, impacted heavily by attenuation in rain, are available at a central location (gateway station) in real-time making the entire setup usable in practice. The communication satellites also outnumber the spaceborne weather radars such as NASA's Tropical Rainfall Measurement Mission (TRMM) and Global Precipitation Measurement (GPM) (Hou et al., 2008).

Communication satellites operate at Ka-band where link signals suffer from strong attenuation in the rain medium (Mishra et al., 2012; Seto and Iguchi, 2015). Ground-based weather radars are typically not employed at millimeter wavelengths for estimating rainfall due to heavy signal attenuation. However, they are quite useful for observation of small hydrometeors such as clouds, drizzle and light snow as well as short-range rain rate retrievals (Chandra et al., 2015; Mishra, 2012). Additionally, Mie scattering effects at Ka-band may not be small causing the computation of scattering amplitudes difficult (Beard et al., 2010; Bringi et al., 2008; Nakamura et al., 2018). Nonetheless, at the locations where low-frequency weather radars may not be available, valuable but less accurate precipitation estimates have been obtained by Ka-band weather radars (Matrosov, 2005) and ground microwave links for cellular communication (Ostrometzky and Messer, 2018). The rainfall estimation procedure at Ka-band exploits the fact that both the rain rate R and specific attenuation A are approximately proportional to the 3.65th rain drop size distributions (DSD) moment at Ka-band (Matrosov et al., 2006) leading to a nearly linear relation between R and A. It is also fortuitous that this relationship has relatively less, $\sim 10\%$, variability to temperature and DSD (Matrosov, 2005).

The carrier-to-noise-ratio (C/N) measurements (Gharanjik et al., 2018b) of the link are predominantly related to A allowing derivation of R estimates. However, the linear R-A relation holds good only for heavy stratiform rain storms. In light rain, the attenuation is less significant and, consequently, difficult to estimate A. The R-A linearity is also affected by the wind shear (Mittermaier et al., 2004) during convective storms. These various rainfall regimes are usually classified by the variability of radar measurables such as reflectivity, Doppler velocity, spectrum width, differential reflectivity, specific differential phase and copolar correlation coefficient that are estimated through advanced weather radar processing (Geerts and Dawei, 2004). The satellite user terminals (UT), on the other hand, are single-polarized passive receivers, and lack the ability to extract even the simplest parameters such as reflectivity and Doppler velocity which are necessary in order to differentiate between storm types and rainfall intensities. Despite these shortcomings, the presence of large number of satellite terminals is a motivation to exploit their measurements for rainfall estimation.

Due to the unavailability of radar-based products critical to correctly apply the R-A algorithm, an alternative is to utilize learning methods which have the ability to extrapolate new features from a limited set of features contained in a training set (Lecun et al., 2015). Prior research (Orlandini and Morlini, 2000; Vulpiani et al., 2009) on S-, C-, X-, and Ku-band weather radars has adopted artificial neural network (ANN) for estimating rainfall wherein the difference between radar estimates and those obtained through *in situ* instruments such as rain gauges is used to train the network to adjust the radar relation parameters

until it converges on an optimal solution. We refer the reader to Testik and Gebremichael (2013) for an overview of these techniques that benefit from the availability of highly-parameterized data through the use of dual-polarization, high-resolution sampling and frequencies with minimal attenuation.

In contrast, our goal is to apply learning for rainfall estimation in a more information-limited setup from satellite communication signals. We first estimate A by processing the received signal C/N and then feed these estimates to a learning network to broadly classifies the storms based on their intensities so that the linear R-A relationship can be appropriately exploited. Our previous work (Gharanjik et al., 2018a) has demonstrated the potential of Ka-band link for rainfall estimation by employing machine learning (ML) (Michalski et al., 2013) to classify dry and wet conditions. In Gharanjik et al. (2018b), we extended this work to enhance the retrieval performance by training the ML network to recognize dry, light and heavy rain regimes using data from the nearest weather radar and collocated rain gauges. Our analysis showed that our rain accumulations were in better agreement with the rain gauge than those from the nearest German weather service Deutscher Wetterdienst (DWD) radar. In comparison with the existing satellite link-based precipitation estimates obtained through conventional methods (Barthès and Mallet, 2013; Mugnai et al., 2015), our experimental set up comprises of broadband satellite systems that allow centralized rainfall estimation from gateway station.

In this work, we investigate deep learning (DL) (Lecun et al., 2015) in the specific context of rainfall estimation using the data from single-polarized passive receivers of ground terminals. The DL is a type of ML technique that works directly on the data rather than the user-defined data features and has been shown to provide state-of-the-art performance in a variety of applications (Elbir et al., 2018; Lecun et al., 2015). While classifying given C/N, it helps to look into the data before and after the present values. In this context, the recurrent neural networks (RNNs) (Medsker and Jain, 2001) are a class of DL architectures that are well suited to learn the time-dependent sequences of varying length. In this paper, specifically we use long short-term memory (LSTM) network (Hochreiter and Schmidhuber, 1997) - a type of RNN that is very efficient in exploiting dependencies over a long period of time and have been used successfully even on non-stationary data (Graves et al., 2005). Unlike our earlier work in Gharanjik et al. (2018b) which derived features such as mean and standard deviation of C/N time series to input in an ML network for dry/wet classification, we directly use the C/N series to train the LSTM. We aggregate the rainfall estimates from 35 UTs located in the Southwest Germany to generate an approximate rainfall map. We then compare our results with the observations from the nearest DWD radar in Southwest Germany. To the best of our knowledge, this is the first work that employs LSTM for the passive satellite links to generate rainfall estimates. Our initial results presented in this paper show reasonable accuracy wherein the 24-hour rain rate accumulations estimated by our proposed method has a difference of 1.8 mm with that of the weather radar.

The paper is organized as follows. In the next section, we provide the details of the link setup and details of obtaining C/N parameter. In Section 3, we describe the DL technique to classify the data into dry/wet regions and aggregate estimates from all UTs to generate a rainfall map. The performance evaluation and comparison with DWD radar is detailed in Section 4 followed by concluding remarks in Section 5.

2. Communication Satellite Network

Broadband satellite systems offer bidirectional communications between the gateway (GW) stations and UTs enabling interactive satellite services (such as Internet provisioning), see Fig. 1. The link from the GW to UTs is called the forward (FWD) link and the link from UTs to the GW is the return (RTN) link.

2.1. System Description

In order to maintain a certain level of quality of service for users, GW stations continuously monitor the FWD and RTN links. The C/N parameter measures quality of the communication link and received signals. The GW has access to end-to-end C/N on both the links. However, we use only FWD links C/N for rainfall estimation due to limitations in accessing RTN data. Average C/N is available at the GW station every five minutes (average C/N over five minutes) and stored in a database. It is generally assumed that the link between GW and the satellite (feeder link) is ideal. This is due to the fact that the transmit/receive antenna gain of the GW is very high. Therefore, the end-to-end C/N is dominated by the C/N of the user link (links between satellite and UTs). As a result, it can be assumed that variations of the end-to-end C/N are mainly caused by the user links. The C/N parameter is mainly affected by the rain attenuation at the operational Ka-band frequencies (broadband satellite) (Gharanjik et al., 2015). Therefore, there is a clear correlation between the C/N variations and amount of the rainfall.

2.2. Experimental Set-up

In order to illustrate our proposed method, we have exploited the experimental system installed in Betzdorf, Luxembourg. The system includes a broadband satellite UT and a weather station equipped with rain gauge. The UT receives broadband

services from ASTRA 2F satellite located at the orbital position of 28.2 E. The links from satellite to UT operate at K-Band (19.70-20.20 GHz) while the links from UT to satellite is at Ka-Band (29.40-30.00 GHz). The elevation and azimuth angles of the links are 29.4° and 151.8°, respectively. We also used rainfall data from the C-band DWD weather radar (located in Southwest Germany) for studying the rain events over the satellite link. Fig. 2 depicts the relative locations of our set-up.

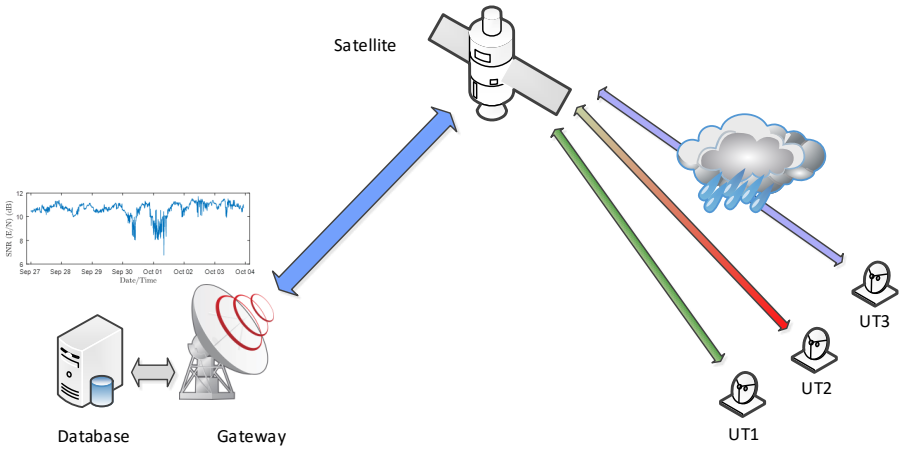


Figure 1: Architecture of a Broadband Satellite Communication Systems. The C/N data of the FWD and RTN links are collected by the gateway and stored at a database. We use these data for rainfall estimation.

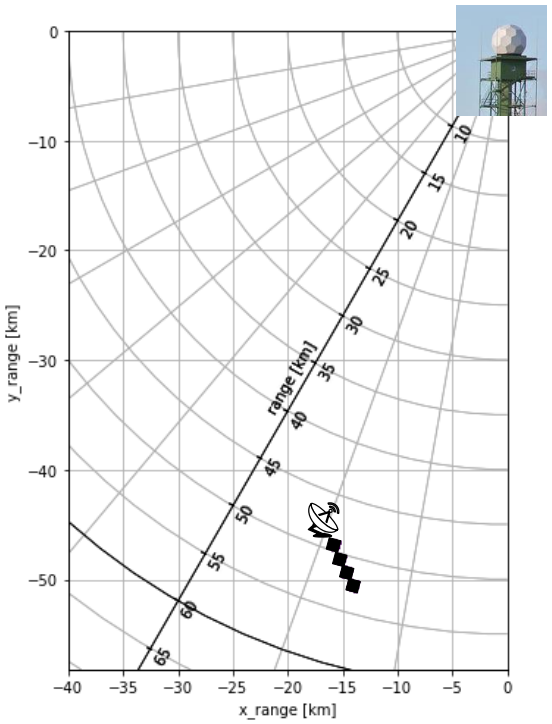


Figure 2: Approximate projection of the satellite slant path on four radar bins shown by dark color. The first top left of these four black bins shows the location of the UT as well as the collocated rain gauge. The Southwest Germany DWD radar is about 50 km away from the UT.

After training the rainfall estimation algorithm using the experimental set-up in Beztdorf, we applied it to C/N data of 35 UTs. These UTs are distributed in 25 km $\times$ 20 km area in Southwest Germany. Fig. 3 shows the distribution and location of the 35 UTs in this region.

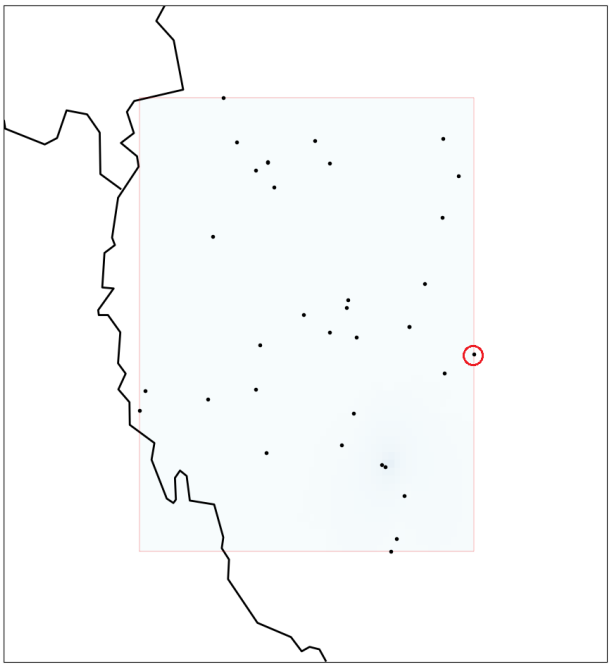


Figure 3: Location of 35 satellite terminals in Southwest Germany (25km by 20km).

2.3. Components of C/N

The first step towards estimating the rainfall from C/N measurements is to determine the amount of signal attenuation caused by rainfall during the rain event. Central to this, is an understanding of the various components constituting the C/N and the impact of rainfall on them. To this end, let us denote C/N by $C(n)$, where n is the index of measurement (data sample). Note that the data indexing starts from midnight and has a temporal resolution of 5 minutes, i.e., $n = 2$ represents 0005 UTC time of the first day of data collection.

Radio-wave propagation (and C/N) on Earth-Space links in millimeter wave frequencies is impacted by different tropospheric effects (Panagopoulos et al.), the major factor being the signal attenuation due to rain medium. We remark that co-channel interference also affects C/N. However, our set up does not employ multibeam coverage and frequency reuse. Consequently, the effect of co-channel interference is limited. Therefore, we assume that C/N is only impacted by rain attenuation and can decompose C/N (in dB) as,

$$C(n) = B(n) - D(n), \tag{2.1}$$

where, $B(n)$ is the baseline (reference level) that corresponds to the expected C/N in dry (no-rain) situation assuming a fixed position. The $B(n)$ includes impact of gaseous absorption, cloud attenuation, scintillations and noise in the microwave link. The $D(n)$ accounts for attenuation in rain and is zero in dry situations.

3. Rainfall Estimation Algorithm

In this section, we detail the proposed rainfall estimation algorithm. It consists of two steps: rain regime classification and rain rate calculation. Classification is required to find the baseline and signal attenuation ($B(n)$ and $D(n)$, respectively). We calculate the rain rate using $D(n)$ as recommended by the ITU-R model (ITU, 2013, 2005).

3.1. Rainfall Classification: LSTM algorithm

The goal of the classification algorithm is to distinguish between two classes: rain and dry given the C/N measurements. We consider LSTM here which is an RNN technique designed to efficiently find and infer long-range temporal dependencies in the time series. It was developed to counter the exponential blow-up or decay of the backpropagated error in existing RNNs leading to inaccessibility of long time lags.

The LSTM network can be considered as a sequence-to-label system. Its hidden layer consists of memory blocks which comprises of one or more recurrently connected memory cells and multiplicative units such as the input, output and forget gates. The latter three are the continuous analogues of write, read and reset operations for the memory cells. The network

interacts with the memory cells only via the gates. The cell input, network output and previous cell values are multiplied by the activation of the input, output and forget gate, respectively.

3.2. Rainfall Estimation: R-A Relation

After identifying the rain and dry events, we use a procedure similar to the one discussed in (Gharanjik et al., 2018a) to estimate the signal attenuation due to rain, i.e., $D(n)$. The ITU recommends (ITU, 2013, 2005) following power-law relationship between the specific attenuation A (dB/km) and rain rate R (mm/h)

$$A = kR^{\alpha}, \tag{3.1}$$

where the coefficients k and α depend on the frequency and polarization of the link. For the considered experimental setup at FWD link, we compute these values as follows: $k = 0.0939$ and $\alpha = 1.0199$. The specific attenuation is obtained as $A = D/L_s$ where D is the signal attenuation defined in (2.1). Here, $L_s = 4.9276$ km is the slant path length of the satellite link (Gharanjik et al., 2018a).

3.3. Rainfall Map Generation

After converting the C/N time-series to R, our objective is to generate a rainfall map for the region in Southwest Germany with 35 *in situ* UTs. We used the trained LSTM to estimate the rainfall rate for each UT. Thereafter, we applied inverse distance weighting (IDW) interpolation technique (Lu and Wong, 2008) create an approximate rainfall distribution over the entire region (see Fig. 3). The IDW assumes that the regions close to one another experience similar rain intensities than those that are farther apart. For each point on the map, we considered 5 closest neighboring UTs for computing the IDW weights.

4. Numerical Results

In this section, we present some numerical results for the proposed rainfall estimation approach. We employ an LSTM layer with 5 units and two outputs, each representing a class (dry or wet). Each LSTM unit looks back to the last 10 time steps in order to determine the class of the current C/N value. The classification output layer consists of y_1 and y_2 that provide the probability of rain and dry events, respectively. Fig. 4 shows the architecture of the LSTM network. Here, we standardized the input data (C/N) (rescaling the data so that the mean of C/N values is 0 and the standard deviation is 1) in order to speed-up the learning and convergence of the network.

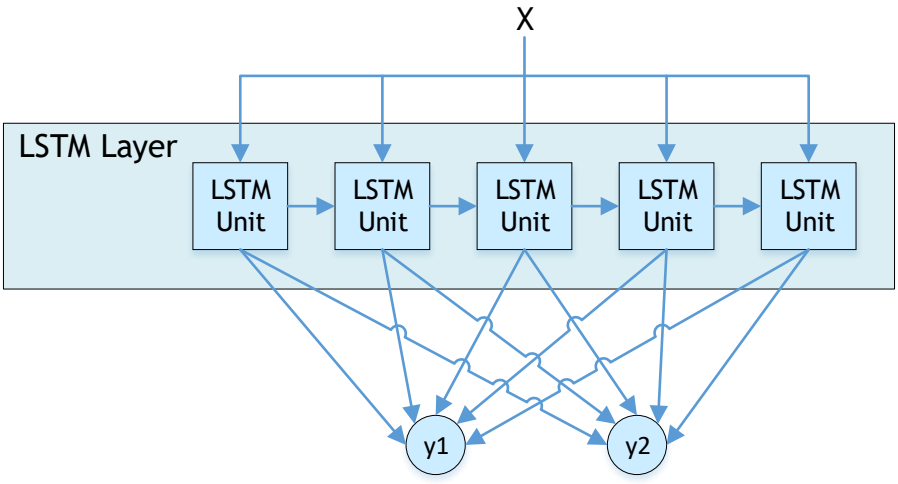


Figure 4: Structure of LSTM network for rain/dry classification.

All LSTM blocks had the following activation functions: logistic sigmoids in the range [-1, 1] for the input and output activation functions of the cell, and in the range [0, 1] for the forget gates. We used data from the set-up mentioned in Section 2 and partitioned them into LSTM training and test data. All nets were trained with gradient descent, using a learning rate of 10^{-1} and a momentum of 0.9. At the end of each iteration, the weights were updated and network activations were reset to zero. The output layers had softmax classifers, and the cross entropy objective function was used for training.

Following the procedure outlined in Section 3.2, we obtained estimates of R for each UT. Fig. 5 shows rain rates and rain accumulations over 24 hour period from 1200 UTC on 22 May 2018 to 1200 UTC on 23 May 2018 as estimated by the Southwest Germany DWD radar (dashed blue line) and the satellite link UT (encircled terminal on Fig. 3) using our proposed algorithm (solid red line). The UT estimates follows the radar closely leading to a single-day accumulation difference of ~ 1.5 mm only.

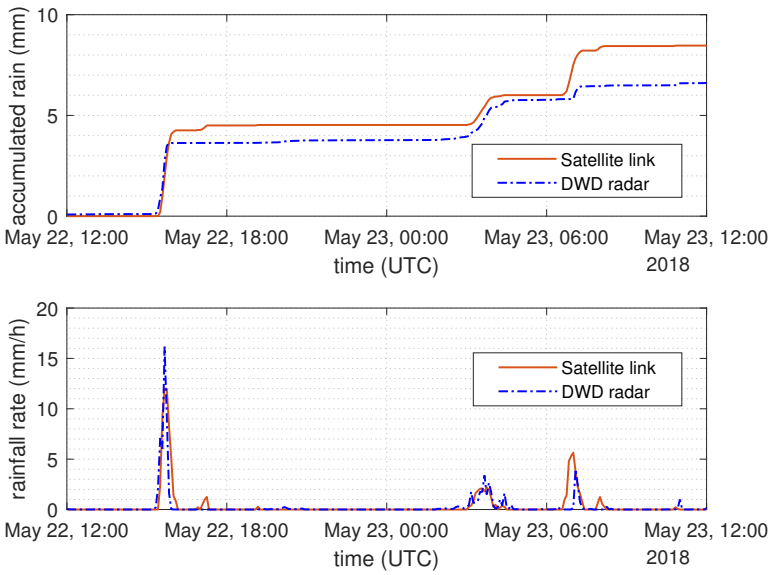
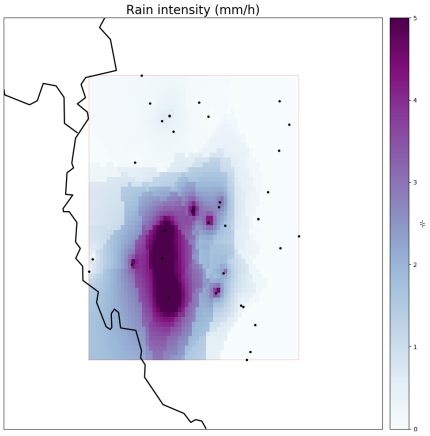


Figure 5: Rain accumulations during 24 hours from 1200 UTC on 22 May 2018 till 1200 UTC on 23 May 2018 as observed by the Southwest Germany DWD radar (dashed blue line) and satellite link (encircled UT in Fig. 3) using our proposed algorithm (solid red line).

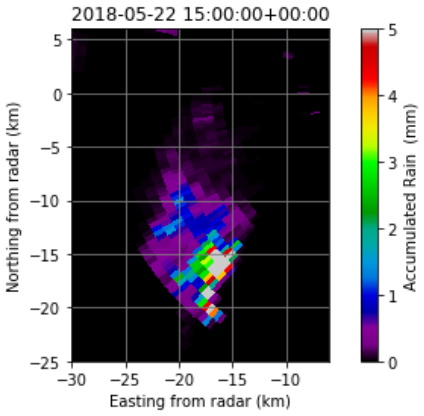
Finally, Fig. 6 compares 5-minute accumulations of the Southwest Germany DWD radar with the rainfall distribution generated by LSTM-based UT estimates at two different time intervals for a passing storm on 22 May 2018 UTC. The two snapshots which are about 35 minutes apart show that UT estimates capture the general direction and locations of the storms as observed by the radar. Note that the location of the radar beam is higher than the ground while the estimates from the UTs are closer to the ground. Several other factors such as differences in resolutions and sampling rates enhance the dissimilarities between the two estimates. As we show in Gharanjik et al. (2018b), the UT estimates are improved by training with the rain gauge data wherever possible. Nonetheless, our study demonstrates that DL can be effectively used to obtain valuable estimates of rainfall from UTs in regions where radar coverage may be missing.

5. Summary

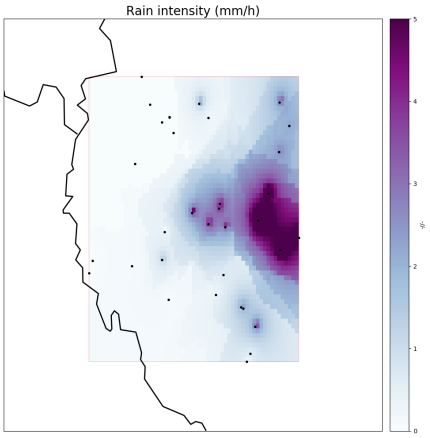
We proposed and investigated a DL framework for rainfall estimation based on opportunistic use of C/N measurements from broadband satellite communication networks. The learning network was modeled after LSTM which searches and recognizes long-term temporal dependencies in time-series data. We trained LSTM to directly classify the C/N data from the satellite links into dry and wet weather without using any user-defined data features. Thereafter, the events classified as rain storms were estimated for rain rates using the R-A expression following the ITU-R recommendations. Our comparisons of the rainfall distribution map generated from LSTM-based UT estimates with the nearest weather radar shows that our algorithm captures the major features of the storm even though very limited information about the weather was available to the UT set-up. This study demonstrates that DL is a promising framework to extract valuable, although less accurate, precipitation retrievals via the communication satellite links. In future, our goal is to continue improving the UT estimates through use of other advanced DL techniques and better training data.



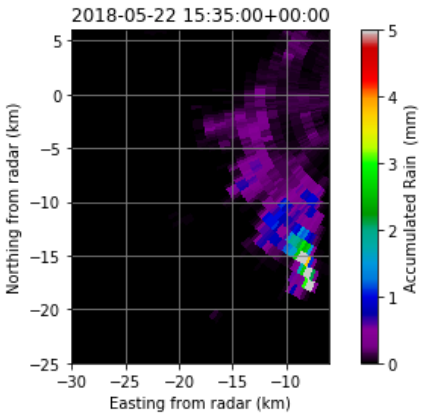
(a) Rainfall map (intensity) generated using C/N data from 35 satellite terminals at 1500 UTC on 22 May 2018



(b) Rainfall map (accumulation over 5 minutes) from DWD radar at 1500 UTC on 22 May 2018



(c) Rainfall map (intensity) generated using C/N data from 35 satellite terminals at 1535 UTC on 22 May 2018



(d) Rainfall map (accumulation over 5 minutes) from DWD radar at 1535 UTC on 22 May 2018

Figure 6: Comparison of the rainfall maps produced by our LSTM-based algorithm and the nearest DWD radar at two different intervals for a storm passing over Southwest Germany on 22 May 2018 UTC.

Acknowledgement

This work was partially funded by the Luxembourg National Research Fund (FNR) for the Proof of Concept project RAFAEL bearing contract POC/17/ 11648950.

References

"Propagation data and prediction method required for the design of the Earth-space telecommunication systems," ITU-R Recommendation P.618-11, Geneva, Switzerland, Tech. Rep., 2013.

"Specific attenuation model for rain for use in prediction methods," ITU-R Recommendation P.838-3, Geneva, Switzerland, Tech. Rep., 2005.

L. Barthès and C. Mallet, "Rainfall measurement from opportunistic use of earth-space link in Ku band," *Atmospheric Measurement Techniques*, vol. 6, no. 8, pp. 2181–2193, 2013.

K. V. Beard, V. Bringi, and M. Thurai, "A new understanding of raindrop shape," *Atmospheric Research*, vol. 97, no. 4, pp. 396–415, 2010.

V. Bringi, M. Thurai, and D. Brunkow, "Measurements and inferences of raindrop canting angles," *Electronics Letters*, vol. 44, no. 24, pp. 1425–1426, 2008.

A. Chandra, C. Zhang, P. Kollias, S. Matrosov, and W. Szyrmer, "Automated rain rate estimates using the Ka-band ARM zenith radar (KAZR)," *Atmospheric Measurement Techniques*, vol. 8, no. 9, p. 3685, 2015.

A. M. Elbir, K. V. Mishra, and Y. C. Eldar, "Cognitive radar antenna selection via deep learning," *arXiv preprint arXiv:1802.09736*, 2018.

B. Geerts and Y. Dawei, "Classification and characterization of tropical precipitation based on high-resolution airborne vertical incidence radar. Part I: Classification," *Journal of Applied Meteorology*, vol. 43, no. 11, pp. 1554–1566, 2004.

A. Gharanjik, M. R. Bhavani Shankar, P.-D. Arapoglou, and B. Ottersten, "Multiple gateway transmit diversity in Q/V band feeder links," *IEEE Transactions on Communications*, vol. 63, no. 3, pp. 916–926, 2015.

A. Gharanjik, M. R. Bhavani Shankar, F. Zimmer, and B. Ottersten, "Centralized rainfall estimation using carrier-to-noise of satellite communication links," *IEEE Journal on Selected Areas in Communications*, 2018, in press.

A. Gharanjik, K. V. Mishra, M. R. Bhavani Shankar, and B. Ottersten, "Learning-based rainfall estimation via communication satellite links," in *IEEE Statistical Signal Processing Workshop*, 2018.

A. Graves, S. Fernández, and J. Schmidhuber, "Bidirectional LSTM networks for improved phoneme classification and recognition," in *International Conference on Artificial Neural Networks*, 2005, pp. 799–804.

S. Hochreiter and J. Schmidhuber, "Long short-term memory," *Neural computation*, vol. 9, no. 8, pp. 1735–1780, 1997.

A. Y. Hou, G. Skofronick-Jackson, C. D. Kummerow, and J. M. Shepherd, "Global precipitation measurement," in *Precipitation: Advances in Measurement, Estimation and Prediction*, S. C. Michaelides, Ed. Springer, 2008.

W. Krajewski and J. Smith, "Radar hydrology: Rainfall estimation," *Advances in Water Resources*, vol. 25, no. 8-12, pp. 1387–1394, 2002.

Y. Lecun, Y. Bengio, and G. Hinton, "Deep learning," *Nature*, vol. 521, no. 7553, pp. 436–444, 2015.

G. Y. Lu and D. W. Wong, "An adaptive inverse-distance weighting spatial interpolation technique," *Computers & geosciences*, vol. 34, no. 9, pp. 1044–1055, 2008.

S. Y. Matrosov, "Attenuation-based estimates of rainfall rates aloft with vertically pointing Ka-band radars," *Journal of Atmospheric and Oceanic Technology*, vol. 22, no. 1, pp. 43–54, 2005.

S. Y. Matrosov, P. T. May, and M. D. Shupe, "Rainfall profiling using atmospheric radiation measurement program vertically pointing 8-mm wavelength radars," *Journal of Atmospheric and Oceanic Technology*, vol. 23, no. 11, pp. 1478–1491, 2006.

L. Medsker and L. Jain, "Recurrent neural networks," *Design and Applications*, vol. 5, 2001.

R. S. Michalski, J. G. Carbonell, and T. M. Mitchell, *Machine learning: An artificial intelligence approach*. Springer Science & Business Media, 2013.

K. V. Mishra, "Frequency diversity wideband digital receiver and signal processor for solid-state dual-polarimetric weather radars," Master's thesis, Colorado State University, 2012.

K. V. Mishra, V. Chandrasekar, C. Nguyen, and M. Vega, "The signal processor system for the NASA dual-frequency dual-polarized Doppler radar," in *IEEE International Geoscience and Remote Sensing Symposium*, 2012, pp. 4774–4777.

K. V. Mishra, A. Kruger, and W. F. Krajewski, "Monitoring cross-channel correlation solar scan measurements using the Iowa X-band polarimetric radars," in *IEEE International Geoscience and Remote Sensing Symposium*, 2013, pp. 1688–1691.

K. V. Mishra, W. F. Krajewski, R. Goska, D. Ceynar, B.-C. Seo, A. Kruger, J. J. Niemeier, M. B. Galvez, M. Thurai, V. Bringi *et al.*, "Deployment and performance analyses of high-resolution Iowa XPOL radar system during the NASA IFloodS campaign," *Journal of Hydrometeorology*, vol. 17, no. 2, pp. 455–479, 2016.

M. P. Mittermaier, R. J. Hogan, and A. J. Illingworth, "Using mesoscale model winds for correcting wind-drift errors in radar estimates of surface rainfall," *Quarterly Journal of the Royal Meteorological Society*, vol. 130, no. 601, pp. 2105–2123, 2004.

C. Mugnai, F. Sermi, F. Cuccoli, and L. Facheris, "Rainfall estimation with a commercial tool for satellite internet in Ka band: Model evolution and results," in *IEEE International Geoscience and Remote Sensing Symposium*, 2015, pp. 890–893.

K. Nakamura, Y. Kaneko, K. Nakagawa, H. Hanado, and M. Nishikawa, "Measurement method for specific attenuation in the melting layer using a dual Ka-band radar system," *IEEE Transactions on Geoscience and Remote Sensing*, vol. 56, no. 6, pp. 3511–3519, 2018.

S. Orlandini and I. Morlini, "Artificial neural network estimation of rainfall intensity from radar observations," *Journal of Geophysical Research: Atmospheres*, vol. 105, no. D20, pp. 24 849–24 861, 2000.

J. Ostrometzky and H. Messer, "Dynamic determination of the baseline level in microwave links for rain monitoring from minimum attenuation values," *IEEE Journal of Selected Topics in Applied Earth Observations and Remote Sensing*, vol. 11, no. 1, pp. 24–33, 2018.

A. D. Panagopoulos, P.-D. M. Arapoglou, and P. G. Cottis, "Satellite communications at Ku, Ka, and V bands: Propagation impairments and mitigation techniques," *IEEE Communications Surveys and Tutorials*, vol. 6, no. 3, pp. 2–14.

B.-C. Seo, W. F. Krajewski, and K. V. Mishra, "Using the new dual-polarimetric capability of WSR-88D to eliminate anomalous propagation and wind turbine effects in radar-rainfall," *Atmospheric Research*, vol. 153, pp. 296–309, 2015.

S. Seto and T. Iguchi, "Intercomparison of attenuation correction methods for the GPM dual-frequency precipitation radar," *Journal of Atmospheric and Oceanic Technology*, vol. 32, no. 5, pp. 915–926, 2015.

F. Y. Testik and M. Gebremichael, *Rainfall: State of the science*. John Wiley & Sons, 2013, vol. 191.

M. Thurai, K. V. Mishra, V. Bringi, and W. F. Krajewski, "Initial results of a new composite-weighted algorithm for dual-polarized X-band rainfall estimation," *Journal of Hydrometeorology*, vol. 18, no. 4, pp. 1081–1100, 2017.

G. Villarini and W. F. Krajewski, "Review of the different sources of uncertainty in single polarization radar-based estimates of rainfall," *Surveys in Geophysics*, vol. 31, no. 1, pp. 107–129, 2010.

G. Vulpiani, S. Giangrande, and F. S. Marzano, "Rainfall estimation from polarimetric S-band radar measurements: Validation

of a neural network approach," *Journal of Applied Meteorology and Climatology*, vol. 48, no. 10, pp. 2022–2036, 2009.

Potential for use of radar data for climate monitoring

Elena Saltikoff[1], Andreas Becker[2], Bernard Urban[3], Katja Friedrich[4],
Rainer Hollmann[2], Joshua Soderholm[5], Caterina Tassone[6]

[1]*Finnish Meteorological Institute, Finland*
2 Deutscher Wetterdienst, Germany
3 Meteo France, France
4 University of Colorado, United States
5 Bureau of Meteorology, Australia
6 Global Climate Observation System, Switzerland
[2]

(Dated: 21 June 2018)

1 Introduction

Many NMHSes have now archives of over 10 years of radar data, and there is growing need to use this data also for climate monitoring. This implies an additional archival and documentation requirement on top of those that had been addressed for the canonical use of radar systems for real-time purposes like warning.

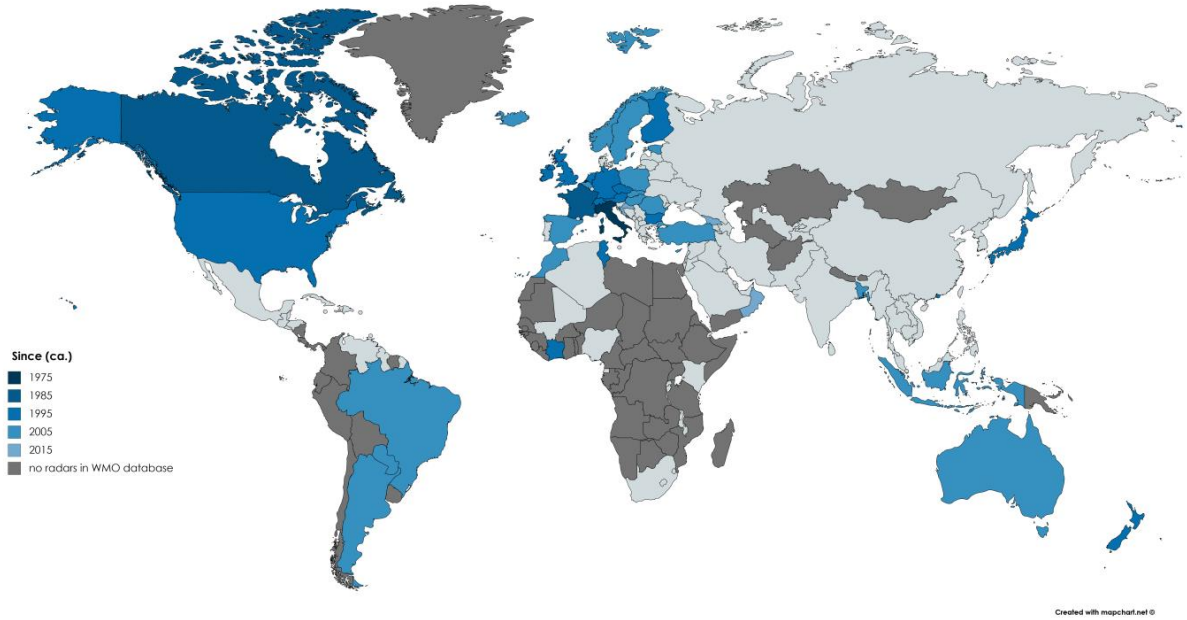


Figure 1:Approximated length of radar data archives in different WMO member countries.
Note that the entire country is coloured even if there are archives by no more than one radar.

Through WMO and GCOS a Task Team has been initiated leading discussions between climate researchers and radar experts, and preparing recommendations for mandatory and suitable data and metadata to be archived for climate monitoring purposes. This serves the baseline information to develop accepted guidelines and standards, with a view on the rather limited lifetimes of radar systems being shorter than those of stations and the characteristic climate time scale of 30yrs. Therefore it is essential to keep not only the metadata describing the latest hardware and processing, but also a history of important hardware changes such as from non-Doppler to Doppler radars to allow for a full retrieval of the essential information also decades after the measurements had been taken and to avoid false interpretations of apparent trends which come from changes in equipment, not changes in climate.

The phenomena to be monitored with weather radars include in addition to precipitation also severe mesoscale phenomena such as hailstorms and tornadoes.

The central parameter is horizontal reflectivity, ZH, which is basis of precipitation estimates. The other key parameters have importance for improving the quality of precipitation estimates and as independent variables for process and climate studies. As for the extreme precipitation, radar systems are the only instruments that can claim to fully resolve and fetch the scale of such meteorological events giving their unique capacity to study their developments during the first decades where climate change impacts the hydrometeorology.

2 Recommendations

2.1 What data to save

The task team recommends that radar data for climate monitoring shall be saved as Level 2 files, ie Derived radar variables or moments (reflectivity, radial velocity, differential reflectivity, etc.) at full resolution after aggregation and filtering. Organised in polar coordinates by rays, range bins and quantities. Also, known as "sweep" and "volume scan" data. (Full definition of radar data levels by WMO's Inpert-Programme Expert team of Operational Weather Radars, IPET-OWR, is as Annex 1)

While it is acknowledged, that there are still single polarization radars in use and data saved from non-Doppler radars, the key parameters listed are

- Equivalent reflectivity factor (DBZH)
- Radial velocity of scatterers away from instrument (VRAD)
- Doppler spectrum width (WRAD)
- Log differential reflectivity H/V (ZDR)
- Correlation Coefficient (RHOHV)
- Differential phase (PHIDP)

For ease-of-use, archive managers can be tempted to save Level 3 products such as rainfall rate or hydrometeor classification. As processing algorithms develop over years, maintaining homogeneity in the time series is challenging, and for reprocessing purposes saving also the Level 2 data is strongly recommended. The difference in amounts of stored data is not significant. 3D data are 10-30 times larger than 2D, but it is very easy to compress (e.g. zip). In OPERA, 150 radars produce 1-2 Gb a day for reflectivity, and even if we include all parameters the dataset grows to 10 Gb a day. Problem is not the disk space, but the management of data.

2.2 What about metadata

Data alone is not useful, if it is not accompanied with a sufficient set of metadata. Minimum and goal sets of metadata parameters have been defined e.g. by WMO WIGOS and IPET-OWR (Annex 2). For use of climate studies, there is has one strong recommendation: save history of metadata.

Because a lifetime of a radar is 10-20 years, most climatologically interesting time series would be containing data from different instruments at the same places. Even if the instrument has not been replaced, typically several upgrades have been implemented, so the present metadata is not describing the oldest data. Dates and types of major changes (such as from non-Doppler to Doppler capability, from single to dual polarization) should be indicated carefully. The logs of such changes is typically saved separately from the data; if not earlier then at least in data rescue projects these should be connected. The engineering logs may connect other information also useful for data use, such as calibration records. Combining these with the actual data is an important task to support the climatological studies. We are facing a risk of interpretation of changes in instruments or data processing to trends or seasonal variation of climate. (Have you heard the anecdote of three-year cycle of wind speed, which proved to be the maintenance interval of Wild anemometers? A counterpart in radar world is yet to be found - or not.)

2.3 We have some very old data

Existing archives are a treasure at risk. Data rescue projects and digital archiving are not only interest of radar meteorologist, our entire society is thinking what to do with old data formats and old physical media such as magnetic tapes.

For reprocessing of data, it is advisable to save intermittent products comparable to Level 2 data, including at least minimal metadata with a posteriori analysis. It is likely, that the reprocessing will be a repeated activity, and the goal is that the most cumbersome issues such as reading old data formats can be repeated only once. Bear in mind,that the technology needed for reading very old media (such as magnetic tapes) may not be available in the future decades.

Homogenization and potential reanalysis of archives containing several years and several radars is an effort of several man months, not something one can do in his/her spare time. For example, the operational Australian radar archive consists of approximately 800 years of data across more than 50 sites. Consolidation, quality control and post-processing of multiple archive sources has required several months of full-time work and remains an ongoing effort.

3 Examples of data use

Climatologists have already published local and regional climatological studies based on national radar archives. The analyzed parameters include

- High-resolution maps of annual average precipitation and frequency of precipitation rate (Fairman et al, 2015)
- Exceedance probability of 1h rainfall (Overeem et al., 2009)

- Relative frequency of severe weather as a function of time of day (Brimelow et al., 2014)
- Hovmöller diagram of > 40 dBZ (longitunal average) (Chen et al, 2012)
- Distribution by numbers of significant tornado events for convective mode by season (Grams et al., 2012)
- Number of hail days detected in the period 2003-2012 (Lukach et al, 2017)
- Hourly radar-derived hail frequency (normalized) for the entire domain and six sub-regions in the Alps. (Nisi et al. 2015)
- Distribution of the GEV parameters derived from satellite (HRC and CHRC) and radar datasets. (Marra et al. 2017)
- Rose diagrams of thunderstorm movement distributions for different months (Liu et Li, 2016)
- Climatology of progressive derecho events for the warm season (May–August) of 1996–2013. (Guastini & Bosart, 2016).

This is by no means a comprehensive list, just examples of what all can be studied with radar data time series! A mosaic of corresponding figures from these articles is included in the poster.

4 Conclusions and next steps

The team recommends, that while everyone saves the data you are measuring now, they also think if it can be read and understood in 2050, improve your documentation, and document the link between your data and supporting technical metadata (such as maintenance and upgrade logs).

Those who have existing archives, should think about the data you have saved over the years, especially think if it can be read and understood in 2050, and probably plan a data rescue project. Improving the documentation and document the link between your data and supporting technical metadata (such as maintenance and upgrade logs) should be done as soon as possible – not only the storage media are fading, but also the people who were responsible for changes such as Doppler upgrade projects, are soon getting retired in many countries.

This would also be a great subject for an international project to plan and prototype a portal with uniform access for different archives.

Acknowledgement

The authors wish to thank Paul Joe, Mark Curtis, Mike Dixon and Daniel Michelson from IPET-OWR for sharing the documents still in progress.

References

Brimelow J. C., G. W. Reuter, A. Bellon and D. Hudak,2004: A radar-based methodology for preparing a severe thunderstorm climatology in central Alberta. *Atmosphere-Ocean*. https://doi.org/10.3137/ao.420102

Chen M., Y Wang, F Gao and X Xiang 2012: Diurnal variations in convective storm activity over contiguous North China during the warm season based on radar mosaic climatology. *J. Geo. Res*. https://doi.org/10.1029/2012JD018158

Fairman J, D M. Schultz, ,D J. Kirshbaum, ,S L. Gray and A I. Barrett 2015, A radar-based rainfall climatology of Great Britain and Ireland. *Weather*, 70, 5. https://doi.org/10.1002/wea.2486

Grams J. S. and R. L. Thompson,. 2012: A Climatology and Comparison of Parameters for Significant Tornado Events in the United States. *Wea.Forec*. https://doi.org/10.1175/WAF-D-11-00008.1

Guastini C G. and L. F. Bosart, 2016: Analysis of a Progressive Derecho Climatology and Associated Formation Environments: *Mon. Wea.Rev*. https://doi.org/10.1175/MWR-D-15-0256.1

Liu W and X. Li, 2016: Life Cycle Characteristics of Warm-Season Severe Thunderstorms in Central United States from 2010 to 2014. *Climate* 4(3) 45. https://doi.org/10.3390/cli4030045

Lukach, M., L. Foresti, O. Giot and L. Delobbe (2017): Estimating Occurrence and Severity of Hail Based on 10-years Observations From Weather Radar in Belgium. *Meteor. Appl*. https://doi.org/10.1002/met.1623

Marra, F., Morin, E., Peleg, N., Mei, Y., and Anagnostou, E. N.: Intensity–duration–frequency curves from remote sensing rainfall estimates: comparing satellite and weather radar over the eastern Mediterranean, *Hydrol. Earth Syst. Sci*., 21, 2389-2404, https://doi.org/10.5194/hess-21-2389-2017.

Nisi, L. , Martius, O. , Hering, A. , Kunz, M. and Germann, U. (2016), Spatial and temporal distribution of hailstorms in the Alpine region: a long-term, high resolution, radar-based analysis. *Q.J.R. Meteorol. Soc*., 142: 1590-1604. doi:10.1002/qj.2771

Overeem A., I Holleman, A. Buishand, 2009: Derivation of a 10-Year Radar-Based Climatology of Rainfall. *J Appl. Met. Cli* https://doi.org/10.1175/2009JAMC1954.1

Annex 1: Proposed Standard Definitions for Weather Radar Data Levels

The table below is proposed by WMO IPET-OWR as the standard wording to describe 'levels' of weather radar data.

Level	Description
0	Data at full resolution as received at the sampling rate of the receiver. Generally only available internal to the system. Special equipment may be required to measure and record such data.
1	Data in sensor units also known as "time series" or "I/Q" (in-phase and quadrature) data. Produced and processed by the instrument's signal processor. Generally not recorded except for limited durations on operational radars. Commonly recorded on research radars.
2	Derived radar variables or moments (reflectivity, radial velocity, differential reflectivity, etc.) at full resolution after aggregation and filtering. Organised in polar coordinates by rays, range bins and quantities. Also, known as "sweep" and "volume scan" data.
3	Radar products which are derived primarily from level 2 data. May be in the level 2 polar coordinates (particle ID, quality metrics, etc.), or in other coordinates systems such as vertical profiles or Cartesian grids (CAPPI, rain rate estimates, etc.).
4	Higher order products which may include data from multiple measurements. This includes products which composite multiple radars (mosaics) as well as those that blend data from other sources (satellites, rain gauges, NWP etc.).

5 Annex 2. Draft for Mandatory Weather Radar Metadata for International Exchange by IPET-OWR

This table lists weather radar related metadata which are considered mandatory for the international exchange of weather radar data. The metadata are listed according to their definition in the WMO Information Model for Radial Radar and Lidar Data. An additional column 'CfRadial' identifies the corresponding dimension, variable or attribute name which implements the metadata within the CfRadial 2.0 file format. Note that this is still work in progress.

IMID	Description	CfRadial
	Volume metadata	
1.0	Instrument type, distinguishing between "radar" and "lidar"	instrument_type
1.1	Site identifier, WIGOS identifier (see below)	instrument_name
1.2	Volume start time	time_coverage_start
1.3	Volume end time	time_coverage_end
2.0	Site longitude	longitude
2.1	Site latitude	latitude
2.2	Site altitude above geodetic datum. For a scanning instrument this is the center of rotation of the antenna.	altitude
2.3	Geodetic datum name	
3.2	Antenna beam width H	radar_beam_width_h
3.3	Antenna beam width V	radar_beam_width_v
3.5	Frequency	frequency
	Sweep metadata	
5.1	Target fixed angle	fixed_angle
5.4	PRT mode	prt_mode
5.5	Distance to centre of first range bin	meters_to_center_of_first_gate
	Ray metadata	
8.0	Elevation angle	elevation

8.1	Azimuth angle	azimuth
8.2	Time of acquisition (relative to volume start time)	time
8.8	Pulse repetition time(s)	prt
8.9	Nyquist velocity	nyquist_velocity
	Range bin metadata	
11.0	Length of range bin	meters_between_gates
	Dataset metadata	
12.0	Dataset identifier (user specified)	variable name
12.1	Quantity name	standard_name
12.2	Quantity units	units
12.3	Quantity value used to indicate missing data	_FillValue
12.4	Quantity value used to indicate no signal	_Undetect
13.0	Identifiers of datasets which are qualified by this dataset	qualified_variables

The site shall be identified (IMID 1.1) by its WIGOS identifier, the structure of which consists of four parts[1]. The part of the structure called "Local identifier" is the only part consisting of characters. Following the ODIM NOD identifier convention (Michelson et al., 2014)[2], it is suggested as a best practice that the local identifier be harmonized to a five-character string, where the first two characters are the member country's ISO 3166-1 alpha 2 ccTLD[3] code (lower case), and the latter three characters are freely-selectable (also lower case).

[1] http://wis.wmo.int/page=WIGOS-Identifiers

[2] Michelson D.B., Lewandowski R., Szewczykowski M., Beekhuis H., and Haase G., 2014: EUMETNET OPERA weather radar information model for implementation with the HDF5 file format. Version 2.2. EUMETNET OPERA Output O4. 38 pp.

[3] http://www.iso.org/iso/country_codes

OPERA – past, present and future

Elena Saltikoff[1], Günther Haase[2], Hidde Leijnse[3], Petr Novák[4], Laurent Delobbe[5]

[1]FMI, Finland , [2]SMHI, Sweden, [3]KNMI, The Netherlands, [4]CHMI, Czech Republic, [5]RMI, Belgium

(Dated: 21 June 2018)

1 Introduction

The EUMETNET Radar project OPERA (Operational Program on the Exchange of Weather Radar Information) is approaching its 20th birthday. Its most visible achievement is the Pan-European composite (fig.1), but there is much more.

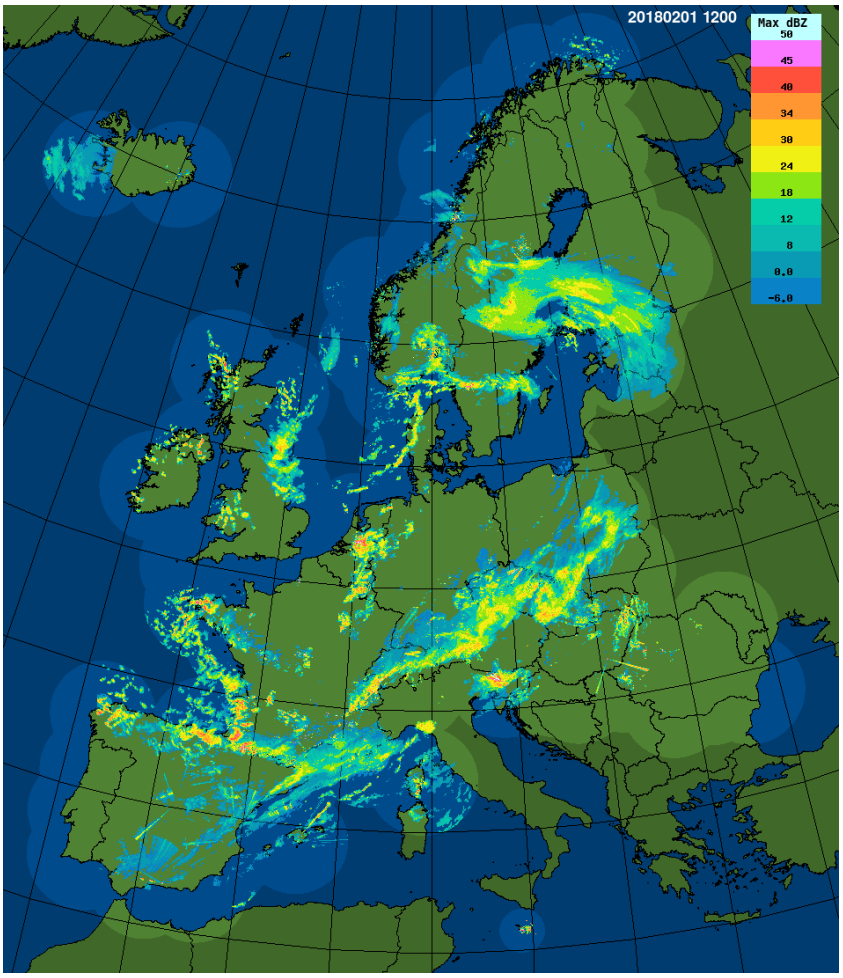


Figure 1. OPERA Maximum reflectivity composite 1 February 2018 12 UTC

2 History is history

Weather radar experts in Europe started organized co-operation in COST activities 72 (Measurement of precipitation by radar, 1979-1985) and 73 (Weather radar networking, 1985-1991). After this, operationally-oriented GORN group (Liaison Group of Radar Networking, 1992-1998) was established, which, in 1999, led to establishment of OPERA (Operational Program on the Exchange of Weather Radar Information) under the umbrella of EUMETNET (the Network of European Meteorological Services). The task given to this program was "To harmonize and improve the operational exchange of weather radar information between National Meteorological Services" (Holleman et al., 2008).

At that time, several regional exchange groups existed. Actually, bilateral exchange of data between neighbouring countries was developed in late 1980s (e.g. UK and Ireland, France and Switzerland), using "existing national codes (what we now call data formats) developed for a particular radar installation, and dedicated communication links". The COST 72 data exchange pilot project used four different formats. COST 73 proposed modifications to WMO BUFR-94 wishing that in the future the same standard format could be used everywhere (Collier, 1990).

GORN and OPERA continued the development of the data format and the software supporting it. In 2008, the OPERA Data Information Model (ODIM) was developed "…with which the encoding, decoding and management of data and products from weather radar systems may be facilitated, primarily for the purpose of international exchange in Europe" (Michelson et al., 2008, 2011 and 2014). Implementations of this information model were specified in BUFR and in HDF-5. This data model has become the standard for radar data exchange in Europe and beyond. It is vital for running the OPERA Data Center and it has also accelerated bilateral exchange of radar (volume) data between meteorological services. Most importantly, all major radar manufacturers provide conversion software between their data format and the ODIM formats.

In 2004 EUMETNET decided that OPERA should be more operational, and move from supporting bilateral exchange to running a data hub. The OPERA Pilot Data Hub received single-site Cartesian products and national composites from members and created a composite. Variability in the quality of input was surprisingly large, and the projection conversion led to loss of resolution. For creating a more homogenous product, a data centre was designed. It was called Opera Data Centre, ODC, which is pronounced same way as *Odyssée*, so it is now referred to as Odyssey. (Unlike some legends say, the name has nothing to do with a long journey.)

In order to get as homogenous products as possible, the idea from 2011 was to collect data as raw as possible, and then run all quality control centrally. Centralized clutter cancellation was running from late 2015, but the quality was still less than optimal, and more alarmingly, it was destroying some real precipitation. We've corrected this latter issue and learned from this that algorithms should be thoroughly tested before implementation. Meanwhile, several members upgraded their radars and could use locally very advanced signal processing techniques, which cannot to be repeated in ODC. Hence, in March 2017, a new agreement was made: to collect the best possible data, document how it was processed, and collect also the unfiltered data (TH) as a separate parameter. By May 2018, this decision has been implemented by 11 members.

Changes can be seen by studying the Pan-European composites, and especially by calculating long-term sums and averages. The area covered by the composite has been substantially increased by the progressive incorporation of new radars. The quality and the homogeneity of the composite have increased as well. During the first year, the homogenization was mainly due to improvements in incoming data, but from late 2015 the central processing has been removing more unwanted echoes than before through non-meteorological echo detection algorithms and the application of a satellite-based cloud mask. This increase in quality has been confirmed with quantitative studies. The negative bias in the northern areas is also obvious, and applications for VPR and different ZR for snow have been developed but not yet applied operationally.

3 Present status is an example to the rest of the world

In 2018, OPERA had 31 members. Its metadata database lists 225 radars, 152 of these (from 24 countries) are exchanging data regularly. Of the OPERA radars, 75 are from last century. The majority (178) are C-band radars, complemented by 18 S-band, 3 X-band radars. 122 radars are dual-polarization. Generally 30-40 people attend the Expert team meetings which are held two times a year. This makes OPERA by far the largest, most heterogeneous body of radar experts anywhere in the world.

To understand both the variability and common factors in this grouping, and to share experiences between members, OPERA has performed several surveys and studies. Results from a survey about maintenance show large differences in national maintenance policies, and reveals that the primary causes of missing data are not with the radar itself but are related to issues with the electricity supplies or telecommunications (Saltikoff et al., 2017). A survey about application priorities shows that the most important uses of radar data are aviation and severe weather warnings. Importance of other applications such as hydrological applications, NWP assimilation and verification, and information for general public has a large variability across Europe. These differences of priorities of national meteorological services are the main reason of the wide variability in measurement scan strategies and schedules observed over Europe.

The use of polarimetric radar variables in Europe was also subject of a survey. Currently the largest benefit of dual-polarization radars is in the quality improvement of other data (reflectivity and Doppler), especially in removal of unwanted signals such as radio interference and wind turbines. Only a limited number of OPERA members are testing dual-pol attenuation correction, and even less have started using this operationally.

For quality assessment, OPERA has benefited of co-operation with data users such as NWP, nowcasting for flood warning (Park et al.,2017) and the ENRAM community studying animal (e.g., birds, insects, etc.) movements (Bauer et al,2017), but also carried out its own studies.

Assessment of rain rate composites shows, that the homogeneity of composites increased significantly between 2012 and2015 due to national improvements both at the radars themselves and the data sent to ODC. The quality improvement tools (beam blocking and satellite-based removal of residual clutter) changed the amount of non-precipitating echoes from the end of 2015.

Assessment of accumulated precipitation (compared to a mesoscale analysis MESAN, Häggmark et al., 2000) shows that OPERA generally underestimates precipitation in winter, most prominently along the Norwegian coast. It confirms that the

monthly clutter fraction (pixels with precipitation intensities greater than 0.0 mm/h) decreased at the end of 2015, which coincides with the implementation of the new clutter filters.

Proof of a cake is in its eating, and the real value of OPERA's efforts comes from use of the exchanged radar data. The composites are visualized to operational forecasters in many participating institutes, and on some of their websites. The data is assimilated in limited-area NWP models and used for verification. Several international organizations, such as EUMETSAT and ECMWF have licenses for their duties, and a few external users have acquired a license which is available via ECOMET. These users are represented in the OPERA User Group, of which the chair attends each Expert Team meeting and provides feedback to OPERA.

4 Future is bright

In the next EUMETNET program phase, 2019-2023, OPERA is focusing even harder on the needs of users outside the radar community. We have identified several different user types, and split the production lines accordingly. There are work packages for harmonization of metadata and for quality management, assessment of new technologies, and plans for real-time exchange of data and status reports. What will certainly continue is the exchange of knowledge, information and experiences between European radar experts, which has been the heart of OPERA for 20 years.

Acknowledgement

The authors would most of all want to thank all the past and present members of OPERA expert team who have participated in lively, sometimes even fierce, discussion and thus exchanged expertise and contributed to the so-called grey knowledge.

Secondly, there have been several enthusiastic users, whose questions and feedback have helped us to improve the products and their documentation.

Most of the activities have been funded by EIG EUMETNET and its members, the European weather services.

References

C Bauer, S, J.W.Chapman, D.R:Reynolds, J.A.Alves, A.M.Dokter, M.M.H Menz, N Shapir, M ciach, L.B.Pettersson, J.F.Kelly, H. Leijnse, J. Shamoun-Barades, 2017: From Agricultural Benefits to Aviation Safety: Realizing the Potential of Continent-Wide Radar Networks BioScience, 67, 10, 912–918, https://doi.org/10.1093/biosci/bix074

Collier, C. G., 1990: COST-73: The development of a weather radar network in Western Europe. In: Collier & Chapuis (ed.) Weather Radar Networking. Seminar on COST 73 project. ISBN 0-7923-0672-4

Häggmark L, K-I Ivarsson, S Gollvik and P-O Olofsson (2016) Mesan, an operational mesoscale analysis system, Tellus A: Dynamic Meteorology and Oceanography, 52:1, 2-20, DOI: 10.3402/tellusa.v52i1.12250

Holleman, I., L. Delobbe and A. Zgonc, 2008: Update on the Weather Radar Network (OPERA).WMO TECO. Available online at https://www.wmo.int/pages/prog/www/IMOP/publications/IOM-96_TECO-2008/1(11)_Holleman_The_Netherlands.pdf

Huuskonen A., E.Saltikoff, and I.Holleman, 2014: The operational weather radar network in Europe. *Bull. Amer. Meteor. Soc.* , 95, 897–907, https://doi.org/10.1175/BAMS-D-12-00216.1.

Michelson, D., R. Lewandowski, M. Szewczykowski, H. Beekhuis, and G.Haase, 2009, 2011 and 2014: EUMETNET OPERA weather radar information model for implementation with the HDF5 file format. OPERA Deliverable OPERA_2008_03, 36 pp. Version 2.2 available online at http://eumetnet.eu/wp-content/uploads/2017/01/OPERA_hdf_description_2014.pdf

Park, S, M. M. Berenguer and D. Sempere-Torres, 2017: Use of OPERA Data for Real-Time Pan-European Flash-Flood Hazard Assessment and Nowcasting. AMS Radar conference 2017. Available online at https://ams.confex.com/ams/38RADAR/webprogram/Paper321114.html

Saltikoff E., M. Kurri, H. Leijnse, S. Barbosa and K. Stiansen, 2017: Maintenance keeps radars running. *Bull.Am.Met.Soc.* https://doi.org/10.1175/BAMS-D-16-0095.1

Ice microphysical retrievals using polarimetric radar data

A. Ryzhkov, P. Bukovcic, A. Murphy, P. Zhang, and G. McFarquhar

Cooperative Institute for Mesoscale Meteorological Studies, University of Oklahoma, 120 David L Boren Blvd., Norman, OK 73072

1. Introduction

Accurate estimation of bulk microphysical characteristics of ice and snow such as ice water content (IWC), mean volume diameter (D_m), and total concentration (N_t) is a challenging task due to extreme variability of ice/snow habits, size distributions, densities, shapes, and orientations. The radar reflectivity *Z* was the primary radar measurement for estimating ice water content *IWC* for decades. There have been a number of studies suggesting various *IWC*(*Z*) relations in ice / snow clouds (e.g., Sassen 1987; Atlas et al. 1995; Liu and Illingworth 2000; Hogan et al. 2006; Delanoe et al. 2014; Heymsfield et al. 2005, 2016; Protat et al. 2016). The inherent uncertainty in the *IWC*(*Z*) estimate is caused by the variability of the size distribution (SD) of ice / snow particles and (to lesser extent) by the variations of density. The IWC(Z) relations are parameterized by either D_m or N_t (e.g., Hogan et al. 2006; Bukovcic et al. 2018) which have to be estimated independently.

Any generic IWC(Z) relation tends to severely underestimate high ice water content (HIWC) of very small ice crystals in high concentrations commonly encountered by commercial aviation in tropical cyclones, thunderstorm anvils, and stratiform parts of mesoscale convective systems. These encounters pose a serious risk for commercial airplanes due to possible engine power loss and damage. The values of IWC in the HIWC regions can be as high as 3 - 4 g m^{-3} with typical median volume diameters of ice particles less than 0.5 mm (Fridlind et al. 2015; Strapp et al. 2016; Leroy et al. 2017). Because the corresponding Z is much lower than the aviation safety threshold of 20 dBZ, commuter planes do not expect high amount of ice there.

Existing cloud models experience serious problems with adequate representation of ice microphysical processes partially due to the lack of reliable information about IWC, D_m, and N_t from atmospheric remote sensors and multiparameter dual-polarization measurements offer a unique opportunity to fill the gap in the existing knowledge.

2. Polarimetric method for ice retrieval

Simple expressions for *Z* and *IWC* can be obtained assuming the exponential size distribution

$$N(D) = N_{0s} \exp(-\Lambda_s D) \qquad (1)$$

and a power-law dependence of the snow density ρ_s on the equivolume diameter *D*

$$\rho_s(D) = \alpha D^{-\beta} \qquad (2)$$

where the exponent β is close to 1 (Brown and Francis 1995; Heymsfield et al. 2004; Matrosov 2007; Brandes et al. 2007; Erfani and Mitchell 2016; Tiira et al. 2016) and the multiplier α is much more variable and proportional to the degree of riming. Following derivations by Hogan et al. (2006) and Bukovcic et al. (2018), one can obtain analytical expressions for the *IWC*(*Z*) parameterized either by the intercept N_{0s} of the size distributions

$$IWC = 3.81\,10^{-4}\,\alpha^{-0.2} N_{0s}^{0.4} Z^{0.6}, \qquad (3)$$

or by the mean volume diameter $D_m = 4/\Lambda_s$ of ice particles

$$IWC = 3.09\,10^{-3}\,\frac{Z}{\alpha D_m^2} \qquad (4)$$

In (1) – (4), *IWC* is in g m^{-3}, D_m is in mm, N_{0s} is in $m^{-3}mm^{-1}$, and *Z* is in mm^6m^{-3}.

It follows from (3) and (4) that the multipliers in the power-law *IWC*(*Z*) relations are almost entirely dependent on N_{0s} or the product αD_m^2. Therefore, the knowledge of D_m (or N_{0s}) is essential. We suggest using the measurements of specific differential phase K_{DP} to estimate D_m from the ratio of Z and K_{DP}. This is based on the fundamental fact that the radar reflectivity factor *Z* is proportional to the 4th moment of snow size distribution and the specific differential phase K_{DP} is proportional to the 1st moment if snow density is inversely proportional to the diameter of snow particle. Therefore, their ratio is approximately proportional to the cube of D_m.

Indeed, the expressions for *Z* and K_{DP} in the Rayleigh approximation are (Bukovcic et al. 2018)

$$Z = \frac{|K_i|^2}{|K_w|^2}\frac{1}{\rho_i^2}\int \rho_s^2(D)D^6 N(D)dD \qquad (5)$$

and

$$K_{DP} = \frac{0.27\pi}{\lambda\rho_i^2}\left(\frac{\varepsilon_i - 1}{\varepsilon_i + 2}\right)^2 \int F_{shape}F_{orient}\rho_s^2(D)D^3 N(D)dD\,. \qquad (6)$$

In (5) – (6), $K_i = (\varepsilon_i - 1)/(\varepsilon_i + 2)$, $K_w = (\varepsilon_w - 1)/(\varepsilon_w + 2)$, ε_i and ε_w are the dielectric constants of solid ice and water, and ρ_i = 0.917 g cm^{-3} is the density of solid ice, λ is the radar wavelength, F_{shape} is the "shape factor" determined by the aspect ratio of the particle, and F_{orient} is the "orientation factor" depending on the width of the canting angle distribution σ (Ryzhkov 2001):

$$F_{orient} = \frac{1}{2}\exp(-2\sigma^2)[1 + \exp(-2\sigma^2)] \qquad (7) \quad ,$$

The dependence of F_{shape} on the aspect ratio of oblate spheroids is illustrated in Fig. 1. The dependence of F_{orient} on σ is shown in Fig. 2.

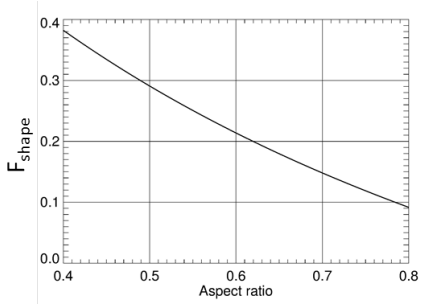


Fig. 1. Shape factor F_{shape} as a function of the aspect ratio of oblate spheroid.

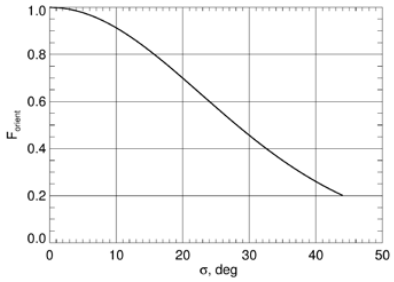


Fig. 2. Orientation factor F_{orient} as a function of σ.

Eqs (5) and (6) can be simplified using (1) and (2) and assuming that β = 1 and the shape and orientation of the particles do not change across the size spectrum

$$Z = 5.30\,10^{-3}\alpha^2 N_{0s} D_m^5 \qquad (8)$$

$$K_{DP} = 1.02\,10^{-2} F_{shape}F_{orient}\frac{\alpha^2 N_{0s}}{\lambda}D_m^2 \quad . \qquad (9)$$

Therefore,

$$\frac{Z}{K_{DP}\lambda} = 0.520\frac{D_m^3}{F_{shape}F_{orient}} \qquad (10)$$

and the mean volume diameter D_m can be estimated from a cubic root of the ratio Z/K_{DP} (or $Z/(K_{DP}\lambda)$ if the shapes and orientations of ice particles are roughly known:

$$D_{\rm m} = 1.24\,[F_{shape}F_{orient}]^{1/3}\left(\frac{Z}{K_{\rm DP}\lambda}\right)^{1/3} \qquad (11)$$

where $D_{\rm m}$ and λ are expressed in mm, Z is in $\rm mm^6m^{-3}$, and $K_{\rm DP}$ is in deg $\rm km^{-1}$. The dependence of the mean volume diameter $D_{\rm m}$ on the parameter $\xi = [Z/(K_{\rm DP}\lambda]^{1/3}$ for irregular shape / aggregated snow for different aspect ratios a/b and two widths of the canting angle distributions is shown in Fig. 3.

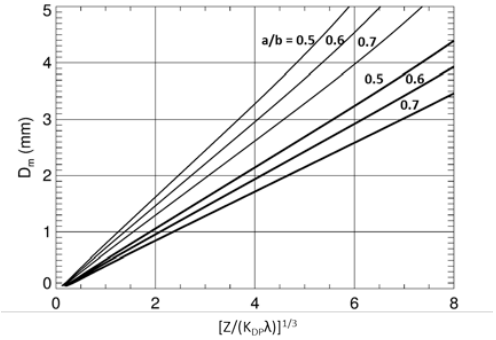


Fig. 3. Dependence of the mean volume diameter $D_{\rm m}$ of ice particles on the parameter $\xi = [Z/(K_{\rm DP}\lambda]^{1/3}$ for irregular shape / aggregated snow for different aspect ratios a/b and two widths of the canting angle distributions: σ = 10° (thin curves) and σ = 40° (thick curves). Exponential size distribution of snowflakes is assumed.

For the gamma size distribution the $D_{\rm m}(\xi)$ estimate is somewhat sensitive to the size distribution shape factor μ in the range between -1 and 1 (Fig. 4). This range contains the majority of μ estimates from in situ observations (Brandes et al. 2007; Delanoe et al. 2014; Tiira et al. 2016; Matrosov and Heymsfield 2017).

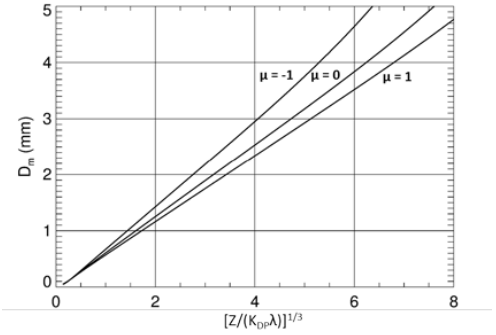


Fig. 4. Dependence of the mean volume diameter $D_{\rm m}$ of ice particles on the parameter $\xi = [Z/(K_{\rm DP}\lambda]^{1/3}$ for irregular shape / aggregated snow and different values of the shape parameter μ of the gamma size distribution. The assumed aspect ratio a/b = 0.6 and the width of the canting angle distribution σ = 25°.

The advantage of the $D_{\rm m}$ estimator based on the $Z/K_{\rm DP}$ ratio is its low sensitivity to the size distribution variability and changes of snow density and degree of riming (the latter because both Z and $K_{\rm DP}$ are proportional to α^2). However, this estimator does not account for the diversity of ice particle shapes and orientations both of which strongly affect $K_{\rm DP}$. Therefore, the estimator is better suited to work for irregular shape and aggregated snow (for which the aspect ratio does not vary much around the value of 0.6) assuming that the width σ of the canting angle distribution of ice is roughly known. Following Ryzhkov et al. (2017), the width σ can be estimated using linear depolarization ratio $\rm L_{dr}$, $\rm Z_{DR}$, and $\rho_{\rm hv}$

$$\sigma = \frac{180}{\pi}\frac{L_{dr}^{1/2}}{(1+Z_{dr}^{-1}-2\rho_{hv}Z_{dr}^{-1/2})^{1/2}} \qquad (12)$$

where σ is in deg and $\rm L_{dr}$ and $\rm Z_{dr}$ are expressed in linear units.

Our retrievals of σ from radar observational data indicate that σ can vary between 10 and 40º in snow. Therefore, it is instrumental to develop an estimator of D_m that is immune to the variations of particle shapes and orientations. Such estimator can be built using the ratio Z_{DP}/K_{DP} where $Z_{DP} = Z_h - Z_v$ is the reflectivity difference. The ratio Z_{DP}/K_{DP} is very robust with respect to the variability of the particles' aspect ratios and orientations because these two factors affect similarly Z_{DP} and K_{DP} and, therefore, it remains almost intact (Ryzhkov et al. 1998). It can be shown that Z_{DP} is roughly proportional to 3rd moment of the size distribution of ice / snow. Therefore, the ratio Z_{DP}/K_{DP} is expected to be linearly dependent on D_m^2.

To further substantiate this idea, we present simulated D_m and

$$\eta = \left(\frac{Z_{DP}}{K_{DP}\lambda} \right)^{1/2} \qquad (13)$$

for 12 snow habits consisting of irregular / aggregated snow (with the aspect ratio 0.6) and 11 types of pristine ice crystals listed in Table 1. All particles are modeled as oblate or prolate spheroids with aspect ratios dependence on size approximated by the power-law relation

$$h = cL^d, \qquad (14)$$

where h is the smaller and L is the larger dimension of a crystal, both expressed in mm.

Table 1. Parameters c and d in Eq (14) for different types of crystals (Matrosov et al. 1996)

Crystal habit	c	d
1. Dendrites	0.038	0.377
2. Solid thick plate	0.230	0.778
3. Hexagonal plates	0.047	0.474
4. Solid columns ($L/h < 2$)	0.637	0.958
5. Solid columns ($L/h > 2$)	0.308	0.927
6. Hollow columns ($L/h < 2$)	0.541	0.892
7. Hollow columns ($L/h > 2$)	0.309	0.930
8. Long solid columns	0.128	0.437
9. Solid bullets ($L < 0.3$ mm)	0.250	0.786
10. Hollow bullets ($L > 0.3$ mm)	0.185	0.532
11. Elementary needles	0.073	0.611

The hydrometeors with oblate shapes (irregular / aggregates, dendrites, solid thick plates, and hexagonal plates) are assumed to have a Gaussian distribution of orientation of their rotation axis with zero mean canting angle and the width σ ranging from 10° to 40°. The particles with prolate shape (columns, bullets, needles) are supposed to have random orientation in the horizontal plane.

The results of simulations are presented in Fig. 5 as D_m vs η dependencies. It is remarkable that the curves for the 12 ice habits corresponding to exponential SD and $\alpha = 0.2$ are practically indistinguishable. The average dependence of D_m on η characterizing the 12 curves can be approximated by $D_m = -0.1 + 2.0\eta$. (15)

As opposed to the estimate of $D_m(\xi)$ from (11), the $D_m(\eta)$ estimate is affected by the degree of riming. Hence, it has better chance to work at lower temperatures with lower likelihood of riming.

Once D_m is determined, the ice water content IWC can be estimated from the combination of Z and D_m using (4). In fact, it is

$$\gamma = \alpha D_m^2 \qquad (16)$$

that is needed to compute IWC from (4) rather than D_m It can be shown that the product γ is highly correlated with η^2 :

$$\gamma \approx 0.78\eta^2 = 0.78 \frac{Z_{DP}}{K_{DP}\lambda} \qquad (17)$$

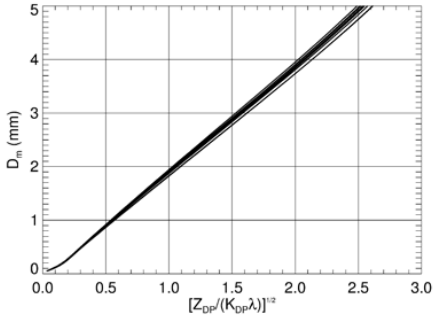


Fig. 5. Dependence of the mean volume diameter D_m of ice particles on $[Z_{DP}/(K_{DP}\lambda)]^{1/2}$ for 12 various ice habits for exponential size distribution and $\alpha = 0.2$.

and the dependence of γ on η is almost insensitive to the ice habit, aspect ratio, orientation, and density (or degree of riming) of the ice particles for an exponential size distribution. Combining (17) with (4) yields

$$IWC \approx 4.010^{-2} \frac{K_{DP}\lambda}{1 - Z_{dr}^{-1}} \qquad (18)$$

which is very close to the relation derived by Ryzhkov et al. (1998).

Total concentration of ice particles N_t can be estimated from the combination of Z and γ. Indeed, for exponential size distribution, $N_t = N_{0s}D_m/4$ and (8) can be modified to

$$Z = 2.12\,10^{-2}\gamma^2 N_t, \qquad (19)$$

where N_t has the units of m^{-3}. Therefore, $\log(N_t)$ can be estimated from

$$\log(N_t) = 0.1Z(\mathrm{dBZ}) - 2\log(\gamma) - 1.33. \qquad (20).$$

In (20), N_t is expressed in (1/L) to facilitate comparisons of the retrieved N_t with in situ probe observations which commonly use the units (1/L) for N_t.

3. Measurement errors

The accurate and reliable measurements of K_{DP} are critical for implementing the polarimetric techniques for the estimation of the mean volume diameter D_m. Big advantage of K_{DP} is that it is not biased by noise, attenuation, and radar miscalibration. On the other hand, the magnitude of K_{DP} in ice and snow is relatively small, particularly at longer radar wavelengths. At S band, K_{DP} in dry ice and snow is usually smaller than 0.3 deg km^{-1} and typical values are below 0.05 deg km^{-1} in aggregated snow at warmer temperatures (Ryzhkov and Zrnic 1998; Griffin et al. 2018). Because the mean volume diameter D_m is inversely proportional to the cubic root of K_{DP}, the fractional standard deviation of the D_m estimate is proportional to the ratio 1/3 SD(K_{DP})/K_{DP}.. The value of the standard deviation of the K_{DP} estimate SD(K_{DP}) is equal to 0.11 deg km^{-1} for typical parameters of the WSR-88D processing at low reflectivity (< 40 dBZ) signals and radial resolution of 6 km. Therefore the fractional standard deviation of the D_m estimate is about 70% if K_{DP} = 0.05 deg km^{-1} and can be much higher if K_{DP} is lower Additional azimuthal averaging helps to reduce the statistical error of the D_m estimate. The quasi-vertical profiles (QVP) methodology (Ryzhkov et al. 2016) prescribes azimuthal averaging of K_{DP} over a full 360° circle and this decreases the SD(K_{DP}) by the factor $(360)^{1/2} \approx 19$ so D_m can be estimated with the accuracy better than 4% (for K_{DP} = 0.05 deg km^{-1}). The corresponding accuracy is about 20% if K_{DP} = 0.01 deg km^{-1}. Averaging in a limited azimuthal sector may be needed if a substantial horizontal nonuniformity of the radar echo occurs within a full circle of the QVP averaging.

Calibration biases of Z and Z_{DR} may affect the $D_m(\xi)$ and $D_m(\eta)$ estimates. Because D_m is proportional to the cubic root of Z in ξ, the impact of the calibration bias of Z is not very significant. The 1 dB and 2 dB biases of Z would cause 8% and 16% fractional bias of D_m. The adverse effect of miscalibrated Z_{DR} on the quality of the $D_m(\eta)$ estimate depends on the actual value of Z_{DR}. It rapidly increases for lower Z_{DR}. It can be shown that a Z_{DR} bias of 0.2 dB would produce a 5.5% fractional bias in D_m if Z_{DR} = 1.0 dB and the bias exceeds 25% if Z_{DR} < 0.2 dB. Therefore, the estimator $D_m(\eta)$ is expected to be much better in areas of high Z_{DR} (like the dendritic growth layer).

Given the enhanced sensitivity of the $D_m(\eta)$ estimator to the degree of riming and Z_{DR} biases (at small Z_{DR}) the method is expected to be more accurate at relatively low temperatures (say, lower than -10 to -15°C) in stratiform clouds where

significant riming is less likely and in areas of higher Z_{DR} (exceeding 0.2 dB). The $D_m(\xi)$ estimator might be the preferred choice at higher temperatures (> -10°C) in mixed-phase clouds where riming can be significant.

4. Validation of the algorithm

The algorithm for snow size distribution retrieval described in a previous section may require further refinement and is a subject of extensive testing and validation. Herein, we provide initial validation results using snow disdrometer measurements at the surface and in situ measurements onboard of research airplane.

The disdrometer measurements of snow during 16 winter events in Oklahoma (Bukovcic et al. 2018) have been used to test the procedure for estimating the mean volume diameter of snowflakes D_m from the ratio Z/K_{DP}. A scatterplot of D_m measured by the disdrometer versus the retrieved value is in Fig. 6. Note the values of Z and K_{DP} in this example are calculated from the disdrometer data assuming fixed aspect ratio a/b and the width of the canting angle distribution σ and using the multiplier in (11) matched with the selected a/b and σ. Therefore, the difference between the actual and retrieved values of D_m is attributed to the variability of snow density and size distributions which are not considered in the theoretical simulations and the disdrometer measurement errors. The agreement between actual and retrieved D_m (Fig. 6) is quite good although the retrieved values are slightly higher.

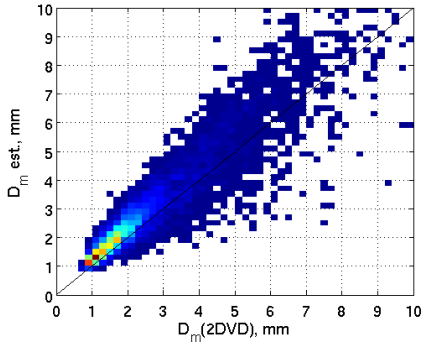


Fig. 6. Scatterplot of the mean volume diameter D_m estimated from the ratio Z/K_{DP} vs measurement with the 2D-video disdrometer. Data are from 16 snow events in Oklahoma.

Because K_{DP} in snow is low and noisy, aggressive spatial averaging is required to ensure suitable quality of the K_{DP} estimates. The QVP methodology implies azimuthal averaging of radar data at high elevation over a whole 360° circle. The QVP product is radar-centric and has relatively coarse horizontal resolution degrading with altitude because the azimuthal averaging is performed on a conical surface (Ryzhkov et al. 2016). For direct comparison of the ground-based radar and aircraft data, the Columnar Vertical Profiles (CVP) methodology for processing and displaying the radar data might be more appropriate (Murphy et al. 2018). As opposed to QVP, the CVP technique prescribes azimuthal averaging in a limited azimuthal sector using all available tilts of radar data instead of one. As a result, vertical profiles of polarimetric radar variables are generated in a column with much smaller horizontal dimension. This column can follow the aircraft track to facilitate direct comparison of the radar and in situ aircraft data.

An example of the CVP product generated from the KVNX WSR-88D radar data for the case of mesoscale convective system observed during the Midlatitude Continental Convective Clouds Experiment (MC3E) on 20 May 2011 is shown in Fig. 7 (panels (a) – (d)). Horizontal size of the vertical column is 20 km x 20° (shown at the top of the plot). The aircraft altitude at any given time is depicted by a black line in the plot. It is important to contrast the CVP product with a 4D-grid WSR-88D product suggested by Homeyer (2014) and Homeyer and Kumjian (2015) in a column following aircraft for the same storm (panel (e), Tian et al. 2016). The latter has horizontal and vertical resolution of 2 km and 1 km respectively. It is obvious that the CVP product has better vertical resolution (at the expense of degraded horizontal resolution) compared to the 4D-grid product.

The retrieved D_m, N_t, and IWC from polarimetric data in ice regions outside of the time intervals when aircraft flew within the melting layer and below are presented in Fig. 8. The best agreement of the retrieved microphysical parameters (dots) and in situ measurements (solid curves) is achieved for the mean volume diameter and ice water content in the dendritic growth layer at the temperature between -10 and -20°C (top panel in Fig. 8). The initial validation results are promising and call for a more comprehensive and systematic studies.

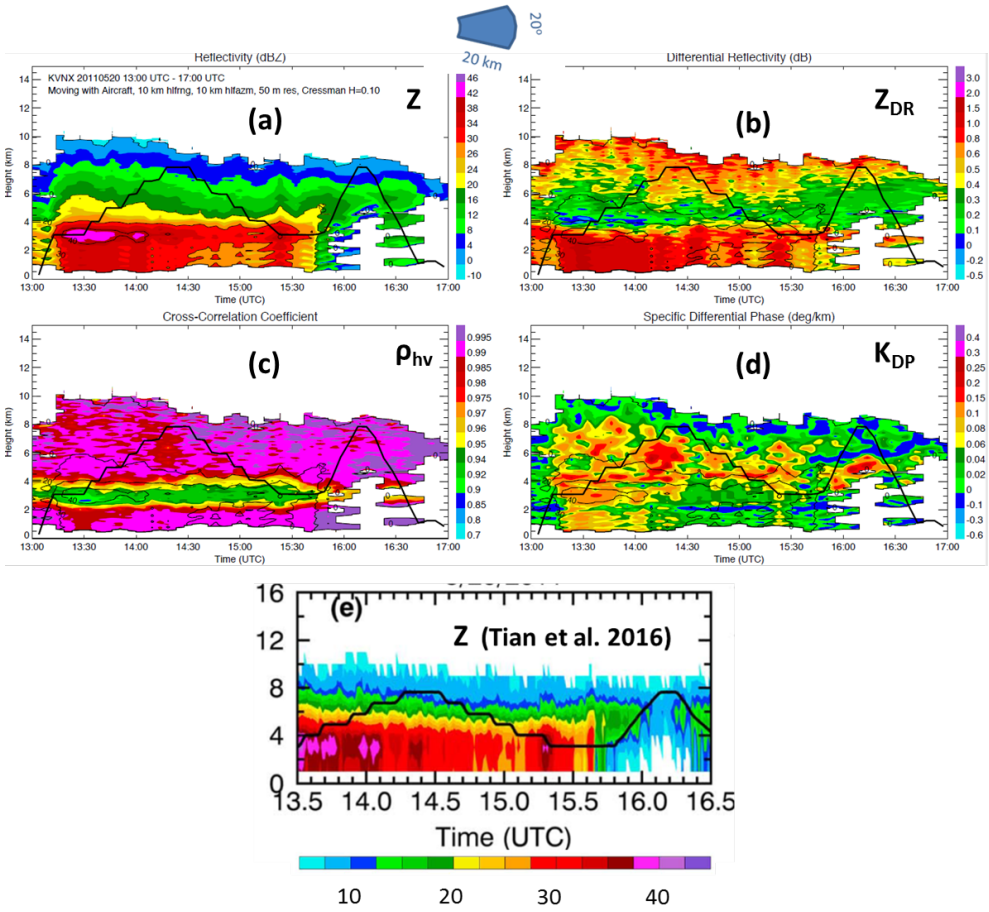


Fig. 7. Vertical profiles of polarimetric variables in a vertical column following the aircraft represented in a height vs time format for the MCS on 20 May 2011. Panels (a) – (d): Z, Z_{DR}, ρ_{hv}, and K_{DP} estimated from the WSR-88D data using the CVP methodology. Panel (e): 4D-grid Z product from WSR-88D (Tian et al. 2016). Aircraft height vs time is depicted with black line.

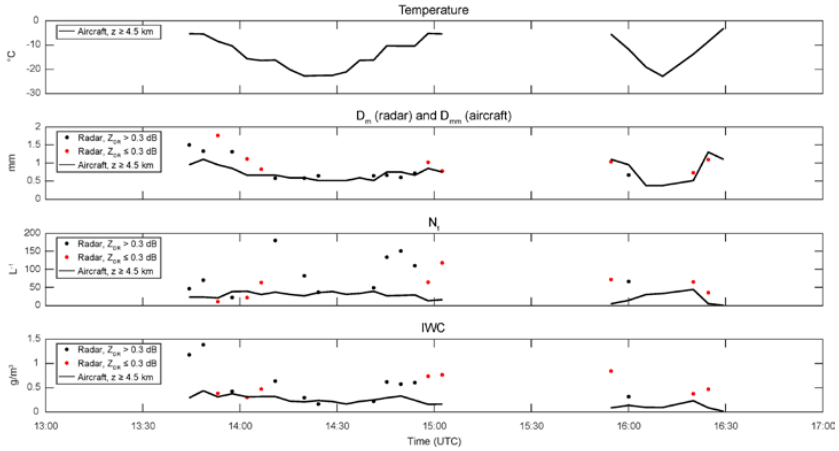


Fig. 8. Comparison of D_m, N_t, and *IWC* retrieved from the radar measurements (dots) and in situ aircraft probes (solid lines) for the MCS on May 2011.

5. Retrievals in a tropical cyclone

Polarimetric ice retrievals made in tropical cyclones and hurricanes reveal common microphysical features characterized by very high concentrations of small ice particles aloft. As an example, a composite QVP of Z, Z_{DR}, ρ_{hv}, and K_{DP} retrieved from the KMHX WSR- 88D data collected during the hurricane Irene on 27 August 2011 is presented in Fig. 9. A striking

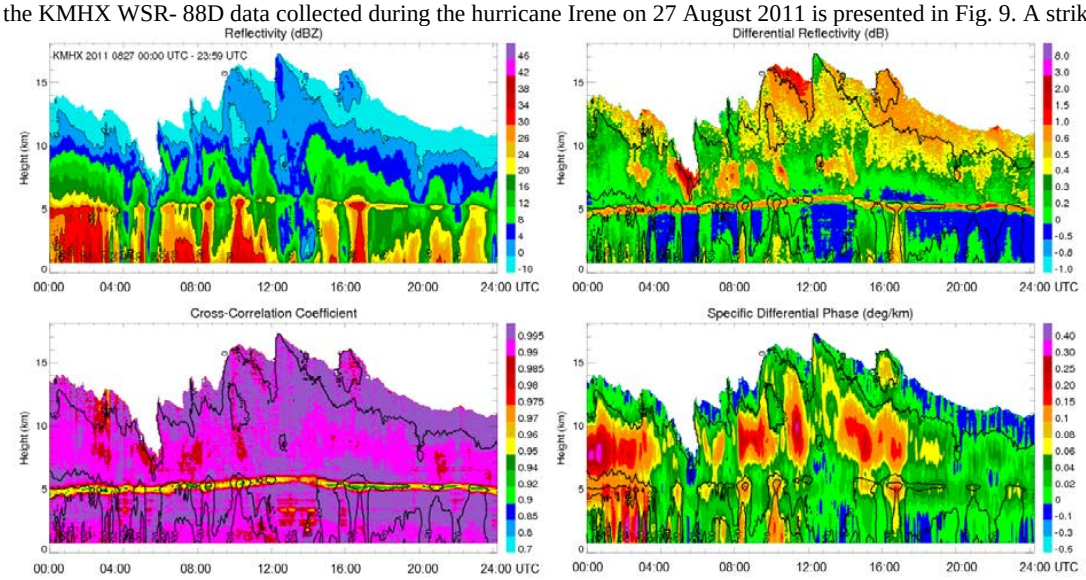


Fig. 9. Composite QVP of Z, Z_{DR}, ρ_{hv}, and K_{DP} retrieved from the KMHX WSR-88D data collected during the hurricane Irene on 27 August 2011. Overlaid are contours of Z = 10, 20, and 30 dBZ.

feature of this storm is the evidence of extended regions of enhanced K_{DP} associated with very low Z above the freezing level. Reflectivity is below 20 dBZ above the melting layer while the maximal K_{DP} is above 0.3 deg km^{-1}. This is a strong indication of high concentrations of very small ice in a whole depth of the cold part of the storm. Another evidence of the dominance of small hydrometeors is a uniformly high ρ_{hv} above and below the melting layer typical for tropical storms. The top of the storm is highest at the time when the eye wall of the hurricane passed in the proximity of the radar between 12 and 15 UTC. This time period is also marked by the ascension of the melting layer clearly visible in the Z_{DR} and ρ_{hv} panels.

The corresponding plot illustrating the time evolution of D_m, log(N_t), and log(IWC) in the vertical cross section of the storm (Fig. 10) shows the mean volume diameter of ice does not exceed 0.1 – 0.2 mm in the large vertically extended areas of the storm where the total ice concentration is higher than 1000 1/L. The resulting IWC in these areas is significant and may be as high as 5 g m^{-3}. These retrieval results are consistent with the documented evidence of high ice water content at the periphery of tropical cyclones which may dramatically impact the performance of airplane engines and therefore pose significant aviation hazard (Fridlind et al. 2015; Strapp et al. 2016; Leroy et al. 2017; Stanford et al. 2017).

Ice water content computed from the $IWC(Z)$ relation (18) is almost an order of magnitude lower than the one obtained from the polarimetric retrieval algorithm using Z, K_{DP}, and Z_{DP}. This is seen in the vertical profiles of Z, IWC(Z), and IWC(K_{DP}, Z_{DP}), (Fig. 11). The reflectivity is generally below 15 dBZ above the freezing level in this storm due to very small dominant size of ice.

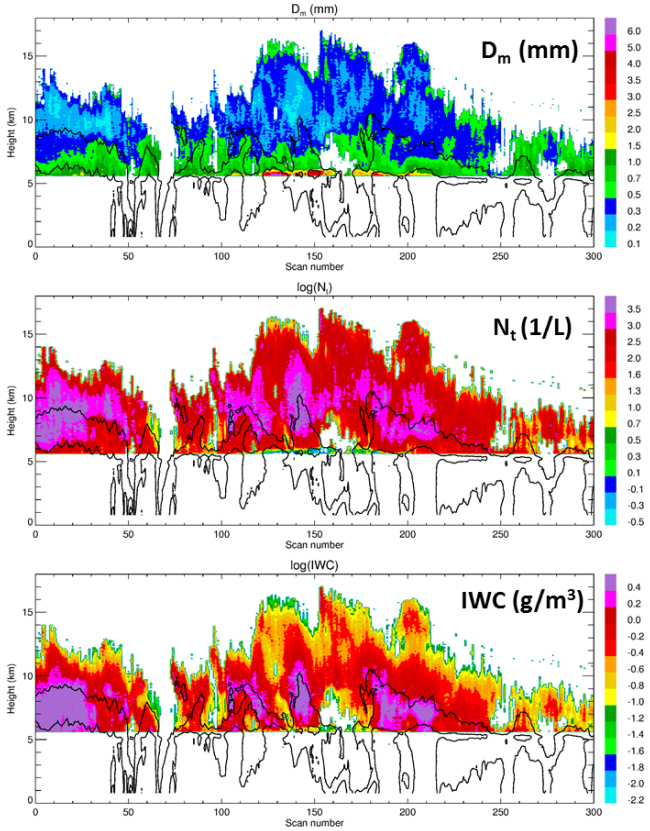


Fig.10. Vertical cross-sections of the mean volume diameter D_m, total number concentration N_t, and ice water content *IWC* above the freezing level retrieved from the QVP displayed in Fig. 11.11 for the hurricane Irene on 27 August 2011. The N_t and *IWC* contours are in logarithmic steps. Overlaid are contours of Z = 10, 20, and 30 dBZ.

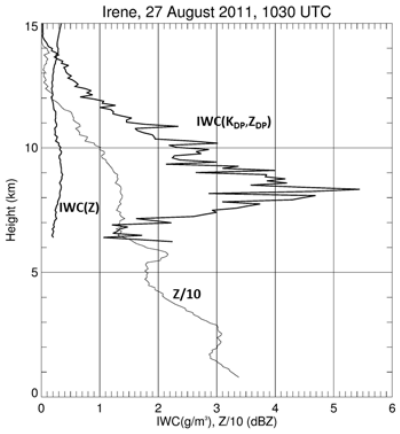


Fig. 11. Vertical profiles of Z/10 and *IWC* retrieved from the *IWC*(Z) and *IWC*(K_{DP},Z_{DP}) relations applied to data from the hurricane Irene observed by the KMHX WSR-88D on 27 August 2011 at 1030 UTC.

References

Atlas, D., S. Matrosov, A. Heymsfield, M. Chou, D. Wolf, 1995: Radar and radiation properties of ice clouds. *J. Appl. Meteor*., **34**, 2329 – 2345.

Brandes, E., K. Ikeda, G. Zhang, M. Schoenhuber, and R. Rasmussen, 2007: A statistical and physical description of hydrometeor distributions in Colorado snowstorms using a video-disdrometer. *J. Appl. Meteor*., **46**, 634 – 650.

Brown, P. R. A., and P. N. Francis, 1995: Improved measurements of ice water content in cirrus using a total-water probe. *J. Atmos. Oceanic Technol.*, **12**, 410–414.

Bukovcic, P., A. Ryzhkov, D. Zrnic, and G. Zhang, 2018: Polarimetric radar relations for quantification of snow based on the disdrometer data. *Journal of Applied Meteorology and Climatology*, **57**, 103 – 120.

Delanoe, J., A. Heymsfield, A. Protat, A. Bansemer, and R. Hogan, 2014: Normalized particle distribution for remote sensing application. *J. Geophys. Res. Atmos*., **119**, 4204 – 4227.

Erfani, E., and D. Mitchell, 2017: Growth of ice particle mass and projected area during riming. *Atmos. Chem. Phys*., **17**, 1241 – 1257.

Fridlind, A., A. Ackerman, A. Grandin, F. Dezitter, M. Weber, J. Strapp, A. Korolev, and C. Williams, 2015: High ice water content at low radar reflectivity near deep convection – Part 1: Consistency of in situ and remote-sensing observations with stratiform rain column simulations. *Atmos. Chem. Phys*., **15**, 11713 – 11728.

Griffin, E., T. Schuur, and A. Ryzhkov, 2018: A polarimetric analysis of ice microphysical processes in snow, using quasi-vertical profiles. *J. Appl. Meteor. Climatol*., **57**, 31 – 50.

Heymsfield, A., A. Bansemer, C. Schmitt, C. Twohy, and M. Poellot, 2004: Effective ice particle densities derived from aircraft data. *J. Atmos. Sci*., **61,** 982 – 1003.

Heymsfield, A., Z. Wang, and S. Matrosov, 2005: Improved radar ice water content retrieval algorithms using coincident microphysical and radar measurements. *J. Appl. Meteor*., **44**, 1391 – 1412.

Heymsfield, A., S. Matrosov, and N. Wood, 2016: Toward improving ice water content and snow-rate retrievals from radars. Part I: X and W bands, emphasizing *CloudSat. J. Appl. Meteor. Climatol.*, **55**, 2063 – 2090.

Hogan, R., M. Mittermaier, and A. Illingworth, 2006: The retrievals of ice water content from radar reflectivity factor and temperature and its use in evaluating a mesoscale model. *J. Appl. Meteor. Clim.*, **45**, 301 – 317.

Homeyer, C., 2014: Formation of the enhanced-V infrared cloud top feature from high-resolution three-dimensional radar observations. *J. Atmos. Sci*., **71**, 332 – 348.

Homeyer, C., and M. Kumjian, 2015: Microphysical characteristics of overshooting convection from polarimetric radar observations. *J. Atmos. Sci*., **72**, 870 – 891.

Leroy, D., E. Fontane, A. Schwarzenboeck, J. Strapp, A. Korolev, G. McFarquhar, R. Dupuy, C. Courbeyre, L. Lilie, A. Protat, J. Delanoe, F. Dezitter, and A. Grandin, 2017: Ice crystal sizes in high ice water content clouds. Part II: Statistics of mass diameter percentiles in tropical convection observed during the HAIC/HIWC project. *J. Atmos. Oceanic Technol.*, **34**, 117 – 136.

Liu, C., and A. Illingworth, 2000: Toward more accurate retrievals of ice water content from radar measurements of clouds. *J. Appl. Meteor*., **39**, 1130 – 1146.

Matrosov, S., R. Reinking, R. Kropfli, and B. Bartram, 1996: Estimation of ice hydrometeor types and shapes from radar polarization measurements. *J. Atmos. Oceanic Technol.*, **13**, 85 – 96.

Matrosov, S., 2007: Modeling backscatter properties of snowfall at millimeter wavelengths. *J. Atmos. Sci*., **64**, 1727 – 1736.

Matrosov, S., and A. Heymsfield, 2017: Empirical relations between size parameters of ice hydrometeor populations and radar reflectivity. *J. Appl. Meteorol. Clim*., **56**, 2479 – 2488.

Protat, A., and Coauthors, 2016: The measured relationship between ice water content and cloud radar reflectivity in tropical convective clouds. *J. Appl. Meteor. Climatol*., **55**, 1707 – 1729.

Ryzhkov, A.V., 2001: Interpretation of polarimetric radar covariance matrix for meteorological scatterers. Theoretical analysis. *Journal of Atmospheric and Oceanic Technology,* **18,** 315 - 328.

Ryzhkov, A., and D. Zrnic, 1998: Discrimination between rain and snow with a polarimetric radar. *J. Appl. Meteor*., **37**, 1228 – 1240.

Ryzhkov, A., D. Zrnic and B. Gordon, 1998: Polarimetric method for ice water content determination. *Journal of Applied Meteorology*, **37**, 125-134.

Ryzhkov, A., S. Matrosov, V. Melnikov, D. Zrnic, P. Zhang, Q. Cao, M. Knight, C Simmer, and S. Troemel, 2017: Estimation of depolarization ratio using radars with simultaneous transmission / reception. *J. Appl. Meteorol. Clim.*, **56**, 1797 – 1816.

Sassen, K., 1987: Ice cloud content from radar reflectivity. *J. Climate Appl. Meteor*., **26**, 1050 – 1053.

Ryzhkov, A., S. Matrosov, V. Melnikov, D. Zrnic, P. Zhang, Q. Cao, M. Knight, C Simmer, and S. Troemel, 2017: Estimation of depolarization ratio using radars with simultaneous transmission / reception. *J. Appl. Meteorol. Clim.*, **56**, 1797 – 1816.

Stanford, M., A. Warble, E. Zipser, J. Strapp, D. Leroy, A. Schwarzenboeck, R. Potts, and A. Protat, 2017: A ubiquitous ice size bias in simulations of tropical deep convection. *Atmos. Chem. Phys.,* **17,** 9599 – 9621.

Strapp, J. W., and Coauthors, 2016: The High Ice Water Content (HIWC) study of deep convective clouds: Report on science and technical plan. FAA Rep. DOT/FAA/TC-14/31, 105 pp. [Available online at www.tc.faa.gov/its/worldpac/techrpt/tc14-31.pdf.]

Tian, J., X. Dong, B. Xi, J. Wang, C. Homeyer, G. McFarquhar, and J. Fan, 2016: Retrievals of ice cloud microphysical properties of deep convective systems using radar measurements. *J. Geophys. Res. Atmos.*, **121**, 10820 – 10839.

Tiira, J., D. Moisseev, A. Lerber, D. Ori, A. Tokay, L. Bliven, and W. Petersen, 2016: Ensemble mean density and its connection to other microphysical properties of falling snow as observed in Southern Finland. *Atmos. Meas. Tech*., **9**, 4825 – 4841.

A Hydrometeor Classification Algorithm for the UK C-Band Weather Radar Network

Steven Best[1] and Dawn Harrison[1]

[1]*Observations R&D, Met Office, Fitzroy Road, Exeter, EX1 3PB, UK*

(Dated: 22 June 2018)

1. Introduction

The UK Met Office completed the upgrade of its C-band weather radar network to dual-polarisation capability in early 2018. Ongoing improvements to the in-house processing software, Radarnet IV, have recently included new algorithms designed to extract the benefit from the supply of polarimetric data. The latest of these developments is a hydrometeor classification algorithm (HCA), which is currently designed to distinguish between seven different classes of hydrometeor: rain, drizzle, wet snow, dry snow, hail, graupel, and ice crystals.

The HCA is based on a fuzzy logic approach, which combines the likelihood of a given hydrometeor type based on both the polarimetric variable signatures and the atmospheric temperature profile (though a classification may also be made using either of these data sources individually). The likelihoods associated with the polarimetric data are calculated using bivariate membership functions – many of which are modified versions of those used in the operational Météo France HCA (Al-Sakka *et al*., 2013). The temperature-derived likelihoods are based on NWP model wet-bulb freezing level information – where a melting layer region is defined in 3D space, and the cross-sectional radar beam power profile is integrated for each measurement to determine the fractional power returned from the regions above, below, and within the melting layer. A novel approach is also introduced here by allowing the melting layer depth to be perturbed in order to account for deviations from the assumed 'average' depth. The polarimetric- and temperature-derived membership values are combined multiplicatively to calculate the final likelihood for each hydrometeor type, and a tier-based method is employed to ensure that the maximum number of classifications is made by using likelihood values based on reduced variable sets where the full variable set returns likelihoods of zero.

Two case studies are presented here – using both Plan Position Indicator (PPI) and Range-Height Indicator (RHI) type datasets – which illustrate certain components of the classification procedure, and provide an insight into the skill of the classification, based on subjective qualitative analysis. Possible improvements, verification methods, as well as future requirements of the algorithm are also discussed prior to its scheduled operational release later in 2018.

2. Algorithm Description

The principle of a hydrometeor classification algorithm (HCA) is to combine multiple types of radar measurement – each providing different information relating to each hydrometeor type – in order to produce an estimate of the most likely type in a given radar sampling volume. Several examples of operational HCAs have been reported in the literature in the past couple of decades (see, for example, Chandrasekar *et al*., 2013 for a useful summary); many of which employ the fuzzy-logic approach – owing to the relative simplicity, ease of implementation, and flexibility of the method. The scheme developed here is also based on a fuzzy logic approach, and borrows concepts and components from other algorithms, whilst providing new features which improve its performance in the context of the UK radar network.

The polarimetric variables provided by the UK network are: the standard reflectivity measurement in the horizontal polarisation (Z_H), the differential reflectivity (Z_{DR}); the cross-correlation coefficient (ρ_{HV}); the specific differential phase (K_{DP} – via the propagation differential phase, ϕ_{DP}); and the linear depolarisation ratio (LDR). Of these, all except LDR are used in the algorithm; LDR is not used as it requires a different measurement mode (i.e. a separate scan) to the other parameters, meaning that the datasets are not concurrent with the other measurements, and are therefore not directly comparable. Note also that currently K_{DP} is only calculated in regions corresponding to high correlation coefficient (> 0.97), and so it plays a relatively small part in the classification procedure.

2.1 Polarimetric membership functions

At the core of a fuzzy logic algorithm are the functions which relate the input (i.e. the radar measurement) to a degree of likeliness of association with a given output (i.e. a particular hydrometeor class). Initially, the membership functions used in the UK Met Office (UKMO) scheme were borrowed from the operational HCA employed by Météo France – for details of this algorithm, see the report by Al-Sakka *et al*. (2013). These membership functions are bivariate, or two-dimensional, and define the variation of the given 'secondary' parameter (i.e. Z_{DR}, ρ_{HV}, or K_{DP}) with respect to the reflectivity, Z_H. The

advantage of employing 2D membership functions is that when two measurements are not independent from each other, then this dependence can be captured, and any points in the two-dimensional space which do not follow this dependence can be fixed to return a likelihood of zero; thus reducing the chances of false classification. An example of such a function, illustrating the expected association between Z_H and Z_{DR}, is shown in Figure 1.

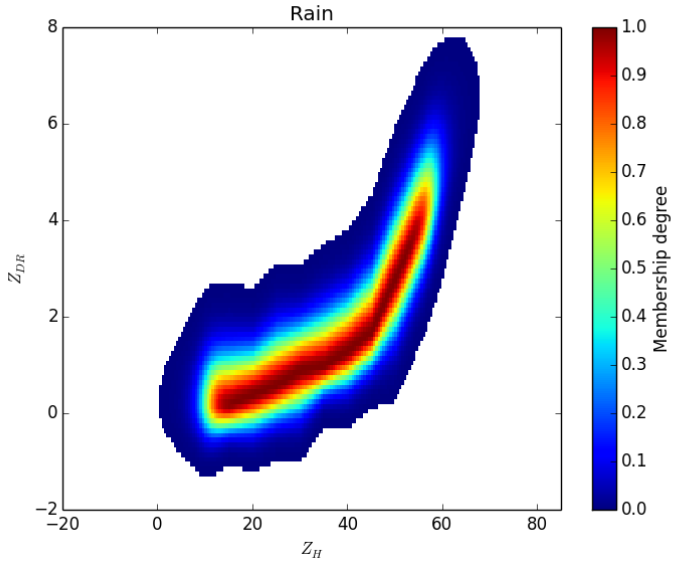


Figure 1. Membership function showing the degree of association of each point in the (Z_H, Z_{DR}) space with the rain class.

This membership function was initially borrowed from the Al-Sakka *et al.* (2013) scheme, though it has since been modified by applying a beta function weighing to the to the *x*- (Z_H -) axis in order to smoothen the transitions to zero membership at the boundaries (the original membership function employed a trapezoidal *x*-axis weighting). The Al-Sakka scheme membership functions were generated using real datasets – that is, measurements corresponding to (what was presumed to be) each hydrometeor type were collected, and the membership functions were then constructed around these measurements in order to best capture their variation. The advantage of this approach, over, say, the use of scattering simulation results, is that the real-life measurements – rather than the output from a simplified model – are used as the reference; and therefore the 'imperfect' data are not forced to conform with idealized predictions. The membership functions of the Al-Sakka scheme were all initially trialled with the UK radar network data, and modifications were eventually made, as described above, in order to better capture the behaviour of the measurements provided by the UK radar network. Outlines of all of the modified membership functions can be seen later in Figure 7. Note that, because the Al-Sakka algorithm does not include membership functions for either of the classes graupel and drizzle, these were generated *ad hoc* using reports in the literature – specifically, using a combination of 1D beta-functions from Dolan *et al*. (2013) for drizzle, and the 2D functions defined by Marzano *et al*. (2007) for graupel.

2.2 Use of temperature data

Although an HCA which is based entirely on radar data would be highly desirable, in practice it is very difficult to distinguish between some types of hydrometeor without the use of temperature information. A good example of this is in considering rain and dry snow, which can both occupy similar regions in the (Z_H, Z_{DR}) space, and which are generally also both associated with high correlation coefficient. Another example might be wet snow and graupel, which are types associated with different precipitation mechanisms, but which nevertheless produce similar polarimetric signatures. An example of a classification made using only polarimetric information can be seen later in Figure 6, in which the erroneous presence of dry snow below the melting layer – and graupel within it – can be noticed.

There are various potential methods of acquiring temperature information for an HCA scheme – these include radiosonde measurements, numerical weather prediction (NWP) forecast data, or estimation of the height of the 0 ºC isotherm using the polarimetric radar data itself. Of these, the most robust and reliable method is thought to be the use of NWP forecast data, due to the high spatial / temporal resolution available, the extent of coverage, and the generally good accuracy (a study by Mittermaier and Illingworth (2003), for example, showed the UKMO Unified Model to predict the height of the wet-bulb freezing level accurately to within 200 m, with an RMS error of 147 m). For these reasons, the selected source of temperature information for the HCA is a wet-bulb freezing level field derived from the UKMO UK-domain operational NWP model output. Specifically, these data provide the height (above ground level) of the wet-bulb 0 ºC isotherm – which allows the atmospheric wet-bulb temperature at any height above ground level to be calculated using a standard lapse rate of

-6.5 ºC/km. Note that although use of this lapse rate is an adequate approximation in most cases, the quality of the output of the HCA may be expected to improve with the provision of full 3D temperature data – a development which is likely to be considered in the future.

Many published fuzzy logic HCA schemes make use of temperature information in a similar way to the polarimetric information – that is, the inferred temperature at (the centre of) a given resolution volume is used to calculate the association with each class using pre-defined one-dimensional membership functions. These functions may be trapezoids, beta functions, or otherwise, which are fixed to represent approximately the transition from frozen to melting to liquid hydrometeors with increasing temperature. Although this approach is fairly simple to implement, it is not clear how the membership function shapes or parameters should be determined, nor how they may vary with increasing range from the radar (with which the beam cross-sectional area becomes larger, and therefore the chances of simultaneously sampling multiple hydrometeor types increases – see Figure 2). It is therefore suggested that an improvement to this aspect of the scheme would be to consider the problem in more geometric terms – i.e. define, in terms of height, a melting layer region directly beneath the 0 ºC isotherm, with a depth of ~500 m, and calculate the likelihood of a particular hydrometeor type dynamically, based on the integrated fractional beam power returned from its associated region (i.e. below, within, or above the melting layer). In this way, the *a priori* likelihoods of all hydrometeors in a given sampling volume are calculated; leaving the polarimetric signatures with the final input in determining the dominant type. This avoids making any assumptions as to the dominant hydrometeor type in a volume based only on the location of the beam axis relative to the 0 ºC isotherm (when in fact, the dominant power return from the sampling volume may originate from a different region of the beam cross-section). An example of the calculated 'probability' of wet snow during a winter stratiform event is shown later in Figure 5. Note here how the observed probability distribution is skewed towards the bottom of the melting layer, where the beam power is still relatively concentrated within the melting layer; whereas, further out, the fractional beam power within the melting layer is reduced due to the greater total beam width.

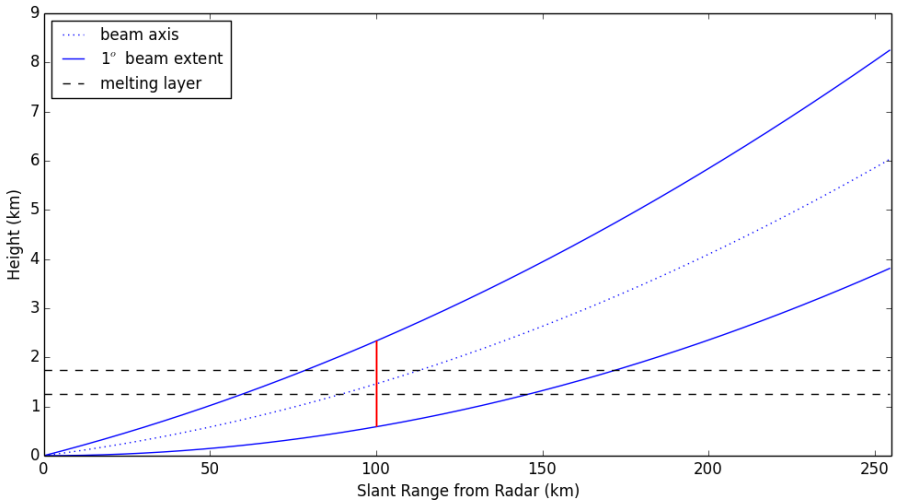


Figure 2. Example radar beam profile for a 0.5 degree elevation angle, with a melting layer superimposed between 1.25 and 1.75 km height. At 100 km range, the beam axis will be located within the melting layer region, though the outer extents of the beam may also be sampling liquid and/or frozen particles.

2.3 Combination and inference

The combination of the membership function (MF) outputs – including the temperature-based weightings – in a fuzzy logic scheme is something which can generally be chosen to suit purposes. Some HCA schemes described in the literature use the membership functions outputs additively (e.g. Zrnic *et al*., 2001); and some use a combination of multiplication and addition in order to give increased influence to certain parameters (e.g. Dolan *et al*., 2013; Al-Sakka *et al*., 2013). Furthermore, when outputs are added together, a 'confidence' or 'weighting' factor may be applied to some, or all variables, in order to control the influence they have on the classification. As such, the possibilities for constructing the combination formula are effectively limitless. For the UKMO algorithm, the decision was made to use all function outputs (including the temperature-derived values) multiplicatively, so as to assign them equal weighting and influence. This approach is thought to have a couple of distinct benefits: firstly, it avoids making assumptions about the efficacy of certain parameters relative to others, and thereby removes the need to apply arbitrary weightings within the formula – this effectively makes the formula as simple and as scientifically robust as possible. Secondly, it reduces the numbers of false classifications – as, if a given class has zero likelihood based on one of the membership function outputs, then that class will be suppressed no matter what the outputs

from the other membership functions are. The corresponding drawback here is that the total number of classifications made is reduced, which can result in large gaps in the resulting classification images. This issue has been addressed here by introducing secondary and tertiary classification stages, in which the probabilities of each class are re-calculated, but using one less input parameter, to increase the chances of an overall non-zero probability. As such, the probability (not a probability in the strict sense, but more of a 'likelihood') of a given class may be written as follows:

$$P(class) = F(Z_H, Z_{DR}) * F(Z_H, \rho_{HV}) * F(Z_H, K_{DP}) * F(T) \mid F(Z_H, Z_{DR}) * F(Z_H, \rho_{HV}) * F(T) \mid F(Z_H, \rho_{HV}) * F(T),$$

where F represents the membership function output for a given parameter (pair), and the '|' symbols separate the effective 'tiers' of calculation – with the first tier in the sequence to produce a non-zero output taking precedence over those following. In this way, the total number of classifications made can be improved, with the caveat that the second- and third-tier classifications will be less reliable than the primary. As a final classification stage, in order to fill in any remaining un-classified pixels, a nearest-neighbour interpolation is applied.

3. Results / case studies

The following examples are provided in order to demonstrate the methodology of the HCA, and to help assess the accuracy of the final classification. The examples are restricted to stratiform cases, which are more useful for illustrating how the use of temperature data affects the final classification.

3.1 Winter stratiform – PPI

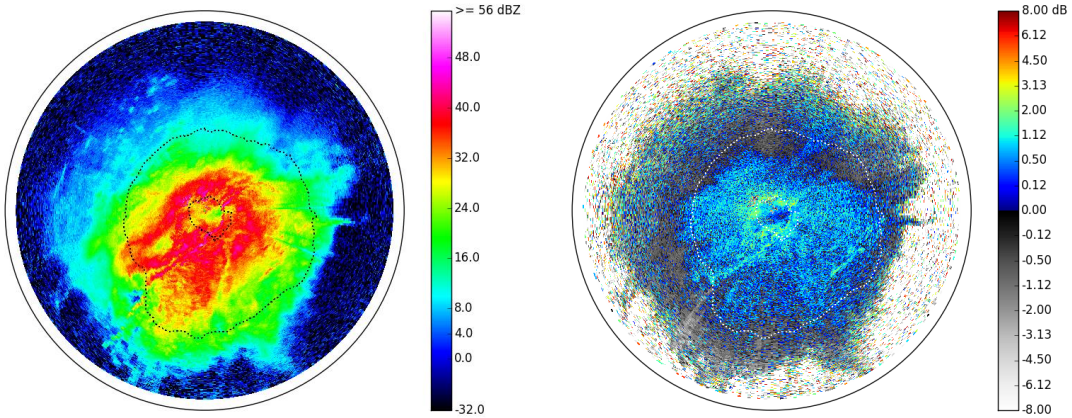


Figure 3. Reflectivity (left) and differential reflectivity (right) from a stratiform event over the south-west UK at 201701121139, captured by Predannack radar. The inner and outer dashed lines represent the points of intersection of the beam top with the melting layer bottom (assuming a 500 m melting layer depth); and the beam bottom with the melting layer top, respectively. The image corresponds to the lowest elevation (0.5°) scan.

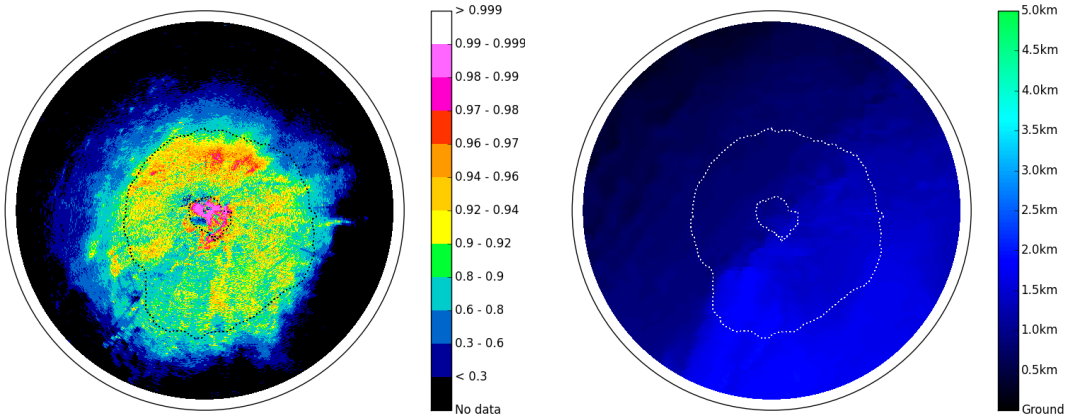


Figure 4. As for Figure 3, but now showing the correlation coefficient (left) and the NWP-derived wet-bulb freezing level height (right).

The first case study is an event which took place over the south-west of the UK in January 2017. The wet-bulb freezing level on this occasion was at around 1 km height in the vicinity of the radar, and the precipitation was fairly heavy, uniform, and widespread – providing useful conditions to test the classifier's output at the transitions between different regimes (i.e. liquid, melting, frozen).

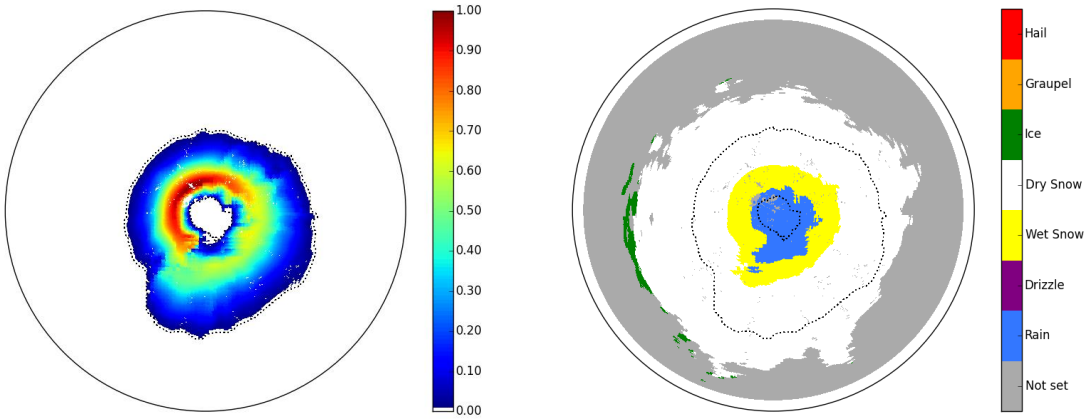


Figure 5. As in Figure 3, but now showing the 'probability' of wet snow calculated using NWP temperature data only (left), and the full classification based on temperature data only (right).

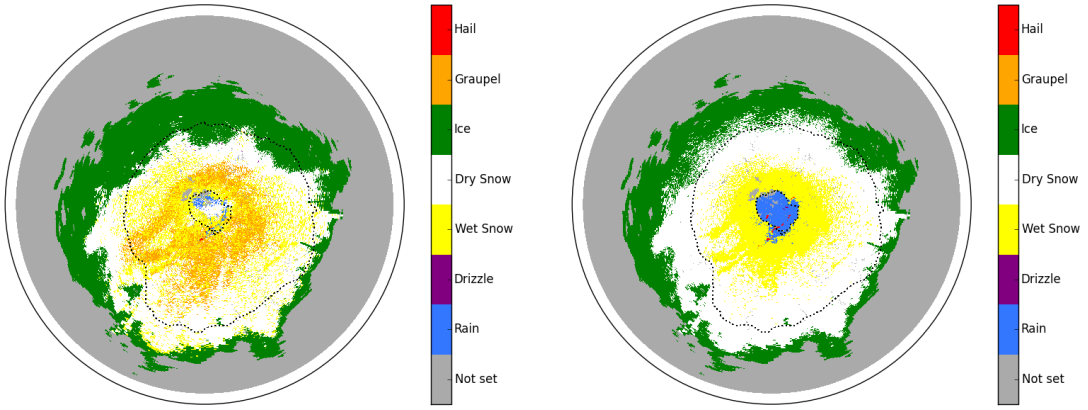


Figure 6. As in Figure 3, but now showing the classification based on polarimetric information only (left), and the classification using both polarimetric and temperature information (right).

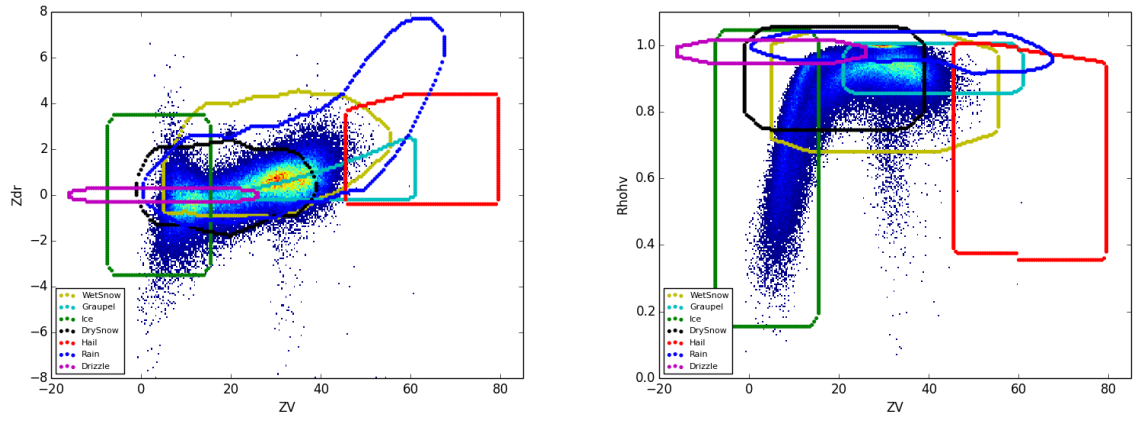


Figure 7. Scatterplots showing the distribution of (Z_H, Z_{DR}) (left) and (Z_H, ρ_{HV}) (right) measurement pairs associated with Figure 3 - Figure 6, with the polarimetric membership function outlines superimposed.

The raw polarimetric variables (with the exception of K_{DP}) and the NWP freezing level height field are shown in Figure 3 - Figure 4, whilst some of the derived probabilities / classifications, based on the input data, are show in Figure 5 - Figure 6. Figure 7 shows the distributions of the polarimetric measurements in relation to the membership functions used in the classification.

From Figure 3 - Figure 4, it can be seen that the gradient in freezing level – which increases towards the south-east – causes a 'widening' of the melting layer as seen by the radar (indicated by the sets of dashed lines). The melting layer is also clearly visible in the polarimetric data, though note that the expected extent of the melting layer region (as indicated by the dashed lines) and the pattern of the polarimetric variables do not completely match up due to a couple of reasons: firstly, the dashed lines take into account the beam width – so that just within the outer dashed line, part of the beam is still within the melting layer, but presumably the majority of the beam power originates from outside it, so that the measurement is more representative of the snow region. Secondly, the dashed lines correspond to the NWP model-defined wet-bulb freezing level, and by assuming a melting layer depth of 500 m – when in reality, the model may be subject to slight errors, and the melting layer depth may not conform to this value.

The left-hand panel of figure 5 illustrates how the 'probability' of wet snow – as calculated using the method described in Section 2.2 – varies with distance from the radar. Towards the north-west of the radar, where the freezing level is lower, the radar samples the melting layer in higher resolution, which produces a high, narrow peak in probability where the majority of the beam is within the melting layer. Conversely, towards the south-east, where the freezing level is higher, the beam width is larger than the melting layer depth by the time it encounters it, meaning the probability peak is shorter and wider. The full temperature-only classification – seen in the right-hand panel of Figure 5 – shows how rain is allowed to overlap into the melting layer region – in particular towards the south-east – because in these regions, the beam has only just entered the melting layer, and the majority of its power still originates from the rain region. The purpose of this temperature-only calculation is not to give a definitive classification, but to give fair representation to all types of hydrometeor which the beam may be sampling in a given region. As seen from the 'best' classification – shown in the right-hand panel of Figure 6 – once the polarimetric variables are added into the equation, the classification indicates the presence of wet snow right down to the point at which the beam enters the melting layer – meaning that in these regions, although the actual axis of the beam may lie below the melting layer, the strength of the signal from the wet snow in the outer beam regions makes it the dominant hydrometeor type.

The radar-only classification, shown in the left-hand panel of Figure 6, shows how the distribution of hydrometeor types is generally fairly well represented in the absence of temperature information. The obvious exceptions here are, as mentioned in Section 2.2, the appearance of dry snow below the melting layer, and graupel within it. Besides this, there is also a small region of wet snow which appears below the melting layer at close range to the south-west of the radar. It is likely that the reduced correlation coefficient in this region – which manifests due to side-lobe reflection from the sea – is the cause of this.

It is also worth giving a brief mention to the plots shown in Figure 7, which illustrate the distribution of the raw polarimetric measurements in relation to the membership functions used to classify them. Of particular note is the long 'tail' in the (Z_H, ρ_{HV}) measurements – where the correlation coefficient drops dramatically as the reflectivity values become smaller. As such low values of ρ_{HV} (< ~0.7) are not generally associated with hydrometeors of any type, these measurements must be subject to physical effects associated with the sampling conditions – in particular partial beam filling (and the associated drop in signal-to-noise ratio). As this effect typically comes into play at longer ranges (and greater heights) from the radar, which are often associated with ice conditions, the ice (Z_H, ρ_{HV}) membership function has been specially modified to allow these lower values of ρ_{HV} – note the elongated green rectangle in the right-hand panel of Figure 7. Although this suffices as a 'quick fix' to the problem of classifying measurements with reduced signal-to-noise ratio, investigation is needed into understanding the effects of signal degradation on the resulting measurements, which may then allow correction of the raw data to be carried out.

3.2 Autumn stratiform – RHI

Figure 8 shows the raw data from an RHI scan taken from Wardon Hill radar, in the south-west of England, during a stratiform event in October 2014. In this example, the melting layer is clearly visible in the form of a bright band at around 2 km in height, and extending from directly overhead the radar to roughly 30 km in range. What is also clear is that the melting layer varies in depth with increasing range from the radar. The dashed lines on the figures show the assumed melting layer profile, which is defined to extend 500 m below the NWP model wet-bulb freezing level height; and it is clear that the actual depth – particularly noticeable in the reflectivity image – fluctuates between roughly this figure and a significantly smaller value in some areas.

The resulting classification of this example is shown in Figure 9 – where the top panel illustrates the result when the fixed 500 m melting layer depth is assumed. In this case, the area of wet snow comprising the melting layer is seen to be tightly constrained within the pre-defined region, in a manner which is not entirely consistent with the polarimetric data.

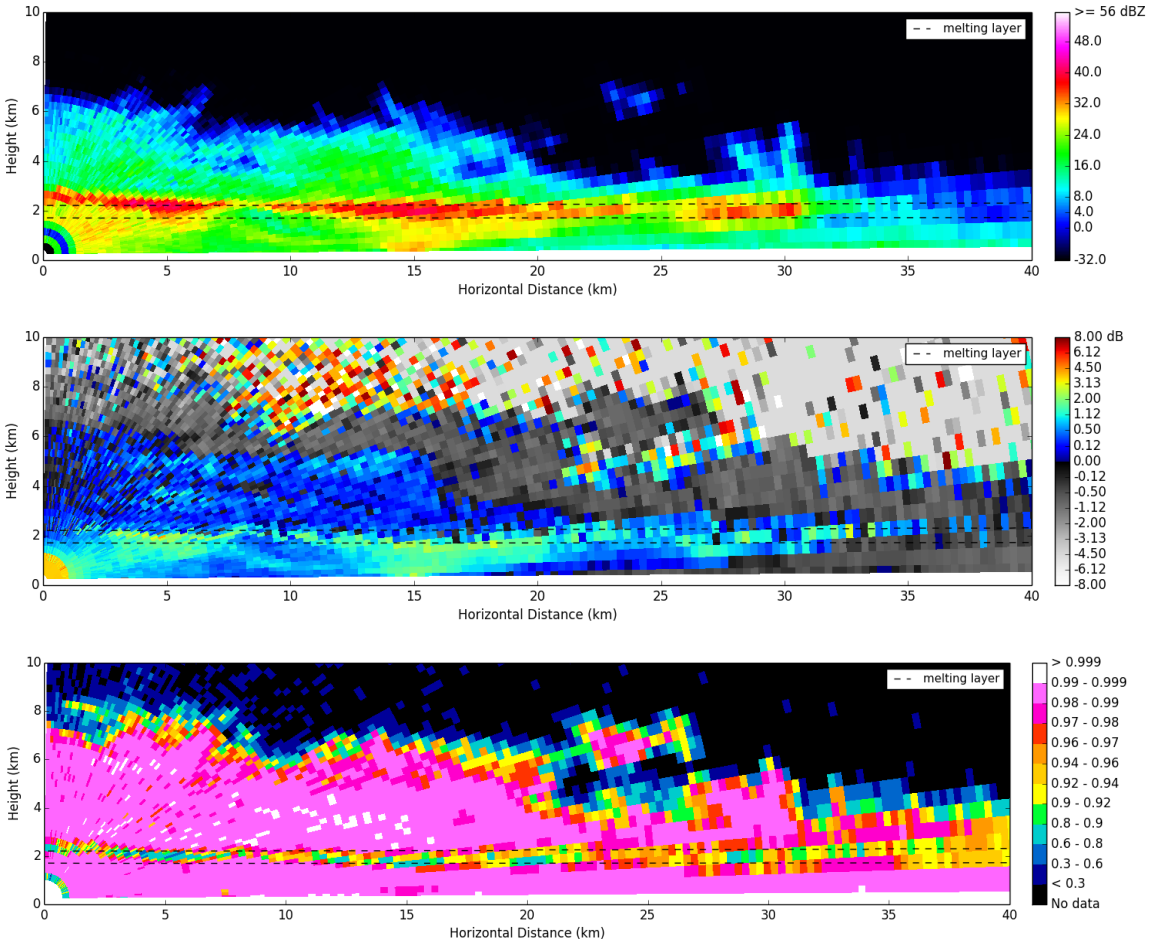


Figure 8. Reflectivity (top), differential reflectivity (middle) and correlation coefficient (bottom) from an RHI scan captured during an autumn stratiform event (201410131335) in the south of the UK. The dashed lines represent the assumed boundaries of the melting layer.

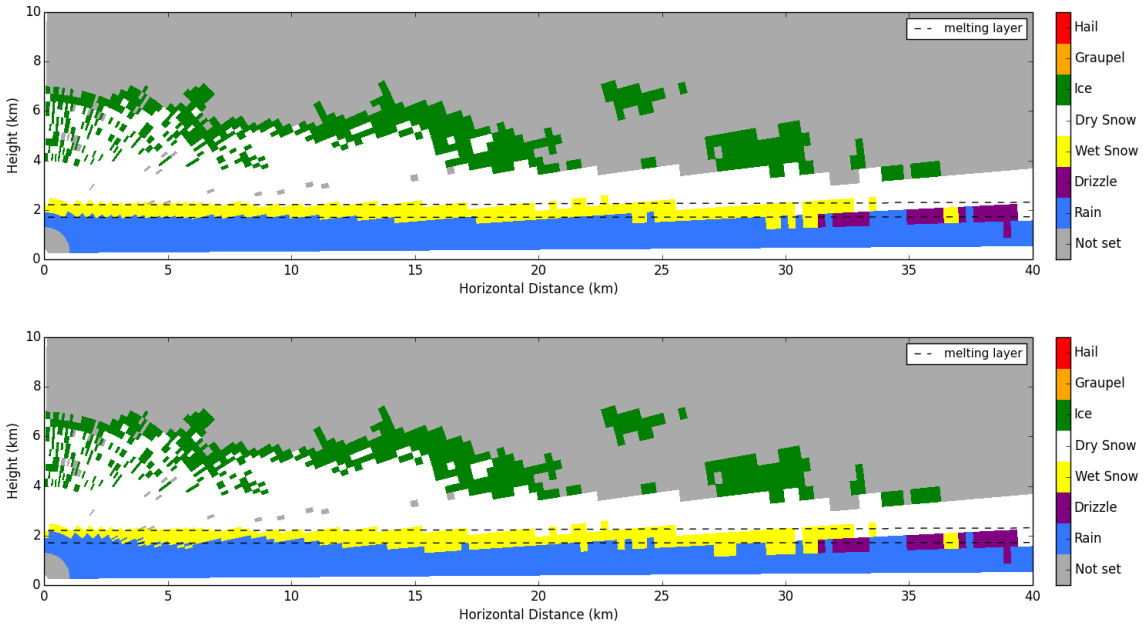


Figure 9. Classification corresponding to Figure 8 – using a fixed (500 m) melting layer depth (top); and allowing the melting layer to be perturbed by +/- 200 m (bottom).

This is particularly noticeable at close range, where the relatively small beam width results in minimal overlap into neighbouring regions. The lower panel of Figure 9 shows the result when, instead of fixing the melting layer depth at 500 m, it is perturbed by +/- 200 m. In this case, the temperature-derived likelihoods are re-calculated (as described in Section 2.2) for bright band depths of 300 m, 500 m, and 700 m, and the final likelihood for each grid point is chosen as the maximum of all of those calculated, so that each scenario is given fair representation. Looking at the result in the lower panel, it is noticeable that the wet snow classifications are no longer so tightly constrained within the pre-defined melting layer region, and that they more closely match the pattern seen in the polarimetric signatures – in particular, the twin 'bulges' in the melting layer – seen in the reflectivity image – are now also recognisable in the classification.

The depth of the melting layer does not appear to be something which has been given fair consideration in HCA studies reported in the literature, especially considering its obvious impact on a classification. Because it is something which varies dynamically, and which currently has no NWP-defined field associated with it (at least in the case of the UKMO model), it is suggested that this perturbation method represents a useful means of allowing for its departure from a pre-defined (or assumed) value in real-time. The key to this method lies in retaining the temperature-derived probability information generated for each perturbation – this way a range of scenarios are allowed, leaving the polarimetric data to determine the most accurate one.

4. Summary / future development

This report has described a new fuzzy logic hydrometeor classification algorithm (HCA) which has been implemented in a non-operational mode at the UK Met Office. The algorithm essentially combines the calculated likelihoods of different hydrometeor types based on the polarimetric signatures with those based on an NWP-derived environmental temperature profile. The polarimetric-derived likelihoods are calculated using 2D membership functions, some of which are modified versions of those employed in the operational Météo France algorithm (Al-Sakka *et al*., 2013). In calculating the temperature-based likelihoods, a rigorous approach is taken by determining the fractional beam power originating from different regions associated with a pre-defined melting layer – which allows for the possibility of simultaneously sampling more than one region, and hence more than one hydrometeor type. Additionally, the pre-defined melting layer region is perturbed in order to allow for departures from the assumed standard depth of 500 m. Based on visual analysis of case study examples – both those presented in this report, and a range of others considered – this treatment of the temperature data in particular appears to produce encouraging improvements, particularly in stratiform cases, when compared to more conventional approaches.

The HCA described here is scheduled to become operational later in 2018, though it is envisaged that further work will be carried out to improve and refine it in the intervening period. The planned future developments can be loosely summarised as follows:

- Because the temperature data used in the HCA are currently in the form of a 2D field (the height of the wet-bulb freezing level in the radar domain), the atmospheric temperature below and above this height must essentially be 'guessed' based on the use of a standard atmospheric lapse rate, which may not be accurate, and in some cases – for example that of an atmospheric temperature inversion – may be the opposite of the true profile. Accurate 3D NWP temperature data would therefore probably offer a slight improvement in classification skill in many cases; and in some cases it would conceivably offer a significant one.
- The HCA currently classifies radar scan data as it is provided, and hence the classification results are obviously only valid at altitude. Because the weather at the surface is sometimes of greater importance than that aloft, it is useful to extrapolate – using a source of (ideally 3D) temperature data – the HCA results to the surface, in order to extract maximum benefit from them. Currently the UKMO generates an operational surface precipitation type product which is based on a combination of (2D) freezing level information and the UK surface rain rate product. It is planned, in due course, to update this product using the HCA output – which would provide more detailed information on hydrometeor types of the same phase (e.g. rain / drizzle), as well as new information on types which are not currently represented in the product (e.g. hail, graupel).
- Until now, verification of the HCA has been limited to subjective visual analysis of case study results, which is a method with obvious limitations. More formal verification of HCA output is generally a challenge due to the lack of 'truth' measurements; though the UKMO has recently been involved in a campaign which has used the FAAM (Facility for Airborne Atmospheric Measurement) aircraft to make controlled flights through various weather events in order to collect *in situ* data concerning the types and distributions of hydrometeors associated with them. It is hoped that these data can be used in conjunction with the classification outputs of scans coincident with the flights in order to form some sort of formal verification framework. Additionally, various sources of ground-truth data may be available – including disdrometer and rain gauge measurements, routine weather station reports, and crowd-sourced data; all of which may be compared with a forthcoming surface precipitation type product.
- There are several other classes of hydrometeor that are not currently considered within the HCA; and indeed the built-in set of classes in any HCA is somewhat determined by the requirements of the end user. For example, up to this point, it has been deemed sufficient to simply attempt to distinguish between single ice crystals and aggregates

(or 'dry snow'); whereas in reality there are several different species of ice crystal that can feasibly be discriminated using polarimetric radars. If there were a requirement to do so in the future therefore, then such functionality could potentially be added to the algorithm.

5. References

Al-Sakka, H., Boumahmoud, A., Fradon, B., Frasier, S. J., Tabary, P. 2013. "A New Fuzzy Logic Hydrometeor Classification Scheme Applied to the French X-, C-, and S-Band Polarimetric Radars." *J. Appl. Meteor. Climatol.* 52: 2328–2344.

Chandrasekar, V., Keränen, R., Lim, S., Moisseev, D. 2013. "Recent advances in classification of observations from dual polarization weather radars." *Atmospheric Research* 119: 97-111.

Dolan, B., Rutledge, S. A., Lim, S., Chandrasekar, V., and Thurai, M. 2013. "A Robust C-Band Hydrometeor Identification Algorithm and Application to a Long-Term Polarimetric Radar Dataset." *J. Appl. Meteor. Climatol.* 52: 2162–2186.

Marzano, F. S., Scaranari, D., and Vulpiani, G. 2007. "Supervised Fuzzy-Logic Classification of Hydrometeors Using C-Band Weather Radars." *IEEE Transactions on Geoscience and Remote Sensing* 45 (11): 3784-3799.

Mittermaier, M. P., Illingworth, A. J. 2003. "Comparison of model-derived and radar-observed freezing-level heights: Implications for vertical reflectivity profile-correction schemes." *Q. J. R. Meteorol. Soc.* 129: 83-95.

Zrnic, D. S., Ryzhkov, A., Straka, J., Liu, Y., Vivekanandan, J. 2001. "Testing a Procedure for Automatic Classification of Hydrometeor Types." *Journal of Atmospheric and Oceanic Technology* 18: 892-913.

Observations of the atmospheric boundary layer from a vertically pointing, S-band, FMCW radar in northern Alabama, U.S.A. during VORTEX-Southeast



Robin Tanamachi

Robin L. Tanamachi[1], S. J. Frasier[2], J. Waldinger[2], A. T. LaFleur[1], and F. Rocadenbosch[3]

[1]*Department of Earth, Atmospheric, and Planetary Sciences, Purdue University, West Lafayette, Indiana, U.S.A.*
[2]*Microwave Remote Sensing Laboratory, University of Massachusetts, Amherst, Massachusetts, U.S.A.*
[3]*CommSensLab, Department of Signal Theory and Communications, Universitat Politècnica de Catalunya (UPC), Barcelona, Spain*

(Dated: 23 June 2018)

1 Introduction

The use of S-band (~10 cm wavelength) radars for boundary layer (BL) profiling is generally accepted practice (Gossard 1990; Wilczak et al. 1995). S-band straddles the Bragg regime (which dominates in clear air at wavelengths just below 10 cm) and the Rayleigh regime (which dominates in most classes of precipitation at wavelengths above 10 cm). Therefore, S-band radar is useful both for clear-air BL studies and precipitation studies, a property that led to its adoption in the U.S. National Weather Service Radar – 1988 Doppler (WSR-88D). S-band radar observations can be used for real-time monitoring of the convective BL, where insect concentrations and Bragg scatter illuminate the horizontal structures within the convective BL (Gossard and Strauch 1983; Gossard 1990; Melnikov and Zrnić 2017). The vertical resolution of WSR-88D observations of clear air, however, is limited in horizontal and vertical extent by the volume coverage pattern used by the WSR-88D in non-precipitation monitoring mode, and in temporal coverage by the volume update time (~ 5 – 6 min). In precipitation, the WSR-88D-observed components of motion are predominantly horizontal owing to shallow elevation angles used (< 20°). The vertical component of motion is poorly observed and must usually be retrieved using some type of retrieval such as multi-Doppler synthesis (e.g., Armijo 1969) or ensemble Kalman filter data assimilation (e.g., Dowell et al. 2004). For the same reason, WSR-88D Doppler spectra are of limited use for ascertaining drop size distributions.

During spring 2016 and spring 2017, a vertically pointing, S-band radar was deployed in northern Alabama as part of the Verification of the Origins of Rotation in Tornadoes Experiment (VORTEX) – Southeast (VSE). VSE was instigated to intensively investigate tornadoes, their environments, and their societal impact in the Southeast United States (Rasmussen and Koch 2016). The University of Massachusetts frequency modulated continuous wave radar (hereafter UMass FMCW) was deployed in support of the objective of characterizing the BL evolution, which can strongly modulate the character of developing storms, in the VSE domain in northern Alabama, U.S.A. Approximately eight (six) weeks' worth of vertical Doppler spectra were collected over Belle Mina (Scottsboro), Alabama in 2016 (2017) (Figure 1), including observations of BL stratification and precipitation. Conditions during the deployment ranged from quiescent clear skies to severe thunderstorms containing heavy rain and hail (e.g., Figure 2).

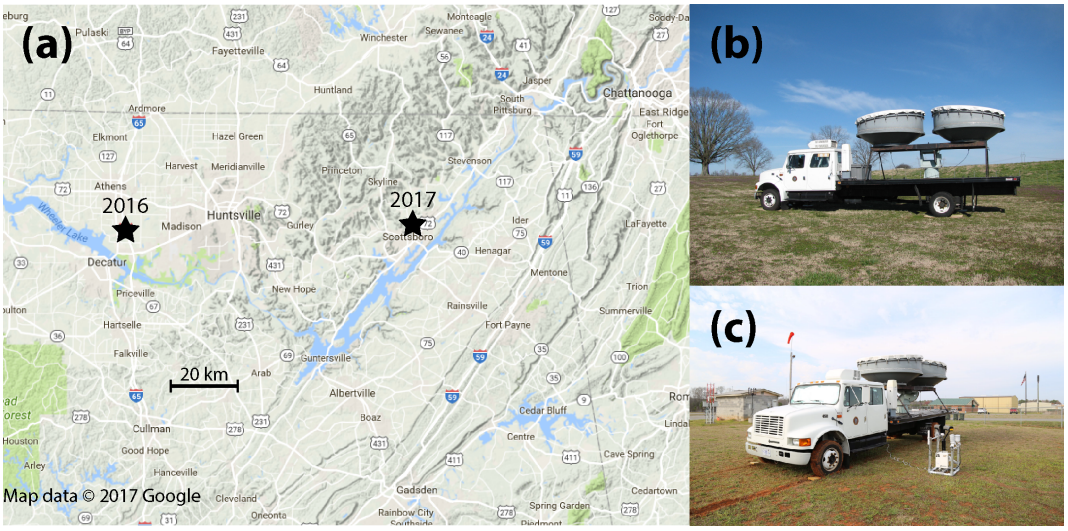


Figure 1: (a) VORTEX-SE deployment sites for UMass FMCW in Northern Alabama during the 2016 and 2017 field campaigns. (b) UMass FMCW deployed at the Tennessee Valley Authority site near Belle Mina, Alabama in 2016. (c) UMass FMCW deployed at Scottsboro municipal airport in 2017. A collocated Portable In Situ Precipitation Station (Dawson et al. 2017) sits beside the truck, and a Vaisala CL31 ceilometer sits on the truck bed just behind the cab.

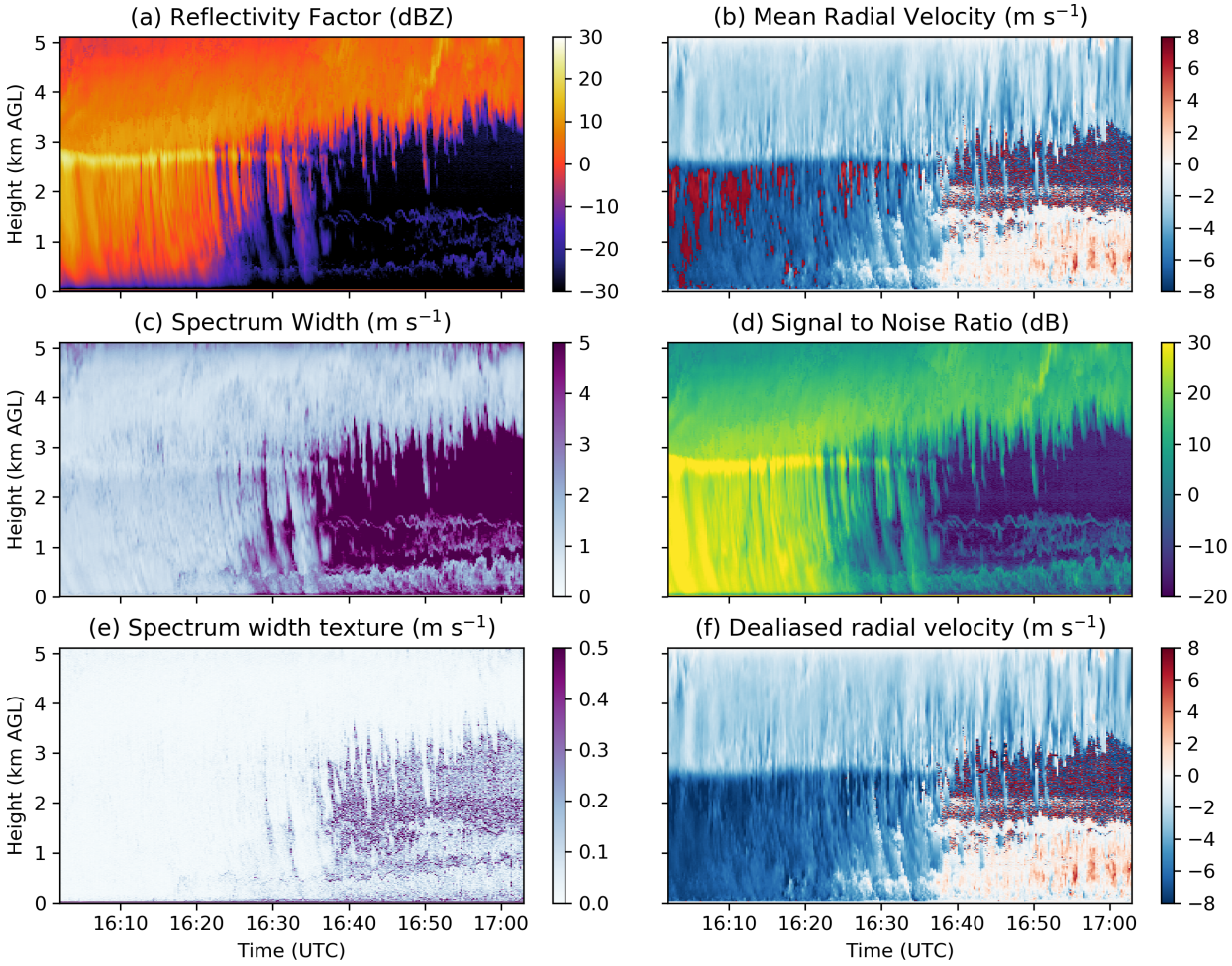


Figure 2: UMass FMCW observations of (a) reflectivity factor (in dBZ), (b) raw Doppler radial velocity (in m s^{-1}), (c) spectrum width (in m s^{-1}), and (d) signal to noise ratio (in dB) from 1600 to 1700 UTC on 3 April 2017 above the Scottsboro, Alabama airport. The end of a stratiform precipitation event with an evident melting layer (around 2.8 km AGL) can be seen, following which at least two elevated, convective layers (at approximately 1.0 and 1.5 km AGL) are visible in the hydrometeor-free air. Derived quantities (e) spectrum width texture (in m s^{-1}) and (f) dealiased Doppler radial velocity (in m s^{-1}) are also shown.

This presentation documents the VSE deployments of UMass FMCW and updates the system description. Additionally, we present results of application of three algorithms to these data: (1) a simple-but-flexible echo classification scheme to separate precipitation from non-precipitation, (2) a bright band identification algorithm, and (3) an extended Kalman filter-based BL height detection algorithm. The latter technique will be discussed in greater detail in a separate presentation at this conference (Rocadenbosch et al., abstract no. 29).

2 UMass FMCW

UMass FMCW (Figure 1b, c) is a single-polarized, pulse compression radar (İnce et al. 2000; İnce et al. 2003; Waldinger et al. 2017). During VSE data collection, UMass FMCW operated as follows. Over a 1.34 s interval, 256 frequency modulated sweeps were collected to produce a Doppler spectrum. Twelve such spectra, spanning a 16.1 s interval, were then averaged, and moments calculated from the averaged spectra. Reflectivity (η, units: mm^6 m^{-3}) was estimated from system signal-to-noise ratio (SNR) using the radar equation (e.g., Doviak and Zrnić 1993, their Eqn. 4.16) and nominal system parameters (**Error! Reference source not found.**). Linear radar reflectivity factor (z) was calculated from η, while radial (vertical) Doppler velocity (w), and spectrum width (σ_w) were calculated from the Doppler spectra. In a change from previous field campaigns, Doppler spectra were also recorded for VSE deployments.

In 2017, UMass FMCW was upgraded with a solid state (gallium nitride) amplifier, replacing the traveling wave tube (TWT) amplifier used in 2016 and prior seasons (Waldinger et al. 2017). This upgrade increased the maximum unambiguous velocity of the system from 4.9 to 7.3 m s^{-1}, and eliminated power spurs in the Doppler spectra resulting from the TWT amplifier's switching power supply. While the majority of these spurs were small in amplitude and could be removed using median filtering, the stronger spurs persisted and led to spurious echoes appearing at constant range (height; Figure 3a-d). The spurs drifted in frequency and occasionally overwhelmed weak meteorological returns, making them difficult to remove using

conventional automated filtering methods and flummoxing the automated dealiasing algorithm (Herráez et al. 2002) applied to these data (Figure 3f). The 2017 solid state amplifier upgrade virtually eliminated these issues (Figure 2f). For these reasons, the scatterer classification algorithm described later in this manuscript was developed using only the observations made in 2017.

Table 1: Selected parameters of the UMass FMCW radar system as configured for VSE.

Parameter	Value
Frequency	2.92 GHz
Bandwidth	30 MHz
Sweep interval	5.24 ms
Sweep rate (PRF)	190.735 Hz
Amplifier type	Traveling wave tube (2016) Solid state GaN (2017)
Transmitted power (continuous)	250 W
Antenna gain	34 dB
Compression gain	50.2 dB
Noise level	-97.4 dBm
3-dB beam width	3.5°
Maximum unambiguous range	5.12 km
Maximum unambiguous velocity	±4.9 m s^{-1} (2016) ±7.3 m s^{-1} (2017)
Sampling period	1.34 sec
Averaging period	16.1 sec
Range resolution	5.0 m

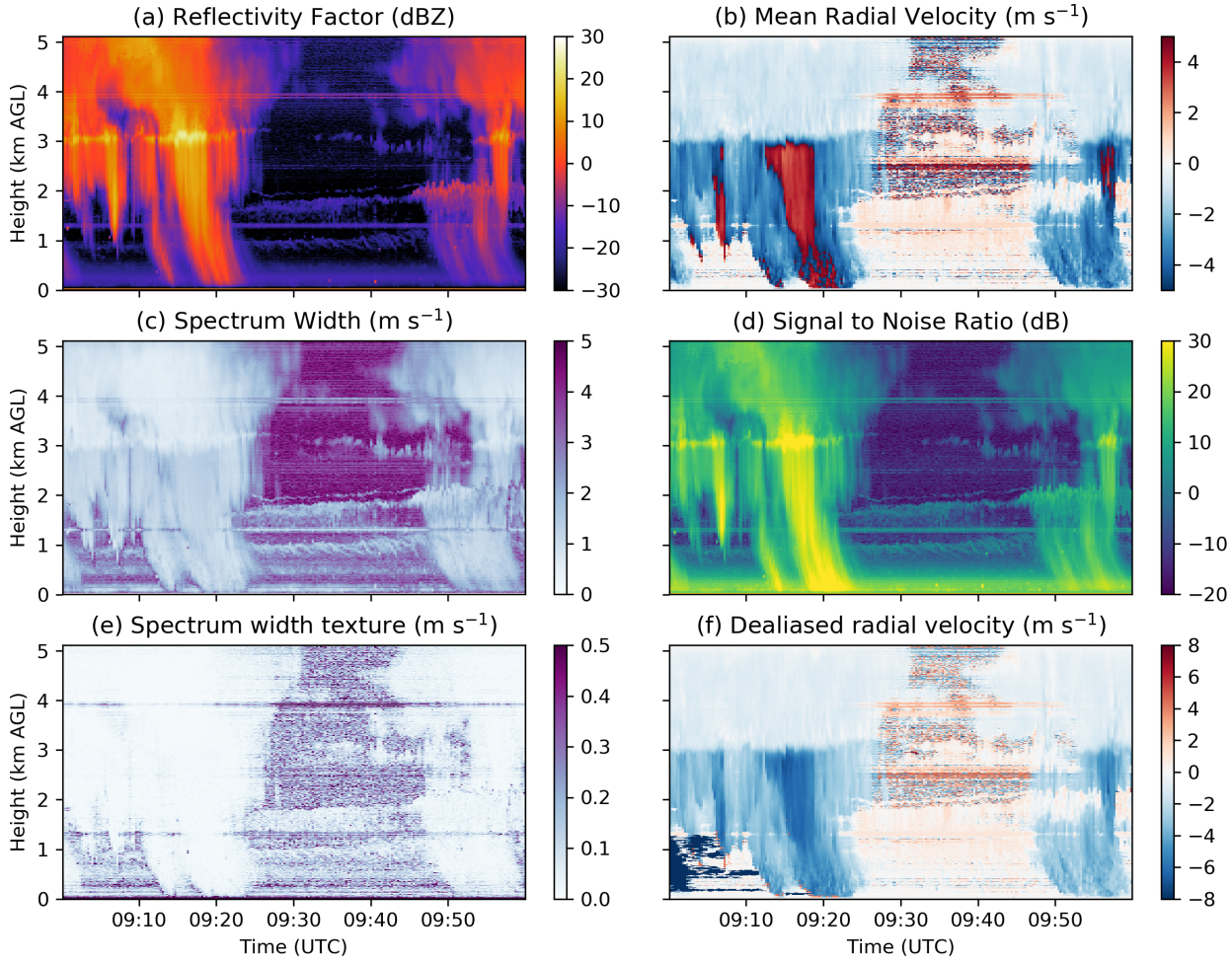


Figure 3: As in Figure 2, but for observations from 0900 to 1000 UTC on 31 March 2016 over Belle Mina, Alabama. A light precipitation / virga event is depicted. The melting layer can be seen at 3.0 km AGL, and the top of the convective boundary layer is evident at about 2.0 km AGL, following the cessation of rain. These data were collected prior to the solid state amplifier upgrade, and show the effects of power spurs (appearing as spurious echoes at constant height) in all the fields. These spurious echoes cause the automated dealiasing algorithm (panel f) to fail from 0900 to 0915 UTC, below the precipitation.

3 Scatterer classification algorithm

Two VSE-associated research projects undertaken using UMass FMCW data required separation of non-precipitation (predominantly Bragg scatter) from precipitation (predominantly Rayleigh scatter) observations. Because ~14 weeks' worth of observations were collected, manual separation of these two classes of echoes would be quite time-consuming, so we pursued an automated technique. We chose to use the generalized fuzzy logic technique described by Gourley et al. (2007). While developed for C-band polarimetric radar, this techniqueis agnostic to the choice of band, polarimetry, and variables used in the classification. The only requirement is that sufficient differences exist in the measured variables between the classes to be assigned that the kernel density estimators (KDEs) have relatively small overlap.

The fuzzy logic algorithm used in this study was trained on the four primary variables in the UMass FMCW data: logarithmic reflectivity factor (Z), w, signal-to-noise ratio (SNR), and σ_w. Attenuated echoes (with associated noisy Doppler velocities) were occasionally observed at high altitudes in convective precipitation. To eliminate attenuated precipitation observations, the texture of σ_w^2 (e.g., Figure 4e) was used. The texture (spatial variability in the vertical) of a variable f at a height index h over a kernel size n is given by the root-mean-square-difference formula:

$$\text{Texture}(f_h) = \sqrt{\frac{\sum_{i=-(n-1)/2}^{(n-1)/2}(f_h - f_{h+i})^2}{n}} \qquad (3.1)$$

This texture formula is the same as that given by Gourley et al. (2007; their Eqn. 1) but reduced to a single (vertical) spatial dimension. Precipitation data were censored where Texture(σ_w^2) exceeded 0.2 m s^{-1}, a value inferred by inspection to correspond to attenuated precipitation observations, but not to hydrometeor-free air observations.

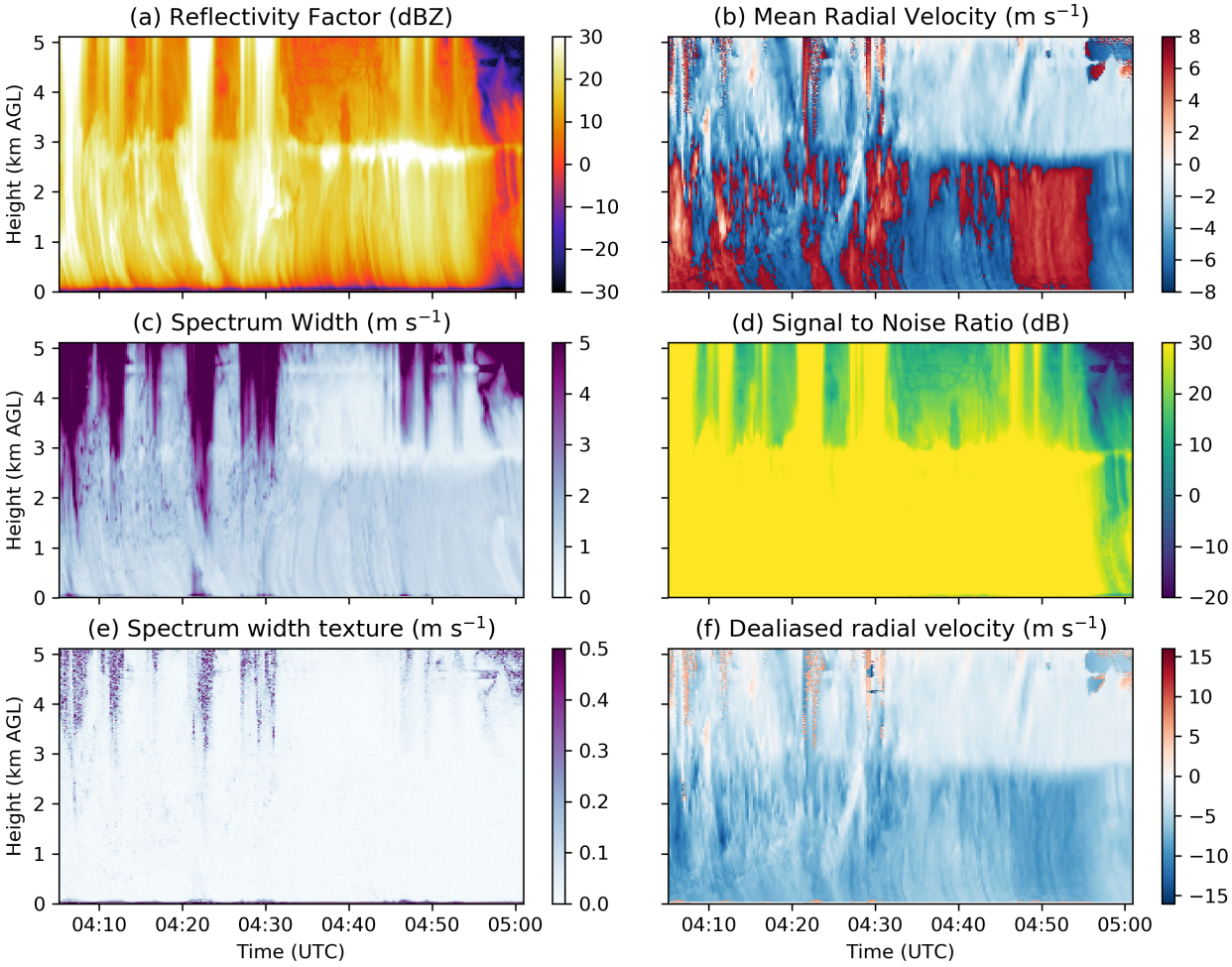


Figure 4: As in Figure 2, but for 0400 to 0500 UTC on 28 March 2017, during a transition from convective (pre-0430 UTC) to stratiform (post-0430 UTC) precipitation.

To "train" the fuzzy logic algorithm (i.e., populate the KDEs) as was done by Gourley et al. (2007), we selected subsets of the observations of the desired categories. The nine-hour "precipitation" subset of the UMass FMCW data was composed of examples of stratiform, convective, warm rain (i.e., no ice processes), and drizzle. KDEs for nonprecpitation were generated similarly using a nine-hour subset of observations of scatterer-free air, bioscatterer activity, or Bragg scatter in the convective BL (e.g., Figure 5). These two sets of training data were selected to capture a plausible range of the measured and derived variables, and contained observations spanning the 2017 deployment period in order to account for any long-term variability in the radar's performance. One additional category ("no data") was defined for those observations that were censored by the UMass FMCW signal processor (signified by Z = -99.0 dBZ).

The normalized Gaussian KDEs (Silverman 1986) were generated using the scikit-learn (Pedregosa et al. 2011) package for Python (Figure 6). As in Gourley et al. (2007), the overlap area of the KDEs was used to assign weights to each variable for each class. The smaller the KDE overlap area, the better a discriminator the variable was, and the larger the weight assigned to that variable. Following training, the three variables found to have the largest weights were (in descending order) Z, SNR, and σ_w^2. These three variables are used to classify precipitation and nonprecipitation for the 2016 and 2017 data sets. Radial velocity (w) was found to have a relatively small weight compared to the other variables. It was also noted that the KDE for clear air appeared to have artificially inflated "wings" close to the edges of the radar Nyquist interval (7.3 m s^{-1}; Figure 6b), signifying that low-SNR clear-air observations resisted dealiasing. Therefore, in spite of previous studies showing its potential power as a precipitation discriminator (Ralph et al. 1996), w was not included in the set of variables used to make the scatterer classifications in these data.

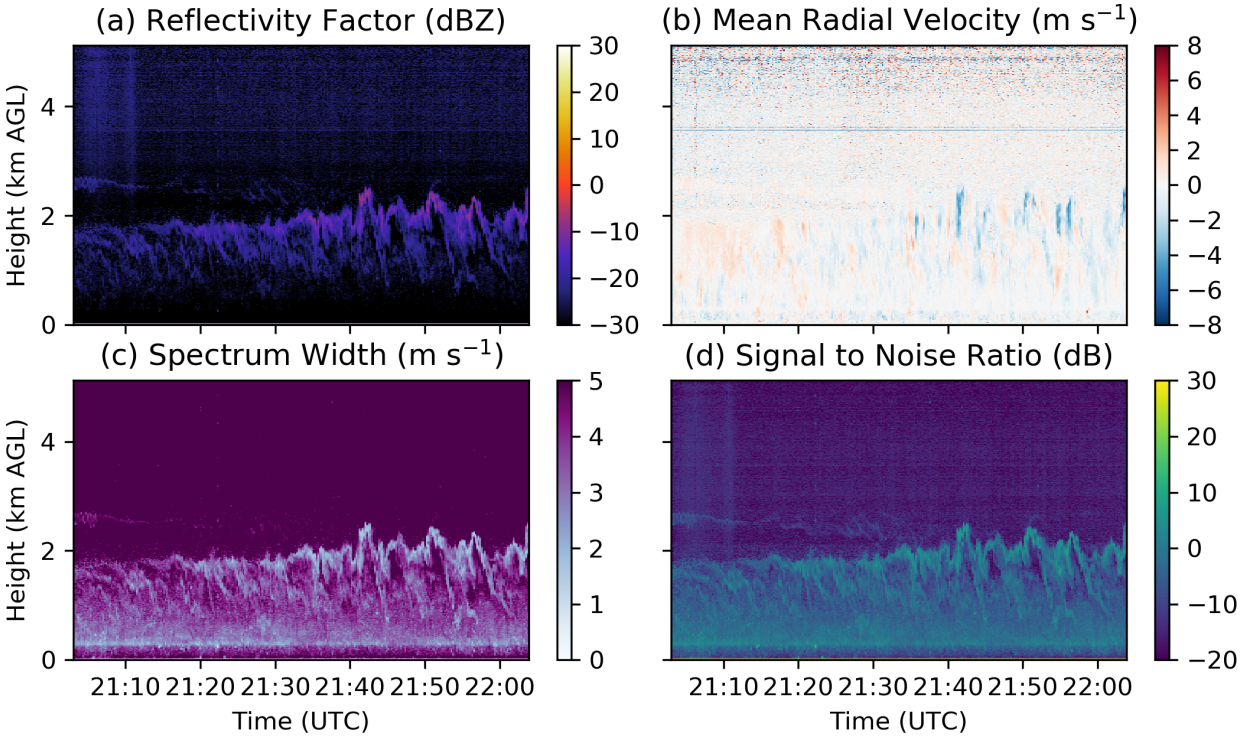


Figure 5. As in Figure 2(a-d), but for 2100 to 2200 UTC on 3 April 2017, showing the growth of the convective boundary layer.

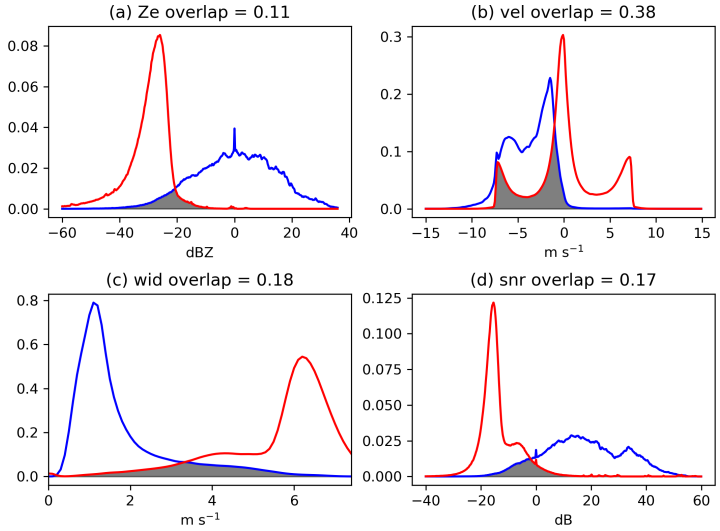


Figure 6. Kernel density estimators for (a) reflectivity (in dBZ), (b) dealiased Doppler radial velocity (in m s^{-1}), (c) spectrum width (in m s^{-1}), and (d) signal to noise ratio (in dB) for precipitation (blue curves) and non-precipitation (red curves). The normalized area where the two curves overlap (representing ambiguous classification) is shaded in dark gray.

Examples of the resulting classifications, based on the observations shown in Figures Figure 2 through Figure 5, are shown in Figure 7. On first glance, the algorithm appears to be working fairly well. There are, however, a few issues of note. Firstly, in the 2016 data (e.g., Figure 7b), the spurious echoes from the TWT power spurs are misclassified as precipitation. We estimate that approximately 5-10% of the precipitation classifications in the 2016 data are likely erroneous results of power spur artifacts. These observations reinforce the notion that some additional quality control needs to be performed on the 2016 data.

Secondly, some regions near the top of the convective BL (e.g., Figure 7a and d) are classified as precipitation, but it is ambiguous whether the echoes are Bragg scatter or light virga within convective clouds (Figures Figure 2 and Figure 5, respectively). While vertical velocity oscillates from positive to negative in these regions (Figures Figure 2b and Figure 5b, respectively), suggesting that Bragg scatter is the dominant scattering mechanism, cloud bases were detected (Figure 8) by a collocated Vaisala CL31 ceilometer (Figure 1b, c) in some instances (e.g., Figure 8b). We conclude that Bragg scatter is being misclassified as precipitation in some instances where cloud bases were not detected (e.g., Figure 7a at and after 1630 UTC

around 500 m AGL), but that light virga was likely present within convective clouds (e.g., Figure 7b). In the former case, the precipitation classification is incorrect, but in the latter, it is correct. The ceilometer observations will likely be introduced as an additional check on this classification scheme in the future.

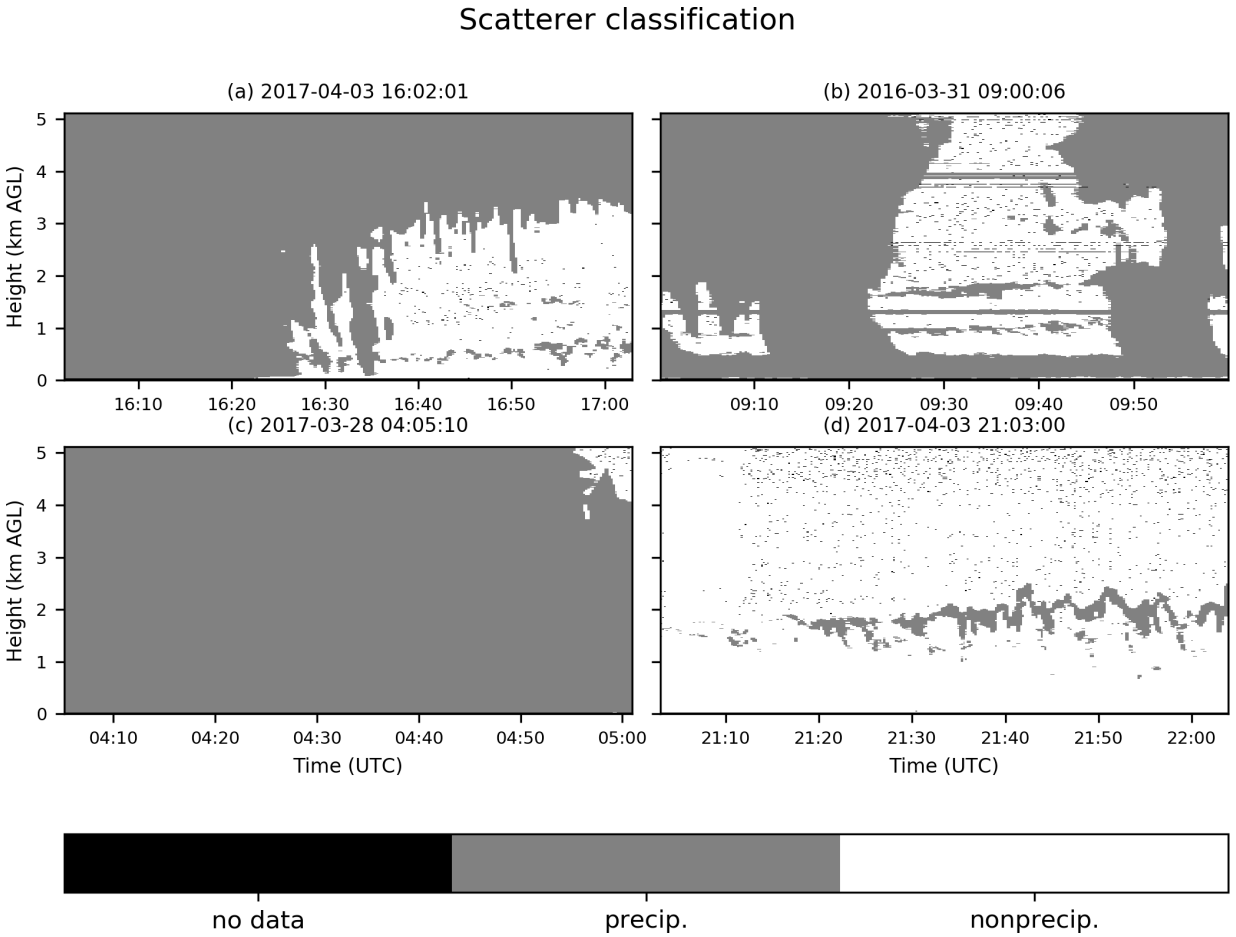


Figure 7: Scatterer classifications (precipitation / non-precipitation) based upon the observations shown in Figures Figure 2 through Figure 5, respectively.

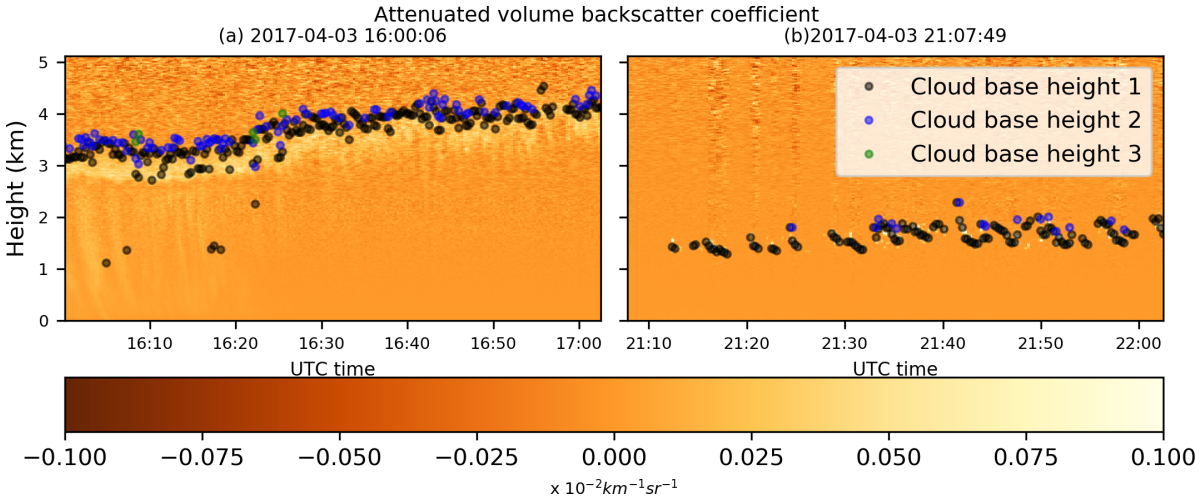


Figure 8: Attenuated volume backscatter coefficient (color fill in km^{-1} sr^{-1}) and cloud base heights (colored dots) detected by a ceilometer collocated with UMass FMCW at the times the measurements shown in (a) Figure 2 and (b) Figure 5 were collected.

4 Melting layer (bright band) identification in precipitation

With our precipitation classifications in hand, we proceed to automated identification of the melting layer (ML) in order to further segregate frozen from liquid precipitation, and convective from stratiform precipitation. Our methodology for bright

band identification (BBID) is patterned after that formulated by Zhang et al. (2008) for stratiform regions. The principal differences are (1) we use measured vertical profiles of reflectivity from the UMass FMCW radar, rather than vertical profiles of predominantly horizontally polarized reflectivity derived from a volume coverage pattern, and (2) when needed, we use estimated 0 °C height from an independent, collocated instrument rather than an operational numerical model field. The 0 °C height, which is used as a first guess for the altitude of the top of the ML, is iteratively estimated either from the bright band top calculated at a previous time step, or from temperature profiles produced by the Collaborative Lower Atmospheric Profiling System (CLAMPS) (Blumberg et al. 2015) if the former quantity was not available. CLAMPS was collocated with UMass FMCW for both the 2016 and 2017 VSE field campaigns (Turner 2016). The scatterer classification was used to constrain ML identifications to precipitation only. Results of the ML identification for a 12-hour rain event during VSE on 3 April 2017 are shown in Figure 9. Good agreement can be seen between the CLAMPS 0 °C height and the ML identification, lending confidence that the identified ML can be used to separate frozen (above) and liquid (below) hydrometeors.

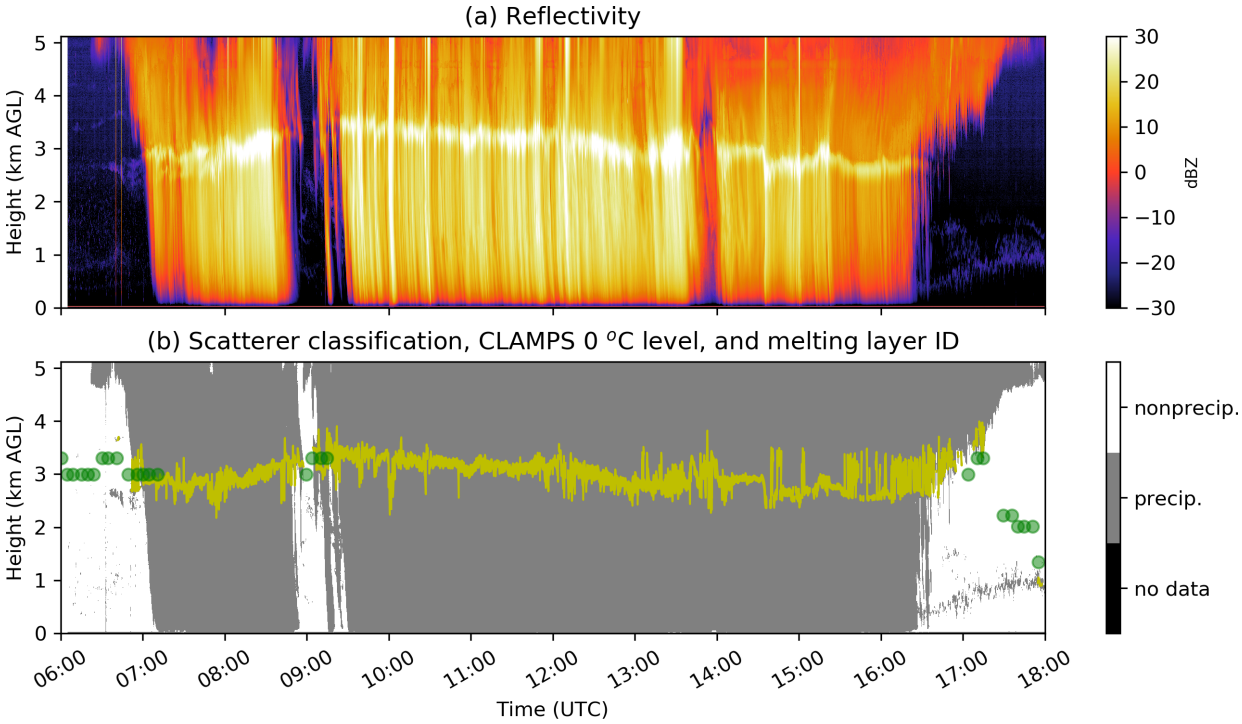


Figure 9: (a) Reflectivity (in dBZ) for a 12-hour precipitation event on 3 April 2017, with a bright band in clear evidence. (b) Corresponding scatterer classification (gray shading) and melting layer identification (yellow fill), overlaid with CLAMPS 0 °C level (green dots).

5 Identification of the top of the convective BL using an extended Kalman filter technique

We turn our attention to the non-precipitation regions identified using our scatterer classification algorithm. Within this section, we assumed that Bragg scatter was the predominant mechanism generating echo in these regions, even though it has been documented that UMass FMCW can detect bioscatterers (Contreras and Frasier 2008) and that some regions of Bragg scatter may be misclassified as light precipitation (e.g., Figure 7a).

Lange et al. (2015) described a technique for automatic identification of the top of the convective BL in UMass FMCW reflectivity observations using an extended Kalman filter (EKF). The application of this technique to UMass FMCW VSE observations will be discussed in detail in a separate presentation at this conference (Rocadenbosch et al., abstract no. 29). An example of this application to the 2016 UMass FMCW reflectivity observations is shown Figure 10. For the 2016 data, the algorithm was modified to avoid identifying the spurious echo artifact from the TWT power spur as the top of the BL. It can be seen that the algorithm successfully avoids misidentifying this artifact as the top of the BL at all but a handful of time steps. We intend to apply this algorithm in a semi-supervised fashion to all the UMass FMCW non-precipitation observations in an effort to characterize the diurnal cycle of convective BL growth and decay over the VSE domain.

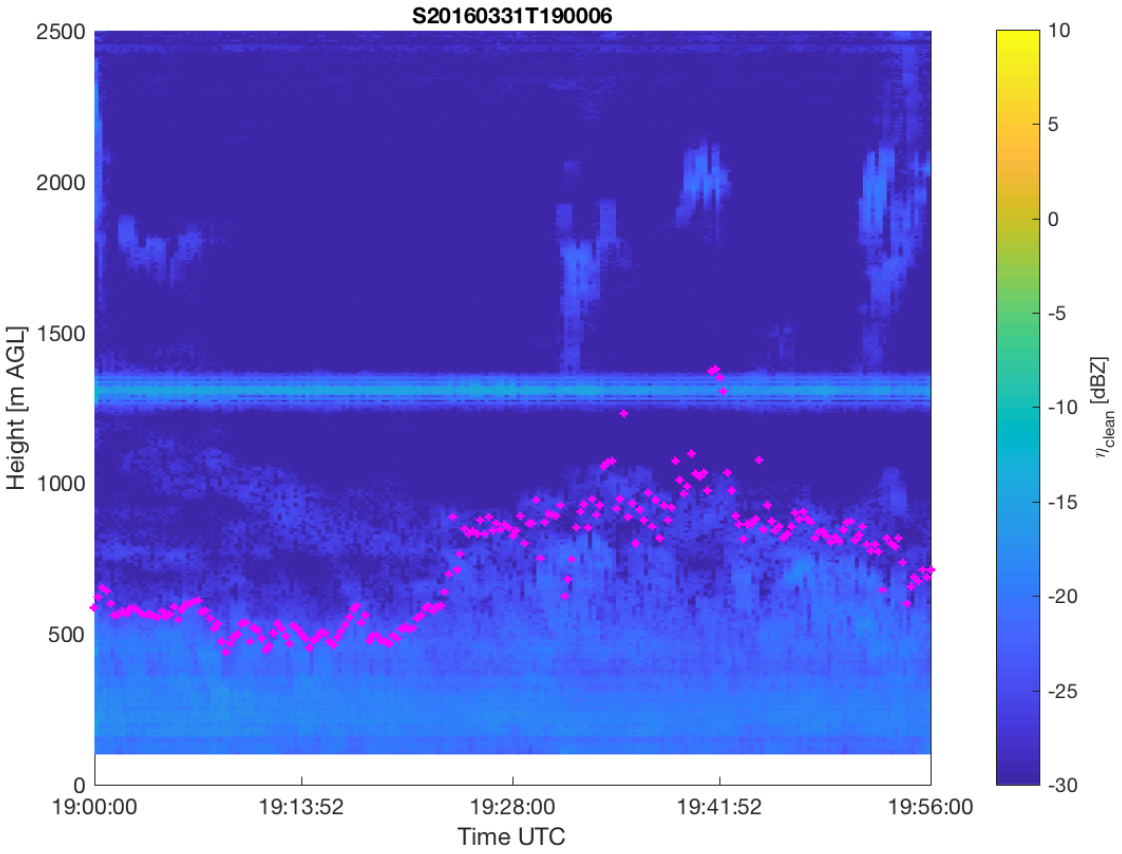


Figure 10: Bioscatterer-free ("clean") UMass FMCW reflectivity (in dBZ) from 1900 to 2000 UTC on 31 March 2016, overlaid with BL top identifications (magenta crosses) from the EKF-based technique. The reader is referred to Lange et al. (2015) for additional detail regarding the reflectivity preprocessing.

6 Conclusions

We developed a scatterer identification algorithm for observations collected during VORTEX-SE by a vertically-pointing, S-band, single-polarized FMCW radar. This algorithm automatically separated UMass FMCW observations of precipitation and nonprecipitation, and allowed for further identification of salient BL features of interest to the VSE cohort. The products produced by our postprocessing include:

1. Dealiased vertical velocities in precipitation
2. Scatterer classification (precipitation and nonprecipitation)
3. Bright band top and bottom heights
4. Convective boundary layer top heights

These products serve as a stepping stone toward a comprehensive characterization of the BL over northern Alabama during early spring. It is anticipated that these products will be used to derive additional conceptual models, such as those for convective BL growth based on composites of BL evolution, and estimated precipitation drop size distributions verified by collocated disdrometer observations (Dawson et al. 2017) (Figure 1c). We also intend to add additional subclasses to the non-precipitation scatterer category, specifically refractive index turbulence (RIT), biological scatterers (insects, birds, etc.), and unknown non-meteorological targets.

Acknowledgements

This work was funded by NOAA grants NA15OAR4590231 and NA16OAR4590208. Dr. Kevin Knupp of the University of Alabama Huntsville played critical facilitating roles in the deployment of the UMass FMCW in both 2016 and 2017. Dr. Temple Lee and Dr. Bruce Baker of NOAA secured the use of and power supply for the Belle Mina deployment site in 2016. The Python packages Matplotlib (Hunter 2007), scikit-image (van der Walt et al. 2014), and Py-ART (Helmus and Collis 2016) were used in the preparation of this manuscript. We would like to express our gratitude to Dr. David Turner of NOAA/ESRL for valuable input regarding the quality of the CLAMPS temperature profiles, and to Dr. Robert Jackson of Argonne National Laboratory for providing the code for the texture calculations.

References

Armijo, L., 1969: A theory for the determination of wind and precipitation velocities with Doppler radars. *J. Atmos. Sci.*, **26,** 570-573, doi:doi:10.1175/1520-0469(1969)026<0570:ATFTDO>2.0.CO;2.

Blumberg, W. G., D. D. Turner, U. Löhnert, and S. Castleberry, 2015: Ground-based temperature and humidity profiling using spectral infrared and microwave observations. Part II: Actual retrieval performance in clear-sky and cloudy conditions. *J. Climate Appl. Meteor.*, **54,** 2305-2319, doi:10.1175/JAMC-D-15-0005.1.

Contreras, R. F., and S. J. Frasier, 2008: High-resolution observations of insects in the atmospheric boundary layer. *J. Atmos. Oceanic Technol.*, **25,** 2176-2187, doi:10.1175/2008JTECHA1059.1.

Dawson, D. T., M. E. Baldwin, J. Bozell, J. Buckingham, D. R. Chavas, W. L. Downing, M. Guo, R. L. Tanamachi, A. N. Griffin, H. M. Mallinson, S. J. Frasier, W. Heberling, J. Waldinger, M. I. Biggerstaff, and S. M. Waugh, 2017: Overview of Purdue's mobile disdrometer operations during VORTEX-SE 2016-2017. *38th Conf. on Radar Meteorology*, Chicago, Illinois, American Meteorological Society,

Doviak, R. J., and D. S. Zrnić, 1993: *Doppler Weather Radar and Observations.* 2 ed. Academic Press, 562 pp.

Dowell, D. C., F. Zhang, L. J. Wicker, C. Snyder, and N. A. Crook, 2004: Wind and temperature retrievals in the 17 May 1981 Arcadia, Oklahoma, supercell: Ensemble Kalman filter experiments. *Mon. Wea. Rev.*, **132,** 1982-2005,

Gossard, E. E., 1990: Radar Research on the Atmospheric Boundary Layer. *Radar in Meteorology: Battan Memorial and 40th Anniversary Radar Meteorology Conference*, D. Atlas, Ed., American Meteorological Society, 477-527.

Gossard, E. E., and R. G. Strauch, 1983: *Radar observations of clear air and clouds.* Vol. 110, Elsevier Scientific Publishing Co., John Wiley & Sons, Ltd, 280 pp.

Gourley, J. J., P. Tabary, and J. Parent du Chatelet, 2007: A fuzzy logic algorithm for the separation of precipitating from nonprecipitating echoes using polarimetric radar observations. *J. Atmos. Oceanic Technol.*, **24,** 1439-1451, doi:10.1175/JTECH2035.1.

Helmus, J. J., and S. Collis, 2016: The Python ARM Radar Toolkit (Py-ART), a library for working with weather radar data in the Python programming language. *Journal of Open Research Software*, **4,** e25, doi:http://doi.org/10.5334/jors.119.

Herráez, M. A., D. R. Burton, M. J. Lalor, and M. A. Gdeisat, 2002: Fast two-dimensional phase-unwrapping algorithm based on sorting by reliability following a noncontinuous path. *Appl. Opt.*, **41,** 7437-7444, doi:10.1364/AO.41.007437.

Hunter, J. D., 2007: Matplotlib: A 2D graphics environment. *Computing In Science & Engineering*, **9,** 90-95, doi:10.1109/MCSE.2007.55.

İnce, T., A. L. Pazmany, and S. J. Frasier, 2000: High resolution profiling of the atmospheric boundary layer. *IGARSS 2000: IEEE 2000 International Geoscience and Remote Sensing Symposium, Vol I - VI, Proceedings*, New York, IEEE, 209-211,

İnce, T., S. J. Frasier, A. Muschinski, and A. L. Pazmany, 2003: An S-band frequency-modulated continuous-wave boundary layer profiler: Description and initial results. *Radio Science*, **38,** 1-10, doi:10.1029/2002RS002753.

Lange, D., F. Rocadenbosch, J. Tiana-Alsina, and S. J. Frasier, 2015: Atmospheric boundary layer height estimation using a Kalman filter and a frequency-modulated continuous-wave radar. *Geoscience and Remote Sensing, IEEE Transactions on*, **53,** 3338-3349, doi:10.1109/TGRS.2014.2374233.

Melnikov, V., and D. S. Zrnić, 2017: Observations of convective thermals with weather radar. *J. Atmos. Oceanic Technol.*, **34,** 1585-1590, doi:10.1175/JTECH-D-17-0068.1.

Pedregosa, F., G. Varoquaux, A. Gramfort, V. Michel, B. Thirion, O. Grisel, M. Blondel, P. Prettenhofer, R. Weiss, V. Dubourg, J. Vanderplas, A. Passos, D. Cournapeau, M. Brucher, M. Perrot, and E. Duchesnay, 2011: Scikit-learn: Machine Learning in Python. *Journal of Machine Learning Research*, **12,** 2825-2830,

Ralph, F. M., P. J. Neiman, and D. Ruffieux, 1996: Precipitation identification from radar wind profiler spectral moment data: Vertical velocity histograms, velocity variance, and signal power–vertical velocity correlations. *J. Atmos. Oceanic Technol.*, **13,** 545-559, doi:10.1175/1520-0426(1996)013<0545:PIFRWP>2.0.CO;2.

Rasmussen, E. N., and S. Koch, 2016: VORTEX-SE: Lessons learned and early results. *28th Conf. on Severe Local Storms*, Portland, Oregon, American Meteorological Society, 3.2,

Silverman, B. W., 1986: *Density Estimation for Statistics and Data Analysis.* CRC Press.

Turner, D. D., 2016: CLAMPS boundary layer evolution observations during VORTEX-SE-2016. *28th Conf. on Severe Local Storms*, Portland, Oregon, American Meteorological Society, 3.7,

van der Walt, S., J. L. Schönberger, J. Nunez-Iglesias, F. Boulogne, J. D. Warner, N. Yager, E. Gouillart, and T. Yu, 2014: scikit-image: image processing in Python. *PeerJ*, **2,** e453, doi:https://doi.org/10.7717/peerj.453.

Waldinger, J., T. Hartley, W. Heberling, S. J. Frasier, and R. L. Tanamachi, 2017: S-band FMCW boundary layer profiler: System upgrades and results. *2017 IEEE International Geoscience and Remote Sensing Symposium (IGARSS)*, Austin, Texas, IEEE, doi:10.1109/IGARSS.2017.8128008.

Wilczak, J. M., R. G. Strauch, F. M. Ralph, B. L. Weber, D. A. Merritt, J. R. Jordan, D. E. Wolfe, L. K. Lewis, D. B. Wuertz, J. E. Gaynor, S. A. McLaughlin, R. R. Rogers, A. C. Riddle, and T. S. Dye, 1995: Contamination of wind profiler data by migrating birds: Characteristics of corrupted data and potential solutions. *J. Atmos. Oceanic Technol.*, **12,** 449-467,

Zhang, J., C. Langston, and K. Howard, 2008: Brightband identification based on vertical profiles of reflectivity from the WSR-88D. *J. Atmos. Oceanic Technol.*, **25,** 1859-1872, doi:10.1175/2008JTECHA1039.1.

WHY THE GENERALIZED GAMMA? - AN ANSWER BASED ON MEASUREMENTS WITH METEOROLOGICAL PARTICLE SPECTROMETER AND 2D VIDEO DISDROMETER

Merhala Thurai[1], V.N. Bringi[1], Patrick Gatlin[2], Walter Petersen[2] and Matt Wingo[3]

[1]*Dept. of ECE, Colorado State University, Fort Collins, Colorado 80523, United States*
[2] *NASA Marshall Space Flight Center, Huntsville, United States*
[3] *University of Alabama, Huntsville, United States*
(Dated: June 2018)

1 Introduction

The generalized gamma (GG) formulation for representing hydrometeor particle size distributions (PSD) has been considered by several researchers in the past several decades, ranging from cloud droplet and fog PSDs (Deirmendjian 1969; Hess et al. 1998; Vivekanandan et al. 1999, also referred to as modified gamma distribution) to ice PSDs (Delanoe et al., 2005, Petty and Huang, 2011). For rain, the use of GG formulation has been somewhat more recent (Auf der Maur, 2001, Lee et al., 2004, Kuo et al., 2004, Raupach and Berne, 2017, Thurai and Bringi 2018).

From theory, the GG form is mathematically sound and has the following desired properties: (a) it reduces to standard gamma, exponential, and Weibull forms (which are special cases) and as a limiting case to the log-normal form, (b) any power law of drop diameter (D) such as mass or mass flux also falls in the GG form and (c) it maximizes relative entropy under moment constraints (Wu and McFarquhar, 2018). As shown in the latter, it is very difficult from measurements alone to prove via statistical methods that the GG is optimal compared to standard gamma (SG) or log-normal forms. While the SG distribution is widely adopted in radar rainfall studies as well as in multi-moment numerical schemes, some studies have shown via rigorous statistical (Kolmogorov-Smirnov) goodness-of-fit tests that around 50% or more of 1-min measured DSDs reject the SG model as a fit to the data (Adirosi et al. 2014).

Following Auf der Maur (2001), in the GG formulation, the rain drop size distribution (DSD), represented by N(D), can be expressed as:

$$N(D) = M_0 \frac{c\lambda}{\Gamma(\mu_{GG})} (\lambda D)^{c\mu_{GG}-1} \exp[-(\lambda D^c)] \qquad (1)$$

where M_0 is the zeroth moment (= total number of drops per m^3) and μ_{GG} and c are two shape parameters, and λ can be expressed in terms of two reference moments, M_i and M_j (Lee et al., 2004), leading to the double-moment normalized version of eq. (1), given by:

$$N(D) = N_0' \; h_{GG(i,j,\mu,c)}(x) \qquad (2)$$

where $N_0' = M_i^{(j+1)/(j-i)} M_j^{(i+1)/(i-j)}$ and $D_m' = (M_j / M_i)^{1/(j-i)}$

$$h_{GG(i,j,\mu,c)}(x) = c\,\Gamma_i^{\frac{(j+c\mu_{GG})}{(i-j)}} \Gamma_j^{\frac{(-i-c\mu_{GG})}{(i-j)}} x^{c\mu_{GG}-1} \exp\left[-\left(\frac{\Gamma_i}{\Gamma_j}\right)^{\frac{c}{(i-j)}} x^c\right]$$

$$\Gamma_i = \Gamma\left(\mu_{GG} + \frac{i}{c}\right) \quad \text{and} \quad \Gamma_j = \Gamma\left(\mu_{GG} + \frac{j}{c}\right) \quad \text{and}$$

$$x = \left(\frac{D}{D_m'}\right)$$

If we set i=3 and j=4, then D_m' becomes equal to D_m, the mass-weighted mean diameter. Note also that eq. (2) will reduce to the SG model (for c=1) defined by the three parameters [N_W, D_0 or D_m and μ_{SG})] where $\mu_{SG} = \mu_{GG} - 1$ and N_W, the normalized intercept parameter, is simply related to N_0' via $N_W=[4^4/6]N_0'$. Furthermore, eq. (2) further reduces to an exponential distribution when $\mu_{SG} = 0$ (or $\mu_{GG} = 1$).

The DSD formulation used herein is also based on double-moment normalization using the 3rd and 4th moments as the reference moments (M_3,M_4) and the intrinsic shape of the normalized distribution h(x) where $x=D/D_{43}$ is the scaled diameter and D_{43} (i.e., D_m), i.e. the ratio of M_4 to M_3. N(D) can be expressed in compact form as $N(D)=M_3/D_{43}^4\, h(x; \mu_{GG}, c)=N_0'\, h(x; \mu_{GG}, c)$. This form has the advantage that any moment of the DSD can be expressed as power laws of the two reference moments and (μ_{GG}, c); in particular the lower order moments (M_0, M_1, M_2) which are involved in modeling microphysical processes such as coalescence and break-up which control the DSD shape at the small drop and large drop ends as well as the plateau region in between. Most currently available disdrometers cannot accurately measure the small drop end (D<0.5-0.7 mm) due to poor resolution and sensitivity issues.

2. Data

We consider here measurements of rain drop size distributions (DSD) using collocated high resolution (50 microns) Meteorological Particle Spectrometer (MPS) and moderate resolution (170 microns) 2D-video disdrometer from two different rain climatologies (Greeley, Colorado, and Huntsville, Alabama, USA). In both locations, the instruments were installed within a DFIR double wind-fence in order to mitigate wind effects, especially for small drops, The combination of data from the two instruments yields what we term as the "full" or composite DSD spectra, e.g. over 1-minute, covering the size range from 100 microns to large rain drops whose shapes were found to be not very well represented by the standard gamma model, but required the additional flexibility offered by eq. (2), with the two abovementioned shape parameters (μ_{GG}, c). We define the composite spectra as using the MPS for 0.1<D<1 mm and 2DVD for D > 1 mm based on resolution and sample volume considerations. An example is given below in Fig. 1 where the 2DVD data are shown in blue, the MPS data in black and the composite DSD in green. Also shown is the fitted GG curve in red, where the estimation of μ and c is done with a global search using nonlinear least squares, as mentioned in Thurai and Bringi, (2018). Note also that we allow μ to go negative to capture the drizzle mode (Raupach et al., 2018a, 2018b).

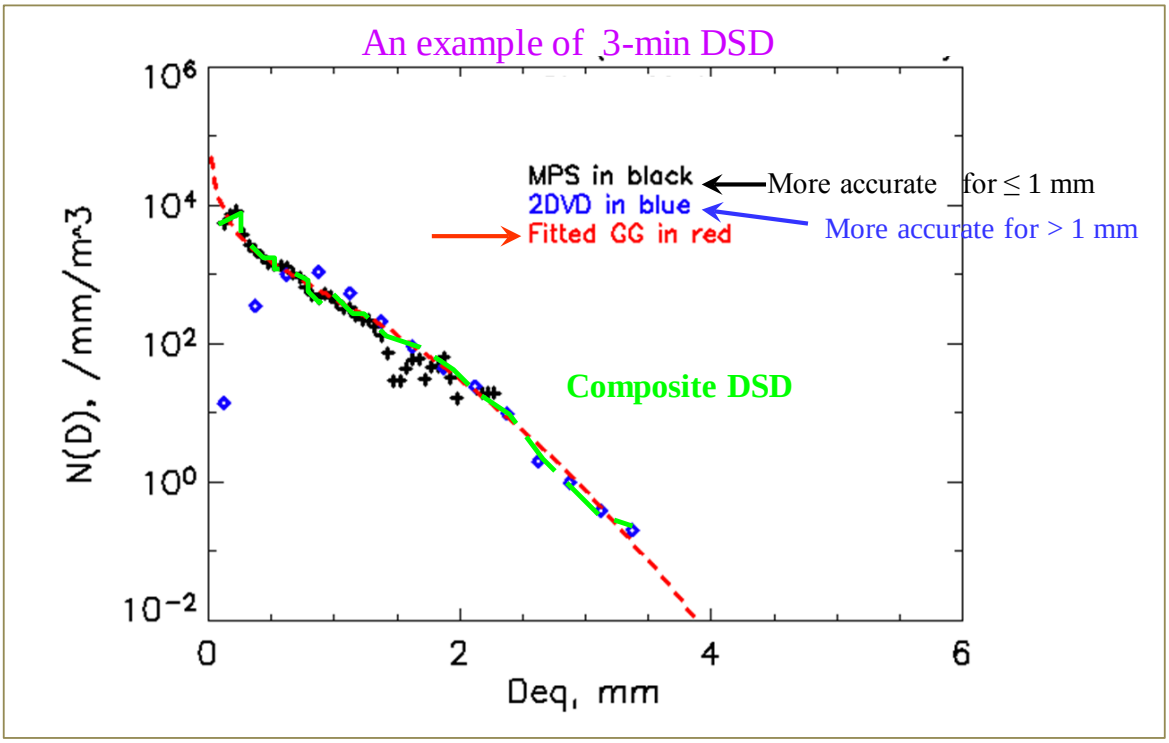


Fig. 1: *An example of a 3-minute DSD from the MPS and the 2DVD, together with the composite DSD and the fitted GG to eq. (2).*

Examples of events presented here include light, shallow rain, stratiform rain, and convective rain events in Greeley, as well as outer bands of hurricane Irma and tropical storm Nate. The latter two are special cases, which fortuitously had crossed our instrumentation site in Huntsville (HSV).

2 Greeley examples

The first two examples from Greeley are taken from long duration but intermittent rain event, which was part of a mid-latitude synoptic-scale cyclone that produced different types of rain ranging from light stratiform to strong convective (Thurai et al., 2017). The set of plots in panel (a) in Fig. 2 show the 3-min DSD measurements (09:48 - 10:00 UTC) during light precipitation. Superimposed is their corresponding generalized gamma fitted curves in red. Values of D_m for these cases were ~ 0.5 mm, which is expected for DSDs mostly consisting of small drops (maximum drop diameters < 1.2 mm). CSU-CHILL S-band radar RHI scan made over the instrument site (panel (b)) shows around 10 dBZ at 13 km range to the instrumented site. The rain system was shallow with low echo tops and no bright-band. LDR (linear depolarization ratio in panel (c)) does not show any bright-band either. The drizzle mode is clear for D<0.5 mm with a distinct concave upwards shape; this mode causes the D_m to be smaller and the spectral width to be larger than DSDs measured only by 2DVD as described in Thurai et al. (2017).

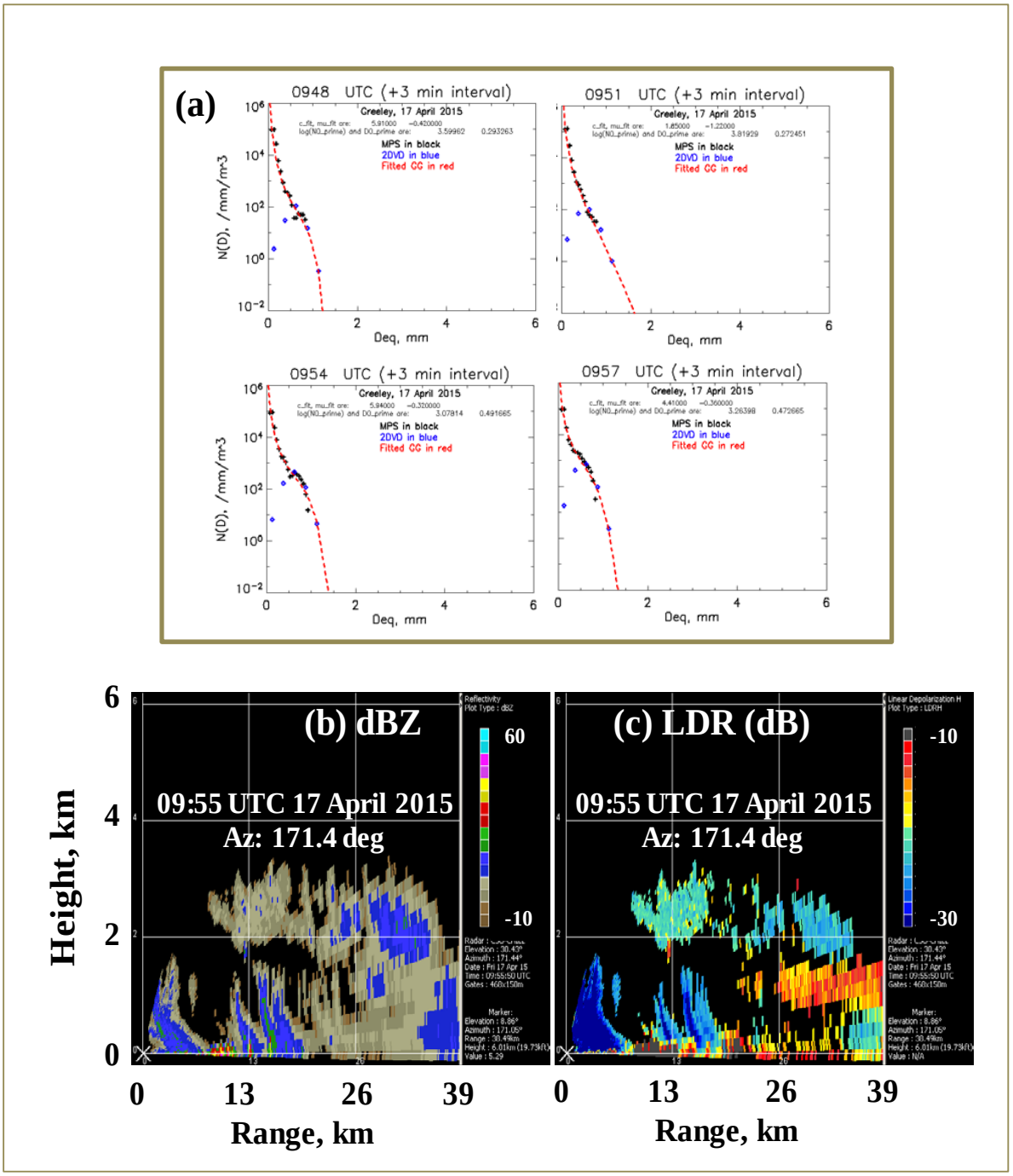


Fig. 2: *(a) Light rain DSDs during the 17 April 2015 event at Greeley (GXY). (b) dBZ from CHILL S-band RHI over the disdrometer site (13 km range); (c) the corresponding LDR. In (a) MPS data are in black, 2DVD data in blue and the GG fitted curve in red.*

The second example, shown in Fig. 3 is taken during stratiform rain period at the disdrometer site (on the same day). Panel (a) shows two 3-minute DSD measurements at 13:21 to 13:27 UTC. Somewhat larger drops were recorded, and D_m values were around 1 and 0.8 mm respectively. Once again, the drizzle mode is evident. The CHILL S-band RHIs over the disdrometer site at 13:23 UTC are shown in panels (b) and (c). Very clear bright band can be seen from the LDR plot.

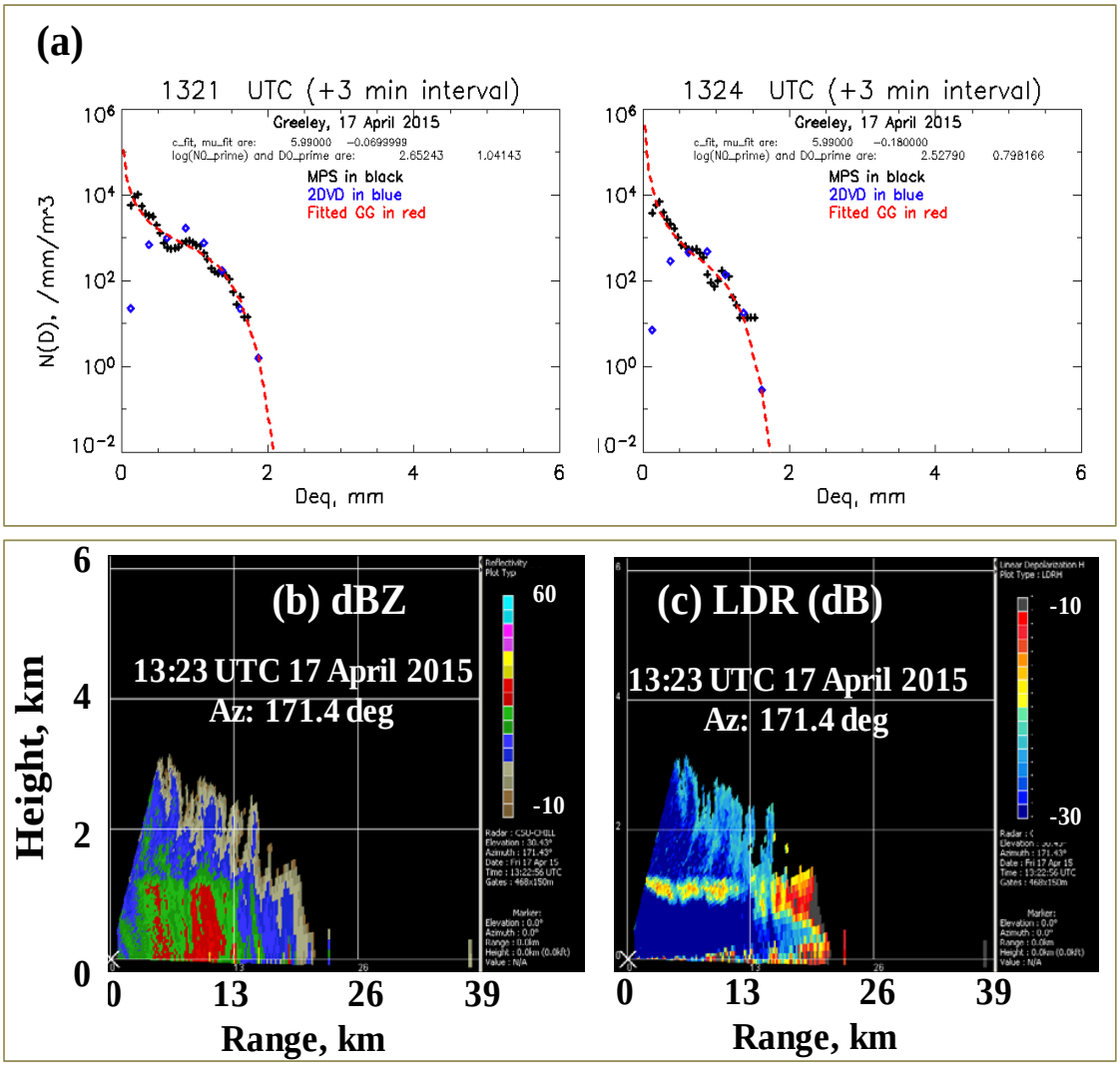


Fig. 3: *(a) Stratiform rain DSDs during the 17 April 2015 event at Greeley (GXY). (b) dBZ from CHILL S-band RHI over the disdrometer site (13 km range); (c) the corresponding LDR. In (a) MPS data are in black, 2DVD data in blue and the GG fitted curve in red.*

The third example is from a convective event which occurred on 10 Aug 2015 and which lasted for about 35 minutes over the disdrometer site. Panel (a) shows two 3-minute DSD measurements at 21:57 to 22:03 UTC. Significantly larger drops were recorded (D_{max} > 4.5 mm), and D_m values were around 2.4 and 2.1 mm respectively. Once again, the drizzle mode is evident. The CHILL S-band Z over the disdrometer site taken at 22:02 UTC is shown in panel (b) and the corresponding Z_{dr} is shown in panel (c). 40-45 dBZ values can be seen at 13 km range, and ~2 dB Z_{dr}, being consistent with the large drops seen in panel (a).

In all three cases, i.e. Fig. 2, 3, and 4, the fitted GG curves are seen to closely represent the composite DSDs. A further example can be seen in Thurai et al., (2017b), which shows animation of a 90-minute event on 23 May 2015 during which the 3-minute rainfall rate reached a maximum of over 60 mm/h. There too the fitted curves can be seen to closely represent the composite DSD data throughout the 90 minute period.

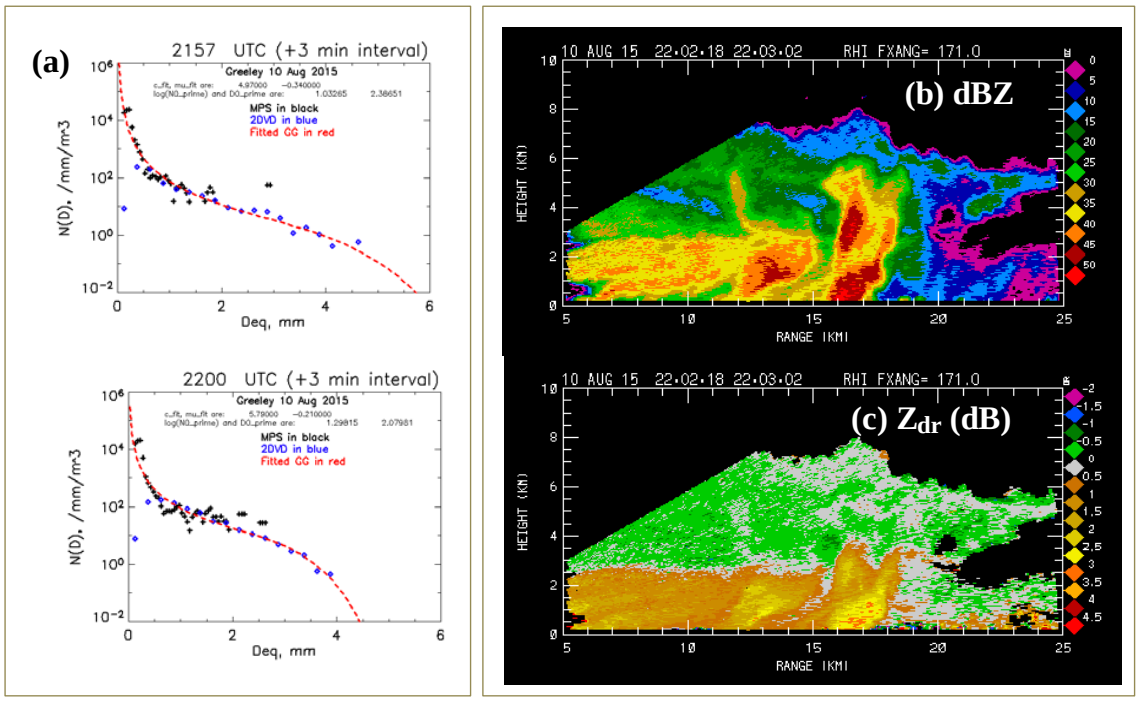


Fig. 4: *(a) Convective rain DSDs during the 10 Aug 2015 event at Greeley (GXY). (b) dBZ from CHILL S-band RHI over the disdrometer site (13 km range); (c) the corresponding Z_{dr}. In (a) MPS data are in black, 2DVD data in blue and the GG fitted curve in red.*

3 Huntsville examples

3.1 Outer bands of Hurricane Irma

On 11-12 September 2017, the outer rain bands of Hurricane Irma produced rainfall for more than 8 h over our instrumented site at UAH leading to unique data sets of the evolution of the drop size, shape, and fall speed distributions over the entire size range. The radar mosaic map of the Irma outer bands at 00:55 UTC on 12 Sept 2017 is shown in Panel (a) of Fig. 5. Collocated with the MPS and 2DVD (inside the DFIR as mentioned earlier) was a Precipitation Occurrence Sensor System (POSS, Sheppard and Joe, 2008). A 1-hour DSD comparison between the composite DSD and the POSS-based (calibrated) DSD is shown in panel (b). The agreement is very close, and the rise in the drop concentration in the sub-mm region is also evident in both datasets.

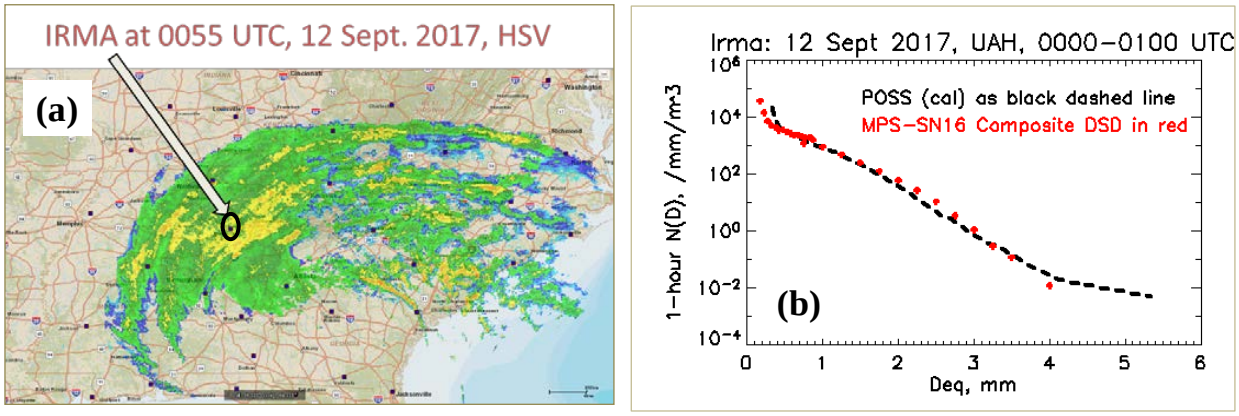


Fig. 5(a): *Radar mosaic image over SE US at 00:55 UTC on 12 Sept. 2017 (University of Alabama, Huntsville, UAH, is marked with an arrow); (b) a 1-hour DSD comparison between the MPS+2DVD (SN16) composite DSD and (calibrated, collocated) POSS-based DSD during the passage of Hurricane Irma outer bands, from 00 – 01 hr UTC on 12 Sept 2017.*

Four examples of 3-minute averaged "composite" DSDs constructed from MPS and 2DVD measurements on 12 Sept 2017 are shown in Fig. 6(a-d) in green, along with their fitted GG model in red. Once again, the fitted curves represent the measured data very well.

Panel (e) shows the reflectivity-height profiles from the UAH-XPR (after calibration) vertically-pointing X-band Doppler radar, from 00:00 to 06:00 UTC. Melting layer is evident throughout the event but with variable thickness and intensity. Panels (f) and (g) show the N_W and D_m variations derived from the 1-minute composite DSDs for 00 – 06 hr UTC. Some variation in D_m can be seen; during the thick bright-band period of 03-04 hr, Dm values reach 1.5 mm whereas during weak rain period after 05:30 UTC, they go below 1 mm. Fitted values of [μ_{GG}, c] are shown in panels (h) and (i), respectively. The shape parameter μ_{GG} appears to be relatively steady whereas the second shape parameter c exhibits somewhat more variability, attaining some of its lowest values during the thick BB period. Panel (d), at 03:15 UTC shows that N(D) of 10^{-2} /mm/m^3 from the fitted GG corresponds to the highest drop diameter (~ 4.5 mm) amongst the four panels.

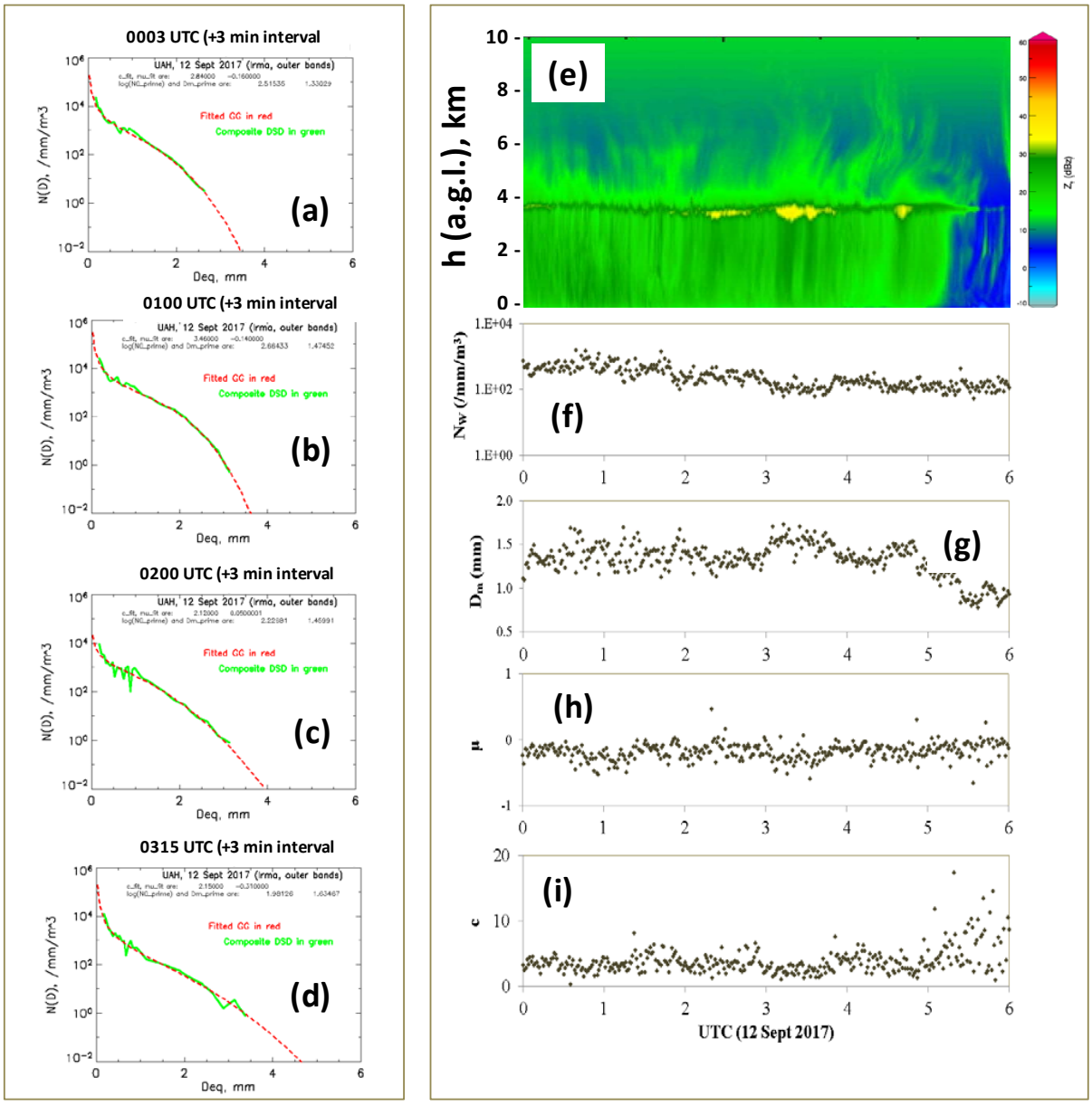


Fig. 6: *(a) to (d): Four examples of 3-minute composite DSDs (light green) from Irma outer bands, along with their GG fits; (e) Vertical profiles of reflectivity from UAH-XPR Doppler radar (courtesy of Prof. Knupp et al., at UAH); (f) N_W from the ground-based 1-minute composite DSD; (g) the corresponding D_m; (h) the fitted μ, and (i) the fitted c values.*

3.2 Tropical storm Nate

Fig. 7 shows an example of shallow or weak rain, which was part of the tropical storm Nate that had also traversed our instrument site at UAH. Panels (a) and (b) show, respectively, the Z and mean Doppler velocity versus time from the XPR for 17-18 UTC. A weak bright-band is noted near 5 km with echo tops < 5.6 km height, which is apparent in the mean Doppler velocity starting at 1700 UTC when the DSD shows a drizzle mode (panel c). After 1754 UTC, the echo tops are very shallow and entirely warm rain; the DSD now has a distinctly different shape at the small drop end (convex down). While these echoes are from the remnants of Nate after landfall, nevertheless they could have some oceanic characteristics. Martner et al. (2008) report on such shallow echoes without bright-band as well as echoes with BB and note very distinct DSDs between the two.(In general however, oceanic rain tend to have more dominant component of small drops concentration, for example, Thompson eta l. 2015).

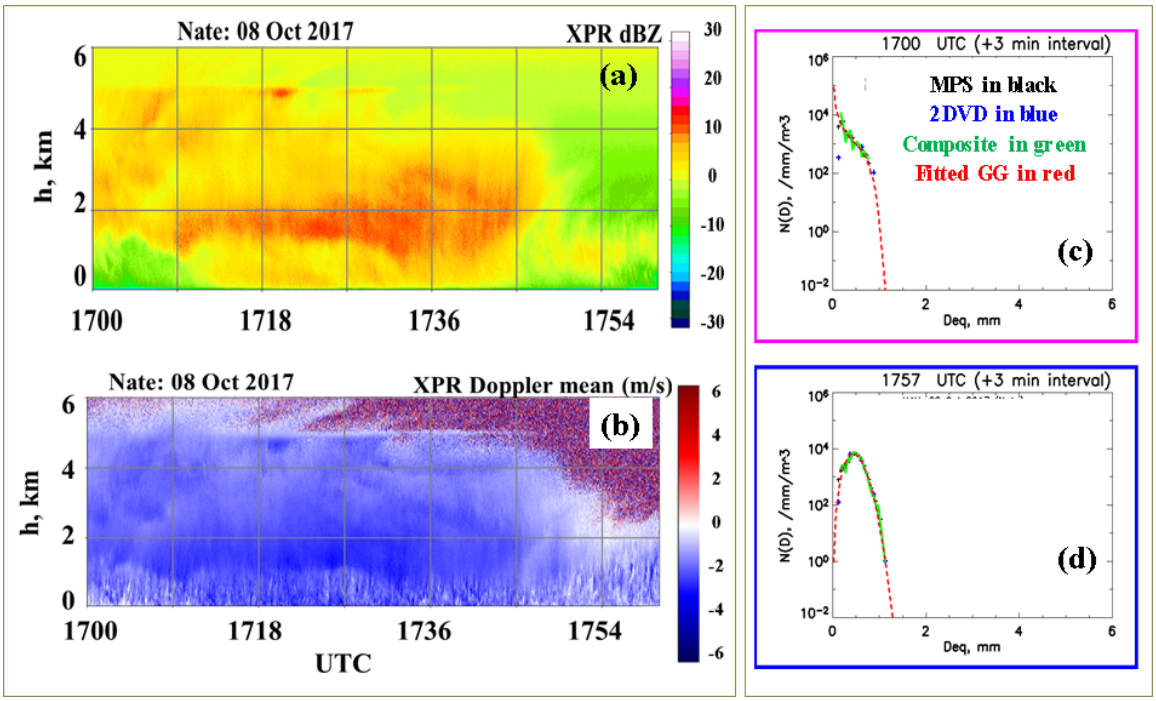


Fig. 7: (a) *XPR observations of dBZ (time-height cross-sections) during tropical storm Nate; (b)mean Doppler velocity (courtesy of Dustin Conrad and Prof. Kevin Knupp); (c) DSDs during weak bright-band, low Z/R, period (in pink box) and shallow warm rain (in blue box). The composite DSDs are shown as green curve in panel (c). As in Fig. 1(a), the GG curves show excellent fits to the composite DSDs.*

Another time period during Nate is shown in Fig. 8. The middle panel shows the XPR Z plot for 1500-1600 UTC. Some examples of the 3-min composite DSDs are shown surrounding panels whose times are 'connected' to the center panel with blue lines. At 15:24 there is some discrepancy between the MPS and 2DVD data, which corresponds to the highly bent vertical profiles of Z. This observation is noteworthy. It is possible that unusual size sorting may be occurring during this time period. It also appears that there may be some growth occurring in the lowest 1-km. Other cases show (as before) very close representativeness of the GG fitted curves to the data.

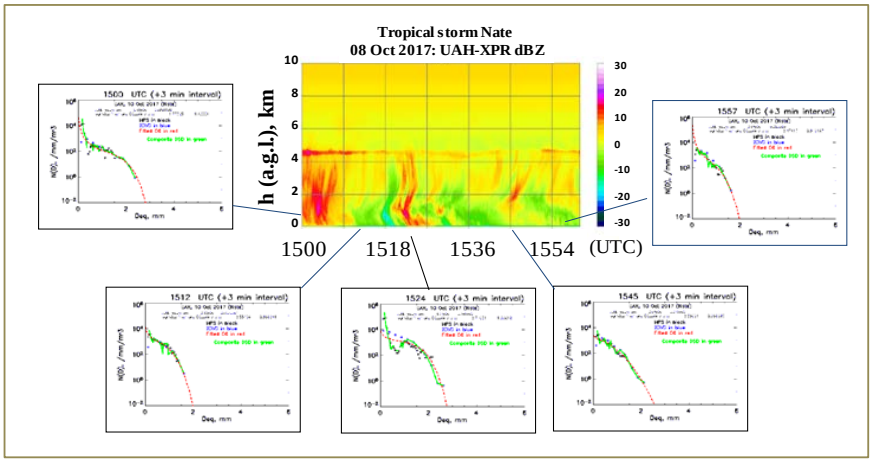


Fig. 8: *15:00-16:00 UTC during Nate. Center panel shows the dBZ height profiles from UAH-XPR and the surround panels show examples of 3-minute DSDs at various times.*

4 Overall assessment

In section 1 we referred to the compact representation for $N(D)=N_0$' h(x), as shown by Lee et al. (2004; their eq. (43), and based on earlier work by Testud et al., 2001). In our composite DSD datasets, we have seen that h(x) can be best represented in terms of the generalized gamma form with the two shape parameters (μ_{GG} , c) so that it can simultaneously fit the small drop and large drop ends together with a 'shoulder' region in between (Thurai and Bringi, 2018). The stability of h(x) has been demonstrated using Parsivel disdrometer data for stratiform rain by Raupach and Berne (2017), but with the caveat that the small drop end could not be accurately characterized. Here we show the stability of h(x) at the Greeley site (GXY) in Fig. 9, panel (a) using contoured frequency of occurrence plots of $h(x) = N(D)/N_W$ versus $x = D/D_m$, for a large number of 1-minute DSDs during rain-only events. Overlaid onto the plot is the optimized, or most probable, GG fit where the small drop end (actually x<0.5) has a concave up shape while the large drop end (x>2) falls faster than an equivalent exponential (e.g., due to drop break-up). Histograms of the fitted values of the two shape parameters are shown in panels (b) and (c). Whereas μ shows a narrow histogram, mostly within -1 to +0.2, values of c show wider distribution. In panel (b), the standard gamma value for c=1 is marked in magenta. Clearly, it is not the most probable value. In fact, in Thurai and Bringi (2018), we show in Table 2, that less than 17% of the cases had c values in the range 0.5 to 1.5. Moreover, heuristic goodness-of-fit methods were used to demonstrate that the generalized gamma model outperforms the SG model which has only one shape parameter.

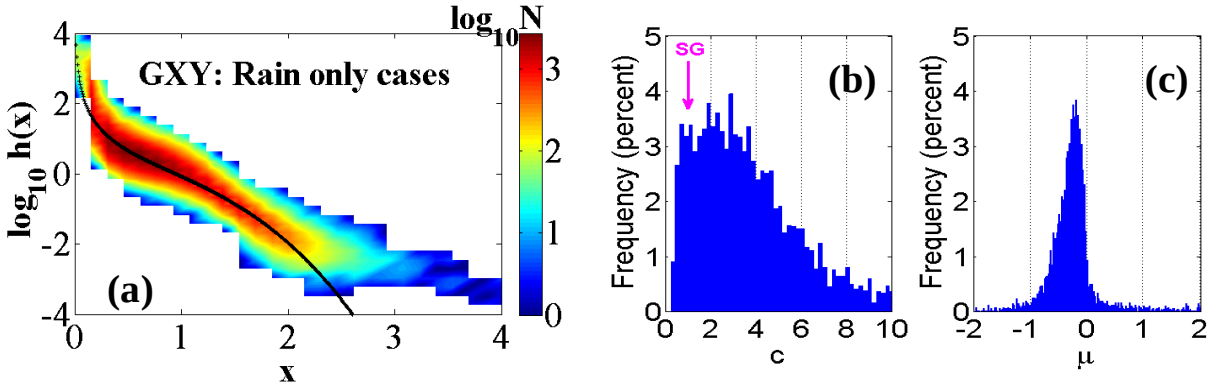


Fig. 9: *(a) h(x) versus x in terms of frequency of occurrence (color) and the most probable variation (black curve); (b) and (c) histograms of fitted c and μ values from a large number of 1-minute DSDs from rain-only events at Greeley.*

To illustrate the goodness of fit, in Fig. 10 we show histograms of the normalized bias for various drop diameter intervals. For each histogram, the center diameter (in mm) is shown on top. For the small drops, diameter interval in 0.05 mm (MPS resolution), and for the larger drops (> 0.75 mm), the diameter interval was set to 0.25 mm. In most cases, the bias appear to be fairly close to 0, and histograms are Gaussian-like, but larger diameters have broader histograms because of less no. of points, which is to be expected. The total number of 1-minute points, altogether, was 12177, taken from both GXY and HSV events.

Finally in Fig. 11 we show the variation of D_m versus σ_M, the standard deviation of mass spectrum, derived for the same 12177 1-minute DSDs. The color intensity plot represents the frequency of occurrence corresponding to the data itself and those derived from the GG fits are shown as black dots. Most of these points lie well within the 'higher frequency region', giving further confirmation of the high representativeness of the GG fits. We have also included three curves, one in black and the other two in gray. They represent the equations (22) – (24), given in Williams et al. (2014), with the black curve showing the most likely variation and the gray lines the upper and lower bounds. The underestimation of σ_M from these curves is largely due to lack of the small drops (MPS) data being included in their DSD data.

5. Conclusions

We believe that we have answered the question in the title 'Why Generalized Gamma" not necessarily via statistical testing but based on fidelity of the visual fits to our composite DSD data, especially for those which have double curvature. Also when μ_{GG} is slightly negative, it controls the shape at the small drop end simultaneously with c controlling the shape at the large drop end. This, the standard gamma with c=1 and negative μ_{SG} cannot do. Although the generalized gamma has been shown to better represent the full DSD spectrum, additional research is required on the sensitivity of its shape parameters, especially c, to rainfall type and meteorological regime in order to apply this DSD model to existing radar-based rainfall retrieval algorithms.

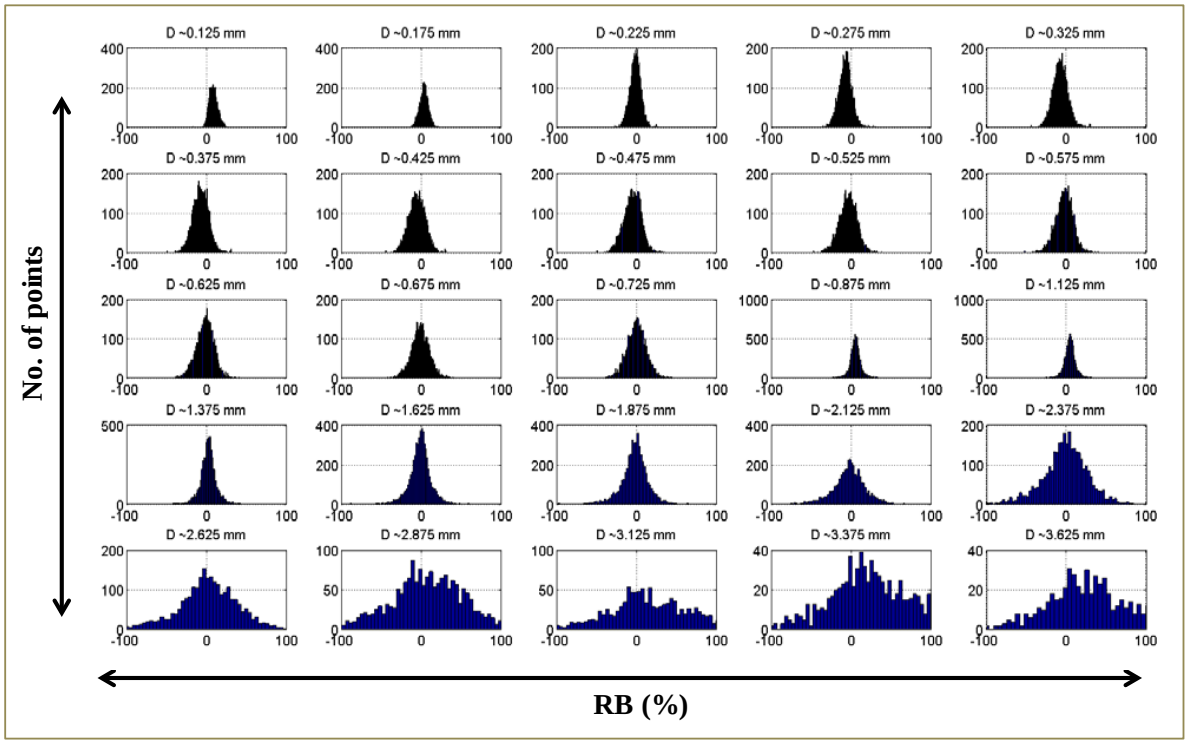


Fig. 10: *Histograms of the normalized bias for various drop diameter range. The center diameter is on top of each panel*

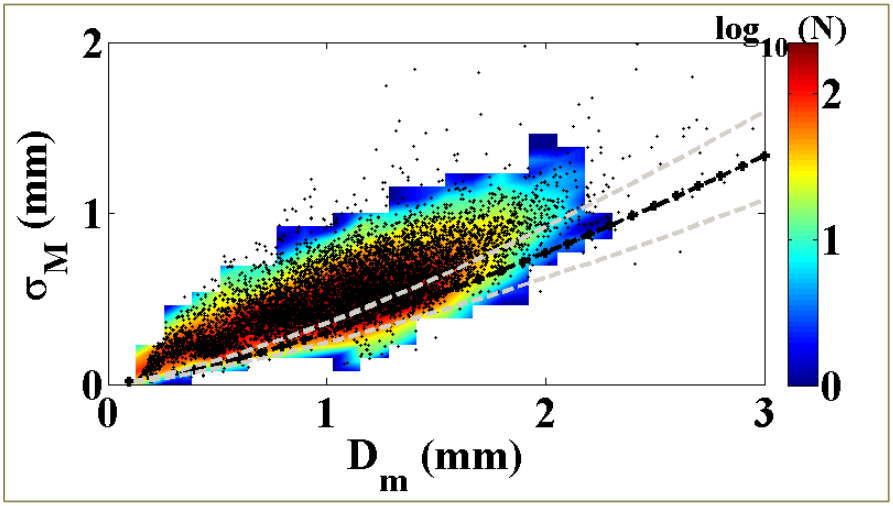


Fig. 11: *D_m versus σ_M from 7435 1-minute DSDs (color intensity) compared with the corresponding GG-fitted variations. The black line is eq. (22) of Williams et al (2014) and the grey lines are their eq. (23) and eq. (24).*

Acknowledgements

We would like to thank Professor Kevin Knupp of University of Alabama, Huntsville, and his team for supplying the XPR data/images during the Hurricane Irma event as well as tropical storm Nate. We also wish to thank Drs. Tim Raupach and Alexis Berne for their collaboration in the data analyses presented in this paper. MT and VNB acknowledge support by the U.S. National Science Foundation under Grant AGS-1431127, and additional support from NASA's Global Precipitation Measurement program through Award NNX16AD47G.

References

Adirosi, E., Gorgucci, E. Baldini, L., and Tokay, A. Evaluation of gamma raindrop size distribution assumption through comparison of rain rates of measured and radar-equivalent gamma DSD. J. Appl. Met. Clim. 2014: Vol 53, pp. 1618–1635.

Auf der Maur, A. N. Statistical tools for drop size distribution: Moments and generalized gamma. J. Atmos. Sci. 2001: Vol. 58, pp. 407–418.

Deirmendjian, D. Electromagnetic Scattering on Spherical Polydispersions. Elsevier. 1969: 290 pp

Delanoe, J. M. E., Heymsfield, A. J. Protat, A. Bansemer, A. and Hogan, R. J. Normalized particle size distribution for remote sensing application. J. Geophys. Res. – Atmospheres. 2014: Vol. 119 (7), pp. 4204-4227.

Hess, M., Koepke, P. and Schult, **I.** Optical properties of aerosols and clouds: The software package OPAC. Bull. Amer. Meteor. Soc. 1998: Vol. 79, pp. 831–844.

Kuo, K., Smith, E. A., Haddad, Z., Im, E., Iguchi, T., and Mugnai, A. Mathematical–Physical Framework for Retrieval of Rain DSD Properties from Dual-Frequency Ku–Ka-Band Satellite Radar. J. Atmos. Sci., 2004: Vol. 61, pp. 2349–2369.

Lee, G., Zawadzki, I. Szyrmer, W. Sempere-Torres, D. and Uijlenhoet, **R.** A general approach to double-moment normalization of drop size distributions. J. Appl. Meteor. 2004: Vol. 43, pp. 264–281.

Martner, B. E., Yuter, S. E. White, A. B. Matrosov, S. Y. Kingsmill, D. E. and Ralph F. M. Raindrop size distributions and rain characteristics in California coastal rainfall for periods with and without a radar bright band. J. Hydrometeorol. 2008: Vol. 9, pp. 408–425.

Petty, G. W., and Huang, W. The modified gamma size distribution applied to inhomogeneous and non-spherical particles: Key relationships and conversions. J. Atmos. Sci. 2011: Vol. 68, pp. 1460–1473.

Raupach, T. H., and Berne, A. Invariance of the double-moment normalized raindrop size distribution through 3D spatial displacement in stratiform rain. J. Appl. Meteor. Climatol. 2017: Vol. 56, pp. 1663–1680.

Raupach, T. H., Thurai, M., Bringi, V. N. and Berne, A. Reconstruction of the drizzle mode of the raindrop size distribution: An approach using double-moment normalization, 2018a: 10th European Conference on Radar in Meteorology and Hydrology (ERAD 2018), organized by KNMI and Wageningen University, Netherlands, 1 - 6 July 2018.

Raupach, T. H., Thurai, M. Bringi, V. N. and Berne, A. Reconstructing the drizzle mode of the raindrop size distribution using double-moment normalization, 2018b: Manuscript submitted.

Sheppard, B. E., and Joe, P. I. Performance of the precipitation occurrence sensor system as a precipitation gauge, J. Atmos. Oceanic Technol. 2008: Vol. 25, pp. 196 –212.

Testud, J., Oury, S., Black, R. A. Amayenc, P. and Dou, X. K. The concept of ‘‘normalized’’ distribution to describe raindrop spectra: A tool for cloud physics and cloud remote sensing. J. Appl. Meteor., 2001: Vol. 40, pp. 1118–1140.

Thompson, E. J., Rutledge, S. A. Dolan, B. and Thurai, M. Drop size distributions and radar observations of convective and stratiform rain over the equatorial Indian and west Pacific Oceans. J. Atmos. Sci., 2015: Vol. 72, pp. 4091–4125,

Thurai, M., Gatlin, P. Bringi, V. N. Petersen, W. Kennedy, P. Notaros, B. and Carey, **L.** Toward completing the raindrop size spectrum: Case studies involving 2D-video disdrometer, droplet spectrometer, and polarimetric radar measurements, J. Appl. Meteor. Climatol., 2017a: Vol. 56, pp. 877–896.

Thurai, M., Kennedy, P. C. and Bringi, **V.N.** Modeling observed drop size distributions: 23 May 2015. CSU-CHILL National Radar Facility Website, 2017b: accessed 1 October 2017, available online: *http://www.chill.colostate.edu/w/DPWX/Modeling_observed_drop_size_distributions:_23_May_2015.*

Thurai, M., and Bringi, V. N. Application of the generalized gamma model to represent the full DSD spectra. J. Appl. Meteorol. and Climat., 2018: Vol. 57, pp. 1197–1210.

Vivekanandan, J., Martner, B. E. Politovich, M. K. and Zhang, G. Retrieval of atmospheric liquid and ice characteristics using dual-wavelength radar observations. IEEE Trans. Geosci. Remote Sens., 1999: Vol. 37, pp. 2325–2334.

Williams, C. R., and Coauthors. Describing the Shape of Raindrop Size Distributions Using Uncorrelated Raindrop Mass Spectrum Parameters. J. Appl. Meteor. Climatol., 2014: Vol. 53, pp. 1282–1296.

Wu W. and McFarquhar, G. M. Statistical theory on the analytical form of cloud particle size distributions, J. Atmos. Sci. 2018: Accepted for publication

QUANTITATIVE PRECIPITATION ESTIMATION BY X-BAND POLARIMETRIC RADAR NETWORK OF KOCHI UNIVERSITY

Akira Nishii[1] and Koji Sassa[2]

[1]*Graduate school of Kochi University, 2-5-1, 780-8072 Akebono-cho, Kochi-shi, Kochi, Japan*
[2]*Kochi University, Kochi, 2-5-1, 780-8072 Akebono-cho, Kochi-shi, Kochi, Japan*

(Dated: 2 July 2018)

1 Introduction

Kochi prefecture locates in the south part of Shikoku Island divided by Shikoku mountains of more than 1500 m in height, and it also faces warm and moist Pacific Ocean. Then, this area is one of the heaviest rainfall area in Japan. Annual precipitation amounts in Kochi city and in mountain area are about 2,500 mm and more than 3000 mm, respectively. Heavy rain events of more than 50 mm/h occur frequently. Many heavy rain events are affected by complex terrain of Kochi Prefecture. Warm rain events are also frequently observed. Moreover, tornadoes often occur. Japan Meteorological Agency (JMA) provides the 2km CAPPI data obtained from its C-band radar network every 5miniutes. We often miss cumulonimbi developing rapidly and approaching tornadoes. As another monitoring system, Ministry of Land, Infrastructure and Transport (MLIT) has constructed X- and/or C- band polarimetric radar network called XRAIN providing the data every 1 minute. However, only a C-band polarimetric radar located in a high mountain (1500 m above sea level) covers Kochi prefecture and there is no X-band polarimetric radar covering this area. Therefore, we have been constructing our own X-band polarimetric radar network to complement the other radar networks in Kochi prefecture. At this time, we have installed 5 X-band polarimetric radars and one more radar will be installed in October 2018. We have also developed quasi-real time Quantitative Precipitation Estimation (QPE) system providing 1km CAPPI data of 150 m in spatial resolution every 1 minute from our radar network. QPE by X-band polarimetric radar have achieved very high performance in many studies (e.g., Maki et al., 2005). Especially QPE with specific differential phase K_{DP} achieves high performance because K_{DP} is less sensible of the variation of Drop Size Distribution (DSD) and can compensate attenuation by rainfall (Park, et al., 2005). The present study aims to verify our QPE system. We evaluated of QPE from three radars at Asakura, Monobe, and Aki radar sights. We also introduce our polarimetric radar network system.

2 Kochi University Polarimetric Radar Network

Figure 1 shows the arrangement of Kochi University X-band polarimetric radar network. 5 radars have currently installed and they cover the most part of Kochi prefecture. Asakura, Monobe, Aki radars shown in green circles have been operated for more than three years. In this year, we installed Susaki and Tosashimizu radars shown by yellow circles in western Kochi. Kuroshio radar shown by red circle will be settled in October 2018. The observation range of Asakura radar is 80 km and those of the other radars are 30km. In the present study, we evaluated QPE for three radars; Asakura, Monobe and Aki because they have a lot of data for more than two years. The specifications of these radars are listed in table 1. Our radars are relatively

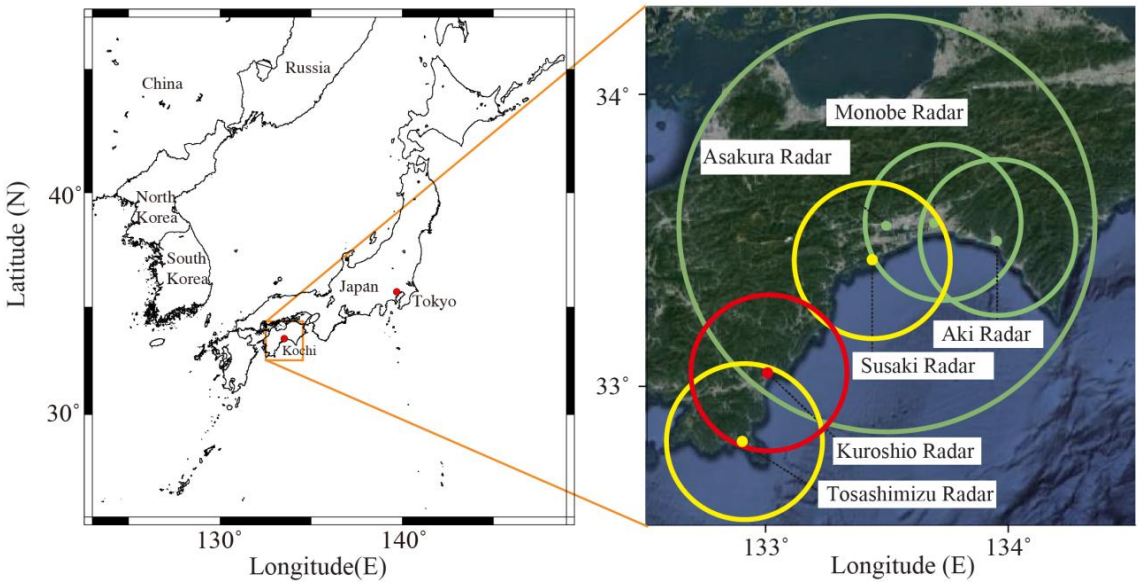


Figure 1:The location of Kochi and Kochi University radar network.
Points and circles represent radar locations and observation ranges, respectively.

Table 1: System specifications of Kochi University's radars.

	Asakura	Monobe, Aki
Frequency	9.39 GHz	9.47 GHz
Beam width	2.0 deg	2.7 deg.
Range resolution	150 m	50 m
Observation range	80 km	30 km
Update time	1 min (low elev.) 5 min (high elev.)	1 min

cheap and compact then the beam widths are slightly wide. But, range resolutions are high. At this time, we operate Asakura radar in the volume scan mode composed of 3 PPI scans of 2.5, 4.0 and 6.0 deg. in elevation angle every 1 minute and 5 PPI scans at higher angles up to 20 deg. every 5 minutes though the elevation angles employed for the validation of QPE were slightly different as mentioned later. Monobe and Aki radars are operated in 5 PPI scans from 3.0 deg. to 16 deg. every 1 minutes. These observation data are immediately transferred to science cloud at National Institute of Information and Communications Technology (NICT) and converted into rainfall intensity R [mm/h]. R is provided as 1km CAPPI data with of 150 m × 150 m in spatial resolution. It takes less than one minute from the volume scan of each radar to make radar network data. We adopted lower altitude for CAPPI data than those provided by JMA or XRAIN (2 km altitude) because we wanted to observe the altitude near the surface as well as possible in complex terrain of Kochi prefecture and expected to observe warm rain which developed at lower altitude. To make CAPPI from PPI data observed by each radar, we employed Cressman interpolation method (Cressman, 1959). The sampling radius of the interpolation are defined as follows;

For Asakura radar (r is a distance from radar [km]);

Horizontal sampling radius [km]: $0.01r + 0.1$ *(2.1)*

Vertical sampling radius [km]: 0.75 (constant.) *(2.2)*

For other radars;

Horizontal sampling radius [km]: $0.02r + 0.2$ *(2.3)*

Vertical sampling radius [km]: 2.5 (constant.) *(2.4)*

The difference in sampling radius is based on the observation range and the adopted PPI elevations for CAPPI. Figure 2 shows the example of CAPPI data of our radar network. We employed the highest value of precipitation intensity among each radar data in the area where more than two radars cover in order to compensate rain attenuation.

3 Quality Control of Our Radar Network

Our radars are settled at relatively lower altitude in complex terrain area. Therefore, our radars are strongly affected by clutters and beam blockage by mountains. Moving Target Indicator (MTI) is applied in our radars to remove contamination by clutters (Aoyagi, 1983). However, it is not enough to remove clutters and many echoes remain even in sunny days as shown in the upper figures of Fig. 3. Then we made additional processing to remove clutters. For Asakura radar, both the original received power Pr and the MTI-processed power Pr_{MTI} are available. The reflectivity data are employed when the difference between Pr_{MTI} and Pr is more than 5 dBZ as shown in following inequality,

$$Pr_{MTI} - Pr \geq 5\ dBZ. \qquad (3.1)$$

Otherwise, the data were eliminated as clutters. Monobe and Aki radars do not output original Pr and do only MTI-processed radar reflectively Z. Therefore, we removed clutters by mapping. We checked strong reflectivity Z areas in sunny days affected by clutters and removed them. Results of these elimination processes are shown in the lower figures of Fig. 3. Most of clutters are dramatically removed by these processes. Terrains also become as partial blockages of radar beam. In far side of such terrains, Z becomes lower even heavy rainfall and QPE is underestimated. To avoid such situation, we masked partial beam blocked area. Figure 4 shows the examples of masked areas. We employed the PPI data obtained at higher elevation angles to interpolate Z and K_{DP} eliminated as clutters. Moreover, the data in the region where ρ_{hv} was less than 0.60 were eliminated to remove echo returning from a non-meteorological target. We also made the attenuation correction with the method of Maesaka et al.(2014) to correct rain attenuation.

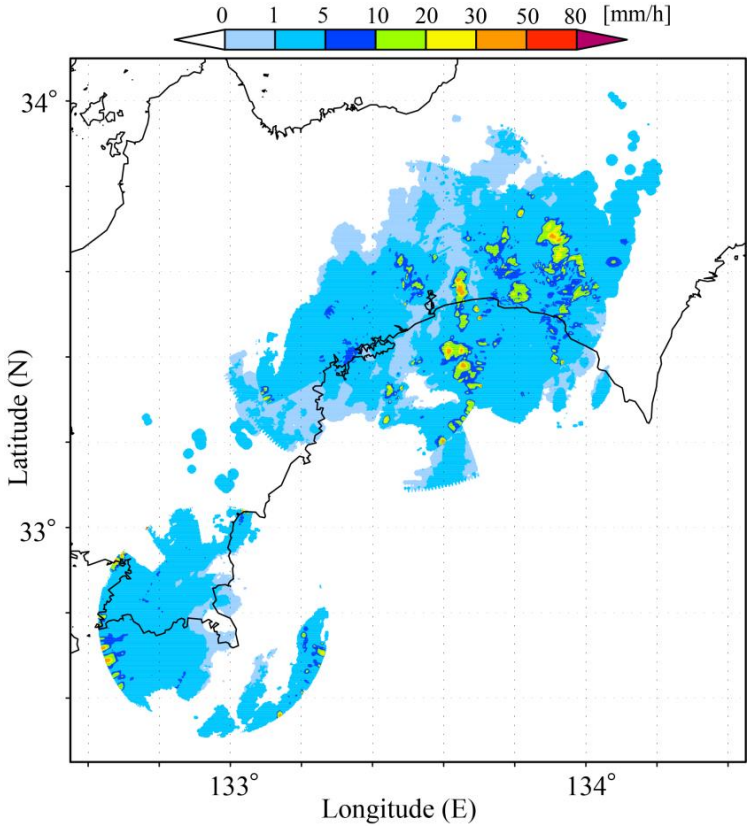


Figure 2: A picture of rainfall intensity derived from the radar network. This shows CAPPI at a height of 1 km. (At 09:06 UTC, May 13, 2018)

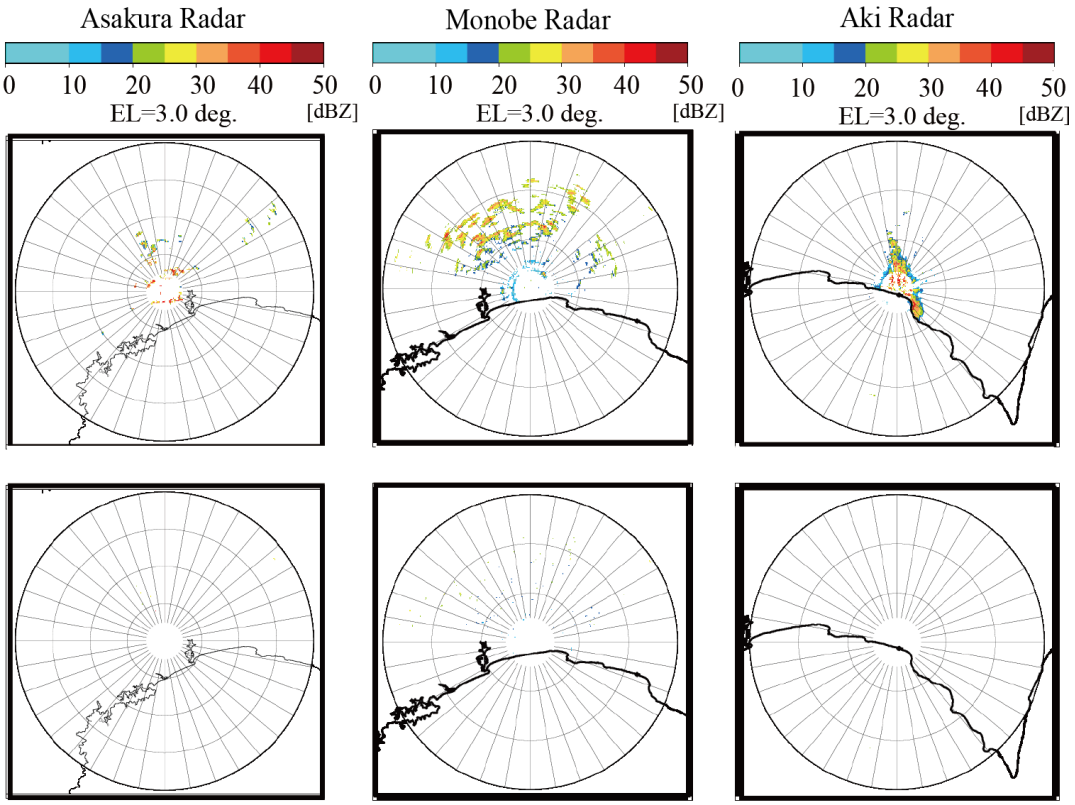


Figure 3 PPI images of reflectivity before (a) and after (b) removing clutter by our methods.

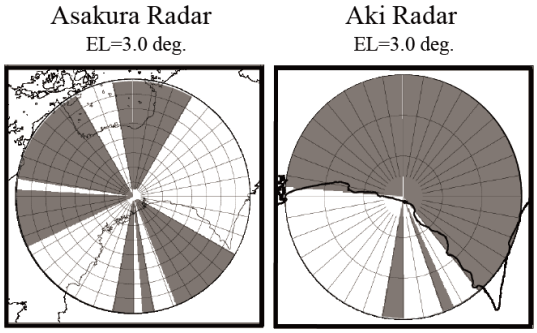


Figure 4 Examples of masked area shown in gray shade.

4 QPE by radars

We employed specific differential phase K_{DP} [deg./km] and horizontal radar reflectively Z [mm^6/m^3] in QPE. We converted these parameters to rainfall intensity R [mm/h] by the following equations,

$$K_{DP} = \alpha \times 19.6 K_{DP}^{0.825} \ (Z \geq 30 \text{ dBZ and } K_{DP} \geq 0.3), \quad (4.1)$$

$$Z = BZ^{\beta}. \quad (4.2)$$

K_{DP}–R relationship (eq. 4,1) is based on Maki et al. (2005)'s equation derived from DSD observation in Tsukuba, Japan. But we found that this relationship underestimates rainfall intensity. Therefore, we introduced the correction coefficient, α=1.3. Such underestimation also occurs in XRAIN which uses the same α (Maesaka et al., 2014). K_{DP} is a good parameter for QPE because of its less sensitivity to DSD variation than Z and resistance to attenuation by rain (Park et al., 2005). But in weak rainfall, the value of K_{DP} is quite low and noise contamination is not negligible. Therefore, Z-R relationship was adopted for weak rain. The values of constant B and β in Z-R relationship (eq. 4,2) are decided for each radar by comparing between hourly rainfall observed by rain gauges and the integrated value of instantaneous Z for one hour as mentioned later.

5 Verification of QPE

To evaluate the accuracy of QPE defined in chapter 4, we compared radar rainfall R_r [mm] and gauge rainfall R_g [mm]. We picked up 4 heavy rainfall events (max hourly rainfall was more than 20 mm/h.) as shown in Table 2.

Table 2 Periods of events.
Note that date is in UTC and all event occurred in 2017.

Rainfall period
09:00 May 12 – 0:00 May 13
08:00 June 20 – 23:00 June 20
01:00 August 6 – 07:00 August 7
14:00 September 16 – 14:00 September 17

We used the PPI scan data of 3, 4, and 5 deg. in elevation angle for Asakura radar in order to validate QPE. The elevation angles slightly different from the current observation mode. For the validation of Monobe radar and Aki radar, we used 5 PPI scan data from 3 deg. to 16 deg. We also used 10 minutes rainfall intensity obtained from 30 rain gauges of JMA AMeDAS and POTEKA installed by us as shown in Fig. 5, in order to compare with rainfall intensity obtained by our radars. All rain gauges were tipping bucket type and minimum resolution is 0.5 mm. We compared with the radar data at 1 km height because we provided the CAPPI data at that height. But radar beam does not reach at some rain gauge sites because it is blocked by terrain. In such case we employed the data obtained from the PPI scan higher elevation angles but close to 1 km height.

Even after quality control, the observation error and the radio wave dissipation sometimes occur. Thus we removed the data in the following situations,

- R_g and/or R_r was 0 mm.
- There was at least 1 missing data in R_r.

6 Result of verification

Results of validation of *Z-R* relations are shown in Figure 6. We employed stratified average per 1 dBZ radar reflectivity from 20 dBZ to 30 dBZ for Z to calculate *B* and β. In addition to *Z-R* relationship variability for radar calibration, it is also largely affected by the variation of DSD and coefficients differs each rainfall type (e.g. Fujiwara (1965). It is impossible to

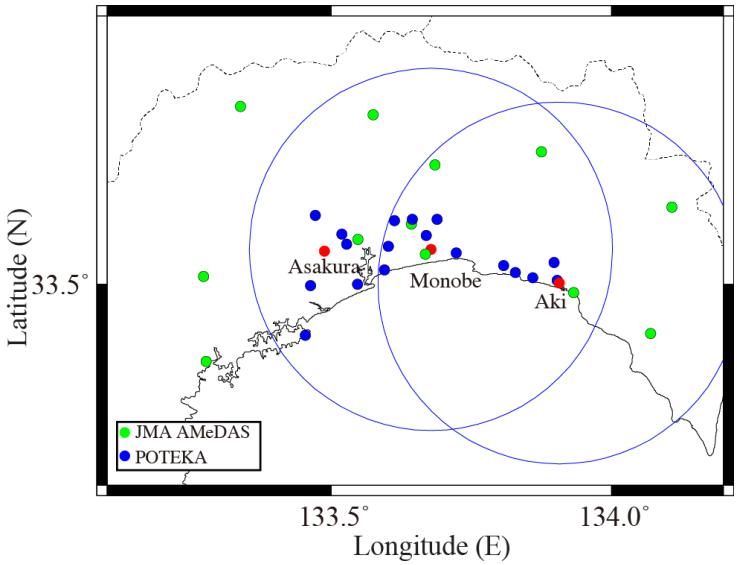


Figure 5 Map of rain gauges. Green dots and Blue dots denote the locations of JMA AMeDAS rain gauge and POTEKA rain gauge, respectively. Red points denote radar sites and blue circles represent the observation ranges of Monobe radar and Aki radar.

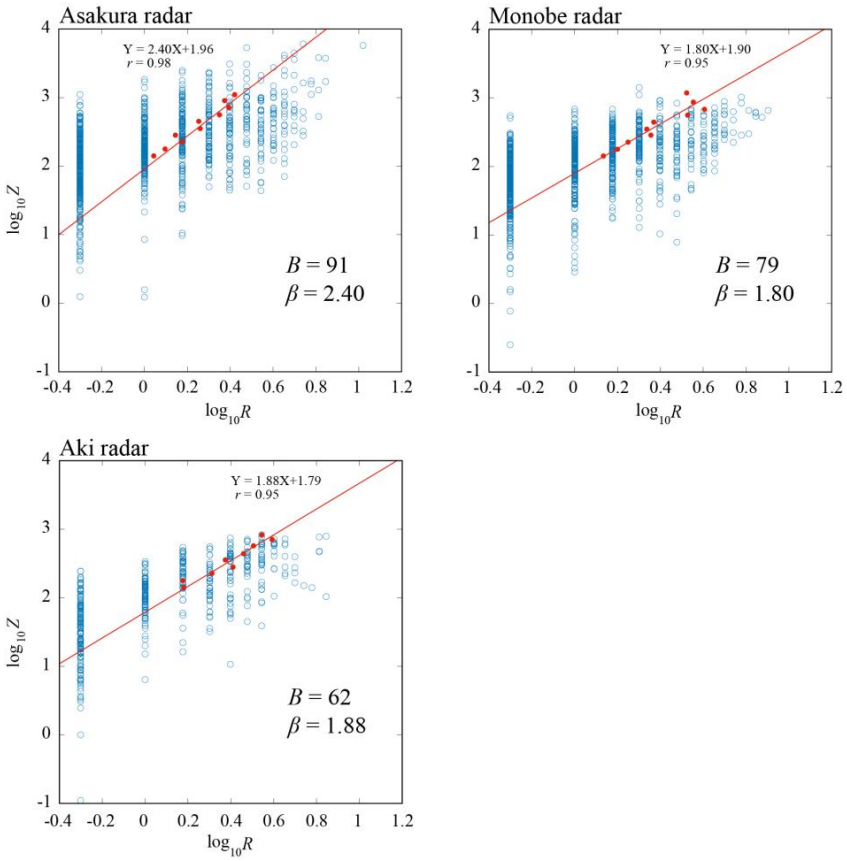


Figure 6 Logarithmic plots of Z-R relationship.
Red points show layer averages to calculate Z-R relationships and red lines shows regression line.

adopt *Z-R* relationship for each rain event, thus we employed unique coefficients for each radar.

Figure 7 shows the result of verification of total QPE. Asakura radar and Aki radar were found to slightly underestimate rainfall however correlation coefficients achieved about 0.80. each radar estimated rainfall almost accurately. For heavy rain case, K_{DP}-*R* relationship shown by green plots mainly contributes to QPE. We found that QPE with K_{DP}-*R* relationship showed high performance. The reason of underestimate is due to radio wave dissipation blocked by complex terrain. Especially, Aki radar locates near mountains. The PPI data at higher elevation angle to interpolate such masked region may not represent the actual clouds well. Asakura radar is also affected by complex terrain. On the other hand, Monobe radar locates at open plain field and not affected by clutters. Therefore, Monobe radar showed good performance, i.e., a = 1.01 and r = 0.79.

Figure 8 shows the result of a typical irregular observation point. The rain gauge at Kochi city hall located 3.8 km from Asakrua radar. In this case, Asakura radar strongly over-estimated the rainfall intensity. This rain gauge is also covered by Monobe radar but it did not show the abnormal data. Therefore, such results were not caused by the error of the rain gauge. Figure 9 shows the range dependence of differential phase φ_{DP} at the azimuth of 72 deg. which showed the direction of Kochi city hall. There is a peak of φ_{DP} near 5 km from Asakura radar. It is abnormal value because φ_{DP} should increase monotonically below a melting layer. It is not caused by switching between short and long pulses because the change from short pulse to long pulse is made at 10km from Asakura radar. In this study, we applied smoothing filter twice to smooth the fluctuation of φ_{DP}. Hubbert and Bringi (1995) used moving average filter for 10 times to remove φ_{DP} noises. But, the jump of φ_{DP} at 5 km will not be smoothed by filters. This may be caused by the ghost echo due to clutter in far distance, power cable crossing between Asakura radar and Kochi city hall and so on. The investigation of the reason is one of our future work.

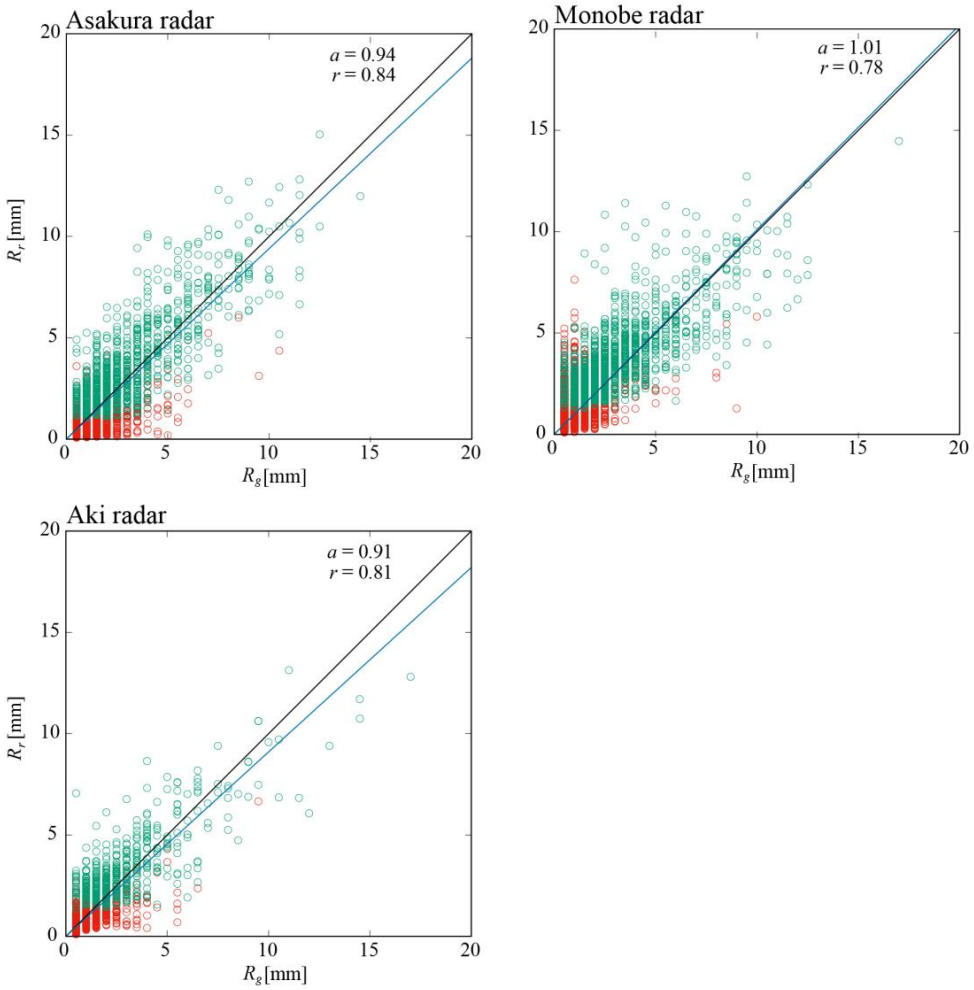


Figure 5 Scatter plots of Rr and Rg for each radar. Blue line and black line represent Rr=Rg and Regression line, respectively. Green plots indicate Rr estimated with K_{DP}-R relationship more than 50 % in estimated time and Red plots show Rr with Z-R relationship.

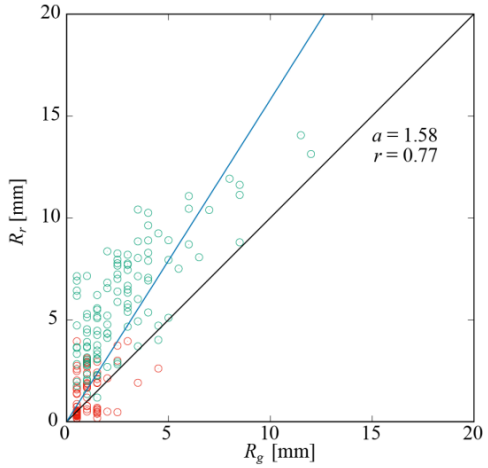


Figure 6 Scatter plots of Rr derived from Asakura radar and Rg at Kochi city hall. Blue line and black line represent Rr=Rg, Regression line, respectively. Green plots indicate Rr is estimated with K_{DP}-R relationship equal or more than 50 % in estimating time.

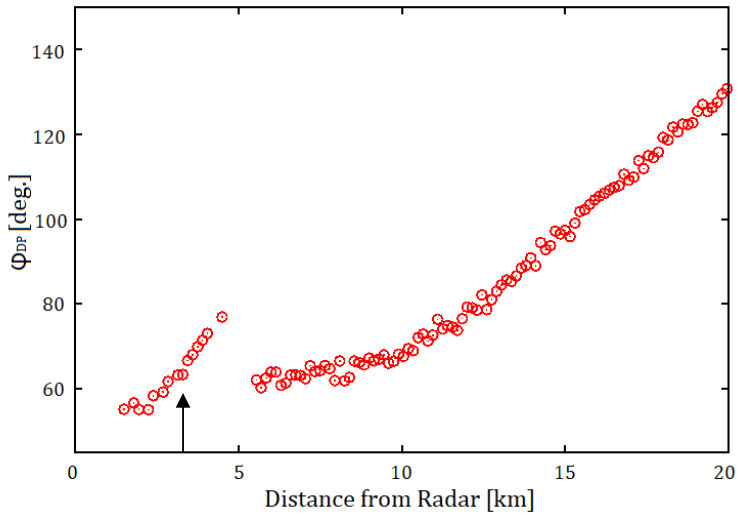


Figure 7 Range distribution of φDP observed by Asakura radar at PPI scan of 5.0 deg. in elevation angle. at 15: 28 JST, Sep. 17, 201. An arrow shows the location of Kochi city hall.

Table 3 shows the result of verification of QPE for each distance from radar. Except Monobe radar, the tendency of underestimation became remarkable at farer regions from radar. We considered that it was caused by two reasons. The first is the effect of altitude estimating *Rr*. The observation height becomes higher with the distance from radars. When cloud yielding rainfall developed lower altitude like as warm rain case, the radar beam passing in high altitude may return just weak echoes. Aki radar showed strongly this trend because low elevation beams blocked by mountains near Aki radar site and *Rr* farer than 10 km was estimated from the PPI scan at higher elevation angles. The altitude of about 3 km. Second is the azimuth resolution of radar beam. Because our radars are compact, beam widths are large as shown in Table 1. Then, the azimuth and height

Table 3 Regression and correlation coefficient at each distance

Distance from radar [km]	Asakura		Monobe		Aki	
	a	*r*	*a*	*r*	*a*	*r*
0-10	1.07	0.88	1.01	0.81	0.95	0.87
10-20	0.88	0.84	1.04	0.79	1.31	0.78
20-30	0.81	0.75	0.99	0.7	0.78	0.56
30-	0.72	0.68	-	-	-	-

resolution becomes worse with the distance from radars. At 20 km distance from a radar, the azimuth resolution of Asakura radar is approximately 670 and those of Monobe and Aki radar are 940 m.

7 Conclusion

We evaluated the accuracy of Quantitative Precipitation Estimation obtained from Asakura, Monobe, and Aki radars by comparing with rainfall intensity obtained by rain gauges. Asakura and Aki radars slightly underestimated rainfall intensity and Monobe radar showed good performance. The correlation between the radars and rain gauges were almost 0.8, which shows that QPE by our radars were accurate. On the other hand, radar underestimated rainfall at the regions far from radars. But we expect that this problem will be solved by merging radar data in our radar network.

We will make quality control of each radar data more to improve the accuracy of QPE and investigate the reason of abnormal reflectivity at some observation points as future works.

Acknowledgements

This research and development work was supported by the MIC/SCOPE 165009001. A part of rain gauge data was provided from Japan Meteorological Agency and Railway Technical Research Institute.

References

Aoyagi, J. ,1983: A study on the MTI weather radar system for rejecting ground clutter, Papers in Meteorology and Geophysics, Vol. 33, No. 4, pp. 187-243.

Cressman, G.P., 1959 : An operational objective analysis system, Monthly Weather Review, 87, pp. 367-374.

Fujiwara, M., 1965: Raindrop-size distribution from individual storms, Journal of Atmospheric Sciences, 22, 5, pp.585-591.

Hubbert, J. and Bringi, V.N., 1995: An iterative filtering technique for the analysis of copolar differential phase and dual-frequency radar measurements, J. Atmos. Ocean. Technol., 12, pp.643-648.

Maesaka, T., Maki,M., Iwanami, K., Tsuchiya, S., Kieda,K., and Hoshi, A. 2011: Operational rainfall estimation by X-band MP radar network in MLIT, Japan, Proc. of 35th Conf. on Radar Meteor, 142.

Maki, M., Part, S.-G., and Bringi, V.N., 2005: Effect of variations in rain drop size distributions on rain rate estimations of 3 cm wavelength polarimetric radar, Journal of the Meteorological Society of Japan, Vol. 83, No. 5, pp.871-893

Park, S.G., M. Maki, K. Iwanami, V. N. Bringi, and V. Chandrasekar, 2005: Correction of radar reflectivity and differential reflectivity for rain attenuation at X band. Part II: evaluation and application, J. Atmos. Ocean. Technol., 22, pp. 1633-1655.

Standard Operation Procedures (SOP) for Weather Radars Operation, Monitoring, Maintenance and Calibration.

Ljubov Liman,Timo Posio and Mikko Kurri
Finnish Meteorological Institute, Finland
(Dated: 21 June 2018)

1 Introduction

A standard operating procedure, or SOP, is a set of step-by-step instructions compiled by an organization to help workers carry out complex routine operations. SOPs aim to achieve efficiency, quality output and uniformity of performance, while reducing miscommunication and failure to comply regulations. The information collected in to SOP will help the present maintenance personnel in their work as well as the new maintenance personnel familiarizing themselves with operation, monitoring, maintenance and calibration procedures of radars.

This document was prepared as an example of a SOP document and is written in generic way enabling it to be used independently of the radar manufacturer or radar type. With the help of such SOP, the maintenance personnel can monitor, maintain and calibrate the weather radars and make sure that all operations and tasks are made and taken care of. These procedures are to be followed to minimize variation, reduce errors, and ensure accuracy in measurement of meteorological radar parameters.

Procedures should be provide a description of who does what, and when. An SOP characterizes relationships and control measures. It defines the roles and responsibilities to help workers “find themselves” in the process. Procedures should be clarify different decision points and provide the necessary guidance on criteria to make a decision.

This SOP will have a two-tiered system that includes both procedures and work instructions. The procedures provide a general view of the higher level steps, whereas work instructions are significantly more detailed. One advantage of a two-tiered system is that SOP change less often, whereas work instructions may need to be changed or updated more frequently due to changes in radar network structure, equipment, or software. In this document, examples of instructions are not specified.

SOP is written in a concise, step-by-step, easy-to-read format. Also, is used a flow charts to illustrate the process being described.

The SOP is prepared based on FMI radar team experience, Timo Posio’s engineering degree thesis “Functions, maintenance and calibration of the WRM200 weather radar" and an article "MAINTENANCE KEEPS RADARS RUNNING", BAMS 2017, Saltikoff et.al. …

2 Content of the Standard Operation Procedures (SOP) for Weather Radars Operation, Monitoring, Maintenance & Calibration

Standard Operation Procedures described in this document consists of five parts (Fig. 1).

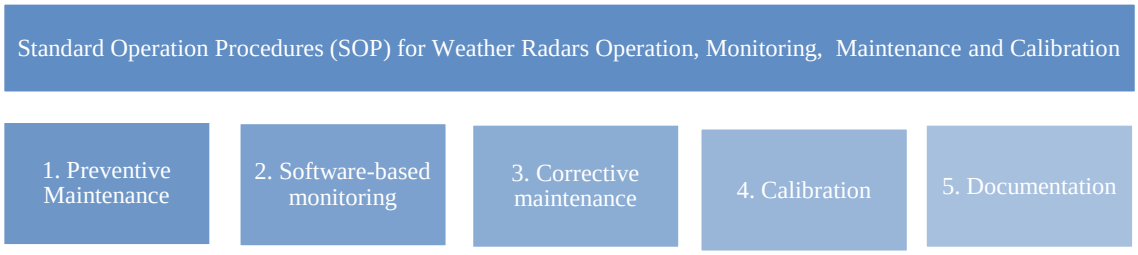


Figure 1: Contents of the Standard Operation Procedures (SOP) for Weather Radars Operation, Monitoring, Maintenance and Calibration.

The preventive maintenance (1) has an important impact on the quality of radar measurements and radar reliability. It is divided into groups: monthly maintenance, every six months maintenance, annual maintenance, three-year maintenance and larger maintenance every five years.

Software-based monitoring (2) checks the quality of the data and can give early indications of component degradation. Several software-based monitoring methods available allow the radar operator to perform monitoring without interrupting radar operation. Some of them are presented in this section.

The radar components are not eternal and some of the components may break down during use. Corrective maintenance (3) is carried out for troubleshooting.

Keeping the radar calibrated is as important as keeping the radar running and ensuring that the radar produces the best-quality data. Calibration (4) can be used to ensure that the radar measures correctly and adjustments are set correctly. Calibration can also detect defective performance, such as broken or broken components.

The documentation (5) shall include all the information required to the operation, monitoring, calibration and maintenance of the radars.

Each part should include the following sub parties. Sub particles are indicated in the tables.

1. Preventive Maintenance

1. Preventive Maintenance				
1.1 Monthly maintenance	1.2 Every six months maintenance	1.3 Annual maintenance	1.4 Three-year maintenance	1.5 Five-year maintenance

Figure 2: Preventive Maintenance

2. Monitoring

2. Software-based monitoring							
2.1. Sun	2.2. Fixed clutter targets	2.3. Birdbath scan	2.4. ZDR	2.5. Daily averages	2.6. Pair comparison	2.7. BITE	2.8. Etc.

Figure 3: Software–based monitoring.

3. Corrective Maintenance

3. Corrective Maintenance	
3.1.Corrective maintenance if necessary	3.2. Spare parts

Figure 4: Corrective maintenance

4. Calibration

4. Calibration				
4.1 Returning power measurements and return damping control	4.2 Measuring pulse lengths	4.3 Measurement of power and pulse force calculation	4.4 Calibration of the receiver	4.5 Calibration Measuring Instruments

Figure 5: Calibration

5. Documentation.

5. Documentation	
5.1. Metadata	5.2. Major database elements

Figure 6: Documentation.

3 Summary

The SOP for final work can be presented in the form of a general scheme. The SOP can be edited as separate documents in the future, which will facilitate their exchange within the meteorological institutions. The documents

can be specially designed for printing, which makes it easier and safer to archive them. Files can be added to electronic databases of institutions, where they can be changed if necessary. Even if the lists have already been tested, they can be updated or added to them. Therefore, documents are well stored as unencrypted files in Microsoft Excel.

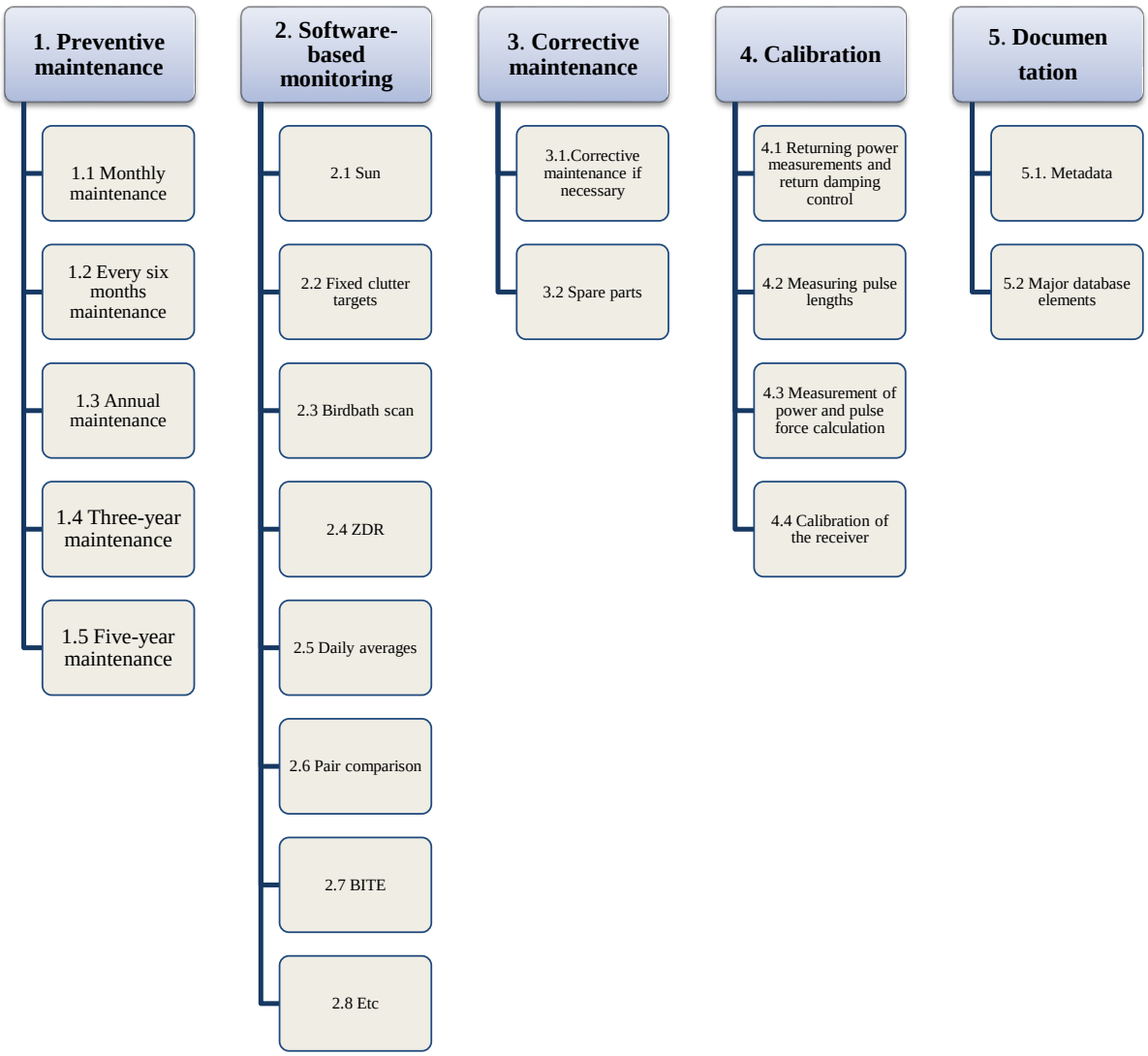


Figure 8: SOP in table

Acknowledgement

Thank You Elena Saltikov, Timo Possio, Mikko Kurri and Hannu Kärki for their help in preparing this document.

References

Saltikoff et.al. "MAINTENANCE KEEPS RADARS RUNNING", BAMS 2017.

Timo Posio “Functions, maintenance and calibration of the WRM200 weather radar”, engineering degree thesis 2014, Metropolia University of Applied Sciences.

FMI 2018 Training on weather radar.

USING EUSKALMET RADAR FOR ANALYSIS OF INTENSE AND PERSISTENCE PRECIPITATION EVENT IN BASQUE COUNTRY DURING WINTER: THE 11 JANUARY 2018 CASE.

Joseba Egaña[1,2] , Santiago Gaztelumendi[1,2] , Olatz Principe[1,2] , Virginia Palacio[1,2] and Mercedes Maruri[1,2]

[1]*Basque Meteorology Agency, Basque Country, Spain.*
[2]*Meteorology Area, Energy and Environmet Division,Tecnalia, Basque Country, Spain.*

(Dated: 17 April 2018)

1 Introduction

In this work, a study of a severe weather episode (11 January 2018) is performed focusing on synoptic, mesoscale and local aspects based on different data available in the studied area including Radar products provided by Basque Meteorology Agency (Euskalmet). Euskalmet Radar is sited in Kapildui Mountain (1174 m), near the capital of the Basque Country (fig.1). It is a METEOR 1500 Doppler Weather Radar with Dual polarization capabilities. This Radar is based on a Klystron transmitter system and operates in C-band frequency (Gaztelumendi, 2006).

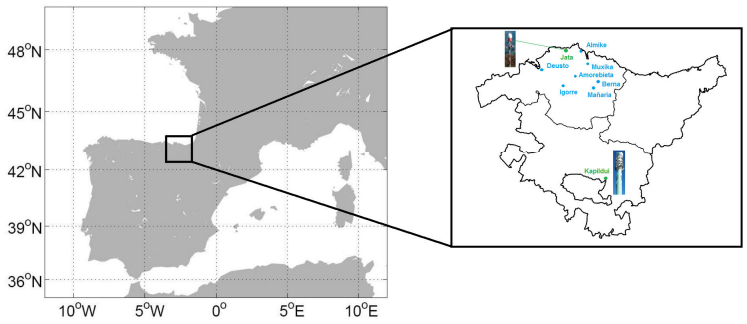


Figure 1: Location of the Basque Country, radars and some automatic weather stations.

Very high intensities of precipitation are not normal in Basque winter season (December-January-February), since air masses are usually cold and cannot contain enough water vapor to generate very heavy rainfall. In summer, intensities of precipitation can exceed 30 mm in one hour instead, due to storms with great vertical development and deep convection; because warm air masses can contain abundant water vapor and can potentially generate very heavy rainfall intensity. These situations are related to deep convection and convective parameters (Egaña, 2005), (Egaña, 2007), (Egaña, 2011), (Gaztelumendi, 2009).

In this case, accumulated precipitations reach up to almost 80 mm in Gernika area, in particular in Muxika station (fig. 2) where maximum precipitation is registered, due to a stationary front and to the activation of part of that front later, generating a rapid rise of local rivers in the affected area where activation takes place. In addition, most of total rainfall is recorded in 12 hours, although accumulated precipitation is close to 30 mm in just one hour.

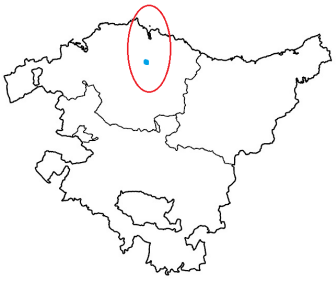


Figure 2: The most affected zone is Gernika area (red circle) where Muxika station is localized (blue point).

For the study of this episode, we have divided this work into four sections. First, we do an analysis of the situation on a synoptic and local scale. Then radar products are analyzed and finally, we complete this work with some conclusions.

2 Synoptic environment

In surface, there are an anticyclone and a depression over Madeira and the Tyrrhenian Sea, respectively. Thus, an inflow of humid sea air gets inside. On the other hand, meteorological situation is uncertain due to the formation of a small

depression with an erratic movement over the Bay of Biscay (fig. 3). In these latitudes, depressions usually move from west to east, but in this case, the area of low pressure goes to the east towards the Brittany coast and it descends to the south while pressure increases. This situation modifies the pressure field in the Basque Country and, in turn, generates a convergent wind field in surface.

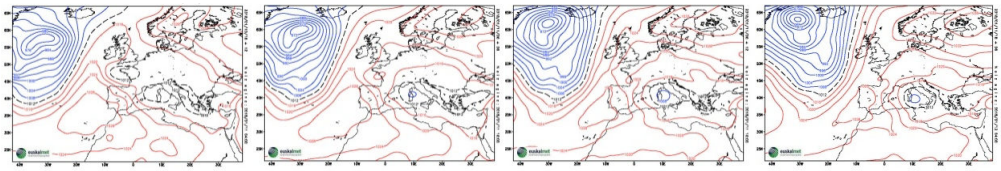


Figure 3: Evolution of sea level pressure during the episode at 06, 12, 18 and 24 UTC, on January 11, 2018

In fact, primary center of the depression is in a final phase located in France, even so a secondary center is formed in the Basque Country. Therefore there is an absence of wind in this zone and the air mass gets colder, thanks to persistent and abundant precipitation. This pressure field generates a convergence zone in Gernika and Muxika area. West winds come from the west, and weak east and southeast winds come from the east part of Bizkaia, where two different air masses join among them. A warmer one that places to the west and a cold one, that stagnates in Bizkaia, especially to the east. Besides this situation, there is an occluded front (fig. 4) associated with that low which gets active in that area.

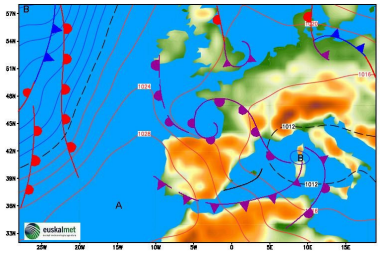


Figure 4: Sea level pressure and fronts map at 12 UTC, on January 11, 2018

At 500 hPa level, a cut-off low (with a cold air mass inside) is over France at the beginning of the day and, as the journey progresses, it moves towards the Mediterranean Sea and arrives in the west of Italy (fig. 5). At the same time, the mass of air that affects us is relatively cold in lower layers (fig. 6).

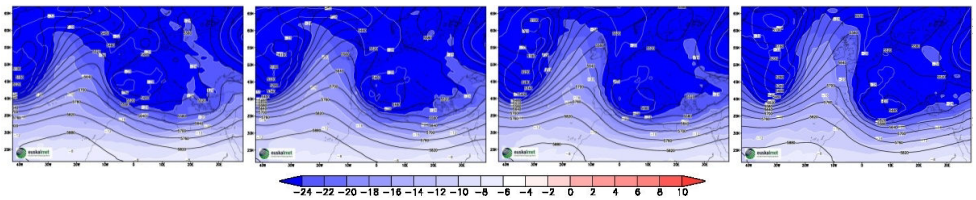


Figure 5: Geopotential and temperature at 500 hPa at 06, 12, 18 and 24 UTC, on January 11, 2018

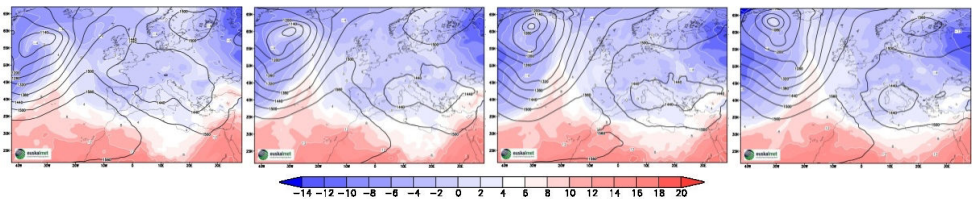


Figure 6: Geopotential and temperature at 850 hPa at 06, 12, 18 and 24 UTC, on January 11, 2018

3 Local environment

The occluded front is associated with the secondary depression formed over the Basque Country and remains stationary on aforesaid region, especially affecting an area oriented northwest-southeast. During the afternoon, snow level drops to 400 meters in eastern Bizkaia and western Gipuzkoa due to persistence and intensity of precipitation. In these situations, the melting causes a remarkable cooling effect. This secondary low favors absence of wind over the Basque Country and therefore air mass gets colder. From 6:00 pm, a winds convergence area (fig. 7) is formed where heavy precipitation is generated afterwards.

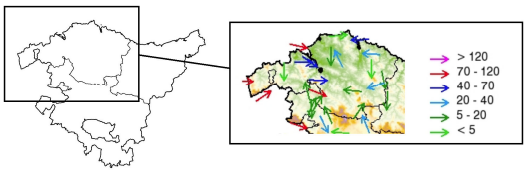


Figure 7: Wind convergence where two air masses join among them at 17:10 UTC, on January 11, 2018

On the one hand, temperatures are low in eastern Bizkaia with east and southeast winds; on the other hand, due to strong northeast wind, a much milder air mass of maritime origin arrives from the west. In Deusto weather station (fig. 8), temperature rises from 4ºC to 9-10ºC in one hour, and wind turns from southeast to northwest and gets stronger (fig. 9). In this way, in addition to the convergence zone, two very different air masses join in a short period of time activating the precipitation, especially in Gernika-Muxika area.

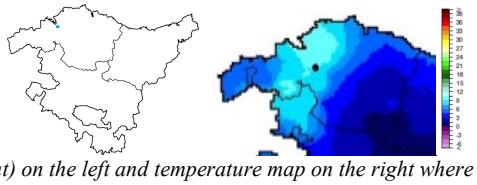


Figure 8: Deusto station location (blue point) on the left and temperature map on the right where we can see very different air masses join

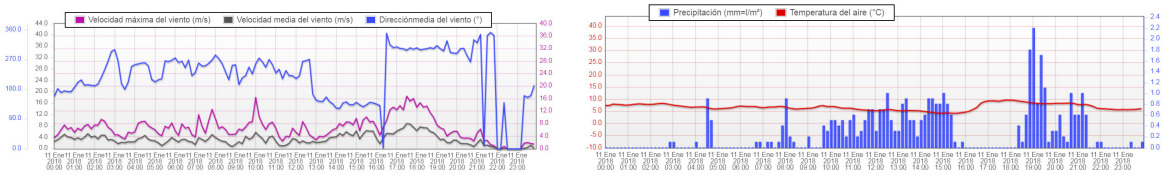


Figure 9: Evolution of wind (left) and temperature and precipitation (right), in Deusto station, on January 11, 2018

As we have seen, convergence and union of two different air masses cause the maximum precipitation. This moment of maximum activity only lasts one or two hours, time enough to generate problems, on the one hand, due to saturation and precipitation just fallen before the peak of precipitation and, on the other hand, due to the intensity of precipitation in the moment of maximum activity.

Table 1: Maximum precipitation in ten minutes, in one hour and total precipitation during the day, on January 11, 2018

Station	Precipitation in 10 min (l/m^2)	Time (UTC)	Precipitation in 1 hour (l/m^2)	Time (UTC)	Precipitation in 24 hours (l/m^2)
Muxika	8.5	17:50	26.2	18:00	76.5
Almike	5.1	17:30	15	16:20	70.9
Derio	4	18:30	7.4	21:20	48.4
Igorre	3.5	18:50	10.9	19:10	55
Berna	2.8	18:00	13.1	18:30	50.9
Amorebieta	2.5	18:00	12.7	18:40	58
Mañaria	2.3	17:40	10.3	18:00	61.1

Intensity of precipitation reaches a record and Muxika station registers 26.2 mm in one hour (table 1 and fig. 10, 11). This data is an absolute record; in other words, in winter there has never been such high intensity of precipitation in weather stations network in the Basque Country. Intensities are also exceptional in ten minutes (8.5 mm) for this season. Maximum precipitation of the day takes place in Urdaibai area, in Muxika and Almike weather stations (table 1).

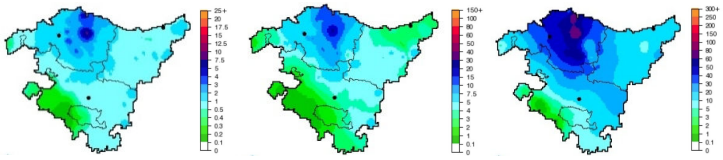


Figure 10: Maximum precipitation in ten minutes, in one hour and total precipitation during the day, on January 11, 2018

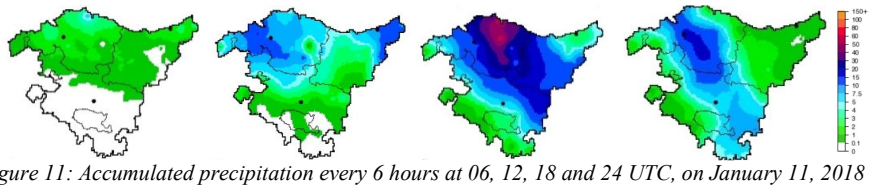


Figure 11: Accumulated precipitation every 6 hours at 06, 12, 18 and 24 UTC, on January 11, 2018

At the time of more intense precipitation, around 7:00 pm, temperature rises in the area very noticeably (fig. 12).

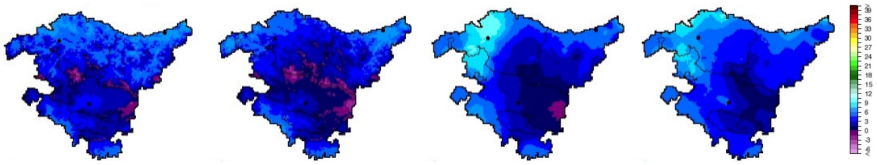


Figure 12: Temperature at 06, 12, 18 and 24 UTC, on January 11, 2018

In the most affected area, river levels rise rapidly because of intense rainfall, such as drainage basin in Oka and Ibaizabal. Consequently, rivers exceed stablished level (for Muxika and Amorebieta stations, yellow levels are 2.5 m and 2.75 m and orange levels are 3 m and 3.25 m, respectively). Finally, they reach 4.19 m and 3.56 m in Muxika and Amorebieta stations, respectively (fig. 13).

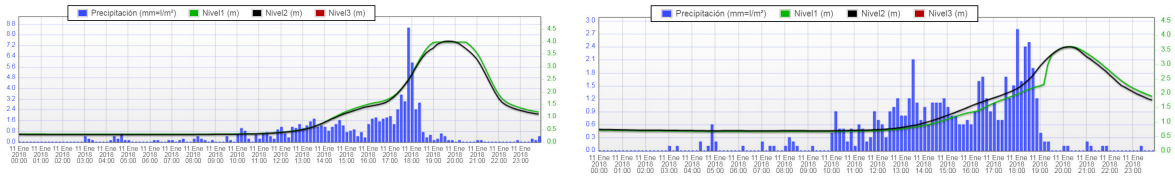


Figure 13: River levels and precipitation in Muxika (left) and Amorebieta (right) stations, on January 11, 2018

4 Radar analysis

This extraordinary episode of intense precipitation is analyzed using different Radar products. Convective precipitation is detected in the affected area by Kapildui Radar images, although vertical development is not very deep since it is a cold season. For example, Echotop product shows cloud tops of six or seven kilometers at maximum precipitation moment (fig. 14).

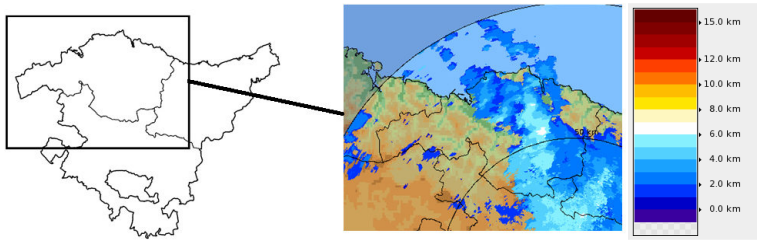


Figure 14: Echotop product of Kapildui Radar at 17:42 UTC, on January 11, 2018

Another product of Kapildui Radar that can be analyzed is the sequence of max 2-10 km (fig. 15). The precipitation band associated with the mentioned front is observed, with the activation in the study area where maximum reflectivities can be seen. In addition, precipitation line is almost stationary and, for a relatively long period of time, it is maintained over the affected area.

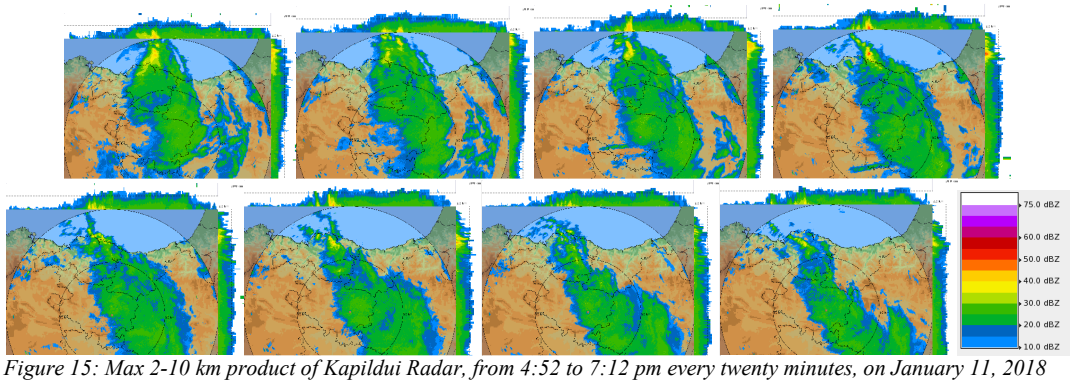


Figure 15: Max 2-10 km product of Kapildui Radar, from 4:52 to 7:12 pm every twenty minutes, on January 11, 2018

However, Kapildui Radar is on the top of a mountain and can hardly analyze this kind of situations at very low altitudes in the study zone. In order to analyze reflectivity near the surface, it is necessary to use Jata Radar which belongs to Aemet (Spanish Meteorological Agency) and is localized in Plentzia-Mungia area, next to Bilbao. The available information can be used operationally to obtain some products.

Both maximum precipitations in one hour and in ten minutes are ephemeris in winter. This intensity of precipitation could be equivalent to surface reflectivity close to 50 dBz and these values can be verified by Jata Radar (fig. 16). During one or two hours, precipitation line remains almost stationary or even with a certain retrograde movement. Nevertheless, after this time, the precipitation activity decreases because convergence zone disappears and precipitation line moves to the south due to north wind at medium levels.

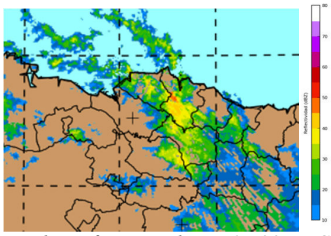


Figure 16: PPI 0.5º dBz product of Jata Radar at 17:30 UTC, on January 11, 2018

Taking into account the combination of both Radars (Kapildui and Jata), we can obtain also different products and results. This combination can calculate an estimated precipitation, obtaining the reflectivity value of the closest layer to the surface in every zone. This value is transformed into intensity of precipitation, through Marshall-Palmer relation and information every ten minutes to obtain accumulated precipitation in one hour and in 24 hours. In addition, this information is corrected with weather station data and is based on calculated factors, such as the intensity of precipitation ratio calculated by the radar and that calculated by the station at the location of each station (fig. 17 and 18). In this way we obtain the QPE (Quantitative Precipitation Estimation).

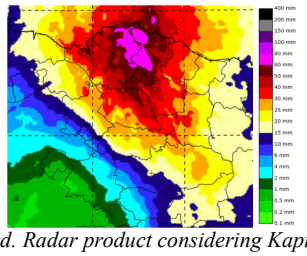


Figure 17: Precipitation Accumulated in 24 h Adjusted. Radar product considering Kapildui and Jata Radars and a correction of stations, on January 11, 2018

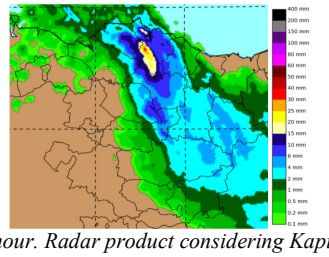


Figure 18: Precipitation Accumulated in one hour. Radar product considering Kapildui and Jata Radar, on January 11, 2018

So considering both radars, the amount of precipitation estimated in 24 hours is between 60 and 80 mm in the most affected area, reaching 80 mm punctually (fig. 17). Maximum hourly precipitation occurs between 6:00 and 7:00 pm and the values of PAC in one hour exceed 20-25 mm, even 30 m (fig. 18).

If we only consider Kapildui Radar and the correction of weather stations, the result obtained underestimates the data calculated with the combination of both Radars (Kapildui and Jata), which is closer to the real data (fig. 19). So, in this case, the resolution of both Radars together is much better.

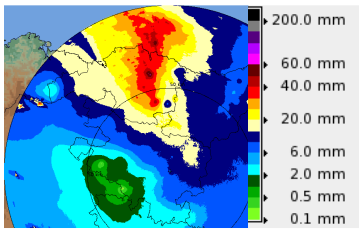


Figure 19: Precipitation Accumulated in 24 h Adjusted. Radar product considering Kapildui Radar and a correction of weather stations, on January 11, 2018

5 Summary and conclusions

To sum up, different circumstances creates a convergence zone, which activates an occluded front over the Basque Country in Bizkaia province, in particular in Gernika and Muxika area. This convergent zone lasts a short period of time, just around two hours. However, it is time enough to activate the front in that area in an extraordinary way. This convergent zone has a slight retrograde movement for a couple of hours, and after that it tends to deactivate and move to the south. In addition, two different air masses join at this converging zone and the activation is even more relevant. A secondary low is created in the Basque Country, so temperatures fall down, especially in east area of Biscay. Consequently, this cold air mass joins a warmer one arriving from west; therefore, the front gets more active.

Due to this abundant and intense precipitation, there are so many problems in different zones from affected area. There are water accumulations in the streets. Several rivers overflow in different areas, such as Oka and Ibaizabal, which generates local floods and numerous problems on the roads. The most affected area is the surroundings of Gernika. In fact, Firemen have to rescue several people from cars trapped by water between Gernika and Muxika, where material damage is considerable with floods in the ground floor, garages and shops (fig. 20).

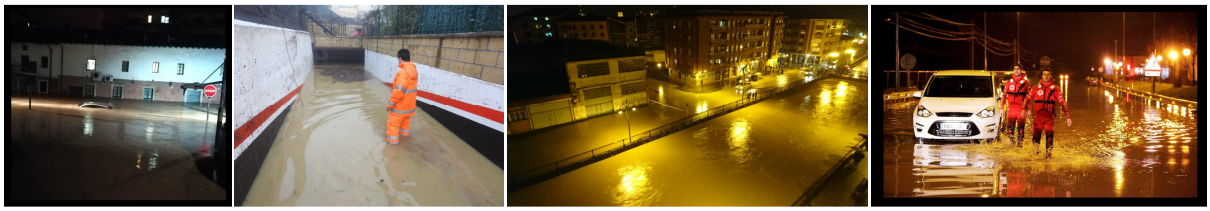


Figure 20: Pictures of floods in the streets. Muxika, Gernika and Mungia are some of the most affected towns.

Throughout the day, persistence of precipitation leaves more than 70 mm in 24 hours in different parts of the territory, with more than 25 mm of precipitation in one hour and more than 8 mm in ten minutes. In winter, those quantities are unusual in our territory.

For the study of this episode, we use different products of Kapildui Radar and the combination of this one with Jata Radar (from Aemet), together with the correction of weather stations network available for Euskalmet, obtaining QPE close to reality. In different Radar products we can see the location of the convergence zone and the areas of maximum activity.

Acknowledgement

The authors would like to thank the Emergencies and Meteorology Directorate - Security Department – Basque Government for public provision of data and operational service financial support. We also would like to thank all our colleagues from TECNALIA and EUSKALMET for their daily effort in promoting valuable services for the Basque community.

References

Aranda J.A., Morais A., 2006: The new weather-radar of the Basque meteorology agency (Euskalmet): site selection, construction andinstallation. 4th European Conference on Radar in Meteorology and Hydrology, Barcelona (Spain).

Doviak R.J., Zrnić D.S., 1984: Doppler radar and weather observations. Academic Press, USACommittee to assess NEXRAD Flash Flood Forecasting Capabilities at Suphur Mountain California, 2005: Flash Flood Forecasting Over

Egaña J., Gaztelumendi S, Mugerza I, Gelpi I.R. 2005:Synoptic patterns associated to very heavy precipitation events in the Basque Country. 5th EMS. Utrech(Netherlands).

Egaña, J.; Gaztelumendi, S.; Gelpi, I.R.; Otxoa de Alda, K. 2007. A preliminary analysis of summer severe storms in the Basque Country area: synoptic characteristics". ECSS 2007. Fourth European Conference on Severe Storms. Trieste (Italy).

Egaña, J., Gaztelumendi, S., Pierna, D., Otxoa de Alda, K., Hernández, R., Gelpi, I.R., 2011: A study of instability indexes in summer severe storms case in the Basque Country area. 6th European Conference on Severe Storms (ECSS 2011). Palma de Mallorca, (Spain) 03 - 07 October 2011.

Gaztelumendi S., Egaña J., Gelpi I.R., Otxoa de Alda K., Maruri M., Hernandez R., 2006: The new radar of Basque meteorology Agency:Configuration and some considerations for its operative use. 4th European Conference on Radar in Meteorology and Hydrology, Barcelona (Spain).

Gaztelumendi S., Otxoa de Alda K., Egaña J., Gelpi I.R.,Pierna D., Carreño S., 2009: Summer showers characterization in the Basque Country. 5th ECSS.Landshut (Deutschland).

Lacmann G. Midlatitude synoptic meteorology. Dynamics, analysis and forecasting. February 2015. American Meteorological Society.

Marigo, G., Robert-Luciani, T., Crepaz, A., 2008: Snow level forecasting methods and parameters; two practical examples on Eastern italian alps. Conference on Mountain Meteorology.

Meischnner P., Collier C, Illingworth A., Joss J. Randeu W, (1997). “Advanced Weather Radar Systems in Europe: The Cost 75 Action”Vol 78, No 7, July 1997, pp 1411-1430. Bulletin of the American Meteorological Society.

Using Euskalmet radar for analysis of a heavy storms event in Basque Country during summer: the 30 August 2017 case.

Joseba Egaña[1,2] , Santiago Gaztelumendi[1,2] , Olatz Principe[1,2] , Virginia Palacio[1,2] and Mercedes Maruri[1,2]

[1]Basque Meteorology Agency, Basque Country, Spain.

[2]*Meteorology Area, Energy and Environmet Division,Tecnalia, Basque Country, Spain.*

(Dated: 17 April 2018)

1 Introduction

In warm season (from May to September) storms generated by deep convection are frequent in the Basque Country (see Fig.1), although not in all cases storms produce severe conditions. Impacts are usually caused by intense showers exceeding 30 mm in 1 hour or 10 mm in 10 minutes (see Gaztelumendi et al, 2009 and Egaña et al, 2007a,b), especially if the showers affect urban areas, and by hail and wind gusts associated with storms (see Gaztelumendi et al, 2010). In these situations surface pressure patterns are not very defined, with barometric swamp or relative thermal lows. In high levels, southwest wind usually predominates and there is often a trough configuration with its axe over the west of the Iberian Peninsula. This configuration generates positive vorticity advection (see Egaña et al, 2007). Besides, in this period, warmth accumulated during the day favours atmospheric thermal instability. When instability degree is high, storms might be very active and vertically quite developed and the top of the clouds could reach the tropopause. In many cases, storms are created in the south or southwest, outside the Basque Country, although they can also be generated within. This depends on the convergence areas in low levels and instability degree above the Basque Country. In this region, storms usually move from southwest to northeast, as a consequence of frequent southwest high levels flow. In some circumstances, storms deviation might be relevant in relation to the main flow. Severe storms dynamic is complex and many factors should be taken into account, including instability index and other parameters, such as wind shear or storm relative helicity (e.g. Wesiman and Rotunno, 2000, Doswell 2001).

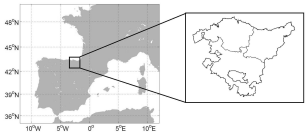


Figure 1: The Basque Country located in the north of Iberian Peninsula.

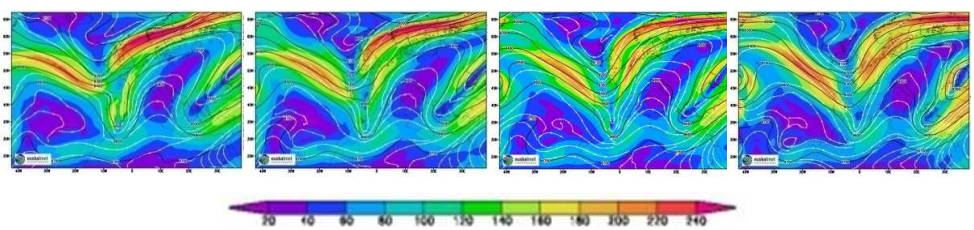
2 Synoptic Environment

A depression isolated in high levels of the atmosphere affects the days before the west part of the Iberian Peninsula. During August 30, in 500 hPa and 300 hPa levels (see Fig. 2), a deep trough formed in Atlantic Ocean traverse the Iberian Peninsula causing dynamic instability. The temperature is relatively low in the 500 hPa layer, around -13 ºC, and in 850 hPa level the air mass it is not very hot (approximately 13 ºC), therefore the thermal instability it is not very pronounced.

In surface, the Iberian Peninsula is in a barometric swamp during the first part of the day. The anticyclone of Azores lengthens through the Atlantic Ocean until the British Isles latitude and moves towards the east during the day reaching the Gulf of Biscay and at the end of the day it extends as a wedge along the Cantabrian Sea. In addition an occluded front crosses the Gulf of Biscay towards the Mediterranean Sea.

On the other hand, instability indices are not very high, Total Totals index (TTI) is around 50 ºC and Lift Index around -2 ºC, however those values indicate certain instability and are enough to have events with heavy rainfall in the Basque Country (Egaña et al., 2017). Precipitable water values are significant for this area, around 25-30 kg/m^2.

This situation and especially the dynamic instability allow the development of storms which moves from southwest to northeast during the second part of the day.



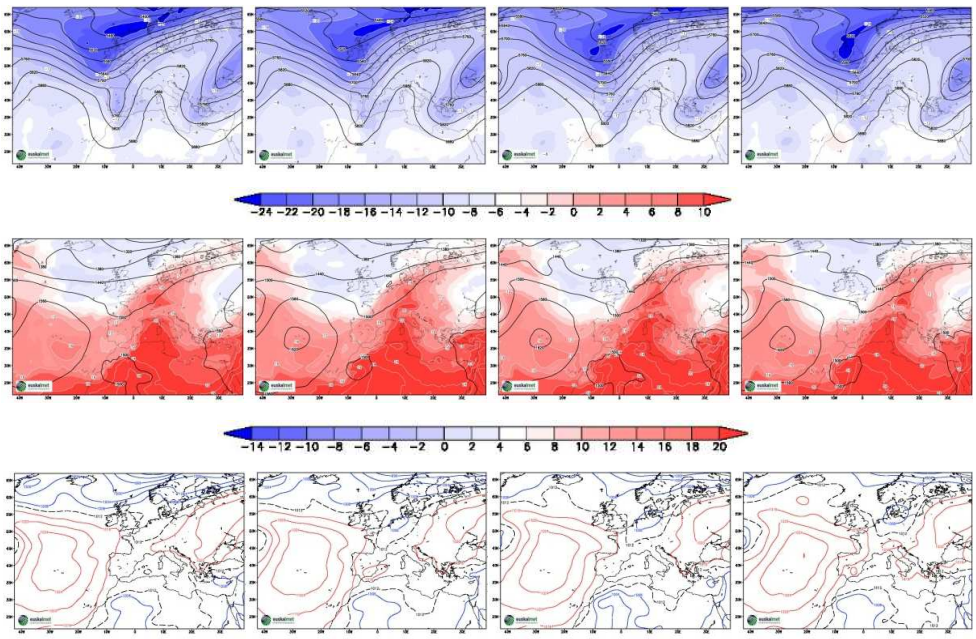


Figure 2: Jet stream and geopotential in 300 hPa, geopotential and isotherms in 500 hPa and 850 hPa, and sea level pressure at 06, 12, 18 and 24, on 30/08/2017.

3 Episode description and radar analysis

The morning is sunny and the temperature is soft in the coast and higher in the interior of the region (maximum around 28-29 ºC in the south and the east). Around midday clouds tend to develop in the west of the area and first heavy storms (>15mm/hour) take place. It is noteworthy the register of Ordunte automatic weather station (AWS) at 15:30 local hour, with 13.5 mm/10-min and 15.1 mm/h (see Fig. 3 and Table 1). After, they extend to Bilbao, the most populated city of the Basque Country and at 16:30 local hour 10 mm are registered in 10 minutes (17 mm/h) (see Fig. 3 and Table 1). The duration of these showers is quite short and the electrical activity is high (see Fig. 11 at 14:50 UTC). In addition showers are accompanied by hail of approximately 2 cm. Z-based Hail Detection (ZHAIL) radar product shows a high probability of hail (see Fig. 6) above 80 %. Waldvogel criterion is used to make the calculus and it studies the echotop 45 dBz above 1.4 km over 0 ºC isotherm (see Waldvogel et al., 1979)

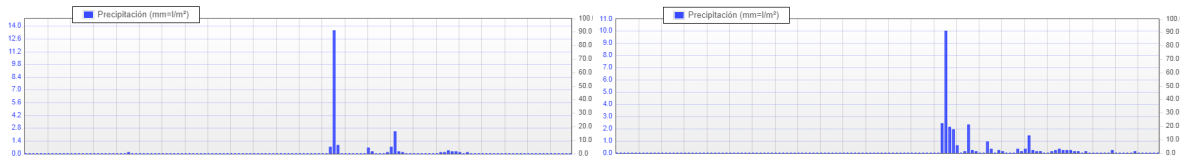


Figure 3. Hourly precipitation in Ordunte and Abusu (Bilbao) AWS on 30/08/2017.

After, storms develop also in east and in northeast of the region. They do not lose intensity, on the contrary they are more intense than those of the west. As a result, rainfall are heavy and very heavy (>30mm/hour) in the east part of the region, in the interior and also in the coast between 18:20 and 19:10 local hour. In Ereñozu, Oiartzun and Behobia stations exceed 30 mm/h and 10 mm/10-min (in Oiartzun 33.2 mm/h and 12.9 mm/10-min, and in Behobia 32.6 mm/h and 12.8 mm/10-min), and the maximum of precipitation is recorded in Ereñozu with 44 mm/h and 15.4 mm/10-min (see Table 1).

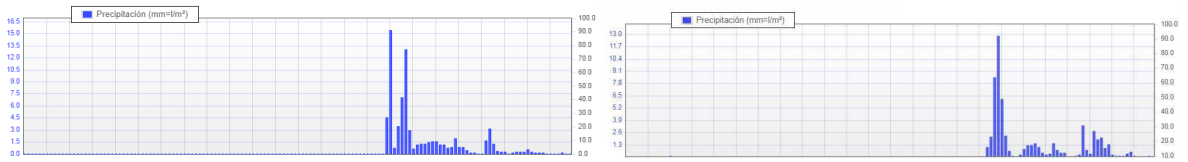




Figure 4. Hourly precipitation in Ereñozu, Behobia and Oiartzun AWS on 30/08/2017.

Convective and electrical activity starts in the west part of the Basque Country and extends to the east and northeast as can be seen in the images of MAX (2-10 km) with lightning (see Fig. 5). Crosses represent cloud-ground strikes and points represent the cloud-cloud discharges. MAX product of the radar, ranging from 2 km to 10 km (see Fig. 6) shows maximum reflectivities up to 55-60 dBz in the heaviest storms in the west and also in those of the east part of the region. They development reaches around 11-12 km as Echotop product reveal (see Fig. 6), which represents the maximum height at which reflectivity is greater than 15 dBz.

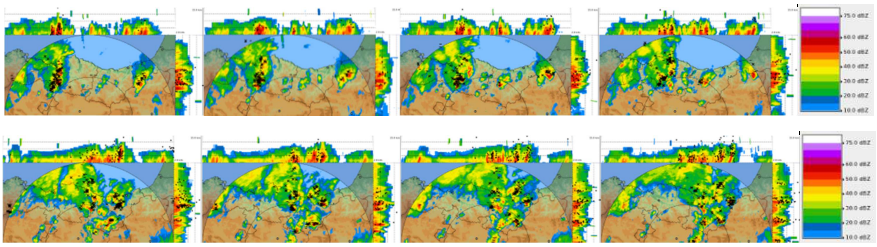


Figure 5. MAX (2-10 km) images with lightning activity from 14:10 to 14:40 and from 15:20 to 15:50 UTC every 10 minutes.

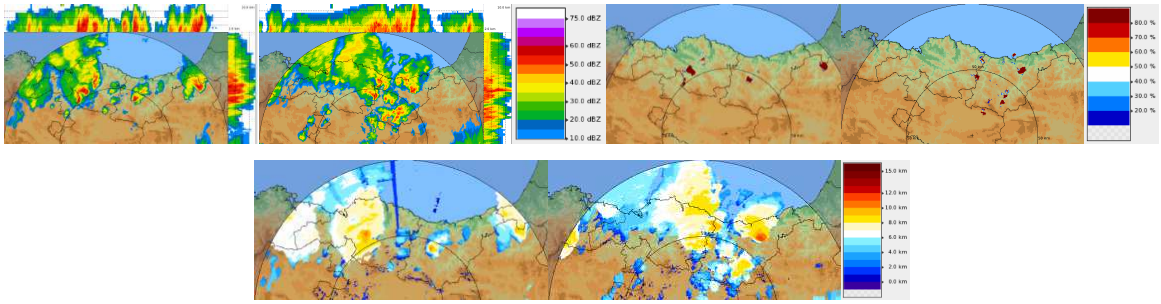


Figure 6. MAX (2-10 km), ZHAIL and Echotop-15 dBz products at 14:10 and 15:20 UTC on 30/08/2017.

In late afternoon storms lose intensity, although it continues raining quite heavily in the east, as a result of which the precipitation accumulated in 24 hours exceeds 60 l/m2 in Oiartzun and Ereñozu AWS (see Fig. 4). In many other places precipitation is very abundant (>30 mm/24h) (see Table 1).

The spatial and temporal distribution of this precipitation can be seen in Kriging maps of maximum rainfall in 10 minutes, hourly and total in 24 hours (see Fig. 8 and Table 1). It is consistent with PAC product of Kapildui radar which gathers the precipitation accumulated hourly or in 24 hours not only with radar data, but also with values registered by AWS.

Table 1: Maximum accumulated precipitation in one hour, in 10 minutes and in 24 hours.

Station	Hourly precipitation (mm)	Time UTC	Precipitation in 10 min. (mm)	Time UTC	Precipitation in 24 hours (mm)
Ereñozu	44	16:40	15.4	16:00	71.6
Oiartzun	33.2	17:00	12.9	16:30	64.9
Behobia	32.6	17:10	12.8	16:50	57.8
Zarautz	29.7	16:20	8.3	15:40	42.5

Lasarte	26.6	16:30	11	16:10	49
Abusu	17	15:10	10	14:30	25.5
Ordunte	15.1	14:10	13.5	13:30	20.6

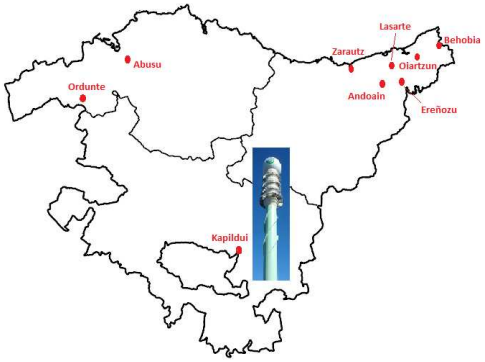


Figure 7. Location of some AWS and Kapildui radar in the Basque Country.

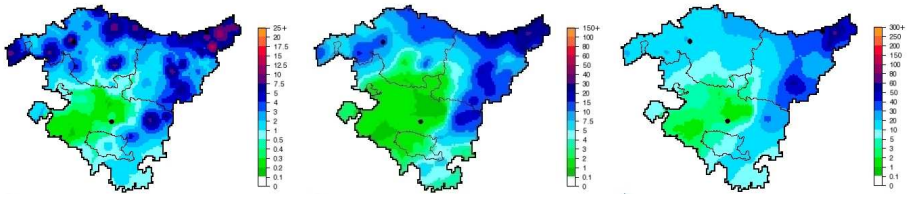


Figure 8. Precipitation in 10 minutes, in one hour and in 24 hours on 30/08/2017.

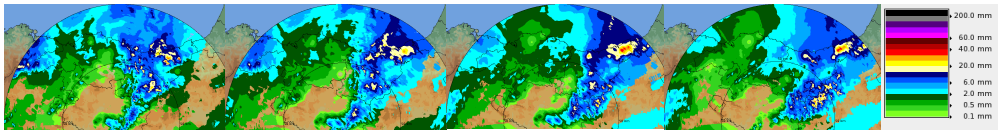


Figure 9. PAC 1h product: hourly precipitation during very heavy storms, at 16:20, 16:40, 17:00 and 17:20 UTC.

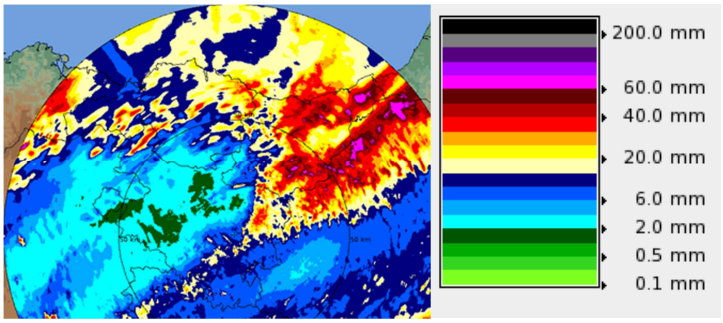


Figure 10. PAC 24 h product: precipitation in 24 hours on 30/08/2017.

The amount of precipitation accumulated causes some temporary problems in urban roads (see Fig. 13, Fig. 14 and Fig. 15) and flooding of certain rivers as Jaizubia in Bidasoa basin that reaches yellow warning level. Associated to certain storms very strong wind gusts are registered in some places as Zarautz (73 km/h). Nevertheless, comparing with other similar events, wind gusts are not very significant.

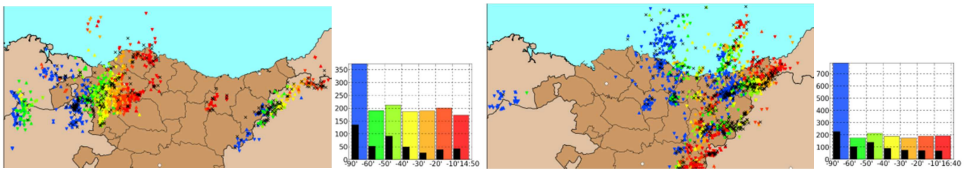


Figure 11. Spatial distribution and intensity of CG (cloud-ground) and IC (intracloud) strokes during 90 minutes between 14:50 and 16:40 UTC on 30/08/2017.

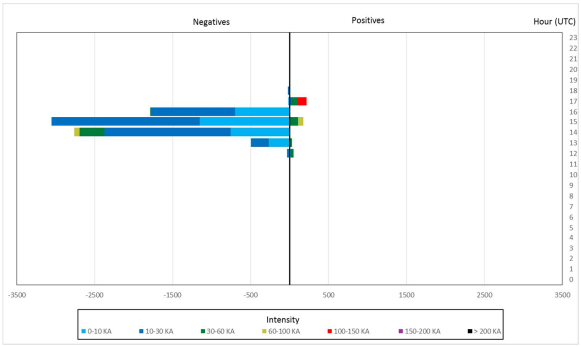


Figure 12. Hourly distribution of CG (cloud-ground) strokes on 30/08/2017.

The higher electrical activity during the event it produces during 5 hours. In this episode, 1378 lightning strokes are registered, of which 330 are positive and 1048 negative, and they are recorded in the first part of the evening together with the heaviest thunderstorms happen. The most intense positive strike is 115.2 kA and the negative one -64 kA.

4 Summary and conclusions

The convective cells trajectory is eastward and northeastward, a common movement in storm events in the Basque Country due to a deep trough coming from Atlantic Ocean. In studied episode the major factor that leads to the development of heavy storms is the dynamic instability caused by the trough crossing the Basque Country from west to east. Instability indexes are not very high, but enough to originate heavy and very heavy rainfall.

The radar products and data are essential to tracking storms, not only to do nowcasting following in real-time the movement and development of the storms, but also to quantify the heavy rainfall that take place in zones where there is not an AWS. Products as PAC that combine radar and AWS data, allows to estimate the QPE (quantitative precipitacitation estimation) in any place of the region in order to know the impact .

The damages generated by heavy rain are not too important. The most populated city affected is Donostia-San Sebastián, in the northeast of the region. Big pools are formed in many streets making driving complicated and drains overflow. Other locations are also affected, with power cutoffs, dropped trees and small floods. In addition some rivers grow fast and reach warning yellow level. Although the rainfall is heavy also in the west of the region, impact is not so relevant.

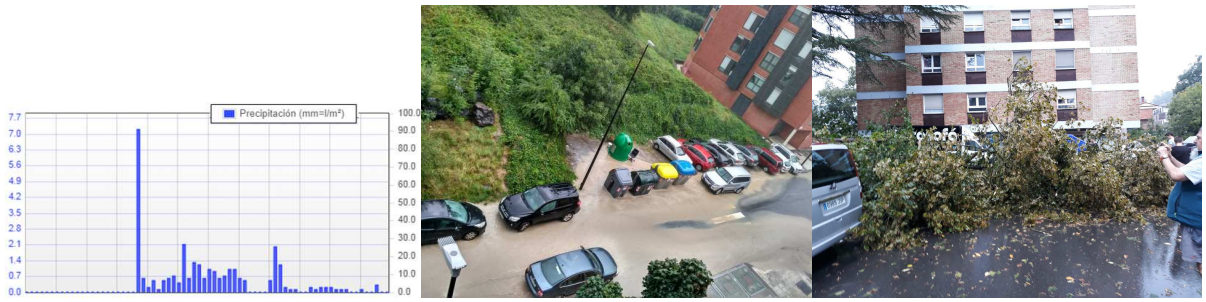


Figure 13. Hourly precipitation in Andoain AWS from 12 to 24 UTC and impact in the town with pools in roads and dropped trees on 30/08/2017.

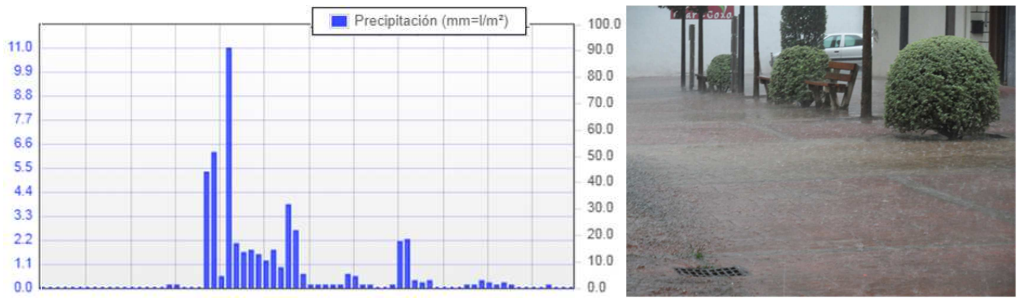


Figure 14. Hourly precipitation in Donostia-San Sebastián from 12 to 24 UTC and heavy rainfall in Usurbil (Lasarte AWS) on 30/08/2017.

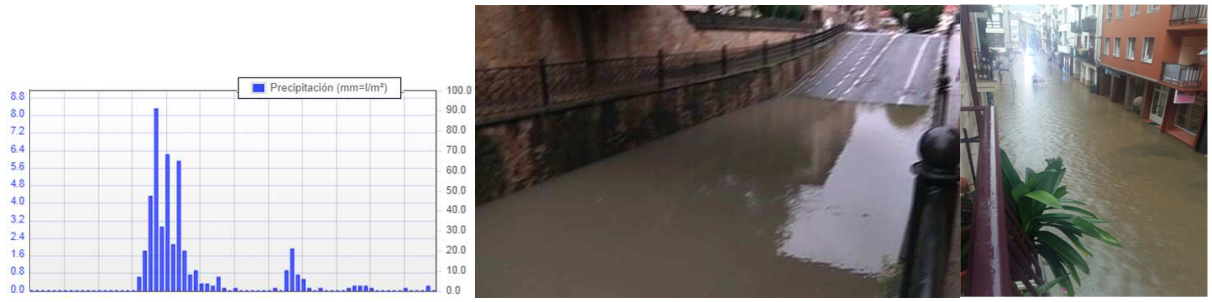


Figure 15. Precipitation from 12 to 24 UTC in Zarautz AWS and floods on 30/08/2017.

Acknowledgement

The authors would like to thank the Emergencies and Meteorology Directorate - Security Department – Basque Government for public provision of data and operational service financial support. We also would like to thank all our colleagues from TECNALIA and EUSKALMET for their daily effort in promoting valuable services for the Basque community. Finally, we would also like to thank the Free Software Movement and all institutions and people that maintain and support availability of free data and tools for scientific community.

References

Doswell, C. A. III, 2001. Severe Convective Storms, Meteor. Monogr., No. 50, Amer. Meteor. Soc, doi: 10.1175/0065-9401-28.50.433.

Egaña, J., Gaztelumendi, S., Gelpi, I.R., Otxoa de Alda, K, 2007a. A preliminary analysis of summer severe storms in the Basque Country area: synoptic characteristics". ECSS 2007. Fourth European Conference on Severe Storms. Trieste (Italy).

Egaña, J., Gaztelumendi, S., Gelpi, I.R., Otxoa de Alda, K., 2007b. Synoptic patterns associated to severe storms in the Basque Country. 7th EMS 8th ECAM.

Egaña J., Gaztelumendi S., Pierna D., Príncipe O., 2017c. A study of convective severe storms in Basque Country during XXI century. 9th European Conference on Severe Storms (ECSS), 2017. Pula, Croatia.

Gaztelumendi, S., Egaña, J., Gelpi, I.R., Otxoa de Alda, K., 2007. Study of a case: the 4th july 2006 storm over the city of Bilbao. 4th European Conference on Severe Storms (ECSS).

Gaztelumendi, S., Otxoa de Alda, K., Egaña, J., Gelpi, I.R., Pierna, D., Carreño, S.,2009. Summer showers characterization in the Basque Country. 5th ECSS 2009.

Gaztelumendi, S., Egaña, J., Gelpi, I.R., Otxoa de Alda, K., Maruri M., Hernández R., 2010. Using Euskalmet Radar data for analysis on July 1st Hailstone storms in Vitoria city. 6th ERAD 2010.

Waldvogel, A., Federer, B., Grimm, P., 1979. Criteria for the detection of hail cells. Atmospheric Physics. ETH, 8093 Zurich, Switzerland

Weisman, M. L., and R. Rotunno, 2000. The use of vertical wind shear versus helicity in interpreting supercell dynamics. J. Atmos. Sci., 57, 1452–1472.

Results of the monitoring tasks and co-creation activities of the precipitation products of Kapildui weather radar

M. Maruri[1 2] (mercedes.maruri@tecnalia.com), S. Gaztelumendi[1 2], K. Otxoa de Alda[1 2], R. Hernandez[1 2], C. Stocker[3]. J. Salazar[3], I. Eguiara[4], J.A.. Aranda[1 5] .

[1] *Basque Meteorology Agency, Basque Country, Spain.*

[2] *Meteorology Area, Energy and Environmet Division,Tecnalia R&I, Basque Country, Spain.*

[3] *Basque Water Agency, Basque Country, Spain.*

[4] *Traffic Directorate, Security Department, Basque Country, Spain.*

[5] *Emergencies and Meteorology Directorate, Security Department, Basque Country, Spain.*

(Dated: June 2018)

1 Introduction

The estimation of surface rainfall in real time is one of the challenges of meteorological services, given its discrete behavior, spatially heterogeneous, and its variability with time and type of meteorological event. In areas of complex terrain, there are meteorological situations in which the meteorological observations present a high uncertainty. Those inaccuracies are important to know and identify (Koistinen and Michelson, 2002). On the other hand, our users (meteorological services, hydrological modelers, traffic control, public safety authorities, and environmental/tourism departments among others) demand more complex products in real time such as, the amount of rainfall that falls, the type of hydrometeors and the trend in the next few hours (Holleman et al, 2008). For a long time, in situ measurements were made of rain gauges from surface meteorological stations (manual/automatic), to make way for more advanced technologies with meteorological radars (with high spatial and temporal resolution). During the last years it has been working with the integration of available observation systems as a solution to the problem and the creation of new products that consider the needs of different users (Germann et al, 2006).

In this way, different products that represent the distribution of surface rainfall naturally arise. The interpolation maps obtained from the surface hydro-meteorological network, integrated PPIs with low elevations free of blockages that convert reflectivity to rainfall, SRIs (Surface Rainfall Intensity), integrated radar products with other types of observations (disdrometers and rain gauges) and even the integration of several radars. The present paper has a double objective, to establish a methodology of analysis the accuracy of the different precipitation products that are used in the operative and surveillance tasks, and to describe, in different situations typical of the study area, the quality and capacity that different products have to describe the evolution of particular meteorological phenomena (Maruri et al, 2010, Argota et al 2012, Lakshmanan et al, 2012). The classification of the results is aimed to introduce improvements or define limitations that can be of great knowledge value for the end users that use this data in the chain of decision making (Lakshmanan and Smith, 2007).

2 Study area and input data

The study area is the Basque country, located at the eastern end of the Cantabrian Sea, with an extension of 7234 km2, between the Cantabrian Mountains of Picos de Europa to the west and the Pyrenees to the east, being a very complex area geographically and climatologically by the Mediterranean influences that come from the Ebro valley and the northern Atlantic ones. All these factors interact with different weights according to the zone, time of year and synoptic situation, and configure different meteorological patterns that are affected by the quality problems typical of a meteorological radar, resulting in the cases to be analysed being complex. In the Basque Country, the dense network of surface stations complements the meteorological radar information and is a great value that helps to describe certainly the evolution of the rainfall field.

The input data with which we have worked to carry out this work have been, on the one hand, the observations of the Basque hydro-meteorological network (the Basque Government´s AWS network) Maruri 2001, the meteorological radar of Kapildui (of the Basque Government) Aranda and Morais 2006 and Gaztelumendi et al 2006, the meteorological radar of Jata (AEMET-State Meteorological Agency) and the reports of the data quality of the products derived from these systems independently and integrated (web pages EUSKALMET and AEMET).

3 Methodology

Although it seems quite clear that the integration of the observations is the best solution and the one that gives rise to the most real representation of surface rainfall, this is not always the case since the representativeness of the automatic stations in their location is not always correct or the radar data, in the lowest elevation without blockages, can be extrapolated to the surface without great uncertainties or that finally both systems fail because there is a low density of the stations and blockages (total or partial) in the radar vision in the study area J. Koistinen and D. Michelson, 2002.

It is also known that certain meteorological patterns can be associated with systematic errors in the observation systems, therefore making an assessment of the data quality of the historical database is crucial for a better interpretation of the data in real time by the different users and from this study to know the limitations and establish the future lines of improvement.

This paper presents two phases, a first one that gathers codification the information of the relative differences of the "rainfall products", starting as information referring to the Kapildui radar, this information is extracted from the monthly monitoring reports of the Kapildui radar operation, and a second phase that analyses statistically, in a structured way, the differences through the different products along the different meteorological patterns. This document includes the methodology used to collect all the information and presents some meteorological situations detected during the process of preparation de data. The data is prepared for a future classification statistical analysis; each group will be analysed independently discussing its quality and representativeness with respect to the meteorological pattern it represents

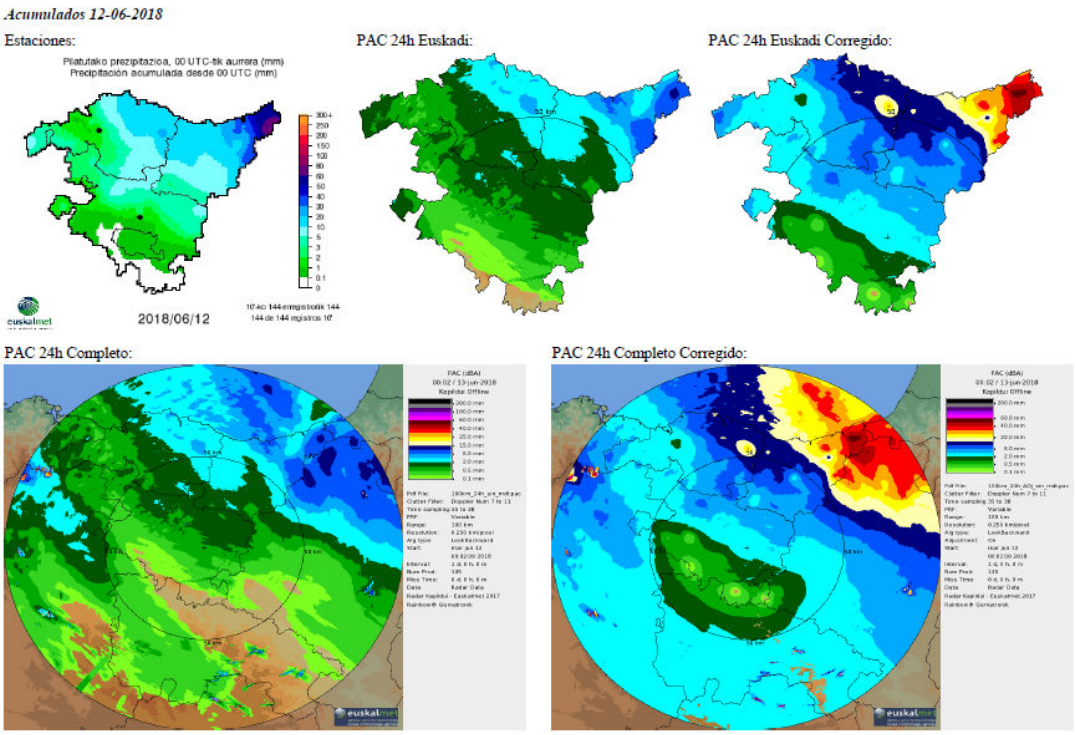
We will work with the database from 2014 to the present and in particular with the information of the documents of accumulated 24 precipitation and tables of pac24 (24hour-accumulated precipitation).

The accumulated documents have a daily resolution and contain the information of the different products "PACs of 24 hours". The figure presented below is obtained for June 12, 2018, where persistent rainfall leaves accumulated up to 93.1 mm in the Eskas station at the east border of the Basque Country, with a complex hydrological situation for decision-making derived from a rapid response of the rivers.

In the first row the 24-hour pac is observed with information from the surface network, followed by the 24-hour pac derived from the radar information and finally the integrated 24-hour pac (surface network + radar) is observed, restricting the data to the Basque autonomous community, in a second row are the products PAC-24h as they are visualized with the software of the manufacturer "rainbow" and integrated with surface stations in range. The latest KED graphic is a self-developed alternative that intelligently combine the information of the surface stations and the two radars available in the region.

All the graphs are useful in monitoring tasks; the observations of these graphs are collected in tables that will be presented below.

The visual comparison of independent way allows seeing the representativeness of the measures face to the episode (jams in the rain gauges, blockages in the radars), the integration of the systems emphasizes especially the problem associated to the measure´s systems, the most frequent, in jammed rain gauges in surface and interferences that accumulate in the radar or poor resolution of the observation in an area. The Kapildui radar blocks are reduced when the Jata radar is integrated.



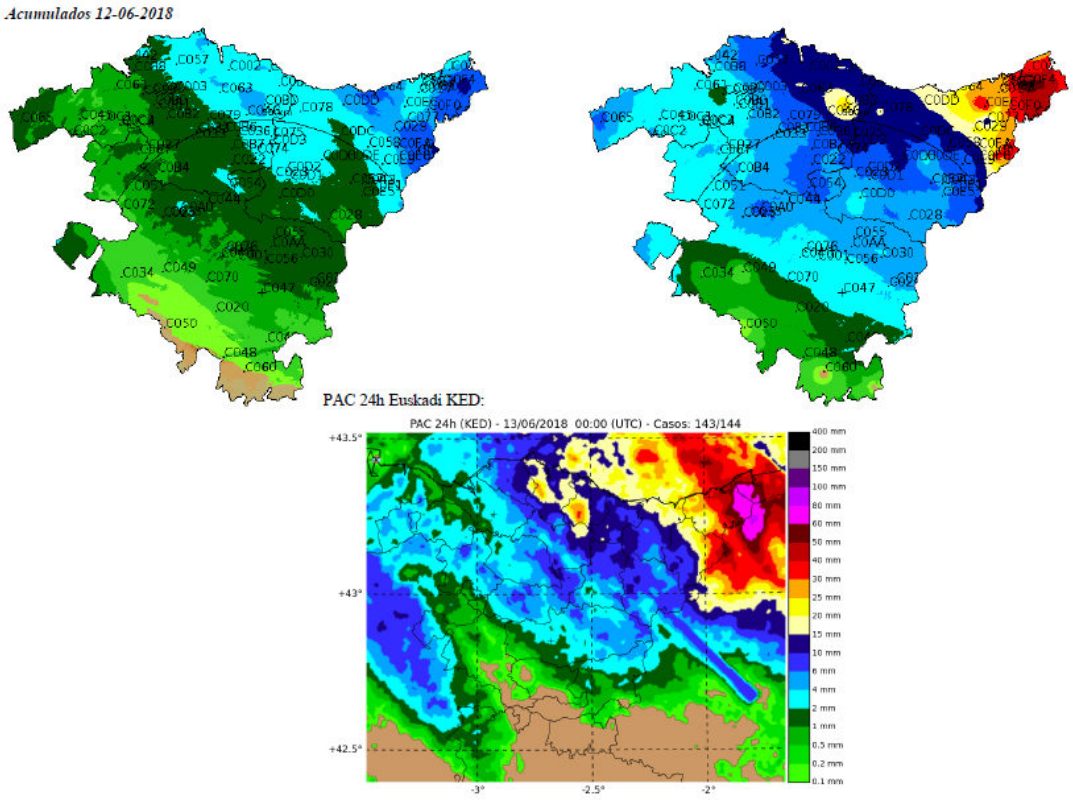


Figure 1:Daily 24-hour PACs products. On June 12 2018.

In this example underestimations of rainfall in the study area by a surface station can be seen, interference of Wi-Fi antennas that accumulate over time and especially great spatial variability of rainfall in the region and the importance of having a spatial representativeness in blockade areas and close to relevant urban cities of the region such as Bilbao and San Sebastian, particularly in this case in the Bilbao area.

Pac tables: the last work table of June 2018 is included. It is a double entry table where the information of the pacs products of 24 hours is codified (Pac = only radar of Kapildui, Pac AK = Pac adjusted Kapildui + Stations, Pac AJ = Pac adjusted Jata + Stations, Pac A-KED = Pac adjusted Kapildui + Jata + Stations, B + G + A, area where rainfall is concentrated), by days of the month. The rainfall is coded by a "p" followed by a number that is associated with the colour scale of the radar product and a series of specific codes of whether the rainfall is storm type with its zone identification. There are other codes "letters" associated with the presence of clutter in the product and even a colour code on top of the day that makes the day stand out from others for potential future studies.

	Monday	Tuesday	Wednesday	Thursday	Friday	Saturday	Sunday
Day					**1**	**2**	**3**
PAC					P3(T-A)	P2 (T-Inter)	P3(T-B,G)
PAC A-K					=	=	P5(T-Inter)
PAC A-J							
PAC A-KED					P5 T-Alava	P4 T-(inter)	=
B+G+A							
Day	**4**	**5**	**6**	**7**	**8**	**9**	**10**
PAC	P	P2	0	P(G)	Pp (B)	Ppp(T+1)*	pp
PAC A-K	+2	+2 (T-Añarbe)	+1(G)	+	+	Ppp(T+3)*	=
PAC A-J							
PAC A-KED	P4(B)	P5(T-Añarbe)	+1(G)	P5(T-G) Interference	P4(T-B)	P6(T) Midle CAPVa	P3
B+G+A							
Day	**11**	**12**	**13**	**14**	**...**	**...**	**...**
PAC	P4 (littoral)	P3 (G)	p- (G)				
PAC A-K	+	P6(G)	P4 (G)*				

PAC A-J							
PAC A-KED	P4 (littoral)	P7 (G) Interference	P4 (G) Interference				
B+G+A							

Leyenda		
No rainfall		
	0	No rainfall
	0 + C	No rainfall and clutter areas
	p-	rainfall < 0.2 mm
	p- + C	rainfall < 0.2 mm y clutter areas
rainfall		
	P	Maximum rainfall 4 mm
	Pp=p2	Maximum rainfall 15 mm (low percentage)
	Ppp=p3	Maximum rainfall 15 mm (high percentage)
	Pppp=p4	Maximum rainfall 25 mm
	Ppppp=p5	Maximum rainfall 40 mm
	Pppppp=p6	Rainfall between 40 and 60 mm (Adverse weather limit)
	Ppppppp=p7	Rainfall high then 60 mm (Adverse weather)
Others		
	Error	
*	The product is very artificial. It does not represent reality.	
+,-	Add or subtract symbol (something more than that category or something less and add some information).	
C	Clutter symbol. C_b (low C.) C_m (C._moderer) C_a (high C.)	
T	The origin of the rainfall is due to storms.	

B-Bizkaia->Bizkaia´s area G-Guipúzcoa->Guipuzkoa´s área (Zarautz and Berastegi) A-Alava->Alava´s area.
L-Littoral I- Intermediate zone CAPV
B-Burgos N-Navarra
Other phenomena that are observed: Melting layer-Non fainfall targets
CR-> Accumulated reflectivity more accentuated in clutter areas but not very strong
NN:
Number of data with which the accumulated pac has been made.
Pluv: Problems in rain meters
Storm codes T: Storms pN: Number accumulated category Zone -(Cantabria-Ca,Bizkaia-B,Guipuzkoa-G,Alava-A, Rioja-R, Navarra-N)

Table 1:A detail of the table used to code the precipitation 24-hour accumulated precipitation products.

Currently, an encrypted spreadsheet containing the information of these tables from 2014 to the present is being created. All those comments subject to subjectivity are being eliminated and giving more homogeneity to all entries, over the years, so that they can be treated jointly.

Although, there are many studies which will try to find the best adjusted Z-R for a meteorological situation, the aim of this paper is to find an inventory of non-representative situations by the products available along the meteorological situations of the region.

4 Some case studies and discussion

4.1 Clear air echoes; Biological targets, second trips signatures and ground clutter.

There are clean air situations in which no return signal is expected that does not come from ground clutter, but instead reflectivity values are observed below the rainfall detection value but when doing the accumulated 24 hours, it represents a light rain. These cases are very easy to detect in real time and do not generate problems except for those situations of change of time, where the cloudiness begins or the beginning of storms and everything overlaps and accumulates. As seen in the example presented below. These false echoes disappear when the information of the automatic surface stations that provide non-rainfall information is integrated. As seen in the Pac24-KED. The target which causes this pattern during spring and summer is biological (birds or insects).

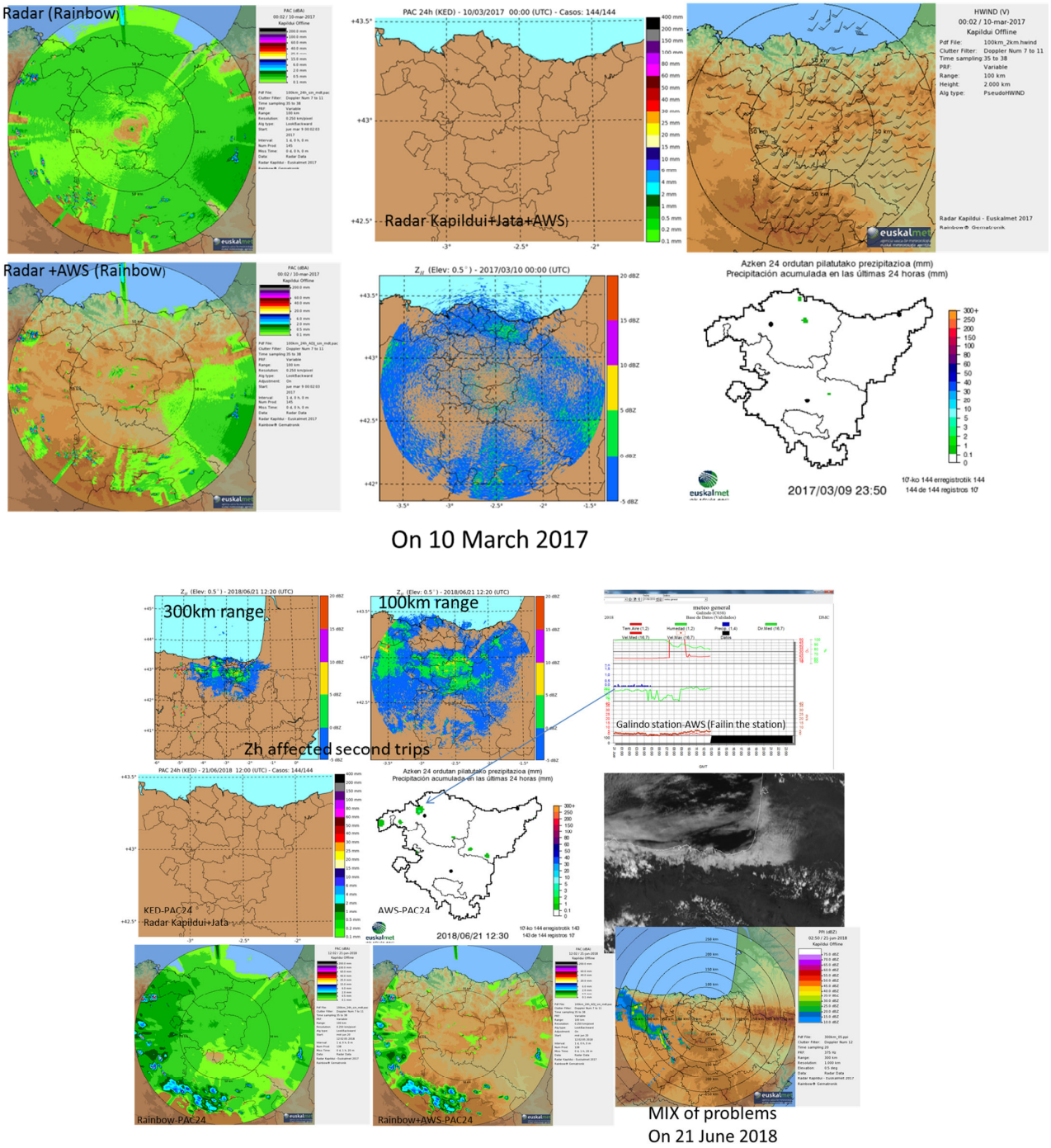


Figure 2. On 10 March 2017. Biological targets. On 21 June 2018. A mix of clear air targets; Biological, Interferences+ Aws errors+Second trips

4.2 Representativeness's analysis of the products in the main urban centers and surroundings of the Basque Country: Bilbao, Donostia y Gasteiz

The three study populations are Bilbao, Donosti and Gasteiz, are three basins with historical flood history, the cases of Bilbao and Donosti present the added problem of having points affected by the tides, special attention must be paid to these areas and their accesses. Bilbao and Donosti are in blocked areas and the lowest elevation (0,5) is 2 km above sea level at that point (100 km from Kapildui radar), which makes the presence of other observation systems to improve quality essential of these measure. When the weather phenomena of precipitation affect only the coastline and are developed below 4 km it is necessary to incorporate information from both radar and the automatic weather surface station network.

This integration is required, on the left bank of Bilbao, in addition it is recommended to improve the resolution of the surface stations in this area because there are automatic weather stations on exposed surface sites, which underestimate the measurements. In the example presented below, 24-hour integrations are observed where the lack of Jata radar data generates underestimates in the blocking zones. The radar of Kapildui presents good coverage and quality in a range of 50 km, which includes the third population centre that is Gasteiz, for this, a product that considers the lowest elevation and that saves the land as surface data is created "MejorZ".

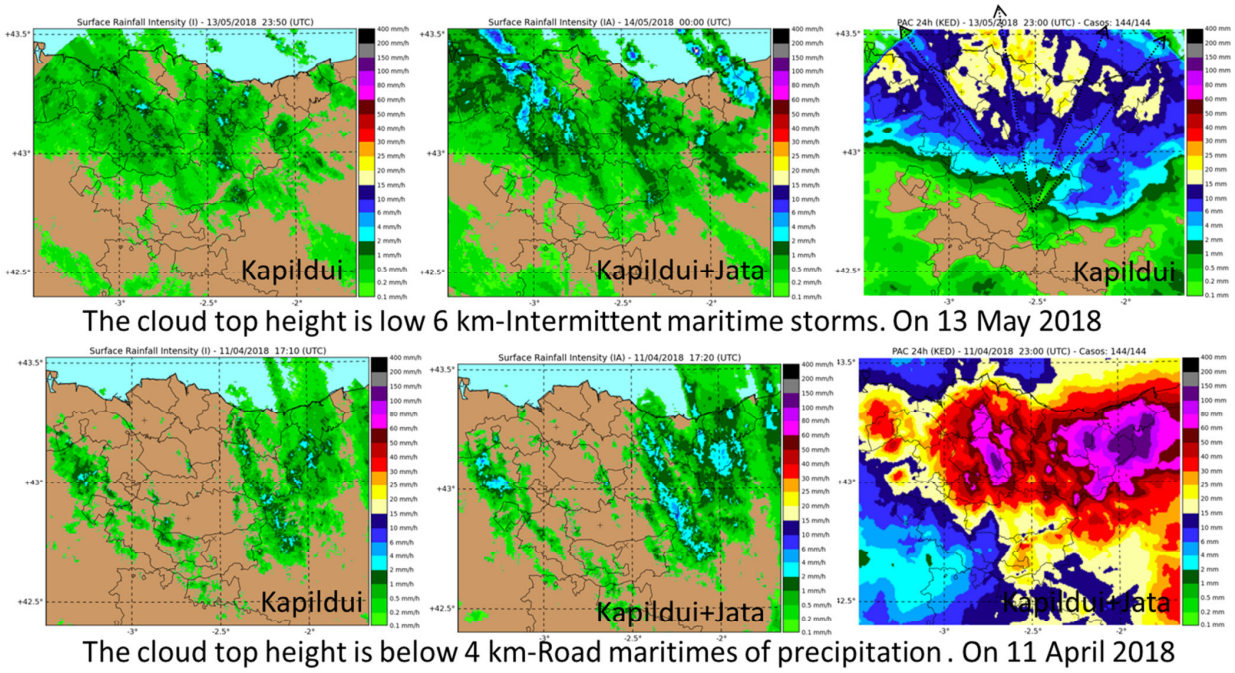


Figure 3. Blocking areas close to the most population urban cities. Jata radar reduces the blocking areas.

4.3 Winter case

Both the cases of stratiform and convective precipitation (scarce evolution in height), the Kapildui radar data can lead to underestimations in the littoral due to lack of information in the lower layers, and the integration with shore surface stations can reinforce this underestimation because the sensors are in exposed areas. In this case the radar of Jata plays an important role to correct these underestimations. Heterogeneous radome attenuation are frequents and sectorial subestimations must be detected.

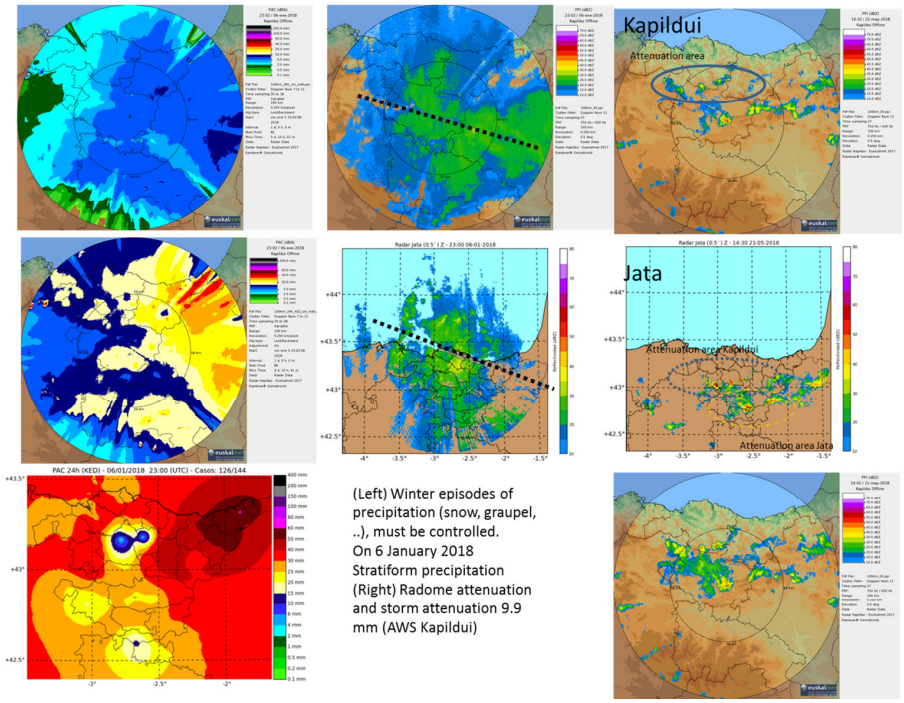


Figure 4. Attenuations. AWS errors.

4.4 Summer case

The summer situation is associated with storms, for these cases the Kapildui radar information is essential to observe not only the evolution of the storms in the territory itself, but what is happening in the border regions since it can be a good indicator of what may appear in the region itself. For cases in which the storms pass over the radome or are close to the radar, the radar loses information of the spatial distribution at ranges greater than 50 km and in these cases the surface information is relevant, Jata does not provide quality information and sometimes the integration of the information of both systems (radar + raingauges) gives rise to spatial distributions mathematically very contrived.

In general, the integration of radar and rain gauges in the Kapildui station itself sometimes leads to problems.

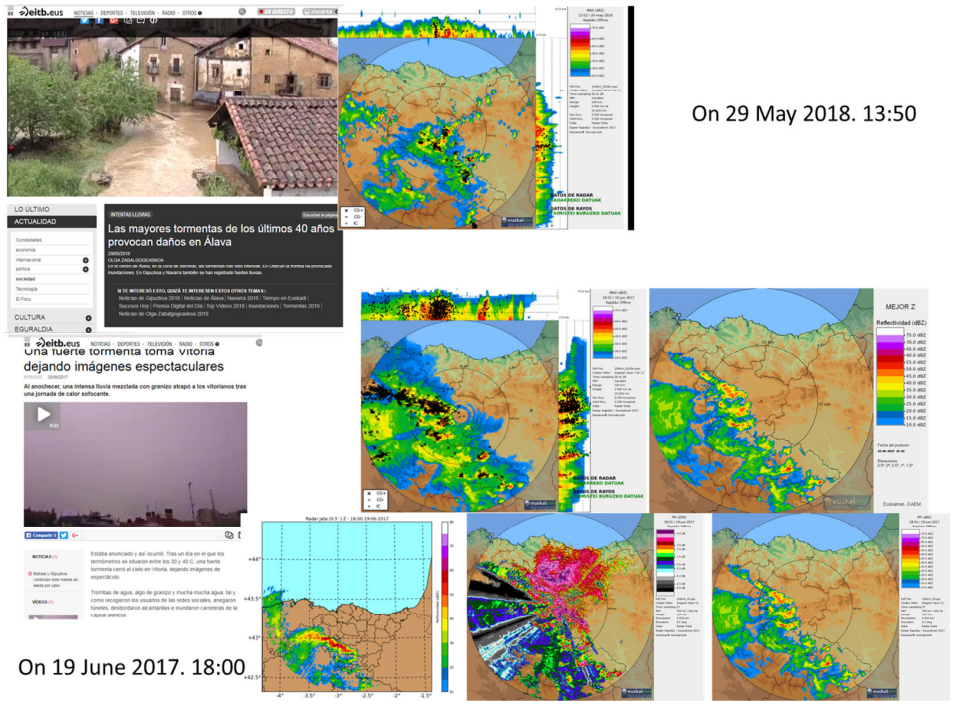


Figure 5. South storms.

5 Conclusion

The integration of all observation systems is the one that offers the best results, but always the integration must be done under control. Not always the use of all the rain gauges available in the automatic surface network is the one that gives the best result, there are situations where the errors are systematic because the representativeness of the rain gauges in the area is poor and the surface data introduce artificial behaviours in the integration/interpolation that it results in a strange distributions of the rain in a complex terrain.

Knowing the systems and their potentials/limitations is essential to define improvements. But, on the other hand, documenting them is even more important in terms of the end use of users.

Currently, radar products are input data for decision making in adverse situations, so they must be analysed in detail to know to what extent they are able to respond to the needs of users and describe the problem with the spatial resolution that is necessary.

Acknowledgement

We would like to thank all the users who use the data of the Basque Government network and their direct collaboration with the emergency and meteorology management, and the Basque meteorological agency for facilitating, managing and disseminating, at no additional cost, the public information of the observations, creating a feedback that makes the knowledge service grow.

References

Aranda., J.A.; Morais., A.(2006). The new weather-radar of the Basque Meteorology Agency (Euskalmet): site selection, construction and installation. ERAD 2006 - THE SEVENTH EUROPEAN CONFERENCE ON RADAR IN METEOROLOGY AND HYDROLOGY

Gaztelumendi, S.; Egaña., J.; Gelpi., I.R.; Otxoa de Alda, K.; Maruri., M.; Hernandez., R (2006). The new radar of Basque meteorology Agency: Configuration and some considerations for its operative use. ERAD 2006 - THE SEVENTH EUROPEAN CONFERENCE ON RADAR IN METEOROLOGY AND HYDROLOGY

German U. Galli G. Boscacci M and Bolliger M (2006). Radar precipitation measurement in mountainous region, Q.J.R. Meteorology Society 2006,132, pp. 1669-1692. Doi:10.1256/qj.05.190

Holleman, I., L. Delobbe, and A. Zgonc, 2008: Update on the European Weather Radar Network (OPERA). Proc. Fifth European Conf. of Radar Meteorology and Hydrology, Helsinki, Finland, ERAD, 3.3. Google Scholar

Koistinen, J. & Michelson, D.B. 2002: BALTEX weather radar-based precipitation products and their accuracies. — Boreal Env. Res. 7: 253–263.

Lakshmanan, V., T. Smith, G. J. Stumpf, and K. Hondl, 2007: The Warning Decision Support System–Integrated Information. Wea. Forecasting, 22, 596–612, doi:https://doi.org/10.1175/WAF1009.1. Link, Google Scholar

Lakshmanan, V., C. Karstens, J. Krause, and L. Tang, 2014: Quality control of weather radar data using polarimetric variables. J. Atmos. Oceanic Technol., 31, 1234–1249, doi:https://doi.org/10.1175/JTECH-D-13-00073.1. Link, Google Scholar

M. Maruri 2001. Validación en tiempo real de datos de redes meteorológicas. Tesis Univ. País Vasco UPV/EHU.

M. Maruri, J. López, J.A. Aranda, S. Gaztelumendi 2010. Effects of the meteorological conditions over the radome of kapildui weather radar and studies of their quality impacts. ERAD 2010 - THE SIXTH EUROPEAN CONFERENCE ON RADAR IN METEOROLOGY AND HYDROLOGY

Juan Antonio Romo Argota, Mercedes Maruri Machado, Ivan Iglesias, Sabina Ustamujic 2012. Characterization tools for estimate radar signals with partial Obstructions. ERAD 2012 - THE SEVENTH EUROPEAN CONFERENCE ON RADAR IN METEOROLOGY AND HYDROLOGY

Web pages:

EUSKALMET: http://www.euskalmet.euskadi.eus/. Last visited 2018, 21 June

AEMET: http://www.aemet.es/es/portada. Last visited 2018, 21 June

Evolution of the configuration of the lightning protection system of the Kapildui weather radar installation

M. Maruri[1 2 3] (mercedes.maruri@tecnalia.com), J.A. Aranda[1 4] .
[1] *Basque Meteorology Agency, Basque Country, Spain.*
[2] *Meteorology Area, Energy and Environmet Division, Tecnalia R&I, Basque Country, Spain.*
[3] *University of the Basque Country UPV/EHU, Spain.*
[4] *Emergencies and Meteorology Directorate, Security Department, Basque Country, Spain.*
(Dated: June 2018)

1 Introduction and problem description

The selection of a site of weather radar in a complex terrain is not an easy task. The WMO in collaboration with the CIMO (Web Wmo-Cimo-Opag-Cb, 2005) gives to the operator some critical issues to evaluate, for identification the site; radar coverage, meteorological phenomena detection, electromagnetic interferences, wind turbine parks, environmental impact and potential integration with other systems. In the case of Kapildui weather radar, the site was mainly selected to complement the observations available (Jata weather radar from AEMET (Meteorological Spanish Agency). Kapildui is a good place to observer the storm events of the region during the summer season (Maruri et al 2014, Gaztelumendi et al 2014, Egaña et al 2014). In addition both radars are in the border of the Basque region; this means that the resolution and quality is high if it is used both radar in an integrate product. Both have strategical meteorological views, the Spanish radar (Jata Radar) registers all the meteorological phenomenons at the coast (synoptic and coastal weather) and the regional radar registers all the mountain phenomenons. In addition the sites are close to two main cities, Bilbao and Gasteiz and this is a great value for monitoring and nowcasting potential floods in urban areas and the surrondings. Finally, the Basque meteorological agency (EUSKALMET) operates a dual-Doppler polarimetric weather radar located at the top of Kapildui mountain (1,1 km above sea level). The radar system is installed over a 50 meter metal tower to avoid the obstacles of a complex terrain (Figure 1) .

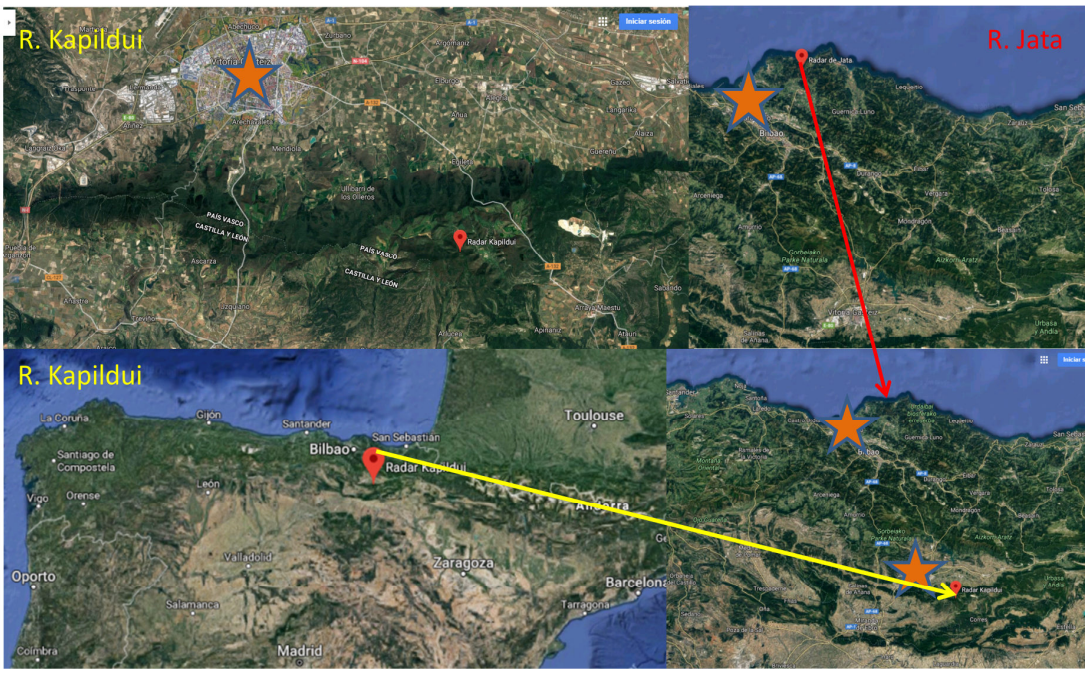


Figure 1:Geographical locations of Kapildui (yellow) and Jata (red) Weather Radars(Ref: Google maps). The stars are the locations of the most populated cities of the Basque Country.

Studies of the lightning activity in Spain reveal that higher activity areas are located in the south and the east border of the Basque region, Ebro Basin (Web Aemet-publications). One of the most severe episodes of severe storm registered in the historical database of the weather radar is described in the (Gaztelumendi et al, 2015).

There are two typical extremes groups behavior of the lightning activity in the Basque Country, the cold and the warm seasons and a great variety of them between them. In a previous study, cold seasons have associated to less activity than warm seasons. In terms of severity, impacts to the population, the winter episodes are associated to grapple precipitation and traffic incidents in the littoral and the spring and summer episodes are related to agricola damage and local flash flood (Maruri et al, 2014). In general, the lightning activity affect to communication links and is the main cause of electrical

damage of the communication systems. The Basque government communications network is affected in many ways by the lightning strokes.

2 History of the evolution of the lightning protection systems of Kapildui weather radar

One of the critical components of a weather radar system has been the lightning protection system, in the case of the Kapildui weather radar system there are three periods completely different in the history of the system;

The first period is from the installation (November 2005) to January, 2009. The lightning protection system (LPS) was installed as provided by the manufacturer, a single central lightning rod and two equidistant 35 mm2 copper down-conductors connected to the ground.

Along this period direct lightning impacts occurred during cold and warm seasons, the impacts were on the joints of the radome pieces and screws. Although the fiber glass of the radome apparently looks sufficient strong to make its functions, that it is not true, the composition of the fiberglass changes its property and it is vulnerable to the humidity, over time. The degradation starts in the impact moment and in a short period, severe meteorological episodes could be the reason of the collapse of the radome. In this period was the cyclogenesis episode associated to the Klaus sub-tropical cyclone in January 2009 (Lopez et al 2010), that it collapses the system as it shown in the figure 2.



Figure 2. Situation of the status of the radome after Klaus, in January 2009.

The second period started, in spring of 2009 to October 2014. The radome was substituted an alternative system was installed, a CTS-type. Its operation is based on the de-ionization of the electrical environment to inhibit the lightning strokes in the surroundings of the radar. This protection system has a good performance in communication towers along the Basque region that they belongs to the Basque Goverment. During the warm season, the system was a good performance, no direct impacts where registered although many thunderstorms passed over the site. But in the cold season (at the end of the year-2009), two thunderstorms impacted in the inner face of the radome. No evidence of direct impacts was found and a lack of knowledge of the lightning mechanism in the area of the site was the motivation of a thesis doctoral (Lopez et al, 2012).

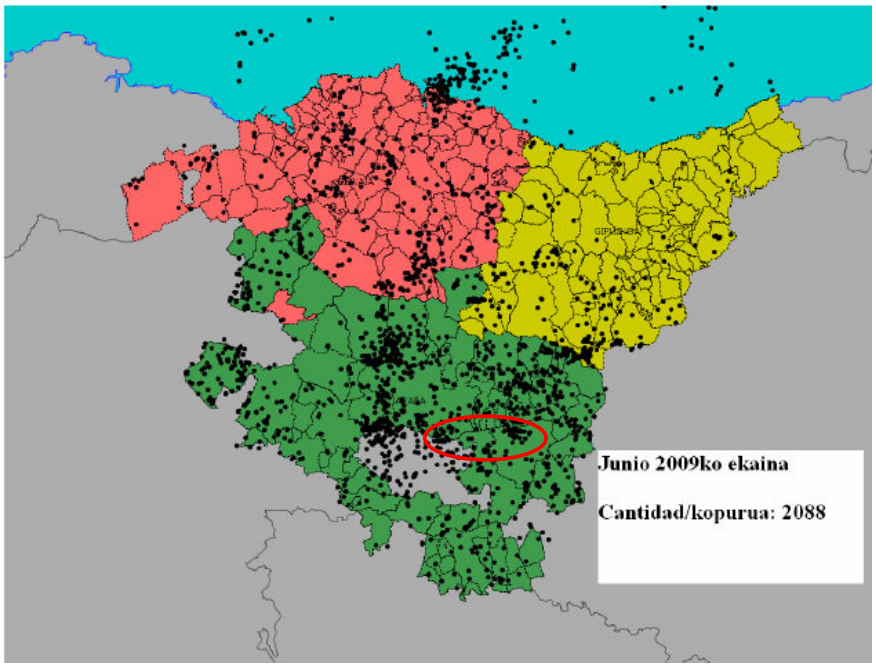


Figure 3. Example of the representation of the lightnings distribution in the warm season. Legend: Total count (June 2009).

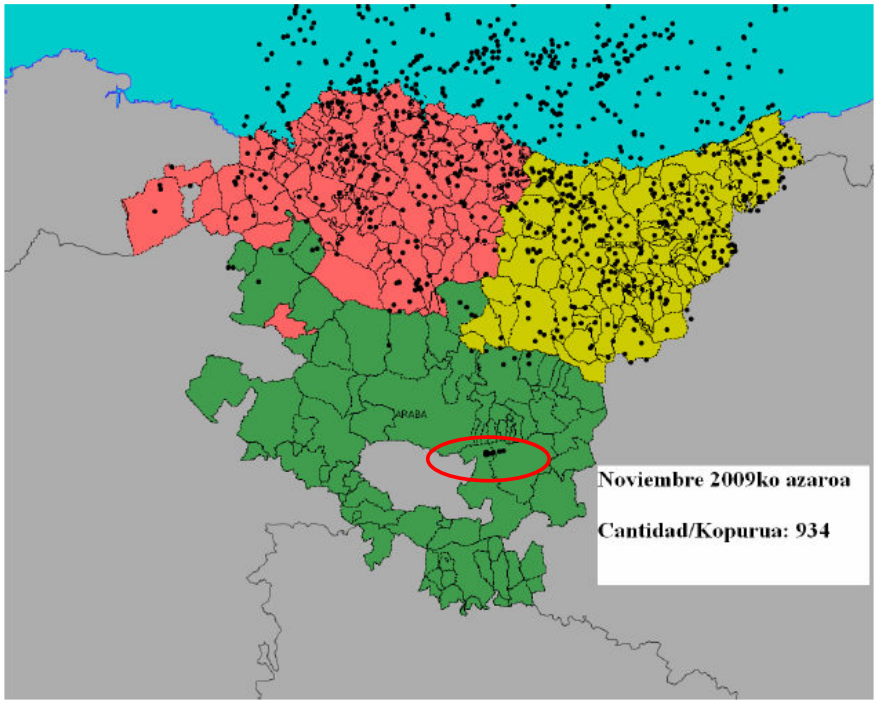


Figure 4. Example of the representation of the lightnings distribution in the cold season. Legend: Total count (November 2009). This period belongs to the strike ligthning impact.

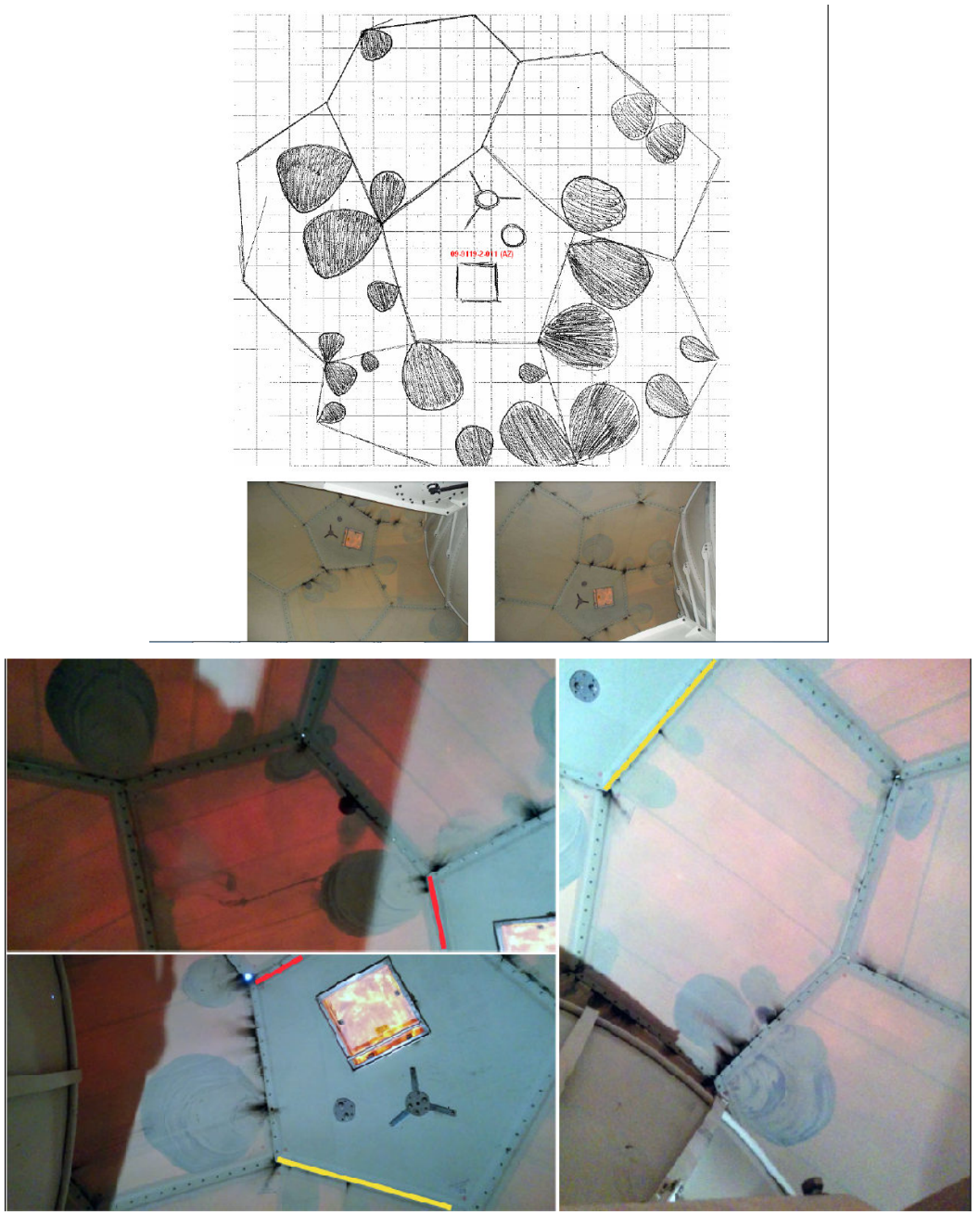


Figure 5. Maintenance photos of the radome status in February 2012. The radome stains have enlarged over the years and presented problems of leaks and moisture.

The thesis is based on the study of the electrical field in high structures considering the meteorology of the site. The relevant results of the thesis about the best protection system of the Kapildui weather radar base on the results of the Slim model are:

-In a basic case in which there is no static accumulation on the radome and the base of the cloud is far away from it, the lightning rods at the top of the radome and below the radome (lateral) are more significant than external ground cables to protect the structure. This situation could be considered in a warm season.

-In the situation, in which there is accumulation of static charge on the radome, the cables on the outer face of the radome are essential in order to attenuate the effect of the static surface charge. The cables increase the stabilization of the structural tower and in particular the metallic elements (screws…). In case of lightning discharges, this one will occur on the protection system installed for that purpose.

The lasted and third period started, in October 2014, the lightning protection system installed was a combination of CTS-type, lateral lightning rods and extra copper cables that they cover radome screws in the outer face of the radome.



Maintenence file of the random status. Situation of the status of the radome. First report of the semi-annual maintenance 2015.

Additional comments, it is important to take into account related to the maintenance team, the people involved in this task has to be qualified to work in tall structures. Periodically, visual inspections of the radome are required to be included not only in the maintenance task but also in more situations. In the daily monitoring two events are analyzed lightning activity close to the radar (less than 10 km) and electrical instability that it generates lost of data with a lightning activity with radius superiors to 10 km.

3 Discussion of the historical evolution

Little can be said about the first two periods, neither of the two lightning protection systems worked with the installation of the radar and with the climatology of the study area, Kapildui. Therefore, the discussion will be based on the last period.

Statistically the electrical activity in this period indicates a decrease in the density of the lightning with respect to the previous periods in the vicinity of the radar, even passing the storms above the tower. On the other hand, electrical current instabilities have been recorded with data losses associated with the passage of storms, but the lightning strikes have been channeled through the correct paths without affecting the screws or the radome.

The Impact in the quality of the raw data of the new system remained to be evaluated, beeing important to find a balance between, losses of data quality in a particular application, economically profitable operating system and availability of a complete historical database available for different meteorological studies and users. Regarding this point, none of the products derived from the raw data related to precipitation or detection of other targets or meteorological phenomenons that are monitored with the radar in situations of adverse weather have been compromised.

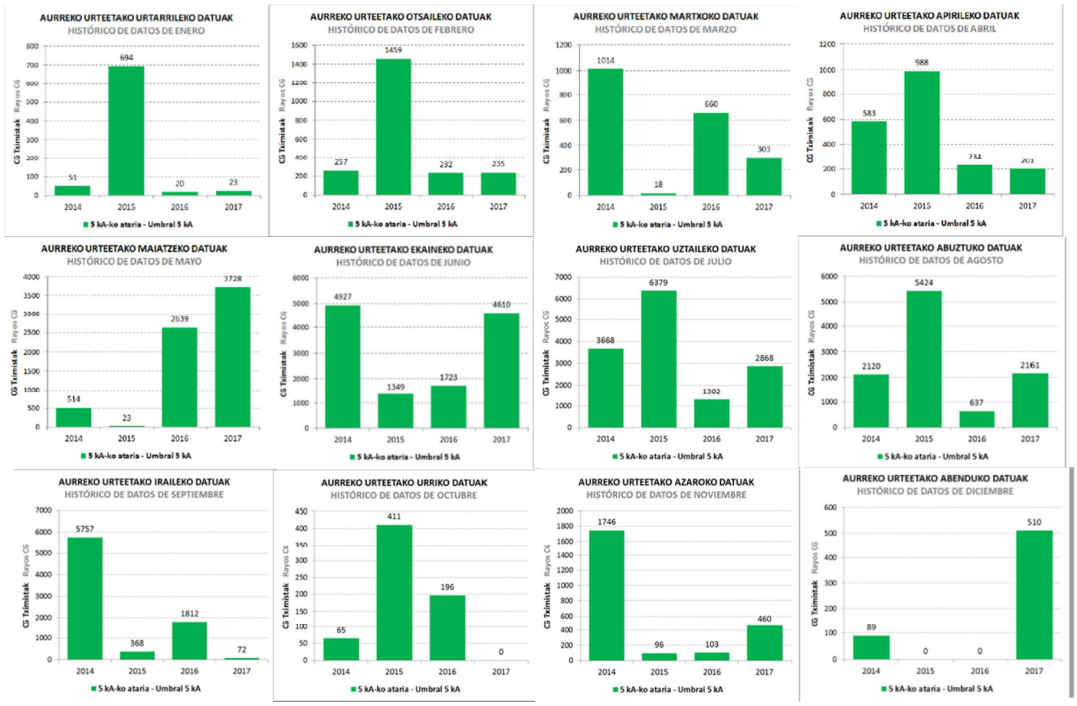
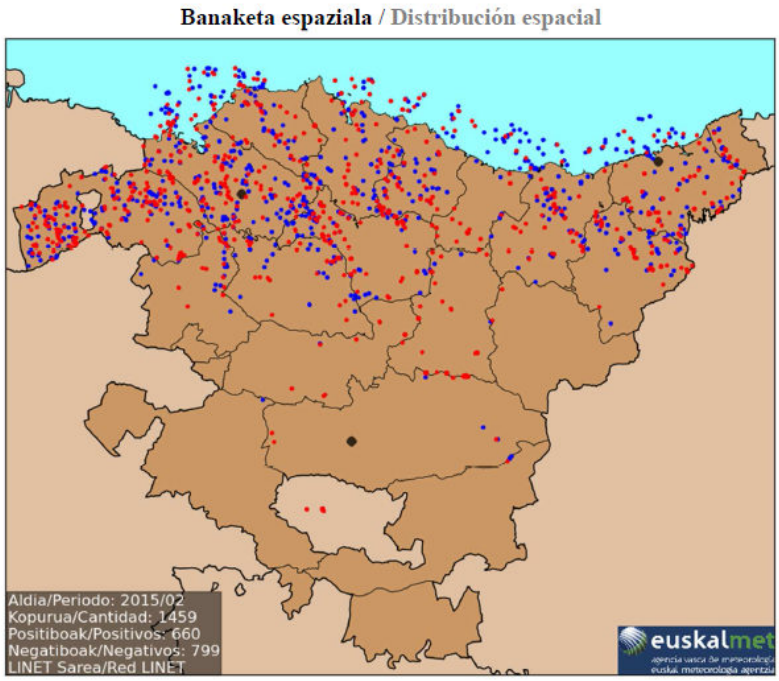


Figure 6. Histogram of frequency of strikes last years, by months.



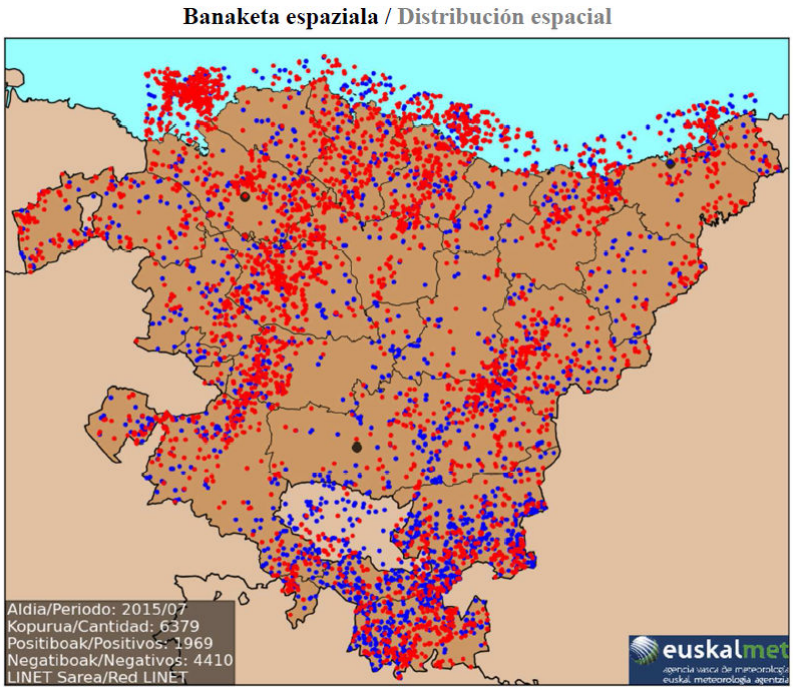


Figure 7. Example of the representation of the lightning distribution in cold / warm seasons and total count, February and July 2015 (last period).

4 Conclusions

A Previous study of the location must be made taking into account the incidence that stormy activities may have on the system. It is important that the site is suitable for observing meteorological phenomena but the lightning protection system must be optimal to protect the installation in all kinds of situations

The direct impact of lightning on the structure accelerates the deterioration of the material that can be compromised in adverse weather situations.

It is necessary to take a good supervision of the state of the radome after any episode that makes suspect a high probability of impact in the structure, with or without adverse effects in radome or screws.

A loss in the quality of the data, in complex locations but of great meteorological interest for a support service for citizen security, can compensate the decision to opt for a more robust protection system.

the economic cost of changing a radome and above all for a regional meteorological service should not be ignored, the decisions to make are a compromise of many factors that must be evaluated before operating a system like these in complex terrain .

Finally, to say that this work is methodologically based on trial and error and therefore wants to make known to the radar community other alternatives that can work in locations such as the study.

Acknowledgement

The authors thank their colleagues from Euskalmet/DAEM (Basque Meteorological Agency/Directorate of emergency and meteorology), for supplying the raw data used in this analysis.

References

Evelio Álvarez Lamata, Francisco Espejo Gil, Francisco José Cortés Rabinad, Cristina Lafragüeta Pérez y Roberto Serrano Notivoli. "Caracterización sinóptica de los procesos convectivos en el interior del nordeste peninsular". Nota técnica 3 de AEMET, NIPO: 784-11-008-8. <http://www.aemet.es/documentos/es/conocermas/recursos_en_linea/publicaciones_y_estudios/publicaciones/Sinoptica/NT_AEMET_3.pdf>, visit on June 11, 2018.

Joseba Egaña, Santiago Gaztelumendi, Virginia Palacio, Olatz Principe, Mercedes Maruri (2014). "Using radar data for analysis of a very heavy precipitation episode in Bilbao area", 8th European Conference on Radar in Meteorology and Hydrology. 1-5 September 2014.

Santiago Gaztelumendi, Joseba Egaña, Olatz Principe, Virginia Palacio, Mercedes Maruri (2014). "Analysis of a heavy storms episode in Basque Country: the 19-20 jul 2013 case", 8th European Conference on Radar in Meteorology and Hydrology. 1-5 September 2014.

Santiago Gaztelumendi, Joseba Egaña, Arkaitz Etxezarreta, Mercedes Maruri, Maialen Martija, José Antonio Aranda and Pedro Anitua (2015). "A tornado in Basque Country?: the 23 june 2014 case". European Conference on Severe Storms 2015. 14–18 September 2015, Wiener Neustadt, Austria. ECSS2015-71

Javier López ; Joan Montanyà ; Mercedes Maruri ; Jose Antonio Aranda ; Santiago Gaztelumendi, (2010). "A case of winter lightning initiation from a tall structure in the Basque Country ", 30th International Conference on Lightning Protection (ICLP) . 13-17 Sept. 2010. DOI: 10.1109/ICLP.2010.7845841

J.López , J.Montanyà, M.Maruri, D.De la Vega, J.A.Aranda, S.Gaztelumendi (2012). Lightning initiation from a tall structure in the Basque Country. Atmospheric Research. Volume 117, 1 November 2012, Pages 28-36 https://doi.org/10.1016/j.atmosres.2011.07.006

J. López (2012). Estudio de las condiciones del inicio de rayos ascendentes en torres radar y evaluación de los sistemas de protección. UPV/EHU. Directores David de la Vega y Mercedes Maruri

Mercedes Maruri, Arkaitz Etxezarreta, Jose Antonio Aranda, Maialen Martija, Eugenia Iturritxa, Iñaki Eguiara, Jesus Torres, Joseba Egaña, Pedro Anitua, Santiago Gaztelumendi (2014). "Study of radar signatures of hail in the Basque Country", 8th European Conference on Radar in Meteorology and Hydrology. 1-5 September 2014.

WMO-CIMO-OPAG-CB. "Training course on weather radar systems (2005), Expert team on training activities and training materials,". <https://www.wmo.int/pages/prog/www/IMOP/publications/IOM-88_TM-Radars/IOM-88_Module-F.pdf>, visit on June 11, 2018.

Severe Hail Detection: Hydrometeor Classification for Polarimetric C-band Radars Using Fuzzy-Logic and T-matrix Scattering Simulations

Mari L. Schmidt[1], Silke Trömel[1], Alexander V. Ryzhkov[2], and Clemens Simmer[1]

[1]*Institute of Meteorology/Univ. of Bonn, Bonn, Germany*
[2]*CIMMS/Univ. of Oklahoma, Norman, Oklahoma, USA*

(Dated: 19 June 2018)

1. Introduction

Detecting and discriminating hail size is done operationally for S-band radars *e.g.* in the US using published and discussed algorithms (e.g. Ryzhkov et al. (2013a), Ortega et al. (2016)). However, these algorithms were designed for S band and may require different approaches or at least adjustment to work at C band. During summertime convective events large hail is frequently reported in the growing European severe weather database (ESWD) and can cause severe damage. Therefore, a hail discrimination algorithm needs to be developed for utilization on operational weather radar networks in Europe, including Germany, which consist mainly of C-band radars.

C-band radars are more affected by attenuation especially in hail cases. The usability to detect hail due to attenuation and methods to mitigate attenuation in C band have been discussed Schmidt et al. (2017). Furthermore, current operational algorithms were designed for S band and do not consider specific attenuation A_h at all for the classification. Modifications to operational algorithms, like the hydrometeor classification algorithm (HCA) from Park et al. (2009) and the hail size discrimination algorithm (HSDA), described in Ryzhkov et al. (2013a) and Ortega et al. (2016), to include A_h and use proper parameter ranges for C band are possible. We present here an approach to determine proper parameters for C-band radars using backscattering simulation.

2. Data and Model

2.1. Radar Data

For the development and as a testbed of the algorithms, we use the German polarimetric radar network of the German Weather Service (DWD) covering an area of more than $357\,000\,\mathrm{km}^2$ as primary radar data source. To compare the performance on S-band and C-band data, same radar volumes should be collected by both type of systems. For the comparison of S band and C band we use data of two quasi-collocated radar sites in Alabama, KEOX (S band) and EEC (C band). The sites are approximately $40\,\mathrm{km}$ apart from each other.

2.2. Scattering Model

We use a two-layer T-matrix scattering model to obtain backscattering amplitudes of dry and wet hail. For rain or dry hail a single-layer T-matrix scattering would be sufficient, but to cope with the scattering properties of water coated, wet hail, a two-layer model performs better Ryzhkov et al. (2010). The code for the model used here is the same as in Ryzhkov et al. (2013b). To calculate scattering, temperature dependent dielectric constants of the simulated medium are necessary. These are calculated using the equations from Cole and Cole (1941).

Also, scattering is not only dependent on the material, but on the shape as well. Two-layered spheroids are assumed, but the outer axis-ratio of the shape is variable. Here the axis-ratio γ for rain droplets with diameter D (in mm) is assumed to follow Ryzhkov et al. (2010):

$$\gamma = 0.9951 + 0.02510 \cdot D - 0.03644 \cdot D^2 + 0.005303 \cdot D^3 - 0.0002492 \cdot D^4 \,. \tag{2.1}$$

For dry, small hail/graupel with Diameter D the axis-ratio γ is assumed to follow Ryzhkov et al. (2010)

$$\gamma = \begin{cases} 1 - 0.02 \cdot D & if\ D < 10\,\mathrm{mm}, \\ 0.8 & if\ D \geq 10\,\mathrm{mm} \end{cases} \tag{2.2}$$

Tumbling of hydrometeors is considered with a "two-dimensional axissymmetric gaussian distribution of orientations" Ryzhkov et al. (2010). By providing a standard deviation of the canting angle, angular moments can be calculated. The

polarimetric variables are then calculated using the scattering amplitudes obtained by the T-matrix and the angular moments as described in Ryzhkov et al. (2010).

3. Hydrometeor Classification

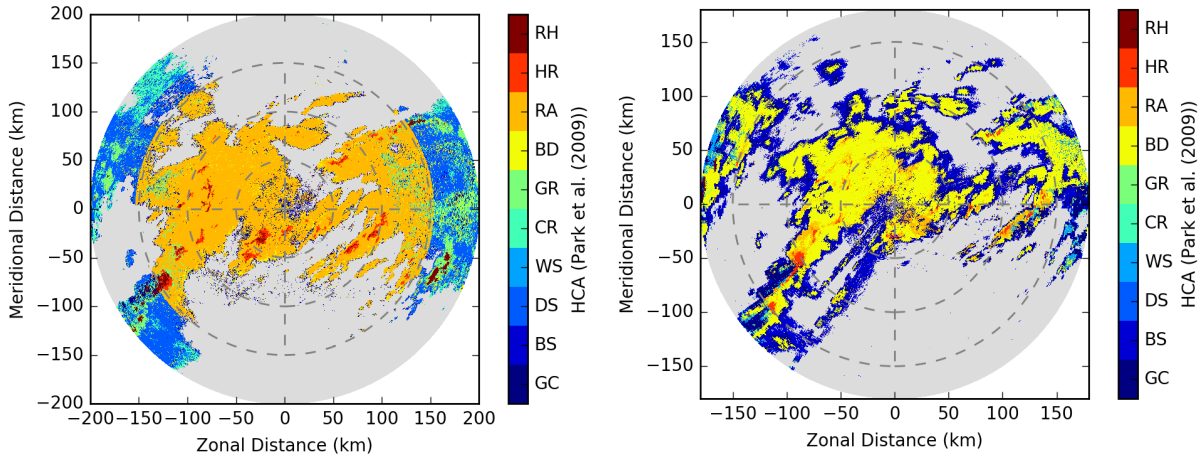
3.1. Performance of unmodified algorithm

Reference Park et al. (2009) presented a well working hydrometeor-classification algorithm (HCA). It is used operationally and was extended to discriminate between small, large and giant hail (see Ortega et al. (2016)). But with the parameters provided, the algorithm does not work well at C band. This is shown exemplarily in Fig. 1, where we compare the application of HCA to S-band data and C-band data of two quasi-colocated radars.

For the S-band data, shown in Fig. 1a, most of the area is detected to contain rain with some cells bearing heavy rain and hail. Further away only snow is detected as the melting layer is passed. The classification seems to be quite plausible for this example at S band.

For the same date and time the closeby C-band radar captured the same storm. Using the same algorithms as before, the resulting classification, shown in Fig. 1b, appears to be quite different. First of all, the C-band radar suffers from strong attenuation at locations where hail was detected with S-band data. This is not a shortcoming of the applied algorithm as this problem is related to wavelength properties. However, for a successful hydrometeor classification and hail detection at C band, attenuation is highly recommended being monitored and included in the algorithm (compare with Schmidt et al. (2017)).

Secondly, most of the area is classified to contain big drops instead of rain. This is a clear indication, that the parameters provided by Park et al. (2009) do not fit for C band. Also, almost no hail was clearly classified. One obvious reason might be, that the reflectively for hail at C band is generally lower than at S band (see *e.g.* Fig. 8 and 15 in Ryzhkov et al. (2013b)).



(a) S band (KEOX) *(b) C band (EEC)*

Figure 1: The hydrometeor classification algorithm (HCA) as in Park et al. (2009) for two quasi-colocated radar sites (KEOX and EEC) in Alabama, USA. The ordinate shows the meridional and the abscissa the zonal distance from the radar site in km. The gray color marks areas without classifiable echoes inside the radar range. According to the colorbar the different determined hydrometeor classes are given by color. Here stands RH for rain and hail mixture, HR for heavy rain, RA for rain, BD for big drops, GR for graupel, CR for ice crystals, WS for wet snow, DS for dry snow, BS for biological scatter and GC for ground clutter (compare with Park et al. (2009)). The data used has been measured on Jan., 21th 2017 16:43 (local time).

3.2. Simulation Setups

To obtain useful parameters for the fuzzy-logic, a broad variety of hydrometeors needs to be simulated. Most crucial is the distinction between rain and hail. Therefore, we will focus on those two (main-)classes here.

To simulate all possible rain drops, which could appear in the radar volume, a variety of different settings has to be considered in the simulations. The following specifications of simulation parameters should cope with all probable kind of rain drops to some extent:

- Medium (inner and outer) is liquid water
- Dielectric constants for 30 °C, 20 °C, 10 °C and 0 °C

- Drop diameters from $0.1\,\mathrm{mm}$ and up to $50\,\mathrm{mm}$ with step size of $0.1\,\mathrm{mm}$
- Tumbling: Canting angle distributions have standard deviations of $7°$, $20°$ or $45°$.
- Axis-ratio of droplets depends on drop diameter and follows (2.1).

For hail - in general - other specifications are important. Not only can hail be dry and wet, but also appear in various combinations of size, shape and density. Later on three size categories for hail will be used: small hail ($D < 2.5\,\mathrm{cm}$), large hail ($2.5\,\mathrm{cm} \geq D < 5\,\mathrm{cm}$) or giant hail ($D \geq 5\,\mathrm{cm}$). Therefore, the simulation results will be split into these three groups as well. In certain heights only dry hail appears and in lower heights only wet hail may appear. Therefore, in the later classification additionally discrimination for range gates in dependency on the temperature of the radar volume has to take place (compare with Ortega et al. (2016)). Following specifications will be considered in the simulations:

- Inner medium is ice (with variable density) and outer medium is either ice (with same density as inner medium) or liquid water.
- If outer medium is liquid, the water coat will be simulated to be $0.5\,\mathrm{mm}$ thick.
- Dielectric constants at $20\,°\mathrm{C}$, $0\,°\mathrm{C}$ and $-10\,°\mathrm{C}$ for each medium (*i.e.* various combinations of different temperature are possible with mixed media)
- Particle diameters from $1\,\mathrm{mm}$ up to $25\,\mathrm{mm}$ (small hail), $26\,\mathrm{mm}$ up to $50\,\mathrm{mm}$ (large hail) and $51\,\mathrm{mm}$ up to $100\,\mathrm{mm}$ (giant hail). Each with $1\,\mathrm{mm}$ step-size.
- Axis-ratio for small hail will follow (2.2). For large and giant hail it will be set to 0.5, 0.6, 0.7, 0.8, 0.85, 0.9, 0.95, 1.0.

With the simulation results trapezoidal membership functions can be defined. E.g. for differential reflectivity Z_{DR} for rain we obtain values as shown in Fig. 2. The probability shown (blue histogram) is determined by the occurrence of the respective value and the total number of simulations for this class (here rain). The edges of the trapezoidal function are here determined by the 5, 25, 75 and 95 percentiles of all simulated values of this class. Most values are found to be around $+0.2\,\mathrm{dB}$. With these values a fuzzy-logic algorithm (*e.g.* as in Park et al. (2009)) could be fed to consider Z_{DR} at C band. With this approach, parameters based on simulations instead of empirical values can be set for all polarimetric values. However, the simulations reflect every variation of a simulated hydrometeor alike. This does not necessarily mean, that all variations appear in observation equally. But no polarimetric signal of any variation is hereby missed or underestimated by probability assumptions of appearance (*e.g.* by a drop-size distribution).

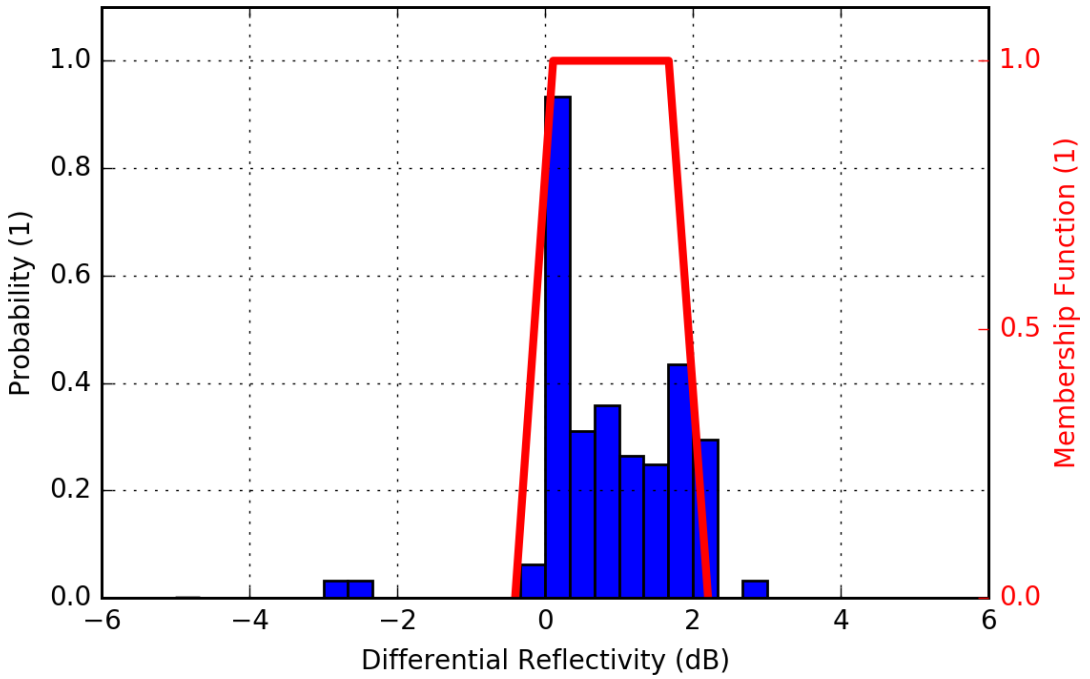


Figure 2: Probability of occurrence of differential reflectivity in T-matrix backscattering simulation for rain shown as histogram in blue. See text for simulation specifications. Trapezoidal membership function in red is obtained by 5, 25, 75 and 95 percentiles of simulated values.

4. Limits of this approach

Some assumptions have been made during developing the proposed method. Therefore, limits and drawbacks of the approach are mentioned here. Without making claims of being a complete list of all flaws, here are some of which should be kept in mind:

- the used scattering model may not be able to correctly model ice crystals and biological scatter. For these two classes empirical values may be much more accurate.
- all possible kind of hail variations were meant to be thought of and realized in the simulations. However, some hail variations are missing. *E.g.* only regular shapes are possible to be simulated and non-regular shapes (*e.g.* spiky hailstones) could not be simulated.
- every simulation is weighted to be equally important as every other simulation. In nature, some "simulations" may appear more often than others and lead to different polarimetric observations.
- each simulation considers currently only a single set of hydrometeors (*e.g.* large rain drops). In nature all kind of different hydrometeors could appear in the same radar volume and lead to different scattering results.

5. Conclusion and Current Work

We have shown that the unmodified HCA with default parameters is not suitable for the application on C-band radars. Adjustments to the parameters used for the fuzzy-logic are required. This could be done reliably by scattering simulations - although with limits - as proposed here.

As concluded in former work, the specific attenuation A_h is a unique polarimetric variable for hail size discrimination as it is the only polarimetric variable known so far, which monotonically increases with size diameter at C band (see Schmidt et al. (2017)). Therefore, we highly recommend including A_h in hydrometeor classification algorithms.

Lastly, a third modification is recommended: different hail classes for differently sized hail, since scattering behavior of hail varies with size. Not only provides a separation of hail into sized subclasses (e.g. small, large and giant hail) more information, it may improve the reliability to detect hail too.

The current approach being tested is well suited for nowcasting in operational systems. With the required radar data loaded, the discrimination algorithm yields hydrometeor classes and hail size classes for a given set of fuzzy-logic parameters in less than a few seconds on a modern Linux PC. With multiprocessing this can be reduced even further.

At the time being not all simulations are finished and not all results are available yet. However, work is in progress and further results (*e.g.* parameters range for fuzzy-logic) are currently being produced. Once testing and evaluation is done, these parameters will be published separately.

Once all parameters have been determined, the modified algorithm will be applied to the German polarimetric radar network. Using the hail size reports of the growing European Severe Weather Database (ESWD), the hail classification and discrimination will be evaluated.

Acknowledgments

This project is supported by the German Weather Service (DWD) under grant *2015EMF-07*. The Alabama radar data was kindly provided by Pengfei Zhang. Also, we would like to thank Jeffrey Snyder and Alexander V. Ryzhkov for providing the code and support for the two-layer T-matrix scattering model.

References

K. S. Cole and R. H. Cole, "Dispersion and absorption in dielectrics i. alternating current characteristics," *The Journal of chemical physics*, vol. 9, no. 4, pp. 341–351, 1941.

K. L. Ortega, J. M. Krause, and A. V. Ryzhkov, "Polarimetric radar characteristics of melting hail. part III: Validation of the algorithm for hail size discrimination," *J. Appl. Meteor. Climatol.*, vol. 55, no. 4, pp. 829–848, apr 2016. [Online]. Available: http://dx.doi.org/10.1175/JAMC-D-15-0203.1

H. S. Park, A. V. Ryzhkov, D. S. Zrnić, and K.-E. Kim, "The hydrometeor classification algorithm for the polarimetric WSR-88d: Description and application to an MCS," *Weather and Forecasting*, vol. 24, no. 3, pp. 730–748, jun 2009. [Online]. Available: http://journals.ametsoc.org/doi/abs/10.1175/2008WAF2222205.1

A. Ryzhkov, M. Pinsky, A. Pokrovsky, and A. Khain, "Polarimetric radar observation operator for a cloud model with spectral microphysics," *Journal of Applied Meteorology and Climatology*, vol. 50, no. 4, pp. 873–894, apr 2010. [Online]. Available: http://journals.ametsoc.org/doi/abs/10.1175/2010JAMC2363.1

A. V. Ryzhkov, M. R. Kumjian, S. M. Ganson, and A. P. Khain, "Polarimetric radar characteristics of melting hail. part i: Theoretical simulations using spectral microphysical modeling," *Journal of Applied Meteorology and Climatology*, vol. 52, no. 12, pp. 2849–2870, dec 2013. [Online]. Available: http://dx.doi.org/10.1175/JAMC-D-13-073.1

A. V. Ryzhkov, M. R. Kumjian, S. M. Ganson, and P. Zhang, "Polarimetric radar characteristics of melting hail. part II: Practical implications," *Journal of Applied Meteorology and Climatology*, vol. 52, no. 12, pp. 2871–2886, dec 2013. [Online]. Available: http://dx.doi.org/10.1175/JAMC-D-13-074.1

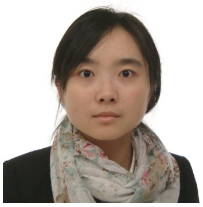
M. Schmidt, S. Troemel, A. V. Ryzhkov, and C. Simmer, "Severe hail detection: An adaptive algorithm for anomalous attenuation correction and new insights from scattering simulations at c-band," in *38th Conference on Radar Meteorology, AMS, Chicago, IL, 28 Aug. 2017*, 2017. [Online]. Available: https://ams.confex.com/ams/38RADAR/meetingapp.cgi/Paper/320715

Effect of Urban Environment on summer precipitation in Stuttgart

Yaoyao Zheng[1], Jan Handwerker[1], and Norbert Kalthoff[1]

[1]*Karlsruhe Institute of Technology, Hermann-von-Helmholtz-Platz 1, 76344 Eggenstein-Leopoldshafen, Germany*

(Dated: 22 June 2018)



Yaoyao Zheng

1. Introduction

Urban region is characterized with unique thermal and dynamical properties, differing from other natural environments. One well-established illustration is the heat island effect. Besides air temperature, urban environment might also affect precipitation. Research (Han et al., 2014; Lowry, 1998; Shepherd, 2005) has shown that the urban-specific perturbations have potential to change the genesis, intensity and movement of precipitation systems within/surrounding the cities, while such changes might vary for cities of different sizes, climate and topography. The urban effect on precipitation is indefinite, hence requiring further investigations to answer several questions, for instance, whether the presence of an urban environment would suppress or favor the initiation and development of precipitation systems.

What renders the issue of urban effect on precipitation more intricate is the possible additional topographic effect, since some cities have complex topographic features. One exemplar is Stuttgart–one of largest metropolitan areas in Germany. The downtown of Stuttgart is located in a sink-like basin and its perimeter is across several hills and valleys. The complex terrain of Stuttgart complicates the study on urban environment, however, selecting Stuttgart as our target city may bring about potential investigations of combination of urban effect and topographic effect on precipitation. Furthermore, as a consequence of such topography, Stuttgart is vulnerable to flash flooding, necessitating the studies on precipitation, such as quantitative precipitation estimation, for the hydrologic applications including flooding prediction and mitigation.

Precipitation is fairly inhomogeneous in terms of both time and space, which necessitates observations of high spatial and temporal resolution. In comparison with S-band and C-band weather radar, X-band has a superior spatial-temporal resolution capacity. Additionally, the spatial coverage of X-band is compatible with scale of most major cities. Thus, X-band radar is suitable for studying urban precipitation. Nevertheless, similar to any other weather radars, data quality of X-radar measurement is subject to numerous factors such as scan strategy (Zheng et al., 2017). After our pre-experiment chose a suitable scan strategy (Zheng et al., 2017), further valuation of X-band radar dataset can be achieved by comparing X-band radar precipitation measurements to other precipitation measurements provided by other independent sources, which can give more credence to our further research that relies upon the X-band radar dataset. For example, measurement from a vertical-looking Micro Rain radar (MRR) can be used for evaluation of measurement in vertical direction, while rain gauge network distributed within the radar coverage provides possibility for areal comparison.

Above all, this extended abstract will focus on the assessment of X-band radar measurement in Stuttgart using other available independent precipitation measurements, in order to facilitate the subsequent research on utilization of X-band radar measurement to resolve the spatial distribution and temporal evolution of precipitation systems within or surrounding the urban regions. Section 2 will introduce the instruments and measurements, while Section 3 will propose a customized height-dependent Z-R relation. The discussion of comparisons of precipitation measurements between our X-band radar and other instrument will be presented in detail in Section 4.

2. Measurements

High-resolved X-band radar dataset was obtained from X-band radar measurement in Stuttgart from May 23-September 17, 2017. During that time, a dual-polarized X-band radar from Institute of Meteorology and Climate Research of Karlsruhe Institute of Technology was operated in two scan strategies. One is defined as fine scan and the other one as coarse scan (see Table 1). In accord with the high-resolved measurement we aim at, the fine scan strategy was operated with a radial resolution of 75 meters, which was nearly the highest spatial resolution available in our X-band radar setup. During the operation, a unit time period of each 10 time consisted of three fine scans and one coarse scan, which means the temporal resolution of our measurement can be as short as 90 seconds.

Table 1: Scan strategy of X-band radar measurements.

Scan strategy	Radial resolution(m)	Radius(km)	Number of elevation	Number of measurement per hour
Fine	75	75	3	18
Coarse	250	100	10	6

Besides the above X-band radar measurement, a vertical-pointing MRR operated by University of Stuttgart, which is situated in Stuttgart and 13 km away from X-band radar, also provides datatset of radar reflectivity (Z_{MRR}) in dBZ and rainfall rate (RR_{MRR}) in mm/hr, with the time resolution of 1 minute and the height resolution of 100 meters starting from 0.1 km to 3.1 km above the surface. Validation of MRR measurements is conducted by comparing precipitation measurement from MRR to simultaneous precipitation measurement from a weighing rain gauge named Pluvios. Pluvios updates rainfall rate (RR_{Pluv}) at a 5-minute interval. Since the Pluvios is located just a few meters away from MRR, precipitation measurement from Pluvios should serve as a good reference for the precipitation measurement from MRR.

Atmospheric hydrometers at different altitudes is much likely to differ from the rain falling on the land surface, partially due to change of phase such as evaporation. Moreover, strong winds enable to shift the precipitation to other locations that are not directly above the ground-based instruments. Additionally, radar-derived rainfall estimation depends on sizes of scattering volumes. For instance, the measurement volume of MRR at 2km high is in the order of magnitude of 100 times as that of MRR at 200m high. Large scattering volume is characterized by more significant spatial variation, probably introducing extra uncertainties. For the purpose of validation, it is preferred to use MRR rainfall measurement at lower attitude to compare with Pluvios. For instance, figure 1 shows an excellent linear correlation for precipitation measurements from MRR and Pluvios. In figure 1, the orthogonal linear fitting is applied, producing the slope equal to one and the intercept equal to 0. In general, the linear relation between MRR and Pluvios precipitation measurements tends to deteriorate with height. However, this linear relation in our study is still quite obvious up to 2km of the measuring height of MRR.

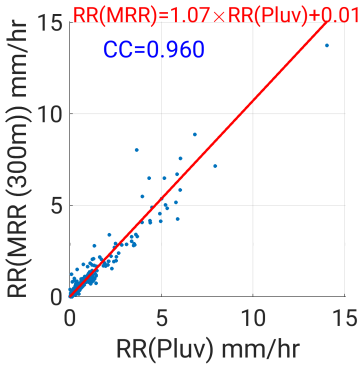


Figure 1: Comparison of precipitation measurements between rain gauge (Pluvio) and MRR at a 300-meter height above surface

Although measurements of MRR can be used for validation at different vertical levels, it is only a point comparison, which implies the demand of more measurements for validation. Thus, hourly precipitation rate from (DWD-CDC) from rain gauges from German Weather Service–Deutscher Wetterdienst (DWD) will be involved for validation of X-band radar data as well (more details in Section 4.2).

3. Z-R relation

Radar reflectivity (Z) rather than rainfall rate is the variable directly provided by X-band radar. The empiric relation between radar reflectivity and rainfall rate (Z-R relation) is prone to a number of external factors such as precipitation type and atmospheric thermodynamic condition. Due to variability of drop size distribution (DSD) and radar measuring volume, there is also variability of Z-R relationship with height.

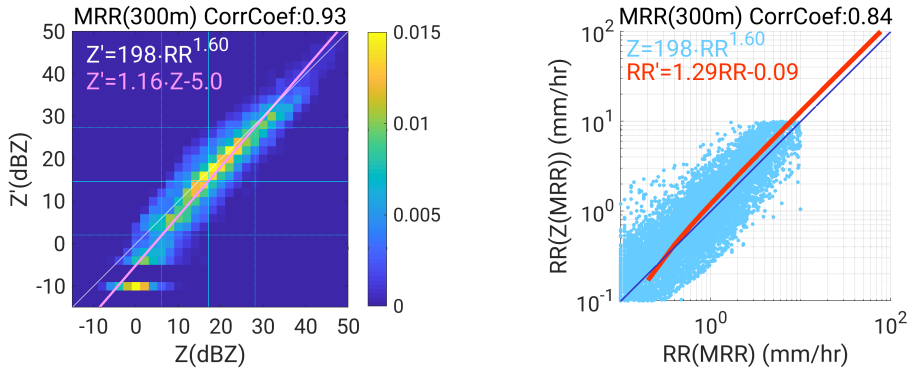
Among the aforementioned measurements in Section 2, MRR provides dataset of radar reflectivity and rainfall rate, but rain gauge is only able to measure rainfall rate. In order to guarantee the reliability of comparison between X-band with other instruments, Z-R relation is needed and should be selected with caution.

Datasets of both reflectivity and rainfall rate are derived using DSD measured directly by MRR, and accordingly rainfall rate estimation of MRR is not based Z-R relation (METEK, 2012). In contrast, simultaneous datasets of reflectivity and rainfall rate from MRR can be used for deriving individual Z-R relations, in regards to the suggestion (Peters et al., 2002) about updating Z-R relation using MRR. Moreover, there are dataset of MRR at different altitudes, which offers opportunities to derive Z-R relations at corresponding altitudes. To reduce the uncertainties, MRR dataset obtained during the same period of X-band measurement are involved here. For example, a MRR-based Z-R relation is derived as

$$Z = aR^b \tag{3.1}$$

, where a=198 and b=1.6 for MRR of 300-meter height, which is accidentally similar to the well-known Marsh-Palmer relation.

One way to assess the MRR-based Z-R relation is to convert rainfall rate into corresponding reflectivity based on specific Z-R relation, which can be referred as the equivalent Z'_{MRR}. Figure 2(a) is a two-dimensional histogram of reflectivity between MRR-measured Z and equivalent Z'_{MRR}. Reversely, the reflectivity can be converted into the corresponding rainfall rate based on the inverse form of Z-R relation, which is then referred as the equivalent R'_{MRR}. Figure 2(b) is the scatterplot of the MRR-measured R and the equivalent R'_{MRR}. Both figures demonstrate good linear correlations, between Z_{MRR} and equivalent Z'_{MRR}, or between R_{MRR} and equivalent R'_{MRR}, supporting the reliability of the MRR-derived Z-R relation.



(a) dBZ comparison (b) RR comparison

Figure 2: Evaluation of Z-R relations derived from MRR measurements

However, on condition that the increasing altitudes is accompanied by more measurement errors related to vertical wind and ice phase (METEK, 2012) in higher altitudes, the MRR-derived Z-R relation at higher altitude might exhibit less robust linear relations, compared to figure 2. For that sake, the variations of correlation coefficients of these quasi-linear relations with heights is presented in figure 3. Correlation coefficients at most heights, such as lower than 1-km, are sufficiently high, imply the MRR-derived Z-R relation could be reliable. Correlation coefficients for Z are usually larger than those for rainfall rate. It may be due to the fact that radar reflectivity in unit of dBZ is quasi-logarithmic, where measurements from heavy precipitation weight less.

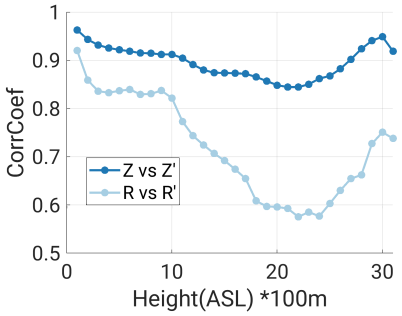


Figure 3: Variation of correlation for MRR-based ZR relations

4. Evaluation

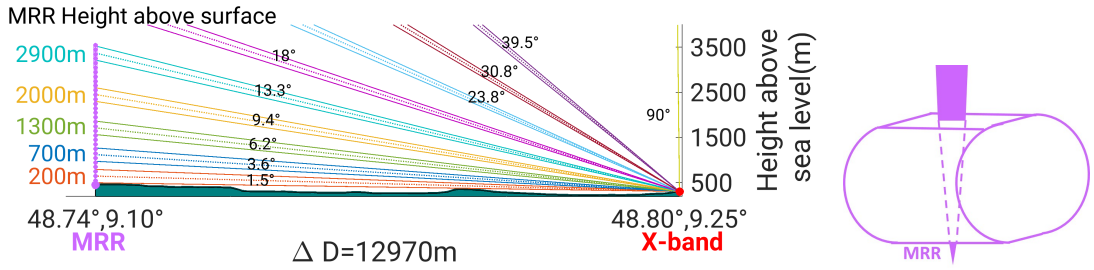
The man propose of this section is to 1) compare the X-band radar reflectivity Z_{Xband} with Z_{MRR}; 2) compare Z_{Xband} with RR_{MRR}; 3) compare Z_{Xband} with hourly rainfall rate from DWD rain gauge network–RR_{DWD}. These comparisons are supposed to examine the data quality of our X-band radar measurements.

4.1. Evaluation of Z with a vertically-looking MRR

Since MRR is within the coverage of X-band radar and MRR has been validated with ground reference data (see Section 2), we can use the coincident and co-located radar reflectivity measurements of MRR and X-band radar to evaluate the data quality of Z_{Xband}. The geometry of the intercepting scattering volumes of MRR and X-band radar is shown in figure 4. From figure 4(b), we find that the radar beams of first five elevations of the coarse scan strategy intercept the MRR measuring heights of 200m, 700m, 1300m, 2000m and 2900m.

Although both X-band radar and MRR offer radar reflectivity measurement, there are distinctions between them. One difference is that MRR yields the veritcal-pointing scattering volume (see figure 4(a)) and is less vulnerable to the attenuation

issue. The second difference is the size of scattering volume. Given that the beamwidths of MRR and X-band radar are 2° and 1.3° and the aforementioned radial resolutions of MRR and X-band radar measurements, the scatter volumes for MRR, X-band radar including both fine scan and coarse scan strategies can be approximately calculated based on the geometry, shown as Table 2. From the Table 2, the scattering volume of MRR is much smaller than that of X-band radar measurement at the location of MRR.



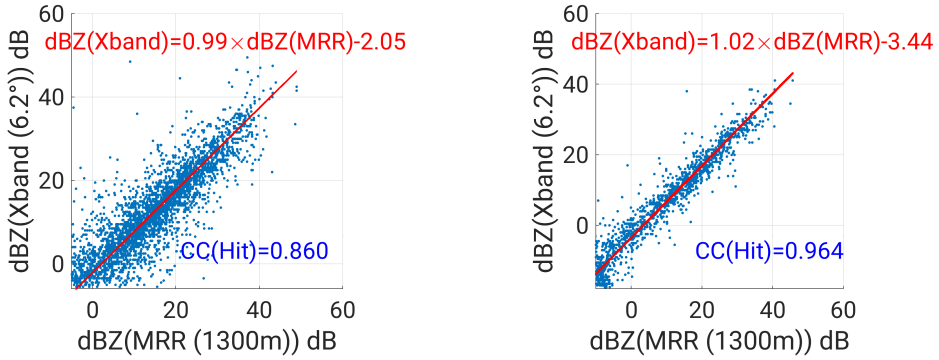
(a) Fine scan (b) Coarse scan

Figure 4: Illustration of interception between MRR and X-band radar

Table 2: Scattering volumes of MRR and X-band radar MRR (level=200m) as a unit)

MRR level	200m	700m	1300	2000	2900	Xband (fine)	Xband (coarse)
Volume	1	12	40	95	200	1240	4200

In spite of the difference between MRR and X-band radar, radar reflectivity from both instruments is highly correlated. Figure 5 shows good correlation under the circumstance that the intercepted volume is at the height of 1300 meters above the surface. When it comes to the difference of correlation between the fine scan and coarse scan, correlation coefficient of fine scan is slightly lower than that of coarse scan. A possible explanation is that the total number of measurement of fine scan is as three times as that of coarse scan within the same measuring period, as the aforementioned setup for scan strategy (see Section 2). Apparently, the negative values of both intercepts of fine scan and coarse scan indicate the X-band radar underestimates the radar reflectivity, but it appears that X-band radar measurements operating in the coarse scan strategy underestimate the reflectivity to a greater extent than fine scan strategy. A probable reason is due to the size of scatter volume. With large scatter volume, the extreme value will be 'diluted'.



(a) Fine scan (b) Coarse scan

Figure 5: Z_{MRR} vs Z_{Xband}

Figure 6 presents vertical variations of relation between MRR and X-band radar reflectivity. Correlation coefficients (see figure 6 a)) of MRR and X-band radar reflectivity decrease slightly with height, but all of them are sufficiently high. The slopes (see figure 6 b)) of linear regression equation increase with height, mostly close to unit 1 around 700 and 1300 meters. Besides, the absolute magnitudes of intercepts (see figure 6 c)) in the linear regression increase with the height as well, implying that the underestimation of X-band radar reflectivity intensifies with heights, given that the slopes are close to one. Provided that orthogonal fitting is used, deviation in figure 6 d) is defined as the summation of the shortest distances of all data points to the regression line. Figure 6 d) reveals that the liner regressions using the radar reflectivity of fine scan strategies rather than coarse scan strategies exhibit larger deviations in the higher altitudes. Hit rate (HR) and false alarm rate (FAR) in figure 6 f) are expressed as

$$HR = \frac{h}{a+b} \tag{4.1}$$

$$FAR = \frac{c}{c+d} \tag{4.2}$$

where a, b, c and d is explained in Table 3. Figure 6 f) shows that fine scan strategy provides higher HR and lower FAR, and both HR and FAR do not change too much for different heights. Contradictorily, for the coarse scan strategy, HR decreases and FAR decreases noticeably with increasing heights. The mean radar reflectivitiy in figure 6 e) is the the mean of radar reflecitivity on condition that radar reflectivity of both X-band radar and MRR are above certain thresholds, and these thresholds approximately represent the capability to detect signals from meteorology echos. The higher mean reflecitivity provided by fine scan strategies is for the reason that a number of weak signals tend to be regarded as noise in fine scan strategy, indicating deteriorating detectability related to the higher spatial (radial) resolution, which corresponds to the previous data quality analysis (Zheng et al., 2017).

Table 3: Contingency table for rain detection of X-band radar and MRR

–	MRR detects rain	MRR detects non-rain
X-band radar detects rain	a	b
X-band radar detect non-rain	c	d

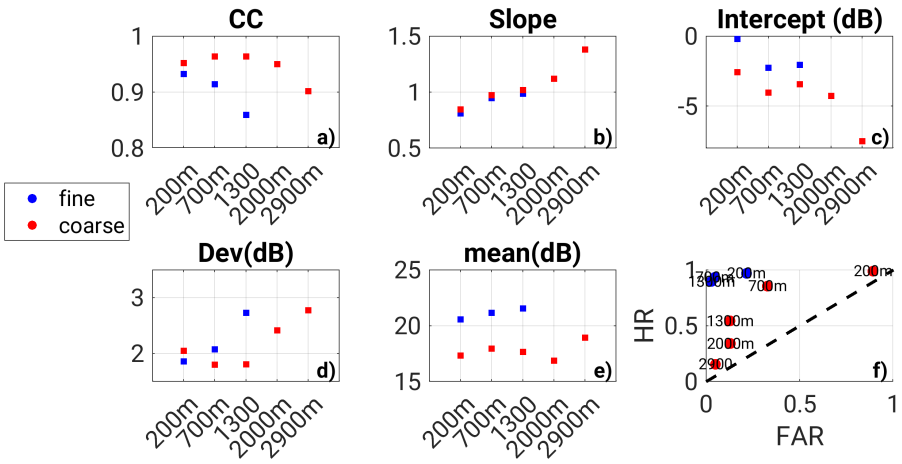


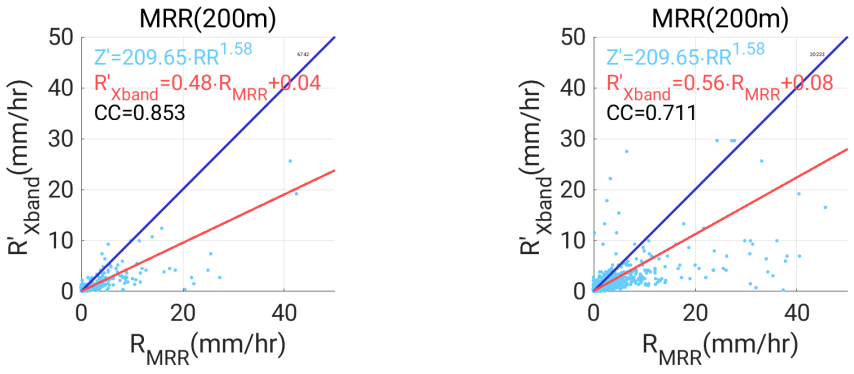
Figure 6: Vertical variation of statistics for comparison of radar reflectivity between X-band radar (both fine and coarse scan strategies) and MRR measurements. a) correlation coefficient; b) slope in linear regression equation; c) intercept in linear regression equation; d) deviation to the linear regression equation; e) mean radar reflectivity; f) scatter plot of hit rate (HR) and false alarm rate (FAR).

4.2. Evaluation of RR with a vertically-looking MRR

The procedure to compare RR between the X-band radar and MRR is similar to the comparison for reflectivity in Section 4.1, except that radar reflectivity of X-band Z_{Xband} needs to be transformed into the equivalent rainfall rate RR'_{Xband} before comparison. Similar to Section 4.1, comparisons will be conducted at different heights. Due to the variability of Z-R relation with altitudes (see Section 3), the height-dependent Z-R relations are applied. The preliminary attempt is to use MRR-derived Z-R relations from Section 3. The comparison specific at height of 200m, shown in figure 7, supports a good linear relation between RR_{Xband} and RR_{MRR}. Nevertheless, from the slope and intercept, it appears that X-band radar measurements underestimate the rainfall rate, corresponding to the underestimation of radar reflectivity in Section 4.1. However, differing from results in Section 4.1 is that the linear relations degrade more rapidly with the increasing altitudes for the comparisons of RR, while the linear relations for the comparison of radar reflectivitiy are strong enough through most heights of the MRR scattering volumes intercepted by the radarbeam of X-band radar.

4.3. Evaluation with DWD rain gauge network

Eleven stations (Table 4) are selected from DWD ground-based rain gauge network within 75 km from X-band radar. The section criteria are contingent on the heights of stations compared to the heights of scattering volumes above the stations, and the availability of radar measurements (see figure 8). The later criterion is intended to remove the stations where our X-band radar measurements are not available.



(a) Fine scan (b) Coarse scan

Figure 7: RR $_{MRR}$ vs RR'$_{Xband}$

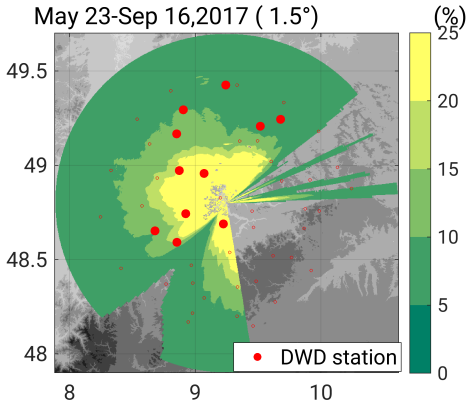


Figure 8: Map of frequency of detection of rain over the coverage of X-band radar

In order to assess the correlation of radar reflectivity from X-band radar measurement and the hourly precipitation rate from DWD rain gauges, the radar reflectivity is converted into rainfall rate refered as R'$_{X\text{-band}}$ using Z-R relation and then we compare RR$_{DWD}$ with R'$_{X\text{-band}}$. An alternative way is to converted the rainfall rate of DWD into equivalent radar reflectivity referred as Z'$_{DWD}$, and then to compare Z'$_{DWD}$ with Z$_{X\text{-band}}$.

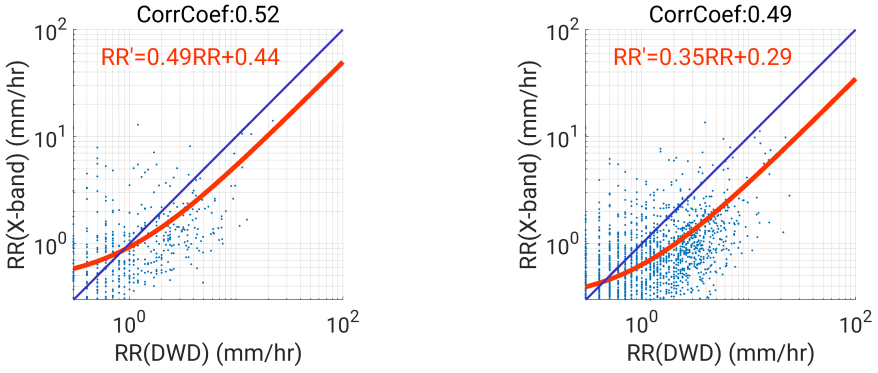
Table 4: Information of selected DWD rain gauge station

id	distance(km)	height above seal level(m)	interception height above surface level(*100m)
#1255	70	220	14
#1216	68	312	18
#13674	65	237	17
#2787	58	354	15
#3761	49	276	13
#5562	45	570	9
#2159	37	430	9
#3362	34	244	10
#4160	25	478	5
#4349	22	248	6
#4931	12	371	3

From Table 4, the radar beams of X-band radar measure the precipitation above the rain gauges at varying height for different DWD stations, instead of the precipitation falling into the surface. As mentioned in Section 3, Z-R relation varies with height. Therefore, the height-dependent Z-R relation should be taken into account. Provided that our measurement period was within 4 months and the coverage of X-band radar is 120-km in radius, the assumption that vertical variability of Z-R relation remains similar within the coverage of radar during our measurement period could be acceptable. Therefore, the MRR-derived height-dependent Z-R relations can be adopted here as well, which means that Z-R relation varies for different rain gauges, based on the intercepting height (see Table 4) different scattering volumes above the rain gauges.

The comparison on a basis of rainfall rate is presented in figure 9. Regardless the high variability of precipitation, the

comparison over 11 stations still reveals moderate correlation between RR_{DWD} and RR'_{Xband}. A reason for the moderate correlation is owing to the various interception height of scattering volumes. In figure 9, the red line representing the linear regression is lower that the diagonal line, indicating that X-band radar underestimate the precipitation, which is in agreement to the results presented in Section 4.2.



(a) Fine scan (b) Coarse scan

Figure 9: RR_{DWD} vs RR'_{Xband}

5. summary

This extended abstract provides detailed evaluation of X-band radar in two different scan strategies in aid of other precipitation instruments. Height-varying Z-R relation are developed to favor the comparison between precipitation measurement and radar reflectivity measurement. The results show that high correlations between X-band radar measurement with other instruments, which can corroborate the further utilization of X-band radar data for characterizations of precipitation in an urban environment.

Acknowledgement

We acknowledge that Dr. Jochen Seidel from University of Stuttgart provided the MRR measurement dataset.

References

D. W. D. C. D. C. DWD-CDC, "Recently hourly station observations of precipitation for germany, quality control no completed yet, version recent," last accessed: 2017-05-14.

J.-Y. Han, J.-J. Baik, and H. Lee, "Urban impacts on precipitation," *Asia-Pacific Journal of Atmospheric Sciences*, vol. 50, no. 1, pp. 17–30, January 2014.

W. Lowry, "Urban effects on precipitation amount," *Progress in Physical Geography*, vol. 22, no. 4, pp. 477–520, December 1998.

METEK, *Metek Micro Rain Radar MRR-2 User Manual*, Meteorologische Messtechnik GmbH, Fritz-Strassmann-Strasse 4, 25337 Elmshorn, Germany, March 2012.

G. Peters, B. Fisher, and T. Andersson, "Rain observations with a vertical looking micro rain radar(mrr)," *Boreal environment research*, vol. 7, no. 4, pp. 353–362, December 2002.

J. M. Shepherd, "A review of current investigation of urban-induced rainfall and recommendations for the future," *Earth Interactions*, vol. 9, no. 12, pp. 1–27, July 2005.

Y. Zheng, J. Handwerker, and N. Kalthoff, "Optimal scan strategy for fine resolved x-band radar measurements." Europen Meteorologic Society, September 2017. [Online]. Available: https://presentations.copernicus.org/EMS2017-360_presentation.pdf

Multi-Frequency Radar Retrieval of Snowfall Microphysics

Jussi Leinonen[1], Matthew D. Lebsock[1], Ousmane O. Sy[1], Simone Tanelli[1], Brenda Dolan[2], Randy J. Chase[3], Joseph A. Finlon[3], Dmitri Moisseev[4,5], and Annakaisa von Lerber[5]

[1]*Jet Propulsion Laboratory, California Institute of Technology, Pasadena, California, USA*
[2]*Department of Atmospheric Science, Colorado State University, Fort Collins, Colorado, USA*
[3]*Department of Atmospheric Sciences, University of Illinois at Urbana-Champaign, Urbana, Illinois, USA*
[4]*Institute for Atmospheric and Earth System Research / Physics,, University of Helsinki, Helsinki, Finland*
[5]*Radar Science, Finnish Meteorological Institute, Helsinki, Finland*

(Dated: 14 June 2018)

1. Introduction

Multi-frequency cloud and precipitation radars reveal information about the measurement target through differential backscattering at different frequencies. While the radar reflectivity is independent of frequency at the Rayleigh regime, i.e. for scatterers much smaller than the wavelength, the reflectivities at different wavelength diverge when the scatterer size approaches or exceeds the wavelength. On the other hand, the number concentration of scatterers affects the radar signal equally at all frequencies. Therefore it is intuitive that the dual-wavelength ratio (DWR), defined as the ratio of reflectivities at two different frequencies, carries information about the size of the hydrometeors. Accordingly, dual-frequency techniques have been developed for radar retrievals of rainfall (e.g. Meneghini et al., 1989, 1992) and adopted in the Ku/Ka-band radar on the Global Precipitation Measurement (GPM) core satellite (Kuo et al., 2004).

Radar retrievals of ice and snow particles are more complicated than those of liquid water drops, owing to the variable density and complex internal structure of icy hydrometeors. Snowflakes grow as a consequence of several different processes, most importantly vapor deposition growth, aggregation and riming. Each of these processes leads to different relationships between the snowflake size and mass, and each is strongly affected by environmental variables such as temperature and humidity (Lamb and Verlinde, 2011; Pruppacher and Klett, 1997). This variability is a source of significant uncertainty in radar retrievals. Nevertheless, dual-frequency methods have proved useful for snow retrievals (Hogan et al., 2000; Liao et al., 2005; Matrosov, 1993, 1998).

Recently, experimental, modeling and theoretical studies have established that radars using *three* different frequencies can convey information about the snowflake density, in addition to the size (e.g Kneifel et al., 2011; Kulie et al., 2014; Leinonen et al., 2012; Leinonen and Moisseev, 2015; Stein et al., 2015; Yin et al., 2017). This can be understood in terms of the relationship between the frequency dependence of radar reflectivity, and the spatial correlation of the mass distribution of the snowflake (Leinonen et al., 2013). This understanding is now complemented with the availability of datasets that contain the scattering properties of snowflakes at wide ranges of size and density (e.g. Kuo et al., 2016; Leinonen and Szyrmer, 2015). This has made it possible to develop a multi-frequency retrieval algorithm for the microphysical properties of falling snow.

Leinonen et al. (2018) described a Bayesian multi-frequency algorithm for microphysical retrievals and tested it with cases from the Olympic Mountain Experiment / ACE Radar Definition Experiment 2015 (OLYMPEX/RADEX'15), where the National Aeronautics and Space Administration (NASA) DC-8 operated a radar at 13.4 GHz (Ku band), 35.6 GHz (Ka band) and 94.9 GHz (W band) frequencies. In this extended abstract, we will review the methodology used in the retrieval method (section 2). We will then show retrievals from three additional cases that were not analyzed by Leinonen et al. (2018), further demonstrating the capability of the algorithm to retrieve snowflake properties (section 3). Finally, we will discuss the new cases and summarize the findings in section 4.

2. Algorithm overview

Here, we give an overview of the retrieval algorithm. A more detailed description, with further discussion of the choices involved in formulating the algorithm, can be found in Leinonen et al. (2018).

The algorithm uses a probabilistic framework to retrieve a state vector $\mathbf{x}$ from a measurement vector $\mathbf{y}$. For the state vector, we assume an exponential particle size distribution (PSD)

$$N(D) = N_0 \exp(-\Lambda D) \tag{2.1}$$

where D is the maximum diameter of a snowflake and N_0 and Λ are the intercept and slope parameters, respectively. We also assume a mass-dimensional relationship of the form

$$m(D) = \alpha D^\beta. \tag{2.2}$$

where m is the mass and α and β are the prefactor and the exponent of the relationship, respectively. The state vector for each radar bin is

$$\mathbf{x} = \begin{bmatrix} \ln\ N_0 & \ln\ \Lambda & \ln\ \alpha \end{bmatrix}^T. \tag{2.3}$$

We retrieve the logarithms of the parameters on order to cover a larger dynamic range of values and to make the forward model more linear. The exponent of the m–D relationship is fixed to $\beta = 2.1$.

The forward model is based on the snowflake scattering databases of (Leinonen and Szyrmer, 2015) and (Kuo et al., 2016). To calculate the radar reflectivity, we first use the scattering databases to derive the backscattering cross section as a function of size and mass: $\sigma_{\mathrm{bsc}}(\ln\ D, \ln\ m)$. The reflectivity is then derived by integrating over this function according to the PSD and the m–D relationship. The attenuation is calculated similarly, but using the extinction cross section instead. The reflectivity is corrected for attenuation using a relationship between the Ku-band reflectivity (which is practically unattenuated in snow) and the attenuation at Ka and W bands. The relationship is derived by drawing samples from the *a priori* distribution, calculating the reflectivity and the attenuation for each data point, and fitting a function giving the attenuation as a function of reflectivity. The measurement vector for the three-frequency retrieval is

$$\mathbf{y} = \begin{bmatrix} Z_{\mathrm{dB,Ku}} & \mathrm{DWR}_{\mathrm{Ka/W}} & \mathrm{DWR}_{\mathrm{Ku/Ka}} \end{bmatrix}^T. \tag{2.4}$$

where $Z_{\mathrm{dB,Ku}}$ is the Ku-band reflectivity in dBZ units, $\mathrm{DWR}_{\mathrm{Ka/W}}$ is the DWR between Ka and W bands, and $\mathrm{DWR}_{\mathrm{Ku/Ka}}$ is the DWR between Ku and Ka bands.

We retrieve the state vector as the conditional expectation of $\mathbf{x}$ given $\mathbf{y}$: $\mathrm{E}[\mathbf{x}|\mathbf{y}]$. We can calculate this using Bayes' rule as

$$\mathrm{E}[\mathbf{x}|\mathbf{y}] = \int \mathbf{x}\, p(\mathbf{x}|\mathbf{y})\, \mathrm{d}\mathbf{x} = \frac{1}{p(\mathbf{y})} \int \mathbf{x}\, p(\mathbf{y}|\mathbf{x})\, p(\mathbf{x})\, \mathrm{d}\mathbf{x}. \tag{2.5}$$

Here, $p(\mathbf{y}|\mathbf{x})$ is given by the forward model and the assumed radar error, and $p(\mathbf{x})$ is the *a priori* probability of $\mathbf{x}$ that was derived from *in-situ* observations from both OLYMPEX and the Biogenic Aerosols-Effects on Clouds and Climate (BAECC) campaign in Finland. Since we do the retrieval separately for each bin, the dimensionality of the problem is not very large: Both the $\mathbf{x}$ and $\mathbf{y}$ are three-dimensional. It is thus possible to directly compute the integral of Eq. 2.5 numerically. This allows us to build a lookup table mapping each $\mathbf{y}$ (within realistic finite ranges) to a corresponding $\mathbf{x}$. This lookup table is then used, together with interpolation, to retrieve the state vector for each bin. The retrieval is very robust, and gives reliable error estimates, because an iterative method is not used.

The retrieved state vector and its error covariance can be used to derive other microphysical parameters and their error estimates. In this extended abstract, we examine the ice water content (W_{ice}), the mass-weighted mean diameter (D_m) and the bulk density (ρ_{bulk}); see Leinonen et al. (2018) for detailed definitions.

3. Case studies

3.1. Overview

The cases shown here are from the OLYMPEX/RADEX'15 field campaign, which studied precipitation on the Olympic Peninsula of Washington State, USA, in late 2015. The region experiences large amounts of precipitation as a result of the interaction of the Pacific Ocean midlatitude weather systems with the mountains of the peninsula. During OLYMPEX, the surface precipitation was even heavier than usual, and produced many excellent cases for precipitation measurements using both *in-situ* and remote sensing instruments. As part of the experiment, the NASA DC-8 aircraft operated the Airborne Third Generation Precipitation Radar (APR-3; Sadowy et al., 2003). This radar gathered data during many precipitation cases that covered different synoptic conditions with pre-frontal and post-frontal precipitation, with precipitation rates ranging from light rainfall to "atmospheric river" conditions.

Leinonen et al. (2018) examined two cases from OLYMPEX in detail, with comparisons to ground-based dual-polarization radar observations, and to aircraft-based *in-situ* observations. Below, we shall examine the triple-frequency retrievals from three more cases that occurred in days other than those considered by the Leinonen et al. (2018) study.

3.2. December 1, 2015: Stratiform precipitation modified by orography

On December 1, 2015, a widespread area of stratiform rain passed over the Olympic Peninsula (Houze et al., 2015). The overflights ranging from the peninsula to the ocean captured many cases of this precipitation being modified by its interaction with the mountainous terrain. The top panel in Fig. 1 shows the Ku-band reflectivity in one such flight leg, which indicated a stable melting layer typical of stratiform snowfall consisting of aggregates, with distinct fallstreaks in the rain below. The precipitation can be seen to interact with the mountains, which can be identified from the radar ground echo on the left of the

panel. The precipitation weakened significantly as it passed over the mountains, evident on the leftmost part of the top panel.

Three microphysical parameters retrieved from the triple-frequency data can be seen on the bottom three panels of Fig. 1: W_{ice}, D_m and α. In these panels, the Ku-band reflectivity data is shown in grayscale in the areas where the retrieval was not performed due to unavailability of one of the other two channels, or where the signal is not from snow.

Over the ocean and the coastal area, the retrieved W_{ice} exhibits little variation, with only a few areas of slight enhancement. D_m and α show a region of large, less dense particles with little change in ice water content at around $120\ \mathrm{km}$ on the distance scale, indicating enhanced aggregation. Otherwise these parameters are fairly similar over all of the ocean and low-lying land areas. On the other hand, near the mountains the patterns become much more complicated. The most conspicuous feature is the streak arising from around $60\ \mathrm{km}$ on the vertical scale, becoming a horizontally oriented region of enhanced W_{ice} and α with an increase in D_m just below. We interpret this as a layer of riming induced by the lifting of supercooled water into the stratiform precipitation by orographic forcing. All parameters exhibit much higher variability over the mountains than over the ocean, likely owing to the updrafts and downdrafts forced by the mountains.

3.3. December 8, 2015: Stratiform precipitation modified by orography

In the December 8–9 rain event, an atmospheric river — a narrow band of high moisture originating in the tropics — brought heavy precipitation on the windward side of the Olympic Mountains (Barnes et al., 2015a). The heavy surface rain, and its strengthening as it interacted with the mountains, is evident in Fig. 2. The significant spatial variability of the precipitation, compared to the December 1 case, is also clear from this plot.

Perhaps the most interesting feature in the microphysical variables retrieved from this case is the band of high bulk density that meets the melting layer around $100\ \mathrm{km}$ on the distance scale (ρ_{bulk} is shown instead of α on Fig. 2 because this feature more distinct using ρ_{bulk}). A strong enhancement of the density in a layer approximately $1\ \mathrm{km}$ high reaches from this point to approximately $60\ \mathrm{km}$ on the distance scale, and somewhat less clearly all the way to $20\ \mathrm{km}$. Beneath this layer is a region of large, lower density snow, indicating aggregates. Another region where the density is high is approximately $1\ \mathrm{km}$ above the melting layer around $40\ \mathrm{km}$ on the horizontal scale. In this region, the ice water content is also fairly high. This is in contrast to the high-density band at higher altitudes, where the ice water content does not seem to be affected much by the change in density.

Another notable result of the retrieval is related to the relationship of snow above the melting layer and the rain below it. The top panel of Fig. 2 shows the strongest Ka-band reflectivity in the rain occurring between 40 and $60\ \mathrm{km}$ on the horizontal scale. However, the reflectivity in the snow in this area barely differs from that elsewhere in the 0–$100\ \mathrm{km}$ range. Nevertheless, the retrieval indicates high ice water content, moderately large snowflakes, and low density of snow in this area, all of which stand out from the surrounding areas. We suspect that this results from convective lifting of moisture above the melting level, forming new snow in this area. Thus, the retrieved quantities can be seen to connect to rain below the melting layer in a manner that is not obvious from the single-frequency radar reflectivity alone.

3.4. December 13, 2015: Convective plumes

In this case, we consider a much shorter leg than in the previous two cases, occurring completely over the ocean. The December 13 event consisted of post-frontal convection (Barnes et al., 2015b), thus offering an opportunity to test the capabilities of the algorithm in convective conditions. The Ku-band reflectivity on the top panel of Fig. 3 shows a low melting layer, highly variable precipitation and a particularly strong convective plume on the left side of the figure.

The plume on the left is notable for its very high retrieved density and small particle size, suggesting that riming is occurring, as one might expect in such a convective plume. The ice water content is high in this plume: The riming is apparently strongly increasing particle density without having much effect on the size. In cases such as this, some of the dual-frequency signal may be due to differential liquid water attenuation. Indeed, liquid water attenuation is probably the reason why the retrieval is not performed in the bottom part of the plume, as the dual-frequency ratios reach values outside the limits of the retrieval table. However, further up in the plume small snowflakes are still detected; if liquid water were to blame for all of the signal, one would also expect a false detection of large snowflakes because both dual-frequency ratios would become large. This implies that there is a genuine signal of strong riming in this plume, even though the results should be interpreted with caution.

Elsewhere in this case, another conspicuous feature of this case is the transition between 40 and $70\ \mathrm{km}$ on the horizontal scale. Starting from the left, large low-density snowflakes with low ice water content around $40\ \mathrm{km}$ indicate small numbers of aggregates. Between 50 and $60\ \mathrm{km}$, the ice water content increases strongly, with an accompanying drop in the retrieved size and a slight increase in density. This suggests that riming takes over as the primary mode of snowflake growth. To the right from $60\ \mathrm{km}$, aggregation seems to dominate again.

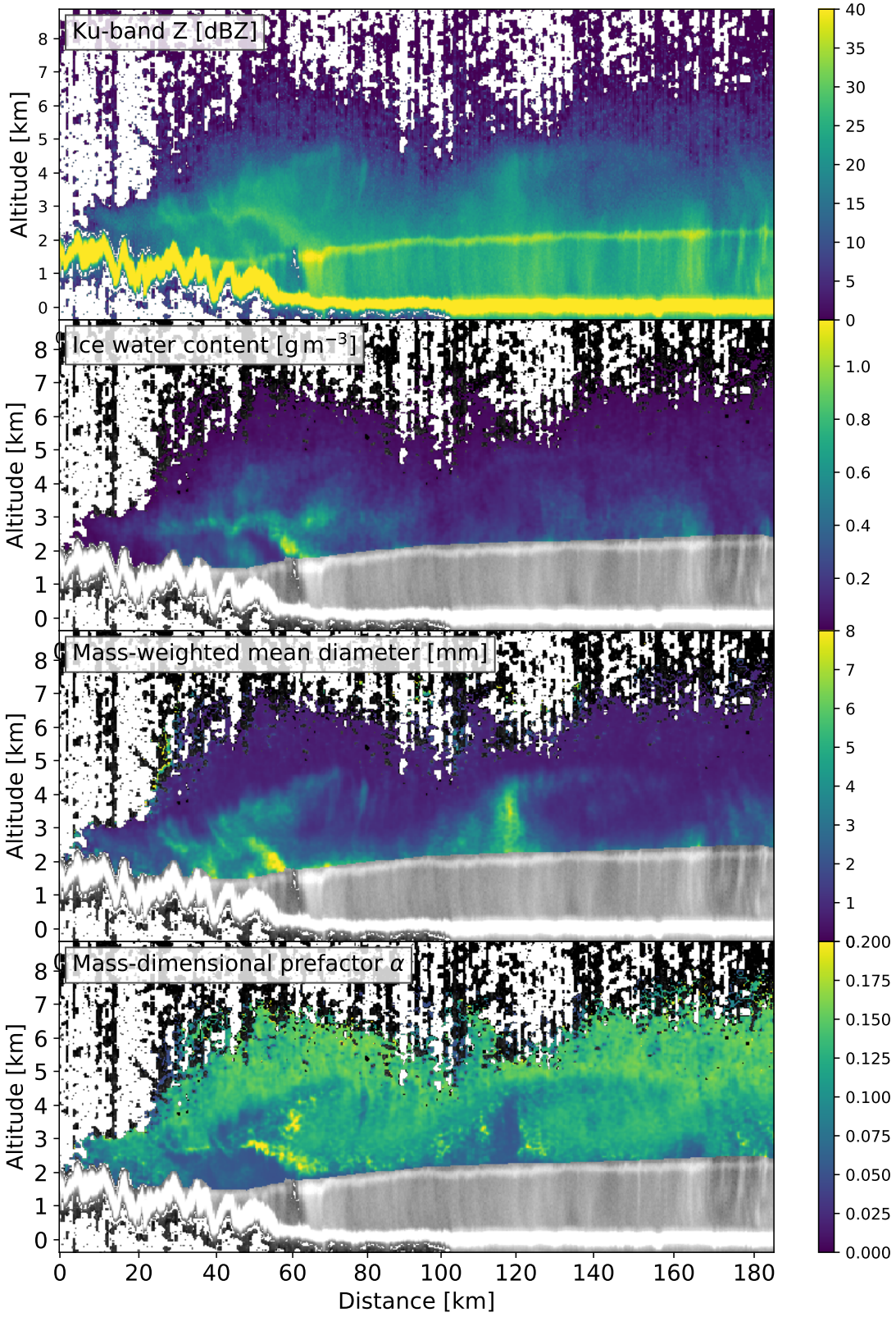


Figure 1: The Ku-band radar reflectivity (top panel) and the retrieved microphysical parameters (other three panels) from the December 1 case. The gray background on each of the bottom three panels shows the radar reflectivity in areas where the retrieval was not run.

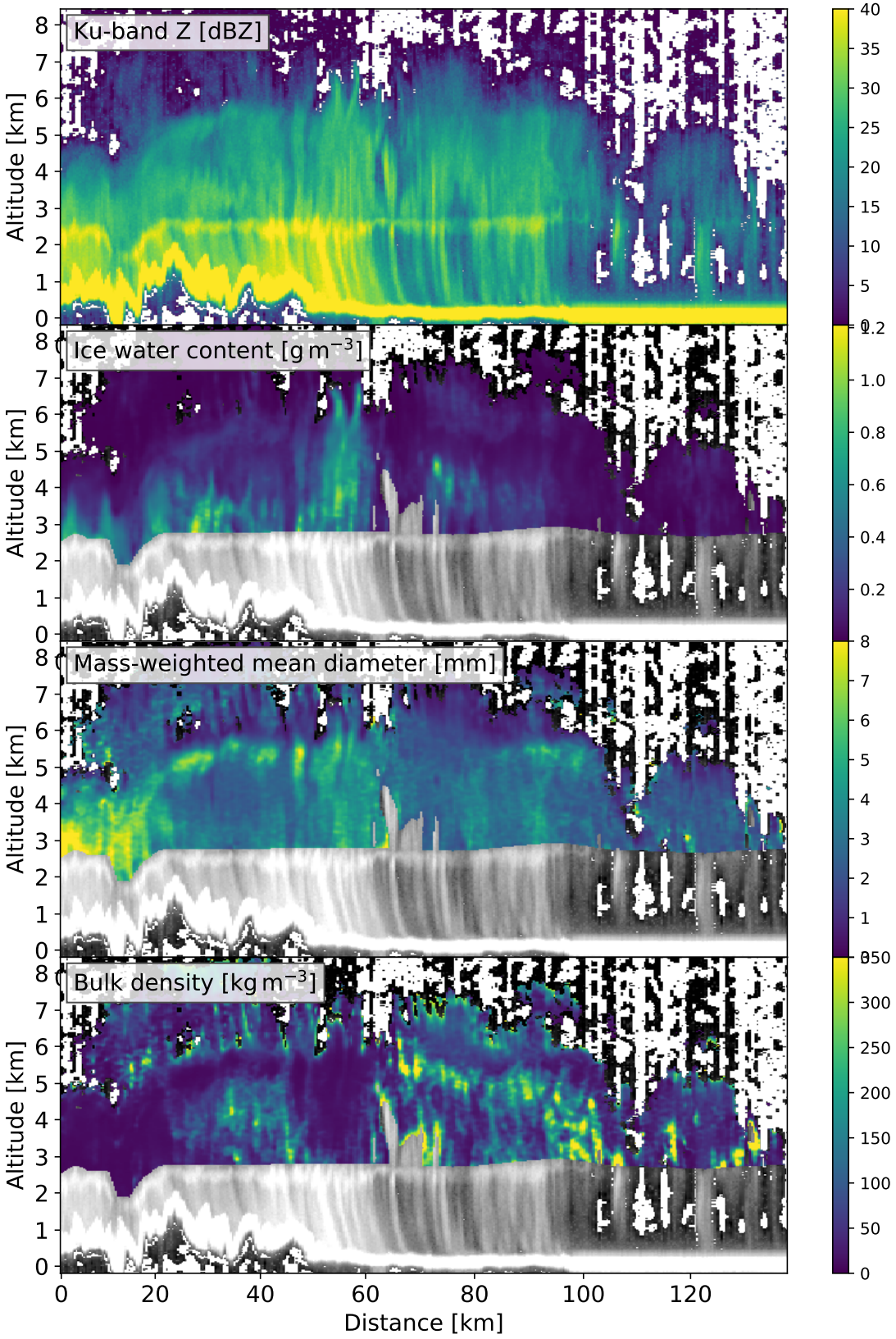


Figure 2: As Fig. 1, but for the December 8 case, and the bulk density (ρ_{bulk}) is shown on the bottom panel instead.

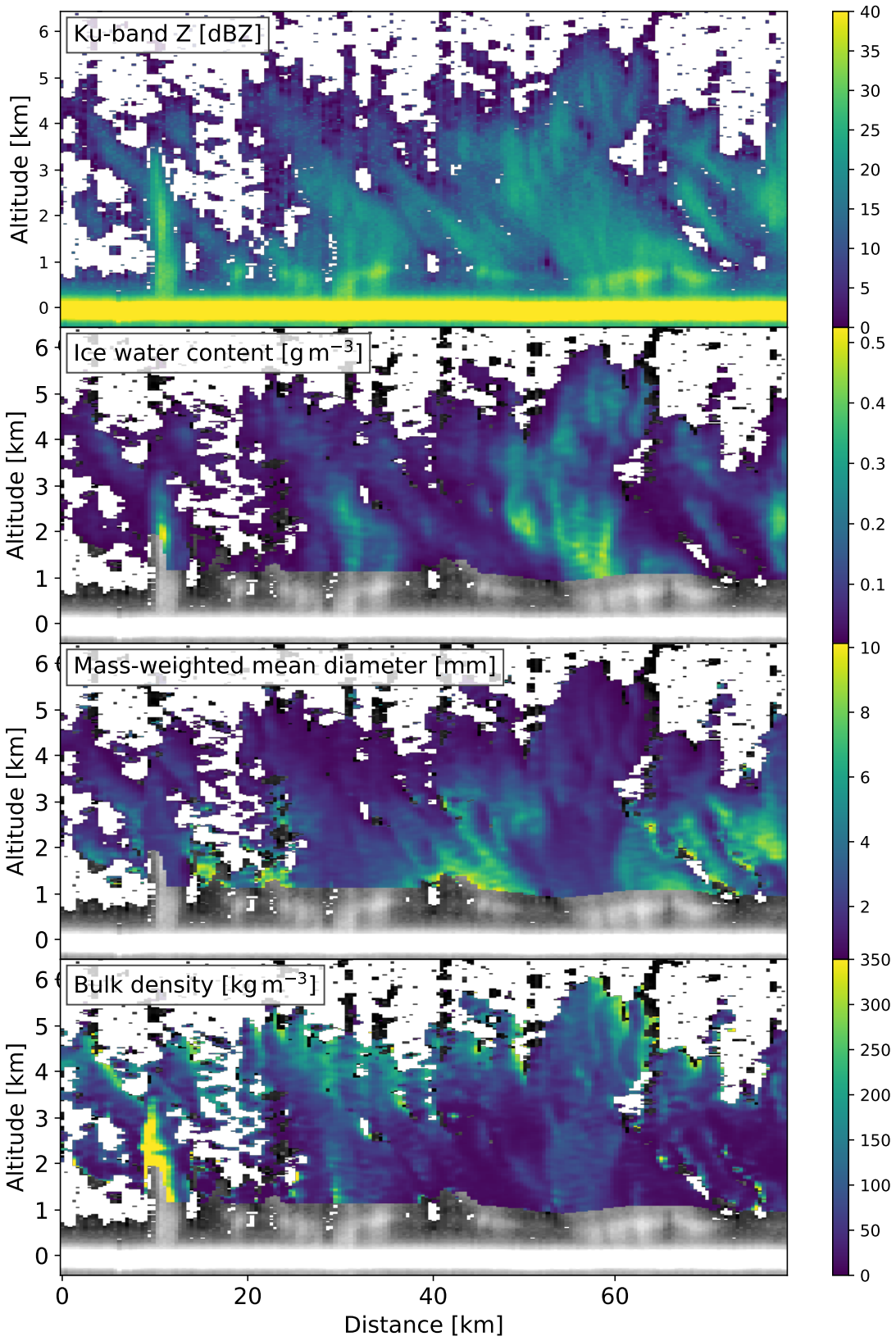


Figure 3: As Fig. 2, but for the December 13 case.

4. Summary

In this extended abstract, we have given an overview of the multi-frequency radar retrieval algorithm for snowfall, introduced by (Leinonen et al., 2018). The algorithm is based on the Bayesian principle and uses a direct numerical solution of the expected value of the state, utilizing lookup tables for efficiency. The algorithm produces estimates of the ice water content as well as the size and density of snowflakes, along with their error estimates.

We have also presented the retrievals performed in three additional cases that were not considered in the original study. Collectively, the cases discussed in this abstract demonstrate the capability of triple-frequency radars, when combined with a suitable retrieval algorithm, to provide information about the microphysics of ice-phase precipitation. Our algorithm is able to estimate snowflake size and density, and thus distinguish between snowflake growth driven by aggregation and growth caused by riming. While we are unable to provide *in-situ* validation in these cases, the retrieved values are consistent with the large-scale conditions: Stratiform precipitation is mostly characterized by aggregation, while regions of riming are seen in more convective cases. We also see the retrieved values relate in a consistent way to the rain found below the melting layer.

Acknowledgement

The research of JL, ML, ST and OS was carried out at the Jet Propulsion Laboratory (JPL), California Institute of Technology, under contract with NASA. The work of JL and ML was supported by the NASA Aerosol-Cloud-Ecosystem and CloudSat missions under RTOP WBS 103930/6.1 and 103428/8.A.1.6, respectively. JL was partly funded under subcontract 1559252 from JPL to UCLA. ST and OS acknowledge support from the GPM GV program and the ACE Science Working Group funding for the acquisition and initial processing of APR-3 data, and support from the U.S. Participating Investigator program for the detailed analysis of W-band Doppler data. Funding for the research of BD, RC and JF was provided by NASA Precipitation Measurement Missions grants NNX16AI11G (BD) and NNX16AD80G (RC and JF) under Ramesh Kakar. DM acknowledges the funding received through ERA-PLANET, trans-national project iCUPE (Grant Agreement 689443), funded under the EU Horizon 2020 Framework Programme, and the Academy of Finland (grants 307331 and 305175). The research work of AvL was funded by EU's Horizon 2020 research and innovation programme (EC-HORIZON2020-PR700099-ANYWHERE).

References

H. C. Barnes, R. A. Houze, Jr, S. Braun, S. Durden, J. Mace, C. Mass, L. McMurdie, J. Wurman, and J. Zagrodnik, "OLYMPEX science summary for 8-9 december 2015," http://olympex.atmos.washington.edu/archive/reports/20151208-9/20151208-9Science_summary.html, 2015, last access: May 30 2018.

H. C. Barnes, R. A. Houze, Jr, B. Dolan, M. Chaplin, J. Zagrodnik, S. Braun, J. Munchak, and S. Durden, "OLYMPEX science summary for 13 december 2015," http://olympex.atmos.washington.edu/archive/reports/20151213/20151213Science_summary.html, 2015, last access: May 30 2018.

R. J. Hogan, A. J. Illingworth, and H. Sauvageot, "Measuring crystal size in cirrus using 35- and 94-GHz radars," *J. Atmos. Oceanic Technol.*, vol. 17, no. 1, pp. 27–37, 2000.

R. A. Houze, Jr, L. McMurdie, J. Mace, S. Tanelli, S. Nesbitt, J. Zagrodnik, and M. Zuluaga, "OLYMPEX science summary for 1-2 december 2015," http://olympex.atmos.washington.edu/archive/reports/20151201-2/20151201-2Science_summary.html, 2015, last access: May 30 2018.

S. Kneifel, M. S. Kulie, and R. Bennartz, "A triple frequency approach to retrieve microphysical snowfall parameters," *J. Geophys. Res.*, vol. 116, 2011.

M. S. Kulie, M. J. Hiley, R. Bennartz, S. Kneifel, and S. Tanelli, "Triple frequency radar reflectivity signatures of snow: Observations and comparisons to theoretical ice particle scattering models," *J. Appl. Meteor. Climatol.*, pp. 1080–1098, 2014.

K.-S. Kuo, E. A. Smith, Z. Haddad, E. Im, T. Iguchi, and A. Mugnai, "Mathematical-physical framework for retrieval of rain DSD properties from dual-frequency Ku-Ka-band satellite radar," *J. Atmos. Sci.*, vol. 61, no. 19, pp. 2349–2369, 2004.

K.-S. Kuo, W. S. Olson, B. T. Johnson, M. Grecu, L. Tian, T. L. Clune, B. H. van Aartsen, A. J. Heymsfield, L. Liao, and R. Meneghini, "The microwave radiative properties of falling snow derived from nonspherical ice particle models. Part I: An extensive database of simulated pristine crystals and aggregate particles, and their scattering properties," *J. Appl. Meteor. Climatol.*, vol. 55, no. 3, pp. 691–708, 2016.

D. Lamb and J. Verlinde, *Physics and Chemistry of Clouds*. Cambridge, UK: Cambridge University Press, 2011.

J. Leinonen, S. Kneifel, D. Moisseev, J. Tyynelä, S. Tanelli, and T. Nousiainen, "Evidence of nonspheroidal behavior in millimeter-wavelength radar observations of snowfall," *J. Geophys. Res.*, vol. 117, 2012.

J. Leinonen, D. Moisseev, and T. Nousiainen, "Linking snowflake microstructure to multi-frequency radar observations," *J. Geophys. Res.*, vol. 118, pp. 3259—-3270, 2013.

J. Leinonen, M. D. Lebsock, S. Tanelli, O. O. Sy, B. Dolan, R. J. Chase, J. A. Finlon, A. von Lerber, and D. Moisseev, "Retrieval

of snowflake microphysical properties from multi-frequency radar observations," *Atmospheric Measurement Techniques*, 2018, pre-review discussion paper available.

J. Leinonen and D. Moisseev, "What do triple-frequency radar signatures reveal about aggregate snowflakes?" *J. Geophys. Res.*, vol. 120, pp. 229–239, 2015.

J. Leinonen and W. Szyrmer, "Radar signatures of snowflake riming: A modeling study," *Earth Space Sci.*, vol. 2, pp. 346–358, 2015.

L. Liao, R. Meneghini, T. Iguchi, and A. Detwiler, "Use of dual-wavelength radar for snow parameter estimates," *J. Atmos. Oceanic Technol.*, vol. 22, no. 10, pp. 1494–1506, Oct. 2005.

S. Y. Matrosov, "Possibilities of cirrus particle sizing from dual-frequency radar measurements," *J. Geophys. Res.*, vol. 98, pp. 20 675–20 683, 1993.

——, "A dual-wavelength radar method to measure snowfall rate," *J. Appl. Meteor.*, vol. 37, no. 11, pp. 1510–1521, 1998.

R. Meneghini, K. Nakamura, C. W. Ulbrich, and D. Atlas, "Experimental tests of methods for the measurement of rainfall rate using an airborne dual-wavelength radar," *J. Atmos. Oceanic Technol.*, vol. 6, no. 4, pp. 637–651, 1989.

R. Meneghini, T. Kozu, H. Kumagai, and W. C. Boncyk, "A study of rain estimation methods from space using dual-wavelength radar measurements at near-nadir incidence over ocean," *J. Atmos. Oceanic Technol.*, vol. 9, no. 4, pp. 364–382, 1992.

H. R. Pruppacher and J. D. Klett, *Microphysics of clouds and precipitation*, 2nd ed. Rordrecht, The Netherlands: Springer, 1997.

G. A. Sadowy, A. C. Berkun, W. Chun, E. Im, and S. L. Durden, "Development of an advanced airborne precipitation radar," *Microwave J.*, vol. 46, no. 1, p. 84, 2003. [Online]. Available: http://www.microwavejournal.com/articles/3577-development-of-an-advanced-airborne-precipitation-radar

T. H. M. Stein, C. D. Westbrook, and J. C. Nicol, "Fractal geometry of aggregate snowflakes revealed by triple-wavelength radar measurements," *Geophys. Res. Lett.*, vol. 43, pp. 176—-183, 2015.

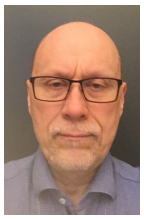
M. Yin, G. Liu, R. Honeyager, and F. J. Turk, "Observed differences of triple-frequency radar signatures between snowflakes in stratiform and convective clouds," *J. Quant. Spectrosc. Radiat. Transfer*, vol. 193, pp. 13–20, 2017.

Operational Solar Monitoring for Improving the Homogeneity of the European Radar Network

Asko Huuskonen[1], Günther Haase[2], Daniel Michelson[3], Hidde Leijnse[4], Iwan Holleman[5], Matt Probert[6], Rashpal Gill[7], Michael Frech[8], Mikko Kurri[1], and Harri Hohti[1]

[1]*Finnish Meteorological Institute, Helsinki, Finland*
[2]*Swedish Meteorological and Hydrological Institute, Norrköping, Sweden*
[3]*Environment and Climate Change Canada, Toronto, Canada*
[4]*Royal Netherlands Meteorolodical Institute, De Bilt, The Netherlands*
[5]*Radboud University, Faculty of Science, Nijmegen, The Netherlands*
[6]*Met Office, Exeter, United Kingdom*
[7]*Danish Meteorological Institute, Copenhagen, Denmark*
[8]*German Meteorological Service, Hohenpeißenberg, Germany*

(Dated: 11 June 2018)



Asko Huuskonen

1. Introduction

The solar monitoring is a method in which the data collected during the normal operational scanning of a radar are used to determine antenna azimuth and elevation biases (Huuskonen and Holleman, 2007), to monitor the receiver stability (Holleman et al., 2010b), the width of the solar image as seen by a radar antenna (Altube et al., 2015; Huuskonen et al., 2014a) and the polarimetric properties of a radar (Figueras i Ventura et al., 2012; Frech, 2013; Gabella et al., 2015; Holleman et al., 2010a; Huuskonen et al., 2016b). A recent summary of the method is given by (Huuskonen et al., 2016b).

EUMETNET, the network of European Meteorological Services, runs a number of projects and operational services dealing with various observation systems and networks (http://eumetnet.eu). OPERA (Operational Exchange of Weather Radar Information) deals with weather radar and has been running since 1999 (Huuskonen et al., 2014b). For the present six year period (OPERA 4, 2013-2018) a work package (known as OD5 within OPERA) is established to extend the solar signal analysis to the whole OPERA radar network, so that 31 OPERA members need not all establish such a facility themselves. The centralized processing makes use of the radar volume data which are collected by Odyssey, the OPERA data center, for producing European wide composites (Matthews et al., 2012). This paper summarizes the results of the work and gives an update for the first results presented by Huuskonen et al. (2016a).

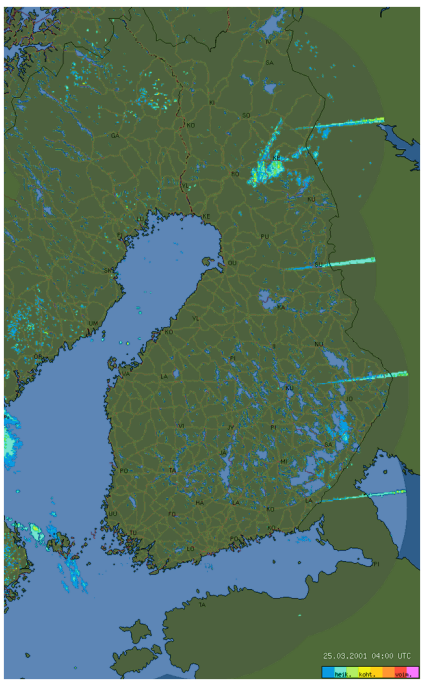


Figure 1: Solar signal observed simultaneously by four radars in Finland on March 25, 2001 at 4:00 UTC (Huuskonen et al., 2016b).

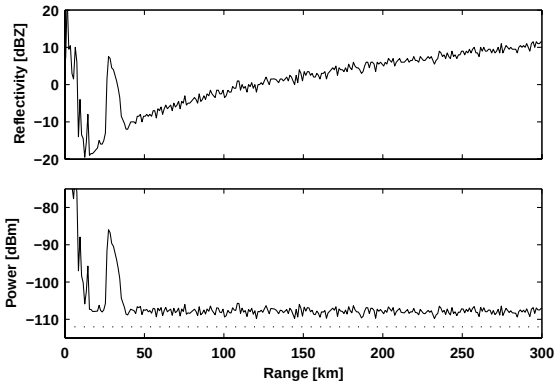


Figure 2: The reflectivity data with a sun signal uncorrected (upper panel) and the received power calculated applying Eq.2.1 (lower panel). The noise level of the radar is indicated by the dotted line (Huuskonen and Holleman, 2007).

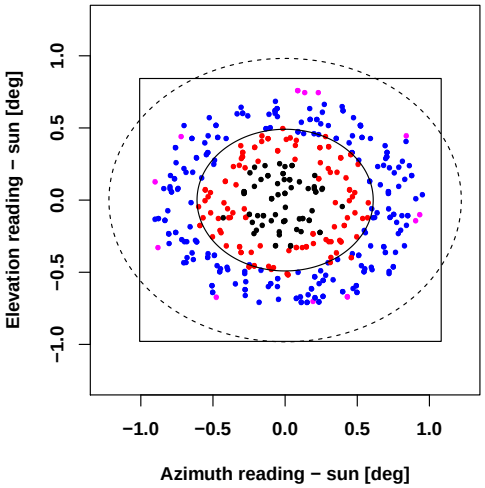


Figure 3: Solar hits as a function of azimuth and elevation. The sun hit power is shown relative to maximum (black within 1 dB of maximum, red 1 ... 3 dB below the maximum, blue 3 ... 7 dB below the maximum, and magenta more than 7 dB below the maximum). An ellipse shows the half power (3 dB) widths in elevation and azimuth, respectively. The dashed lines show ellipses with axes lengths twice that. The rectangular box is the data selection area as described in the text.

2. Method

The detection and analysis of solar signatures in radar volume data is described in a series of papers mentioned in the Introduction. We will summarize the main points of the method here for convenience. In the method a reflectivity signal originating from a continuous microwave source are searched along radials in the operational scan data. Figure 1 shows an example where four radars observe the solar signal simultaneously close to the spring equinox. As a radar signal processor usually corrects the received echoes for the range dependence and the atmospheric attenuation, the signals from the sun appear to increase with the range. The received solar spectral power at the antenna feed P (per MHz in dBm) can be calculated from the reflectivity signature as a function of the range $Z(r)$ (in dBZ) using:

$$P = Z(r) - 20\log_{10} r - 2ar - C - 10\log_{10} \Delta f \tag{2.1}$$

where C is the radar constant in dB according to Probert-Jones (1962), a is the one-way gaseous attenuation in dB km^{-1}, and Δf is the receiver 3 dB bandwidth in MHz. In the case of a proper solar signal the power P is constant along the range (> 50 km), as illustrated in Fig. 2.

The mean and standard deviation of this signal, together with the antenna pointing and timing information, are the data used in the subsequent analysis. The possible contamination by rain and ground clutter can be avoided by using data from far ranges only. As this would reduce the amount of usable data unnecessarily, we use the two-stage estimation method by Huuskonen et al. (2016b) in which first an estimate of the mean and standard deviation is calculated from the long ranges and these are used to filter out the contaminated range bins at the shorter ranges. In the present work the first estimate is made using data measured above 8 km, and the final estimate using data measured above 4 km altitude and using a fixed width of 2 dB for the outlier filtering window. This is roughly 3 times the standard deviation of a typical solar hit. A solar hit estimate is stored if more than 70% of the data passes the filtering, i.e. less than 30% of the data points are contaminated by rain or clutter.

Depending on the hardware of the radar, the volume coverage pattern, the season and the latitude of the radar, several tens of sun hits are found per day. When these hits are plotted as a function of the azimuth and elevation, a symmetric distribution is seen which is slightly wider in azimuth than in elevation, as shown in Fig. 3. Uncorrected reflectivity data are rather used for this analysis as (time-domain) Doppler clutter filters can attenuate the solar signal by several dBs, and the interference filtering applied to remove RLAN signatures efficiently remove solar signal as well. In some networks the background is estimated on a ray-to-ray basis. Then a solar interference is interpreted as an increase in the background noise and the noise subtraction removes the solar signal. As the determined background power is stored in the metadata, the solar analysis can be carried out as presented below using the stored powers.

The sun hit distribution of linear powers is well approximated by a Gaussian form, and hence the power P in dB can be written as:

$$P(x, y) \equiv a_x \cdot x^2 + a_y \cdot y^2 + b_x \cdot x + b_y \cdot y + c \tag{2.2}$$

where the coordinates x and y are defined as:

$$x = (\phi_{\text{read}} - \phi_{\text{sun}}) \cdot \cos\theta_{\text{sun}} \tag{2.3}$$

$$y = \theta_{\text{read}} - \theta_{\text{sun}} \tag{2.4}$$

where ϕ and θ denote azimuth and elevation, respectively, "read" refers to the angle reading of the radar antenna and "sun" refers to the calculated sun position. The observed azimuth differences are multiplied by $\cos\theta_{\text{sun}}$ to make them invariant to the elevation (e.g. Doviak and Zrnić, 1993, p. 516). For refraction we use the analytical formulas of Holleman and Huuskonen (2013) with $k = 5/4$.

The elevation and azimuth biases (B_θ, B_ϕ), and widths (Δ_θ, Δ_ϕ), and the power when the antenna is pointing directly to the sun, $\hat{P}_{\text{sun}}$, can be calculated from the linear parameters a_x to c solved from Eq. 2.2 (Huuskonen and Holleman, 2007; Huuskonen et al., 2016b):

$$\Delta^2_{\phi,\theta} = -\frac{40\log_{10} 2}{a_{x,y}} \approx -\frac{12}{a_{x,y}}, \tag{2.5}$$

$$B_{\phi,\theta} = -\frac{b_{x,y}}{2a_{x,y}}, \tag{2.6}$$

$$\hat{P} = c - \frac{b_x^2}{4a_x} - \frac{b_y^2}{4a_y}. \tag{2.7}$$

In case the number of data points is not sufficient for a full 5-parameter analysis, the widths can be fixed to values based either on data collected over long times, or calculated based on the known properties of the antenna and the azimuth scanning.

One cannot assume *a priori* that a radar is correctly pointed. Hence the usual method in which only solar hits within, say, 2° of the known solar position is not usable. We instead assume that the majority of the data points are genuine solar hits and analyze the distribution of the hits. We have noticed than in the present dataset a robust estimate of the distribution limits is obtained by calculating the median m and the median absolute deviation (MAD) and including all points X_i for which

$$|X_i - m| < 2.9652\ \text{MAD} \tag{2.8}$$

For a Gaussian distribution this means that data points within the 2σ width are used. This operation is carried out separately for azimuth and elevation and any point beyond the rectangular area defined by the limits is discarded from the further analysis (see Fig. 3). This removes strong outliers, such as RLAN signatures, before the fitting, unless they are close to the solar direction. The fitting is carried out twice so that any solar hit which is further away from the fit curve than a set limit is removed before the second fit is performed. This is an efficient method if a small number of outliers is present in the data. In addition data measured at elevations below 1° are discarded to avoid severe refraction. The upper elevation limit is set to 10° to reduce the effects of possible non-linearities of the antenna readings.

For polarimetric radars the above procedure is applied separately to horizontal and vertical polarization. In case the radar measures P_H and the differential reflectivity Z_{dr}, the vertical power is calculated first as $P_V = P_H - Z_{\text{dr}}$. An estimate of the solar Z_{dr} is then obtained as a difference of the estimated horizontal and vertical solar fluxes. This method is better than performing the analysis directly to the measured Z_{dr}, as pointed out by Huuskonen et al. (2016b). A separate analysis of the two polarization sets gives also the pointing biases separately and show how well the pointings of the two polarizations agree.

As part of the work package OD5, the processing improvements described above have been included in the solar hit detection algorithm of KNMI (Royal Netherlands Meteorological Institute) and this code has been integrated into the BALTRAD software (Michelson et al., 2018), deployed at Odyssey. The present solar hit analysis is built on the FMI analysis program, with additions described in this paper.

3. Data and Results

The OPERA Radar Data Center Odyssey collects radar volume data and produces a European composite at every 15 minutes. For compositing Odyssey uses corrected reflectivity (Z_H) but for some radars Odyssey receives also uncorrected reflectivity and radial velocity data. In March 2018, altogether 156 radars of 24 OPERA members supplied Z_H and 96 radars of 13 OPERA members uncorrected reflectivity as well. The frequency of data varies so that roughly half of the radars report at every 5 minutes, and the remaining at every 6-15 minutes.

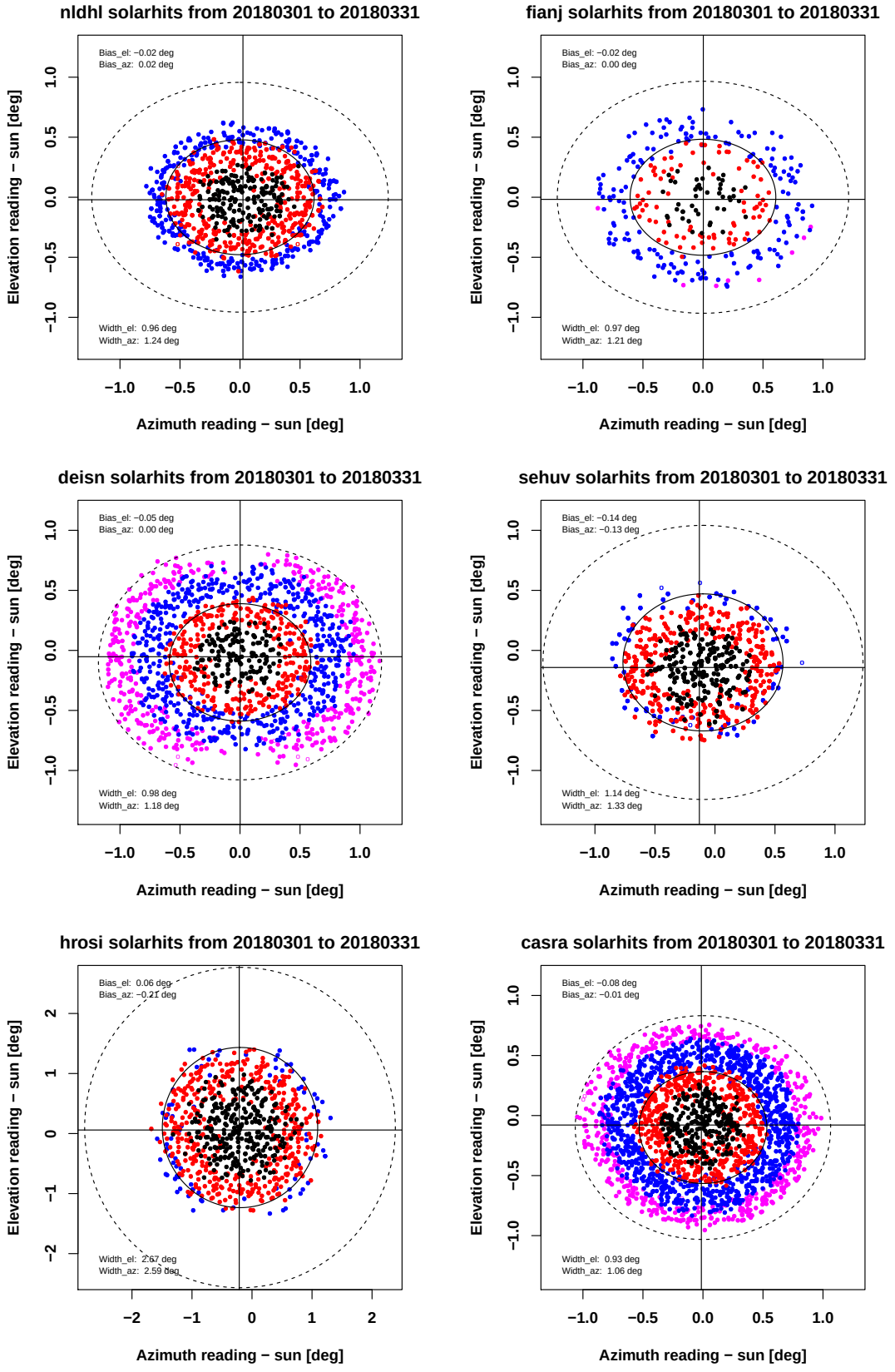


Figure 4: Solar hits for one month for radars at Den Helder (nldhl, Netherlands), Anjalankoski (fianj, Finland), Isen (deisn, Germany), Hudiksvall (sehuv, Sweden), Osijek (hrosi, Croatia) and Radisson (casra, Canada) radars. The colours and ellipses are as in Fig. 3. The elevation and azimuth biases are shown in the upper left corner and are also designated by the horizontal and vertical lines, respectively. The elevation and azimuth widths are shown in the lower left corner.

Figure 4 shows six example cases. In each panel all hits for one month are displayed together with the results on antenna pointing and widths. The examples include both C and S-band radars, with variable reporting frequency. The differences in the solar hit distribution can be explained by these facts. All data are based on uncorrected reflectivity.

The Den Helder radar (nldhl, upper left panel) provides data at every 5 minutes. The total number of solar hits exceeds 1000 and hence the data can be analyzed on a daily basis as more than 30 solar hits are found each day. The antenna biases are small, and the width values typical. The Anjalankoski radar (fianj, upper right panel) data are very similar except that the number of solar hits is roughly one third compare to the Den Helder radar. Volumes are measured at every 5 minutes but the reporting frequency to the OPERA data center is once in every 15 minutes which explains the difference.

The center panels show two other C-band examples. The Isen radar (deisn, left panel) has a very good sensitivity; the weakeast solar echoes are 12 dB below the maximum. Also in this case the number of solar hits is sufficient for a daily analysis. The Hudiksvall radar (sehuv, right panel) detects solar hits down to 3 dB below the peak. Yet the data is fully sufficient for a 5-par analysis of data.

The Osijek radar (hrosi, lower left panel) data shows a large number of solar hits with a much higher width of the distribution. The radar operates in the S-band with a small antenna, and hence the beam width is larger than in the other examples which are all from the C-band. The widths in azimuth and elevation are roughly identical, contrary to the other cases in which the azimuth widths are larger than the elevation widths. As described by Huuskonen et al. (2014a), the width in azimuth depends also on the windowing which is applied in the azimuth direction. The OPERA/BALTRAD solar hit detection code has also found use outside the OPERA community. An example is the Radisson radar in Canada (casra, lower right panel) which is an S-band radar with a 9.15 m antenna. The sensitivity of the radar is good and the radar produces sufficient number of solar hits for daily analysis of data.

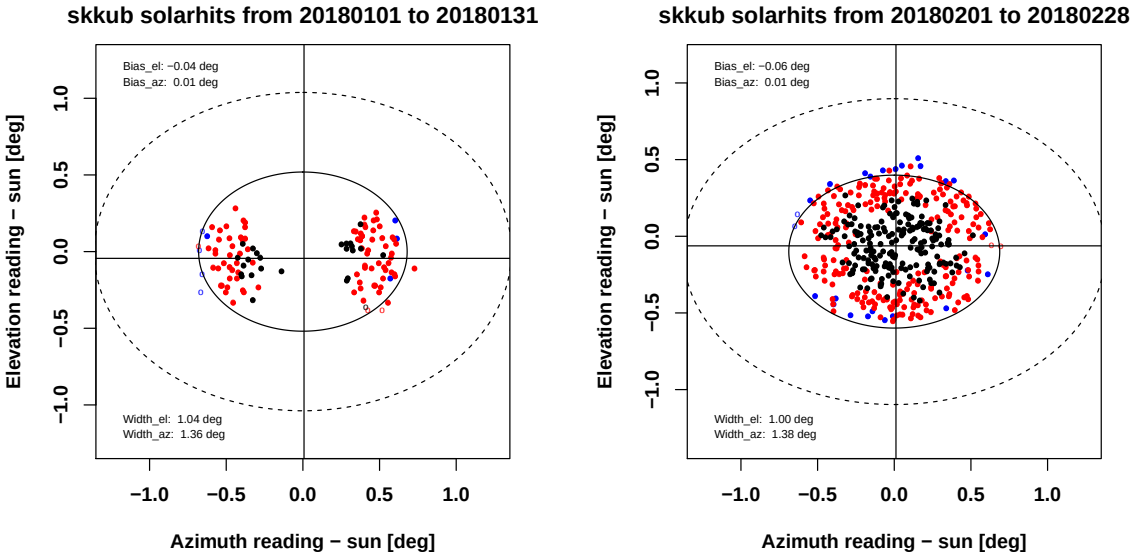


Figure 5: Solar hits collected at the OPERA data center during January and February 2018 in Skubinska Hola (skkub, Slovak Republic). The colours and ellipses are as in Fig. 3 and labels as in Fig. 4.

The number of solar hits varies greatly from radar to radar in the OPERA network. Roughly 100 radars produce more than 15 solar hits in a month. In the this group of radars, the maximum number is about 1200, the median is 300 and the quartiles are found at 150 and 760. This means that roughly one quarter of the radars provide sufficient number of data points for a daily analysis and three quarters for a weekly based analysis. Others are best analyzed on a monthly basis. A 5-parameter fit is not successful for all the 100 radars; in such case we provide median values of the observed azimuth and elevation biases as results.

Huuskonen et al. (2016a) presented data from the Norwegian Andenes radar where no solar hits were seen close to the solar direction. The left hand panel of Figure 5 shows a similar case but based on uncorrected reflectivity and hence the disappearance of the solar hits cannot be connected to the calculation of the corrected reflectivity which was mentioned as a probable cause for the disappearance by Huuskonen et al. (2016a). Recently, Jurasek and Okon (2018) have found out that the solar hits are removed by the spatial filter (2-D speckle filter) which is applied to all data when active. When a strong solar spoke is visible only in one ray, it is removed by the filter. When the solar spoke spans two adjacent azimuths, it is not removed. The right hand panel of Figure 5 shows the solar image of the same radar after the spatial filter was turned off. Comparison of the results shows that reliable bias estimates are obtained also based on the filtered data. Azimuth width value also seems

to be rather reliable but the elevation width is not determined equally well from the filtered data. This case is another example showing that the solar method is valuable also in revealing workings of the signal processing, just like the cases presented by Huuskonen et al. (2014a).

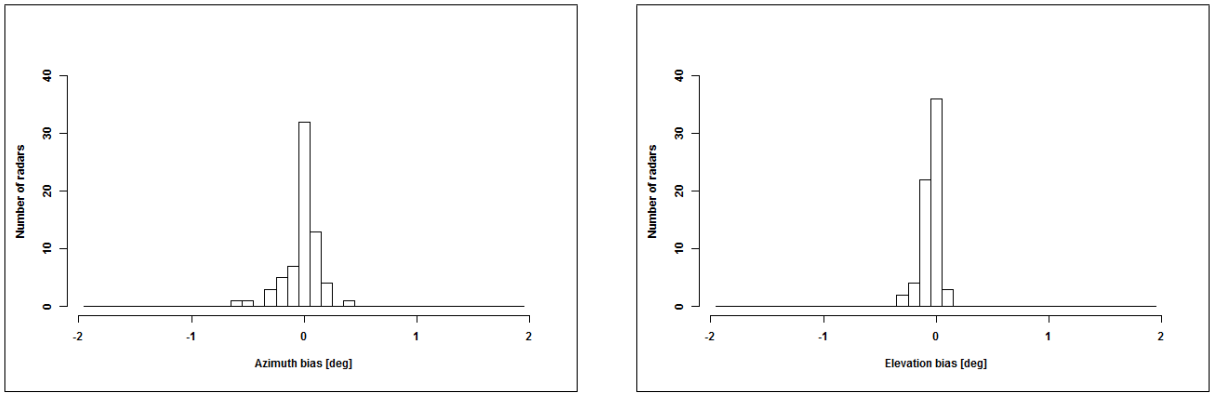


Figure 6: The distribution of the azimuth and elevation biases in March 2018 for the OPERA network.

Figure 6 shows a summary of the azimuth and elevation biases based on the solar hit data recorded in March 2018 for the 74 radars providing 5-parameter fit results. We note that the azimuth bias for a majority of radars is less than 0.2°, and the elevation bias is less than 0.1°. These results are very useful in improving the pointing, especially in elevation, where other suitable reference sources are difficult to find.

4. Discussion

The results demonstrate that an operational solar hit detection and analysis system is now available for the OPERA community. We can provide a full set of results for 75 OPERA radars which is 50 % of the radars used in OPERA compositing. For additional 25 radars we provide azimuth and elevation biases. During the last few years we have been able to increase the number of successfully analyzed radars. We also receive more uncorrected reflectivity data and data with higher transmission frequency. In reality there are more than 100 radars in the network detecting solar interferences. Approximately 40 radars are such that the solar interferences are removed from the data before sending data to the OPERA data center, and hence their solar data have not been analyzed in the present study.

A future goal is to extend the analysis to the receiver stability and calibration levels. Correct estimation of the solar flux requires metadata which are not needed in the compositing (e.g. radar constant, pulse widths, receiver band width, receiver losses) and hence are considered optional and are still missing in many radar data sets sent to the OPERA data center. Hence the fluxes determined are at present mostly on an arbitrary scale. However, they can be used to monitor the receiver stability of a radar as long as the metadata mentioned above remain unchanged. Further extensions to comparisons of calibration levels within radar networks require that the metadata are made available, noting the fact that the solar method is able to monitor the receiver chain only, and changes in the transmitter chain will remain unnoticed. Another future goal is the analysis of polarimetric data. As soon as either differential reflectivity or vertical reflectivity is available, the analysis system is able to provide results on the solar LDR bias as well as information on the pointing biases of the two polarizations and how well they agree.

Since its introduction in 2004 the solar monitoring method has proven to be a valuable tool for monitoring the antenna pointing, antenna system stability, and receiver stability. In addition it is a good tool for studying the workings of the data processing which affect the width of the solar image. With the introduction of polarimetry it has found new uses in monitoring the differences in the polarization channels of the radar. The present work demonstrates the extension of the use of the method to the OPERA radar network which covers a whole continent. Results on antenna pointing are now delivered to the OPERA members on a regular basis. When appropriate data from all the network are available, full harmonization of the measurement angles is possible. Future work will then continue towards monitoring the receiver stability, and to the use of the solar fluxes in harmonization of the calibration levels.

Acknowledgement

The OPERA project work is financed by the EUMETNET members. The authors wish to thank the OPERA members for providing the data for this work and the OPERA Expert Team members for their support. The numerical analysis and the figures have been prepared using the R software (R Core Team, 2015).

References

P. Altube, J. Bech, O. Argemí, and T. Rigo, "Quality control of antenna alignment and receiver calibration using the sun: adaptation to mid range weather radar observations at low elevation angles," *J. Atmos. Ocean. Technol.*, vol. 32, pp. 927–942, 2015.

R. J. Doviak and D. S. Zrnić, *Doppler Radar and Weather Observations*, Second ed. Academic Press, 1993.

J. Figueras i Ventura, A.-A. Boumahmoud, R. Fradon, P. Dupuy, and P. Tabary, "Long-term monitoring of french polarimetric radar data quality and evaluation of several polarimetric quantitative precipitation estimators in ideal conditions for operational implementation at c-band," *Q. J. R. Meteorol. Soc.*, vol. 138, pp. 2212–2228, 2012.

M. Frech, "Monitoring the data quality of the new polarimetric weather radar network of the german meteorological service," in *36th Conference on Radar Meteorology*. AMS, 2013.

M. Gabella, M. Sartori, M. Boscacci, and U. Germann, "Vertical and horizontal polarization observations of slowly varying solar emissions from operational swiss weather radars," *Atmosphere*, vol. 6(1), pp. 50–59, 2015.

I. Holleman and A. Huuskonen, "Analytical formulas for refraction of radiowaves from exoatmospheric sources," *Radio Science*, vol. 48, pp. 226–231, 2013.

I. Holleman, A. Huuskonen, R. Gill, and P. Tabary, "Operational monitoring of radar differential reflectivity using the sun," *J. Atmos. Ocean. Technol.*, vol. 27, pp. 881–887, 2010a.

I. Holleman, A. Huuskonen, M. Kurri, and H. Beekhuis, "Operational monitoring of weather radar receiving chain using the sun," *J. Atmos. Ocean. Technol.*, vol. 27, pp. 159–166, 2010b.

A. Huuskonen and I. Holleman, "Determining weather radar antenna pointing using signals detected from the sun at low antenna elevations," *J. Atmos. Ocean. Technol.*, vol. 24, pp. 476–483, 2007.

A. Huuskonen, M. Kurri, H. Hohti, H. Beekhuis, H. Leijnse, and I. Holleman, "Radar performance monitoring using the angular width of the solar image," *J. Atmos. Ocean. Technol.*, vol. 31, pp. 1704–1712, 2014a.

A. Huuskonen, E. Saltikoff, and I. Holleman, "The operational weather radar network in Europe," *Bull. Amer. Meteor. Soc.*, vol. 95, pp. 897–907, 2014b.

A. Huuskonen, G. Haase, D. Michelson, H. Leijnse, I. Holleman, M. Probert, R. Gill, M. Frech, M. Kurri, and H. Hohti, "Solar monitoring as a tool for improving the homogeneity of radar networks," in *Ninth European Conference of Radar Meteorology and Hydrology (ERAD), Antalya, Turkey*, 2016a. [Online]. Available: https://erad2016.mgm.gov.tr/storage/images/_abstract/extended_abstract/6.6.pdf

A. Huuskonen, M. Kurri, and I. Holleman, "Improved analysis of solar signals for differential reflectivity monitoring," *Atmos. Meas. Techn.*, vol. 9, pp. 3183–3192, 2016b.

M. Jurasek and L. Okon, "Slovakian national report to OPERA," in *39^{th} OPERA meeting, Bellizona, Switzerland*, 2018.

S. Matthews, P. Dupuy, R. Scovell, A. Kergomard, B. Urban, A. Huuskonen, A. Smith, and N. Gaussiat, "Eumetnet OPERA radar data center: providing operational, homogeneous european radar rainfall composites," in *Proceedings of a symposium held in Exeter, UK, April 2011, IAHS publication, 351*, 2012, pp. 9–14.

D. Michelson, A. Henja, S. Ernes, G. Haase, J. Koistinen, K. Ośródka, T. Peltonen, M. Szeszczykowski, and J. Szturc, "BALTRAD advanced weather radar networking," *Journal of Open Research Software*, vol. 6 (1), p. 12, 2018. [Online]. Available: http://doi.org/10.5334/jors.193

J. R. Probert-Jones, "The radar equation in meteorology," *Q. J. R. Meteorol. Soc.*, vol. 88, pp. 486–495, 1962.

R Core Team, *R: A Language and Environment for Statistical Computing*, R Foundation for Statistical Computing, Vienna, Austria, 2015. [Online]. Available: https://www.R-project.org/

NETWORK OF WEATHER RADARS IN REPUBLIC OF SRPSKA, BOSNIA AND HERZEGOVINA

Tihomir Dejanovic[1], Velimir Vranic[1] and Zoran Vucinic[2]

[1]*JP "Protivgradna preventiva RS" a.d., Kozarskih brigada bb, 78400 Gradiška, Republic of Srpska, Bosnia and Herzegovina*
[2]*Republic hydrometeorological service of Serbia, Kneza Viseslava 66, 11000 Belgrade, Serbia*
(Dated: 20 June 2018)


Tihomir Dejanovic

1 Introduction

This paper will present a new weather radar network in the region of the Western Balkans. This new radar network will very well fit into the existing radar networks in Croatia and Serbia, so that by establishing it, most of the Western Balkan region will be covered by high quality radar data. As can be seen from Figure 1, it is currently the southwestern and southern part of the Balkans without quality radar data. In the next few years, it is expected that the efforts of Croatia, Bosnia and Herzegovina (Republic of Srpska) and Serbia in the procurement and installation of new radars will significantly change the existing state to better.

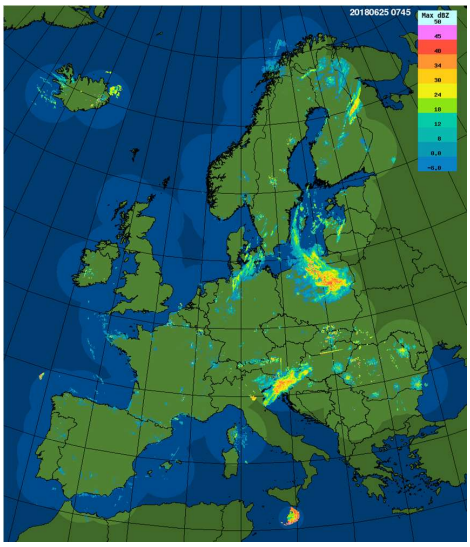


Figure 1:Opera European weather radar composite products 09/25/2018 07:45. It is adopted from the OPERA webpage.

2 Weather Radar at the location Borje

During July 2017, JP "Protivgradna preventiva RS" a.d. has installed the EEC DWSR-3501C SDP Doppler Weather Radar at the location of Borje, Republic of Srpska, Bosnia and Herzegovina. The location of the new radar is Lat 44.58326400ºN, Long 17.60608900ºE and height 1075 m. From this location in the range of 200 km, most of the territory of Bosnia and Herzegovina, as well as parts of the territory of Croatia, are covered. Figure 2 shows the technical characteristics of this radar:

DWSR-3501C SDP System Level Technical Characteristics	
Transmitter Type	Magnetron (EEC-5257-35)
Frequency	5,200 – 5,700 MHz
Transmitter Power	350 kW
Pulse Repetition Frequency	200 - 2400 PPS (within the duty cycle)
Pulse Width	0.4 to 2.0 µsec
Maximum Effective Range	>500 km (Reflectivity) and >250 km (Velocity) (Range Error is less than 1% of the range)
Maximum Velocity Detection	No Unfolding ~ 25 m/s 3:2 Unfolding ~ 50 m/s 4:3 Unfolding ~ 75 m/s 5:4 Unfolding ~ 100 m/s
Receiver Sensitivity – MDS	-114 dBm @ 2µsec
Noise Ratio	< 2.5 dB
Ground Clutter Suppression	≥ 40 dB (typically ~ 45 dB)
System Operational Availability	Better than 99.0%
System Power Requirements	Single Phase 220-240 VAC ± 10%, 50/60 Hz ± 10%

Figure 2: Technical characteristics EEC DWSR-3501C SDP Doppler Weather Radar

DWSR-3501C SDP Transmitter Performance Characteristics	
Transmitter Type	Magnetron (EEC-5257-35)
RF Power Output	250 kW (nominal)

IQ2 Receiver and Signal Processor Performance Characteristics	
Dynamic range:	> 105 dB at 0.5-MHz bandwidth
Range Resolution:	15.625 m standard for 4 channels with 76.72MHz clock, other combinations by option, for example 15m with 80MHz clock
Number of Range Gates	4096 (typical), 8192 (optional)
Flexibility:	All IQ2 firmware and software can be updated through the server

IQ2 Signal Processor Moments	
Reflectivity	Zh, Zv (corrected), [dBZ] / UZh, UZv (uncorrected), [dBZ]
Radial Velocity	Vh, Vv, [m/s]
Spectral Width	Wh, Wv, [m/s]
Differential Phase	ΦDP, [degrees]
Correlation Coefficient	ρHV, [0.00 – 1.00]
Linear Depolarization Ratio	LDR, [dB]
Specific Differential Phase	KDP, [degrees]
Differential Reflectivity	ZDR, [dB]
Clutter power	CCORh, CCORv, [dB]
Signal quality index	SQI

D-Series Pedestal Performance Characteristics		
Type	Elevation over Azimuth	
Azimuth Velocity	> 36°/sec maximum	
Azimuth Acceleration	> 15°/sec2	
Azimuth Deceleration	> 15°/sec2	
Azimuth Rotation	360°, clockwise or counterclockwise	
Elevation Movement Range	Manual Mode -2° to + 92° (Bumper Stops)	Automatic Mode -0.5° to + 90° (Software)
Elevation Velocity	Manual Mode Variable from 0°/sec to 15°/sec	Automatic Mode Software controlled up to 5 scans per minute
Azimuth & Elevation Pointing Accuracy	Better than ± 0.1°	
Azimuth & Elevation Display Resolution	Better than ± 0.1°	
Safety Devices	Safe switch on Pedestal and Access door interlock, Latched Key Maintenance Control	

4.2 Meter (14-Foot) Reflector Performance Characteristics	
Reflector Type	Varies (Spun Aluminum or Composite)
Feed Horn Type	Orthogonal (Dual Polarization)
Beam width	< 1.0° (0.95° typical above 5600 MHz)
Gain	≥ 45 dB (typical)
Operating Frequency	5200-5700 MHz
Wavelength	5.0 cm at 5625 MHz
Standard Polarization	Dual Polarization (SIDPOL)
Side Lobes	≥ 25 dB down from main lobe @ ≤10° (nominal)
VSWR (at Reflector)	1.15:1 (typical)

Figure 2: Technical characteristics EEC DWSR-3501C SDP Doppler Weather Radar

Figure 3 shows the tower at the location of Borje:



Figure 3: The tower at location of Borje

3 Network of weather radars

By the end of 2018, it is planned to set up another EEC DWSR-3501C SDP Doppler Weather Radar at Jahorina, Republic of Srpska, Bosnia and Herzegovina. Location of the planned radar is Lat 43.72019944ºN, Long 18.56186110ºE and height 1911.5 m. In this way, in the 200km range, both radars would cover the entire territory of the Republic of Srpska, Bosnia and Herzegovina, parts of the territory of Croatia, Serbia and almost the entire territory of Montenegro. Coverage of the territory of the new radar network and its integration into existing radar networks in Croatia and Serbia will be shown.

Figure 4 shows the coverage at locations of Borje and Jahorina in the 200 km range



Figure 4: The coverage at locations of Borje and Jahorina in the 200 km range

Figure 5 shows the coverage at locations of Borje ,Jahorina (Republic of Srpska, Bosnia and Herzegovina), Bilogora(Croatia), Fruska gora and Jastrebac (Serbia) in the 200 km range:

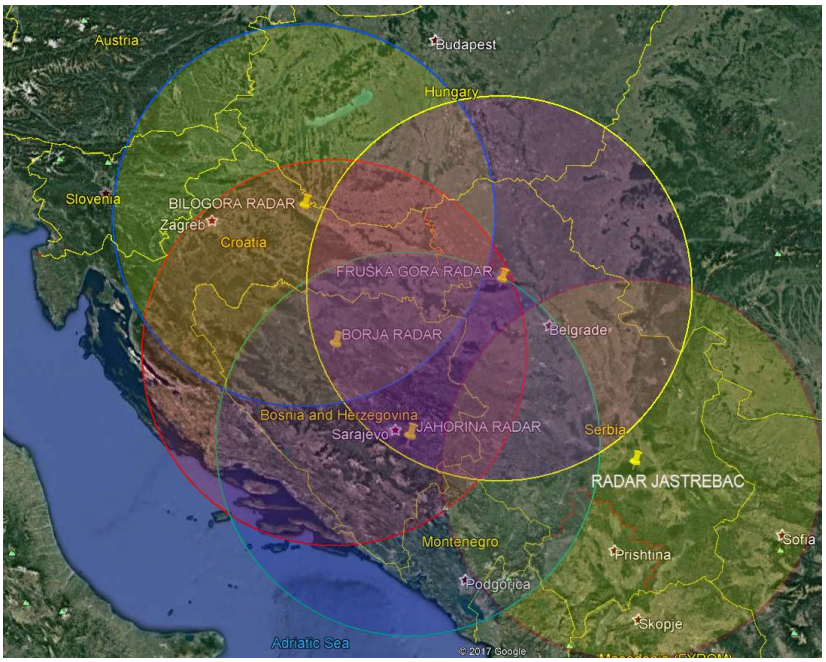


Figure 5: The coverage at locations of Borje ,Jahorina (Republic of Srpska, Bosnia and Herzegovina), Bilogora(Croatia), Fruska gora and Jastrebac (Serbia) in the 200 km range

Also, the connection of a new radar network in Republic of Srpska, Bosnia and Herzegovina to European and regional radar networks is planned, especially in the OPERA (Operational Programme for the Exchange of Weather Radar Information).

References

Enterprise Electronics Corporation, Technical Documentation Set Operations and Technical Manual DWSR-3501C SDP - 24 September 2015
Enterprise Electronics Corporation, EDGE 6 User Manual - 29 January 2015
Enterprise Electronics Corporation, EDGE 6 Technical Manual - 29 January 2015
OPERA radar animation is available online.: http://eumetnet.eu/activities/observations-programme/current-activities/opera-radar-animation/ - Url visited 25.06.2018.

Monitoring the ongoing upgrade of the Swedish weather radar network

David Dufton[1], Günther Haase[1], Daniel Johnson[1], and Gianfranco Vulpiani[1, 2]

[1]*Swedish Meteorological and Hydrological Institute, Norrköping, Sweden*
[2]*Department of Civil Protection, Presidency of the Council of Ministers, Rome, Italy*

(Dated: 22 June 2018)

1. Introduction

Dual polarisation weather radars have long been considered advantageous but it is only more recently that national weather networks have begun to incorporate dual polarisation radars. Sweden's plans for a fully dual polarised network started over 10 years ago, the first of its twelve radars was upgraded to dual polarisation in 2014 and the final radar is due to be completed in 2019. The process involves upgrading existing radars to dual polarisation while retaining existing components where possible, rather than a complete renewal. To obtain the greatest benefit from the upgrade it is clear that the radars need to be well calibrated and monitored to ensure system stability and homogeneity across the network. Recent events clearly show this is not the case for the upgraded radars, with inconsistent radar calibration and temporal instabilities clear within the network as seen in figure 1. An offset between radars within the network is clearly visible in March 2018 but not clear in October 2017 suggesting a potential shift in radar calibrations across the network in the six month period between these images. As differences in radar composites can be hard to attribute clearly to radar calibration due to possible differences in observation height and sensitivity in the interesecting region which can vary with changes in propagation conditions additional tools are required to investigate the true cause of the differences observed in the composites.

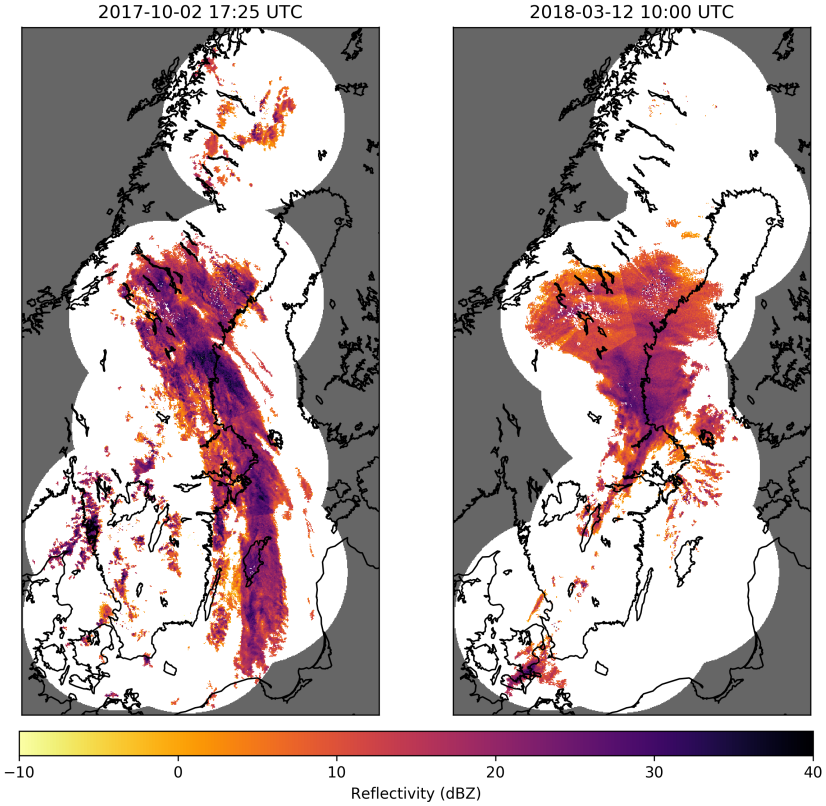


Figure 1: Two Swedish horizontal reflectivity composites (lowest ppi, 2km resolution, stereographic projection). The boundaries between different radars are clearer in the later image (2018-03-12 10:00 UTC) suggesting a drift in radar calibration could have led to an increased difference in absolute calibration between radar sites.

To investigate these differences SMHI has been implementing a number of techniques to allow monitoring of the network and to adjust radar calibrations where appropriate. This is a critical stage in the development of all downstream data products as they are all dependant on accurate measurements from the radar network. Weather radar monitoring and calibration has long

been a topic of research and many methods are already well established within the literature (Goddard et al., 1994; Gorgucci et al., 1992; Gourley et al., 2006; Ryzhkov et al., 2005, for example) and recently efforts have been made to improve the sharing of non published techniques, and more importantly experiences, across the weather radar community (for example the Weather Radar Calibration & Monitoring workshop (WXRCalMon) hosted by DWD in 2017[1]). This extended abstract should be viewed in this context and covers the implementation of existing techniques to monitor the SMHI network, focusing on challenges, changes and improvements that are relevant when adapting each of them to a national network. To aid the reader we provide the names and locations of each of the upgraded radars mentioned in the following work in table 1, below.

Table 1: Names and locations of upgraded radars in the Swedish weather radar network

Name	Abbreviation	Latitude (°N)	Longitude (°E)
Ängelholm	ang	56.37	12.85
Hemse	hem	57.30	18.40
Hudiksvall	huv	61.58	16.71
Leksand	lek	60.72	14.88
Örnskoldsvik	oer	63.63	14.76
Österund	osd	63.29	14.76
Vara	vax	58.26	12.83

2. Monitoring Reflectivity

There are two challenges when considering the calibration of a weather radar network, one is that each radar functions stably through time and the other being that measurements from each radar are consistent with the other radars in the network. Ideally both of these are accomplished through absolute calibration of each radar during installation and at regular intervals thenceforth but it is clear that during intervening periods the calibration can drift as already shown in figure 1. To detect these changes it is important to monitor the network therefore SMHI has implemented several methods to do so at a range of complementary time scales from monthly to volume by volume.

2.1. Statistical analysis maps

A simple, yet effective, method for qualitatively assessing the stability of each radar is to produce statistical maps, such as echo occurrence frequency, or average observed reflectivity, for fixed time intervals (Harrison et al., 2014). These maps are easy to generate and provide a quick, visual guide to potential changes in the network. For example, figure 2 shows three consecutive monthly mean reflectivity maps from the Vara weather radar which show a clear decrease in the observed values for October 2017 compared to September and November. However using these maps it is not possible to pinpoint the exact timing of any system changes, and determine whether they occur gradually or represent a jump in system calibration. To allow more precise monitoring of the radars we have implemented the relative calibration adjustment (RCA) method of Silberstein et al. (2008) to complement this visual approach. Our experience of implementing RCA for monitoring is discussed in the following section.

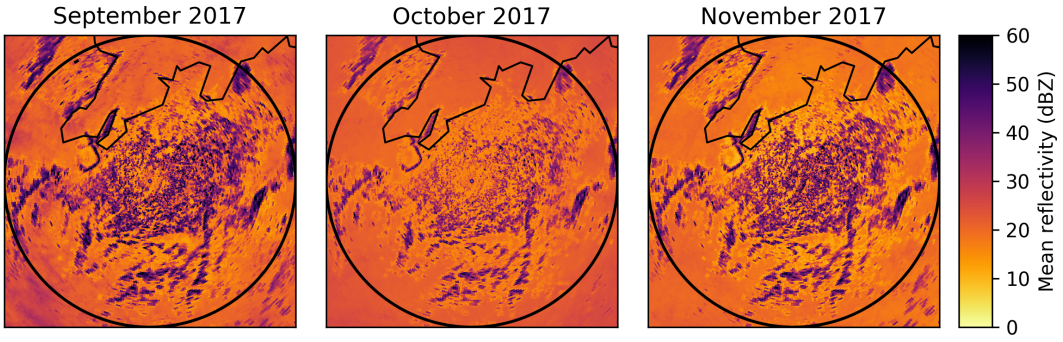


Figure 2: Monthly mean reflectivity for radar Vara. Each panel is a 100km box centred on the radar, with a 50km range ring shown. Also shown is the coastline of Lake Vänern.

[1]See www.dwd.de/EN/specialusers/research_education/seminar/2017/wxrcalmon2017/wxrcalmon_en_node.html

2.2. Relative Calibration Adjustment - Ground Clutter monitoring

The RCA method was first proposed by Silberstein et al. (2008) and its wider implementation has been discussed in further detail by Wolff et al. (2015). In summary the method uses the distribution of reflectivity measurements from ground clutter targets to track the relative stability of the radar system through time relative to a baseline.

$$\mathrm{RCA_t} = \mathrm{C95_t} - \mathrm{C95_{base}} \tag{2.1}$$

Where C95 is the 95$^{\mathrm{th}}$ percentile of the clutter distibution and base is a fixed baseline value. The most important assumptions are that the reflectivity returns from the highest percentiles of the clutter distribution should remain constant if the radar system does not change and that meteorological echoes of sufficient magnitude occur infrequently enough to not shift the highest percentiles of the distribution. Originally the method used daily clutter distributions, and more recent work has shown the method to also produce stable results with higher temporal resolution.

The first observation from our implementation of RCA is that the radars in the Swedish network have significantly less high reflectivity clutter targets than the radars used in previous work. For example the Kwajalein radar used by Silberstein et al. (2008) has more than 5000 range gates (1° x 264 m) with a reflectivity above 50 dBZ within 10 km while the Swedish radar at Vara has only 51 range gates (1° x 500 m) which meet the same criteria. It is also important to note that due to the upgraded Swedish radars being located in rural areas the majority of ground clutter returns come from vegetated slopes which provide lower and less stable reflectivity measurements than man made targets. An initial implementation of RCA was made using a very loose definition of acceptable clutter targets (Z>30 dBZ, range<25 km, probability>95%) to obtain a much greater number of observations per sweep. This was then tracked on a scan by scan update basis and found to be useful in monitoring the network but susceptible to both noise and environmental changes in the clutter targets. Figure 3 shows the results of this monitoring for the Vara weather radar, previously shown in figure 2. During the second half of 2017 there were several issues with the radar which were identified with the help of the RCA monitoring including re-pressurising the waveguide in September, replacement of the fibre optic rotary joint in October and finally replacement of the magnetron and refixing of the drivetrain at the end of November 2017.

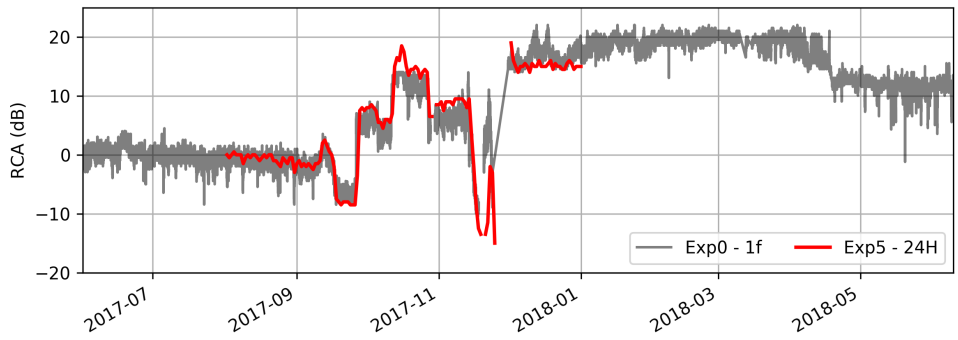


Figure 3: RCA monitoring for the Vara radar. The grey line is the relative change in the 95th percentile of a file by file clutter distribution using a trial clutter mask. The red line is a revised approach where daily distributions are considered using a revised clutter map (experiment 5). The baseline for each RCA is the median value within the first 3 days of each timeseries to track the relative change, in the future a baseline will be defined based on a fixed point in time where the radar is believed to be well calibrated.

Despite the value of this monitoring being clear further analysis has been undertaken to refine the calculation of the RCA, to obtain more stable results. This analysis included changing the clutter definition used and varying the time interval of the distribution from 1 file to 1 day. Three different parameters can be changed in the clutter definition to alter the number of range gates included in the distribution. First one can change the reflectivity threshold, secondly one can change the maximum range at which gates are used and finally one can vary the echo occurrence frequency (EoF) threshold. Seven different variations (table 2) of these parameters were trialled for two radar sites using both 3 hourly and daily time periods over a 30 day test period.

Table 2: RCA sensitivity experiments. Both the thresholds used to build a clutter map and the standard deviation of the RCA results from a 30 day test period for two radars are shown. The column N for each radar is the number of range gates defined by the clutter map. All clutter maps were defined using a single, rain free day apart from the operation test map (experiment 0) which used a whole month of reflectivity observations.

Experiment	Min. Z	Range	EoF	Vara			Hudiksvall		
number	(dBZ)	(km)	(%)	N	3 Hour σ	24 Hour σ	N	3 Hour σ	24 Hour σ
1	50	10	50	51	1.44	0.83	23	1.01	0.71
2	50	10	25	130	1.40	1.07	25	0.99	0.71
3	50	25	25	720	0.68	0.42	38	0.93	0.71
4	50	25	50	360	0.86	0.50	31	0.93	0.67
5	45	10	50	260	0.86	0.64	30	0.94	0.67
6	45	25	50	1199	0.68	0.39	46	0.90	0.61
7	30	25	50	5302	0.67	0.46	307	0.58	0.47
0	30	25	95	2311	1.79	1.80	131	0.71	0.47

The analysis indicated that options which increased the number of range gates in the distribution provided more stable results and that reducing the Z threshold is the most stable option for increasing range gates. The analysis also showed that a universal set of thresholds is not suitable for the network, and should be varied depending on the clutter characteristics of each radar site. The most unexpected result is seen for the original trial implementation of RCA for the Vara site, where variability is significant despite a large number of range gates being used in the distribution. This is due to an unexplained diurnal variation which occurs for several days during the trial period. The variation occurs only for the higher percentiles of this distribution and is not seen in any of the other experiments and is well correlated with external temperature variation at the radar site. we postulate the variation is due to a temperature dependant variation of the propagation conditions or, more likely, the clutter targets themselves, although an exact cause is as yet unknown. Additional testing also shows that experiments using a maximum range of 25 km are affected more by anomalous propagation events, suggesting a compromise solution is required which maximises range gates without increasing range too far or reducing reflectivity to include more variable "soft" targets.

For the radar at Vara we believe experiment 5 represents the best compromise, while using a lower reflectivity threshold of 30 dBZ is more appropriate for Hudiksvall. Results from the application of the thresholds from experiment 5 with a daily distribution period are shown in figure 3 and are clearly more stable than the original implementation while retaining the same indicators of malfunction during September, October and November 2017. The RCA method has provided us with a useful tool for monitoring our systems during and beyond the upgrade period but our results are not as stable as those shown by Silberstein et al. (2008). We believe this difference is partly a result of the reduced number and "softer" nature of the clutter targets available at our sites and we would advise other services to consider RCA a useful tool while acknowledging its performance will vary from site to site. Our next step for the implementation of RCA is to provide an automated method for monitoring the results. Given the variability shown a fixed threshold may lead to false positives so we are also considering the implementation of a time integrated RCA, to account for the stability of any changes in time. This should lead to transient affects such as AP or wet-radome being ignored, providing a less sensitive monitoring system.

2.3. Sensitivity monitoring

We have also implemented monitoring of each radar's sensitivity, by fitting a 2 parameter relationship to the range - reflectivity data on a daily basis. Radar sensitivity should be a function of receiver noise and radar calibration with deviations indicating instability in the radar system. Figure 4 displays the minimum detected reflectivity at 100 km range for each upgraded radar over the previous year. There are significant deviations within some of the records which coincide with known changes to radar hardware or calibration but some of the transient jumps remain unexplained.

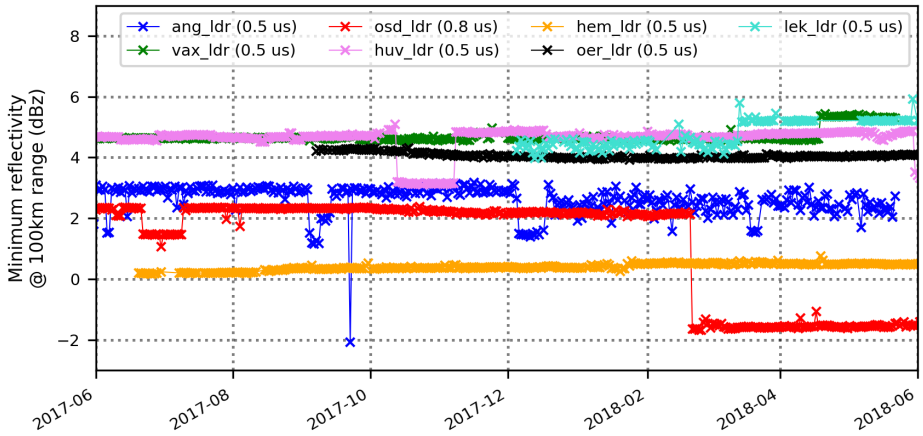


Figure 4: Monitoring of daily sensitivity at 100km range for the upgraded radars in the Swedish network. All the results shown are for the radars operating in LDR mode, where only horizontally polarised radiation is transmitted, with the operational pulse width shown in brackets on the legend. The pulse width shown is currently used for all operational scans irrespective of elevation.

Information from sensitivity monitoring can be combined with those from RCA to indicate whether any changes are likely to be the result of radar calibration or a change in environmental condition or even antenna pointing. For example the sensitivity results for the radar at Vara (vax) shown little deviation between September and December 2017 while the RCA varies by over 30 dB during this period. This suggests that the wide RCA variations were more likely to be a result of significant angular pointing errors associated with the broken drivetrain though the faulty magnetron may also have contributed to a lesser degree. It is also possible to infer an idea of radar miss-calibration across the radar network as each radar contains the same receiving hardware which means large deviations in sensitivity after accounting for the difference in known radar constant are not likely to occur. For example the current sensitivity difference between the Östersund radar (osd) and its neighbour at Hudiksvall (huv) is 6.4 dB, which is explained through the difference in radar constant and change in receiver bandwidth as a result of the different pulse widths, whereas the 4.3 dB difference between Hudiksvall and Hemse (hem) is calculated to be a result of differences in receiver MDS unless one of the radars is currently miss-calibrated.

2.4. Radar inter-comparison

As the Swedish radar composite (figure 1, for example) often indicates potential differences in radar calibration across the Swedish network we have begun to investigate the use of direct radar to radar comparison of reflectivity as a potential means of homogenising the network. Seo et al. (2014) previously demonstrated one application of the technique to radars within the US NEXRAD network. Our current implementation collocates range gates in both space and time using the range gate centroid, with no allowances currently made for attenuation or beam blockage (comparisons of raw reflectivity from both radars). Figure 5 shows a comparison between the Östersund radar and its neighbour at Hudiksvall on the 2$^{\text{nd}}$ October 2017 and the 12$^{\text{th}}$ March 2018 representing the time periods displayed in figure 1.

While there is a large degree of scatter across both plots due to the direct comparison of reflectivity without beam propagation corrections and the relatively coarse limits of collocation used (15 seconds, 125 m altitude and 0.001° of latitude and 0.003° of longitude) there is a clear shift in the distributions between the two events with the mean difference changing from 0.6 dB to 4.4 dB. Research at SMHI will now focus on the optimal limits to use for collocation and how the results are affected when data corrected for beam propagation effects is used. As there are 26 possible comparisons between overlapping radars in the network we hope to utilise these comparisons to homogenise the network, although as this would only be a relative calibration we are hoping to find a solution where the relative differences can be supported with absolute values to provide an accurately calibrated, homogeneous network.

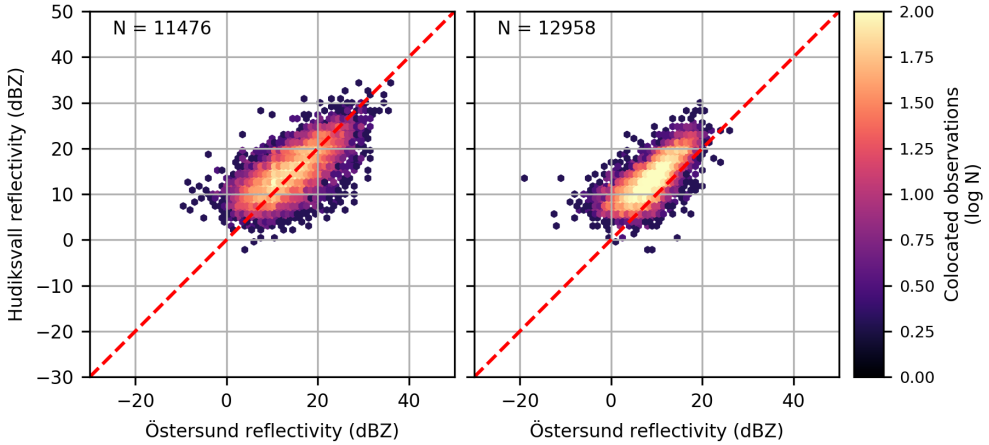


Figure 5: Radar to radar comparison of horizontal reflectivity for the radars at Östersund and Hudiksvall. Reflectivity values are corrected for ground clutter during signal processing but have not been corrected for partial beam blockage or attenuation.

2.5. Solar monitoring of the receiver

One methodology that provides a measure of the absolute calibration of the radar receiver channel is the monitoring of solar radiation detected by the radar with comparison to solar reference measurements (Holleman et al., 2010a). OPERA has now implemented solar monitoring for its members using their online operational radar data on a monthly basis which provides information both on radar antenna pointing and receiver calibration relative to the sun, provided all the metadata provided is accurate (Huuskonen et al., 2013, 2018). SMHI runs the solar hit detection aspect of this system locally within the Baltrad system (Michelson et al., 2018), producing contiguous records of online solar hits for our radars. SMHI's upgraded radars are now generating enough online solar hits for it to be possible to implement the OPERA fitting methodology on a shorter timeseries of data of the order of 2-5 days and we are now experimenting with developing a rolling window solar monitoring process with a daily update cycle. We hope this will provide further information to diagnose the likely source of any changes within our network and complement the RCA and sensitivity monitoring tools described above.

2.6. Self-consistent calibration

Another potential method for determining an absolute calibration of dual polarisation weather radars is to use the principle of self consistency between dual polarisation moments. There are two variations of the approach being considered at SMHI, the first using the self consistency of reflectivity, differential reflectivity and specific differential phase shift (Gorgucci et al., 1992; Gourley et al., 2009) and the second which considers the consistency of reflectivity and specific attenuation determined with the constraint of differential phase shift (Diederich et al., 2014). Both methods have previously shown good results and will be considered once processing of the required parameters at sufficient accuracy becomes operational at SMHI. The biggest challenge to implementation of these methods will be their reliance on contiguous measurements within the liquid only region of precipitation over moderate to long distances, which will not always be available given the climatology of Sweden.

3. Monitoring Differential Reflectivity

Numerous methods also exist to monitor the system differential reflectivity (ZDR) offset, caused by asymmetries in the horizontal and vertical transmit and receive paths. Although these asymmetries should theoretically be accounted for through accurate absolute calibration of reflectivity in both channels it is often considered more feasible to directly monitor and adjust ZDR using a target or targets of a known ZDR. These include the sun (ZDR = 0 dB), rain viewed at vertical incidence (ZDR = 0 dB) or drizzle viewed at horizontal incidence (ZDR $\approx$ 0.2 dB). Each of these methods has its limitations and a combined approach offers the best solution when attempting to calibrate to within the 0.1 dB to 0.2 dB accuracy needed to reliably use ZDR for radar QPE (Ryzhkov et al., 2005).

3.1. Bird-bath scans

The often cited accurate method for ZDR calibration is to use a so-called "birdbath" scan at vertical incidence (90 degrees elevation) where rain drops should not exhibit any difference in reflectivity measurements. Often interference from the radome and radar side lobes can cause non-zero differences which fluctuate depending on azimuth so the radar dish is rotated during the

birdbath to allow an average to be taken. Gorgucci et al. (1999) first proposed the method to be used during rain events but it is common for national weather services to apply the method without distinguishing between liquid and ice phase hydrometeors as ice phase hydrometeors should also have an average ZDR of 0 dB when viewed at vertical incidence (Gourley et al., 2006, for example).

In Sweden it is clear that birdbath scans incorporating only rainfall measurements would generally only be possible from spring to autumn, especially at higher latitudes, due to the climatologically low melting layer height throughout the year and the need to avoid the radar near-field when determining the ZDR calibration. To determine the impact of using ice phase measurements for ZDR calibration three approaches were taken to produce ZDR calibration estimates from the birdbath scans. The first approach was a simple bulk thresholding, where SNR must be greater than 20 dB, the co-polar correlation coefficient must be greater than 0.98, horizontal reflectivity must be greater than 10 dBZ and the observation range must be greater than 1200 m. The second was to add the restriction that the Doppler Velocity measured at vertical incidence must be less than $-3\,\mathrm{ms}^{-1}$ (where negative velocities are towards the radar) generally constraining the results to rain only and the third was to restrict Doppler Velocity to between $-1\,\mathrm{ms}^{-1}$ and $-3\,\mathrm{ms}^{-1}$ and the altitude of observations to greater than 1500 m to constrain the results to the ice phase. An example of this masking is seen in figure 6 where it can be seen that the thresholding successfully removes the melting layer and separates the rain region from the ice region of this event.

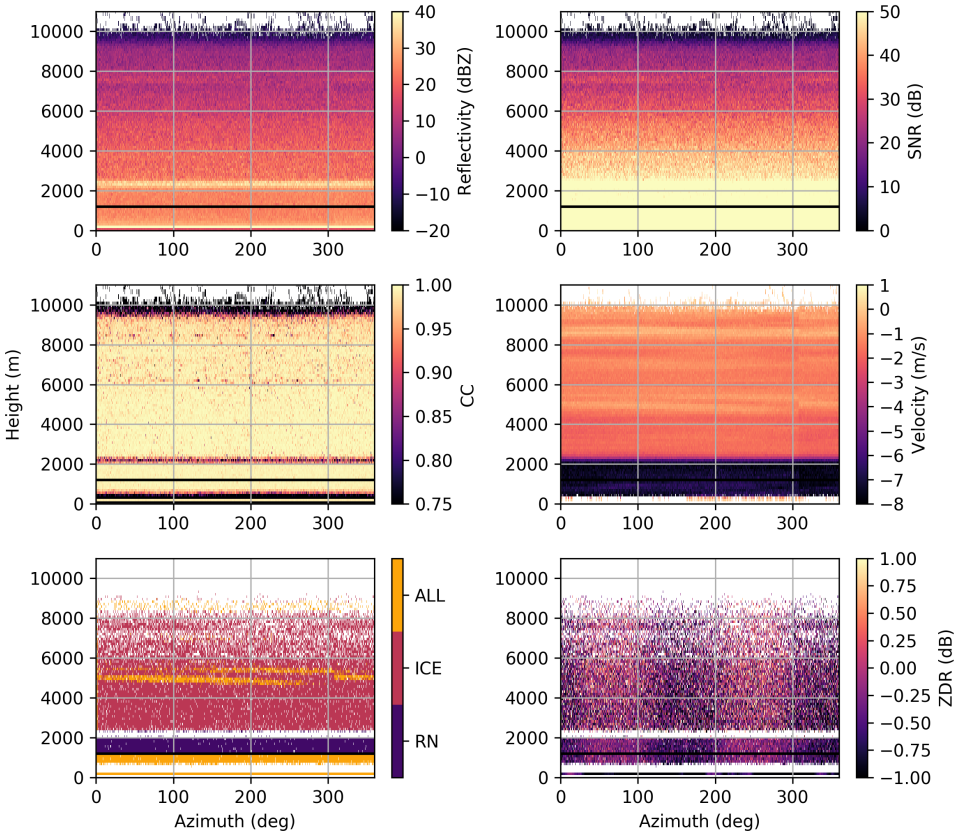


Figure 6: Calibration scan at vertical incidence for radar Leksand, 2018-05-11 15:43 UTC. Panels are as follows: top right - horizontal reflectivity, top left - signal to noise ratio, middle right - co-polar cross correlation, middle left - radial velocity, bottom left - valid gate masking and bottom right - ZDR masked using the ALL calibration mask. On the figure valid gates below 1200 m *are shown but these are omitted in the calibration analysis. The solid black horizontal line denotes this limit on the other plots.*

While it would be expected that the ZDR offset calculated in both rain and ice should be equivalent using these three thresholds indicate this not to be the case, with systematic differences of up to 0.13 dB observed between the second and third approach. These differences were even greater when using a range threshold of only 875 m which suggests some of the difference was due to contamination at low altitude and indicates the importance of setting a suitable minimum height when configuring such a calibration. Figure 7 shows the variability in the results from the Vara and Örnskoldsvik radars, while table 3 summarises the mean difference for each radar. In all cases only instances which contain at least 1200 range gates which meet the thresholding criteria are used. This threshold was determined by checking the variation in the stability of the calibration results as a function of the number of valid range gates and 1200 was found to offer the best compromise between stability and obtaining a reasonable number of results to allow monitoring in time.

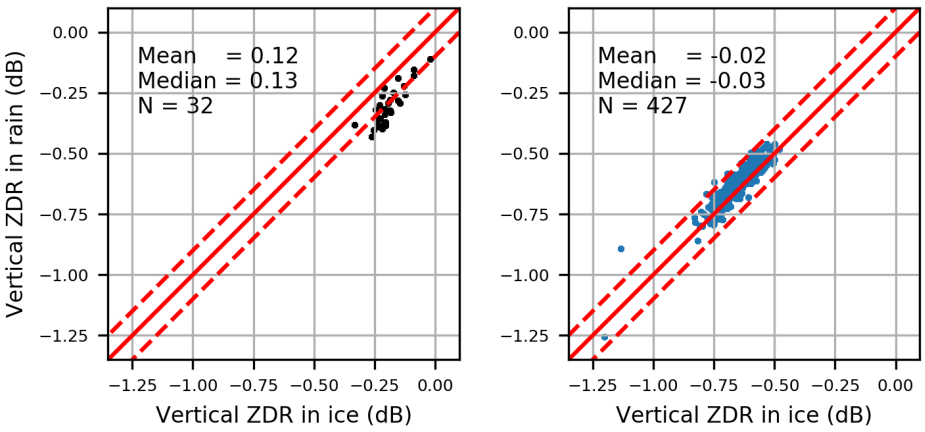


Figure 7: Comparison between observed vertical ZDR in rain and in ice for Leksand (left panel) and Vara (right panel). Each cross represents a birdbath scan where both the rain and ice thresholding produces at least 1200 valid range gates for each phase. The solid red line is the 1:1 line and each dashed line represents an offset of ± 0.1 dB.

Table 3: Median difference between system ZDR measured at vertical incidence in ice and in rain for each radar in the Swedish radar network

Weather Radar	$\mathrm{Med.}\Delta\mathrm{ZDR}_{\mathrm{ICE-RAIN}}$	Weather Radar	$\mathrm{Med.}\Delta\mathrm{ZDR}_{\mathrm{ICE-RAIN}}$
Ängelholm	0.03 dB	Örnskoldsvik	0.11 dB
Leksand	0.13 dB	Östersund	0.06 dB
Ase	0.02 dB	Vara	−0.03 dB
Hudiksvall	0.01 dB		

As the ZDR bias from the bulk approach deviates between that of ice and rain depending on whether the majority of observed precipitation has a large or small Doppler velocity, it is possible that bulk bias adjustment could be influenced beyond the required lower accuracy limits. However for the majority of radar sites the difference is not significant suggesting a bulk approach can be utilised for calibration, however monitoring both rain and ice values has other advantages for checking system stability as the following curious example demonstrates (figure 8).

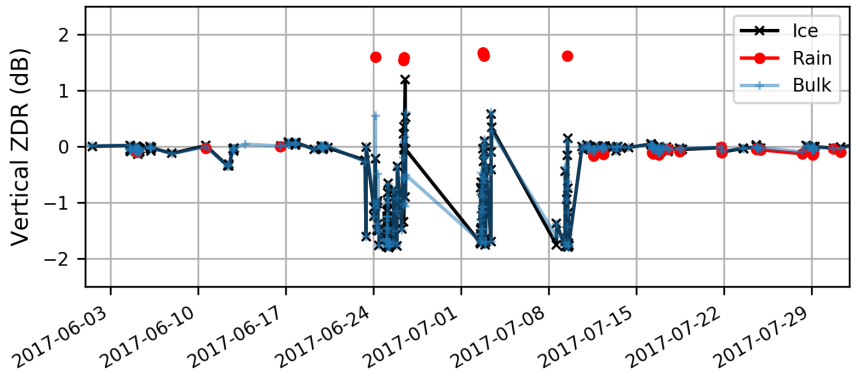


Figure 8: Vertical ZDR bias for the Östersund radar. Red dots are the mean bias from rain, black crosses the mean bias from ice and blue pluses the bias from the bulk filtering which ignores velocity. Results are only shown when at least 1200 range gates in the vertical scan meet the required thresholding criteria.

During processing of the available archive of vertical scans it was noted that results from rain and ice differed significantly for a period of over two weeks at the Östersund radar. Further investigation showed that scans at horizontal incidence were also affected by a shift in ZDR occurring at a variable range from the radar. Two similar events have been found for one of the other radars in the network but in all cases the events do not correspond to any reported changes in radar hardware, software or calibration with the radars returning to their original state after a period of time. Currently we have no explanation for these

transient events but monitoring each of the rain, ice and bulk calibrations should allow them to be detected and investigated if they occur again. For this reason we implement a consistency check for any vertical scans which return a valid result for either rain or ice, raising a warning where a deviation greater than 0.2 dB is observed between results.

3.2. Solar monitoring

In addition to solar monitoring of reflectivity the online monitoring system run by SMHI also captures the ZDR of any solar hits if the radar is operating in simultaneous transmit/receive mode. The expected ZDR of these solar spikes is 0 dB if the radar is perfectly aligned to the sun as the sun is a unpolarized source of radiation. Due to the antenna pattern any off axis hits deviate from the expected result and a multi parameter fit is required to obtain a true offset for the receiver calibration using the sun (Holleman et al., 2010b). Such a method has not yet been implemented at SMHI but the raw data has been used to support investigation of ZDR bias changes detected by the vertical scans. For example the solar data collected at Östersund during the time period shown in figure 8 has been analysed and shows a clear decrease of between 1.5 dB and 2.0 dB matching the change indicated by many of the ice phase results collected during the same period suggesting that the issue shown is more likely to be occurring in the receive chain of the radar rather than a transmit fault. Once a multi parameter fit has been applied to the online results the solar monitoring of ZDR will complement the results obtained from the birdbath and provide additional information when determining the cause of any changes to ZDR bias observed.

3.3. "Known target" calibration

It will also be necessary for SMHI to implement a form of “known target” ZDR calibration where scans at horizontal incidence are analysed. The vertical scans investigated show a clear azimuthal dependant variation likely to be a result of the lightning protection installed on each radome but it is unlikely the variation will be manifested the same at low elevation angles. Using a target such as light snow or drizzle will allow the azimuthal variation to be investigated while also potentially accounting for bias introduced as a result of differential beam blocking. (Ryzhkov et al., 2005). Using horizontal scans will also increase the temporal availability of ZDR bias results once azimuthal variation has been accounted for.

4. Discussion and conclusions

The techniques discussed in this paper have been / will be implemented by SMHI to assist in the monitoring of its radar network. During the process of implementing techniques available in the literature it has become clear that many require adaptations and produce unexpected variations as a result of the individual nature of the radar network and we hope our experiences reported here assist other national services when applying these techniques to their own networks. Using vertical observations of ice phase particles to monitor system ZDR bias significantly expands the temporal availability of results, and has the additional benefit of potentially detecting transient features which are range dependant through a comparison with the results from rain.

While each technique alone has merit we advocate using multiple techniques for the purposes of monitoring both reflectivity and differential reflectivity both for redundancy and to allow more nuanced analysis of the likely cause of any problems which are detected. As more of these techniques become operational the next challenge will be to automate their combination to provide monitoring which not only detects changes across the network but which also indicates the likely cause of such a change, whether that be a failure in antenna pointing, the radar transmitter or the receiver hardware for example.

Acknowledgement

The authors would like to thank our SWERAD colleagues here at SMHI for all the discussions we have had during the development of this work along with those at SAAB and EEC who we have also had discussions with. We would also like to thank our partners in OPERA, particularly Asko, for help with our solar monitoring development and also the participants, and particularly the organisers, of the WXRCalMon workshop where many useful discussions were had regarding the monitoring of a national radar network.

References

M. Diederich, A. Ryzhkov, C. Simmer, P. Zhang, and S. Trömel, “Use of Specific Attenuation for Rainfall Measurement at X-Band Radar Wavelengths. Part I: Radar Calibration and Partial Beam Blockage Estimation,” *Journal of Hydrometeorology*, vol. 16, no. 2, pp. 487–502, Nov. 2014. [Online]. Available: http://journals.ametsoc.org/doi/abs/10.1175/JHM-D-14-0066.1

J. W. F. Goddard, J. Tan, and M. Thurai, “Technique for calibration of meteorological radars using differential phase,” *Electronics Letters*, vol. 30, no. 2, pp. 166–167, Jan. 1994.

E. Gorgucci, G. Scarchilli, and V. Chandrasekar, "Calibration of radars using polarimetric techniques," *IEEE Transactions on Geoscience and Remote Sensing*, vol. 30, no. 5, pp. 853–858, Sep. 1992.

——, "A procedure to calibrate multiparameter weather radar using properties of the rain medium," *IEEE Transactions on Geoscience and Remote Sensing*, vol. 37, no. 1, pp. 269–276, Jan. 1999.

J. J. Gourley, P. Tabary, and J. Parent du Chatelet, "Data Quality of the Meteo-France C-Band Polarimetric Radar," *Journal of Atmospheric and Oceanic Technology*, vol. 23, no. 10, pp. 1340–1356, Oct. 2006. [Online]. Available: http://journals.ametsoc.org/doi/abs/10.1175/jtech1912.1

J. J. Gourley, A. J. Illingworth, and P. Tabary, "Absolute Calibration of Radar Reflectivity Using Redundancy of the Polarization Observations and Implied Constraints on Drop Shapes," *Journal of Atmospheric and Oceanic Technology*, vol. 26, no. 4, pp. 689–703, Apr. 2009. [Online]. Available: http://journals.ametsoc.org/doi/abs/10.1175/2008JTECHA1152.1

D. Harrison, S. Georgiou, N. Gaussiat, and A. Curtis, "Long-term diagnostics of precipitation estimates and the development of radar hardware monitoring within a radar product data quality management system," *Hydrological Sciences Journal*, vol. 59, no. 7, pp. 1277–1292, Jul. 2014. [Online]. Available: https://doi.org/10.1080/02626667.2013.841316

I. Holleman, A. Huuskonen, R. Gill, and P. Tabary, "Operational Monitoring of Radar Differential Reflectivity Using the Sun," *Journal of Atmospheric and Oceanic Technology*, vol. 27, no. 5, pp. 881–887, Jan. 2010. [Online]. Available: https://journals.ametsoc.org/doi/abs/10.1175/2010JTECHA1381.1

I. Holleman, A. Huuskonen, M. Kurri, and H. Beekhuis, "Operational Monitoring of Weather Radar Receiving Chain Using the Sun," *Journal of Atmospheric and Oceanic Technology*, vol. 27, no. 1, pp. 159–166, Jan. 2010. [Online]. Available: https://journals.ametsoc.org/doi/full/10.1175/2009JTECHA1213.1

A. Huuskonen, E. Saltikoff, and I. Holleman, "The Operational Weather Radar Network in Europe," *Bulletin of the American Meteorological Society*, vol. 95, no. 6, pp. 897–907, Oct. 2013. [Online]. Available: https://journals.ametsoc.org/doi/abs/10.1175/BAMS-D-12-00216.1

A. Huuskonen, G. Haase, D. Michelson, H. Leijnse, I. Holleman, M. Probert, R. Gill, M. Frech, M. Kurri, and H. Hohti, "Operational solar monitoring for improving the homogeneity of the European radar network," in *Tenth European Conference of Radar Meteorology and Hydrology (ERAD), Ede, The Netherlands*, 2018.

D. Michelson, A. Henja, S. Ernes, G. Haase, J. Koistinen, K. Ośródka, T. Peltonen, M. Szewczykowski, and J. Szturc, "BALTRAD Advanced Weather Radar Networking," *Journal of Open Research Software*, vol. 6, no. 1, Mar. 2018. [Online]. Available: http://openresearchsoftware.metajnl.com/articles/10.5334/jors.193/

A. V. Ryzhkov, S. E. Giangrande, V. M. Melnikov, and T. J. Schuur, "Calibration Issues of Dual-Polarization Radar Measurements," *Journal of Atmospheric and Oceanic Technology*, vol. 22, no. 8, pp. 1138–1155, Aug. 2005. [Online]. Available: http://journals.ametsoc.org/doi/abs/10.1175/JTECH1772.1

B.-C. Seo, W. F. Krajewski, and J. A. Smith, "Four-dimensional reflectivity data comparison between two ground-based radars: methodology and statistical analysis," *Hydrological Sciences Journal*, vol. 59, no. 7, pp. 1320–1334, Jul. 2014. [Online]. Available: https://doi.org/10.1080/02626667.2013.839872

D. S. Silberstein, D. B. Wolff, D. A. Marks, D. Atlas, and J. L. Pippitt, "Ground Clutter as a Monitor of Radar Stability at Kwajalein, RMI," *Journal of Atmospheric and Oceanic Technology*, vol. 25, no. 11, pp. 2037–2045, Nov. 2008. [Online]. Available: http://journals.ametsoc.org/doi/abs/10.1175/2008JTECHA1063.1

D. B. Wolff, D. A. Marks, and W. A. Petersen, "General Application of the Relative Calibration Adjustment (RCA) Technique for Monitoring and Correcting Radar Reflectivity Calibration," *Journal of Atmospheric and Oceanic Technology*, vol. 32, no. 3, pp. 496–506, Jan. 2015. [Online]. Available: http://journals.ametsoc.org/doi/abs/10.1175/JTECH-D-13-00185.1

Assimilation of different radar data for a better forecasting of severe weather phenomena

Luca Rovai[1], Andrea Antonini[2], Samantha Melani[1,2], Valerio Capecchi[2], Riccardo Benedetti[2], Luca Fibbi[1,2], Bernardo Gozzini[2], Gianni Messeri[1,2], Alberto Ortolani[1,2], and Francesco Pasi[1,2]

[1]*CNR-IBIMET, Via G. Caproni, 8 50145 Florence, ITALY*
[2]*LaMMA Consortium, Via Madonna Del Piano, 10 50019 Sesto Fiorentino (FI), ITALY*
(Dated: 22 June 2018)

1 Introduction

In recent years, a succession of severe weather conditions throughout the Mediterranean basin has led many regional and European meteorological centers to attempt for increasingly reliable forecasts of such events (Zsoter, 2006) (Dutra, et al., 2013). Because of the extreme phenomena intensity and their very limited spatial and temporal scale, the most promising approach relies on short-term forecasts (Hou, et al., 2013) (Ji-Hyun, et al., 2012). Many studies have confirmed the importance of assimilating local conventional and unconventional observations for short-term forecasts and nowcasting at high spatial resolution (Schwitalla, et al., 2014) (Maiello, et al., 2017). An analysis of the impacts of assimilating ground stations and radar measurements in a numerical atmospheric model (WRF-ARW) is here presented for two intense rainfall events that struck Tuscany (central Italy) in the last three years. The first one occurred on Aug. 1, 2015, when a weak trough located in the Tyrrhenian Sea between Corse and Tuscany led to a multicellular convective storm, rapidly moving to the hinterland. Around 5 p.m. UTC a severe wet microburst hit the town of Florence, dumping 45 mm of rain and hail in 45 min. 15 people were injured, 330 trees felled by wind gusts and hundreds of vehicles and buildings were strongly damaged. The second studied event occurred on Sep. 9, 2017. During the day a slow-moving long wave trough deepened over Western Mediterranean Sea. The trough was characterised by strong South-Westerly upper level forcing and mild, very moist, southerly low level flow, converging towards the Italian Tyrrhenian coasts. This synoptic set-up, combined with local winds convergences, resulted in heavy rain (250mm in 4h, 100mm in 1h) and flash floods, causing eight casualties.

The objective of the study presented here consists in testing some possible forecast approaches, rather than attempting a reanalysis or a hindcasting of the events. So only data acquired before the events, just in time to be assimilated into a NWP model for a realistic short-tem forecasting and nowcasting activity, are taken into account.

2 Instruments and methods

2.1 Radar systems and data

Two kinds of data are considered: conventional data acquired by ground weather stations, namely values of atmospheric pressure (P), temperature (T) and relative humidity (RH) as well as wind speed and direction, and meteorological Radar observations in the form of reflectivity values and Doppler radial velocity, when available.

Conventional data are collected from more than one thousand of ground stations, part of them distributed all over the Italian peninsula and connected to the WMO's Global Telecommunication System (GTS) and part concentrated on the Tuscany territory belonging to the meteorological regional network.

Radar observations come from two sources:

- the Leghorn X-band radar, providing reflectivity values in a range of about 110 Km, with an observation time resolution of 15 min. and a radial resolution of 450 m, at 4 different elevations;
- the Aleria S-band radar, providing reflectivity and radial velocity values in a range of about 250 km, with an observation time resolution of 15 min. and a radial resolution of 1000 m, at 5 different elevations.

2.2 WRF NWP model

The forecast system architecture tested on the two case studies is based on the numerical weather prediction (NWP) model ARW (Advanced Research WRF), version 3.8.1, equipped with the WRF-DA package for 3DVar data assimilation (WRFweb). We chose to run the model on 50 vertical levels at 3km of horizontal resolution, taking as initial and boundary conditions the ones provided every three hours by the ECMWF global model IFS, at 0.125° of resolution.

2.3 Experiment description

We performed four different assimilation experiments for each case study, always using the same 3DVar assimilation schema. The first forecast run starts in “cold” mode (i.e. using the low resolution global model as initialization) 12 hours before the beginning of the event under study, for example at 00 UTC for an event starting at 12 UTC. Once the model has completed the first three hours of integration, a period considered sufficient for its “spin-up”, the 3DVar assimilation process

rovai@lamma.rete.toscana.it

starts, always taking as background atmospheric state the high resolution forecast ARW fields. This "hot" restart allows to get physically realistic fields, and hence reliable forecasts, even soon after the assimilation instants, which are set every three hours of integration time, ingesting observations made within a temporal window of one hour (centered in the assimilation reference time). Parallel runs are maintained all the lead time long, so that at the end of computation we have four different forecasts, as schematically shown in Figure 1:

A0. control run (CTRL), without any assimilation;

A1. One stage assimilation run, with a single assimilation 9 hours before the event starts;

A2. Two stages assimilation run, with two assimilations 9 and 6 hours before the event;

A3. Three stages assimilation run, with assimilations 9, 6 and 3 hours before the event;

A4. Four stages assimilation run, with assimilations 9, 6, 3 and zero hours before the event, i.e. up to the beginning of the event itself.

The comparison between these forecasts provides an indication of the effectiveness of the assimilated data, as well as information on how well and with how much advance the event can be predicted.

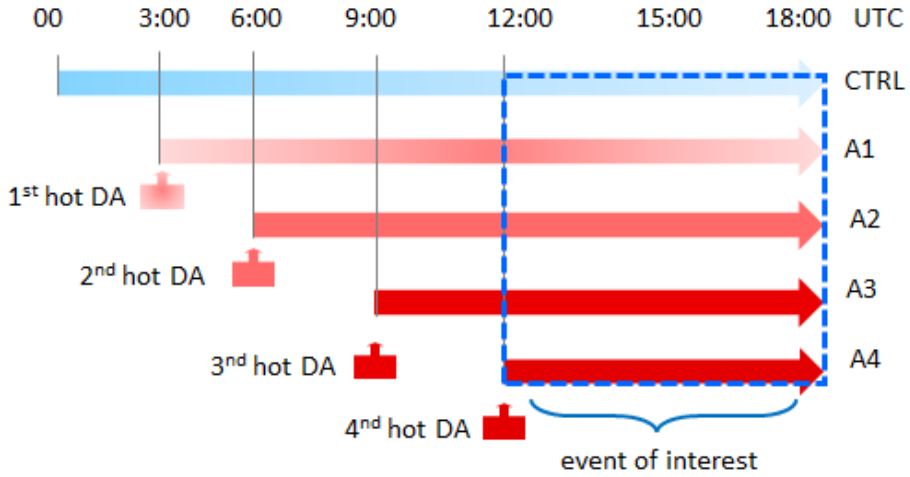


Figure 1 Timetable of the control run (CTRL) and the three nested assimilation experiments. The event of interested is here assumed to start at 12:00 UTC.

3 Results and conclusions

For both the case studies the duration of the event of interest has been considered of 6 hours, even if the heaviest rainfall concentrates in two hours or less, especially for the convective storm on Aug. 1, 2015. The cumulated precipitation measured by the local network of rain gauges during the 6 h nominal duration of the two events is the physical quantity on which the goodness of the forecasts has been evaluated.

3.1 Florence, Aug. 1, 2015 case study

The convective storm on Aug. 1, 2015 and the microburst that hit the town of Florence at 5 p.m. is probably one of the most difficult event to be predicted, because of its sudden formation and the extremely localised area (less than 2 km^2) of the microburst. Indeed the CTRL run (top right panel of Figure 2) provides no indication of the possible occurrence of such an event and, more or less, the same happens with the one and two stages assimilation run (A1 and A2). The three stages assimilation run (A3, bottom left panel of Figure 2) begins to indicate convective rains in the hinterland, clearly reinforced and extended to coastal areas with the four stages assimilation run (A4, bottom right panel of Figure 2). Anyway, both the intensity and mostly the localization of the precipitation remain in poor agreement with the actually measured values. From a point view of the weather alert it should however be noted that short term forecasts, like the ones obtained with radar and ground stations data assimilation three hours before the event (A3) or just at the first signs (A4), would at least allow the alerting of the civil protection. Thus, also in this case, the hot-start 3DVar assimilation of local observations could support such an action.

3.2 Leghorn, Sept. 9-10, 2017 case study

The heavy precipitation event on Sept. 9-10, 2017 involved a wider area with respect to the one of Florence 2015, following a different dynamics. As clearly visible by the radar reflectivity images, the phenomenon began to develop in the

afternoon, offshore Tuscany, slowly approaching the coast where it arrived in the night. In fact the assimilation of radar reflectivity data, in addition to ground stations, produces remarkably positive effects as early as 6 hours before the start of the most severe event, assumed at 00 UTC of September 10th 2017 (see bottom left image of Figure 3).

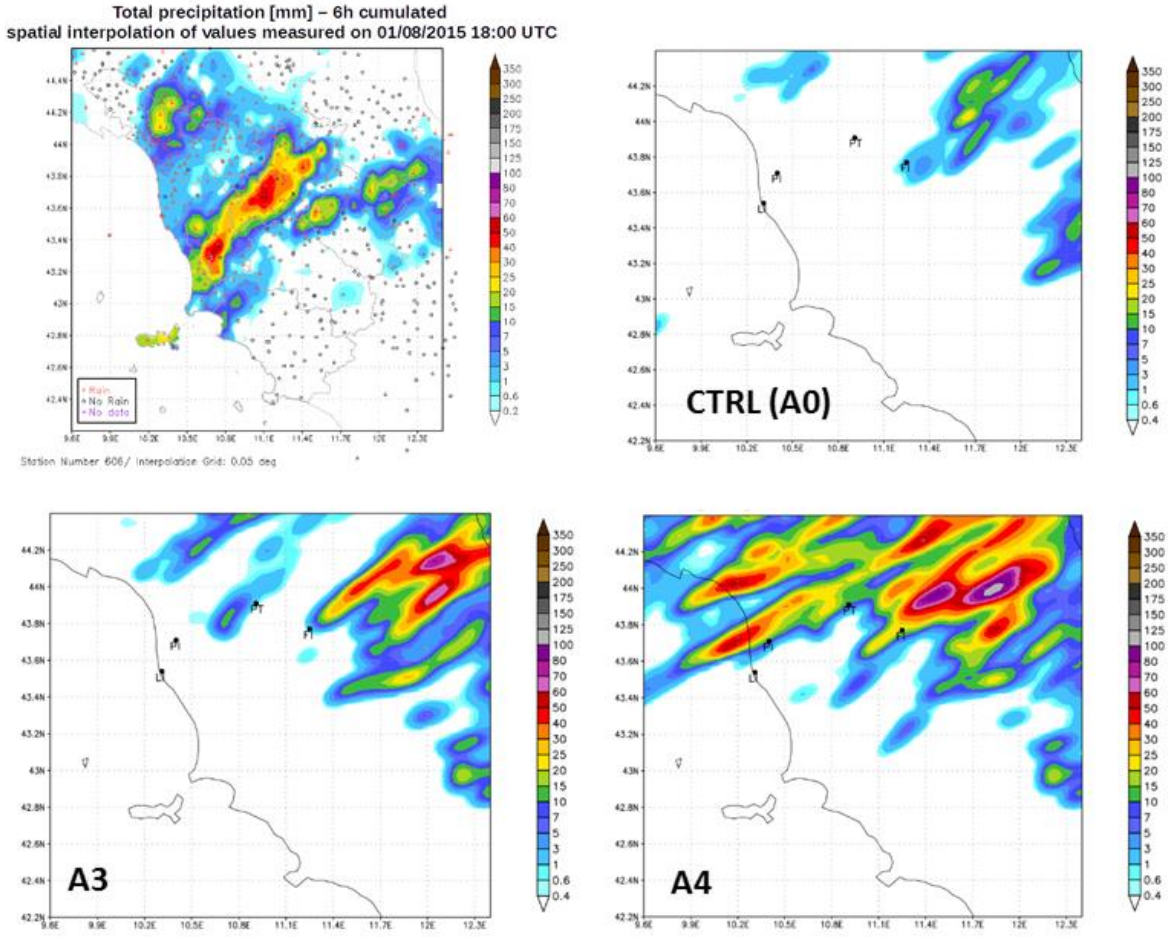


Figure 2 Assimilation experiments results for the case study of Florence. The top left image show the spatial interpolation of measured values for the 6 hours cumulated precipitation, from 12:00 to 18:00 UTC, and the ground stations where the rain gauges are located. The other images report the same field as predicted by the simulated forecast experiments: the control run CTRL (top right), the A3 (bottom left) and the A4 (bottom right) assimilation experiments.

To better quantify the effect, and in general to evaluate the forecasts goodness, we have calculated the RMSE between the predicted 6h-cumulated precipitation and the one actually measured by 65 rain gauges distributed all over the area most heavily hit by the storm (the red circle in the images of Figure 3). The so calculated RMSE values (reported as $RMSE_0$ in the images of Figure 3) include both the "intensity" error, due to the over/underestimation of the phenomenon, and the "location" error, due to some possible misplacement of the event. These two different sources of error have been disentangled by applying a rigid roto-translation in lat-lon space to the set of 65 rain gauges, finding the three roto-translation parameters (ΔLat, ΔLon and ΔΦ) that minimise the RMSE (blu circles in images of Figure 3) within the domain of interest (42.2-44.4°N, 9.6-12.32°E). As shown in Figure 3, the A2 assimilation of ground stations and radar observations, six hours before the event, significantly reduces both the "intensity" and the "location" error. Such improvement, especially as concerns the location, is somehow surprisingly less evident both in the A3 (bottom right image of Figure 3) and in the A4 assimilation experiment (the latter not shown however similar if not worse than A3).

3.3 Conclusions

For both the case studies of Florence 2015 and Leghorn 2017, the data assimilation of radar reflectivity and Doppler velocity from the Leghorn X-band and the Aleria S-band radars, added to more conventional observations (P, T, RH and wind speed and direction) from ground stations, improves the short-term prediction of the the severe weather events occurred. In the case of Florence the ARW numerical forecast control run (i.e. without any assimilation) fails to predict the occurrence of any heavy rain phenomenon. The assimilation of observations made 3 hours before the event forces the model to output precipitation fields whose intensity resembles the one actually observed. Anyway a higher location error, 60-80 km

NE, remains. For the case of Leghorn the control run predicts the occurrence of heavy rains, even if of lower intensity and located about 50 km N the actual location. The data assimilation clearly improves the location and also the event intensity, with the best result obtained by the two stages assimilation, up to six hours before the event start.

In conclusion the study here presented confirms that the assimilation of data coming from local network of ground stations and meteorological radar installations improves the short term predictability of severe weather events, as reproduced by high resolution numerical prediction models. However further analyses are needed especially to understand why in some cases adding information closer to the event (through the data assimilation process of later observations), can bring to a worsening of the model forecasts.

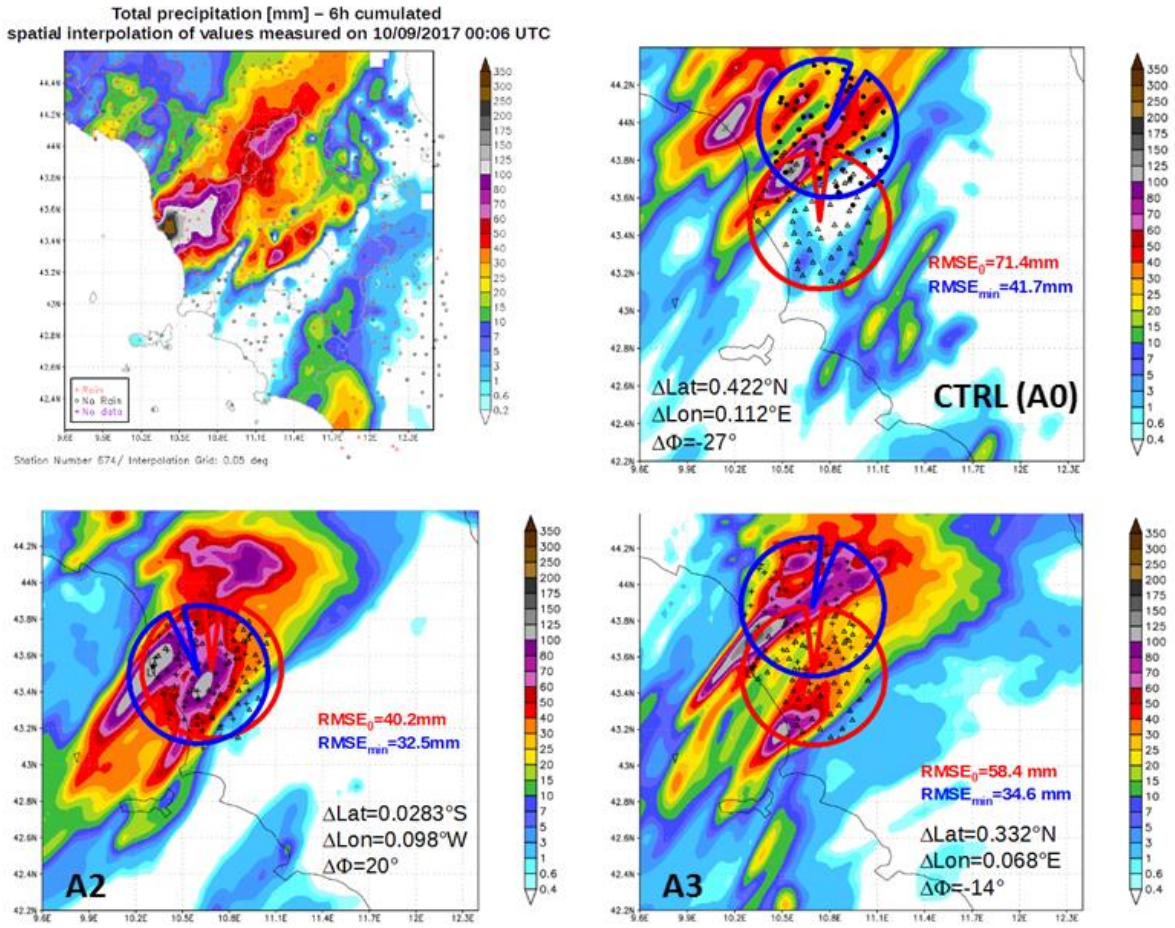


Figure 3 Assimilation experiments results for the case study of Leghorn. The top left image show the spatial interpolation of measured values for the 6 hours cumulated precipitation, from 00:00 to 06:00 UTC, and the ground stations where the rain gauges are located. The other images report the same field as predicted by the simulated forecast experiments: the control run CTRL (top right), the A2 (bottom left) and the A3 (bottom right) assimilation experiments.

Acknowledgement

This work was partially supported within the SWAMM project of the FAR-FAS programme of Regione Toscana. The authors express special thanks to Dr. Andrea Orlandi, for his valuable and constructive suggestions to gain a deeper insight in numerical weather prediction modelling.

4 References

Dutra E. [et al.] The extreme forecast index at the seasonal scale [Article]. - 2013. - Vol. 14. - pp. 256-262.

Hou Tuanjie [et al.] Impact of 3DVAR Data Assimilation on the Prediction of Heavy Rainfall over Southern China [Article] // Advances in Meteorology. - 2013. - Vol. 2013.

Ji-Hyun L. and Dong-Kyou H. Effect of Length Scale Tuning of Background Error in WRF-3DVAR System on Assimilation of High-Resolution Surface Data for Heavy Rainfall Simulation [Article] // Advances in Atmospheric Sciences. - 2012. - 6 : Vol. 29. - pp. 1142-1158.

Maiello Ida [et al.] Impact of multiple radar reflectivity data assimilation on the numerical simulation of a flash flood event during the HyMeX campaign [Journal] // Hydrology and Earth System Sciences / ed. Union European Geoscience. - [s.l.] : Copernicus Pubblications, 2017. - Vol. 21. - pp. 5459-5476.
Schwitalla Thomas and Wulfmeyer Volker Radar data assimilation experiments using the IPM WRF Rapid Update Cycle [Article]. - March 2014. - 1 : Vol. 23. - pp. 79-102.
WRF - Weather Research & Forecasting Model [Online] // UCAR NCAR web site. - https://www.mmm.ucar.edu/weather-research-and-forecasting-model.
Zsoter E. Recent developments in extreme weather forecasting [Journal] // ECMWF Newsletter. - 2006. - 107.

Time-series based approach to identify and process biological targets in radar wind profiler data for cross disciplinary purposes

Nadja Weisshaupt[1], Volker Lehmann[2], Alexander Haefele[3], Mercedes Maruri[1,4,5]

[1] University of the Basque Country UPV/EHU, Spain
[2] Meteorologisches Observatorium Lindenberg, Germany
[3] Federal Office of Meteorology and Climatology, MeteoSwiss, Payerne, Switzerland
[4] Basque Meteorology Agency (EUSKALMET), Spain
[5] Meteorology Area-TECNALIA R&I, Spain

1. Introduction

Operational radar wind profilers used in meteorology have been known to register biological targets, such as birds (e.g. Wilczak et al. 1994). Migrating birds seriously affect the quality of meteorological data, i.e. wind measurements. Existing signal processing approaches have contributed to improved data quality, in particular the Gabor frame based clutter filtering (Lehmann and Teschke 2008, Lehmann 2012), so that the data products are suitable for operational meteorological purposes. However, there is still a potential for further refinement. These radars accumulate a great treasure of data based on their continuous operation mode and widespread use in networks worldwide. In regard to today's budget constraints, it would be reasonable to make use of the large data pool and share its information with other disciplines. The non-meteorological data content and its potential use in related areas, such as biology or even risk assessment studies is still poorly understood. For example, as these radars register birds, the altitudinal profile of bird densities could be a valuable piece of information in bird strike prevention. Similar efforts to broaden the use of radar data have already been started for weather radars, in particular by the COST Action ENRAM (European Network for the Radar surveillance of Animal Movement 2013-2017).

Previous analyses by Weisshaupt et al. (2017) have shown that time series data (and derived Gabor spectrograms) is the only appropriate level to deal with biological data content, both for meteorological and biological purposes, as it is the only level permitting unambiguous separation of atmospheric vs. non-atmospheric targets.

The aim of this paper is to present new findings from the application of the previously developed methodology to three radar wind profilers with different specifications and from different manufacturers. Signal characteristics of biological echoes were compared between the different systems taking into account the system specifications and operational parameters to verify the utility of the developed manual methodology.

2. Main matter

Time series data was obtained from two UHF-band RWPs (Lindenberg and Bayreuth, Germany) from the Deutsche Wetterdienst and from the RWP in Payerne, Switzerland, from the MeteoSwiss. The RWP from the Basque Meteorology Agency (Euskalmet) at Punta Galea (Spain) served as a reference because it was part of an ornithological calibration campaign with simultaneous measurements by thermal imaging and moonwatching (Weisshaupt et al. 2017). The specifications are given in Table 1 below.
Vertical data was obtained for the Swiss, in line with the method developed for the Basque radar.
In the two German tropospheric RWPs, the scans use a 4-beam configuration without any vertical beam. This implies that the methodology by Weisshaupt et al. (2017) can be only partially applied. Both tropospheric systems exhibit slight differences related to the sampling volume. In both cases the pulse width is longer than the boundary layer RWP and both use the oversampling to reduce the pulse width. Therefore a single bird could extend to several gates (between 3□5 gates). The same effect of oversampling is found in the Swiss radar, where birds extend to about 7 gates.

	Tropospheric RWP Lindenberg / Bayreuth	Boundary Layer RWP, Payerne, CH (Low Mode)	Boundary Layer RWP, Punta Galea, Spain (Low Mode)
Operational frequency	Both 482 MHz (62 cm)	1290 MHz (23 cm)	1290 MHz (23 cm)
Vertical resolution	150 m (pulse width 1000 ns), sampled range: 0.45-9.38 km /250 m	150 m (gate spacing 60 m), sampled range: 0.105-3.345 km	60 m (pulse width 417 ns), sampled range: 0.133-2.001 km

	(pulse width 1700 ns), sampled range: 0.55-10.52 km		
Number of gates	96 / 70	55	32
Sampled season/Location	Summer, Autumn/Lindenberg, GERMANY	Autumn	Spring/Punta Galea-SPAIN
Manufacturer	Vaisala	Degreane	Vaisala
Beam configuration	4 beams, no vertical: BAY: N-E-S-W LIN: NE-NW-SW-SE	5 beams: N, S, E, W, vertical	5 beams: N, S, E, W, vertical

Table 1. Specifications of the four Radar Wind Profilers used in this study.

Gabor spectrograms derived from time series were generated for all radars. Spectrograms offer additional information for target identification and allow for a more profound study of target signal characteristics.
MTRs and high profiles were calculated for the Swiss radar based on the method described in Weisshaupt et al. (2017).

3 Results & Discussion

3.1 Comparison of signal characteristics and general pattern in TS

Biological and atmospheric echoes exhibited similar characteristics in all four radars, i.e. a typical transient zigzag pattern for point targets (birds, Fig. 1) and continuous patterns for stationary or distributed atmospheric targets (Fig. 2). Bird echo strength was in all radars superior to atmospheric signals. Depending on the system specifications, especially in the Swiss radar, bird signals spread more or less to adjacent gates. In the tropospheric RWPs birds spread into 3-5 gates (Fig. 3a), while the Swiss radar exhibited the highest "contamination" with single echoes spreading into up to seven gates (Fig. 3b). The spreading of a single echo in as much as seven gates implies a serious issue for data quality, compared to a system where an echo spreads into three gates or less. In particular also in higher bird densities, this leads to large sampling areas of poor or no value for the wind measurements.

3.2 Effect of beam configurations

As to beam configurations, in the data of the two vertical beams the birds passed through the zero line in spectrograms when they flew through the centre of the beam (Fig. 1). In the two radars with only inclined beam directions, birds were either above or below the zero line, while there was frequently a faint copy of the actual true signal on the opposite side of the zero line (Fig. 4). The position of the echo in a particular beam direction, i.e. on the positive or the negative side of the zero line, indicates the directional component. For example, if the echo is on the positive side in the east and north beam, but negative in the south and west, it indicates a migration direction from NE to SW. Thus, combining the information of the four beams, a general migration direction can be derived based on raw data in the time series.

3.3 Implementation of qualitative selection criteria

After establishing the qualitative selection criteria for bird echoes in the Punta Galea RWP (see Weisshaupt et al. 2017), the question arises, if this approach is also applicable to RWPs from other manufacturers where the data visualization differs, e.g. based on the software used. The use of an equivalent echo selection would be the prerequisite to calculate migration intensities (i.e. migration traffic rates, MTRs) and derived height profiles that could then be compared between different RWPs. We therefore applied the qualitative approach established for the Vaisala radar in PG to the Swiss RWP from Degreane. Also in the Swiss data there were different qualitative levels of bird echoes. The parameters were adapted to the system specific patterns to obtain a visually comparable data set as follows: targets were selected, if they showed bird characteristics (e.g. zigzag, transient), passed the zero line and if signal strength (of SNR) was at least 200 units. This corresponded visually to the selection criteria of "good" and "very good" in Weisshaupt et al. (2017). This allowed then the calculation of MTRs and height profile with good quality data for the Swiss radar (Fig 5).
Apart from the single bird echoes, the study of the Swiss data revealed also transient cloud-like echoes (Fig. 6). Based on previous findings, it is known that frequencies of multiple echoes passing simultaneously would overlap and produce a mixed pattern in TS. Weisshaupt et al. (2017) hypothesized that flocks might potentially show as several birds depicted in a line of zigzags in the spectrograms. While this is probably true for loose flocks of few individuals, the Swiss data now indicates, that larger dense flocks of small passerines as found in

diurnal migration would be rather represented as a big cloud like shape as the numerous small birds fly too close together to be resolved as individual echoes, each with its own movement, comparable to the pattern of rain which also shows as a broad band, compared to the narrow line of clear air. However, this finding needs further verification.

Conclusions

The current results show that the methodology to identify biological targets is applicable to radar wind profilers with different system specifications. Biological echoes can be distinguished from atmospheric ones, and migration intensity and height distribution could be calculated for data from RWPs with different system specifications and of different manufacturers.

Even though the approach had originally an ornithological motivation, the findings are also valuable for the meteorological community, as the information on the biological signal characteristics provides novel insights potentially valuable for the improvement of wind data quality and related services. It also helps understand the interactions between meteorology and biology as well as the effect and limitations of filter mechanisms and their impact on the data output. Additionally, as the methodology allows the calculation of the height distribution (vertical profile) and intensity of bird migration (so-called migration traffic rates), radar wind profiler data offers a valuable source for flight safety and collision hazard evaluation in impact assessments, e.g. for wind parks. Currently the discrimination of biological and meteorological signals is based on manual processing. However, it would be of great value to obtain such information automatically and the authors would like to encourage further research to automatize this processing for the benefit of both meteorological and ecological services.

References

Lehmann, V. (2012) Optimal gabor-frame-expansion-based intermittent-clutter- filtering method for radar wind profiler. Journal of Atmospheric and Oceanic Technology, 29, pp. 141–158.

Lehmann, V. and Teschke, G. (2008) Advanced intermittent clutter filtering for radar wind profiler: signal separation through a Gabor frame expansion and its statistics. Annales Geophysicae, 26, pp. 759–783.

Weisshaupt, N., Lehmann, V., Arizaga J. and Maruri, M. (2017) Radar wind profilers and avian migration - a qualitative and quantitative assessment verified by thermal imaging and moon watching. Methods in Ecology and Evolution, 8(9): pp. 1133-1145. doi:10.1111/2041-210X.12763.

Figures

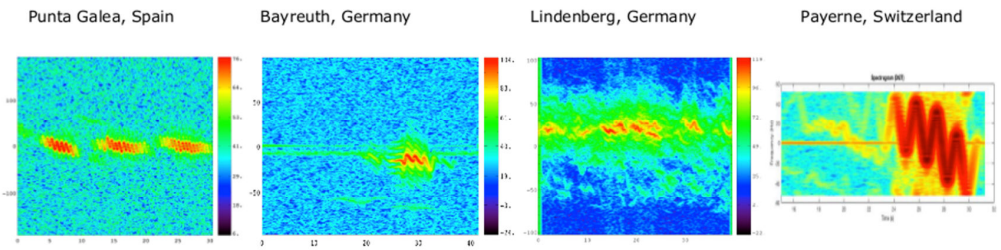


Fig. 1. Comparison of bird echoes in the four RWPs Punta Galea, Bayreuth, Lindenberg and Payerne.

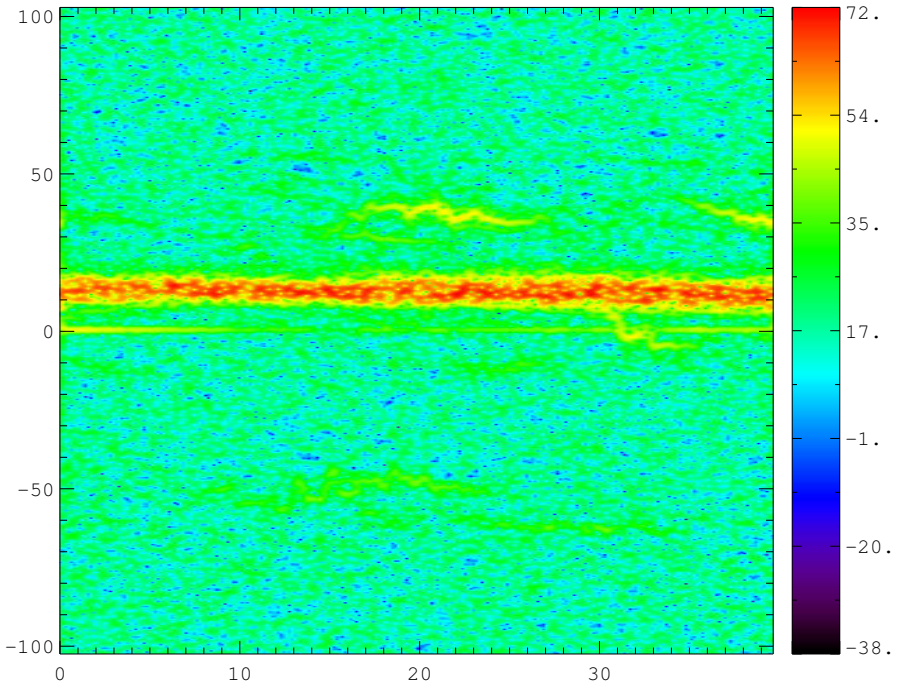


Fig. 2. Atmospheric signal in north-east beam, Gate 20, of the Lindenberg RWP on 17:43:01 UTC, 4 Oct 2016.

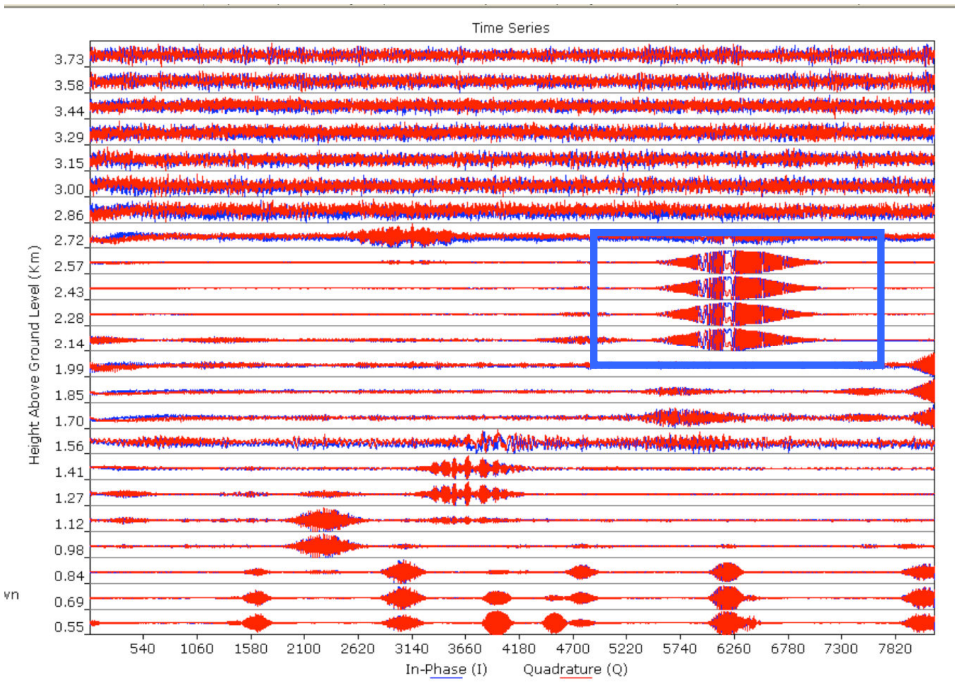


Fig. 3a. Time series of west beam of Bayreuth RWP with an example of a single bird echo spreading in four adjacent gates, 17:41:09, 4 Oct 2016.

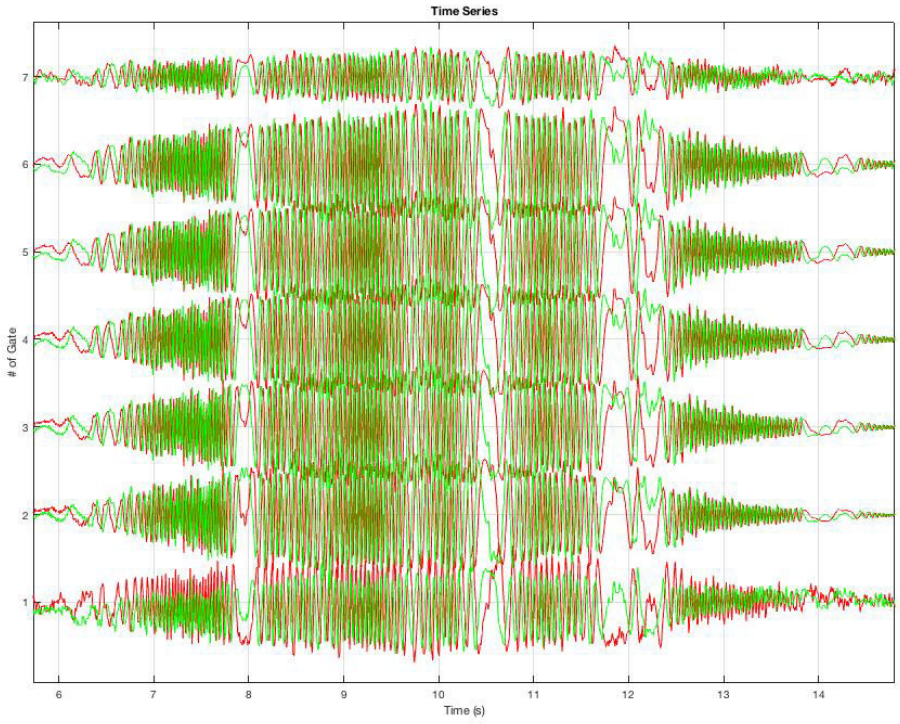


Fig. 3b. Time series of vertical beam of Payerne RWP with an example of a single bird echo spreading in seven adjacent gates on 9 Oct 2017.

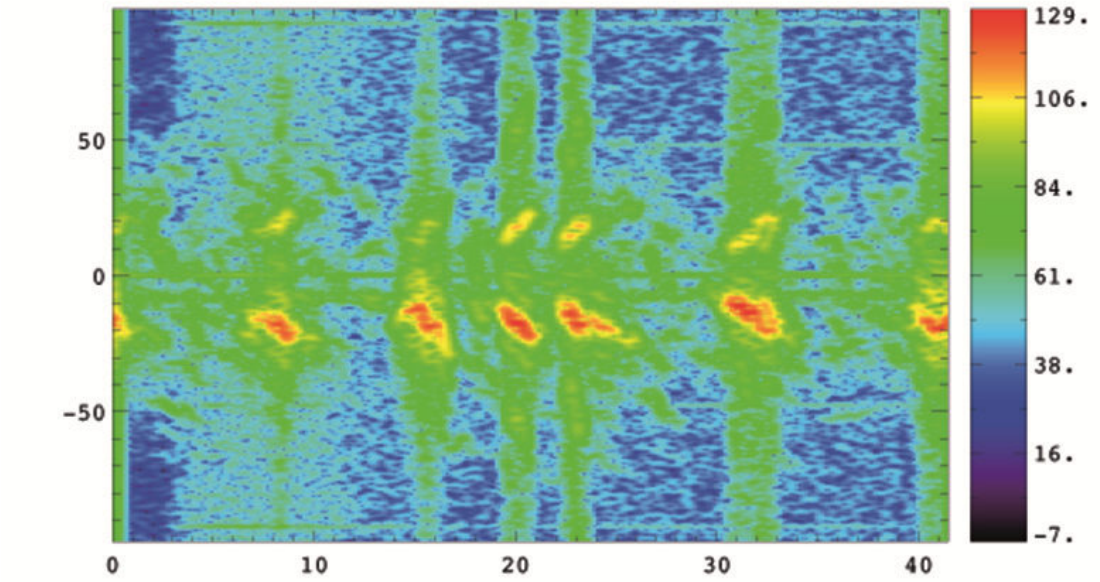


Fig. 4. True bird echoes showing on the negative side of the zero line and copies on positive side in west beam of Bayreuth RWP on 17:41:09 UTC, 4 Oct 2016.

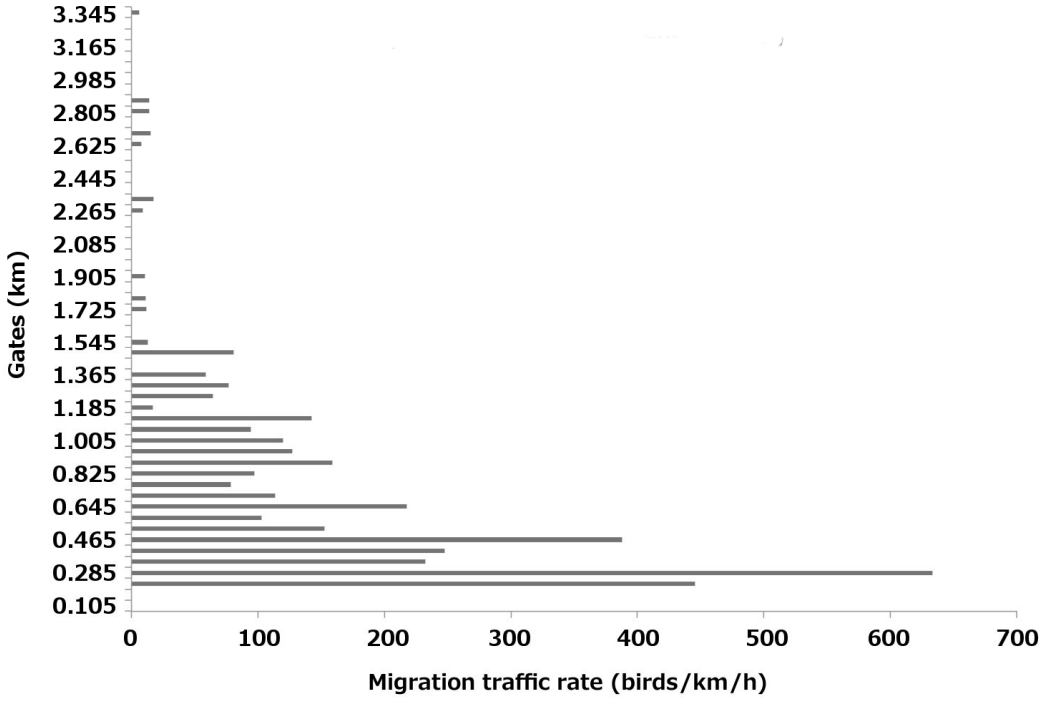


Fig. 5. Vertical height profile of nocturnal bird migration intensity (migration traffic rate, MTR) for the 55 gates of the Payerne RWP on 9 Oct 2017.

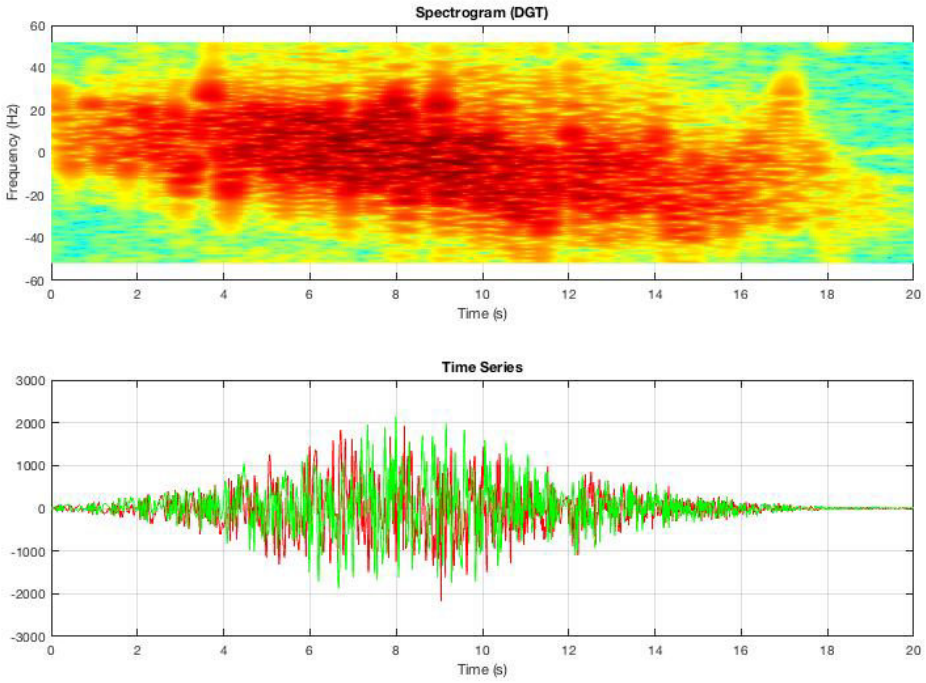


Fig. 6. Overlapping frequencies causing a cloud-like pattern in spectrogram (above) and a beat frequency in time series (below) from several targets passing simultaneously through the Payerne RWP on 9 Oct 2017.

Differential phase upon transmission as a new radar parameter

Valery Melnikov

The University of Oklahoma, CIMMS and NOAA/OAR National Severe Storms Laboratory
120 Boren Bulvd, Norman, Oklahoma. USA, 73072
(Dated: 21 June 2018)

1 Introduction

The main radar parameters are the wavelength, pulse repetition frequency, beamwidth, minimal detectable signal, and polarization configuration. These parameters are determined by the radar transmitter, receiver, antenna, and waveform of the radar pulse (e.g., pulse compression). The majority of polarimetric weather radars employ simultaneous transmission and reception of orthogonally polarized waves (STAR configuration). Typically, the differential phase between the transmitted waves is not controlled in STAR radars. The total system differential phase **(**Φ_{DPsys}**)** is the sum of the system differential phases upon transmission (ψ_t) and reception (ψ_r) and is measured as a differential phase in the closest to radar edge of a radar echo: $\Phi_{DPsys} = \psi_t + \psi_r$.

The differential phase Φ_{DP} is not yet used as a distinct parameter, its radial gradient (K_{DP}) is widely utilized in radar observations. Measured Φ_{DP} consists of the propagation contribution and differential phase upon scattering δ. Radar observations show that phase δ varies in clouds and can be used as an additional source of information about scattering media. It is shown here that δ depends not only on the sizes and shapes of hydrometeors, but also on differential phase upon transmission. If ψ_t is known, i.e., it has been measured, the phase can be used in the retrievals of the scatterers' properties. A variable ψ_t allows obtaining additional information about scatterers in the radar resolution volume.

2 Radar Observations

Our radar observations with S-band WSR-88D KOUN (Norman, Oklahoma, USA) show a "strange" dependence of measured Φ_{DP} on the antenna elevation angle. An example of a vertical cross section (RHI) of nonprecipitating ice clouds is shown in Fig. 1(a, b, and c). The freezing level was at a height of 3.5 km therefore the clouds observed above 5 km contained ice particles. The propagation differential phase is negligible at S frequency band in icy nonprecipitating clouds, therefore the phase Φ_{DP} in such situations depends on differential phase upon scattering δ. In the clouds above 5 km, differential reflectivity (Z_{DR}, panel b) decreases with elevation as it should be because the media exhibits more scattering symmetry at high elevations. A similar patterns can be expected for Φ_{DP} and the phase values close to zero are expected at vertical sensing. The WSR-88D's antenna cannot be point at zenith; the highest elevation angle is 60°. The measured Φ_{DP} in the clouds (Fig. 1c) increases with elevation that "contradicts" the above statement about the increasing symmetry in scattering media. This pattern could be caused by clouds particles of different habits. However, our radar observations show that such a signature is observed routinely. One more example is shown in Fig. 1(d, e, and f).

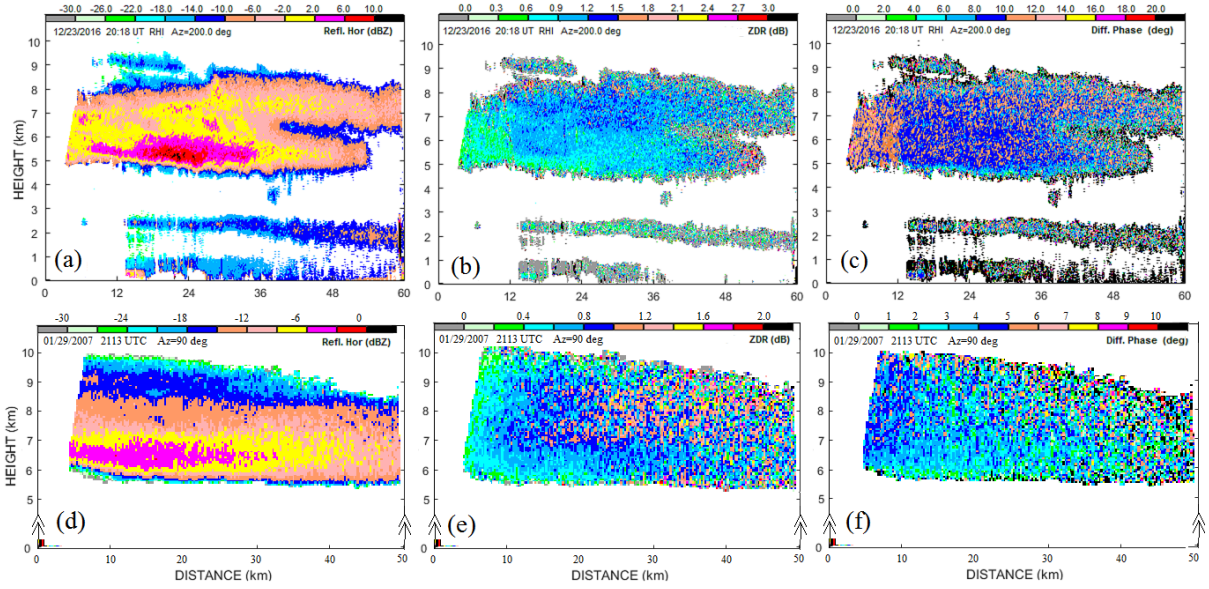


Fig. 1. (top row): Vertical cross sections of nonprecipitating clouds collected with WSR-88D KOUN on 23 Dec. 2016 at 2018 UTC at an azimuth of 200°; (a), (b) and (c) are fields of Z, Z_{DR} and Φ_{DP}. (bottom row): Same as in the top row, but collected on 29 Jan. 2007 at 2113 UTC at an azimuth of 90°.

Fig. 2 presents results of simultaneous observations of nonprecipitating clouds with KOUN and the X-band mobile NSLL's radar NOXP. On that day, NOXP was located 4.7 km to the South of KOUN so that RHI observations from the two radars in azimuths of 0^o and 180^o captured the same cloud areas. Fig. 2 present images for an azimuth of 0^o. One can see increasing Φ_{DP} with elevation observed with KOUN (panel c), but Φ_{DP} from NOXP (panel f) decreases with elevation. Z_{DR} values decrease with elevations for both radars. These different Φ_{DP} dependences are explained in the next section.

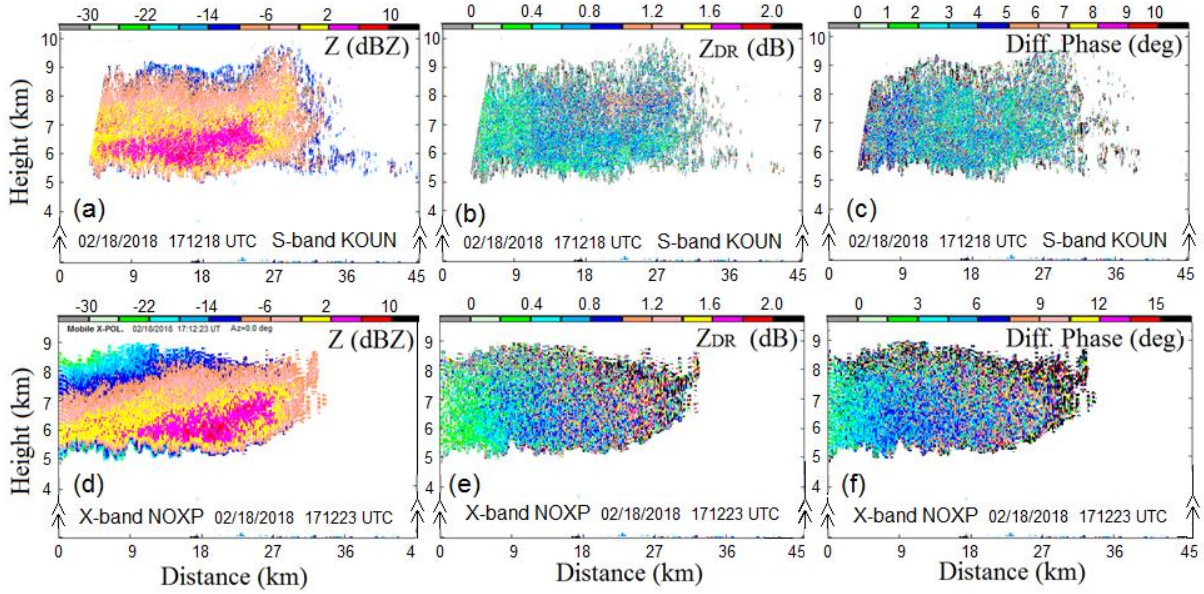


Fig. 2.RHI of Z, Z_{DR}, and Φ_{DP} (panels a, b, and c respectively) collected with S-band KOUN on 18 Feb. 2018 at 171218 UTC at an azimuth of 0^o. (d, e, f): same as in the top row, but collected with X-band NOXP at 171223 UTC.

3 Theoretical considerations

Geometry of scattering of two orthogonally polarized waves E_h and E_v scattered by an ice crystal is presented in Fig. 3, where the ice particle is shown with yellow. The incident direction is indicated with the vector ***k***. The incident angle γ equals the antenna elevation angle. The axis ON is orthogonal to the particle's plane and OZ is vertical so that θ is the canting angle of the particle. The plane OXY is horizontal.

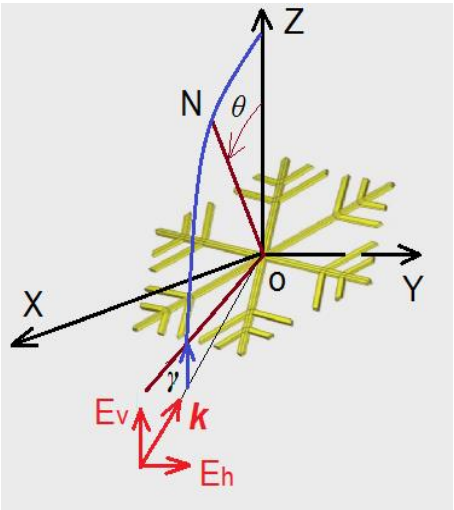


Fig. 3. Geometry of scattering of the orthogonally polarized waves E_h and E_v by an ice crystal (in yellow). Angles θ and γ are the canting angle and elevation of the antenna respectively. OZ is the vertical axis. The plane OXY is horizontal.

Complete considerations of scattering by ice particles can be found in Melnikov (2017), where received voltages are designated as E_{hr} and E_{vr}. From these voltages, all radar variables can be obtained. The mean received powers P_h and P_v in the polarization channels are obtained as,

$$P_h = <| E_{hr} |^2> \text{ and } P_v = <| E_{vr} |^2> \ , \quad (1)$$

where the brackets stand for time averaging. Values of Z_{DR} and ρ_{hv} are

$$Z_{DR} = 10 \log_{10}[(P_h - n_h)/(P_v - n_v)] \ , \quad (2)$$

$$R_{hv} = < E_{hr}^* E_{vr} > \ , \quad (3)$$

$$\rho_{hv} = |R_{hv}|/[(P_h - n_h)(P_v - n_v)]^{1/2} \ , \quad (4)$$

$$\delta = \arg(R_{hv}) \ , \quad (5)$$

where n_h and n_v are the mean noise powers in the channels and the asterisk indicates complex conjugate. Averaging in (1) and (3) yields

$$P_h = < |\alpha_h|^2 > + J_1 Re(< \alpha_h^* \Delta\alpha >) + < |\Delta\alpha|^2 > C_1, \quad (6)$$

$$P_v = < |\alpha_h|^2 > + 2\mathrm{Re}(< \alpha_h^* \Delta\alpha >) C_2 + < |\Delta\alpha|^2 > C_3] \ , \quad (7)$$

$$R_{hv} = e^{j\Phi_{DPsys}}[< |\alpha_h|^2 > + \mathrm{Re}(< \alpha_h \Delta\alpha^* >) C_4 + j\mathrm{Im}(< \alpha_h \Delta\alpha^* >) C_5 + < |\Delta\alpha|^2 > C_6], \quad (8)$$

$$C_1 = [3J_2 + 4(J_1 - J_2) + (5J_2 - 4J_1)\sin^2\gamma]/8 \ , \quad (9a)$$

$$C_2 = 1 - J_1 - (1 - 3J_1/2)\sin^2\gamma \ , \quad (9b)$$

$$C_3 = (J_1 - J_2)/2 + (1 - 2J_1 + J_2) + [(5J_2 - 4J_1)/8 - \beta_t^2(2 - 7J_1 + 5J_2)]\sin^2\gamma + (1 - 5J_1 + 35J_2/8)\sin^4\gamma \ , \quad (9c)$$

$$C_4 = 1 - J_1/2 + (3J_1/2 - 1)\sin^2\gamma \ , \quad (9d)$$

$$C_5 = (1 - 3J_1/2)\cos^2\gamma \ , \quad (9e)$$

$$C_6 = e^{-j\psi_t} cos\psi_t [J_1 - J_2 + (5J_2/4 - J_1)\sin^2\gamma] \ , \quad (9f)$$

$$\Phi_{DPsys} = \psi_t + \psi_r, \quad (9g)$$

where Re(x) and Im(x) stand for the real and imaginary parts of x and

$$J_1 = < \sin^2\theta > , \ \ J_2 = < \sin^4\theta > \quad (10)$$

are the moments of the θ-distribution. Values of α_h and α_v are polarizabilities in the horizontal and vertical directions of the scatterer oriented horizontally and $\Delta\alpha = \alpha_v - \alpha_h$. Measurables (2) - (5) are explicitly expressed via polarizabilities $\alpha_{h,v}$, the moments of the θ-distribution in (10), elevation angle γ, and differential phases in transmit and receive $\psi_{t,r}$.

Radar variables for plate-like ice particles as a function of the antenna elevation are shown in Fig. 4 for various phase ψ_t. It is assumed that ice particles flutter in the air with the standard deviation in θ of 30°. Phase ψ_r does not affect Z_{DR}, ρ_{hv}, and δ, but this phase must be accounted for in the system differential phase Φ_{DPsys} (9g). One can see from Fig. 4c that phase δ can be an increasing or decreasing function of elevation and this signature depends on ψ_t. Positive (negative) ψ_t values mean that H-polarized wave is behind (ahead) the V-polarized one. In STAR radars, the system differential phase is made positive regardless of the sign of ψ_t. This is achieved by changing ψ_r. Such changes shift the Φ_{DP} curve to positive values leaving its shape unchanged. So we see that measurable Φ_{DP} can increase or decrease with increasing antenna elevation and this signature depends on ψ_t. If ψ_t is known, i.e., has been measured, the elevation dependences of Φ_{DP} and ρ_{hv} can be used for retrievals of ice particles' parameters if clouds are horizontally uniform as it is, for instance, in Fig. 1(d, e, f). Variations in ψ_t change Φ_{DP} and ρ_{hv} measured in a single radar resolution volume and thus can be used for retrievals of scatterers' properties in non-uniform clouds. It can be concluded that phase ψ_t is a valuable radar parameter which affects radar variables and can be used in the retrievals of scatterers' properties.

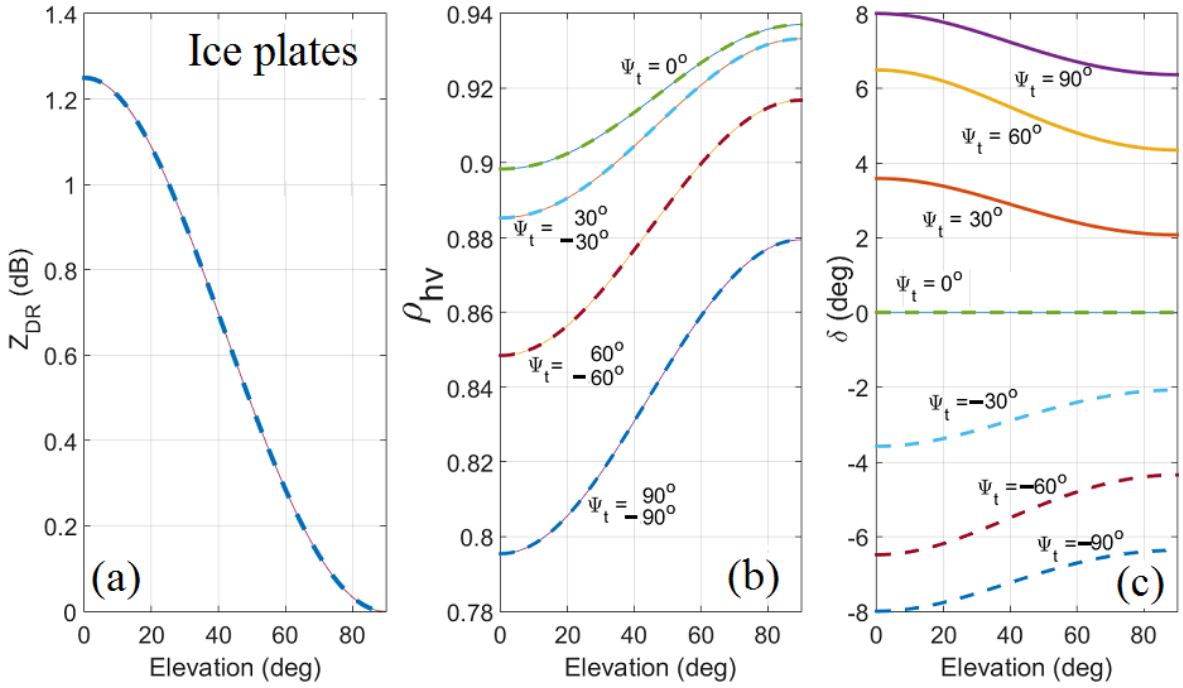


Fig. 4. Elevation dependences of Z_{DR} (a), ρ_{hv} (b), and δ (c) for ice plate-like crystals and for various phase ψ_t.

The dependence of ρ_{hv} on polarization configurations was observed by Krehbiel et al. (2005) in thunderstorms. They reported on significant drops in ρ_{hv} when their X-band radar switched polarization from simultaneous to circular. Circular polarization is the one when there is a phase shift of 90° upon transmission. At circular polarization, ρ_{hv} was measured by Scott et al. (2001) and Kreihbel et al. (2005) in a typical STAR configuration with ψ_t= 90° (or –90°) upon transmission. Such a drop can be explained with Fig. 4b for ψ_t = 0° and ±90°.

Examinations of Φ_{DP} fields in clouds can reveal areas occupied by particles of various habits. An example is shown in Fig. 5 (right panel). One can see an increase in Φ_{DP} with antenna elevation at the very left part of radar echo at heights of 3-6 km. Well pronounced areas of low Φ_{DP} are seen at the bottom of the clouds at distances of 10 – 50 km. This feature could be due to melting of the ice particles; the freezing level was at a height of 3.6 km. A similar feature is seen in Fig. 1c in the Φ_{DP} field at a height of 5 km. In this case the decrease in Φ_{DP} most likely is a result of aggregation of ice particles; the freezing level was at a height of 3.5 km. Since Φ_{DP} in ice clouds is directly linked to phase δ and ψ_t, known $\psi_t$can be used to obtain δ, which, in its turn, can be utilized in the retrieval procedure.

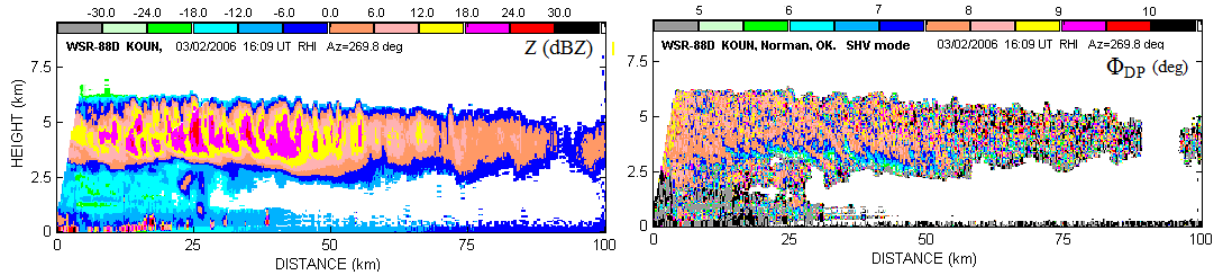


Fig. 5. RHI of nonprecipitating clouds collected with KOUN on 2 March 2006 at 1609 UTC at an azimuth of 270°.

Phase $\psi_t$affects the radar variables from hail. Fig. 6 presents Z_{DR}, δ, and ρ_{hv} as functions of hailstone diameter. The hailstones are modelled with oblate spheroids with axis ratio of 0.7. It is assumed that the hailstones flutter in the air with the standard deviation of their canting angle of 40° and are observed at an antenna elevation angle of 0°. Hail contains a water film of a thickness determined by the hailstone's diameter according to Rasmussen and Heimsfield (1987). Phase δ is a function of the hail diameter (Fig. 6b). Variations in $\psi_t$change the phase by 1 – 2° for hailstones larger than 3 cm. Such phase changes are measurable. Values of ρ_{hv} significantly drop with increasing ψ_t that can also be used for hailstone sizing.

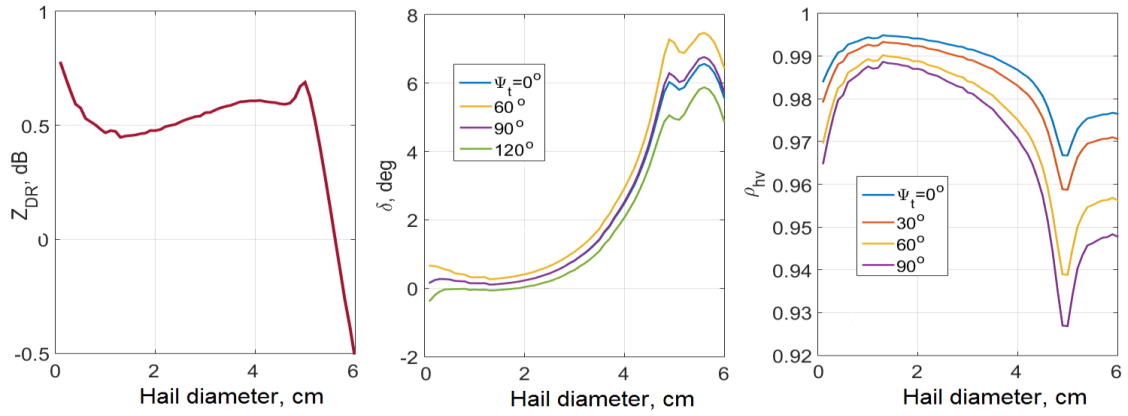


Fig. 6. Z_{DR}, δ, and ρ_{hv} as functions of the diameter of wet hailstones at various ψ_t and for horizontal sensing.

4 Observations in "clear air"

Radar echoes from clear air are caused by turbulent air vortexes, birds, insects, and bats. Biological echoes typically are characterized by larger Z_{DR} and lower ρ_{hv} values than those form precipitation and air vortexes (Bragg scatters). Some properties of the biological scatterers are obtained with radars (Drake and Reynolds, 2012). Due to variety of species' shapes and sizes, it is difficult to obtain species' properties from weather radar variables. The number of unknown properties of species is larger than the number of measurable radar variables that makes the retrievals of species' properties uncertain. A variable ψ_t could make the retrievals more certain.

To demonstrate the influence of ψ_t on radar variables in echoes from insects, data were collected with KOUN at ψ_t = 30°. A retrieval procedure described by Melnikov et al. (2015) allows obtaining the insects' properties and their orientations in the air. Using these properties, it is possible to generate radar fields at any ψ_t. Radar fields at ψ_t = 0° and 90° are shown in Fig. 7. One can see that a 90° change in ψ_t drastically changes all the fields. Values of Z, Z_{DR}, Φ_{DP}, and ρ_{hv} can change by 5 dB, 7 dB, 80°, and 0.7respectively in a single range gate. This means that variable ψ_t can deliver additional information about biological scatterers which cannot be obtained via other remote sensing methods.

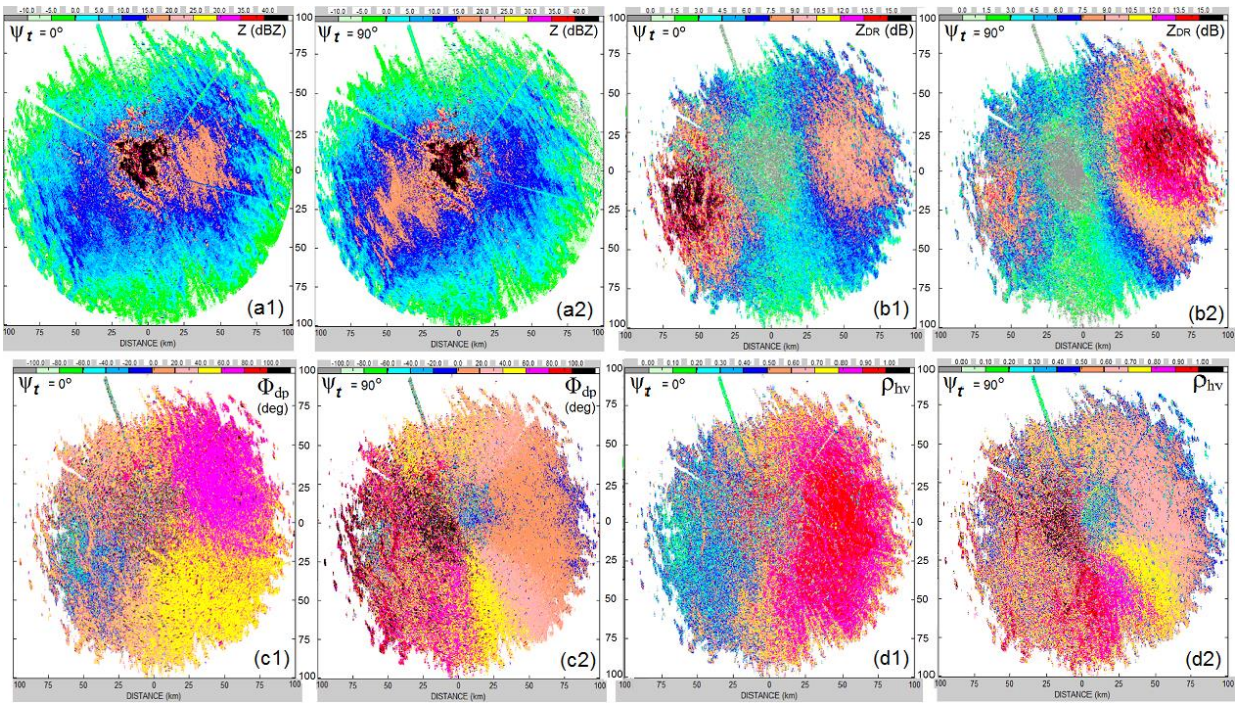


Fig. 7. (a1, a2): PPIs of reflectivity from insects obtained at ψ_t = 0° and 90°. Other panels present pairs of Z_{DR} (b1,b2), Φ_{DP} (c1, c2), and ρ_{hv} (d1, d2) obtained at ψ_t = 0° and 90°. WSR-88D KOUN, 1 Nov. 2013 at 1111 UTC at an elevation of 1°.

5 Conclusions

Values of Z_{DR}, Φ_{DP}, and ρ_{hv} measured with STAR radars depend not only on the sizes, shapes, and orientations of scatterers, but also on the radar differential phase ψ_t upon transmission. A variable ψ_t allows obtaining new information about scattering media such as the shapes and axis ratios of ice cloud particles and the parameters of hailstones. A variable ψ_t is a powerful tool for obtaining the shapes of insects and birds and their headings in the air. These capabilities make the phase upon transmission a new radar parameter.

Variable ψ_t can be implemented using phase shifters which are mechanical devices at the cm/mm radar wavelength and require seconds to change ψ_t. In a phased array radar, variations in ψ_t can be made electronically, i.e., fast. Variations in ψ_t during the dwell time in an operational phased array radar could be used for a better detection of hail and electrified cloud areas dangerous for aviation.

References

Drake, V.A. and D.R. Reynolds // Radar Entomology: Observing Insect Flight and Migration. CABI, 2012, - 489 pp.

Krehbiel, P, W. Rison, R. Thomas, C. Maggio, T. Marshall, M. Stolzenberg, T. Hamlin, K. Wiens, R. Scott. Lightning and dual-polarization radar structure of small convective storms. // 32nd Radar Meteorology Conference, Albuquerque, NM, October 2005.

Melnikov, V., M. Istok, and J. Westbrook. Asymmetric radar echo patterns from insects. //J. Atmos. Oceanic Technol. – April 2015, Vol. 32, pp. 659-674.

Melnikov, V. Parameters of cloud ice particles retrieved from radar data. //J. Atmos. Oceanic Technol. - March 2017.: Vol. 34. - pp. 717 - 728.

Rasmussen, R. M. and **A. J. Heimsfield**. Melting and shedding of groupel and hail. Part 1. Model physics. //J. Atmos. Sci. - 1987, Vol 44. - pp. 2754 - 2763.

Scott, R.D., P. R. Krehbiel, and W. Rison. The use of simultaneous horizontal and vertical transmissions for dual-polarization radar meteorological observations.// J. Atmos. Oceanic Technol., - April 2001,Vol. 18, pp. 629-648.

Geostatistical merging of X-band weather radar and a sparse rain gauge network over an urban catchment

I.seck[1] (i.seck@opgc.univ-bpclermont.fr), J. van baelen[1]
[1]Laboratoire de Météorologie Physique, Université Clermont Auvergne (France)

1 Introduction:

Optimal Quantitative Precipitation Estimation (QPE) of rainfall have been proven to be crucial to the accuracy of hydrological models, especially over urban catchments. Small to medium-size towns are often equipped with a sparse rain gauge networks that struggle to catch the variability of rainfall over high spatio-temporal resolutions. X-band Local Weather Radars (LAWRs) provide a cost effective solution to meet this challenge.

In this study, we examine two geostatistical methods to merge X-band weather radar data with the combination of rain gauge networks of Clermont-Ferrand (13 gauges with a 5 minutes temporal resolution) and Meteo France (5 gauges with a 6 mintes temporal resolution): Conditional merging and Kriging with an external drift according to Velasco-Forero et al (2009). The effects of attenuation correction, using the Hitchfeld Bordan (1954) algorithm as well as correcting the mean field bias of radar data were also investigated.

This extended abstract is organized into four sections. After the introduction, the geostatistical methods are presented in the Methodology section as well as the performance assessment criteria applied to compare the methodes. Section 3 presents the study area as well as the steps taken to pre-process the radar data. Finally, section 4 presents the results of the study.

2 Methodology

Two geostatistical methods: Kriging with External Drift (KED) and Conditional Merging (CM), were chosen to merge the radar and rain gauge data at three different temporal resolutions: 5, 30 and 60 minutes. Similar studies such as Berndt et al (2014) and Goudenhoofdt et al (2008) used a C-band weather radar and a relatively dense rain gauge network in order to compare several merging techniques including

geostatistical ones, and found that KED and CM performed the best at several network densities and temporal resolutions scenarios.

Hereafter, we present briefly these two methods, as well as the performance assessment measures chosen to determine the best one at every temporal resoltion investigated.

2.1 Geostatistical Merging methods of rain gauge and radar data:

Both merging techniques use Ordinary Kriging OK, as an intermediate step. A detailed description of OK can be found in geostatistical texbooks (Goovaerts,1997; Isaaks and Srivastava,1990), it uses an experimental variogram capturing the spatial variabiliy of data, which is then fitted to a theoretical one in order to resolve a linear system minimizing the kriging variance.

In this study, a single variogram standardized by the variance was used for every temporal resolution, thanks to averaging variograms of several time steps across the study period using radar data. The exponential model was found to fit best across the three resolutions investigated

2.1.1 KED: Kriging with an External Drift

For practical reasons, we use the Velasco-Forero et al (2009) modified version of KED, because it is more suitable for real time applications, which is the end goal of this study in the Clermont-Ferrand catchment.

The procedure is as follows:

1. First Radar pixels corresponding to the location of every rain gauge is selected and then interpolated over the study area.
2. A deviation map is then computed between observed radar grid and interpolated radar grid.
3. The deviation map is then used to compute the corresponding variogram
4. The variogram computed in in step 3 is then used to interpolate the rain gauge data over the study area.

2.1.2 CM: Conditional Merging

Conditional Merging (CM) described by Ehret (2003) follows the same steps as KED, however the deviation map is used to introduce the radar detected variability of rainfall to the field obtained by OK, through a simple addition.

2.1.3 Performane assessment criteria:

Three criteria are used to measure the performance of every geostatistical technique including OK:

- The bias criterion:

$$Bias = \frac{1}{n}\sum_{i=1}^{n}[Z'(x) - Z(x)]$$

  Where n is the number of rain gauges, Z is the observation value of gauge number i at location x and Z' is the estimation at the same location.

- The root mean square error normalized with the average of the observations Z:

$$RMSE = \frac{1}{Z}\sqrt{\sum_{i=1}^{n}[Z'(x) - Z(x)]}$$

- The variance ratio Rvar:

$$Rvar = \frac{Var[Z'(x)]}{Var[Z(x)]}$$

These criteria were also used in the study of Berndt et al (2014), although the study was carried out in Lower Saxony (Germany) using a C-band radar, it is still interesting to compare how these methods compare in different configurations.

3 Study area and data

The Clermont-Ferrand catchment is located in Central France in the mountainous Massif Central geological region. The average annual precipitation rate is about 600 mm/yr. The city of Clermont-Ferrand monitors precipitations through a network of 13 gauges scattered around the city, operating with a 5 minutes temporal resolution, five gauges belonging to the National Meteorological Service Météo-France operating with a 6 minutes temporal resolution also operate in the study area. Fig. 1 shows the rain gauge network as well as the Digital Elevation Model (DEM) of the terrain and the location of the X-band radar.

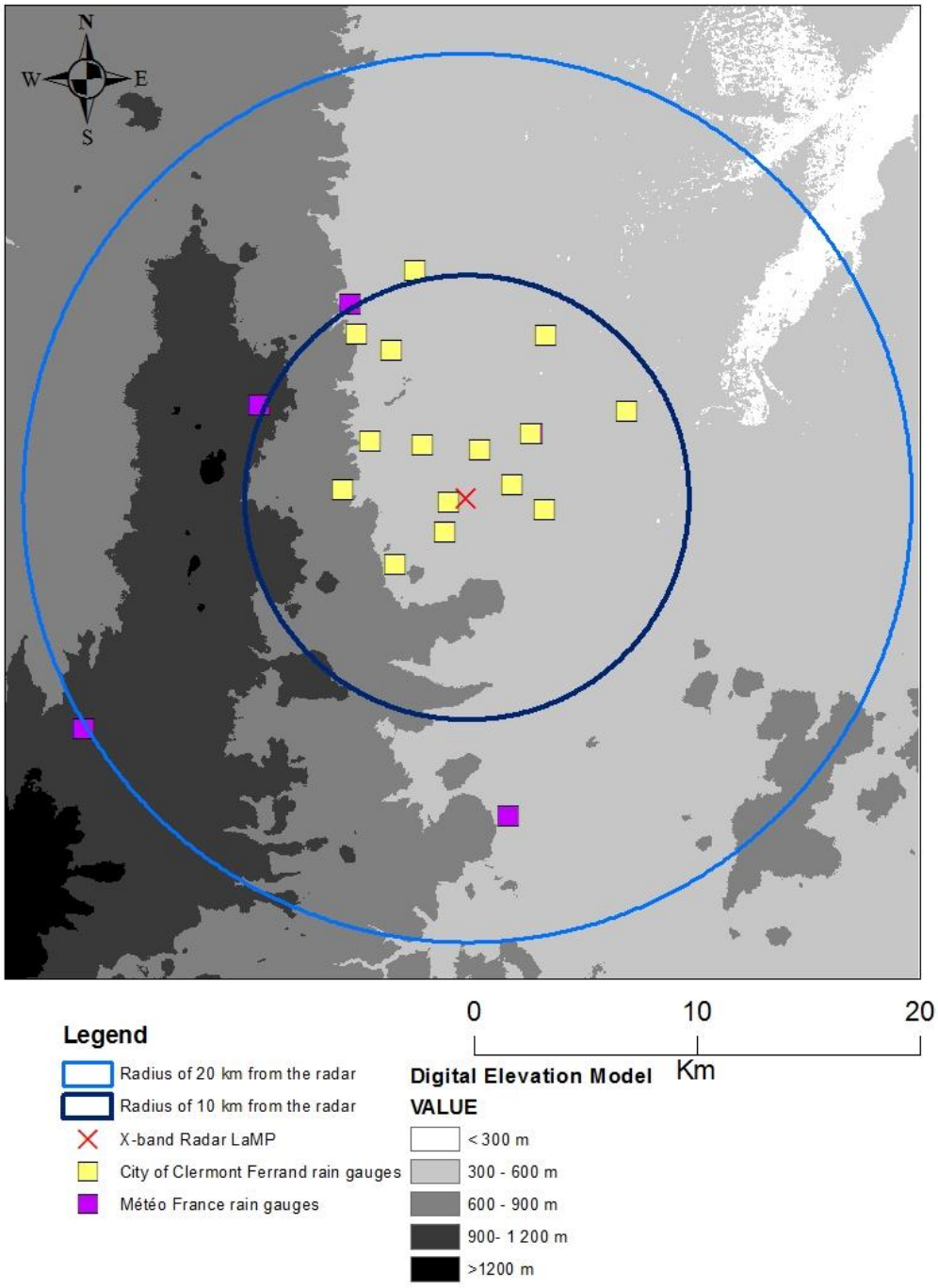


Figure 1:Location of the study area and the rain gauge network

The 6- minutes temporal resolution gauges were disaggregated to 5 minutes using a moving six hours window centered around the target time step. Both the 5 and 6 minutes rain gauges were also aggregated to 30 and 60 minutes.

The technical characteristics of the radar are specified in Table 1

Table 1:The X-band radar characteristics

A	B
Transmitted frequency	9.41 GHz
Peak power	24 kW
Pulse length	80 ns
Pulse repetition frequency	2100 Hz
Antenna information	*Parabolic with fixed elevation (5°), 2.5° power beam width at 3 dB*

3.1 Pre-processing of radar Data:

The radar have a radial resolution of 60 m, all non clutter radar pixels were interpolated on a 100*100 m grid. The X-band weather radar is well-known for being affected by attenuation. We use Hitscfeld-Bordan (1954) algorithm to correct the raw radar data, clutter is corrected through a clear sky radar reflectivity field corresponding to the study period (The summer of 2013).

The raw reflectivities Z were converted into rainfall intensities R using the Marshall Palmer relationship:

$$Z = 200 * R^{1.6}$$

We apply a Mean Field Bias correction (MFB) to the radar data , assuming that it is affected by a uniform multiplicative error. Goudenfoodt et al (2009) found that this method improves the agreement between tha radar and gauge data.

The MFB factor is expressed as:

$$MFB = \frac{\sum_{i=1}^{n} \mathrm{Gi}}{\sum_{i=1}^{n} Ri}$$

G_i is the rainfall intensity value corresponding to rain gauge i, R_i is the corresponding radar pixel.

Both the attenuation correction algorithm and the radar mean field bias correction method were used seperately then combined to see how it affects the KED and CM merging techniques.

4 Results:

The results are presented in Table 2. Att refers to the application of the attenuation algorithm, while "mfb" refers to the Mean Field Bias correction Method.

The performance assessment tests were applied on a small selection of the time steps where rainfall was detected by both the radar and the gauges for at least 12 of the 18 locations, and where a bright band have not distorted the data (visual check).

Table 2: Performance assessment results

		5 min			30 min			60 min		
		BIAS	RMSE	RVAR	BIAS	RMSE	RVAR	BIAS	RMSE	RVAR
No Att	OK	0.164	0.778	0.351	0.057	0.786	0.333	0.050	0.678	0.123
	KED	0.156	0.812	0.479	0.048	0.852	0.496	0.042	0.736	0.417
	CM	0.338	0.873	0.437	0.119	0.964	0.793	0.097	0.843	0.453
Att	KED	0.165	0.840	0.508	0.042	0.856	0.494	0.042	0.738	0.419
	CM	0.397	0.875	0.451	0.113	1.026	0.994	0.099	0.879	0.570
No Att mfb	KED	0.159	0.813	0.483	0.047	0.851	0.493	0.042	0.739	0.417
	CM	0.346	0.872	0.432	0.108	0.889	0.540	0.089	0.804	0.336
Att mfb	KED	0.170	0.842	0.514	0.044	0.855	0.492	0.047	0.736	0.420
	CM	0.367	0.863	0.426	0.095	0.913	0.587	0.086	0.821	0.392

One of the surprizing findings of this study is that KED have performed marginally better the OK. The attenuation correction algorithm and the mean field bias correction of radar data have not improved the performance of the two interpolation techniques at all, worsening it in most cases. The Conditional Merging technique performed the worst, it was slightly improved by the MFB method when it comes to reducing the bias and the root mean square error normalized by the average of the observations, however it reduced the variance ratio as well which was the only advantage it had compared to KED and OK.

The study is ongoing, the objective is to cover more seasons in order to investigate the effects of seasonal change in the drop size distribution of rainfall as well as their nature (stratiform, convective, mixed…) over the performance of the merging techniques.

5 Acknowledgement

The reseach leading to this work is funded by the Ministry of Higher Education and Research in France. The rain gauge data used in this work is privided by Météo-France and the city of Clermont-Ferrand. Moreover the authors would like to thank the team maintaining the X-band radar in the Phydical Meteorology Laboratory in Clermont-Ferrand (LaMP).

6 References

Berndt, C.; Rabiei, E.; Haberlandt, U. Geostatistical merging of rain gauge and radar data for high temporal resolutions and various station density scenarios. J. Hydrol. 2014, 508, 88–101

Ehret, U., 2003. Rainfall and Flood Nowcasting in Small Catchments using Weather Radar, 1st ed. Mitteilungen. Eigenverlag des Instituts für Wasserbau der Universität Stuttgart, Stuttgart.

Hitschfeld, W., and J. Bordan, 1954: Errors inherent in the radar measurement of rainfall at attenuating wavelengths. J. Meteor., 11, 58–67, doi:10.1175/1520-0469(1954)011,0058: EIITRM.2.0.CO;2.

Goovaerts, P., 1997. Geostatistics for Natural Resources Evaluation. Oxford University Press, USA.

Goudenhoofdt, E., Delobbe, L., 2009. Evaluation of radar-gauge merging methods for quantitative precipitation estimates. Hydrology and Earth System Sciences 13,195–203.

Velasco-Forero, C.A., Sempere-Torres, D., Cassiraga, E.F., Jaime Gómez-Hernández, J.,2009. A non-parametric automatic blending methodology to estimate rainfall fields from rain gauge and radar data. Advances in Water Resources 32, 986–1002.

Development of a Detection System of Heavy Rainfall using X-band Phased-Array Weather Radar

Kazuhiro Yoshimi[1] , Fumihiko Mizutani[1] , Nobuhiro Takahashi[2], Tomoo Ushio[3, 4]

[1]*Toshiba Infrastructure Systems and Solutions Corp., 1, Komukai, Toshiba-cho, Saiwai-ku, Kawasaki 212-8551 Japan*
[2]*National Institute of Information and Commuications Technology (NICT), 4-2-1, Nukui-Kitamachi, Koganei, Tokyo 184-8795, Japan*
[3]*Osaka Universtiy, 1-1 Ymadaoka, Suita, Osaka 565-0871, Japan*
[4]*Tokyo Metropolitan University, 6-6 Asahigaoka, Hino-shi, Tokyo, Japan 191-0065*

1 Introduction

Due to global warming and the rapid urbanization of emerging countries, torrential rain disasters occur frequently in various parts of the world and become social problems. Sediment disasters and flood damage are also frequent in Japan due to extreme weather phenomena such as super typhoon and torrential rain. Under such circumstances, the Government of Japan cites "Enhancement of societal resiliency against Natural Disasters" as one of the "Cross-ministerial Strategic Innovation Promotion Program (SIP)" led by the Cabinet Office. In preparation for natural disasters such as heavy rain and tornado, Industry-Academia-Government works together to establish a mechanism to share disaster information in real time, and is promoting realization of responding ability. This demonstration experiment is being conducting under the support of SIP from 2015 and TOSHIBA has been developing a detection system of heavy rainfall for users who conduct disaster prevention caused by rainfall

The purpose of this research and development is to aim at constructing a system based on user's view by conducting applied research on information obtained from heavy rain / tornado prediction technology. For the purpose of aiming at constructing a system based on such a user's perspective, we are conducting demonstration experiments to introduce a system to an actual site and to verify the problems for practical application.

2 Scheme of the developed system

2.1 Detection system of heavy rainfall

The developed heavy rain detection system (Figure 1) aims to distribute alarms as preliminary information of heavy rain to users such as municipalities. The heavy rain detection alarm is based on the information observed by the phased array weather radar (hereinafter, this is called “PAWR”) (Anraku et al, 2013/Wada et al, 2012/2014) and the information of the weather radar network called “XRAIN” distributed, by the Ministry of Land, Infrastructure, Transport and Tourism. Although rainfall prediction is carried out by many research institutes, the purpose of the detection system developed by TOSHIBA is to notify the heavy rain information more simply. Observation data delivered from each weather radar is processed in the cloud managed by TOSHIBA and delivered by e-mail and LED beacon as warning information of heavy rain. In addition, rainfall distribution is also delivered at the same time by the web display function which is one of the functions of the heavy rain detection system.

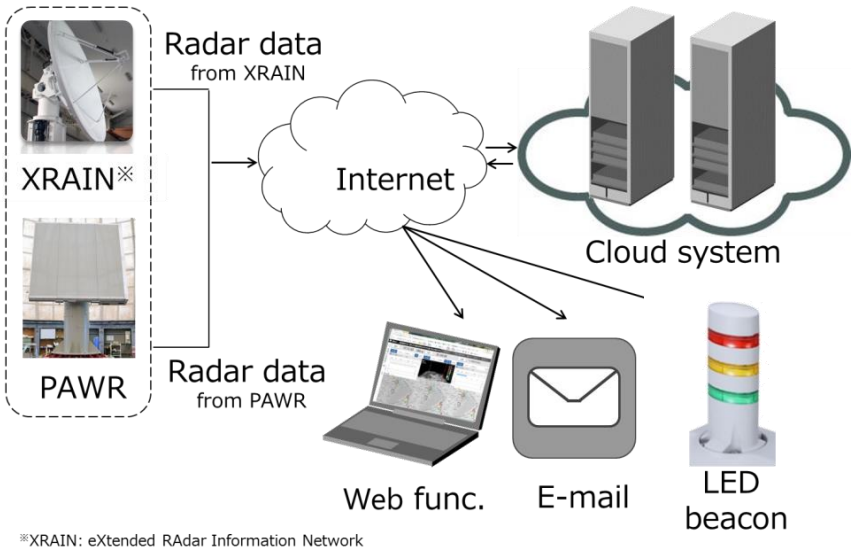


Figure 1: Conceptual diagram of the developed system

2.2 Definition of alarm

In this demonstration experiment, two types of alarms are distributed to the user as alarm information of heavy rain. The definitions of these alarms are as follows. In addition, a conceptual diagram of alarm notification is shown in Figure 2.

- WATCH alarm: early warning information to be announced based on predicted rainfall, VIL, ETOP
- WARNING alarm: current condition information to be reported when heavy rain is observed near the ground

where VIL: Vertical Integrated Liquid is the total mass of precipitation in the clouds (Hirano and Maki, 2010) and ETOP is the cloud top height. The predicted rainfall uses a prediction model that three-dimensionally tracks individual rain clouds.

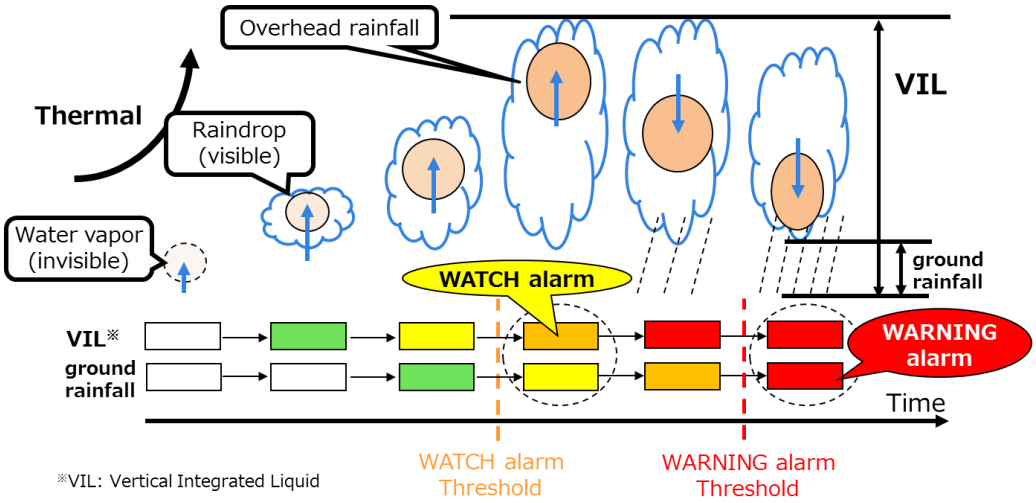


Figure 2: The conceptual diagram of the alarms

Next, we show the evaluation index of the demonstration experiment system in Table 1. "Threat Score (TS)", "False Alarm Ratio (FAR)" and "Undetected Error Rate (Ur)" with respect to alarm accuracy are defined as follows. True Positive is defined as the case where WARNING alarm is issued with WATCH alarm issued. Also, a state in which WATCH alarm is reported, but WARNING alarm is not reported is defined as False Positive. False Negative is defined as a state in which WARNING alarm is issued in a state where WATCH alarm has not been reported, and the other is defined as True Negative.

Table 1: Verification Indices for the two types of detection alarm

		WARNING alarm	
		Observed	NOT Observed
WATCH alarm	Forecasted	TP (True Positive)	FP (False Positive)
	NOT Forecasted	FN (False Negative)	TN (True Negative)

The threat score (TS) can be written as

$$\text{Threat Score (TS)} = \frac{\text{TP}}{\text{TP} + \text{FP} + \text{FN}} \quad (0 \leq \text{TS} \leq 1) \tag{1}$$

The false alarm ratio (FAR) can be written as

$$\text{False Alarm Ratio (FAR)} = \frac{\text{FP}}{\text{TP} + \text{FP}} \quad (0 \leq \text{FAR} \leq 1) \tag{2}$$

The undetected error rate (Ur) can be written as

$$\text{Undetected Error Rate (Ur)} = \frac{\text{FN}}{\text{TP} + \text{FN}} \quad (0 \leq \text{Ur} \leq 1) \tag{3}$$

2.3 Condition of alarm activation

The conceptual diagram of Figure 3 shows the distributed condition of WATCH alarm. The characteristic of the alarm using VIL and ETOP is that it uses three-dimensional rainfall information observed by PAWR. Therefore, in the demonstration experiment conducted in 2017, as mentioned above, an alarm was issued when VIL, ETOP, CAPE and 3D analysis exceeded the set thresholds. Table 2 shows the thresholds of the indices actually used as the alarm issued conditions. The thresholds of VIL and ETOP are supposed to follow the values of the demonstration experiment in 2016. Where, CAPE is an indicator of atmospheric instability and is very valuable for predicting serious weather. In addition, the threshold of CAPE was determined after analysis in all cases of past torrential rains in demonstration experiments (from 2015 to 2016).

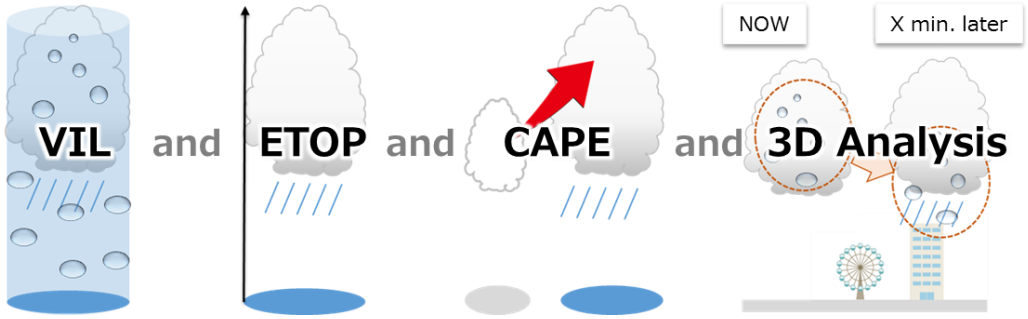


Figure 3: The WATCH alarm condition and its index

Table 2: The threshold of the index (VIL, ETOP, CAPE, 3D analysis)

Index	VIL [kg/m^2]	ETOP [m]	CAPE [J/kg]	3D analysis [mm]
Threshold	5	4000	800	8.33

3 Results of demonstration experiment using the system

3.1 Precipitation events and target site

Table 3 shows precipitation events where an alarm was distributed in the demonstration experiment conducted in the 2017. The total number of alarms reported from July to November during the period of the demonstration experiment was 15. When judging from the indicator expressing the state of the atmosphere and the weather chart, the case which can be defined as heavy rain was two cases occurred on August 18 and August 23. In other cases, an alarm was reported due to the heavy rainfall in the front line or torrential rain caused by the typhoon.

Moreover, in this demonstration experiment, we target users who may have flood prevention activities due to local heavy rain, such as sewerage division, park manager and road administrator. In showing the effectiveness of the observation data of PAWR, the following is example of the water park where remarkable results were obtained.

Table 3: Rainfall events during demonstration experiment in 2017(1/2)

No.	Period			Number		Remarks
				WATCH	WARNING	
1	2017/07/09 13:00	~	2017/07/09 21:00	20	36	Frontal rain
2	2017/07/17 21:00	~	2017/07/18 00:00	0	4	Frontal rain
3	2017/07/18 14:00	~	2017/07/18 21:00	2	4	Frontal rain
4	2017/07/26 01:00	~	2017/07/26 08:00	0	9	Frontal rain

Table 3: Rainfall events during demonstration experiment in 2017(2/2)

No.	Period			Number of times		Remarks
				WATCH	WARNING	
5	2017/08/07 15:00	~	2017/08/08 00:00	0	4	Typhoon
6	2017/08/08 12:00	~	2017/08/08 19:00	0	3	Typhoon
7	2017/08/18 05:00	~	2017/08/18 12:00	10	15	Torrential heavy rain
8	2017/08/23 13:00	~	2017/08/23 20:00	11	12	Torrential heavy rain
9	2017/08/26 03:00	~	2017/08/26 10:00	2	2	Frontal rain
10	2017/09/07 10:00	~	2017/09/07 15:00	0	8	Frontal rain
11	2017/09/12 03:00	~	2017/09/12 10:00	14	41	Frontal rain
12	2017/09/16 12:00	~	2017/09/17 00:00	0	1	Frontal rain
13	2017/09/17 17:00	~	2017/09/18 02:00	0	13	Typhoon
14	2017/09/28 04:00	~	2017/09/28 11:00	0	10	Frontal rain
15	2017/10/22 19:00	~	2017/10/23 00:00	0	1	Typhoon

3.2 Typical successful event

In the demonstration experiment in 2017, a water park managed by Osaka prefecture was also newly added as a target institution of the demonstration experiment. The water park is adjacent to the river, and a hydrophilic area where park users can freely access the riverside was constructed.

On the other hand, it is known that the water level of a river rises sharply due to sudden heavy rain in the hydrophilic area adjacent to urban areas. It is a very dangerous place for park users, as typified by a water accident at the Toga River.

In the demonstration experiment in 2017, in order to confirm whether alarms to such a hydrophilic area manager are useful, we asked the river administrator to use the system and whether alarm notification to the water park is useful. As a result, in the case of August 18, a case where the water level of urban river rose sharply was observed. We confirmed that alarm distribution in basin unit is effective not for local alarm distribution to targeted area. In other words, we showed that alarm distribution based on observation information of PAWR delivered in this demonstration experiment is effective for the water park (Figure 4).

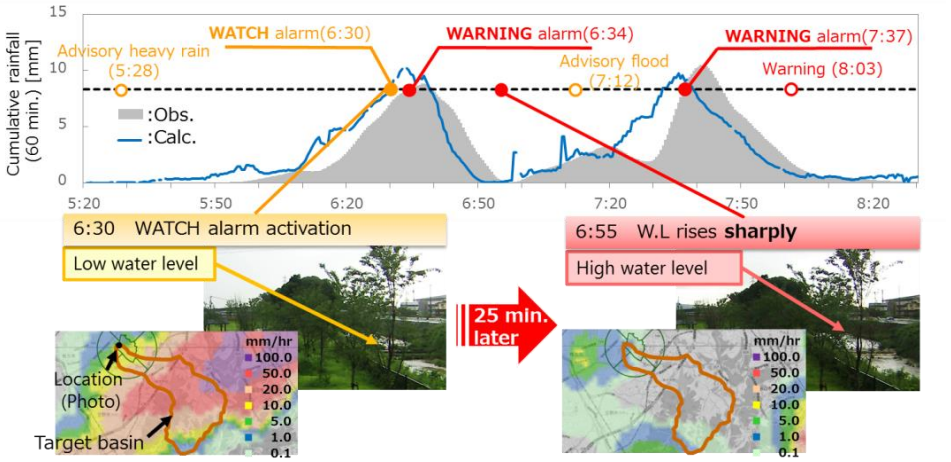


Figure 4: A successful case of alarm system at a water park in Osaka, Japan

3.3 Scores of the alarm in demonstration experiment in 2017

In this chapter, we show the results of the accuracy verification of the WATCH alarm for the heavy rain events in the demonstration experiment conducted in the 2017. As a result, it was found that the alarm distributing algorithm adopted in the demonstration experiment in 2017 showed that the frequent occurrence of the false alarm, which was the subject of the demonstration experiment in 2016, was greatly improved (Table 4). On the other hand, we found that the undetected error rate which was 0% last year was somewhat higher in score, 25.9%. Moreover, due to a large decrease in the false alarm ratio, the threat score has improved considerably compared with the demonstration experiment in 2016.

Table 4: Annual scores of the alarm

	2016 (num. of times)	2017 (num. of times)
TS	23.2% (38)	71.4% (20)
FAR	76.8% (126)	4.8% (1)
Ur	0% (0)	25.9% (7)

4 Discussions

As mentioned earlier, in the alarm distributing system of the demonstration experiment in 2017, it was found that the number of undetected error's cases of WATCH alarm increased while cases of torrential rain decreased. This is thought to be because the alarm was set to be distributed when all the indexes exceeded the threshold value, so that the alarm condition was too severe for the heavy rain case compared with demonstration experiment in 2016.

Therefore, as shown in Figure 5, We tried to improve the TS by permitting deterioration of the score of FAR, making a distinction between a judgment index based on measured value and a judgment index based on analysis value, and making it OR condition. There are two main reasons for roughly classifying. The first is to reduce the Ur by improving the alarm distributing algorithm in which an alarm is issued when any one of the determination indices matches. The second reason for roughly classifying judgment indicators is not only to report cases of heavy rain but also alarms for non-heavy rain cases. Because we hope users to utilize the demonstration experiment system in a wider sense for water defense activities. Here, the determination index based on the measured value is determined from the viewpoint of utilizing the observation information of the weather radar such as VIL and ETOP. Further, the analysis index based determination index is used as a determination index based on a so-called predicted value.

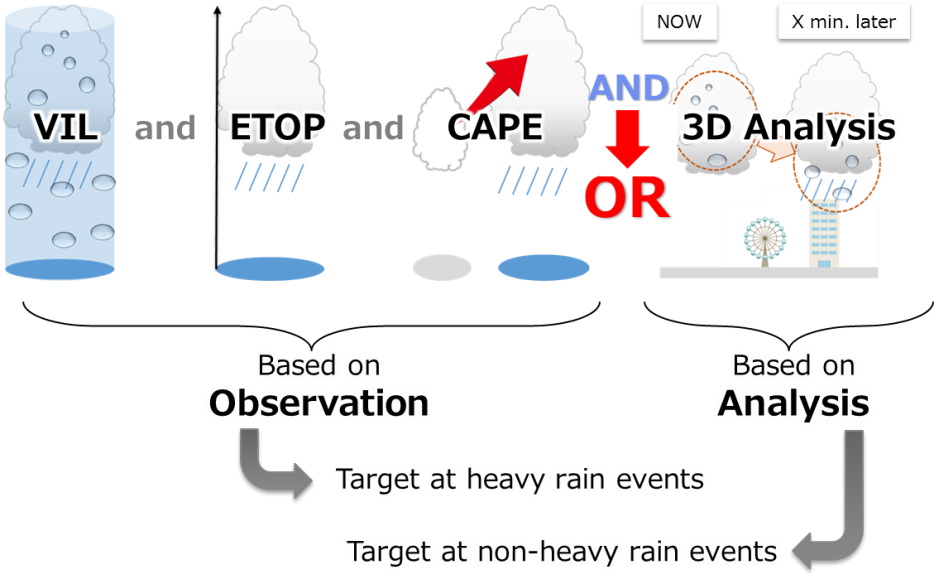


Figure 5: An improvement plan of the condition to distribute the alarm

5 Conclusions

TOSHIBA developed a heavy rain detection system based on observation data of the single polarized phased array weather radar and conducted a demonstration experiment using the system together with Osaka local governments. As a result, it was found that the three - dimensional rainfall information observed by PAWR is useful as the input of the system for securing the safety of the users of green space parks and water parks managed by municipalities. In addition, as a result of the demonstration experiments, we were able to obtain many cases where the alarm notification succeeded immediately before heavy rain. From the above, it is being acknowledged that local governments' flood prevention activities are carried out smoothly, and alarms are announced beforehand from heavy rain, which is an effective system for actual disaster prevention work. We will continue demonstration experiments from July in 2018, and verify the utility of PAWR data and the practicality of heavy rain detection system. Moreover, TOSHIBA has been developed high precision dual polarization phased-array weather radars which utilize solid-state transmitters which allow fast three-dimensional observation. In 2018, we will conduct demonstration experiments using observed data by this latest weather radar developed by TOSHIBA

Acknowledgement

This research is (partially) supported by the "Cross-ministerial Strategic Innovation Promotion Program (SIP)" from Japan Science and Technology Agency, JST.

References

Naoki Anraku, Fumihiko Mizutani, Masakazu Wada, Hironori Handa, Tomoo Ushio, Shinsuke Satoh, 2013: Development of Phased-Array Weather Radar system for 3D observation of cumulonimbus clouds. extended abstract, 36th Conf. on Radar Meteorology, Albuquerque, U.S, Amer. Meteor. Soc. 146.

Masakazu Wada, Naoki Anraku, Hiroshi Yamauchi, Ahoro Adachi, Ushio Tomoo and Shinsuke Satoh, 2014: Development of advanced radar technologies for weather application. ERAD 2014 - THE EIGHTH EUROPEAN CONFERENCE ON RADAR IN METEOROLOGY AND HYDROLOGY. Abstract ID 074.

Masakazu Wada, Naoki Anraku, Hiroshi Yamauchi, Ahoro Adachi, 2012: Operational usage of Solid-State Weather Radar. TECO 2012. WMO TECHNICAL CONFERENCE ON METEOROLOGICAL AND ENVIRONMENTAL INSTRUMENTS AND METHODS OF OBSERVATION.

Kohin Hirano and Masayuki Maki, 2010: Method of VIL Calculation for X–band Polarimetric Radar and Potential of VIL for Nowcasting of Localized Severe Rainfall – Case Study of the Zoshigaya Downpour, 5 August 2008 –, SOLA, 2010, Vol. 6, 089−092.

Solar Energy Perspective on the Data Assimilation of Radar Reflectivity Data in a Limited Area NWP Model

Tuuli Perttula[1], Sami Niemelä[1], Anders V. Lindfors[1] and Elena Saltikoff[1]

[1]*Finnish Meteorological Institute, Erik Palménin aukio 1, 00560 Helsinki, Finland*

(Dated: 21 June 2018)

1 Introduction

Radar reflectivity observations are operationally assimilated only by few meteorological services. However, a lot of research has been done and is going on in this field. Radar reflectivity is very indirectly connected to the model variables and therefore it is not self-evident how it should be optimally assimilated to get the best impact out of the observations. Research in assimilation of radar reflectivity observations directly with both three-dimensional variational (3D-Var) (Wang et al. 2013a) and four-dimensional variational (4D-Var) (Wang et al. 2013b; Sun and Wang 2013) schemes has given promising results. However, this development has not yet led to operational implementations. An indirect 1D+3D-Var method (Caumont et al. 2010) is used to assimilate radar reflectivity operationally for instance by Météo-France (Wattrelot et al. 2014) and some members of the HIRLAM consortia (Gustafsson et al. 2017) including the Metcoop collaboration between Sweden, Norway and Finland (Müller et al. 2017).

Radar reflectivity provides information about precipitation and therefore traditionally in the renewable energy sector the main user of radar reflectivity data has been the hydropower industry. However, when assimilated into a numerical weather prediction (NWP) model the 3-D radar data can improve also cloudiness inside the model analysis and forecasts. Since cloudiness has a direct impact on solar radiation, assimilation of radar reflectivity data may bring improvements to the model that are of interest for solar energy applications.

The aim of the present study was to evaluate the possible improvement in the representation of solar radiation in a NWP model when assimilating radar data. For that, we use the HARMONIE-AROME configuration of the limited area ALADIN-HIRLAM NWP system, in which the radar reflectivities are assimilated using an indirect 1D+3D-Var assimilation method (Caumont et al. 2010; Wattrelot et al. 2014). In this method, humidity profiles are retrieved from the radar reflectivity volumes and these profiles are then assimilated through the 3D-Var scheme. Earlier impact studies using this method in assimilating radar reflectivity have given neutral to positive impact (Ridal and Dahlbom 2017).

As we are specifically focusing on solar radiation, we use ground-based measurements of global radiation from the Finnish network as a reference. From the point of view of development of radar data assimilation, the solar radiation observations provide an independent source of reference observations, suitable for comparisons with modeled radiation. In many verification studies, the humidity and temperature measurements from radiosondes are used as a reference. Compared to them, the solar radiation data has a higher spatial and temporal resolution. A previous study, for example, compared the performance of different radiation schemes in the HARMONIE-AROME NWP model with solar radiation measurements during spring in Finland (Rontu and Lindfors, 2018). They found good agreement between the model and measurements in clear-sky cases, while under cloudy skies, the modeled surface solar radiation tended to be too high.

2 Data and methods

2.1 NWP Model

Radar reflectivity assimilation experiments were run using the HARMONIE-AROME configuration of ALADIN-HIRLAM NWP system (Bengtsson et al. 2017). ALADIN-HIRLAM NWP-system is a non-hydrostatic limited area model including different choices for model components. In this study we run the system with AROME physics (Seity et al. 2011; Brousseau et al. 2011) using the model version cy40h1.1. The model domain covers the Scandinavian countries and the whole Baltic Sea area. It consists of 720x800 points in horizontal with 2,5 km resolution and 65 model levels in vertical with the model top at 10 hPa. The model domain can be seen in Fig. 3.

The boundary conditions for the HARMONIE-AROME come from the European Center for Medium-Range Weather Forecasts (ECMWF) Integrated Forecast System (IFS). Boundary fields are updated every 3 hours.

Upper air observations are assimilated in HARMONIE-AROME inside the three-dimensional variational (3D-Var) data assimilation scheme. In this study we assimilated in-situ observations in model experiments with and without the radar reflectivity observations. Assimilated in-situ observations included surface synoptic observations (SYNOP), sea-based SYNOP-stations (SHIP), aircraft reports (AMDAR, AIREP, ACARS), buoy observations (BUOY), radiosondes (TEMP) and wind profiler (PILOT) observations.

2.2 Radar data, its pre-processing and assimilation

Volume scans of radar reflectivity from Finland, Sweden, Norway and Denmark were assimilated in our study. In 2016, FMI in Finland operated 10 C-band weather radars. Sweden had 12 radars, Norway 9 and Denmark 5. The data were quality controlled using the BALTRAD toolbox (Michelson and Henja, 2012). The operational international radar data flow for data assimilation is described more in detail by Ridal and Dahlbom (2017).

Before the radar data are assimilated in the HARMONIE-AROME model some quality control steps are performed as described by Ridal and Dahlbom (2017) and Gustafsson et al. (2017). The radar data from different countries were checked for errors and format differences and corrected to be in uniform format. Horizontal thinning of data was also applied. To avoid either residual clutter or incontinuities due to intensive clutter cancellation, the lowest elevation scan of each volume was not used.

Radar reflectivity data are assimilated using a 1D+3DVar method introduced by Caumont et al. (2010) and later operationally implemented by Wattrelot et al. (2014). This method consists of two parts: First a one-dimensional (1D) Bayesian method is used to retrieve humidity profiles from the radar reflectivity volume scans, which are then assimilated using the three-dimensional variational data assimilation (3D-Var) technique. Radar reflectivity assimilation brings moisture to areas where radar detects precipitation. It also dries areas where the model forecasts rain but the radar sees no precipitation.

Main motivation for reflectivity assimilation has been to improve precipitation estimation. The microwaves are also scattered from non-precipitating clouds, especially in cases when there are hydrometeors in clouds which do not fall to ground (Fig 1). Assimilation of radar data, and its potential use for verification, can help to improve the cloud forecasts.

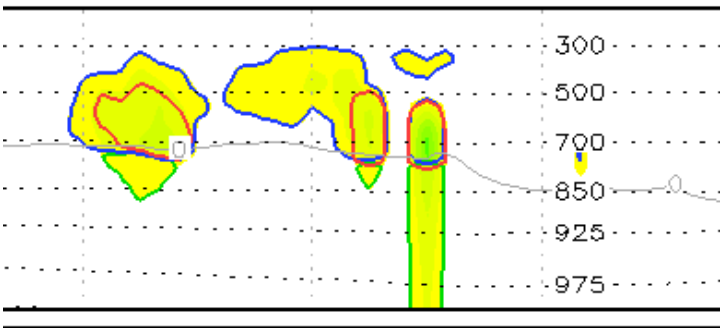


Figure 1a. An example of rain (green outline), graupel (red) and snow (blue) in HARMONIE-AROME model. The green and yellow shades represent the hydrometeor density in g/m3. Assimilation of 3-dimensional radar data with a method using humidity profiles can improve this information, and hence also the cloudiness forecasts.

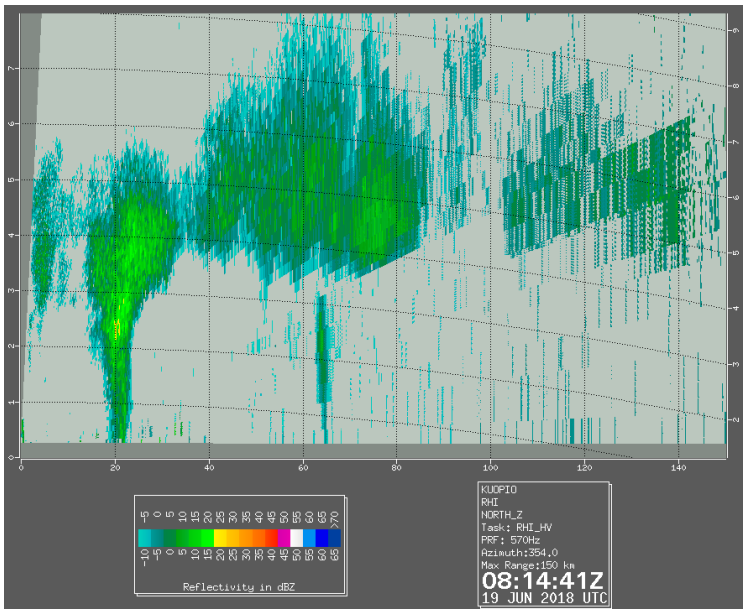


Fig 1b. Range-height plot north from FMI Kuopio weather radar 19.6.2018 describing the 3-dimensional structure of precipitation.



Fig 1c. Precipitation falling from clouds but evaporating before it reaches ground. Photo from Nötö, Finland, 8.5.2018 (The three examples are not from the same situation)

2.3 Solar radiation measurements

A map of the global radiation measurement stations used in this study is shown in Fig. 2. These stations belong to the solar radiation measurement network of the Finnish Meteorological Institute (FMI), where global radiation is measured using ventilated Kipp and Zonen CM11 secondary standard pyranometers. The instruments are calibrated regularly and the measurement data have been tested using the quality assurance procedures defined for the Baseline Surface Radiation Network (Long and Shi, 2008), with minor modifications to better suit Finnish conditions. In this study, hourly values of the global radiation were used, covering the whole one-month experiment period. Based on a more detailed analysis of the Swedish radiation measurement network (Persson, 2000), the uncertainty of these hourly values is estimated to be roughly 4%, except for low Sun conditions when larger uncertainty is expected.



Figure 2: Finnish radiation stations marked with red dots.

3 Results

3.1 Experimental setup

Two HARMONIE model experiments were run to evaluate the impact of the assimilation of the radar reflectivity data. In the control run only in-situ observations were assimilated. Radar assimilation run included assimilation of radar reflectivity, otherwise the setup was exactly same as in the control run. Assimilated observations are listed in table 1.

Table 1: Assimilated observations.

Experiment	Assimilated observations
Control run	SYNOP, SHIP, AMDAR, AIREP, ACARS, BUOY, TEMP, PILOT
Radar data assimilation run	SYNOP, SHIP, AMDAR, AIREP, ACARS, BUOY, TEMP, PILOT, RADAR

Experiment period lasted from 1st to 31st July 2016. Analysis was run every 3 hours and 48-hour-long forecasts were started at 00 and 12 UTC cycles. Short 3-hour-long forecasts were started at 03, 06, 09, 15, 18 and 21 UTC cycles. Radar data were assimilated at every analysis cycle i.e. every 3 hours. Radar locations can be seen in Fig. 1.

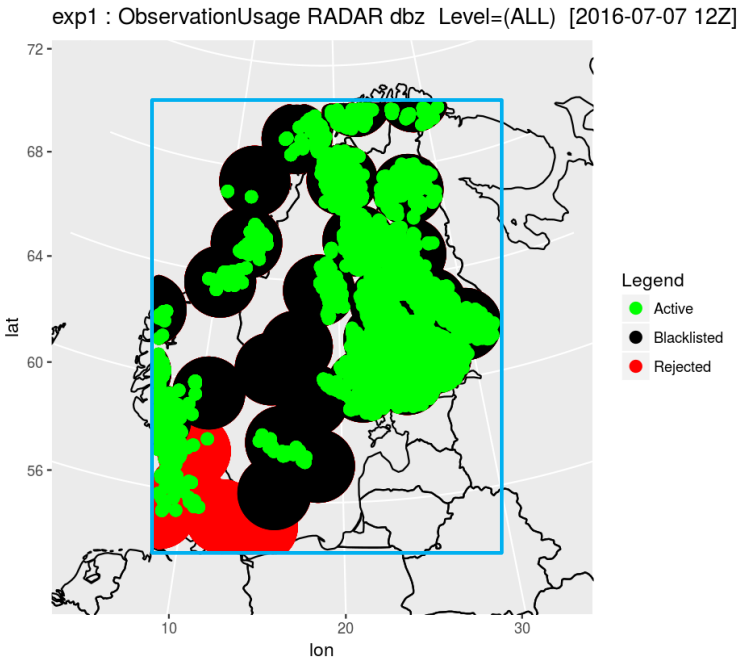


Figure 3: Radar observations entering screening on 7 July 2016 at 12 UTC forecast cycle. The used HARMONIE-AROME domain is marked with blue square. Red dots indicate rejected observations, black dots blacklisted observations and green dots active observations. Figure includes radar observations from all elevation angles. It is to be noted that the lowest elevation angle from every radar scan is blacklisted automatically regardless of quality.

3.2 Verification against SYNOP and radiosonde observations

The overall meteorological performance of HARMONIE-AROME model was verified against SYNOP and radiosonde observations. These included observations from 635 SYNOP stations and 23 radiosonde stations. Impact of radar reflectivity assimilation over the one-month period was neutral for most parameters. Very small negative bias could be seen in the mean sea level pressure, however the difference between the two experiments was a lot smaller than for example normal differences between different operational NWP models. In verification against radiosonde observations there was a slight negative impact on temperature between 200 hPa and 700 hPa. The impact on specific humidity was slightly positive between 300 hPa and 700 hPa (Fig. 4).

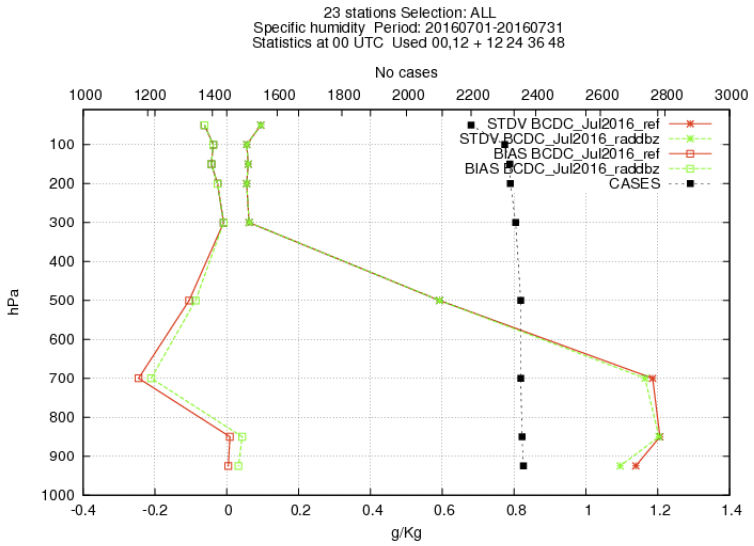
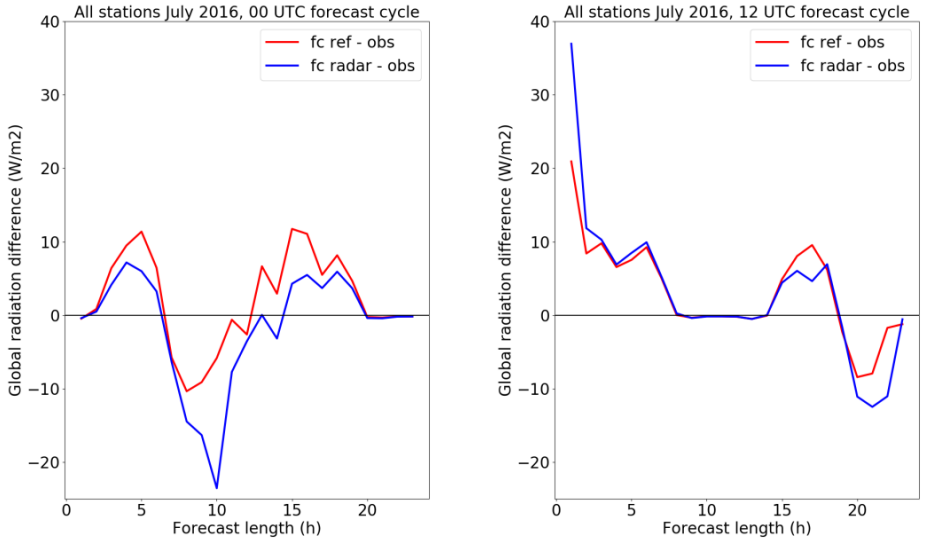


Figure 4: Verification of radar (green) and control (red) runs against radiosonde observations. Standard deviation (stars) and bias (boxes) of specific humidity.

3.3 Impact on global radiation

Global radiation values at the radiation station locations were extracted from the forecasted HARMONIE model fields, both for the radar experiment and for the control run. Observations were compared separately to 00 UTC and 12 UTC forecast cycles so that for example 6-hour-long forecast started at 00 UTC corresponded to the global radiation observation made at 6 UTC and 6-hour-long forecast started at 12 UTC corresponded to the global radiation observation made at 18 UTC. The local time during the period when the radiation observations were made was East European Summer Time (EEST), which corresponds to UTC + 3 hours.

Figure 5 shows global radiation differences between forecasts and observations. These differences were averaged over the whole experiment period of July 2016 and over all the 26 radiation stations. Red curve indicates the difference between the reference experiment and observations and blue curve the difference between the radar data assimilation experiment and observations. The smaller the difference between forecast and observation is i.e. closer to zero the better the forecast is. In the figure a) the used forecasts were started at 00 UTC and in figure b) at 12 UTC.

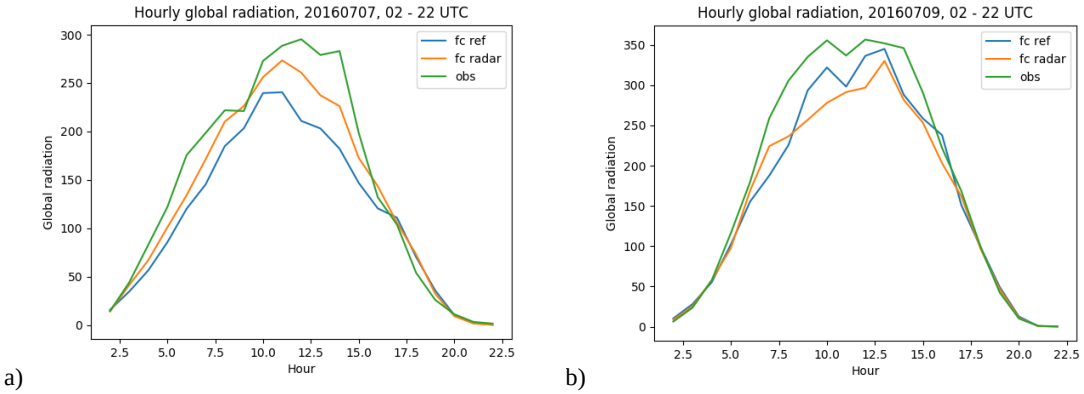


a) b)

Figure 5: Difference between observed and forecast global radiation averaged over whole experiment period and all 26 observation stations. Blue: Radar data assimilation experiment, red: control run. a) Forecasts started at 00 UTC, b) Forecast started at 12 UTC.

Radar reflectivity data assimilation has a positive impact on global radiation forecasts started at 00 UTC on forecast lengths 1-6 hours and 12-19 hours. However, the impact is negative at forecast lengths 6-12 hours. For forecasts started at 12 UTC the impact is mainly negative, only at forecast lengths 16-19 hours the impact is positive. Overall, the radar experiment has less global radiation (i.e. more clouds) than the control run. The great difference between the forecast cycles is explained by the fact that the global radiation varies diurnally.

The results in Fig. 5 are averaged over the whole month and all the stations. Therefore, we wanted to investigate the diurnal behaviour related to different weather situations. We classified three different type of days: 1) No significant impact from the radar reflectivity assimilation or the impact is partly negative and partly positive (14/31 days), 2) Radar reflectivity assimilation has clearly positive impact on global radiation (10/31 days) and 3) Radar reflectivity assimilation has clearly negative impact on global radiation (7/31 days). We decided to look more carefully into the cases where the impact of radar data assimilation was clearly positive or negative. Examples of these cases are shown in Fig. 6 and 7.



a) b)

Figure 6: Hourly global radiation averaged over 26 radiation stations. Green: Global radiation observations, Orange: Radar experiment forecast, Blue: Control run forecast. a) Example of a case where radar data assimilation has positive impact 7 July 2016 b) Example of a case where radar data assimilation has negative impact 9 July 2016.

The study of individual stations and forecasts showed that in some cases the radar reflectivity assimilation brought global radiation forecast very close to the observation. In other cases radar reflectivity assimilation affected the forecast negatively. For instance, on 9th of July (Fig 6b.), the radar run eventually performs worse (i.e. not enough radiation, too much clouds) than the control run, although in the beginning of the forecast the impact of the radar data to radiation forecast seem to be slightly positive. Analysis increments and cloud profiles from the different cases were studied but unfortunately, we did not yet find a clear reason for why the impact is sometimes positive and sometimes negative.

The 24-hourly precipitation sums form radar, and the satellite images (Fig 7) show that nature of precipitation and cloudiness was different on these two days. 7th July the precipitation was more widespread especially in western and northern parts of the country, while on the July 9th the weather was more convective and precipitation consisted mainly of isolated showers. Before any conclusions can be drawn from this, more studies of different weather types should be done.

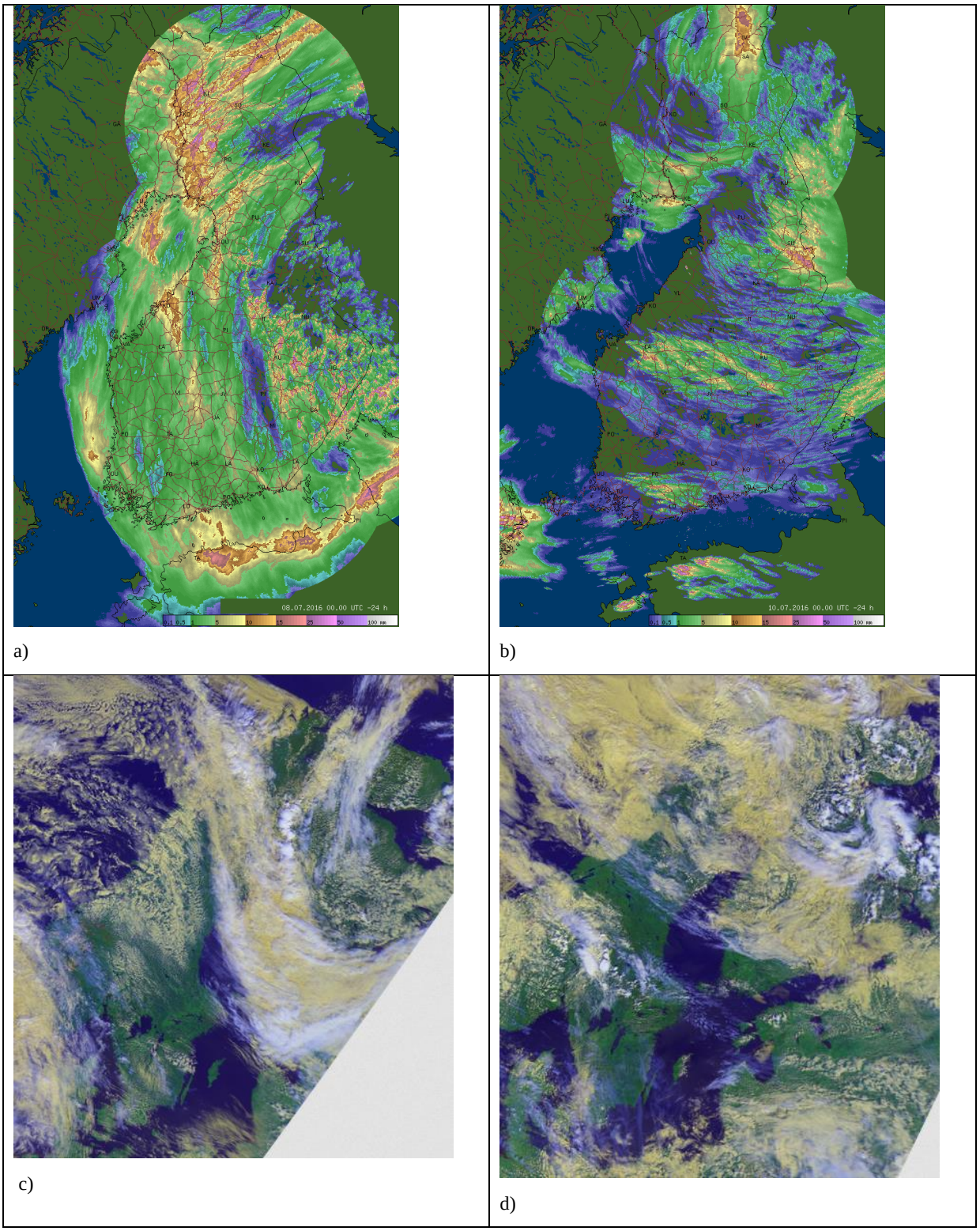


Figure 7: a) 24-h precipitation sum based on FMI radars from 7 July 2016 b) 24-h precipitation sum based on FMI radars from 9 July 2016 c) Satellite image 7 July 2016 at 10:26 UTC and d) Satellite image from 9 July 2016 at 9:45 UTC.

4 Conclusions

Radar reflectivity data was assimilated into HARMONIE-AROME NWP model. To study its impact, two one-month-long model experiments were run, one with radar data assimilation and one without. Radar reflectivity assimilation had a slightly positive impact on specific humidity forecast and slightly negative impact on temperature forecast in verification against SYNOP and radiosonde observations. Otherwise the impact was neutral.

To study the impact of radar reflectivity assimilation from the point of view of solar energy applications, we compared the forecasts from the two model experiments to observations from Finnish global radiation stations. In general, the radar data increased the amount of clouds in forecast leading to less global radiation reaching to surface. The positive impact on radiation was seen in morning and late afternoon. However, the impact during midday was overall negative. During individual days the impact on global solar radiation forecast varied a lot. The reasons behind positive and negative cases were studied in more detail, but we did not find definite answer for such variable behavior. Therefore, further studies should be done looking at more into reasons on why global radiation is sometimes well forecast and sometimes not and why the impact of radar reflectivity assimilation varies.

Acknowledgement

We thank the Strategic Research Council at the Academy of Finland for funding through the BCDC Energy project (decision 292854 and 314167).

References

Bengtsson, L., and Coauthors, 2017: The HARMONIE–AROME model configuration in the ALADIN–HIRLAM NWP system. Mon. Wea. Rev., **145**, 1919–1935, *https://doi.org/10.1175/MWR-D-16-0417.1*.
Brousseau, P., L. Berre, F. Bouttier and G. Desroziers, 2011: Background-error covariances for a convective-scale data-assimilation system: AROME–France 3D-Var. Q.J.R. Meteorol. Soc., 137: 409–422. doi:10.1002/qj.750
Caumont, O., Ducrocq, V., Wattrelot, É., Jaubert, G., & Pradier-Vabre, 2010: 1D+3DVar assimilation of radar reflectivity data: a proof of concept. Tellus A, 62(2). doi:*http://dx.doi.org/10.3402/tellusa.v62i2.15678*.
Gustafsson, N., Janjić, T., Schraff, C., Leuenberger, D., Weissman, M., Reich, H., Brousseau, P., Montmerle, T., Wattrelot, E., Bučánek, A., Mile, M., Hamdi, R., Lindskog, M., Barkmeijer, J., Dahlbom, M., Macpherson, B., Ballard, S., Inverarity, G., Carley, J., Alexander, C., Dowell, D., Liu, S., Ikuta, Y. and Fujita, T., 2017: Survey of data assimilation methods for convective-scale numerical weather prediction at operational centres. Q.J.R. Meteorol. Soc.. Accepted Author Manuscript. doi:10.1002/qj.3179.
Long, C. and Shi, Y., 2008**:** An Automated Quality Assessment and Control Algorithm for Surface Radiation Measurements, Open Atmos. Sci. J., 12, 23–37, *https://doi.org/10.2174/1874282300802010023*.
Michelson, D., and A. Henja, 2012: Opera work package 3.6: Odyssey additions, task 3: Tuning and evaluation of "andre" tool. OPERA Tech. Rep. Working Doc. WD-2012-02c, 20 pp.
Müller, M., and Coauthors, 2017: AROME-MetCoOp: A Nordic convective-scale operational weather prediction model. Wea. Forecasting, **32**, 609–627, *https://doi.org/10.1175/WAF-D-16-0099.1*.
Persson, T., 2000**:** Measurements of solar radiation in Sweden 1983–1998, SMHI Reports Meteorology and Climatology, vol. RMK No. 89, Swedish Meteorological and Hydrological Institute, Norrköping, Sweden.
Ridal, M. and M. Dahlbom, 2017: Assimilation of Multinational Radar Reflectivity Data in a Mesoscale Model: A Proof of Concept. Journal of Applied Meteorology and Climatology **56**:6, 1739-1751, doi:*https://doi.org/10.1175/JAMC-D-16-0247.1*.
Rontu, L. and A.V. Lindfors, 2018**:** Comparison of radiation parametrizations within the HARMONIE–AROME NWP model. Advances in Science and Research, 15:81–90. doi: *https://doi.org/10.5194/asr-15-81-2018*
Seity, Y., P. Brousseau., S. Malardel, G. Hello, P. Bénard, F. Bouttier, C. Lac and V. Masson, 2011: The AROME-France Convective-Scale Operational Model. Mon. Wea. Rev., 139, 976–991. Doi: *http://dx.doi.org/10.1175/2010MWR3425.1*
Sun, J., and H. Wang, 2013: Radar data assimilation with WRF 4D-Var. Part II: Comparison with 3D-Var for a squall line over the U.S. Great Plains. Mon. Wea. Rev., **141**, 2245–2264, doi:*https://doi.org/10.1175/MWR-D-12-00169.1*.
Wang, H., J. Sun, S. Fan, and X.-Y. Huang, 2013a: Indirect assimilation of radar reflectivity with WRF 3D-Var and its impact on prediction of four summertime convective events. J. Appl. Meteor. Climatol., **52**, 889–902, doi:*https://doi.org/10.1175/JAMC-D-12-0120.1*.
Wang, H., J. Sun, X. Zhang, X. Y. Huang, and T. Auligné, 2013b: Radar data assimilation with WRF 4D-Var. Part I: System development and preliminary testing. Mon. Wea. Rev., **141**, 2224–2244, doi:*https://doi.org/10.1175/MWR-D-12-00168.1*.
Wattrelot, E., O. Caumont, and J.-F. Mahfouf, 2014: Operational Implementation of the 1D+3D-Var Assimilation Method of Radar Reflectivity in the AROME Model. Monthly Weather Review. Vol. 142. 1852-1873.

IMPLEMENTATION AND OPERATIONAL USE OF A HETEROGENEOUS RADAR NETWORK IN THE COMPLEX OROGRAPHY OF ABRUZZO REGION

Errico Picciotti[1], Saverio Di Fabio[1], Stefano Barbieri[1], Mario Montopoli[2], Renato Zauri[3], Andrea Cipollone[3], Francesco Luigi Rossi[3] and Frank Silvio Marzano[1,4]

[1] *CETEMPS, University of L'Aquila (Italy)*
[2] *CNR, Institute of Atmospheric Sciences and Climate of Rome (Italy)*
[3] *CFA, Functional Centre of Abruzzo Region Civil Protection (Italy)*
[4] *DIET, University of Rome (Italy)*
(Dated: 22 June 2018)

1 Introduction

This work shows recent advancements in terms of structure, processing and mosaicking methods specifically implemented for the local radar network covering the Abruzzo region, in central Italy. The hydrological risks are further enhanced by the complex topography of Abruzzo region, which is characterized by high mountainous, relatively small catchments, river basins and Adriatic Sea side. Complex orographic environment introduces additional difficulties in the matching of observations of the same phenomenon from different radars during the mosaicking.

The Abruzzo radar network is constituted by two single-polarization radars at C- and X-band, respectively and by two dual-polarization X-band radars jointly operated by the CFA and CETEMPS, respectively. Moreover in the south part of Abruzzo region, a dual-polarization C-band radar managed by the Italian Department of Civil Protection, is also operative.

Functional Centre of Abruzzo Region (CFA) is part of Civil Protection Regional System with functions of forecast, monitoring and warning regarding meteorological, hydrological, hydraulic and wildfire risk. It is the regional meteorological service for Abruzzo and includes the institutional duties of the daily operational meteorological surveillance. For its activities, CFA uses data in real time from the hydro-meteorological network of Abruzzo Region and from radar network. The Center of Excellence (CETEMPS) of the University of L'Aquila is a joint effort of the Dept. of Physics and the Dept. of Electrical Engineering, funded by the Ministry of Education and University of Italy starting from 2001. The research activity concerns mainly remote sensing, atmospheric physics, meteorology and hydrology. It support the CFA in the the daily operational meteorological forecast and surveillance.

The Abruzzo radar network design (section 2) was driven by the needs of the CFA for the detection and warning of severe weather and related hydrological risks, which requires high redundancy, availability and accuracy of radar data. As known, any fruitful usage of network radar data either for quantitative precipitation estimation or just for operational monitoring, must deal with a careful check of data quality. This aspect is particularly critical for networks with heterogeneity radar having different system features. In this respect, a dedicated algorithmic chain, able to process raw data, enhance their quality, extract from them accurate and useful hydro-meteorological products have been developed and customized for the different installations (section 3). The mosaicking procedure is presented and some merging strategies of reflectivity data have been tested in the composite domain (section 4) in real-time and on archived data cases, in diverse storm regimes. Two case studies occurred on May 3, 2018 and June 8, 2018 are presented and discussed (section 5).

Conclusions and future developments are provided in the last section.

2 The Abruzzo Region Radar Network

The Abruzzo radar network is constituted by four radars located at the sites of M. Midia, Cepagatti, Tortoreto and L'Aquila respectively. The main criteria taken into account to support the choice of the sites were:
1) identification of priority coverage areas for population centers based on the expected paths of storms; 2) environmental impacts, terrain features and local obstructions; 3) electromagnetic interference; 4) financial resources and costs; 5) communications to the site, namely, accessible roads, electrical lines, phone lines enabled for data connections, water supply, etc.

During 2006 a new project for installing a C-band weather radar in Central Italy, at Monte Midia site, has been successfully accomplished. The site is at the border between the Abruzzo and Lazio regions in Central Italy. Mt. Midia top height is at 1710 meter and covering most Central Italy, including the Abruzzo inland and the urban area of Rome. The project, sponsored by the Italian Department of Civil Protection (DPC), has been a synergic work, coordinated by the CETEMPS and including both regional authorities (CFA) and Italian companies (Telespazio, Icarus and Eldes) [Marzano, 2012]. It's part of the Italian operational weather radar network and it's jointly operated by the CFA and CETEMPS.

In the framework of two European projects, AdriaRadNet [Picciotti, 2014] and CapRadNet (successfully completed and funded by IPA Adriatic CBC Programme) and spin-off activities of HYDRORAD project [Picciotti, 2013] (successfully

completed and funded by Seventh Framework Programme, FP7) three new X-band radar systems have been installed in Abruzzo Region. One X-band radar has been installed in 2012 at L'Aquila, another in 2014 at Tortoreto and the third one at Cepagatti five km far from Pescara airport in 2017. These systems cover almost all the regional coasts and partially overlap and complement the existing national radar network, their choice derived from a balance between the available economic and financial resources of the related projects and the need for qualitatively valuable observations, related to the CFA activities for civil protection purposes. All these systems are jointly operated by the CFA and CETEMPS.

Moreover, in the south part of Abruzzo region, a dual-polarization C-band radar, located in Tufillo, has been installed and managed by the Italian Department of Civil Protection (DPC). The Tufillo radar is operative since 2008 and it's part of the Italian operational weather radar network [Vulpiani, 2008]. The latter is currently composed of 21 systems, managed by a federation of national and regional bodies including the Department of Civil Protection (DPC), the Air Force, the regional weather services, and the National Aviation Authority. Composite products such as Constant Altitude Plan Position Indicator (CAPPI), Vertical Maximum Indicator (VMI), Surface Rainfall Intensity (SRI) and Surface Rainfall Total (SRT) are generated in real time by DPC and disseminated at national and regional level.

Some general technical specifications of all radar systems installed in Abruzzo Region are shown in Table 1 while their location and pictures are given in Figure 1.

Table 1: Technical specifications of the installed radars in Abruzzo Region

Features	Units	M. Midia	Tortoreto	Cepagatti	L'Aquila	Tufillo
Owner	---	CFA	CFA	CFA	CETEMPS	DPC
System Model	---	DWSR-93C	WR-25XP	WR-10X	WR-25XP	Meteor 660C
Latitude	[deg]	42,06	42,78	42,40	42,37	41,94
Longitude	[deg]	13,18	13,94	14,14	13,35	14,25
Height (over sea level)	[m]	1710	10	50	665	692
Polarization capability	---	NO	YES	NO	YES	YES
Band	---	C	X	X	X	C
Peak Power	[kW]	250	25	10	25	500
Antenna Gain	[dB]	40,5	35	35	35	45
Beamwidth	[deg]	1,6	3,0	3,0	3,0	1,0
Temporal resolution	[min]	10	10	10	10	10

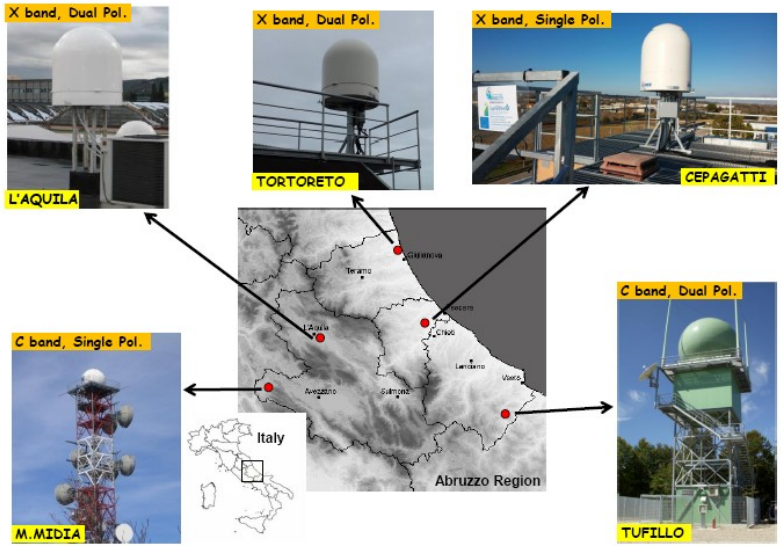


Figure 1: Location and pictures of the radars installed in Abruzzo Region in the center of Italy

3 Radar data pre-processing chain

There are numerous sources of errors that may affect radar measurements. Among these, the most important are the following: radar calibration, ground clutter, beam blockage, wet-radome attenuation, rain attenuation, beam-broadening, non-uniform beam filling, vertical variability of precipitation and WLAN interferences. At X-band, attenuation may generate detrimental effects in quantitative precipitation applications, especially in convective events. Dual-polarization radars have

the potential to provide additional information to overcome many of the uncertainties in contrast to situation when only the conventional reflectivity Z and Doppler information are available.

Due to the complexity of radar measurement and processing it is practically impossible to eliminate these errors completely or at least to evaluate each error separately. On the other hand, precise information about the data reliability is important for the end user.

Before the compositing, once a raw volume scan is fully received, the data are processed through a specific processing chain called RAMP (Radar Advanced Multiband Processing) to eliminating, compensating or at least to identifying the most common error sources for each device (Figure 2).

The employed algorithms are functionally divided into two paths: one for data corrections and the second for data quality characterization. Particular quality algorithms can be switched on or off in the scheme. Processing by means of data correction algorithms allows the reduction of uncertainty in the data, whereas quality characterization algorithms generate a map of total quality index (TQI) that can be attached to the data [Osrodka, 2012].
The scheme should be an objective procedure, i.e. independent of platform (quality of data from different radar could be easy to compare) and the final application of the analysed data. Although it is not possible to make all Abruzzo region radar systems identical, it is possible to ensure harmonized technical and software platforms on which each radar data can be processed.

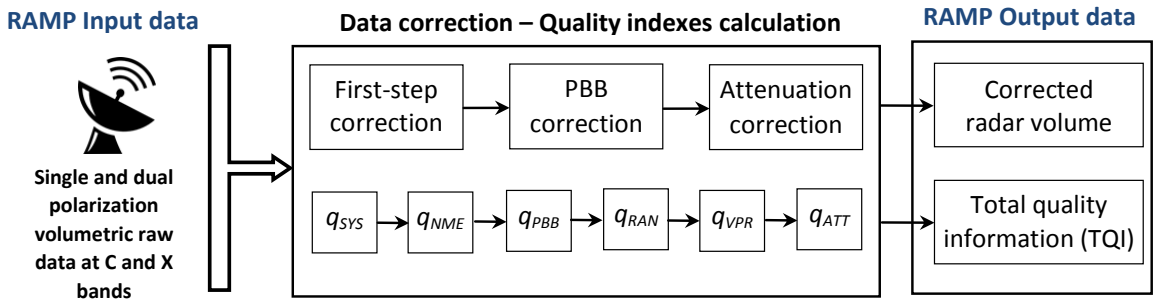


Figure 2: Weather radar data pre-processing chain (RAMP)

The main steps of data correction and quality characterization within the proposed RAMP chain can be summarized as follows:

3.1 First-step correction

For each radar, a specific first-step correction of volumetric data is applied. Ground-clutter, specks, WLAN interference, biological and others non-meteorological echoes have been removed from the reflectivity (Z) field by exploiting the textural spatial correlation of meteorological targets with respect to artifacts [Barbieri, 2017]. Uncertain data are flagged but not removed. For dual-polarization systems a median smoothing filter and bias correction has been applied to the differential reflectivity (Z_{dr}), a compensation is applied to the correlation coefficient (ρ_{hv}) and the differential phase (Φ_{dp}) has been processed by a multistage smoothing filter for K_{dp} estimation [Barbieri, 2014].

3.2 Partial beam blockage correction

Due to the complex topography of Abruzzo region, which is characterized by high mountainous, all radars system suffered by beam blockage along several direction especially at the lower elevation scan. Thus, the second step of the pre-processing chain is the partial beam blockage (PBB) correction. When a radar beam intercepts a mountain, two situations are possible: 1) only part of the beam cross section illuminates the intercepted topography (partial blockage), or 2) the radar beam is completely blocked (total blockage). An occlusion of the beam of the order of less than 10% is considered negligible and is not corrected while an occlusion that exceeds 60% is rejected. If radar bins are partially shielded between 10% and 60% the radar reflectivity factor measurements is modified by adding 1-4 dB depending on the degree of occultation [Bech, 2003].

3.3 Path attenuation correction

For single -polarization systems the attenuation is computed with an iterative procedure that involves the estimation of the two-way path integrated attenuation (PIA) along the entire beam path [Osrodka, 2012].

For dual polarization systems the PIA is calculated by using Φ_{dp} which is filtered as described in previous section:

$$_{hc} = \ _{h} + \alpha\left[\Phi_{dp}(r_N) - \Phi_{dp}(r_0)\right] \qquad _{drc} = \ _{dr} + \beta\left[\Phi_{dp}(r_N) - \Phi_{dp}(r_0)\right] \tag{1}$$

In (1) Z_{hc} and Z_{drc} are the corrected reflectivity and differential reflectivity, α = 0.28, β = 0.04 for X-band and α = 0.08, β = 0.03 for C-band while r_N and r_0 are, respectively, the farthest and the initial radar bin along the path.

It is worth mentioning which at X-band frequencies, path attenuation of radar signal caused by rain can be quite significant, and especially in case of heavy rain, it may reach several dB.

3.4 Total quality information

Assuming the radar systems are well maintained, the quality analysis has been focused on the following error sources: radar technical parameters, non meteorological echoes, beam blocking, distance from the radar, attenuation and height of measurement (Table 2). For each error an individual quality index (q_i) is calculated in each radar pixel through appropriate tests, giving as output an unitless quantity expressed by numbers from 0 (bad quality) to 1 (excellent quality).

Table 2: Group of quality index and related source of errors to which they refers

Quality Index	Source of error	Note
q_{SYS}	Radar system technical parameters	It is static within the whole radar range as well as in time and taken into account several factors as in [Osrodka, 2012]
q_{NME}	Non meteorological echo	Pixel affected by non meteorological echoes are removed, for the uncertain pixel a value of 0.5 is applied, the others data are set to 1.
q_{PBB}	Partial beam blocking	It is computed from the corrected data taking into account the PBB value as in [Barbieri 2017]
q_{RAN}	Long range measurement	This quality factor decreases with increasing distance from the radar, it is computed as in [Rinollo et al. 2013]
q_{ATT}	Rain path attenuation	It is computed from the corrected data taking into account the PIA value as in [Barbieri 2017]
q_{VPR}	Inhomogeneous vertical profile of reflectivity	The compensation of this effect is not performed in RAMP, the quality index associated is estimated as in [Friedrich et al. 2006]

The final data quality in each radar pixel can be retrieved by combining all the individual quality indicators. A multiplicative combination rule is here used:

$$TQI = q_{SYS} \cdot q_{NME} \cdot q_{PBB} \cdot q_{RAN} \cdot q_{ATT} \cdot q_{VPR} \quad (2)$$

In the Figure 3 is shown an example of RAMP application at M. Midia radar data for the rainy event occurred in Italy on September 1, 2017.

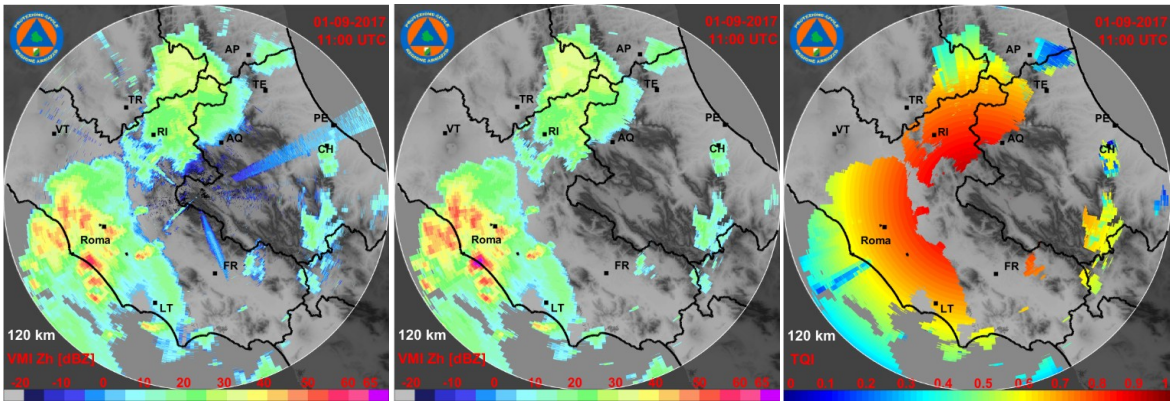


Figure 3: An example of RAMP application: Monte Midia reflectivity before (left) and after (center) data correction, the total quality index (TQI) associated is also shown (right)

4 The mosaicking procedure

In operational configuration the implemented mosaicking software takes as input a complete volume scan from L'Aquila (AQ), M. Midia (MM), Cepagatti (CE) and Tortoreto (TO) radars are routinely collected every 10 minutes with synchronised start time.

As described in the previous section once a radar volume scan is fully received, the data are pre-processed through RAMP chain in the native radar (spherical) coordinates. After that, single radar reflectivity data are remapped from their native

spherical coordinates to a cartesian coordinates system and then some valuable products (such as VMI, VIL, SRI) are generated at single radar level (Figure 4, left panel).
These products derived from the different radar systems are remapped onto a common cartesian 2D grid with a resolution of 0.4 x 0.4 km^2 and with a composite area of about 83.000 km^2, see (Figure 4, right panel) where the coverage area utilized for each device (do not considering obstacles due to orography) is also depicted.
The mosaicking domain was defined taking into account the technical characteristics of the radars, their geographical location and the peculiarities of the territory concerned, for each radar, the coverage area was set compatible with the size of the mosaicking domain.
The DPC composite products, if temporally available, are also used as input data by cutting out on a 60 km domain from Tufillo (TU) radar site to optimally cover the southern part of the region.

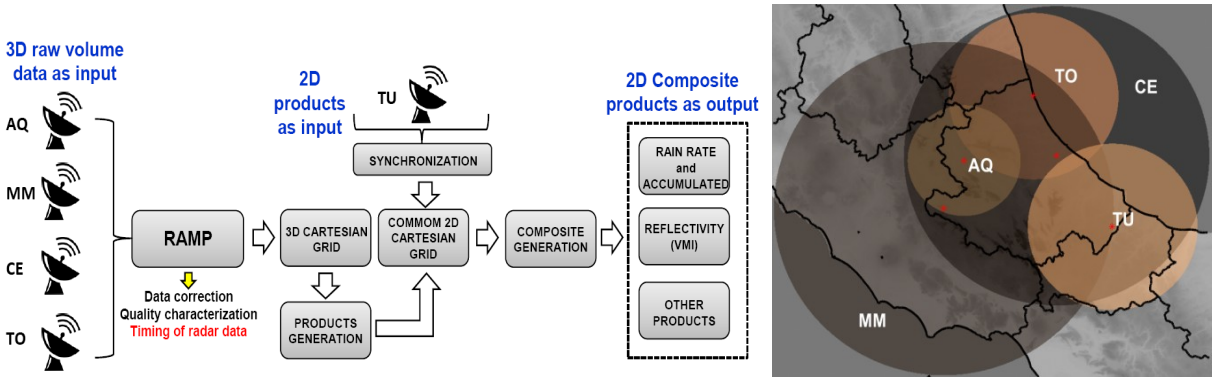


Figure 4: An overview flowchart of the 2D radar mosaic system (left) and the composite domain with the maximum coverage area chosen for each radar system (right)

After the remapping some 2D composite products are created in real time each 10 minutes. It is worth mentioning which 2D mosaic is the simplest compromise, to reduce the computational complexity and the data rate although 2D products lack the height information that is critical for severe weather forecasting. This is the approach suggested by [Charba, 2005] and carried by the U.S. National Weather Service to create mosaics operationally at 2 km resolution.
Selecting an optimal way to merge radar data is significant and must consider a number of factors such as the size and shape of the domain of interest, number and location of the network's nodes, and the resolution and type of the desired products. Our goal is to assess how different merging techniques can improve the total quality of reflectivity over the composite domain of figure 4. There are several ways to generate a composite of radar data, in Table 3 are resumed the methods still under testing. The latter have been tested in real-time and on archived data cases, in diverse storm regimes.

Table 3: Different merging strategies tested in the composite domain

	Method	Description
1	Assign to the common pixel the mean or maximum value of reflectivity	[Zhang ,2004]
2	Assign to the common pixel a value weighted with the distance from the radars, using linear and exponential weighting functions	[Einfalt, 2012] [Zhang, 2004]
3	Assign to the common pixel the value corresponding to the maximum final quality (TQI) calculated by RAMP	[Fornasiero, 2006] [Peura, 2007]
4	Assign to the common pixel the value corresponding to the minimum PIA (path integrated attenuation) or minimum distance	[Domaszczynski, 2012]

Preliminary results show how the principle of Maximum Quality is a good compromise between the tested methods since it is comprehensive of the major problems affecting radar data.
In radar image composites, Maximum measurement value is a conventional choice for a compositing principle, however, even unreliable data is easily passed through. Another conventional principle of Average, has the advantage of compensating for data discrepancy; but at the same time, it tends to equalize the values especially in presence of convective cells.
The Minimum PIA gives variable results for the presence of radar systems with different wavelengths that provide a different attenuation correction.
Finally, the conventional Weighted Nearest-Radar composites are rather similar: the distance from a radar is used as a quality indication. Both weight monotonically decrease with range but the exponential weight decreases faster than the linear one: this causes underestimation in the farthest overlapping points of the mosaic.

5 Example of application in case studies

Two case studies with different weather regimes have been selected to apply the proposed merging strategies. The first one is a widespread event occurred on 3 May 2018. The second case, occurred on 08 June 2018, corresponds to a strong atmospheric instability that developed into several convective precipitation phenomena.

5.1 Event occurred on 3 May 2018

The case study of May 3, 2018, 10:40 UTC, refers to a phenomenon of low pressure located in the central Tyrrhenian area, characterized by widespread precipitation and strong winds coming from the eastern quadrants.
The event presents local precipitations of showers or thunderstorm nature, especially on the eastern slopes of the mountains.
This has been identified only by the Maximum method and by the Maximum Quality method, (Figure 5A and 5B) while the other cases show lower reflectivity.
The Maximum method, retaining the highest reflectivity intensities in the data fields, possibly mitigates attenuation losses due to regions of intense rainfall but could provide a biased estimate due to radars that provide higher reflectivity values as a result of calibration differences.
The applied methods do not impose any smoothing when creating a mosaic from multiple radars. However, discontinuities may appear at the boundaries of the radar range.
Figure 5D shows the lower reflectivity values in the overlapping area presumably due to low PIA values as expected in a widespread case.

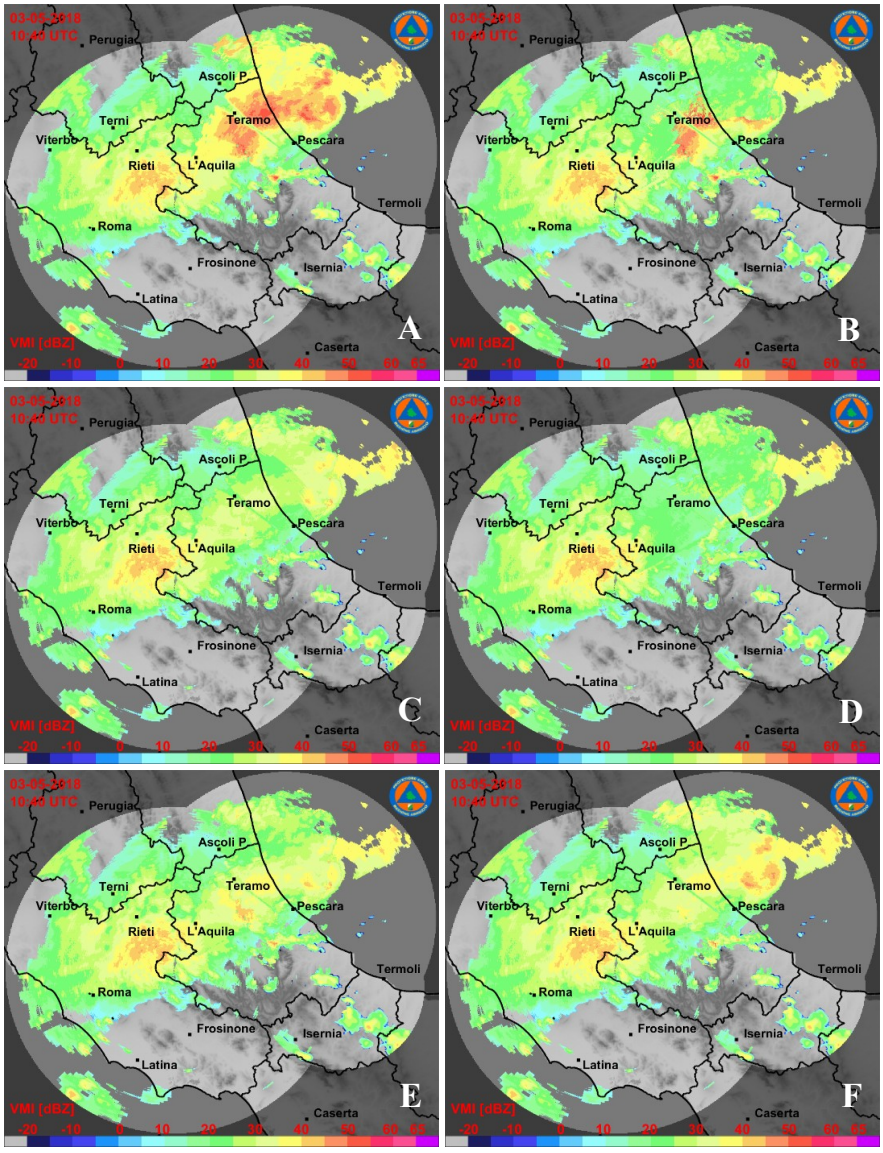


Figure 5: Example of reflectivity composite techniques in the composite domain on 3 May 2018 at 10:40 UTC. MAXIMUM reflectivity (A), MAXIMUM QUALITY (B), AVERAGE (C), MINIMUM PIA (D), EXPONENTIAL WEIGHTED with the distance (E) and LINEAR WEIGHTED with the distance (F)

5.2 Event occurred on 8 June 2018

The case study of June 8, 2018, 13:40 UTC, is part of a perturbation coming from the west that crossed central Italy in the previous hours and characterized by a strong atmospheric instability that has developed several phenomena with hail and thunderstorms appeared in the eastern composite domain.
Among the present radars, the X-band systems have a better characterization of the precipitation cells along the Adriatic coast, but sometimes may have partial loss of reflectivity signal due to the greater attenuation of the X-band wavelength, compensated by C-band radars in the overlapped observation area.
Visual comparison of Figure 6 panels shows discrepancies with respect to the different compositing techniques. The highest observed reflectivity values in convective cells are better reproduced in the panel 6A than in the other panels.
Moreover, the mosaics obtained with Weighted Nearest-Radar methods (Figure 6E and 6F) are more similar to each other, in particular showing an underestimation of the convective cells.
Figures 6B and 6D show a better representation of the cells, although the effect of the PIA influence both methods of mosaicking. In fact, both the Maximum Quality and the Minimum PIA algorithms use the minimum attenuation as quality indicator. For this reason, in case of strong attenuation, convective cells could be partially represented in the mosaic domain.

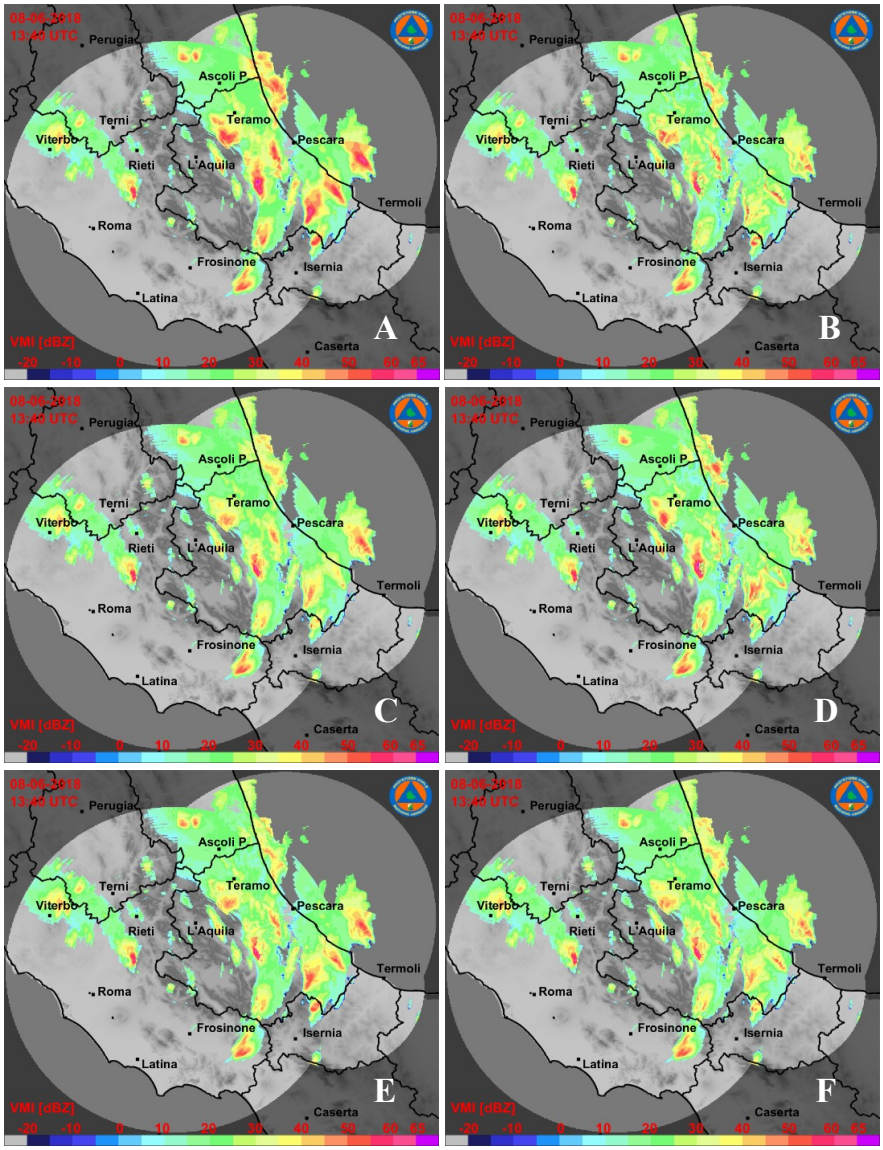


Figure 6: Example of reflectivity composite techniques in the composite domain on 8 June 2018 at 13:40 UTC. MAXIMUM reflectivity (A), MAXIMUM QUALITY (B), AVERAGE (C), MINIMUM PIA (D), EXPONENTIAL WEIGHTED with the distance (E) and LINEAR WEIGHTED with the distance (F)

6 Conclusion

The primary justification for a weather radar network in Abruzzo Region is the support on the CFA activities for detection and warning of severe weather and related hydrological risks. The Abruzzo radar network is constituted by five systems at C- and X band which operate in a complex topography, in such circumstances, a part from path attenuation that might be severe at X band, the quality of the retrieved radar products is further conditioned by the presence of topographic obstacles. Raw volume scans are processed through a specific processing chain called RAMP to compensating or at least to identifying the most common error sources for each device. That to ensure harmonized technical and software platforms on which each radar data, with different features, can be processed before the composite. A 2D radar mosaic system has been implemented in which, all data are routinely collected every 10 minutes with synchronised start time and the related composite products are generated in real time as output.

In this work the performances of the different mosaicking methods have been qualitatively assessed, the quality information is prone to be used into composition procedures especially when the quality function is comprehensive of the major problems affecting radar data.

Future developments will be devoted to include in the analysis rain gauge network data to provide performance evaluation with ground reference information [Fornasiero, 2006], new algorithms for adjusting the radar composite in real-time are also currently in progress as well as the tests of 3D compositing methods.

Acknowledgement

This work is partly supported by EU co-financing and the Interreg Italy-Croatia CBC Programme through the AdriaMORE project.

References

Barbieri S., Picciotti E., Montopoli M., Di Fabio S., Lidori R., Marzano F.S., Kalogiros J., Anagnostou M. and Baldini L. "Intercomparison of dual-polarization X-band miniradar performances with reference radar systems at X and C band in Rome supersite" Proc. ERAD2014, Garmisch-Partenkirchen (Germany), 1-5 September **2014**.

Barbieri S. "Testing of dual-polarization processing algorithms for radar rainfall estimation in tropical scenarios" HSAF, Visiting Scientist H_AS17_01 report, **2017**.

Bech J., Codina B., Lorente J. and Bebbington D. "The sensitivity of single polarization weather radar beam blockage correction to variability in the vertical refractivity gradient", J. Atmos. Oc. Tech., vol. 20, pp. 845-855, **2003**.

Charba J. and F. Liang "Quality control of gridded national radar reflectivity data," in 21st Conf. on Wea. Analysis and Forecasting/17th Conf. on Numerical Wea. Prediction, (Washington, DC), p. 6A.5, Aug. **2005**.

Domaszczynski P. "Performance evaluation of a network of polarimetric X-Band radars used for rainfall estimation." PhD diss., University of Iowa, **2012**.

Einfalt T., Lobbrecht A., Leung K. and Lempio G. "Preparation and evaluation of a Dutch-German radar composite to enhance precipitation information in border areas", Journal of Hydrologic Engineering, Vol. 18 Issue 2, **2012**.

Friedrich K., Hagen M., and Einfalt T. A quality control concept for radar reflectivity, polarimetric parameters, and Doppler velocity, J. Atmos. Ocean. Tech., 23, 865–887, **2006**.

Fornasiero A., Alberoni P. P., Amorati R., Marsigli C. "Improving the radar data mosaicking procedure by means of a quality descriptor." In ERAD Publication Series, volume 3, pages 378–341, **2006.**

Marzano F.S., Ronzoni M., Montopoli M., Di Fabio S., Picciotti E. and Vulpiani G. "Statistical characterization of C-band single-polarization radar retrieval space-time error in complex orography" Proc. of ERAD2012, Tolouse (France), 25-29 June **2012**.

Osrodka K., Szturc J. and Jurczyk A. "Chain of data quality algorithms for 3-D single polarization radar reflectivity (RADVOL-QC system)", Meteorol. Appl., DOI: 10.1002/met.1323, **2012.**

Peura M., and J. Koistinen "Using radar data quality in computing composites and nowcasting products" 33rd Conference on Radar Meteorology, Cairns, Australia, American Meteorological Society, **2007.**

Picciotti E. and other authors "Coupling X-band dual-polarized mini-radars and hydro-meteorological forecast models: the HYDRORAD project", Nat. Hazards and Earth Syst. Sciences, vol. 13, pp. 1229-1241, **2013**.

Picciotti E. et al. "The ADRIARadNet project: ADRIAtic integrated RADar-based and web-oriented information processing system NETwork to support hydrometeorological monitoring and civil protection decision" Proc. ERAD2014, Garmisch-Partenkirchen (Germany), 1-5 September **2014**.

Rinollo A., Vulpiani G., Puca S., Pagliara P., Kaňák J., Lábó E., Okon Ł., Roulin E., Baguis P., Cattani E., Laviola S., and Levizzani V. "Definition and impact of a quality index for radar-based reference measurements in the H-SAF precipitation product validation" Nat. Hazards Earth Syst. Sci., 13, 2695-2705 **2013**.

Vulpiani G. and other authors "The Italian radar network within the national early-warning system for multi-risks management" Proc. of ERAD08, Helsinki, 30 June-4 July **2008**.

Zhang, J., K. Howard, and J. J. Gourley "Constructing Three-Dimensional Multiple-Radar Reflectivity Mosaics: Examples of Convective Storms and Stratiform Rain Echoes". Journal of Atmospheric and Oceanic Technology, **22,** 30-42, **2004**.

ANALYSIS OF HAIL EVENT IN FIELD OF REFLECIVITY AND DIFFERENTIAL REFLECIVITY *131

S.STEVANOVIĆ[1] (svetlana.stevanovic@hidmet.gov.rs)
S.BILJIĆ[1], M.VASIĆ[1], G.BOGUNOVIĆ[1]
[1]Republic Hydrometeorological Service of Serbia, Kneza Viseslava 66,
11030 Belgrade, Serbia

Introduction

The aim of the analysis is to detect spatial characteristics and intensity in the field of reflectivity and differential reflectivity, their comparison with the occurrences of small hail and hail, as well as the potential of the storm to produce the hail. The reason for the resulting analysis is stormy weather on the territory of two radar centers in Central Serbia, which are close to the position of Dual–pol Doppler radar Jastrebac. Hail and small hail, as well as damage from individual storms, were recorded. During the analysis products MAX, CAPPI Z, ZDR, CC (RohHV), KDP and ZHAIL, were used. Product analysis is dictated by the values of reflexivity, the probability of occurrence of hail and temperature conditions. Three dates were selected with recorded damage from hail and small hail of different intensity. The dates are May 3rd, July 22nd and August 12th. In order to make the analysis as precise as possible, products are defined as follows:

VIL1- observes the precipitation zone, VIL2 – observes the area above zero isotherms. VIL products were made for two layers (VIL1 for a layer up to 3.5 km and VIL2 for a higher layer from 4 to 10 km, taking into account the height of the zero isotherm, based on the prognostic isotherms of the ECMWF model for the current day and emagrams of the ETA model. For the VIL product, values of convective precipitation parameters are taken.

ZHAIL - accounted for above 80% of the values, in order to increase reliability compared to recorded occurrences of hail and small hail on the ground.

Z, ZDR, CC (Rohv), KDP - are primarily observed in the zone of maximum reflexivity (45-60 dBZ and higher data values), which should signify the presence of the hail. These products are made on height of 1km, in order to compare with the actual phenomena of the hail and small hail recorded on the radar centers. The temporal continuity was rarely disturbed by the lack of a scan at certain time intervals (a technical problem in the radar operation).

All occurrences of the hail and small hail are recorded locally, but time period are matched here for analysis with UTC time for which products are made. The time period for which the analysis was carried out is determined by the life cycle of the storm and the product ZHAIL. Only those with a probability of over 80% were taken for the observed storms, and then reduced for storms that have caused damage. The tables, analyzes and conclusions are given only for storms that have caused damage.

Time data for the life cycle of all storms relate only to recorded data in the territory of the centers of Besnjanja and Krusevac. Actual life time for some storms is longer, but storms are outside the observed territory. Note: The values of ZDR in the tables 1.,2.,3. are given for the immediate surroundings of the spot where the appearance of the hail and small hail is observed, for CC (RhoHV) and KDP values are given in somewhat wider area within the indicated high reflexivity.

Discussion

On May third, a total of 4 storms give rise to damage. Storms that caused damage are multicell storms (the number is given in the table.1) which had their own life cycle from 10 to 16 UTC. One of the parameters of the analysis is the zero isotherm. The prognostic isotherms are according to ECMWF for 12 UTC is H [0] = 3.6 km. Emagrams of the ETA model at 09, 12 and 15 UTC show successive values of 602J / kg, 1113J / kg and 1254J / kg. In the time of CAPE maximum, the life cycle of the storm No.27 was the one that gave it the greatest damage. Fig.1 emagram 15 h for 03.05.2017.

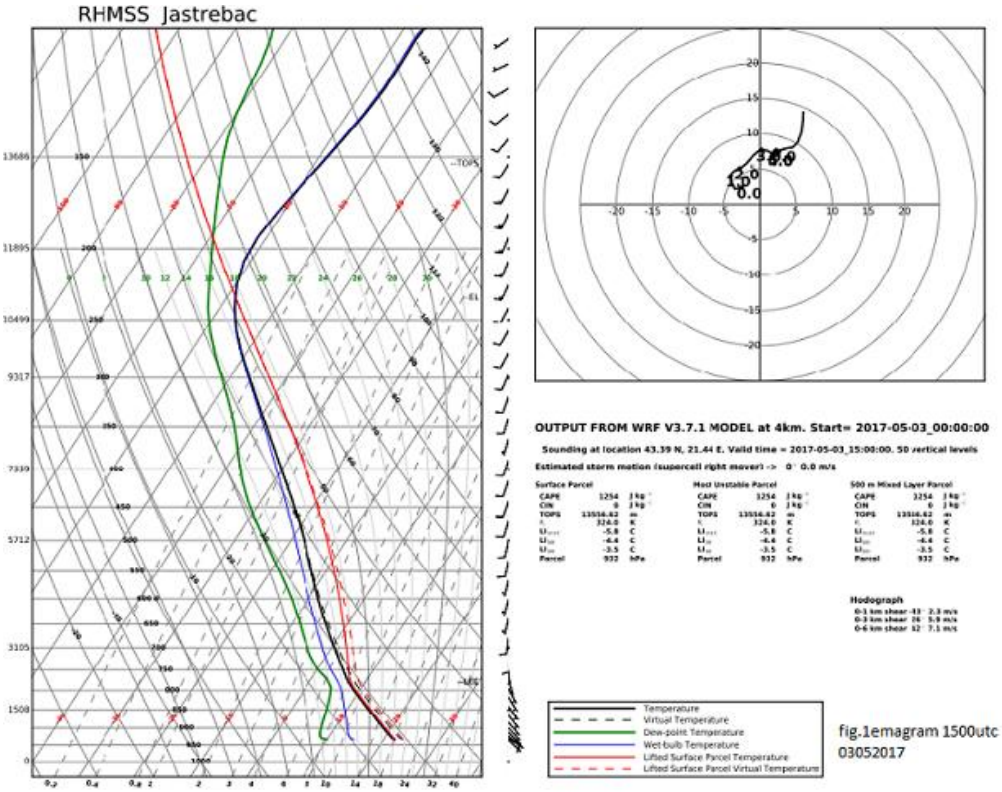


fig.1emagram 1500utc
03052017

From the table .1 values, (products VIL2, MAX), it can be noticed that the greatest potential for the production of the hail has storm No.27 and then storm No. 13., but realized potential for hail production it is shown from the values of the products VIL1 and ZDR. Intensity of the precipitation zone is in compliance with the recorded phenomena of the hail.

For the storms No. 12 and No. 4, there are significantly lower values of VIL2 and VIL1 that indicates much lower potential for the production of the hail, which is confirmed by the values of KDP that indicate low water content. In the same time values of the product CC (RhoHV) indicate mainly the melting of the hail and small hail. In the case of reflection No. 4 for terms 1050 and 1055 values for ZDR are relatively high, but the appearance of a dry hail is recorded, and there is a discrepancy that should lead to further check.

Also for the storm No. 13 the value for ZDR at 1415 is high, which does not coincide with the observed phenomenon, but in the next 1420 values for the ZDR coincide well, so the observed phenomenon cannot be reliable. KDP for storm No. 13 is in a larger range than in the two

preceding cases (storm No.4and12), which implies melting and increased water content, and this is confirmed by the product VIL1.
For the storm No.27 at 1505, the small hail and rainfall was recorded, while for other time period dry hail and small hail, and both with rain, which is to a great extent confirmed by the values for ZDR. The values for CC (RhoHV) also indicate melting , but that does not necessarily have to be in contradiction the phenomena, while the values of the KDP implies melting and increased water content, and that is confirmed by the product VIL1. Some spatial characteristics and the likelihood of the appearance of the hail are given in the following figures: 2 and 4. Spatial characteristic for the storm in the table are very similar, but some different occurred for storm No.22, which is not in the table. Only storm for which phenomena of hail and small hail has not been recorded on May third, it is one with a clearly visible sign of TBSS (storm No.22). This storm develops before storm No. 27(in the immediate vicinity) and in mature stage splits in to a two cells. Right cell moves to the NE, and left to the NW and merges with cloud mass in which storm No.27 develops. Fig.3. Hail probability is on fig.4.

Table1.

Hail/small hail time	StormNo.12 /LS No.	ZDR (dB)	CC(RhoHV)	KDP deg/km	cappiZ(dBZ)	MAX(dBZ)	VIL1(mm)	VIL2(mm)
1350sh	95	2 - 3	0.87 - 1.0	-0.6 - 1.4	47 - 55	47- 55	7.1 - 17.1	17.1 - 71
1355sh	95	1 - 3	0.87 - 1.0	-1.0 - 1.4	47 - 60	47 - 60	7.1 - 17.1	17.1 - 41.4
1400h	95,116	3 - 4	0.87 - 1.0	-1.0 - 2.6	47 - 60	47 - 60	17.1 - 29.1	17.1 - 41.4
1405h	95	2 - 4	0.87 - 1.0	-1.0 - 1.0	47 - 60	47 - 60	17.1 - 29.1	17.1 - 71
Hail/small hail time	Storm No.4 /LS No.	ZDR (dB)	CC(RhoHV)	KDP deg/km	cappiZ(dBZ)	MAX(dBZ)	VIL1(mm)	VIL2(mm)
1025gr,sh,h	406	1 - 5	0.87 - 1.00	0.2 - 1.4	47 - 60	47 do 60	5,1 - 17,1	17.1 - 41.4
1030h	406	1 - 4	0.87 - 1.00	-0.2 - 1.0	47 - 55	47 do 55	7.1 - 17.1	17.1- 29.1
1050h	403	3 - 4	0.87 - 1.00	-0.6 - 1.4	47 - 55	47 do 55	7.1 - 17.1	7.1 - 17.1
1055h	403	3 - 4	0.87 - 1.00	-0.6 - 1.0	47 - 55	47 do 55	7.1 - 17.1	17.1 - 29.1
Hail/small hail time	StormNo.13 /LS No.	ZDR (dB)	CC(RhoHV)	KDP deg/km	cappiZ(dBZ)	MAX(dBZ)	VIL1(mm)	VIL2(mm)
1325sh	412	0 - 4	0.87 - 1.0	-0.2 - 3.0	47 - 60	47 - 60	17.1 - 29.1	29.1 - 71
1330sh,h	412,409	3 - 4	0.87 - 1.0	-0.6 - 2.2	47 - 55	47 - 55	17.1 - 29.1	29.1 - 100
1335sh,h	412 ,403,409	3 - 4	0.87 - 1.0	-0.6 - 2.2	47 – 60	47 - 60	17.1 - 41.4	29.1 - 100
1340h	412, 403	3 - 4	0.87 - 1.0	-0.6 - 3.0	47 – 60	47 - 60	17.1 - 41.4	29.1 - 41.4
1415sh	402	4 - 6	0.87 - 1.0	-0.6 - 1.4	47 – 60	47 - 60	17.1 - 41.4	17.1 - 41.4
1420sh	402	1 - 4	0.87 - 1.0	-1.0 - 1.4	47 - 55	47 - 55	12.1 - 17.1	17.1 - 41.4
Hail/small hail time	StormNo.27 /LS No.	ZDR (dB)	CC(RhoHV)	KDP deg/km	cappiZ(dBZ)	MAX(dBZ)	VIL1(mm)	VIL2(mm)
1505 sh	324	3 - 5	0.87 - 1.0	-0.6 - 1.8	55 - 60	55 - 60	41.4 – 100	71 - 100
1510 h	307	2 - 4	0.87 - 1.0	-0.2 - 2.2	55 - 60	55 - 60	41.4 - 71	71 - 100
1515 sh,h	307,306	0 - 3	0.93 - 1.0	-0.2 - 2.2	55 - 60	55 - 60	41.4 - 71	71 - 100
1520h	307,306	2 - 4	0.87 - 1.0	-1.0 - 2.6	55 - 60	55 - 60	41.4 - 100	71 - 100
1525h	307,306	2 - 3	0.87 - 1.0	-1.0 - 1.4	55 - 60	55 - 60	41.4 - 71	71 - 100
1530h	306	1 - 3	0.87 - 1.0	-1.0 - 1.8	55 - 60	55 - 60	41.4 - 100	71 - 100
1535h	305	1 - 3	0.87 - 1.0	-0.2 - 2.2	55 - 60	55 - 60	29.1 - 41.4	29.1- 71

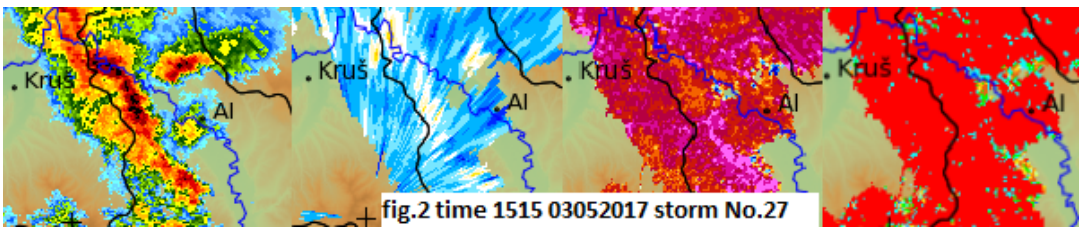


fig.2 time 1515 03052017 storm No.27

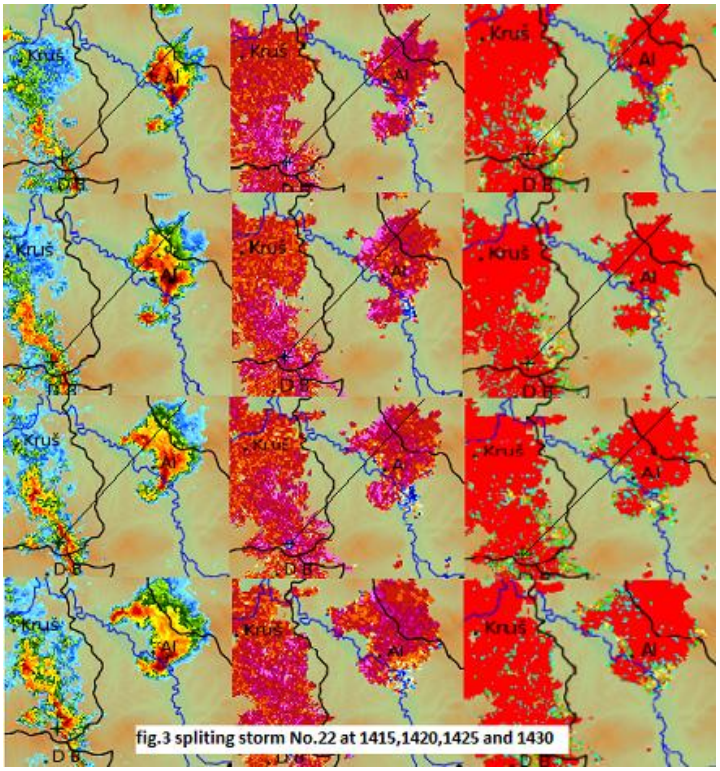


fig.3 spliting storm No.22 at 1415,1420,1425 and 1430

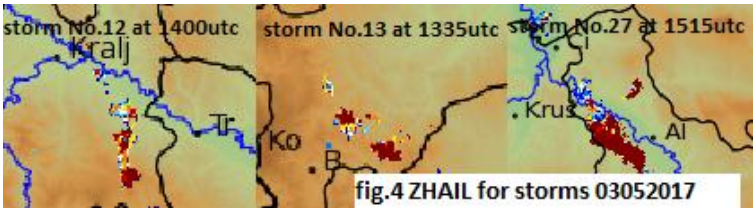


fig.4 ZHAIL for storms 03052017

On July 22nd, two storms give rise to damage.Storms that caused damage (the numbering is given in the table) had their own life cycle from 1737 to 2003 UTC. The storm No.5 is multicell storm and storm No.10 has some characteristics of the supercell storm. The prognostic isotherms are according to ECMWF for 18UTC, for this case H [0] = 4.8 km. Emagrams of the ETA model at 12, 15 and 18 UTC show successive values of 1336J / kg, 1800J / kg and 525J / kg, so the maximum is at 15UTC. The life cycle of both storms is after the CAPE maximum. Fig no.5 emagram 15 h for 22072017.

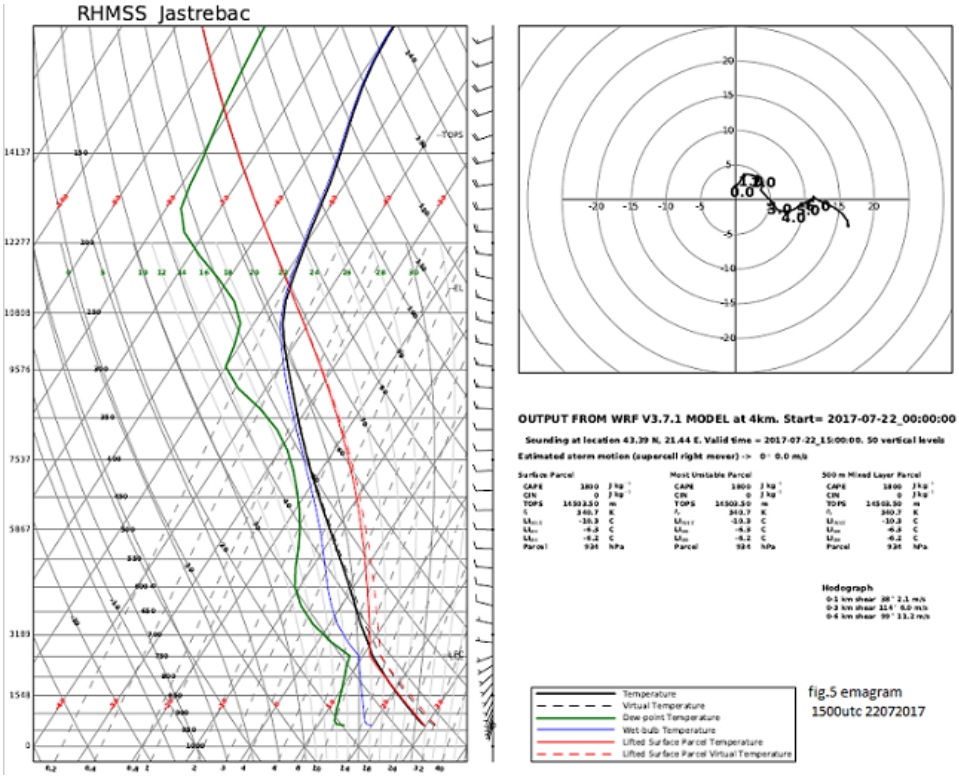
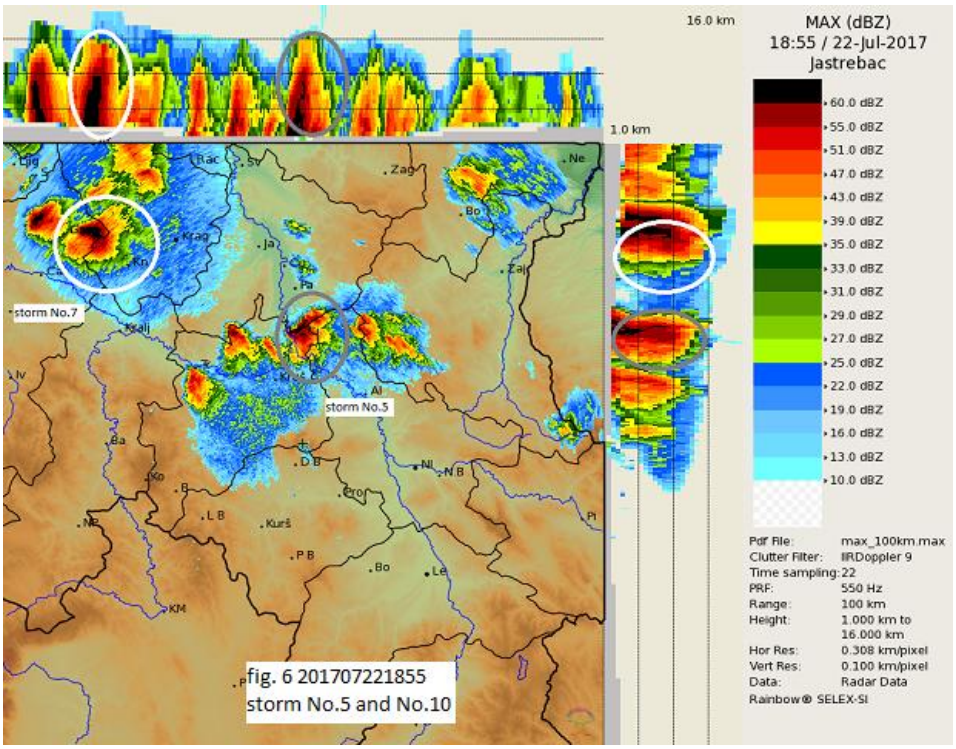


fig.5 emagram
1500utc 22072017

According to the values of the products MAX and VIL2 in the table 2., storms No. 5 and 10 shows more pronounced potential for the production of the hail and according to the values of the products CAPPI Z, VIL1 realized potential in the precipitation zone. Fig.6
Reflection No. 5 in all periods in which the hail occurs, have values for KDP and CC (RhoHV), which mainly refer to the melting hail, while the ZDR gives gradual decreases in value over time. Since the entire hail occurrence is with rain, the values of these products are more in line with these occurrences. However at 1840 station 61 that records the hail phenomenon more corresponds to the earlier term of 1825 or 1830 when the cloudy mass is closest to the station.
Reflection No. 10 is storm that also takes on the characteristics of the supercell, which is confirmed by the high values of the MAX products, CAPPI Z, VIL1 and VIL2. Values for KDP products vary slightly but refer to the melting of the hail, as well as the value for the product CC (RhoHV). The values of the ZDR product are relatively high, especially in the periods 1920 and 1925, but the occurrence of hail with rain is recorded in that period of time, so these values cannot be excluded. The values that are in question are related to the first two terms when the station 175 is far ahead of the cloud mass, so probably mistake appears in the time of occurrence i.e. report. Later this station is in cloudy mass and then the reported phenomena are realistic to be recorded. Spatial characteristics of TBSS for storm No.5, and hook echo for the storm No.10 are present. Fig.7, 8 and 9.

Table2

Hail/small hail time	Storm No.5 /LS No.	ZDR (dB)	CC(RhoHV)	KDP deg/km	cappiZ(dBZ)	MAX(dBZ)	VIL1(mm)	VIL2(mm)
1810 tbss	74	3 - 4	0.87-1.0	-0.6 - 1.8	50 - 55	50 - 60	29.1 - 41.4	41.4 - 100
1840 h	61	4 - 4	0.87-1.0	0.6 - 2.6	50 - 55	50 - 60	29.1 - 70	41.4 - 100
1845 h	61,68	1 - 3	0.80-1.0	-0.6 - 3.0	50 - 55	50 - 60	41.4 - 100	41.4 - 100
1850 h	68,281	2 - 3	0.87-1.0	0.2 - 3.0	50 - 60	50 - 60	29.1 - 100	41.4 - 100
1855	281	2 - 3	0.87-1.0	-1.0 - 3.4	50 - 60	50 - 60	29.1 - 100	41.4 - 100
Hail/small hail time	Storm No.10 /LS No.	ZDR (dB)	CC(RhoHV)	KDP deg/km	cappiZ(dBZ)	MAX(dBZ)	VIL1(mm)	VIL2(mm)
1840 sh	175	3 - 4	0.87-1.0	-0.2 - 1.8	30 - 47	47 - 55	1.2 - 7.1	17.1 – 41.4
1845 h,sh	**175,175**	3 - 5	0.87-1.0	-0.2 - 2.2	47 - 50	47 - 55	7.1 - 17.1	29.1 - 100
1850 sh	175	3 - 4	0.87-1.0	0.6 - 1.8	47 - 50	50 - 60	17.1 - 29.1	41.4 - 100
1855 h,sh	175,175	3 - 4	0.87-1.0	0.2 - 2.2	47 - 55	50 - 60	17.1 - 29.1	41.4 - 100
1920 h	164	4 - 5	0.87-1.0	-0.2 - 1.4	47 - 55	50 - 60	17.1 - 29.1	41.4 - 100
1925 h	164	4 - 5	0.93-1.0	-0.2 - 1.0	50 - 55	50 - 60	17.1 – 41.4	41.4 - 100
1930 h	164,167	2 - 4	0.87-1.0	-0.2 - 1.4	50 - 60	50 - 60	17.1 – 41.4	41.4 - 100
1935 h	165,167	3 - 4	0.87-1.0	-0.2 - 1.8	55 - 60	55 - 60	17.1 - 29.1	41.4 - 100
1940 h	167	1 - 3	0.87-1.0	-1.0 - 3.0	55 - 60	50 - 60	17.1 - 29.1	41.4 - 100



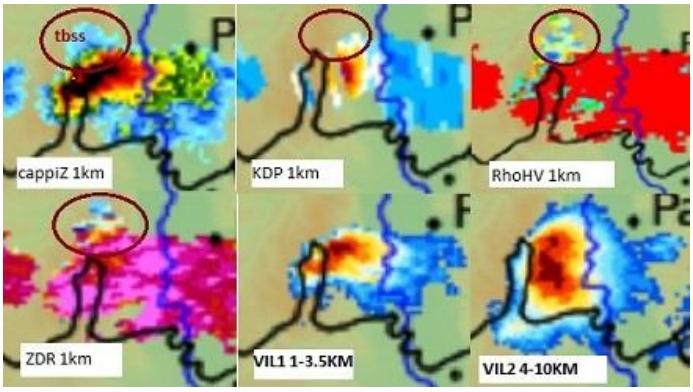


fig.7 storm No.5 22072017 at 1815UTC

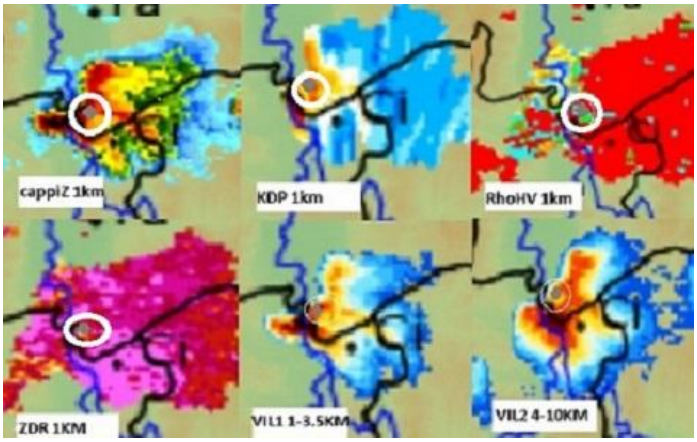


fig.8 storm No.5 22072017 at 1845 UTC hail on station 61

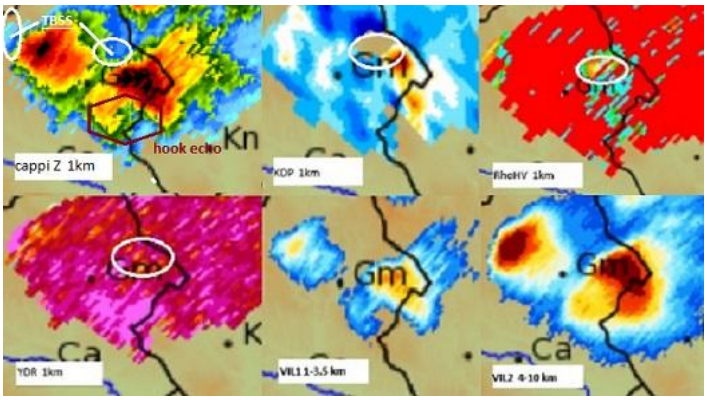


fig.9 storm No.10 22072017 at 1855UTC

<u>On August 12th</u> one storm gives rise to damage. Supercell storm that caused damage (the numbering is given in the table) had her own life cycle from 1737 to 2003 UTC (real time is longer,

but supercell is outside of the observed territory). The prognostic isotherms are according to ECMWF for 15UTC, for this case H [0] = 4.3 km. Emagrams of the ETA model at 12, 15 and 18 UTC show successive values of 1858 / kg, 1256J / kg and 1058J / kg, so the maximum is at 12UTC. The life cycle of the storm is after the maximum CAPE. Fig 10. emagram 12 h for 12082017.

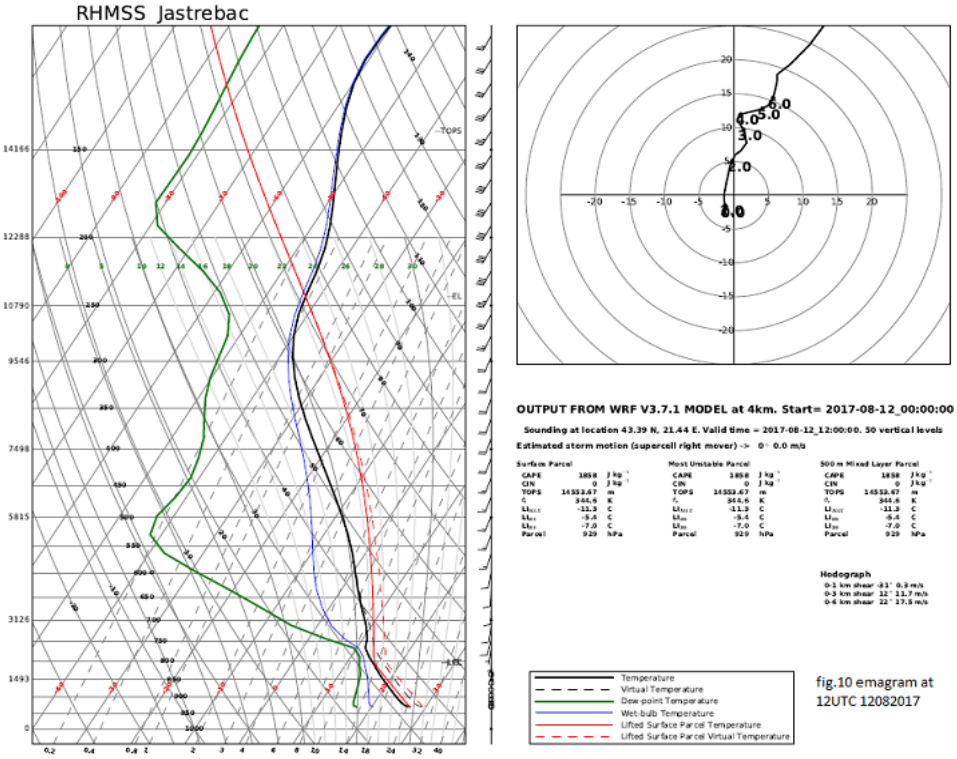


fig.10 emagram at 12UTC 12082017

According to the given values in the table, all recorded phenomena were are from the storm with high potential of production of the hail and small hail, as can be seen from the values of products MAX, CAPPI Z, VIL1 and VIL2. The products of KDP, CC, and ZDR also have significantly higher values, and the fact that all the phenomena of the hail and small hail are registered with heavy rain and shower fits in the values that are in the immediate vicinity of the place where the phenomenon is recorded. It should be noted that for ZDR observation sites values are rarely higher than 4dB, but the immediate environment has values up to 7dB. For this date other storms are multicell and there were no records of damage from it (so there are not in the table).

The table shows the first values for super cells that caused great damage in the territory of two neighboring municipalities Knic and Kragujevac. In the initial terms 1450 and 1455, there is a problem of identifying the value of the products given for the precipitation zone at a height of 1km, because the site is out of the cloudy mass, indicating the possibility of error in the observation period of the phenomenon or on precipitation from the anvil of the super cell. Already, the values of CC (RhoHV) refer to the melting hail, while the high values for the KDP refer to the shower as well as the ZDR values. Furthermore, in terms of 1505 and 1510, the values of CC (RhoHV) refer

also to a large hail, but the values of KDP and ZDR indicate melting and again on the shower, which is confirmed by recorded phenomena. In the period from 1515 to 1545, values for CC (RhoHV) and ZDR are changed in accordance with recorded occurrence of hail, but the KDP slightly deviates for the period 1530 when it reaches minimum. In that time 1530 three lunch station recorded hail size bigger than 2,5cm, so the KDP value it is not contrary to the values for CC (RhoHV) and ZDR. Values for CAPPI Z, VIL1 are still high, and confirm values for CC (RhoHV) and ZDR in precipitation zone. Some spatial characteristics are shown on fig.11 and 12.

Table3.

Hail/small hail time	Storm No.7 /LS No.	ZDR (dB)	CC (RhoHV)	KDP deg/km	cappiZ(dBZ)	MAX(dBZ)	VIL1(mm)	VIL1(mm)
1450 h,sh	19	2 - 7	0.80 - 1.0	-0.2 - 4.6	55 - 60	60	41.4 - 71	41.4 - 71
1455 h,sh	19	1 - 7	0.80 - 1.0	-1.0 - 5.0	60	60	71 - 100	100
1505h	175,164	3 - 7	0.73 - 1.0	-1.0 - 4.6	60 - 65	60 - 65	71 - 100	100
1510 h	13,161,163,175	0 - 4	0.73 - 1.0	-1.0 - 5.0	60 - 65	60 - 65	71 - 100	100
1515 h	13,22,29,160, 161,163,175	1 - 5	0.80 - 1.0	-1.0 - 3.0	60 - 65	60 - 65	71 - 100	100
1525 h	5,10,15,17, 29,160,161, 163	2 - 5	0.80 - 1.0	-1.0 - 3.0	60 - 65	60 - 65	71 - 100	100
1530 h	10,11,16,16,17,29,30,163	0 - 5	0.73 - 1.0	-1.0 - 2.6	60 - 65	60 - 65	71 - 100	100
1535 h	10,11,16	1 - 5	0.80 - 1.0	-1.0 - 3.8	60 - 65	60 - 65	100	100
1540 h	10	1 - 5	0.73 - 1.0	-1.0 - 3.8	60 - 65	60 - 65	71 - 100	100
1545 h	35	1 - 5	0.80 - 1.0	0.2 - 4.6	60 - 65	60 - 65	41.4 - 71	41.4 - 71

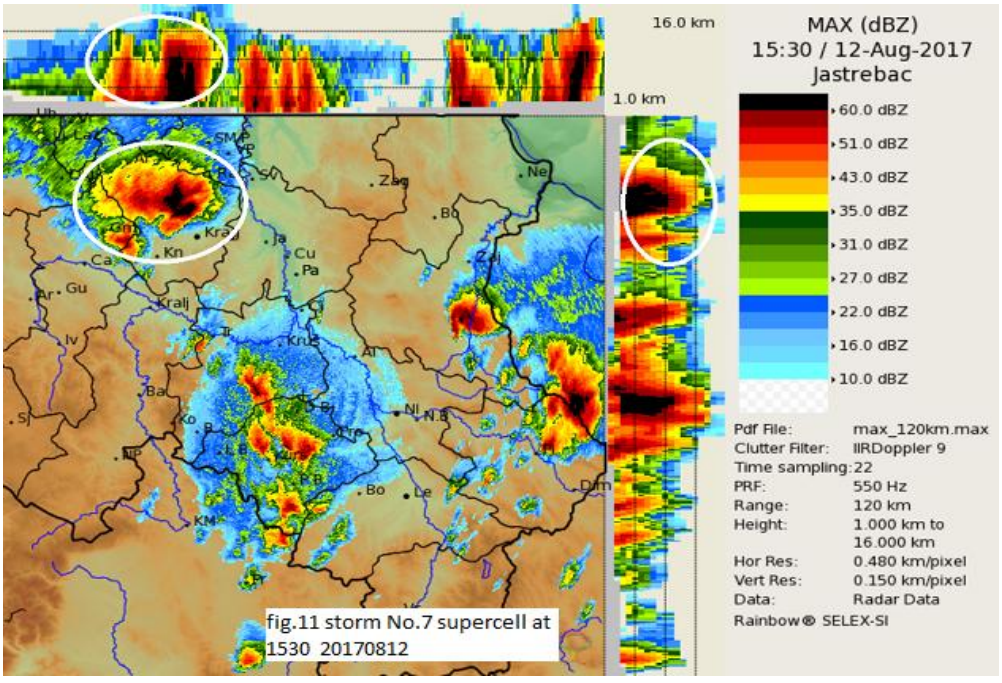


fig.11 storm No.7 supercell at 1530 20170812

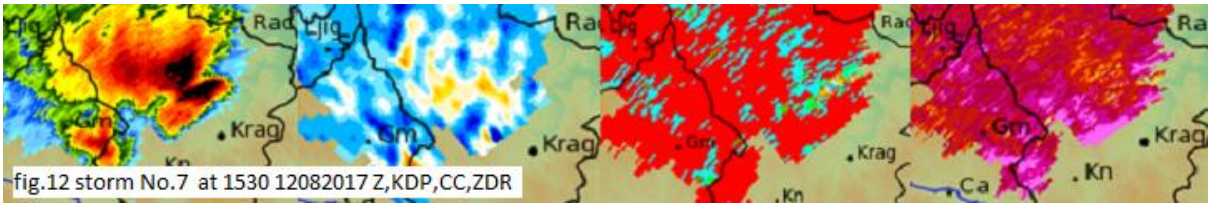


fig.12 storm No.7 at 1530 12082017 Z,KDP,CC,ZDR

Conclusion

For all three dates there are some deviations that indicate spatial and temporal differences in product values (ZDR, CC, and KDP) and recorded phenomena, but there are also a large number of matches with recorded phenomena. The analysis shows that it is necessary, especially when it comes to storms in the spring season, to compare the recorded phenomena with product values(ZDR, CC,KDP), in order to get a more precise assessment of precipitation and damage area. Summer situations, show higher matching with the recorded data, but even then the above differences occurs and checking with products (ZDR, CC, and KDP) is inevitable.

Acknowledgement

I owe all my gratitude to the co-authors mentioned above and Julijana Nađ, Tatjana Komlen, Ilija Jovičić, Ljiljna Dekić.

References

Don Burgess,2011 -Introduction to the Dual-Polarized WSR-88D

Jeff Duda -How to use and interpret Doppler weather radar

Cathy Kessinger, 2009- Selected Topics in Radar Meteorology and Theory

Carin Goodall, Hal Austin, Robert Frederick, David Glenn, and Lara Pagano, 2012-Experiences with

DUAL POLARIZATION Radar in Operations at Newport/Morehead City NC

WSR-88D Dual-Polarization Radar Detection Aid

Dual-Pol Reference Guide

Software Manual Rainbow® 5-Products & Algorithms-2013

QUALITY-BASED RADAR DATA PROCESSING AND QPE AT THE SLOVAK HYDROMETEOROLOGICAL INSTITUTE

Ladislav Méri[1], Marián Jurašek[1], Ján Kaňák[1], Ľuboslav Okon[1]

[1]*Slovak Hydrometeorological Institute (SHMÚ), Jeséniova 17, 833 15 Bratislava, Slovakia*

(Dated: 22 June 2018)

1 Introduction

By the growing demand for meteorological radar data and products the question of its accuracy and quality rises more often and often. While the issue of radar measurement quality is resonating many years among the community of users of meteorological radars (e.g. projects like OPERA, BALTRAD, but also INCA-CE, H-SAF …), radar manufacturers are offering only limited capabilities in this field. One possible reason for such lack of capabilities in the radar data processing products may be the fact that they were developed primarily for processing single radar data and the compositing possibilities were added only as supplementary features. Improvement in the area of international radar data exchange and networking enables deeper analysis and a bit new approach, where data from different radars are mutually controllable, comparable and combinable. Integration of measurements form other sources (e.g. satellites, rain-gauges, numerical weather prediction outputs, lightning detection systems, cameras …) opens other opportunities to improve the quality of radar data and also other meteorological products. This approach could be potentially advantageous also in the field of X-band radars, where the quality issues could be especially challenging. As this approach requires such a broad spectrum of supporting meteorological data, it`s development is probably best fitted to national meteorological services, where these data are available. The meteorological services are than benefiting from the newly developed products with a very high additional value.

These considerations led to the development of the qRad radar data processing and the qPrec precipitation estimating software at the SHMÚ. The software uses a more network-centered view to the radar data processing, where the data form different radars are not processed independently, but together with other data sources are compared, controlled and combined by each other. The software is written in C++ in a modular way for easy portability and uses parallel processing techniques for fast run.

The qRad software estimates the actual quality of the radar volume data by various quality indexes and tries to correct some undesirable effect on the measurement (e.g. beam-blockage, ground-clutter, non-meteorological echoes …). The corrected volume data are then directly processed to composite radar product and quality maps. The resulting radar products are used by the forecasters and for QPE, and are used for validation of the EUMETSAT H-SAF precipitation products. The software was installed also at the Hungarian Meteorological Service to support the H-SAF validation efforts.

The qPrec package uses estimation theory and probabilistic approach to estimate the rainfall intensity as accurate as possible based on heterogeneous input data (rain-gauges, radars, satellites, lightning detection in the future…). The calibrated input data fields are combined according to their precision and actual quality. The resulting precipitation estimates are regularly validated by the climatological rainfall amounts and by hydrological model runs. The first results are showing dramatic improvement of the precipitation estimation against the methods used previously at the institute.

The development is in progress, so the near future plans are also mentioned.

2 Radar data quality estimation

The result of meteorological radar measurements is influenced by a variety of factors. Some of these factors derive from the radar hardware and from the measurement parameters settings (power, polarity, beam-width, noise, detection range, various filters on the hardware site …). Others are caused by the surrounding environment (beam height above the terrain, beam-blockage, sea-clutter, interference with other electronic devices …), or by the actual meteorological situation (beam propagation, partial beam-filling, bright-band, overshooting of the low clouds, second-trip echoes …). The majority of these factors can be directly calculated, estimated or at least estimate their probability. After the quantification of these quality factors, they are rescaled to a dimensionless number between 0.0 and 1.0 – the so called quality index (QI), where the value 0.0 stands for the lowest quality and 1.0 for the best quality. The qRad software estimates the quality of each measured bin in the volume data by different quality indexes. An example of the actually used quality indexes are shown on the Fig. 1. So far the next quality indexes were implemented:

2.1 Constant quality index

The quality factor in this case is the radar itself – it`s position, hardware, and settings. Measurements of the reliable and properly set radars are evaluated as good quality (QI=1.0), while the data of less reliable or less precise radar sites are

labelled with lower QI values. This quality index is useful also when some other quality index was not computed (due to some missing data). Then the missing quality index can be replaced with a constant number.

2.2 Quality index according to the distance from the radar

Each radar bin is evaluated according to its distance from the radar. The radar beam is broadening and its volume is growing as it propagates in the atmosphere. The resulting measurement is then representing an average of a larger volume. In this case the next linear relationship is used:

$$qi = \begin{cases} 1.0; & r < r_{min} \\ 1.0 - \dfrac{r - r_{min}}{r_{max} - r_{min}}; & r_{min} \le r \le r_m \\ 0.0; & r > r_{max} \end{cases} \qquad (2.1)$$

, where r is the distance from the radar and r_{min} and r_{max} are parameters of the computation (with default values of 0.0 and max. range of the radar).

2.3 Similarity with the surrounding bins

Two bins are considered as similar when their value differs less than a given threshold. The similarity QI is than the percentage of the similar bins in a defined window around the given bin. This QI is aimed to find some spikes or smaller holes and to evaluate the bins on the borders of the detected clouds. The software enables to replace the value of the bin with QI lower than a defined threshold with a QI-weighted average of the surrounding values.

2.4 Beam-blockage by the terrain

The percentage of the transmitted energy blocked by the terrain is computed according to the energy distribution along across the radar beam. The 10-meter resolution ASTER GDEM digital terrain model is used in the computation. The resulting QI is then

$$qi = \begin{cases} 1 - block; & block \le block_{max} \\ 0; & block > block_{max} \end{cases} \qquad (2.2)$$

, where $block_{max}$ is a user-defined threshold of blocking. The software offers the possibility to correct the blockage by dividing the measured energy by the blockage.

2.5 Beam height above the terrain

Some quality factors are influencing only certain type of radar products. The beam height above the terrain should be useful especially for rainfall estimating products - the estimated rainfall should be more precise, when the used bin is near the surface of the terrain. The QI is computed according to the next equation:

$$qi = \begin{cases} 1 - \dfrac{h_{above}}{h_{max}}; & 0 \le h_{above} \le h_{max} \\ 0; & h_{above} < 0 \; or \; h_{above} > h_{max} \end{cases} \qquad (2.3)$$

, where h_{above} is the bin height above the terrain and h_{max} is the user defined maximum height above the terrain.

2.6 Cloud type QI

The NWCSAF Cloud-Type product is used in this QI. Non-undetected bins are evaluated according to the cloud type in their position. The QI is associated according to the next table:

Table 1:QI according to cloud-type

Cloud-type	QI
Cloud-free (land, see, snow…)	0.01
Fractional	0.1
Height semi-transparent thin	0.1

Other clouds	1.0

The software enables to replace the low QI bins with an undetected value according to user settings.

2.7 Cloud top height QI

This test uses the NWCSAF Clout Top Temperature and Height product to assign low QI (0.01) to the non-undetected bins found above the cloud tops. The software enables to replace suspicious bins with an undetected value.

2.8 Time QI

The time of the measurement is evaluated in this QI. It is computed as a linear relationship of the difference between the time of the measurement and a given product validity time:

$$qi = \begin{cases} 1 - \dfrac{\Delta T}{\Delta T_{max}}; \ \Delta T \leq \Delta T_{max} \\ 0; \ \Delta T > \Delta T_{max} \end{cases} \quad (2.4)$$

, where ΔT_{max} is a user-defined maximal allowed time-difference.

2.9 Average QI

This QI is computed as an average of user-selected QIs from a couple of last measurements. This could be useful to detect some ground-clutters or other permanent error sources. In our application the combination of Cloud-type and Cloud-top-height QIs is used in this test.

3 QI-based radar product generation

The resulting QI of each radar bin is computed by multiplying the used partial QIs for the given product:

$$qi_{R_i} = \prod_{j=1}^{n} qi_{R_i}^{j} \quad (3.1)$$

, where qi_{R_i} is the QI of then bin from the *i*-th radar and $qi_{R_i}^{j}$ is the *j-th* QI from the actually used QIs. The value of the product is then computed as a QI-weighted average from all available radars in the given point:

$$z = \frac{\sum_{i=1}^{N} qi_{R_i} z_{R_i}}{\sum_{i=1}^{N} qi_{R_i}} \quad (3.2)$$

, where *z* is the value of the resulting product, and z_{R_i} is the value from the *i-th* radar. The resulting QI of the product in the given point is computed with a probabilistic approach, where qi_{R_i} is treated as the probability of good measurement.. The resulting QI than a 1.0 minus the probability of bad measurement in the given point:

$$\begin{aligned} qi &= 1{,}0 - P' = \\ &= 1{,}0 - \prod_{i=1}^{N} P'_i = \\ &= 1{,}0 - \prod_{i=1}^{N} (1{,}0 - qi_{R_i}) \end{aligned} \quad (3.3)$$

, where P' and P'_i is the probability of bad measurement for the resulting product and for the *i-th* radar. In this way the fact that the point covered with more radars will have a higher QI. An example visualization of the CMAX composite and the resulting QI composite is shown on the Fig. 2. The software is capable at this time to compute the PPI, CMAX, 3D-CAPPI and the PP products. The PP product stands for Precipitation Potential. It is a product developed at the SHMÚ, and it

computes the average reflectivity in the layer above the terrain. The thickness of the layer is user-defined (2km used as default). The input bins are weighted according to their height above the terrain (the beam-height QI used for this purpose).

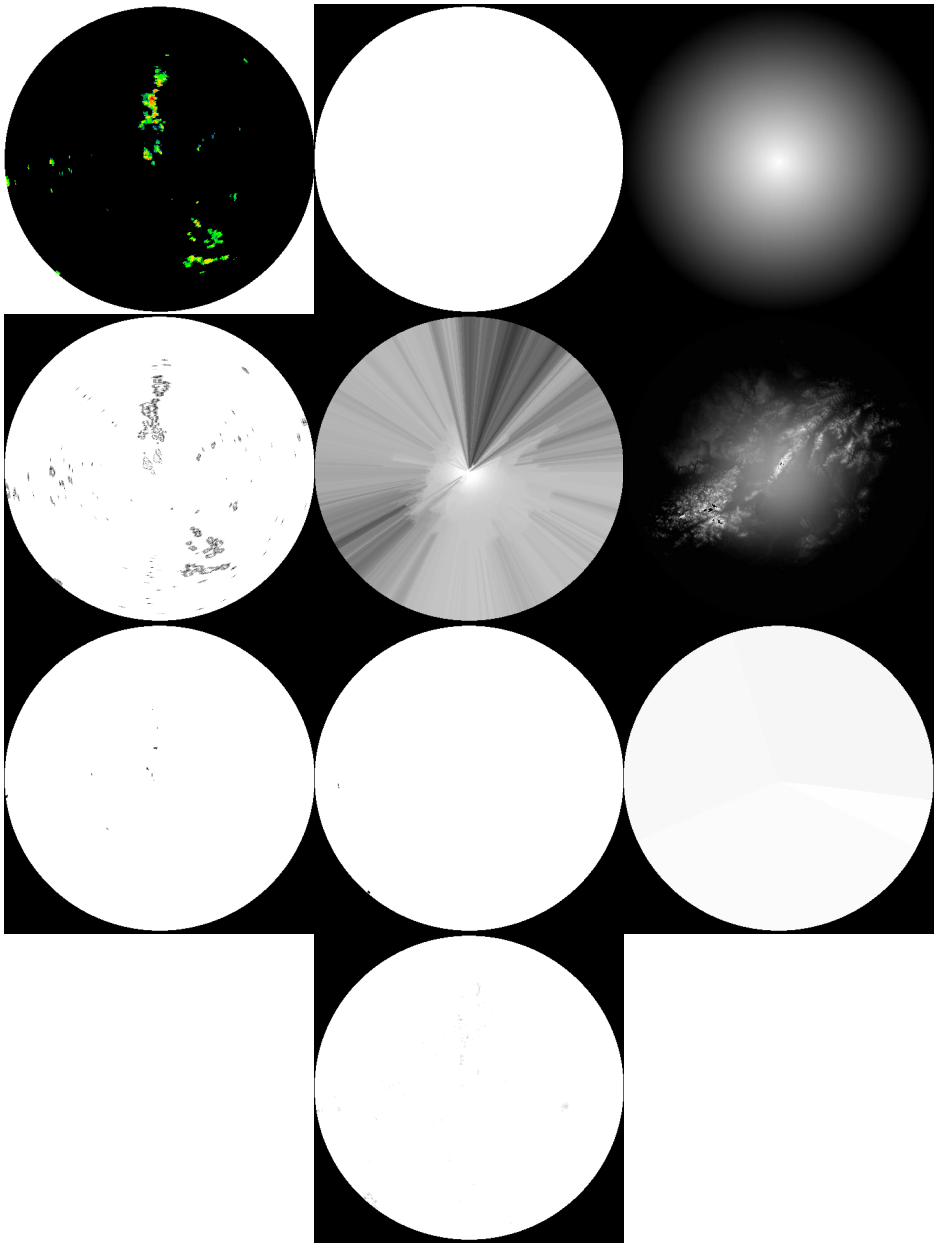


Figure 1:Example visualization of the so far implemented quality indexes. From the top-left corner: PPI of the DBZH, Constant QI, Distance QI, Similarity QI, Beam-blockage QI, Beam-height QI, Cloud-type QI, Cloud-top-height QI, Time QI, Average QI

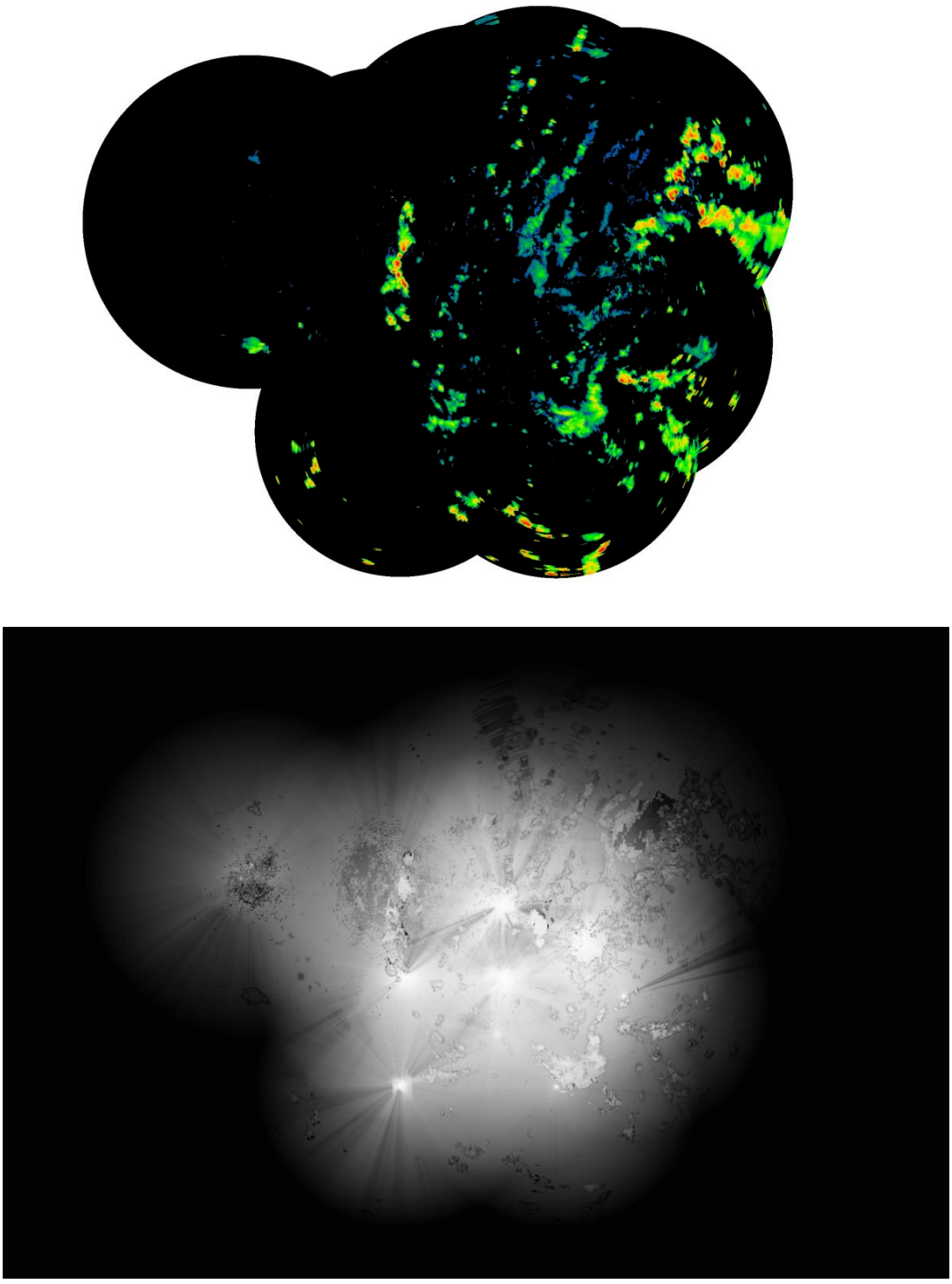


Figure 2: Example visualization of the CMAX composite product and the associated QI field from a network of 13 radars.

4 QI-based QPE

The design and development of the qPrec precipitation estimation software was started from the basics. The distribution of rainfall values measured by the automatic rain-gauges for different radar products was examined and a combination of probabilistic and variational approach was chosen. The processing chain is sketched on the Fig. 3.

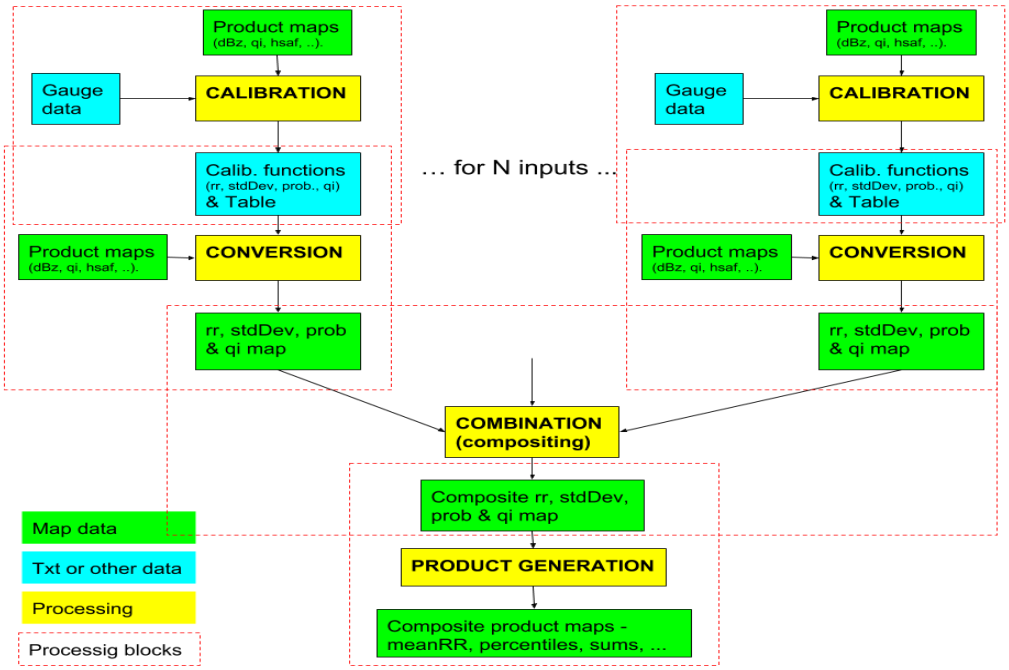


Figure 3: Processing chain in the qPrec software.

The processing chain consists of four processing blocks. The first block is the calibration step. Here the input fields, which may be related to the precipitation, are calibrated by the rain-gauge data to obtain an unbiased estimate of the rainfall-rate from the given product. The outputs of this step are four functions to describe the actual relationship between the input field and the probability of precipitation, the mean rainfall rate, the standard deviation of the rainfall-rate and the average QI of the inputs (Fig. 4).

The second processing block is the conversion. In this step the input maps are converted by the calibration functions to maps of mean rainfall-rate, standard deviation of the rainfall-rate, probability of precipitation, and quality index.

The third block is the combination, where converted input maps from different sources (different radars, other precipipataion products …) are combined to a common map of mean rainfall-rate, standard deviation of the rainfall-rate, probability of precipitation, and quality index. The second and third step can be described by the equations below:

$$P_a = \frac{\sum QI_i \times f_P(y_i)}{\sum QI_i} \qquad (4.1)$$

$$RR_a = \frac{\sum f_{mean}(y_i)/\sigma_i^2}{\sum 1/\sigma_i^2} \qquad (4.2)$$

$$\sigma_a^2 = \frac{1}{\sum 1/\sigma_i^2} \qquad (4.3)$$

$$\sigma_i = \frac{\overline{QI}}{QI_i} \times f_\sigma(y_i) \qquad (4.4)$$

, where P_a, RR_a and σ_a^2 are the resulting combined probability of precipitation, mean rainfall-rate and standard deviation of the rainfall rate. The combined quality index is computed by the equation 3.3. y_i is the *i-th* input value (e.g. reflectivity) in the given point and QI_i is the quality of the *i-th* input value in the given point. f_P, f_{mean} and f_σ are the calibration functions for the probability of precipitation, mean rainfall-rate and standard deviation of the rainfall rate and $\overline{QI}$ is the mean quality index of the inputs used in the calibration step (lower right in the Fig. 4). As seen in the equation 4.4, the actual QI is used to scale the standard deviation of the actual input value, which is then used as the weighting factor in the equation 4.2.

The last processing block is the product generation. Given the probability of zero precipitation (1- P_a) and the parameters of the non-zero rainfall-rate distribution (RR_a, σ_a^2), the probability density function of the rainfall rate is known in the given point and several products can be generated – actual rainfall-rate ($P_a * RR_a$), probability of some rainfall-rate levels, percentiles, sums …

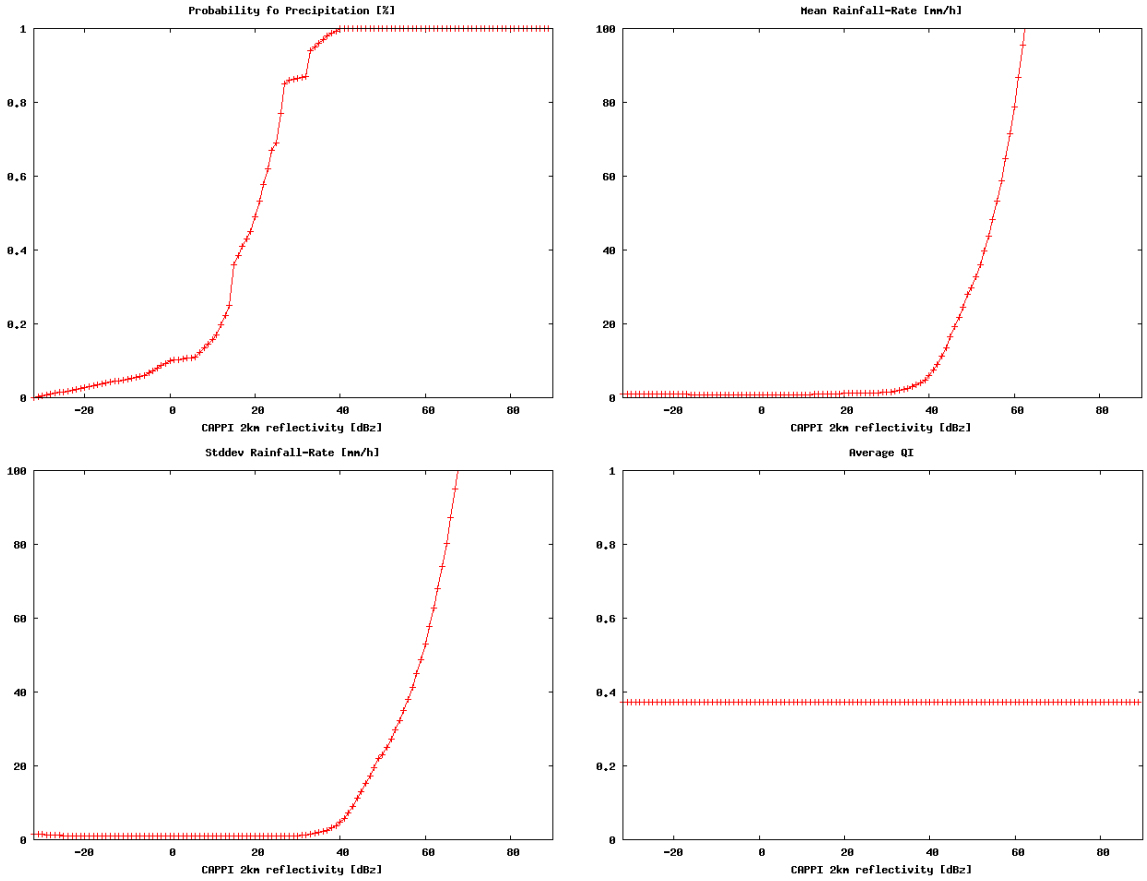


Figure 4: Example of calibration functions of the CAPPI-2km product from a given radar.

5 Usability and validation of QIs and QI-based products

As the definition of individual QIs, its scaling or its combination technique is rather subjective and not standardized, there isn`t a common objective way to validate the QIs itself. Their usefulness depends on the user's application and on the method their usage (weighting, thresholding, max. QI …). Probably the different QI algorithms should be validated by their benefits in the different use-cases. For example when the radar data are used for QPE, the benefit of the QI algorithm should be evaluated as the improvement of the QPE precision using the given QI algorithm. Similarly when the radar data are used in NWP, the QI should be evaluated by his influence on the NWP results.

5.1 Subjective visual improvement

Our forecasters and other internal users of the radar products are using these QI-based products in our visualization tool and are very satisfied by their quality. Almost all of our contributors on the Facebook page of our institute (mostly our forecasters) are choosing the qRad outputs against the products from the software of our radar manufacturer, when some interesting radar data needs to be presented.

5.2 Improvement in the H-SAF precipitation validation project

The Slovak Hydrometeorological Institute is an active contributor to the EUMETSAT H-SAF project especially in the precipitation validation working group. Since the beginning of the work the CAPPI-2km product from our radar manufacturer software - scaled by the Marshal-Palmer equation – was used in the validation of the satellite products. After using the CAPPI-2km product generated by the qRad software (and scaled by the Marshal-Palmer equation in the same manner as the old product), the magnitude of the detected deviations went lower and the distribution of the deviations became more symmetric than in the case of the old CAPPI-2km product (Fig. 5). Using qRad validation data we experienced more reliable H05 H-SAF product quality in terms of statistical scores than it used to be in the past when we used radar data from simple mosaic software that basically maximized rainfall values at every point, where data from more than one radar were available. The qRad software was installed also in the Hungarian Meteorological Service to support the H-SAF validation tasks in this institute.

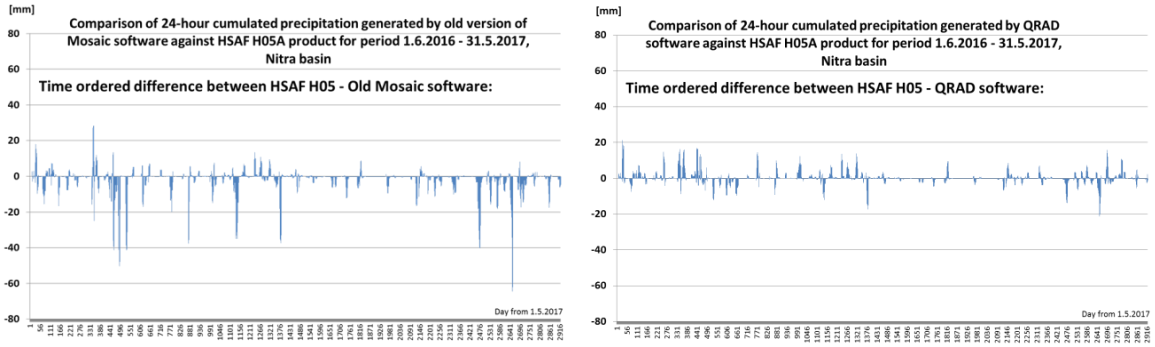


Figure 5: Difference in the usage of the old radar manufacturer generated CAPPI and the qRad generated CAPPI in the H-SAF validation project.

5.3 Improvement in our iterative QPE development project

The qPrec software is developed in an iterative approach. Each new version or change of the software (usage of a new QI, new input field, new algorithm …) is validated against the 24-hour climatological precipitation sum from our 600 climatological precipitation stations. Gradual addition of QIs to the processing had the consequence of improving the precision of the 24-hour precipitation estimation of the qPrec software (Fig. 6).

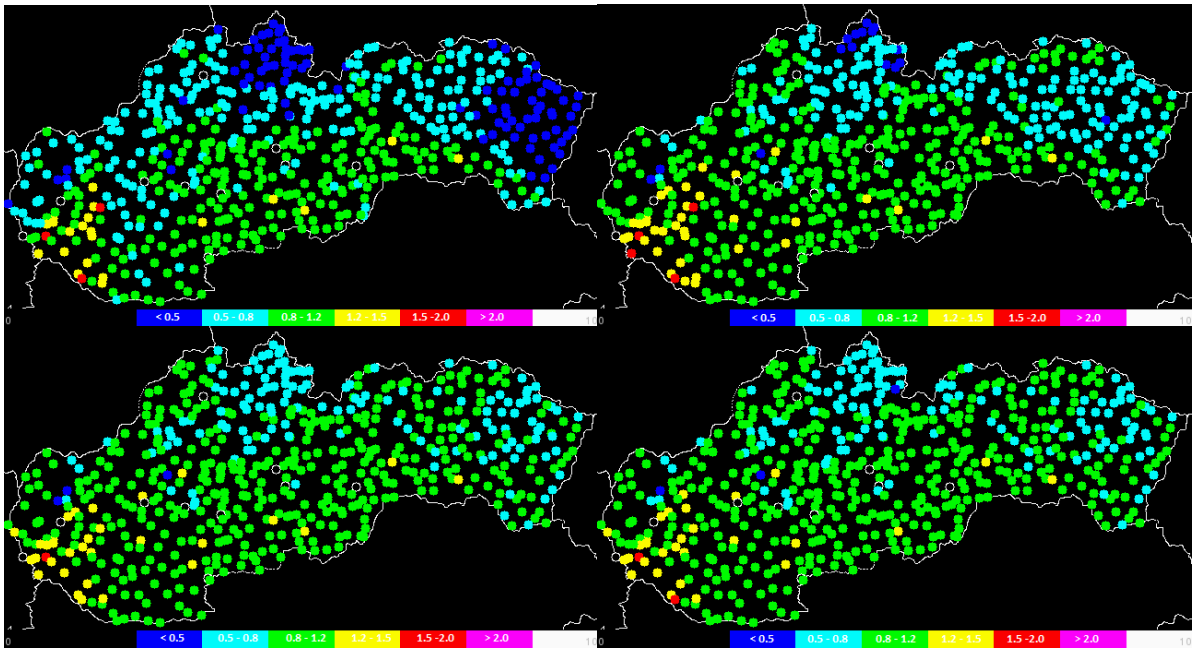


Figure 6: Average ratio of 24-hour precipitation sums from the qPrec software and from the climatological stations - qPrec / clim – for the period of 1.5.2017 – 30.9.2017. Upper left – without QI, upper right – distance QI added, lower left – beam-blockage QI added, lower right – similarity QI added. The number of points with ratio between 0.8 and 1.2 (green) is increasing by adding the QIs. Some residual underestimation in the north and east and some overestimation in south-west needs to be treated by additional changes in the future.

5.4 Improvement in the hydrological applications

An improvement in the hydrological modelling outputs was also reported by our hydrological forecasting department when the outputs of the qPrec software were used instead of the previously used INCA precipitation analyses (Fig. 7). The hydrological validation is also a part of the iterative development process of the qPrec software.

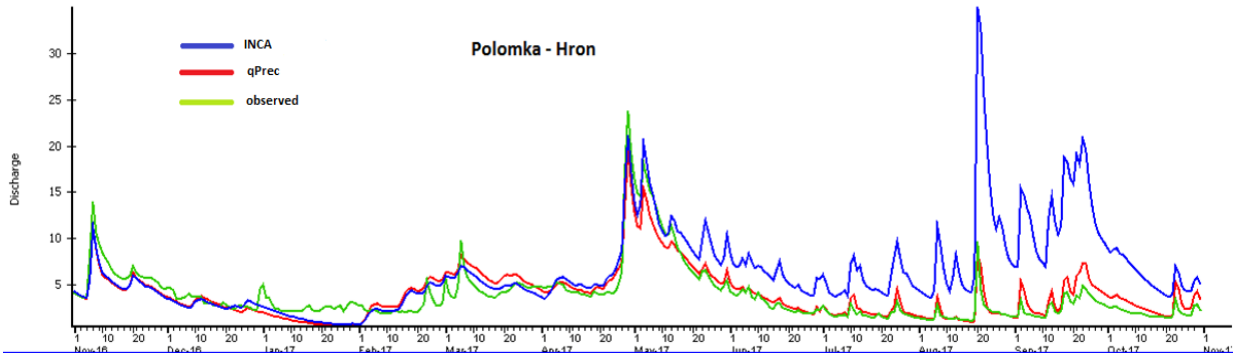


Figure 7: Hydrological model outputs for the Hron river in the central part of Slovakia from 1.10.2016 to 1.10.2017. Model using the qPrec product was producing more precise estimation of the observed outflow than with the INCA precipitation analyses.

6 Summary

The qRad quality-based radar data processing software and the qPrec quality-based precipitation estimation software is under development in the Slovak Hydrometeorological Institute. This quality-based approach combined with the iterative development process seems to give promising results (improved visual and statistical parameters of the radar products, improved precision of the precipitation estimates). The development is ongoing: new QIs and product are planned to the qRad software, while usage of the new QIs and testing of some new input fields are planned for the qPrec software.

MULTI-RADAR DATA FUSION FOR HIGH-RESOLUTION QPE IN URBAN AREA

Brandon Hickman[1,2] Jussi Tiira[2], Roberto Cremoni[2,3], Dmitri Moisseev[2,4]

[1] *University of Bonn, Germany*

[2] *Institute for Atmospheric and Earth System Research / Physics, University of Helsinki, Finland*

[3] *ARPA-Piemonte, Turin, Italy*

[4] *Finnish Meteorological Institute, Helsinki, Finland*

1. Introduction

Urban areas are at a high risk of extremes in precipitation where flooding can have large socio-economic impacts. High-quality observations are required in urban areas to allow adequate warnings and understanding of how precipitation affects the urban area. Weather radar, with their large large temporal and spatial coverage, are ideal instruments for precipitation observations (Saltikoff et al 2010). However, radars suffer from several challenges which are compounded for urban areas (Einfalt et al 2004; Berne et al 2004). Radar signal quality can be degraded due to several issues, including ground clutter, beam blockage, signal and radome attenuation and filtering techniques employed.



Figure 1:Helsinki area with three C band radars

The Helsinki region hosts three C band radars, the Vantaa radar (VAN) owned by the Finnish Meteorological Institute (FMI) and which is part of thee Finnish national radar grid, the Kumpula radar (KUM) maintained by the University of Helsinki, and the Kerava radar owned and operated by the Vaisala corporation, both of which are for research operations. The radars can be seen in Figure 1. Friedrich et al. (2006) used index fields to define the radar data quality. It is shown here, that by combining the three radars, after a series of quality control steps, into a single composite improves the possibility of quantitative precipitation estimation in urban areas. The sources of uncertainty we address here are 1) the removal of non-meteorological targets, 2) absolute calibration of radar reflectivity, 3) identification and correction of beam blockage, 4) ground clutter , 5) attenuation of the path and radome attenuation, 6) and beam broadening and precipitation overshooting.

2. Methods

2.1.Radar Composite and Quality Control

In order to produce the highest quality precipitation field for the urban area a three radar composite was created form the three Helsinki based radars: KER, KUM, and VAN. Prior to radar compositing the radar undergo a series of quality control steps to reduce the impact of various errors. These uncertainties are converted to a series of weights which are then applied to $Z_{H,}$ and K_{DP}. The weights for Z_H are as follows: non-meteorological targets (WNM), Beam Blockage (W_{BB}), path

attenuation (Watt), wet radome attenuation (W_{WR}), Doppler-filter clutter suppression (W_{vel}), ground clutter (W_{CSR}), and range (W_{range}). For K_{dp}, which suffers from fewer uncertainties than Z_H such as calibration, attenuation, and ground clutter, only the weights for range was used to correct for height differences in the beam. Additionally noise in light rain was accounted for by removing K_{dp}<0.1 ° km^{-1}. Additional filter, based on the self-consistency theory (Gorgucci et al 1992) was used to remove spurious results (W_{KDP}). The weights were combined as seen in (2.1) and the composite was created by the joining of the three quality controlled radars W_{KER}, W_{KUM}, W_{VAN} (2.2),

$$W_{(KER,KUM,VAN)} = \begin{cases} 0, W_{BB} = 0 \quad OR \quad W_{NM} = 0, \quad OR \quad W_{Kdp} = 0 \\ W_{att} + W_{wr} + W_{range} + W_{vel} + W_{CSR}, else \end{cases} \tag{2.1}$$

$$Z_{composite} = \frac{W_{KER} \times Z_{KER} + W_{KUM} \times Z_{KUM} + W_{VAN} \times Z_{VAN}}{W_{KER} + W_{KUM} + W_{VAN}} \tag{2.2}$$

The initial steps are as follows:

1. The Removal of non-meteorological targets (W_{NM}) by utilizing the weather echo classification from each radar. The weather echo class is determined by a fuzzy logic algorithm which utilizes the dual-polarimetric parameters to classify the echoes (Keräinen et al 2014).
2. Absolute calibration of Z_H using the self-consistency between Zh and Φ_{dp} for rain (Gorgucci et al. 1992; Goddard et al 1994), and follows the procedures presented by Gourley et al. (2009).

With these steps accomplished, a set of weights are calculated for each radar. Beam blockage from buildings and trees was determined for the radars by utilising laser scanning data fro the National Land Survey of Finland, providing an accurate elevation of elevation of the objects in the radar's horizon. A beam was classified as suffering form partial beam blockage by using a 3 dB Gaussian beam shape which is a ratio of the unblocked and blocked total power. A beam is considered free from beam blockage when the ratio is less than 1 dB. Beams with no beam blockage have a weight (W_{BB}) equal to 1, else equal to 0. Ground clutter is accounted for with two weights: W_{VEl} and W_{CSR}. All radars undergo a Doppler ground clutter filter, the Gaussian model adaptive processing or GMAP (Siggia and Passarelli 2004). Signal loss when velocities of precipitation are close to zero and some ground clutter can escape the filter. W_{vel} was created to account for this signal loss. When the mean velocity normalized by the unambiguous velocity is less than 0.1, indicating ground clutter, W_{vel} is set to 0.01, and greater than 0.1 receives the full weight. Though K_{dp} is typically immune to clutter, there appeared an unknown error at the edges of W_{vel} field, while the source of this uncertainty is known it was accounted for in the K_{DP} composite. An additional clutter filter was created using the clutter-to-signal ratio (W_{CSR}) for residual clutter. Echoes where the CSR was greater than 25 dB was determined as classified as clutter and the W_{CSR} was set to 0.01, and when CSR was less than 20 the echo received the full weight. Values in between followed the following, $W_{CSR} = (25 + CSR_{obs}) / (25-20)$.

Two forms of attenuation were accounted for: path attenuation and wet radome attenuation. Path attenuation was determined on a ray by ray case. A linear relationship between Z_H loss and Φ_{dp} (Ryzhkov and Zrnić 1995) was used to determine the attenuation as following : $0.0688 \times \Phi_{dp}$ (Carey et al 2000). The maximum allowed attenuation as set to 3 dB (Watt=0.01), and the minimum qualifying as attenuation was set to 1 dB (W_{att}=1). Between these values, W_{att} was calculated as W_{att}=3-A_{obs}/(3-1). Wet radome attenuation, when a radar's radome is covered in water leading to signal loss at the radar site, was determined by utilizing Z_H from the other radars above the radar in question. A third degree polynomial, in the form $A_{wr} = -0.001566 \times Z_H^2 - 0.01516 \times Z_H + 0.03765$, was found to represent the loss of Z_H well. W_{WR} was set to 0. 01, when the A_{wr} was greater than 3dB, and 1 when A_{wr} was less than 1. Between 1 and 3, the $W_{WR} = (3-A_{wr})/(3-1)$.

The correction for overshooting and echo height discrepancies due to differing elevation angles was taken into account with W_{range}. As the radars can operate at different elevation angles, and even equal distance echoes can represent different heights. To correct for this, the height of the echo was used, calculated form by utilizing the 4/3 earth model. An adapted calculation for the W_{range} from Zhang et al (2005) was used to create a less steep gradient. This is due to the relatively close ranges of the radars to one another. W_{range} was calculated is seen in (2.3)

$$W_{range} = \begin{cases} 1, R < R_{min} \\ exp(-\frac{H^2}{2H_{max}^2}) + H_{min}, R \geqslant R_{min} \end{cases} \tag{2.3}$$

where H_{max} is 2 km, and H_{min} is the height of the beam at 0.3 km. Near radar echoes (range<0.3km) is set to 1 to utilize the nearest radar.

K_{DP} required an additional filter to remove spurious results. A self-consistency filter (W_{KDP}) was applied to correct remove these. This utilized the relationship defined in Gourley et al (2009), and removed values values that varied more than $\pm 10^{-3}$ ° km^{-1}. Values outside this range received a weight of 0, and inside received the full weight of 1.

2.2. Quantitative Precipitation Estimation and interpolation of Precipitation

Utilising the composited Z_H and K_{dp} fields, the rain rate was computed using the formulations found specifically fro five years of disdrometer data in Finland from Leinonen et al. (2012), and the relationships can be found therein. A blended QPE decision method was used to created to take into account the strengths and weaknesses of K_{dp} and Z_H and to increase the accuracy and reliability of the QPE (Giangrande and Ryzhkov 2008). R(ZH) was used for light rain and drizzle, where the rain rate was less than 4 m/s. R(K_{DP}) was used for possible hail cases, defined here when Z_H was above 50 dBZ, and heavy rain, when Z_H was greater than 20 dBZ and K_{dp} was greater than 0.1 ° km^{-1}.

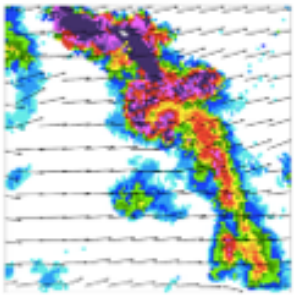


Figure XXX: Motion vectors of precipitation estimate. Black arrows show direction of motion.

Interpolation was performed on the precipitation fields to increase the number of observations, from every five minutes to 1 minute. An example of the calculated motion fields is seen in Figure XXX. Interpolation was performed by calculating the motion vectors based on the optic flow algorithm, which utilizes the changing position of objects to recognise motion. We used a python packaged Optflow (Pulkinnen 2016) for the interpolation process.

3. Results

3.1. Composite

Compositing was performed for the summer months of 2016. Events were chosen based on the presence of precipitation and the lack of a bright band, which would require additional quality control steps. An example of corrected and composited Z_H and K_{DP} can seen in Figure 3.

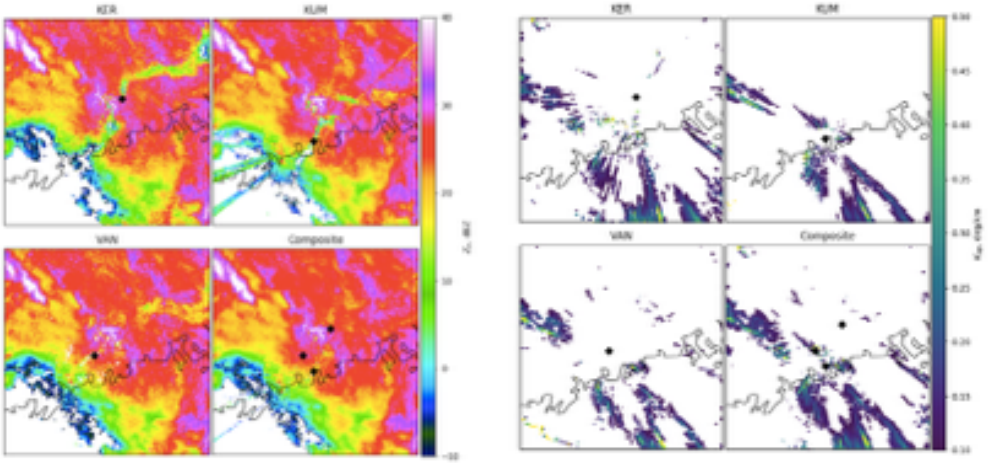


Figure 3: Reflectivity (left) and Specific differential phase (right) for two separate events. KER, KUM, VAN, and the composite are shown. Note low Kdp (<0.1° km^{-1}) have been removed.

Figure 3 shows the Zh and Kdp for KER, KUM, VAN and the composite. Large improvements can be seen in the composited Z_H over individual scans. The effect of W_{vel} , can be seen in all three radars, seen as a zone of decreased Z_H

snaking out from the radar. In the composite this error is removed and realistic Z_H are shown. Path attenuation is taken in all radars, but can be seen especially in KUM towards the east. This is corrected in the composite with higher Z_H. All three radars are being rained on eat this moment. However the reflectivity above KUM is the lowest and falls below the minimum A value (1dB) and receive the full W_{wr} weight, as opposed to the other two which are reduced. a KUM also suffers from 2nd trip echoes; these are removed/weakened with the combination of the other radars. However the composite does include weakened 2nd trip echoes that were not present in the other radars. So some sleight errors, including some speckle, are transferred to the composite. The K_{dp} composite shows how the K_{dp} can be blended. Large values of K_{DP} seen in the south west in KUM and VAN are removed in the composite. This is due to the W_{KDP} filter removing spurious values.

3.2. QPE

Composite was verified with a gauge comparison of rain rates from the summer 2017. Five rain gauges fall within the composite area used. Two of these gauges are in the city, one of which is located in at the KUM radar location, and another in the city center (Kaisaniemi). Figure 4 shows the gauge comparison for the Kaisaniemi gauge, and all five gauges combined for the FMI VAN radar, and the composite.

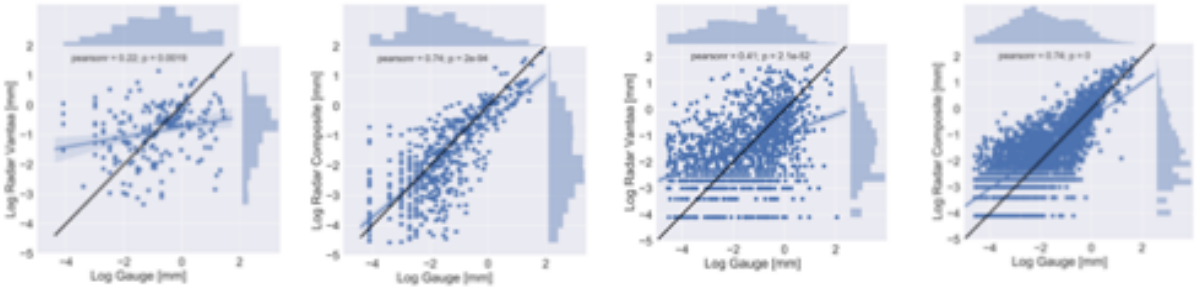


Figure 4: Radar to gauge comparisons for the FMI VAN radar at the Kaisaniemi gauge (A) and all gauge (B), and radar to gauge comparison for the composite Kaisaniemi gauge (C) and all gauges (D). All plots are in log-log format. Black line indicates the 1-1 relationship, and a linear fit is shown as a blue line in each plot. The distribution for all gauges and radar are seen in the margins.

The comparison for the Kaisaniemi gauge and the VAN radar and composite is clear. The composite greatly outperforms the VAN radar for city precipitation estimation in the city center. VAN suffers from considerable echo removal due to clutter suppression techniques. The composite is able to correct for this. The composite also overestimates all low rain rates. This is possibly due to the interpolation adding additional observations. The gauges are 10 minute averages accumulations. Therefore in very low precipitation rates the radar may out perform the gauges. The composite also shows improvement over VAN for all gauges, however to a lesser degree. The bias, standard deviation, and root mean square error can be seen in Table 1. The table shows that the composite outperforms VAN alone.

Table 1:Mean biases, standard deviations, and root mean square error for the composite and VAN radar for both Kaisaniemi and all gauges (including Kaisaniemi).

	Bias [mm]	SD [mm]	RMSE [mm]
Composite Kaisaniemi	-0.07	0.08	0.28
VAN Kaisaniemi	3	0.48	0.70
Composite All Guages	-0.05	0.09	0.30
VAN All Guages	-0.1	0.49	0.70

Finally, Figure 5 shows the VAN radar and composite 24 hour accumulation for a single day in 16.06.2016. The effect of VAN's clutter suppression is highly visible in the accumulation. This leaves large gaps over the city, located to the south east of VAN (black dot)

3. Discussion

In order to produce the highest quality precipitation estimate over the city of Helsinki in Finland and quality controlled composite was created from three C band radars. A series of quality controlled weights and an absolute calibration of the three radars were implemented to create the highest quality data. The composited data was then used to create a precipitation estimate. A blended precipitation rate was created with $R(Z_H)$ and $R(K_{DP})$ to increase the reliability of the measurements.

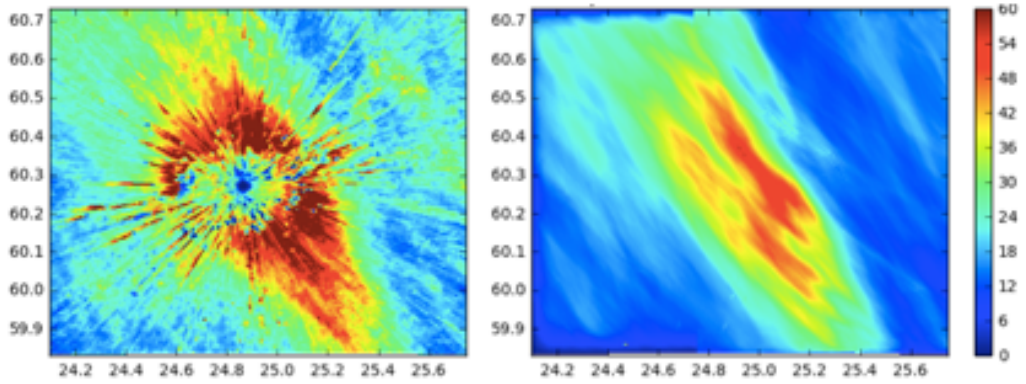


Figure 5 VAN (right) and composite (left) 24 hour precipitation accumulation fro 16.06.2016.

By utilising five gauges within the Helsinki region to compare the rain rate estimate to surface observations a significant improvement can be seen between the FMI VAN radar, which is part of the Finnish national radar grid, and the Helsinki composite, and errors are reduced for composite. However, errors can be transferred from individual radars to the composite. The most prominent errors consist of 2nd trip echoes, and speckle.

Acknowledgement

I would like to than AnnaKaisa von Lerber for her help in providing all the vantaa radar data and gauge data.

References

Berne, A. Delrieu, G. Creutin, J. and Obled, C. 2004: Temporal and spatial resolution of rain- fall measurements required for urban hydrology. *Journal of Hydrology*, 299 (3-4), 166–179,

Carey, L. Rutledge, S. Ahijevych, D. and Keenan, T. 2000: Correcting propagation effects in c-band polarimetric radar observations of tropical convection using differential propagation phase. *Journal of Applied Meteorology*, 39 (9), 1405–1433.

Einfalt, T. Arnbjerg-Nielsen, K. Golz, C. Jensen, N. Quirmbach, M. Vaes, G. and Vieux, B. 2004: Towards a roadmap for use of radar rainfall data in urban drainage. *Journal of Hydrology*, 299 (34), 186 – 202

Friedrich, K. Hagen, M. and Einfalt, T. 2006: A quality control concept for radar reflectivity, polarimetric parameters, and doppler velocity. *Journal of Atmospheric and Oceanic Technology*, 23 (7), 865–887,

Giangrande, S. and Ryzhkov, A. 2008: Estimation of rainfall based on the results of polarimetric echo classification. *Journal of Applied Meteorology and Climatology*, 47 (9), 2445–2462

Goddard, J. Tan, , J. and Thurai, M. 1994: Technique for calibration of meteorological radars using differential phase. *Electronics Letters*, 30 (2), 166–167.

Gorgucci, E. Bechini, R. Baldini, L. Cremonini, R. and Chandrasekar, V. 2013: The influence of antenna radome on weather radar calibration and its real-time assessment. *Journal of Atmospheric and Oceanic Technology*, 30 (4), 676–689

Gourley, J. Illingworth, A. and Tabary, P. 2009: Absolute calibration of radar reflectivity using redundancy of the polarization observations and implied constraints on drop shapes. *Journal of Atmospheric and Oceanic Technology*, 26 (4), 689–703

Leinonen, J. Moisseev, , D. Leskinen, M. and Petersen, W. 2012: A climatology of disdrometer measurements of rainfall in Finland over five years with implications for global radar observations. *Journal of Applied Meteorology and Climatology*, 51 (2), 392–404

Pulkinnen, S. 2016: C++/Python implementations of optical flow algorithms. https://github.com/pulkkins/Optflow, Url visited on 21.06.2018

Ryzhkov, A. and Zrnic´, D. 1995: Comparison of dual-polarization radar estimators of rain. *Journal of Atmospheric and Oceanic Technology*, 12 (2), 249–256

Saltikoff, E. Huuskonen, A. ,Hohti, H. , Koistinen, J. and J. Heikki, 2010: Quality assurance in the FMI doppler weather radar network. *Boreal environment research*, 15 (6), 579–594.

Siggia, A. and Passarelli, J. 2004: Gaussian model adaptive processing (gmap) for improved ground clutter cancellation and moment calculation, Visby, Sweden. ERAD, 67–73, [Available online at http://copernicus.org/erad/2004/online/ERAD04 P 67.pdf.].

Operative correction of dual-PRF outliers

Patricia Altube[1], Tomeu Rigo[1], OriolArgemí[1], Nicolau Pineda[1], Joan Bech[2], Scott Collis[3], and Jonathan Helmus[4]

[1]*Servei Meteorològic de Catalunya, Barcelona*
[2]*Universitat de Barcelona, Barcelona*
[3]*Argonne National Laboratory, Argonne, Illinois*
[4]*Anaconda Inc., Austin, Texas*
(Dated: 22 June 2018)


P. Altube & T. Rigo

1. Introduction

Doppler radars estimate the radial velocity of the weather targets from the phase shift between consecutive backscattered pulses. Since phase measurements are confined within the $\pm\pi$ interval, the radar can unambiguously estimate only radial speeds below an upper limit, which is known as the *aliasing velocity*, V_a. For scatterers moving faster than V_a, the velocity estimate is given folded back within the unambiguous interval, in a phenomenon called *aliasing*, and differs from the actual value in a factor $2nV_a$, where n is an integer number.

The dual-PRF technique (Dazhang et al., 1984) stands, in this context, as a procedure for extending V_a at the processing level without compromising the maximum measurable range. The technique works with two different PRFs (Pulse Repetition Frequencies). These frequencies are continuously alternated, such that all gates along a radial are probed with one PRF and all gates along the contiguous radial with the other PRF. With this scanning mode, the velocity estimates from two contiguous gates can be combined to derive a velocity estimate in an extended unambiguous interval, as long as the actual velocity of both gates is assumed equal.

However, weather radar velocity images obtained using the dual-PRF technique display characteristic unfolding errors which appear as remarkable outliers in the radial velocity field (Jorgensen et al., 2000; May, 2001). These outliers result when the equal velocity requirement of the technique is violated, in situations of high azimuthal shear, turbulence or due to a high uncertainty in the velocity estimates, for instance. Correction of these velocity discontinuities is essential for a reliable use of velocity data in downstream applications such as severe weather detection algorithms, nowcasting systems and assimilation in numerical models.

Recently, a new methodology to correct dual-PRF characteristic outliers has been developed and validated (Altube et al., 2017). The technique is particularly robust in the correction of clustered outliers and can be applied when extended aliasing is present. Since the beginning of 2018, the correction methodology has been operatively implemented for the weather radar network (XRAD) of the Meteorological Service of Catalonia (SMC). In the upcoming sections the correction methodology, its quantitative evaluation and operative implementation are briefly described. The main objective of the present work is a qualitative evaluation of the correction methodology. Hence, we have collected examples of outlier correction for nine real-case severe weather events that have taken place in Catalonia during the last 4 years. The cases presented in the following include tornadoes, downbursts and gust fronts.

2. Radar network

The XRAD weather radar network operated by the SMC constitutes a key tool for weather surveillance and short-term forecasting, for quantitative precipitation estimation and for the study of heavy precipitation events in Catalonia, a region covering an area of about 32000 km^2 in the Northeastern territory of the Iberian Peninsula. The XRAD is composed of four C-band (5.33 cm wavelength) single-polarisation Doppler weather radars: Creu del Vent (CDV), La Miranda (LMI), Puig Bernat (PBE) and Puig d'Arques (PDA). The location and coverage of the four radars is shown in Figure 1. The operation of PBE radar temporarily ceased in 2012 and was resumed in October 2016 (Argemí et al., 2018).

The operative scanning strategy of XRAD radar systems is divided in three sub-tasks during which each of the radars perform Plan Position Indicator (PPI) scans at several fixed elevations. This duty cycle is repeated continuously on a 6-minute basis and consists of a long range single-PRF scanning sub-task at 0.6°elevation, designed for fast weather surveillance, and two short range, dual-PRF, multiple elevation volumetric sub-tasks. Short range sub-tasks are preset at fixed elevations ranging from 0.6° to 27°. The output files for the short range tasks, in SIGMET-VAISALA in RAW format (Vaisala, 2014), store uncorrected reflectivity (T, i.e. noise corrected but without application of the Doppler clutter filter), reflectivity (Z) and Doppler velocity (V) base data in polar coordinates. The spectral width (W) is computed and used for Signal Quality Index (SQI) filtering in the processor.

Regarding the dual-PRF sampling scheme, the dual-PRF factor defining the ratio between the two PRFs ($\mathrm{PRF}_H/\mathrm{PRF}_L = (N+1)/N$) is $N = 3$ for all four radars but the particular PRFs (and, hence, also the aliasing velocity V_a) vary depending on

the radar. In the particular case of the CDV radar, the corresponding high and low PRFs chosen allow to enlarge its coverage up to a range of 150 km, in order to supply the Vall d'Aran region at the Northwestern extreme of Catalonia with volumetric radar data including the Doppler velocity estimates.

Table 1: Scanning and sampling settings of the operative XRAD radars.

Task description	Radar	PRF [s^{-1}]	V_a [m/s]	Max. range [km]
Long range	CDV LMI PBE PDA	450	6.0	250
Short range	CDV	1000 / 750	40.0	150
	LMI	1150 / 862	46.0	130
	PBE	1140 / 855	45.4	130
	PDA	1150 / 862	46.0	130

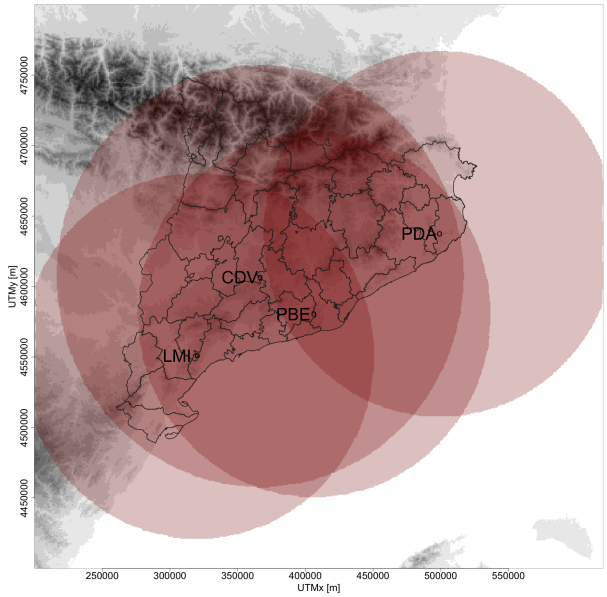


Figure 1: XRAD network weather radars and their coverage of the Catalonia region at the lowest elevation of the short-range volumetric scan.

3. Correction methodology

The nature and characteristics of the dual-PRF outliers are well known (Joe and May, 2003; Jorgensen et al., 2000) and it is possible to identify the affected gates in comparison with the correct gates in their local neighbourhood. Existing correction methods propose to use local statistical moments of the velocity field as reference for outlier identification (Holleman and Beekhuis, 2003; Joe and May, 2003).

The correction method proposed in Altube et al. (2017) works similar to these existing techniques but works in the phase space instead of the velocity space. The procedure consists of two differentiated stages in which the outliers are identified first and corrected next.

In the **identification stage**, the phase of each gate in the image is scaled based on the PRF at which it has been scanned. Then, from the scaled phases of the close neighbours of each gate, PRF-specific local means are computed using circular statistics, that is, accounting for the angular differences between them instead of the arithmetic distances (Fisher, 1993). These specific means are considered together to derive a local reference phase which, after converted back to velocity space, is compared with the gate velocity. If the absolute difference between the gate velocity and the reference is above V_a, the gate is identified as an outlier. Since the computations are carried out in phase space, the so calculated reference velocity is not biased in the presence of extended aliasing (in the $2V_a$ interval). In addition, thanks to the PRF-specific phase scaling, the reference is also robust to the presence of outliers in the local neighbourhood. These are differentiating characteristics of the methodology that offer increased flexibility for the design of quality control procedures.

In the **correction stage**, only gates identified as outliers are corrected. The correction factor in each case is again calculated

from the difference between the gate velocity and a reference velocity. In this stage, however, the reference is calculated as the local median in the velocity space, after all gates labelled as outliers have been removed in order to minimise the bias of the reference (Hengstebeck et al., 2014).

4. Pre-operative validation

The quantitative testing and validation of the dual-PRF outlier correction method requires a *true* radial velocity field without outliers that serves as reference for comparison with the corrected field. Two different quantitative tests were performed prior to the operative implementation of the method for the XRAD.

The first evaluation of the method, which used **simulated dual-PRF fields** is detailed in Altube et al. (2017). The simulations were derived from analytical functions modeling vertical profiles of wind fields, as in Brown and Wood (2007). In the simulation procedure, Gaussian random noise of fixed standard deviation was added to the radial velocities. Multiple simulations were tested, each with a different standard deviation value for the random noise. The performance of the correction method was evaluated using verification metrics such as the Probability of Detection (POD) index. The results of the test showed that the outlier miss rate is below 10% (and significantly lower than for other existing correction methods) even when half of the gates in the image are outliers and 80% of the outliers are clustered in groups of more than 4 contiguous members.

Note that, in this case, the outliers in the dual-PRF image simulations arise uniquely as a result of random velocity differences. However, in real situations, wind fields are often inhomogeneous, velocity uncertainties are heteroscedastic and radial velocity fields contain regions of missing data (filtered out or without significant echoes).

Therefore, a second quantitative test for the dual-PRF outlier correction technique was carried out, this time applied to **dual-PRF velocity fields constructed from real single-PRF velocity fields**. In the analysis, raw data from the C-band Scanning ARM Precipitation Radar (CSAPR), located in the Southern Great Plains ARM facility (SGP I7 site) in Oklahoma (ARM, 2011), was used. The CSAPR radar provides PPI Doppler velocity data estimated at a single-PRF of $1240\,\mathrm{s}^{-1}$, corresponding to a Nyquist velocity of $16.5\,\mathrm{m/s}$. Further information about the CSAPR radar can be found in Giangrande et al. (2014).

On 20 June 2011 a low pressure system in Kansas and associated frontal passage was directing a south-south-westerly flow across the plains. Large regions of winds greater than 50 knots led to large regions of aliasing, especially in sweeps at higher radar elevations. A post-processing dealiasing algorithm was run over radial velocity fields collected by the CSAPR between 1817UTC and 1859UTC (ARM, 2011), and four well-dealiased PPI images at $4.4°$ elevation were selected. Non-valid gates were filtered out below a Signal Quality Index (SQI, a.k.a, normalised coherent power) threshold of 0.25. The four selected velocity fields, used as *reference* in the validation process, were then artificially folded in alternate radials into Nyquist intervals of $12\,\mathrm{m/s}$ and $9\,\mathrm{m/s}$ and further unfolded within the extended Nyquist interval of $36\,\mathrm{m/s}$ using the dual-PRF technique. The resulting dual-PRF images contained a 4.74% of dual-PRF outliers out of the total number of valid gates.

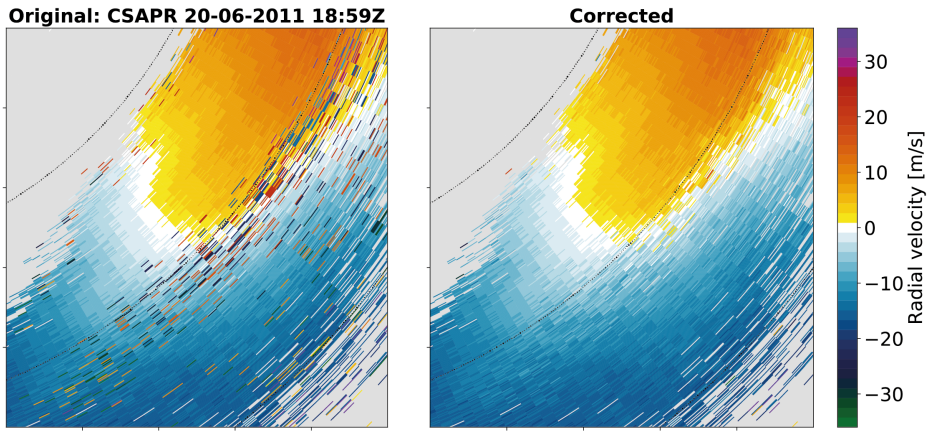


Figure 2: Example of outlier correction in a dual-PRF velocity field built from single-PRF velocity data collected by ARM CSAPR radar on 20 June 2011 at an elevation of $4.4°$*. Gates with a non-valid velocity value are filled in light grey colour and the two dotted rings indicate* $60\,km$ *and* $80\,km$ *ranges from the radar, respectively.*

Figure 2 illustrates the performance of the correction technique and Table 2 gives its hit, miss and false alarm percentages (out of the total number of outliers) when applied to the series dual-PRF velocity fields built from the data collected by the ARM CSAPR radar on 20 June 2011. The hit values given are *effective hits*, for which the false alarm number has been removed. These results indicate that the miss and false alarm rate of the correction method in the identification stage may increase under real measurement conditions. In addition, it is derived that the outliers remaining at the end of the process

correspond mostly to the misses. That is, the correction stage works more effectively for the false alarms than for the misses.

Table 2: Percentage of gates labelled as hits, misses and false alarms out of the total number of outliers, analysed separately for the dual-PRF outlier identification and correction stages.

	Identification	Correction
Hits (eff.)	85.4%	88.9%
Misses	4.3%	9.3%
False alarms	10.3%	1.8%

5. Operative implementation

The operative (real-time) correction of the dual-PRF velocity imagery of the XRAD was implemented during the second half of 2017 and was definitive and oficial at the beginning of the new 2018 year. The operative module includes three stages: (1) correction of the velocity data, (2) writing the output file and (3) ingestion in the automated processing chain.

The correction algorithm has been implemented in Python language (Python, 2001) and works with *radar* objects defined in the Py-ART library (Py-ART, 2013). The Py-ART library includes a function that reads the data from the input SIGMET-VAISALA file in RAW format (Vaisala, 2014) and stores them in the *radar* object. The *radar* object contains the moment data for all gates in each elevation and also the metadata (instrument, task and product parameters) specified in the input file headers.

In the second stage of the operative implementation project, a Python function that generates SIGMET-VAISALA binary files in RAW format has been developed. The generation of such a RAW format file consists on building an extensive binary header that contains all the required metadata and also on compressing the moment data in binary format, applying a SIGMET-VAISALA *ad hoc* compression algorithm that removes series of consecutive zeros. The current implementation recycles the headers of the input file, modifying the apropriate fields.

Once the output RAW file containing the corrected velocity data is generated, it is ingested into the post-processing chain of the XRAD, which is, in its most part, carried out by the SIGMET-VAISALA IRIS software. This way, and as shown in Figure 3, the data is visualised in near-real-time on the default IRIS visor.

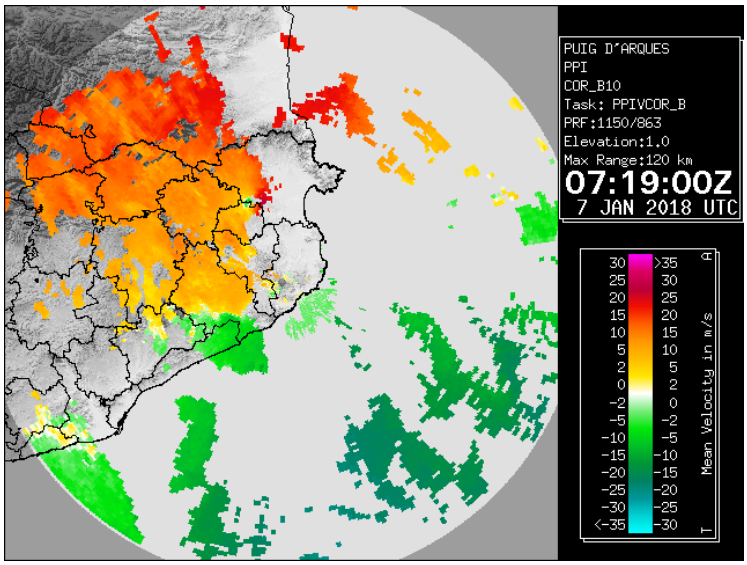


Figure 3: Example of PPI (Plan Position Indicator) product display of the corrected data in IRIS user visualisation interface (Cistella tornado event 07 January 2018, see Table 3).

6. Real-case application

We have considered a set of seven severe wind (straight-line and/or tornadoes) events that have affected different points of Catalonia in the last five years. The events are listed and described in Table 3. Two of them are double cases affecting two slightly different regions. The cases have been selected according to two different criteria that need to be met at the same time: the thunderstorm had hit a dense populated area and there is enough information available regarding the damages at surface; or, in cases when the reports about surface observations are scarce, the pattern in the radar imagery is clear enough to confirm

the occurrence of the event. No casualties were registered in any of the events, but most thunderstorms produced important damages in buildings, vegetation or urban equipment.

Table 3: List and description of the selected severe-weather events.

Location	Type	Date	Time	Description
Alguaire	Downburst	2014-09-04 2014-09-05	23:00-01:00	The thunderstorm moved during mid night, with moderate speed (60 km/h), affecting a scarcely populated region, but causing important damages in rural buildings.
Montblanc	Downburst	2016-05-22	12:00-14:00	The fastest thunderstorm analysed in this study (180 km/h), which produced strong winds affecting small populations. Few damages were reported.
Cercs	Wind gust	2016-09-09	15:00-17:00	Quasi-stationary thunderstorm (the maximum speed was 15 km/h) that produced locally strong winds. More thunderstorms followed the path of the first one (convective train).
Badalona	Downburst	2016-09-13 2016-09-14	23:00-01:00	Another nightly event, occurring in a densely populated coastal area, with damages in different structures of the city. The thunderstorm moved with moderate speed (40 km/h).
Alguaire Montsec d'Ares	Wind gust	2017-05-11	09:30-11:30 18:00-20:00	Two similar, bowed structures affected the NW area of Catalonia, producing damages in rural areas, with several incidences in small villages.
Valls	Squall line	2017-10-18	13:00-17:00	The unique case of a squall line, which formed perpendicular to the coast and moved from SW to NE, crossing all the Catalonia region. Largest damages were produced in Valls.
Cardona Cistella	Tornado	2018-01-06 2018-01-07	23:30-01:30 05:00-09:00	Two different tornadic events took place during the same day (a very rare case: few tornadic outbreaks in Catalonia, none in winter) The populations affected were small but the damages important.

The proposed correction technique has been applied to all nine cases described in Table 3. Two of the cases (Cardona and Cistella tornadoes) took place on 7 January 2018, when the operative correction module was already implemented and running. For the rest of the cases, the methodology has been retroactively applied. Figure 4 displays the study zone corresponding to each and all events analysed.

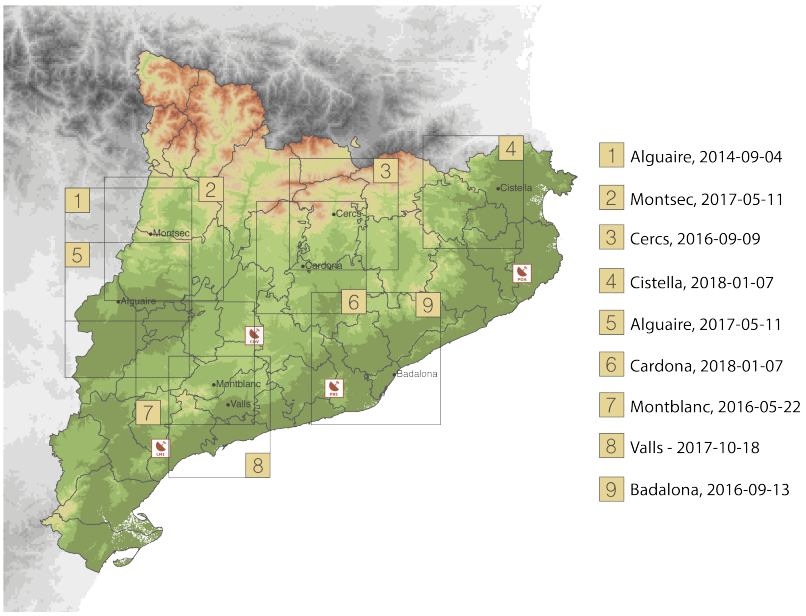


Figure 4: Study zones within Catalonia region of each of the severe weather episodes analysed.

Table 3 summarises for each event the relevant gate labelling results derived from the correction process. Given are: the fraction of valid correct velocity gates, the fraction of filtered gates and the fraction of outliers corrected. The fraction of filtered gates corresponds to the gates filtered out in the velocity image when compared with the corresponding corrected reflectivity image. In the case of the CDV radar, these gates are, essentially, gates automatically SQI filtered in the processor. For the rest of the radars the fraction of filtered gates is not estimable, because the SQI filter is applied to both V and Z moments. These results indicate that the percentage of outliers generally rounds 2-5% after SQI filtering. They also evidence the aggressiveness of the filtering, which can remove a significative number (10-20% on average) of gates with a valid reflectivity value.

Table 4: Percentage of valid gates, filtered gates and corrected outlier gates in the study zone for each of the analysed severe weather cases. The best located XRAD radar (regarding coverage in the study zone) is indicated in each case.

ID	Type	Location	Radar	valid	filtered	corrected
1	downburst	Alguaire	CDV	60.7%	35.3%	4.0%
2	windgust	Montsec	CDV	83.9%	11.3%	4.8%
3	windgust	Cercs	CDV	78.8%	18.8%	2.4%
4	tornado	Cistella	PDA	98.0%	–	2.0%
5	windgust	Alguaire	CDV	85.9%	9.4%	4.7%
6	tornado	**Cardona**	CDV	84.0%	12.0%	4.0%
7	downburst	**Montblanc**	CDV	72.3%	8.5%	2.4%
8	squall line	**Valls**	LMI	97.0%	–	3.0%
9	downburst	Badalona	PDA	96.3%	–	3.7%

Three events have been marked in bold in Table 3 and Table 4: a downburst in Montblanc (2016-05-22), a squall line crossing the territory and passing over Valls (2017-10-18) and a tornado in Cardona (2018-01-07). Selected velocity fields for these events are shown in Figure 5, Figure 6 and Figure 7, respectively. The images collect, in each case, the dual-PRF field before (original) and after (corrected) application of the outlier correction technique. In addition, besides the velocity images, the standard deviation of the velocity field is displayed for a sub-region highlighted in a dashed square. Figure 5 and Figure 7 also include a schematic depiction of the expected Doppler velocity patterns for axisymmetric divergence and rotation, respectively, adapted from (Brown and Wood, 2007).

These figures exemplify how the corrected velocity fields display a remarkably higher quality. After application of the correction procedure, the divergent structure of the downburst (Figure 5) and the couplet associated with the mesocyclone rotation can be clearly identified (Figure 7). The velocity field regions displaying high local standard deviation values (approximately above $6\,\mathrm{m/s}$) coincide with the zones where the majority of dual-PRF outliers arise and where most of the SQI filtering takes place (Collis et al., 2015). The image of the squall line moving towards Valls in Figure 6 is a example chosen to evidence how in cases of strong shear (somewhat quantified by the local field variability, in the standard deviation sub-figure) the procedure may sporadically raise false alarms or/and miss a few outliers. These method failures are attributed to large differences in the average *true* radial velocities between the local high-PRF and low-PRF scanned gates. Since these averages are used to estimate the reference velocity, significative differences lead to a biased reference and to identification errors.

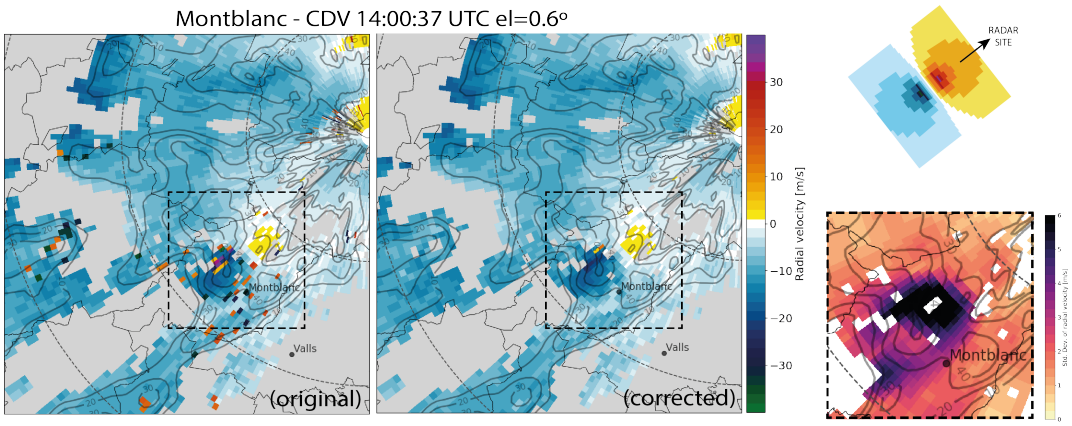


Figure 5: Montblanc downburst, 22 May 2016. Real-case example of dual-PRF outlier correction: original and corrected radial velocity images (left), standard deviation or radial velocities for the region enclosed in a dashed square (bottom right) and depiction of a sample radial velocity field for a downburst (top right, adapted from Brown and Wood (2007)).

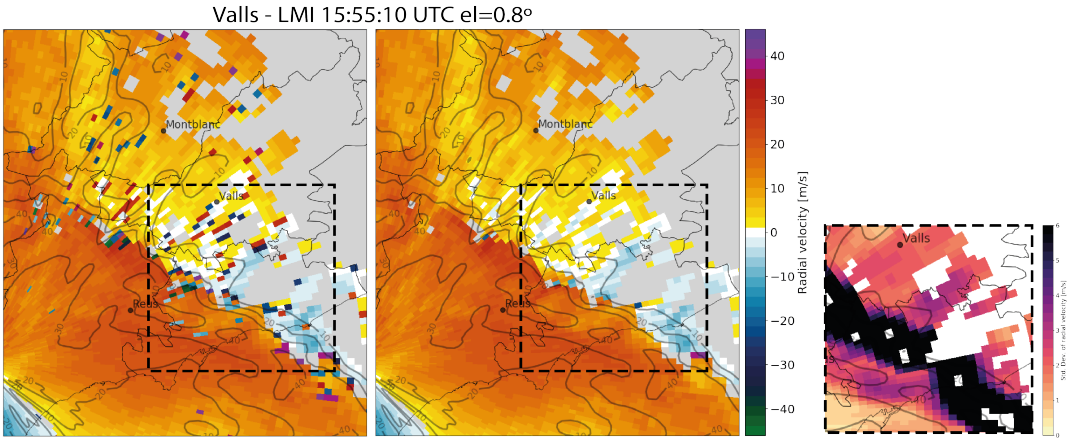


Figure 6: Valls windgust, 18 October 2017. See caption in Figure 5.

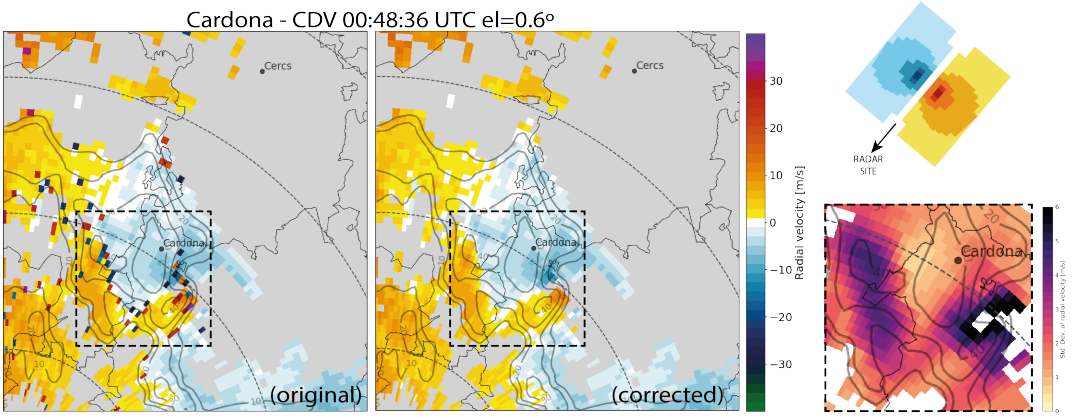


Figure 7: Cardona tornado, 07 January 2018. See caption in Figure 5. Top right sub-figure corresponds to a depiction of a sample radial velocity field for a tornado (adapted from Brown and Wood (2007)).

7. Conclusions and outlook

Unfolding errors or outliers in dual-PRF velocity data appear as clear discontinuities in the velocity field. An image processing methodology to correct these dual-PRF outliers and improve the quality of the Doppler radar velocity data has been devised and operatively implemented for the weather radar network of the Meteorological Service of Catalonia. Similar to other existing techniques, the implemented technique identifies and corrects the outliers by comparison with a reference velocity estimated from the field in the immediate vicinity. However, this methodology estimates the reference velocity using circular statistics applied to the phase of the surrounding gates instead of classical statistics applied to their velocities. In addition, the algorithm uses the phases scaled based on the scanning PRF to derive the reference velocity. These characteristics make the method more robust to the presence of outliers in the neighbourhood or to extended Nyquist aliasing in the estimated velocity field.

A previous quantitative validation of the method using simulations had shown a high performance of the algorithm in correcting clustered outliers, when these outliers result from a variability of random nature in the local velocity field. In the present work, we describe a further quantitative assessment using dual-PRF fields derived from actual single-PRF fields, which evidences that the performance of the method slightly declines under real measurement conditions.

Following the quantitative validation, we present a qualitative assessment based on nine real, severe-weather events that have taken place in the Catalonia region since 2014. The analysis has pointed out that the percentage of dual-PRF outliers can reach the 5% and that with the current SQI filter threshold settings, up to 20% of the velocity gates with a valid reflectivity value may be removed. We focus on three particular events, corresponding to a downburst, a mesocyclone and a squall line. The latter

in particular has evidenced that the algorithm is sensitive to systematic local velocity field variabilities, resulting in sporadical failures. However, overall, the examples presented show how the corrected velocity fields display a remarkably higher quality and are, in contrast with the primary fields, well-suited for their use in complex downstream applications.

The capabilities of the dual-PRF outlier correction method are expected to make it advantageous for a flexible design of the Doppler velocity quality control flow of the XRAD. Indeed, the next step in the project consists on investigating whether and how the correction algorithm can help minimising the SQI filter threshold. Such an analysis is to be carried out using unfiltered single-PRF Doppler velocity data together with the corresponding spectral width information. With this setting, dual-PRF fields with varying degrees of filtering can be derived, keeping the single-PRF fields as reference for quantification.

Acknowledgements

The authors are very grateful to Carme Farnell, Oriol Rodríguez, Miquel Montaner and the firefighters of the Fire Department of Catalonia for the photos and for the damage reports provided, which were indispensable for the selection of the study cases.

References

P. Altube, J. Bech, O. Argemí, T. Rigo, N. Pineda, S. Collis, and J. Helmus, "Correction of dual-prf doppler velocity outliers in the presence of aliasing," *J. Atmos. Oceanic Technol.*, vol. 34, pp. 1529–1543, 2017.

O. Argemí, P. Altube, and T. Rigo, "A first analysis of the Vallirana radar data quality and its contribution to the radar network of the Meteorological Service of Catalonia (XRAD)," in *Proceedings, 10th European Conference on Radar Meteorology and Hydrology*. Ede-Wageningen, Netherlands: ERAD, 2018, poster presentation.

ARM, "Atmospheric Radiation Measurement (ARM) Climate Research Facility. C-Band ARM Precipitation Radar (CSAPR). 2011-06-11, 36.7962 N 97.4484 W: Southern Great Plains (SGP) Nardin, OK (C-band radar site, Intermediate/Auxiliary) (I7)," 2011, compiled by N. Bharadwaj, D. Nelson, B. Isom, J. Hardin, I. Lindenmaier, S. Collis and A. Matthews. Atmospheric Radiation Measurement (ARM) Climate Research Facility Data Archive: Oak Ridge, Tennessee, USA. [Data set accessed 2015-09-20 at http://dx.doi.org/10.5439/1025169.].

R. A. Brown and V. T. Wood, *A guide for interpreting Doppler velocity patterns: Northern Hemisphere Edition*, 2nd ed. Norman, Oklahoma: U.S. Dept. of Commerce, National Weather Service, 2007.

S. Collis, J. Helmus, S. E. Giangrande, K. Muehlbauer, K. North, and P. Kollias, "An open framework for polarimetric radar measurement processing," in *37th Conference on Radar Meteorology*. Norman (OK), US: AMS, 2015, oral presentation: [https://ams.confex.com/ams/37RADAR/webprogram/Paper276120.html].

T. Dazhang, S. G. Geotis, R. E. P. Jr., A. L. Hansen, and C. L. Frush, "Evaluation of an alternating-PRF method for extending the range of unambiguous Doppler velocity," in *Preprints, 22nd Conference on Radar Meteorology*. Zurich, Switzerland: Amer. Meteor. Soc., 1984, pp. 523–527.

N. I. Fisher, *Statistical analysis of circular data.*, 1st ed. New York: Cambridge University Press, 1993.

S. E. Giangrande, S. Collis, A. K. Theisen, and A. Tokay, "Precipitation estimation from the ARM distributed radar network during the MC3E campaign," *J. Appl. Meteor. Climatol.*, vol. 53, pp. 2130–2147, 2014.

T. Hengstebeck, D. Heizenreder, and P. Joe, "Detection of atmospheric rotation by means of the DWD radar network," in *Proceedings, 8th European Conference on Radar Meteorology and Hydrology*. Garmisch-Partenkirchen, Germany: ERAD, 2014.

I. Holleman and H. Beekhuis, "Analysis and correction of dual PRF velocity data," *J. Atmos. Oceanic Technol.*, vol. 20, pp. 443–453, 2003.

P. Joe and P. T. May, "Correction of dual PRF errors for operational weather radars," *J. Atmos. Oceanic Technol.*, vol. 20, pp. 429–442, 2003.

D. P. Jorgensen, T. R. Shepherd, and A. S. Goldstein, "A dual-pulse repetition frequency scheme for mitigating velocity ambiguities of the NOAA P-3 airborne doppler radar," *J. Atmos. Oceanic Technol.*, vol. 17, pp. 586–594, 2000.

P. T. May, "Mesocyclone and microburst signature distortion with dual-PRT radar," *J. Atmos. Oceanic Technol.*, vol. 18, pp. 1229–1233, 2001.

Py-ART, "Python ARM Radar Toolkit," 2013, [http://arm-doe.github.io/pyart/].

Python, "Python language reference," 2001, [https://www.python.org/].

Vaisala, *USER'S MANUAL: Digital IF receiver/Doppler signal processor, RVP8*, Vaisala Oyj, Helsinki, Finland, 2014.

Performance of a new algorithm for nowcasting anomalous trajectories

Anna del Moral[1,3], Tomeu Rigo[2] and Maria Carmen Llasat[1,3]

[1] *GAMA, Dpt. Física Aplicada, Universitat de Barcelona, Martí i Franquès 1, 08028 Barcelona, Spain*
[2] *Servei Meteorològic de Catalunya, Berlin 38-48, 08029 Barcelona, Spain*
[3] *Institut de Recerca de l'Aigua, Universitat de Barcelona, Montalegre 6, 08001 Barcelona, Spain*

(Dated: 15 June 2018)

1 Introduction

Severe weather events are common phenomena around the world, sometimes devastating. According to the National Weather Service of the United States, these events are mainly caused by severe thunderstorms which may produce hailstones ≥ 2.5cm in diameter, wind gusts ≥ 25 $m \cdot s^{-1}$ and/or tornados. Some studies in Catalonia (NE of the Iberian Peninsula) have demonstrated that this type of severe thunderstorms usually present some kind of anomalous motion (i.e. split, merge, stationarity or sudden changes of direction) during their life cycle (del Moral et al., 2017; Pascual, 2005).

According to Cotton et al., 2001 the motion of a thunderstorm is basically composed by three types of movement: the translation (synoptic factors), the forced propagation (mesoscale factors), and the auto-propagation (thunderstorm itself factors). Orographic boundaries, a veering and/or shear of the environmental wind, as well as the precipitation of the thunderstorm itself, which produces density currents from evaporating cooling, are some elements that may influence directly in these types of motion, among others (Lin, 2007). In order to obtain an accurate knowledge of what is causing a thunderstorm to suffer an anomalous movement, usually, it is necessary to combine several data sources (i.e. radiosoundings, radar, numerical weather predictions, etc.), or to conduct complex calculus and simulations, mainly out of the operative arena. Nevertheless, especially when it comes to forecasting a split or merge process, it is expected that the thunderstorm will break or join gradually in time and that the process will be visible in the reflectivity field of it the cell, if a 3D identification is being carried out.

With the objective of detecting split and merge processes in severe thunderstorms in Catalonia, the present study shows the performance of a new version of the algorithm of the 3D thunderstorm identification and tracking (del Moral et al., 2018) which is expected to assist the current radar-based operative nowcasting tool in the Meteorological Service of Catalonia (*Servei Meteorològic de Catalunya*, SMC). As stated before, this algorithm is based on the current version of the SMC algorithm (Rigo and Llasat, 2004), which in turns is an adaptation from the SCIT (Storm Cell Identification and Tracking algorithm, Johnson et al., 1998). The new algorithm is also performed in two stages; the 3D thunderstorm (hereinafter cell) identification and the tracking module. The 3D cell identification, in its turn, is carried out in two phases; the 2D structures identification in each vertical level, based on reflectivity and area thresholds, and the construction of the final 3D cell from the 2D structures. A double reflectivity thresholding method plus an overlapping technique allows a better definition of the convective structures, making it possible to identify changing processes within the same cell, such split or merge. Furthermore, the dynamic distance threshold technique that has been adopted to correctly track cells improves the identification of the anomalous movements and the current construction of the cell paths.

The present study shows how is performed the new algorithm version and discusses the first results that are being obtained within the ongoing validation process. To accomplish with these goals, the manuscript is structured as it follows; Section 2 shows the performance of different types of algorithms used to nowcast convective cells; Section 3 explains the area of study, while Section 4 is focused on the data used; Section 5 describes the new algorithm and the statistical methods used for its evaluation; Section 6 describes the results depending on the type of cells found during the study and, finally, in Section 7 the results are discussed and it is proposed some further studies.

2 A brief review of the tracking and nowcasting algorithms in the literature

Thunderstorm identification, tracking and short-range forecasting of the future cells trajectories throughout their life cycle, constitute the basis of severe weather warning operations (see, for instance, Roberts et al., 2005), and the most important techniques in research of severe phenomena. According to Wilson et al. (1998 and 2004), the historical treatment of thunderstorm extrapolation techniques can be divided in two main groups: assuming no change in motion, size and intensity (steady-state assumption) and allowing changes based on past trends. The first one technique, can also be divided in two main groups depending on the way they track the identified thunderstorms: cross-correlation tracking and centroid tracking and matching.

The cross-correlation technique uses correlated radar images to calculate the displacement vector, extrapolates the area to future images separated in time, and takes the translation that gives the maximum correlation as the final echo displacement. This technique is really effective when it comes to nowcast convective precipitation embedded in stratiform one, because its capability to distinguish between both types of precipitation. However, it is not so efficient identifying and tracking

individual convective cells. The second methodology, centroid tracking, is based on the identification and tracking of the centroid of every single cell within a convective system, obtaining also other properties. Nevertheless, most of the time is unable to identify stratiform precipitation, mainly because it is focused in deep convection analysis. On the other hand, Tsonis and Austin (1981) proved that those algorithms allowing changes of the thunderstorms' features based on past trends, don't necessary improve the nowcasting techniques.

One of the most well-known centroid-type algorithm is the TITAN (Thunderstorm Identification, Tracking, Analysis and Nowcasting) (Dixon and Wiener, 1993). This algorithm uses unique and fixed reflectivity and volume thresholds to define convective cells. Then, cells are tracked across consecutive radar scans applying a combinatorial optimisation technique plus a geometric algorithm, handling, then, anomalous movements of thunderstorms such splitting or merging. The Enhanced TITAN algorithm (Han et al., 2009) goes one step further and introduces a dual threshold process during the convective cells identification, which is followed by a growth and dilation operation to avoid false mergers when there are dense severe convective cells and clusters. Moreover, during the tracking process, the technique is changed to an overlapping one, which, combined with a dynamic constrain-based combinatorial optimization method, handles possible violations of the maximum speed constrain when cells shapes change constantly and rapidly.

Another world-wide known centroid-type algorithm is the SCIT (Storm Cell Identification and Tracking Algorithm) (Johnson et al., 1998). In the SCIT algorithm, a 3D cell identification is done by stages. First, 2D storm structures are created using 7 thresholds and imposing a minimum, isolating this cells from surrounding areas of lower reflectivity and obtaining their centroids. Finally, 3D cells are obtained by associating 2D storm cores in consecutive elevation scans, and connecting their centroid by imposing distance constrains, and solving multiple associations by taking the core with the largest mass (equivalent liquid water content estimated from reflectivity). Non-associated components are matched by imposing larger research distances. For the tracking module, the SCIT algorithm makes a first guess of the locations of the cells, by calculating the motion vector of the past scans using linear least squares fit. Then, the current cell locations are compared to the first guess, and the track is constructed by connecting the centroids that, again, match a distance threshold. This algorithm was adapted to the Spanish region by the Service of Applied Techniques (Servicio de Técnicas Aplicadas, STAP) of the National Weather Service of Spain (Agencia Estatal de Meteorología, AEMET), who added some constrains in the identification process, as well as slightly changed the way the first guess is calculated during the tracking, where it was also added the wind fields from numerical models (Martin et al., 2007). It was also adapted to the Catalan area by the Meteorological Hazards Analysis Team (Grup d'Anàlisi de situacions Meteorològiques Adverses, GAMA) from the University of Barcelona (Rigo and Llasat, 2002 a, b).

3 Area of study

The study is centered in Catalonia (NE of the Iberian Peninsula), a region covering an area of 32,000 km^2, favored for the development of different kinds of thunderstorms due to the proximity to the sea and its own orography (Fig. 1); the Pyrenees to the north at an altitude over 3,000 m; the Central Depression to the west and the Littoral and Pre-Littoral ranges to the east. Convective activity mainly takes place during summer and autumn (Farnell et al., 2017; Rigo and Llasat, 2016; Rigo and Pineda, 2016; Cortès et al., 2017) and, as explained in the introduction section, a high amount of these thunderstorms present anomalous motion during their life cycle, such splitting, merging or stationarity (del Moral et al., 2017; Pascual 2005).

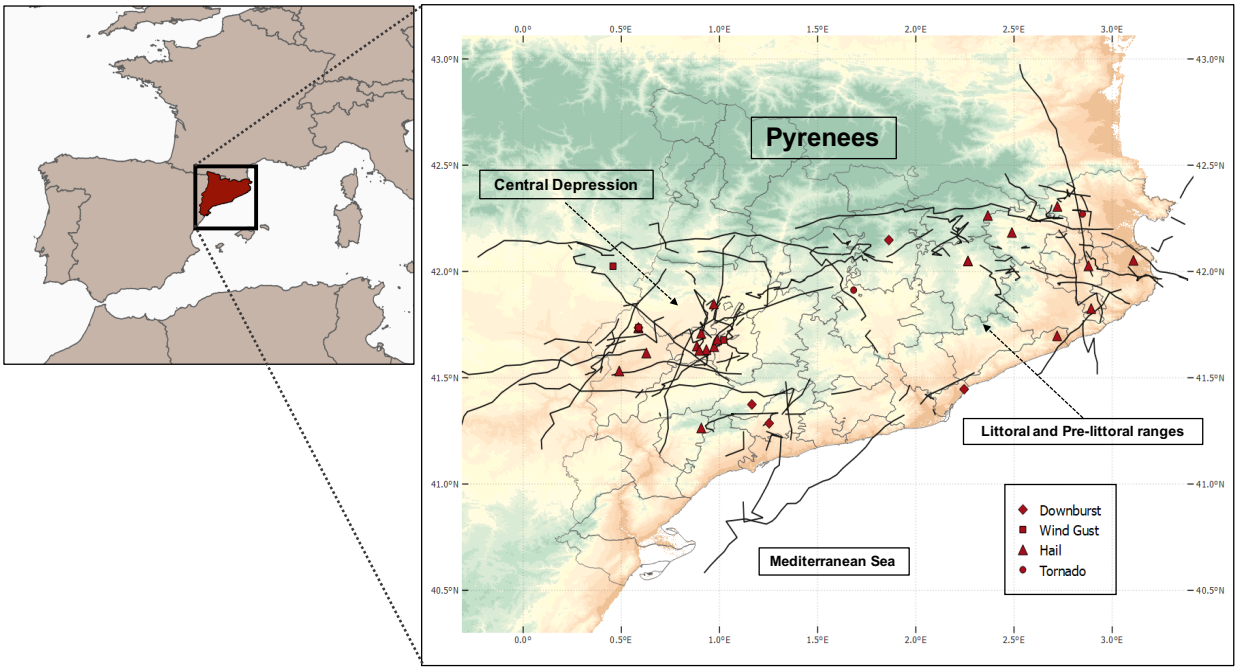


Figure 1: Map showing the region of study (Catalonia) with the tracked cells involved in the analyzed cases.

4 Dataset

It has been selected 31 days from the databases of the SMC (internal) and the INUNGAMA (Llasat et al., 2014), which have presented reported damages due to severe weather phenomena and of which most of them there was a proof of anomalous motion. In total, the database is formed by 21 cases of hail, 8 cases of severe wind gusts (downburst or gust front) and 2 tornado cases (Table 1). Figure 2 presents some radar images with different examples.

Table 1: List of the analyzed cases of severe weather, with date and time of occurrence and type of phenomena at surface. Cases with asterisk also recorded strong wind gusts.

Date	Time (UTC)	Type
17/09/2007	15:00	Hail
31/08/2011	13:00	Hail
05/07/2012	16:30	Hail
27/07/2012 (a)	17:00	Hail
27/07/2012 (b)	17:30	Hail
18/06/2013	14:00	Hail*
10/07/2013	16:00	Gust Front
10/07/2013	17:30	Hail
19/07/2013	14:30	Hail
23/07/2013	14:30	Hail
02/07/2014	16:30	Hail
04/09/2014	23:30	Downburst
06/09/2014 (a)	16:00	Hai*
06/09/2014 (b)	16:30	Hail
14/09/2014	14:30	Hail
15/09/2014	15:30	Hail
23/06/2015	16:30	Hail
22/05/2016	13:30	Downburst

16/08/2016	19:30	Hail
09/09/2016	22:00	Downburst
13/09/2016	23:30	Downburst
14/10/2016 (a)	13:30	Hail
14/10/2016 (b)	14:30	Hail
11/05/2017 (a)	12:30	Gust Front
11/05/2017 (b)	19:00	Gust Front
06/07/2017	16:00	Hail
10/07/2017	17:00	Hail
18/10/2017	19:00	Hail
18/10/2017	20:00	Downburst
07/01/2018	01:00	Tornado
07/01/2018	07:30	Tornado

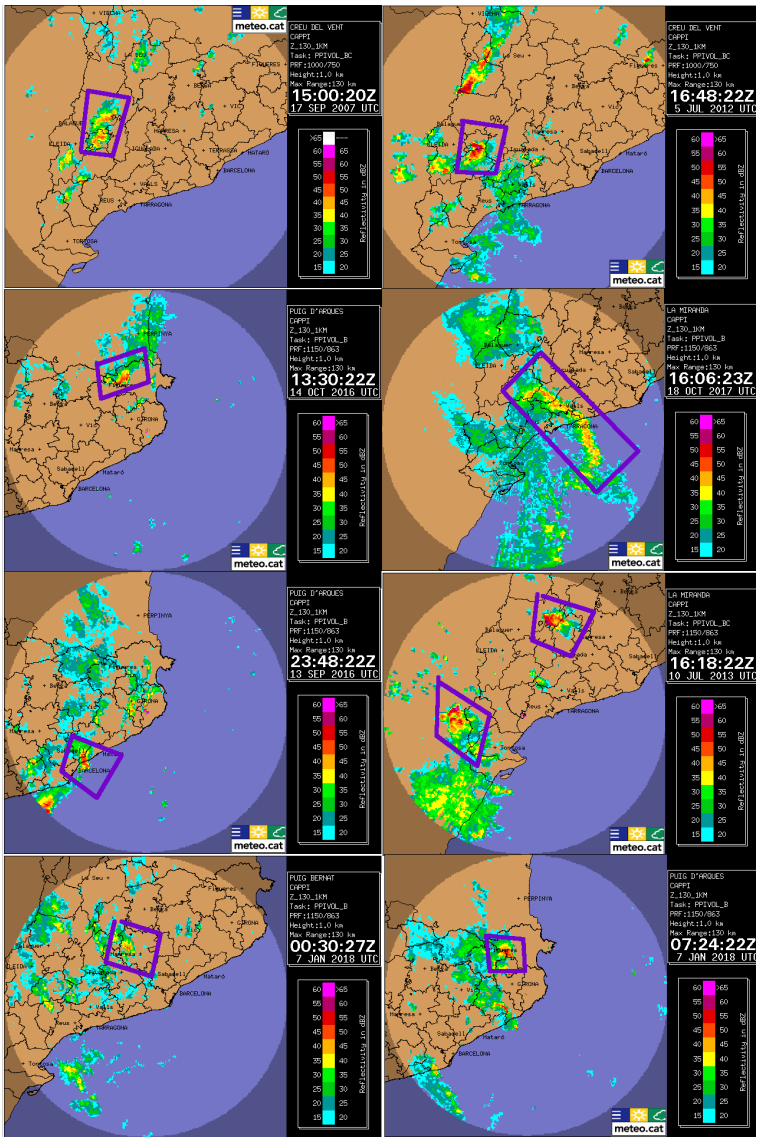


Figure 2: Some examples of the radar structures (inside the purple rectangle) that produced the severe weather in different episodes.

The new algorithm runs over a volumetric composite product of 10 CAPPs (Constant Altitude Plan Position Indicator) that goes from 1 to 10 km in 1km increments. The composite product, provided by the SMC, combines short-range CAPPI volumes (130 or 150 km, depending on the radar) from each of the four radars of the SMC's Meteorological Radar Network, (Altube et al., 2015) with a spatial and temporal resolution of 2 x 2 km^2 and 6 min, respectively (Rigo et al., 2008). In total, the algorithm has been performed on 7440 10-layer-composite GeoTIFFs (Georeferenced Tagged Image File Format), 240 for each day. The dataset was reduced once identified the severe thunderstorms for each case.

5 Methodology

The analysis of the cases was done mainly in three steps; visual recognition of the thunderstorms' motion; automatic detection and tracking of the radar cells with the new algorithm, and the final verification. During the first stage, it was necessary to rigorously visually identify the motion of all the cells involved in each case of study, which meant to analyze each radar animation, discerning whether a thunderstorm was suffering a split/merge or not. For those days where there was a high convective activity, it was more difficult to identify each severe phenomenon with its causing thunderstorms. In these cases, it was imposed the rule of the closest cell to the observation spot, the maximum of the reflectivity field (i.e. $\geq$ 60 dBZ in cases of hail) and the shape of the cell (i.e. the bow echo in cases of severe wind). It is important to remark the issues of a human-based visual recognition and tracking of shapes which, according to Rasmusen and Hager 2001, can be divided into three problems; *agile motion*, when the object movement exceeds the dynamic prediction abilities of the tracker person; *distraction*, when another object has a similar shape to the object being tracked; and *occlusion*, when another scene element is interposed between the tracker and the object tracked. Furthermore, orographic blocking, interferences or precipitation attenuation, among other factors, may occasionally lead to visually recognize as a split or merge process when sometimes it is not real. In the present study, it has been tried to minimize these handicaps.

5.1 Convective cell identification and tracking

As explained in the Introduction section, the new algorithm is performed in three steps; the 2D identification of structures in each level (here CAPPIs), the 3D construction of the cell (identification module) and the final tracking of the 3D cells. The construction of the cell is done in two steps; 2D identification of the structures in each CAPPI level, and final 3D formation of the cell within the entire volume. The main difference from the previous algorithms are listed above. For detailed explanation see del Moral et al., 2018.

3D identification

- Pre-processing of the entire image, CAPPI by CAPPI to remove false echoes from external sources, or anomalous echo propagation (ANAPROP).
- Queen's case adjacency neighbor pixel labelling (8 neighbors; 4 vertexes and 4 sides) to group pixels and construct the 2D structures (Lloyd, 2010), and filtering of 2D structures smaller than 10 pixels (40 km^2).
- Double 7-threshold reflectivity technique to delimit the final area of the 2D structure; first applied from the highest value to the lowest, and finally bottom-up. This allows a major continuity in the identification, especially in the area of the structure, since it is not just saved the core of it, prone to major fluctuations form image to image, as it is done in the SMC algorithm.
- Construction of the 3D cell by the overlapping technique, instead of by matching closest centroids imposing vertical distance thresholds. This allows to identifying multiplicity of 2D structures in the same CAPPI (M2D), which will announce a possible anomalous motion.

Tracking

- Connection of the centroids in consecutive images (6-min time lapse) with a dynamical threshold that depends on the area of the cell, allowing multiple match if the conditions are met. This allows to save a warning if a possible splitting or merging processes has occurred (PS "possible splitting" and PM "possible merging").
- Connection of the centroids in images with 12-min time lapse, imposing the minimum variance of some selected characteristics of the cell (maximum reflectivity, ZMAX, highest altitude at which there is a reflectivity of 40 dBZ, HTOP40, and area, NPIX), and a maximum distance of connection. Allowing, again, a major continuity of

the cell features during its life cycle, which ideally may follow a normal distribution (growing and decaying pattern).

- Identification of unconnected cells with high development. This is, cells that present a top (HTOP) greater than 7 km at the beginning of their life cycle, will appear as a new warning (HTOP7) and will be targets to consider further.

The possible warnings that may conclude in the identification of a split/merge process, which are used during the entire present manuscript, are resumed in Table 2. It is important to remark that these appear at different stages of the entire identification of the process. For instance, several M2D, with an increasing pattern before a split/merge process will be considered as the indicator, in advance, that some anomalous movement may take place with the cell. If a M2D pattern is not recognizable during the identification, the new tracking module will warn with a PS or PM warn if, during the tracking, the connection results in this kind of patterns. Finally, if all of the above has failed, the appearance of a cell with a high development during the tracking, will be considered as an indicator that the cell could be a resulting one from a splitting process.

Table 2: Different possible indicators of splitting and merging processes with their time of appearance during the identification. M2D is the "multiplicity of 2D structures" in a CAPPI; PS/MG is "possible splitting" and "possible merging" flags; HTOP7 represents a height of the cell top above 7 km.

Indicator/flag	Time to split/merge	Module	Evaluation
M2D	Previous	3D identification	Prognosis
PS/PM flag	On time	Tracking	Diagnosis
HTOP7	After time	Tracking	Diagnosis

5.2 Analysis Method

The entire analysis has been divided in two sections; evaluation of the M2D warnings (prognosis), and evaluation of the PS and PM or HTOP7 warnings during the tracking module (diagnosis). Hereinafter the different types of cells will be named as follows: possible Splitting (PS) or Merging (PM) cells, newborn cells with high development (HTOP7) and cells with no anomalous motion (NAM). It must be explained that he HTOP cells not necessary represent resulting cells from merging and splitting processes all the time, but, for instance, it can also represent cells that have been identified as new ones because the tracking has failed, or for missing radar data during consecutive images.

It is necessary to specify the methods used for the evaluation of the new algorithm in terms of the capability to warn with PS and PM in the tracking module. First, for the first analysis, it has been applied a double dichotomous forecasting verification (Yes/No). The first one has considered the visual recognition of the split/merge of the cells as the observed targets, and the PS/PM flags during the tracking module as the forecasted targets. The second one (different contingency table), has only considered the "forecast no" targets as the total sampling (no PS/MG flag in the tracking module), and has taken the HTOP7 flag as the new forecasting target, comparing it against the visual recognition of split/merges, again as observed targets. This second verification has been done to prove the capability of having some kind of information when an anomalous process takes place, even if the first indicator has failed. If a cell has suffered an anomalous process, the resulting "daughter cells" may appear with a high development (HTOP7 flag). The accuracy and the skillness of the method has been tested with the Probability of Detection (POD), Probability of False Alarm Detection (POFD) and the Peirce's Skill Score (PSS) indexes described below:

$$POD = \frac{hits}{hits + misses} \tag{3.2.1}$$

$$POFD = \frac{false\ alarm}{correct\ negatives + false\ alarm} \tag{3.2.2}$$

$$PSS = POD - POFD \tag{3.2.3}$$

6 Results

More than 75% of the cases were recorded during the JASO season (July, August, September and October), and almost 90 % took place *Post Meridian* (12-00 UTC). Table 3 summarizes the 31 cases characteristics depending on the motion and phenomena presented:

Table 3: Studied cases according to type of motion and severe weather event. SP, MG and NAM. represent "splitting", "merging", and "not anomalous" motions.

	PS	PM	NAM
Hail	7	6	8
Downburst/Gust Front	2	3	3
Tornado	1	0	1

6.1 M2D evaluation and patterns (identification module)

As stated in Section 5, M2D flags are displayed during the 3D identification process, representing a prognosis indicator that a possible split/merge will happen. This is always emitted when a 3D cell, in a given time of its life cycle, has more than one 2D structures in a same CAPPI. Figure 3a shows the frequency of M2D flags emitted for the observed PS/PM cells, a total of 19. The 63.2 % of the cases (12) contained M2D flags before the split/merge process, representing a good indicator that something may happen with the cell; 10.5 % of cases (2) presented M2D flags in a moment of the entire life cycle of the cell, and another 2 cases presented M2D at the moment of the split or merge. Finally, 15.8 % cases (3) did not present any M2D flag.

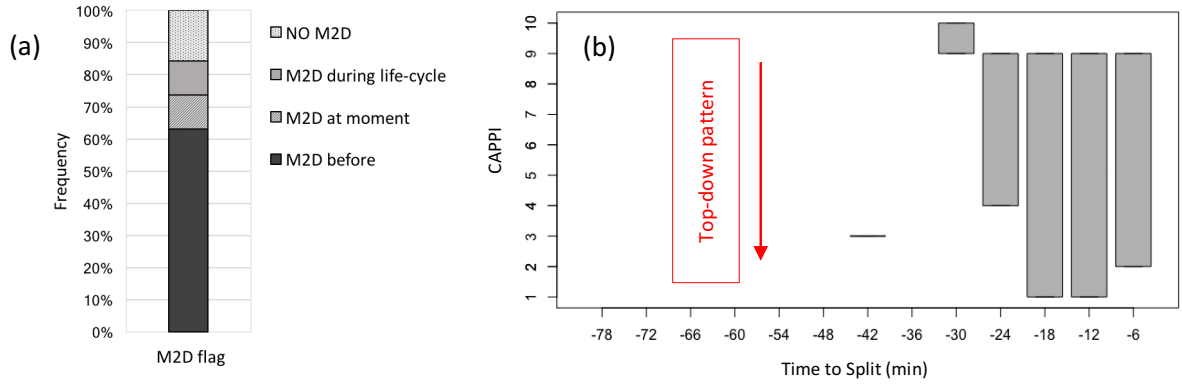


Figure 3: (a) Frequency of M2D flags during for the cells visual recognized as PS/MG, depending on the time of occurrence. (b) Pattern of M2D flags for the splitting cell of 10 July 2013. Bars represent intervals of CAPPIs with multiplicity.

Furthermore, in all the cases except those with no flag available, M2D warnings where visible not only in one sequence of the entire life cycle but in consecutive image with a mean lead time of 30 minutes. For instance, Figure 3b shows the consecutive M2D flags of the splitting cell of 10 July 2013 case, visible 30 min before the split process, where it also can be distinguished a top-down pattern of appearance. The first M2D flags are registered at CAPPIs 9 and 10 km, and then it starts to descend to lower CAPPIs until almost all the CAPPIs register M2D flags. It is also found a M2D at CAPPI 3 km 42 min before the split, which has not been considered a valid flag. This type of pattern was common in some cases, but not all the cases presented a clear top-down/bottom- up pattern.

6.2 Performance of the PS/PM and HTOP7 warnings (tracking module)

Table 4 shows the skill scores for the evaluation of the different possible warnings displayed in the tracking module. It can be seen how the new tracking scheme detected correctly the PS/PM process of 63 % of the cases observed (POD = 0.63), and only the 8 % (POFD = 0.08) of the cases where incorrectly warned. This results in a good ability (0.55) of the algorithm to separate PS/PM and NAM events (notice that the PSS score is comprised between -1 and 1, and a 0 indicates no skill). Moreover, if the first chance of warning does not appear, a second chance is available if a HTOP7 warning is issued. In this case, the results show that 100 % of the cases that were not detected at first, presented an HTOP7 warning in the first identification of the resulting cells of the process.

Table 4: Skill scores for the evaluation of the PS/PM warnings (first chance) and HTOP7 warnings (second chance) in the tracking module.

	PS/PM	HTOP7
POD	0.63	1.00
POFD	0.08	0.08
PSS	0.55	0.92

7 Conclusions

The present study shows the first results obtained from the validation of 31 cases of severe weather in Catalonia, which is still ongoing and that aims to validate the new version of the 3D identification and tracking algorithm (del Moral et al. 2018). The new version algorithm identifies and track the convective cells in a different way that the current operative in the SMC, in order to try to anticipate an anomalous movements (split/merge), and also to perform more realistic tracks of all type of cells, especially those which present such movements. In this way, the algorithm has been validated from two perspectives; the capability to foresee split/merge movements in the identification module (M2D warnings), and the capability to identify split/merge movements in the tracking module (PS/PM and HTOP7 warnings).

The first study shows that almost 85 % of the cases with anomalous motion presented M2D warnings, in some stage of their life cycle, and that more than 65 % where displayed in advance (lead time of 30 min in average), constituting a possible tool for foreseeing this type of processes. As seen from the splitting case of 10 July 2013, it is expected that a split/merge of a cell will appear gradually in time, and therefore, should be visible in the volumetric structure of the cell as time passes. In the present study, most of the splitting cases presented a top-down pattern in the M2D warnings, spreading form upper to lower CAPPI levels. However, it is necessary to conduct more studies on merging thunderstorms, since it wasn't able to distinguish a valid pattern of M2D (bottom-up expected against top-down sometimes found).

Finally, the second study shows the performance of the tracking module when the split/merge process takes place. The results demonstrate that is the module that works better, since it has two chances of identification. As a first stage, the POD score resulted in 0.63, which was highly (1.00) increased when the second stage (HTOP7 warnings) was performed. This allowed to correctly identify the split/merge process seen previously in the identification module (M2D), with a great accuracy.

The results are promising, but the validation is still ongoing with more severe thunderstorms with and without anomalous motion, and also with heavy precipitation events. In this sense, the currently work is focused in expanding the study among a wider range of cases, as well as to study the different behavior during the life cycle of each type of thunderstorm described above. It is also necessary to discern whether is possible or not to find a M2D flag pattern for merging storms, as well as to know the differences of the characteristics of the cells when identified with the new or the SMC version, in order to find strong and weak points to improve. Furthermore, it is expected to study other anomalous movements such stationarity or changes of direction by studying not just the target cell but the motion of its neighbors.

Unless it is necessary to conduct deep studies on how the wind field acts in every case of study, as well as to evaluate the influence of the complex topography and the sea, which is modulating this type of thunderstorms in the region of study, the present study shows some promising indicators that may constitute a good tool to introduce in an early warning system.

Acknowledgement

This research was carried out under the framework of the Spanish projects HOPE (CGL2014-52571-R) and M-CostAdapt (CTM2017- 83655-C2-2-Ra), of the Ministry of Economy, Industry and Competitiveness, and the HYMEX international program. The authors would like to thank the Meteorological Service of Catalonia for providing all the radar data used to develop the algorithm, and to Dr. Aitor Atencia for the valuable suggestions and discussion with the statistical analysis.

References

Altube, P., Bech, J., Argemí, O., and Rigo, T., 2015: Quality control of antenna alignment and receiver calibration using the sun: Adaptation to midrange weather radar observations at low elevation angles. Journal of Atmospheric and Oceanic Technology, 32(5), 927-942.

Cortès, M., M. C. Llasat, J. Gilabert, M. Llasat-Botija, M. Turco, R. Marcos, J. P. Martín Vide, and L. Falcón, 2017: Towards a better understanding of the evolution of the flood risk in Mediterranean urban areas: the case of Barcelona. Natural Hazards, 1–22, doi:10.1007/s11069-017-3014-0.

Cotton, W., Bryan, G., Bryan and G., van den Heever, S.,2001: Storm and Cloud Dynamics. The Dynamics of Clouds and Precipitating Mesoscale Systems, vol. 99. Elsevier, pp. 1–809.

del Moral, A., M. del C. Llasat, and T. Rigo, 2017: Identification of anomalous motion of thunderstorms using daily rainfall fields. Atmospheric Research, **185**, 92–100, doi: 10.1016/j.atmosres.2016.11.001.

Dixon, M. and G., Wiener, 1993: TITAN: thunderstorm identification, tracking, analysis, and Nowcasting—a radar-based methodology. J. Atmos. Ocean. Technol. 10 (6), 785–797. http://dx.doi.org/10.1175/1520-0426 (1993)010<0785: TTITAA>2.0. CO; 2.

Farnell, C., T. Rigo, and N. Pineda, 2017: Lightning jump as a nowcast predictor: Application to severe weather events in Catalonia. Atmospheric Research, **183**, 130–141, doi: 10.1016/j.atmosres.2016.08.021.

Han, L., S., Fu, L., Zhao, Y., Zheng, H., Wang and Y., Lin, 2009: 3D convective storm iden- tification, tracking, and forecasting - an enhanced TITAN algorithm. J. Atmos. Ocean. Technol. 26, 719–732. http://dx.doi.org/10.1175/2008JTECHA1084.1.

Johnson, J.T., MacKeen, P.L., Witt, A., Mitchell, E.D.W., Stumpf, G.J., Eilts, M.D., Thomas,

Johnson, J. T., P. L. MacKeen, A. Witt, E. D. W. Mitchell, G. J. Stumpf, M. D. Eilts, and K. W. Thomas, 1998: The Storm Cell Identification and Tracking Algorithm: An Enhanced WSR-88D Algorithm. Weather Forecasing, **13**, 263–276

Lin, Y.-L., 2007: Mesoscale dynamics. 1st ed. Cambridge University Press.

Llasat, M. C., R. Marcos, M. Llasat-Botija, J. Gilabert, M. Turco, and P. Quintana-Seguí, 2014: Flash flood evolution in North-Western Mediterranean. Atmospheric Research, 149, 230–243, doi: 10.1016/j.atmosres.2014.05.024.

Lloyd, C. D., 2010: Spatial data analysis: an introduction for GIS users. Oxford University Press, 206 pp.

Martín, F., F., Elizaga, O., Carretero and I., San Ambrosio, 2007: Diagnóstico y predicción de la convección profunda (in Spanish). In: Technical Note n. 35 of the Analysis and Forecasting Technical Service of the Spanish Weather Service, pp. 174.

Pascual, R., 2005: Convective storm initiation in western Catalonia: characteristics and uncertainties of the methodology used. Wolr weather research program symposium on nowcasting and very short range forecasting. Toulouse (France) 5-9 September 2005.

Rasmussen, C. and G. D. Hager, 2001: Probabilistic data association methods for tracking complex visual objects. IEEE transactions on pattern analysis and machine intelligence, 23, 560-576.

Rigo, T. and M.C., Llasat, 2002a: Analysis of Convective Structures that Produce Heavy Rainfall Events in Catalonia (NE of Spain) using Meteorological Radar. In: Proceedings of Second European Conference on Radar Meteorology (ERAD), Delft, Netherlands. vol. 18–22 (November 45–48).

Rigo, T., and M.C., Llasat, 2002b: Analysis of convection in events with high amounts of precipitation using meteorological radar. In: Proceedings of 4th Plinius Conference on Mediterranean Storms, Mallorca, Spain. vol. 2–4 (October 1–4)

Rigo, T., and Llasat, M.C., 2004: A methodology for the classification of convective structures using meteorological radar: application to heavy rainfall events on the Mediterranean coast of the Iberian Peninsula. Natural Hazards and Earth System Sciences, 4 (1), 59–68. http://dx. doi.org/10.5194/nhess-4-59-2004

Rigo, T., and M. C. Llasat, 2016: Forecasting hailfall using parameters for convective cells identified by radar. Atmospheric Research, **169**, 366–376, doi: 10.1016/j.atmosres.2015.10.021.

Rigo, T., and N. Pineda, 2016: Inferring the Severity of a Multicell Thunderstorm Evolving to Supercell, by Means of Radar and Total Lightning. Electronic Journal of Severe Storms Meteoroly, **11**, 1–21.

Roberts, R., D., Burgess and M., Meister, 2006. Developing tools for nowcasting storm se- verity. Weather Forecast. 87 (11), 540–558. http://dx.doi.org/10.1175/WAF930.1.

Tsonis, A.A. and G.L., Austin, 1981: An evaluation of extrapolation techniques for the short- term prediction of rain amounts. Atmosphere-Ocean 19, 54–65. http://dx.doi.org/10. 1080/07055900.1981.9649100.

Wilson, J.W., N.A., Crook, C.K., Mueller, J., Sun and M., Dixon, 1998: Nowcasting thunder- storms: a status report. Bull. Am. Meteorol. Soc. 79, 2079–2099. http://dx.doi.org/ 10.1175/1520-0477 (1998)079<2079: NTASR>2.0.CO; 2.

Wilson, J.W., E.E., Ebert, T.R., Saxen, R.D., Roberts, C.K., Mueller, M., Sleigh, C.E., Pierce and A., Seed, 2004: Sydney 2000 forecast demonstration project: convective storm Nowcasting. Weather Forecast. 19 (1), 131–150.

Information sparseness, a key obstacle to radar data assimilation in convection

Frédéric Fabry

McGill University, 805 Sherbrooke West, H4X1G9 Montreal, Canada
(Dated: 15 June 2018)



Frédéric Fabry

1 Preamble: How Data Assimilation Works and How It Can Fail

To better capture the significance of the work presented below, one must first understand how data assimilation functions conceptually, and how it can fail. Not being familiar with any conceptual introduction on assimilation, I chose to write one.

1.1 Atmospheric Data Assimilation: Goal, Available Information, Process

Data assimilation refers to techniques designed to combine optimally the information available about the state of the atmosphere at a particular time. The result of that optimal combination, referred to as the analysis, generally serves as the initial conditions for numerical weather forecasting. The information available to compute this analysis originates from two sources (Fig. 1):

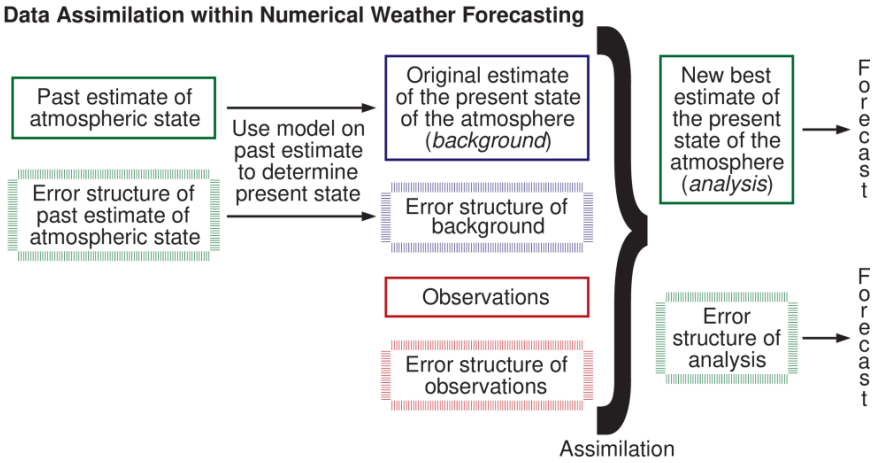


Figure 1: Flowchart illustrating the context within which assimilation is performed. Adapted from (Fabry, 2015).

1. Background, or a-priori, information on the state of the atmosphere. This generally comes from a forecast made in the past but valid at the time of interest. It has the advantage of having information about all the atmospheric fields needed for a forecast, but this information has errors that need to be corrected;
2. Observations of the atmosphere made at or near the time of interest. These observations will be incomplete (in coverage, in atmospheric state variables) to generate an analysis on their own, but they can be used to correct the errors of the background. One should not forget that these observations also have errors, either of measurement or of representativeness (e.g., the mismatch between the sampling volume of the observation and the volume represented by the analysis grid-point).

Because the background and observations are imperfect, the analysis cannot perfectly respect both sets of constraints. It is hence the task of the data assimilation system to generate the analysis that best combines the information provided by both sources of data. The assimilation system computes the new analysis by *updating the background to better respect the constraints provided by observations* (the change to the background made by the assimilation system, or the difference between the analysis and the background, is referred to as the innovation). It attains this goal by simultaneously:

- Minimizing the mismatch between the analysis and the background, taking into account background errors;
- Minimizing the mismatch between actual observations and expected observations simulated using the analysis, taking into account the errors of observation, measurement simulation, and observation representativeness;
- Spreading the innovation induced by observations from the locations and variables where these adjustments occur to other locations and variables.

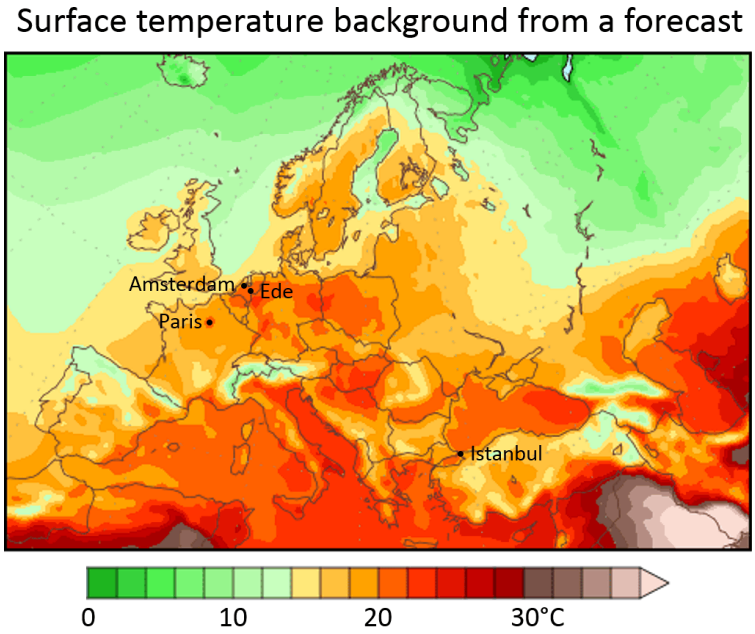


Figure 2: Example of a surface temperature forecast (courtesy of wxmaps.org), used as background to assimilate a measurement at Ede.

1.2 Error Dependencies: The Powerful Idea behind All Data Assimilation Approaches

The real power and magic of data assimilation results from the dependencies between errors, as this is what allows the assimilation system to optimally spread the information coming from new measurements. Let us illustrate this process by analyzing the assimilation of a single measurement.

Consider a forecast for temperature such as Fig. 2 that we shall use as the background in an assimilation system. The expected temperature for Ede is 21°C, with a background error of ±2°C (not shown). Let us say that we have an observation at 24°C, with an observation error of ±1°C. Given the uncertainties on each, the optimum blend of these two constraints (21±2 and 24±1) is 23°C. The innovation at Ede resulting from the assimilated measurement is hence 23−21=+2°C. The analysis temperature at Ede is now computed (and its new uncertainty can also be estimated).

Since we raised the temperature at Ede, should we change temperatures elsewhere? Consider Amsterdam. Common sense suggests that it is very likely that the reason we made a mistake forecasting the temperature in Ede also applies in Amsterdam; hence, it is reasonable to assume that we should also raise the temperature in Amsterdam. By how much? Given the short distance between the two cities, the errors in their forecast are probably highly correlated, and we should probably raise Amsterdam's temperature by, say, +1.5°C. How about Paris? It is also possible that the reason we made a mistake forecasting the temperature in Ede also applies in Paris, but not as likely as in Amsterdam. Since there is a greater than 50% chance that the temperature in Paris is also too low, we should slightly raise the temperature in Paris too. For Istanbul however, the processes that led to a temperature error in Ede are probably irrelevant there, and we have no reason to change temperatures that far from Ede.

The next question we should ask ourselves is: What were the causes of this forecast error in Ede, and what have been its consequences? Causes may include reduced cloudiness, or stronger southerly winds; consequences may be a thicker planetary boundary layer, and somewhat higher temperatures and reduced humidity in it as a result. We should hence probably adjust those too. Suddenly, because we know that the surface temperature in Ede is wrong, we are capable of modifying many fields, and not only in Ede. This is only possible because errors in one quantity at one place, here the temperature at Ede, are statistically linked with errors in other quantities or in other locations. Note that depending on the expected cause of forecast error, the sphere of influence of a correction will vary in size: If the likely cause of error is due to synoptic-scale processes, a single measurement can correct fields over large areas; if that cause is due to a localized phenomenon (e.g., convection), that sphere of influence will be more limited.

The dependencies between errors are what allows data assimilation systems to correct much of the background with a relatively small number of incomplete observations and obtain a new analysis. In general, these dependencies are assumed to be linear in variance, i.e., $\sigma^2_{variable\ 1} = k^2\sigma^2_{variable\ 2} + \sigma^2_{unexplained}$; if you know $\sigma_{variable\ 1}$, $\sigma_{variable\ 2}$, and k that is linked to the correlation between the errors in the two variables, you can propagate an innovation in *variable 2* ($\Delta_{variable\ 2}$) into *variable 1* using $\Delta_{variable\ 1} = k\Delta_{variable\ 2}$, and have *variable 1* benefit from the reduction in uncertainty on *variable 2*. The many existing assimilation approaches (3DVar, 4DVar, EnKF, LETKF, EnVar, etc.) primarily differ in the assumptions, approaches and algorithms used to estimate $\sigma_{variable\ 1}$, $\sigma_{variable\ 2}$, and k for every combination of variables and locations.

1.3 Conditions of Success of Assimilation

Based on this conceptual understanding we can gather from the two subsections above, we may make a list of the conditions that must be met for data assimilation to lead to a useful innovation and ultimately to a reduction in forecast errors. First, there must be a sufficient number of observations adding value or somewhat contradicting the background (mismatch condition), and they must be unbiased (unbiased measurements condition). Second, the model must be capable of reproducing the observations it is trying to assimilate (reproducibility condition). Next, the assimilation system must be able to use the contradictory observation and efficiently innovate the needed state variables to account for that mismatch (usability condition). Then, the assimilation system has to establish and/or use the relationship between state variable errors to propagate the innovation to surrounding areas and state variables (information propagation condition). Finally, the innovated state variables must play a significant role in determining the future state of the atmosphere (relevance condition). For each of these conditions of success, one can find associated causes of assimilation failure. Table 1 summarizes this admittedly complicated but important list.

Table 1: Conditions of success and resulting possible causes of failure of data assimilation systems used to improve weather forecasts.

Conditions of success	Possible causes of failure
Mismatch condition: The analysis will differ from the background if real observations do not agree with observations simulated using the background	Insufficient contradictory information from observations (too few in number, or too small in mismatch magnitude compared to observation uncertainty)
Unbiased measurements condition: Observations and their simulation must be statistically unbiased	Biased data (e.g., incorrect calibration, bad bias correction) or systematically incorrect measurement simulation
Reproducibility condition: The model must have the variables, physics, and resolution needed to 1) generate the real current atmospheric state and 2) simulate accurately the physics of the measurement process	1) Incorrect/insufficient physics in model; 2) Insufficient effective resolution to simulate the observed processes; or 3) Lack of ability or insufficient information to simulate observations (e.g., no 6^{th} moment of rain computed in the model to simulate *Z*)
Usability condition: The assimilation system must be able to use the observation-background mismatch to efficiently adjust the model state at the grid-point where the observation occurred	1) Ill-behaved or unknown relationship between observation mismatch and model-state innovation (e.g., behaving non-linearly when it is assumed to be linear); 2) Bad background errors; or 3) Bad observation errors or incorrect estimate of their correlation
Information propagation condition: Innovations in each variable at each location can be propagated to other variables at other locations if usable relationships between them exist and are known to the assimilation system	1) No systematic/determinable relationships between errors; or 2) Unknown functional form(s) or magnitude of these relationships
Relevance condition: Changed fields must play a significant role in the future evolution of the weather patterns of interest for forecasts to be improved	Changed fields do not significantly affect future atmospheric evolution, and fields of importance to the forecast are not significantly affected

This table is worth coming back to as we analyze the challenges of radar data assimilation.

2 A Reflection on Radar Data Assimilation and its Challenges

Radar is our best instrument to monitor and study storms; data assimilation is our best method to merge information; numerical forecasting is our best forecasting tool. We should therefore expect that the assimilation of radar data into convective-scale models will provide the best forecasts. Yet it does not appear to be the case (Fig. 3). For precipitation, simple extrapolation of rainfall patterns still regularly beat numerical forecasting with radar data assimilation for a couple of hours. More curious are the facts that a) the skill of numerical forecasting aided by radar data assimilation drops very rapidly in the first forecast hour, and b) assimilated radar data shows positive effect for much shorter periods (e.g., about two hours) than other instruments (e.g., six hours for surface observations; L. Fillion, 2017, private communication).

This very rapid drop in skill and the short duration of increased skills sparked questions in me. Specifically, *what is fundamentally and/or practically different between the data from radar and that of other sources that may affect their assimilation*, in particular in the context of convective-scale forecasting? Note that this question is different and complementary to the more traditional "*what makes convective-scale assimilation difficult*" for which we already have many answers.

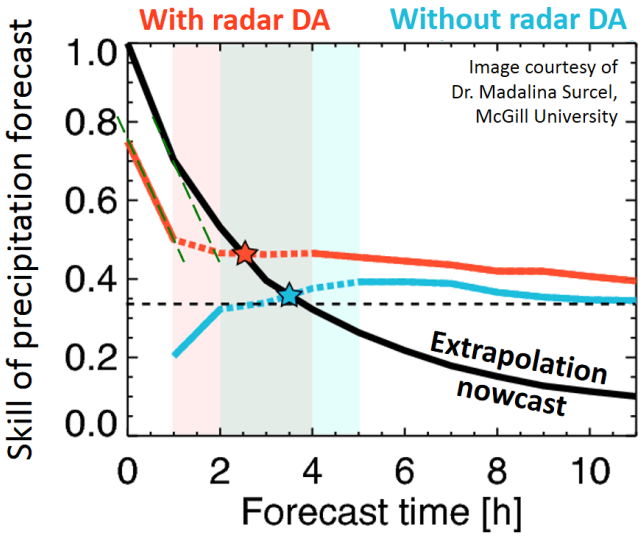


Figure 3: Skill of precipitation forecasts with (orange) and without (cyan) using radar data assimilation for the US Spring Experiment of 2008. The skill of echo nowcasting (black) is also shown. Note the rapid skill drop in the first hour for forecasts using radar assimilation.

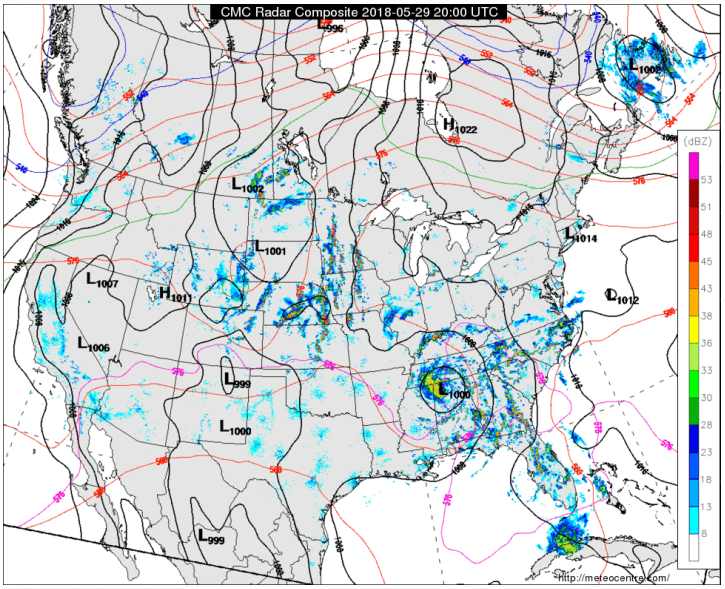


Figure 4: Reflectivity composite and sea-level pressure over southern Canada and the United States on a late spring afternoon.

3 The Sparseness of Radar Innovation and its Implications

If the assimilation of radar data behaves differently than that of other datasets, the answer is likely in the characteristics of the radar data itself. This brings us to our first question: What does radar measure?

First and foremost, radar measures echo strength. Echoes come primarily from precipitation, and a large fraction of the other echoes (ground, interference, birds, and sometimes insects) is filtered prior to assimilation. Then, only in areas with echoes can we measure other properties such as Doppler velocity or dual-polarization characteristics.

Precipitation is an unusual atmospheric field. First, it is zero over more than 90% of the troposphere. Non-zero values tend to form small clusters and be close to normally distributed in logarithmic units (this is why reflectivity maps in dBZ are esthetically pleasing, more so than those in linear Z units). This distribution in magnitude and in space is very different from that of other atmospheric fields. For example, contrast the fields of pressure and of reflectivity largely from rain in Fig. 4: pressure is smooth and has large-scale patterns, and its value varies continuously; precipitation has a lot more small-scale variability and forms clusters with large areas of zeroes in between.

As a result, the innovation from radar data is clustered to small areas: For much of the model grid-space, the background and the measurements agree perfectly that precipitation is zero. There is hence no innovation in these areas, and no reason to improve on the background (see the mismatch condition in Table 1). Radar observations will induce an innovation only in regions where either the background or observations have precipitation. This limits the reach of radar data assimilation.

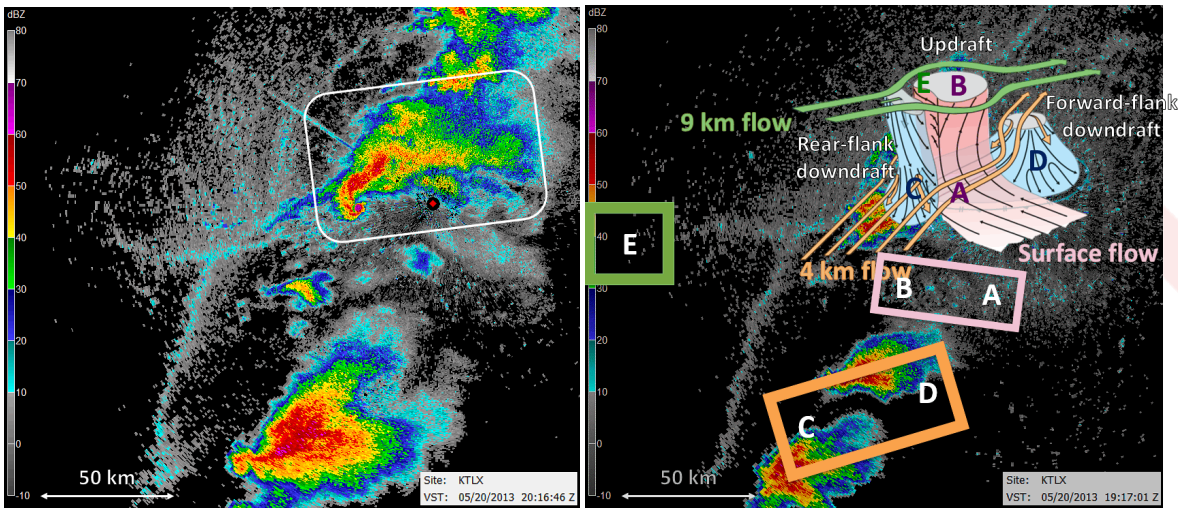


Figure 5: Left: Reflectivity PPI of a supercell to forecast (in the rectangle). Right: The same image one hour before, with a cartoon of the supercell positioned where the storm will be an hour later. White letters show the location of the air that will feed different areas of the storm (matched colored letters). Note how many of those fall in no-echo areas, especially the crucial A-B set (storm inflow).

Figure 5 provides a great illustration of this issue and its implications. Consider the tornadic supercell storm in the rounded rectangle on the left image that struck Moore OK in 2013. It is a perfect example of the type of events we want to forecast well in advance, say with a lead-time of an hour. To forecast such a storm, we need to know the inflow that will provide its heat and moisture (identified as the colored letters A and B on the right of Fig. 5). We also need to know the properties of the air that will make up the surrounding environment and feed its downdrafts (colored letters C to E). An hour before, where is the air that will make up the future storm components? In the areas bounding the white letters on the right of Figure 5. Most of those are devoid of radar echoes; therefore, radar cannot obtain much information about them, at least directly.

This implies that most of the improvement in forecasts that radar can provide must be indirect: information has to propagate from the regions of echoes to the regions identified in the white letters. This is possible only if there are useful and known relationships between the observed characteristics of radar echoes and atmospheric properties in the identified regions. In the absence of such relationships, radar information is of limited use for improving key forecasts like this one. This illustrates the critical importance of having useful error dependencies between echo areas and other regions.

4 Radar: Strong to Detect the Impacts of a Storm, Poor to Observe its Causes

Radar has become a valued operational instrument for weather surveillance thanks to its ability to characterize storms and monitor their impacts. Warnings of anticipated and current storm damages rely largely on radar imagery. It is hence natural to think of radar as our best tool to monitor storms. This success explains why we naturally think that its data should be equally skillful at helping us forecast these storms numerically. But radar is much better at detecting the threats of storms than at inferring their causes.

Radars actually detect storms only late in their life cycle. Consider the time sequence of the evolution of storms illustrated in Fig. 6. Storms begin thanks to the combination of environment conditions that provide its fuel (temperature profile, humidity at the base of the storm), and a forcing mechanism that breaks the capping inversion preventing the storm to form earlier (e.g., via low-level convergence). Except perhaps for the forcing mechanism itself, radar is largely blind to these environmental conditions. As the unstable air parcel accelerates upwards, clouds form rapidly. But again, radar is largely blind to water clouds. Only when coalescence or ice crystal growth is significant enough do echoes appear aloft (Fig. 7). By that time, the storm is well underway, and precipitation starts very quickly. It is at the latter stages of storm evolution that radar provides its best information. Unfortunately, this does not give us much time to use radar information to make a forecast.

Let us complement the time-evolution view above with information obtained by considering atmospheric evolution in a process-oriented context. The box-and-arrow diagram in Fig. 8 illustrates the many interactions between different atmospheric properties relevant at weather timescales. Radars detect precipitation, and one component of the 3D wind where echoes are available. But the main driving force of storm dynamics is the pressure gradient arising from temperature and/or density contrasts, while the main control on storm intensity is low-level temperature and humidity. In fact, the property best constrained by radar measurements, precipitation, 1) is the furthest from storm causes, 2) has limited feedback on them, and 3) is short-lived without support. Indeed, if precipitation is modified in a model analysis and nothing else, that precipitation will rain out quickly without having had much time to influence the evolution of other atmospheric properties. Only if assimilation properly changes the fields that result in precipitation may it have a lasting positive effect.

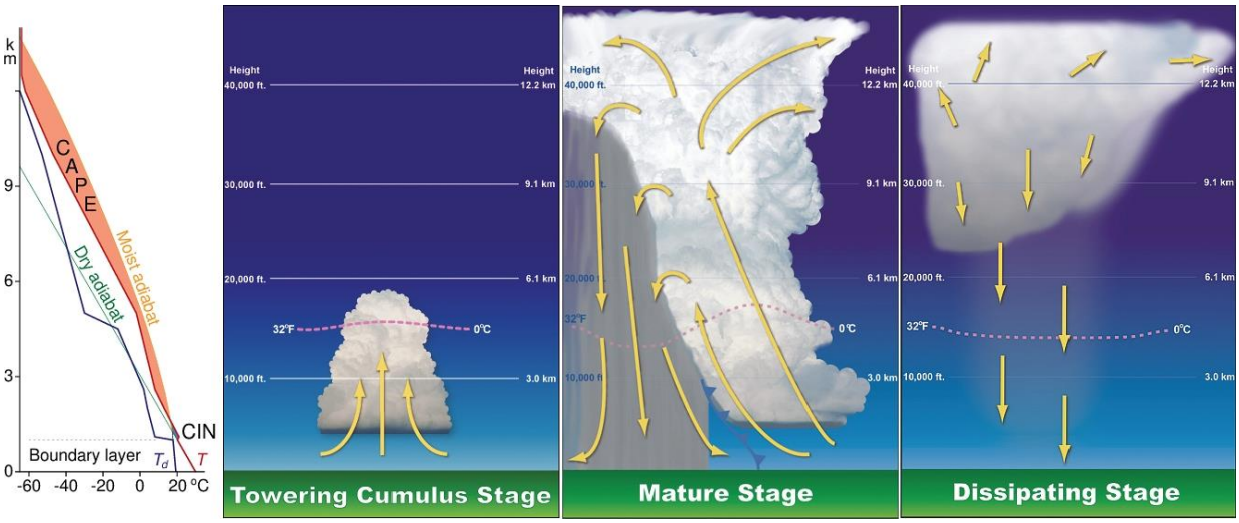


Figure 6: Idealized vertical section of the time evolution of convective cell in a weak vertical wind shear environment during its growing stage, mature stage, and dissipation stage. Source: NOAA JetStream. Added on the left is a vertical profile of the environmental temperature (T) and of dew point temperature (T_d) associated with this event illustrating the vertical structure of the well-mixed boundary layer at the base of the troposphere, superposed with a zone of convective inhibition (CIN) offering some resistance to the formation of thunderstorms, itself superposed with a large conditionally unstable region with much convective available potential energy (CAPE)..

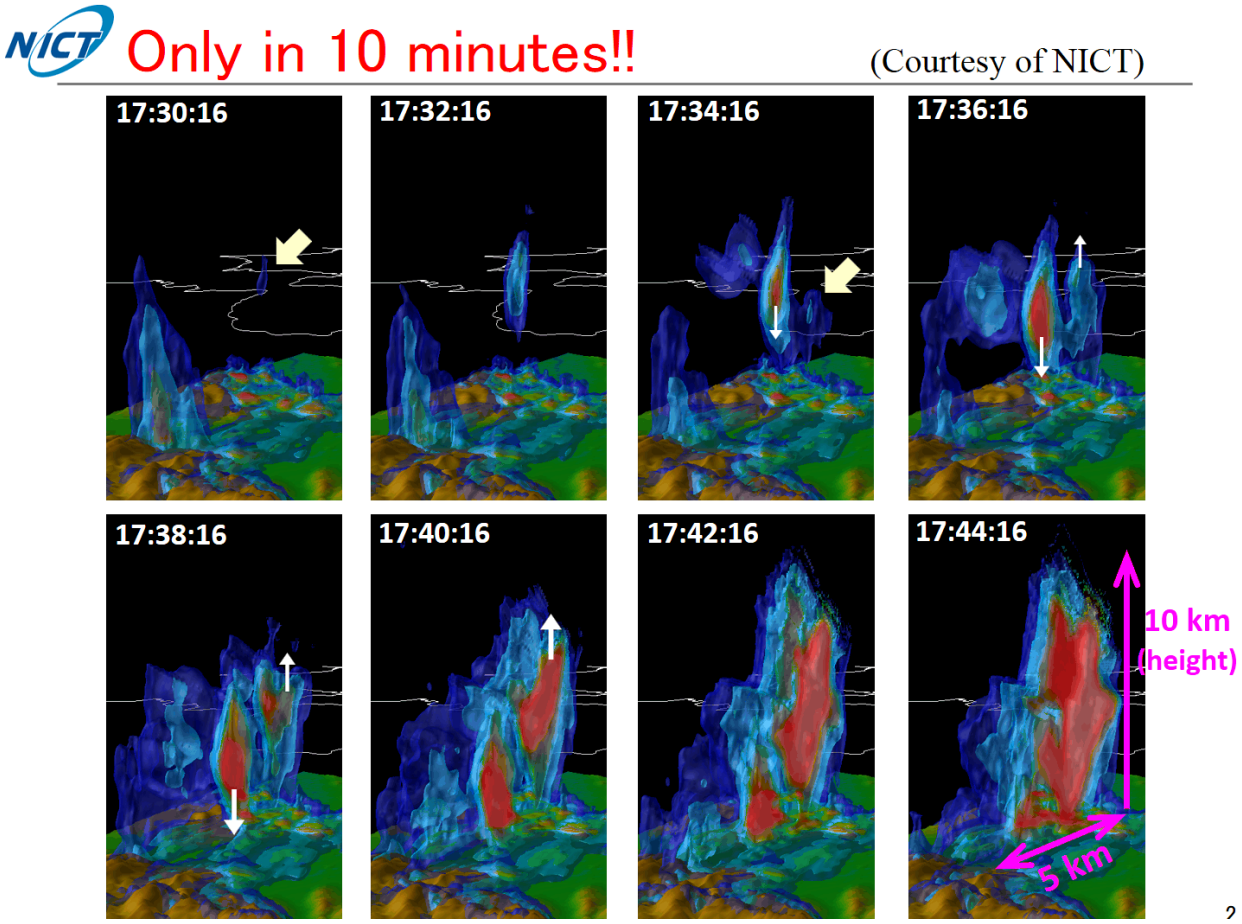


Figure 7: Time sequence of the evolution of the echoes from two convective cells as observed by a phased-array radar. Contrast these images with Fig. 6, and note how late radar detects a storm in progress. From a presentation by (Miyoshi T., 2018).

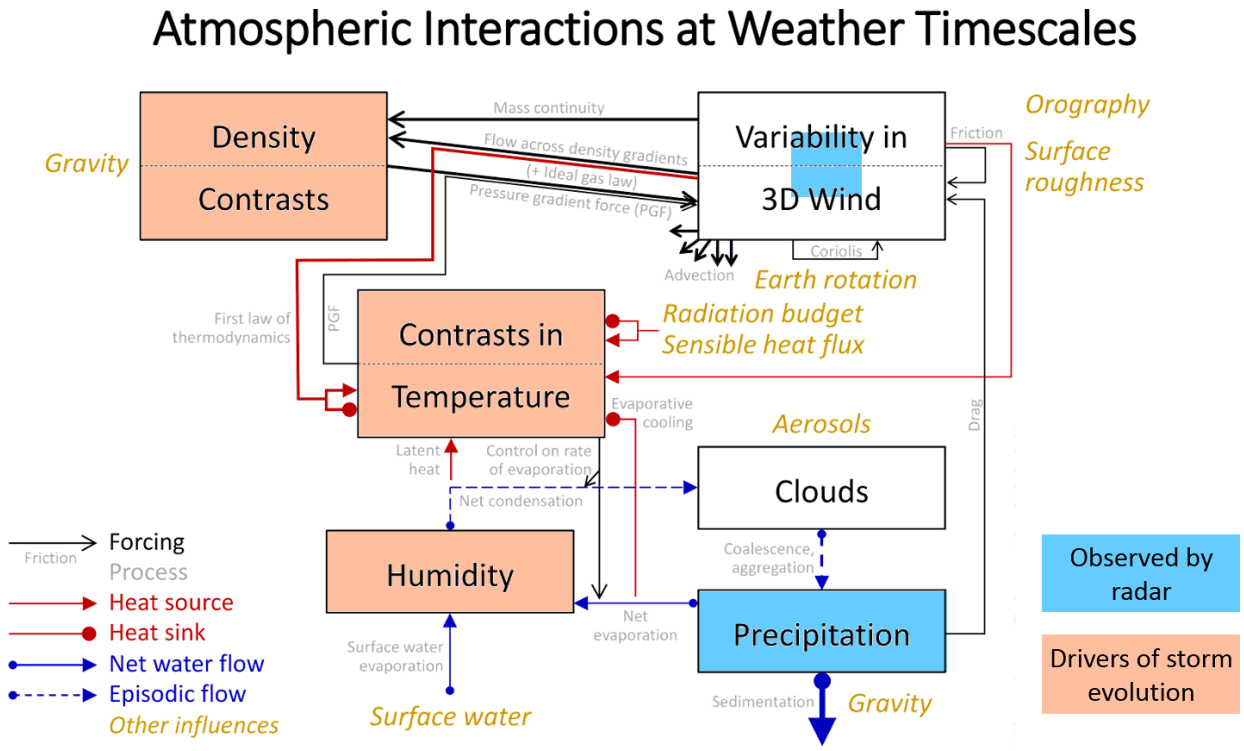


Figure 8: Box-and-arrow diagram of how atmospheric properties influence each other based on the prognostic equations of forecasting models. Atmospheric properties that drive storm evolution are shaded in orange while the ones observed by radar are shaded in cyan.

The discussions around Figs. 6 and 8 illustrate two key limitations of radar data for convective-scale assimilation: Direct information on storm properties arrive late in the time evolution of storms, and the atmospheric fields well measured by radar do not significantly shape the evolution of present and future events. We must hence largely rely on indirect information, namely what can current storm characteristics tell us about storm drivers in the past, and what can we infer from them concerning storm drivers in the future.

5 Compounding Difficulties to Radar Data Assimilation

The sparseness of the radar innovation and the lack of relevancy of the properties directly estimated to the improvement of forecasts are two fundamental obstacles to the successful assimilation of radar data. We should not however forget additional challenges linked with the field of precipitation, its sampling with radar, and its modeling.

5.1 The Lack of Large-Scale Variability of Rainfall

As illustrated in Fig. 4, compared to other atmospheric fields, rainfall lacks large-scale variability (or has considerable small-scale variability). As a result, the errors in forecasted rainfall will also be smaller-scale errors. Because such forecasts are used as background fields by assimilation systems, two additional obstacles arise. First, the successful modeling of rainfall relies on the ability of models to simulate detailed smaller-scale processes, something they often do poorly because of limited resolution and microphysics. The lack of effective model resolution limits the model's ability to simulate what can be observed and hence the benefit of innovation from observations. A case could be made that since models cannot simulate the finest-scale processes of precipitation shaping what radars measure, maybe we should not assimilate measurements at the highest available resolution. Second, the lack of large-scale errors in precipitation limits the sphere of influence of any assimilated measurement: If errors are largely at smaller-scales, than the correlation between errors here and further out is reduced (Fig. 9). Hence, projecting information originating from precipitation is more difficult than doing so from other data sets. And yet, as illustrated in Fig. 5 and Section 3, we have specifically identified a need to project information at "large" distances out from radar echo areas. Figuring out how to do so effectively should significantly increase the effectiveness of radar data assimilation.

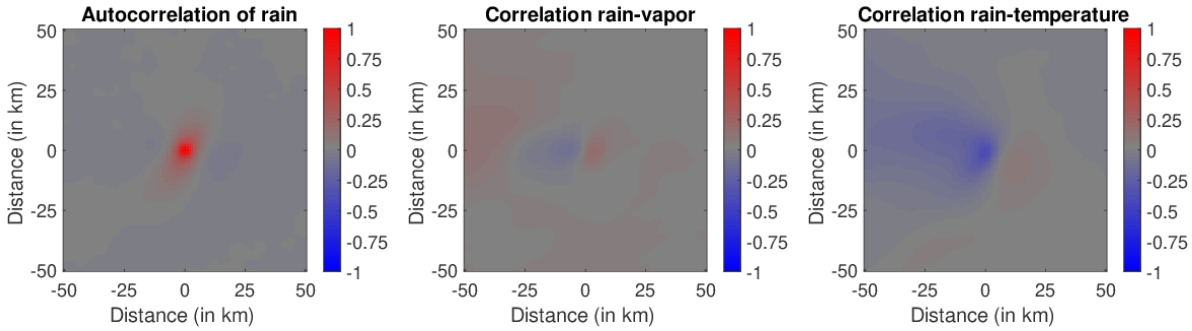


Figure 9: Correlation between errors in rainfall at one point and those of rainfall (left), vapor mixing ratio (middle) and temperature (right) at 750-m altitude from the 1000-member ensemble from (Jacques D., 2015).

5.2 Radar-Measured vs Modelled Properties

Radar measures beam- and range-weighted reflectivity, a property linked with the sixth moment of precipitation. In echo areas, it also measures other properties beam, range, and reflectivity weighted. Models simulate a few moments of precipitation on a grid, but generally not the sixth. In the process of simulating radar observations, the assimilation system must convert the moments simulated by models into reflectivity, a process not unlike what we do with *Z-R* relationships. It must do so taking into account the geometry of radar measurements. These two processes will come with errors that are correlated in space. For example, the same microphysical processes that cause drops to be unusually large or small at one location also act in nearby areas. In the 70 years we have had *Z-R* relationships, we have not definitely characterized the statistical properties of their error, especially its spatial correlation. This must now be achieved to help data assimilation.

Additionally, assimilation approaches are based on the hypothesis that data are not biased. Calibrated data everywhere are hence a necessity, and so are unbiased observation simulations.

5.3 The Convective-Scale Context

At larger scales, there exists some reasonably well respected approximations linking atmospheric properties: hydrostatic balance, quasi-geostrophy, etc. These help assimilation systems fill missing information. At convective scales, these approximations break down, and we need additional information to compensate.

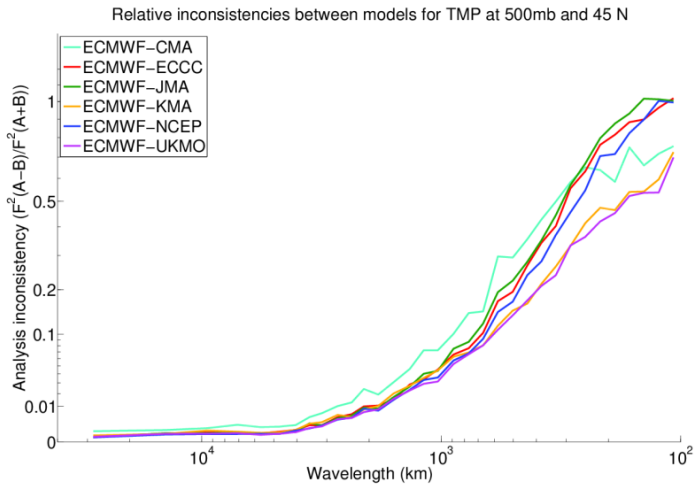


Figure 10: Fractional inconsistency in variance between the analysis of ECMWF and of other global models for temperature at 50 kPa and 45°N computed from the power spectrum of the difference and of the sum between two model fields. A fractional inconsistency of 1 means that fields at that scale are completely decorrelated. At scales below 300 km, the different analyses are more than 50% inconsistent.

The need for information at smaller scales is particularly acute given that the global analyses that will often serve as the first background information to meso- and convective-scale forecasts are largely inconsistent at smaller scales (Fig. 10), and hence all probably have large errors. Correcting those errors is hence the task of data assimilation at high-resolution; failure to achieve this correction will result in significant errors at the mesoscale that will affect the model's ability to forecast events at those scales. And because radar is the most important data source at those scales (Table 2), it will have to play a key role in that task if storm forecasts at convective scales are to become the way of the future.

Table 2: Measurements of any atmospheric variable per hour over a 10×10 km area comparable to the size of a convective cell. For this exercise, a typical surface station reports information for five variables (pressure, temperature, dew point, winds, and precipitation).

Data source	Number of observations
Upper air observation of any variable using planes, radiosondes, GNSS receivers, etc.	≈ 0−10 (0−8 about thermodynamics)
Surface observations of any variable	≈ 0−10 (0−4 about thermodynamics)
Geostationary satellite (per channel)	≈ 1,200 (largely from cloud top up)
Radar reflectivity	≈ 25,000
Radial velocity (assuming 60% echo coverage in storms)	≈ 15,000 in storms, 0 in no echo areas

6 Summarizing Conclusion: A Sobering Table (Table 3)

Table 3: Possible causes of failure of data assimilation systems used to improve weather forecasts and radar-specific challenges.

Possible causes of assimilation failure	Some radar-specific challenges
Mismatch condition: Insufficient contradictory information from observations (too few in number, or too small in mismatch magnitude compared to observation uncertainty)	1) The richest information from radar come from areas with echoes (<10% coverage); and 2) over most of the model domain, there are no mismatch in precipitation
Unbiased measurements condition: Biased data (e.g., incorrect calibration, bad bias correction) or systematically incorrect measurement simulation	Reflectivity measurements are often biased; so can their simulation given the limited microphysics of models
Reproducibility condition: 1) Incorrect/insufficient physics in model; 2) Insufficient effective resolution to simulate the observed processes; or 3) Lack of ability or insufficient information to simulate observations (e.g., no 6^{th} moment of rain computed in the model to simulate *Z*)	1) Small-scale processes that shape rainfall and its reflectivity are often not resolvable; and, 2) most model microphysics cannot be used to unambiguously compute reflectivity
Usability condition: 1) Ill-behaved or unknown relationship between observation mismatch and model-state innovation (e.g., behaving non-linearly when it is assumed to be linear); 2) Bad background errors; or 3) Bad observation errors or incorrect estimate of their correlation	1) Observation operators must include all measurement physics (beam smoothing, reflectivity weighting…); and, 2) the correlation distance of errors in simulated reflectivity arising from assumed rain-reflectivity relationships is unknown
Information propagation condition: 1) No systematic/determinable relationships between errors; or 2) Unknown functional form(s) or magnitude of these relationships	Limited or complex relationships exist between rainfall and other errors, especially at larger distances
Relevance condition: Changed fields do not significantly affect future atmospheric evolution, and fields of importance to the forecast are not significantly affected	Changing rainfall has the least impact of the future outcome of storms; key fields such as temperature and humidity are harder to modify using radar data

Acknowledgement

This work was made possible by a grant from Environment and Climate Change Canada.

References

Fabry F. Radar Meteorology - Principles and Practice [Book]. - [s.l.] : Cambridge University Press, 2015. - Vol. ISBN 1107070465.

Jacques D. and Zawadzki, I. The impacts of representing the correlation of errors in radar data assimilation. Part II: Model output as background estimates [Article] // Monthly Weather Review. - [s.l.] : American Meteorological Society, March 2015. - Vol. 143. - pp. 71 - 75. - 71 - 75.

Miyoshi T. J. Ruiz, G.-Y. Lien, T. Teramura, Y. Maejima, K. Kondo, H. Sakamoto How fast shall we go? Lessons learned from 30-second-update, 100-m-mesh data assimilation experiments [Conference] // 8th EnKF Workshop. - Mont Gabriel : [s.n.], 2018.

WIND TURBINES SEEN IN RADAR DATA WITH THE BIG DIFFERENCE METHOD

Willi Schmid[1] and Stefan C. Müller[2]
[1]*meteoradar gmbh, Räbacher 4, CH-8143 Stallikon, Switzerland*
[2]*Meteotest AG, Fabrikstrasse 14, CH-3012 Bern, Switzerland*
(Dated: 18 June 2018)

1 Introduction

The effectiveness of filtering wind turbines in radar data is degraded by the moving rotor blades. Therefore, the echoes of wind turbines may remain visible in radar images of precipitation. The degree of disturbance by the wind turbines is not really clear in a given setting. It is argued that the radar data are affected even far away from the wind turbines, due to multi-body scattering and side-lobe effects of the radar antenna (DWD 2013a). For these reasons, the users of radar data, especially weather services, are concerned about the growing number of wind turbines in the vicinity of radar stations. Based on a recommendation by (WMO 2010), the German Weather Service does not allow the construction of wind turbines closer than 5 km to a radar site (DWD 2013b). In the range 5-15 km from a radar the construction of wind turbines is only allowed as long as the peaks of the rotor blades remain below the altitude of the radar antenna. These restrictions inhibit the plans of manufacturers of wind turbines, since the economic benefits of big turbines are better than those of smaller ones.

In that conflict, there is a need for a better understanding of the effects of wind turbines on radar data. Studies of these effects are typically done with multi-year data samples (Norin, 2015), (Teschl, et al., 2016), in order to isolate the effects of the wind turbines in probability distributions of the quantities of interest, e.g., radar reflectivity (Z, dBZ) or Doppler velocity (V, m/s). The main reason for the need of long-term radar data is the natural variability of these quantities.

In this contribution, we investigate the differences of Z (dB) and V (m/s), measured in two plan position indicators (PPI's) at adjacent elevation angles. The echoes of precipitation show small differences in a proper setting (short distance from the radar, short time lag between the radar measurements, no melting layer, smooth radar patterns, negligible advection), but the differences increase dramatically under the influence of wind turbines and other sources of clutter. So, using proper threshold values applied to the measured differences lead to an objective detection of the areas affected by wind turbines. The dramatic advantage of this method is that much shorter time series of radar data than used in the studies mentioned above are required for a quantitative assessment of the effects of wind turbines on radar data.

We use in this study the radar data of a 12 hour period in early summer 2017, measured with the radar Türkheim in Southern Germany. This period covers dry weather and a cluster of thunderstorms followed by stratiform precipitation. Four wind turbines are in a distance of 2.5 km from the radar. A communication tower (the "tower" hereafter) is, not far away, in the same distance from the radar as the wind turbines. We investigate the differences of Z and V in various sectors: in free air above shadowed ground, above visible ground, at the locations of the tower and the wind turbines and in various distances from these obstacles. We found that each sector has its characteristic "footprint": a characteristic percentage number of big differences as a function of precipitation intensity. We show and discuss hereafter some examples for illustration and summarize our findings on how the effects of wind turbines depend on distance from the turbines.

2 Data and procedure

The radar Türkheim is located in a complex relief, composed of flat hills, steep valleys, free fields, forests and a variety of mostly small settlements. About 10 wind farms can be found within a distance of 15 km from the radar. For this study, we have selected the wind farm Aufhausen, consisting of 4 wind turbines in a distance of about 2.5 km from the radar. A tower is located a bit north of the turbines. Fig. 1 shows the positions of the turbines, the tower and the radar.

The radar operates continuously, providing 11 PPI scans of radar reflectivity Z (dBZ) and Doppler velocity V (m/s) every 5 min. We analyze the PPI data at the elevation angles 0.5, 1.5, 2.5 and 3.5 deg. The differences DZ and DV are defined in Equations (1) and (2), the indices *up* and *lo* correspond to these pairs of elevation angles: 1.5/0.5, 2.5/1.5 and 3.5/2.5 deg.

$$DZ = Z_{up} - Z_{lo}(dB) \qquad (1)$$

$$DV = V_{up} - V_{lo}(m/s) \qquad (2)$$

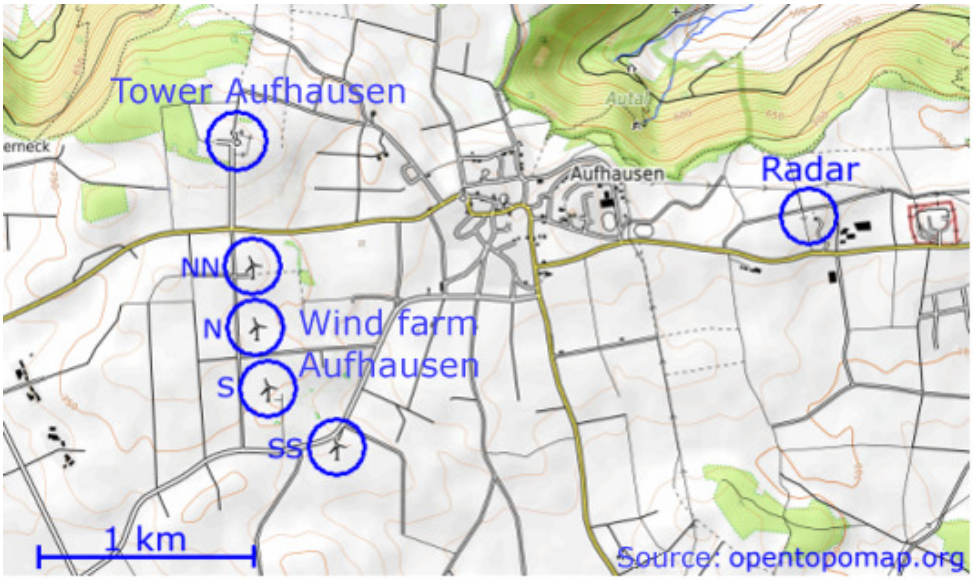


Fig. 1: The radar, the wind turbines and a communication tower nearby.

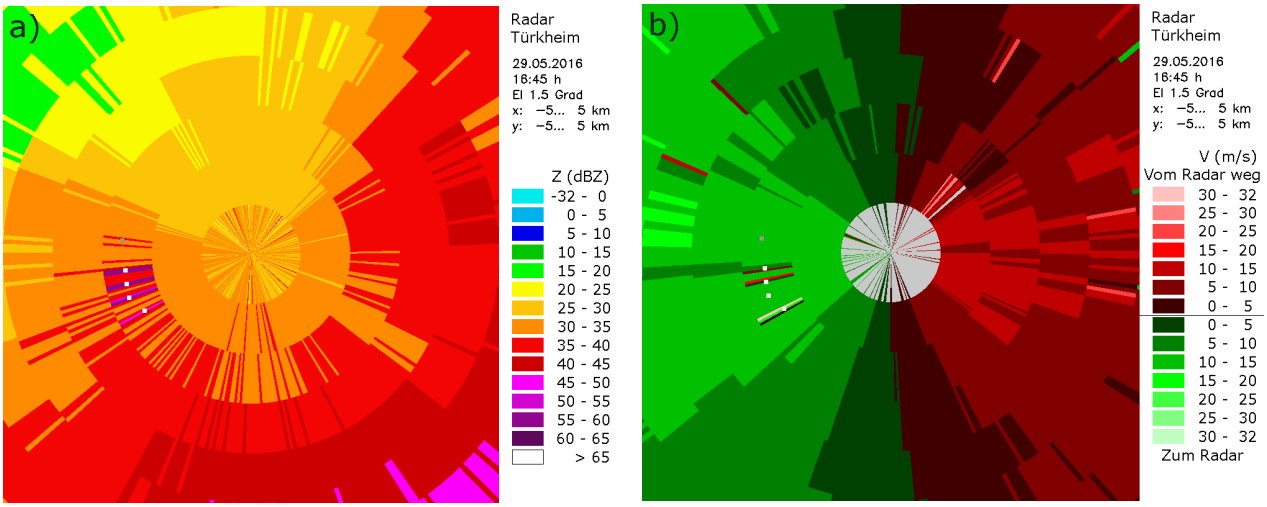


Fig. 2: Radar reflectivity (a) and Doppler velocity (b) at 16:45 UTC on 29 May 2016

The radar data cover a time period of 12 hours (1000-2200 UTC on 29 May 2016) and have a resolution of 1 km in range and 1 deg. in azimuth. The data passed a clutter filter based on Doppler criteria (DWD 2013a) but they did not pass the new quality management system called RADOLAN (DWD 2017). This system includes an improved filtering of radar data based on polarisation criteria. We recently obtained the same data but optimized with RADOLAN, but the time to consider these data here was too short. Fig. 2 illustrates the effects of the wind turbines on the radar data. The reflectivity pattern (Fig. 2a) shows higher values at the locations of the wind turbines (white dots) than elsewhere. The Doppler velocities (Fig. 2b) are affected as well, but one can find isolated erroneous values of Doppler velocity also far away from the wind turbines.

We define various sectors of interest, typically composed of a couple of neighboring radar pixels. Fig. 3 gives an overview of the sectors in the vicinity of the wind turbines and the tower. The **core sectors** are defined by three neighboring radar pixels in azimuthal direction, surrounding one obstacle. In addition, we define four **neighboring sectors**, two of them on the left and right side of a core sector, and two of them on the back side, seen from the radar. We also define sectors far away from any towers, above shadowed terrain and above visible terrain when viewed from the radar. For brevity, we do not show the locations of these sectors here. The sector above shadowed terrain is called the **clean sector** hereafter, it is assumed that this sector is not affected by ground clutter echoes.

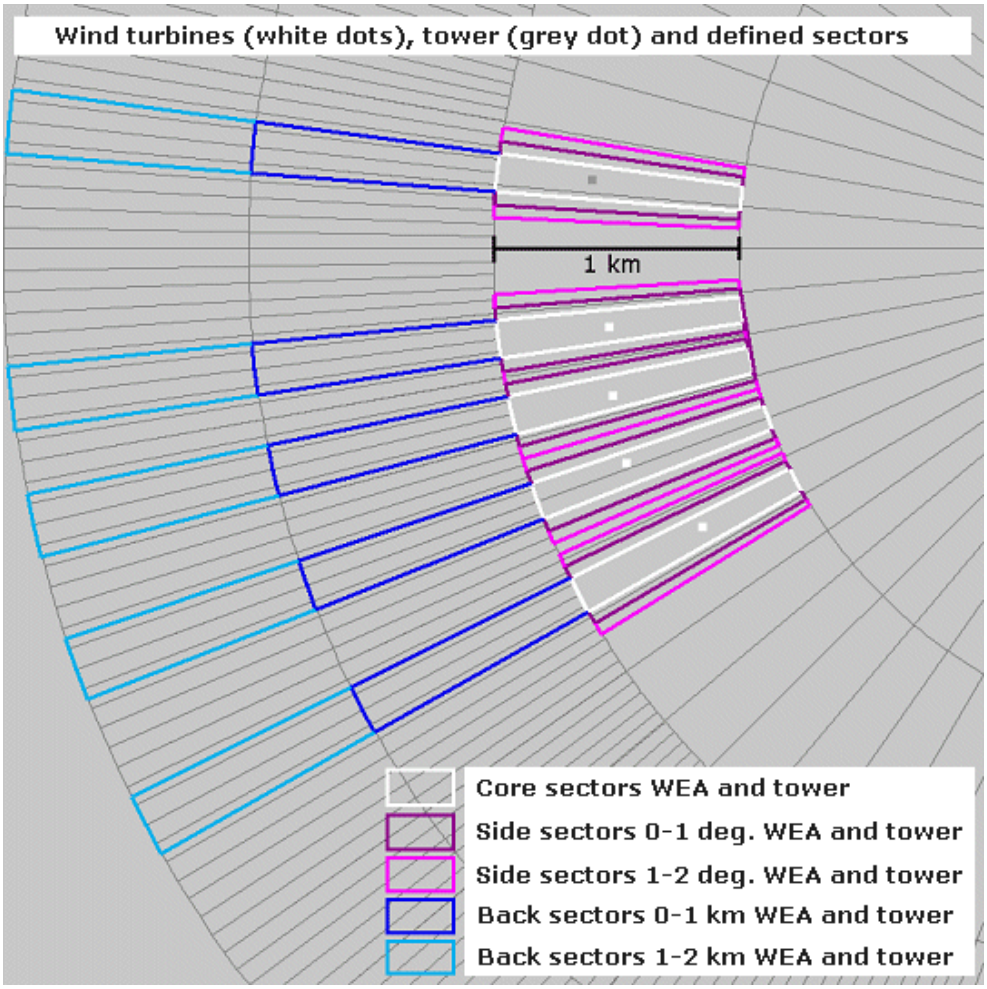


Fig. 3: The sectors defined in the vicinity of the wind turbines and the tower.

We compute the quantities DZ and DV for each radar pixel inside a sector or a group of several sectors. After processing the available time period of 12 hours, we obtain a sample of difference values that is ready for further evaluation. The number of data values representing a sector depends on the number of radar pixels within a sector but typically varies between some 100 and some 1000. Fig. 4 shows the histograms of DZ and DV for the clean sector (Fig. 4a), and for the core sectors attributed to the four wind turbines of the wind farm Aufhausen (Fig. 4b). In both figures, the PPI's at the elevation angles 0.5 and 1.5 deg. have been evaluated. In Fig. 4a we note that almost all difference values are within a threshold of 6.5 (dB or m/s, vertical lines in Fig. 4a). We take this threshold as a separator between **clean** and **affected** data values. In Fig. 4b, many data values are beyond the given threshold and can be attributed to the effects of the wind turbines (plus possibly of the ground) to the radar measurements. A significant amount of data values remain close to zero and still produce a peak in the histogram inside the interval bounded by 6.5 (dB or m/s). These data are considered as being clean, unaffected by the wind turbines, i.e. they can be used for an estimate of Z and V due to precipitation in the core sectors.

We use these properties for an estimate of the percentage amount of affected data values as a function of average radar reflectivity due to precipitation. For this, all difference values are categorized as clean or affected as described in the last paragraph. The clean values are used to calculate the average radar reflectivity (dBZ), which gives an estimate of the average precipitation intensity at a given time for a given sector. The scale of average radar reflectivity is divided into these intervals: 0-10, 10-20, 20-30, 30-40 and > 40 dBZ, and the percentage amounts of affected data on the total data sample is computed for each interval, taking into account the complete time period of 12 hours. The resulting diagrams, showing the percentage number of affected values vs. average radar reflectivity, can be considered as **footprint diagrams**, showing the degree of clutter effects (ground, buildings or wind turbines) on the radar data as a function of radar reflectivity.

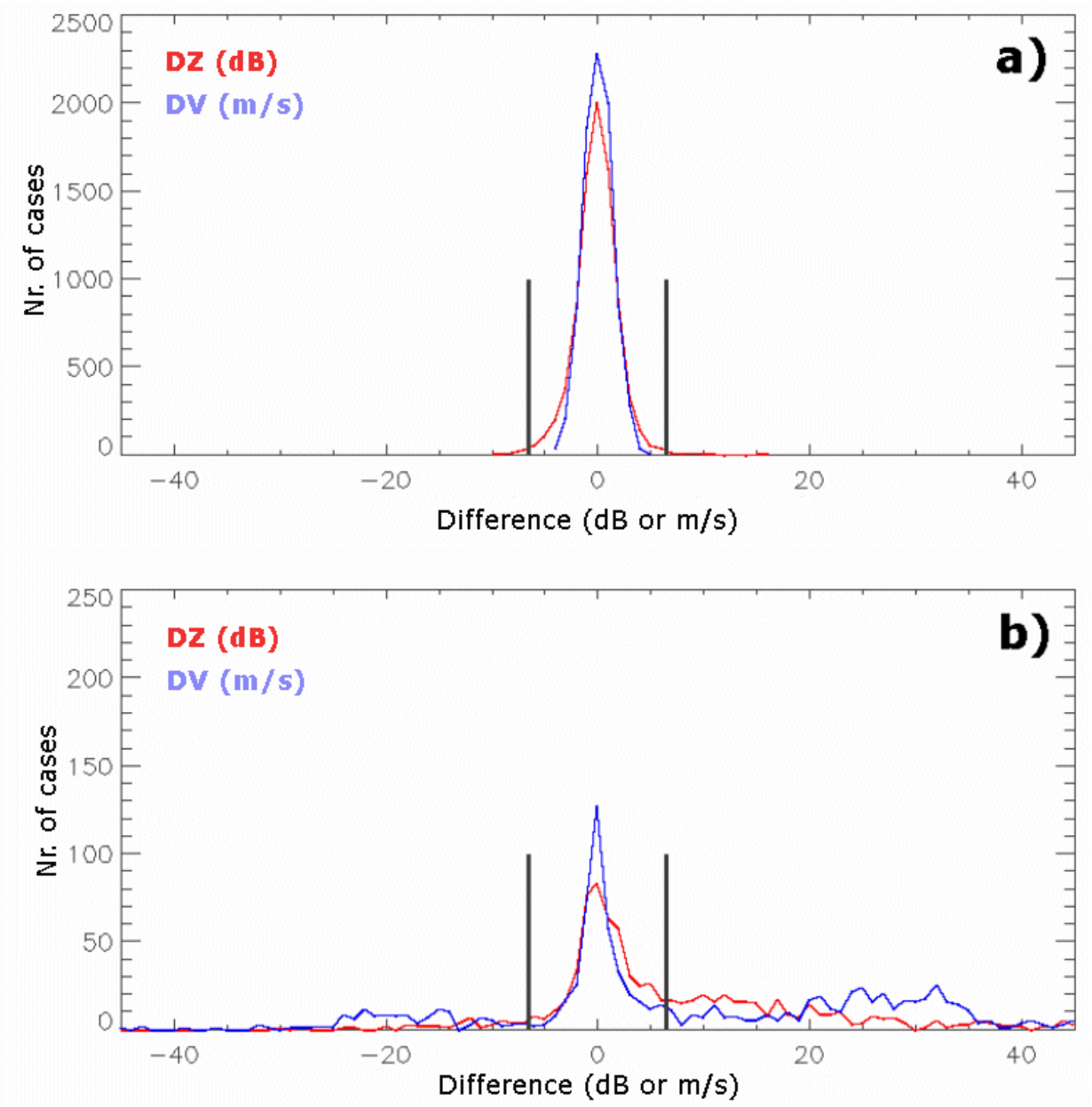


Fig. 4: Histograms of the differences DZ and DV, for a „clean“ sector (a) and the core region of the wind turbines (b) shown in Fig. 2. The vertical lines mark a threshold of 6.5 dB or m/s.

3 Results

We show and discuss a limited selection of footprint diagrams. We have to consider that the tower and additional obstacles (buildings, forests or even free fields) may affect the data in a comparable manner as the wind turbines. First, we discuss these effects with the help of Fig. 5, showing the footprint diagrams of the clean sector at the elevations 0.5/1.5 deg., and of the tower Aufhausen at the elevations 0.5/1.5 and 1.5/2.5 deg. The diagram of Fig. 5a is almost free of affected data. This corresponds to the fact that the surface below the clean sector is shadowed by hills in between the radar site and the sector. A contamination of the radar data by the ground is not possible. It is nevertheless possible that spurious effects, e.g., aircrafts or birds or random noise at low reflectivities may cause affected data values.

In contrast, the core region of the tower is heavily affected when considering the lowest possible couple of elevations (0.5/1.5 deg., see Fig. 5b). The contamination diminishes when considering the next higher couple of elevations (1.5/2.5 deg., see Fig. 5c), at least for reflectivities above 10 dBZ. This difference between the lowest possible level and the next higher level is surprising at a first glance. We explain the difference with the effects of additional obstacles on the ground, mainly trees that move with the winds and create Doppler velocities different from zero. The base height of the tower is above the height of the radar antenna. This means that not only the tower, but also trees and buildings in the neighbourhood may act as obstacles in the path of the 1 deg. wide radar beam at the elevation 0.5 deg. As a consequence, the clutter filtering based on the Doppler effect is not effective since the moving trees due to wind may produce Doppler signals different from zero m/s. At the next higher elevation, the effects of the ground are almost negligible. The tower acts as a motionless obstacle, and the clutter filter works much better than close to the ground. However, few affected data are still present up to 30 dBZ in Fig. 5c.

In order to isolate the effects of the wind turbines and to neglect the effects of other targets on the ground, it is best to consider the elevation pair 1.5/2.5 deg. At the elevation 1.5 deg., the towers and the rotor blades of the wind turbines are significant obstacles in the radar beam. The effects of these obstacles are pronounced over the whole range of reflectivity in the core sectors (Fig. 6a). In the neighboring side sectors (Fig. 6b), the percentage number of affected data diminishes above 10 dBZ, but affected data are still present up to 50 dBZ. A bit more far away from the core region (Fig. 6c) the number of affected data decreases to almost zero above 10 dBZ. We conclude that the wind turbines mainly affect a sector of five neighboring radar pixels in azimuthal direction. There may be a direct effect of the rotor blades when they are oriented perpendicular to the radar, or, there may be sidelobe effects of the radar antenna. Outside the core regions, the effects of the wind turbines are reduced to reflectivities below 10 dBZ.

The effects seen in the back sectors are given in Fig. 7. We find affected data in the reflectivity ranges up to 20 dBZ at a distance 0-2 km from the core sectors (Fig. 7 a and b). We defined additional sectors 4-7 km in the back of the core sectors. There, we find affected data up to 10 dBZ (Fig. 7c). Multi-body scattering is the probable source of the effects that are found in the sectors behind the wind turbines, seen from the radar site. The effects seem to decrease with increasing distance from the wind turbines. We did not evaluate the range 2-4 km from the core sectors, because that range is above a forested hill and may be affected by ground clutter at the elevation 1.5 deg.

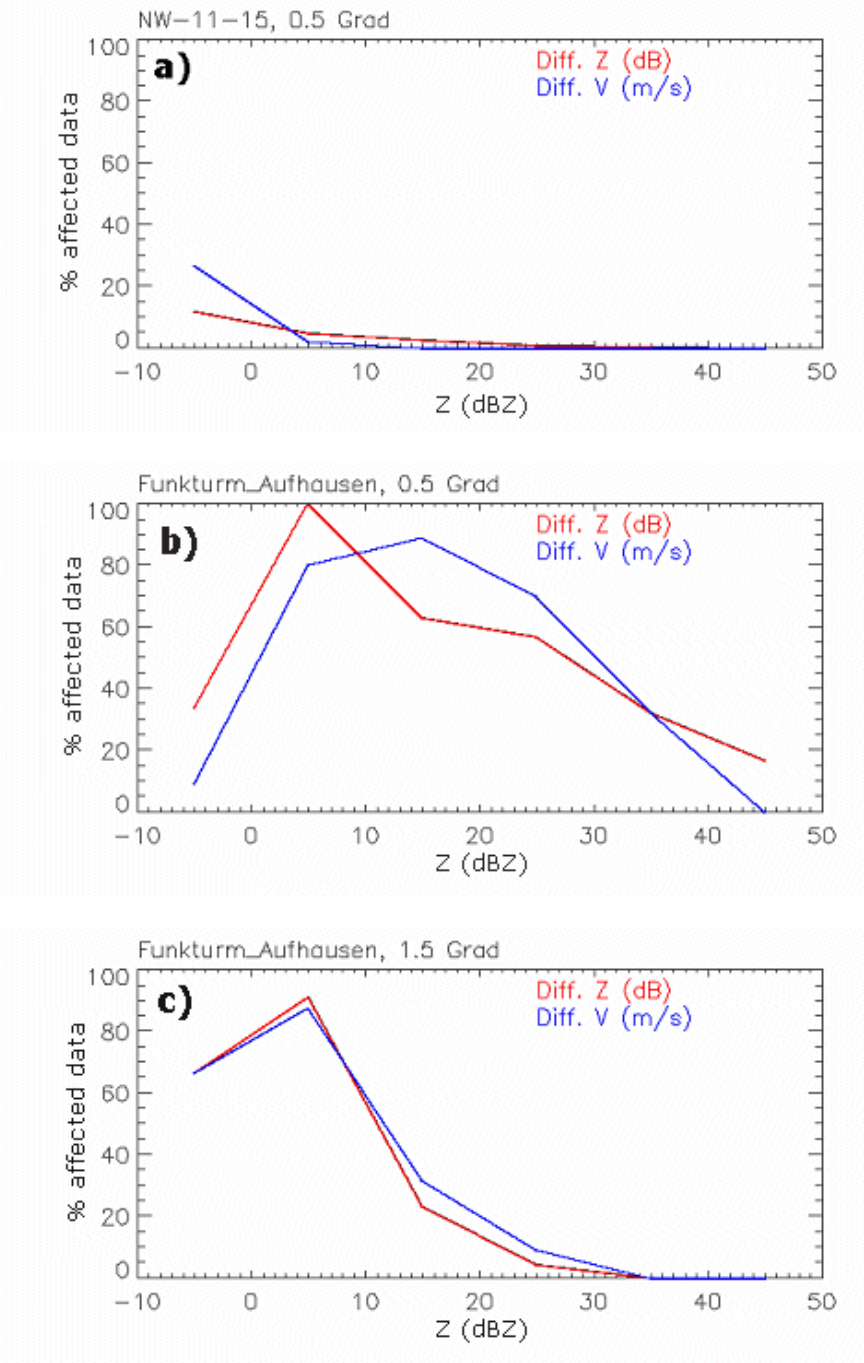


*Fig. 5: Footpri*nt diagrams for a clean sector *at elevations 0.5/1.5 deg. (a), for the core sector of the tower Aufhausen at elevations 0.5/1.5 deg. (b), and for the core sector of the tower Aufhausen at elevations 1.5/2.5 deg. (c).*

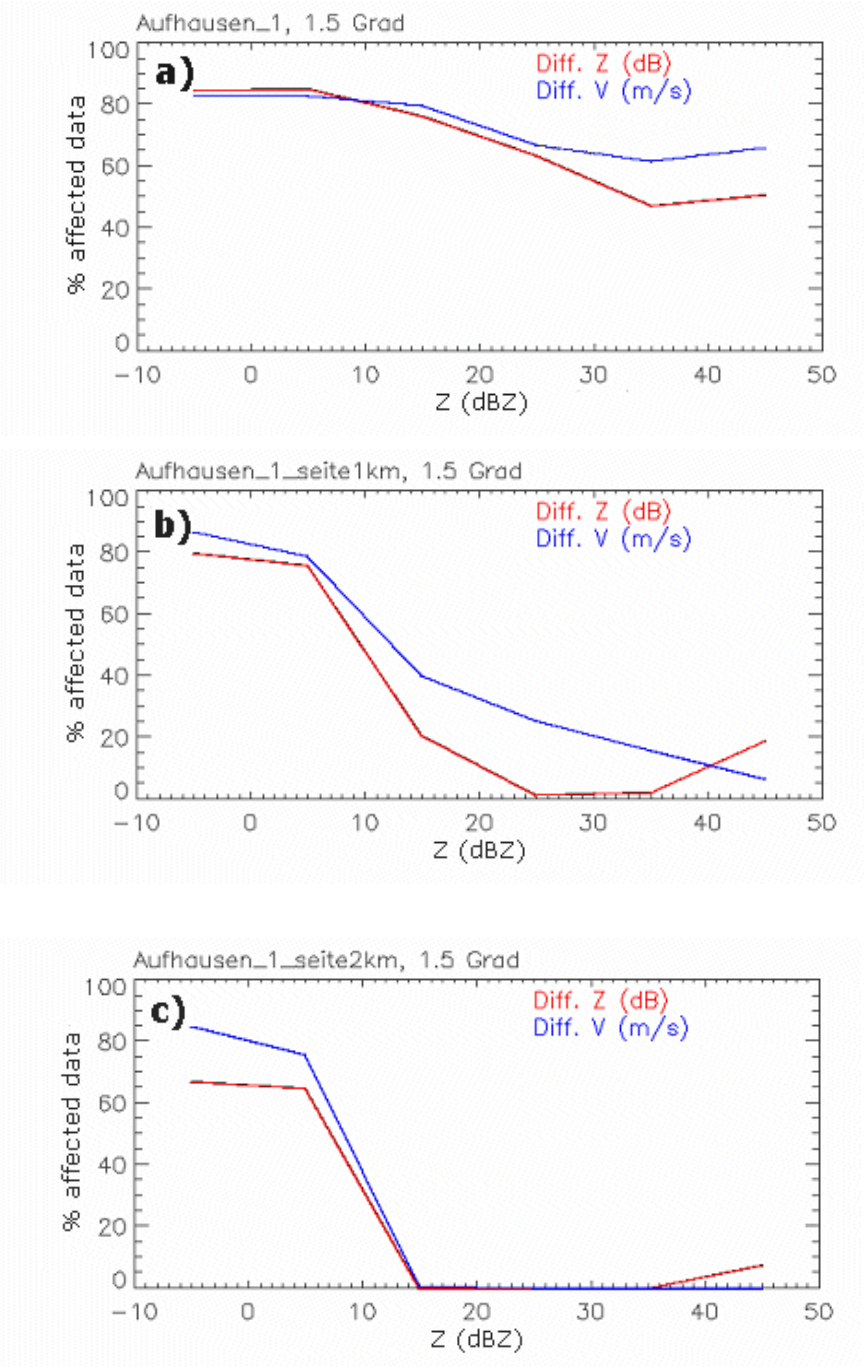


Fig. 6: Footprint diagrams of the wind farm Aufhausen at elevations 1.5/2.5 deg., for the core sectors (a), for the side sectors 0-1 km (b), and for the side sectors 1-2 km (c).

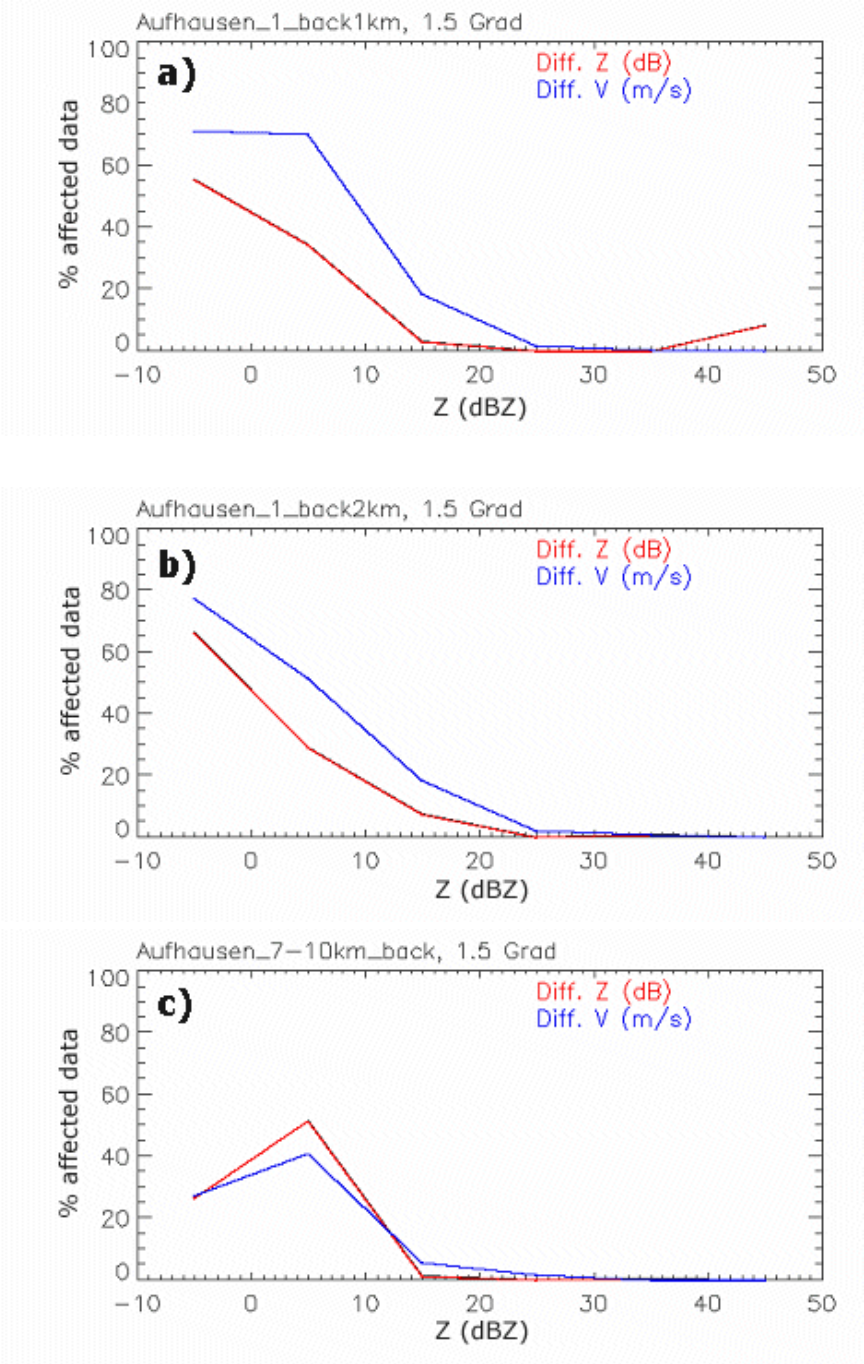


Fig. 7: Footprint diagrams of the wind farm Aufhausen at elevations 1.5/2.5 deg., for the back sectors 0-1 km (a) 1-2 km (b) and 4-7 km (c).

4 Conclusions

We propose the "big difference" method for assessment of the degree of disturbances caused by wind farms. The differences between the PPI data of two adjacent elevation angles can be used to obtain an estimate of the percentage number of data affected by the wind turbines. The effects can already be identified by means of relatively short periods of radar data. This means a big advantage compared to traditional methods that need several years of radar data for reliable statistical results. We have demonstrated the use of the big difference method with a 12-hour data sample, covering a period with clear weather, thunderstorms and stratiform precipitation on 29 May 2016.

A detailed analysis of a wind farm located at a distance of 2.5 km from the radar showed that the data up to 50 dBZ may be affected by the wind turbines in sectors around the turbines that are 5 degs wide in azimuthal direction and 1 km wide in radial direction. In the neighboring sectors, effects of the turbines are still found up to 10 dBZ on the left and right hand sides of the core sector, up to 20 dBZ on the back side within 0-2 km distance from the turbines, and up 10 dBZ in 4 to 7 km distance from the turbines. These findings are in a good agreement to the long-term studies by (Norin, 2015) and (Teschl, et al., 2016). Both studies showed that the effects outside the core sectors around wind turbines can be associated exclusively to low reflectivities, typically in the range of -30 to 10 dBZ. This is a range which is attributed either to clear-air echos (turbulence or insects) or to very weak precipitation. This range is therefore almost unimportant for operational use, e,g., for monitoring hail and heavy precipitation. A potential exception is the monitoring of weak snowfall in winter which may produce slippery conditions for traffic.

These results have been found with radar data that passed a traditional clutter filtering based on Doppler criteria. In the meantime, the German Weather Service came out with a new quality management system (called RADOLAN, (DWD 2017)) using polarisation criteria for filtering radar measurements. We are curious to analyse the effects of the wind turbines with data that passed the new RADOLAN scheme.

One should consider some requirements when the big difference method is planned for use in a specific setting. The scatter of the differences should be first tested in an environment that is not influenced by wind farms or other types of ground clutter. It should be noted that not all weather types are suitable for use of the big difference method. Fast echo motions, melting snowfall or large horizontal gradients in radar reflectivity or Doppler velocity may mask the effects of wind turbines when using the big difference method. Finally, ground clutter, especially the clutter of moving trees may also mask the effects of wind turbines.

Acknowledgement

We thank the German Weather Service for providing the radar data used in this study. In addition, we are grateful to customers and partners for valuable and constructive discussions and suggestions.

References

DWD 2013a Einfluss des Betriebes von Windenergieanlagen auf die Wetterradarmessung und Warnprodukte beim DWD. - Sept 2013. - Available from German Weather Service [Bericht].
DWD 2013b Informationen zur Errichtung von Windenergieanlagen im Nahbereich der Messsysteme des Deutschen Wetterdienstes. - https://www.energieatlas.bayern.de/file/pdf/944/2012_05_10_Anforderungen%20_DWD_WEA_Radar_V1.3.pdf – Jan 2013 [Bericht].
DWD 2017 RADOLAN-Information Nr. 45 vom 25. Oktober 2017. - https://www.dwd.de/DE/leistungen/radolan/radolan_info/radolan_info_nr_45.pdf?__blob=publicationFile&v=3 – Oct 2017 [Artikel].
Norin L. A quantitative analysis of the impact of wind turbines on operational Doppler weather radar data. - Atmos. Meas. Tech., 8, 593–609 – 2015 [Artikel]. - 2015.
Teschl R, Paulitsch H und Teschl F Investigations on the spatial extent of the effect of wind turbines on radar data. - ERAD 2016, Antalya, Turkey - https://erad2016.mgm.gov.tr/storage/images/_abstract/extended_abstract/7.2.pdf – Oct 2016 [Artikel]. - 2016.
WMO 2010 Executive summary of the WMO statement in weather modification. [Bericht].

Rapid Scan Experiment of Doppler Weather Radar for Monitoring Rainstorms and Tropical Cyclones in Hong Kong

Wai Kong[1] and Ying-wa Chan[1]

[1]*Hong Kong Observatory, 134A Nathan Road, Hong Kong, China*

(Dated: 2 July 2018)

1 Introduction

The Hong Kong Observatory (HKO) operates two long-range S-band weather radars for monitoring severe weather such as rainstorms and tropical cyclones. The radars are located at two mountain peaks, namely Tai Mo Shan and Tate's Cairn which are around 950 metres and 570 metres above the mean sea level respectively. Both radars adopt a 6-minute volume scan with 10 elevations in the range of 0°-34° for probing the atmosphere. The two radars operate in tandem to provide redundancy in the provision of radar data and imageries to various internal users and the public.

The merit of volume scan is to acquire 3D radar data for analyzing the vertical structure of rainstorms. However, a volume scan usually requires around 5 to 10 minutes to complete a cycle which limits its capability of monitoring short-lived or rapid evolving weather systems. On the other hand, low-level elevation scans can reflect better the weather conditions near ground level. Some meteorological agents thus adopt special scanning strategy to increase the update frequency of low-level elevation scans to meet their operational needs. For example, the National Oceanic and Atmospheric Administration (NOAA) introduced the Supplemental Adaptive Intra-Volume Low-Level Scan (SAILS) in their NEXRAD network a few years ago, which inserted an additional 0.5° elevation scan during the 5-minute volume scan (Daniel, 2014).

To enhance radar observations, HKO commenced a rapid scan experiment using the Tai Mo Shan weather radar (TMSWR) in 2017. A "One-minute one slice" scanning mode at 0° elevation was chosen to enhance monitoring of severe weather. TMSWR one-minute rapid scan enabled early reception of radar data at higher update frequency of radar imageries than that of the conventional 6-minute volume scan. It provided better continuity in observing the evolution of rainstorms and tropical cyclones that would be useful for weather diagnosis, nowcasting and numerical weather prediction. When TMSWR was switched to rapid scan mode, the Tate's Cairn weather radar (TCWR) continued to operate the 6-minute volume scan. As TMSWR and TCWR are only 12 kilometres apart with similar detection coverages, the two radars with one performing rapid scan while another maintaining volume scan enabled collection of 3D radar data and rapid update of low-level radar data simultaneously, thereby maximizing operational benefits in monitoring severe weather.

This paper introduces the radar scanning strategy adopted in the TMSWR rapid scan experiment and describes the enhanced observations for several rainstorms and Tropical Cyclone (TC) Hato. Potential operational applications of rapid scan are also discussed.

2 Strategy for rapid scan mode

In normal operation, TMSWR and TCWR carry out volume scan with 10 elevations in the range of 0°-34° (Table 1) at 6-minute repetition intervals. As Tai Mo Shan is the highest peak in Hong Kong with no apparent blockage around, TMSWR was chosen to perform low elevation angle rapid scan in the experiment. A total of 7 rapid scan test modes taking into account the repetition interval, no. of elevations, data quality and hardware loading have been tried (Table 2).

	Volume Scan Elevations
TMSWR	0°, 0.9°, 1.8°, 2.7°, 3.6°, 5.4°, 10°, 15°, 22°, 34°
TCWR	0.1°, 0.9°, 1.8°, 2.7°, 3.6°, 5.4°, 10°, 15°, 22°, 34°

Table 1 Volume scan elevations of TMSWR and TCWR.

Rapid scan test mode	Repetition Interval	Number of Slices	Elevation	Antenna Rotation Speed	Chance of Catastrophic Error (Doviak, 2006) (at ω = 4 m/s, SNR ≥ 20 dB)
1	0.5-min	1	0°	15°/s, (2.5 rpm)	0.1%
2	1-min	2	0°, 3.6°	15°/s, (2.5 rpm)	0.1%
3	1-min	3	0°, 3.6°, 10°	21°/s, (3.5 rpm)	0.5%
4	1.5-min	3	0°, 3.6°, 10°	15°/s, (2.5 rpm)	0.1%
5	2-min	3	0°, 3.6°, 10°	11°/s, (1.8 rpm)	0.01%
6	2-min	4	0°, 3.6°, 10°, 15°	15°/s, (2.5 rpm)	0.1%
7	1-min	1	0°	7°/s, (1.2 rpm)	0.0002%

Table 2 Seven test scan modes tried in the TMSWR rapid scan experiment.

All the seven rapid scan test modes in Table 2 had the same dual pulse repetition frequencies (PRFs) of 576/432 Hz and Nyquist velocity of 46 m/s as the existing 0° Plan Position Indicator (PPI) scan of TMSWR. Regarding antenna operation, the existing TMSWR 0° PPI scan has an antenna rotation speed of 8°/s with a chance of catastrophic error of ~0.0007% (Doviak, 2006). Rapid scan test modes 1 to 6 required higher antenna rotation speeds (11°/s to 21°/s) which would reduce the sampled pulses per radial and lower data quality, resulting in higher chance of catastrophic errors (maximum 0.5%) in velocity aliasing.

TMSWR has an 8.5 metres antenna which is relatively large and heavy. Hardware loading has to be considered in designing the optimal scanning strategy. There would be larger hardware stress to motors and gearboxes for faster antenna rotation speed, particularly for conducting multiple elevation scans with short repetition interval like test modes 2 to 6 that required rapid upward and downward motions within 1 to 2 minutes. In conducting test mode 3, noise was generated from the radar antenna, suggesting stress on the equipment.

The role of higher elevation scans is for understanding vertical structure of storms. However, if only limited slices are available, interpolation of these slices when performing cross-section cut can be misleading. For example, the cross-section of echoes using rapid scan mode with only two slices (0° and 3.6°) is shown in Figure 1. The reflectivity cross-section is limited in its ability of revealing the rainstorm structure when compared with the cross-section obtained by the volume scan of TCWR (Figure 2). The number of elevation angles in such rapid scan mode is unable to reveal appropriately the vertical storm structure such as the reflectivity core. The echo intensities as shown from 3-km CAPPI imageries in Figure 1 and Figure 2 are quite different with the former hampered by fewer elevation scans of the rapid scan data.

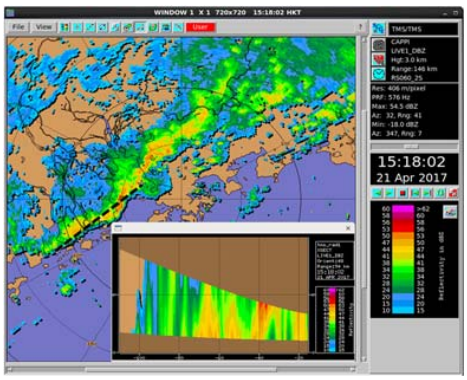


Figure 1 Cross-section of echoes along the black dashed line using TMSWR rapid scan data (scan elevations of 0° and 3.6°, test mode 2 in Table 1).

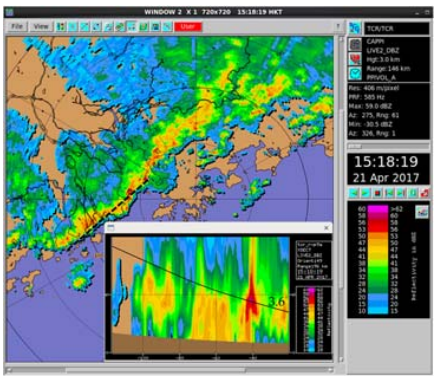


Figure 2 Cross-section of echoes along the black dashed line using TCWR volume scan data.

After considering the relevant factors as discussed above, the "one-minute one-slice" rapid scan mode at 0° elevation (mode 7 in Table 2) was chosen in the TMSWR rapid scan experiment. Although test mode 7 did not have higher elevation scans, this could be complemented by TCWR volume scan. The advantage of test mode 7 was the slower antenna rotation speed of 7°/s (less than the existing 0° PPI scan of 8°/s) which would have a lower chance of catastrophic error of ~0.0002%. With such scan mode, the stress on radar's hardware was reduced compared with that of a volume scan as no vertical movement of the radar antenna was required for scanning at higher elevations.

3 Operational benefits of rapid scan

3.1 Timeliness

TMSWR rapid scan (mode 7 in Table 2) enabled up to 5 minutes earlier reception of low-level (0° elevation) radar data compared with volume scan which was conducted every 6 minutes at 00, 06, 12, ..., 54 Hong Kong Time (HKT). For example, at T + 6 minutes HKT, forecasters might still refer to the T + 00 minutes HKT 0° PPI imageries from the 6-minute volume scan but the one-minute rapid scan radar imageries could be updated to T + 5 minutes HKT, suggesting an early reception by 5 minutes.

3.2 Better continuity

With higher update frequency of radar data, TMSWR rapid scan provided 6 times more low-level radar observations to users compared with the 6-minute volume scan mode. The continuity in monitoring the development of storms could be improved. In fact, TMSWR rapid scan experiment demonstrated better tracking of echo evolution and better appreciation of small and short-lived features including low-level convergence and divergence, downburst and hook echoes (further discussion in Sections 4.1 to 4.4). This facilitated better diagnosis of precipitation mechanism and radar quantitative precipitation estimation. In the case of TC Hato, rapid scan imageries depicted more clearly the accelerated rotation of Hato's spiral rainbands around its centre as well as contraction of the eye structure when Hato approached the coast of Guangdong (to be elaborated further in Section 4.5). It would be very difficult to observe such phenomena using TCWR's 6-minute volume scan imageries.

4 Enhanced observations

4.1 Low-level convergence

In the afternoon of 21 April 2017, a squall line associated with a cold front swept across Hong Kong (Figure 3). Doppler radar imageries generated by 6-minute PPI scan depicted appearance of two low-level convergence lines around 40 kilometres north of Hong Kong (red dashed lines in Figure 4a). Only one convergence line was observed 6 minutes later (red dashed line in Figure 4b). Based on 6-minute radar imageries, it would be difficult to assess which of the following scenarios has occurred.

(i) the two convergence lines have merged into one; or
(ii) the convergence line further north dissipated while the one to its south persisted and moved slowly; or
(iii) the convergence line further north persisted and moved slowly while the one to its south dissipated.

One-minute rapid scan imageries between 1536 HKT and 1539 HKT (Figure 5a to Figure 5d) clearly revealed the gradual dissipation of the convergence line further north, i.e. scenario (ii). This thus enhanced forecasters' capability in diagnosing the evolution of weather systems.

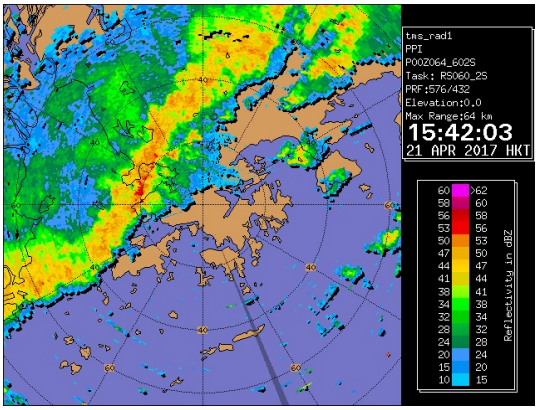
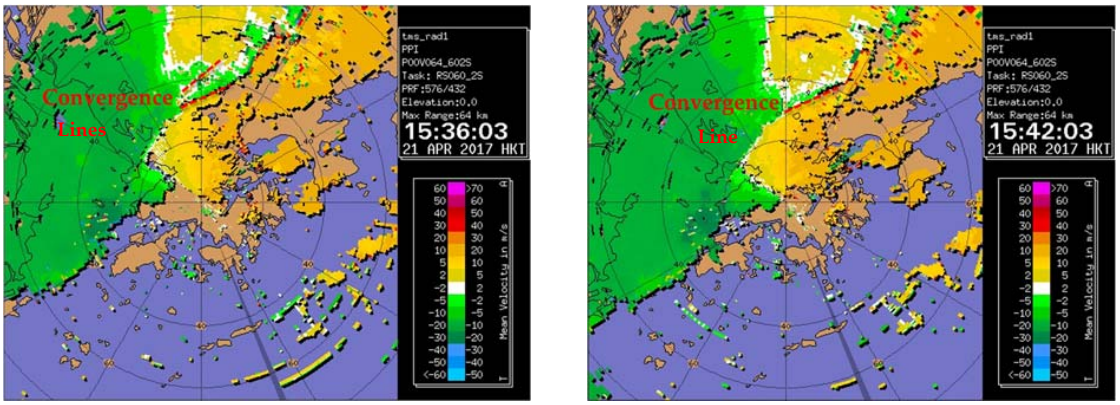
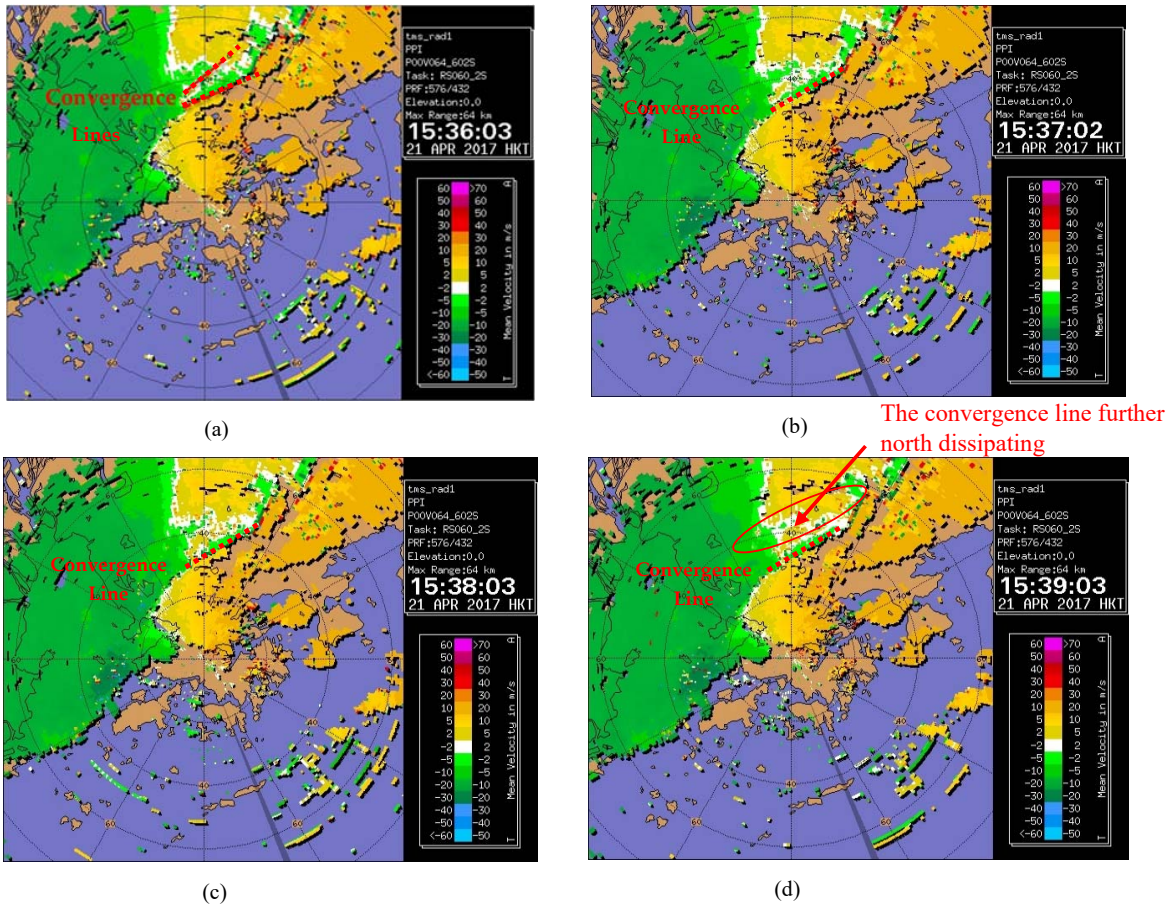


Figure 3 A squall line associated with a cold front swept across Hong Kong in the afternoon of 21 April 2017.



(a) (b)

Figure 4 Evolution of convergence lines as observed from the TMSWR 6-minute Doppler radar imageries (PPI scan) at 1536 HKT and 1542 HKT on 21 April 2017.



(a) (b)

(c) (d)

Figure 5 Evolution of convergence lines as observed from the TMSWR 1-minute rapid scan Doppler imageries from 1536 HKT to 1539 HKT on 21 April 2017 (The convergence line further north dissipated gradually).

4.2 Downburst

On 22 August 2017, the coast of Guangdong came under TC Hato's subsidence air at its outer circulation. The convective storm developed over inland Guangdong to the north of Hong Kong drifted southwards following the prevailing northerly winds. The reflectivity cross-section based on TCWR 6-minute volume scan data revealed descending of the reflectivity core at the height of about 5 kilometres near the storm centre at 1636 HKT (Figure 6b) to near the ground surface at 1642 HKT (Figure 6c). The rapid scan radar imageries captured the subsequent outspreading of echoes (Figure 7a to Figure 7l) and suggested the presence of gust front after the downburst hit the ground. It would be difficult to observe this outspreading process (in the mesoscale of ~20 km) using the 6-minute volume scan radar imageries. Thus the combined use of rapid scan and volume scan could provide a wider perspective in observing the evolution and impact of severe weather.

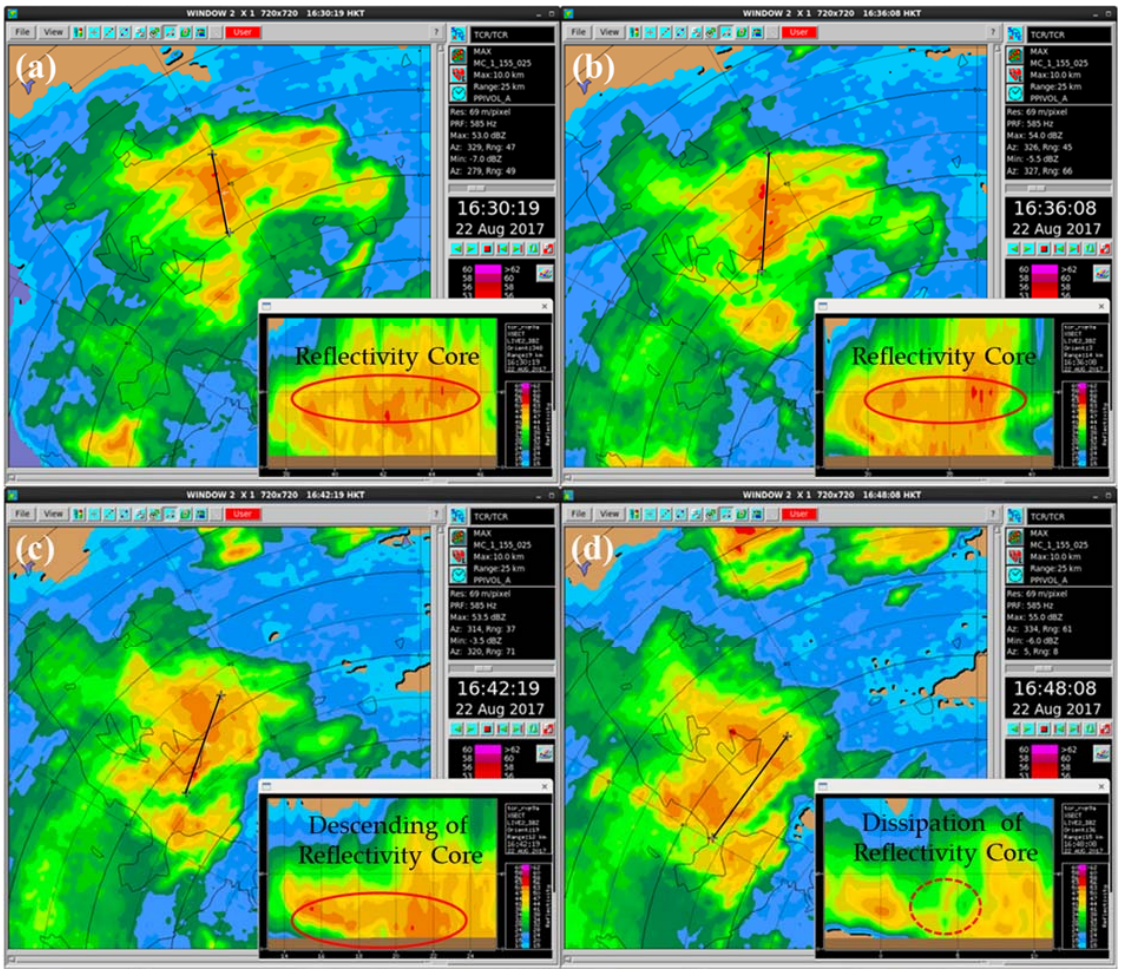


Figure 6 Maximum reflectivity as observed from TCWR 6-minute volume scan Doppler imageries from 1630 HKT to 1648 HKT on 22 August 2017. Cross-section of echoes along the black line are shown in the insets. The reflectivity core was observed to descend from the height of around 5 kilometres at 1636 HKT and it reached the ground and dissipated quickly by 1648 HKT.

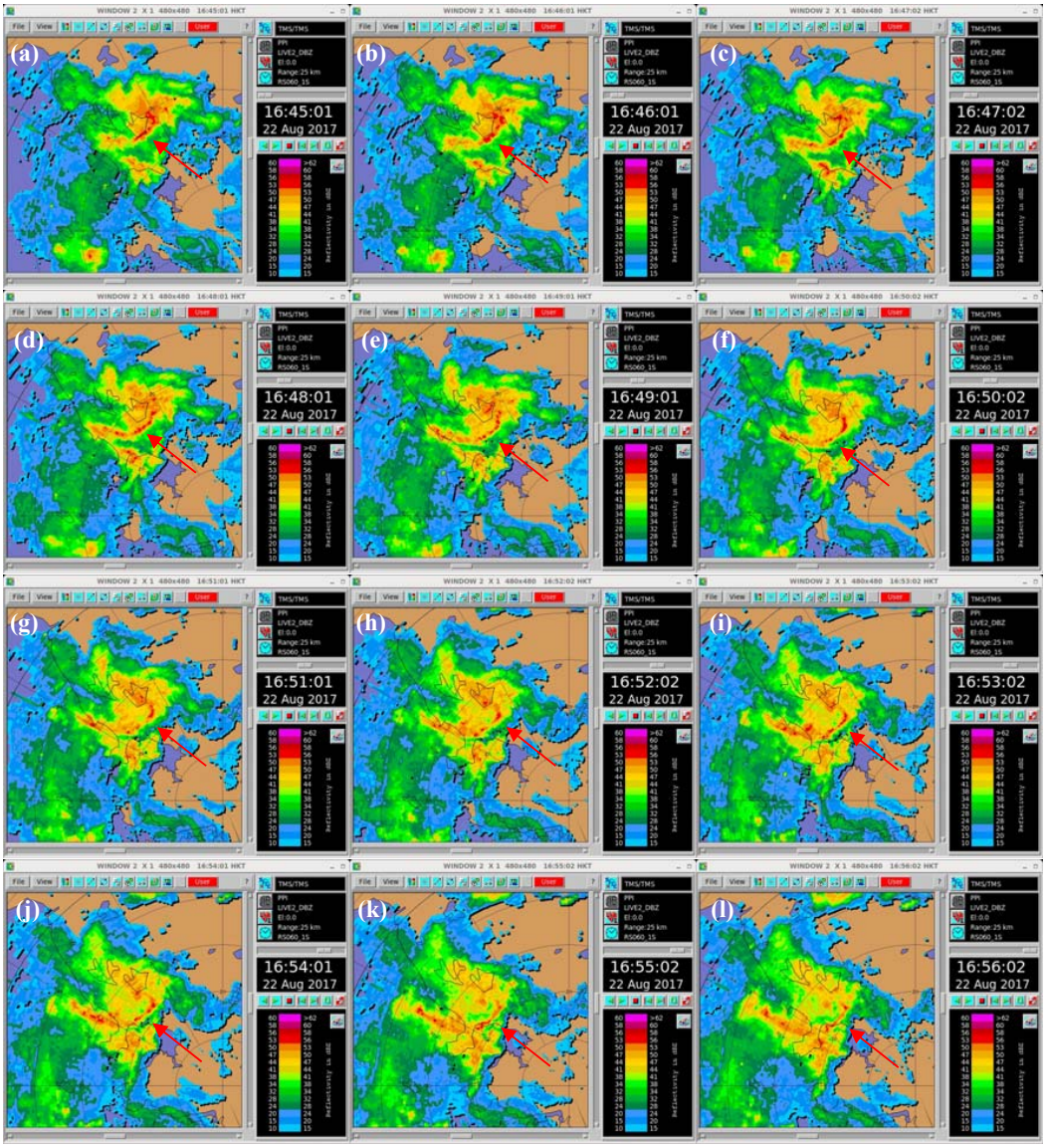


Figure 7 Evolution of downburst as observed from the TMSWR 1-minute rapid scan radar imageries from 1645 HKT to 1656 HKT on 22 August 2017 (The red arrows indicated the outspreading gust front).

4.3 Hook Echo

Hook echo is recognized as a key signature of hail and tornado development on radar imageries. In the past, TMSWR and TCWR 6-minute volume scans could show the occurrences of hook echoes over southern China but the imageries covered at best a few discontinued snapshots. The evolution of hook echo was seldom captured by 6-minute volume scan and identification of hook echo was sometimes quite difficult. With better continuity using 1-minute rapid scan data, the formation and dissipation of hook echoes could be well-captured. This was exemplified by a case with hook echo forming and dissipating quickly over the western part of Hong Kong based on 1-minute rapid scan radar imageries from 0955 HKT to 1036 HKT on 9 May 2018 (Figure 8 to Figure 10). Both the formation and dissipation processes lasted for around 6 minutes or less, implying that it would be difficult to observe these processes using 6-minute radar imageries. The 1-minute rapid scan imageries also revealed the rear flank downdraft, forward flank downdraft and weak echo region features associated with the hook echo when it reached the mature stage (Figure 9). While cross-section radar product was not available in rapid scan, the cross-section of TCWR 6-minute volume scan successfully depicted the overhang echo associated with the hook echo (Figure 11). The advantage of combined use of rapid scan and volume scan data was again illustrated in this example.

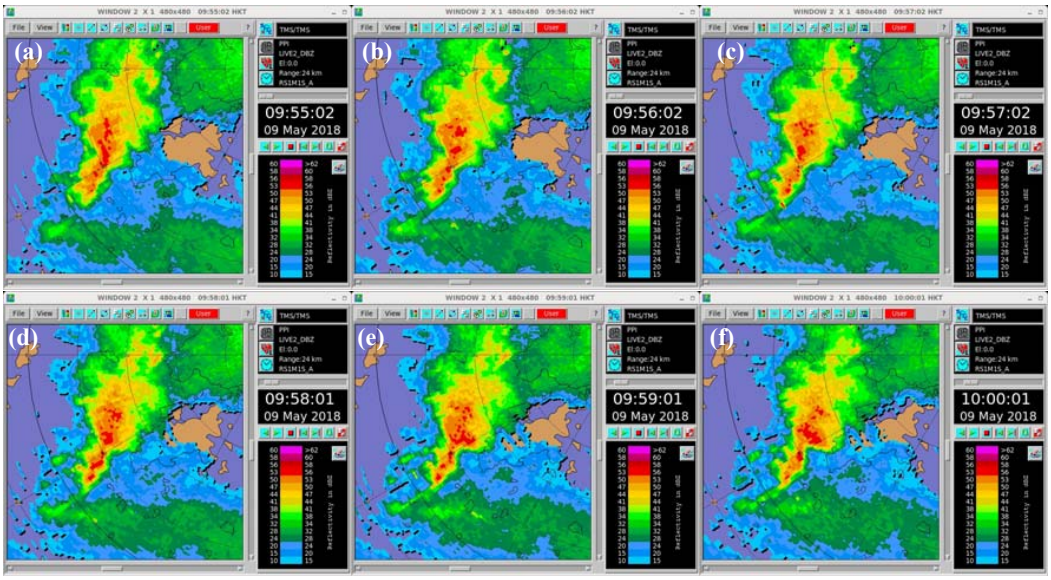


Figure 8 Formation of hook echo from 0955 HKT to 1000 HKT on 9 May 2018.

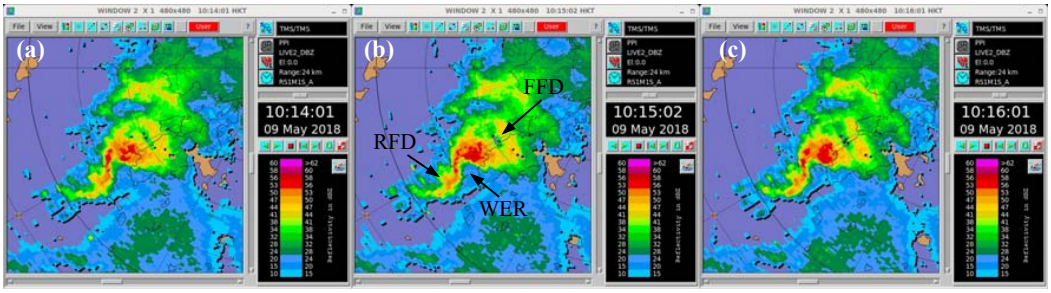


Figure 9 Hook echo reaching mature stage from around 1014 HKT to 1016 HKT on 9 May 2018 and showing features like rear flank downdraft (RFD), forward flank downdraft (FFD) and weak echo region (WER).

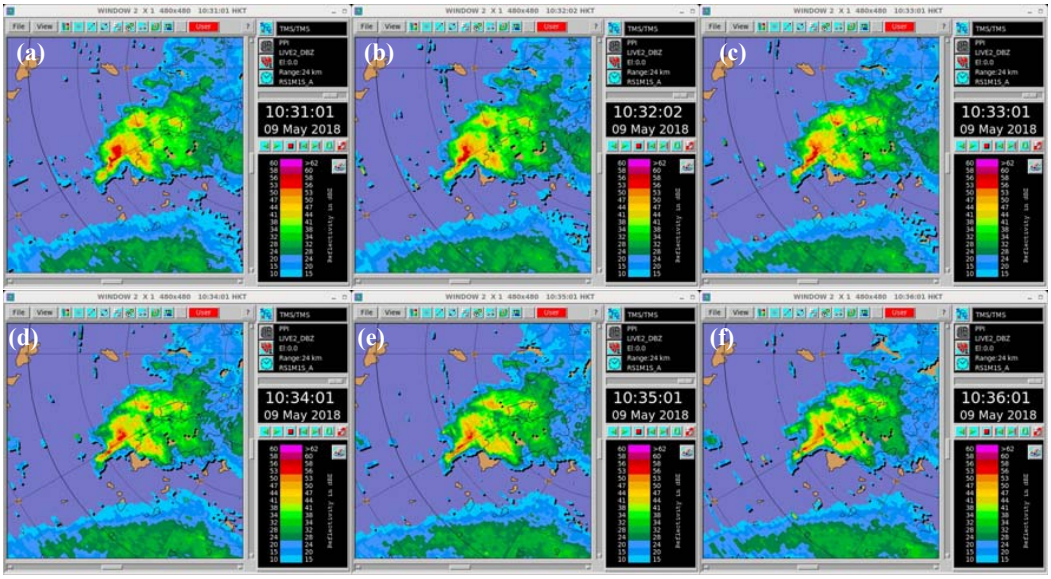


Figure 10 Dissipation of hook echo from 1031 HKT to 1036 HKT on 9 May 2018.

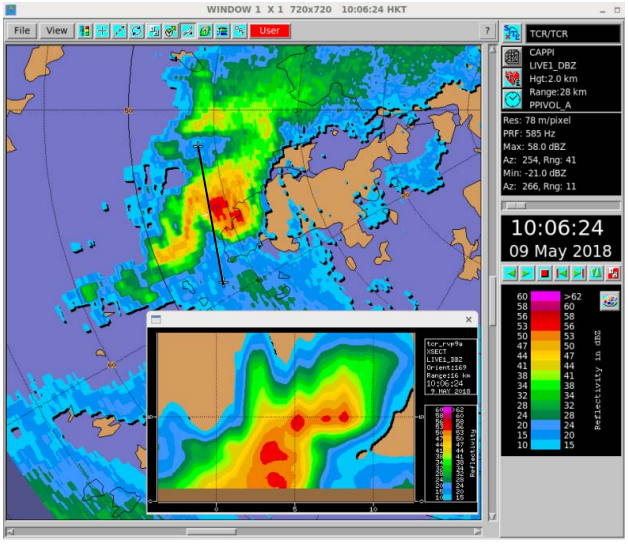


Figure 11 Overhang echo as observed from the cross-section of echoes along the black line using TCWR volume scan data at 1006 HKT on 9 May 2018.

4.4 Rapid intensification and decay of short-lived echoes

In radar quantitative precipitation estimation (QPE) using volume scan data, it is usually assumed little change of the echo intensity between two consecutive volume scans. For example, the radar imageries at 1254 HKT (Figure 12a) and 1300 HKT (Figure 12b) on 22 August 2017 showed that the echoes as highlighted by the red dashed circle intensified slightly from yellow (41 to 44 dBZ) to orange (47 to 50 dBZ) colour. As there was a lack of radar data from 1254 HKT to 1300 HKT, the echo intensity was assumed to maintain either at yellow or orange colour within this 6-minute interval. Such assumption was acceptable with no significant systematic errors if the change of echo intensity was not significant. However, it was observed that the echoes intensified and weakened rapidly between 1254 HKT and 1300 HKT (Figure 13a to Figure 13g) which could lead to incorrect calculation of the QPE.

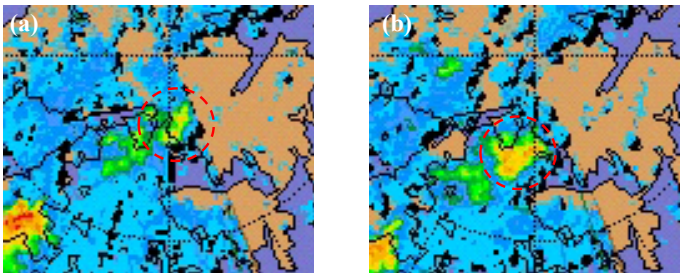


Figure 12 Six-minute volume scan radar reflectivity imageries between 1254 HKT (Figure 10a) and 1300 HKT (Figure 10b) on 22 August 2017. The echoes as highlighted by the red dashed circle showed apparent intensification. Refer to Figure 14 for the radar reflectivity colour scheme.

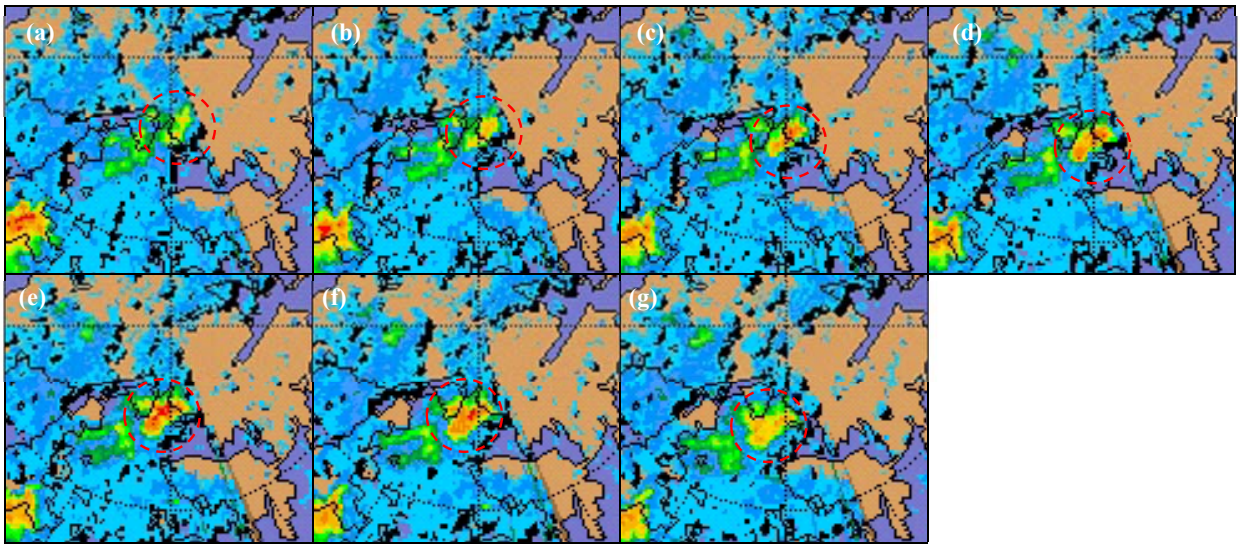


Figure 13 One-minute rapid scan radar reflectivity imageries between 1254 HKT and 1300 HKT on 22 August 2017 (each imagery is 1 minute apart) showed rapid intensification and decay of the echoes as highlighted by the red dashed circle. Refer to Figure 14 for the radar reflectivity colour scheme.

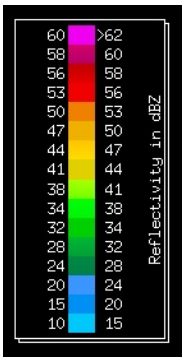


Figure 14 Colour scheme of radar reflectivity.

4.5 Estimation of tropical cyclone intensity

In the morning of 28 August 2017, TC Hato intensified rapidly into a Super Typhoon as it moved towards the coast of Guangdong. Animation of TMSWR one-minute rapid scan reflectivity imageries captured the accelerated rotation of Hato's spiral rainbands around its centre as well as contraction of its eye structure when it approached the coastal areas. Similar signs were hardly observed from TCWR 6-minute volume scan imageries. The rapid scan reflectivity radar imageries could thus be used for estimating the maximum wind speed of Hato and its intensity changes.

The method is to track the displacements of echo features around the TC's centre based on two successive radar reflectivity imageries using pattern recognition techniques similar to those adopted in rainstorm nowcasting. The motion vector fields derived by the above feature tracking method using simulated 6-minute volume scan data and 1-minute rapid scan data are shown in Figure 15 and Figure 16 respectively. The figures demonstrate better continuity in deriving the motion vector fields if 1-minute radar imageries are used instead of 6-minute imageries.

In practice, the calculation should take into account the short-term fluctuation of echo intensity. A time-lag ensemble approach could be used to minimize the potential errors related to this factor. In the case of Hato, the feature tracking method using 1-minute rapid scan data estimated that the rotation speeds of radar echoes near the eye wall of Hato in the short time intervals of 0500-0508 HKT and 0930-0938 HKT on 23 August 2017 increased from around 80 knots to about 90 knots (Figure 17 and Figure 18), i.e. an intensity change of +13%.

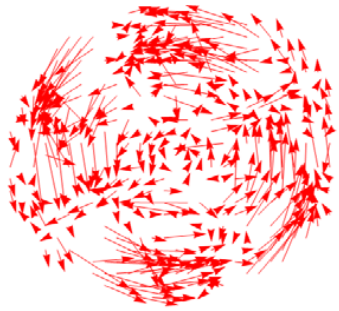


Figure 15 TC motion vector fields derived using two successive simulated 6-minute volume scan data.

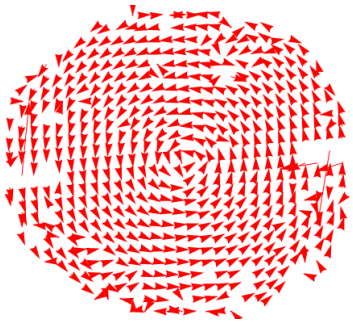


Figure 16 TC motion vector fields derived using two successive simulated 1-minute rapid scan data.

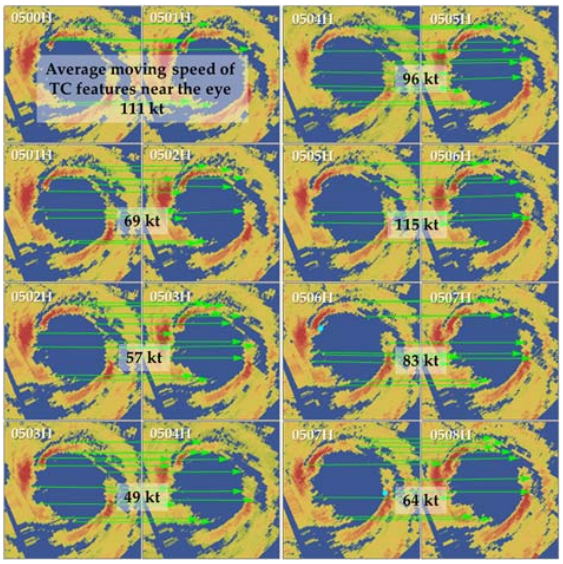


Figure 17 Average moving speed of echo features near the eye of TC Hato calculated by feature tracking method from 0500 HKT to 0508 HKT on 23 August 2017.

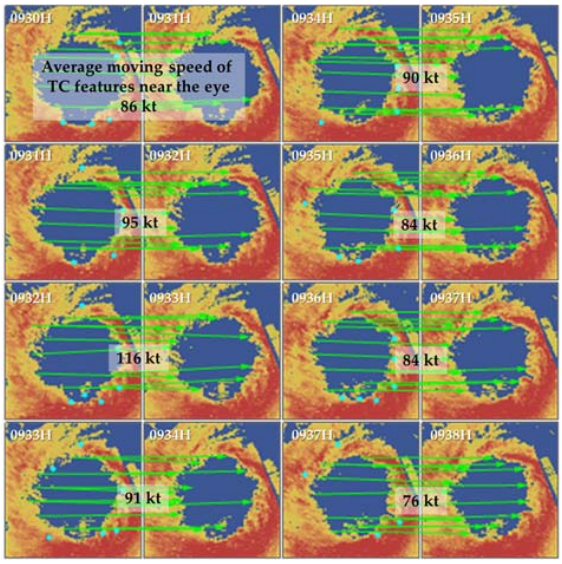


Figure 18 Average moving speed of echo features near the eye of TC Hato calculated by feature tracking method from 0930 HKT to 0938 HKT on 23 August 2017.

TC Hato was the only TC case captured by TMSWR rapid scan after the experiment started in 2017. More TC cases would be required to verify if the average moving speeds of echo features near the TC centre found by feature tracking method could well represent the maximum wind speed near the centre of a TC. Nonetheless, a brief comparison with the HKO Best Track data of TC Hato is given in Table 3. The feature tracking method seems to provide a good reference in estimating the TC maximum wind speed and its intensity change.

Figure 19 shows the circulation and eye wall structure of TC Hato based on radar reflectivity imageries at 0952 HKT on 23 August 2018. The spectrum width near TC centre is usually large which increases the chance of catastrophic errors in the Doppler wind fields derived from dual-PRFs technique. Figure 20 shows significant catastrophic errors near the eye wall of Hato which increases the difficulty to estimate TC intensity using Doppler velocity information. In contrast, the feature tracking method discussed above requires only radar reflectivity imageries. As no dual-PRFs technique is involved, poorer radar data quality may still be used for TC intensity estimation. This provides another diagnostic method to estimate TC intensity even when the catastrophic errors are significant.

	Maximum Wind Speed from HKO Best Track data	TC feature tracking method
0500 HKT, 23 Aug 2017	80 knots	80 knots (average speed based on 0500-0508 HKT 1-minute rapid scan radar imageries)

0930 HKT, 23 Aug 2017	97.5 knots*	90 knots (average speed based on 0930-0938 HKT 1-minute rapid scan radar imageries)
Percentage of Intensity Change	+22%	13%

*Table 3 Comparison of TC Hato's maximum wind speed and intensity change obtained from HKO Best Track data and those derived from TC feature tracking method (*The value is derived from the mean of maximum wind speed of Hato at 0900 HKT (95 knots) and 1000 HKT (100 knots) in HKO Best Track data.)*

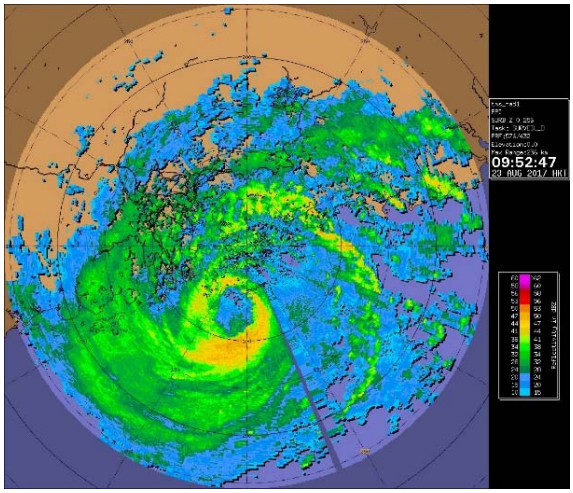


Figure 19 Radar reflectivity imagery of TC Hato at 0952 HKT on 23 August 2017.

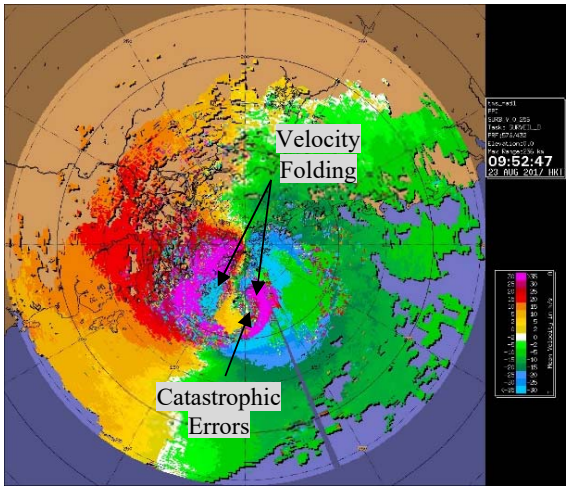


Figure 20 Catastrophic errors and velocity folding problems as reflected from the Doppler radar imagery of TC Hato at 0952 HKT on 23 August 2017.

5 Conclusion

The TMSWR one-minute rapid scan experiment demonstrated the advantages of early reception of radar data by up to 5 minutes and better continuity in tracking the evolution of weather systems, particularly those small-scale and short-lived weather phenomena such as low-level convergence, downburst and hook echoes etc. As illustrated by the case of TC Hato, the feature tracking method could be used to evaluate the change of rotation speeds of Hato's spiral rainbands, allowing estimation of its maximum wind speed and intensity change.

The early availability and faster update of radar data also facilitated nowcasting operation and timely issuance of weather warnings as a result of better weather diagnosis and more accurate and timely QPE. More rapid scan data will be collected in the rain and TC seasons of 2018 for further analysis.

References

Daniel A. E., J. N. Chrisman, C. A. Ray, S. D. Smith, and M. W. Miller New WSR-88D operational techniques: Responding to recent weather events [Conference] // Proc. 30th Conf. on Environmental Information Processing Technologies. - Atlanta, GA : Amer. Meteor. Soc., 2014. - Vol. 5.2. - pp. 71 - 75.

Doviak R. J., Zrnic, D. S. Doppler Radar and Weather Observations [Buch]. - New York : Dover Publications, 2006. - Bd. 2nd ed. : S. 103-119.

RADAR-DERIVED QUANTITATIVE PRECIPITATION ESTIMATION BASED ON VERTICAL-RAINCLOUD TRAJECTORY PROFILES

Hanggar G Mawandha[1] and Satoru Oishi[2]

[1]*Graduate School of Engineering, Kobe University, Japan.*
E-mail: mawandha@stu.kobe-u.ac.jp
[2]*Professor, Research Center for Urban Safety and Security, Kobe University, Japan.*
E-mail: tetsu@phoenix.kobe-u.ac.jp
(Dated: 22 June 2018)

1 Introduction

Radar-derived precipitation is subject in the hydrological field following an advanced development of remote monitoring system used for many disaster mitigation purposes. A high space-time resolution of radar-based quantitative precipitation estimates (QPE) is appealing features for the spatially characterized hydrological condition. However, its quantification accuracy is a challenging task. A network of rain gauges provides more accurate point-wise measurements however the spatial representativity is limited. In contrast, radar provides proper spatial rainfall distribution, but the possibility to inaccurate determination of ground measured value due to uncertain discrepancy factor is high. Hence, combining radar-rain gauge is one of the solutions for generating better QPE in advance. However, radar-rain gauge-based QPE tends to have less precision when limited rain gauge with sparse spatial distribution existed. In this case, a method based on radar-rain gauge merging algorithms (Cecinati, 2010; Germann, 2006; Lee, 2015) to discriminate discrepancy contained in QPE is no longer appropriate to be used.

This study aims to assess the factor of interspace discrepancy between radar bins and rain gauges to generate better QPE algorithm based on the vertical profile of raincloud. This study is taking the case of a radar set up at Mt. Merapi located in the Southern part of Java Island, Indonesia Country (see Figure 1-a). In a mountainous area, the rain gauge network is usually sparse and sufficient point rainfall measurements are not available, which are often unable to characterize the spatial distribution of highly variable rainfall. On the other hand, the void interspace under the available radar tilting beam due to beam distance or beam blockage has caused some valuable rainfall data missing, which is recognized contributing to discrepancy toward the ground. Furthermore, such discrepancies are known aggravated during the raincloud formation processes under developing, mature, and dissipating stages. The method proposed in this study is considering the correlation between vertically-raincloud profile and their composing physical component. Once its correlation has been recognized, the vertically-trajectory pattern of raincloud above the rain gauge could be depicted in the form of rain intensity. These trajectory fields are then used to estimate the probabilities of rain intensity for lower altitudes. Here, the discrepancy factor contained in QPE product can be discriminated against various raincloud formation stages.

2 Methodology

Generally, trajectory profiling comes up with non-parametric and parametric estimates (Jo, 2014). Non-parametric estimators have no fixed structure and depend upon all the data points to get an estimate while parametric estimators concern the nominal values used for every parameter. The problem to use non-parametric estimators requires many data from the prior trajectories. In this case, to collect an adequate data used for raincloud profiling is difficult since rainfalls mostly occur within a short period with a limited height of the vertical column. Hence, application of parametric model will be emphasized based on a physical component which formulates vertically-raincloud profiles. The atmospheric sounding data generated from radiosonde is used to see the correlation among the physical components and calculate the parametric coefficient values which can describe the relationship of rain rate product with the corresponding atmospheric factors (see Figure 2). Radiosonde observations provide an independent and unique reference for many altitudes meteorological variables such as water vapor content, temperature and humidity profiles. However, they are unevenly distributed. Here, the atmospheric water vapor content and relative humidity data are used to generate parametric regression model. The atmospheric water vapor content can explain the extreme precipitation event through the relationship with the surface air temperature (Fujita & Sato, 2017).

The atmospheric data is retrieved from the University of Wyoming (United States) website: http://weather.uwyo.edu/upperair/sounding.html. The upper air map information about water vapor distribution in the study area is shown in Figure 1-b. Two rainfall events on 20/12/2017 and 11/02/2018 are selected representing the heavy rainfall cases. For checking the consistency of the spatial variance over the radar coverage area, several available rain gauges, representing radar range various distance (i.e., $\leq$ 10 km and $\geq$ 15 km), are utilized to validate the result. Statistical variables used to evaluate the model performance are zero phase and maximum phase correlation, lag time, and mean absolute bias value.

In parametric regression, we can model the relationship using any combination of single or multiple predictor variables, and use the least squares approach to estimate the parametric coefficient either linearly or non-linearly. A linear model uses a linear function f(x) to represent the relationship between a dependent random variable $\boldsymbol{Y}$ and a k-dimensional vector of

predictor variables $\boldsymbol{X}$ (Ghasemi Hamed et al., 2013). The parameters (different weights for each input and bias) of the regression are adjusted to minimize the difference between the retrieved variables and real variables in the sense of least squares. The following is general equation form of the linear parametric model.

$$= \boldsymbol{X}\beta + \varepsilon \qquad (2.1)$$

$$\boldsymbol{X} = \begin{pmatrix} 1 & x_{11} \cdots x_{1k} \\ . & . \quad \cdots \quad . \\ . & . \quad \cdots \quad . \\ 1 & x_{n1} \cdots x_{nk} \end{pmatrix}_{(n \times p)}, \varepsilon = (\varepsilon_1, \ldots, \varepsilon_n)^T \qquad (2.2)$$

Where $\boldsymbol{Y}$ is the vector of response variables, $\boldsymbol{X}$ represents a matrix of observed values for the predictor variables. In the parameter estimation phase, we are searching for the vector of parameters β through the set of n points in a way to minimize the sum of the squared error function. The most commonly used type of linear regression is the Ordinary Least Square Estimation (OLSE) which is described through as follows.

$$\widehat{\beta} = (X^T X)^{-1} X^T Y \qquad (2.3)$$

where $\widehat{\beta}$ is a least square solution function to minimize the error sum of squares $\varepsilon^T \varepsilon$. Once the parametric coefficient value has been obtained, it can be used to generate response value at void interspace through reverse multiplication process. For model validating step, cross-correlation technique is applied into data sets between QPE product and rain gauge data observed along the rainfall duration. By using the Fourier-shift method, correlation at zero phase and phase at a maximum value can be obtained. Also, the lag in time series between the data sets can be seen.

3 Results

3.1 Overall Discrepancy Assessment

Radar-derived precipitation estimate method is commonly generated from Constant Altitude Plan Position Indicator (CAPPI) either a maximum value or lowest altitude value. A maximum CAPPI product is computed from 3-D radar volume scan by projecting the maximum value within a vertical column to a 2-D plane. A lowest CAPPI value is obtained from 3-D volume scan by projecting the first CAPPI containing a value within a vertical column to a 2-D plane. In this study, we have three different QPE methods to be compared namely, “max” stands for maximum CAPPI product, “lowest” for lowest CAPPI product, and “model” for parametric model proposed in this study. The size of radar pixel used in this analysis is 300 x 300 m and time resolution is 2 minutes.

The overall QPE performances from three different methods are summarized in Table 1. All QPE methods are assessed based on radar beam distance factor to see the spatial consistency performance. From the statistical test, it concludes that for radar range less than 10 km the maximum CAPPI or lowest CAPPI method performs better than the parametric model. However, compensate result achieved by the parametric model in case of lag time and maximum phase correlation indicator. Regarding lag time, it shows at what delay/lag values time series are similar. Here, lag=1 represents 2 minutes delay of which positive value means radar time series are shifting step ahead than rain gauge while negative means the opposite. When lag ≠ 0 it will slight decrease in correlation while lag=0 both datasets will have a perfect correlation. In case of radar beam reach up to 15 km range or more, the parametric model performs much better than two other methods. Although the overall correlation value is not so high, however small lag time (close to 0) performed by parametric model-based QPE indicates a strong correlation on temporal variance toward actual ground value. The QPE showing the spatial outlook generated by each method over the entire radar range is shown in Figure 3.

Table 1: Statistical test-based QPE performance

Radar beam distance factor	≤ 10 km			≥15 km		
QPE method	max	lowest	model	max	lowest	model
zero phase correlation	0.87	0.90	0.84	0.77	0.72	0.79
maximum phase correlation	0.93	0.93	0.93	0.86	0.83	0.86
lag time (2 minutes interval)						
case of 20/12/2017	1	1	1	2	2	1
case of 11/02/2018	0	0	0	-1	-2	0
mean absolute bias (mm)	7.94	8.66	8.53	19.46	20.03	14.89

3.2 Raincloud stages-based Discrepancy Assessment

The purpose of this analysis is intended to verify such discrepancy caused by raincloud formation processes. At this step, we separated rainfall event based on raincloud formation which consists of developing, mature, and dissipating stage. In Figure 4 we have separate windows showing different raincloud formation stage based on the vertical profile of rain intensity. Under the developing stage along 10 minutes rainfall duration, the maximum CAPPI, the lowest CAPPI, and the parametric model obtained 57 mm h^{-1}, 49 mm h^{-1}, and 19 mm h^{-1}, respectively while the rain gauge recorded 29 mm h^{-1}. Under the mature stage, the maximum CAPPI, the lowest CAPPI, and the parametric model obtained 61 mm h^{-1}, 38 mm h^{-1}, and 48 mm h^{-1}, respectively while the rain gauge recorded 47 mm h^{-1}. Under the dissipating stage, the maximum CAPPI, the lowest CAPPI, and the parametric model obtained 17 mm h^{-1}, 12 mm h^{-1}, and 25 mm h^{-1}, respectively while the rain gauge recorded 18 mm h^{-1}.

The results show that the use of the parametric model can reduce the discrepancy showing from less mean bias value obtained. The highest mean bias value exhibits under developing stage phase where radar indicates rainfall in the air, but rain gauge does not. At this stage, the maximum CAPPI and lowest CAPPI value prone to give high discrepancy when is used as QPE. The discrepancy of radar and rain gauge measurement is recognized through discriminating of each stage of raincloud formation process. However, these stages were not always clearly seen especially for raincloud under convective circumstances where horizontal wind drift plays the dominant role than wind updraft and downdraft.

4 Discussion

Radar-derived QPE based on the parametric model has shown a robust performance compared to maximum CAPPI or lowest CAPPI value as currently used for QPE method. It has revealed showing less mean bias value with a lag time close to zero, especially for longer radar range distance condition. Through the use of atmospheric sounding data as a reference for many altitudes, it has proven that water vapor content and relative humidity configuration deals with vertical raincloud profile. In the model, the physical atmospheric data are assumed to be constant over the simulation of rainfall event since it generally does not change dramatically within a short period. Moreover, the parametric model provides a better approach to figure out discrepancy under different raincloud formation process.

Acknowledgment

We appreciate ERAD committee for the opportunity to present this research work. We are sincerely grateful to Gadjah Mada University and Sabo Office for providing all valuable rainfall data.

References

Cecinati, F., Rico-ramirez, M. A., & Han, D. (2010). Model radar rainfall uncertainty using ensembles REAL method : model radar rainfall errors through their covariance New method : model radar rainfall error spatial correlation with a lowpass filter, *22*(1999), 1999.

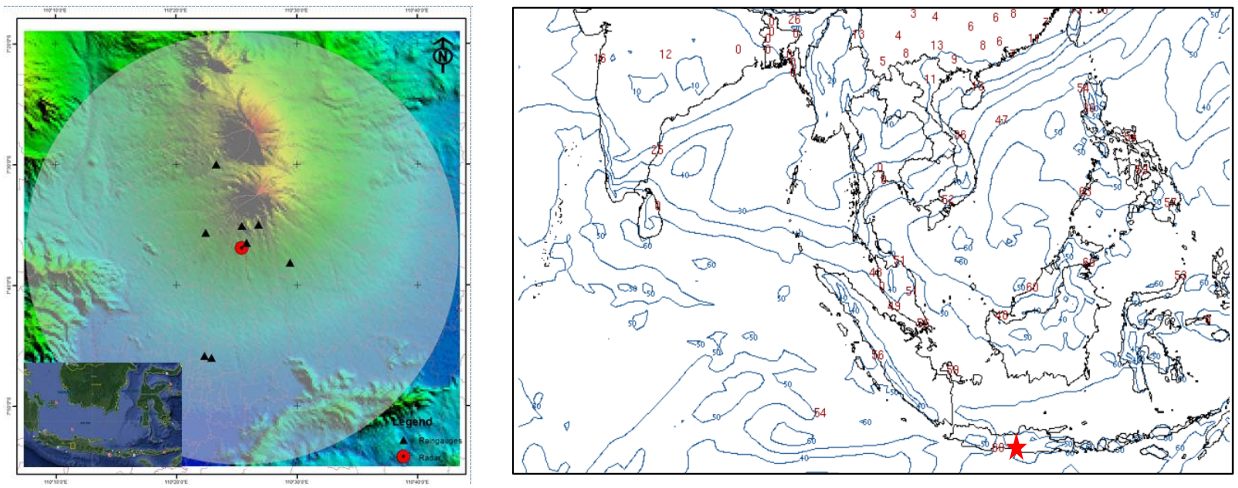
Fujita, M., & Sato, T. (2017). Observed behaviours of precipitable water vapour and precipitation intensity in response to upper air profiles estimated from surface air temperature. *Scientific Reports*, *7*(1). https://doi.org/10.1038/s41598-017-04443-9

Germann, U., Hering, A., Berenguer Ferrer, M., Sempere Torres, D., & Salvadè, G. (2006). Ensemble radar precipitation estimation for nowcasting and hydrology in the Alps. *MAP D-PHASE Scientific Meeting*, (August), 58–61. Retrieved from http://www.univie.ac.at/IMG-Wien/meetings/map_d-phase/short/24-ensradar-germann.pdf

Ghasemi Hamed, M., Gianazza, D., Serrurier, M., & Durand, N. (2013). Statistical prediction of aircraft trajectory: regression methods vs point-mass model. *10th USA/Europe Air Traffic Management Research and Development Seminar, Chicago, United States*.

Jo, J. (2014). Statistical model for aircraft trajectory prediction.

Lee, J.-K., Kim, J.-H., & Suk, M.-K. (2015). Application of bias correction methods to improve the accuracy of quantitative radar rainfall in Korea. *Atmospheric Measurement Techniques Discussions*, *8*(4), 4011–4047. https://doi.org/10.5194/amtd-8-4011-2015



(a) (b)

Figure 1: (a) Raingauges distribution and radar set up at Mt.Merapi, (b) Precipitable water vapor map at 12Z 20 Dec 2017.

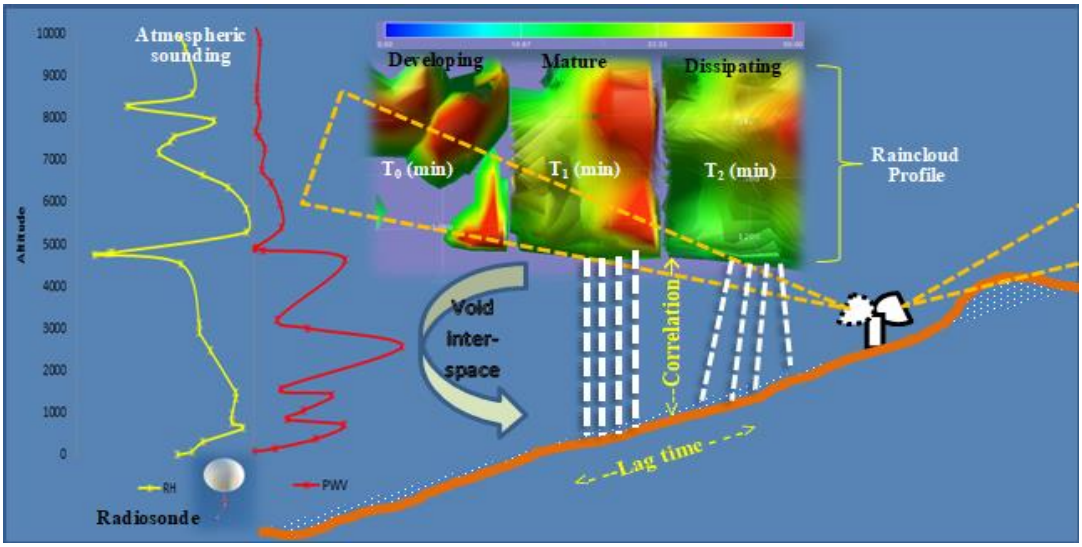
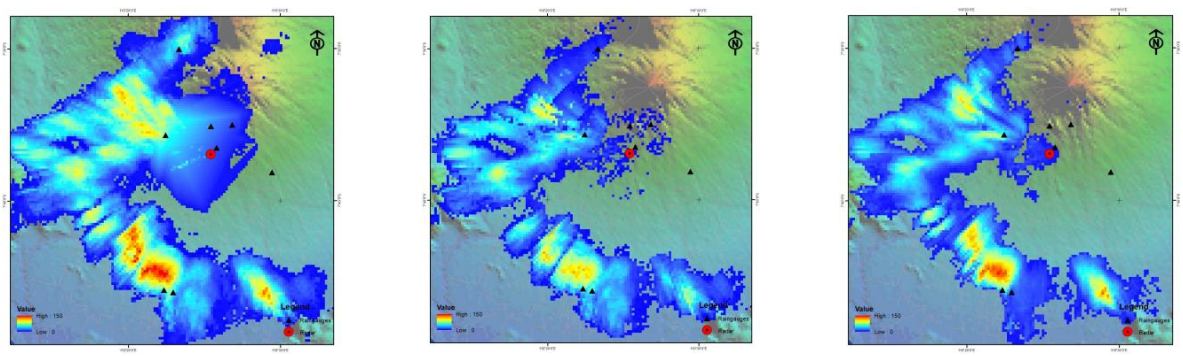
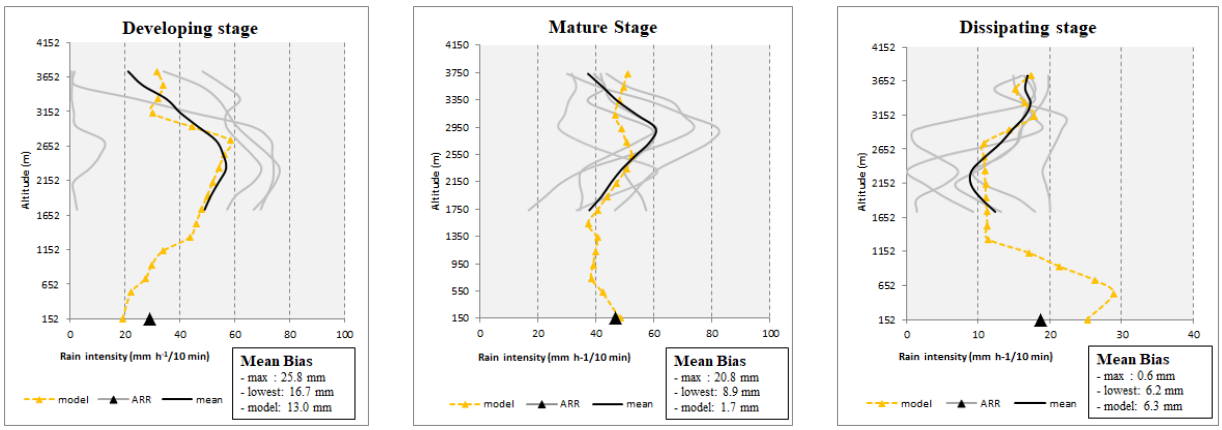


Figure 2: Vertically-raincloud trajectory profiling model scheme.



(a) (b) (c)

Figure 3: (a) Maximum CAPPI-based QPE, (b) Lowest CAPPI-based QPE, (c) Parametric model-based QPE.



(a) (b) (c)

Figure 4: (a) Projected rain intensity under raincloud developing stage phase, (b) Projected rain intensity under raincloud mature stage phase, (c) Projected rain intensity under raincloud dissipating stage phase.

NowPrecip: an algorithm for localized probabilistic precipitation nowcasting in the complex terrain of Switzerland

I.V. Sideris[1], L. Foresti[1], D. Nerini[1,2], and U. Germann[1]

[1] *Swiss Federal Office of Meteorology and Climatology, MeteoSwiss, Switzerland*
[2] *Institute for Atmospheric and Climate Science, ETH, Zürich, Switzerland*

(Dated: 20 June 2018)



Ioannis V. Sideris

1 Introduction

Nowcasting is a statistical technique for very-short weather forecasting. Precipitation nowcasting follows two distinct strategies, cell tracking and area tracking. Cell tracking (e.g. Dixon, and Wiener, 1993; Herring, 2006) detects precipitating cells, treats and tracks them as individual entities, and forecasts their future position based on their observed motion. It focuses on severe storms and usually produces forecasts for thirty minutes to one hour. Area tracking (e.g. Golding, 1998; Germann and Zawadzki, 2002; Bowler et al., 2006; Haiden et al., 2011), on the other hand, cares about tracking a continuous precipitation field covering a large, typically rectangular, domain. It usually makes predictions for several hours (six hours is typical) and often merges slowly the nowcast with the corresponding numerical weather prediction (NWP) forecast. The skill of such nowcasts is commonly superior to those of the NWP for the first 2-4 hours (Lin et al., 2005; Mandapaka et al., 2012), although this really depends on the weather conditions too. Areal-trackers consist of two main parts. First, they analyze the bulk motion of the precipitation and produce a velocity field that describes it. Second, they extrapolate the most recent rainfall into the future using the computed velocity field. In advanced schemes, the variation of the forecasted field in different scales can be taken care of by employing autoregressive schemes that include appropriately correlated noise in the form of a shock term. This term is consistent with the spatiotemporal statistical characteristics of the recent observations and assures that the lifetime of features in different scales are reproduced properly (also see Bowler et al., 2006).

Forecasting precipitation as accurately as possible in the first few hours after real time connects with the fact that rainfall has an important social and economic impact. Heavy rainfalls can function as trigger events (Sättele et al. 2012) for geographically localized hazards like flash floods, debris flows, and spontaneous landslides. Such hazards are especially prominent in the topographically complex Swiss terrain where the Alps cover 60 per cent of the country and the landscape is characterized by numerous rivers and over 1500 lakes (Spreafico et al., 2005). Moreover, rainfalls are associated with a high density of lightning flashes, which can cause damages in the power supply, as well as with strong wind gusts and shear turbulence which can affect aviation severely. Directly or indirectly, extreme rainfall can cause human injuries and fatalities as well as damages in material assets, traffic lines and infrastructure, and forestry or agricultural land (Hilker et al., 2007). During the period 1972-2007 in Switzerland there were 102 fatalities, while the cost damages of thunderstorms alone was estimated to be 1.85 billion Euros. Thunderstorm-related damages comprise about 23 per cent of the total cost of storm related damages for this period (while 75 percent or 6 billion Euros has been attributed to long-lasting rainfall). 95 per cent of the total costs happened during May and October. Early warnings based on nowcasting or using nowcasting output as forcing for hydrological models are critical in diminishing both human fatalities and financial costs since in most cases the impact is not only weather sensitive but also weather-information-sensitive, in the sense that correct information can minimize the impact (Cuo et al., 2011). Even when rainfall is not intense, accurate nowcasting has a positive financial and social impact in the sectors of transportation, tourism, and business activities.

Regarding the comparison between the output of nowcasting and NWP, there are a few reasons that typical extrapolation-based forecasts are still superior to NWP outputs in the nowcasting range (0-4h). First, NWP schemes go through an assimilation process (the merging of observations distributed in time with the dynamical numerical model of the flow in order to determine the state of the atmosphere as accurately as possible (Talagrand, 1997) and produce appropriate initial conditions). Even for high resolution models some information is lost in this process leading to discontinuities between the last radar precipitation map or even radar-raingauge merged precipitation map when this is used (Reyniers, 2008; Sideris et al., 2014). This affects the result of the NWP for the first few hours considerably. Second, even for rapid update cycles the forecast of NWP models is available quite some time after real time. This means that small-scale weather features such as thunderstorms, which typically has a size from a few kilometers to a few tens of kilometers maximum, and survive between 30 and 60 minutes, cannot be forecasted in time. A third reason lies within the statistical nature of precipitation. Rainfall is characterized by strong spatiotemporal variability due to the complexity of the underlying macrophysical and microphysical processes that act in scales smaller than the mesoscale (or sometimes comparable or smaller to the grid scale of NWP models), a fact that makes difficult the accurate prediction in fine-scale especially when convective and orographic processes take place (Cuo et al., 2011; Golding 2000; Ebert et al., 2003). In particular, problems with forecasting displacement have been reported and claimed to be the main source of quantitative precipitation forecasting (QPF) errors (Ebert and McBride 2000). Such errors can affect hydrologic applications significantly, especially the streamflow forecasting operations (Cuo et

al., 2011). Moreover, precipitation is not a prognostic variable of the NWP model and can only be indirectly assimilated into the model using latent heat nudging, etc. Nowcasting offers the opportunity for at least partial improvements for short lead times.

In order for a nowcasting scheme to be useful for a wide range of applications it has to: (a) be probabilistic, so it can produce an ensemble of several members, each of which reflects the underlying statistical properties of the most recent observations, (b) blend seamlessly with the members of the NWP (the nowcasting is superior for the first hours until the initial conditions wash out, then the NWP takes over), (c) be localized in the sense that it has to capture diverse behaviours happening at different parts of the domain at the same time (a situation which may occur either when the domain size is large or when the topography is very complex), and (d) provide some information about the growth and decay associated with topographic features. One additional expectation could be to incorporate information from object-based nowcasting in an areal-based nowcasting. For example satellites may detect convective initiation at some locations with some certainty before the convective cell appears in the radar map. The nowcasting algorithm that produces a field of precipitation should ideally be able to take this piece of information into consideration by generating convective cells at these locations in a seamless fashion.

2 Description of NowPrecip

NowPrecip is a probabilistic areal tracking nowcasting system. It uses advanced techniques that have been employed by other areal-trackers in the past, but it also introduces several new ideas that we hope the nowcasting community will find constructive. The main parts of the NowPrecip algorithm is summarized in the following five sections.

2.1 Motion Field

The motion field is computed using a combination of feature-tracking and a geostatistical technique. The main idea is to detect with high accuracy the displacements *dx* and *dy* of a small but representative number of points on the precipitation map using the last two precipitation observations and then interpolate them over the entire domain using kriging. The steps can be briefly summarized as follows. (a) A few hundreds of pixels with precipitation greater than 0.05 mm are chosen randomly in the domain at time t_1. (b) A 65x65km box is defined around each of these pixels. (c) A cross-correlation technique is used to compare this box with boxes in the neighborhood of the next time-frame t_2. The best match is recorded. (d) A hierarchical scheme is employed to center this box even better in several scales smaller than that of the original 65x65km^2 box. At the end of this computation, displacements *dx* and *dy* for all the chosen pixels have been computed. These will play the role of our measurements to interpolate with kriging. Each velocity vector is accompanied by the computed Pearson correlation between the two matched boxes.

The goal is to determine the quantities *dx* and *dy* everywhere on the raster. To this end we use ordinary kriging to interpolate *dx* and *dy* and provide the motion field we are seeking for. Motion at the chosen pixels has been determined as precisely as possible and now we use this information to interpolate everywhere on the field. Points with small correlation coefficient are rejected. The exact choice for the threshold below which a measurement is rejected is a factor that plays the fundamental role regarding the smoothness of the motion field. Setting this threshold too high is equivalent to computing the motion field in a large scale. As we set it lower and lower, local motion behaviour becomes more apparent. There is an additional mechanism to minimize discontinuities. Occasionally some displacements of our close-by chosen pixels (or measurements) may differ significantly. Such discrepancies are treated by employing spatial measures of local correlation and rejecting outliers. The idea is based on the simple concept of comparing each vector with the neighboring ones and rejecting it if it is much different.

Application of ordinary kriging is the final step for producing a continuous domain motion field (Figure 1). Moreover it extrapolates the result in regions where there is no precipitation in real time. This is important, since precipitation will eventually be advected to the originally dry regions of the domain. Unacceptably erroneous vectors or artefacts would therefore handicap the result. First tests have shown that the outcome has also a good temporal continuity.

There are two enhancements of this scheme that we have found to be useful.

The first is to use the velocity field produced by the aforementioned kriging technique to move the observation before the most recent one into the same Lagrangian frame of the most recent one. In this sense we "center" the two last observations in the same frame. We can then run the aforementioned feature-tracking and kriging scheme anew for these two "centered" observations: doing so, will produce a new field of small velocity corrections. The original field describes in some sense the motion of the body of precipitation in a large scale, while the corrections add localized features. The velocity field can be conceptually described as:

$$\boldsymbol{v}(t) = \boldsymbol{v_g}(t) + \boldsymbol{v_l}(t) + \boldsymbol{\varepsilon}(t) \qquad (1)$$

where $\boldsymbol{v_g}(t)$ refers to the global or large scale velocity field and $\boldsymbol{v_l}(t)$ refers to to the local or small scale velocity field that differ from the large scale motion, while $\boldsymbol{\varepsilon}(t)$ represents the errors. These corrections are local not only in space but also in time and they will be irrelevant after short time, usually about one hour. But during the first hour of the nowcast they can

help the motion field to follow as precisely as possible even small (but occasionally important) features. A typical case occurs with splitting storms, where one storm propagates to the right and one to the left. We proceed by relaxing the sum of large scale motion field plus the small scale corrections (at time zero) towards the large-scale motion field in an-hour time (at lead time +1h). This can take place with a simple weight-based merging in time. After lead time +1h the corrections have been zeroed and the precipitation is advected using the large-scale motion field alone, which also reflects the gradual loss of predictability of the motion associated with small scale features. In this way our motion field is time-dependent only during the first hour of nowcasting and static afterwards. We have to observe that one problem with determining the optical flow as in equation (1) is that the exact point at which the motion is separated in global and local should be prescribed. One could potentially formalize this relation as a sum of an infinite number of terms, each associated with a smaller and smaller scale. The spatial resolution of the domain (in our case $1km^2$) would then define the cut-off scale to keep only a finite number of terms in this relation.

Another observation is that the velocity field is, in reality, time-dependent but this time-dependence depends on the future unknown evolution of the motion. This brings us to a second way to make the motion field dynamic, which is to employ our geostatistical scheme to compute the motion field of the NWP precipitation field(s) for a small number of lead times, e.g. +2,3,4,5 and 6h or any subset of these. Then one can use weights to merge the observation field at real time with the motion field at time +2h, and continue doing the same for connecting seamlessly hours 2 to 3, 3 to 4 and so on. The net result is a time-dependent motion field that starts from the observation-based motion field and evolves using as steps the NWP derived motion field. One can also observe that the two enhancements of the kriging scheme can actually be used together: the first hour can include small-scale corrections which relax towards the observation large-scale motion field after one hour and then moves towards the NWP-derived motion fields.

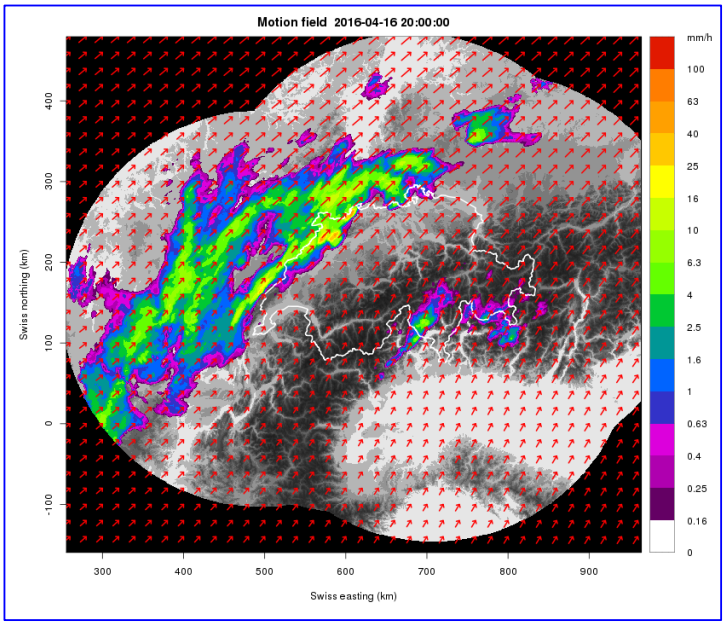


Figure 1: Typical velocity field of NowPrecip

Finally it is worth mentioning that since our technique is based on kriging, its outcome is not only the expected values of motion vectors but also their associated variances (which are produced at no additional computational cost). This variance is getting larger with increasing distance from the measurements. One can employ this variance to generate perturbations for the velocity vectors and eventually produce an ensemble of stochastic motion fields.

2.2 Localization

NowPrecip relies on an autoregression scheme as its main engine to produce nowcasts. Similar schemes have been employed in the past, for instance Berenguer et al. 2011, and Pegram and Clothier, 2001. However, NowPrecip adds a localization approach to address evolution more precisely. This additional scheme can help considerably when there is significant difference in the weather in different parts of the domain, due for instance to complex terrain, or when the domain is too large to be characterized by a singular type of weather.

The autoregression scheme utilizes the last two images plus a stochastic term with predefined spatially correlated noise to produce the next image in the nowcasting sequence:

$$\boldsymbol{R}(t + n\Delta t) = \varphi_1 \cdot \boldsymbol{R}(t + (n-1) \cdot \Delta t) + \varphi_2 \cdot \boldsymbol{R}(t + (n-2) \cdot \Delta t) + \boldsymbol{A_s}(t + n \cdot \Delta t) \qquad (2)$$

Where $\boldsymbol{R}$ is the rainfall, φ_1 and φ_2 are the Yule-Walker coefficients and $\boldsymbol{A_s}(t + n \cdot \Delta t)$ is the stochastic term of the autoregressive process which is essentially a 0-mean spatiotemporally correlated noise with variance:

$$v^2 = \frac{(1+\varphi_2)(1+\varphi_1-\varphi_2)(1-\varphi_1-\varphi_2)}{1-\varphi_2} \qquad (3)$$

The Yule-Walker coefficients are the solution of the system:

$$\begin{bmatrix}\varphi_1\\ \varphi_2\end{bmatrix} = \begin{bmatrix}\rho_0 & \rho_1\\ \rho_1 & \rho_0\end{bmatrix}^{-1}\begin{bmatrix}\rho_1\\ \rho_2\end{bmatrix} \qquad (4)$$

where ρ represents the Lagrangian auto-correlation between the most recent observation and the two observations preceding it. Fields generated this way are second-order stationary (Priestley 1981).

Sequences of spatiotemporally correlated noise are produced employing an FFT-based scheme which is typical in probabilistic nowcasting (Pegram et al. 2001; Bowler et al., 2006; Berenguer et al., 2011). Localized noise characterized by different anisotropy in different locations of the domain can also be introduced. A technique for producing localized noise has been introduced by Nerini et al. in 2017.

Starting from the last two 10-minute observations we advect them according to the computed motion field, then we place them in the autoregressive equation and add the correlated noise to produce the next image in the sequence. This process continues until we have reached the desired number of frames. This completes the first part of our nowcasting sequence production.

NowPrecip has been constructed to operate in a localized scale. We construct a regular grid of points which covers the domain of interest. We call this the "standard grid." The chosen grid length is 32km both in *x* and *y* dimensions. We now consider a box of size 65x65km^2 centered at each of the grid points. (The same system can also work well for sizes 129x129 and 33x33km^2 and the optimal choice of the box size is a matter of experimentation of the particular domain and weather in question.)

Consider the grid point located at coordinates (x_d, y_d). We refer to this location (x_d, y_d) as "destination." Using the computed motion field we easily derive where this point was located in the previous time frame. We refer to this location as "origin" and its coordinates are signified as (x_o, y_o). Centered on (x_o, y_o) is the origin box of size 65x65km^2. We compute the values of two variables of interest: (a) the mean value (hereafter IMF or image mean flux after Pegram and Clothier, 2001) and (b) the wetted area ratio (hereafter WAR) of the box. We do the same for each of the grid points of our domain. Using the concept of Lagrangian persistence we assume that the values of IMF and WAR of each origin box are conserved in time, therefore these values are conserved between origin in time t_o and destination in time t_d.

At the end of this process we have assigned at each grid point of the standard grid a value of IMF and value of WAR. For example the value of IMF and WAR at some grid point (x, y) determines the IMF and WAR the 65x65km^2 box centered in (x, y) should have at time t_d. We will define them as IMF_d and WAR_d.

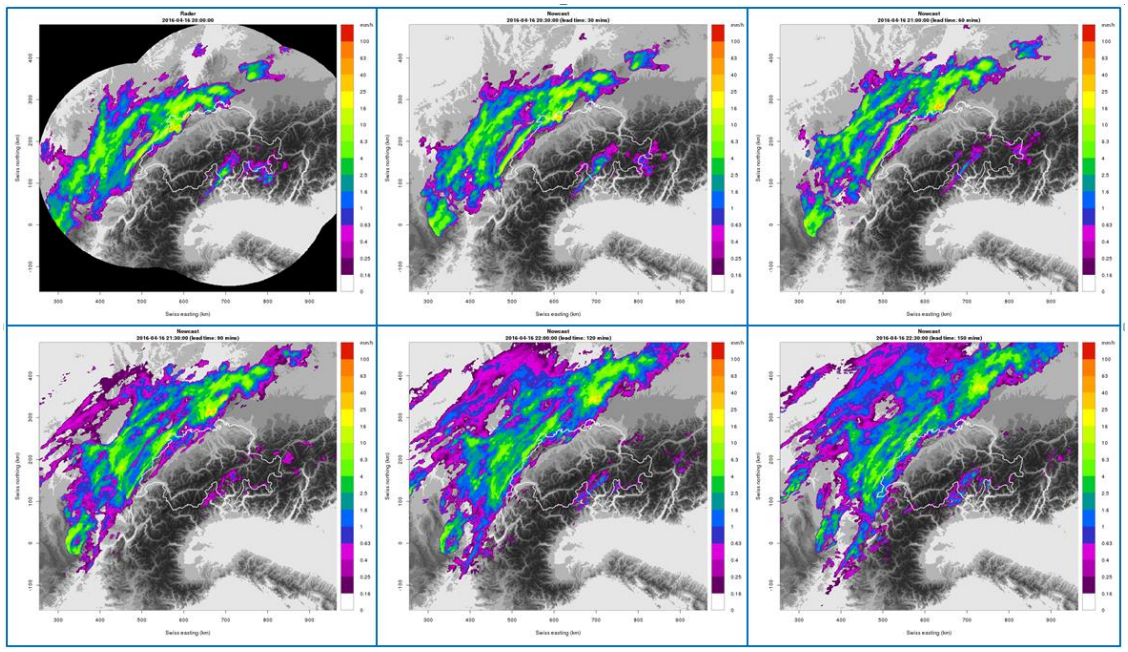


Figure 2: A sequence of a typical NowPrecip nowcast. The first image is the real time observation. The nowcasting images are each 30 min apart. Typically NowPrecip produces sequences that have frequency 10 minutes and extent to lead time equal to 5 hours.

We now employ the autoregressed image we have prepared using equation (2) which corresponds to time t_d. This image has to be adjusted to be consistent with the grid of IMF_d and WAR_d. We now compute the IMF and WAR of the autoregressed image for each point of the standard grid. We adjust them to be equal to the IMF_d and WAR_d through a straightforward shift and scale procedure similar to the one described in Clothier and Pegram, 2002. In particular, for each grid point we compute the values of the variables α and λ so that if we subtract α by all the pixels of the box, zero all negative values, and then multiply the outcome by λ the resulting box will have the desired IMF and WAR (that is $IMF=IMF_d$ and $WAR=WAR_d$). In this way we end up assigning at each grid point of the standard grid a value of α and λ. Then we can easily interpolate α and λ and produce continuous images, where we have values of α and λ computed for each pixel. We will define these maps as $\boldsymbol{A}$ and $\boldsymbol{\Lambda}$. Subtracting $\boldsymbol{A}$ from the autoregressed image, and then multiplying the result by $\boldsymbol{\Lambda}$ will produce the final image where the local properties at the chosen scale are consistent with the concept of Lagrangian persistence, and at the same time there are no spatial discontinuities. We repeat this process for the rest of the time-frames. We emphasize that the finalized images has the same resolution as the observations, i.e. $1km^2$, while the grid we use refers to the scale where Lagrangian persistence is applied.

The nowcasting sequence is finally merged with the corresponding NWP output (Figures 2, 3, and 4). The merging is taking place using an weighted sum of nowcasts and NWP images, with weights which gradually decrease for the nowcasts and increase for the NWP. The weights vector can be nonlinear and it depends on the mean correlation coefficient between the last hour observations and the corresponding NWP images:

$$\boldsymbol{F}_i = (1 - w_i(\rho))\boldsymbol{R}_i + w_i(\rho)\boldsymbol{M}_i \qquad (5)$$

where $\boldsymbol{F}$ is the finalized merged image, $\boldsymbol{R}$ the nowcast and $\boldsymbol{M}$ the NWP model and ρ is the mean Pearson correlation between the last six 10-minute observations and the corresponding images of the NWP and w the vector of the weights.

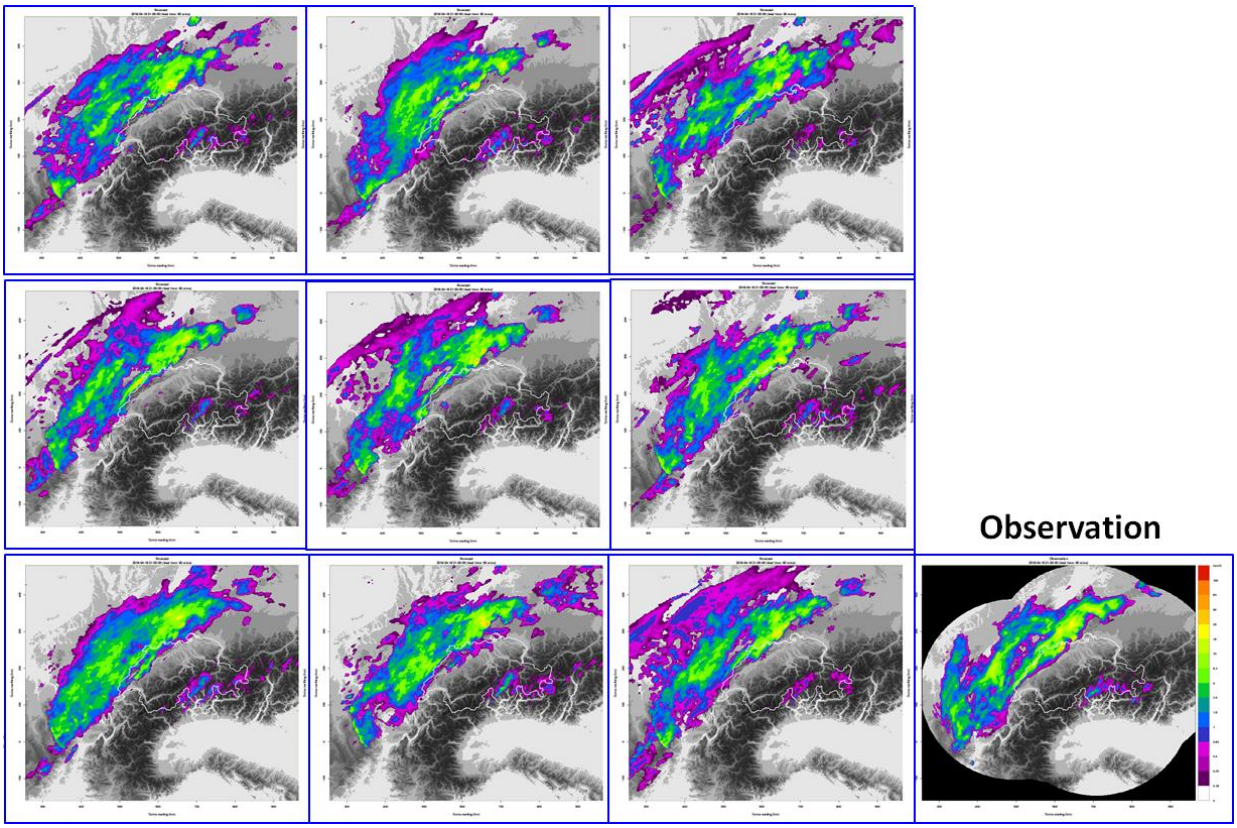


Figure 3: Several realizations for lead time +1h performed by NowPrecip. Each simulation blends slowly with a different member of the NWP COSMO-E in Switzerland. The last image on the bottom right is the radar observatio for comparison.

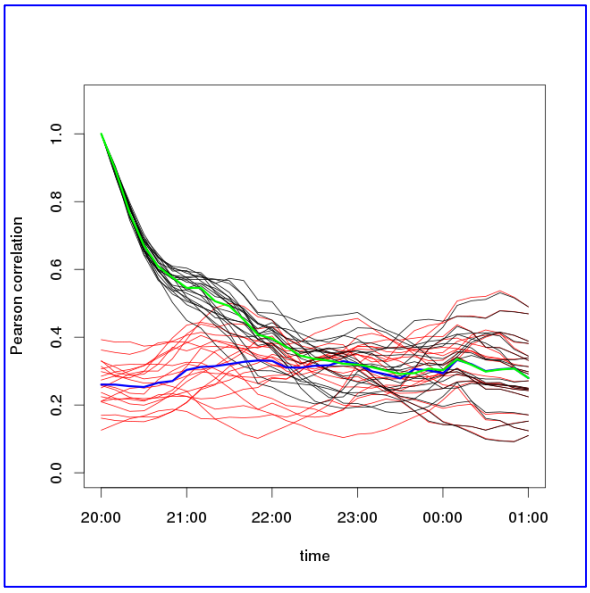


Figure 4: Pearson correlation of NowPrecip (black) for each of the 21 members of an ensemble. Each member is blended with one member of the COSMO-E ensemble (red) in Switzerland. The green line signifies the mean value of NowPrecip, while the blue line signifies the mean value of COSMO-E. The blending is complete after 5 hours.

2.3 Machine learning

The localized nowcasting approach of NowPrecip makes it straightforward to introduce machine-learning capabilities into the scheme. There are two possible ways tested so far.

The first way employs the last hour or last few hours of observations. The goal is to create a dataset of the IMF and WAR at origin and destination for every grid point (x_d, y_d) of the standard grid. We can do that by employing the techniques described in section 2.2. Having created this dataset we can use it to train any machine learning algorithm, for example decision trees or neural networks. The question we ask is the following: given the IMF and WAR of the origin box in time t_o what is the IMF and WAR at destination grid point (x_d, y_d) in time t_d? This is practically a regression method which can replace the Lagrangian persistence assumption. It essentially uses as predictors the IMF and WAR of the origin box at time t_o the coordinates at destination x_d, y_d, and the IMF and WAR of the destination box at the time of origin t_o. It attempts to predict the IMF and WAR at (x_d, y_d) at time t_d. Training a machine learning algorithm this way, that is, using one or few hours of data, is not computationally expensive and can take place in real-time.

The second approach involves radar observations from a multi-year radar archive. The process is practically the same as the aforementioned but the amount of observations is now much larger. We again create a dataset of the IMF and WAR for each of the grid points of the standard grid. This dataset can now be introduced into a machine learning algorithm or even a combination of machine learning algorithms to train a prediction scheme with the goal to predict the IMF and WAR at each grid point in the next time frame. While the training of this type of regression is computationally expensive, one has to prepare it a single time, and its result is an object that provides the desired prediction. We emphasize it is the training process that is computationally expensive while the prediction process which uses this object is not: it can be employed without problems by a nowcasting system running in operational mode. This method is rather climatological in nature. It may provide statistically significant results of expected value and the variability but it is also prone to errors since it uses analogues from many different events. How many of these events are true analogues to the situation in hand is a matter of debate. In this sense, it may not always be able to narrow down adequately to the particulars of the situation which takes place in real time. There is however a large potential on this method and its success depends on how accurate this selection of predictors and analogues is.

Machine-learning-based prediction is an analogue-based replacement for the Lagrangian persistence. Growth and decay is incorporated within the estimation. Decision trees, in particular, gather in sets (formally called leaves) similar initial conditions (similar IMF, WAR, x_o, y_o and any other predictors) and provide statistics of the IMF and WAR at destination. The advantage of using decision trees is that the statistics they provide are not limited to only the mean value but they can also provide broader statistical information like quantiles of the distributions of IMF and WAR at destination. This is an important fact when it comes to probabilistic nowcasting, because the quantiles can be used to assign different values to different members of the ensemble, while the spread of the output at every location will capture the spread determined by the data in the radar-archive. Where analogues, in general, fail is in cases of extremes, because there recorded analogues do not yet exist or may be extremely few. This can be resolved by extrapolating the machine learning results linearly or nonlinearly

to cover extreme cases. Work on the radar-archive machine learning was described by Sideris et al. in 2015, while a paper by Foresti et al. in 2018 is currently accepted and an additional one by Foresti et al. is currently in preparation.

2.4 Growth and Decay

NowPrecip does not rely only on Lagrangian persistence but it can add a growth/decay factor to it by incorporating a technique which computes a systematic growth and decay of precipitation. We emphasize that we attempt to assign a growth and decay trend at certain locations of the domain. This trend is systematic and a function of geographic location. Additional to that is an unpredictable growth and decay component which is instead modeled via the correlated noise in the autoregressive process that moves the evolution. The spatiotemporal characteristics of this correlated noise are responsible for simulating this random growth and decay, in a probabilistic fashion, meaning that an ensemble of nowcasts should be able to produce in a localized area a set of possible scenarios with the appropriate variability, neither over- nor under-dispersive.

The growth and decay trend, on the other hand, is typically associated with topographic features, like for example a mountainous terrain. The NWP uses a solid mathematical foundation which takes into consideration the role of numerous meteorological variables and their interaction with the topography to make weather predictions. This is an opportunity for enhancing the input of a nowcasting system. The idea is to analyze the NWP output in order to detect any systematic growth and decay patterns.

This can be achieved by using the aforementioned already built-in structure of the standard grid and localized boxes. Specifically, for each of the sequential images of the NWP output we can detect the change in IMF and WAR between origin and destination for each of the boxes. We fit IMF at origin versus IMF at destination in such a way that the least squares line crosses the origin (0, 0). We do the same for WAR too. The slopes of the fitting process are practically the multiplicative growth and decay factors we need for IMF and WAR. The result is a standard grid of growth decay for IMF and one for WAR. By using bilinear interpolation we can turn the grid into a continuous map as in Figure 5.

It is useful to enhance this method by quantifying how persistent the behaviour is. Therefore we count the number of times a grid point has been subject to growth and how many times to decay. When the one or other trend is persistent, for example when for grid point (x, y) the large majority of the n NWP frames have been subject to growth, it is safe to assume that growth and decay at this point is indeed characterized by the slopes we have computed. Otherwise the growth and decay is considered to be zero. This additional step can therefore act as a mask so we avoid incorporating non-persistent behaviours in our map.

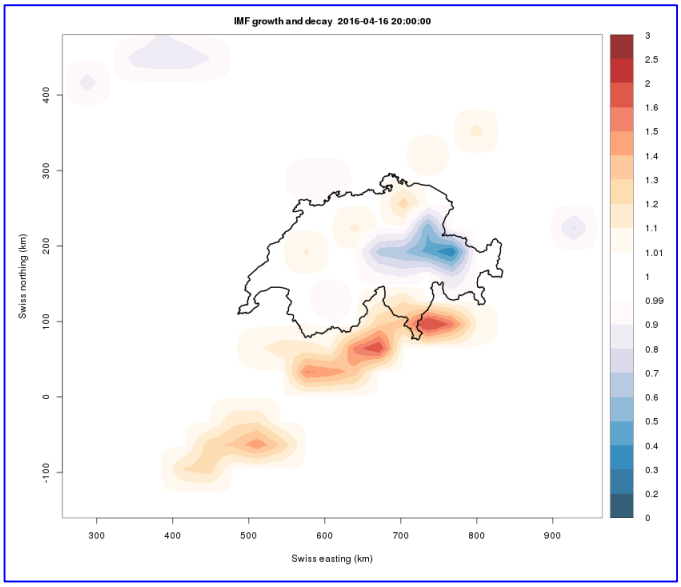


Figure 5: Growth and decay map of NowPrecip. For this particular time-stamp there is enhancement of precipitation south of the Alps (orange region) followed by decay (blue region). Often intense growth and decay areas are associated with the topographic features.

There is an additional possibility on this method which could be useful. The same method as above can be employed for the last hour or last two hours of observations. This can produce an observation-based growth-decay map which is not exactly the same as the NWP-based growth-decay map, although it commonly shares a good number of similarities. This observation-based map is useful to capture the systematic trends on growth and decay that have taken place over the last few observations. Our testing suggests that such trends can be useful for the first hour of the nowcast. It is finally possible to blend the two growth and decay maps (observation-based and NWP-based), using a vector of linear weights, by starting from the observation-based one at real-time and relaxing it after one hour to the NWP-based one.

2.5 Generation of convective cells

During the first tens of minutes of a nowcast there may occasionally be additional information regarding the evolution of individual cells of high precipitation intensity. For example, satellite imagery may be able to detect signatures of convection initiation at some location some minutes before the cell appears in the radar. This is an important piece of information that can improve the very early nowcast considerably especially in alerting situations, therefore efforts to this end are worth to be made. The introduction of this information could potentially take place by adding some growth in the box of interest. But we have developed one additional method which gives more control over the evolution of the cell.

We have constructed a module that builds realistic cells bottom up, pixel by pixel. We can control the size, the intensity and the anisotropy of the cell as well as the coordinates of its evolution in time. The realization of each cell is stochastic, so two realizations with the same parameter values result in two different cells (although with similar statistical properties and appearance). Provided that we have some information over the course the cell is about to follow and over the evolution of its size intensity and anisotropy we can blend it inside the sequence of our nowcasting evolution. This blending is not a simple overlap of the nowcast with the generated cell. The cell instead becomes an integral part of the evolution and interacts with its environment (Figure 6). This way one can grow a cell anywhere inside the domain if additional information, from the satellite usually, provides clues that such a cell has high probability to happen. Obviously the characteristics of such cells, size, intensity and anisotropy, can also be probabilistic, in the sense that they can be drawn by predefined or on-the-fly defined distributions, resulting to cells with different statistical characteristics and appearance for different members of an ensemble.

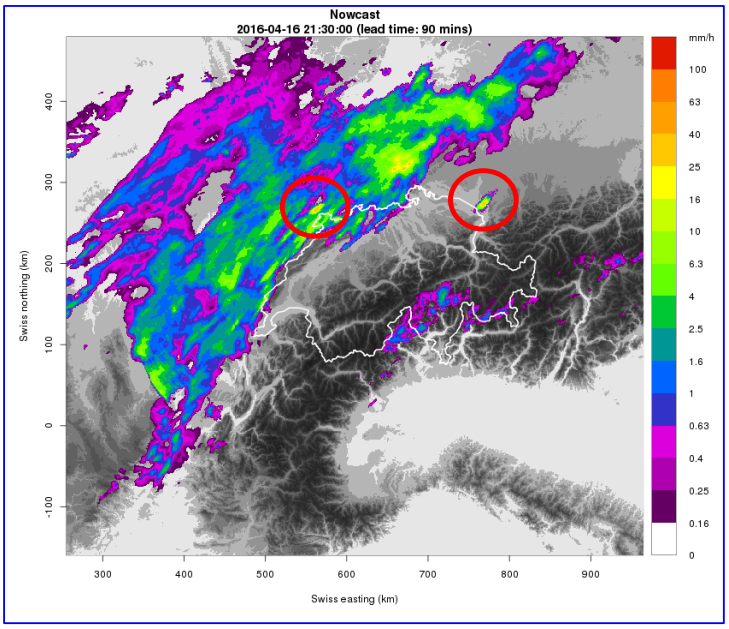


Figure 6: The two high intensity cells in the red circles have been artificially introduced within the map. These cells become part of the evolution and interact with the surrounding precipitation cells seamlessly.

This technique is capable of generating convective cells in specific locations and controlling their properties when reliable information on convection initiation and further evolution happens to be available. At the time of this writing accuracy of such information is still a major issue; it depends nonlinearly on numerous sensitive factors. Work involving machine learning operating on multi-year archives has already started taking place within MeteoSwiss. The purpose of this module, which is currently in a testing phase, is rather to bridge the gap between areal tracking nowcasting systems and object nowcasting systems which care mostly about cell initiation and evolution making good use of convection initiation information when this is reliable.

3 Summary

NowPrecip is a new areal-tracking nowcasting system developed in MeteoSwiss. It is currently in testing mode and aspires to be operational in 2019. It incorporates several innovative features. It proposes a new scheme for producing motion fields based on geostatistics. It is fully probabilistic and can produce ensembles of realizations blended with the output of NWP system COSMO. It uses a grid technology to describe the precipitation in localized fashion, and in this sense it is appropriated for cases where the weather pattern is diverse throughout the domain of interest, as it commonly happens in the complex terrain of Switzerland. It offers the possibility of replacing the Lagrangian persistence assumption with the nonlinear regression of machine-learning algorithms. It includes a growth-decay mechanism produced by the analysis of the

NWP. And finally it offers a solution for introducing and controlling the details of high intensity cells in places of choice within the domain.

Acknowledgement

We would like to acknowledge our colleagues from several divisions in MeteoSwiss for their continuous support over the time of development of this project.

References

Berenguer, M., Sempere-Torres, D. and Pegram, G.G., 2011. SBMcast–An ensemble nowcasting technique to assess the uncertainty in rainfall forecasts by Lagrangian extrapolation. *Journal of Hydrology*, *404*(3-4), pp.226-240.

Bowler, N.E., Pierce, C.E. and Seed, A.W., 2006. STEPS: A probabilistic precipitation forecasting scheme which merges an extrapolation nowcast with downscaled NWP. *Quarterly Journal of the Royal Meteorological Society*, *132*(620), pp.2127-2155.

Clothier, A. and Pegram, G.G.S., 2002. *Space-time modelling of rainfall using the string of beads model: integration of radar and raingauge data*. Water Research Commission.

Cuo, L., Pagano, T.C. and Wang, Q.J., 2011. A review of quantitative precipitation forecasts and their use in short-to medium-range streamflow forecasting. *Journal of hydrometeorology*, *12*(5), pp.713-728.

Dixon, M. and Wiener, G., 1993. TITAN: Thunderstorm identification, tracking, analysis, and nowcasting—A radar-based methodology. *Journal of atmospheric and oceanic technology*, *10*(6), pp.785-797.

Ebert, E.E. and McBride, J.L., 2000. Verification of precipitation in weather systems: Determination of systematic errors. *Journal of Hydrology*, *239*(1-4), pp.179-202.

Ebert, E.E., Damrath, U., Wergen, W. and Baldwin, M.E., 2003. The WGNE assessment of short-term quantitative precipitation forecasts. *Bulletin of the American Meteorological Society*, *84*(4), pp.481-492.

Foresti L., Sideris I.V., Panziera L., Nerini D., and Germann U., 2018. *A 10-year radar-based analysis of orographic precipitation growth and decay patterns over the Swiss Alpine region.* Quarterly Journal of the Royal Meteorological Society, accepted.

Germann, U. and Zawadzki, I., 2002. Scale-dependence of the predictability of precipitation from continental radar images. Part I: Description of the methodology. *Monthly Weather Review*, *130*(12), pp.2859-2873.

Golding, B.W., 1998. Nimrod: A system for generating automated very short range forecasts. *Meteorological Applications*, *5*(1), pp.1-16.

Haiden, T., Kann, A., Wittmann, C., Pistotnik, G., Bica, B. and Gruber, C., 2011. The Integrated Nowcasting through Comprehensive Analysis (INCA) system and its validation over the Eastern Alpine region. *Weather and Forecasting*, *26*(2), pp.166-183.

Hering, A.M., Germann, U., Boscacci, M. and Sénési, S., 2006. Operational thunderstorm nowcasting in the Alpine region using 3D-radar severe weather parameters and lightning data. *ERAD 2006 proceedings*.

Golding, B.W., 2000. Quantitative precipitation forecasting in the UK. *Journal of Hydrology*, *239*(1-4), pp.286-305.

Hilker, N., Badoux, A. and Hegg, C., 2009. The Swiss flood and landslide damage database 1972-2007. *Natural Hazards and Earth System Sciences*, *9*(3), p.913.

Lin, C., Vasić, S., Kilambi, A., Turner, B. and Zawadzki, I., 2005. Precipitation forecast skill of numerical weather prediction models and radar nowcasts. *Geophysical research letters*, *32*(14).

Mandapaka, P.V., Germann, U., Panziera, L. and Hering, A., 2012. Can Lagrangian extrapolation of radar fields be used for precipitation nowcasting over complex Alpine orography?. *Weather and Forecasting*, *27*(1), pp.28-49.

Nerini, D., Besic, N., Sideris, I., Germann, U. and Foresti, L., 2017. A non-stationary stochastic ensemble generator for radar rainfall fields based on the short-space Fourier transform. *Hydrology and Earth System Sciences*, *21*(6), p.2777.

Pegram, G.G.S. and Clothier, A.N., 2001. High resolution space–time modelling of rainfall: the "String of Beads" model. *Journal of Hydrology*, *241*(1-2), pp.26-41.

Priestley, M.B., 1981. Spectral analysis and time series.

Reyniers, M., 2008. *Quantitative precipitation forecasts based on radar observations: Principles, algorithms and operational systems*. Institut Royal Météorologique de Belgique.

Sättele, M., Bründl, M. and Straub, D., 2012, November. A classification of warning system for natural hazards. In *10th International Probabilistic Workshop, edited by: Moormann, C., Huber, M., and Proske, D., Stuttgart: Institut für Geotechnik der Universität Stuttgart* (pp. 257-270).

Spreafico, M.; Weingartner, R.: Hydrologie der Schweiz - Ausgewählte Aspekte und Resultate. Berichte des BWG, Serie Wasser Nr. 7. Bern: Bundesamt für Wasser und Geologie BWG, 2005

Sideris, I.V., Gabella, M., Erdin, R. and Germann, U., 2014. Real-time radar–rain-gauge merging using spatio-temporal co-kriging with external drift in the alpine terrain of Switzerland. *Quarterly Journal of the Royal Meteorological Society*, *140*(680), pp.1097-1111.

Sideris, I.V., Germann, U., Gabella, M., and Panziera, L.. 2015. Nowcasting and large-radar-archive statistical learning in Switzerland. *In Proceedings of the 10th International Workshop on Precipitation in Urban Areas (UrbanRain15)*, Pontresina, Switzerland.

Talagrand, O., 1997. Assimilation of Observations, an Introduction (gtSpecial IssueltData Assimilation in Meteology and Oceanography: Theory and Practice). *Journal of the Meteorological Society of Japan. Ser. II*, *75*(1B), pp.191-209.

Continental-Scale Weather Radar Data Assimilation Using North American Data

Dominik Jacques[1], Daniel Michelson[1], Bjarne Hansen[1], Jean-François Caron[1], and Luc Fillion[1]

[1]*Environment and Climate Change Canada (ECCC)*

(Dated: 22 June 2018)

1. Introduction

Determining the impact of assimilating weather-radar data in numerical weather prediction models at continental scales is still relatively uncommon. This is partly due to data availability, but also due to data quality issues when data are available. This study reports on recent progress towards the assimilation of radar data in the Canadian Regional Deterministic Prediction System (RDPS). Two-dimensional reflectivity composites are assimilated using the method of Latent Heat Nudging (LHN) (Jones and Macpherson, 1997; Manobianco et al., 1994). This work marks the introduction of systematic weather radar data assimilation at ECCC which is one component of the plan towards a rapidly refreshed assimilation system that operates at convective scales. LHN was selected because of its computational efficiency and its well-documented use at other operational centers. LHN gives us a baseline that will allow for future comparisons with other radar data assimilation approaches.

Early results for the application of LHN in the RDPS have been reported at the previous AMS radar conference (Jacques et al., 2017) and are described in a manuscript (Jacques et al., 2018) currently under review. Here, we specifically report on the impact of applying LHN within a continuously cycled assimilation system.

2. The generation of North American composites

Weather-radar data from three sources are used in this study.

1. Environment and Climate Change Canada's weather-radar network consists of 30 C-band Doppler radars. 19 of these radars have an antenna with a 1.1° half-power beamwidth, while the remaining 11 radars have a half-power beamwidth of 0.62°. All radars have magnetron transmitters, and Sigmet-Vaisala antenna controllers and signal processors. Data are acquired using a ten-minute cycle that starts with a descending 24-sweep volume containing only uncorrected reflectivities, i.e. they are not corrected using Doppler signal processing. Maximum range is 256 km, with resolutions of one kilometer in range and one degree in azimuth. With some exceptions, for example radars in mountainous regions, the baseline scan strategy's highest elevation angle is 24°; lowest elevation angle is 0.3° in summer and 0.1° in winter. The volume is followed up by collecting three dedicated sweeps to 112.5 km range containing reflectivity and radial wind velocity data with 500 m resolution in range and 0.5° resolution in azimuth. The combination of the reflectivity volume and the dedicated sweeps containing Doppler data are the data used in this study.
2. McGill University's S-band dual-polarization radar located west of Montréal. This radar has a klystron transmitter and an antenna with a half-power beamwidth of 0.85°. While this is a radar designed and used for research purposes, it is run operationally to contribute data to ECCC's network. Data received by ECCC are in the McGill in-house format that has a resolution of one degree in azimuth and variable (1-4 km) resolution in range, with a maximum range of 480 km. An ascending 24-sweep volume is collected every five minutes, yet ten-minute data are used in this study. ECCC receives reflectivity and radial wind velocity data from McGill, but only the former are assimilated in this study.
3. The American Next Generation Weather Radar (NEXRAD) network. This is a network of S-band dual-polarization radars with klystron transmitters and an antenna with a half-power beamwidth of around 0.92°. The data used in this study are Level II data from the radars in the contiguous United States and Alaska. Data are generally acquired with a cycle of around six minutes, although this can vary depending on which Volume Coverage Pattern (scan strategy) is being run on any given radar. The data resolution is 0.5° in azimuth and 250 m in range, with a maximum range of 458 km. In this study, NEXRAD data have been used to a maximum range of 250 km. ECCC receives conventional and dual-polarization moment data, but only conventional (reflectivity) data are assimilated in this study.

The software framework for quality controlling all radar data and generating composite (mosaic) products is the BALTRAD Toolbox (Michelson et al., 2018) The first step is to harmonize all data to a common file format, in this case ODIM_H5 (Michelson et al., 2014). With the exception of the McGill radar, Canadian data are available natively in the proprietary IRIS format, and these data are read into the BALTRAD Toolbox using new decoding functionality. McGill data are likewise read with a new decoder. NEXRAD data are decoded using functionality found in Py-ART software (Helmus and Collis, 2016). All data and composites are represented in ODIM_H5.

Quality control is performed using specific data processing chains for each type of input radar data. The Canadian C-band data require the most quality control because the 256 km data are effectively non-Doppler reflectivities[1]. The complete quality control chain is given in the following points:

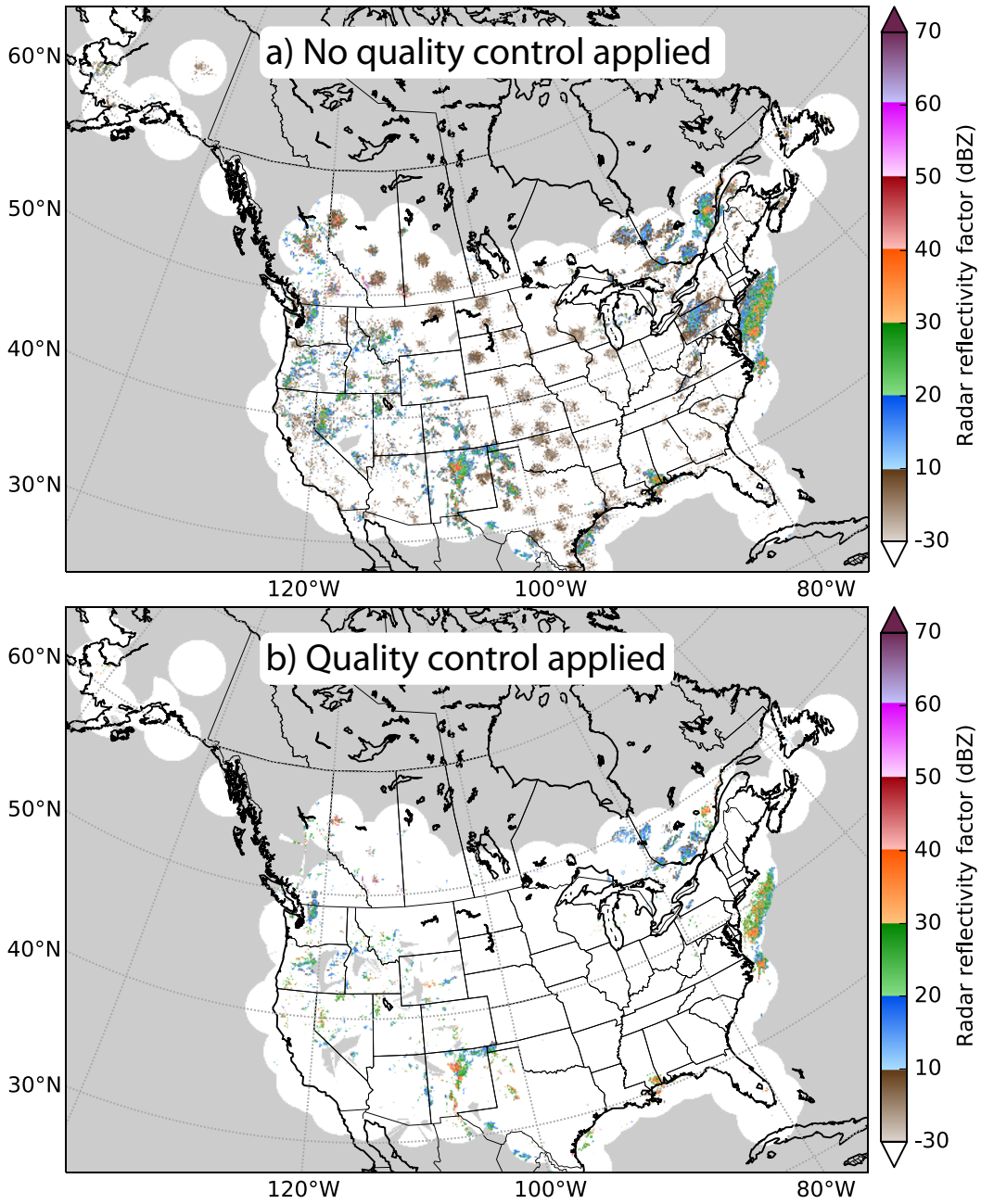


Figure 1: Example of a reflectivity composites (valid on 8 July, 2014 at 0600 UTC) a) without and b) with quality control being applied. Grey shadings indicate areas with no radar coverage.

1. An ECCC in-house algorithm is applied. It combines the 256 km non-Doppler data with the shorter-range (112.5 km) Doppler data and vertical structure analyses to yield a lowest sweep of quality-controlled reflectivity.

2. A hit-accumulation clutter filter is applied whereby echoes are removed if their monthly frequency of occurrence exceeds 60% [2] Such polar bins are replaced with the "no data" special value which represents areas that have not been radiated. (There are two special values, the second representing areas that have been radiated but which have not produced valid echoes, referred to as "undetect".)

[1] In the absence of Doppler velocity, the detection of ground clutter is more difficult.

[2] Val d'Irène is an exception. This radar's lowest elevation angle is negative in order to detect shallow precipitation over the St. Lawrence River. There is significant topography in the area, which leads to systematically high clutter contamination which is mitigated using a higher threshold with data from this radar.

3. Non-precipitation identification and removal, according to Peura (2002), addressing biometeor targets (birds, insects), speckle, and external emitters (e.g. radio interference). Echoes identified as not originating from precipitation are assigned the "undetect" value, and the probability of being non-precipitation is represented in a quality indicator array with the same polar geometry as the sweep of data.

4. Beam-blockage identification and correction. The BALTRAD approach was developed in Northern Europe, where access to international digital elevation model (DEM) information at high latitudes was limited to GTOPO30 (a global digital elevation model (DEM) with a horizontal grid spacing of approximately 1 kilometer) produced by the United States Geological Survey[3]. This approach has been extended using GTOPO30 DEM tiles covering North America. For each scan of radar data, the percentage of beam blockage is determined, and it is added to this scan as a quality indicator array. Data in sectors with partial blockage up to 60% are corrected. Data in sectors with blockage exceeding 60% are assigned the "no data" special value.

5. Conventional attenuation correction according to Ośródka et al. (2014). The path-integrated attenuation is represented in a quality-indicator array with the same geometry as the sweep of data.

6. Range-related beam broadening effects. This is a descriptive quality characterization algorithm (Ośródka et al., 2014), basically indicating decreasing data quality as the radar beam broadens with increasing range from the radar. This information is also represented as a quality-indicator array with the same polar geometry as the sweep of data.

7. "Total quality" according to Ośródka et al. (2014). All the quality-indicator fields mentioned above represent data quality continuously between 0 (lowest quality) and 1 (highest quality). For the purposes of this study, a single quality metric value per polar bin is desired for subsequent processing, e.g. composite generation. The metric representing "total quality" in this case is the minimum quality among those determined in the beam blockage, attenuation, and beam broadening steps outlined above. Pixels identified as "undetect" are assigned a quality of 0.

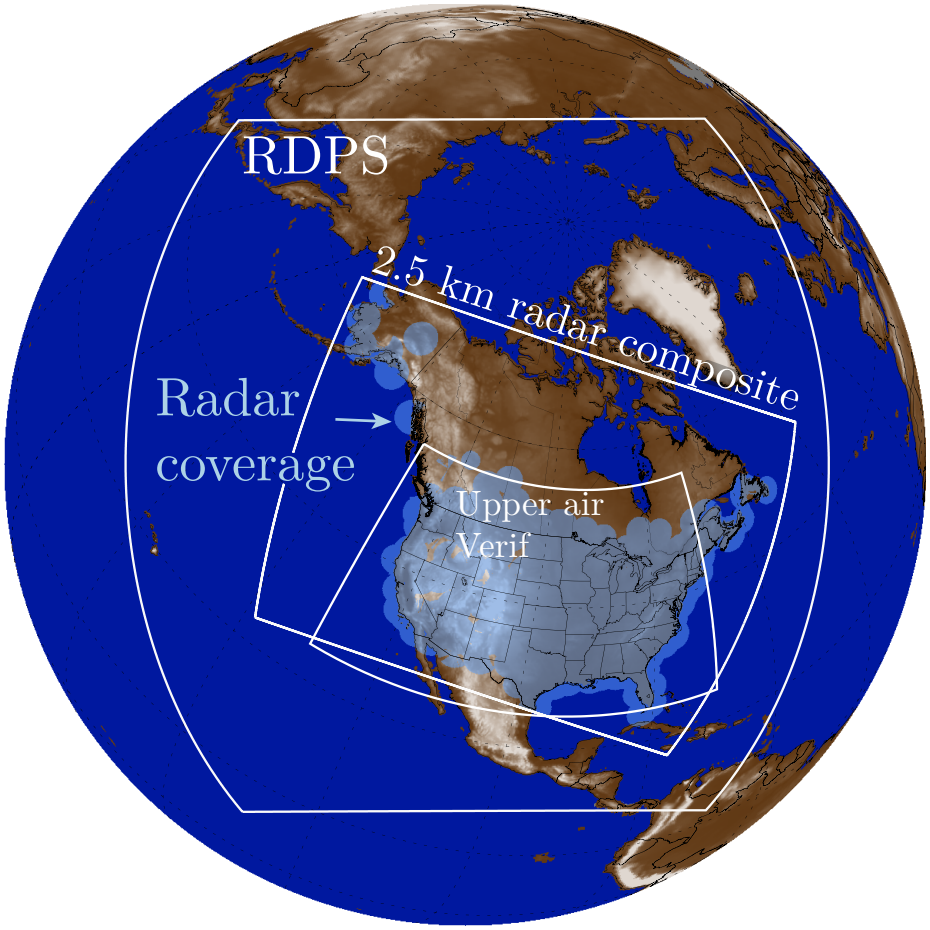


Figure 2: Domains relevant to this study.

[3]See https://lta.cr.usgs.gov/GTOPO30 for more information.

NEXRAD Level II data are processed according to steps 3-7 above using attenuation coefficients for S-band. The McGill data require the least amount of processing because they arrive already quality controlled for clutter and speckle; steps 4-7 are performed using attenuation coefficients for S band.

The processing of input polar data in this way and using the BALTRAD Toolbox is already being performed in Europe, e.g. Ridal and Dahlbom (2017). Noteworthy for our study, however, besides the application of the processing and data quality framework with North American data, is that the quality controls have been used aggressively to suppress as much non-precipitation information content as possible. We know that there is a price to pay for this, in the form of some real precipitation echoes being rejected, but the nature of the LHN approach makes the consequence of assimilating contaminated pixels much more detrimental than the incorrect representation of actual precipitation as "no data".

Composites are generated every 10 minutes containing both uncorrected and quality-controlled reflectivities, along with the associated quality metrics that have been carried over from polar to Cartesian space. Figure 1 shows the impact of the quality controls being applied. All reflectivity and data quality arrays are written to the same ODIM_H5 file. The output grid's horizontal resolution is 2.5 km on a domain shown in Figs. 1 and 2. The higher resolution of the composites relative to the 10 km resolution of RDPS was selected to accommodate future assimilation projects at higher resolution. In generating the composite, data are selected directly from the input polar volumes with no intermediate steps. The basic product being composited is a pseudo-CAPPI (constant altitude plan position indicator) at an altitude of 1 km. In locations where measurements from more than one radar are available, the selection criterion for choosing the input polar data is maximum data quality as represented by the "total quality" field explained above. When the input data are selected for the composite, their surface distance to the corresponding radar is calculated (km) on-the-fly and added to an additional quality array for use in downstream processing.

3. Experiment setup

3.1. The RDPS system

The RDPS is a 10 km forecasting system that operates on the continental-scale domain illustrated in Fig. 2. For these experiments, the RDPS runs with a 6h continuous assimilation cycle that is illustrated in Fig. 3. This continuous cycle setup is currently being tested for an operational implementation planned in September 2018.

From this figure, it can be seen that the background for each assimilation cycle comes from a forecast originating from the previous assimilation cycle. The assimilation of all the non-radar observations (radiosondes, aircrafts reports, satellite measurements, etc) is performed by a 4DEnVAR system described in (Buehner et al., 2015; Caron et al., 2015). This assimilation system generates analysis increments (gray arrows) that are applied during the first six hours of the ensuing forecast using an Incremental Analysis Update (IAU) approach. In Fig. 3 the pink areas represent the IAU period at the beginning of each forecast.

At 0000 and 1200 UTC, two forecasts are integrated from the same Initial Conditions (IC's) and analysis increments. Except for their duration and the possible application of LHN, the two forecasts are identical. Only the 48h forecasts are verified here so that a total of 60 forecasts are considered here.

The RDPS was run during the month of August 2016 which is part of a standard verification period used at ECCC.

Three different configurations have been tested:

1. **No_LHN** is the control experiment where radars measurements are not assimilated. This setup is identical to the operational version of the RDPS currently in use.
2. **LHN_fcst_only** is a setup where radar observations are only assimilated during the 48h forecasts initialized at 0000 and 1200 UTC every day (turquoise shadings). In this configuration, the changes brought to the atmospheric state cannot impact subsequent analyses.
3. **LHN_fcst+cycle** is a setup in which LHN is applied in the 48h forecasts (turquoise shadings) as well as in the cycle forecasts (light green shadings). Because the cycle forecasts are used as background estimates, improvements brought by the LHN can impact subsequent analyses.

By comparing the results of **LHN_fcst_only** and **LHN_fcst+cycle** we can assess the impact of including LHN within a continuous assimilation cycle.

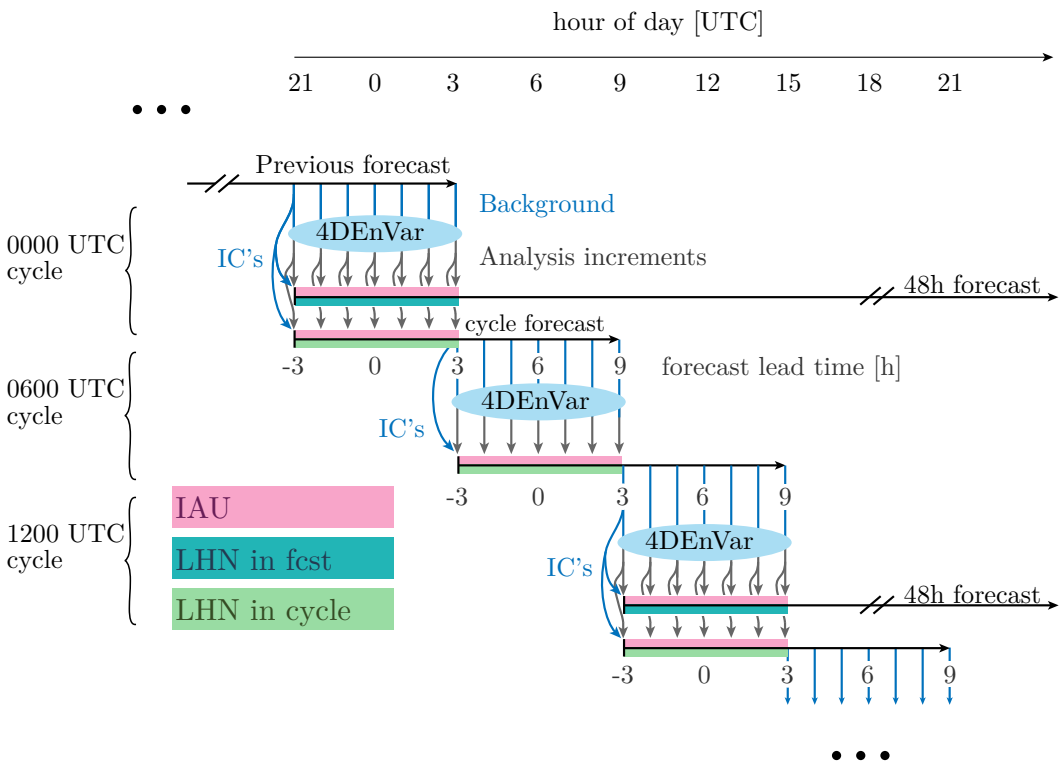


Figure 3: Schematic diagram of the continuously cycled RDPS system.

3.2. Latent Heat Nudging

The implementation details of the LHN algorithm used in this study are described in (Jacques et al., 2018). The method is conceptually similar to that described by Jones and Macpherson (1997). Very briefly, profiles of temperature tendencies are modified during the first six hours of model integration to obtain a better match between the precipitation generated by the model and the precipitation inferred from radar observations.

The 2.5 km radar composites are first interpolated to the 10 km model grid using a circular smoothing window with a radius of 12 km. This smoothing was found to yield the best match between the spectral density of observed precipitation fields compared to those simulated by the 10 km model.

During the first six hours of model integration, the LHN algorithm is applied independently for each grid point of the model grid. The quality index associated with a given radar observation is used to determine whether this observations will be assimilated. No assimilation is performed when the quality index associated with a given measurement is below 0.2. Such low quality occurs outside of the radar range, where beam blockage occurs and wherever non-precipitation echoes are detected by one of the quality controls.

In the trivial case where precipitation is neither simulated or observed, nothing is done.

In locations where precipitation is observed by the radars *and* generated by the model, profiles of temperature tendencies due to latent heat release are scaled for a better match with the observed precipitation. For more precipitation, the column is warmed and moistened; for less precipitation, the column is cooled and dried. Atmospheric water vapor is also adjusted to conserve relative humidity under the temperature change attributed to LHN.

In locations where precipitation is observed but not simulated, special "initiating profiles" are used to warm and moisten the modeled atmosphere according the precipitation rate being observed. These profiles are illustrated in Fig 6 of (Jacques et al., 2018) and are shown to effectively cause the model to precipitate within approximately 20 minutes.

Finally, in locations where the model generates precipitation but none is observed by the radars, the modeled atmospheric warming due to latent heating is reduced by 50%.

4. Verification results

Previous experiments with LHN (Jacques et al., 2017, 2018) in the RDPS have established that this method improves the forecasted instantaneous precipitation rates up to 3h lead times. Also, small (2%) in improvements in RMSE for 12-24h lead time have been documented in verifications against aircraft and radiosonde measurements. With the new experiments presented here, we wished to document if and how the LHN could prove beneficial in the context of a continuously cycled assimilation system.

Precipitation, winds and moisture are examined in the following sections.

4.1. Precipitation scores

Figure 4 shows common contingency scores for the three experiments that have been conducted. The Probability of Detection (POD), False Alarm Rate (FAR), and Critical Success Index (CSI) (Schaefer, 1990) are shown. A threshold of 1 mm/h was used for the computation of these scores. The verification of precipitation was performed wherever radar data with a minimum quality index of 0.2 is available. The radar coverage is shown in Fig. 2.

Figure 4 shows that including LHN within the continuous cycle has no impact on the model's ability to predict instantaneous precipitation rates. After the 6h period where LHN is actively applied (turquoise shading), verification scores of **LHN_fcst_only** and the **LHN_fcst+cycle** experiments similarly converge to those of the **No_LHN** control experiment.

The only difference between the **LHN_fcst_only** and the **LHN_fcst+cycle** experiments can be observed at the onset of the forecast. During the first hour, the **LHN_fcst+cycle** performs better since its initial condition had already benefited from the LHN in the previous assimilation cycle.

Because LHN improves precipitation forecasts at short lead times, it is interesting to compare its impact to those of a simple extrapolation method for predicting precipitation. Here, the MAPLE algorithm (Germann and Zawadzki, 2002) was used to make predictions by advecting the radar composite available at the end of the assimilation window. by construction, MAPLE forecasts are initialized at +3h such that they are perfect at this lead time. However, because this method allows no evolution of the precipitation field other than displacement, its skill decreases rapidly. In Fig. 4, the skill of MAPLE forecasts becomes comparable to that of the **No_LHN** forecasts at lead times of approximately 3.5h. For the POD and CSI scores, this is approximately half an hour later than the moment where the **LHN_fcst_only** and the **LHN_fcst+cycle** experiments reach the level of the **No_LHN** experiment.

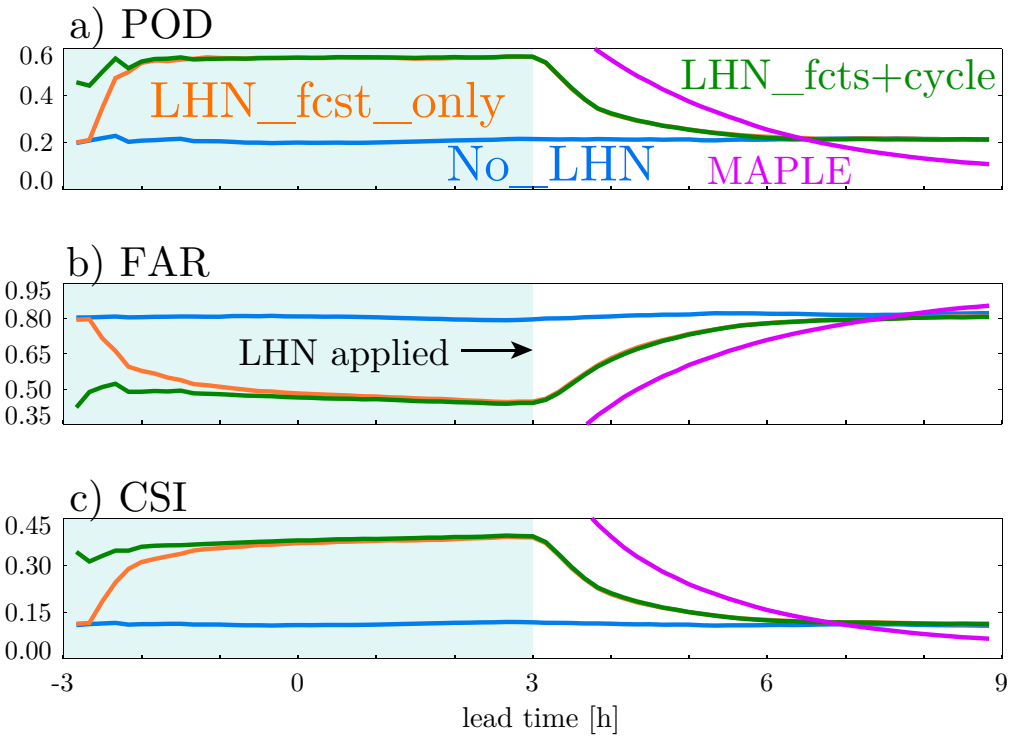


Figure 4: Average score for instantaneous precipitation rates from 60 forecasts in the month of August 2016.

4.2. Upper air verifications

The differences between the **LHN_fcst_only** and the **LHN_fcst+cycle** experiments start to appear in verifications against upper-air atmospheric variables.

Figure 5 shows the percent difference in RMSE (compared to the **No_LHN** control experiment) against aircraft wind measurements. For each panel of this figure, the x-axis represents forecast lead time in bins of 12 hours while the y-axis represents pressure levels in bins of 100 hPa. The color green indicates the reduction in RMSE associated with better, more accurate, forecasts; the color pink indicates deteriorations. An F-test is used to assess the significance of the results being presented. The value of this test is indicated for significance levels greater than 90%.

As before, the RMSE differences shown in Fig. 5 represent averages over the 60 forecasts that have been performed. The domain over which this upper air verification was conducted is indicated in Fig. 2.

Results for the **LHN_fcst_only** experiment appear on the left side. Mixed results are obtained for the U-component of the wind (Fig. 5a) while small improvements are observed for the V-component of the wind (Fig. 5c).

Results for the **LHN_fcst+cycle** experiment appear on the right side. For this experiment, we observe approximately 2% improvement RMSE errors up to 12h lead time for the U-component of the wind (Fig. 5b) and up to 24h lead time for the V-component of the wind (Fig. 5d).

By comparing the left and right side of Fig. 5 we can see that the assimilation of reflectivity composites improves atmospheric winds. This result is noteworthy since winds are not directly influenced by the LHN technique.

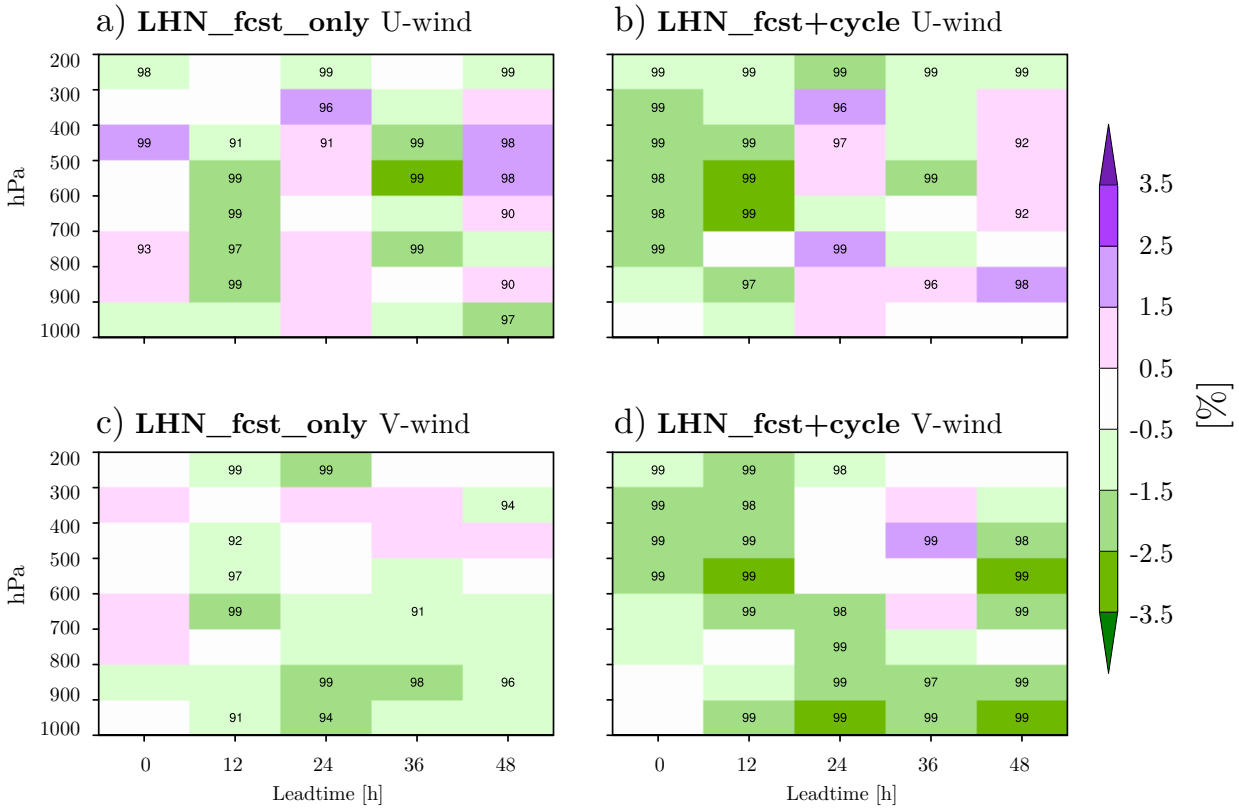


*Figure 5: Percentage difference RMSE (estimated against aircraft observations) for the U- and V-components of the wind between the control run and the **LHN_fcst_only** experiment (panels a and c) and the **LHN_fcst+cycle** experiment (panels b and d).*

For moisture, which is directly modified by the LHN procedure, the difference between the **LHN_fcst_only** and the **LHN_fcst+cycle** experiment is even more pronounced. Figure 6 shows the percent difference in RMSE (compared to the **No_LHN** control experiment) against radiosonde observations of dew point depression. We can see that applying LHN in **LHN_fcst_only** (Fig. 6a) has a mostly neutral impact on the atmospheric moisture. Conversely, the feedback allowed by the **LHN_fcst+cycle** experiment allows a 2-3% improvement in RMSE throughout the atmospheric column and at lead times up to 48h (Fig. 6b).

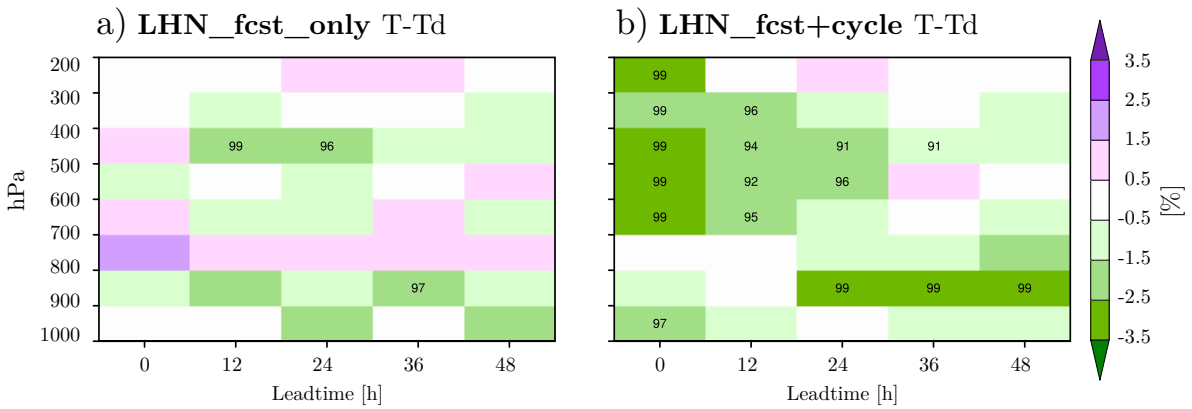


*Figure 6: Percentage difference RMSE (estimated against radiosonde observations) between the control run and the **LHN_fcst_only**.*

5. Discussion and Conclusion

This work reports on advances towards the operational assimilation of radar observations in the Canadian Regional Deterministic Prediction System (RDPS). The goal pursued here was to assess the impact of appling LHN in the continuously cycled assimilation system compared to only applying it in the 48h forecasts issued at 0000 and 1200 UTC every day. Including LHN in the continuous cycle allows radar observations to modify the background and feedback on the subsequent assimilation results.

It is found that using LHN in the continuous cycle does not impact the skill at which precipitation can be forecasted. However, applying LHN in the assimilation cycle improves the RMSE of winds and moisture forecast by approximately 2% and at lead times of 24h and 48h respectively.

LHN primarily modifies temperature for a better correspondence between the simulated and observed precipitation rates. Moisture is also modified by ensuring that the relative humidity remains constant after the temperature change caused by the LHN. When we considered RMSE of temperature forecasts (not shown here), we did do not find major differences between the experiments with and without LHN in the continuous assimilation cycle. This contrasts with the significant improvements we obtain for moisture forecasts (shown in Fig. 6). The reasons for this difference is unclear and will be investigated.

Future work with this project will involve repeating these experiments for the month of July 2016. This will double the number of forecast examined and improve the significance of the results.

When it comes to the processing and quality control of the input radar data, improvements are expected by introducing methods that exploit the polarization moments from those radars that provide them. The availability of Canadian dual-polarization data is expected to increase steadily over the coming years with the roll-out of new S-band radars as part of ECCC's radar network renewal. Using satellite data from GOES-R and S may also help remove residual non-precipitation echoes.

The RDPS assimilation system is also being tested at a resolution of 2.5 km on a domain that covers most of Canada and half of the continental United-States. At this resolution, it becomes relevant to include information on measurement height provided by the quality control within the LHN algorithm. This research avenue will be investigated.

Acknowledgements

Thanks to Thomas Milewski for his help with the RDPS system. Thanks also to Marc Verville for his support with the MAPLE algorithm.

References

M. Buehner, R. McTaggart-Cowan, A. Beaulne, C. Charette, L. Garand, S. Heilliette, E. Lapalme, S. Laroche, S. R. Macpherson, J. Morneau, and A. Zadra, "Implementation of deterministic weather forecasting systems based on ensemble–variational data assimilation at environment canada. part I: The global system," *Monthly Weather Review*, vol. 143, no. 7, pp. 2532–2559, 2015.

J.-F. Caron, T. Milewski, M. Buehner, L. Fillion, M. Reszka, S. Macpherson, and J. St-James, "Implementation of deterministic weather forecasting systems based on ensemble–variational data assimilation at environment canada. part II: The regional system," *Monthly Weather Review*, vol. 143, no. 7, pp. 2560–2580, 2015.

U. Germann and I. Zawadzki, "Scale-dependence of the predictability of precipitation from continental radar images. part I: Description of the methodology," *Monthly Weather Review*, vol. 130, no. 12, pp. 2859–2873, 2014/08/26 2002.

J. J. Helmus and S. M. Collis, "The Python ARM radar toolkit (Py-ART), a library for working with weather radar data in the Python programming language," *Journal of Open Research Software*, no. 1, 2016.

D. Jacques, D. Michelson, J.-F. Caron, and L. Fillion, "Implementing the Latent Heat Nudging algorithm in the Canadian Regional Deterministic Prediction System (RDPS)," in *38th Conference on Radar Meteorology, Chicago, IL, Amer. Meteor. Soc. [Available online at https://ams.confex.com/ams/38RADAR/meetingapp.cgi/Paper/320749]*, 2017.

——, "Latent Heat Nudging in the Canadian Regional Deterministic Prediction System," *Manuscript submitted for publication at the Monthly Weather Review*, 2018.

C. D. Jones and B. Macpherson, "A latent heat nudging scheme for the assimilation of precipitation data into an operational mesoscale model," *Meteorological Applications*, vol. 4, no. 3, pp. 269–277, 1997.

J. Manobianco, S. Koch, V. M. Karyampudi, and A. J. Negri, "The impact of assimilating satellite-derived precipitation rates on numerical simulations of the ERICA IOP 4 cyclone," *Monthly Weather Review*, vol. 122, no. 2, pp. 341–365, 1994.

D. Michelson, A. Henja, S. Ernes, G. Haase, J. Koistinen, K. Ośródka, T. Peltonen, M. Szewczykowski, and J. Szturc, "BALTRAD advanced weather radar networking," *Journal of Open Research Software*, vol. 6, no. 1, 2018.

D. B. Michelson, R. Lewandowski, M. Szewczykowski, H. Beekhuis, and G. Haase. (2014) EUMETNET OPERA weather radar information model implementation with the HDF5 file format. Version 2.2. 42 pp. [Online]. Available: http://eumetnet.eu/wp-content/uploads/2017/01/OPERA_hdf_description_2014.pdf

K. Ośródka, J. Szturc, and A. Jurczyk, "Chain of data quality algorithms for 3-D single-polarization radar reflectivity (RADVOL-QC system)," *Meteorological Applications*, vol. 21, no. 2, pp. 256–270, 2014. [Online]. Available: http://dx.doi.org/10.1002/met.1323

M. Peura, "Computer vision methods for anomaly removal," in *Proc. ERAD (2002)*, EMS. Copernicus GmbH, 2002, pp. 312–317.

M. Ridal and M. Dahlbom, "Assimilation of multinational radar reflectivity data in a mesoscale model: A proof of concept," *Journal of Applied Meteorology and Climatology*, vol. 56, no. 6, pp. 1739–1751, 2017.

J. T. Schaefer, "The critical success index as an indicator of warning skill," *Weather and Forecasting*, vol. 5, no. 4, pp. 570–575, 1990.

FILCOH, a Method to Eliminate Ground Echoes for Weather Radar Operating in Multiple PRT Mode by using The Available Autocorrelation Coefficients.

Mohammed Tahanout[1] and Jacques Parent Du Chatelet[2]

[1]*University Mouloud Mammeri of Tizi-Ouzou, Algeria.*
[2]*Météo-France, France*

1 Introduction

The ground clutter radar returns are the most regular disturbing echoes in the weather radar observations. These echoes are the result of interaction of a part of the radar antenna beam with ground area around the radar. Therefore, the received signal is a combination of different signals incoming from the different scatterers of weather atmospheric phenomena and ground clutter. The intensity of ground clutter echoes are much more important near the radar and in complex area whose radar reflectivity can reach very high value beyond 60 dBZ. Moreover, in some atmospheric conditions, ground clutters echoes could appear far away from the radar because of anomalous propagation (anaprops). Mitigation of ground clutters echoes is fundamentally required in order to estimate accurately the precipitation rate and Doppler radial velocity so, eventually, get reliable data for meteorological forecasting model or air traffic. In this purpose, many techniques are used in modern weather radar. Mainly, in the ARAMIS radar network, the variability pulse to pulse of the signal is tested. Since the variability of the signal of ground clutter is lower, the corresponding echoes are identified and removed from the received signal in time domain (Delrieu et al, 2009). Proceeding in this way, almost all of data collected in the area of ground clutter echoes are missed or not usable. The digital filters are often used for uniform PRT (Period Repetition Time) radar observation (Skolnik, 2008). Narrow low-pass filters attenuate with high efficiency the band around the 0-velocity representing the ground clutter echoes in frequency domain. This technique, also, provide missing information of the weather phenomenon in the filtered band. Whatsoever, the missed values are estimated by interpolation process leading to some information retrieval.

Extending the Doppler velocity measurements with staggered multiple PRT as 2-PRT or 3-PRT, the signal becomes not uniformly sampled which generate a complex signal of ground clutter with upper variability. Actually, the ground clutter spectrum is characterized by the classic narrow band at the 0 velocity and further bands which are the replica of the main band located at uniform gap across the extended Nyquist interval (Tahanout et al , 2015). To perform the ground clutter filtering in this case, it is necessary to mitigate all the lines of ground clutter over the extended Nyquist interval. Nevertheless, for the 2- or 3-PRT signal of C- or X-band radar, the number of replica lines is very high, up to 41 replicas for a C-band radar (Parent Du Chatelet et al, 2010). This leads to high losses of wanted information necessary to the reflectivity or mean velocity estimates. To overcome such difficulties, (Sachidananda et al, 1999) have proposed a method to mitigate the ground clutter echoes by estimation of the replica lines from the main band at 0-velocity in the extended Nyquist interval of 2-PRT S-band radar pulses scheme. More recently, (Torres et al, 2014) and (Warde et al, 2017) have proposed a method based on autocorrelation spectral density which is adapted to 2-PRT scheme and achieve a ground clutter attenuation up to 30 dB for NEXRAD radar operating in S-band. In the same purpose, we have developed a novel technique to mitigate the ground clutter echoes in order to enhance the estimates of the reflectivity and radial mean velocity of the observed weather phenomenon, particularly, in the context ARAMIS radar network using staggered 3-PRT pulses sequences. This technique, named 'FILCOH[@]', is based on the analysis of the autocorrelation function coefficients, mainly the coefficients that are representative of ground clutter signal, to perform the filtering.

In this paper, we illustrate the basics of FILCOH filtering and its performance to attenuate the ground clutter echoes. To do so, in the second section we give the basics and the main important characteristics of the filter in the uniform PRT. The next section is dedicated to the adaptability to staggered PRT sequences. In the four section, some simulation results are presented for different CSR (Clutter to Signal Ratio) using staggered 2- and 3-PRT pulses scheme. The fifth section illustrate the results for the Nice X-band radar data operating with 3-PRT sequences. The conclusions and perspectives of the present work are given in the last section.

2 Basics of FILCOH filtering

For weather radar, the received signal $s(t)$ is considered as a linear combination of the whole signals incoming from the scatterers in interaction within the bin volume of electromagnetic wave radar pulse along the antenna beam. Mainly, for the weather observation with uniform PRT of duration T, the time series of received signal is written as a composite of three components as follow:

$$s(t = kT) = s_w(t) + s_c(t) + s_n(t) \qquad (1)$$

where, $s_w(t)$ the weather signal, $s_c(t)$ the ground clutter signal and the $s_n(t)$ noise signal.

The corresponding autocorrelation function is estimated, in a dwell time $T_d = N\,T$, by:

$$R(\tau = l\,T) = \frac{1}{N}\sum_{k=0}^{N-1} s(k)s^*(k-l) \qquad (2)$$

After developing, the autocorrelation function $R(\tau)$ becomes:

$$R(\tau) = R_w(\tau) + R_c(\tau) + R_n(\tau) + \sum_{x\neq y} R_{xy}(\tau) \qquad (3)$$

Assuming that the signals $s_w(t)$, $s_c(t)$ and $s_n(t)$ independent in the considered dwell time, the cross-correlation term $\sum_{x\neq y} R_{xy}(\tau)$ is considered trivial, where, the couple (x,y) represent two among the composite signals. Thus, the autocorrelation is reduced to a combination of three autocorrelation functions, $R_w(\tau)$, $R_c(\tau)$ and $R_n(\tau)$, corresponding respectively to the weather signal $s_w(t)$, the clutter's signal $s_c(t)$ and the noise $s_n(t)$. $R(\tau)$ can be written as follow:

$$R(\tau) = R_w(\tau) + R_c(\tau) + R_n(\tau) \qquad (4)$$

As the characteristics of the composite signals are different, we can distinguish particular intervals in such autocorrelation function as the time lag is varied within the interval $[-T_d/2, Td/2]$, i.e:

- For $|\tau| \leq T_c$. In this case, $R(\tau) = R_w(\tau) + R_c(\tau) + R_n(\tau)$ and $R(\tau) = R_w(\tau) + R_c(\tau)$ if $\tau \neq 0$.
- For $T_c < |\tau| < T_d/2$, $R_w(\tau) \cong 0$. In this case, the autocorrelation of the received signal represent actually the autocorrelation function of the ground clutter signal, $R(\tau) \cong R_c(\tau)$. Where T_c is the lag time beyond which the autocorrelation of the weather signal become trivial. In this interval $T_c < |\tau| < T_d/2$, $R(\tau)$ represent the coherent part of the autocorrelation function of the ground clutter.

The figure 1 shows the amplitude of autocorrelation function of the weather signal and ground clutter echoes for a simulated signal. In this example, the phase is omitted for better illustration. Actually, the phase of the weather signal fluctuates as the mean velocity and the spectral width are high, while, the phase of the ground clutter do not vary significantly. The effect of the noise appears practically only in the coefficient at the lag 0. The CSR of this example is set to 0 dB to get the same comparison scale between the weather and ground clutter autocorrelation functions. The corresponding spectral widths are respectively σ_v = 4 m s^{-1} and σ_c = 0.3 m s^{-1}. As one can see, $R_w(\tau)$ decreases much rapidly than the autocorrelation of the clutter $R_c(\tau)$. The interval $[T_c, T_m]$ represent the interval where the global autocorrelation represent practically the ground clutter and $R_w(\tau)$ becomes remarkably low.

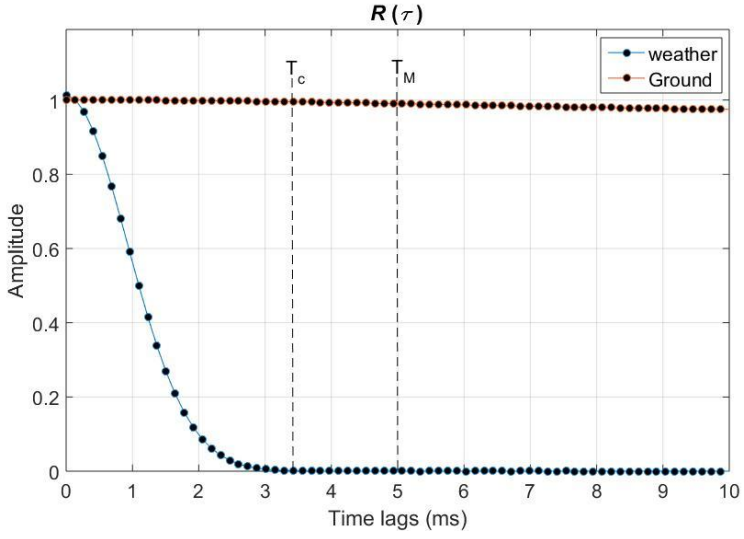


Figure 1: Composite autocorrelation function of simulated received signal. CSR= 0 dB, λ = 3.3 cm, T = 0.317 ms, N=180, SNR=20 dB.

The basic of FILCOH filtering consist of estimation of the autocorrelation function of the ground clutter in the coherent part and evaluation of the corresponding coefficients values in the interval of $|\tau| \leq T_c$ by extrapolation under some prior assumptions. Hence, the autocorrelation coefficients of the weather signal are obtained merely by subtraction.

As first approach, we have considered the case of the ground clutter defined by small spectral width at the 0-velocity. In this case, the autocorrelation function of the ground clutter echoes is quasi-constant, $R_c(0 \leq |\tau| \leq T_c) \cong R_c(T_c < |\tau| < T_d) \cong \tilde{R}_c$. Under these assumptions, the autocorrelation function is adjusted and the ground clutter is filtered out as follow:

$$R_f(\tau) = R(\tau) - \tilde{R}_c \qquad (5)$$

For high SNR (Signal to Noise Ratio), the autocorrelation function of the weather signal is deduced directly from $R_w(\tau)=R_f(\tau)$, otherwise, $R_w(\tau)=R_f(\tau \neq 0)$. For moderate fluctuations, the estimate of the ground cutter is performed by calculating the mean of the coherent part of $R(\tau)$ defined as:

$$\tilde{R}_c = \frac{1}{2m}\left(\sum_{l=l_c+1}^{l_m} R(l\,T) + \sum_{l=-l_m}^{-l_c-1} R(l\,T)\right) \qquad (6)$$

where, l_c et l_m integers so that $T_c = l_c T$, $T_m = l_m\, T < T_d/2$ and $m = l_m - l_c$ (see figure 1).

To strengthen the condition under the assumption considered in this first approach, we use:

- Circular autocorrelation function computation.
- Rectangular windowing.

For larger spectral width of the ground clutter echoes, the analysis is performed using a rectangular window sliding over the time series of dwell time duration with an overlap α between the consecutive windows defined in percentage. The length L_w of the window is determined according to a spectral resolution chosen so as the main power of the ground clutter become within the line at 0-velocity. The dwell time T_d is then the duration of the considered window. This is achieved running the following global algorithm steps:

1. For each rectangular i^{th} sliding window, compute the autocorrelation function of the received signal $R_i(\tau)$.
2. Compute the ground clutter estimate $\tilde{R}_c^i$ in the coherent part using equation (6).
3. Filter out the ground clutter using the equation (5) : $R_f^i(\tau) = R_i(\tau) - \tilde{R}_{ci}$; $R_w^i(\tau \neq 0) = R_i(\tau \neq 0) - \tilde{R}_c^i$
4. Compute the global autocorrelation function: $R_f(\tau) = \frac{1}{N_w}\sum_{i=1}^{N_w} R_f^i(\tau)$; $R_w(\tau \neq 0) = \frac{1}{N_w}\sum_{i=1}^{N_w} R_f^i(\tau \neq 0)$; N_w the number of estimates over the dwell time by the sliding window.
5. Estimate the power (reflectivity) and the mean velocity of the weather phenomenon via the appropriate autocorrelation coefficients in $R_w(\tau)$, particularly, $R_w(T)$.

The above algorithm has been implemented and tested on simulated and real data of uniform PRT. In this section, we just present an illustration of FILCOH filtering applied on data acquired by a UHF Doppler radar operating in Clermont-Ferrand airport as a wind profiler. The radar explore particular azimuthal angles following a specific protocol using a uniform PRT at a wavelength λ = 22.3 cm. After a study on a rain event occurred during the day, we have defined the parameters of FILCOH filter given in the table 1.

Table 1: FILCOH Parameters for UHF radar.

T	2.2 ms
T_d	281.6 ms ($T_d/2$ = 140.8ms)
T_c	80 ms
L_w	128
l_c	36
l_m	64
N_w	6
α	60%

T_c was determined observing the behavior of the time of coherence T_w of the rain signal that we have defined using the following empirical formula:

$$T_w = \frac{T}{2\,R(0)} \sum_{k=0}^{\frac{N}{2}-1} |R(\tau = kT)| \qquad (7)$$

The fig.2 shows two examples of obtained power spectra before and after FILCOH filtering observed at the lowest elevation angles and different ranges (r_1=2 km, r_2= 12 km). The first example illustrate the case of the rain spectrum overlapped with the ground clutter at the 0-velocity (figure 2.a). As one can see on this figure, the line at 0 m s^{-1} is mitigated about 54 dB retrieving precisely the level of the Gaussian shape spectrum representing the rain. The second example shows the case of the rain spectrum off ground clutter (figure 2.b). In this case, the attenuation is about 40 dB reaching the noise level. These two examples illustrate the adaptive behavior of FILCOH filtering. This behavior turns out to be very interesting for M-PRT signals demonstrated hereafter.

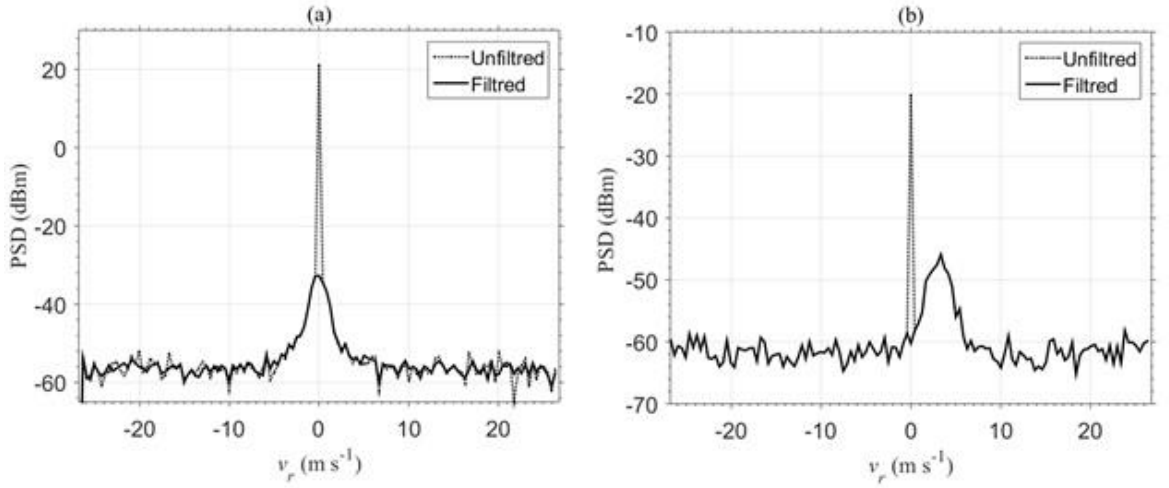


Figure 2: UHF radar profiler power spectra before and after FLCOH filtering. (a) range at 2 km and (b) range at 12 km.

3 M-PRT FILCOH filtering

FILCOH filtering applied to M-PRT autocorrelation function $R(\tau)$, in our case 2- or 3-PRT, yields limited performance. This is due to the features of $R(\tau)$ which is known only for lags obtained by combination of the periods of the M-PRT scheme T_i (i= 1, 2, …, M). Furthermore, the coefficients $R(\tau)$ are estimated with a bias depending of the number of the available samples in the analysis widow. To be able to implement correctly the FILCOH filtering, it is necessary to consider $R(\tau)$ as the combination of secondary autocorrelation functions $R_i(\tau)$ so that $R(\tau) = \Sigma R_i(\tau)$ with $R_i(\tau) = R(T_i + k\Sigma T_i)$ k an integer from 0 to T_d/T and $R_i(\tau) = 0$ pour $\tau \neq T_i + k\Sigma T_i$. Then, FILCOH filtering is run to each of the secondary autocorrelation function $R_i(\tau)$. Proceeding in this way, this is equivalent to working in Doppler frequency interval $\pm\, 1/\Sigma T_i$ corresponding to uniform PRT of ΣT_i. Hence, the ground clutter $\tilde{R}_{ci}$ is estimated for each $R_i(\tau)$. For i= 1,2, ..,M, we write:

$$\tilde{R}_{wi}(\tau) = R_i(\tau) - \tilde{R}_{ci} \qquad (8)$$

The global estimated autocorrelation of the weather phenomenon is obtained by:

$$\tilde{R}_w(\tau) = \sum_{i=1}^{M} R_{wi}(\tau) \qquad (9)$$

The figure 3 illustrate the 3-PRT FILCOH filtering operated on simulated signal. The uniform spectrum is generated within the extended Nyquist interval, then, uniform time series are calculated using inverse FFT. The time series is resampled with 3-PRT sequence using ratios (T_1/T_2, T_2/T_3) = (4/5, 5/6) (Tabary et al, 2006), then, the algorithm of FILCOH is applied considering the adaptation by calculating the autocorrelation functions according to the equations (8) and (9) before calculating the corresponding spectra. As shown on this figure, the Clutter's 15 lines are spread over the extended Nyquist interval with periodicity corresponding to λ/(2 ΣTi) (Tahanout et al, 2009). The attenuation of these lines is performed in adaptive way on each line reaching accurately the rain 3-PRT spectrum.

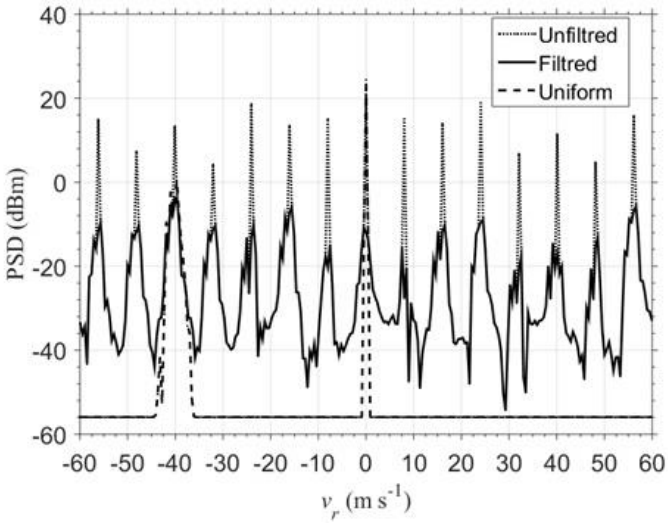


Figure 3: Example of spectra before and after FILCOH filtering of 3-PRTsimulated signal. CSR = 20 dB, σ_c = 0.15 m s^{-1}, $v_m = -40$ m s^{-1}, σ_v = 1 m s^{-1}, SNR = 20 dB.

3 Simulation results

To get an overview of the FICOH filtering performance, we have carried out simulation in 2-PRT with ratio T_1/T_2 = 2/3 and 3-PRT with ratios (T_1/T_2, T_2/T_3) = (4/5, 5/6) (Zrnic, 1975). The filter is applied on M-PRT time series, then, the weather power and mean velocity are estimated and compared to the inputs. The CSR is varied from –30 to 60 dB with step of 1 dB and the mean velocity v_m is incremented in the normalized extended Nyquist interval [–0.5, 0.5]. The spectral width of ground clutter is kept to normalized values respectively 0.003 and 0.0025 for the 2- and 3-PRT. These values are corresponding to 0.3 m s^{-1} respectively for an extended Nyquist interval of ± 50 m s^{-1} in 2-PRT and ± 60 m s^{-1} in the 3-PRT. The parameters of FILCOH are summarized on the table 2 for the two M-PRT schemes.

Table 2: FILCOH normalized parameters.

	2-PRT	3-PRT
L_w (0-pading)	45 (18 pulses)	45 (9 pulses)
l_c	5	15
l_m	22	22
N_w	4	*7*
α	75%	75%

The bias and standard deviation of the estimated power and mean velocity are shown respectively in figure 4 and 5 for the 2- and 3-PRT considering two normalized spectral widths of weather phenomenon. Generally, the errors present a wave variation around the ground clutter lines positions. The figure 4 shows the results for a CSR = 60 dB. In this case, The bias and standard deviation of estimate of the received weather power P_r is relatively low, particularly, for the normalized spectral width of the weather phenomenon σ_v = 0.04 for which the bias is under ± 1 dB and the standard deviation is below 2 dB (figure 4.a and 4.b). The performance for mean velocity recovery is limited for CSR > 50 dB. The results shown in the figure 4.c and 4.d illustrate the performance for a CSR = 50 dB. The bias of the mean velocity is within ± 0.02 and the standard deviation is relatively low.

The errors induced by the 3-PRT sequence are much undulating, particularly for the smallest spectral width. This is caused by the high number of replica lines of the ground clutter which is 15 for the 3-PRT periods ratio under study. However, the bias and standard deviation obtained for the received power P_r are convincing for CSR < 45 dB (figure 5.a and 5.b). The bias is less than 1.7 dB for the normalized spectral width of 0.033 and the standard deviation is practically regular around 1.5 dB. The performance of FILCOH is decreased to the mean velocity measurements for CSR > 35 dB. The figure 5.a shows an interesting bias obtained practically within ± 0.03. Nevertheless, the standard deviation is very high. This is probably due to L_w the length of analysis window (sliding window) which is corresponding only to 9 radar pulses in order to deal with the relative high ground clutter spectral width considered in this study.

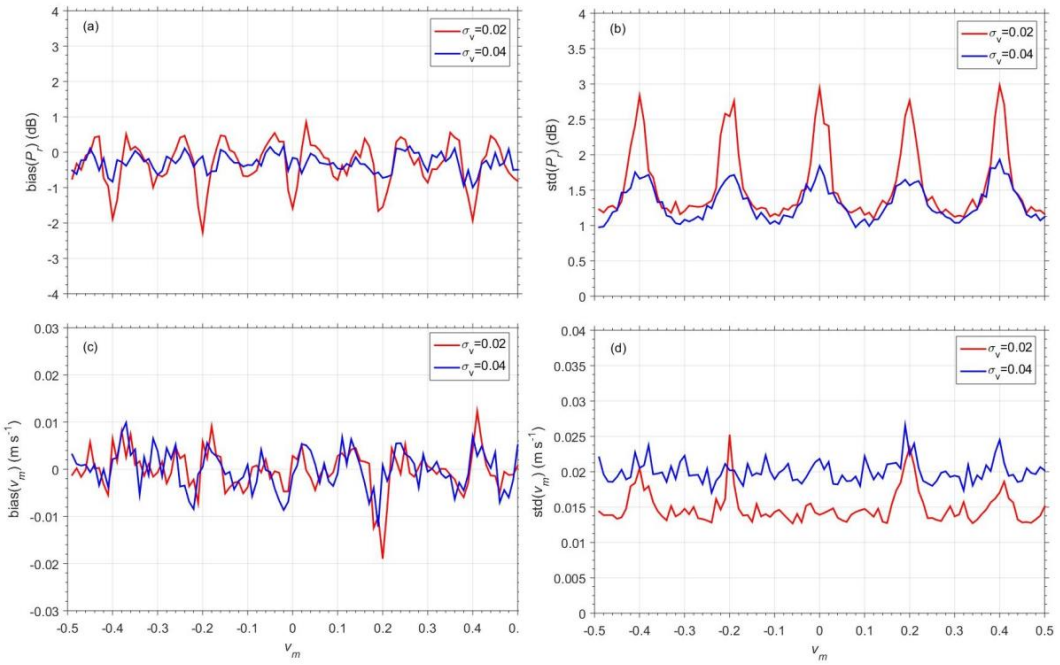


Figure 4: Bias and standard deviation (std) of the estimates of received power P_r and mean velocity v_m for 2-PRT. (a) bias(P_r) and (b) std (P_r) for CSR=60 dB. (c) bias(v_m) and (d) std(v_m) for CSR=50 dB. SNR=20 dB.

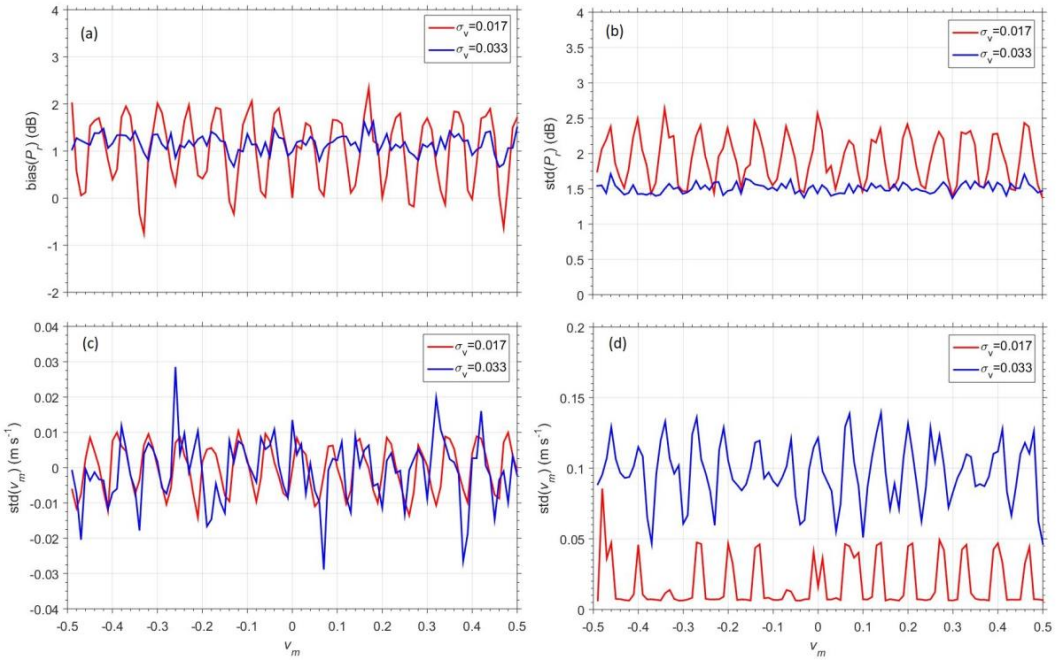


Figure 5: Bias and standard deviation (std) of the estimates of received power P_r and mean velocity v_m for 3-PRT. (a) bias(P_r) and (b) std (P_r) for CSR=45 dB. (c) bias(v_m) and (d) std(v_m) for CSR=35 dB. SNR=20 dB.

4 Real data results

Using the parameters of the table 2, FILCOH filtering was also tested on real data collected by the X-band radar operating in Nice (France). The radar pulses are emitted with 3-PRT scheme according the (4/5, 5/6) periods ratios and T_1 = 0.548 ms. The peak power P_e is about 110 kW at the wavelength $\lambda \cong 3.3$ cm. The I and Q times series are collected in restricted area very close, spreading out along the 30 km away from the radar over an azimuthal angle of 20° from 330 to 350°. The selected area is characterized by diversity echoes, strong, moderate and weak echoes from the ground clutter. The study is limited to the moderate rain event occurred during 3 hours in june 5th 2011 between 12h00 and 15h00 UTC.

The figure 6.a shows an example of the relative received power (P_r/P_e) from the study area before filtering. The corresponding mean radial velocity is illustrated on the figure 6.b on which one can distinguish the 0-velocity characterizing of the strong ground clutter area. The figure 6.e provides the related relative coherent time ($T_w/(2T_d)$) where T_w is computed using the equation (7). This parameter takes value in the interval [0, 1]. The high value of the coherent time identify clearly the strong ground clutter echoes. After FILCOH filtering, we obtain respectively the figures 6.c, 6.d and 6.f. The comparison of the amplitude of the relative power between the figure 6.a and 6.c, we can deduce that the attenuation of the ground clutter is performed up to 30 dB. Furthermore, we notice the decrease of the 0-velocity surface on the figure 6.d.

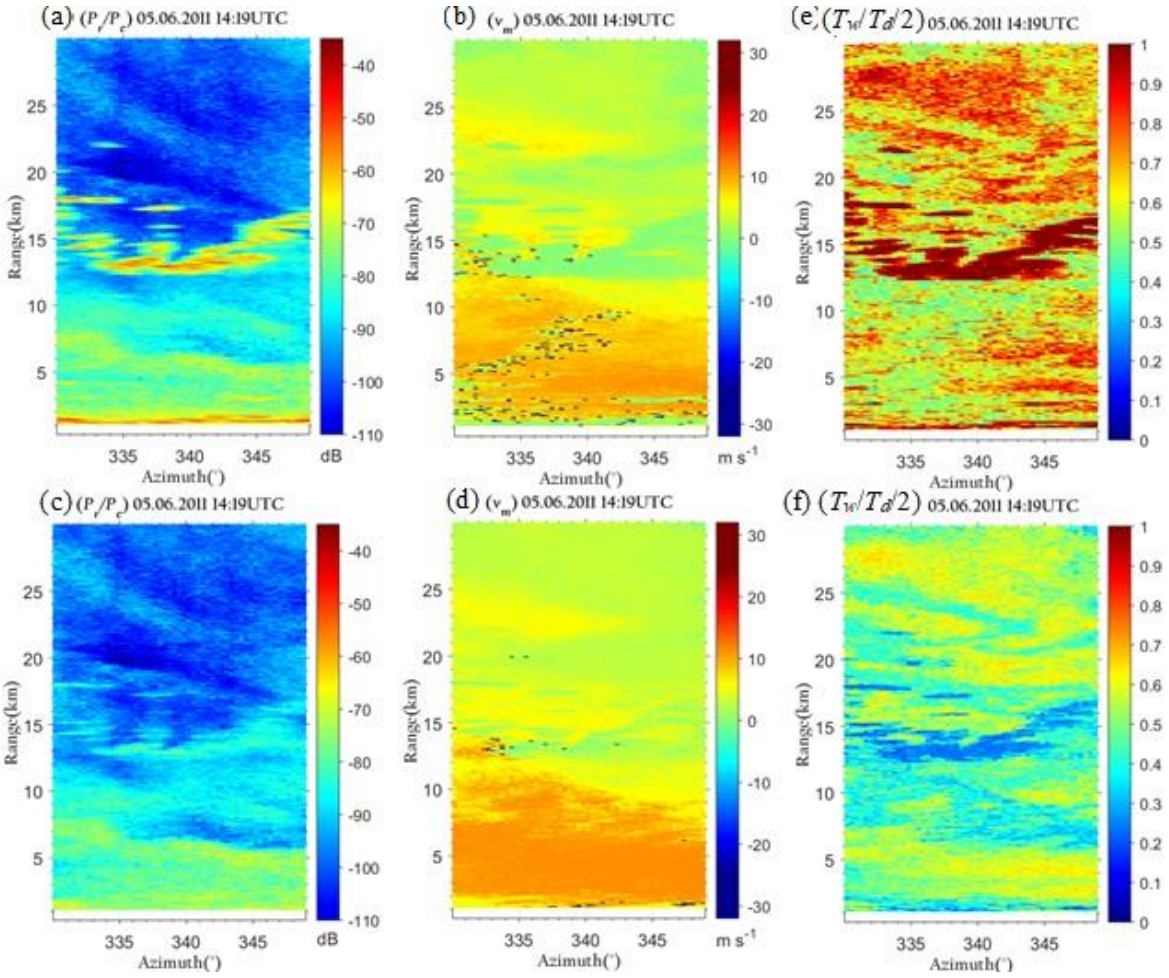


Figure 6: Example of FILCOH filtering. (a) Relative received power, (b) mean radial velocity and (e) relative coherent time, before filtering. (c) Relative received power, (d) mean radial velocity and (f) relative coherent time, after filtering.

To get a quantitative overview of the performance of the FILCOH filtering, we have plotted the statistics curves of the figure 7. The figure 7.a shows the regression of filtered received power versus the unfiltered one for the whole event. As we can see, the attenuation of the ground clutter reaches 40 dB particularly for strong echoes at around −50 dB. This figure reveals also a positive bias less than 2 dB observed yet in simulation results (see figure 5.a). The figure 7.b shows the distribution of the received power (P_r/P_e) for the main zone of the ground clutter between 10 and 20 km in range before and after FILCOH filtering. We notice that the strong ground echoes between −78 and −50 dB are efficiently mitigated getting a Gaussian shape distribution after FILCOH filtering representing probably the weather phenomenon. Following the same representation for the velocity, the figure 7.c illustrate the regression of filtered velocity versus the unfiltered one zooming on the interval of true velocities between −10 and 20 m s^{-1} in the zone of strong ground clutter. As it is shown by this figure, the population of 0-velocities spread over the interval of the measured of the weather velocities signifying the attenuation of the ground clutter echoes. As expected by simulation, the undulating behavior of the bias appears for velocities in the interval [2.5, 17] m s^{-1}. The figure 7.d demonstrate the high mitigation of the ground clutter where the population of 0-velocities is decreased strongly.

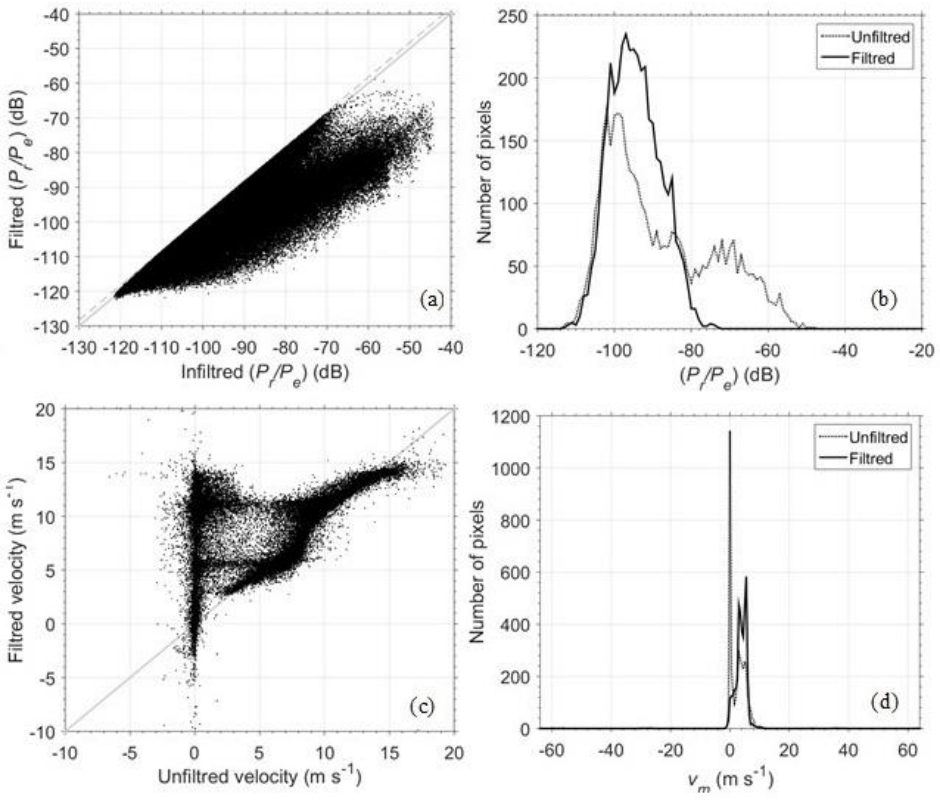


Figure 7: Performance of FILCOH filtering. (a) Received power regression, (b) received power distributions, (c) velocity regression (d) velocity distributions.

5 Conclusion

FILCOH is a simple and efficient technique designed to radar ground clutter echoes filtering. The performance of this filter has been verified by simulation and application on true radar data obtained with non-conventional pulse radar scheme 2- and 3-PRT. It was shown by simulation that FILCOH mitigate the ground clutter echoes with high CSR up to 60 dB for the power retrieving and up to 50 dB for mean radial velocity measurement using staggered 2-PRT. For the 3-PRT radar pulses scheme the performance is relatively decreased, but still very interesting. The simulation results demonstrated that the power recovery after filtering is performed for CSR < 45 dB and the mean radial velocity measurement is performed up to CSR= 35 dB. These results are confirmed with an example of application on real data of X-band radar of a moderate rain event. Elementary statistics have demonstrated a performance of mitigation of ground clutter about 40 dB and high efficiency of velocity recovery. However, FILCOH has a disadvantage for high CSR when using mean of the coherent part of the 3-PRT autocorrelation function. Indeed, the variance of the velocity measurement is very high because of the length of analysis window. To overcome this limitation, further work are expected. For example, instead to estimate only one moment of the coherent part, we project to make more sophisticated analysis by introducing an harmonic analysis of the coherent part of the autocorrelation function corresponding to the ground clutter echoes so that the FILCOH filtering get the possibility to mitigate several harmonic lines around 0-velocity.

Acknowledgement

The authors would like to thank DSO and CMR, teams of Météo-France, for providing the X-band radar data and the DEGREANE team for making available the UHF radar profiler data.

References

Delrieu G., Boudevillain B., Nicol J., Chapon B. and Kirstetter P. E. : Bollène-2002 Experiment: Radar Quantitative Precipitation Estimation in the Cévennes–Vivarais Region, France, Journal Of Applied Meteorology And Climatology, 2009.

Parent Du Chatelet J., Tahanout M., Curtis C. D: Experimental validation of a multiple PRT weather radar transmitting scheme optimized to mitigate wind speed ambiguities and to filter-out ground clutter, International Conference on weather radar, ERAD2010, 2010.

Skolnik M. I.: Radar Handbook, New York, Mc Graw-Hill, 3rd edition, 2008.

Sachidananda M. and Zrnic D. S.: "Ground Clutter Filtering Dual Polarization, Staggered PRT Sequences", Journal of Atmospheric and Oceanic Technology, Vol. 23, 1114-1130, 2006.

Tabary P., Guibert F., L. Perier, and J. Parent du Chatelet: An operational triple-PRT scheme for the French radar network, Journal of atmospheric and Oceanic Technology, 23, 1645– 1656, 2006.

Tahanout M., Adane A.E.H., Parent Du Chatelet J.: An Improved M-PRT Technique for Spectral Analysis of Weather Radar Observations, IEEE Transactions on Geoscience and Remote Sensing, 53, 5572 – 5582, 2015.

Tahanout, M., J. Parent Du Chatelet and C. Augros : A new multiple-PRT scheme for Météo-France Doppler radar network to improve spectral moment estimation of weather radar signal and ground clutter filtering, *34th AMS international conference on Radar Meteorology*, USA, 2009.

Torres S. M. and Warde D. A. : Ground Clutter Mitigation for Weather Radars Using the Autocorrelation Spectral Density, , Journal of Atmospheric and Oceanic Technology, 2014.

Warde D. A. and Torres S. M.: Staggered-PRT Sequences for Doppler Weather Radars. Part II: Ground Clutter Mitigation on the NEXRAD Network Using the CLEAN-AP Filter, Journal of Atmospheric and Oceanic Technology, 2017.

Zrnić D. S.: Simulation of weather like Doppler spectra and signals. Journal of Applied Meteorology, 14, 619–620, 1975.

Impact of the vertical gradients of precipitation on the radar QPE bias in the French Alps

Dominique Faure[1], Nicolas Gaussiat[1] , and Guy Delrieu [2]

[1]*Météo-France, 42, avenue Gustave Coriolis, 31057 Toulouse Cedex, France*
[2]*IGE/HMCIS, CS 40700, 38058 Grenoble Cedex 9, France*

(Dated: 10 June 2018)

1 Introduction : General radar QPE bias observed in the French Alps

In the French Alps, the quality of the radar Quantitative Precipitation Estimation (QPE) provided by the French weather radar network, can be locally limited due to radar beam blockages, the distance to the radars, and the altitude of measurement: distant C band radars, or X band radars installed within the mountain range between 1740 m and 2580 m of altitude, scan the atmosphere above the mountains and cannot detect precipitation into the valleys. The individual radar QPE produced from the volume scanning of each radar are merged every 5 minutes in a national radar QPE composite. A study realized in 2017 on data of the entire year 2016 in all the French Alps (Faure, 2017), has shown a general bias between values of this national radar QPE composite and the measurement of 430 rain gauges: a radar QPE over-estimation for rain gauges at low altitude, and an increasing underestimation for rain gauges at high altitudes (up to 2100 m). A detailed analysis confirmed this tendency for each massif and great valley. This trend has been linked to altitudinal gradients of precipitation observed at ground level in the Alps, and not taken into account by the current radar data processing. In order to test this link, a simple uniform linear correction have been applied, only function of the rain gauges altitudes, and this correction produced a great improvement of the radar QPE, both for the ratios and correlation between radar and rain gauges annual precipitation (figure 1).

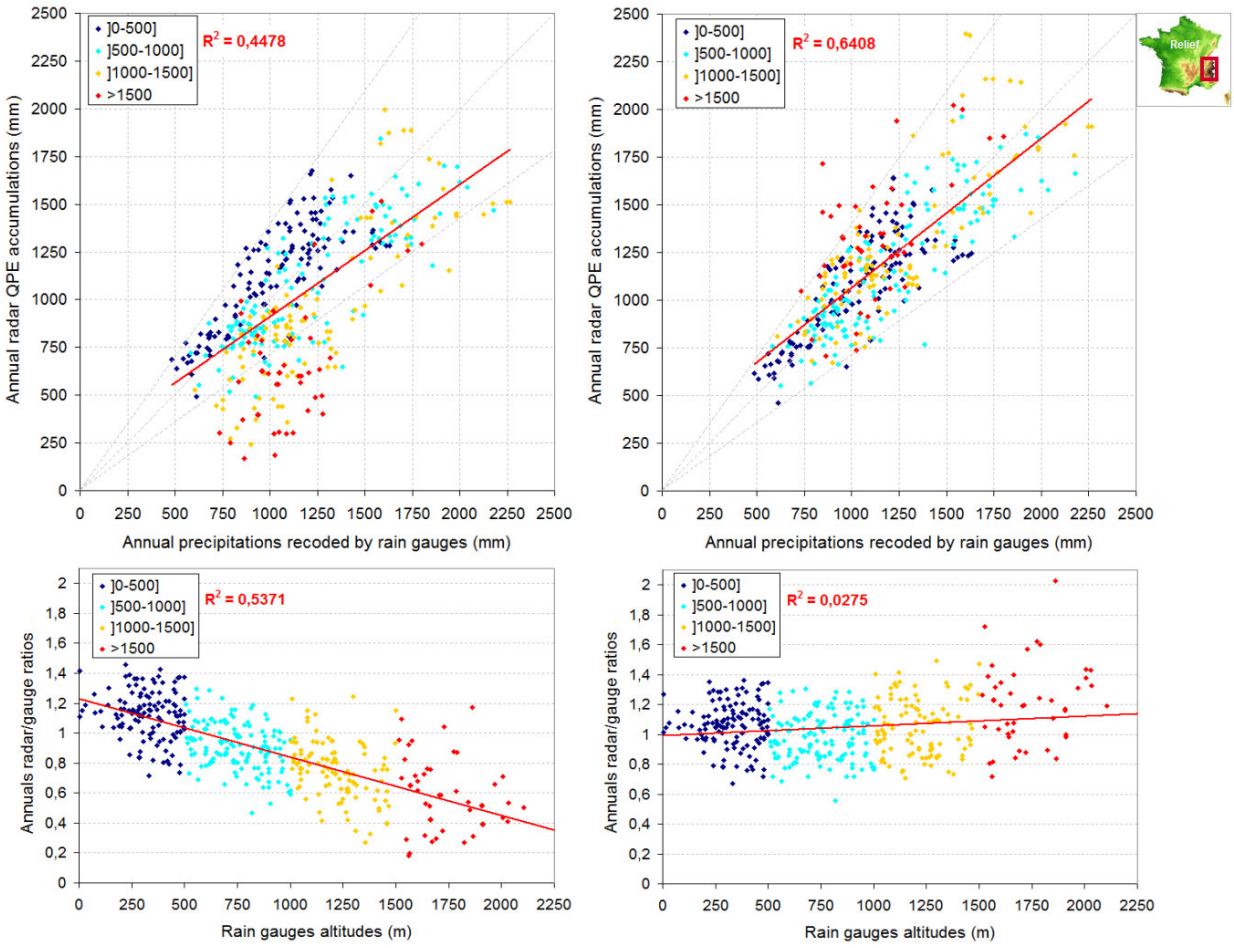


Figure 1: Top, correlation between radar QPE and rain gauges measurements. Bottom, radar QPE bias in function of the rain gauges altitudes. Left, operational data ; right, after the correction. For 430 rain gauges in the French Alps in 2016.

Several analysis of precipitation in the French Alps have been carried out, both on climatology and trends (Durand, 1993), (Durand, 2009), (Barry, 2012), and the impact of relief on precipitation has been studied in two thesis in the region-between de cities of Lyon and Grenoble, using data from a one-dimensional dense rain gauges network (a transect) through the Bas-Dauphiné, Chartreuse and Belledonne massifs (Desurosne, 1994). Climatological vertical profiles of precipitation have been defined for each massif in the French Alps an Pyrenees, and are used in the SAFRAN Analysis system, initially designed to provide atmospheric forcing data in mountainous areas for snow models and avalanche hazard forecasting (Durand, 1993), (Birman, 2017).

The altitudinal gradients of precipitation varying in time and space and depending on several factors, a more detailed analysis of the 2016 data has been carried out over a limited area around the Grenoble conurbation, and for a subset of 23 daily rain gauges. This paper focuses on the vertical gradients of precipitation observed at ground level for different temporal accumulations (yearly, three months periods, monthly, daily) and for three neighboring massifs. The corresponding values of the radar QPE composite are also presented, in order to explain the impact of the altitudinal gradients of precipitation on the bias between radar QPEs and rain gauges measurements.

2 Grenoble site and instrumentation

Grenoble, the greatest French Alps conurbation (500 000 inhabitants), is situated at the confluence of three valleys, and surrounded by three massifs rising up to 2000 m and 3000 m high (figure 2). Several studies as been realized on precipitation in this region, and 23 daily rain gauges are located both at the bottom of the valleys (around 220 m a.s.l.) and on the slopes and top of the three massifs (up to 1730 m a.s.l.). A radar of the national operational network (Moucherotte polarimetric X band radar, 1910 m a.s.l.) is located inside the studied area at the top of the Vercors massif, which guarantees a good radar coverage. The volume scans of the polarimetric XPORT research radar, a vertically pointing Micro Rain Radar and a disdrometer, installed by IGE in the Grenoble Alpes University campus (227 m a.s.l.), complete the observation of the atmosphere inside the valley. Three subsets of rain gauges have been allocated to the Chartreuse, Vercors, and Belledonne massifs, in order to estimate altitudinal gradients of precipitation at ground level.

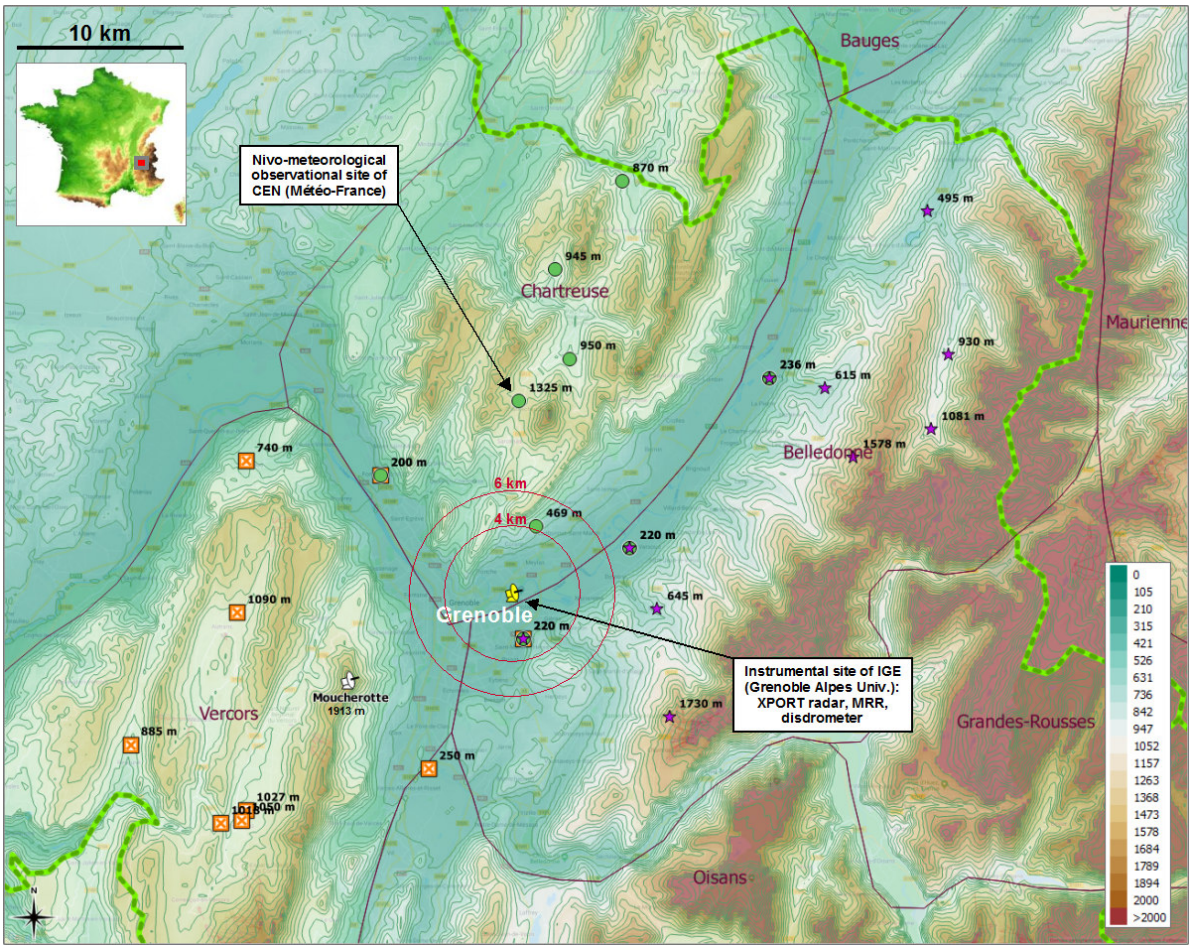


Figure 2: Relief (m) and instrumentation. Brown lines = massifs limits.
Rain gauges distribution: Chartreuse (green rounds), Vercors (orange squares), and Belledonne (purple stars)
Remark: in the valleys, four rain gauges have been used in several subsets.

3 Altitudinal gradients of precipitation and radar QPE bias

In figure 3, for each massif surrounding Grenoble, the 2016 annual amount of precipitation measured by a subset of about ten daily rain gauges are compared to the corresponding radar QPE values. The rain gauges values, consistent with the literature on the annual amount of precipitation for each massif, show an accumulation at ground level increasing with the altitude of the gauges. But the annual radar QPEs appear independent of the altitude considered. For each massif, a similar difference between radar QPE and rain gauges measurements is also obtained for seasonal and monthly accumulations in 2016.

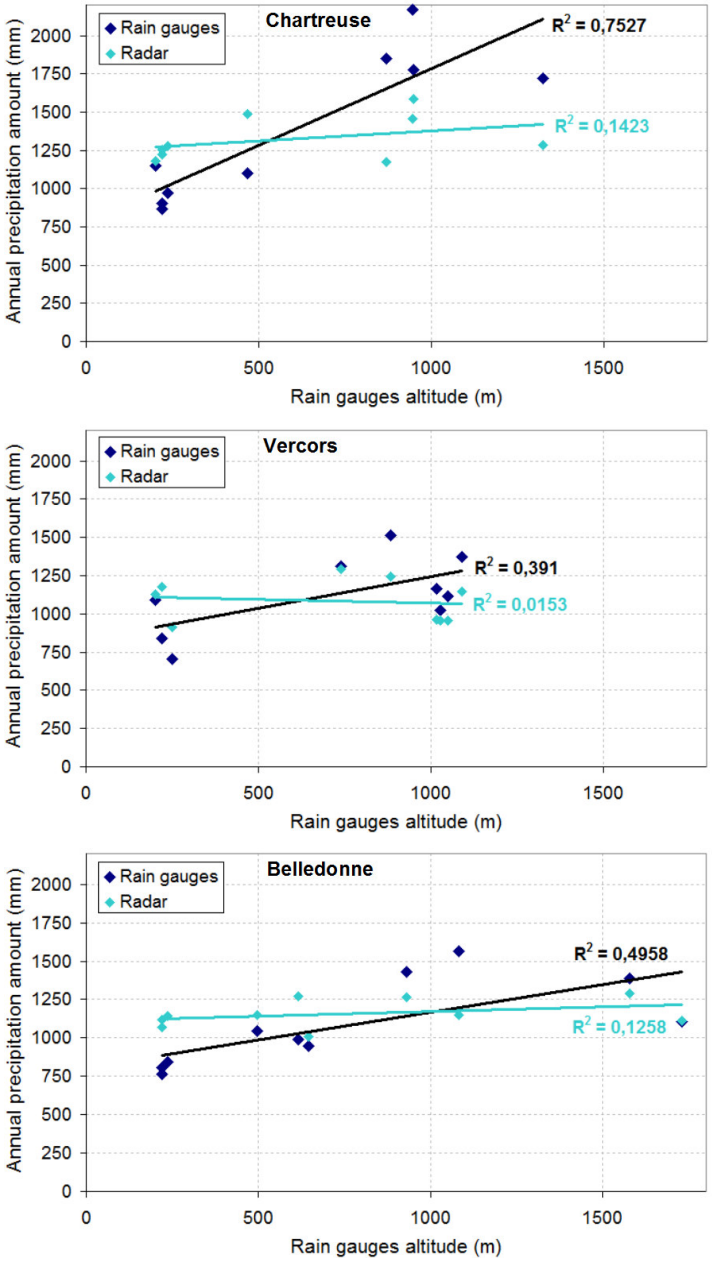


Figure 3: Comparison of rain gauges annual accumulation and the corresponding radar QPEs in 2016 (in mm), for a subset of 9 or 10 rain gauges by massif.

This general tendency bas been related to the local radar data processing used, which does not take into account the relief or any altitudinal gradient of precipitation, but tends to estimate precipitation on a constant level for all the radar coverage:

- first, at the altitude of the local radar for the VPR treatment, the VPR being considered constant below the radar altitude, and also below the melting layer ;
- then, at the mean altitude of the rain gauges used by an hourly radar/gauges calibration, which is variable in time but constant in space. We can note that for the Moucherotte radar QPE calibration, in 2016 the mean altitude of the rain gauges selected was equal to 1155 m (91% located between 800 m a.sl. and 1860 m a.s.l.).

These two treatments thus contribute for a significant part to the annual values of the general bias observed at the French Alps scale, with a common overestimation of the radar QPE compared to rain gauge measurements at the bottom of the valleys, and a systematic underestimation at the highest altitudes.

The next section investigates the estimated values of the altitudinal gradients of precipitation, and their variability for different time steps for each massif.

4 Comparison of annual, seasonal, monthly, and daily gradients estimates

4.1 Need of normalization

For each massif, seasonal, monthly or daily altitudinal gradients of precipitation estimates (mm m^{-1}) depend linearly of the mean precipitation, or of the maximal precipitation, recorded by the rain gauges for the massif (figure 4). The correlation is better for the maximal value, which we suppose more representative of the rain event magnitude, and less influenced by the spatial variability of the precipitation over the massif.

To compare altitudinal gradients estimates for different temporal accumulations, it is thus necessary to normalize these estimations in order to express the gradients for an identical precipitation amount, chosen equal to 1mm. The normalized gradients are then expressed in mm m^{-1} mm^{-1}.

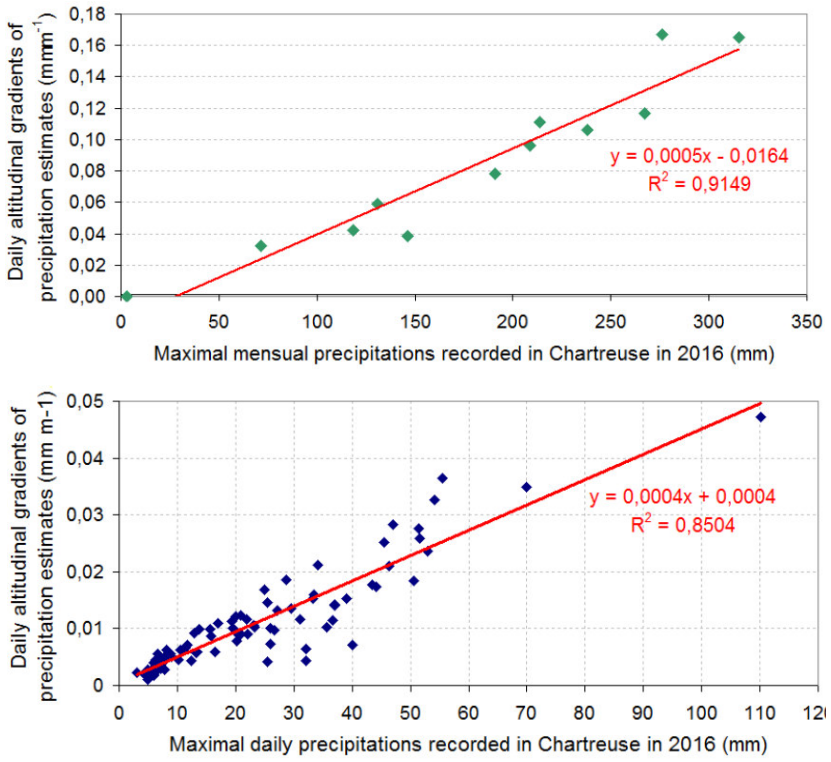


Figure 4: Relation between gradient estimates and magnitude of the precipitation.

4.2 Comparison of altitudinal gradient of precipitation estimates for different temporal accumulations

Figure 5 presents altitudinal gradient estimates for different temporal accumulations. Four seasons as been defined by the following triplets of months: DJF, MAM, JJA, SON.

For each massif, the normalized gradient values are very consistent for all the temporal accumulations (yearly, seasonal, monthly, daily), the gradient estimates for short duration varying around the annual value. For daily accumulations, the variability of the gradient estimates is large, but a great part is due to weak precipitation on the massif (mean of the daily values for the subset of gauges < 1mm/day, and maximal value < 3mm/day). An other part is due to the absence of gradient (determination coefficient R^2 between precipitation and altitude < 0.25), which can be due to the meteorological situation (as convective precipitation), but also frequently to the great spatial variability of daily precipitation over the rain gauges network: in this case, ground level measurements uniquely show the spatial repartition of precipitation. After filtering the non significant gradients estimates, we can observe that all the residual gradient estimates are positive.

We can also note that the normalization doesn't produce the same annual gradient value for different massifs, these gradients depending of factors characteristic of each massif.

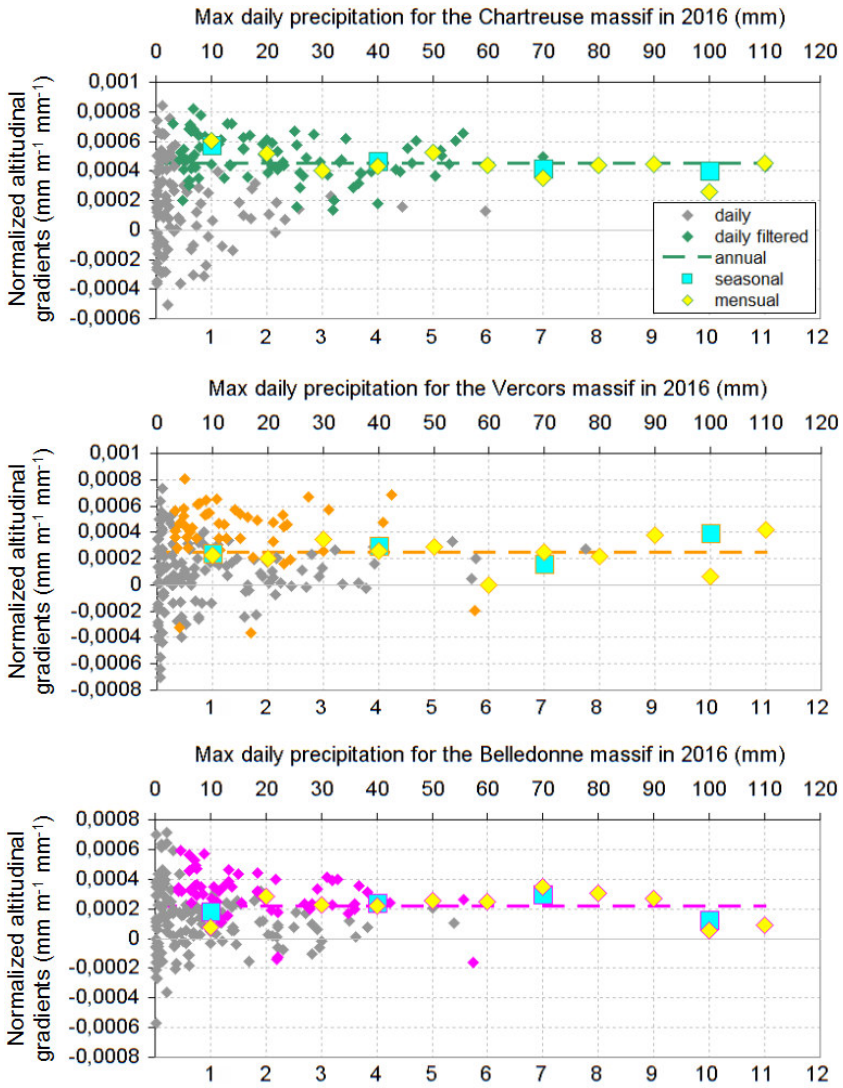


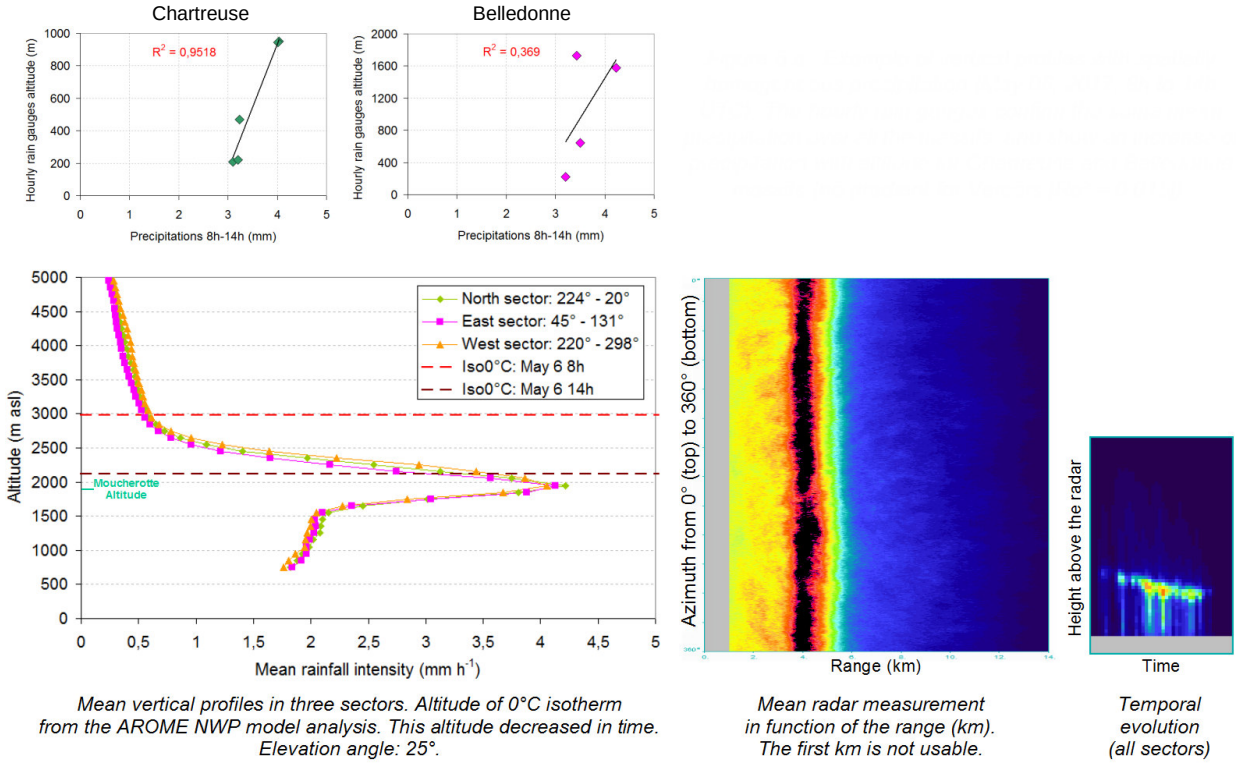
Figure 5: Comparison of the gradients estimates. In grey: non significant gradients estimates (weak precipitation or absence of gradient). Top scales: maximal daily precipitation in mm. Bottom scales: number of the months. Remark: practically all the filtered daily values (not grey) are positives.

5 Measurement of the XPORT radar from the bottom of the valley

The XPORT research radar provides the opportunity to test the contribution of a local X band radar at the bottom of a valley to complete the radar coverage of the national network. Even if the XPORT range is limited by large radar beam blockages and ground clutter, the scanning at high elevation angles allows to describe the structure of the atmosphere into the valley both vertically and spatially. This contribution is particularly important when the melting layer is near the altitude of the operational Moucherotte radar, which is common in the winter season.

XPORT provides vertical profiles of precipitation within and below the melting layer, at altitudes close to those of the rain gauges. This capacity allows to show that the spatial variability of these profiles into the valley widely fluctuates in function of the weather situation. The figures 6 and 7 present two examples of situations, one with spatially homogeneous precipitation, and the other with small rain cells moving quickly mainly on a part of the valley. Mean vertical profiles have been estimated in three sectors positioned in direction of the three massifs, but with measurements performed within the valley: at the elevation angle used to be free from masks and ground clutter (25°), the radar beam axis reach 2000 m a.s.l. at only 4.2 km from the radar, and 2800 m a.s.l. at 6 km (red circles in figure 2). For the second example, with heterogeneous precipitation, the three profiles are quite different.

Figures 6 and 7 equally show the altitudinal gradients estimated from the rain gauges data, but these gradients are not directly comparable to the XPORT profiles for short durations: the rain gauges measurements have been realized in the same direction but at greater distance from the radar, and on the massifs not in the valley. Therefore it is difficult to better analyze the relation between the altitudinal gradients observed at ground level and the radar vertical profiles in the atmosphere, even if they have the same sign (positive in these two examples).

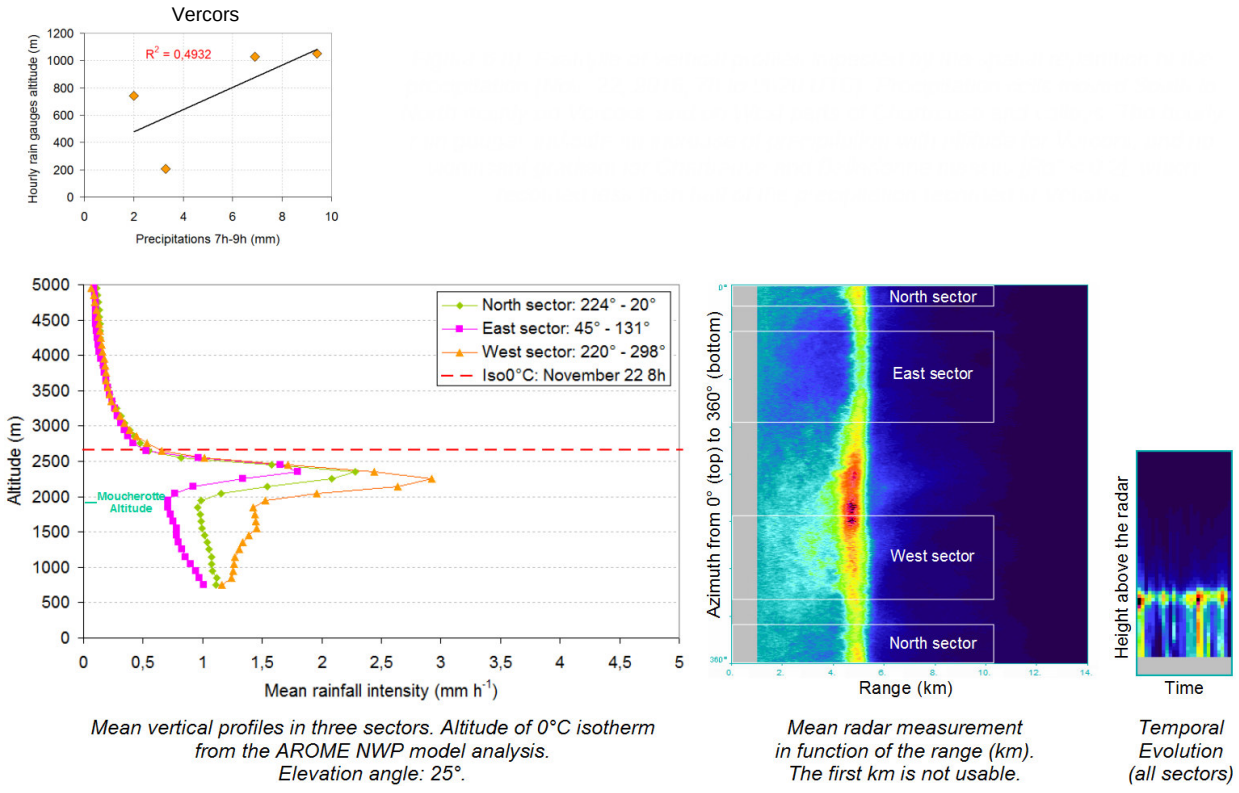


Mean vertical profiles in three sectors. Altitude of 0°C isotherm from the AROME NWP model analysis. This altitude decreased in time. Elevation angle: 25°.

Mean radar measurement in function of the range (km). The first km is not usable.

Temporal evolution (all sectors)

Figure 6: Example of vertical profiles with spatially homogeneous precipitation into the valley (May 06, 2017, 8h to 14h UTC). The hourly rain gauges confirm the same mean precipitation on all the massifs, and show an increase of precipitation with altitude for Chartreuse and Belledonne massifs (no significant gradient for Vercors [R² = 0.015]).



Mean vertical profiles in three sectors. Altitude of 0°C isotherm from the AROME NWP model analysis. Elevation angle: 25°.

Mean radar measurement in function of the range (km). The first km is not usable.

Temporal Evolution (all sectors)

Figure 7: Example of vertical profiles impacted by the spatial repartition of the precipitation into the valley (Nov. 22, 2016, 7h to 9h20 UTC). Precipitation cells moved South to North mainly on Vercors, and on West parts of Chartreuse and valleys. The hourly rain gauges indicate an increase of precipitation with altitude for Vercors, and no significant gradient for Chartreuse and Belledonne massifs [R² < 0.2], which recorded less than half of the amount of precipitation recorded in Vercors.

6 Conclusion

For the three massifs surrounding the Grenoble conurbation, the annual, seasonal, and monthly analysis confirm the same difference between radar QPE and rain gauges measurements: a precipitation amount at ground level increasing with the altitude of the gauges, and a relatively constant radar QPE in space. This difference explains the general bias observed in the French Alps between radar and rain gauges estimates, with a general tendency for the radar QPE to overestimate precipitation at low altitude, and underestimate at high altitude. The parts of the data processing which could influence the value of this bias was also pointed out.

The analysis at the daily time step has shown difficulties to estimate altitudinal gradients each day and for each massifs. This is probably due to factors specifics to each massifs varying in space and time (orientation of the slopes, orographic phenomena), but we also observed the impact of the weather situation (weak precipitation, convective precipitation) and of the spatial variability of daily precipitation, which can hide a possible altitudinal gradient of precipitation. Nevertheless, the temporal integration on longer durations systematically reveals a positive altitudinal gradient of precipitation for the three massifs. The utilization of the XPORT research radar data, acquired from the bottom of the valley, has also been the occasion to use few hours accumulations, which is closer to the operational conditions in real time. And the XPORT vertical profiles estimated in three different angular sectors confirmed the possibility of wide spatial variability of the precipitation in few kilometers, even at the bottom of a valley. This spatial variability contributes to the difficulties to estimate altitudinal gradients of precipitation at the daily time steep, and to the variability of the results from a massif to an other.

These results has been obtained for three neighboring massifs in the north-western part of the French Alps, but the previous results obtained with 430 rain gauges in all the French Alps (Faure, 2017) suggest that these new results could be extrapolated to a great part of the mountain range. Therefore, the general bias of the radar QPE with altitude in mountain, in comparison with ground measurements, could widely impact hydrology, nivology, and prevention of natural hazards, affecting the correct estimation of the precipitation amount on the massifs at all altitudes, and the accurate determination of the snow pack.

Future works should be necessary to better analyze the relation between altitudinal gradients of precipitation observed at ground level and vertical profiles of precipitation estimated in the atmosphere with radar measurements.

Acknowledgement

This work benefit from the collaboration and exchanges between the CMR team of Météo-France and the researchers of the HMCIS team of IGE. It also benefit from exchanges with researchers of the French Snow Research Center (CEN), a research unit of the CNRM (Centre National de Recherches Météorologiques).

References

Barry R. G. Recent advances in mountain climate research [Theor Appl Climatol] - December 2012. : Vol. 110. - pp. 549 - 553. DOI 10.1007/s00704-012-0695-x

Birman C., Karbou F., Mahfouf J., Lafaysse M., Durand Y., Giraud G., Mérindol L. and Hermozo L. Precipitation analysis over the French Alps using a variational approach and study of potential added value of ground based radar observations [J. Hydrometeor.] - May 2017. : Vol. 18(5) - pp. 1425 - 1451. DOI:10.1175/JHM-D-16-0144.1

Desurosne I. Oberlin G. and Blanchet G. Towards a better knowledge of high basin rainfall fields at small time and space steps: analysis of rainfall data from an unidirectional northern pre-Alps network [Proceeding of the Braunschweig FRIEND Conference] : [IAHS Publ.], January 1994. - N°. 221 - pp. 323 - 342.

Durand Y., Brun E., Mérindol L., Guyomarc'h G., Lesaffre B. and Martin E. A meteorological estimation of relevant parameters for snow models [Ann. Glaciol.] - January 1993. : Vol. 18. - pp. 65 - 71. DOI:10.1017/S0260305500011277.

Durand Y., Laternser M., Giraud G., Etchevers P., Lesaffre B. and Mérindol L. Reanalysis of 44 yr of climate in the French Alps (1958–2002): Methodology, model validation, climatology, and trends for air temperature and precipitation [J. Appl. Meteor. Climatol.] - January 2009 : Vol. 48. - pp. 429 - 449. DOI:10.1175/2008JAMC1808.1.

Faure D., Gaussiat N., Dupuy P., Delrieu G., Yu N. and Sarter F. Quality analysis of the 2016 quantitative precipitation estimates in the French Alps [38th Conference on radar meteorology] - Chicago : [AMS] https://ams.confex.com/ams/38RADAR/meetingapp.cgi/Paper/320389. August 2017

Deriving and compositing motion fields – speed and quality challenges


Markus Peura

Markus Peura[1], Tuuli Perttula[1], and Harri Hohti[1]

[1]*Finnish Meteorological Institute, P.O. Box 503, FIN-00101 Helsinki, Finland*
(Dated: 27 June 2018)

1 Introduction

In weather radar data, atmospheric motion vectors can be extracted using two alternative approaches: by using Doppler measurement, when operationally available, and by detecting apparent, visual motion in consecutive reflectivity images. Both approaches involve ambiguity and quality issues. Firstly, Doppler measurement is radial, hence principally one-dimensional, and further subject to aliasing (folding) around a limited velocity range. Secondly, detection of visual motion depends critically on applied window scale and level of detail in image frames, suggesting computation in several scales which may be practically unfeasible.

This work combines our earlier work on optical flow (Peura and Hohti; 2004), quality based compositing (Peura et al.; 2006), and Doppler dealiasing using sliding windows (Peura; 2017).

First, we present the general formulations of these two motion extraction problems. As their practical computating times are potentially large, we present speed-up techniques based on sliding windows that continuously update involved cumulants. The same techniques also apply to averaging (smoothing) which is useful when computing optical flow on radar data.

All the presented methods support using and generating quality information which is an advantage in preprocessing, post-processing, and visualizing motion fields. In experiments, we show how two-dimensional atmospheric motion fields generated from Doppler data and optical flow algorithm can be combined smoothly using quality information.

2 Detecting motion in radar images

2.1 Motion field from doppler data

Consider wind $\mathbf{v} = [u\ v]^{\mathrm{T}}$ observed with Doppler radar. For simplicity, we limit to low elevation angles, hence the vertical component can be discarded. Let us model a radar beam at azimuthal direction α as as unit vector $\mathbf{b}(\alpha) = [\cos\alpha\ \sin\alpha]^{\mathrm{T}}$. Observed wind v_b is the component projected on the beam: $v_b(\alpha) = \mathbf{v}^{\mathrm{T}}\mathbf{b}(\alpha) = u\cos\alpha + v\sin\alpha$.

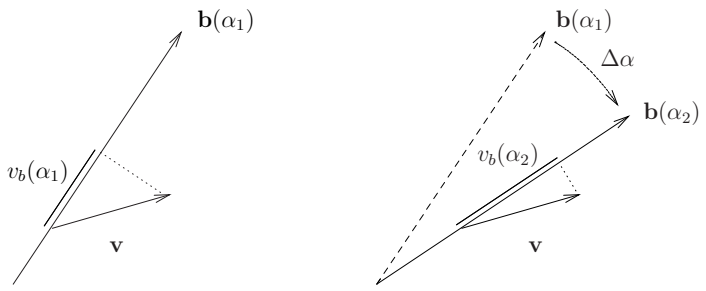


Figure 1: Observing changes in projected and aliased wind v_b. (Azimuthal beam resolution $\Delta\alpha$ drawn large for illustration.)

Our basic idea is to observe *changes* of v_b instead of its absolute values (Fig. 1). In this respect our Doppler dealiasing algorithm differs from that of Haase and Landelius (2004), for example. Specifically, we match measured change d against theoretical derivative of v_b:

$$d = \frac{\Delta v_b}{\Delta\alpha} \approx \frac{\partial v_b}{\partial\alpha} = \mathbf{v}^{\mathrm{T}}\mathbf{b}'(\alpha) = -u\sin\alpha + v\cos\alpha \tag{2.1}$$

Practically, azimuthal scanning resolution $\Delta\alpha = \alpha_2 - \alpha_1$ is small, typically around one degree, hence the changes in v_b are small and exceeding $[-V_{\mathrm{Nyq}}, +V_{\mathrm{Nyq}}]$ is robustly cancelled. In other worlds, we can rely on that we obtain a "true" Δv_b for computations.

Assuming that wind is nearly constant within a neigbourhood of a focused radar bin, we use least-squares fitting to retrieve wind $\mathbf{v} = [u\ v]^{\mathrm{T}}$ that best explains the changes observed in radial speed. Consider Doppler measurements within a window of $m \times n$ radar bins (Fig. 2) having azimuthal coordinates $i \in \{1, 2, ..., m\}$. radial coordinates $j \in \{1, 2, ..., n\}$ and

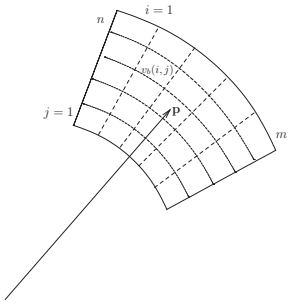


Figure 2: A Doppler window Ω of $m \times n$ (azimuthal $\times$ radial) bins located around a radar bin at position $\mathbf{p}$.

In this context, least-squares fitting means solving a set of $m \times n$ equations, in matrix form minimizing $||\mathbf{e}||$ in

$$\begin{bmatrix} d_{1,1} \\ d_{2,1} \\ \vdots \\ d_{m,1} \\ d_{1,2} \\ \vdots \\ d_{m,n} \end{bmatrix} - \begin{bmatrix} -\sin\alpha_1 & \cos\alpha_1 \\ -\sin\alpha_2 & \cos\alpha_1 \\ \vdots & \vdots \\ -\sin\alpha_m & \cos\alpha_1 \\ -\sin\alpha_1 & \cos\alpha_2 \\ \vdots & \vdots \\ -\sin\alpha_m & \cos\alpha_n \end{bmatrix} \begin{bmatrix} u \\ v \end{bmatrix} = \mathbf{d} - \mathbf{B}\mathbf{v} = \mathbf{e} \tag{2.2}$$

where $\mathbf{d}$ is a column vector of observed speed changes, $\mathbf{B}$ is a matrix of beam direction derivatives $\mathbf{b}'(\alpha)$, and $\mathbf{v} = [u\ v]^{\mathrm{T}}$ is our unknown. (Since $\alpha_{i,j} \equiv \alpha_i$ the elements on each row have positional correspondancy $d_{i,j} \leftrightarrow \alpha_i$ and $\mathbf{B}$ contains repeated elements.) Least-squares approximation of (2.2) yields a pseudoinverse:

$$\hat{\mathbf{v}} = (\mathbf{B}^{\mathrm{T}}\mathbf{B})^{-1}\mathbf{B}^{\mathrm{T}}\mathbf{d} \tag{2.3}$$

Rewriting $\mathbf{B} = [\mathbf{s}\ \mathbf{c}]$ and expanding the simple 2×2 matrix inversion we finally get

$$\hat{\mathbf{v}} = \begin{bmatrix} \mathbf{s}^{\mathrm{T}}\mathbf{s} & \mathbf{s}^{\mathrm{T}}\mathbf{c} \\ \mathbf{c}^{\mathrm{T}}\mathbf{s} & \mathbf{c}^{\mathrm{T}}\mathbf{c} \end{bmatrix}^{-1} \begin{bmatrix} \mathbf{s}^{\mathrm{T}} \\ \mathbf{c}^{\mathrm{T}} \end{bmatrix} \mathbf{d} = \frac{1}{(\mathbf{s}^{\mathrm{T}}\mathbf{s})(\mathbf{c}^{\mathrm{T}}\mathbf{c}) - (\mathbf{c}^{\mathrm{T}}\mathbf{s})^2} \begin{bmatrix} \mathbf{c}^{\mathrm{T}}\mathbf{c} & -\mathbf{c}^{\mathrm{T}}\mathbf{s} \\ -\mathbf{c}^{\mathrm{T}}\mathbf{s} & \mathbf{s}^{\mathrm{T}}\mathbf{s} \end{bmatrix} \begin{bmatrix} \mathbf{s}^{\mathrm{T}}\mathbf{d} \\ \mathbf{c}^{\mathrm{T}}\mathbf{d} \end{bmatrix}. \tag{2.4}$$

Practically, (2.4) means that in each bin location of a radar sweep five sums of mn elements are computed within a $m \times n$ neighbourhood window: $\mathbf{c}^{\mathrm{T}}\mathbf{c}$, $\mathbf{c}^{\mathrm{T}}\mathbf{s}$, $\mathbf{s}^{\mathrm{T}}\mathbf{s}$, $\mathbf{s}^{\mathrm{T}}\mathbf{d}$, and $\mathbf{c}^{\mathrm{T}}\mathbf{d}$. Involved computational issues are discussed further in 3, but first another similar yet more general approach is presented.

2.2 Motion field from optical flow

Optical flow is a name for a group of methods deriving motion in images, typically Cartesian ones. The underlying model links spatical and temporal intensity changes to motion $\mathbf{v} = [u\ v]^{\mathrm{T}}$ much in a same way as in meteorological advection equations:

$$\frac{df}{dt} = \frac{\partial f}{\partial t} + \frac{\partial f}{\partial x}\frac{\partial x}{\partial t} + \frac{\partial f}{\partial x}\frac{\partial x}{\partial t} = f_t + f_x u + f_y v = f_t + \nabla f \cdot \mathbf{v}. \tag{2.5}$$

A basic least squares solution involves minimizing error in a window Ω of $m \times n$ elements, yielding matrix formulation similar to (2.3)

$$\mathbf{v} = -(\mathbf{G}\mathbf{W}\mathbf{G}^{\mathrm{T}})^{-1}\mathbf{G}\mathbf{W}\mathbf{f_t} \tag{2.6}$$

where $\mathbf{G}$ is a $2 \times n$ matrix of gradients, $\mathbf{W}$ is an optional $n \times n$ diagonal matrix of weights and $\mathbf{f_t}$ is a $2 \times n$ matrix of intensity differences between two subsequent images. Again, $\mathbf{G}\mathbf{W}\mathbf{G}^{\mathrm{T}}$ is a 2×2 matrix, hence quickly invertible and we obtain a result similar to (2.4):

$$\mathbf{v} = \frac{1}{G_{xy}^2 - G_{xx}G_{yy}} \begin{bmatrix} G_{yy} & -G_{xy} \\ -G_{xy} & +G_{xx} \end{bmatrix} \begin{bmatrix} G_{xt} \\ G_{yt} \end{bmatrix} \tag{2.7}$$

It essentially involves five sums: $G_{xx} = \sum w f_x f_x$, $G_{xy} = \sum w f_y f_x$, $G_{yy} = \sum w f_y f_y$, $G_{xt} = \sum w f_x f_t$, and $G_{yt} = \sum w f_y f_t$.

2.3 Using and producing quality information

As mentioned above, computations may involve weighting of data like diagonal weighting matrix $\mathbf{W}$ in (2.6). Elements w_i of the matrix determine how much each input value contributes to the result. Note that similar weighting could be also applied in the Doppler inversion scheme (2.3). Radar data is often subject to anomalies, for example echoes originating from non-meteorological targets. Discussing quality control in detail is beyond the scope of this paper, but let us assume that input data – polar volumes – have been quality controlled by a process that assigns each bin a *quality index* between 0.0 and 1.0 (Holleman et al.; 2006). Values near one suggest high reliability, relevancy or usability. Respectively, values near zero suggest that the actual data values should be discarded. Hence, quality indices are a natural source for the elements of $\mathbf{W}$, resulting in end products where data of good quality contributes the most.

The computation process should also generate quality infomation – ideally not replacing input quality information $\mathbf{W}$ but modifying and extending it. For example, in the motion detection algoritms presented, a natural source of quality information are the determinants in the required matrix inversions. In Doppler inversion (2.4), the determinant $(\mathbf{s}^{\mathrm{T}}\mathbf{s})(\mathbf{c}^{\mathrm{T}}\mathbf{c}) - (\mathbf{c}^{\mathrm{T}}\mathbf{s})^2$ is however data invariant – it is essentially a function of window width M. (We consider testing circular Doppler variance in future.) In the case of optical flow (2.7), the determinant $G_{xy}^2 - G_{xx}G_{yy}$ depends on data. We suggest designing a quality index as a monotonously increasing function of type $f(x) = x/(x+a)$ which takes values in $[0, 1[$ and positive decay coefficient a determines the "half-width": $f(a) = 1/2$. So, a can be used for connecting 50% data rejection threshold to computation.

3 Computational issues and solutions

3.1 Motivation

The motion detection algorithms presented above have rather different types of input data: Doppler velocity measurements in polar coordinates and intensity data in Cartesian coordinates. Nevertheless, under least squares minimisation their mathematical formulations become similar. Consequently, given an image of $M \times N$ pixels (bins) and applying a $m \times n$ window, the resulting computational complexity is $\mathcal{O}(MNmn)$ if implemented as four nesting loops. Practically, Doppler motion extraction in one elevation sweep could involve $500 \cdot 360 \cdot 90 \cdot 5 = 8.1 \cdot 10^7$ operations which may be unfeasible. Likewise, a nowcasting application using optical flow would easily need much more, $1000 \cdot 1000 \cdot 50 \cdot 50 = 2.5 \cdot 10^9$ operations making it even less tempting.

3.2 Sliding windows

First, consider a simple averaging problem with an $M \times N$ input image. In the result image, each pixel is assigned the average intensity in a rectangular $m \times n$ window in the input image: $\hat{f}(k,l) = \sum_i \sum_j f(k+i, l+j)$. This example is similar to the above motion detection problems: straightforward looping yields $MNmn$ operations. On the other hand, the average can be computed cumulatively as follows: when the window is moved one step, one row of elements is subtracted and one row is added in the sum, resulting in MNn operations. This "pipeline" approach, a sliding window, is illustrated in Fig. 3

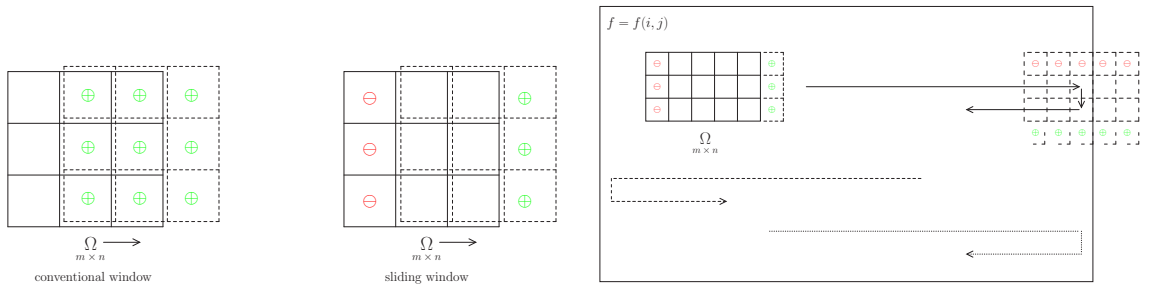
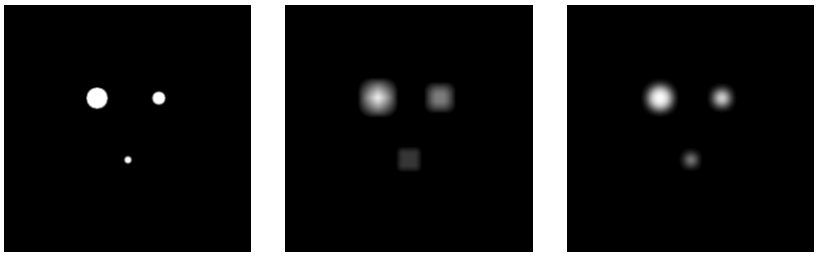


Figure 3: Sliding windows. Computations saved in accumulation (a) and image traversal (b).

As was pointed earlier, computation of Doppler motion (2.3) and optical flow (2.7) is essentially accumulation. This means that they can also be implemented using sliding windows, with complexity $\mathcal{O}(MNn)$. Some experiments are shown in Sec. 4.

Averaging can be accelerated even more: instead of processing in an input with a $m \times n$ window one can process the image with $m \times 1$ window and then the result with $1 \times n$ window, obtaining an equivalent final result. We say that the operation is *separable*. Rectangular averaging implemented this ways requires only $\mathcal{O}(MN)$ computations.

Rectangular averaging is sometimes not desired, as it produces rentangular shapes around original targets as shown in Fig. 4b.



(a) (b) (c)

Figure 4: Sample image (a) blurred with rectangular averaging (b) and Gaussian averaging (c).

Gaussian averaging means convolving an image with a kernel of type

$$g(i,j) = AB \exp^{-ai^2-bj^2} . \tag{3.1}$$

Theoretically, the kernel continues to infinity; practically it is truncated to width and height, say, twice the peak halfwidth. Gaussian averaging is also separable, since

$$\bar{f}(k,l) = \sum_i \sum_j f(k+i,l+j)g(i,j) = A \sum_i \exp^{-ai^2} B \sum_j \exp^{-bj^2} f(k+i,l+j) \tag{3.2}$$

Gaussian averaging separated to horizontal ($m \times 1$) and vertical ($1 \times n$) processing requires $\mathcal{O}(MN(m+n))$ computations. The speed of fast rectangular averaging is not achieved because Gaussian kernels weight pixels unequally.

These averaging operations are mentioned here not only as easier examples and motivations for accelerating motion extraction. Radar data typically contain large empty ("undetected") areas, so motion detection algorithms – like optical flow – typically require smoothing as preprocessing.

3.3 Distance transform

Distance transform is an operation for quickly computing distances in digital images. More specifically, it computes minimal path lengths between two pixels; the paths are sequences of adjacent pixels. Typically 4 or 8-adjacency is applied (Gonzales and Woods; 1992; Sonka et al.; 1993). Hence, it provides an approximation of the Euclidean distance. The basic idea is to iteratively update a distance by incrementing the intensity values when moving away from points of interest.

An input image is passed through twice, first traversing each row from left to right, starting from the top, and then reversing from the bottom, row by row, right-to-left. The window applied in traversing is small and asymmetrically contains neighboring elements of the visited pixel. Three simple processing elements (topologies) and resulting images are displayed in Fig. 5. During a traversal each focused pixel is assigned the minimum in the set of neighbouring values added by the step distance D. The basic version uses rectangular pixel-to-pixel distances (D_r) only, producing in diamond-like shapes. Extended versions apply also diagonal (D_d) and further "chess knight" distances (D_{kn}). In processing 8 or 16 bit digital images, real values (1, $\sqrt{2}$, $\sqrt{5}$) have to be replaced with appropriate integers with similar ratios. One the other hand, especially with floating point images one can use exponential decay function instead of the linear one presented.

As to computational complexity, consider finally a brute-force algorithm – in this case the "true" Euclidean distance is obtained. Given k target pixels of interest, an approach could be to traverese, once for each target, all the pixels of the result image, updating minima (or maxima, for obtaining results like in Fig. 5). Such operation would require "only" $\mathcal{O}(MNk)$ operations, but if the number k is unpredictable and occasionally large, like in the case of observing convective cells and distances thereof, unconfortable load peaks may occur.

In our undestanding, the speed advantage of fast distance transform cannot be imported to the motion detection algorithms presented. However, the algorithm is reviewed here because it has potential in preprocessing – like rectangular and Gaussian averaging above – and in spreading obtained motion fields, as explained in Sec. 4.4.

3.4 On computational complexity

Finally, let us summarize the computational complexities of the suggested fast algorithms by comparing them with the brute-force counterparts (Table 1). For the fast versions of the proposed motion detection algorithms, the computational complexity can be accelerated even more by using temporary arrays in computations. Then, the complexity drops to $\mathcal{O}(MN)$ but five

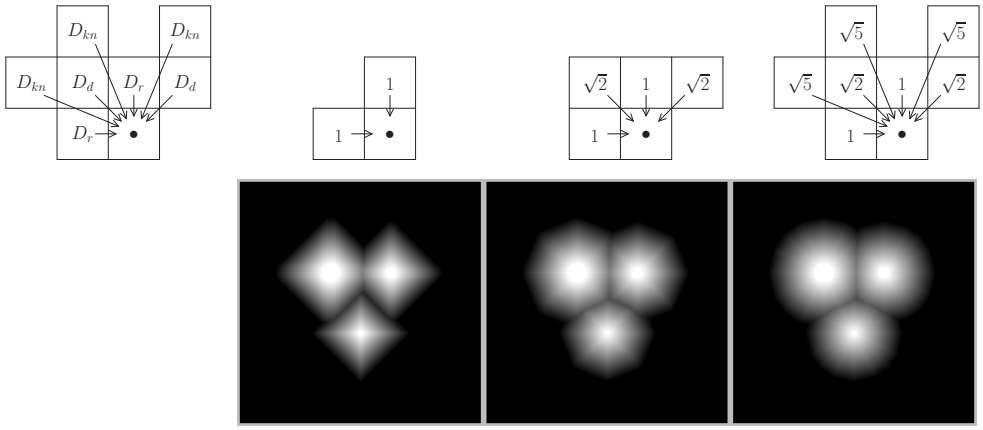


Figure 5: Distance transforms. For comparability with rectangular and Gaussian smoothing illustrated in Fig. 4, we have used inverse distance transform, and the same input image. The resulting sizes reflect the intensities of the sample dots.

extra arrays are allocated storing the accumulants involved. This kind of time-memory trade-off when analysing computational complexity (Papadimitriou; 1994).

Table 1: Computational complexities when using $M \times N$ input image and $m \times n$ window.

Distance brute-force	Distance transform	Averaging, rect., brute-force	Averaging, rect., sliding.	Averaging, Gaussian, separable	Optical flow, brute-force	Optical flow sliding
$MNmn$	MN	$MNmn$	MN	$MN(m+n)$	$MNmn$	$MN \min(m,n)$

4 Experiments

4.1 Doppler fields

We tested the proposed Doppler inversion scheme on three cases using a small composites with data from FMI weather radars (C-band). Doppler data with V_{Nyq}=7.6m/s of the lowest sweep (0.3°) was used[1]. The computation was performed with a window of 5×95 bins (2500m,95°). We have noticed that the window should be azimuthally wide, some tens of degrees to obtain enough information on azimuthal differentials whereas a couple of kilometers in radial direction seems sufficient, providing mainly a smoothing effect. Finally, the motion fields from each radar were composited using quality-weighted compositing (Peura et al.; 2006). In these experiments and the demonstrations of Sec. 3, FMI software "Rack" was used (Peura; 2012).

A frontal case (2016/07/05 12:00 UTC) involves motion in opposite directions: an intensive convective area flowing to North-West and a more widespread area going South-East.

Another case with convection (2017/08/12 16:00 UTC) developed to thunderstorms causing urban flash floods, forest damage, and aviation re-routing in Southern Finland.

The third case (2018/02/01 12:00) is a snow event, not exceptionally intensive in Northern climate but one of the strongest ones during the winter.

Result of Doppler inversion are displayed as dark blue arrows on lowest-scan reflectivity images. Principally, the algorithm approximates the motion for every pixel in the composite, but quality has been used as a transparency parameter in this visualisation: opaque vectors have the maximum quality. For this illustration, quality has been defined simply as the percentage of non-empty bins within the Doppler window. By visual inspection, this heuristic correlates well with the actual usablity of vectors. Especially in nowcasting applications, prevailing overall motion is preferred to local convective or divergent fields. (For analysis of convection or birds, one can compute Doppler variance, for which sliding window can be applied as well.)

Looking at the results Fig. 6, one can see that the algorithm performs well in areas of widespread rain. This was expected, since the central assumption with this algorithm is that wind fields be locally smooth. For convective areas, other techniques like optical flow are called for.

[1]To challenge the algorithm, sweep with V_{Nyq}=7.6m/s was preferred to V_{Nyq}=48.0m/s obtained with Dual-PRF.

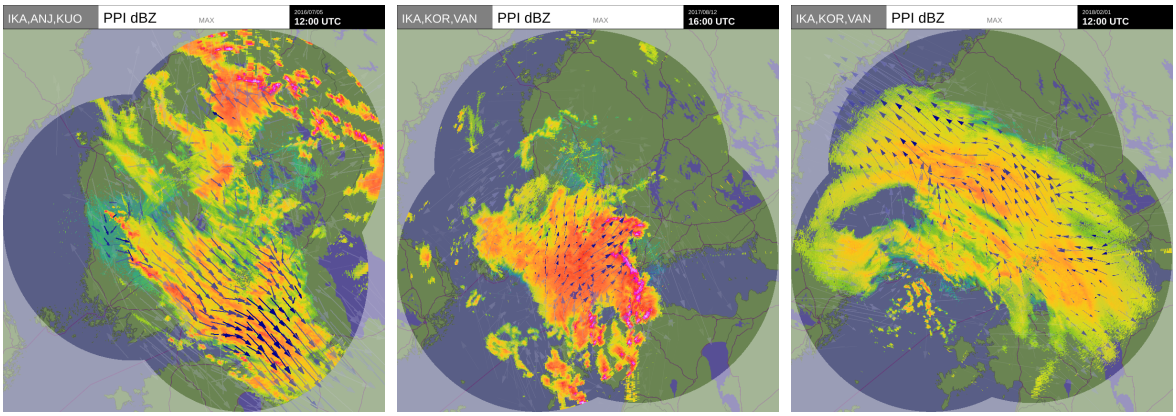


Figure 6: Wind fields obtained by means of Doppler inversion.

4.2 Optical flow

The same cases as above were used as input for optical flow algorithm (Fig. 7). As input, composites with 15 min time differences were used. As preprocessing, the composites were resised to 250×250 pixels and smoothed with Gaussian averaging (3.2). Then, optical flow using a 25×25 window was used, producing motion (u, v) and quality index q defined as a function of determinant (2.7) taking values in $[0.0, 1.0]$.

Compared to Doppler inversion, optical flow performs poorly in large precipitation areas but better in areas of scattered precipitation. This is because optical flow needs visual details like patches, cusps and corners for detecting the motion.

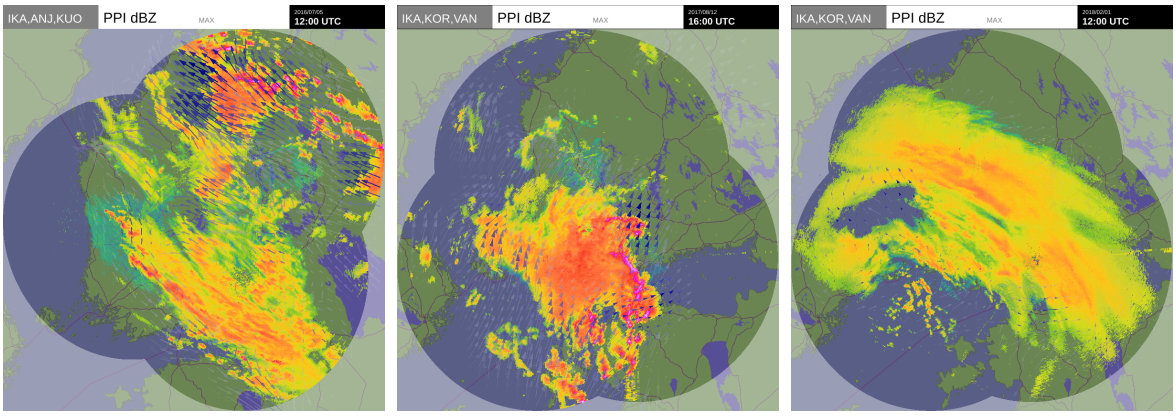


Figure 7: Motion of precipitation areas obtained by means of optical flow.

4.3 Joining Doppler and optical flow data

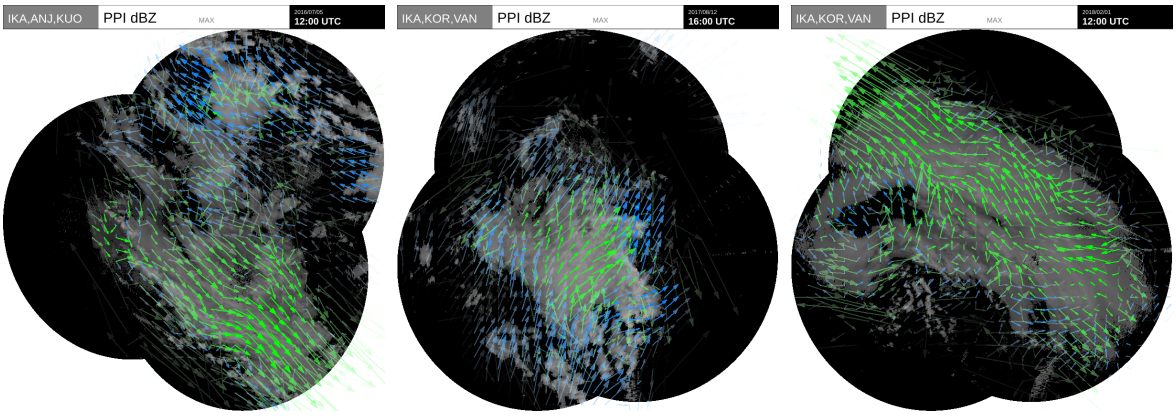
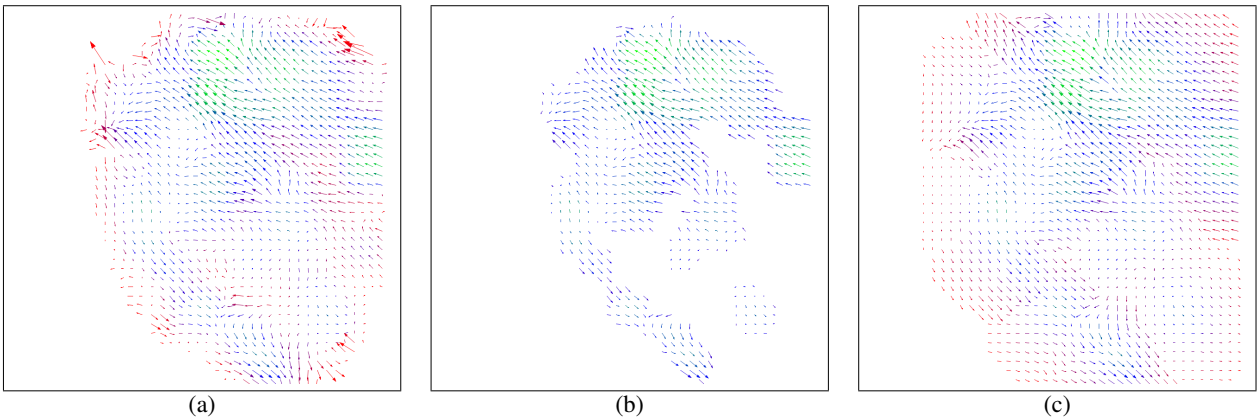


Figure 8: Extracted doppler winds (green) and optical flow (blue) superposed on dBZ.

4.4 Postprocessing: quality-based thresholding and spreading of motion fields

Typically, as in the examples presented in this paper, the obtained motion fields are spatially incomplete. Partly, this is due to radar data itself which may contain large empty areas, hence motion cannot be detected, even though it existed (e.g. clear air motion). Second, applied algorithms provide quality information that suggest discarding some data in the result; this implies *quality based thresholding*. An example is shown in Fig. 9, where the motion field of the leftmost case of Fig. 6 has been coloured such that green and red presents high and low quality, respectively. Vectors of low quality have been removed with quality based thresholding (b). Then, a modified version of distance transform (Sec. 3.3) has been used to spread higher-quality vectors over the lover-quality areas, incuding erased ie. zero-quality area. In the modified version, quality field is processed as in the standard version but data – here motion vectors – are propagated in a separate channel.



(a) (b) (c)

Figure 9: Postprocessing vector field: initial (a), quality thresholded (b) and extended (c) data.

5 Discussion

We addressed two different approaches for detecting motion vectors in radar images: one based on Doppler inversion and another based on optical flow. Experiments demonstrated how these approaches complement each other, Doppler inversion having good performance in widespread precipitation and optical flow more in scattered areas. Clearly, there are challenges shared by both approaches, starting from the two-dimensional input originating from three-dimensional atmosphere. As to potential applications in nowcasting, since these light methods do not involve a physical model, they cannot forecast many dynamic phenomena like onset of convection.

Mathematically, both approaches are based on using least squares method in solving $\mathbf{v} = [u\ v]$ within a window. Further, we presented efficient techniques – sliding windows – that accelerate computation of the involved cumulants.

Quality issues we also addressed, first outlining solutions for using input quality in computation. Because motion detection typically produces data of varying quality, simple procedures for making such quality explicit were presented. Further, we showed how quality data can be used in thresholding and further expanding motion fields. Quality processing involved using heuristic rules, yet potentially compatible to probabilistic schemes defined more strictly.

Compositing the motion of precipitation (hydrometeors, from Doppler) and precipitation areas (from optical flow) does not always make sense. However, when superposed on reflectivity data, they can reveal interesting meteorological information of changing sky conditions. Further, presented methods could be developed further to automatically detect intersecting motion fields, for example.

Finally we would like to stress the speed of the proposed methods. This opens possibilities in computing several parallel motion fields, for example for different altitudes, spatial scales, or precipitation classes (convective vs stratiform).

Acknowledgement

The authors wish to thank Dr.Seppo Pulkkinen and Mr. Joonas Karjalainen for cooperation in motion detection.

References

Gonzales, R. C. and Woods, R. E. (1992). *Digital Image Processing*, Addison-Wesley.

Haase, G. and Landelius, T. (2004). Dealiasing of doppler radar velocities using a torus mapping, *Journal of Atmospheric and Oceanic Technology* **21**(10): 1566–1573.

Holleman, I., Michelson, D., Galli, G., Germann, U. and Peura, M. (2006). Quality information for radars and radar data, *Technical report*, EUMETNET/OPERA. OPERA_2005_19_DataQuality.

Papadimitriou, C. (1994). *Computational complexity*, Addison-Wesley.

Peura, M. (2012). Rack - a program for anomaly detection, product generation, and compositing, *7th European Conference on Radar in Meteorology and Hydrology (ERAD2012)*, Météo France. Software can be downloaded from https://github.com/fmidev/rack.

Peura, M. (2017). Retrieving 2d wind field from aliased doppler data by means of sliding windows, *38th Conference on Radar Meteorology (AMS2017)*, American Meteorological Society.

Peura, M. and Hohti, H. (2004). Optical flow in radar images, *Third European Conference on Radar in Meteorology and Hydrology (ERAD2004)*, Copernicus, pp. 454–458.

Peura, M., Koistinen, J. and Hohti, H. (2006). Quality information in processing weather radar data for varying user needs, *Proceedings of the Fourth European Conference on Radar in Meteorology (ERAD2006)*, Copernicus, pp. 563–566.

Sonka, M., Hlavac, V. and Boyle, R. (1993). *Image Processing, Analysis and Computer Vision*, Chapman & Hall Computing.

Characterisation of the melting layer variability in the Swiss Alps using polarimetric X-band radars

Floor van den Heuvel[1,2], Marco Gabella[2], and Alexis Berne[1]

[1]*Ecole Polytechnique Fédérale de Lausanne (EPFL), Bâtiment GR Station 2, 1015 Lausanne, Switzerland*
[2]*MeteoSwiss, Via-ai-Monti 146, 6605 Locarno, Switzerland*

(Dated: 21 June 2018)

1. Introduction

Although quantitative precipitation estimation (QPE) with radar is complicated by many factors, in complex terrain such as the Alps partial and total beam shielding by mountains is of particular concern (Germann and Joss, 2004). It is common practice to compensate for the lack of direct visibility with the radar by extrapolating the measurements collected at higher elevations to the ground level, using a vertical profile of reflectivity (VPR) to correct for the vertical change in the radar reflectivity measurement (Germann and Joss, 2002). This vertical change in reflectivity is related to changes in size, phase and fallspeed of hydrometeors, which is in turn dependent on both microphysical processes (Fabry and Zawadzki, 1995) and the vertical profiles of temperature and humidity (Stoelinga et al., 2013).

The melting layer (ML) is a typical feature in radar observations of the vertical structure of stratiform precipitation which designates the transition region from solid to liquid precipitation. It has a well-known signature in the (polarimetric) radar variables with a notable increase in the horizontal reflectivity factor (ZH) as well as a reduction of the copolar correlation coefficient (Rhohv) (Battan, 1973; Brandes and Ikeda, 2004). The melting layer is often assumed spatially and temporally homogeneous by algorithms for QPE and VPR correction. However this assumption may not be accurate, especially for wintertime precipitation and in an orographic context. Indeed, according to several studies the melting layer may dip downwards with a few hundred metres in the proximity of terrain (for example Stoelinga et al. (2013)), and melting layer thickness has been related to snowflake density (Matsuo and Sasyo, 1981) and the presence of rimed particles above the melting layer (Wolfensberger et al., 2016). Several studies have reported on the melting layer variability at seasonal and large spatial (for example Harris et al. (2000); Rudolph and Friedrich (2013)) and temporal (Fabry and Zawadzki, 1995) scales. However, none of these studies presented a quantification of the small scale melting layer variability, and none were conducted in an Alpine environment.

This work presents a method based on the Fourier transform for the quantification of the variability of the melting layer at various spatial and temporal scales. The method has been applied to range-height indicator (RHI) scans of two measurement campaigns performed with mobile polarimetric X-band radars in two very different though highly representative regions in Switzerland (Figure 1).

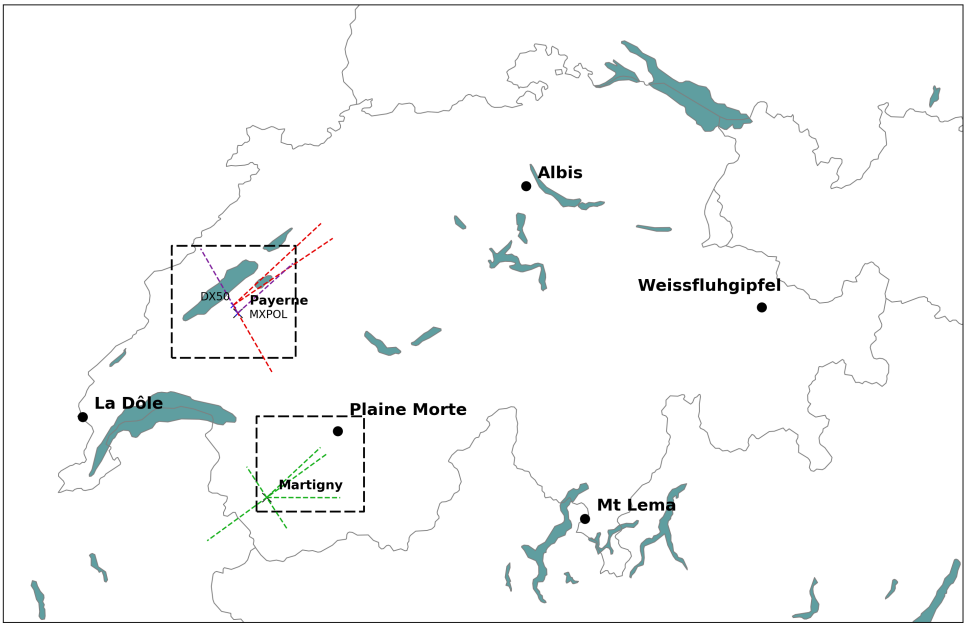


Figure 1: Study area locations; Payerne on the Swiss plateau and Martigny (Valais) in the Swiss Alps.

2. Data and methods

The RHI scans used for this study come from two measurement campaigns in Switzerland (Figure 1) one during early summer in the vicinity of Payerne which is located on the relatively flat, densely populated Swiss plateau. And the second one in winter near Martigny (Valais) in a deep, large and long inner Alpine valley representing locations in Switzerland for which QPE is particularly challenging.

All the RHI scans were subjected to a texture based clutter filter from the ARM Radar Toolkit (Py-ART) (Helmus and Collis, 2016), after which the melting layer detection algorithm developed by Wolfensberger et al. (2016) was applied. The extracted heights of the tops and bottoms of the melting layers as well as the melting layer thickness were de-trended and tapered to minimise the influence of red noise and leakage in the spectra. They were then subjected to a one dimensional Fast Fourier transform. The analysis of this study is based on the fraction of variance explained by component, which is obtained when summing the square of the norm by the total variance:

$$\frac{|\vec{F_A}(n)|^2}{\sigma^2_{\vec{A}}} \tag{2.1}$$

Where the square of the norm of the complex Fourier transform for any frequency n can be obtained by combining the real and the imaginary parts of each of the N coefficients:

$$|\vec{F_A}(n)|^2 = \vec{F}^2_{\mathbb{R}e}(n) + \vec{F}^2_{\mathbb{I}m}(n) \tag{2.2}$$

And the total variance of the original series can be obtained by summing the square of the norm over $n = 1$ to $N - 1$ ($|\vec{F_A}(0)|$ being the mean value).

$$\sigma^2_{\vec{A}} = \frac{1}{N}\sum_{k=0}^{N-1}(\vec{A}_k - \overline{\vec{A}})^2 = \sum_{n=1}^{N-1}|\vec{F_A}(n)|^2 \tag{2.3}$$

These fractions of variance explained by component have the advantage of summarising the spatial variability information into a few components allowing for easy comparison of individual melting layers or the aggregation of the information into distributions for each frequency.

3. Results

3.1. Evaluation of the method

The left panel in Figure 2 shows one melting layer top from the Valais campaign (green line), one from the campaign in Payerne (red line) and an artificial melting layer created by adding white noise to a linear trend (blue line). In the middle panel, the first ten spatial lags (in $1/f$) are given for the fraction of variance explained by component.

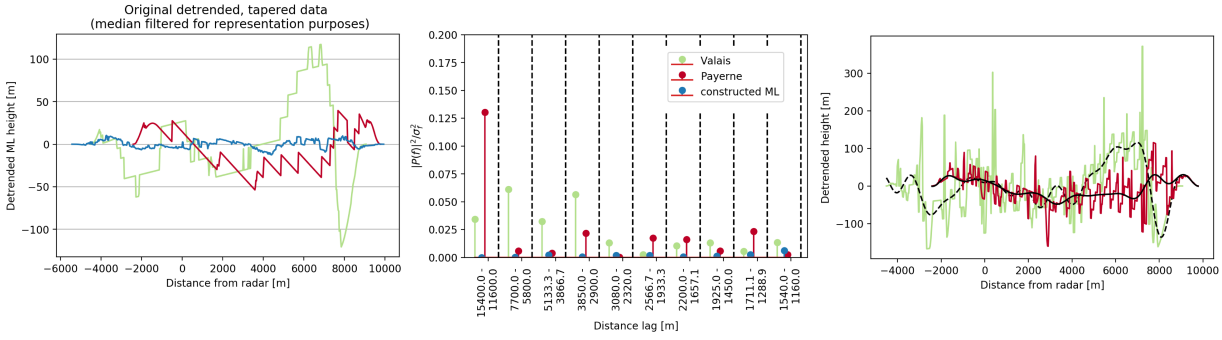


Figure 2: Examples of observed melting layer tops (left panel) and their corresponding fractions of variance explained by component (middle panel) from the the Valais campaign (green), the Payerne campaign (red) and for a constructed melting layer consisting of white noise with a drift (blue). The maximum fraction of variance explained is 0.5, since spectra have not been folded. The reconstituted melting layers by the first ten components (the black lines) are superimposed on the original melting layers in the right panel.

The Payerne melting layer, which displays less spatial variability, has most of its variance explained by the first component. This means that this melting layer top either varies at only the largest spatial scales, or, more likely, at even larger scales not resolved by the obtained spatial frequencies. The Valais melting layer, on the other hand, is spatially more variable and thus displays higher contributions to the total variance from smaller spatial scales. Because the values of the variance explained by the larger spatial lags is based on few realizations, they have a larger associated uncertainty. As an illustration, the black lines in the right panel show the ability first ten components to reconstitute the melting layer tops. Nevertheless, to account for this uncertainty, fractions of variance by component have been regrouped into box plots in this study.

3.2. Melting layer statistics

The distributions of the melting layer tops, bottoms and depths for the two campaigns are given in Figure 3. Both the melting layer tops and bottoms display a bi-modal distribution with approximately a 400 metre shift in height related to the different seasons. This shift in the distributions of the melting layer heights show remarkable coherence as these result in similar distributions of melting layer thickness for both locations. Both the values of the melting layer heights and the bimodal character of the distributions are consistent with the studies by Fabry et al. (1994) and Cluckie et al. (2000). The melting layers are thicker than those reported by Cluckie et al. (2000) but comparable with those found by Fabry et al. (1994).

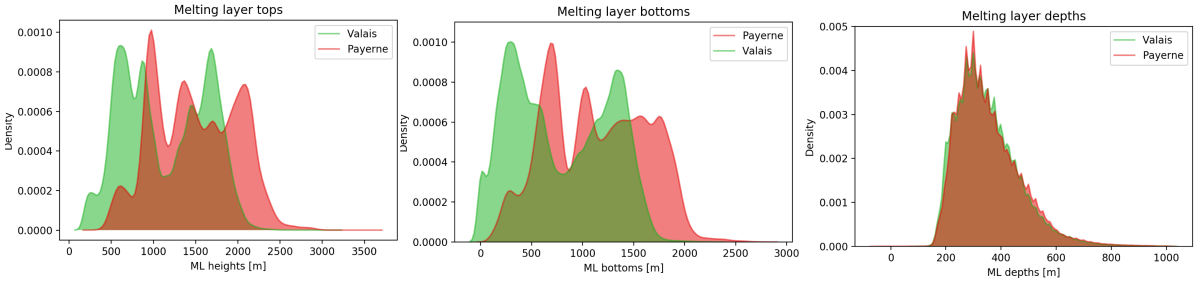


Figure 3: Distributions of the melting layer tops, bottoms and depths for the Payerne and Valais campaigns.

3.3. Melting layer variability

Because the extracted melting layers have different lengths, the fractions of variance explained by component have been regrouped into spatial lags. Figure 4 shows the box plots for the melting layer tops (left panel) and the melting layer thickness (right panel) for both campaigns. Whereas the box plots for the Payerne campaign show higher fractions of variance explained for the first components with an exponential decline towards the smaller spatial lags, the Valais data display a much less pronounced decrease in their fractions of variance explained; indicative of a higher relative importance of variability at smaller scales in the Alpine winter environment. As the box plots indicate, the intra-campaign variability of the fractions of variance explained by component is quite large. However the analysis was also performed on an event basis and showed a similar behaviour of the components across events.

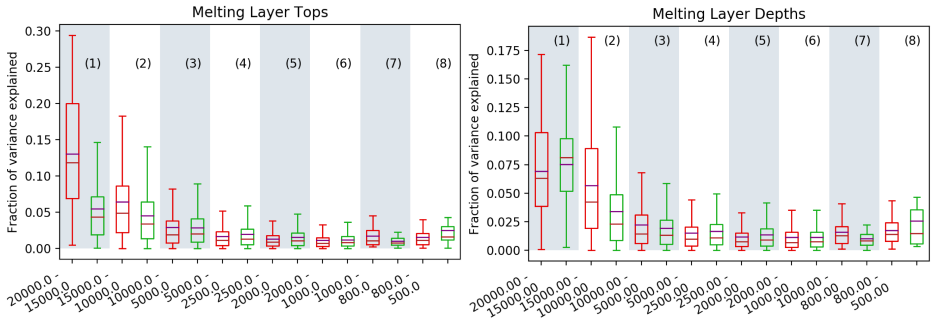


Figure 4: Binned fractions of variance explained by component for the melting layer tops (left) and depths (right) for the Valais data (green) and Payerne data (red).

The box plots of the melting layer depths (thickness) in the right panel of Figure 4 show very little spatial variability. Furthermore, the average and median values for the spatial components of both datasets are much more similar. According to these datasets, the small scale variability of the melting layer thickness is more similar over flat areas and complex topography.

For the analysis of the temporal variability, only precipitation events which were sufficiently long in duration could be used. Vertical PPI scans and the vertical elevations of the RHI scans were blended into time series of at least two minute resolutions and subjected to the melting layer detection algorithm. From the algorithm output, periods of one hour were selected with a sliding window of 12 minutes and subjected to the same Fourier analysis as the spatial data. Though the lengths of the sub selected time series were roughly the same, the data was also re-binned into temporal lags.

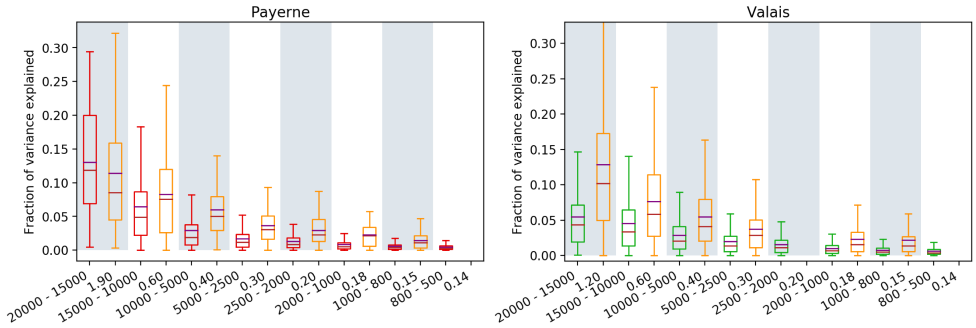


Figure 5: Box plots of the binned fractions of variance explained by component for the melting layer tops of the selected events from the Payerne campaign (left) and the Valais campaign (right). The spatial components are given in red and green for the Payerne and Valais data respectively, and the temporal components in orange.

A comparison of the spatial and temporal components of the two campaigns is given in Figure 5. Overall, the temporal data has slightly lower values, which may be attributed to small discontinuities in rainfall in the temporal data which have the effect of diminishing the spectral slope and as such also the fractions of variance explained by the larger scale components (De Montera et al., 2009; Rysman et al., 2013; Verrier et al., 2011). Nevertheless, for the Payerne case the variability observed at the hourly time scale is very similar to the variability at the 20 to 15 kilometres scale. This could be explained by the fact that the average wind speeds during the events was around 11 km/h which may explain why the air mass scanned by the RHI scans up to a distance of 10 km from the radar was identical to the air mass scanned above the radar within the hour. This result is also comparable to the findings from a study by Rysman et al. (2013) for summer precipitation in the Mediterranean region. They reported similar spectral slopes for the 20-45 minutes temporal range and the 7-20 km spatial range. For the Valais data on the other hand, the one-hourly time scale seems to be responsible for twice as much of the temporal variability in the melting layer tops as the largest spatial component. This could be related to the small-scale topography affecting the RHI scans in the Valais or to the much more variable wind speeds during these events (between 0 and 9.5 km/h). But it is also possible that spatio-temporal coherence in wintertime conditions occurs at larger scales than measured by the X-band radar.

4. Summary and conclusions

This study presented a method based on the Fourier transform which was employed to characterise and quantify the spatio-temporal variability of the melting layer at different scales and at two distinct locations in Switzerland. It is shown that:

- the fractions of variance explained by component are able to concisely describe and distinguish the variability of the observed melting layer at different spatial scales.
- the global statistics of the melting layer heights are consistent with values found in literature and coherent in their seasonal shift in the average heights of the tops and bottoms of the melting layer, with the melting layer thickness remaining the same independent of the season or location .
- the fractions of variance explained by component indicate a higher importance of variability at smaller spatial scales in the case of the Alpine environment for the melting layer tops, but not for the melting layer thickness, suggesting that small-scale topography may have an influence on the melting layer height, but not on it's depth.
- for the data from the relatively flat area (Payerne), variability at the one hourly temporal scale corresponds well with spatial variability at 15-20 km scales. No such link could be established for the data from the Alpine area, possibly due to more variable wind conditions and topography, or perhaps because spatio-temporal coherence occurs at larger scales than could be measured by the X-band radar.

Acknowledgement

The authors would like to thank their colleagues at LTE (EPFL) and MeteoSwiss for their useful suggestions, discussions and support.

References

H. Andrieu and J. D. Creutin, "Identification of Vertical Profiles of Radar Reflectivity for Hydrological Applications Using an Inverse Method. Part I: Formulation," pp. 225–239, 1995.

L. J. Battan, *Radar observation of the atmosphere*. University of Chicago Press, 1973.

C. Bell, "Detection of the Riming Process with a Vertically Pointing Radar," Ph.D. dissertation, McGill University, Montreal, Quebec, 2000.

A. Berne, G. Delrieu, H. Andrieu, and J.-D. Creutin, "Influence of the Vertical Profile of Reflectivity on Radar-Estimated Rain Rates at Short Time Steps," *J. Hydrometeor.*, vol. 5, no. 2, pp. 296–310, 2004.

S. Boodoo, D. Hudak, N. Donaldson, and M. Leduc, "Application of dual-polarization radar melting-layer detection algorithm," *J. Appl. Meteorol. Clim*, vol. 49, no. 8, pp. 1779–1793, 2010.

E. A. Brandes and K. Ikeda, "Freezing-Level Estimation with Polarimetric Radar," *J. Appl. Meteor.*, vol. 43, no. 11, pp. 1541–1553, 2004.

L. S. Campbell and W. J. Steenburgh, "Finescale Orographic Precipitation Variability and Gap-Filling Radar Potential in Little Cottonwood Canyon, Utah," *Weather Forecast*, vol. 29, no. 4, pp. 912–935, 2014. [Online]. Available: http://journals.ametsoc.org/doi/abs/10.1175/WAF-D-13-00129.1

I. D. Cluckie, R. J. Griffith, A. Lane, and K. A. Tilford, "Radar hydrometeorology using a vertically pointing radar," *Hydrol. Earth. Syst. Sc*, vol. 4, no. 4, pp. 565–580, 2000. [Online]. Available: http://www.hydrol-earth-syst-sci.net/4/565/2000/

B. A. Colle, R. B. Smith, and D. A. Wesley, "Theory, Observations, and Predictions of Orographic Precipitation," in *Mountain Weather Research and Forecasting: Recent Progress and Current Challenges*, F. K. Chow, S. F. De Wekker, and B. J. Snyder, Eds. Dordrecht: Springer Netherlands, 2013, pp. 291–344.

S. Das, A. Maitra, and A. K. Shukla, "Melting layer characteristics at different climatic conditions in the Indian region: Ground based measurements and satellite observations," *Atmos. Res.*, vol. 101, no. 1-2, pp. 78–83, 2011.

L. De Montera, L. Barthès, C. Mallet, and P. Golé, "The Effect of Rain —No Rain Intermittency on the Estimation of the Universal Multifractals Model Parameters," *J. Hydrometeor*, vol. 10, no. 2, pp. 493–506, 2009.

F. Fabry and I. Zawadzki, "Long-term radar observations of the melting layer of precipitation and their interpretation," *J. Atmos. Sci*, vol. 52, pp. 838–851, 1995.

F. Fabry, A. Bellon, and I. Zawadzki, "Long Term Observations of the Melting Layer Using Vertically Pointing Radars," Cooperative Centre for Research in Mesometeorology, Montréal, Tech. Rep. MW-101, August, 1994.

U. Germann and J. Joss, "Mesobeta profiles to extrapolate radar precipitation measurements above the Alps to the ground level," *J. Appl. Meteor.*, vol. 41, pp. 542–557, 2002.

——, *Operational Measurement of Precipitation in Mountainous Terrain*. Springer Berlin Heidelberg, 2004, ch. 2, pp. 52–77.

U. Germann, M. Boscacci, M. Gabella, and M. Sartori, "Peak Performance; radar design for prediction in the Swiss Alps," *Meteorological Technology International*, pp. 42–45, apr 2015.

W. R. Gray, M. J. Uddstrom, and H. R. Larsen, "Radar surface rainfall estimates using a typical shape function approach to correct for the variations in the vertical profile of reflectivity," *Int. J. Remote. Sens*, vol. 23, no. 12, pp. 2489–2504, 2002.

J. Harris, K. P. Bowman, and D. B. Shin, "Comparison of freezing-level altitudes from the NCEP reanalysis with TRMM precipitation radar brightband data," *J. Climate*, vol. 13, no. 23, pp. 4137–4148, 2000.

J. J. Helmus and S. M. Collis, "The Python ARM Radar Toolkit (Py-ART), a Library for Working with Weather Radar Data in the Python Programming Language," *Journal of open research software*, vol. 4, no. e25, 2016.

R. A. Houze, "Orographic effects on precipitating clouds," *Rev. Geophys*, vol. 50, no. 1, pp. 1–47, 2012.

R. A. Houze and S. Medina, "Turbulence as a Mechanism for Orographic Precipitation Enhancement," *J. Atmos. Sci*, vol. 62, no. 10, pp. 3599–3623, 2005.

J. Joss and R. Lee, "The Application of Radar-Gauge Comparisons to Operational Precipitation Profile Corrections," *J. Appl. Meteor.*, vol. 34, no. 12, pp. 2612–2630, 1995.

J. Joss and A. Pittini, "Real-time estimation of the vertical profile of radar reflectivity to improve the measurement of precipitation in an Alpine region," *Meteorol. Atmos. Phys*, vol. 47, no. 1, pp. 61–72, 1991.

P. E. Kirstetter, H. Andrieu, B. Boudevillain, and G. Delrieu, "A Physically based identification of vertical profiles of reflectivity from volume scan radar data," *J. Appl. Meteorol. Clim*, vol. 52, no. 7, pp. 1645–1663, 2013.

F. Lumb, "Sharp snow-rain contrasts-an explanation," *Weather*, vol. 38, pp. 71–73, 1983.

G. Marigo, T. Robert-Luciani, and A. Crepaz, "Snow level forecasting methods and parameters: two practical examples on eastern Italian Alps," in *13th Mtn. Meteor. Conf.*, Whistler, Canada, 2008.

J. Marwitz, "The kinematics of orographic flow during Sierra storms," *J. Atmos. Sci*, vol. 40, pp. 1218–1227, 1983.

T. Matsuo and Y. Sasyo, "Melting of Snowflakes below Freezing Level in the Atmosphere," *J. Meteorol. Soc. Jpn*, vol. 59, no. 1, pp. 10–25, 1981.

S. Medina, B. F. Smull, R. a. Houze, and M. Steiner, "Cross-Barrier Flow during Orographic Precipitation Events: Results from MAP and IMPROVE," *J. Atmos. Sci*, vol. 62, no. 1985, pp. 3580–3598, 2005.

G. H. Roe, "Orographic Precipitation," *Annu. Rev. Earth. Pl. Sc*, vol. 33, no. 1, pp. 645–671, 2005.

J. V. Rudolph and K. Friedrich, "Seasonality of vertical structure in radar-observed precipitation over southern Switzerland,"

J. Hydrometeorol, vol. 14, no. 1, pp. 318–330, 2013.

J. F. Rysman, S. Verrier, Y. Lemaître, and E. Moreau, "Space-time variability of the rainfall over the western Mediterranean region: A statistical analysis," *J. Geophys. Res. Atmos*, vol. 118, no. 15, pp. 8448–8459, 2013.

M. T. Stoelinga, R. E. Stewart, G. Thompson, and J. M. Thériault, "Microphysical Processes Within Winter Orographic Cloud and Precipitation Systems," in *Mountain Weather Research and Forecasting: Recent Progress and Current Challenges*, F. K. Chow, S. F. De Wekker, and B. J. Snyder, Eds. Dordrecht: Springer Netherlands, 2013, pp. 345–408.

M. Thurai, E. Deguchi, T. Iguchi, and K. Okamoto, "Freezing height distribution in the tropics," *Int. J. Satell. Co. Netw*, vol. 21, no. 6, pp. 533–545, 2003.

S. Verrier, C. Mallet, and L. Barthès, "Multiscaling properties of rain in the time domain, taking into account rain support biases," *J. Geophys. Res. Atmos*, vol. 116, no. 20, 2011.

B. Vignal, G. Galli, J. Joss, and U. Germann, "Three methods to determine profiles of reflectivity from volumetric radar data to correct precipitation estimates," *J. Appl. Meteorol*, vol. 39, no. 1999, pp. 1715–1726, 2000.

B. Vignal, H. Andrieu, and J. D. Creutin, "Identification of Vertical Profiles of Reflectivity from Volume Scan Radar Data," *J. Appl. Meteorol*, vol. 38, pp. 1214–1228, 1999.

D. Wolfensberger, D. Scipion, and A. Berne, "Detection and characterization of the melting layer based on polarimetric radar scans," *Q. J. Roy. Meteor. Soc.*, vol. 142, no. August, pp. 108–124, 2016.

J. Zhang and Y. Qi, "A Real-Time Algorithm for the Correction of Brightband Effects in Radar-Derived QPE," *J. Hydrometeorol*, vol. 11, no. 5, pp. 1157–1171, 2010.

D. S. Zrnic, N. Balakrishnan, C. L. Ziegler, V. N. Bringi, K. Aydin, and T. Matejka, "Polarimetric Signatures in the Stratiform Region of a Mesoscale Convective System," *J. Appl. Meteorol*, vol. 32, no. 4, pp. 678–693, 1993.

Alternative data processing for Micro Rain Radar (MRR) Observations

Albert Garcia-Benadí[1], Joan Bech[2], Sergi Gonzalez[2,3] and Joaquin del Rio Fernandez[1]

[1]*Universitat Politècnica de Catalunya (UPC), 08800 Vilanova i la Geltrú , Spain*
[2]*Deparment of Applied Physics – Meteorology, University of Barcelona, Spain*
[3]*AEMET, Barcelona, Spain*
(Dated: June 2018)

1 Introduction

The main function of weather radars is to provide a description of the precipitation field, typically in four dimensions: temporal evolution of a 3D field, the determination of precipitation, rainfall intensity and the path of storms. Some radars, as the one used in this study, are designed to observe only vertical profiles.

The radar used in this work a Frequency Modulated Continuous Wave Radar (FMCW) (Strauch et al., 1976) radar. The main difference between a pulsed and a FMCW radar is that the latter transmits continuously and can change its frequency modulation to change the vertical resolution while the pulsed radar emits a great power in a short time at regular intervals. Pulsed transmitters are typically used in weather radars systems working at mid and long ranges while FMCW systems are used in low power transmitters often for shorts ranges applications. The next section describes some characteristics of the FMCW radar used in this study, the Micro Rain Radar (MRR).



Figure 1: Micro Rain Radar from the University of Barcelona installed at Cerdanya (Catalonia) (source: J. Bech)

The MRR manufacturer offers the equipment with its own software of analysis, but some researchers (for example (Maahn and Kollias, 2012), (Adirosi et al., 2016) among others) have proposed other approaches. The premise of the software is to consider that the raindrop is falling at terminal velocity, which is usually valid for stratiform precipitation, but not for convective storms. Another hypothesis is that the hydrometeors always are in liquid phase, but in numerous occasions this conditions is not met. The shape of snow, crystals or flakes, is completely different from water drops and also the terminal velocity and the complex refractive index.

2 Equipment and Measuring principles

2.1 Equipment

The main equipment is the meteorological radar from Metek, model MRR-2 (Micro Rain Radar). The characteristics of the MRR are shown in Table 1

Table 1: Main characteristics of Micro Rain Radar.

Manufacturer	Metek
Model	MRR-2
Frequency (GHz)	24.23
Radar Type	FMCW
Transmit Power (mW)	50
Receiver	Single polarization
Radar Power consumption (W)	25
System power consumption (incl. antenna heating) (W)	225
Number of range gates	32
Range resolution (m)	10-200
Resulting measuring range (km)	3.1
Antenna diameter (m)	0.6
Beam width (2-way,6 dB)	1.5º
Nyquist velocity range (m s^{-1})	±6.0 (0 to +11.9)
Number of spectral bins	64
Spectral resolution (m s^{-1})	0.19
Averaged Spectra (Hz)	5.8

The equipment can be divided in 2 hardware element: the antenna dish with the transmitter, and the processing unit data. A heating system is available in the dish to avoid the accumulation of snow.

In the characteristics from MRR radar the power emission is low (50 mW) and its dish diameter is around 0,6 meters. These values make this radar safe, so it can be located in a city, or town, without a big protecting building as in the case of pulsed radars.

Another important factor is the number of range gates, or number of range bins, that the radar is able to process. In this case, the effective range bins number is 31 because the first gate corresponding to 0 m is removed in the processing. The locations of this height can be changed with the frequency modulation; in this case the vertical resolution can be changed from 10 to 200 meters. The choice in this work is a resolution of 100 meters. The choice of vertical resolution marks the maximum height of measurements, in our choice 3.1 km.

The frequency of the equipment is 24.23 GHz thus the wavelength emission from the equipment is around 12 mm. This point is very important because the wavelength is comparable with the size of the drop, so Rayleigh scattering approximation is not valid and the Mie scattering is used.

The number of spectral bins per range gate is another important parameter. Each spectral bin corresponds to a velocity. The resolution of the spectral bin is given from frequency, speed light, number of bins and number of gates. Table 1 shows the speed resolution is around 0.19 $m \cdot s^{-1}$. This limitation implies that the velocity range is from 0 to 12 $m \cdot s^{-1}$.

2.2 Measurement principles

The radar emits vertically and receives the backscattering signal. This signal is function of the velocity of the hydrometeor that are falling, and also of their dielectric constant (for example liquid water, ice and wet snow). In this work is assumed the hydrometeors are in liquid phase similarly as ordinary weather radars.

From this point there are two physical approaches for the treatment of signal. The first one is to consider that the diameter of the raindrops is similar to the radar wavelength, and the other way is to consider that the raindrops are much smaller than the wavelength. The consequences of this decision transform all necessary calculations to obtain Z (dBZ) and the falling velocity W(m s^{-1}). In fact, this paper analyses and makes comparisons between these two approaches, where the first one is supported by manufacturer (Messtechnik, 2015) because it assumes the wavelength of radar is similar to the diameter of the raindrop. Thus it is necessary to calculate the backscattering cross section with the hypothesis that the raindrops are falling at

terminal velocities using the Mie theory. The second way adopted by (Maahn and Kollias, 2012) and use the Rayleigh approximation because assumes that the diameter of hydrometeors is smaller than the wavelength, and can be used the usual equation for meteorological radar without hypothesis about the terminal velocities.

The paper explains in detail the two ways and the choice chosen.

3 Calculation process

In this section are described all steps necessary to calculate the moments as reflectivity and the falling velocities from the two methods, terminal and non-terminal velocities:

3.1 Format from file

The starting point for both methods is the radar raw data. The values in raw data files are in ASCII and contain several variables: the transfer function (*TF(i)*, specific by each range bin), and the constant of calibration (specific for each radar), and the values of *f(n,i)* expressed in engineer units for all Doppler bin *n* and range bin *i*.

In both methods the conversion of *f(n,i)* to *η(n,i)* is necessary. Figure 2 shows the first lines of a raw data file.

```
MRR 170324000006 UTC DVS 6.10 DSN 0509076064 BW 39275 CC 2245847 MDQ 100 58 58 TYP RAW
H          0      100      200      300      400      500      600      700      800      900
TF  0.003915 0.013457 0.048446 0.112307 0.199046 0.299241 0.406655 0.515048 0.611818 0.701493
F00     1032      345       10       11        9        8        7        9        8        9
F01      599      207       10       13       12       12        9       10       11       10
F02      113       44       12       14       15       17       13       14       14       12
F03        8        8       12       13       14       16       14       16       16       13
F04        3        5       11       15       14       14       12       15       16       15
F05        3        5       12       18       16       13       12       13       15       15
F06        3        7       12       17       16       14       14       14       13       13
F07        3        8       11       13       16       17       15       14       12       12
F08        3        7       10       12       16       19       16       13       12       11
F09        3        6       10       13       17       19       17       13       13       10
F10        2        6       10       14       17       18       17       15       14       11
F11        2        7       12       15       18       17       16       16       15       13
```

Figure 2: Example of data from a MRR raw data file

It is important to notice that the Digital Signal Processing (DSP) of the MRR generates about 10 power spectra per second, and with the standard operation parameters, the DSP transfers averaged spectra every 10 seconds to the data acquisition unit. The data transfer via the serial interface takes about 4 seconds. During this time no measurement is possible. Hence the raw data file is created in 10 seconds where the first 6 seconds are acquisition of data and the other 4 seconds are used to make the raw data file. Thus the stochastic standard deviation of spectral powers is reduced to 13% or 0.53 dB, because the system average 60 spectra instead of 100 spectra.

3.2 Signal determination

An evaluation criterion of variance, to detect per each height if there is relevant signal, is used to improve the speed of processing program. The criteria is detailed in (3.1):

$$\frac{V}{E} \geq \frac{0.6}{\sqrt{\Delta t}} \qquad (3.1)$$

where E is the average spectrum, V is the variance of the spectrum and Δt is the time of the spectrum, in this case 10 s.

If the value of the ratio between E and V is higher than the other terms the spectrum pass the filter and will be evaluated. If the spectrum does not pass the criteria is considered as “no data”. The value of 0.6 is quiet conservative, but it is used as starting point.

The second filter is based in (Hildebrand and Sekhon, 1974) and the filter condition is shown in (3.2). If the spectrum does not pass the filter then it is considered as “no data”

$$\frac{E^2}{V} \geq n \qquad (3.2)$$

where E is the average spectrum and V is the variance of the spectrum. The value of n= 58 is acceptable for a spectrum recorded every 10 s.

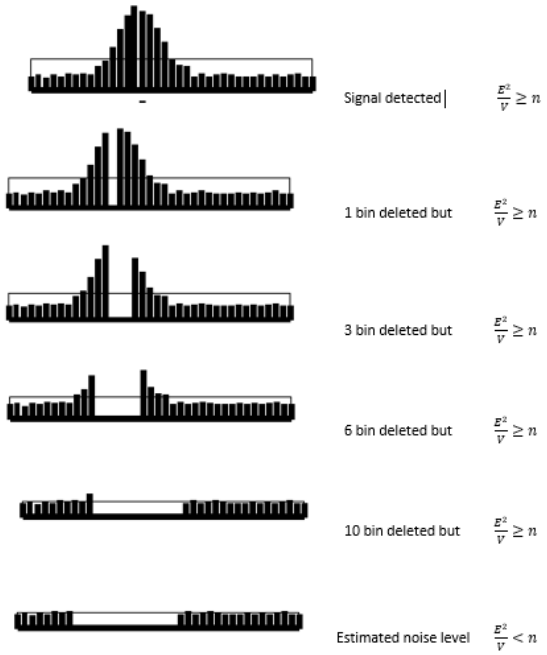


Figure 3: : Process to calculate the noise level in (Messtechnik, 2015) *way*

3.3 Noise determination

In this point resides the main contribution of this work to improve the post-processing of MRR raw data. In the case of signal detection, the noise evaluation from MRR radar data is to consider the noise as "white noise", or independent of the frequency. (3.2) is used to determinate this noise.

In the manufacturer's processing (Messtechnik, 2015) exists a loop where the maximum signal is eliminated and then it checks again the algorithm details in (3.2). This loop stops when the condition is not accomplished. When it occurs, the remained signal value is estimated as noise and subtracted from signal. (See Figure 3.). Following this approach the process of noise determination does not use all bins. Figure 5 shows the minimum bin (blue) until the maximum bin (red) used, hence the manufacturer does not use whole interval of velocities, only a part of available spectral bins.

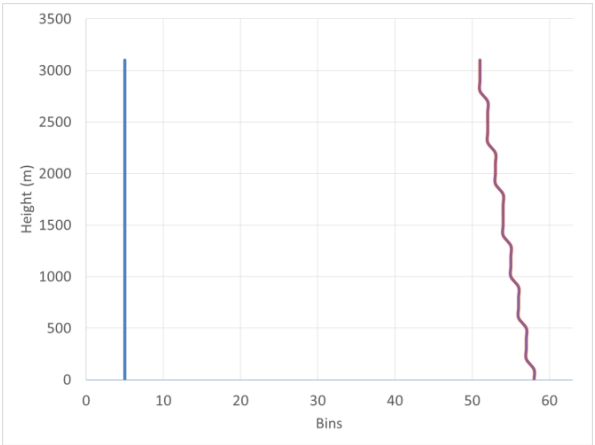


Figure 4: : Relation of the bin used by (Messtechnik, 2015)

In case of (Maahn and Kollias, 2012) the process is dynamic and is calculated for each range bin. The dynamic detection of the noise level at each range allows the detection of weak echoes and the elimination of artifacts caused by radar receiver instabilities. Similar as the (Messtechnik, 2015) method with (3.2), but it only gets the maximum and adjacent bins. Another process to detect false signals has been applied and detailed at (Maahn and Kollias, 2012). In the code of IMProToo from (Maahn and Kollias, 2012) various fields are interpolated for this purpose, specially the gates number 0, 1 and 30, corresponding to heights, and the bins 1, 2 and 64 corresponding to velocities.

In this work the noise determination is realized using an new algorithm to detect the peak value. The advantage of this method is to consider all bins in all heights. Which allows to detect weak echoes.

In Figure 5, the left panel) the detection of a weak echo and the correction of noise level is shown. The middle panel shows the use of bins that the other methodologies have not used and the right panel the algorithm marks as "no data" an input signal.

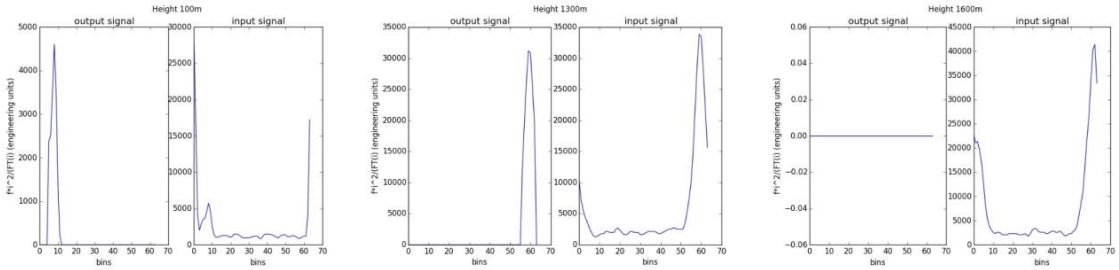


Figure 5: : Example of our own algorithm of noise determination. Left: at 100 m, the first height, of a weak echo from raw data file of real values. (Source: 0116.raw). Middle: at 1300 m. (Source: 0325.raw) Right: at 1600 m (Source: 0325.raw)

3.4 Spectrum average

In section 2.1 it was detailed the processing of the spectrums for all heights created every 10 seconds, but it is interesting to determinate the value for other period. The most usual is 60 seconds. For this reason, it is necessary to average the input signal. This seems easy, but here, the processing task is very important. In this work the program finds the null values and applies a configurable filter. This filter consists in determining the number of null on the number of samples at each height. The number of null number is configurable and is shown in Figure 6 wherein the limit acceptance is set to 50 %. Thus in the best case in a minute the system generates 6 spectrums, with this filter only will be good if the detection ise during 30 seconds.

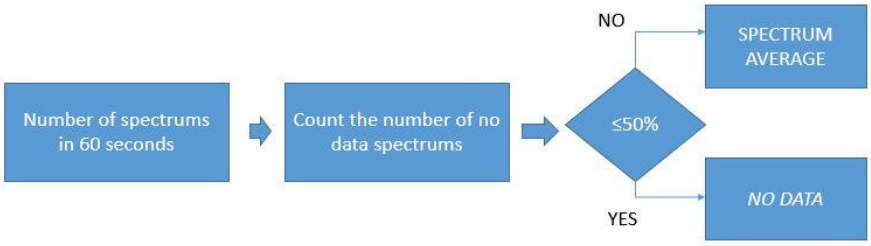


Figure 6: : Filter function in spectrum average

If the numbers of nulls is less than 50% of the size sample the sample is considered good and the averaged is done with the non nulls values. If the number is over 50%, the size sample result is a null sample. This filter allows increasing the threshold of detection.

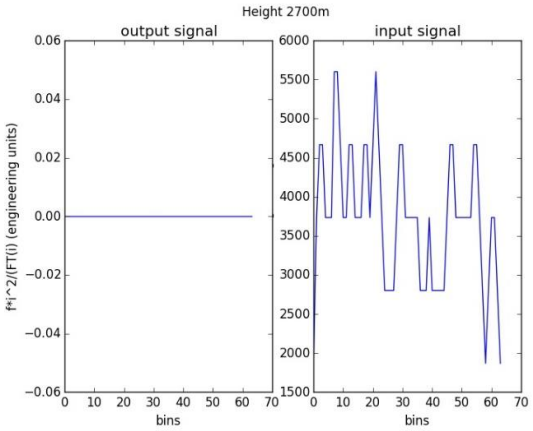


Figure 7: : Example noise detection signal from raw data file of real values. (Source: 0325.raw)

3.5 Dealiasing processing (Velocity folding)

The dealiasing processing is proposed by (Maahn and Kollias, 2012). This phenomenon occurs when the observed Doppler velocity exceeds the Nyquist velocity boundaries (±6 m s^{-1}) of MRR. The MRR Doppler spectra records have a velocity range from 0 to +12 m s^{-1}. Thus, by default the MRR assumes the absence of updrafts (negative velocity) considering that all negative velocities are from hydrometeors with a terminal velocity that exceed +6 m s^{-1}.

This hypothesis of terminal velocity is good enough for rain but does not apply to snow. For this reason to apply the dealiasing methodology is recommended. Figure 8 shows the contribution of the dealiasing process in the analysis of data and Figure 9 shows the detection from this work.

The treatment of dealiasing process consists in the evaluation of the spectrum at one height and the immediately upper and lower range bins at the same time. First it is necessary to calculate the reflectivity at this height, and then to calculate the velocity estimated, using the equation from (Atlas et al., 1973) and doing the average between the velocity estimated by snow and rain.

The dealiasing process consists in the evaluation of three range bins: current, lower and upper bins, where the velocities are from 0 m·s^{-1} to 12 m·s^{-1}, from -12 m·s^{-1} to 0 m·s^{-1} and from 12 m·s^{-1} to 24 m·s^{-1} respectively. The maximum of each height closest to the velocity estimated will be considered to be the true value, and indicates the existence of updrafts if closest maximum is the lower range bin, downdrafts if the closest maximum is the upper range bin or none if the maximum is the current height.

The dealiasing is also implemented in the program done, but note that it is only interesting when there is a snowstorm because then the vertical velocities are very influenced by updrafts and its fall velocities can be less than 2 m s^{-1}.

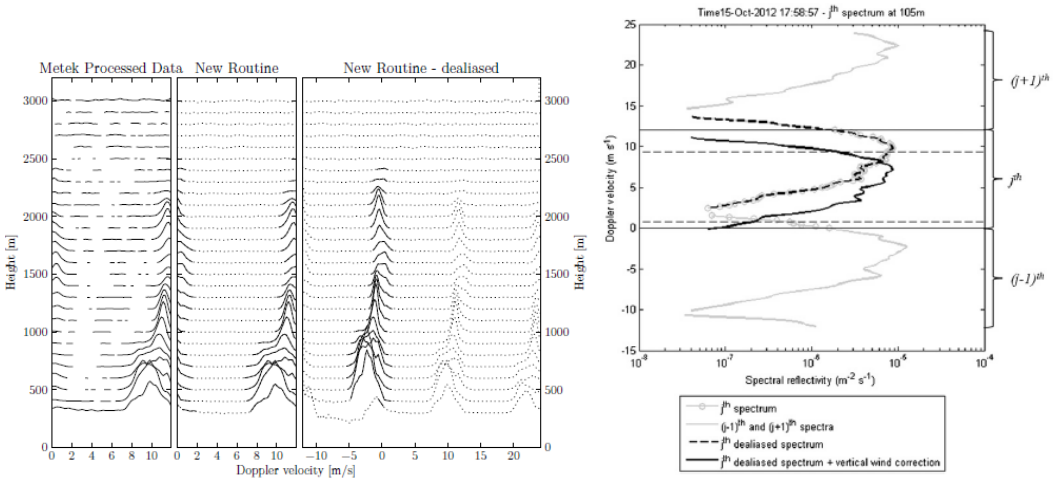


Figure 8: : Right: Example "Waterfall" diagram from (Maahn and Kollias, 2012),*left: Example correction by dealiasing from the work* (Adirosi et al., 2016)

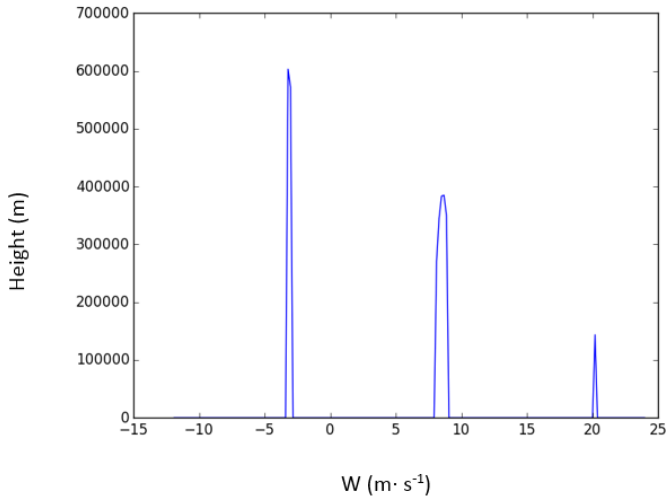


Figure 9: : Example of detection of the three velocities from our application

3.6 Drop size distribution N(D,i)

Assuming that hydrometeors fall with their terminal fall speed is the MRR manufacturers choice (Messtechnik, 2015). This choice allows to relate some parameters as the diameter of the raindrops, with their velocity and then to calculate the backscattering cross sections following the relation of (Atlas et al., 1973) and (Gunn and Kinzer, 1949).

If the diameter is known, the particle backscattering cross section, σ(D) can be calculated using the Mie Theory. However this theory has not an analytical equation. The result is a matrix of values in function of height *(i)* and Doppler spectrum *(n)* where the diameters from raindrop must be calculated detailed in (3.3):

$$D_{nn} = -\frac{1}{0.6} \cdot ln\left\{\frac{1}{10{,}3} \cdot \left(9{,}65 - \left(\frac{v}{\delta v}\right)\right)\right\} \quad (3.3)$$

where :

v is the terminal velocity from (3.4)

$$v(n) = n \cdot \Delta f \cdot \frac{\lambda}{2} \quad (3.4)$$

And δv is the correction for height δv and h is in meters (3.5).

$$\delta v = 1 + 3{,}68 \cdot 10^{-5} \cdot h + 1{,}71 \cdot 10^{-9} \cdot h^2 \quad (3.5)$$

Once the diameters from drops, in every range bin, have been calculated, it is important to remember that the σ(D) is also a function of the complex refractive index *m*. Basically it is necessary to calculate the value for $|K|^2$ following (3.6):

$$|K|^2 = \left|\frac{m^2 - 1}{m^2 + 1}\right|^2 \quad (3.6)$$

where the value of $|K|^2$for liquid water is 0.92 and for ice spheres of 0.18.

In this work, the matrix of the backscattering cross section is implemented using a Matlab functions from (Mätzler, 2002), and the results are saved in a txt file. The txt file will be used in our python code. The reason to use Matlab is because the function of Mie theory in python has not been checked and in Matlab it is implemented.

Once the backscattering cross section has been calculated the next parameter is the drop size distribution N(D) detailed in (3.7), that will be necessary for the moments calculations

$$N(D) = \frac{\eta(D,i)}{\sigma(D)} \quad (3.7)$$

where:

σ(D)is the backscatter cross section

η(D,i) is calculate follows (3.8)

$$\eta(D,i) = \eta(v,i) \cdot 6.18 \cdot \delta v(i \cdot \Delta h) \cdot exp(-0.6 \cdot D) \quad (3.8)$$

where D is the diameter from raindrop in mm.

For the case of (Maahn and Kollias, 2012) these parameters are not necessary because follow the Rayleigh approximation.

The use of Mie Theory or Rayleigh approximation affect at the backscattering cross section as shown in Figure 10,

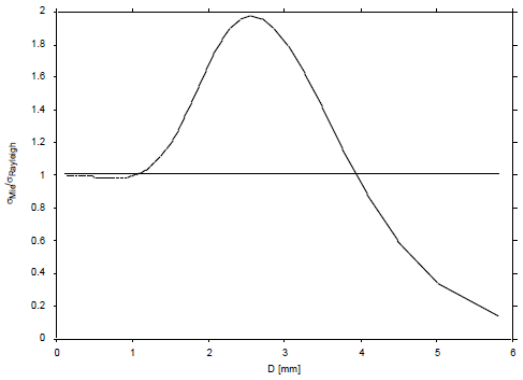


Figure 10: : Single particle backscatter cross section of water droplets at 24,1 GHz normalized with the Rayleigh backscatter cross section. (Extracted from (Messtechnik, 2015)*)*

3.7 N(D) with attenuation correction

The intensity of radar electromagnetic waves is attenuated on the propagation path by different processes. The absorption by water vapour at 24 GHz, around 0,2 dB/km, is neglected because the path considered is around 3 km. But the rain intensity can attenuate significantly at moderate and higher rain rates, when the altitude is considered. To deal this problem, the attenuation correction is implemented follows the method discussed in detail by (Peters et al., 2010). Thus a loop for all height and all Doppler spectra is necessary to calculate the Path Integrated rain Attenuation denoted as PIA. In this loop parameter used is the single particle extinction coefficient, denoted by σ_e, and described in the Mie theory.

The calculation starts in the first range gate *i*=1 ,

$$PIA(r_0) = 1 \tag{3.9}$$

$$N_p(D_{nn}, r_i) = N_a(D_{nn}, r_i) \cdot PIA(r_{i-1}) \tag{3.10}$$

$$\kappa_p(r_i) = \sum_{nn_min(h)}^{nn_max(h)} \sigma_e(D_{nn}) \cdot N_p(D_{nn}, r_i) \cdot \Delta D_{nn} \tag{3.11}$$

$$N(D_{nn}, r_i) = -N_p(D_{nn}, r_i) \cdot \frac{ln(1 - 2 \cdot \kappa_p(r_i) \cdot \Delta r)}{2 \cdot \kappa_p(r_i) \cdot \Delta r} \tag{3.12}$$

$$\kappa(r_i) = \sum_{nn_min(h)}^{nn_max(h)} \sigma_e(D_{nn}) \cdot N(D_{nn}, r_i) \cdot \Delta D_{nn} \tag{3.13}$$

$$PIA(r_i) = PIA(r_{i-1}) \cdot exp(2 \cdot \kappa_p(r_i) \cdot \Delta r) \tag{3.14}$$

If PIA(r_i)>10 then the loop finishes, but if the condition is false then the counter is incrfemented i=i+1 and starts again in equation (3.9). In these equations the subindex a denoted the parameter without attenuation correction, κ is the specific rain attenuation, Δr is the range resolution from the range bins and ΔD_{nn}

$$\Delta D_{nn} = {}^{(D_{nn+1} - D_{nn-1})}/_{2} \tag{3.15}$$

for all nn except for the minimum value of nn where ΔD_{nn}

$$\Delta D_{nn} = D_{nn+1} - D_{nn} \tag{3.16}$$

and except for the maximum value of nn where ΔD_{nn}

$$\Delta D_{nn} = D_{nn} - D_{nn-1} \tag{3.17}$$

This loop is only applied for PIA≤10 because the algorithm becomes unstable for large values

3.8 Reflectivity calculation

Reflectivity is a basic target magnitude for a weather radar. It is obtained from noise detection, filtering and data connection with PIA. Different calculation approaches are used by (METEK, 2016) and (Maahn and Kollias, 2012).

In the case of (METEK, 2016) the equation (3.18) used:

$$Z = 10 \cdot log\left[10^{-3} \sum_{n=n_{min}}^{n=n_{max}} \frac{N_n \cdot D_n^6 + N_{n-1} \cdot D_{n-1}^6}{2} \cdot (D_n - D_{n-1})\right] \quad (3.18)$$

while the option of (Maahn and Kollias, 2012) follows (3.19):

$$Z = 10^{18} \cdot \frac{\lambda^4}{\pi^5} \cdot |K|^2 \cdot \int \eta(v) dv \quad (3.19)$$

this work uses the same equation of (Messtechnik, 2015).

Another important parameter is the fall velocity *W*, which is calculated (METEK, 2016) follows (3.20):

$$W = f_{Nyquist} \cdot \frac{\sum_{n=n_{min}}^{n=n_{max}} n \cdot F_n}{\sum_{n=n_{min}}^{n=n_{max}} F_n} \quad (3.20)$$

where n is the number of spectral bin and the Fn is the spectral reflectivity.

In the approach of Maahn and Kollias (2012) The fall velocity follows (3.21)

$$W = \frac{\int v \cdot \eta(v) dv}{\int \eta(v) dv} \quad (3.21)$$

In our application it uses (3.22) during the dealiasing process runs.

$$W = \frac{\sum v \cdot \eta(v)}{\sum \eta(v)} \quad (3.22)$$

It is interesting to remark that in the processing by Maahn and Kollias (2012) it absence of the terminal velocity assumption allows to work with η(v), but when assuming the terminal velocities works on η(D). Other authors as Adirosi et al (2016) work with both approaches. The relation to transform *η(n,i)* to *η(v,i)* follows (3.23)

$$\eta(v, i) = \eta(n, i) \cdot \frac{2}{\Delta f \cdot \lambda} \quad (3.23)$$

where:

λ is the radar wavelength and Δf is the frequency resolution in power spectra, in Hz.

4 Product comparison and conclusions

This section shows a comparison of the three methods described above((Maahn and Kollias, 2012; METEK, 2016) and the one proposel here) of as precipitation data recorde at the Cerdanya (NE Spain) on the 24 of March of 2017.

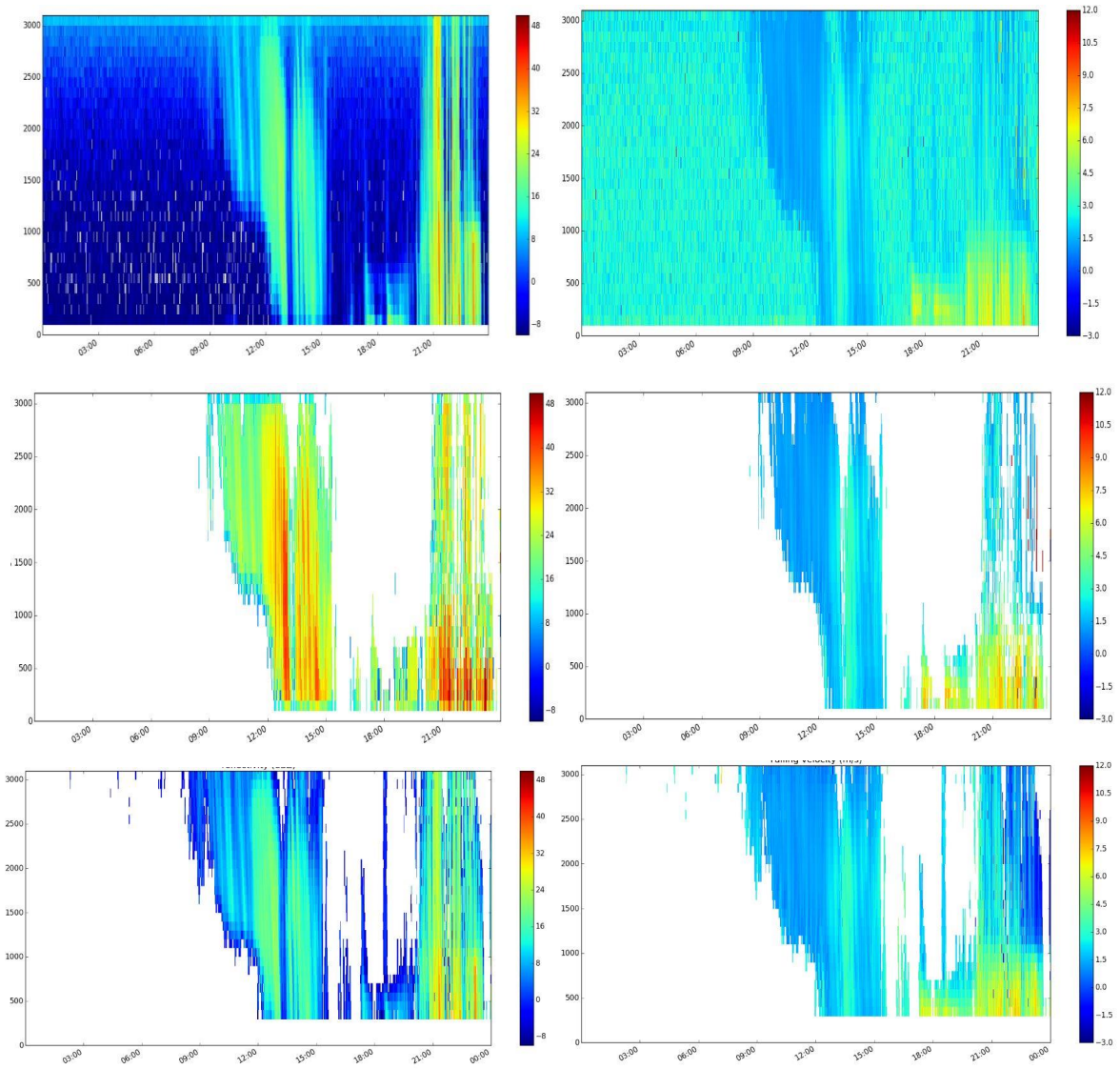


Figure 11: :. Reflectivity (dBZ, left column) and hydrometeor velocity (in m/s, right column) calculated using the methods by (METEK, 2016) *upper panel, the proposal method in middle panel, and lower panel of (Maahn and Kollias, 2012)*

Figure 11 shows various differences between the methodologies. The differences between the manufacturer results and our results are commented because the two methodologies work under the same hypothesis of the terminal velocities. The result of (Maahn and Kollias, 2012) is interesting to see the trend and the noise evaluation of the signal. The first difference is the value of reflectivity (dBZ) higher in our application than the manufacturer. The reason resides in 2 concepts. One is that in our application there are not limit in spectral bins (remember that the manufacturer only uses some spectral bins in function of height, Figure 4) but in our application all bins are used. The other reason is the determination of noise: while the manufacturer may obtain a negative value, in our application this is not possible. Thus the values from the manufacturer always is lower than in our application.

An application for processing data from raw data files has been created trying to improve the noise. The results of the application seem good quantitatively but it is necessary to contrast with other equipment to determinate the possible improvement.

Acknowledgement

This study was partly supported by projects CGL2015-65627-C3-2-R (MINECO/FEDER) and CGL2016-81828-REDT (MINECO)

References

Adirosi, E., Baldini, L., Roberto, N., Gatlin, P., Tokay, A., 2016. Improvement of vertical profiles of raindrop size distribution from micro rain radar using 2D video disdrometer measurements. Atmos. Res. 169, Part, 404–415. doi:https://doi.org/10.1016/j.atmosres.2015.07.002

Atlas, D., Srivastava, R.C., Sekhon, R.S., 1973. Doppler radar characteristics of precipitation at vertical incidence. Rev. Geophys. 11, 1–35. doi:10.1029/RG011i001p00001

Gunn, R., Kinzer, G.D., 1949. THE TERMINAL VELOCITY OF FALL FOR WATER DROPLETS IN STAGNANT AIR. J. Meteorol. 6, 243–248. doi:10.1175/1520-0469(1949)006<0243:TTVOFF>2.0.CO;2

Hildebrand, P.H., Sekhon, R.S., 1974. Objective Determination of the Noise Level in Doppler Spectra. J. Appl. Meteorol. 13, 808–811. doi:10.1175/1520-0450(1974)013<0808:ODOTNL>2.0.CO;2

Maahn, M., Kollias, P., 2012. Improved Micro Rain Radar snow measurements using Doppler spectra post-processing. Atmos. Meas. Tech. 5, 2661–2673. doi:10.5194/amt-5-2661-2012

Mätzler, C., 2002. MATLAB Functions for Mie Scattering and Absorption. IAP Res Rep 2002–8, 1139–1151. doi:10.1039/b811392k

Messtechnik, M., 2015. MRR Physical Basics Valid for MRR Service Version ≥ 5.2.0.9. Elmshorn.

METEK, 2016. MRR-2 Micro Rain RADAR User Manual.

Peters, G., Fischer, B., Clemens, M., 2010. Rain Attenuation of Radar Echoes Considering Finite-Range Resolution and Using Drop Size Distributions. J. Atmos. Ocean. Technol. 27, 829–842. doi:10.1175/2009JTECHA1342.1

Strauch, R.G., Campbell, W.C., Chadwick, R.B., Moran, K.P., 1976. Microwave FM-CW Doppler radar for boundary layer probing. Geophys. Res. Lett. 3, 193–196. doi:10.1029/GL003i003p00193

Blending Field-Based and Cell Tracking Methods for Improved Precipitation Nowcasting



Seppo Pulkkinen

Seppo Pulkkinen[1] and V. Chandrasekar[2]

[1]*Finnish Meteorological Institute, FI-00101, Helsinki, Finland*
[2]*Colorado State University, CO 80523, Fort Collins, USA*
(Dated: 22 June 2018)

1. Introduction

The current radar-based precipitation nowcasting methods can be broadly divided into two main categories: 1) field- and 2) cell-based. The former estimate the advection field over the whole domain and extrapolate radar echoes along the advection field (e.g. Germann and Zawadzki, 2002). The latter isolate cells containing high precipitation intensities and model the evolution of the parameters, such as position and velocity, of each cell or cluster of cells separately (e.g. Dixon and Wiener, 1993; Johnson et al., 1998; Rossi et al., 2015).

Predictability of precipitation is proportional to spatial scale. Therefore, field-based methods typically filter small scales that have low predictability (e.g. Seed, 2003; Turner et al., 2004). Such methods perform well for large homogenous areas of stratiform precipitation, and the scale filtering improves the overall nowcast skill. However, the drawback is that information about small-scale features containing high intensities, such as convective cells, is lost. This leads to reduced nowcast skill for localized heavy precipitation (Pulkkinen et al., 2018). On the other hand, it has been empirically shown that cell tracking methods perform better when nowcasts of highest precipitation intensities are desired (Ebert et al., 2004; Wilson et al., 2004).

The above methods are deterministic so that they produce only a single nowcast, and do not provide uncertainty estimates. This has led to the development of stochastic extensions of both field- and cell-based methods. The STEPS method (Bowler et al., 2006; Seed, 2003) is an extension of S-PROG, where a field of stochastic perturbations is added to the portion of variance not explained by the deterministic S-PROG nowcast. A stochastic perturbation scheme is also applied to the advection field. On the other hand, the cell-based method of Rossi et al. (2015) uses a Kalman filter for producing smooth motion trajectories and modeling the probability distributions of the uncertainties in cell position and velocity estimates.

The objective of this study is to develop a novel nowcasting method that combines the strengths of probabilistic field- and cell-based nowcasts. The former is merged with the latter in areas of high intensity. The experiments are done using radar reflectivity composites from the radar network operated by the Finnish Meteorological Institute (FMI).

2. Methodology

2.1. Field-based nowcasting

As the field-based nowcasting method, we use STEPS (Bowler et al., 2006) that is based on the deterministic S-PROG method (Seed, 2003). A detailed description of the STEPS implementation used here is given in Pulkkinen et al. (2018). In S-PROG, the basic idea is to decompose the input reflectivity field Z into a cascade by applying the fast Fourier transform and a bandpass filter. The decomposition is written as

$$Z_{i,j}(t) = \sum_{k=1}^{n} \sigma_k(t) Y_{k,i,j}(t) + \mu_k(t),$$

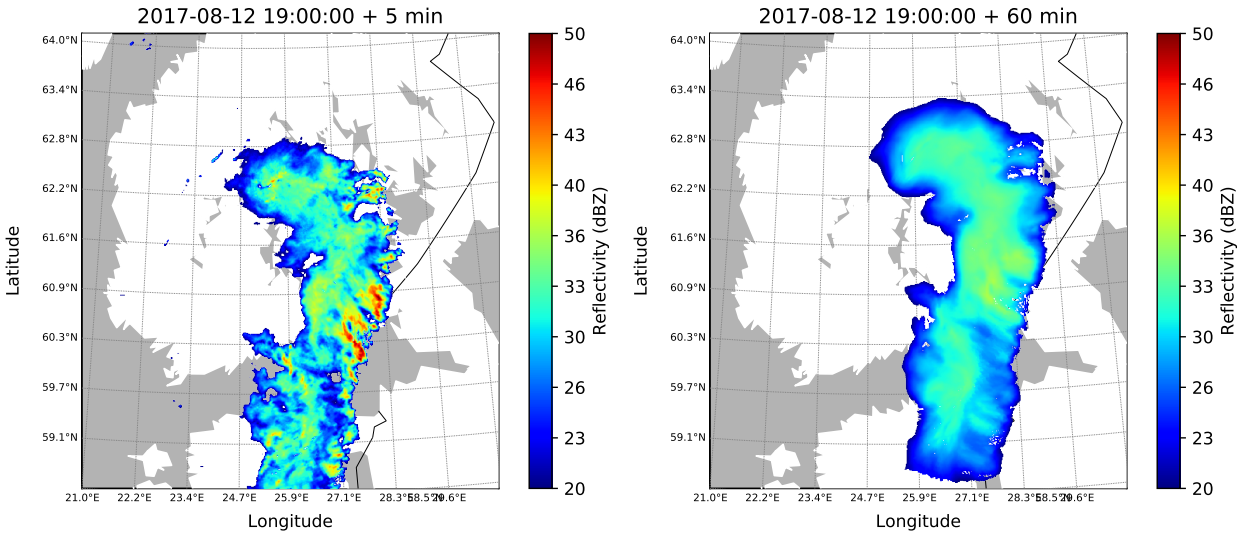
where Z denotes the normalized cascade level, i and j denote spatial coordinates and μ_k and σ_k denote the mean and standard deviation computed for each cascade level. An autoregressive AR(2) model of the form

$$Y^e_{k,i,j}(t+t_l) = \phi_{k,1} Y^e_{k,i,j}(t+t_l-\Delta t) + \phi_{k,2} Y^e_{k,i,j}(t+t_l-2\Delta t) + \phi_{k,0}\varepsilon_{i,j}(t) \tag{2.1}$$

is then applied to each level k. The parameters $\phi_{k,0}$, $\phi_{k,1}$ and $\phi_{k,2}$ are determined from the Yule-Walker equations using time-lagged autocorrelation coefficients of the three most recently measured reflectivity fields. The cascades are in Lagrangian coordinates, so that they are extrapolated to the given time step using the advection field estimated by an optical flow technique and applying a semi-Lagrangian advection scheme (Germann and Zawadzki, 2002). The above model effectively filters small scales having low predictability. This is illustrated in Figure 1 that shows the unperturbed STEPS nowcasts obtained from S-PROG.

Stochastic perturbations are added to account for the variance not explained by the deterministic S-PROG nowcast (the first two terms). The symbol $\varepsilon_{k,i,j}$ in equation (2.1) denotes a Gaussian random field that serves this purpose. In addition,

uncertainties in the advection field are modeled by adding a perturbation field, whose velocity magnitudes are sampled from the exponential distribution and are proportional to the nowcast lead time (Bowler et al., 2006).



(a) 5 minutes

(b) 60 minutes

Figure 1: Unperturbed STEPS nowcasts (S-PROG) with different lead times.

2.2. Cell tracking

The cell-based nowcasting method used here is adapted from Rossi et al. (2015). In our implementation of the method called the Convective Cell Identification, Tracking and Nowcasting (CC-ITN), cells are identified as contour levels of the radar reflectivity mosaic. The identified cells are clustered based on a distance criterion, and intersection area-based matching of cells is applied between consecutive time frames. A Kalman filter model is then employed for estimating smoothed tracks of cluster positions. The model also gives probability distributions of future cell positions, from which nowcast ensembles are generated.

Temporal interpolation is applied in order to enhance robustness of the cell matching. Differently to Rossi et al. (2015), where this is done by using the Kalman filter-estimated velocities, this is done by applying advection-based interpolation to the input data using the optical flow method of Farnebäck (2003), which we have observed to be more robust than the original approach.

A simplified version of the general Kalman filter is applied in Rossi et al. (2015). For a given cluster of cells, the method estimates the unknown state vector $\boldsymbol{x} = (x, \dot{x}, y, \dot{y})^T$ containing the cluster centroid position and velocity based on noisy observations. In the model, the state $\boldsymbol{x}_k$ is assumed to evolve in time according to

$$\boldsymbol{x}_k = \boldsymbol{F}(\Delta t)\boldsymbol{x}_{k-1} + \boldsymbol{w}_{k-1},$$

where the linear state transition model $\boldsymbol{F}(\Delta t)$ is defined as

$$\boldsymbol{F}(\Delta t) = \begin{pmatrix} 1 & \Delta t & 0 & 0 \\ 0 & 1 & 0 & 0 \\ 0 & 0 & 1 & \Delta t \\ 1 & & 0 & 1 \end{pmatrix} \tag{2.2}$$

and Δt denotes the difference between the time steps.

In the above, the term $\boldsymbol{w}_k$ denotes process noise associated with the temporal evolution of the system. In addition, the model assumes that the state $\boldsymbol{x}_k$ is linearly mapped to the observations $\boldsymbol{y}_k$ according to

$$\boldsymbol{y}_k = \boldsymbol{H}_k\boldsymbol{x}_k + \boldsymbol{v}_k,$$

where $\boldsymbol{v}_k$ is a noise term representing measurement uncertainties. In the above, the noise terms $\boldsymbol{w}_k$ and $\boldsymbol{v}_k$ are assumed to be

Gaussian white noise processes with covariance matrices

$$\boldsymbol{Q}(\Delta t) = \sigma_v^2 \begin{pmatrix} \frac{1}{3}\Delta t^2 & \frac{1}{2}\Delta t & 0 & 0 \\ \frac{1}{2}\Delta t & 1 & 0 & 0 \\ 0 & 0 & \frac{1}{3}\Delta t^2 & \frac{1}{2}\Delta t \\ 0 & 0 & \frac{1}{2}\Delta t & 1 \end{pmatrix} \quad \text{and} \quad \boldsymbol{R}_k = \boldsymbol{R} = \begin{pmatrix} r^2 & 0 \\ 0 & r^2 \end{pmatrix}, \tag{2.3}$$

respectively, derived from the white noise acceleration model (Bar-Shalom et al., 1995).

The current state estimate $\boldsymbol{x}_k$ and its covariance matrix $\boldsymbol{P}_k$ are updated via the following two-phase algorithm:

1. Prediction:

$$\hat{\boldsymbol{x}}_k^p = \boldsymbol{F}_{k-1}\hat{\boldsymbol{x}}_{k-1}$$
$$\boldsymbol{P}_k^p = \boldsymbol{F}_{k-1}\boldsymbol{P}_{k-1}\boldsymbol{F}_{k-1}^T + \boldsymbol{Q}_{k-1}$$

2. Update:

$$\hat{\boldsymbol{x}}_k = \hat{\boldsymbol{x}}_k^p + \boldsymbol{K}_\infty(\boldsymbol{y}_k - \boldsymbol{H}_k\hat{\boldsymbol{x}}_k^p),$$

where $\boldsymbol{K}_\infty$ denotes the steady-state Kalman gain to which the iteration converges as the time step k tends to infinity.

The above Kalman filter is applied to computation of 1) smoothed motion trajectories from noisy observations and 2) probabilistic nowcasts of cell positions. For a time step l, the nowcasts are obtained from the prediction equations as

$$\boldsymbol{x}_{k+l} = \boldsymbol{F}(l\Delta t)\boldsymbol{x}_k$$
$$\boldsymbol{P}_{k+l} = \boldsymbol{F}(l\Delta t)\boldsymbol{P}_\infty\boldsymbol{F}(l\Delta t)^T + \boldsymbol{Q}(l\Delta t),$$

where $\boldsymbol{F}$ and $\boldsymbol{Q}$ are defined according to (2.2) and (2.3), respectively, and $\boldsymbol{P}_\infty$ denotes the steady- state covariance matrix. Finally, gridded maps of exceedance probabilities for the given intensity threshold are obtained by approximating the cells by ellipses, and each nowcast ensemble member is obtained by perturbing the centroid positions and setting each pixel in the domain inside/outside the ellipse as one/zero. Empirical exceedance probabilities are computed from the ensembles, and for pixels with multiple overlapping cells, the probability is set to the maximm probability along the individual cells. The ellipse approximations are obtained by applying principal component analysis (PCA) to the vertices of the polygons representing the cells (Rossi et al., 2015).

2.3. The merged probability nowcast

Here we use a simple method for merging the STEPS and CC-ITN nowcasts. We focus on exceedance probabilities that are important for decision making and issuing warnings. The methodology will be extended to quantitative nowcasts of precipitation intensities in a follow-up paper.

The idea is to use a maximum-risk principle, where the exceedance probability is taken as the maximum of the individual nowcasts. That is, the merged probability nowcast is given by

$$P_m^{\mathrm{thr}}(i,j) = \max\{P_{\mathrm{a}}^{\mathrm{thr}}(i,j), P_{\mathrm{c}}^{\mathrm{thr}}(i,j)\},$$

where i and j denote spatial coordinates and $P_{\mathrm{a}}^{\mathrm{thr}}$ and $P_{\mathrm{c}}^{\mathrm{thr}}$ denote the empirical exceedance probabilities of the given intensity threshold computed from the advection- and cell-based nowcast ensembles, respectively. The rationale of this approach is that in order to avoid the loss of nowcast skill, the STEPS nowcast is replaced with the cell-based CC-ITN nowcast in areas where the latter gives predictions of high precipitation intensities. In the following, we use the abbreviation MSC (Merged STEPS and CC-ITN) for the above method.

3. Verification

3.1. Description of the experiments and the verification metrics

Performance of the proposed method was evaluated using eight convective rainfall events in Finland during summers 2016 and 2017. The data was collected using the FMI radar network consisting of 10 C-band radars (see Figure 3). Reflectivity measurements from two lowest elevation angles were interpolated into a 1-kilometer grid with 5-minute temporal resolution, and constant altitude plan position indicator (CAPPI) composites were computed from the gridded measurements. The vertical profile (VPR) correction method of Koistinen and Pohjola (2014) was applied in order to correct range-dependent biases from the radar mosaics. The events in the dataset containing approximately 1000 radar mosaics are listed in Table 1.

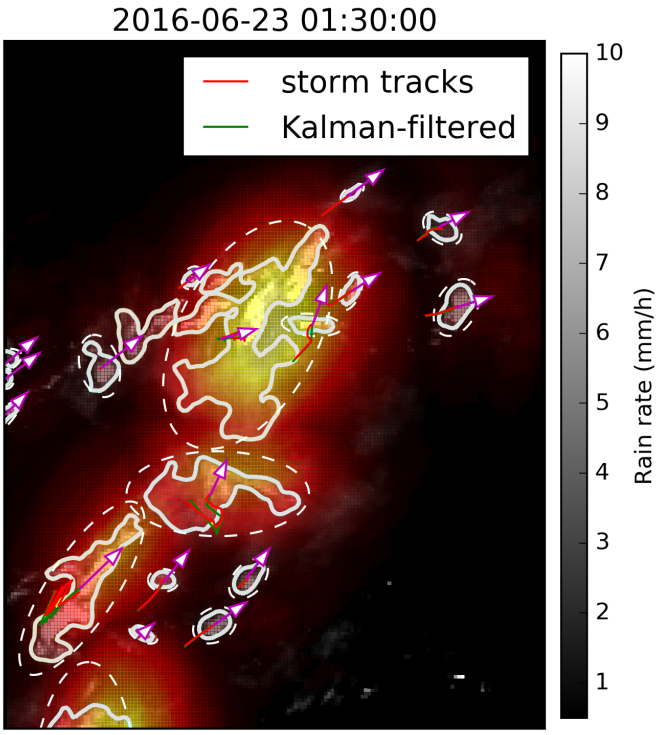


Figure 2: Illustration of a cell-based 20-minute nowcast produced by CC-ITN. The input reflectivity field (converted to rain rate) is plotted with gray shades. The light gray contours represent the cell boundaries corresponding to 35 dBZ threshold. The raw and Kalman-filtered tracks are plotted in red and green, respectively, and the purple arrows illustrate the Kalman filter-based estimates of velocity vectors. Ellipse approximation of the cells are plotted with dashed white lines. Red and yellow colors in the background represent the empirical exceedance probabilities for the 35 dBZ threshold from the nowcast ensembles.

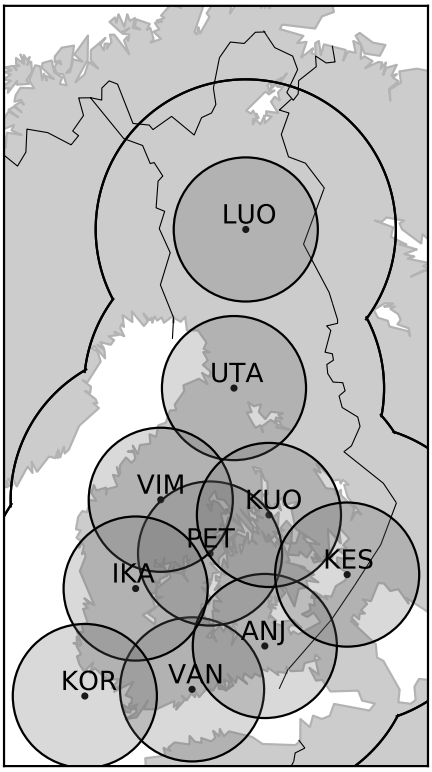


Figure 3: The FMI radar network as of 2016.

For STEPS, the input data was zero-padded in order to obtain square-shaped grids required for the FFT. The nowcasts were generated by using 25 ensemble members and six cascade levels. A detailed description of the STEPS implementation used here is given in Pulkkinen et al. (2018). For CC-ITN, the noise parameters for the Kalman filter were set to $\sigma_v = 5$ km and $r = 5$ km. In the following verification analyses and the CC-ITN method, the intensity threshold for the decision between precipitation and no precipitation is set to 35 dBZ. For computing the STEPS nowcasts, we set this threshold to 10 dBZ.

Table 1: The precipitation events used in the study.

Event	Date	Start time	Duration (hours)
1	27 Jul 2016	04:00	8
2	31 Jul 2016	06:00	15
3	2 Aug 2016	05:00	12
4	3 Aug 2016	07:00	10
5	31 Jul 2017	19:00	8
6	1 Aug 2017	10:00	10
7	12 Aug 2017	14:00	9
8	13 Aug 2017	00:00	11

The reliability diagram (Bröcker and Smith, 2007) measures how well the predicted probabilities of precipitation (intensity above the given threshold) correspond to the observed frequencies. The computations are done by binning the probability range $[0, 1]$ into a set of subintervals. For a reliable forecast, the curve lies on the diagonal (i.e. one-to-one correspondence). The reliability diagram is conditioned on the forecasts: what is the outcome when precipitation was predicted. The diagram is typically accompanied with a sharpness diagram showing a histogram of the predicted probabilities. For a sharp forecast, the probabilities are distributed around one and zero, meaning that the forecast gives definite yes/no predictions.

For the given observation theshold, the Relative Operating Characteristic (ROC) curve (Jolliffe and Stephenson, 2003) measures the ability of the forecast to discriminate between precipitation and no precipitation. The curve is constructed by plotting the probability of detection (POD) against the false alarm rate (POFD) for a set of probability thresholds. The area under the ROC curve is typically used when a summary measure of the plot is desired. As opposed to the reliability diagram, the ROC curve is conditioned on the verifying observations: given that precipitation/no precipitation occurred, what was the outcome of the forecast.

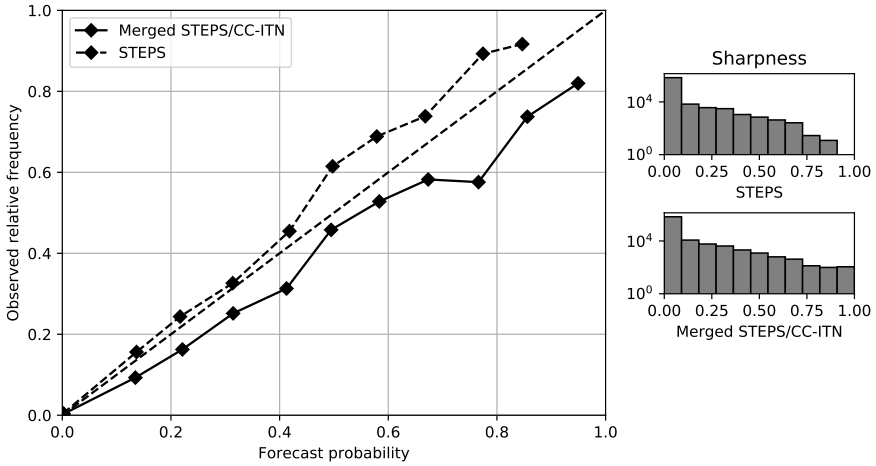
3.2. Results

Figure 4a shows reliability diagrams computed for forecast probabilities that precipitation intensity exceeds the 35 dBZ threshold. The STEPS and MSC methods both show good correspondence between the forecast and observed precipitation probabilities. However, the merged MSC nowcasts show slight overestimation, which indicates that the spread of the ensembles produced by CC-ITN is possibly too small. This could potentially be fixed by using more carefully chosen values of the noise parameters σ_v and r. From Figure 4a, we can also observe that the applying the merging scheme increases the sharpness of the nowcasts. This is attributed to the fact that high-intensity precipitation features, such as convective cells, are typically small, and are thus rapidly filtered out by the STEPS model and replaced with stochastic noise as the lead time is increased (see Figure 1). This results into relatively small number of predicted probabilities at the upper end. On the other hand, CC-ITN is better able to preserve such information, which can be seen as increased sharpness in the upper end of the probability range. Similar results were obtained for all lead times (the results are not shown here for brevity).

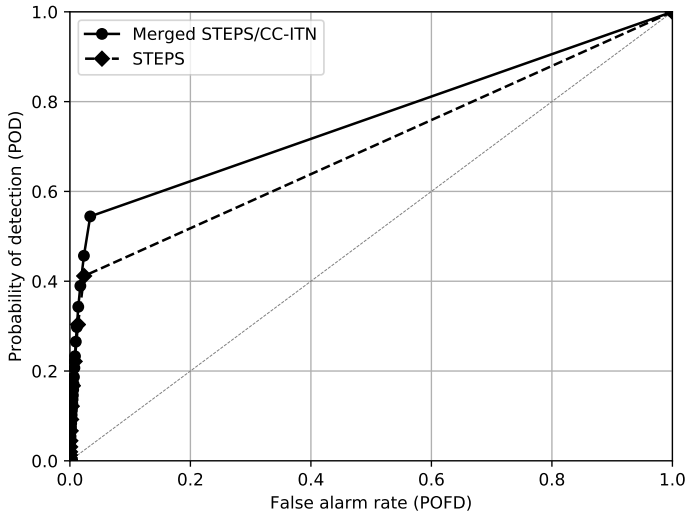
ROC curves for 15-minute STEPS and MSC nowcasts are plotted in Figure 4b for the 35 dBZ threshold. Both methods exhibit similar shape of the curve characterized by low POFD values, and also relatively low POD values. The latter is related to the fact that neither of the methods is able to very accurately predict the higher precipitation intensities that typically have low predicability. Similar behavior was also observed in Pulkkinen et al. (2018) for STEPS nowcasts when the precipitation threshold was set to 35 dBZ. Nevertheless, the merged nowcasts show up to 40% increase in POD compared to the STEPS nowcasts. The areas under the ROC curves are shown in Figure 4c as a function of lead time. For very short lead times (less than 10 minutes), the improvement of the merging compared to the STEPS nowcasts is negligible. However, for longer lead times (over 15 minutes), we can again observe up to a 15% improvement in the nowcast skill. This clearly indicates that for longer lead times, the model used in STEPS discards information about small-scale precipitation features (see Figure 1), whereas this information is better preserved by CC-ITN.

4. Conclusions

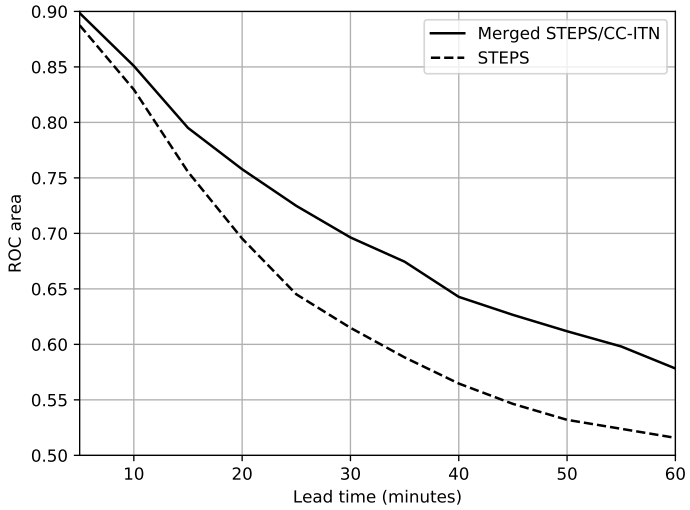
Two different approaches: field- and cell-based methods for radar-based probabilistic precipitation nowcasting were compared, and their strengths and weaknesses were discussed. The STEPS method and the CC-ITN method being developed at FMI were chosen as representative examples of such methods. Promising results were obtained with a simple maximum



(a) Reliability and sharpness diagrams, lead time 15 minutes



(b) ROC curve, lead time 15 minutes



(c) ROC area as a function of lead time

Figure 4: Averaged reliability diagrams, ROC curves for lead time 15 minutes and ROC areas as a function of lead time for the STEPS and MSC nowcasts during the events listed in Table 1.

probability merging scheme that combines the strengths of the two methods: the ability of the former to predict large areas of stratiform precipitation and the ability of the latter to predict the evolution of individual convective cells. The verification scores of the merged nowcasts (MSC) for yes/no forecasts of precipitation above the 35 dBZ threshold showed a significant improvement compared to the STEPS nowcasts.

The cell-based CC-ITN nowcasting method used here is a preliminary implementation that has not been rigorously optimized for the best nowcast skill. Therefore, further improvements in the skill can be expected when merging the STEPS nowcasts with a more advanced cell-based nowcasting scheme. However, the nowcast skill of both methods is limited by the same underlying assumption of Lagrangian persistence, and they share the basic principle of adding stochastic perturbations to the intensity of precipitation features and/or their motion velocities. Therefore, an interesting research direction would be relaxing the above assumptions by incorporating a model for the life cycle of convective cells.

While in this study we considered exceedance probabilities of a fixed intensity threshold (35 dBZ), we are planning to extend the proposed methodology to quantitative nowcasts of precipitation intensities and merging ensembles instead of exceedance probabilities. A more advanced adaptive merging scheme based on the observed skill of the individual nowcasts is also being developed and to be published in a follow-up paper.

Acknowledgement

This research was supported by the Finnish Academy of Science and Letters via the Foundations' Post Doc Pool funding scheme for young scientists working abroad.

References

Y. Bar-Shalom, X. R. Li, and T. Kirubarajan, *Estimation with Applications to Tracking and Navigation: Theory, Algorithms and Software*. Wiley, 1995.

N. E. Bowler, C. E. Pierce, and A. W. Seed, "STEPS: A probabilistic precipitation forecasting scheme which merges an extrapolation nowcast with downscaled NWP," *Quarterly Journal of the Royal Meteorological Society*, vol. 132, no. 620, pp. 2127–2155, 2006.

J. Bröcker and L. A. Smith, "Increasing the reliability of reliability diagrams," *Weather and Forecasting*, vol. 22, no. 3, pp. 651–661, 2007.

M. Dixon and G. Wiener, "TITAN: Thunderstorm identification, tracking, analysis, and nowcasting - a radar-based methodology," *Journal of Atmospheric and Oceanic Technology*, vol. 10, no. 6, pp. 785–797, 1993.

E. E. Ebert, L. J. Wilson, B. G. Brown, P. Nurmi, H. E. Brooks, J. Bally, and M. Jaeneke, "Verification of nowcasts from the WWRP Sydney 2000 forecast demonstration project," *Weather and Forecasting*, vol. 19, no. 1, pp. 73–96, 2004.

G. Farnebäck, "Two-frame motion estimation based on polynomial expansion," in *Image Analysis*, J. Bigun and T. Gustavsson, Eds. Berlin: Springer, 2003, pp. 363–370.

U. Germann and I. Zawadzki, "Scale-dependence of the predictability of precipitation from continental radar images. Part I: Description of the methodology," *Monthly Weather Review*, vol. 130, no. 12, pp. 2859–2873, 2002.

J. T. Johnson, P. L. MacKeen, A. Witt, E. D. W. Mitchell, G. J. Stumpf, M. D. Eilts, and K. W. Thomas, "The storm cell identification and tracking algorithm: An enhanced wsr-88d algorithm," *Weather and Forecasting*, vol. 13, no. 2, pp. 263–276, 1998.

I. T. Jolliffe and D. B. Stephenson, *Forecast Verification: A Practitioner's Guide in Atmospheric Science*. Chichester, UK: John Wiley & Sons, 2003.

J. Koistinen and H. Pohjola, "Estimation of ground-level reflectivity factor in operational weather radar networks using VPR-based correction ensembles," *Journal of Applied Meteorology and Climatology*, vol. 53, no. 10, pp. 2394–2411, 2014.

S. Pulkkinen, V. Chandrasekar, and A.-M. Harri, "Nowcasting of precipitation in the high-resolution Dallas-Fort Worth (DFW) urban radar remote sensing network," *IEEE Journal of Selected Topics in Applied Earth Observations and Remote Sensing*, 2018, accepted, to appear.

P. J. Rossi, V. Chandrasekar, V. Hasu, and D. Moisseev, "Kalman filtering-based probabilistic nowcasting of object-oriented tracked convective storms," *Journal of Atmospheric and Oceanic Technology*, vol. 32, no. 3, pp. 461–477, 2015.

A. W. Seed, "A dynamic and spatial scaling approach to advection forecasting," *Journal of Applied Meteorology*, vol. 42, no. 3, pp. 381–388, 2003.

B. J. Turner, I. Zawadzki, and U. Germann, "Predictability of precipitation from continental radar images. Part III: Operational nowcasting implementation (MAPLE)," *Journal of Applied Meteorology*, vol. 43, no. 2, pp. 231–248, 2004.

J. W. Wilson, E. E. Ebert, T. R. Saxen, R. D. Roberts, C. K. Mueller, M. Sleigh, C. E. Pierce, and A. Seed, "Sydney 2000 forecast demonstration project: Convective storm nowcasting," *Weather and Forecasting*, vol. 19, no. 1, pp. 131–150, 2004.

A probabilistic radar forward model for small ice particles

Robert S. Schrom[1] and Matthew R. Kumjian[1]

[1]*The Pennsylvania State University, 503 Walker Building, 16802 State College, United States*

(Dated: 22 June 2018)

Introduction

A radar forward model connects physical properties of hydrometeors to radar measurements. These forward simulators are important for microphysical model validation and interpreting radar observations. The wide variety of shapes and sizes of ice particles, as well as their importance in precipitation growth, make it difficult to fully understand ice microphysical processes. By evaluating microphysical models with radar measurements, we may be able to make progress in better understanding these processes. The growth of branched planar crystals is particularly important in the development of precipitation in the mid-latitudes (Andrić et al., 2013; Kumjian and Lombardo, 2017) and within mixed-phase Arctic clouds (e.g., Oue et al., 2016)

Forward simulations of the radar variables are performed first by calculating the radar scattering properties of the individual simulated ice particles. Because the bulk radar signal contains samples of numerous hydrometeors within a given volume of the atmosphere, we calculate it using the integrated radar scattering properties of ice particles over probability distributions of their size, orientation, and shape. With exception to the orientation distribution, the distribution quantities are predicted by microphysical models and are input into the forward model. Thus, errors from the forward model are separate from the errors in the microphysical model; the errors and uncertainty in the forward model are the focus of this study.

Because of the errors in simplified representations of branched planar crystals in scattering models (e.g., Schrom and Kumjian, 2018), we need to incorporate detailed-shape scattering calculations into forward models to accurately simulate the polarimetric variables. Given the natural variability in ice crystal shape, we also use these detailed-shape calculations to provide estimates of the uncertainty in the radar scattering properties due to shape ambiguity. We then apply this forward model to microphysical model output with a simplified Monte Carlo method to evaluate the uncertainty in forward model simulations of the polarimetric radar variables.

Scattering calculations

Branched planar crystals have both six-fold symmetry along their characteristic a-axis dimensional plane and reflectional symmetry across their c-axis. Therefore, we introduce a method to generate realistic structures in the "top-view" plane of ice crystals, and use these shapes in the scattering calculations for a forward model. In an effort to generate 2-D branched planar crystal structures that 1) are able to produce a high degree of variability and 2) depend on a limited number of clearly defined physical quantities, we have developed a procedure for generating these 2-D shapes. These physical quantities are illustrated in 1. The similarities between all of the structures we generate with this procedure are that they all have a solid ice core with a given size, six main branches that grow off of the core, evenly spaced subbranches of fixed width that grow off of the main branches, and interiors bounded by a star-shaped outline.

Single-particle radar scattering properties

We use the discrete dipole approximation (DDA) code of Yurkin and Hoekstra (2011) to perform detailed scattering calculations for branched planar crystals. Because the DDA code requires a set of point dipole locations, we use the quantities defined above to generate 2-D polygons for each branched planar crystal and then fill these polygons with a 2-D dipole lattice. We then create the 3-D shape by extending the 2-D structure of dipoles into 3-D along the crystal c-axis.

Both simplified results from ice crystal growth theory (e.g., Sheridan et al., 2009) and observational studies (e.g., Auer and Veal, 1970) suggest that the aspect ratio ($\phi = \frac{c}{a}$, where c is the c-axis length and a is the a-axis length) for branched planar crystals evolves approximately according to a power law during vapor depositional growth. To capture the natural evolution of branched planar crystals, we use a range of power law exponent coefficients to relate the aspect ratio to the size. We assume that all crystals start as hexagonal plates with $\phi = 1$ and a-axis length $a_{min} = 1\mu$m allowing us to use the following relation for the power law:

$$\phi = \left(\frac{a_{min}}{a}\right)^{b}, \tag{2.1}$$

where b is the power law exponent and the units of a are microns.

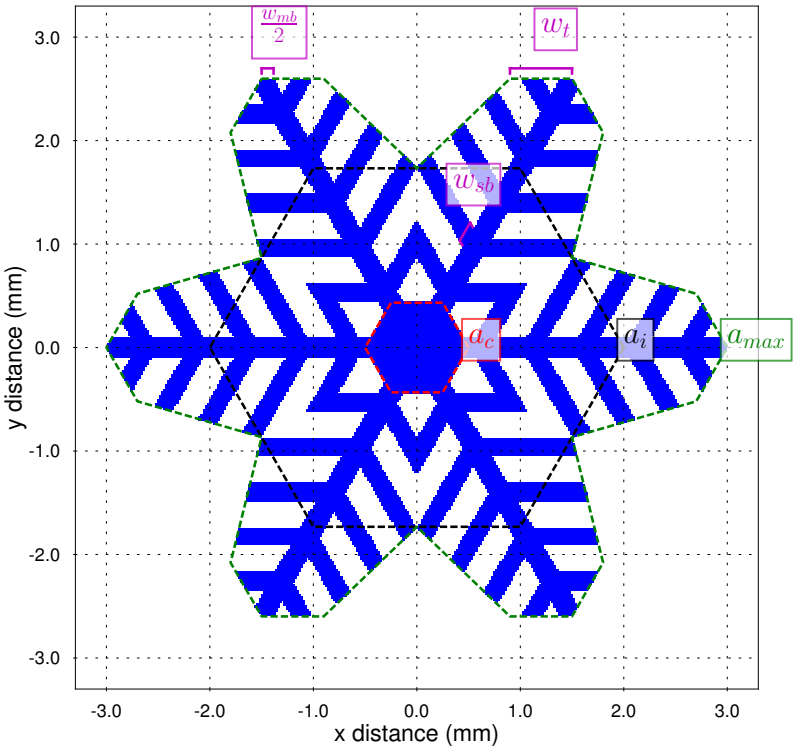


Figure 1: Plot of dipole locations for a branched planar crystal with outlines of the a_c, a_i, and star-shaped regions ploted in dashed red, black, and green lines, respectively. The particular values of w_t, w_{mb} and w_{sb} are labeled and plotted in magenta. The number of subbranches n_{sb} in this example is 5.

Table 1 shows the ranges of each quantity used to generate the 3-D branched planar crystal shapes. The ranges of values of the structure quantities are chosen to generally span the limited observations of effective density (e.g., Jensen et al., 2015). We also set a_{max} to 3 mm and create subsets of the ice particle shapes at 12 a-axis lengths ranging from 0.01 mm to 3 mm and spaced in equal increments according to the square root of their values.

Table 1: Description of the ranges of values (inclusive) used to generate the branched planar crystal shapes and sizes we use for the scattering calculations presented herein. The following values are fixed for all of the ice crystals: number of dipoles along the c axis $n_z = 9$ and $a_{max} = 3$ mm. These ranges of quantities results in a total of 10368 DDA calculations.

Quantity	description	minimum value	maximum value	number of values	spacing
a	crystal a-axis side length	0.01 mm	3.0 mm	12	square-root linear
b	aspect ratio-size power law coefficient	0.40	0.65	6	linear
f_b	subbranch fractional area coverage	0.2	0.9	4	linear
f_i	inscribed hexagon fractional distance	0.1	0.9	3	linear
f_t	tip width fraction	0.3	0.9	2	linear
a_c	core a-axis side length	0.1 mm	0.5 mm	3	linear
n_{sb}	number of subbranches per main branch	2	4 mm	2	linear

Equivalent solid-ice spheroids

For branched planar ice crystals that are small relative to the radar wavelength, we can assume that two pieces of independent information sufficiently describe their backscatter. Therefore, we may represent the detailed-shape scattering by equivalent solid-ice spheroids, where the independent information is contained in the solid-ice spheroid maximum dimension and thickness. These solid-ice spheroids are equivalent in the sense that they have the same backscattering properties as those from detailed-shape calculations (e.g., using DDA). Given our interest in the bulk radar reflectivity factor at horizontal polarization (Z_H) and Z_{DR}, we use σ_h and Z_{DR} from the DDA calculations to constrain the backscatter-equivalent d and h. Therefore, for a given branched planar crystals with σ_h and Z_{DR} calculated from DDA, the equivalent solid-ice spheroid will have the same

σ_h and Z_{DR}.

Given that we focus on small-particle scattering, we perform DDA calculations at S band (with $\lambda = 100$ mm) for branched planar crystals generated using the method described above and the properties listed in Table 1. We then determine the equivalent spheroids from the DDA-calculated σ_h and Z_{DR} for each crystal. Using formulas for the scattering of homogeneous spheroids in the Rayleigh regime from Ryzhkov et al. (2011), we are then able to iteratively determine the maximum dimension and thickness that correspond to the same σ_h and Z_{DR} as those from DDA, using a fixed number of iterations for each particle that results in errors $< 1\%$.

From the equivalent spheroid dimensions and the corresponding maximum dimensions and thicknesses of the branched planar crystals, we calculate the percentage changes in maximum dimension P_d and thickness P_t with:

$$P_d = 100 \times \frac{d_{eqv} - d}{d} \tag{2.2}$$

$$P_h = 100 \times \frac{h_{eqv} - h}{h}, \tag{2.3}$$

where d_{eqv} and h_{eqv} are the maximum dimension and thickness, respectively of the equivalent solid-ice spheroid. In order to simplify the process of mapping bulk physical properties to scattering properties, we can exploit the fact that small-particle scattering is a smooth function of the particle size by performing polynomial fits of P_d and P_h for the branched planar crystals as functions of effective density and aspect ratio; the maximum dimension is then incorporated into the mapping function by determining the dimensions of the equivalent spheroids from (2.2) and (2.3).

To test the accuracy of this mapping procedure, we compare the σ_h and Z_{DR} from the DDA calculations to the σ_h and Z_{DR} from the polynomial fits based on the maximum dimension, aspect ratio, and effective density of the branched planar crystals used in the DDA calculations. The comparison for Z_{DR} is shown in Fig. 2, where the highest counts of particles are found near the one-to-one line. We also find similar results for the comparison of σ_h (not shown).

Forward model evaluation

Estimation of forward model uncertainty

To calculate the bulk radar variables and estimate their uncertainties, we use distributions of aspect ratio, effective density, and number concentration (e.g., from microphysical model output) to first calculate the percentage dimensional changes for particles within each model bin using the polynomials fit to the scattering calculations. We then add random Gaussian noise (corresponding to the single-particle scattering variability) to the percentage dimensional changes calculated for each particle. Using the maximum dimension and thickness simulated by the model and the perturbed dimensional changes, we then calculate the equivalent spheroid dimensions. To calculate the radar scattering properties for each of these equivalent spheroids, we use the formulas for homogeneous spheroids in Ryzhkov et al. (2011) at a given wavelength, and then calculate σ_h, σ_v, and Z_{DR} for the individual ice crystals.

Once we have these bulk radar variables for a given realization of Gaussian noise, we then repeat this process for N_{sam} realizations, randomly sampling percentage dimensional changes for each ice crystal size to calculate N_{sam} bulk radar variables. From these samples of the forward-simulated bulk radar variables, we may then get estimates of their uncertainty solely due to uncertainty in the precise shape of branched planar crystals.

Arctic mixed-phase cloud simulations

To provide an example of the forward model described herein, we examine a case of vapor depositional growth described in Oue et al. (2016). During this case, a cloud was present within the lowest 2 km of the atmosphere; temperatures in this region ranged from between -20 °C to -10 °C. Surface observations taken during the early portion of the case indicated branched planar crystals were the predominant ice crystal habit (see Fig. 3c of Oue et al., 2016).

Radar observations during this case from the Atmospheric Radiation Measurement (ARM) X-band scanning precipitation radar (XSAPR) at Barrow, Alaska show relatively high Z_{DR} throughout the cloud, with low Z_H generally increasing towards the ground (Fig. 3). These radar observations indicate either plate or branched planar crystals growing by vapor deposition and sedimenting. This general microphysical evolution is supported by the sounding that indicates supersaturated conditions throughout the lowest 1-1.5 km of the atmosphere, along with favorable temperatures for vapor depositional growth. In

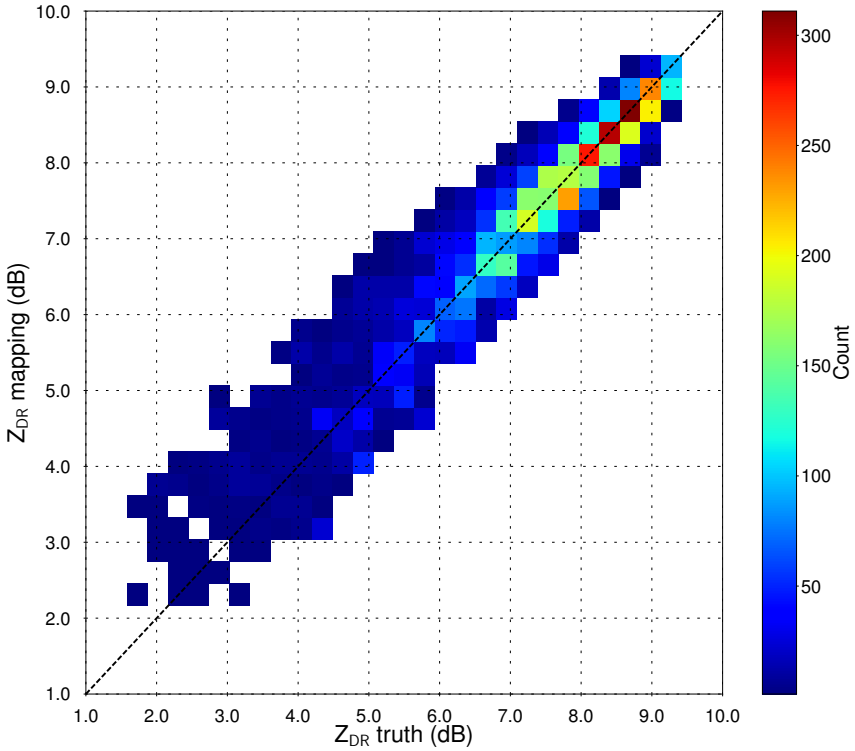


Figure 2: Comparison of Z_{DR} calculated with DDA and using the equivalent-scattering-spheroid mapping procedure for the branched planar crystals defined in Table 1. Pairs of calculations for each branched planar crystal are plotted as counts within given bins of Z_{DR} from DDA (x axis) and from the corresponding Z_{DR} values from the mapping procedure (y axis). The one-to-one line is indicated by the black dashed line.

addition, relatively low liquid water paths through the cloud system at the time of these radar observations suggests that riming was a limited factor in the growth of the ice particles (e.g., Fig. 3b of Oue et al., 2016).

In order to simulate this case, we use an idealized 2-D kinematic model coupled to a bin microphysical model with adaptive habit microphysics that allows for the natural evolution of maximum dimension, aspect ratio, and effective density. This model is similar to that implemented by Harrington et al. (2014) but for explicit prediction of the ice particle properties within each bin. The kinematic framework of this model means that the flow is fixed in time, with one set of idealized updraft and downdraft cells. Both the flow field and the growth/sublimation of ice change the temperature and humidity of the environment. The simulations start with the 2-D domain initialized with the same environment from the sounding and run for 1 hour. After this time, we take profiles of the ice particle size, aspect ratio, and effective density spectral distributions within the updraft and use these profiles to calculate the radar variables. From the uncertainty estimation in our forward model, we derive the standard deviation at each height level in the model profile.

The results for the simulated Arctic mixed-phase cloud case are shown in Fig. 3. Simulations of Z_H show similar shape between the reduced-density spheroid and equivalent-solid ice spheroid calculations, with the equivalent spheroids resulting in a slightly larger Z_H at all heights. The $\pm\sigma$ interval from the forward model ranges from 1 dB to 3 dB, with the largest uncertainty near the highest Z_H, around 700 m above ground level (AGL).

A much larger difference between the reduced-density spheroid calculations and the forward model is present in the simulated Z_{DR} profiles. The shapes of the simulated Z_{DR} profiles show notable differences; the Z_{DR} calculated with the reduced-density spheroids has maximum value at the top of the profiles, decreasing by about 1 dB to the minimum value of 3.7 dB at 700 m height. In contrast, Z_{DR} from the equivalent-spheroid forward model is 1.5-2.5 dB higher and decreases gradually by around 0.5 dB from the top of the profile to around 300 m AGL. The uncertainty in Z_{DR} from the forward model shows a maximum $\pm\sigma$ interval of 0.6 dB around 750 m AGL, where the model-simulated density of branched planar crystals is modestly reduced.

The observations are generally consistent with the simulations; Z_H has a similar shape between 0.9-1.4 km AGL, with

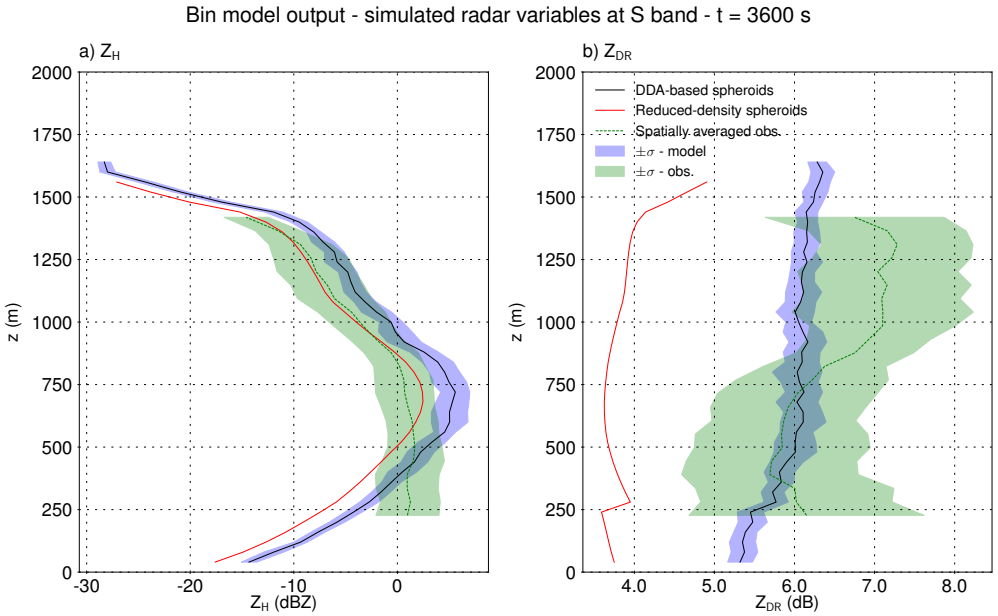


Figure 3: Simulated profiles of a) Z_H and b) Z_{DR} at S band for the model-simulated ice crystals within a profile through the updraft of the simulated cloud. The red lines indicate the simulations of the radar variables using homogeneous, reduced-density spheroids in the Rayleigh approximation, the black lines indicate the mean radar profiles simulated using the forward model described herein, and the blue shading indicates the one-standard-deviation interval of simulated radar variables at each height. Observed profiles of the mean Z_H and Z_{DR} (averaged horizontally from an RHI taken through the cloud) are plotted in green dashed lines. The green shaded regions about the means indicates the one-standard-deviation interval based on the spatial variabilities of the profiles over the averaging region.

values remaining relatively constant below 0.9 km. The spatial variability of Z_H is also larger than that due to the scattering variability from the forward model. The mean observed Z_H happens to be closer to the simulated Z_H from the reduced-density model. However, this correspondence is not particularly meaningful, given the large uncertainties in ice nucleation rates and updraft speeds used in the model. Additionally, the Z_{DR} observations (relatively independent of ice number concentration) show much better correspondence to the equivalent-scattering spheroid forward model simulations. The spatial variability in the observed Z_{DR} is much larger than the scattering uncertainty in the forward model, suggesting that faithfully capturing ice nucleation and microscale dynamic features of Arctic cloud systems are potentially more important than errors that may arise from assuming a particular branched planar crystal. However, using homogeneous, reduced-density spheroids in the scattering model may still produce biases in Z_{DR} that dominate even the processes that govern the spatial variability of the radar observations.

Conclusions

Polarimetric radar measurements of branched planar crystals have the potential to improve our understanding of the growth of these particles within mixed-phase cloud systems. To aid in this goal, we present a forward model that accurately maps bulk ice-crystal physical properties to their microwave scattering properties. Natural variability in the precise ice particle structure that is unspecified by a microphysical model allows us to additionally estimate the uncertainty in forward simulations of the radar variables.

When applied to bin microphysical model output for an Arctic mixed-phase cloud case, we see generally better comparisons to the observed Z_{DR} for the equivalent-spheroid forward model than for the homogeneous, reduced-density spheroid calculations. The spatial variability of the observed Z_H and Z_{DR} is larger than the scattering uncertainty from the forward model. This high spatial variability suggests that accurately comparing radar observations to those simulated from model output requires consideration of the variability in ice growth environments that can be reasonably simulated by the model. If the model provides much coarser or more idealized representations of the precipitation evolution, careful spatial and or temporal averaging of both the observations and model is required.

Acknowledgement

The work contained in this extended abstract is based on a paper in preparation for submission to the Journal of Applied Meteorology and Climatology. Funding for the authors comes from DOE grant No. DE-SC0013953. We thank Jerry Harrington for providing the code for the microphysical model and Hans Verlinde, Eugene Clothiaux, and Kultegin Aydin for their helpful discussions on this work.

References

J. Andrić, M. R. Kumjian, D. S. Zrnić, J. M. Straka, and V. M. Melnikov, "Polarimetric signatures above the melting layer in winter storms: An observational and modeling study," *J. Appl. Meteor. Climatol.*, vol. 52, pp. 682–700, 2013.

A. H. Auer and D. L. Veal, "The dimension of ice crystals in natural clouds," *J. Atmos. Sci.*, vol. 27, pp. 919–926, 1970.

J. Y. Harrington, K. Sulia, and H. Morrison, "A method for adaptive habit prediction in bulk microphysical models. Part I: Theoretical development," *J. Atmos. Sci.*, vol. 70, pp. 349–364, 2014.

M. P. Jensen, W. A. Petersen, A. Bansemer, N. Bharadwaj, L. D. Carey, D. J. Cecil, S. M. Collis, A. D. D. Genio, B. Dolan, J. Gerlach, S. E. Giangrande, A. Heymsfield, G. Heymsfield, P. Kollias, T. J. Lang, S. W. Nesbitt, A. Neumann, M. Poellot, S. A. Rutledge, M. Schwaller, A. Tokay, C. R. Williams, D. B. Wolff, S. Xie, and E. J. Zipser, "The midlatitude continental convective clouds experiment (MC3E)," *Bull. Amer. Meteor. Soc.*, 2015, in press.

M. R. Kumjian and K. A. Lombardo, "Insights into the evolving microphysical and kinematic structure of northeastern U.S. winter storms from dual-polarization Doppler radar," *Mon. Wea. Rev.*, vol. 145, pp. 1033–1061, 2017.

M. Oue, M. Galletti, J. Verlinde, A. Ryzhkov, and Y. Lu, "Use of X-band differential reflectivity measurements to study shallow Arctic mixed-phase clouds," *J. Appl. Meteor. Climatol.*, vol. 55, pp. 403–424, 2016.

A. V. Ryzhkov, M. Pinsky, A. Pokrovsky, and A. Khain, "Polarimetric radar observation operator for a cloud model with spectral microphysics," *J. Appl. Meteor. Climatol.*, vol. 50, pp. 873–894, 2011.

R. S. Schrom and M. R. Kumjian, "Bulk-density representations of branched planar ice crystals: Errors in the polarimetric radar variables," *J. Appl. Meteor. Climatol.*, vol. 57, pp. 333–346, 2018.

L. M. Sheridan, J. Y. Harrington, D. Lamb, and K. Sulia, "Influence of ice crystal aspect ratio on the evolution of ice size spectral during vapor depositional growth," *J. Atmos. Sci.*, vol. 66, pp. 3732–3743, 2009.

M. A. Yurkin and A. G. Hoekstra, "The discrete-dipole-approximation code ADDA: Capabilities and known limitations," *J. Quant. Spectrosc. Radiat. Transfer*, vol. 112, pp. 2234–2247, 2011.

ERAD2018

Radar QPE for an Extreme Precipitation Event in Southern Brazil: January 2018 Flash Flood – 409 mm in 48h

Leonardo Calvetti[1], Cesar Beneti[2], William Coelho[1], Camila Cardoso[3], Tulipa Silva[2], Mario Quadro[3], Dirceu Herdies[4] and Roberto Calheiros[2]

1 Center for Meteorological Research and Forecasting, Federal University of Pelotas (CPMET/UFPEL), Pelotas, Brazil
2 Paraná Meteorological Service (SIMEPAR), Curitiba, Brazil
3 Master Degree in Meteorology, Federal University of Pelotas (PGMET/UFPEL), Pelotas, Brazil
4 Meteorology Department of Federal Institute of Santa Catarina (IFSC), Florianopolis, Brazil
5 Center for Weather Forecasting and Climate Studies (CPTEC/INPE), Cachoeira Paulista, Brazil

1 Introduction

An extreme, multi day rainfall event over eastern Santa Catarina State, Brazil, during 10-12 January 2018 caused a record flooding during a beach tourism season. An unusual synoptic weather pattern induced a record precipitation of 409 mm in three days, registered by the rain gauge network. During all three days, a continuous stratiform rain ranging from 1 to 8 mm/h was predominant. At the end of 10th January and early 11th January severe convective storms developed over Florianopolis City, Capital of the Santa Catarina State. The rain gauge network recorded values of 31.4 mm/h, 25.8 mm/h and a historical record of 31.2 mm in 10 minutes, what generate severe damages due to flash flooding. For the analysis of rainfall spatial distribution it was used Quantitative Precipitation Estimate (QPE) fields obtained by Z-R relationships from a new Dual Polarization S-Band Weather Radar located at Lontras City, about 110 km distance from Florianopolis (figure 1 and 2).

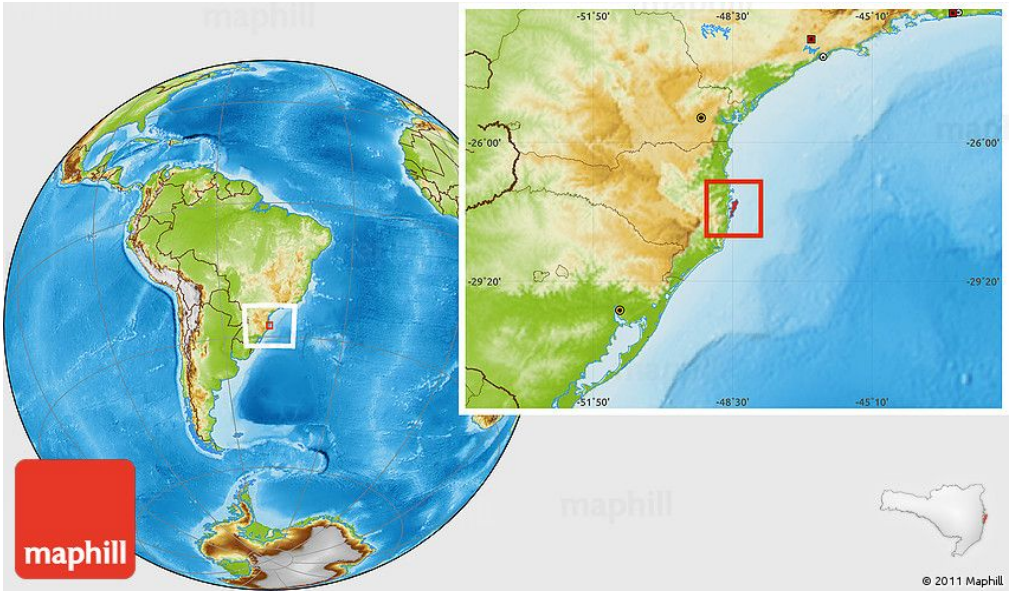


Figure 1: Florianópolis location. The island has 424 km² while the metropolitan area has 2399 km². The sea circulation in the coast of southern Brazil is suppressed by 900 - 1000 m height chain of mountain.

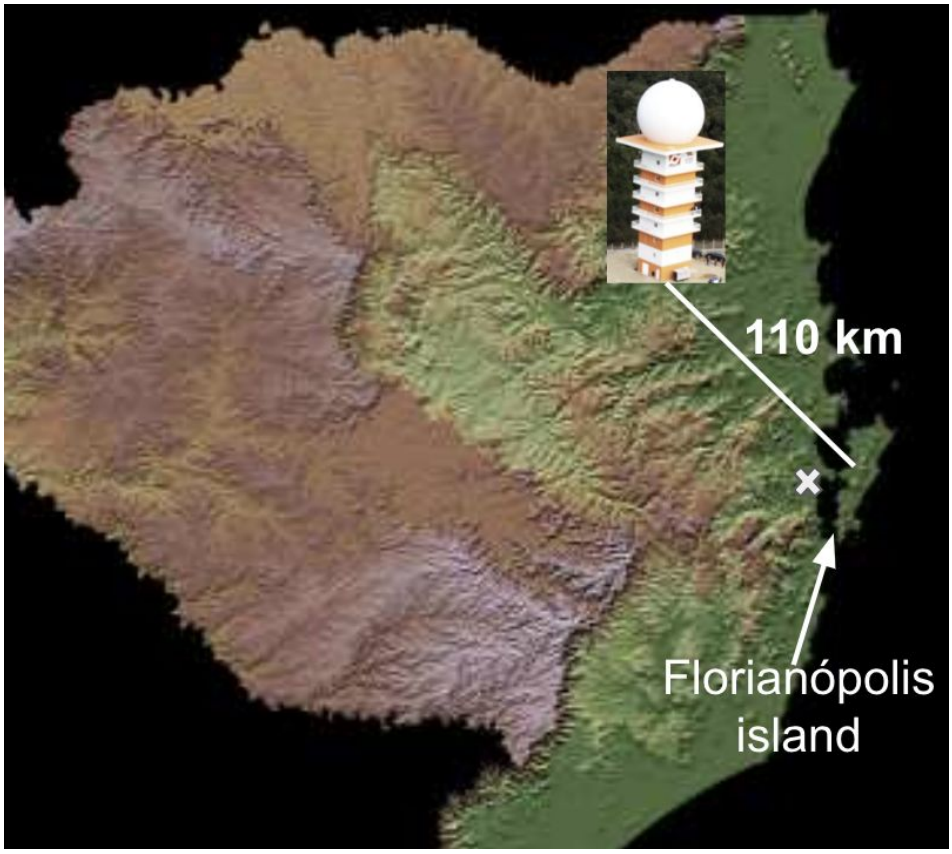


Figure 2: Distance from Lontras-SC Weather Radar to Florianópolis Island. The radar has a good cover for east and southeast areas of Santa Catarina state in Brazil. The x represents the São José rain gauge location.

2 The event and Reflectivity Pattern

The event was characterized by a continue stratiform rain during the three days succeeded by an episode of convection between 10 and 11 January 2018. Even the convective areas the reflectivity was not superior to 45 dBZ (figure 3), i. e., the event was feeded by strong wet wind circulation from the sea. The synoptic pattern (not showed) indicated a typical subtropical high pressure system in the South Atlantic ocean and its west flank close to the Santa Catarina coast blowing a wet northeast wind. The interaction between the winds of the subtropical high system and the Mesoscale Convective System (MCS) produced a continuum cells of heavy precipitation that produced 31.4 mm/h, 25.8 mm/h and a historical record of 31.2 mm in 10 minutes, producing severe damages due to flash floods. As the moisture comes from the sea, the clouds of MSC was not deep as typical storms in Brazil. So, it was a unusual event that most of Z-R relationships could not works properly.

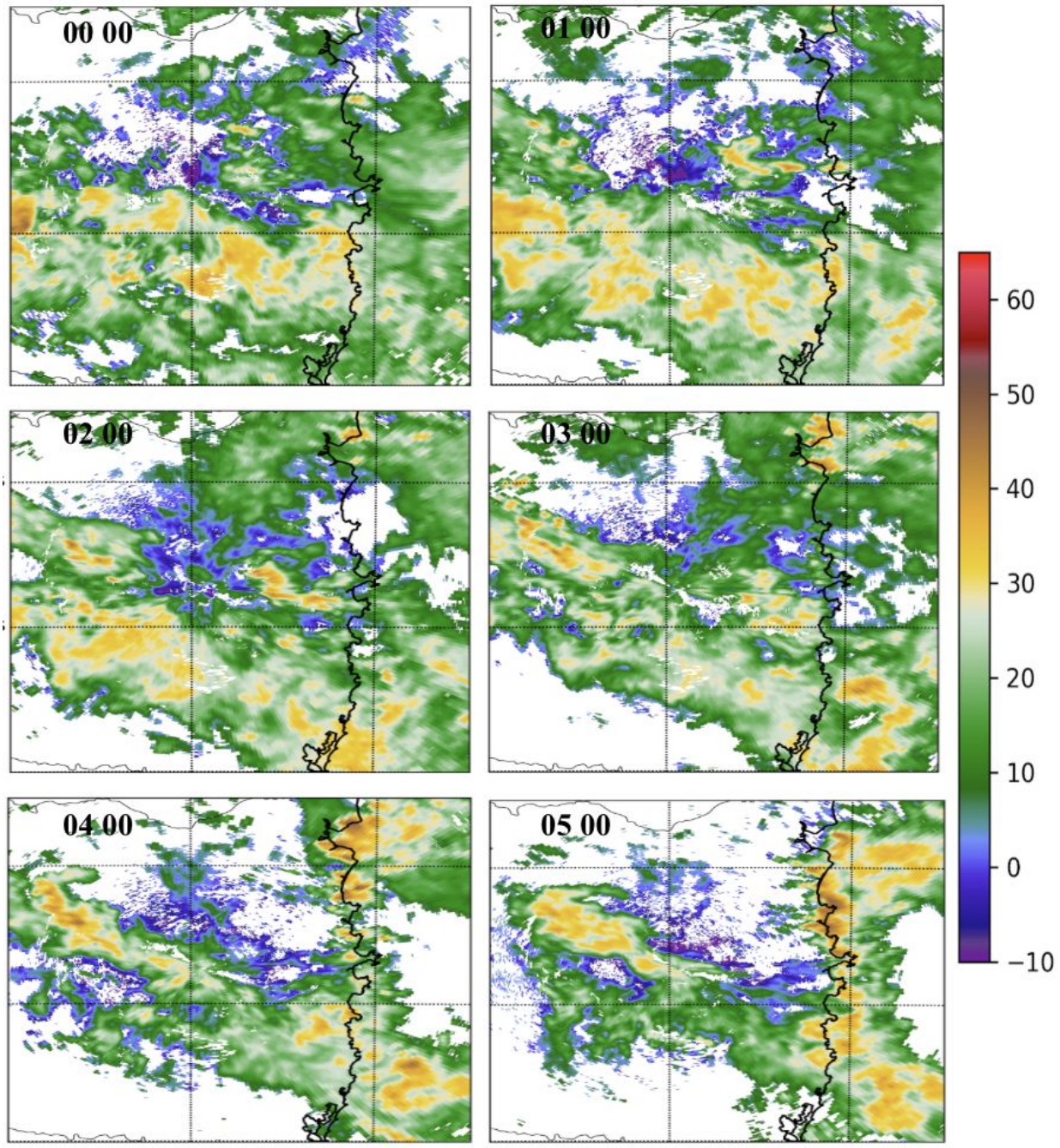


Figure 3: Lontras-SC Weather Radar Reflectivity PPI 0.5˚ sequence for 11 January 2018 from 00h to 05h local time (UTC-3).

One of the objectives in the studies of radar meteorology is the rainfall estimation for extreme events, as was the case of 9,10 and 11 January 2018 in Florianópolis. Therefore, the analysis of the evolution of reflectivity on the Florianópolis region was carried out. First, it has been conduct the analysis if the presence of noises, echoes of terrain, bright band (Oliveira and Beneti, 2014) or other type of "contamination" could interfere the measures of reflectivity (Krajewski et al., 2010, Gorgucci et al. 2015). If there are noises in the signal, the reflectivity does not respond adequately to the meteorological phenomenon. If the return echoes are exclusively due to rain backscattering, the reflectivity signal will vary according to the intensity of the precipitation. Following this theory, the analysis was performed for the precipitation of January 10 between 18 and 23 h over São José - Forquilhinha station, where rainfall reached values of 10 mm in 10 minutes and 88 mm per hour, causing severe flash floods throughout the Florianópolis city. Precipitation peaks are directly associated with radar reflectivity peaks (Figure 3) although the reverse is not true. There is no phase error, which is expected for estimates, as opposed to forecasts.

Trends were also aligned without distortion. It can be concluded that, in this region, the radar of Lontras captured the phenomenon without noise interference in the signal, which is fundamental for a good estimation.

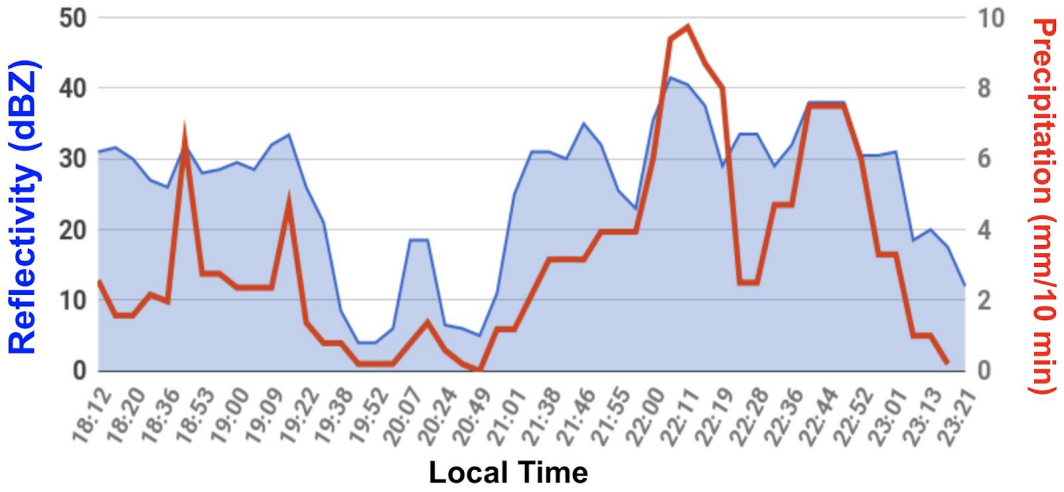


Figure 4: Lontras Radar Reflectivity and Precipitation of São José City rain gauge (lat: -27.60253; lon -48.6201) from 18 to 23h local time at 10 January 2018.

3 Z-R relationships

Since Lontras is a S-Band dual-pol radar, it was possible recovering Z-R relationships by KDP differential reflectivity (ZDR) and phase-specific differential (KDP) variables together with the reflectivity (Z) (CHANDRASEKAR and CIFELLI, 2012; RYZHKOV ET AL., 2005; GIANGRANDE ET AL., 2008). So, for this specific case, it was tested some Z-R used in others researches or which are traditional in radar assumptions. In this way, the experiments were elaborated with six Z-R relationships: traditional Marshall-Palmer (a=200, b=1.6), Joss (a=500;b=1.5), two other Z-R relationships based in studies developed in Brazil, Calheiros (a=236;b=1.5) and Santos (a=52;b=2.7), and two polarimetric Z-R relationships including reflectivity, differential reflectivity and specific differential phase (Table 1). A discussion about the efficiency of the QPE was conducted concerning the rainfall events in a sense of predicting flash foods in urban areas.

Table 1:Z-R relationship experiments and references.

Relationships	Equation
ZR1 (MARSHALL-PALMER, 1948)	$Z = aR^b$ a=200 b=1,6
ZR2 (CALHEIROS ET AL., 2017)	$Z = aR^b$ a=236 b=1,5
ZR3 (SANTOS, 2014)	$Z = aR^b$ a=52 b=2,7
ZR4 (JOSS ET AL., 1970)	$Z = aR^b$ a=500 b=1,5
ZR5 (GIANGRANDE, 2008)	$R(ZDR,KDP) = 52{,}9\|KDP\|^{0,85}ZDR^{-0,53}signal(KDP)$
ZR6 (GIANGRANDE, 2008)	$R(Z,ZDR) = (1{,}42x10^{-2})Z^{0,770}ZDR^{-1,67}$

The tradicional Marshall-Palmer Z-R relationship (ZR1) show good results for the stratiform pattern of all events, but overestimated all convective cells (Figure 5). Using KDP and ZDR variables (ZR5 and ZR6), it was possible to detect the rainfall peaks, but not exactly as observed in rain gauges. However, these polarimetric relationships could be useful for hydrometeorological purposes with a good skill. The ZR3 from Joss et al. 1970 underestimated the cells of heavy rain

(Figure 5), but is in according with other Z-R relationships. The ZR2 and ZR4 get overestimation in convective areas because it was adjusted by typical weather conditions in Brazil, i. e., the heavy rain usually come from thermal and dynamical deep convection. The persistent northeastern maritime influx of moisture in the area lead to a stratiform pattern during the three days. The precipitation peaks were generated by strong convection triggered during a zonal propagation of a mid-level shortwave trough over the coast. Therefore, these two distinct atmospheric regimes with a mix of maritime and continental hydrometeors content led thinking about the use of two type of the Z-R relationship according the precipitation regimen, which will be presented in this conference.

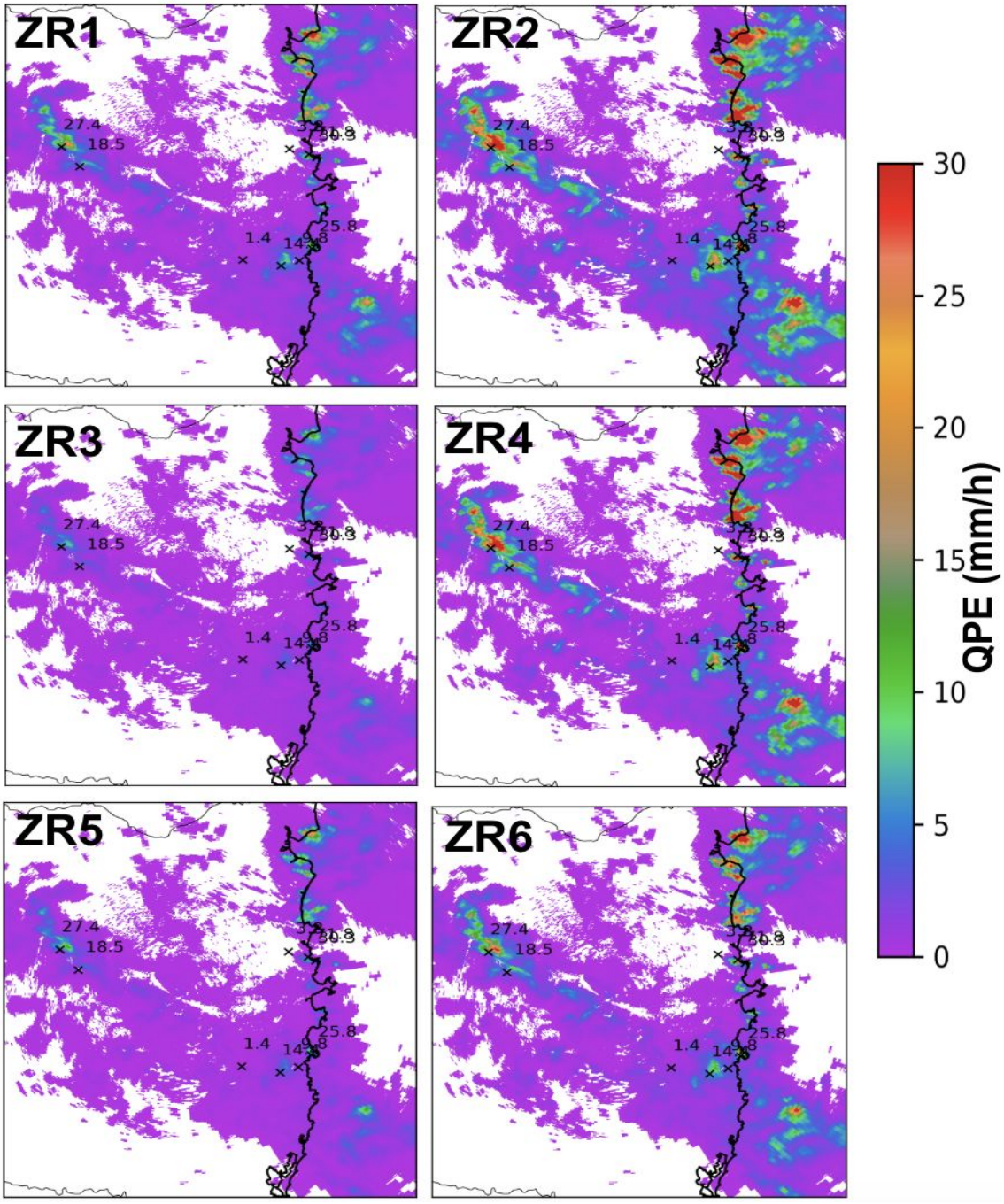


Figure 5: Z-R Relationships from Lontras Weather Radar Reflectivity at 22h local time at 10 January 2018.

The high temporal frequency of rainfall measurements is very important for realistic identification of rainfall and to adjust radar QPE. In Brazil, the Center for Natural Disaster Monitoring and Alert (CEMADEN) maintain several rain gauges in the

main risk areas with 10 minutes of resolution, including Florianopolis area. So, to examine the quality of the rain estimates, it had been plotted São José rain gauge (location is on Figure 2) versus QPE radar estimates by ZR5 experiment between 7pm and 11pm local time 10 January 2018 (Figure 6). This period corresponds rainfall values between 2 and 12 mm in 10 minutes, enough to cause flooding in most urban areas of the Brazil cities. In this case, the use of the variable KDP maybe not result improvements in the estimates, because the clouds that generated the precipitation were not considered of deep convection, although its has a high liquid water content (high mixing ratio) feeded by intense synoptic sea circulation derived by the South Atlantic high pressure system. The values obtained by QPE were very close to the measurements of the rain gauge. At the main peak, near 10 pm the difference was slightly more than 2 mm in 10 min, considered very good for the type of precipitation. Around 6:30 p.m., radar precipitation underestimated the peak. In general the two curves have high correlation and no problems of lag or non-observation are observed. This means that in addition to a good rainfall estimate, there were no radar measurement failures, which is very important at such an extreme time.

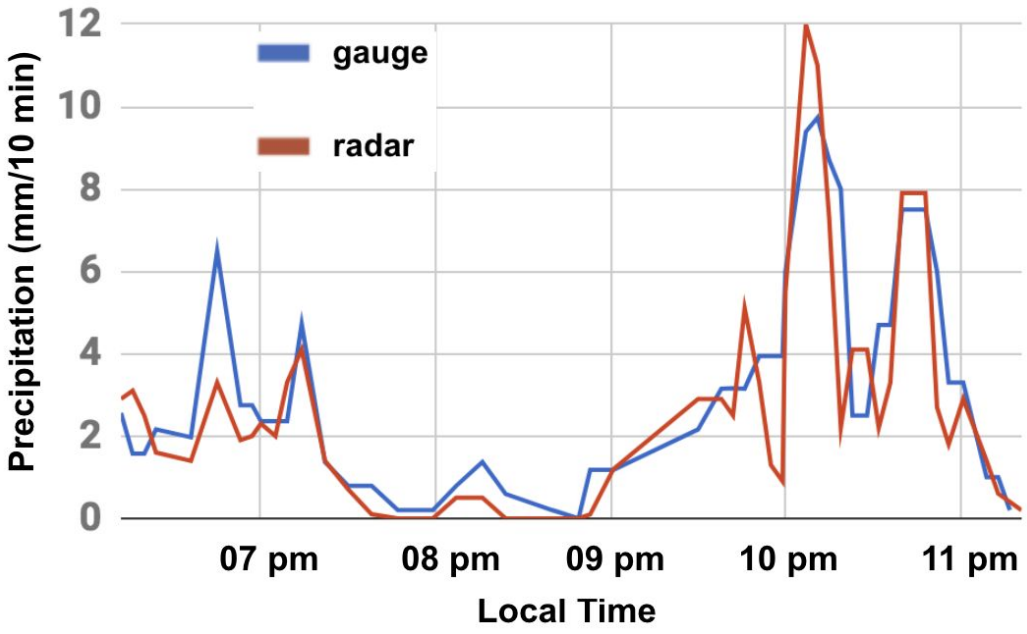


Figure 6: Precipitation Comparison between Z-R Relationship from Lontras Weather Radar and São José rain gauge at 10 January 2018.

Despite the main case of recent months, it is important to verify the performance of the rainfall estimates for a longer period and for all rain gauges under the 200 km range of the Lontras radar, that is, to verify a relation of the distribution of drops in the cloud with surface precipitation (Calheiros et al., 2017). The scattering was obtained with 16 CEMADEN rain gauges which had adequate and fault-free data for the period from 1st October 2017 to 31 January 2018. The period was selected for having the largest rainfall events and reliable radar data. Very high values, above 10 mm in 10 minutes, were close to rain gauges with a tendency to overestimate radar. Values between 5 and 10 mm in 10 minutes had both negative and positive biases, i. e., with non-systematic errors. For the accumulations between 0 and 5 mm in 10 minutes several non-identification of the precipitation occurred, which is typical for observations at such a long distance as the one we are submitting. It is observed that the trend curve is above the diagonal bisector of the graph, which represent overestimation of the QPE.

One positive aspect is that for extreme volumes, values greater than 10 mm in 10 minutes, radar QPE are quite close to rain gauge records. The reason may be due to the type of microphysics monitored so far, since systems with deep convection tend to generate significant overestimations due to the content of ice mixed with the water content in the liquid state.

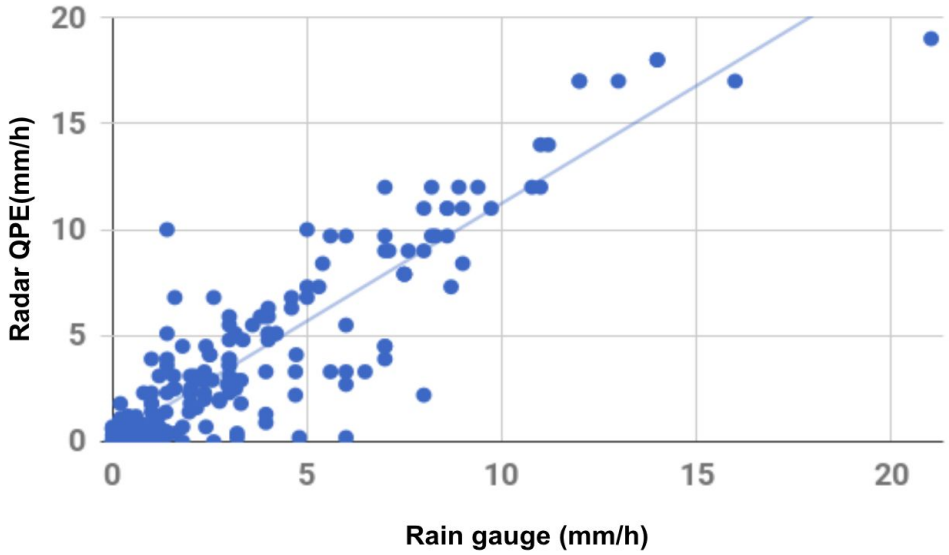


Figure 7: Scatter plot of 10 min precipitation between Rain Gauge and Radar QPE from 1st October 2017 to 31 January 2018.

4 Conclusions

A case study of an unusually heavy precipitation was conducted over southeastern coast Brazil. The event was emblematic for QPE concerns because it was reported extreme rainfall values with no deep convection occurrence. So, traditional Z-R relationship will not works properly for this type of storms in this region due the high interaction with the sea circulation. For this case the best Z-R relationship was those use ZDR and KDP variables and those use "a" parameter greater than 200. Since this type of storms contains a high content of moisture, the Z-R relationships for stratiform could be able to estimate the precipitation, but we recommend to examine a new parameters because the records greater than the climatology.

5 References

Calheiros, R. V., Oliveira, C. e Beneti, C. Distrometric drop size distribution in south brazil: derived z-r relationships. 38th Conference on Radar Meteorology. Chicago, IL,USA. 2017.

Chandrasekar V.; Cifelli R. Concepts and principles of rainfall estimation from radar: Multi-sensor environment and data fusion. *Indian J. Radio Space*, 41 (4), 389-402, 2012.

Giangrande, S. E. e Ryzhkov, A.V. Estimation of Rainfall Based on the Results of Polarimetric Echo Classification. Journal of Applied Meteorology and Climatology. Vol. 47, p. 2445-2462, 2008.

Gorgucci, E.; Baldini, L. Influence of Beam Broadening on the Accuracy of Radar Polarimetric Rainfall Estimation. J. Hydrometeor, 16, 1356–1371, 2015.

Joss, J. K, Schram, K., Thans e Waldvogel, A. On the quantitative determination of precipitation by radar. Research and Development Technical Report (ECOM-02071-2). University of Illinois , EUA, 38p., 1970.

Krajewski, W. F; Villarini, G.; Smith, J. A. Radar Rainfall Uncertainties, Bulletin of the AMS, January, 87-94, 2010.

Marshall, J.S. e Palmer, W. M. The distribution of raindrops with size. Journal of Meteorology. Vol. 5, p. 165-166, 1948.

Oliveira, C. Identificação e correção da Banda Brilhante em dados de Radar Meteorológico. 2014. 73p. Dissertação (Mestrado no Programa de Pós-Graduação de Métodos Numéricos em Engenharia) – Universidade Federal do Paraná, Curitiba – PR, 2014.

Ryzhkov, A.V., Giangrande, S.E., Melnikov, V.M. e Shuur, T.J. Calibration Issues of Dual-Polarization Radar Measurements. Journal of Atmospheric and Oceanic Technology, v. 22, p. 1138-1155, 2005.

A Comparison of Total Lightning Reflectivity Proxies and Weather Radar Data in Southern Brazil for High Impact Weather Monitoring and Nowcasting

William F. Coelho[1] Leonardo Calvetti[2] Cesar A. A. Beneti[3] and Nicole A. Rozin[3]

[1]*Federal University of Pelotas, Ildefonso Simões Lopes 2751, Três Vendas, the Brazil*
[2]*Center of Meteorological Research and Forecasting, Ildefonso Simões Lopes 2751, Três Vendas, the Brazil*
[3] *Meteorological System of Parana, Curitiba, Brazil*
(Dated: 22 July 2018)

1 Introduction

The radar data are widely used for a several activities on meteorology as well as rainfall estimate, storm monitoring and data assimilation in numerical models. The reflectivity factor is the most common variable used because it could infer mesoscale signatures, precipitation estimation and the monitoring of severe storms. Moreover, the coverage of the radar network in Brazil has important gaps, especially in westen where there are concentration of the agriculture. As an alternative, it was proposed the use of total lightning data to generate Lightning Reflectivity Proxies (LRP) or PulseRad as it is also called (LIU et al., 2013).

This study focuses in examining the use of LRP and compare with reflectivity factor for four convective precipitation events in Southern Brazil. Usually, the convection in this area is triggered by advection of heat and moisture from South America low-level jet and its alignment with cold fronts (MARENGO et al ., 2009). For the present work it was choose an event of cold front; a summer ordinary convective cell and two Mesoscale Convective System (MCS). These case studies is a initial assessment of the utility of the LRP in monitoring and nowcasting of convective events, especially in regions that are not covered by the radar network.

2 Data and Methodology

For this work it has been used the Cascavel S-Band Dual-Pol Weather Radar supported by the Paraná Meteorological System (Simepar) which is a EEC Doppler S-band of dual polarization, 1˚ beam width located at 24.87° S and 53.52° W and 720 m altitude and bin resolution of 250 meters.

The LRP data are generated from both IC and CG lightning detected by Earth Network Total Lightning Network (ENTLN). The proxies are calculated by an empirical linear function which can be expressed as dBZ=a*dBR+b, where the coefficients “a” and “b” are obtained empirically for differents regions or seasons, while dBR is the flash rate composed by the total lightning data, that is both intra-cloud and cloud-to-ground lightnings. The LRP data was compared with reflectivity data from radar using radar map images for each event in a subjective analysis.

The four cases were choose in a sense of test all storms type since squall lines, cold fronts and isolated convective cells. The differences between values of LRP and radar reflectivity were analysed using scatter plots which the dBZ values obtained for each rain gauge stations that registered heavy rain rates, taking account the instants before and after the rainy peak to obtain the dBZ value.

3 Results and Discussion

One of the three events was a squall line formed due to the cold front propagation (November 2, 2016), while the other two \were developed embedded in a MCS, one during spring on October 13, 2016 triggered by a high level trough and another during fall on April 26, 2017 associated with an interaction between a cold front and the South America low-level jets. The last case is a typical summer convection of isolated cells occurred on January 09, 2017.

The first case analyzed was a squall line moving northeastward crossing cities that recorded rain rates 12.6mm in 10 minutes (figure 1). The LRP (figure 1e, 1f, 1g and 1h) could capture the squall line signature of spring on October 13, 2016 event (igure 1a, 1b, 1c and 1d) indicating properly the position of convective cells, but underestimate the reflectivity inside the convective cells. by the LRP. However the large stratiform region behind of the squall line (figure 1b, 1c and 1d) is not

identified by the alternative proxies. Comparing 1b and 1f it is possible noting the line still remains organized in the radar image while the alternative proxies indicates a fragmented aspect.

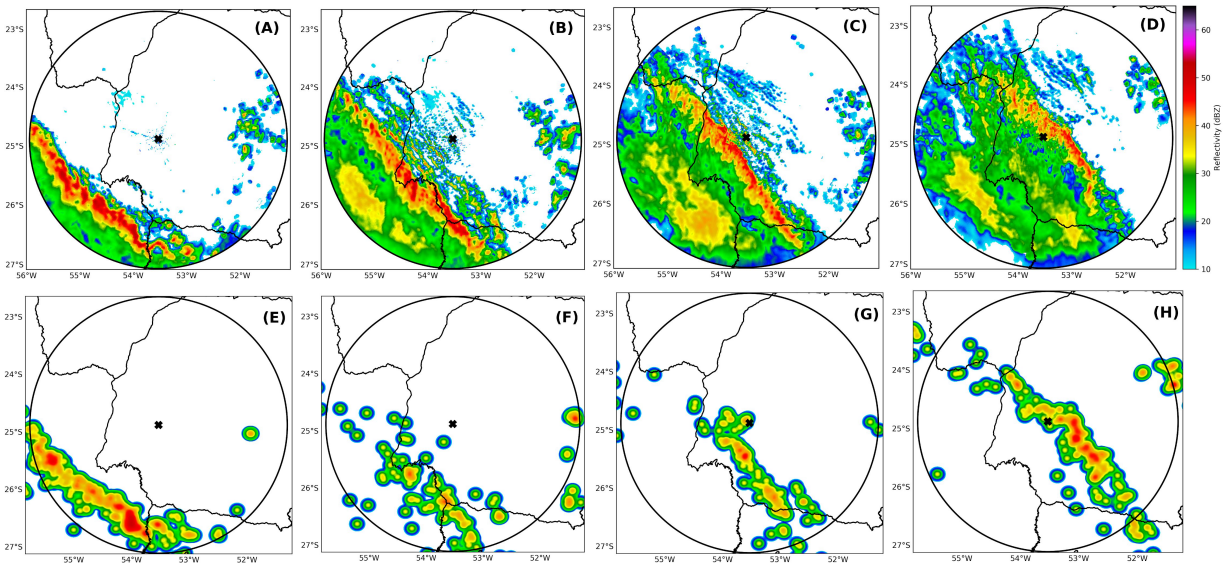


Figure 1: Evolution of the horizontal reflectivity at 3-km altitude over the Cascavel radar at 0400 UTC (a), 0500 UTC (b) 0600 UTC (c) 0700 UTC (d) and LRP at 0400 UTC (e), 0500 UTC (f) 0600 UTC (g) 0700 UTC (h) for the squall line occurred on october 13, 2016.

Similar the first event, the November 02, 2016 squall line was associated with a cold front producing rain rate 15mm in 10 minutes. Differently of the previous case where an underestimate was observed, the values in this case are very close of the radar observations, identifying very well the squall line. However, the broad stratiforme region (< 35 dBZ) behind the line is not represented. The convective cell that can be seen in the figures 2c and 2d at front of the line has its area overestimated by LRP (figures 2g and 2h).

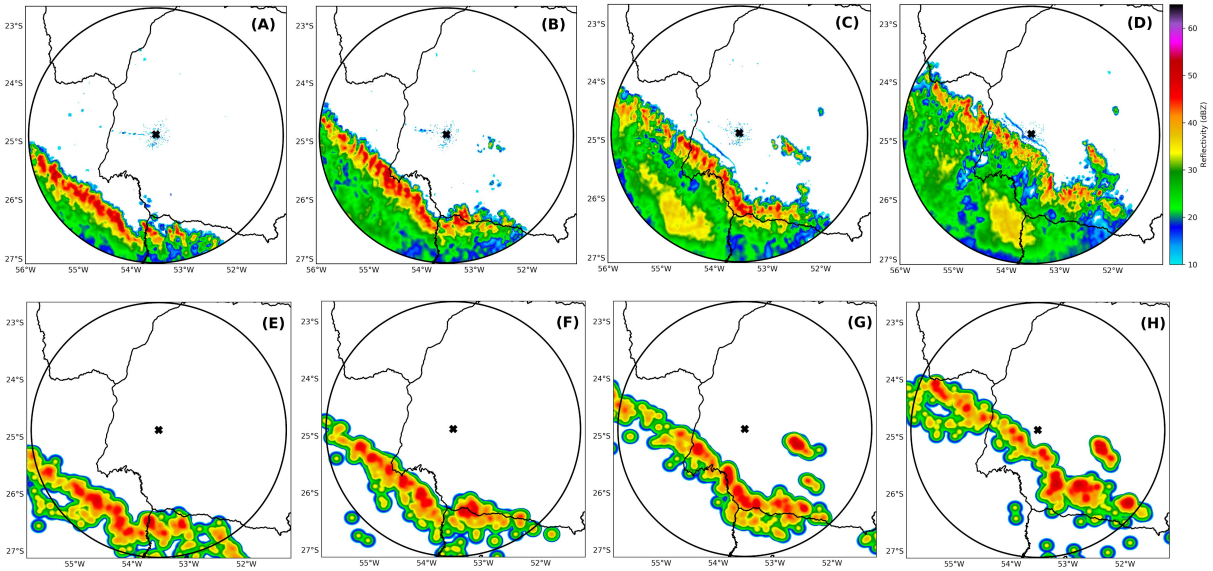


Figure 2: Evolution of the horizontal reflectivity factor (CAPPI 3-km) of the Cascavel radar at 0400 UTC (a), 0500 UTC (b) 0600 UTC (c) 0700 UTC (d) and LRP at 0400 UTC (e), 0500 UTC (f) 0600 UTC (g) 0700 UTC (h) for the squall line occurred on november 02, 2016.

The third case (figure 3) is a squall line associated with a MCC that produced 21mm in 10 min. The values of dBZ over the squall line presented by the LRP are consistent with radar data except in the sense which the LRP system is broader than radar system. This characteristics are noted also in the fourth case (figure 4), which the convective cells appears as wider areas of convection. As in other cases, the stratiform region was not well represented as it was expected because, in theory, the occurrence of lightning in these regions is quite limited, since the upward and downward movements do not act with the same vigor, besides the smaller presence of hydrometeors does not favor the cloud electrification.

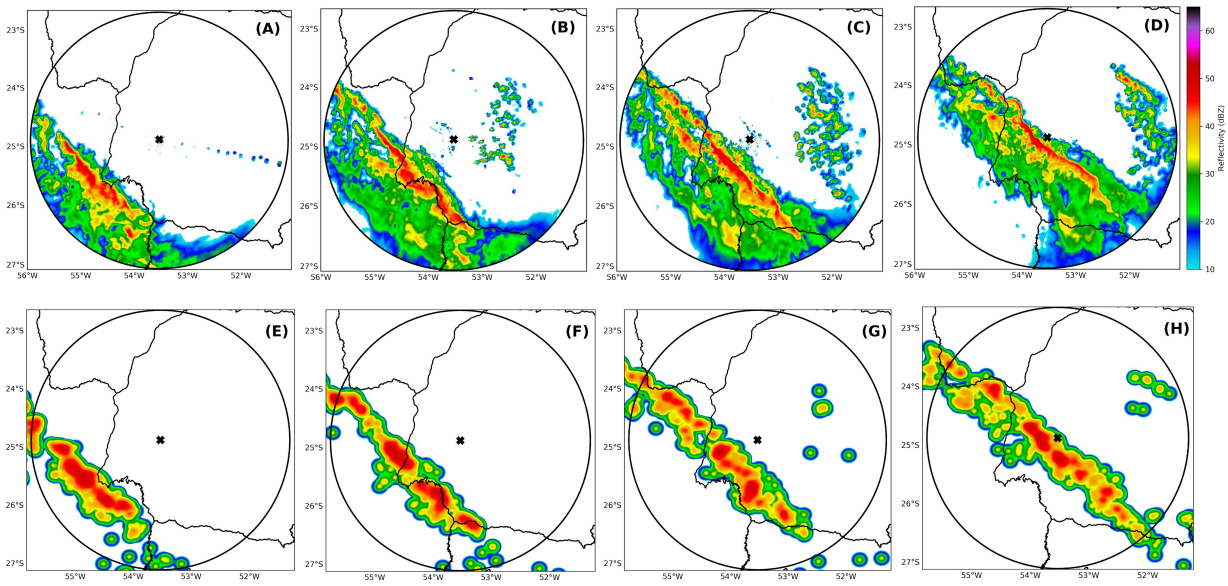


Figure 3: Evolution of the horizontal reflectivity at 3-km altitude over the Cascavel radar at 0200 UTC (a), 0305 UTC (b) 0400 UTC (c) 0500 UTC (d) and LRP at 0200 UTC (e), 0305 UTC (f) 0400 UTC (g) 0500 UTC (h) for the squall line occurred on april 09, 2017.

The fourth event was a typical summer ordinary convective cell which the convection initiate in the evening and produced rain rates 10mm in 10 minutes. The system moved to northeast in order to intensify the cells already placed at this area. (figures 4a to 4d). The LRP estimate a similar distribution to the radar reflectivity fields, but it overestimate the size and values of the cells presented cells with different shapes. These differences could be very important when it want to perform a very localized QPE or even identify any mesoscale signature.

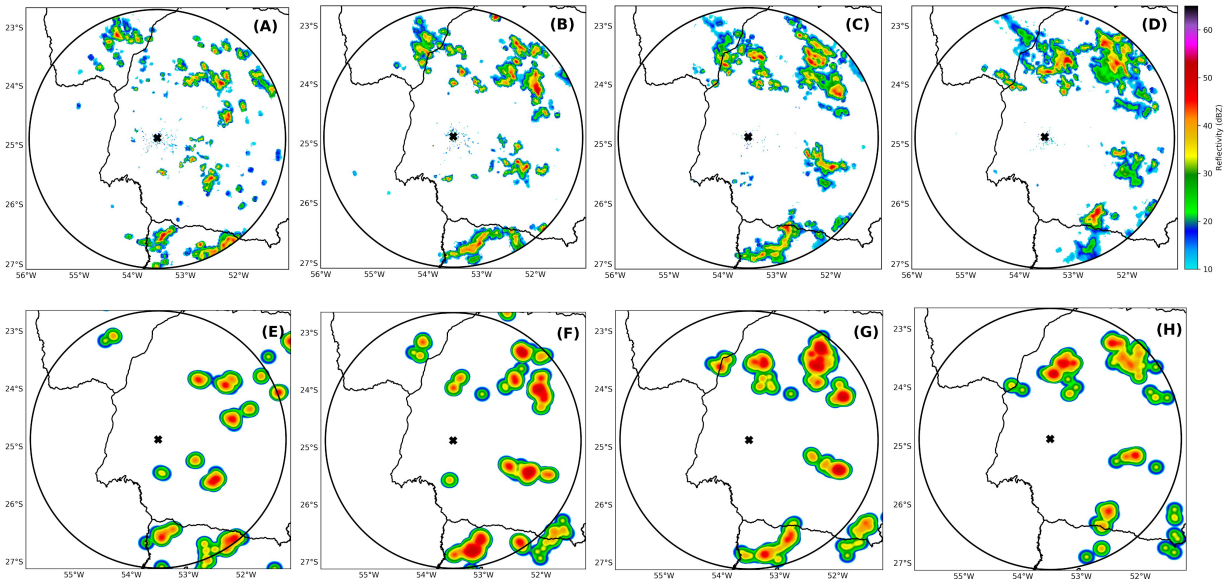


Figure 4: Evolution of the horizontal reflectivity (CAPPI-3km) over the Cascavel radar at 2100 UTC (a), 2200 UTC (b) 2230 UTC (c) 2310 UTC (d) and LRP at 2100 UTC (e), 2200 UTC (f) 2230 UTC (g) 2310 UTC (h) for isolated convection occurred on january 09, 2017

In the scatter plot analyses, (figure 5a) it was noted that a broad spread of the values in the first case, which indicates the large variance. There was a slight tendency of underestimation by LPR given that the most points are positioned below of the diagonal bisectrix. There was a significatively occurrence of the zero values of LPR for a variety of values of the radar reflectivity concentrating in a range of 10 to 40 dBZ (values below the red line in figure 5a). It is due the no detection of lightning in stratiform areas. The second case (figure 5b) does not have such a high occurrence of the zero values of LRP. Besides that, an overestimate is observed which the most points are localized above the blue line. The third case (figure 5c) also indicates a slight overestimate LRP and some points of zero values of LRP. And finally, the figure 5d presents the case related to isolated cells where no overestimate or underestimate it is not clearly observed, and the occurrence of the zero values of LRP is similar to the other cases with the exception of the first case that presented greater occurrence. Whereas the

stratiform regions are represented by values below of 35 dBZ and taking into account that part of the regions is associated with zero values of LRP, the values of radar reflectivity were underestimate or undetected by LRP.

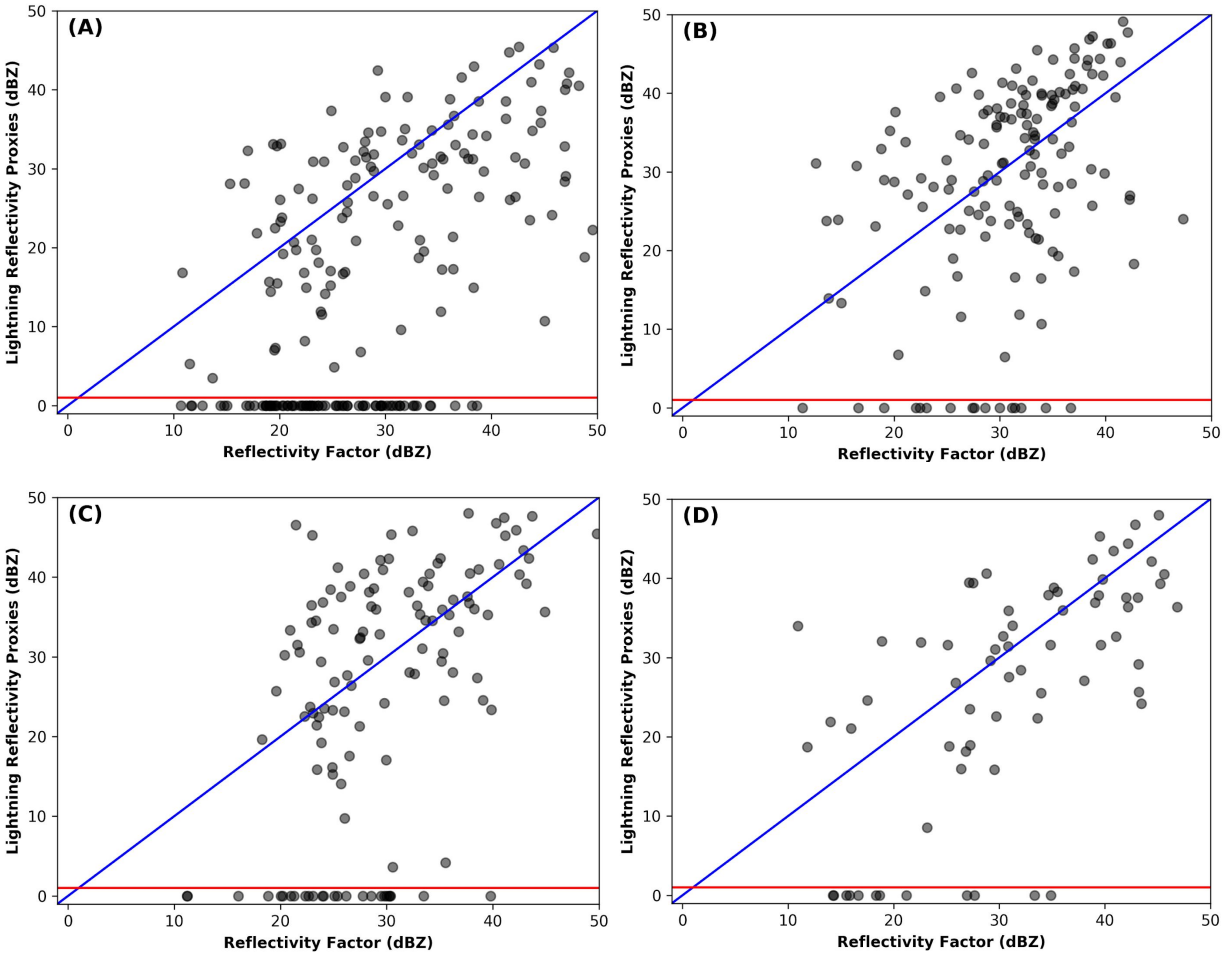


Figure 5: Scatter plot for LPR and radar reflectivity factor in (dBZ) at about 2-km altitude. The values were extracted to positions of rain gauges that registered high rates of precipitation. The events occurring in 13/10/2016 (A), 02/11/2016 (B), 09/01/2017 (C) and 26/04/2017 (D are shown in the figures . The blue line is a bisectrix and the red line is for to indicate the region where values of zero were observed for LPR.

In the scatter plot for all events (figure 6) LRP overestimate the radar reflectivity for rain peaks what could increase the errors in QPE. This result is opposite what was observed in dBZ fields, where the values of the LRP have been below of the radar reflectivity. This occurs because the LPR could not capture the signature of the broad stratiform regions behind the squall lines. Even for high values of the radar reflectivity the variability is high, especially for underestimate values of the LRP.

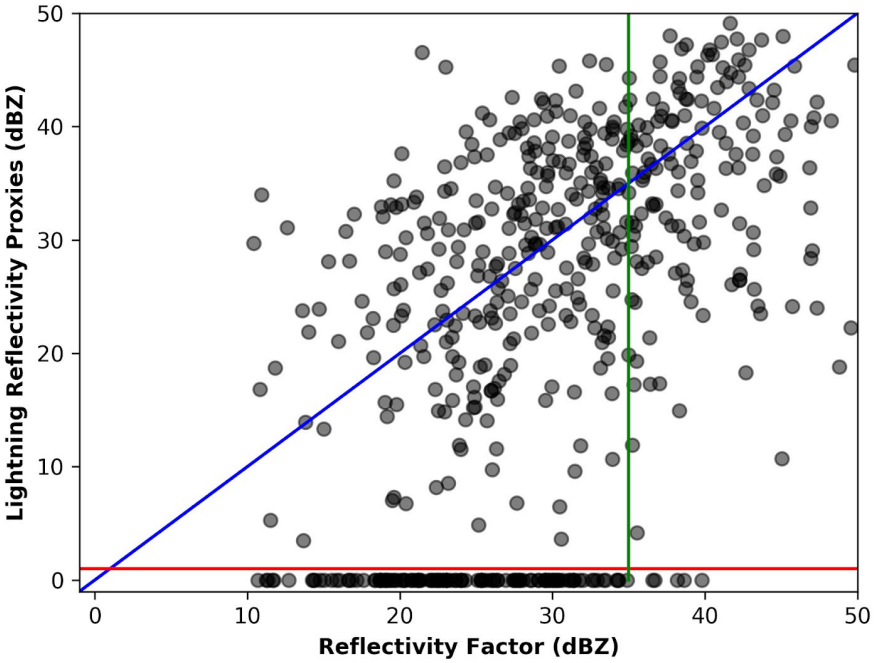


Figure 6: Scatter plot for LPR and radar reflectivity factor in (dBZ) at about 2-km altitude for the four cases. The blue line is a bisectrix, the red line is for to indicate the region where values of zero were observed for LPR and the green line is to separate at left how stratform and at right of the line how convective precipitation.

Conclusion

It was possible to observe that the lightning-based proxies reproduced very well the convective cells of the events. Both the shape and the magnitude of the values were well captured, nevertheless for some applications, such as identified mesoscale signatures, the proxies are not useful. For heavy rain rates the proxies tend to overestimate the values of radar reflectivity. Although this is an analysis of few cases the results of LRP can be very useful to several applications, especially in regions that do not have the presence of meteorological radars. Then, we conclude that the LPR data could be used for weather monitoring and QPE in the major of operational applications. Since most of the lightning data collected have high temporal resolution, this proxies can be very useful for nowcasting that require fast updates of the data for a better result.

Acknowledgement

Thank the Simepar and Earth Networks for provide the data used in this work and also pos graduate program in meteorology at the Federal University of Pelotas.

References

Chonglin L. Robert, S. M. Elena, N. and Christopher, D. L. Using Lightning Data to Generate Proxy reflectivity data. - December 2013. - Patent Application Publication. Vol. 1, p. 14.

Robert H. Cloud Dynamics. Second edition - Elsevier, p. 432, 2014.

Marengo, J. A.; Ambrizzi, T.; Soares, W. R. Jato de baixos níveis ao longo dos Andes. Tempo e clima no Brasil . v. 1, p.169, 2009.

The Development of a Canadian Operational Dual-Polarization Rainfall Estimation Algorithm

S. Boodoo, D. Hudak, N. Donaldson, J. Reid, D. Michelson, P. Rodriguez, M. Couture, V. Stojanovic.

Environment and Climate Change Canada (ECCC)
(Dated: 22 June 2018)

1 Introduction

Environment and Climate Change Canada (ECCC) is evaluating precipitation estimation methods as part of its ongoing upgrade to dual polarized S-band radars. The operational radar network upgrade is undertaken by the Canadian Weather Radar Replacement Program (CWRRP) within the Meteorological Service of Canada (MSC) and installed the first S-band radar in the fall of 2017. The network is scheduled to be completed by 2023 with potentially 32 S-band dual-polarized weather radars covering the most populous regions of the country. In the interim, the network will be a hybrid one comprised of dual-polarized S-bands and Doppler C-bands, two of which are dual polarized. The objective is to develop dual-polarization quantitative precipitation estimation (QPE) algorithms for use in an operational environment for the Canadian network. Algorithm development and evaluation are currently based on the ECCC King City C-band dual-polarized radar (WKR) located 30 km north of Toronto. As more S-band radars come online in the near future, the methodologies and algorithms will be revised to suit the diverse locations and climatology across Canada.

Radar rainfall estimation is known to be subject to significant errors (e.g. Zawadski, 1984; Austin, 1987; Joss and Waldvogel, 1990; Tabary, 2007; Krajewski et al., 2010) such as sensitivity to the variability of the drop size distribution, attenuation, variation of the vertical reflectivity profile, wet radome, clutter, beam blocking non-uniform beam filling and radar mis-calibration. In addition to reflectivity (Z), dual-polarization radars also measure differential reflectivity (Z_{DR}), differential propagation phase (Φ_{DP}), specific differential phase (K_{DP}) and co-polar correlation coefficient (ρ_{HV}), which provides additional information to help mitigate some of these problems. Utilizing this information has shown improvement over traditional Z-only methods in deriving radar rainfall rates. Several dual-polarization rainfall rate estimators can be found in the literature (e.g. Bringi and Chandrasekar, 2001; Gorgucci, 2001; Ryzhkov et al. 2005; Illingworth and Thompson, 2005; Tabary et al. 2011) that are of the forms R(Z, Z_{DR}), R(K_{DP}, Z_{DR}) and R(K_{DP}). Ryzhkov et al., 2014 developed an algorithm based on specific horizontal attenuation (A_H) to derive rainfall rates (R(A_H)) which is immune to radar mis-calibration and partial beam blockage. In Boodoo et al. (2015) several of these algorithms were evaluated for a flooding event that occurred in Toronto in 2013. Very good results were obtained with R(K_{DP}) and R(A_H) algorithms for that case and these are being considered for use in operational environment rather than the traditional reflectivity rainfall (Z-R) relationship (Marshall and Palmer, 1948) that is currently employed. The current work presents the methods and algorithms being developed and their results evaluated with rainfall totals from gauges within 100 km of the radar.

2 Radar data pre-processing.

A significant part of the methodology is assessing the data quality of the polarimetric measurements and the removal of non-precipitation echoes prior to applying rainfall retrieval algorithms. The dual-polarized data are collected at regular 10-minute cycles and Figure 1 shows example raw PPIs of a) Z, b) Z_{DR}, c) ρ_{HV}, d) Φ_{DP} from WKR at 0300Z on June 23 2017.

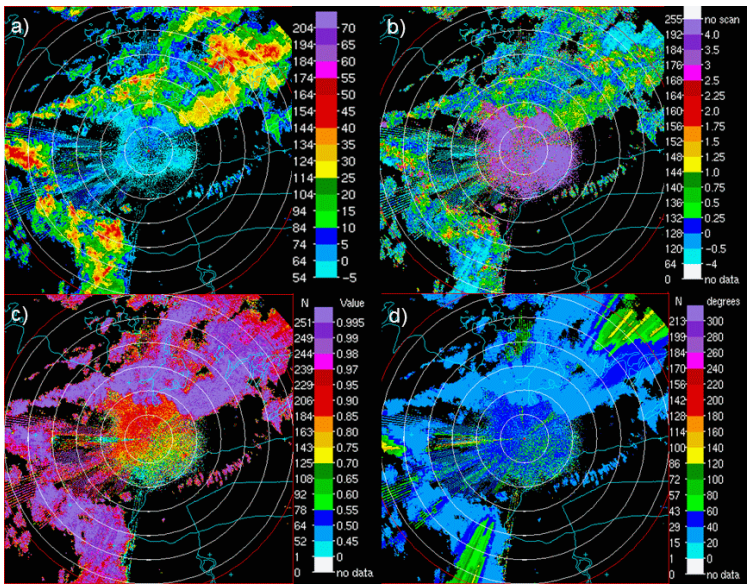


Figure 1: WKR PPIs of a) Z, b) Z_{DR}, c) ρ_{HV}, d) Φ_{DP}, at 0300Z June 23 2017.

As described in Boodoo et al. (2015), separation of precipitating from non-precipitating echoes relies on measurements of ρ_{HV}, signal quality index (SQI) and gradients of Φ_{DP} to determine rainfall regions in the radar scans at 0.5° elevation. Ground clutter contamination is handled by Doppler filters in the signal processor and applied to the polarimetric measurements in addition to low signal-to-noise correction of ρ_{HV} and Z_{DR}. SQI thresholding was effective at removing contamination of radio interference radials and second-trip echoes, but care in the choice of value was required in some rain storm situations with when there is strong shear in the beam. For many QPE applications (e.g. Gourley et. al 2007; Giangrande and Ryzhkov 2008; Park et. al 2009; Cocks et. al 2017) full hydrometeor classification algorithms are used to identify precipitation, but in our case it has not been fully implemented so simple filtering is done using individual variables.

Biases in Z_{DR} measurement produce significant errors in QPE estimates of rainfall and compromise attenuation corrections methods. Scans with precipitation are used to estimate significant deviation of Z_{DR} from the nominal 0 dB that should be attained on the radar system. It also provides a good way of monitoring Z_{DR} in an operational setting. The method works well in most rainfall situations, and care is taken to avoid ground clutter pixels, bright bands and areas of attenuation. Figure 2 is an example of the deviation of Z_{DR} for June 23 2017 at WKR. From about 0000Z to 0300Z, the median Z_{DR} was about 0.1 dB or less as indicated by the thin black line. The colors give an indication of the frequency distribution of the pixels selected for estimating the Z_{DR} deviations. At about 0330Z it began raining moderately over the radar and radome wetting caused a significant reduction in Z. Additionally Z_{DR} was affected by differential attenuation and deviated from zero to reach a maximum of about 0.5 dB at 0420Z while it was raining moderately over the dome.

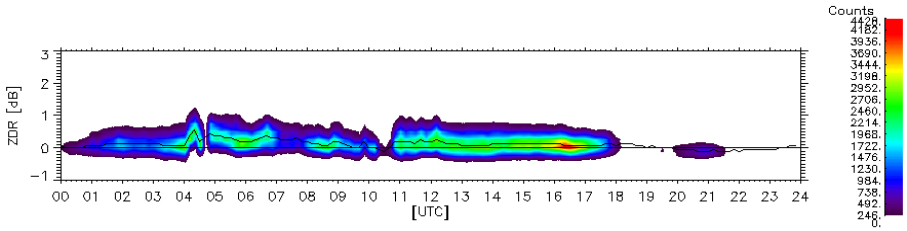


Figure 2: Estimated median Z_{DR} deviation from 0dB at 10 minute intervals derived from light rainfall pixels for June 23 2018 at WKR.

It continued raining over the dome for several hours afterwards with varying intensities, but as the precipitation moved away from the dome, Z_{DR} began to stabilize around 1300Z and remained close to its initial unbiased value of about 0dB. The method of monitoring Z_{DR} deviations during radome wetting scans was used to adjust the overall Z_{DR} field prior to attenuation correction and precipitation estimation. Unfortunately, at this time we have not been able to determine a correction factor for Z under these circumstances.

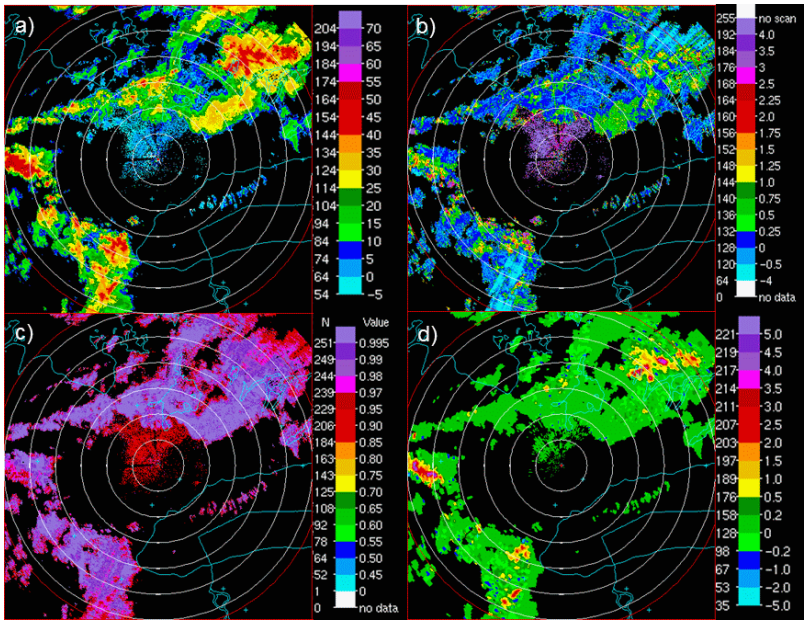


Figure 3: WKR PPIs of a) Z, b) Z_{DR}, c) ρ_{HV}, d) K_{DP}, at 0300Z June 23 2017.

Figure 3 shows PPIs of attenuation corrected Z, attenuation corrected Z_{DR}, ρ_{HV}, and K_{DP} at 0300Z corresponding to the images in Figure 1. Note that most of the second-trip contamination has been removed, but close to the radar weak reflectivity and high Z_{DR} pixels with moderate ρ_{HV} persists (Figs. 3a, 3b, 3c). These returns are likely from insects that have not been adequately filtered out by the pre-processing steps. K_{DP} (Fig. 3d) has been calculated from Φ_{DP} that has been unfolded and smoothed in range and azimuth.

3 QPE algorithms.

Following the methodology described in Boodoo et al. 2015, rainfall retrieval algorithms $R(Z_H)$, $R(Z_H,Z_{DR})$, $R(K_{DP},Z_{DR})$, $R(K_{DP})$ and $R(A_H)$, where K_{DP} and A_H are specific differential phase and specific attenuation, were applied after pre-processing with standard C-band coefficients. Table 1 lists the algorithms presented in the paper.

Table 1: List of QPE estimators used for C-band precipitation estimation.

Source	Algorithm
Marshall and Palmer (1948)	$R = 0.0365Z^{0.625}$
Bringi and Chandrasekar. (2001)	$R = 0.0058Z^{0.91}10^{-0.209Z_{DR}}$
Bringi and Chandrasekar. (2001)	$R = 37.9K_{DP}^{0.89}10^{-0.072Z_{DR}}$
Brandes et al. (2002)	$R = 33.8K_{DP}^{0.79}$
Ryzhkov et al. (2014)	$R = 294A_H^{0.89}$ (T=20^{0}C)

In addition to the above algorithms, two additional precipitation rate estimates were derived by choosing between R(Z) and $R(K_{DP})$ based on rain-rate thresholds as follows:

$$CR1 = \begin{cases} R(Z) \ if \ R(Z) \le 10\ mm/hr \\ R(K_{DP}) \ if \ R(Z) > 10\ mm/hr \end{cases} \qquad CR2 = \begin{cases} R(Z) \ if \ R(K_{DP}) \le 10\ mm/hr \\ R(K_{DP}) \ if \ R(K_{DP}) > 10\ mm/hr \end{cases}$$

where "CR" represents "combined rate" for the two methods and is similar to that of Diederich et al. 2015.

Figure 4 shows examples of derived precipitation rates from the algorithms in Table 1 and the two combined rain-rates based on Z and K_{DP} thresholds (CR1, CR2). The scan is at 0420Z on June 23 2017, and was affected by moderate rain over the radome. At this time both Z and Z_{DR} attenuation correction methods were compromised and Z_{DR} was adjusted for its deviation resulting from radome wetting.

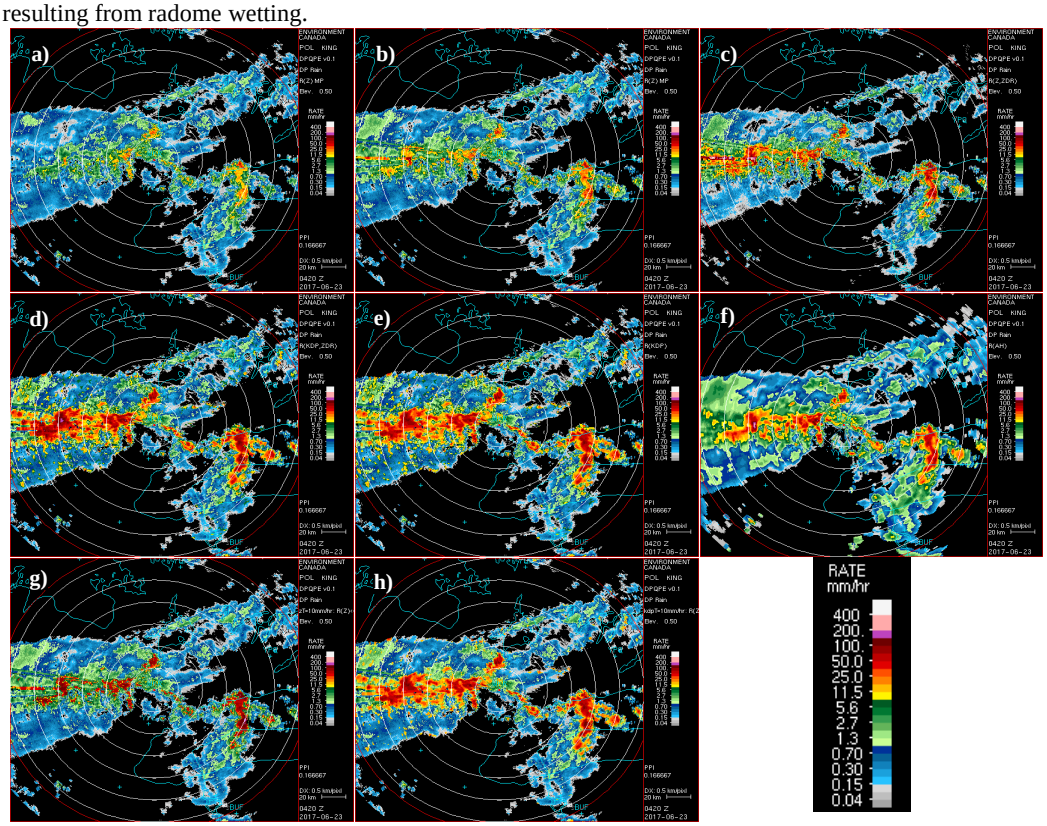


Figure 4: Derived rain-rates from a) R(Z), b) R(Z),Z attenuation corrected, c) R(Z, Z_{DR}), d) R(K_{DP},Z_{DR}), e) R(K_{DP}), f) R(A_H), g) CR1, h) CR2 at 0420Z June 23 2017.

Rainfall rates derived from the various algorithms are shown in Figure 4. Fig. 4a used the conventional R(Z) with the attenuated reflectivity measurements and Fig. 4b used the attenuation corrected reflectivities. The strong rain cells directly west of the radar were severely attenuated and the rates derived from them are low. After attenuation correction, Fig. 4b, rain cells to the west of the radar and also cells south east of the radar show improvement in the rain-rate field, however there are large areas that sill remain affected by the compromised reflectivity correction for the wet radome. Fig. 4c is the rain–rate field derived from $R(Z,Z_{DR})$, and it shows significant improvement in rates with the introduction of Z_{DR}. The Z_{DR} used have been adjusted using the estimated Z_{DR} deviation as described earlier. The same applies to Fig. 4d using the $R(Z,K_{DP})$ algorithm. Much of the heavy rainfall to the west of the radar has been captured, as well as improvement in rates in areas of lighter rainfall. The rainfall rates shown in Fig. 4e ($R(K_{DP})$) is similar to Fig. 4d and is not surprising as K_{DP} is unaffected by path and radome attenuation. Derived rates for $R(A_H)$ in Fig. 4f shows significant improvement in rainfall rates over Z, and very similar values in rainfall intensity as in the K_{DP} algorithms. Additionally there is improvement in areas with lower intensity rainfall that have not been captured as well in the other algorithms. $R(A_H)$ is also unaffected by radome attenuation as the K_{DP} algorithms, but improves rain-fall rates at all intensities encountered in this case. The last two Figures 4g and 4h are the combined Z and K_{DP} algorithms (CR1 and CR2) with thresholding on different variables. Rainfall rates derived from CR1 still look severely attenuated, which is not surprising since Z was under-corrected for attenuation. Using a rate threshold on K_{DP} (CR2) gives better results in this situation. The examples shown here support the idea that under radome wetting conditions rainfall algorithms involving K_{DP} or A_H will generally perform better.

4 Evaluation

To evaluate the performance of the algorithms over numerous cases, daily accumulated rainfall data from rain gauges over southern Ontario were acquired (Mekis et al. 2018). Figure 5 show the areal distribution of the gauges around the radar with total rainfall amounts on June 23 2017, which will be used as an illustration. The maximum accumulation was reported by a gauge located directly west of WKR about 95 km away, and gave a total accumulated rainfall of 152 mm. A nearby gauge, reported 149 mm of accumulated rainfall as indicated by the blue oval in Figure 5. This storm system moved across southern Ontario very quickly and the accumulated rainfall were within a few hours. There was significant flooding at these locations. In the Greater Toronto Area, enclosed in the larger blue oval in Figure 5, a cluster of gauges reported rainfall amounts in the 20 to 60 mm range.

Rainfall accumulations were derived from each of the precipitation rate algorithms, as shown in Figure 4. These were summed at the 10 minute cycles to produce daily accumulations and presented in Figure 6. No adjustments for advection or time sampling were considered and instantaneous rates were simply assumed to persist between scan cycles. In comparison with the accumulation distribution from the gauges, it is evident that accumulations based on R(Z) (Figs. 6a, 6b) whether uncorrected or corrected for path attenuation were significantly lower in the main bands of the precipitation. Additionally, significant radome attenuation and compromised corrections of both Z and Z_{DR} were contributing factors. The $R(Z,Z_{DR})$ algorithm performs a little better in areas with much higher accumulation as in the main band west of the radar and in the band at the north shore of Lake Ontario.

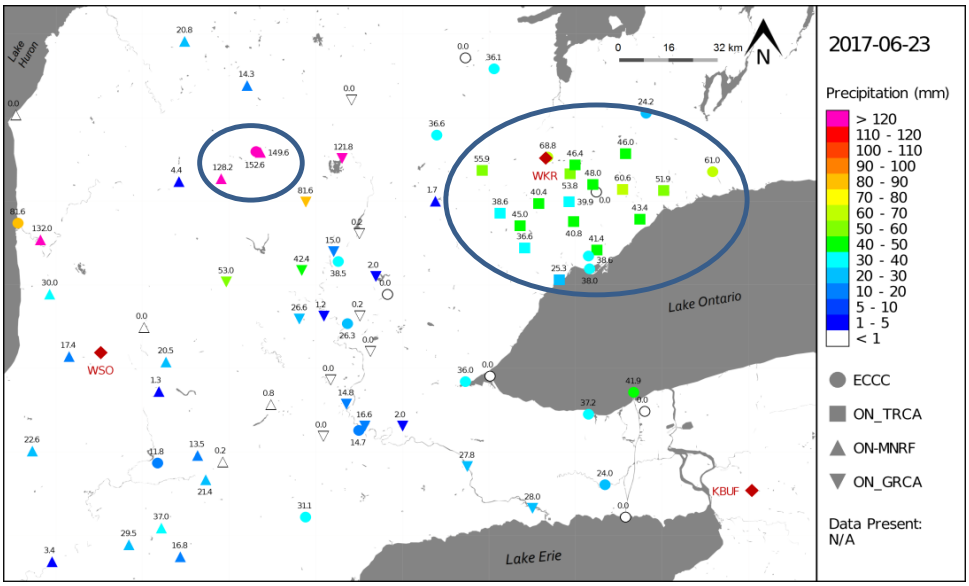


Figure 5: Distribution of rain gauges in southern Ontario showing daily total rainfall accumulation for June 23 2017. Radar locations are marked with red diamonds (King City (WKR), Exeter (WSO) and Buffalo, US Nexrad (KBUF)).

There is however, a circular region of high accumulation (Fig. 6c) within 30 km of the radar that is not realistic and absent in the other accumulation fields. This artifact is a result of the inadequate filtering of high Z_{DR} and low Z, characteristic of

insects near the radar (Figs. 3a, 3b), which was misrepresented as rain and contributed to the total daily accumulation. Although ρ_{HV} is relatively high in this area, Φ_{DP} is noisy, and rain-rate algorithms that depend on Φ_{DP}, namely $R(K_{DP},Z_{DR})$, $R(K_{DP})$, $R(A_H)$, CR1 and CR2 do not show this accumulation artifact (Figs. 6d,e,f,g,h).

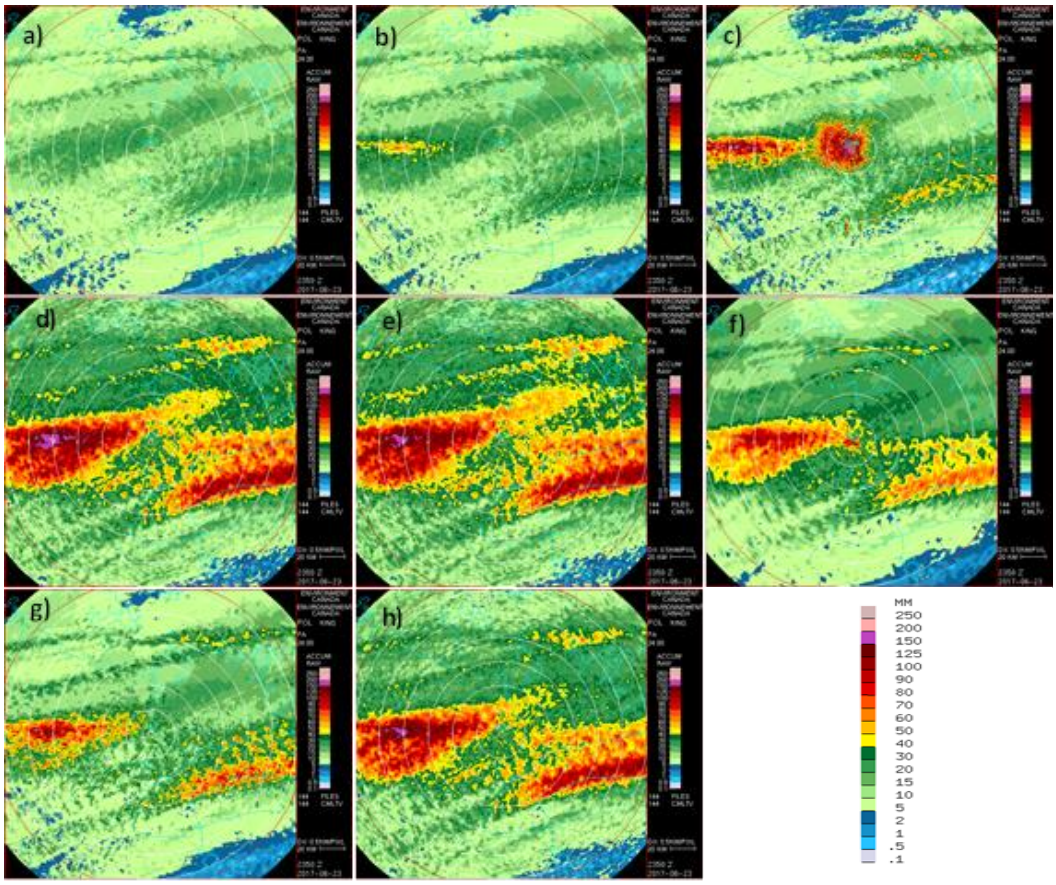


Figure 6: Rainfall accumulation for June 23 2017 from a) R(Z), b) R(Z),Z attenuation corrected, c) R(Z, Z_{DR}), d) R(K_{DP},Z_{DR}), e) R(K_{DP}), f) R(A_H), g) CR1 and h) CR2.

The maximum rainfall accumulation west of the radar is well represented in Figs. 6d,e,h and all these algorithms estimated about 150 mm, which is in good agreement with the gauges in this area. For the Greater Toronto Area, north shore of lake Ontario, rainfall amounts from these algorithms agree well with the gauges. CR1with R(Z) threshold (Fig. 6g), did not perform as well because Z was still under-corrected, and this suggests that if a combination like this were used operationally, the R(Z) threshold would have to be carefully chosen and may need to be adjusted according to the circumstance. The accumulation from $R(A_H)$ (Fig. 6f) is good relative to the K_{DP} dependent relationships, but only estimated about 100 mm compared to the maximum indicated by $R(K_{DP})$, for example. It is likely the coefficients used in the calculation rates and of the specific attenuation were not particularly well-suited for this case as these parameters have temperature and range dependencies (Ryzhkov et al. 2014).

Scatterplots of radar derived daily accumulation total against gauges (44) within 100 km of the radar are shown in Figure 7 for this event. The radar amounts were an average over a small window over each gauge location of approximately 2 km^2. Least absolute deviation fits are shown as solid lines while the one-to-one lines are dotted. Root Mean Square Error (RMSE), Normalized Mean Bias percentage (NMB), and Pearson Correlation coefficient (CORR) for the radar gauge pairs are provided for each of the algorithms in Table 2. It is no surprise that the conventional R(Z) relation used operationally performed poorly, and even with attenuation correction it was only marginally better for this event. Severe attenuation and radome wetting resulted in a 65 to 75 percent lower estimate of rainfall accumulation with these algorithms. The RMSE was greater than 39 mm. Rainfall amounts from the $R(Z,Z_{DR})$ algorithm were underestimated by about 45%. The RMSE was 26 mm and the correlation was 0.9. Relatively low RMSE of about 14 mm were achieved with $R(K_{DP},Z_{DR})$, $R(K_{DP})$ and the combined CR2 algorithms. The normalized mean bias was excellent for the $R(K_{DP},Z_{DR})$, $R(K_{DP})$ estimates, -3 and -1 percent respectively, but the combined CR2 algorithm underestimated the accumulation by 12 percent, which was still good relative to the other algorithms. It was surprising that $R(A_H)$ underestimated by about 30 percent and had a relatively large RMSE, but this could be attributed to the use of improper coefficients in the estimation of specific attenuation. It is expected to perform better once proper coefficients have been established. Overall correlations between the radar gauge pairs for all the algorithms, except R(Z), were excellent.

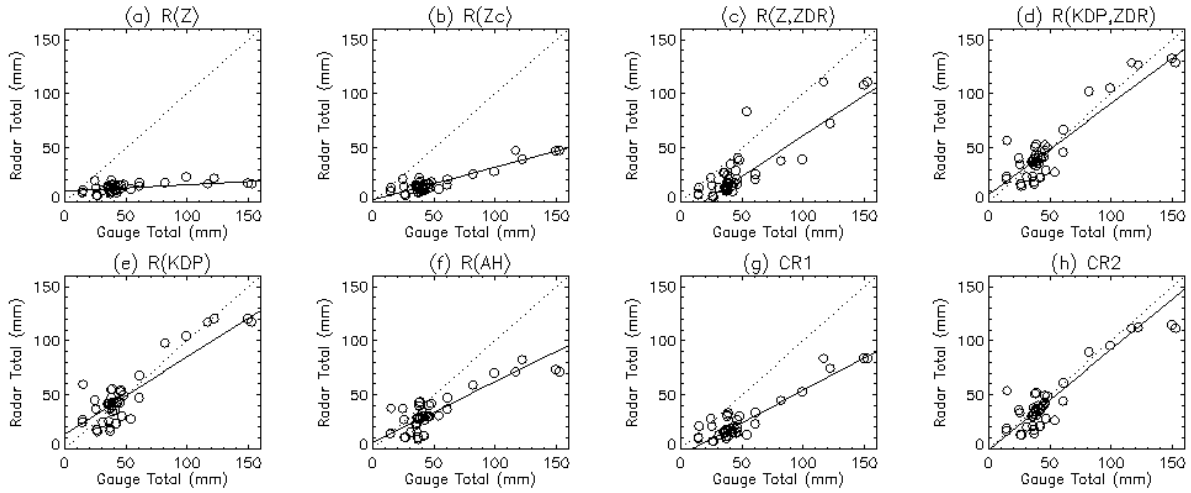


Figure 7: Scatterplots of gauge daily rainfall accumulation against radar derived accumulation from a) R(Z), b) R(Z),Z attenuation corrected, c) R(Z, Z_{DR}), d) R(K_{DP},Z_{DR}), e) R(K_{DP}), f) R(A_H), g) CR1 and h) CR2 on June 23 2017.

Table 2: Relative performance of each algorithm with respect to the gauge total for the June 23 2017 storm, showing values for Root Mean Square Error (RMSE), Normalized Mean Bias percentage (NMB), and Pearson Correlation coefficient (CORR).

Algorithm	RMSE(mm)	NMB(%)	CORR
R(Z)	46.3	-73	0.6
R(Z) attn. corrected	39.2	-65	0.9
R(Z, Z_{DR})	26.3	-44	0.9
R(K_{DP},Z_{DR})	13.2	-3	0.9
R(K_{DP})	14.4	-1	0.9
R(A_H)	24.4	-32	0.9
CR1	27.9	-48	0.9
CR2	14.6	-12	0.9

Over the summer months of June, July and August 2017, 42 days with rainfall were selected to evaluate the rain-rate algorithms over a wide range of rainfall totals. The June 23 event evaluated above was the heaviest rainfall day during this three month period over the King City radar coverage area. It was also the only significant flooding case that we know of during that period. Of the remaining 41 days, except June 23, the daily rainfall accumulations reported from any of the gauges within 100 km of the radar were in the 3 to 65 mm range.

Figure 8 shows the scatter plots of the daily radar versus gauge amounts for the 42 days (including June 23) that were selected from the various algorithms. R(Z) only algorithms show overall under-estimation of daily total rainfall compared to the rain gauges across all amounts. The normalized mean bias in Table 3, give an underestimation of around 50 percent and an average RMSE of 13 mm for these algorithms. The R(Z,Z_{DR}) scatterplot (Fig. 8c) shows a large variance of the radar estimates and poor correlation (0.3) and could possibly be due to inadequate filtering of abnormally high Z_{DR} that are likely not actual precipitation. However the R(K_{DP},Z_{DR}) algorithm (Fig. 8d) show much less spread and gives an NMB of 6 percent and an RMSE of 6 mm. The correlation is also good at 0.9. The R(K_{DP}) RMSE was 6.7 mm while RMSE for R(A_H) was 8.2 mm. For both these algorithms the CORR was 0.9. Normalized mean bias was 6, 11 and -16 percent for R(K_{DP},Z_{DR}), R(K_{DP}) and R(A_H) respectively. Of the two combination algorithms, CR1 and CR2, CR2 performed much better and the NMB was only -1 percent with a RMSE of 6.5 mm for all 42 precipitation days that were analyzed. Furthermore, CR2 outperformed all the other algorithms tested so far in this dataset.

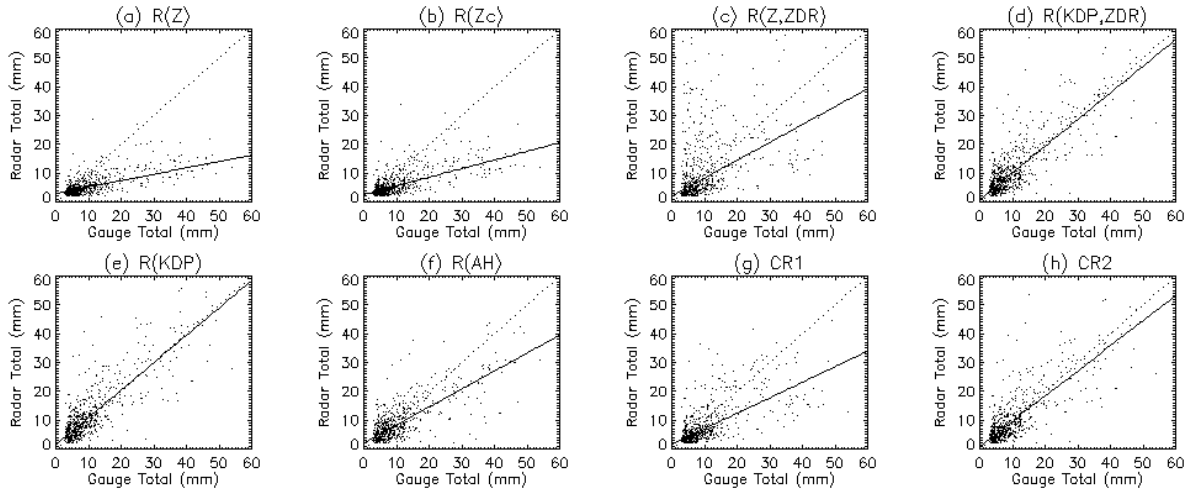


Figure 8: Scatterplots of gauge daily rainfall accumulation against radar derived accumulation from a) R(Z), b) R(Z),Z attenuation corrected, c) R(Z, Z_{DR}), d) R(K_{DP},Z_{DR}), e) R(K_{DP}), f) R(A_H), g) CR1 and h) CR2 for 42 days during June, July and August 2017.

Table 3: Relative performance of each algorithm with respect to the gauge total for 42 days selected during June, July and August 2017, showing values for Root Mean Square Error (RMSE), Normalized Mean Bias percentage (NMB), and Pearson Correlation coefficient (CORR).

Algorithm	RMSE(mm)	NMB(%)	CORR
R(Z)	14	-50	0.7
R(Z) attn. corrected	12.1	-43	0.8
R(Z, Z_{DR})	24.2	40	0.3
R(K_{DP},Z_{DR})	6.4	6	0.9
R(K_{DP})	6.7	11	0.9
R(A_H)	8.2	-16	0.9
CR1	9.1	-23	0.8
CR2	6.5	-1	0.9

5 Summary and conclusions

Environment and Climate Change Canada is undergoing a national weather radar replacement of its existing C-band Doppler network with S-band dual polarized radars, and there is a need to capitalize on the benefits of dual polarization technology for QPE applications in an operational environment. Dual polarization data from the King City C-band radar are being used to develop precipitation estimation and hydrometeor classification algorithms, which will be adapted and tested as S-band installations proceed. Rainfall retrieval algorithms R(Z_H), R(Z_H,Z_{DR}), R(K_{DP}), R(K_{DP},Z_{DR}) and R(A_H) along with combined R(Z) and R(K_{DP}) on rain-rate threshold have been presented. The dual polarization data must be pre-processed and quality controlled before use in these algorithms. SQI thresholding was effective at removing contamination of radio interference radials and second trip echoes. The cross-correlation coefficient was useful for removing residual ground clutter and non-meteorological pixels, although some persisted and caused unrealistic looking accumulation patterns with some algorithms. Systematic Z_{DR} biases are monitored during precipitation but radome wetting complicated Z_{DR} measurements and introduced dynamic positive mean variations in Z_{DR} that should be adjusted for before attenuation correction. Radome wetting also compromised the attenuation correction of Z to the extent that it becomes unusable in many instances. The use of K_{DP} and A_H improved the precipitation estimation dramatically in moderate and heavy rain and in radome wetting situations, but was not as good at lower rainfall intensities. R(Z_H) was better at lower intensities, provided that radome attenuation and path attenuation effects were minimal. A method that selects between R(Z) and R(K_{DP}) using an appropriate threshold on R(K_{DP}) showed promise. The creation of a larger database of rainfall cases spanning five years is being worked on for further algorithm evaluation. Future work also entails investigating appropriate parameters for the calculation of A_H at C and S bands and methods to estimate the reduction of reflectivity during radome wetting and to include hydrometeor

classification output when it becomes available. Some of these algorithms are being run in near real time for both C and S-bands in the radar network.

Acknowledgement

The authors would like to thank Eva Mekis of Environment and Climate Change Canada for providing corrected surface rain gauge measurements used in this work. Thanks to Birathan Somasundaram for processing the raw gauge data to derive the daily accumulations and also for helping with the figures in this paper.

References

Austin, P.M. 1987. Relation between measured radar reflectivity and surface rainfall. Mon. Wea. Rev. 115 (5), 1053–1070.
Boodoo, S., D. Hudak, A. Ryzhkov, P. Zhang, N. Donaldson, D. Sills, and J. Reid, 2015: Quantitative Precipitation Estimation from a C-Band Dual-Polarized Radar for the 8 July 2013 Flood in Toronto, Canada. J. Hydrometeor., 16, 2027–2044, https://doi.org/10.1175/JHM-D-15-0003.1
Brandes, E. A., G. Zhang, and J. Vivekanandan, 2002: Experiments in rainfall estimation with polarimetric radar in a subtropical environment. J. Appl. Meteor. 41, 674–685.
Bringi, V. N. and Chandrasekar, V. 2001: Polarimetric Doppler Weather Radar: Principles and Applications, Cambridge University Press, 636.
Cocks, S.B., J. Zhang, S.M. Martinaitis, Y. Qi, B. Kaney, and K. Howard, 2017: MRMS QPE Performance East of the Rockies during the 2014 Warm Season. J. Hydrometeor., 18, 761–775, https://doi.org/10.1175/JHM-D-16-0179.1
Diederich, M., A. Ryzhkov, C. Simmer, P. Zhang, and S. Trömel, 2015: Use of Specific Attenuation for Rainfall Measurement at X-Band Radar Wavelengths. Part II: Rainfall Estimates and Comparison with Rain Gauges. J. Hydrometeor., 16, 503–516, https://doi.org/10.1175/JHM-D-14-0067.1
Gorgucci, E., G. Scarchilli, V. Chandrasekar, and V. N. Bringi, 2001: Rainfall Estimation from Polarimetric Radar Measurements: Composite Algorithms Immune to Variability in Raindrop Shape-Size Relation. J. Atmos. Oceanic Technol. 18, 1773-1786.
Gourley, J. J., P. Tabary, and J. Parent du Chatelet, 2007: A fuzzy logic algorithm for the separation of precipitating from non-precipitating echoes using polarimetric radar observations. J. Atmos. Oceanic Technol. 24, 1439–1451.
Giangrande, S. and A. Ryzhkov, 2008: Estimation of rainfall based on the results of polarimetric echo classification. J. Appl. Meteor. 47, 2445–2462.
Illingworth, A. J., R.J. Thompson, 2005. The estimation of moderate rain rates with operational polarisation radar. In: 32nd Int. Conf. on Radar Meteorology, Albuquerque, Paper P9R.1, Am. Meteorol. Soc.
Joss, J. and A. Waldvogel, 1990: Precipitation measurement and hydrology. Radar in Meteorology, D. Atlas, Ed. Amer. Meteor. Soc. 577-606.
Krajewski, W. F., G. Villarini, and J. A. Smith, 2010: RADAR-Rainfall Uncertainties. Bull. Amer. Meteor. Soc. 91, 87–94.
Marshall, J. S. and W. M. Palmer, 1948: The Distribution of Raindrops with Size, J. Met. 5, 165-166.
Eva Mekis, Norman Donaldson, Janti Reid, Alex Zucconi, Jeffery Hoover, Qian Li, Rodica Nitu & Stella Melo (2018) An Overview of Surface-Based Precipitation Observations at Environment and Climate Change Canada, Atmosphere-Ocean, 56:2, 71-95, DOI: 10.1080/07055900.2018.1433627
Park, H. S., A. V. Ryzhkov, D. S. Zrnic, and K. E. Kim, 2009: The hydrometeor classification algorithm for the polarimetric WSR-88D: Description and application to an MCS. Wea. Forecasting, 24, 730–748.
Ryzhkov, A. V., S. Giangrande, and T. Schuur, 2005a: Rainfall estimation with a polarimetric prototype of the WSR-88D radar. J. Appl. Meteor. 44, 502–515.
Ryzhkov, A. V., M. Diederich, P. Zhang, C. Simmer, 2014: Potential Utilization of Specific Attenuation for Rainfall Estimation, Mitigation of Partial Beam Blockage, and Radar Networking. J. Atmos. Oceanic Technol. 31, 599–619.
Tabary, P., 2007. The New French Operational Radar Rainfall Product. Part I: Methodology. Wea. Forecasting. 22: 393-408.
Tabary, P., A.-A. Boumahmoud, H. Andrieu, R. J. Thompson, A. J. Illingworth, E. LeBouar, and J. Testud, 2011: Evaluation of two ‘‘integrated’’ polarimetric quantitative precipitation estimation (QPE) algorithms at C-band. J. Hydrol. 405, 248–260.
Zawadzki, I., 1984. Factors affecting the precision of radar measurements of rain. Preprints. In: 22nd Conference on Radar Meteorology, Zurich, Switzerland, Amer. Meteor. Soc. 251–256.

A HYDROMETEORLOGICAL ANALYSIS OF AN EXTREME FLASH FLOOD EVENT IN THE URBAN AREA OF WEST ATTICA, GREECE

Marios N. Anagnostou[1,4,5], George Varlas[2], John Kalogiros[1], Petros Katsafados[2], A. Papadopoulos[3], E. Baltas[4], and E. Anagnostou[6]

[1] *IERSD, National Observatory of Athens, Athens, Greece*
[2] *Department of Geography, Harokopio University of Athens, Greece*
[3] *Institute of Marine Biological Resources and Inland Waters, Hellenic Centre for Marine Research, Greece*
[4] *Department of Water Resources and Environmental Engineering, School of Civil Engineering, National Technical University of Athens, Greece*
[5] *DUTH, School of Engineering, Department of Environmental Engineering, Xanthi, Greece*
[6] *Department of Civil and Environmental Engineering, School of Engineering, University of Connecticut*

(Dated: 22 June 2018)

1 Introduction

Floods are considered the most frequent natural disaster and in 2011 six out of ten biggest natural disasters were flash floods. According to The Centre for Research on the Epidemiology of Disasters (CRED), “flash flood” is usually defined as a rapid inland flood due to intense rainfall with short duration (Guha-Sapir et al., 2012). In this type of phenomena, in highly sloped terrain, the water flows rapidly with high destruction potential while in flat areas it cannot infiltrate into the ground or run off fast enough. Flash floods can be a source of significant damage and serious loss to infrastructures and human lives and are typically associated with thunderstorms which can occur at any place (Karymbalis et al., 2012). Globally the frequency of flooding events has increased and a warmer climate is expected to aggravate the effects on human life (Hirabayashi et al., 2013). All climate model projections show that higher precipitation extremes are expected in warmer climates (Kundzewicz et al., 2007), particularly at mid and high latitudes (Meehl et al., 2005). This directly affects the risk of flash and urban flooding.

Flash floods are a frequent occurrence in several parts of the Mediterranean region due to the local climate, which is prone to short and very intense rainfalls (Gaume et al., 2016). The Mediterranean Basin is a transitional zone between the cold and wet climates of Northern Europe and the hot and dry climates of low latitudes (North Africa) and is characterized by highly diverse climatic conditions (Camarasa Belmonte and Segura Beltran, 2001). Therefore. the types of rainfall that can generate flooding events vary along its coasts (Gaume et al., 2016). In general, convective thunderstorms and showers, which are usually produced in summer and early autumn, due to low level instability and high temperatures, are the dominant cause of flooding episodes (Llasat, et al., 2016). In addition, the form and geometry of the local drainage networks, the morphology of the basin and various anthropogenic interventions modify the catchment response of a basin and its physical properties (Runge and Nguimalet, 2005), potentially exacerbating the phenomenon and its negative effects.

Early warning systems are essential elements in the development of disaster preparedness and response strategies [UNISDR, 2009, Directive 2007/60/EC]. Effectiveness of early warning procedures depends highly on the accuracies of the precipitation monitoring systems involved (Westra et al. 2014). The impact of accurate representation of rainfall spatial variability on simulating the flash flood response has been demonstrated by several studies (Zoccatelli et al. 2010). Moreover, recent studies (Marra et al. 2014) have shown the importance of accurate rainfall estimates at small spatial scales for the prediction of debris flow/landslide initiation. Therefore, to improve the accuracy of flood hazard warning systems, it is critical to acquire accurate estimates of precipitation rates at high resolution. The quantification of precipitation over complex terrains, where these phenomena typically occur, is rather complex, and topography plays a dominant role in shaping precipitation variability (Barros et al. 2000). Current operational rainfall monitoring systems from national weather radar networks do not provide sufficiently accurate measurements of precipitation variability over mountainous areas (Maddox et al. 2002).

Numerical models are employed to predict these adverse phenomena. Nevertheless, flood prediction in urban areas is still an open scientific issue and remains a challenge. A sophisticated approach is the combination of atmospheric-hydrological modeling methods assimilated with high-resolution surface precipitation observations. This approach is becoming more attractive to the scientific community since they are fully coupled in a single advanced observation-modelling system. Many studies performed on flash flooding events focus on numerical modelling, applying a multitude of systems like DRiFt (Discharge River Forecast, Giannoni et al., 2000) and CREST (Coupled Routing and Excess Storage, Shen et al., 2014) for the hydrological part and AROME (Applications of Research to Operations at Mesoscale model, Seity et al., 2011), WRF (Weather Research and Forecasting model, Skamarock et al., 2007) and others for the atmospheric component, with the main issue being the successful prediction of high-intensity rainfall associated with convection (Llasat et al., 2016). Other studies rely on the combination of rain gauges and meteorological radar data (Llasat et al., 2016). In general, a successful numerical simulation of a flash flood event requires the combination of an accurate atmospheric model, a suitable hydrological model and rainfall data of adequate spatial and temporal resolution (Atencia et al., 2011).

Greece experiences a variety of catastrophic weather events, namely floods and flash floods that are frequently followed by severe consequences on the social and economic activity (Papagiannaki et al., 2013) and are primarily connected with strong convective storms developed during the warm season, especially over continental areas. These are mesoscale events with small spatial coverage (5-10 Km) and small-time scales, usually 1-2 hours (Wallace and Hobbs, 2006). The potential of these storms to become hazardous for human life and infrastructure depends on whether the convection organizes into mesoscale convective systems, or into the long-lived convective cells (supercells). In any case they distribute large amounts of water in a limited area very fast. In some cases, the response of watersheds to this type of rainfall events and their runoff rates, are not fast enough, leading to flooding events (Gaume et al., 2016). The negative effects of these phenomena are aggravated in built riverside areas as prevention is a parameter usually ignored during urban planning (Despiniadou and Athanasopoulou, 2006).

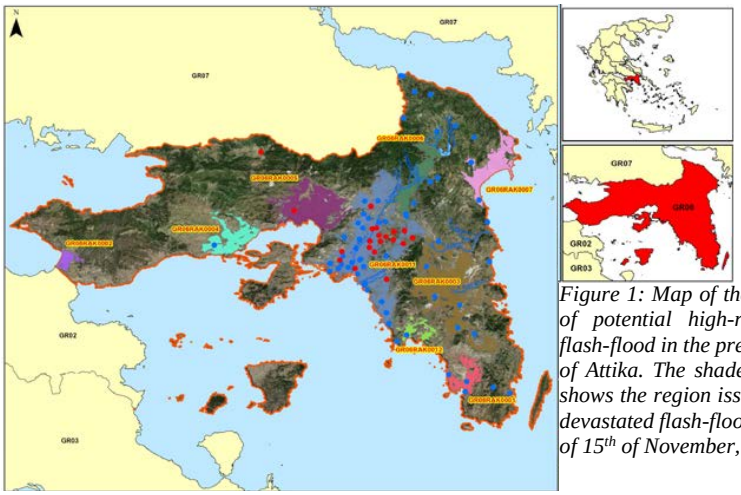


Figure 1: Map of the zones of potential high-risk on flash-flood in the prefecture of Attika. The shaded area shows the region issued the devastated flash-flood event of 15th of November, 2017.

A significant part of the drainage network of Greece consists of mountain torrents and small to medium size drainage basins with limited amount of discharge capabilities for most of the year (Diakakis et al., 2012). Even worse, several parts of the network were diminished, turned into streets or built upon, thus cutting off critical river cross sections (Baltas and Mimikou, 2002). The combination of highly intense convective storms and bad urban planning has led to a series of severe flash flood occurrences in Greece over the past years. A notable event, leading to one of the most devastating flash floods in Attika (suburban city of Mandra), occurred on the 15th of November 2017. Attica prefecture contains the capital, Athens, and it is currently the most populated region in Greece. According to the technical study "FLOOD RISK MANAGEMENT PLAN AND PRIORITIES: for the river basins of Attica prefecture" issued from the Ministry of Environment and Energy, specific secretary of inland waters for the effective elaboration of high risk flood hazard maps and management plans, issued the specific region (GR06RAK0005) of high risk danger and susceptible to flash-flood (see map in Figure 1) This study aims to provide a hydrometeorological analysis to an extreme flash flood event took place in the sub-urban area of Mandra, Attica, Greece.

2 Description of the synoptic and atmospheric instabilities

During the last month of fall 2017 and particularly the last two weeks of November the wider Mediterranean region including the eastern Mediterranean and the Aegean Sea was affected by successively organized barometric lows accompanied by corresponding frontal activities, causing locally strong phenomena. One such rare organized Mediterranean cyclone (named Medican Numa/Zenon), formed on the 11th of November between Tunisia and Libya (Figure 2), which accompanied an organized surface low with its center at the Gulf of Syrtis and a hot front along Sicily - South Italy and the North Ionian Sea. It's the type of storm we're accustomed to seeing in the tropical waters of the Atlantic and Pacific Oceans, perhaps leaving a trail of destruction through the Caribbean and Gulf of Mexico.

This situation affected the western, central and northern parts of Greece with showers and storms, with local adverse phenomena affect the North Ionian - Epirus and particularly the Corfu island. Subsequently, during the 12th of November the above closed low in the upper troposphere moved N-NE during the early hours of 13th November it gradually began to influence from the west - southwest the rest of the country. In the early morning of the 13th of November, a secondly organized instability in the upper tropospheric with cold air masses affect the whole country. In particular, the synoptical behavior of this particular low was the main factor for the shape and evolution of the adverse phenomena in Greece from 14-11-2017 until 19-11-2017. One of the main features of this extended upper low was the fact that it remained almost stationary in the region between Southern Italy - Sicily and the Tyrrhenian Sea.

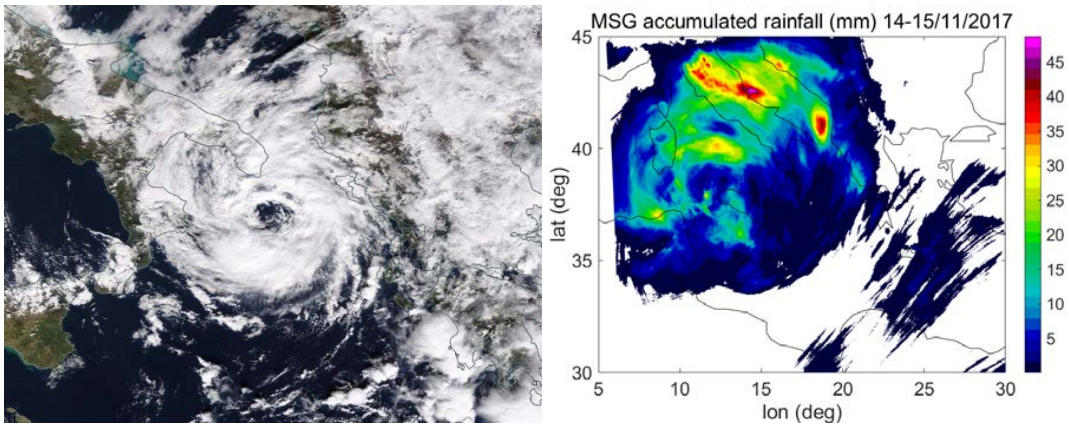


Figure 2: A Mediterranean "hurricane" named Numa struck Greece during 11-19 November 2017. Credit: NASA

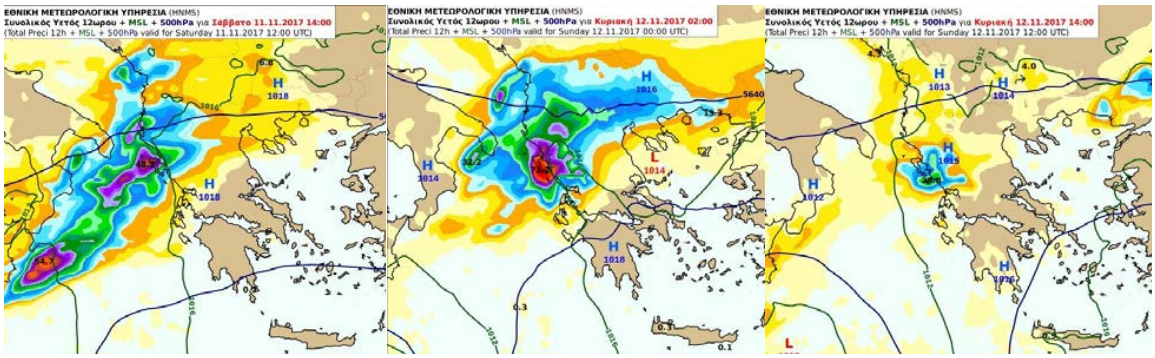


Figure 3: Official prognostic maps (rain accumulation and 500/surface HPa) issued from National Hellenic Meteorological Service (HNMS) associated with the flash flood events during the 11-12 November 2017 in Corfu island. Credit: HNMS

3 The flash flood case study of Mandra, Attika

In the early morning on the 15 of November an intense persistence precipitation event was observed at the mountain of Patera, 10 km north-west of the sub-urban city of Mandra, west of prefecture of Attika, in the preferences of urban capital city of Greece, Athens (see map in Figure 5). The region hosts the largest industrial units in Attica such as refineries, metallurgical industries, factories, shipyards as well as the waste landfill of all Attica prefecture. The intense presence of heavy industrial use, urbanization and other land changes have deteriorated to the worse the environmental pressures while have significantly increasing flood the risk. The anarchy residential and industrial development and activity did not follow any appropriate infrastructure network for flood protection and drainage rainwater collection (Mavrakis et al. 2004).

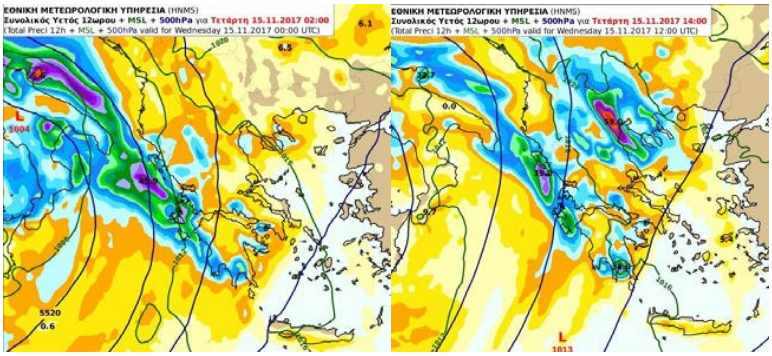


Figure 4: Similar to Figure 3 but for the case of Mandra flash flood in Attica region, during the 15th of November 2017. Credit: HNMS

The hydrographic network (see map in Figure 6) of the water basin that drain the large volumes of surface runoff from the steep gradients of surrounding mountainous end up in the Thriasio plateau (in the city of Elefsina) are extremely rich. The main streams apart this large water basin are the Sarantapotamos and St. Vlasiou (Fig 6b). During this event, rainfall data were collected from the XPOL radar of the National Observatory of Athens located on the Penteli mountain (about 30 km NE of Mandra). The XPOL radar was operated during rain events in plan position indicator (PPI) mode taking measurements in a

sector scan of 180º, at 0.5º, 1.5º and 2.5ºelevation sweeps with a range resolution of 120 m for the total range of 65 km. Antenna rotation rate was 6 deg s^{-1} and he time period for a full volume scan was less than 3 minutes.



Figure 5: map of the west of Attika indicating within the shading area (Thriasio) the main drainage network (with blue lines) and the region affected from the flash flood event of 15th of November 2017

The study domain is also covered by an operational C-band radar of HNMS at the mountain of Hymettus, about 10 km south of XPOL radar. Based on the HNMS official report, the total estimated rainfall accumulation recorded on 15 of November from 00:00 UTC until 12:00 UTC was 80 mm with the highest recorded rainfall rates (at the mountain of Patera) was above the 300 mm/hr.

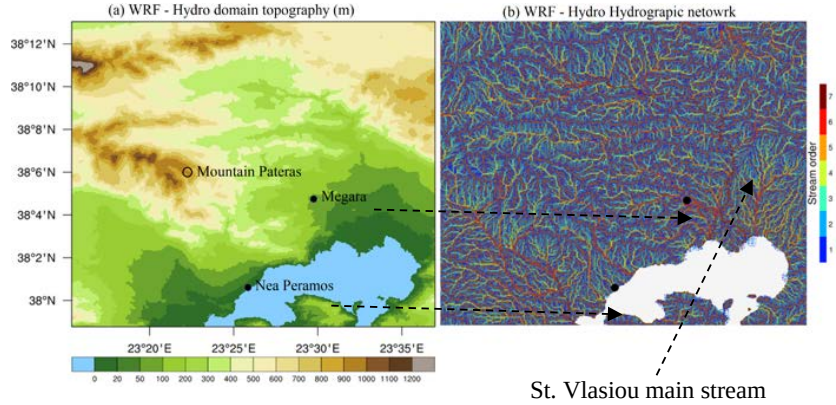


Figure 6: (a) topography and (b) hydrographic map of the water basin used for the hydrological runs

On the other hand, the XPOL recorded total accumulated precipitation (in the core of the storm at the mountain of Patera) of more than 200 mm (Figure 7b). More impressive was the fact that the highest precipitation rates of the core of the storm recorded during the time 03:00 to 06:00 UTC was more than 120 mm/hr (Figure 7a). This caused the sub-basin of St. Aikaterini to overflow and flood the area of Mandra, located in west Attica (see map in Figure 5), causing extensive damages on property and infrastructure, and the death of 23 people.

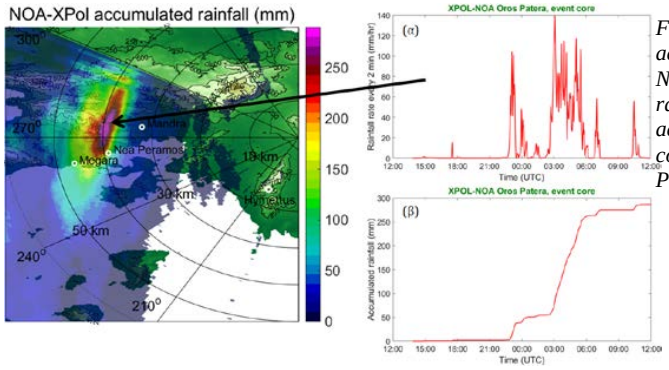


Figure 7: XPOL PPI rain accumulation during the 15th of November flood event with (a) rainfall rate and (b) accumulation rainfall, over the core of the storm in the mountain Patera

Comparisons of the total accumulation rainfall estimations recorded from the IMERG (Integrated Multi-satellitE Retrievals for GPM) satellite precipitation product (Figure 8a) with the aggregated 10x10 km XPOL rainfall product (Figure 8b) agrees very well, indicating of more than 200 mm rainfall (from 00:30 UTC until 07:30 UTC of 15 of November) over the city of Mandra (Figure 8c).

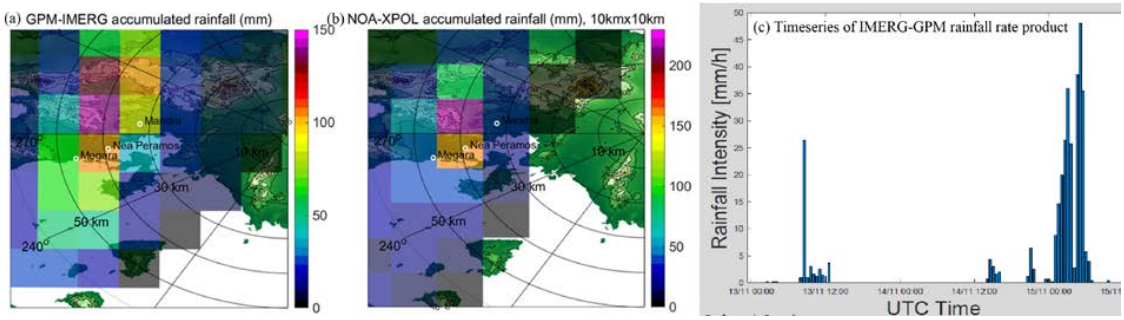


Figure 8: rain accumulation estimates during the 15th of November flood event from (a) GPM-IMERG product, (b) XPOL 10x10 km aggregated product and (c), timeseries rainfall rate from the IMERG-GPM over the city of Mandra.

3.1 Configuration of the Hydrological model based on the CHAOS (WRF-Hydro)

The potential benefit in using short-range X-band dual-polarization high-resolution observations for flood modeling applications is examined by comparing the different radar, satellite and prognostic simulations, with the later used as reference throughout the hydrologic analysis. Dynamic downscaling of the GFS (0.25°×0.25°) setting up the forecasting model of CHAOS (WRF-ARW) in the study domain with horizontal resolution of 9 km × 9 km, 3 km × 3 km, 1 km x 1 km and 0.25 km × 0.25 km covering the Europe, Greece and region of Attica, respectively. Coupling the CHAOS (WRF-Hydro model 50 m × 50 m) with the atmospheric forecasting model precipitation (Varlas et al. 2017), satellite and radar precipitation estimates in the city of Mandra every hour in the 0.25 km x 0.25 km grid. The hydrological configuration of the network is based on a 90 meters digital elevation map and the methodology followed for the stream ordering is on Strahler.

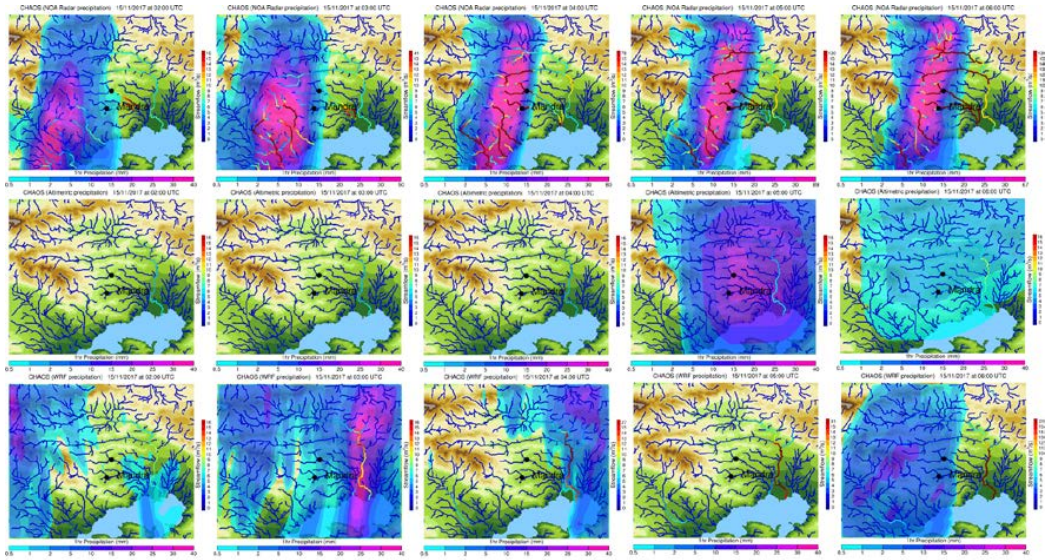


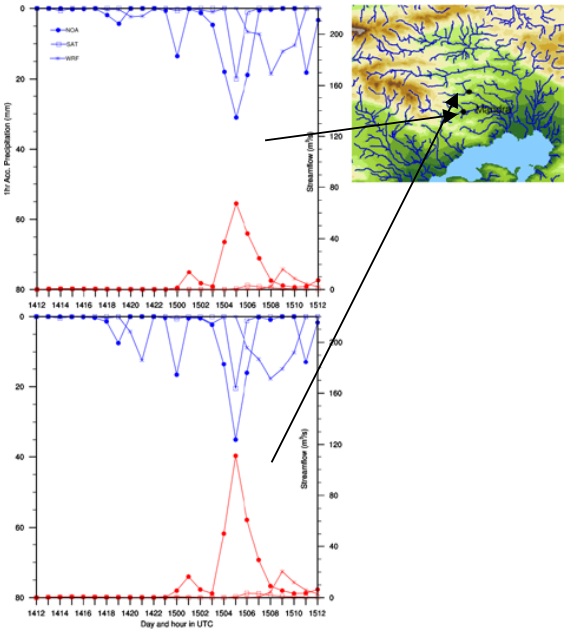
Figure 9: surface hourly rain accumulation estimates from the NOA's XPOL radar (upper five subplots), the IMERG-GPM (middle subplots) and the WRF-ARW (lower subplots). On the same plots are superimposed the simulated streamflows forced from each of the three rainfall estimates.

Simulated streamflow of the 02:00 until 06:00 UTC of 15th of November is shown in Figure 9 superimposed the surface hourly rainfall accumulation (mm) of NOA's XPOL in the upper five subplots, the IMERG-GPM in the middle ones and the WRF-ARW in the lower, ones. Due to the absence of any ground validation stations, a more qualitative approach will be followed. It is obvious that there are different characteristics in the spatial pattern and intensities of all three different the surface precipitation estimates. However, the satellite is missed the majority of the peak of the storm. It only indicates precipitation during the last two hours (i.e. 05 and 06 UTC). On the other hand, the WRF-ARW forecasting model is closer to the radar rainfall estimates, however, not that much in the pattern of the storm but in the total duration and in some cases in the intensity. Similarly, the streamflow simulations assimilated from the three estimates is clearly indicates that the simulation coupled from the radar precipitation estimates is the one that gives the higher streamflows, where in turn this can be assumed as flooding.

Figure 10, on the other hand, is a more quantitative comparison approach, showing the hourly streamflow simulations from 12 UTC of 14 of November up to 12 UTC of 15 of November forced from radar, satellite and forecasting rainfall estimations. Both plots are extract from the two black dotes shown in the upper right map of the figure. We notice that the peak rainfall intensities of radar match with the satellite but underestimate the total rainfall accumulation, while the model estimates, even

though are shifted in time, they are better comparable to the total rainfall accumulation to the radar estimates. Similarly, the streamflow simulations are match better in time between the forcings from radar and satellites, but, in total quantity of streamflow, the forcing of WRF-ARW matches better with the radar estimates.

4 Conclusion



This study presented the hydrometeorological analysis of an extreme flash-flood event in the sub-urban area of west Attika in Greece. A three-day (14–16 November 2017) wave of hazardous weather with intense precipitation rates persisted around the mountain Pateras in the sub-urban town of Mandra, resulting to tremendous flooding with landslides, extensive damages and a total of 23 fatalities. The area is highly urbanized with complex terrain effect. This case study has been simulated by the non-hydrostatic WRF-ARW atmospheric model coupled with an advanced hydrological module CHAOS (WRF-Hydro) able to offer improved simulation of land surface hydrology and energy states and fluxes at a fairly high spatial resolution using a variety of physics-based and conceptual approaches. The CHAOS (WRF-Hydro) simulated this case study under three different precipitation forcings. The first was based on WRF-ARW hindcasts (WRF-Hydro), the second one was based on XPOL and C-Band radar estimates (XPOL-Hydro) and the third on core GMP/IMERG estimated precipitation rates (GMP/IMERG-Hydro). The initial precipitation forcings are evaluated against surface raingauge and disdrometer observations close to the area of interest. Preliminary results indicate that XPOL-Hydro outperforms the WRF-Hydro and the GMP/IMERG-Hydro in terms of water level and surface runoff estimations.

References

Atencia, A., Mediero, L., Llasat, M.C., Garrote, L., 2011. Effect of radar rainfall time resolution on the predictive capability of a distributed hydrologic model. Hydrol. Earth Syst. Sci. 15, 3809–3827.

Baltas, E.A., Mimikou, M.A, (2002). Considerations for the optimum location of a C-band weather radar in the Athens area, Proceedings of ERAD, 348-351, © Copernicus GmbH 2002.

Barros, A. P., Joshi, M., Putkonen, J., and Burbank, D. W., "A study of the 1999 monsoon rainfall in a mountainous region in central Nepal using TRMM products and rain gauge observations," Geophysical Research Letters, 2000, Vol. 27, pp. 3683 – 3686

Camarasa-Belmonte, Ana & Segura, Francesca. (2001). Flood events in Mediterranean ephemeral streams (ramblas) in Valencia region, Spain. CATENA. 45. 229-249. 10.1016/S0341-8162(01)00146-1.

Despiniadou, V. and E. Athanasopoulou, 2006. Flood Prevention and Sustainable Spatial Planning. The Case of the River Diakoniaris in Patras. Proceedings in the 46th Congress of the European Regional Science Association (ERSA), Volos.

Diakakis, M., S., Mavroulis, G., Deligiannakis (2012). Floods in Greece, a statistical and spatial approach, Nat Hazards, doi:10.1007/s11069-012-0090-z.

Gaume, E., M., Borga, M. C., Llassat, S. Maouche, M., Lang, M., Diakakis, 2016: Mediterranean extreme floods and flash floods. The Mediterranean Region under Climate Change. A Scientific Update, IRD Editions, pp.133-144, 2016, Coll. Synthèses, 978-2-7099-2219-7.

Guha-Sapir D, Vos F, Below R, with Ponserre S. Annual Disaster Statistical Review 2011: The Numbers and Trends. Brussels: CRED; 2012. Available online at http://www.cred.be/sites/default/files/ADSR_2011.pdf

Hirabayashi Y, R. Mahendran, S. Koirala, L. Konoshima, D. Yamazaki, S. Watanabe, H. Kim and S. Kanae, 2013, Global flood risk under climate change, Nature Climate Change,3, 816–821 (2013), doi:10.1038/nclimate1911.
Journal of Hydrology, 541, Part A, 2016, pp24-37, doi: 10.1016/j.jhydrol.2016.05.040.

Papagiannaki, K., Lagouvardos, K., Kotroni, V., 2013. A database of high-impact weather events in Greece: a descriptive impact analysis for the period 2001–2011. Nat. Hazards Earth Syst. Sci. 13, 727–736.

Karymbalis, E., P., Katsafados, C., Chalkias and K. Gaki-Papanastassiou, 2012: An integrated study for the evaluation o of natural and anthropogenic causes of flooding in small catchments based on geomorphological and meteorological data and modeling techniques: The case of the Xerias torrent (Corinth, Greece), Zeitschrift für Geomorphologie Vol. 56, Suppl. 1, 045–067, Stuttgart, January 2012.

Llasat, M. C., R., Marcos, M., Turco, J., Gilabert, M. Llasat-Botija, 2016: Trends in flash flood events versus convective precipitation in the Mediterranean region: The case of Catalonia, Journal of Hydrology, Vol. 541, pp. 24-37.

Zoccatelli, D, M. Borga, F. Zanon, B. Antonescu, and G. Stancalie, "Which Rainfall Spatial Information for Flash Flood Response Modelling? a Numerical Investigation Based on Data From the Carpathian Range, Romania." Journal of Hydrology, 2010, Vol. 394, pp: 148 – 161

Marra, F., Nikolopoulos, E. I., Creutin, J. D., Borga, M., Creutin, J. D., "Radar rainfall estimation for the identification of debris-flow occurrence thresholds." J. Hydrol., 2014, Vol. 519, pp. 1607 – 1619.

Mavrakis A., Theoharatos G., Asimakopoulos D., Christides A., 2004. Distribution of the Trace Metals in Sediments of Eleusis Gulf. Mediterranean Marine Science, 5/1, 151-158.

Maddox, R. A., J. Zhang, J. J. Gourley, and K. W. Howard, "Weather Radar Coverage over the Contiguous United States." Weather and Forecasting, 2002, Vol. 17, pp. 927 – 934.

Runge, J. and Nguimalet, C. R.: Physiogeographic features of the Oubangui catchment and environmental trends reflected in discharge and floods at Bangui 1911–1999, Central African Republic, Geomorphology, 70, 311–324, 2005.

Wallace J.M., and P.V. Hobbs (2006), Atmospheric Science. An Introductory Survey, Academic Press, Elsevier, ISBN 13: 978-0-12-732951-2.

Shen, X.; Hong, Y.; Zhang, K.; Hao, Z.; Wang, D. (2014). "CREST v2.1 Refined by a Distributed Linear Reservoir Routing Scheme", American Geophysical Union, Fall Meeting 2014, abstract #H33G-0918.

Skamarock, W. C., J. B. Klemp, J. Dudhia, D. O. Gill, D. M. Barker, W. Wang, and J. G. Powers (2007), A description of the advanced research WRF version 2, 100 pp.,NCAR Tech. Note NCAR/TN–468+STR

Giannoni, F., Roth, G., Rudari, R., 2000. A semi-distributed rainfall–runoff model based on a geomorphologic approach. Phys. Chem. Earth B. 25, 665–671.

Seity, Y., Brousseau, P., Malardel, S., Hello, G., Benard, P., Bouttier, F., Lac, C., Masson, V., 2011. The AROME – France convective-scale operational model. Mon. Weather Rev. 139, 976–991.

Kundzewicz, Z.W., L.J. Mata, N.W. Arnell, P. Döll, P. Kabat, B. Jiménez, K.A. Miller, T. Oki, Z. Sen and I.A. Shiklomanov, 2007: Freshwater resources and their management. Climate Change 2007: Impacts, Adaptation and Vulnerability. Contribution of Working Group II to the Fourth Assessment Report of the Intergovernmental Panel on Climate Change, M.L. Parry, O.F. Canziani, J.P. Palutikof, P.J. van der Linden and C.E. Hanson, Eds., Cambridge University Press, Cambridge, UK, 173-210.

Meehl, G.A., J.M. Arblaster, and C. Tebaldi, 2005: Understanding future patterns of precipitation extremes in climate model simulations. Geophys. Res. Lett., 32, L18719, doi:10.1029/2005GL023680.

Westra, S. et al, "Future changes to the intensity and frequency of short-duration extreme rainfall." Review of Geophysics, 2014, Vol. 52, pp. 522 – 555

Varlas G, Katsafados P, Papadopoulos A, and Korres G, 2017: "Implementation of a two-way coupled atmosphere-ocean wave modeling system for assessing air-sea interaction over the Mediterranean Sea," Atmospheric Research, Vol. 208, pp. 201-217.

UNISDR, 2009. Terminology for Disaster Risk Reduction. Available online: http://www.unisdr.org/we/inform/terminology (accessed on Jan 11, 2013).

European Commission, 2007. Directive 2007/60/EC of the European Parliament and of the Council of 23 October 2007 on the assessment and management of flood risks.

A Method for estimate of range variation of attenuation from dual frequency and dual polarization radar

-Validation using scattering database of snow-



Takahisa Kobayashi

Takahisa Kobayashi[1,2] , Mistuharu Nomura[1] ,Soichiro Sugimoto[1],Ahoro Adachi[2], Nobuhiro Nagumo[2] and Hiromaru Hirakuchi[1].

[1]*Central Research Institute of Electric Power Industry,1646,Abiko,Chiba,Japan,270-1194*
[2]*Meteorological Research Institute, Tsukuba, Japan, 305-0035*

(Dated: 22 June 2018)

1 Introduction

An accurate measurement of snow is one of important topics to be solved in the radar meteorology. The relationships between the equivalent radar reflectivity (Ze) and snowfall rate (s) differs significantly from Ze-r (r: rainfall rate) for rain. In addition, the Ze-s relationship varies significantly with snow type, drysnow, wet snow, mixed-phase precipitation etc. Classification of hydrometeors is, as a first step, needed for quantitative precipitation estimation from Z-r(s) relationship. Traditionally, snow areas are identified from ambient temperature and relative humidity (e.g., Matsuo and Sasyo, 1981). Many hydrometeor classification methods for dual-polarization radars have been also developed (e.g., Kouketsu et al., 2015, Chandrasekar et. al., 2013). Most methods use the polarimetric radar signatures such as reflectivity (Ze), differential reflectivity (Zdr), specific differential phase (Kdp), and the correlation coefficient between horizontal and vertical Ze (ρ_{HV}) measured at each radar resolution volume. These parameters often have similar values for different types of precipitation and it is needed to identify the type of precipitation by combining above signatures.

For reflectivity-based rainfall rate estimate, the specific attenuation is an amount to be removed from radar received signals. Many extensive studies have, therefore, focused on the attenuation correction. Attenuation is closely related to rainfall rate and therefore, methods of rainfall rate estimate based on attenuation properties have been developed (Matrosov, 2005, Ryzhkov et al., 2014). Although attenuation is relatively insensitive to the drop size distribution (DSD), the specific attenuation also depends on the type of precipitation. The attenuation of dry snow is generally small at most radar frequencies. While for rain, large attenuations appear. It has also been reported that melting hail has very large attenuation (Thurai et al., 2015).Hydrometeor classification is also needed in the attenuation-based rainfall estimate. In other words, attenuation can be a useful information for hydrometeor classification.

There are no straightforward methods for accurate estimate of attenuation. Most methods to estimate attenuation utilize redundancy relations among radar observables. The specific attenuation (A) can be estimated if A is related to the intrinsic radar reflectivity factor (Ze^{i}) by a power law (Hitshchfeld and Bordan, 1954). This method was modified by using path-integrated attenuation (PIA) which was used in rainfall rate estimate algorithm in the radar equipped on the Tropical Rainfall Measuring Mission (TRMM) (Meneghini and Nakamura, 1990, Iguchi and Meneneghini, 1994). This method was further modified for the dual frequency space-borne radar (DPR) onboard the Global Precipitation Mission (GPM).

For dual-polarization radars, a linear relationship between the path integrated attenuation (PIA) and the differential phase (Φdp) has been used to estimate attenuation (Bringi et al., 1990, Ryzhkov et al., 2014).The redundancy has been also used for attenuation correction (Adachi et al., 2013, 2015). These methods are useful, however, the coefficients in the relationships between Φdp and A significantly differ, depending on particle size distribution, precipitation type, and temperature.

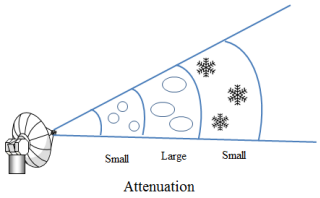
To avoid the variation of the coefficients, We have developed a method by using changing tendency of the radar variables in the radar propagation path instead of the variables at each radar resolution volume (Kobayashi et al., 2015). The method estimates radar range variations of the relative values of attenuation from the dual frequency ratio (DFR) which is defined as the difference of Ze at a frequency of Ku and Ka measured with the DPR. We have also developed a similar method for a dual-polarization radar (Kobayashi et al., 2017). Both methods intend to classify rain and dry snow and have been examined by simulations based on the T-matrix method. In the simulation, snow particles are assumed to be spheroidal shape. This assumption may not be appropriate for radar operated at higher frequency.

In this presentation, we examined the methods for attenuation estimate by simulations using scattering database for irregular snow by Lu et al. (2016).The objective of our study is to examine the methods for snow of irregular shape and for severe conditions of snow to estimate of snow, i.e., snow of large scattering and small attenuation.

2. Methods for attenuation estimate

For dry snow, the attenuations are generally negligible. For rain, on the other hand, large attenuations appear. In our methods, the different attenuation properties are used to hydrometeor classification. As mentioned earlier, attenuation is closely related to specific differential phase (Kdp) as $A=\alpha Kdp$. The coefficient α significantly depends on type of precipitation as well as temperature. To avoid the effects of variation of α, we use the range variation of the radar received signals instead of values at specified ranges. The methods, therefore, do not estimate attenuation at specified range but at some region of radar range in which no significant changes in precipitation properties exist. We estimate attenuation for hydrometeor classification from the relative magnitude of attenuation in the radar propagation path (Fig.1). We have developed two method; one is for a dual-frequency radar and another is for a dual-polarization radar(Kobayashi et al., 2015, 2017).

Fig.2.1 Schematic figure of hydrometeor classification from range variation of attenuation.



2.1 Methods for attenuation estimate from dual frequency radar (MAD)

The DPR onboard the GPM core satellite operates at frequencies of Ku-band (14GHz) and Ka-band (35GHz). The dual frequency ratio (DFR) is obtained from the DPR and is defined as,

$$DFR = Z_e(Ku:dBZ) - Z_e(Ka:dBZ). \qquad (2.1.1)$$

For rain of small size of raindrops, the scattering properties both at Ka and Ku-band radar are in the Rayleigh regime, which results in small values of the DFR unless attenuation is significant. For rain of large size of raindrops, the scattering properties at Ka-band radar is in the Mie regime but are still in the Rayleigh regime at Ku-band radar, which results in larger value of DFR. For snow, on the other hand, the scattering properties are in the Mie regime both for Ka and Ku-band radar. Larger size of particles generally lead to larger values of DFR. DFR associated with the different scattering properties of particles between Ka and Ku-band is called here as 'scattering effect' (DFRs). The different scattering effect can be used to classify hydrometeor type from measurements by using the Dual-frequency precipitation radar (Liao, and Meneghini, 2011). Their method, however, neglects attenuation and therefore needs exact attenuation correction.

In addition to the scattering effects, attenuation due to rain results in increases in DFR. Larger attenuation of the radio wave in rain, in general, occurs at higher radar frequencies. Attenuation due to rain is not significant for Ku-band but is significant for Ka-band. This different attenuation property enhances DFR. For dry snow, attenuation can be usually neglected both for Ka and Ku-band radar. It should be mentioned that "dry snow" is defined here as pure ice snow which is composed of ice and air. DFR associated with the different attenuation is related to rain rate and drop size and is called here as 'attenuation effect'. For dry snow, DFR is determined by only the scattering effects because of almost no attenuation at both 35 and 14 GHz. While for rain, DFR is determined by both the scattering and the attenuation effects. The path integrated attenuation (PIA) increases with total rain rate in the propagation path. Thus, larger decreasing tendency of the measured reflectivity factor in the propagation path should appear at higher frequencies for homogeneous precipitation. The differential PIA between Ka and Ku-band is defined here as the attenuation effects (DFRa), which monotonically increase with the path integral rain rate if the DFRs is constant in the propagation path.

$$DFRa = PIA(Ku) - PIA(Ka) = \int_{r1}^{r2}\int_{d\min}^{d\max}[\sigma_a(Ku) - \sigma_a(Ka)]N(D)dDdr, \qquad (2.1.2)$$

Here, σ_a is attenuation coefficient. A key factor for hydrometeor classification is the attenuation effects which tend to enhance DFR and appear only in precipitation with attenuation like rain.

$$DFR = DFR_s + DFR_a, \quad \text{for rain.} \qquad (2.1.3)$$
$$DFR = DFR_s, \quad \text{for dry snow.}$$

We can, therefore, identify the medium as rain if we can detect DFRa in the measured DFR (DFRm). To detect DFRa, we should firstly remove DFRs from DFRm.

The scattering effects are basically related to the size of particles. Large values of DFRs arise primarily from large particles in size. The increases in the size of particles are, generally, associated with higher precipitation rate, ie. Larger values of Ze at Ku-band. **T**herefore, the DFRs can be expected to increase with intrinsic value of Ze.

Figure 2.2 shows the relationship between DFRs and intrinsic value of Ze (Ze^t) at Ku-band for rain. The DFRs increases with Ze^t(Ku) linearly. For mixed phase precipitation, the DFRs also tends to increase with Ze^t(Ku) (Fig.2.2). Thus, we assume that the DFRs is related Ze^t by power law as,

$$DFR_s = cZe^{t\,d}, \qquad (2.1.4)$$

Coefficients *c* and *d* depend on precipitation type. The ratio of the DFR to Ze^{td}(Ku) is given by

$$Dz \equiv DFR / Ze^{t\,d} = c + DFRa / Ze^{t\,d}, \qquad (2.1.5)$$

The parameter Dz is, therefore, a measure of the DFRa. We assume that Ze^t(Ku) can be approximated as measured value Ze(Ku). Figure 2.3 shows the ratio of the DFR to Ze(Ku) versus the DFRa. The ratio is linearly related to the DFRa except for DFR/Ze<0.1. Although the coefficients *c* and *d* varies with snow properties of the volume equivalent diameter D_0, density etc., the T-matrix calculations suggests that the relationship of Eq.2.1.4 is generally valid at Ze (Ku) larger than 10-20dBZ (Liao and Meneghini, 2005). Here the coefficient *b* was assumed to be 1. The derivative of DFRa with range shows attenuation per unit length of range.

$$\frac{dDz}{dr} \equiv \left(\frac{dDFRa}{dr} Ze^d - DFRa \frac{dZe^d}{dr} \right) / dZe^{2d} \approx, \frac{dDFRa}{dr} / Ze^d \qquad (2.1.6)$$

For snow of low density, the DFRa is generally smaller than the DFRs. Large contributions of DFRs to DFR need accurate estimate of DFRs. For dry snow, we assume Ze(Ku) as Ze(Ka)=c'$Ze^{d'}$(ku) in linear scale instead of Eq. 2.1.4. Figure 2.4 shows the relationship between Ze^tKa) versus Ze^t(Ku) in linear scale for aggregate snow by using the scattering database by Lu et al. (2016).

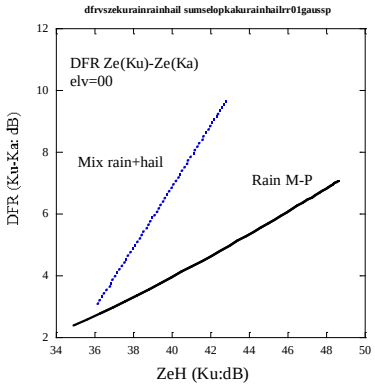


Fig.2.2 DFRs versus Ze(Ku) for rain and mixed-phase precipitation.

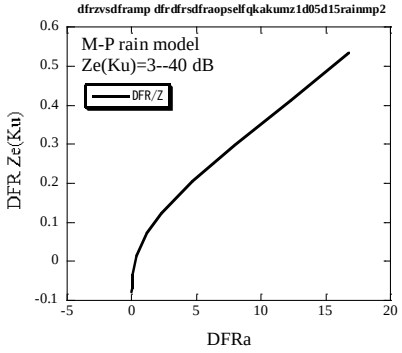


Fig.2.3 DFRs /Ze(Ku) versus DFRa for rain.

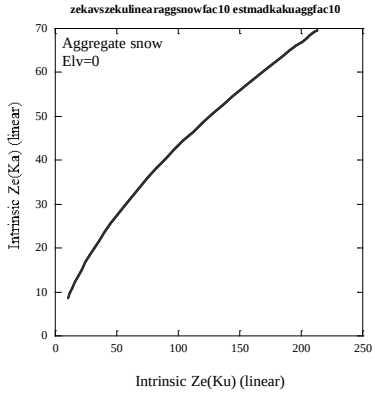


Fig.2.4 Ze^t(Ku) versus Ze^t(Ku) in linear scale for aggregate snow.

2. 2 Method for attenuation estimate from dual polarization radar (MAP)

As mentioned earlier, the attenuation was estimated from the range variation of the DFR calculated from Ze at Ku and Ka-band which have different propagation effect, that is, different attenuation. Similar technique can be applied for a single frequency dual-polarization radar. Various polarization radar signatures have different attenuation effects. Larger attenuation effects appear in the horizontally polarized reflectivity (ZeH) than the vertically polarized (ZeV) for rain of oblate raindrops. The specific differential phase Kdp is not affected by attenuation. We can, therefore, estimate attenuation from the range variation of parameters with different propagation effects.

One-way path-integrated attenuation at range r in linear scale (PIA^L) is given by

$$2PIA^L(r) = Z_e^t(r) - Z_e^m(r). \qquad (2.2.1)$$

Here, Z_e^t is 'intrinsic' (no attenuated) radar reflectivity, and Z_e^m is the measured reflectivity in linear scale. We assume that Z_e^t is related to Kdp by power law) as

$$Z_e^t(r) = aKdp^b. \qquad (2.2.2)$$

From (2.21) and (2.2.2), the path integrated attenuation is given by

$$2PIA^L = aKdp^b - Z_e^m(r). \qquad (2.2.3)$$

Devided by Kdp, (2.2.3) is given by,

$$Q_Z \equiv \frac{2PIA^L}{Kdp^b} = \frac{aKdp^b - Z_e^m}{Kdp^b} = a - \frac{Z_e^m}{Kdp^b}. \qquad (2.2.4)$$

The parameter Qz is related to attenuation. The specific attenuation (Ad) of the difference of Ze can be obtained by taking derivative of (2.2.4) in terms of range assuming that the coefficient of *a* is constant in the range of dr.

$$Ad(\Delta r) = \frac{dPIA^L}{dr} = -Kdp^b \frac{dQ_Z(r)}{2dr} \qquad (2.2.5)$$

or

$$Ad(\Delta r) = -Kdp^b \frac{Q_Z(r+\Delta r) - Q_Z(r)}{2\Delta r} \qquad (2.2.6)$$

In taking derivative, coefficients *a* and *b*, and Kdp are assumed to be constant in the region of range Δr. The unknown term *a* is therefore removed and is the advantage of this method.The shorter length of Δr is better for the assumption of constant values of coefficient a and Kdp. However, larger Δr is better for deriving less noisy Kdp. The coefficient *b* is unknown and is taken to be 1 in this study. We intend to derive range variations of the relative value of attenuation (Fig.2.1), therefore the incorrect value of *b* is not serious unless large variation of *b* in the propagation path Δr. Although, backscattering effect on Kdp may not negligible for X-band radar (Matrosov, 1999, Troomel, et al.,2013), we neglect the effects in the simulation because exact theoretical calculation of the scattering effect is still uncertain (Oguchi T., personal communications).

This method is based on the relationship between Kdp and Ze as shown in Eq.2.2.2. For rain, similar relationships have been reported (eg, Bringi et al., 1990). This is because axis ratio of raindrops is larger for larger size of raindrops. This assumption is therefore reasonable for rain. Figure 2.4 shows the simulation plots of Kdp versus Ze^t at X and C-band for rain of the M-P size distribution. Figure2.5shows the simulation plots of Kdp versus Ze^t at X and C-band for mixture of rain of the M-P size distribution and spherical ice particles. Linear relationships between log(Kdp) and Ze^t(Ku) are obtained both for rain and mixed-phase precipitation. For mixed-phase precipitation, similar relationships have been reported by Balakrishnan and Zrnic (1990). Figure 2.6 shows plots of Kdp versus Ze^t(Ku) at X and C-band for wet snow simulated with the T-matrix method. The shape of snow particles is assumed to be oblate with the axis ratio of 1.6. The refractive index of snow particles was calculated with the Maxwell-Garnet theory. The water fraction varies 0 to 20 percent in volume with range. Linear relationships clearly appear. This method, so called soft oblate model, is a less time consuming simulation process and is useful for studies on polarimetric scattering of snow. The scattering properties calculated from the soft oblate model is different from the correct values of irregular and complex shape of snow. The observed specific differential phase has not clearly related to Ze at C-band (Ryzhkov and Zrnic, 1998). This is because complicated properties of the relation among shape, size,and densities of snow particles and small values of Kdp at C-band for snow. Fortunately, larger values of Kdp appear for radar of higher frequency. We examined the Kdp-Ze relationship for realistic shape of snow particles by using the scattering database for irregular snow particles developed by Lu et al. (2016). Figure 2.7 shows the relation for aggregate snow of M-P size distribution.. Linear relationships can be obtained.

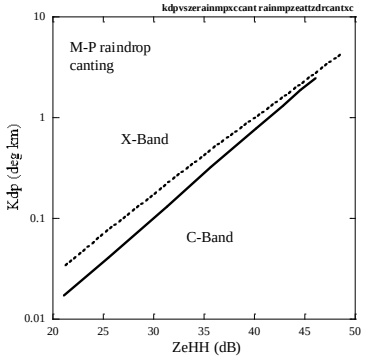


Fig.2.4 Simulation plots of Kdp versus Ze^t at X and C-band for rain of the M-P size distribution.

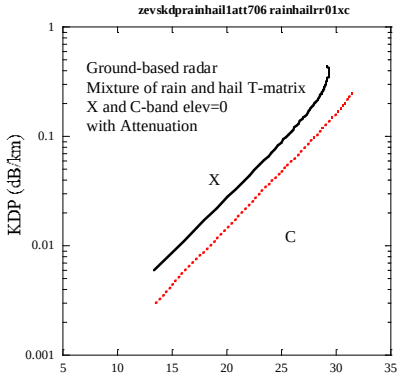


Fig.2.5 Same as Fig.2.4 but for mixed-phase precipitation of rain and hail.

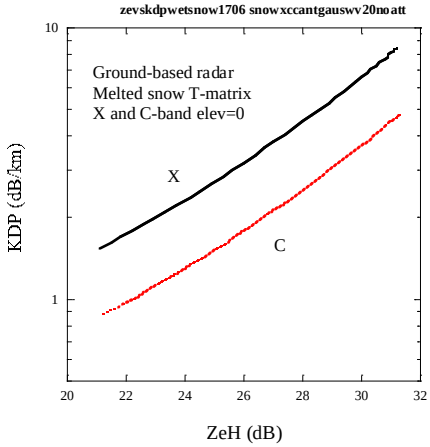


Fig.2.6 Simulation plots of Kdp versus Ze^t at X and C-band for wet snow calculated using T-matrix method.

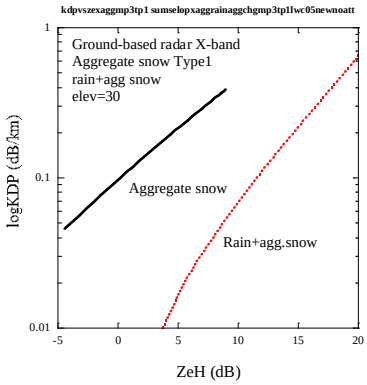


Fig.2.7 Simulation plots of Log(Kdp) versus Ze^t at X and C-band for aggregate snow.

3. Validations: simulations for aggregate snow

Two methods for estimate attenuation, MAD and MAP have been examined by simulation for rain, snow and mixed-phase precipitation (Kobayashi et al., 2016, 2017). In the simulation, scattering properties of raindrops, ice particles and snow particles were calculated with the radar simulator using T-matrix method (Kobayashi et al., 2011). The shape of such hydrometeors was assumed to be oblate. The refractive index for snow is calculated using the Maxwell-Garnett mixing formula associated with various water fraction in snow. The T-matrix approaches have been widely used for snow of complicated shape and are useful for studies on interpretation of radar signals. The scattering properties of irregular snow particles of large size calculated with the T-matrix approach may be , however, inappropriate at higher frequencies of radio wave (Tyynela et al., 2011).

The scattering properties of irregular snow have been calculated using various numerical technique like the Discrete Dipole Approximation (DDA) and have been arranged into a database (Lu et al., 2016, Kuo et al., 2016). Here, we will examine the MAD and MAP by using the scattering database for dry snow by Lu et al. (2016). Attenuation of dry snow is generally negligible. The specific attenuation of snow in the database shows very small in x and Ku-band (Fig.3.1). Even for Ka-band, attenuation is too small to examine the method for estimate attenuation properties for small values of snowfall rate. Thus, we calculate scattering properties of aggregate snow of high snow fall rate. Gaussian range variations of snowfall rate at the maximum of 10 mm/h at the range of 10km are applied. The maximum value may be too high for real snow but for suitable for the validation test.

3.1 MAD

As show in Eq.2.1.4, DFRs is assumed to be due to related to Ze(Ku) as DFRs=cZe^{d}(Ku). This assumption is appropriate for relatively large attenuated precipitation. Figure 3.2 shows the range variations of Range variations of Ze(Ka), Ze(Ku) and DFR for aggregate snow. The DFR does not tend to increase with range monotonically. This is because large contribution of DFRs to DFR. This is because small attenuation and large reflectivity associated with high snowfall rate of dry snow. To derive DFRa, more accurate estimate of DFRs is needed. We assume relationship as Ze(Ka)= c'Ze$^{d'}$(Ku) in linear scale instead of the relation of DFRs=cZe^{d}(Ku) [dB].

$$Ze(Ka) = cZe^{d} \quad [\text{linear} \quad \text{scale}], \qquad (3.1)$$

Figure 3.3 shows the range variations of DFR/Ze^{d}(Ku) as well as Ze(Ka), Ze(Ku) in linear scale. Parameter *d* is taken to be 0.3. Monotonically increase tendency of DFR/Ze^{d}(Ku) with range appears. Figure 3.4 shows the results of estimate. The method successfully estimate range variation of attenuation even for snow of large scattering contribution to DFR.

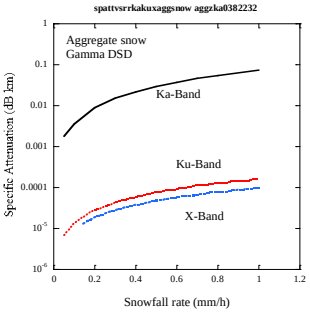


Fig.3.1 Specific attenuations of aggregate snow at Ka, Ku and X-band.

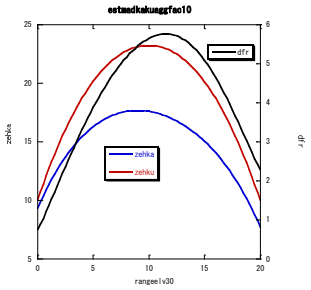


Fig.3.2 Range variations of Ze(Ku), Ze(Ka) and DFR/Ze(Ku) for aggregate snow.

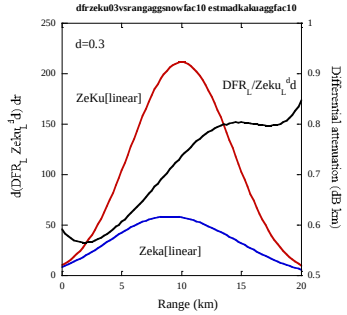


Fig.3.3 Range variations of Ze(Ka) Ze(Ku) and DFR/Ze^{d}(Ku) in linear scale.

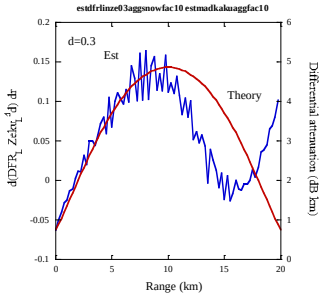


Fig.3.4 The range variation of estimated attenuation and theoretical value for aggregate snow.

3.2 MAP

Figure 3.5 shows the range variation of the intrinsic reflectivity factor (Ze^t) and attenuated value (Zem). Although snowfall rate is the maximum at the range of 10km, the peak of the reflectivity factor Zem is around 8 km because of attenuation. Difference between Ze^t and Zem has a peak at range of 10km and decrease with range associated with largest scattering at 1range of 10km. Figure 3.6 shows the range variation of Q_Z and Kdp. The parameter Q_Z tends to monotonically increase with the range except for short range region in which small values of Kdp. The assumption Eq.2.22 is proved to work well for estimate attenuation for aggregate snow.

Figure3.7 shows the range variation of estimated relative specific attenuation of difference of ZeH (Ad) (solid line) and the theoretically calculated value (dotted line) for aggregate snow. Although there are slight differences at larger radar range, the overall tendencies of the range variation are in good agreement. It should be mentioned that the coefficient b is taken to be 1, therefore, the estimated attenuation is a relative value. The overestimated attenuations appear at range of smaller than 2 km and larger than 17km are associated with errors in the assumption of Eq. 2.1.4. Overall, the method successfully estimate range variation of attenuation even for snow of small attenuation and large scattering properties.

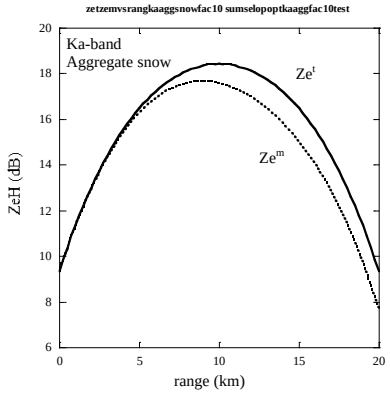


Fig.3.5 Intrinsic value of Ze versus Kdp for aggregate snow.

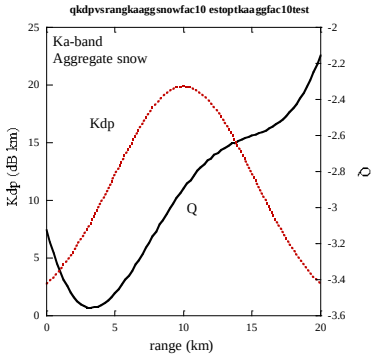


Fig.3.6 The range variation of Q_Z andZe for aggregate snow.

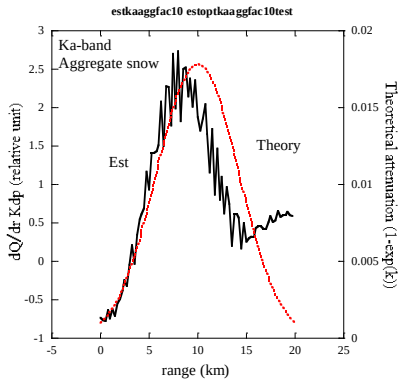


Fig.3.7 The range variation of estimated attenuation and theoretical value for aggregate snow.

4. Summary

We have developed methods to estimate range variation of attenuation from single polarization radars at ka and Ku-band, and a dual polarization radar. We have already examined the methods for rain and snow of spheroidal shape. In this paper, we have examined the methods for aggregate snow by using scattering data base for irregular shape of snow by Lu et al. (2016). Results show that the estimated range variation of attenuation f agrees with the theoretical calculations for aggregate snow. Both methods, MAD and MAP can successfully estimate range variation of attenuation even for severe condition of precipitation to estimate attenuation, that is, snow of large scattering and small attenuation. These methods are useful for precipitation classification from GPM DPR and dual polarization radar. These methods are also useful for more accurate precipitation classification with current classification method.

References

Adachi, A., T. Kobayashi, and H. Yamauchi, 2015: Estimation of raindrop size distribution and rainfall rate from polarimetric radar measurements at attenuating frequency based on the self-consistency principle. *J. Meteor. Soc. Japan*, **93**, 359-388.

Adachi, A., Kobayashi, T., Yamauchi, H., and Onogi, S., 2013: Detection of potentially hazardous convective clouds with a dual-polarized C-band radar. *Atmos. Meas. Tech.*, **6**, 2741-2760.

Balakrishnan, N., and D. S. Zrnic, 1990, Estimation of rain and hail rates in mixed-phase precipitation, J. Atmos. Sci., 47, 565-583. Kobayashi,T., and K. Masuda, H. Yamauchi, and A. Adachi, 2011, Physically-based Simulator for measurements of precipitation with Polarimetric and Space-borne Radars, SPIE Remote Sensing, Cheko, Praha 9/18-9/24, 2011.

Bringi, V. N., and V. Chandrasekar, N.Balakrishnan, D.S. Zrnic, 1990, An examination of propagation effects in rainfall on radar measurements at microwave frequencies, J. Atmos. Oceanic Technol., 7,829-840.2001:Kobayashi T., M. Nomura ,S. Sugimoto, F. Akimoto Furuzawa, A, Adachi, and H. Hirakuchi, 2015: Radar simulation studies for dual-frequency radar measurements of snow from space: Hydrometeor classification. Extended Abstract, 37th Conf. on Radar Meteor., Amer. Meteor.Soc., 108.

Chandrasekar, et.al., 2013, Recent advamces in classification of observations from dual polarization weather radars. *Atmos. Res.*, 119, 97-111

Hitschfeld, W., and J. Bordan, 1954: Errors inherent in the radar measurement of rainfall at attenuating wavelengths. *J. Meteor.* **11,** 58–67.

Iguchi, T., and R. Meneghini, 1994: Intercomparison of single-frequency methods for retrieving a vertical rain profile from airborne spaceborne radar data. *J. Atmos. Oceanic Technol.*, **11,** 1507–1516.

Kobayashi, T. ,M. Nomura ,S. Sugimoto,A. Adachi, N. Nagumo and H. Hirakuchi.2017,Radar simulation studies for hydrometeor classification from range profile of polarimetric radar signatures,Extenden abstract 38th Conf. on Radar Meteor., Amer. Meteor. Soc., 1-10.

Kobayashi, T., S. Sugimoto, M. Nomura and A. Adachi、2015, Radar simulation studies for measurement of precipitation from space-borne radar on GPM、Extended Abstract, Conference on Radar in Meteorology and Hydrology 2014. Extended abstract,

Kouketsu, T. et al., A,2015, A hydrometeor classification method for X-band polarimetric radar: Construction and validation focusing on solid hydrometeors under moist environments, *J. Atmos. Oceanic. Technol.*, 32, 2052-2074.

Kuo, K.-S., and Coauthors, 2016: Themicrowave radiative properties of falling snow derived from nonspherical ice particle models. Part I: An extensive database of simulated pristine crystals andaggregate particles, and their scattering properties. *J. Appl. Meteor. Climatol*., 55, 691–708, doi:10.1175/JAMC-D-15-0130.1.

Liao, L., and R. Meneghini, 2011, A study on the feasibility of dual-wavelength radar for identification of hydrometeor phases, *J. Appl. Meteor. Clim*, 50, 449-456

Lu, Y. et al., 2016, A polarimetric scattering database for non-spherical ice particles at microwave wavelengths, Atmos. Meas. Techniques, 9, 5119-5134.

Matrosov, S., et al., 1999: Prospects for measuring rainfall using propagation differential phase in X- and Ka-radar bands, *J. Appl. Meteor*., 38,766-776.

Matrosov, S., 2005: Attenuation-based estimate of rainfall rates aloft with vertically pointing Ka-band radars. *J. Atmos. Oceanic Technol*., 22,43-54.

Matsuo, T. and Y. Sasyo, 1981, Melting of snow flakes below freezing level in the atmosphere. *J. Meteorl. Soc. Japan*, 59, 10-24.

Meneghini, R., and K. Nakamura, 1990: Range profiling of the rain rate by an airborne weather radar. *Remote Sens. Environ.,* **31,** 193–209.

Ryzhkov, A., and D. S, Zrnic, 1998: Discrimination between rain and snow with polarimetric radar, *J. Appl. Meteor*., 37,12281240.

Ryzhkov, A., M. Diederich,P.,.Zhang, C. Simmer,2014: Potential utilization of specific attenuation for rainfall estimation,mitigation of partial beam blockage, and radar networking, *J. Atmos. Oceanic Technol*., 31,599-619.

Thurai, M., E. Chobanyan, V.N. Bringi and B.M. Notaroš, 2015, Large raindrops against melting hail: calculation of specific differential attenuation, phase and reflectivity, ELECTRONICS LETTERS ,. 51, 1140–1142

Tromel, S., M. R. Kumjian, A. V., Ryzhkov, C. Simmer, and, M. Diederich, 2013: Backscatter differential phase estimation and variability. *J. Appl. Meteor. Climatol.*, 52,2529–2548

Tyynela, J., J.Leinonen, D. Moisseev, and T. Nousianen, 2011, Radar backscattering from snowflakes: comparison of fractal, aggregate, and soft spheroidal model, *J. Atmos. Oceanic Technol*., 28、1365-1372.

Vertical wind profile measurements on the operational weather radar in "wind profiler" mode

Yuri Pavlyukov, Alex Travov, Nadja Eroshkina

Central Aerological Observatory of ROSHYDROMET, 3, Pervomayskaya Str., Dolgoprudny, Moscow Reg., 141700, Russia

(Dated: 22 June 2018)

1 Introduction

Preliminary results of the experiments started in 2017 on the measurement of the vertical wind profile by operational weather radar in a special high-resolution "Vertical Wind Profile" (VWP) observation mode are presented. The main goal of our experiments was to expand the list of radar secondary products of useful and demanded in operational aviation applications, nowcasting and numerical weather prediction.

Radar experimental observations were made in Dolgoprudny (Moscow region) by DMRL-C, Russian operational C-band dual-polarization Doppler weather radar with pulse compression [1]. The special VWP mode on operational radars considered in the report should provide a more accurate estimation of the wind field characteristics in the future.

2 Observation modes

Commonly operational DMRL-C radar make observations in “Reflectivity” and “Velocity” modes consistently every 10 minutes. In the first mode 60-μs step-phase-modulated pulse at PRF=380 Hz and antenna rotation rate - 40 °/s are used. In the second mode 25-μs step-phase-modulated pulse at PRF=1 KHz and antenna rotation rate - 25 °/s are used.

The VWP mode is added after completing of “Velocity” mode. The radar in this third mode performs one elevation scan on 30° (in some experiments – 60°). In the third mode 10-μs step-phase-modulated pulse at PRF=3,3 KHz is used. The 12 °/s antenna rotation rate gives better statistics of 278 distinct azimuthal packs per one degree in comparison with 10 azimuthal packs per degree for “Reflectivity” mode and 40 azimuthal packs per degree in “Velocity” mode. For example, Figure 1 confirms that due to improved statistics in VWP mode, the Doppler velocity observation has a higher quality than the same map obtained in the conventional "Velocity" mode.

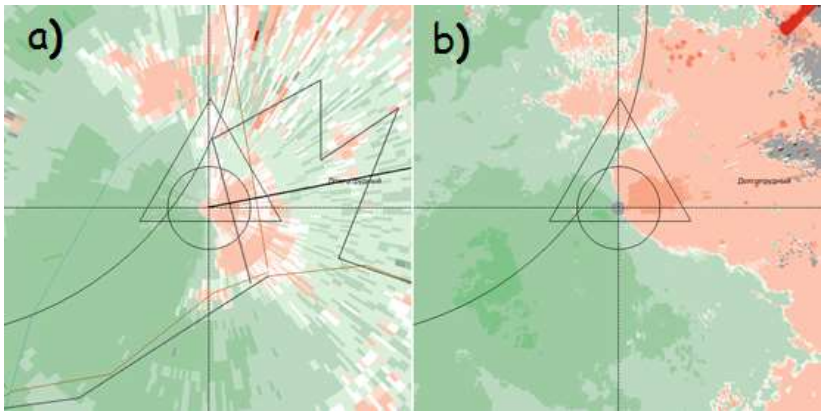


Figure 1: Doppler radial velocity PPI in "Velocity" (a) and "VWP" (b) DMRL-C modes.

3 Data processing procedure

For primary data processing at each range bin in VWP mode the *Discrete Fourier Transformation (DFT)* is used instead *Puls-Pair-Method* that is used in other observation modes. For data processing in VWP mode DMRL-C is equipped with additional processing GPU module based on the NVIDIA CUDA parallel computing platform [2]. The sampling rate of GPU module is 10 MHz compared to 1.25MHz sampling rate for “Reflectivity” and “Velocity” modes so that output data resolution is 15 m on the range and 0.5° on the azimuth compare to 250 m and 1° for “Velocity” mode.

For secondary data processing a conventional VAD technique is used to obtain the averaged horizontal wind profile [3]. Application of VAD to azimuthal circles at every distance of Doppler velocity PPI provides a vertical profile with wind speed components at height resolution *R (m)*:

$$R = 15 * sin(el),$$

where *el* – is the elevation angle. Our experiments were carried out with 30° and 60° elevation angles.

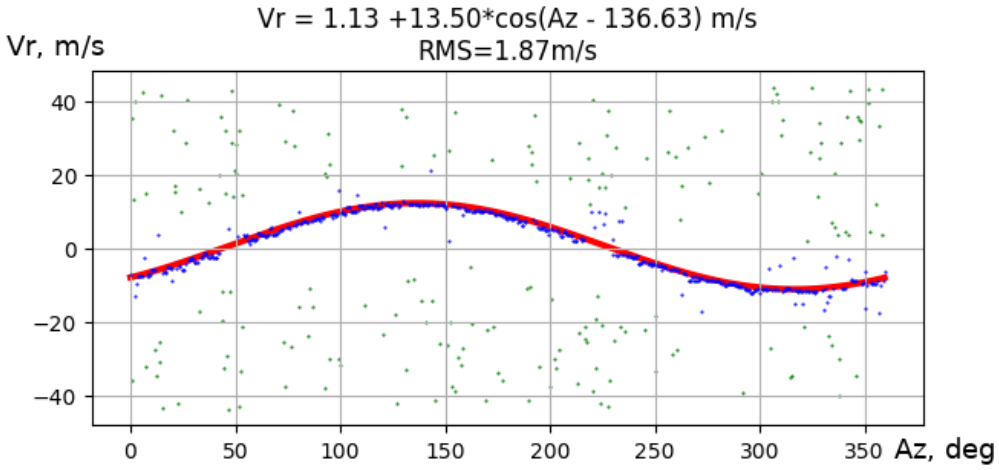


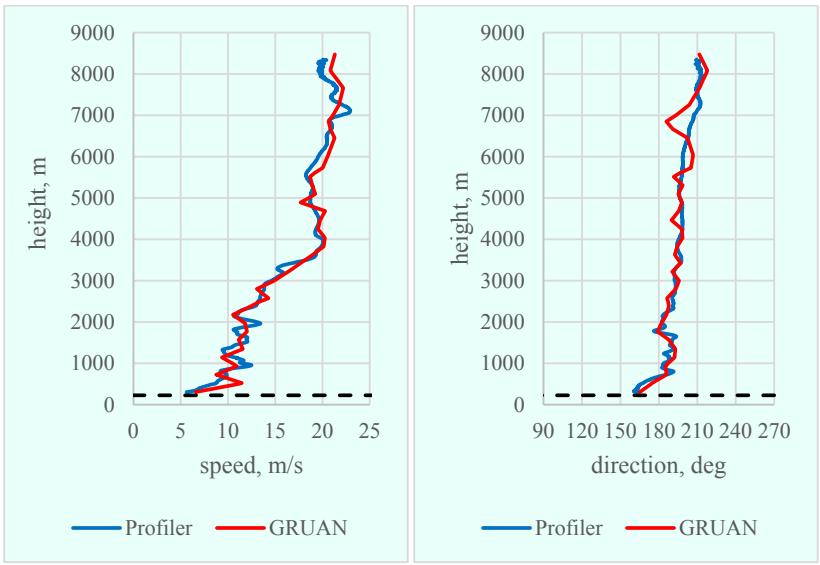
Figure 2: Example of VAD sinusoid fitting for data in VWP mode and filtered values

4 Case study

The radar wind measurements were compared with radiosonde soundings from the GCOS Reference Upper-Air Network (**GRUAN**, 2018 [4]) data of "Dolgoprudny" (DLG) station (WMO code: 27612). DLG is located near the radar. Height resolution of the radiosonde data is 100÷200 m. It is necessary to take into account in data analysis the distance of the radiosonde from the launch site. The results of radar observations in VWP mode were analyzed in the report under two different weather conditions: "Clear-sky" and "cloudy/rainy".

4.1 Cloudy/rainy condition

In cloudy or rainy conditions the number of profile points sometimes exceeded 1000. Each profile point corresponds to one VAD circle with 15 m thick in slanting distance. For example on January 29 at 00:00 UTC our radar was in the convergence zone of air flows with the center of low pressure situated near Stockholm.

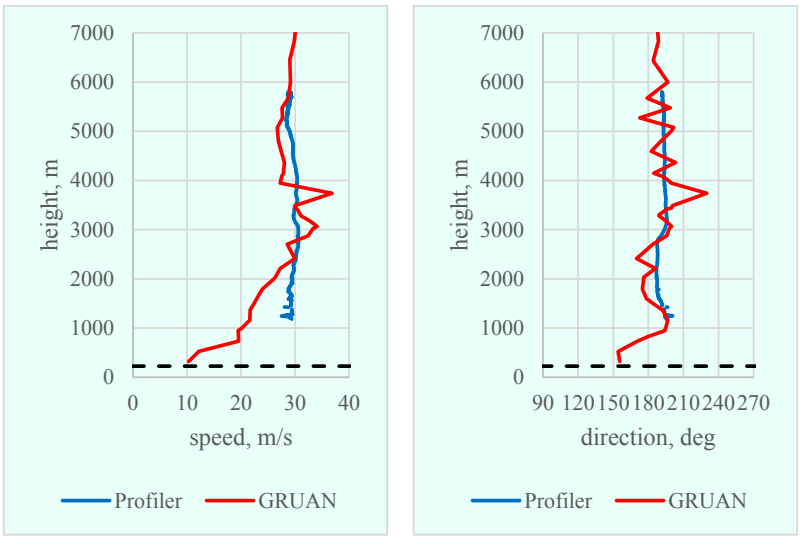


a) b)

Figure 3: Profiles of wind speed (a) and direction (b) according to GRUAN (red) and profiler (blue) 01/29/2018 00 UTC. The black dotted line in the graphs below is the height of the radar installation above mean sea level.

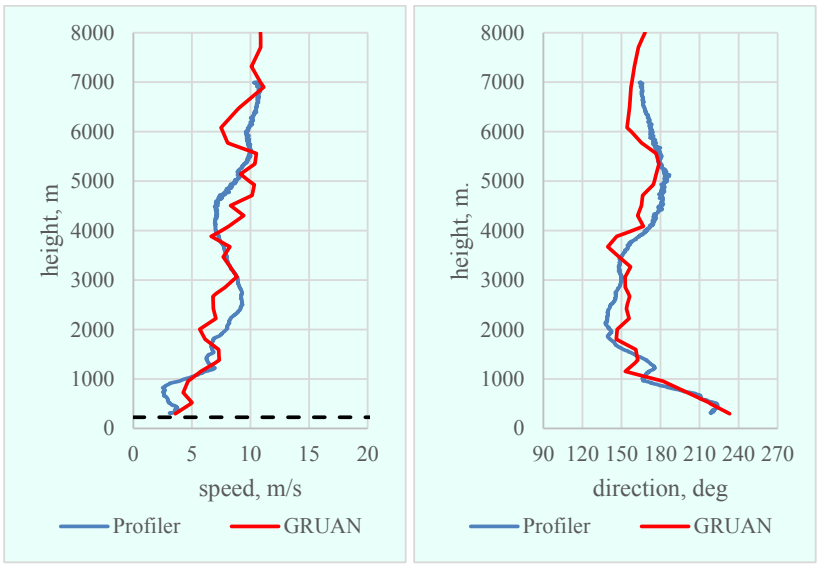
The profiles of wind speed and direction from GRUAN and VWP radar mode ("Profiler") are presented in Figure 3. The upper bound of the profile was ~ 8 350 m, the average deviation of the wind speed – 0,4 m/s and the direction – 0,4 deg. It is possible that the profiler-radiosonde difference increase with altitude is caused primarily by a significant distance of the radiosonde from the launch point (20 km – at height 7 km).

Small deviations of the profiler measurements from the radiosonde measurements are also observed with fewer points. For example, in the case of 04/02/2018 at 12:00 UTC (Figure 4) the average deviations was 0.75 m/s for velocity and 0.2 degrees for wind direction. Separate precipitation areas were in the radar observation zone at that time. The cloudy Echo Top was 5.9 km. The radiosonde quickly migrated from the launch site because high wind speed and its distance was 27 km at height 6 km. In the low troposphere (<1.5 km) the profile has a wide spread, which indicates a numerical instability in this layer.



a) b)

Figure 4: Profiles of wind speed (a) and direction (b) according to GRUAN (red) and profiler (blue) 04/02/2018 12 UTC. The black dotted line in the graphs below is the height of the radar installation above sea level.



a) b)

Figure 5: Profiles of wind speed (a) and direction (b) according to GRUAN (red) and profiler (blue) 05/15/2018 12 UTC. The black dotted line in the graphs below is the height of the radar installation above sea level.

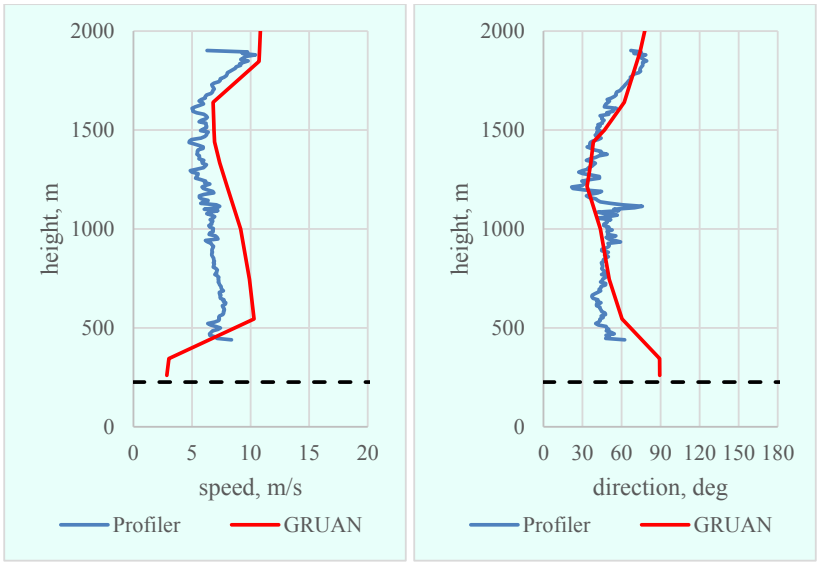
In the frontal systems, generally, strong wind shear is observed. In Figure 5 one of these cases is illustrated: on 05/15/2018 at 12:00 UTC frontal system passed through the Moscow region and frontal showers and thunderstorms were observed. In general, the error of the profiler during this period does not exceed the norm - 0.2 m/s in speed and 2.6 degrees in direction.

In this case the wind shift in the lower troposphere was well retrieved but the wind speed was slightly below the value measured by the radiosonde (the deviation was about 1 m/s). At the same time, the radiosonde distance from the radar was small - 13 km at height of 7 km.

4.2 "Clear-sky" condition

Great attention was paid to the study of the wind profile retrieve in the cases clear-sky or little clouds conditions were above the radar. Analysis showed that in the cold period under these conditions the wind profile is not retrieved in each period and very little number of points pass VAD filters. E.g. on 02/24/2018 at 00:00 UTC in a diffused pressure field, the profile has only 6 points. However, even in such conditions the wind speed deviations was less than 1 m/s and the direction – 8.5 degrees.

In the warm period under conditions of strong warming of the surface and the appearance of the surface boundary layer (SBL), the profiler demonstrated the ability to retrieve the wind profile in the lower troposphere. Thus, on 05/10/2018 at 12:00 UTC in conditions of a cloudless sky (Figure 6) there were wind gusts up to 13 m/s at an altitude of 10 meters. The wind profile was not retrieved quite in "Velocity" mode because of insufficient data in the scan area and was retrieved in VWP mode in the SBL up to a height of 1.9 km but the profiler deviation from the radiosonde in this case was bigger (2.2 m/s for speed and 1.9 degrees for direction).



a) b)

Figure 6: Profiles of wind speed (a) and direction (b) according to GRUAN (red) and profiler (blue) 05/10/2018 12 UTC. The black dotted line in the graphs below is the height of the radar installation above sea level.

5 Results

The 149 cases were analyzed in the period 10/01/18÷01/06/18 (1 case: 1 GRUAN radiosonde launch and 1 radar observation). There is a good agreement of wind data on the speed and direction up to the upper boundary of the radar echo.

The average deviation of VWP radar mode data from GRUAN sounding data was 0.9 m/s for wind speed and 6.8 degrees for wind direction, which meets WMO requirements for wind measurements.

VWP results are better in "cloudy and precipitation" conditions: 0.8 m/s – the difference in wind speed and 5.5 degrees – the difference in wind direction and worse in "Clear-sky" conditions: 1 m/s and 9.3 degrees respectively.

It is important to note that Doppler wind observations in VWP mode for a "Clear-sky" conditions retrieves a less detailed wind profile and in conditions where there are no radar echo above the position, the profile is not retrieved (But mentioned cases take place not so often).

Conclusions:

- the presented VWP radar observations mode has a higher spatial resolution of the vertical wind profile than conventional Doppler observations;
- the presented VWP radar observations mode makes possible the wind characteristics measurements in conditions of significant blocking areas;
- in the "Clear-sky" conditions with a strong surface warming it is possible to obtain a vertical wind profile by the presented VWP radar observations mode observations although the wind speed values are usually lower than that measured by the radiosonde;
- the presented VWP radar observations mode makes it possible to measure the wind profiles even under such conditions when common Doppler observations with a lower PRF do not allow it to be done.

References

1. **WMO Radar Database**, 2018: http://wrd.mgm.gov.tr/db/search-country.aspx?l=en&c=RU&o/,
2. **CUDA Zone**, 2018: https://developer.nvidia.com/cuda-zone ,
3. **Holleman I.,** Scientific Report, KNMI WR-2003-02, 2003: Doppler Radar Wind Profiles,
4. **GRUAN**, GCOS Reference Upper-Air Network, 2018: https://www.gruan.org/network/sites/dolgoprudny/.

Comparison between different QPE based on: Microwave Links, Radar adjusted and Gauges.

Pier Paolo Alberoni[1], Anna Fornasiero[1], Giacomo. Roversi[2,3], Stefania Pasetti[2], Marco Folegani[2], Federico Porcù[3]

[1]*ARPAE Emilia Romagna, Italy*
[2] *MEEO S.r.l., Italy*
[3]*Department of Physics and Astronomy - University of Bologna, Italy*
(Dated: 22 June 2018)

1 Introduction

Currently the most used tools to estimate quantitative precipitation are rain gauges and weather radars, both with relative merits and defects. Rain gauges measurements are not reliable in case of intense precipitation events and have poor spatial representativeness due to high spatial and temporal variability of rainfall field. Weather radars monitor rainfall over large areas with high spatial resolution, but through indirect measurements and affected by various sources of error.

A complementary approach is represented by a technology, not yet been tested in Italy, that consists in the extrapolation of rainfall intensity data from cellular communication infrastructures (i.e. in the identification of rain-induced attenuation of microwave links), usually called Microwave link (MWL) networks or Commercial Microwave links (CML).

A validation activity of these different QPE – Quantitative Precipitation Estimates technologies was done over the Bologna province area (Italy) on the period February 20th - June 30th 2016 in the framework of the RainBO project LIFE15/CCA/IT/000035[1].

An accurate validation exercise was carried out by comparing microwave links QPE (MWL QPE) and radar adjusted QPEusing, as reference field, a Rain gauges measurements spatial analysis (ERG5, a modified Shepard interpolation).

The validation activity was developed in two steps: 1) a Qualitative analysis, mainly based on many daily accumulation maps comparisons; 2) a Quantitative analysis, carried out by using statistical indexes..

In the first phase, a visual inspection of the rainfall fields in the datasets has been done in order to understand the general behavior and to identify, if possible, any problems or drawbacks in the collected data set. A synoptic comparison was conducted by plotting together the rainfall estimates obtained from remote sensing tools (i.e. Microwave links and radar) with the measured reference field (i.e. rain gauges). In the second validation phase, the quantitative one, statistical indicators based on contingency table and continuous verification methods were calculated in order to estimate the reliability of the microwave link and the radar QPE methods.

Additionally some single event analysis was conducted in cases of false precipitation detection by MWL when compared to gauges, as in the case of abnormal attenuation detection by MWL due to the presence of snow or mixed-phase precipitation and a discussion of under sampling of precipitation in the convective season.

2 Validation datasets

The validation has been carried out comparing the rainfall obtained by Microwave links with other rainfall estimates available over the project domain. Further in detail, Microwave QPE have been compared with radar QPE, both raw and Gauge-corrected, rain gauges and the operational precipitation analysis (ERG5) made available by Arpae.

2.1 Microwave Links (MWL) data

Microwave data were collected as historical dataset, starting from February 2016 to June 2016, from two providers: Lepida and Vodafone. Lepida provides also real-time data, while Vodafone is evaluating the possibility to provide a short sample period of 2017, simulating the real-time data that can be provided in case a customer will finance an operative service.

The operative frequency of Vodafone links has a large range, for this reason the frequency window required by original Rainlink algorithm was extended from [12.5 - 40.5] GHz to [5.0 - 45.0] GHz in order not to miss any available information. The Lepida links work at a fixed frequency of 26 GHz.

The pathlength of the MWL varies fairly but most of these links are under 13 km and the average length is 5.6 km.

As the algorithm estimates the rainfall averaged along the link path, we expect an error not lower than the average length of the links. This interval can be even larger in case of less dense links, so we decided to increase the grid resolution from 1 km (the original one used by Wageningen University[2]) to 5 km, in order to filter any possible interpolation's artificial

[1] https://www.rainbolife.eu/
[2] WUR - https://www.wur.nl/en/Persons/dr.ir.-A-Aart-Overeem.htm

effect. The interpolation grid adopted for the RainBO project is the one already in use by Arpae for ERG5 precipitation analysis.

Table 1:Microwaves link characteristics

	Lepida	Vodafone
Number of links	37	422
Coverage area	Bologna Apennines	Bologna metropolitan area
Historical data period	Starting from 28th March 2016 – till today	From 20th February 2016 to 30th June 2016
Temporal frequency	1 minute	15 minutes
Link average length	7.4 km	5.4 km
Frequency range	26 GHz	5-45 GHz
Time format in the original dataset	UTC	UTC+1
ACM – Attenuation Coefficient Measurement	Not used	Active for some links

2.2 Rain-gauge data

Rain gauge hourly data are provided by the Arpae Rirer (regional hydro-meteorological) network, established in 2001 by bringing together existing hydrological and meteorological station networks managed by different public bodies, operating all over the regional area. The network is composed by 498 stations with circa 900 sensors.

Real-time data are collected in the central data archive mainly by radio-link and are available for operational activities. Figure 1 shows the Rirer network and the location of the two radars which form the regional radar network.

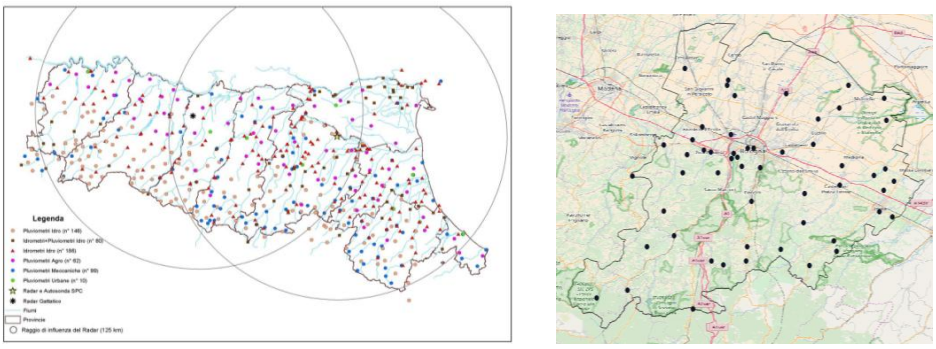


Figure 1: The Rirer network (left), Distribution of the Rirer gauges in the validation area (right)

2.3 Radar data

Radar dataset is based on hourly precipitation estimations obtained from the composit of the regional radar network managed by Arpae-SIMC. The regional network is composed by two C-Band systems, one located at San Pietro Capofiume (Bo) and the other in Gattatico (RE) (Figure 1). For each radar the precipitation rate at the ground is then interpolated from polar coordinates to a 256 X 256 Cartesian grid of 1 km x 1 km resolution, then single rain-rate estimates are merged to obtain a composite of both radar. Rain rates are obtained every 5 minutes and the final rain total over a 1-hour period is computed by an advective algorithm taking into account the movement of precipitating systems. The algorithm is based on the computation of maximum cross-correlation between consecutive maps, leading to the estimate of the displacement vector for each precipitation system. The precipitation field is then reconstructed every minute between the observed maps and finally cumulated over one hour. Finally radar QPE is adjusted with rain gauges data.

2.4 Erg5: rainfall analysis

The ERG5 gridded meteorological data set has been developed by Arpae-SIMC, in order to support agricultural services of Emilia-Romagna. ERG5 data are operationally produced since 2001, interpolating the hourly station data for the main meteorological variables (air temperature, relative humidity, precipitation, wind, solar irradiance) onto a 5x5 km grid covering the Emilia-Romagna region. Within the RainBO project, only ERG5 hourly cumulated precipitation data are considered. With respect to this parameter, ERG5 input data consists of all hourly cumulated precipitation data recorded by the Rirer network. All data are daily checked for their quality and undependable hourly data are not used as input of the analysis. The interpolation method used for hourly precipitation consists of a Shepard modified scheme using topographic distances instead of Cartesian distances. This allows the interpolation to take into account the influence of topography on precipitation, by making locations divided by orographic obstacles more distant than they would be if Cartesian distances were used. For project validation purpose only the erg5 grid point which are within the Bologna province has been used.

3 Qualitative analysis: daily maps

As stated above, daily rainfall amounts of MWL based estimation were visually compared with the others available estimates (radar, calibrated and uncalibrated, and ERG5), in order to get an idea on the quality of precipitation estimates retrieved by MWL. The ERG5 analysis was used as reference.

The daily rainfall pattern retrieved by MWL, as well as the hourly pattern, generally shows a reliable structure that sometimes reproduces the pattern features (rainfall peaks and gradients) observed by the others measuring tools. We state that the agreement between MWL estimates and the other ones is generally promising, even though some drawbacks still need to be addressed. These drawbacks cause a variable time matching of the different precipitation estimates. It is also important to highlight that the performance of the Microwave estimates seems to increase in the second half of the analysed period. The main reason lies, maybe, on the types of clouds producing precipitation. Stratiform precipitations, lasting for hours but mainly with moderate or light rain, were observed in the winter period. The spring period is mainly characterized by convective storm, even embedded in frontal structures, with showers and heavy rain. As the MWL estimate is based on the attenuation occurred along the link path and it is clear that attenuation is strongly related to rainfall intensity and that the signal is consequently stronger in the convective season. This behaviour is sometimes counter-balanced by the difficulty to detect scattered or isolated convective storm; we will further showcase some examples of isolated storms that not intersect, with its core, any microwave link in the project domain.

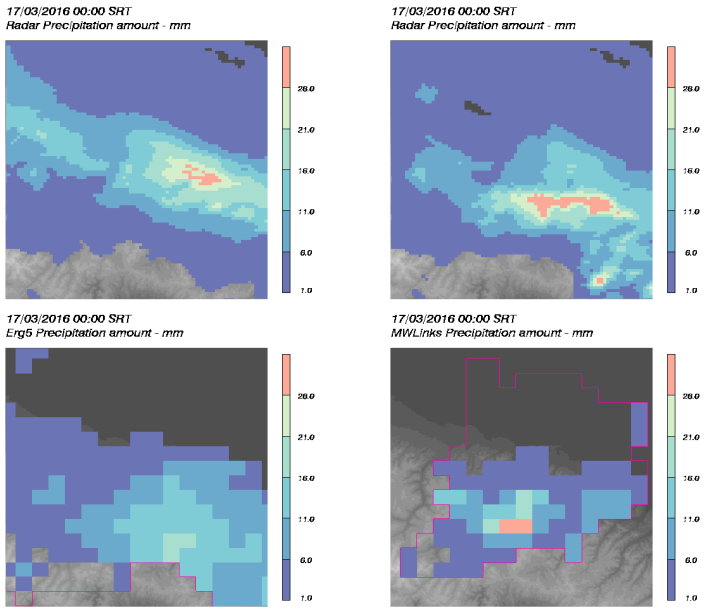


Figure 2: The Quantitative precipitation estimates accumulated from 16/03/2016 00 UTC to 17/03/2016 00 UTC. (Top Left) Radar QPE, (Top Right) Radar adjusted QPE; (Bottom Left) Erg5; (Bottom Right) Microwave Links QPE

On 16 March precipitation is mainly located over the Bologna hilly area, with a local maximum shown in Fig. 2. Both remote sensing methodologies identify correctly this feature, radar estimates spread light precipitation in the flat area north of Bologna while erg5 and MWL does not detect such rainfall.

Excellent results are achieved also in a more convective event such as the one displayed in Fig 3. On 11 May precipitation occurred with a well defined gradient in the West-East direction and some local maxima in the North-West and South-West part of the province. Microwave accumulation slightly underestimate the rainfall field while an overestimation is recorded in

the non adjusted radar. Adjustment procedure well calibrates radar data as displayed in the top right panel of Fig. 3. Fine scale structure of daily amount is well detected in both remote sensing maps.

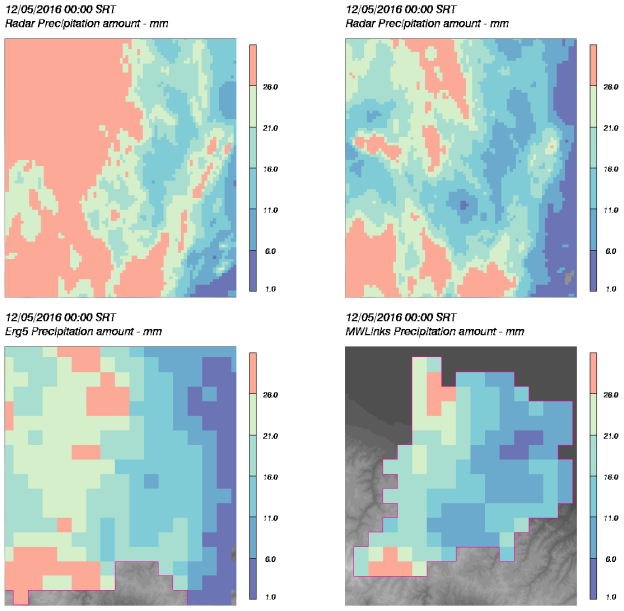


Figure 3: The Quantitative precipitation estimates accumulated from 11/05/2016 00 UTC to 12/05/2016 00 UTC UTC. (Top Left) Radar QPE, (Top Right) Radar adjusted QPE; (Bottom Left) Erg5; (Bottom Right) Microwave Links QPE

Another important result achieved through the qualitative analysis is the need of an enhanced quality check for the Microwave power data. In the punctual analysis carried out on the Budrio station (not reported here) we have found that the link is affected by an antenna structural deformation due to sun heating and/or wind pressure which caused a misalignment between antennas link and consequently a lack of power which is interpreted as an attenuation event. Malfunctioning effects are more frequent and stronger on this link, though we noticed that less severe effects are or could be present in other links. We evaluate that this problem affects roughly 10% of daily maps.

4 Quantitative analysis

Categorical statistics and continuous verification scores are calculated on time series of hourly precipitation distribution parameters (one for all areal mean) over the Bologna metropolitan area and estimated by radar, radar-adjusted (ADJ), Microwave links (MWL) and rain gauges, then compared with erg5 (used as reference field).

4.1 Categorical score verification

The scores are calculated using hourly mean over the area, either on the whole period and in rainy hours (i.e. where no precipitation has been detected; no rainy hour is defined as both hourly mean precipitation = 0 mm for Erg5 and hourly mean precipitation < 0.1 mm for the other estimates). This is done to remove the no rainy event, which is most frequent one (about 80%), from the dataset, focusing then the score computation on the rain occurrence. Categorical scores are computed for two different thresholds. The lower threshold distinguishes between Rain/no Rain (of course for the filtered distributions where no rainy hours has been removed this threshold distinguishes between Rain/VeryLightRain). The upper threshold focuses on the identification of heavy rain events. For the whole period and for the filtered subset the higher threshold was set to 2 mm. In the framework of the whole validation period (Table 2), a comprehensive reading of categorical statistics shows that at the end of the day both adjusted radar and MWL estimates show a comparable skill in the precipitation estimation. A deep analysis indicates that such result comes from two different behaviours: on the one end radar tends to overestimate precipitation (in terms of intensity and number of hours) while MWL tends to underestimate precipitation (in terms of intensity and number of hours).

In order to highlight the effect of different precipitation regimes on the categorical scores, we split the dataset into two sub-periods, the first one for the 'stratiform season' from February 1 to April 15 (Table 3) and the second one for the 'convective season' from April 16 to June 30 (Table 4). This splitting may be questionable, but we deem it very useful to explain the different estimation trends we found. Regarding the first period (Table 3) we duplicate the computation of categorical score removing a melting-layer event from the dataset: therefore we added an additional column to the previous table. For simplicity we refer to the first period as “winter” and to the second one as “convective”.

In these period we observe an opposite behaviour.

In winter time radar over-performs in the low threshold if compared to MWL. A general overestimation from radar is observed. Regarding MWL, we notice the effect of sampling the snow-melting also in terms of validation score as well. By lower threshold the 'cleaned dataset' performs worst results. One possible explanation is that by lower threshold, the hours not considered because of the misleading snow-melting effect, are interpreted as detected phenomena (in the contingency table) regardless the absolute hourly amount (i.e. both observation, erg5, and estimation, MWL, was above the threshold). Looking to higher threshold the rejection has a huge effect: FAR falls to 0, BIAS decreases from 1.53 to 0.79 and Threat Score raises from 0.41 to 0.67. With this threshold, data are wrongly registered as detected phenomena from MWL but not from Erg5, so we have removed a false alarm event. This analysis makes clear that we need to tackle such phenomena before to move to a real-time or near real-time use of MWL.

The performance of the MWL improves during the convective season and from low to high threshold. This is probably due to the better response of MWL to intense events. In the same time radar scores dramatically drops in convective season. Table 4 shows radar ADJ Threat Score falling around 0,5 from the 0,70 winter value. This worsening seems due to the growing of FAR (reflected also in BIAS), while POD has a positive score.

These results make clear the issue about the capability of rain gauges (and as consequence of erg5) and MWL network to sample small-scale phenomena such as thunderstorms captured by radar instead. Therefore radar shows a 'probably false' overestimation when compared to erg5 probably due to convective cores which are not detected by the rain gauges network. MWL, as rain gauges, under-samples convective cores and therefore the areal mean is lower.

Table 2: Categorical statistics scores on the filtered dataset (no rainy hours removed)

	Threshold	Radar	ADJ	Rain gauges	MWL
N. Samples		702	702	586	280
FAR	0,5	0,39	0,37	0,06	0,09
BIAS	0,5	1,57	1,53	0,996	0,67
POD	0,5	0,95	0,95	0,94	0,61
TS	0,5	0,59	0,61	0,89	0,57
FAR	2	0,58	0,39	0,12	0,08
BIAS	2	2,25	1,55	1,05	0,89
POD	2	0,95	0,95	0,93	0,82
TS	2	0,41	0,59	0,82	0,77

Table 3: Categorical statistics scores on the filtered dataset (no rainy hours removed). Period: 1 February- 15 April. Cleaned dataset means MWL discharging period 01:00 – 13:00 UTC of 03/03/2016 .

	Threshold	Radar	ADJ	MWL	'Cleaned ' MWL
N. Samples		347	351	101	87
FAR	0,5	0,27	0,26	0,02	0,03
BIAS	0,5	1,32	1,28	0,59	0,52
POD	0,5	0,96	0,95	0,58	0,5
TS	0,5	0,70	0,71	0,57	0,49
FAR	2	0,5	0,30	0,52	0,09
BIAS	2	2	1,44	1,53	0,79
POD	2	1	1	0,73	0,71
TS	2	0,5	0,70	0,41	0,67

Table 4: Categorical statistics scores on the filtered dataset (no rainy hours removed). Period: 16 April-30 June.

	Threshold	Radar	ADJ	MWL
N. Samples		355	351	179
FAR	0,5	0,50	0,48	0,13
BIAS	0,5	1,91	1,86	0,72
POD	0,5	0,95	0,96	0,63
TS	0,5	0,49	0,51	0,58
FAR	2	0,67	0,49	0,06
BIAS	2	2,61	1,70	0,78
POD	2	0,87	0,87	0,74
TS	2	0,32	0,48	0,71

4.2 Continuous score verification

Continuous verification is focused on the distribution of a continuous variable without performing any stratification as for categorical verification. Tables 5-7 report the mean error, the mean absolute error and the root mean square error for the whole period, the filtered rainy hours sub-set, and the two sub-periods: winter and convective. As already stated, overall behaviours (Table 5) are equivalent for adjusted radar and MWL, with a slightly underestimation (in hourly amount this time) for MWL and a corresponding overestimation for ADJ. Absolute errors and RMSE are very similar.

Table 5: Continuous scores on the filtered dataset (no rainy hours removed). Whole period.

	Radar	ADJ	Rain gauges	MWL
ME	0,506	0,282	0,017	-0,006
MAE	0,570	0,332	0,104	0,532
RMSE	0,908	0,503	0,163	1,064

If the two sub-periods (winter and summer) are considered, an opposite behaviour is registered between them.

In winter time (Table 6) radar ADJ get best scores respect to MWL, even considering the "cleaned" subset. Removing the snow-melting hours highlight the more pronounced underestimation where the mean error (ME) is -0.194 but also the greater (compared to radar ADJ) variability, as could be deducted from RMSE. We point out that MWL is much better than the raw radar estimate, this means that radar needs to be gauge-calibrated.

Table 6: Continuous verification scores on the filtered dataset (no rainy hours removed). Period: 1 February- 15 April. Cleaned dataset means MWL discharging period 01:00 – 13:00 UTC of 03/03/2016 .

	Radar	ADJ	MWL	'Cleaned MWL
ME	0,412	0,179	0,269	-0,194
MAE	0,496	0,241	0,841	0,461
RMSE	0,826	0,319	1,637	0,594

Convective season (Table 7) is characterized by a good estimation by MWL. An underestimation, for MWL, is still present, indeed the mean error is negative. We observe a worsening in the radar indexes. This depend to a greater variability in the rainfall pattern, due to the fine scale structure of precipitation field, which is better sampled by the radar.

Table 7: Continuous verification scores on the filtered dataset (no rainy hours removed). : 16 April-30 June.

	Radar	ADJ	MWL
ME	0,606	0,385	-0,160
MAE	0,642	0,423	0,358
RMSE	0,981	0,635	0,509

5 Single event based analysis

The statistical analysis carried out in the previous sections is not sufficient to present and analyse some data peculiarities needed to get a more complete understanding of the of the behaviours of the different precipitation estimates. Then we run an ad-hoc analysis on each event where different problems occur.

5.1 Detection of abnormal attenuation by MWL

On March 2nd a huge overestimation occurs on MWL estimate, as briefly previously introduced and further underlined in the quantitative analysis both with categorical and continuous scores.

The hourly precipitation analysis shows the passage of a meteorological system heading West, East. Precipitation is then detected and recorded in the datasets. Fig. 4 shows two representative hours. It is evident that MWL strongly overestimate precipitation in the Apennines area. Local hourly maximum reach 40 mm for MWL whereas the other estimate are below 5 mm (Fig. 5). We point out that MWL estimate is based on the measure of power attenuation along the link path. In this area links are normally placed on the top of hills and mountains, their path is free of any obstacle, and they can be located 10 or 100 meters off the ground. MWL detect a different hydrometeors in comparison with the ones collected by gauges (on the ground). the Radar, instead, will sample higher atmospheric volume, in order not to be contaminated by ground return.

Fig. 6 shows instantaneous temperature and hourly precipitation, for two Apennines stations (Sasso Marconi and Vergato). It is clear that the temperature close to the ground falls around 0°C during the precipitation event. We can infer that there was rain at ground, mixed-phase precipitation with the melting of snowflake along microwave link path and snow

at higher levels where radar samples are taken. Microwave attenuation depends on the third power of the hydrometeors dimension: snowflake and aggregates have a huge horizontal dimension in the melting layer but, from an electromagnetic point of view, they act as a drop of water causing a big attenuation. This effect is similar to the well known "bright-band" in the radar meteorology.

Such phenomena occurred on March 3rd and other times, even if we are not able to demonstrate it. Similarities occur in other events as well, even the effect is not so strong.

A quality control is needed to tackle this problem in real-time operation.

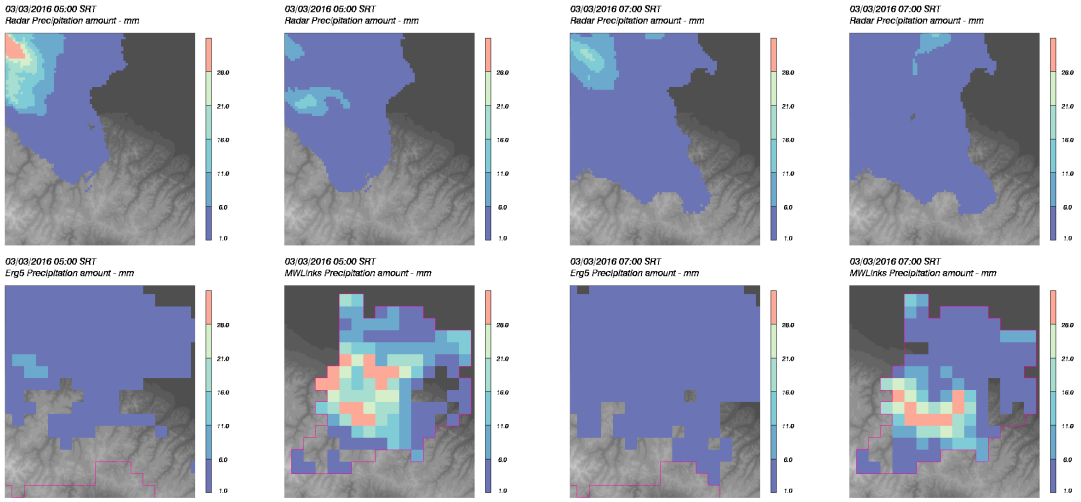


Figure 4: Quantitative precipitation estimates accumulated at 05_00 UTC (Left) and 07:00 UTC (Right) on 10/03/2016. Each group is composed by four panels : (Top Left) Radar, (Top Right) Radar adjusted; (Bottom Left) Erg5 ; (Bottom Right) MWL.

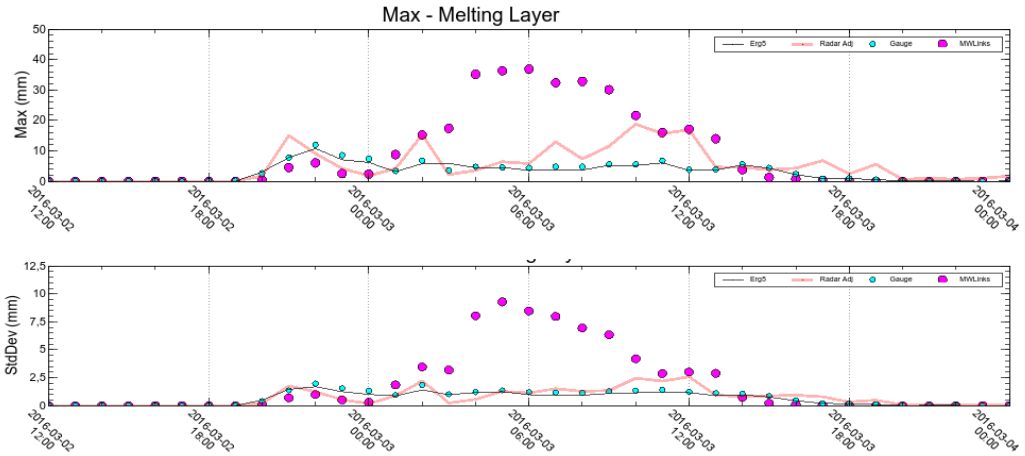


Figure 5: Time series of Hourly maxima (Top Panel) and Standard Deviation (Bottom Panel) from 02/03/2016 12:00 UTC to 04/03/2016 00 UTC

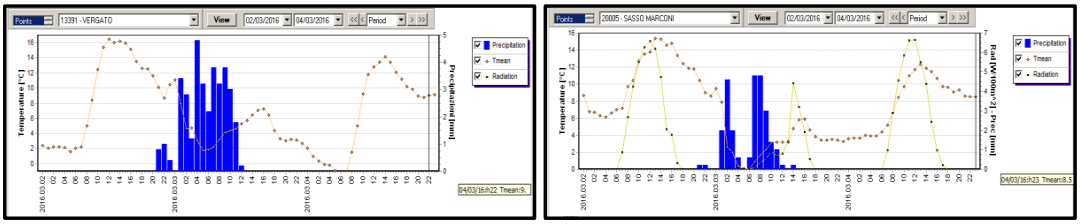


Figure 6: Time series of temperature and hourly precipitation: Sasso Marconi (Left) and Vergato (Right) from 02/03/2016 00:00 UTC to 05/03/2016 00 UTC

5.2 Undersampling of precipitation in convective season

Scattered precipitation is a challenge for every gauge network. We have pointed out in the quantitative analysis section that radar score drop down in the second period considered. On figure 7 the time series of hourly maximum has been plotted for some sub-periods of the convective season to highlight this problem.

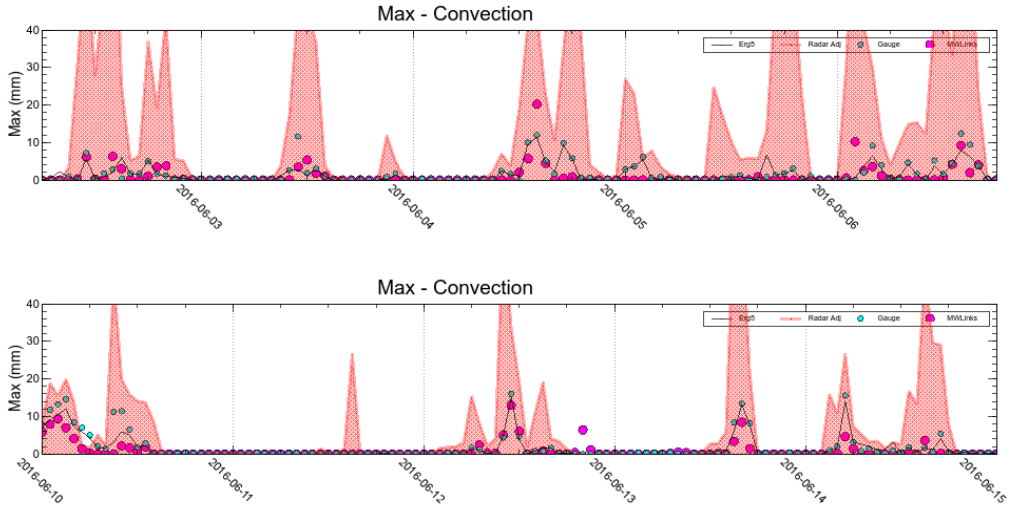


Figure 7: Time series of hourly maximum (Top panel) from 02/06/2016 00 UTC to 07/06/2016 00 UTC, (Bottom panel) from 10/06/2016 00 UTC to 15/06/2016 00 UTC.

In most of events plotted radar catches a signal stronger than in QPE datasets. Few examples of hourly patterns are shown in Fig. 8 and 9.

On May 14 at 20:00 UTC radar detects in the North of Bologna a convective storm, embedded in widespread precipitation pattern (Fig. 8). The storm marginally rides over some gauges and the analysed erg5 field does not detect such structure. MWL shows a local maximum in the same location where radar catch the storm. A closer look to link data shows similar problems in gauge and MWL data. Indeed no link cross the storm's core path. We point out that a merge of MWL data from different providers can increase the sampling capability and at the end precipitation retrieving.

On June 12t at 14:00 UTC a small storm rides over the Apennines slopes (Fig. 9). As in the previous case, gauge network recorded only the widespread precipitation in which storm is embedded and even MWL does not register the storm but only the surrounding precipitation.

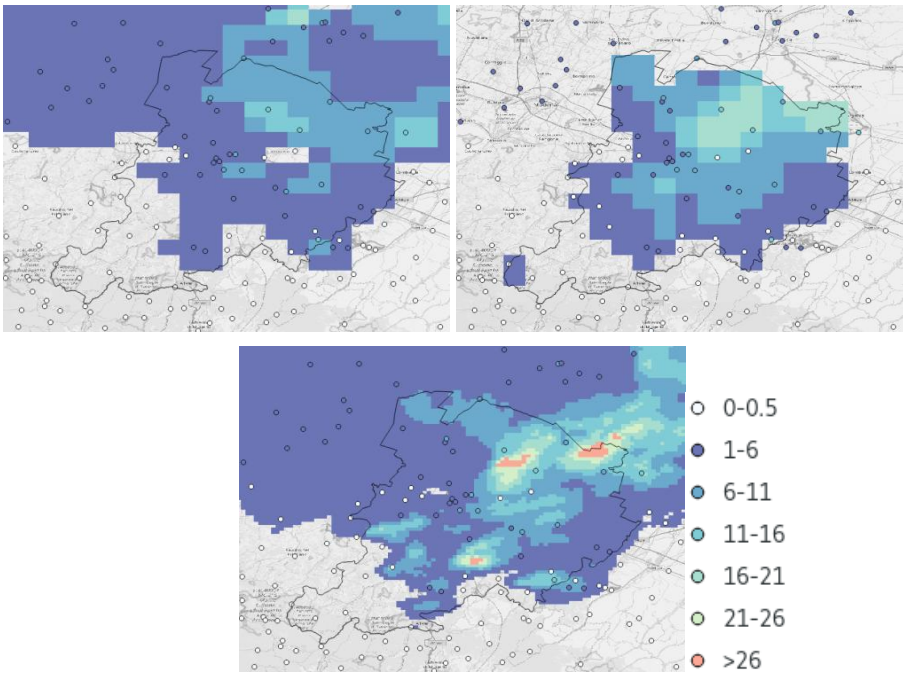


Figure 8: 14/05/2016 20:00 UTC hourly precipitation from different datasets, rain gauge data are overplotted in each panels: (Top Left) Erg5; (Top Right) MWL; Bottom Left) Radar Adj.

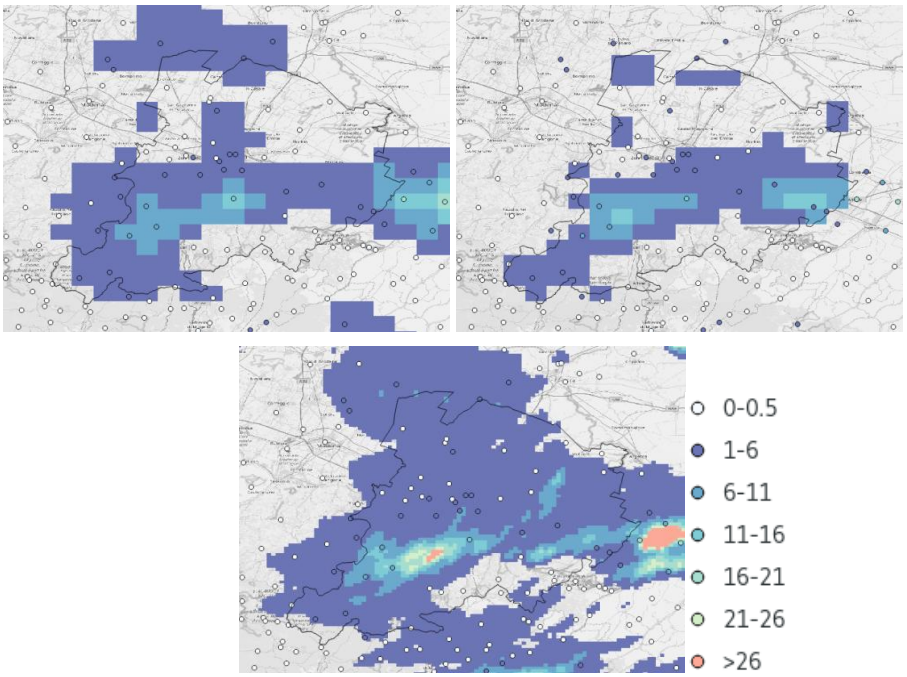


Figure 9: 12/06/2016 14:00 UTC hourly precipitation from different datasets, rain gauge data are overplotted in each panels: (Top Left) Erg5; (Top Right) MWL; Bottom Left) Radar Adj.

6 Conclusions

The agreement between MWL QPE and the other estimates is quite promising even if it requires a tuning activity in order to make the technology used in real-time or near real-time. The qualitative analysis shows that the performance of the MWL estimate seems to increase in the second half of the analyzed period, mainly characterized by convective storms, where showers and heavy rain play a predominant role even if embedded in frontal structures.

This behavior is confirmed by the quantitative analysis done by using statistical indicators: the scores of rainfall estimates by microwave links data get better during Summer and Spring seasons.

The validation has pointed out that a Microwave-based QPE method slightly underestimates precipitation occurrence both in spatial averages and punctual amounts, while Adjusted radar has complementary features.

The low spatial coverage of the microwave link network is an important issue to be addressed in the future, in collaboration with data providers, in order to increase the quality of the retrieved field.

Additional quality control procedures have to be developed during any validation follow-up activities in order to reduce the impact of false signals on the estimated rain fields. The automatic identification of false signals has to be tackled in particular in the following two scenarios: antennas structural deformations due to solar radiation or strong winds and bright-bands detection due to snow-melting layers crossing the microwave link path.

Acknowledgement

This work has been done within the framework of the RainBO project LIFE15/CCA/IT/000035

Impact of rimed and unrimed snow on snowfall retrievals at X, Ka, and W band



Marta Tecla Falconi

M. T. Falconi[1], A. von Lerber[2], D. Ori[3], F. S. Marzano[1], and D. Moisseev[2,4]

[1]*Department of Information Engineering, Sapienza University of Rome, Italy and CETEMPS, L'Aquila, Italy*
[2]*Radar Science, Finnish Meteorological Institute, Finland*
[3]*Institute for Geophysics and Meteorology, University of Cologne, Cologne,*
[4]*Department of Physics, University of Helsinki, Finland*
(Dated: 22 June 2018)

1 Introduction

The correlation between the snowfall rate S and the radar equivalent reflectivity factor Ze is challenging due to their dependence on the microphysical properties of snowfall. The variability of the Ze-S and S-Ze relations at millimeter and centimeter wavelengths is largely affected by microphysical snow growth processes. When a Ze-S power-law relation is assumed, its coefficients depend on different parameters such as the snow type, degree of riming and aggregation, density and terminal velocity (e.g., Von Lerber et al., 2017). The Ze-S relation is also strongly dependent on radar frequency since various electromagnetic wavelengths are more sensitive to different parts of the particle size distribution (PSD).

The radar-based snowfall intensity retrieval at X, Ka and W band has been investigated in previous works (e.g., Falconi et al., 2018) in terms of Ze-S relation using data from four snowfall events, recorded during the Biogenic Aerosols Effects on Clouds and Climate (BAECC) campaign in Finland. The dataset was divided in rimed and unrimed snow using the liquid water path (LWP) as an indicator of riming occurrence and as the driven observable for the k-means clustering of the dataset. This classification highlighted three different regimes: lightly rimed (LR), moderately rimed (MR) and heavy rimed (HR) snow on temporal scales larger than few minutes.

In this work, the four case studies of the 2014 winter from BAECC are used to illustrate the impact of the rimed snow classification for every different instrument available and illustrated in Figure 1.

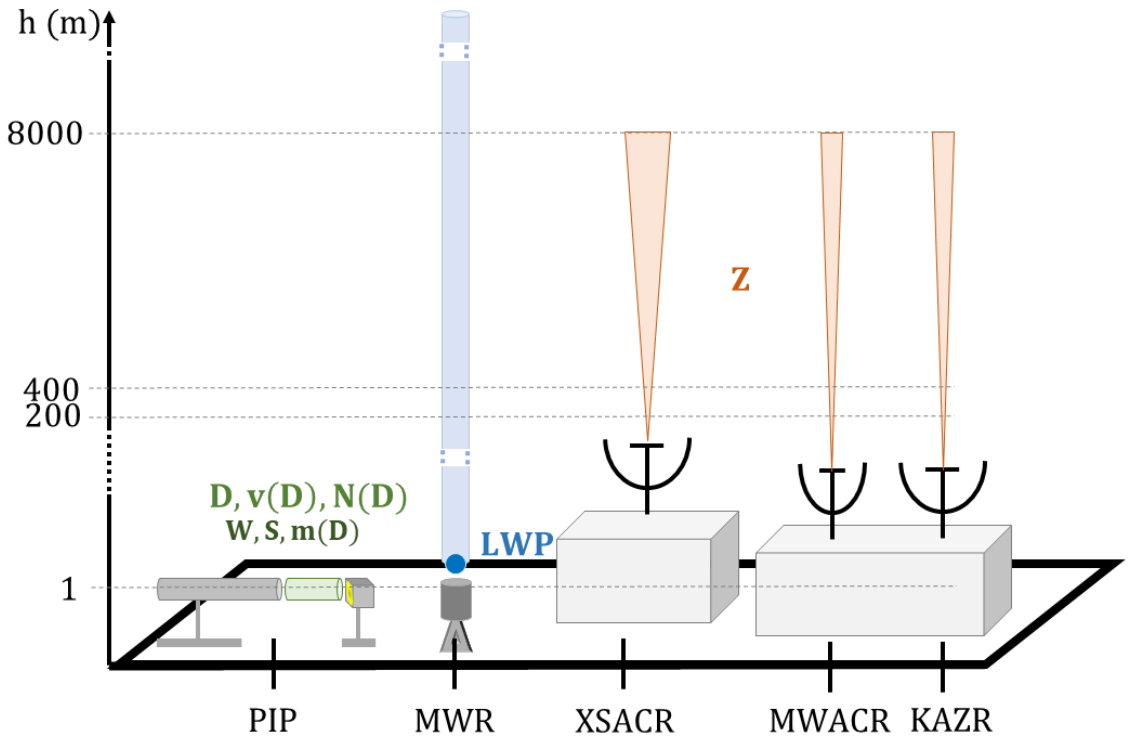


Figure 1:Graphical representation of the measurement site with in situ, video disdrometer (PIP), and remote sensing instruments, microwave radiometer (MWR) and X, Ka and W band radar (XSACR, KAZR, MWACR), deployed during the BAECC campaign.

2 Data, Instruments and Methods

The data used in this study are part of the BAECC campaign organized in 2014 by the University of Helsinki (UH), the US department of Energy ARM program, the Finnish Meteorological Institute (FMI) and other collaborators. The four case studies (12 February, 15-16 February, 21-22 February and 20 March 2014) belong to the snowfall intensive observation period (BAECC SNEX IOP) carried out thanks to a collaboration with the NASA Global Precipitation Measurement (GPM) ground validation program. Figure 1 illustrates the instruments of the BAECC SNEX IOP used in this study. For further information on the single instruments and calibration techniques applied see Falconi et al., 2018.

The focus of this study is to investigate how the impact of the rimed snow classification, made with the microwave radiometer, appears using other instruments.

2.1 Ground-based and microwave radiometer measurements

The rimed snow classification, considered as a reference for this study, was applied in Von Lerber et al., 2017 and Falconi et al., 2018 using the LWP as a proxy of riming. The LWP (gm^{-2}) is an integrated measurements derived from the second Mobile Facility (AMF2) two-channel microwave radiometer (MWR) following the well-known formula:

$$LWP = \int_{h=0}^{\infty} W(h)dh \qquad (2.1)$$

where the W is the liquid water content (in gm^{-3}) and h is the measured height (in m).

As a first proof of this classification we want to use derived variables from the video disdrometer (Particle Imaging Package, PIP). The PIP measures hydrometeor size, fall velocity, an estimate of particle shape and PSD. The liquid water content W and the liquid-water-equivalent snowfall rate S (in mm to hours) are the two variables, evaluated from PIP, used to test the rimed snow classification with in-situ measurements. The W is derived from the third-moment M_3 of the PSD as:

$$W = \frac{\pi}{6}\rho_w 10^{-3} M_3 \qquad (2.2)$$

where ρ_w is the liquid water density (in gcm^{-3}). The S is derived from the mass-flux as

$$S(mmh^{-1}) = 3.6 \int \frac{m(D)}{\rho_w(D)} v(D)\, N(D) dD \qquad (2.3)$$

where D is the particle diameter (in mm), m is the mass (in g) derived as in Von Lerber et al., 2017, v is the velocity (in ms^{-1}) and N is the PSD (in $\mathrm{mm}^{-3}\mathrm{m}^{-1}$). We will use the S(W) to separate the three classes: LR, MR and HR.

2.2 Supervised Classification using radars at X, Ka and W band

The Atmospheric Radiation Measurement (ARM) cloud radars at X, Ka and W band are an important part of the BAECC SNEX IOP. To compare the radars with the ground-based sensors, and also to reduce the beam mismatch, all the data are averaged to 5 min. The near-field influence is also taken into account by selecting all radar data at 400 m (Sekelsky, 2002), as highlighted in Figure 1.

Supervised Maximum Likelihood Classification (MLC) has been used for analysis of rimed classes. The equivalent reflectivity factor Z_e in dBZ, measured by the radar systems at different wavelengths has been divided in three classes (LR, MR, and HR) for each band. The 3x3 matrix of radar measurements is then used to obtain the related probability distribution function (PDF).

The MLC is applied with the arg-max criterion:

$$\hat{c} = \underset{c=LR,MR,HR}{argmax}\ L(Z) \qquad (2.4)$$

where c are the three rimed classes and $\hat{c}$ is the estimated class and the $L(Z)$ is the likelihood function that we define and evaluate as:

(1) $L(Z) = p(Z_{e,X}, Z_{e,Ka}, Z_{e,W})$, the 3D joint-distribution function estimated from the data;

(2) $L(Z) = p_m(Z_{e,X}, Z_{e,Ka}, Z_{e,W})$, the 3D joint-distribution function modelled as a multivariate Gaussian distribution;

(3) $L(Z) = p(Z_{e,X})p(Z_{e,Ka})p(Z_{e,W})$, the independent 3D joint-distribution function.

All the supervised MLC are evaluated in terms of probability of detection (POD), false alarm rate (FAR) and the critical success index (CSI) are also shown.

3 Results

Four snowfall events during the BAECC campaign are used to investigate the impact of the rimed snow classification done in Falconi et al., 2018. In Figure 2 (a) the events were classified into three subgroups using a k-means cluster analysis trained by LWP and D_0. The riming is clearly related to LWP but almost not dependent on the estimated size.

We want now relate the classification made with the LWP evaluated by MWR to ground-based measurements estimated by PIP. For this purpose, a direct relation between the LWP and W, S is expected and visible in Figure 2(b), where W and S are conveniently scaled. In Figure 2(c) the k-means cluster analysis is reported on the W-S space in which the separation of the three-classes is visible and divided in three cones.

To relate the radar observables with the LWP classification three different supervised MLC have been applied. The four events are divided in a training dataset (12 February, 15/16 February and 22 February 2014) and a test dataset (21 February and 20 March 2014). In Table 1 the performance indexes are presented, showing the unlikelihood to classify the three classes. The MLC has been testes for a new classification model separating all the data in two classes: low riming (LOW = LR+MR) and heavy riming (HEAVY= HR) class. Looking at the results for two classes (Table 1), the possibility to classify is more concrete having a POD at around 0.75 for each class.

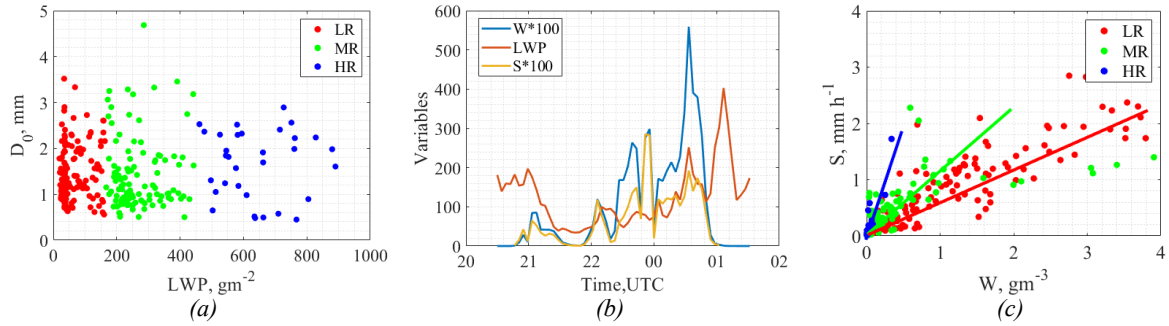


Figure 2: Comparison of ground-based evaluated variables and microwave radiometer measurements: (a) Plot of median diameter D_0 with respect to LWP for the three cluster regions: LR, MR and HR (red, green, blue) obtained on four snowfall days of BAECC IOP campaign; (b) Measurements from 15-16 February 2014 between 20:00 and 02:00 UTC, W and S are estimated by PIP and LWP is evaluated by MWR; (c) Three regions cluster in (b) are mapped into a S-W plane, defining three cones.

Table 1:Performance indexes for the three versions of the MLC.

	Two-classes			Three-classes		
L(z)	CSI	POD	FAR	CSI	POD	FAR
$p(Z_{e,X}, Z_{e,Ka}, Z_{e,W})$	0.68	0.75	0.25	0.13	0.23	0.77
$p_m(Z_{e,X}, Z_{e,Ka}, Z_{e,W})$	0.38	0.42	0.58	0.08	0.14	0.86
$p(Z_{e,X})p(Z_{e,Ka})p(Z_{e,W})$	0.69	0.73	0.27	0.23	0.38	0.62

References

von Lerber, A., Moisseev, D., Bliven, L. F., Petersen, W., Harri, A., and Chandrasekar, V.: Microphysical properties of snow and their link to Ze–S relations during BAECC 2014, J. Appl. Meteorol. Clim., 56, 1561–1582, https://doi.org/10.1175/JAMC-D-16- 0379.1, 2017.

Falconi, M. T., von Lerber, A., Ori, D., Marzano, F. S., and Moisseev, D.: Snowfall retrieval at X, Ka and W bands: consistency of backscattering and microphysical properties using BAECC ground-based measurements, Atmos. Meas. Tech., 11, 3059-3079, https://doi.org/10.5194/amt-11-3059-2018, 2018.

Sekelsky, S. M.: Near-field reflectivity and antenna boresight gain corrections for millimeter-wave atmospheric radars, J. Atmos. Ocean. Tech., 19, 468–477, https://doi.org/10.1175/1520- 0426(2002)0192.0.CO;2, 2002.

How much attenuation at W and Ka bands is caused by melting layer? An answer from multi-frequency radar Doppler spectra

Haoran Li[1] and Dmitri Moisseev[1,2]

[1]*University of Helsinki, P.O. Box 3, Helsinki, Finland*
[2]*Finnish Meteorological Institute, P.O. Box 503, Helsinki, Finland*
(Dated: 22 June 2018)

1 Introduction

Melting layer is known as an area with enhanced radar reflectivity factor in centimeter radar measurements. This enhancement, so-called bright band, is mainly due to the fast increase of the dielectric constant of the melting snow. The bright band feature is significant for radars operating at S, C and X bands, but less obvious for Ka- and W-band radars, at which the dip of reflectivity in the melting layer is reported and known as dark band (Kollias and Albrecht, 2005; Sassen et al., 2005). Accompanied with the weakening bright band when the radar wavelength moves towards millimeter, signal attenuation in the melting layer becomes a knotty problem. The unknown melting layer attenuation blocks the retrieval of ice cloud above for ground-based cloud radars (Illingworth et al., 2007), and hinders the interpretation of rainfall for space-borne radars operating at Ka and W bands which provide global observations from the top to down (Stephens et al., 2002; Hou et al., 2014; Illingworth et al., 2015).

It is believed that if the melting layer model could reproduce the radar reflectivity correctly, the melting process described in the model is confidential. A lot of works have been devoted into develop realistical models to predict microphysical processes inside the melting layer (e.g., Fabry and Zawadzki, 1995; Szyrmer and Zawadzki, 1999; Leinonen and von Lerber, 2018). Matrosov (2008) derived melting layer attenuation relation for X, Ka and W bands based on the existing melting layer models, and matched the model output with X band radar reflectivity profiles. However, Fabry and Szyrmer (1999) found that the bright band model is very sensitive to the assumed electromagnetic properties. Johnson et al. (2016) demonstrated that the electromagnetic properties of the melting snow are highly uncertain because of the water distribution inside. Thus, actual measurements are imperative for better understanding the physical processes in the melting layer as well as constraining the models.

Bellon et al. (1997) determined the melting layer attenuation at X band by the combination of X band and UHF radar measurements. von Lerber et al. (2015) estimated the melting layer attenuation at C band when the melting layer reaches the ground. Recently Nakamura et al. (2018) derived the melting layer attenuation at Ka band via a dual Ka-band radars deployment. However, there is no measurement study on W band melting layer attenuation.

Due to the large data volume, the potential of radar Doppler spectra was not fully investigated in the past. In addition, the combination of radar measurements at different frequencies was demonstrated to reveal more underlying microphysical information (Sekelsky et al., 1999). Tridon et al. (2013) retrieved the rain attenuation at W band by utilizing the flat Rayleigh regime in Ka-W dual-wavelength Doppler spectra ratio. The Rayleigh scattering regime in multi-frequency radar Doppler spectra is also reported in snow by Kneifel et al. (2016). Can we use the Rayleigh regime in multi-frequency radar Doppler spectra to determine the melting layer attenuation at Ka and W bands? This paper provides a roadmap to answer this question.

2 Data

From February to September 2014 Biogenic Aerosols Effects on Clouds and Climate (BAECC) field campaign was carried out at the University of Helsinki Hyytiälä Station (Petäjä et al. 2016),. Dual-frequency (X/Ka) and dual-polarized scanning Atmospheric Radiation Measurement (ARM) cloud radar (X/Ka-SACR) and the zenith-pointing W band ARM cloud radar (MWACR) were deployed during BAECC. The range gate spacing for X/Ka-SACR is 25 m, and 30 m for MWACR. The X/Ka-SACR radars were running different scanning modes during BAECC, we use the vertical pointing data during the precipitation event 12th June 2014 in this study. The original temporal resolution (2 s) is averaged into 1 min for all radar data. More details about the radar products are referred to (Kneifel et al., 2015) and (Petäjä et al. 2016). Radar reflectivity is calibrated by matching the lowest reflectivity to the reflectivity simulated from the video distrometer. Gaseous attenuation is corrected by using the sonding data as input to the millimeterwave propagation model (Liebe, 1985). Since the mispointing of MWACR leads to horizontal shift of W band spectrum, we adopt the method proposed by Kneifel et al. (2016) to correct the W band spectrum by matching the Rayleigh regime of W band to that of Ka band.

3 Method

3.1 Theoretical basis

Regarding the attenuation effects, the measured radar reflectivity factor for a radar operating at the wavelength of λ at the range of *r* can be expressed in the following form (Tridon et al. 2013),

$$Z_{m,\lambda}(r) = Z_{e,\lambda}(r) - 2\int_0^r \alpha_\lambda(s)ds \quad (3.1)$$

where $Z_{e,\lambda}$ is the equivalent radar reflectivity factor, α_λ is the one-way specific attenuation including the attenuation from gases, hydrometeors, and wet radome at the wavelength of λ. Dual-wavelength ratio (DWR) between radars operating at two wavelength λ_1 and λ_2 ($\lambda_1 > \lambda_2$) is defined as,

$$DWR(r) = Z_{m,\lambda_1}(r) - Z_{m,\lambda_2}(r) \quad (3.2)$$

Thus,

$$DWR(r) = Z_{e,\lambda_1}(r) - Z_{e,\lambda_2}(r) + 2\int_0^r [\alpha_{\lambda_2}(s) - \alpha_{\lambda_1}(s)]ds \quad (3.3)$$

where the first and the second terms correspond to Mie scattering effect, and the third term is the attenuation effect. For centimeter-wavelength where most raindrops and snowflakes are good Rayleigh scatters, the Mie scattering effect is 0. After matching the reflectivities from two radars at the bottom of the melting layer, the melting layer attenuation at the higher frequency can be derived after separating the gaseous attenuation. The DWR technique was used to quantify X band melting layer attenuation (Bellon et al., 1997) since most hydrometeors are Rayleigh scatters at X band. However, when it comes to millimeter wavelength, the DWR technique may not be applicable due to the Mie scattering.

3.2 Rain attenuaiton

Nevertheless, there are still small hydrometeors which fall in Rayleigh scattering regime in the millimeter-wavelength radar projected volume. Tridon et al. (2013) demonstrated that the Rayleigh regime in dual-wavelength Doppler spectral ratio (DSR) can be used to untangle the rain attenuation and Mie effect at W band. As shown in Figure 1, the spectrums for X- and Ka-band radars are very similar though the Mie scattering effect starts to emerge when the velocity exceeds 8 m/s. The Mie effect on W band is significant as indicated by the significant dip at around 6.8 m/s in W band spectra. The flat plateau in Ka/W DSR is characterized by the falling velocity within 4 m/s as reported in (Tridon et al., 2013). The flat part in X/Ka DSR is also obvious though a bit noisier. It should be noted that the combination of X and W bands is not applied this study, since the sensitivity of X-band radar is not as good as Ka-band radar and might obscure the Rayleigh regime. The Ka/W DSR in Rayleigh regime at the range of *r* is defined as,

$$DSR_{Rayleigh}(Ka,W,r) = \frac{\int_{v_{Rayleigh,rain}}^{v_{noise,W}} [S_{Ka}(v) - S_W(v)]dv}{v_{noise,W} - v_{Rayleigh,rain}} \quad (3.4)$$

where S_{Ka} and S_W indicate power spectral density at Ka and W bands respectively, $v_{noise,W}$ and $v_{Rayleigh,rain}$ represent the minimum and maximum velocity range in the Rayleigh regime respectively. To ensure the data quality, $v_{noise,W}$ is determined where the power spectral density is 10 dB above the W-band noise level. $v_{Rayleigh,rain}$ is set to 4 m/s. Similarly, the X/Ka DSR in Rayleigh regime for rain at the range of *r* is defined as,

$$DSR_{Rayleigh,rain}(X,Ka,r) = \frac{\int_{v_{Rayleigh,rain}}^{v_{noise,X}} [S_X(v) - S_{Ka}(v)]dv}{v_{noise,X} - v_{Rayleigh,rain}} \quad (3.5)$$

where $v_{noise,X}$ is determined where the power spectral density is 10 dB above the X-band noise level. Thus the rain attenuation at Ka band from ground to *r* can be expressed as,

$$A_{rain}(Ka,r) = DSR_{Rayleigh,rain}(X,Ka,r) + A_{rain}(X,r) + A_{gas}(X,0,r) \quad (3.6)$$

where $A_{rain}(X,r)$ is the rain attenuation at X band from ground to *r*, $A_{gas}(X,0,r)$ is the gaseous attenuation at X band from ground to *r*. The millimeterwave propagation model (Liebe, 1985) is applied to estimate the gaseous attenuation at X, Ka and W bands in this study. Similarly, the rain attenuation at W band from ground to *r* can be written as,

$$A_{rain}(W,r) = DSR_{Rayleigh,rain}(Ka,W,r) + A_{rain}(Ka,r) + A_{gas}(Ka,0,r) \quad (3.7)$$

where $A_{rain}(\mathrm{Ka},\mathrm{r})$ is the rain attenuation at Ka band from ground to *r*, $A_{gas}(Ka,0,\mathrm{r})$ is the gaseous attenuation at Ka band from ground to *r*.

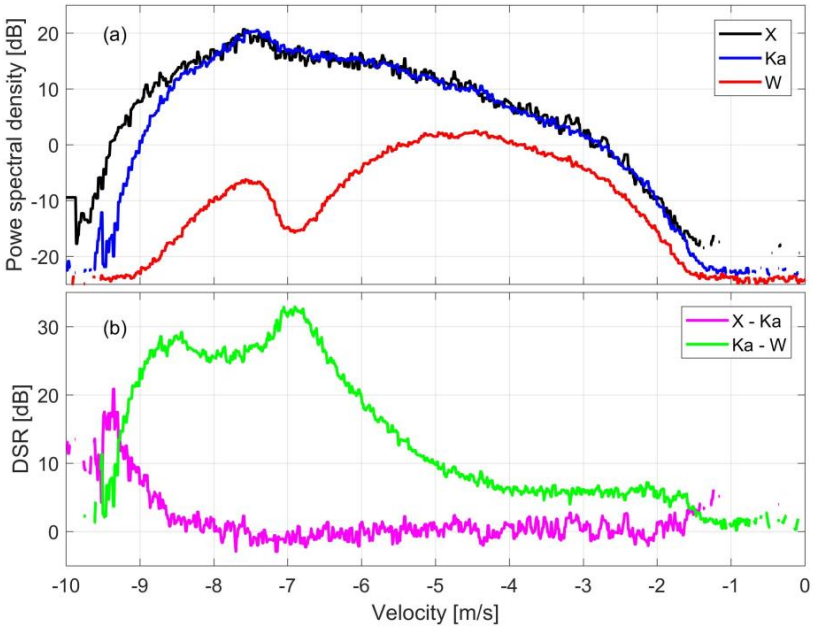


Figure 1: Doppler spectrums of X-, Ka- and W-band radars in rain (a), DSR for X/Ka and Ka/W in rain (b).

3.3 Melting layer location and attenuation

For single-polarized radar, the location of the melting layer is detected by using the reflectivity-based method. During, the multi-frequency radars are dual-polarized and capable of providing additional products such as ρ_{hv}, Z_{dr} and K_{dp}. In this study, we use the local dip of ρ_{hv} to detect the melting layer location.

Kneifel et al. (2016) presented the Rayleigh regime in DSR for Ka/W and X/Ka. As shown in Figue 2, the Doppler spectrum in snow is much narrower than that in rain. The flat Rayleigh regime is around -1.1 m/s ~ -0.8 m/s, which is narrower and noisier than that in rain. As expected, Ka band radar signal has longer wavelength, and the X/Ka DSR flat Rayleigh regime (-1.3 m/s ~ -0.8 m/s) is more significant than that for Ka/W. Thus, the X/Ka DSR in Rayleigh regime for snow at the range of *r* is defined as,

$$DSR_{Rayleigh,snow}(X,Ka,r) = \frac{\int_{v_{Rayleigh,snow,X/Ka}}^{v_{noise,X}} [S_X(v) - S_{Ka}(v)]dv}{v_{noise,X} - v_{Rayleigh,snow,X/Ka}} \quad (3.8)$$

where $v_{Rayleigh,snow,X/Ka}$ indicates the velocity which is 0.3 m/s (absolute value) smaller than the $v_{noise,X}$. For Ka/W DSR,

$$DSR_{Rayleigh,snow}(Ka,W,r) = \frac{\int_{v_{Rayleigh,snow,Ka/W}}^{v_{noise,W}} [S_{Ka}(v) - S_W(v)]dv}{v_{noise,W} - v_{Rayleigh,snow,Ka/W}} \quad (3.9)$$

where $v_{Rayleigh,snow,Ka/W}$ indicates the velocity which is 0.3 m/s (absolute value) smaller than the $v_{noise,W}$. For a meling layer locating from r_1 to r_2 ($r_1 < r_2$), the melting layer attenuation at Ka and W bands can be expressed as,

$$A_{ML}(Ka) = DSR_{Rayleigh,snow}(X,Ka,r_2) - A_{rain}(Ka,r_1) + A_{ML}(X) - A_{gas}(Ka,r_1,r_2) \quad (3.10)$$

$$A_{ML}(W) = DSR_{Rayleigh,snow}(Ka,W,r_2) - A_{rain}(W,r_1) + A_{ML}(Ka) + A_{gas}(Ka,r_1,r_2) - A_{gas}(W,r_1,r_2) \quad (3.11)$$

where $A_{ML}(X)$ indicates the melting layer attenuation at X band incorporating the attenuation from melting snow and the gaseous attenuation at X band throughout the melting layer. As stated before, gaseous attenuation at X band is very small, and is assumed to 0 dB. Matrosov et al. (2008) presented the two-way melting layer attenuation at X-, Ka-, and W-bands as

$$A_{ML}(X) = 0.048R^{1.05} \quad (3.12)$$

$$A_{ML}(Ka) = 0.66R^{1.1} \quad (3.13)$$

$$A_{ML}(W) = 2.6R^{0.87} \quad (3.14)$$

where R is the rain rate (mm/h). Thus,

$$\frac{A_{ML}(X)}{A_{ML}(Ka)} = \frac{1}{13.75R^{0.05}} \ll A_{ML}(Ka)\ (R > 0.1\ mm/h) \qquad (3.15)$$

(3.15) indicates that the melting layer attenuation at Ka band is much larger than that at X band for normal rainfall. Thus, the uncertainty from using the modelled relation for X-band is trivial in estimating Ka band attenuation.

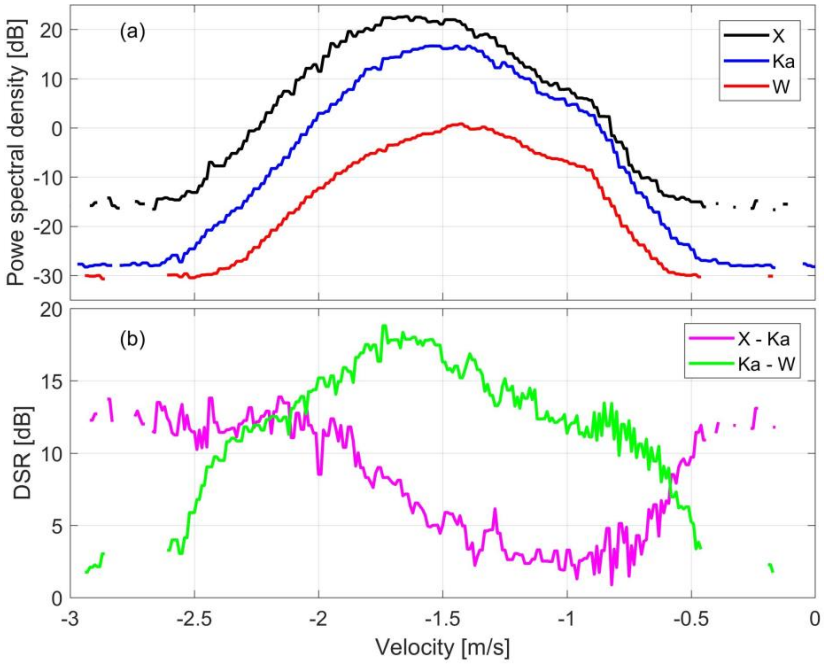


Figure 2: Doppler spectrums of X-, Ka- and W-band radars in snow (a), DSR for X/Ka and Ka/W in snow (b).

3.4 Rayleigh scatters in the cloud top

Except for searching the narrow Rayleigh regime in X/Ka and Ka/W DSR, ice crystals at cloud top can be good Rayleigh scatters at W band as well as at Ka band. Thus the DWR technique could also be utilized to estimate melting layer attenuation. (3.10) and (3.11) could be rewritten as,

$$A_{ML}(Ka) = Z_X(r_3) - Z_{Ka}(r_3) - [A(Ka, r_2, r_3) - A(X, r_2, r_3)] - A_{rain}(Ka, r_1) + A_{ML}(X) - A_{gas}(Ka, r_1, r_2) \qquad (3.16)$$

$$A_{ML}(W) = Z_{Ka}(r_3) - Z_W(r_3) - [A(Ka, r_2, r_3) - A(W, r_2, r_3)] - A_{rain}(W, r_1) + A_{ML}(Ka) + A_{gas}(Ka, r_1, r_2) - A_{gas}(W, r_1, r_2) \qquad (3.17)$$

where $Z_X(r_3)$, $Z_{Ka}(r_3)$, and $Z_W(r_3)$ are radar reflectivity at the range of r_3 (cloud top) for X, Ka and W band radars, respectively; $A(\mathrm{X}, r_2, r_3)$, $A(Ka, r_2, r_3)$ and $A(\mathrm{W}, r_2, r_3)$ are the integrated total attenuation from melting layer top r_2 to cloud top r_3, recpectively. The total attenuation above the melting layer contains the attenuation from dry snow, gaseous attenuation and possibly-existed supercooled water. For this event, only gaseous attenuation is considered.

4 Results

The stratiform rainfall in 12th June 2016 was observed by the multi-frequency radars. The melting layer attenuation is determined by utilizing (3.16) and (3.17). The retrieved melting layer attenuation is presented as a function of the X band radar reflectivity at the rain top (bottom of the melting layer). The rain rate in (3.13) is converted in to the radar reflectivity by using the Marshall-Palmer relation (Marshall and Palmer, 1948), which was used in (Matrosov, 2008). As shown in Figure 3, the measured melting layer attenuation is well matched with the model developed by Matrosov (2008). The increase of the Ka-band attenuation is also well characterized by the increasing radar reflectivity. Figure 4 presents the melting layer attenuation at W band. The measurements in general agree with the modelled ones well, especially for light precipitation (Z_X <17). For relatively intense precipitation, the model seems to underestimate the melting layer attenuation.

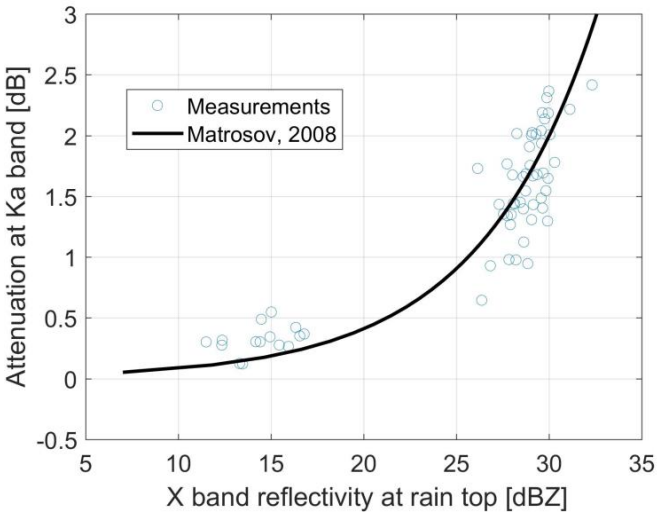


Figure 3: Ka-band melting layer attenuation

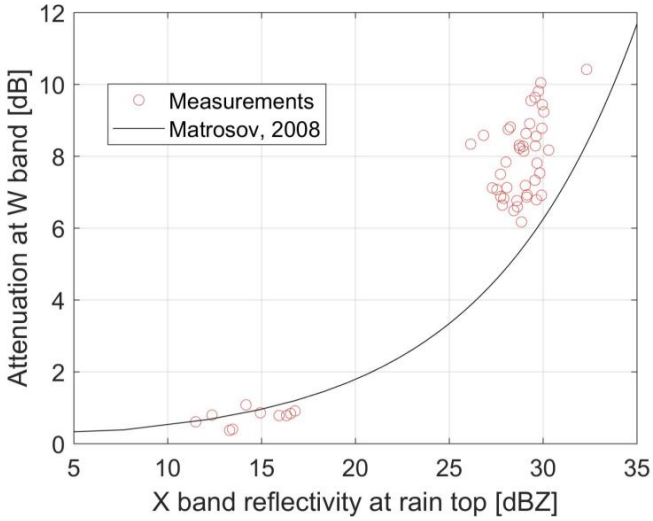


Figure 4: W-band melting layer attenuation

Acknowledgement

We would like to thank the personnel of Hyytiälä station and Matti Leskinen for their support in field observation. Dr. Stefan Kneifel is acknowledged for fruitful discussions. The research of HL and DM was supported by Academy of Finland (Grant no. 305175) and the Academy of Finland Finnish Center of Excellence program (Grant no. 307331). HL was also funded by China Scholarship Council. The instrumentation used in this study was supported by NASA Global Precipitation Measurement Mission ground validation program and by the Office of Science U.S. Department of Energy ARM program. The data used in this study are available from DOE ARM archives.

References

Bellon, A., I. Zawadzki, and F. Fabry, 1997: Measurements of melting layer attenuation at X-band frequencies, *Radio Sci.*, 32(3): 943–955.

Fabry F. and Szyrmer W., 1999: Modeling of the melting layer. Part II: Electromagnetic. *J. Atmos. Sci.*, 56(20): 3593-3600.

Fabry F. and Zawadzki I., 1995: Long-term radar observations of the melting layer of precipitation and their interpretation, *J. Atmos. Sci.*, 52(7): 838-851.

Hou A. Y., R. K. Kakar, S. Neeck, et al., 2014: The global precipitation measurement mission. *Bull. Am. Meteorol. Soc.*, 95(5): 701-722.

Illingworth A. J., H. W. Barker, A. Beljaars, et al., 2015: The EarthCARE satellite: The next step forward in global measurements of clouds, aerosols, precipitation, and radiation. *Bull. Am. Meteorol. Soc.*, 96(8): 1311-1332.

Illingworth A. J., R. J. Hogan, E. J O'connor., et al., 2007: Cloudnet: Continuous evaluation of cloud profiles in seven operational models using ground-based observations. *Bull. Am. Meteorol. Soc.*, 88(6): 883-898.

Johnson B. T., W. S. Olson, and G. Skofronick-Jackson, 2016: The microwave properties of simulated melting precipitation particles: sensitivity to initial melting. *Atmos. Meas. Tech.*, 2016, 9(1): 9.

Kneifel, S., P. Kollias, A. Battaglia, et al., 2016: First observations of triple-frequency radar Doppler spectra in snowfall: Interpretation and applications, *Geophys. Res. Lett.*, 43, 2225–2233, doi:10.1002/2015GL067618.

Kneifel, S., A. von Lerber, J. Tiira, et al., 2015: Observed relations between snowfall microphysics and triple-frequency radar measurements, *J. Geophys. Res. Atmos.*, 120(12), 6034–6055, doi:10.1002/2015JD023156.

Kollias P. and Albrecht B., 2005: Why the melting layer radar reflectivity is not bright at 94 GHz, *Geophys. Res. Lett.*, 32, L24818, doi:10.1029/2005GL024074.

Leinonen J. and von Lerber A., 2018: Snowflake melting simulation using smoothed particle hydrodynamics. *J. Geophys. Res. Atmos.*, 123(3): 1811-1825.

Liebe H. J., 1985: An updated model for millimeter wave propagation in moist air. *Radio Sci.*, 20(5): 1069-1089.

Marshall J. S. and Palmer W. M., 1948: The distribution of raindrops with size, *J. Meteorol.*, 5(4): 165–166.

Matrosov, S. Y.., 2008: Assessment of radar signal attenuation caused by the melting hydrometeor layer, *IEEE Trans. Geosci. Remote Sens.*, 46(4): 1039-1047.

Nakamura K, Y. Kaneko, K. Nakagawa, et al., 2018: Measurement Method for Specific Attenuation in the Melting Layer Using a Dual Ka-Band Radar System. *IEEE Trans. Geosci. Remote Sens.*, 56(6): 3511-3519.

Petäjä, T., et al., 2016: BAECC: A field campaign to elucidate the impact of biogenic aerosols on clouds and climate, *Bull. Amer. Meteor. Soc.*, 97(10), 1909–1928, doi:10.1175/BAMS-D-14-00199.1.

Sassen, K., J. R. Campbell, J. Zhu, P. Kollias, M. Shupe, and C. Williams, 2005: Lidar and triple-wavelength Doppler radar measurements of the melting layer: A revised model for dark- and brightband phenomena, *J. Appl. Meteorol.*, 44, 301 – 312.

Sekelsky S. M., W. L. Ecklund and K. S. Gage., 1999: Multi-frequency radar observations of the melting layer//Geoscience and Remote Sensing Symposium, IGARSS'99 Proceedings. IEEE 1999 International. IEEE, 1: 705-707.

Stephens G. L., Vane D. G., Boain R. J., et al., 2002: The CloudSat mission and the A-Train: A new dimension of space-based observations of clouds and precipitation. *Bull. Am. Meteorol. Soc.*, 83(12): 1771-1790.

Szyrmer W. and Zawadzki I., 1999: Modeling of the melting layer. Part I:Dynamics and microphysics, *J. Atmos. Sci.*, 56(20): 3573-3592.

Tridon, F., A. Battaglia, and P. Kollias, 2013: Disentangling mie and attenuation effects in rain using a Ka-W dual-wavelength Doppler spectral ratio technique, *Geophys. Res. Lett.*, 40(20), 5548–5552, doi:10.1002/2013GL057454.

von Lerber A., D. Moisseev, J. Leinonen, et al., 2015: Modeling radar attenuation by a low melting layer with optimized model parameters at C-ban. *IEEE Trans. Geosci. Remote Sens.*, 53(2): 724-737.

Testing of conventional attenuation estimation algorithms with operational radars in different bands

Aleksandr Lialiushkin[1], Aleksandr Solonin[1], Nikolay Bocharnikov[1], Tatiana Bazlova[1], Nadezhda Yakimainen[1] and Vasiliy Olenev[1]

[1]*Institute of Radar Meteorology (IRAM), p. Voeikovo 15, Saint-Petersburg, Russia*

(Dated: 21 June 2018)



Aleksandr Lialiushkin

1 Introduction

Air traffic controllers of the airports require accurate information about weather phenomena dangerous for aviation such as strong convection and thunderstorms. One of the main function of a terminal weather radar is to provide this information to ATM systems operationally (Bazlova, 2002). However, probability of detection of severe weather associated with convective cloudiness degrades with the distance from the radar. Mainly, because of attenuation in rain. In addition, terminal weather radar data is widely used by airdrome nowcasting systems that require precipitation detection and quantification in advance before it reaches the airdrome territory. This detection and quantification suffer from the attenuation and require practical methods of data correction, as well.

Customary practices of QPE quality enhancement involves raw radar data correction for rain attenuation and adjustment of resultant precipitation field against rain gauge network. The latter allows correcting the large-scale and long-term biases in total precipitation sums even when the former does not perform at its best. In this situation, the remaining errors, which are associated with attenuation correction, are in charge of local transitory variations and range-dependent biases in precipitation fields.

On the other hand, tasks of cloud classification and severe weather detection (except hydrological applications) are not directly connected with QPE and might benefit from rain gauge correction only if this correction of surface rain rate is somehow transferred back to volumetric radar data. This leads to a greater importance of attenuation correction for severe weather detection, especially for automated weather radar systems designed for aeronautical application such as pilot and air traffic controller briefing, terminal airdrome forecasting, present weather reporting and alerting, and finally ATM system integration.

Several methods of in-rain attenuation correction are developed in scientific papers and some of them continue to be extended and improved (Liang Feng, 2016). However, the choice on which one to use for practical solutions is always left to system designers and end users. In order to determine an optimal way of rain attenuation estimation, a base set of these methods has been chosen for evaluation of their operational performance in various weather situations with an emphasis on range-dependent biases and robustness.

Two operational weather radars, one C-band and the other X-band, are used for validating the estimates. The C-band radar data after correction is regarded as a ground truth being less prone to the attenuation effects.

2 Test Procedure

Saint-Petersburg has three operation weather surveillance radars located in the city or in proximity:

Table 1:Operational weather radars in Saint-Petersburg

#	Manufacturer	Model	Software	Band	Pol	Pulse	Year	Placement
1	SELEX	METEOR-500C	MeteoCell	C	Single	Short simple	2006	Pulkovo airport
2	SELEX	METEOR-50DX	MeteoCell	X	Dual	Short simple	2011	City center
3	LEMZ	DMRL-C	GIMET-2010	C	Dual	Long NLFM	2014	City suburbs (Voeikovo)

The radars #1 and #2 have been selected for validation, as they have the same manufacturer and RPG software but work in different frequency bands. The distance between them is 16 km.

Horizontal reflectivity data of the radar #1 is corrected by operational algorithm for in-rain attenuation. This algorithm uses standard for single-polarization weather radars empirical power law relation between horizontal reflectivity Z_H and specific attenuation for C-band (Hitschfeld, et al., 1954). This data is then used as a reference reflectivity field.

Horizontal reflectivity data of the radar #2 is corrected for in-rain attenuation using following basic methods available for dual-polarization X-band radars (Bringi, et al., 1990):

1. No correction,
2. $A = a\, Z_H^b$ with standard coefficients a and b,
3. $A = \alpha K_{DP}$ with standard coefficient a,
4. $A = a\, Z_H^b$ with modified coefficients a and b.

12 days with long-lasting rain events for different baric situations during summer and autumn seasons of 2017 has been picked out.

All reflectivity data from both radars has been converted to the same geographic grid and compared against reference data with range-dependence taken into account. Mean error $E = Z_X - Z_{reference}$ (ME) for the reflectivity values and the root mean square error (RMSE) has been calculated for each 10-km range step in 200 km radius around the radar #2, as well as total ME and RMSE.

3 Test results for selected cases

3.1 8th of June 2017

Weather situation description: baric col, a front passing aside the radar position, stratiform clouds with embedded convective, light to moderate rains and distant thunderstorms.

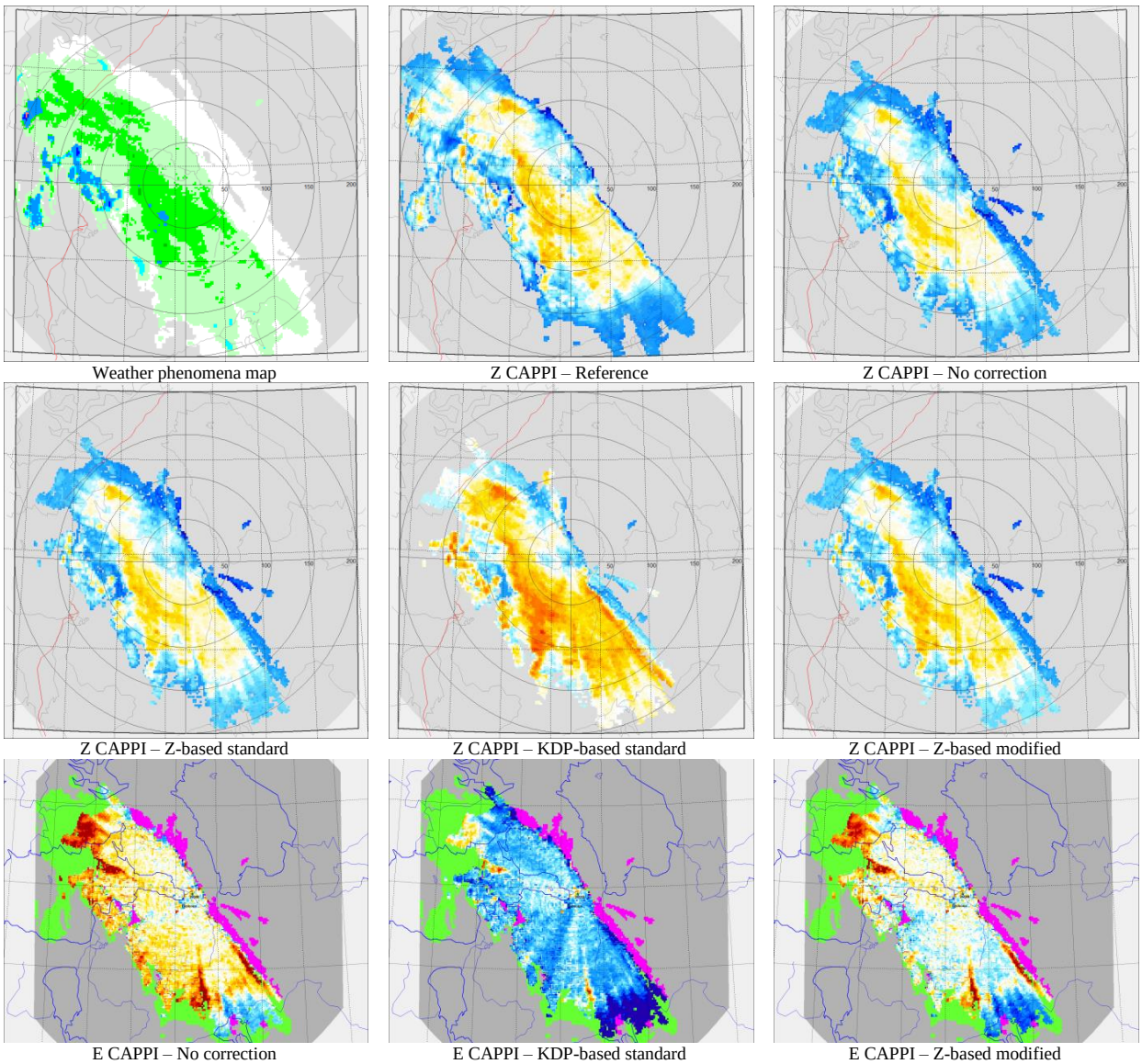


Figure 1: Reflectivity data for 8th of June 2017 22:40 UTC. On weather map greens for stratiform rains, blues for convective. On E-CAPPI maps red for attenuated signal, blues for overcompensated signal, whites for zero error.

Statistics for the whole day:

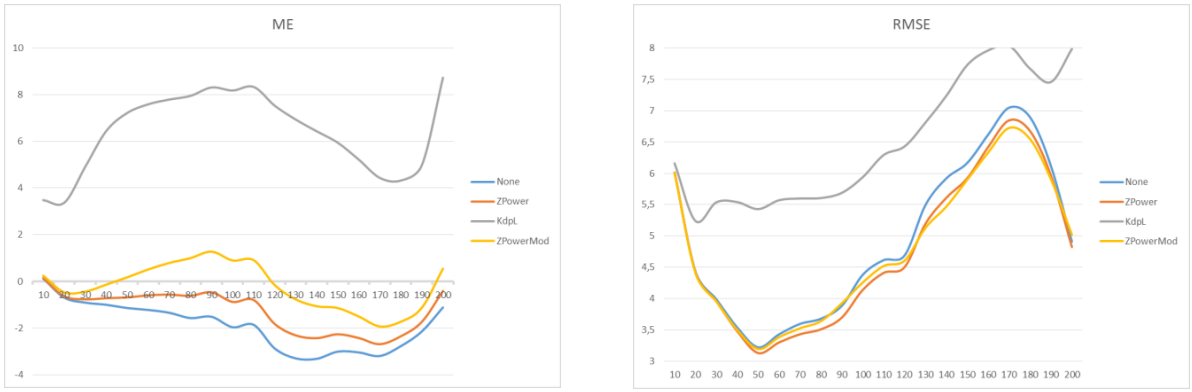
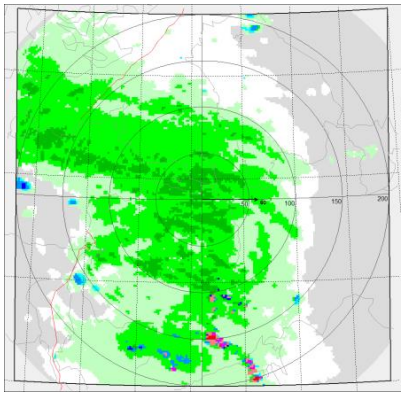


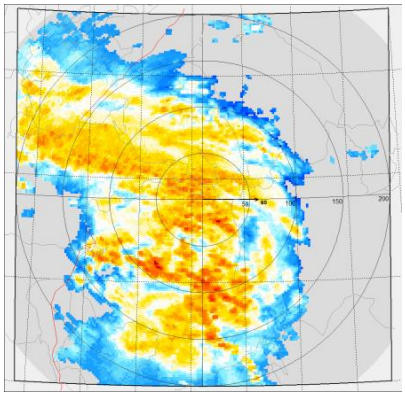
Figure 2: Mean error (dBZ) and RMSE of X-band radar reflectivity compared to C-band radar for the 8th of June 2017

3.2 2nd of August 2017

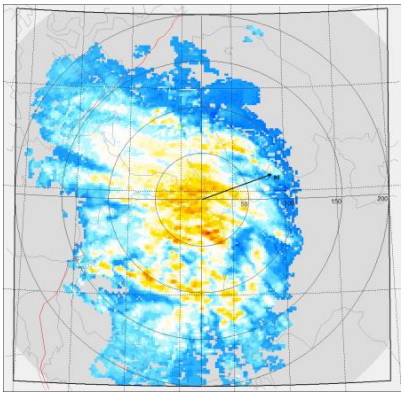
Weather situation description: baric trough, a worm front passing over the radar position, stratiform clouds with embedded convection, light to moderate rains and thunderstorms.



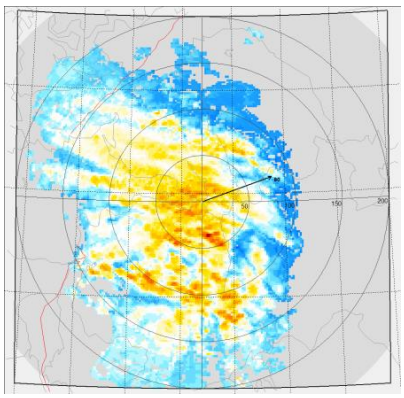
Weather phenomena map



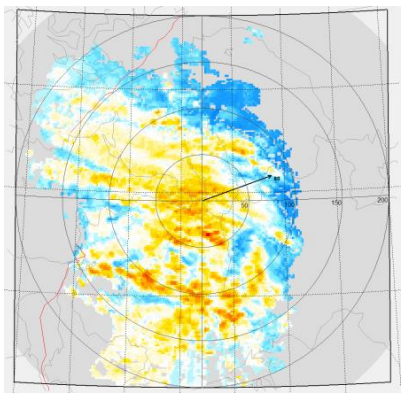
Z CAPPI – Reference



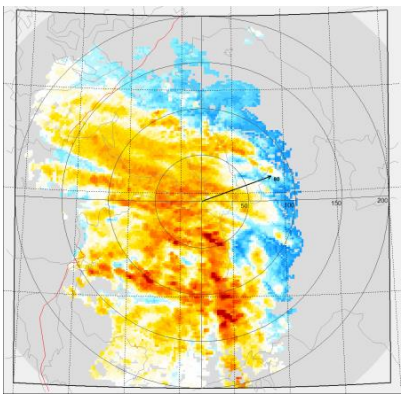
Z CAPPI – No correction



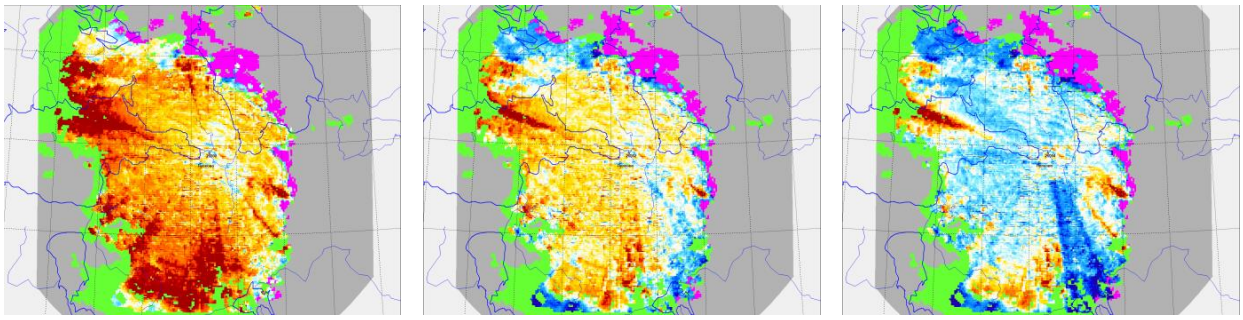
Z CAPPI – Z-based standard



Z CAPPI – KDP-based standard



Z CAPPI – Z-based modified



E CAPPI – No correction | E CAPPI – KDP-based standard | E CAPPI – Z-based modified

Figure 3: Reflectivity data for the 2nd of August 2017 06:00 UTC. On weather map greens for stratiform rains, blues for convective. On E-CAPPI maps red for attenuated signal, blues for overcompensated signal, whites for zero error.

Statistics for the whole day:

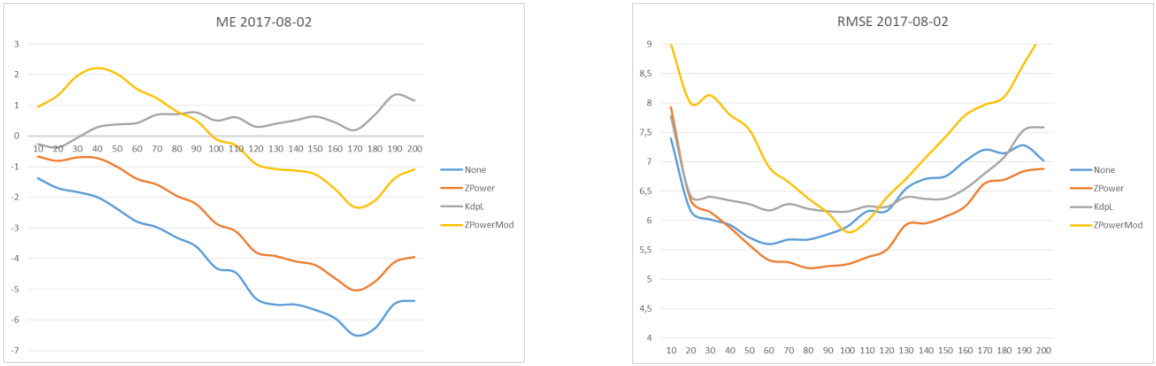


Figure 4: Mean error (dBZ) and RMSE of X-band radar reflectivity compared to C-band radar for the 2nd of June 2017

4 Summary

Fig. 5 shows total statistics for the whole data set of the summer and autumn seasons of 2017 for all weather situations in bulk.

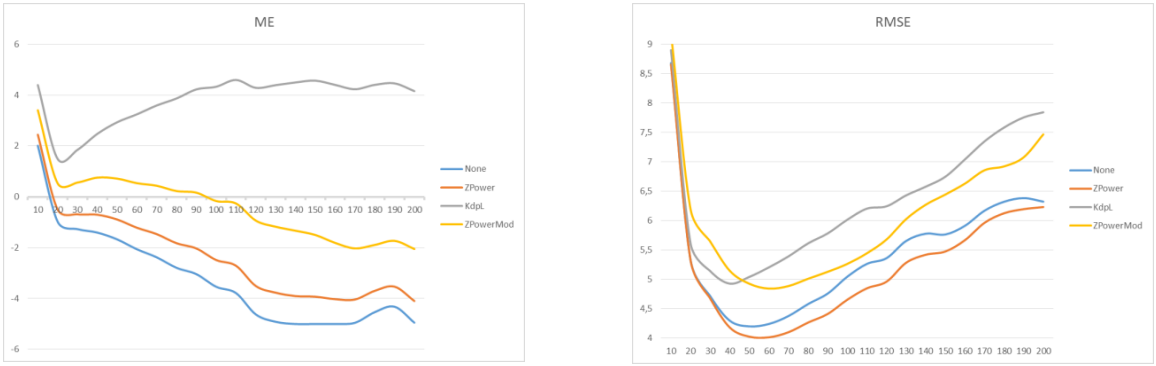


Figure 5: Mean error (dBZ) and RMSE of X-band radar reflectivity compared to C-band radar as functions of range in km

As it can be seen, standard Z- and KDP-based methods reduce at some extent the absolute error in reflectivity field and decrease range-dependence. On average, Z-based method with adjusted coefficients performs better and is flatter than other methods. In some weather situations, KDP-based method turns out to be the best. However, in general situation it overcorrects the data leading to false alarms and even bring in growth of reflectivity over reference with distance.

In addition, as illustrated in Fig. 5 by RMSE graphs, all attenuation correction methods except standard Z introduce some extra nose in the resulting fields because of inherent empirical nature of all this algorithms.

The results, summarized in Table 2, show that for practical operational purposes based method with adjusted coefficients performs relatively better in terms of mean error, RMSE being similar to those obtained using the other methods.

Table 2:Operational performance of attenuation correction methods for the Saint-Petersburg X-band radar compared against C-band radar over 12 days of summer and autumn seasons of 2017

Algorithm	ME	RMSE
No correction	-3,55	5,41
Standard Z	-2,59	5,10
Modified Z	-0,46	5,82
Standard KDP	3,97	6,22

5 Conclusions

Attenuation correction is an essential step for correct severe weather detection with uniform reliability at all ranges using C- and X-band weather radar. It is an important step in quantitative rain estimation, as well. Moreover, the method of choice for operational work should be as robust to miscalibration, system noise, and external interferences as it is achievable.

In the paper, several common methods of attenuation correction in rain are evaluated. It is found that classical single-polarization methods after proper tuning can perform on the whole set of situations in bulk better than other available methods. However, in some weather situations modern algorithms outperform the common ones. Therefore, in practical applications, a combination of Z-based algorithm with ability to switch to some other algorithm in certain situations appears as a good compromise.

References

Bazlova T., N. Bocharnikov, G. Brylev, at al. Meteorological automated radar networks. [Book]. - Saint-Petersburg : Hydrometeoizdat, 2002.

Bringi V.N., Balakrishnan N. and Zrnic D.S. An examination of propagation effects in rainfall on polarimetric variables at microwave frequencies. [Journal] // J. Atmos. Ocean. Technol.. - 1990. - 7. - pp. 829–840.

Hitschfeld W. and Bordan J. Errors inherent in the radar measurement of rainfall at attenuating wavelengths. [Article] // J. Meteorol. - 1954. - 11.

Liang Feng Hui Xiao, Guang Wen, Zongfei Li, Yue Sun, Qi Tang and Yanan Liu Rain Attenuation Correction of Reflectivity for X-Band Dual-Polarization Radar [Journal] // Atmosphere. - 2016. - 7. - S. 174.

The importance of assimilating thermodynamic fields with radar observations in convective-scale weather systems

Ching-Yin Ke, Kao-Shen Chung
Department of Atmospheric Sciences, National Central University, Taiwan

(Dated: 22 June 2018)



Ching-Yin Ke

1 Introduction

Radar data assimilation has greatly improvement QPF at convective scale. By using 3DVAR system, Ge et al. (2013) shows sensitivity tests of assimilating different state variables at storm scale. With WRF-LETKF Radar Assimilation System (WLRAS) which assimilates radar reflectivity and Doppler velocity, this study use OSSEs to examine the impact of assimilating additional observations of temperature and vapor, and provide some guidance for the needs of observations at convective scale.

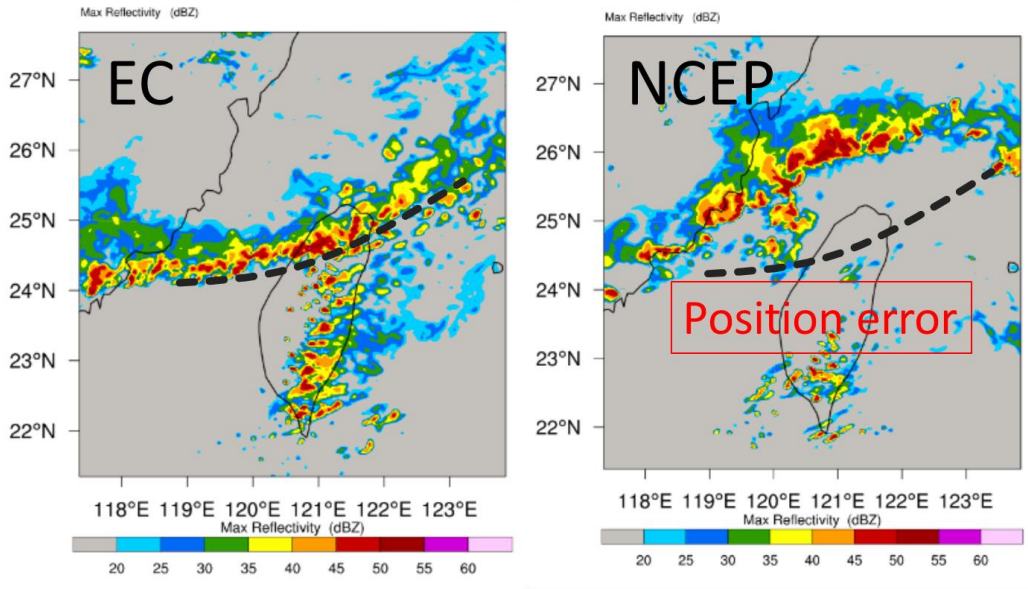


Figure 1:reflectivity of front position error near Taiwan 1400 UTC 11 June 2012

2 Methodology - WLRAS

The radar data assimilation system, WRF-LETKF Radar Assimilation System (after called WLRAS), is developed by Tsai et al. (2014) and it based on WRF-LETKF (Yang et al., 2012 and 2013) that is coupled with the local ensemble transform Kalman filter (LETKF; Hunt et al., 2007) and the WRF model.

In the study, the system uses mixed localization method for different covariance localization radii to different model variables. Observation data update all model variables by cross correlation to simulate the complex process in convective scale.

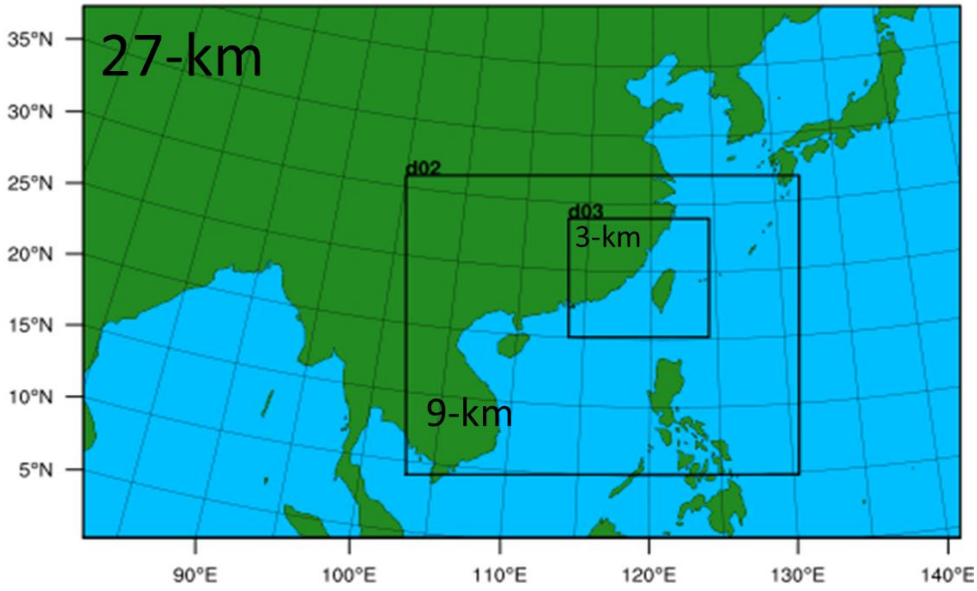


Figure 2: Model domain setup in WRF

3 OSSEs (Observing simulated system experiments)

Two independent models setup from EC reanalysis (Truth) that is wetter environment, from NCEP reanalysis (other experiments) that is drier environment at 0000 UTC 11 June 2012.

RCWF and NCU-CPOL are chosen for the OSSE study at North of Taiwan from Truth run. These radar are designed to have a maximum unambiguous range of 230-km, a volume scan from 0.5o to 19.5o. Simulated lower-resolution observation by superobbing in radial(4-km) and azimuth(4o).

The assimilation strategies is a 15-minute) analysis cycle internal both in 1 and 2 hour assimilation period. We study the data sensitivity of radar only (Z, Vr, ZVr, ZVr2h) and ZVr with additional variable (+T, +QV, +TQv)

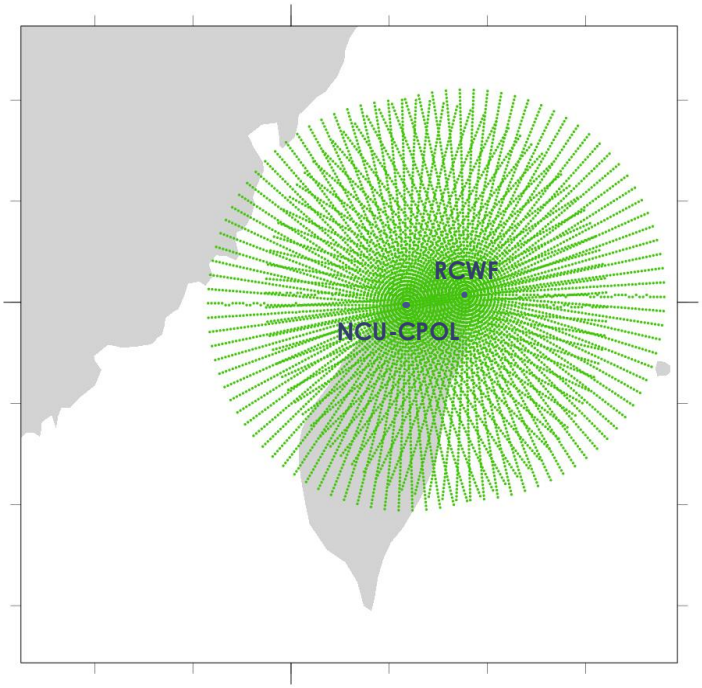


Figure 3: Simulated observation on superobsing space

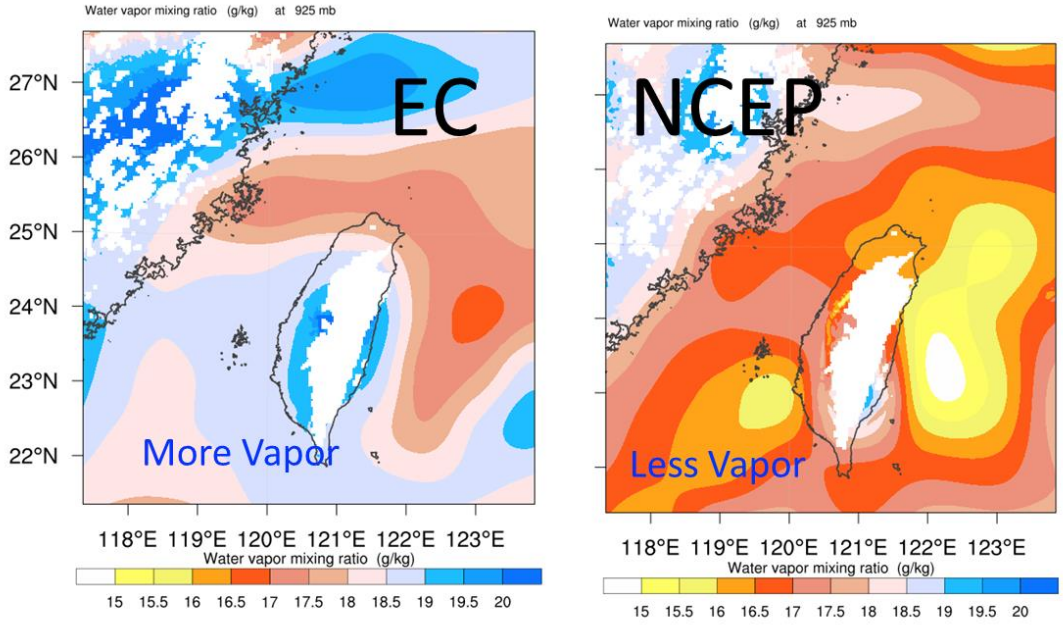


Figure 4: Model initial water vapor on 925-hPa. EC (left) is more vapor than NCEP reanalysis (right).

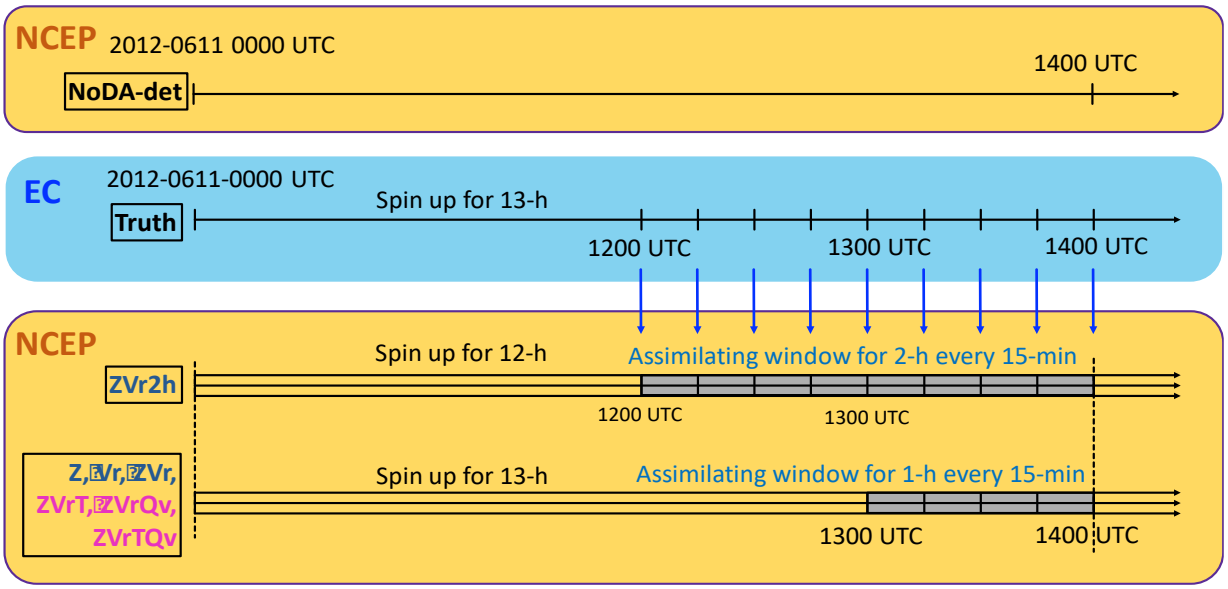


Figure 5: Experiments table

4 Result of analysis

Assimilating radar data improve the position of the front. Additional T or Qv with radar correlated the error reflectivity in stratiform.(Figure 6)

SCC score shows different model variables of every experiments at 1400 UTC. U, V show different score signature by front position. V wind is more important than U wind in frontal system. Assimilating temperature have well effect in ice particle signature. Water vapor is important in warm rain particle.

$$\frac{\sum(x_i - \bar{x_i})(x_t - \bar{x_t})}{\sqrt{\sum(x_i - \bar{x_i})^2 \cdot \sum(x_t - \bar{x_t})^2}}$$

Radar data can modify and capture the strong convection area in the right location, but the error in stratiform is still remains. T and Qv improve the hydrometeo variables in stratifom area. (Figure 8)

ZVrT and ZVrQv have good temperature structure than ZVr and ZVr2h in stratiform area. (Figure 9)

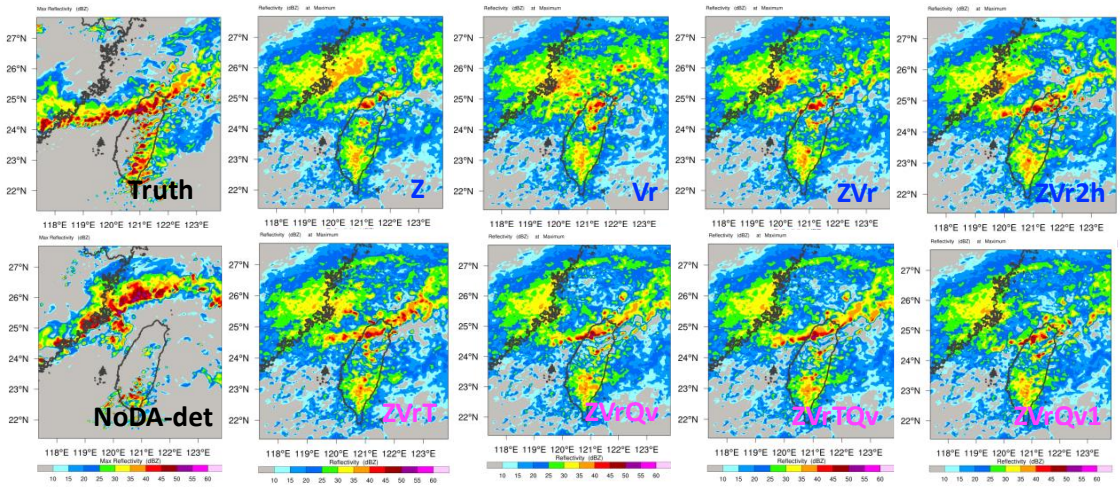


Figure 6: The analysis maximum reflectivity field at 1400 UTC.

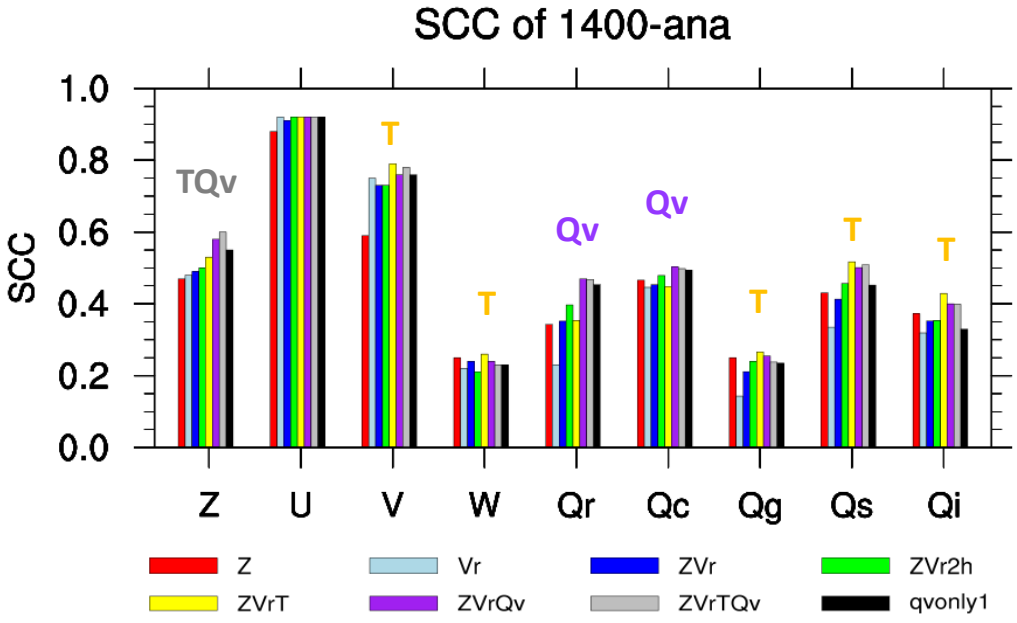


Figure 7: SCC score shows different model variables of every experiments at 1400 UTC (analysis field)

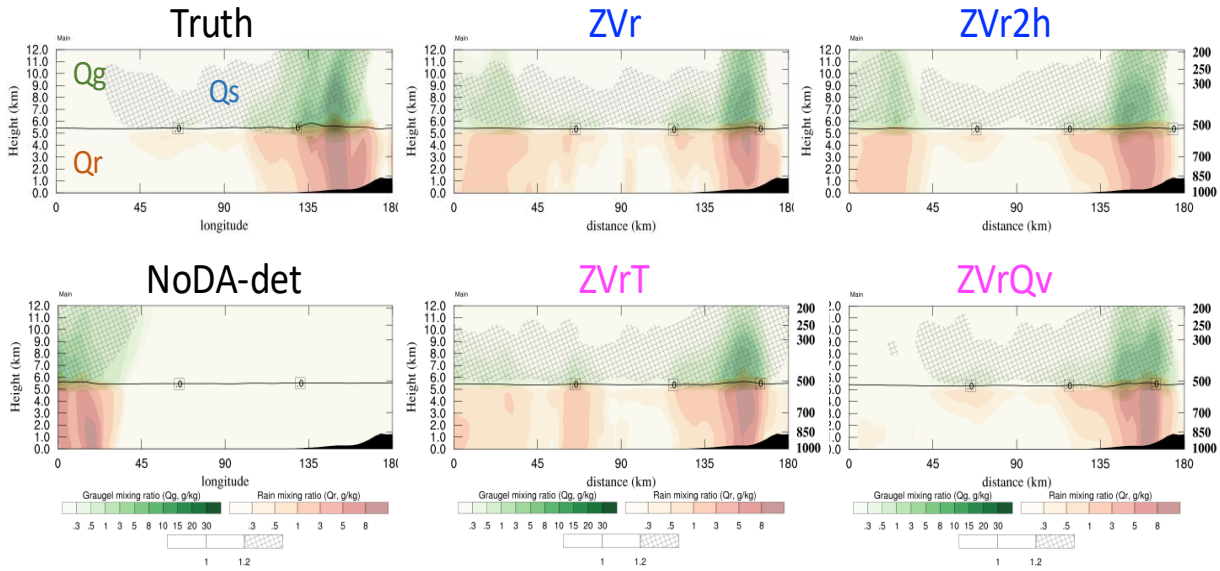


Figure 8: vertical profile of hydrometer rain(red), graupel(green) and snow(cross).

.

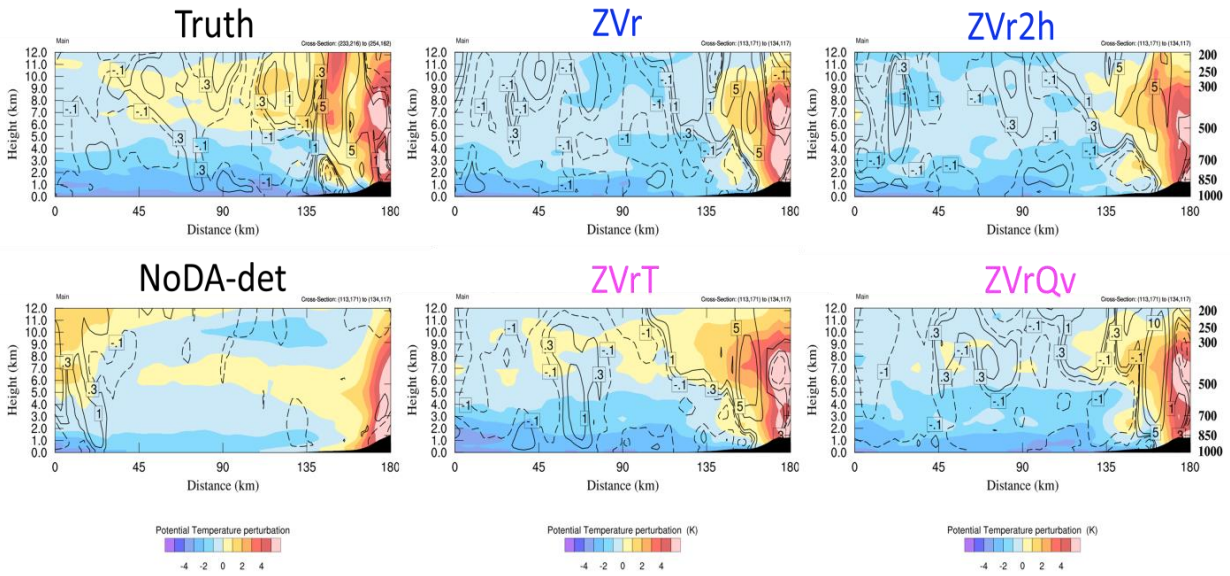


Figure 9: vertical temperature structure (shaded) and vertical velocity (contour)

5 Result of QPF

Rainfall accumulation from 1400 UTC to 1700 UTC. Radar data experiments are improve rainfall accumulation in convectivie area, but the wrose rainfall still ramains. Additional variable of temperature and water vapor shows good strong rainfall and decreas the worse rainfall in stratiform area. (Figure 10)

ETS score of 3-h rainfall shows ZVr2h is better than only one hour asimilation. Additional variable are improve at heavy rainfall. The best important variable is Qv. (Figure 11)

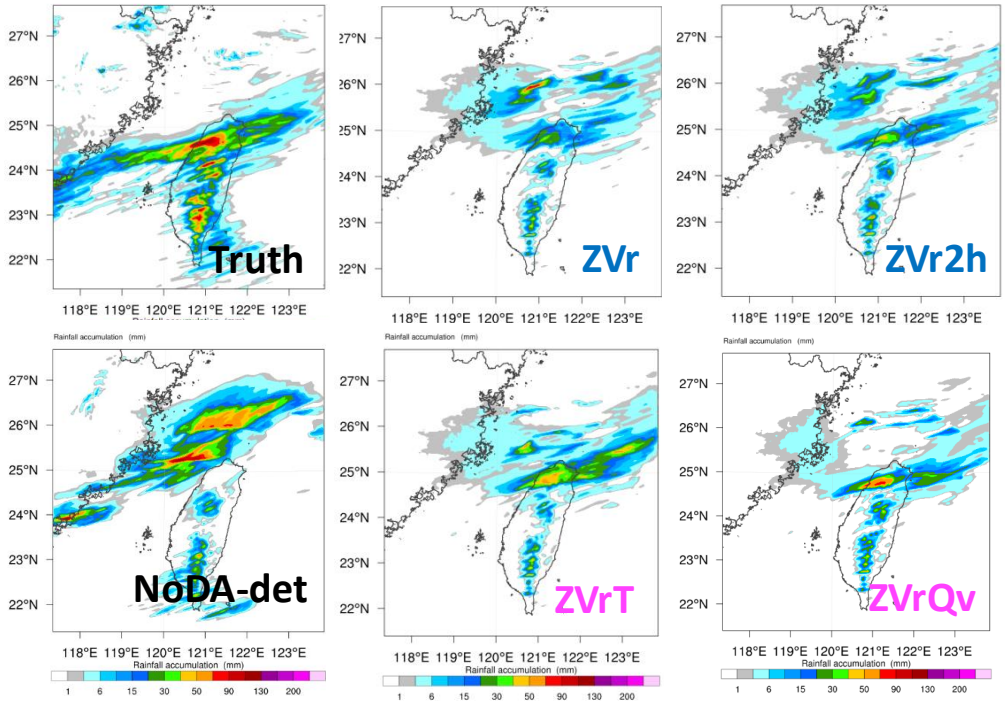


Figure 10: Rainfall accumulation from 1400 UTC to 1700 UTC.

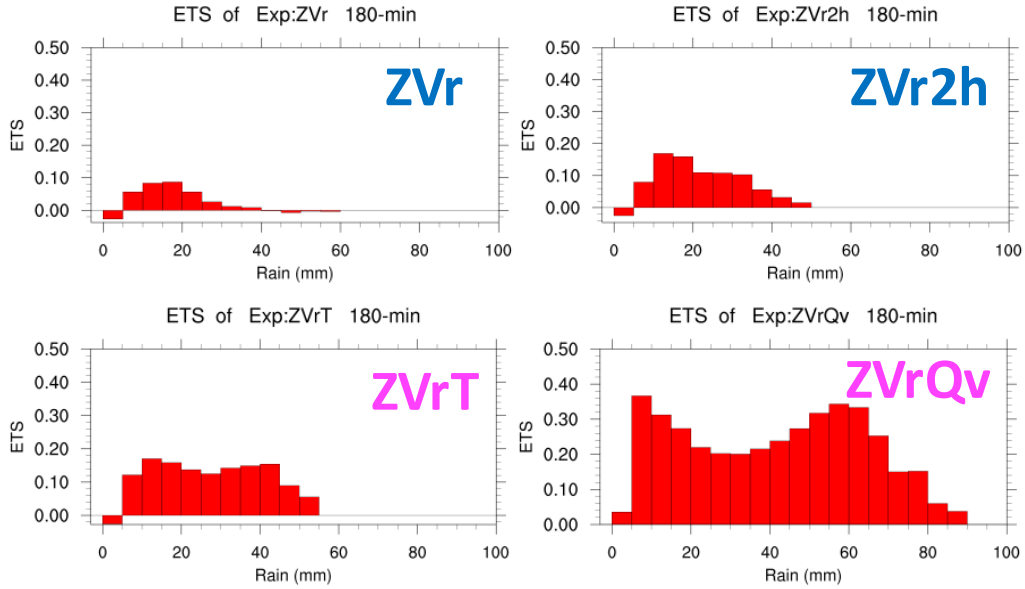


Figure 11: ETS score for 3 hours rainfall accumulation

6 Summary

The study shows the result assimilating of assimilated additional variables of Temperature and vapor through OSSEs by WLRAS.

(1) Radar data (Z, Vr) assimilation show improvement in strong convection. In stratiform region,

rainfall accumulation is overestimated.

(2) Temperature (T) illustrate good vertical structure of temperature in stratiform and ice particle. This is better than ZVr2h at QPF of heavy rain.

(3) Water vapor (Qv) is the best one of the microphysics variable structure, warm rain particle and QPF.

Acknowledgement

Thank You All!

References

Guoqing Ge, Jidong Gao, and Ming Xue, 2013: Impacts of Assimilating Measurements of Different State Variables with a Simulated Supercell Storm and Three-Dimensional Variational Method. *Mon. Wea. Rev.*, 141, 2759–2777.

Tsai, C.-C., S.-C. Yang, and Y.-C. Liou, 2014: Improving Short-Term QPFs with a WRF-LETKF Radar Data assimilation system: OSSEs on Typhoon Morakot (2009). *Tellus A*, **66**, 21804.

Yang, S.-C., E. Kalnay, and T. Miyoshi, 2012: Accelerating the EnKF Spinup for Typhoon Assimilation and Prediction. Weather and Forecasting, 27, 878-897.

Yang, S.-C., M. Corazza, A. Carrassi, E. Kalnay, and T. Miyoshi, 2009: Comparison of local ensemble transform Kalman filter, 3DVAR, and 4DVAR in a quasigeostrophic model. Mon. Wea. Rev., 137, 693-709.

Data assimilation of radar reflectivity volumes in a LETKF scheme

Virginia Poli[1], Thomas Gastaldo[1,2], Chiara Marsigli[1], Pier Paolo Alberoni[1], and Tiziana Paccagnella[1]

[1]*Arpae Emilia-Romagna, HydroMeteoClimate Agency, Viale Silvani 6, 40122 Bologna, Italy*
[2]*University of Bologna, Bologna, Italy*

(Dated: 22 June 2018)

1. Introduction

At Arpae SIMC, the HydroMeteorological Service of Emilia-Romagna Region (Italy), it is operational an ensemble data assimilation system at the convection permitting scale, KENDA, based on a Local Ensemble Transform Kalman Filter (LETKF) scheme. The system has been developed in the Consortium for Small scale Modeling (COSMO) model and, currently, it is used to assimilate only conventional observations. The aim is to improve the accuracy of the analysis to initialize deterministic and ensemble forecast runs. For rapidly evolving systems, such as summer thunderstorms, this requires the assimilation of dense and frequent observations. For this reason in the experimental KENDA set-up, reflectivity volumes from the Italian radar network are assimilated by means of the COSMO Radar Forward Operator.

The quality of the analysis depends on various factors, but the observational error plays a crucial role. It arises from three sources: instrumental error, representativity error and errors derived from observation operator. Since none of these are known and their effects are not distinguishable, the choice of its value is not straightforward. To estimate the error associated to reflectivity observations, a diagnostic based on statistical averages of observation-minus-background and observation-minus-analysis residuals is used. This is performed separately for each radar since the Italian radar network is inhomogeneous both in the acquisition strategy and from an instrumental point of view.

The impact of assimilation of radar volumes is then assessed by means of the verification of forecasted fields.

2. The KENDA system

The Kilometer ENsemble Data Assimilation (KENDA) system (Schraff *et al.*, 2016) implements the LETKF described in Hunt *et al.* (2007). At Arpae it is carried out using an ensemble of 20 members with boundary conditions provided every 3 hours at a 10 km horizontal resolution by the ensemble of the data assimilation system of the Centro Operativo per la Meteorologia (COMet) and a deterministic run which employs hourly boundary conditions provided by a 5 km version of COSMO run at Arpae (COSMO-5M). The inclusion of the deterministic branch is necessary because ensemble mean analyses, that ensue from the mean of a non-Gaussian ensemble, are generally unbalanced (Schraff *et al.*, 2016) and this can lead to inaccuracies in the initialization of deterministic forecasts. KENDA is run operationally with hourly assimilation cycles in which conventional observations (SYNOP, TEMP, AIREP) are assimilated. Furthermore, surface rainfall intensity fields from the radar composite distributed by the National Department of Civil Protection are assimilated by means of a Latent Heat Nudging (LHN) scheme (Jones and Macpherson, 2006). During the assimilation cycles the model derives the innovations as the difference between observations and model first guess. These innovations are taken by the LETKF to produce analyses (Figure 1) that are then used to provide initial conditions to COSMO-2I, the 2.2 km deterministic run initialized twice a day at 00 UTC and 12 UTC and to COSMO-2I EPS, a high resolution ensemble which runs every day at 00 UTC for a 48 hours forecast range.

The KENDA system allows also the assimilation of non-conventional observations. Both reflectivity and radial winds volumes can be assimilated through the use of Efficient Modular VOlume RADar Operator (EMVORADO) expressly designed for the COSMO model. It simulates the radar reflectivity factor and radial velocities processing the COSMO model fields one radar station at a time. Operator characteristics, resolution and the management of no-precipitation information are described in Bick *et al.* (2016). In the present work, only the assimilation of reflectivity volumes is tested (together with conventional data), while radial wind observations are not considered.

3. Reflectivity volumes

Radar reflectivity volumes come from the Italian radar network. For assimilation purposes, input data should be of good quality. For this reason raw reflectivities are pre-processed to remove non meteorological echoes, in particular, to eliminate the clutter signal that would affect the analysis retrieval introducing spurious observations. Due to the fact that the Italian network is not managed by a single agency and volumes from individual radars undergo different pre-processing, it is not possible to define a homogeneous quality criterion. For this reason all data in the volume, that are not rejected from pre-processing step, are supposed to have the same quality and are used into the assimilation cycle.

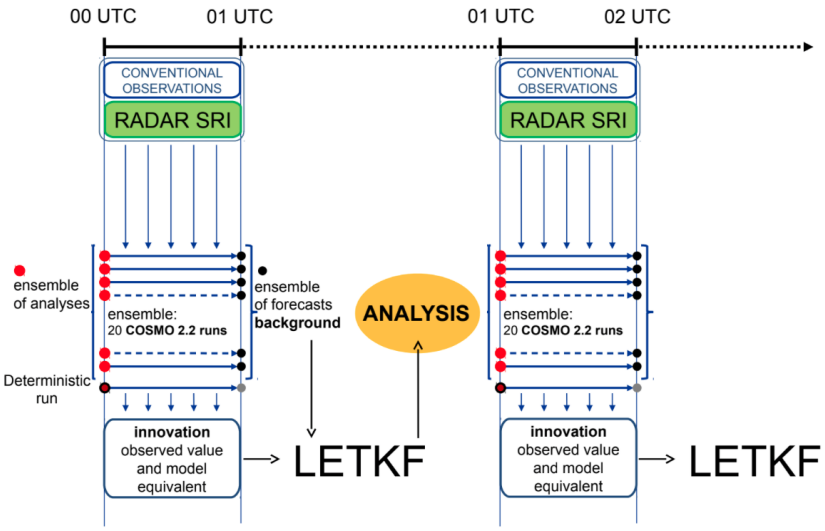


Figure 1: Functional scheme of the KENDA system.

Data have a range resolution of 1 km, while the azimuthal resolution is 1 degree except for San Pietro Capofiume and Gattatico radars where the azimuthal resolution is 0.9 degree. The high temporal and spatial density of observations is precious to estimate the initial state of numerical weather forecast. On the one hand, this allows to gather a lot of information on the real state of the atmosphere, but, on the other hand, this involves an increase in analysis computational cost, in data transfer time and in memory disk occupation. Moreover, a spatial and/or temporal high density violates the assumption made in the most part of assimilation schemes, including LETKF, for which observational errors should be non-correlated. To reduce the total amount of data and to extract essential content of information, the superobbing technique is chosen. In this way, reflectivities over a defined area are combined through a weighted mean into one single observation representative of the desired greater spatial scale. As in Bick *et al.* (2016), the horizontal resolution chosen for the superobbing is equal to 10 km. Furthermore, before performing superobbing, a threshold of 5 dBZ is applied to observed and simulated fields in order to avoid that large innovations (observed minus simulated reflectivities) associated to non-precipitating signals would lead to large analysis increments without physical relevance.

3.1. Observational error

One of the key points of the assimilation of these data is the definition of the observational error. This is influenced by three sources: instrumental error (ε_M), representativity error (ε_R) and errors derived from observation operator (ε_H).

$$\varepsilon_o = \varepsilon_M + \varepsilon_R + \varepsilon_H \tag{3.1}$$

Since none of these are known and their effects are not distinguishable, the choice of its value is not straightforward. As a first value, formerly employed by Bick *et al.* (2016), 10 dBZ has been used, but it is a too large error, in particular for smaller reflectivities. A more advanced method to evaluate the observational error is a diagnostic based on statistical averages of observations-minus-background and observations-minus-analysis residuals, as described in Desroziers *et al.* (2005). This statistics has been applied to different case studies. Due to the complex orography of the considered area, radar are placed at very different altitudes and are inhomogeneous both in the acquisition strategy and from an instrumental point of view. For these reasons the Desroziers statistics has been performed separately for each radar giving observational errors ranging from 3 to 7.7 dBZ.

4. Experiments set-up

Analyses are obtained running KENDA with three different configurations:

1. assimilation of conventional observations + LHN of estimated surface rainfall intensity (*conv*);
2. assimilation of reflectivity volumes with an observational error of 10 dBZ for all the observations (*radar_roe10*);
3. assimilation of reflectivity volumes with an observational error different for each radar (*radar_roevar*).

The biggest difference between the first and the other two configurations is the different use of the radar data. Latent heat nudging is a technique used for the assimilation of precipitations estimated by radar at the surface. It has been used for a long time and its good results in first forecast hours are attested in literature (Stephan *et al.*, 2008). Its strength derives from

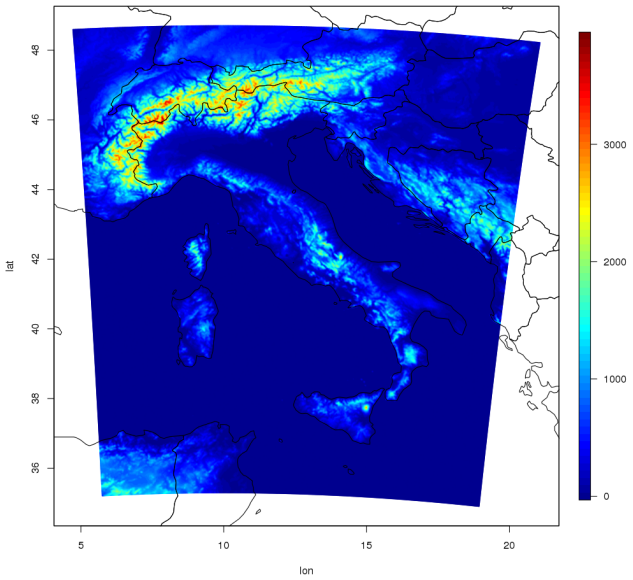


Figure 2: Integration domain and corresponding orography of the COSMO model employed in this study.

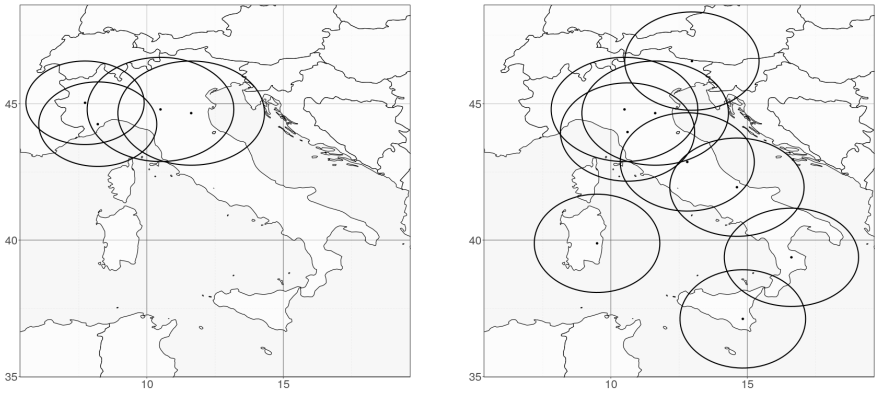


Figure 3: Domain covered by radars at their lowest elevation beam angle in the first case study (on the left) and in the second case study (on the right).

the relationship between observed precipitation and latent heat integrated along the vertical column which allows, during the integration of the model, a continuous and direct adjustment of the temperature and humidity profiles.

While latent heat nudging uses an estimated precipitation field, with all the limitations that result, for example, from the choice of the conversion factors between reflectivity and rain, the assimilation in KENDA using the EMVORADO permits a direct use of the three-dimensional reflectivity data.

To date, there is a limited worldwide experience in the assimilation of reflectivity volumes in a ENKF scheme (Bick *et al.*, 2016; Gastaldo *et al.*, 2018; Dong and Xue, 2008; Dowell *et al.*, 2011; Aksoy *et al.*, 2009), with results attested mainly on single case studies. For this reason, the first goal to be achieved is to, at least, match the results from the benchmark run, *conv*.

The methodology has been tested in two different case studies for which the COSMO model is run at 2.2 km horizontal resolution over the domain presented in Figure 2 and employing 65 terrain-following hybrid layers. In the first experiment, starting the 3th and ending the 6th February 2017, only four radars from the Northern Italy has been assimilated, while for the second case study (16th and 17th January 2018) almost the whole Italian network has been used (Figure 3).

5. Verification

To evaluate the impact of the assimilation of reflectivity volumes and the quality of the obtained analyses, forecasts starting from the KENDA deterministic analyses are performed. For the first case study the forecasts are initialized every three hours, while for the second case they are initialized every hour.

The performance of each experiment is assessed by means of the Fractions Skill Score (FSS) and the SAL technique.

5.1. FSS

The Fractions Skill Score is a spatial verification measure which compares the forecast and observed fractional coverage of grid-box events in spatial windows of increasing size (Roberts and Lean, 2008). It can be defined as

$$FSS = 1 - \frac{\frac{1}{N}\sum_{N}(P_f - P_o)^2}{\frac{1}{N}(\sum_{N} P_f^2 + \sum_{N} P_o^2)} \tag{5.1}$$

where P_f is the forecast fraction, P_o the observed fraction and N is the number of spatial windows in the domain. It ranges from 0 (complete mismatch) to 1 (perfect match).

The FSS was applied to the hourly precipitation fields by combining all the forecasts at the same time to understand how the impact of the assimilated observations varies as forecast time increases. Observations were accumulated rainfall fields from the Italian radar composite adjusted by rain-gauges. Spatial windows were fixed at 0.2 degrees. Events were defined by different precipitation thresholds.

Results from the two case studies are shown in Figure 4. The experiments are identified by line colors, while thresholds can be distinguished by line types. The sample of the second case study is bigger, even if the case study was shorter, as the direct consequence of the fact that for January 2018 forecasts were initialized every hour.

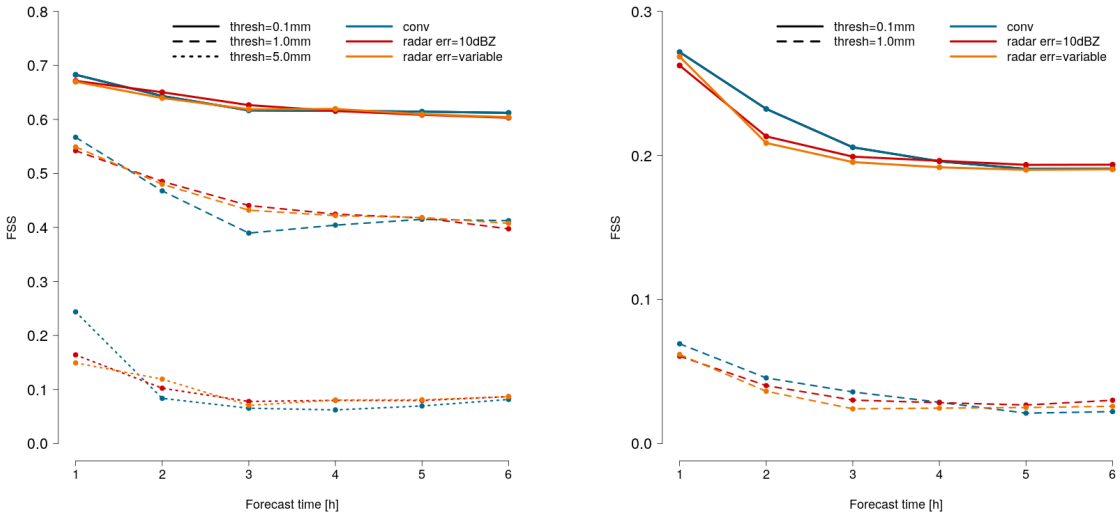


Figure 4: FSS for February 2017 case study (on the left) and for January 2018 case study (on the right).

In the first case the *conv* run outperforms in the first forecast step the other two runs for all the thresholds. This can be probably due to the LHN effect. It is able to capture the dynamical structure and the right rainfall amount of the storm (Leuenberger and Rossa, 2004; Leuenberger and Rossa, 2007), but its efficacy degrades rapidly with forecast time. For forecast times between 2 and 5 hours, and for the two higher thresholds, runs initialized with the analyses coming from assimilation of radar volumes have a good performance. For the threshold equal to 0.1 mm this trend is less clear. Differences between *radar_roe10* and *radar_roevar* are quite small.

For the January 2018 case study, values of FSS are very low. This comes from the fact that the precipitating events occurred in those two days were not well forecasted in any of the experiments. The score shows a better performance of the *conv* for the first three hours. In this case, the run *radar_roevar* has a better result for the first forecast hour respect to *radar_roe10*, in particular for the lower threshold.

5.2. SAL

The SAL metrics (Wernli *et al.*, 2008) is an object based verification score. It detects individual objects in the accumulated precipitation fields by considering continuous areas of grid points exceeding a selected threshold. Comparing objects from observed and forecast fields, SAL provides information about the structure *S*, the amplitude *A* and the location *L* errors of quantitative precipitation forecast. A perfect match between forecast and observations would lead to all the components equal to 0; the more values differ from 0, the greater the disagreement between model and observations. More in detail, a too

sharp/flat (broad/small) structure of forecast precipitation compared to observations is associated to positive (negative) values of *S*; an overestimation (underestimation) of average rainfall over the domain is associated to positive (negative) values of *A*; a misplacement of precipitation nuclei leads to positive values of *L*. *L* can range between 0 and 2, while *S* and *A* between -2 and 2.

In the scatterplot each scatter point is colored by its location component. The gray box spans the middle two quartiles of structure (x axis) and amplitude (y axis) components. Dotted line denotes the median structure and amplitude component scores.

SAL is performed over the limited area shown in 5.

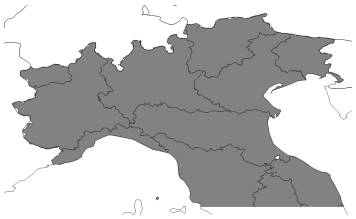


Figure 5: Domain used in SAL computation.

For the February 2017 case study, SAL scores of 3hourly accumulated precipitation, valid at 3 forecast hours, are shown in Figure 6. The chosen threshold is of 1 mm. The *radar_roe10* experiment gives slightly better results in structure and localization components respect to *conv*, while *radar_roevar* shows a little improvement for localization and amplitude components compared to *radar_roe10*.

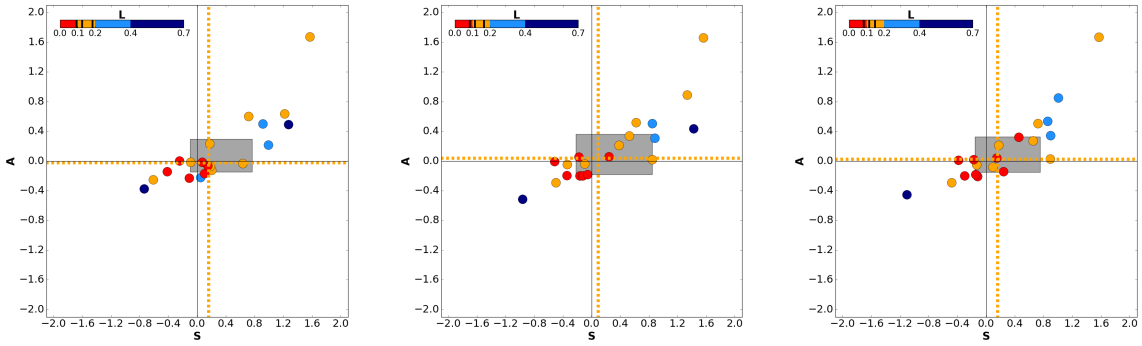


Figure 6: SAL for February 2017 case study for the different experiments: conv on the left, radar_roe10 in the middle and radar_roevar on the right.

For January 2018 case study SAL score confirms the poor results already displayed by the FSS in the previous section, for this reason the scatterplots are not shown.

6. Conclusions and future work

Assimilation of reflectivity volumes has a great potential due to the high spatial and temporal density of this type of observations. The KENDA system has been implemented and run at Arpae with the aim of improving forecasts assimilating radar volumes instead of assimilating conventional observations and surface radar rainfall, thereby taking advantage of the three dimensional structure of radar data.

Even if the assimilation for the first case study is performed only over northern Italy an improvement of forecast is recognized from the second hour forecast, while for the first hour forecast is still outperformed by LHN. The results are different for the two events analyzed. In fact for the second case, although almost all the radars of the Italian network were used, there is no noticeable change improving forecasts.

The methodology implemented has given encouraging results, although some problems should be considered in more detail.

As a first step, the verification should be carried out over longer periods of time, including different types of events. Then different tunings of model must be tested to understand if assimilation of reflectivity volumes can have a higher impact. The definition of the ensemble is also part of this theme. Its size is limited to 20 members which may not be representative of all the possible weather scenarios. For this reason the spread of the ensemble should be increased both by using more members and different inflation techniques.

On observations side, an improvement of the observational error estimation is needed, making it dependent on height range, radar station and flow dependent. Moreover both the correlation between neighboring observations should be exploited and the quality of data should be homogeneously defined and used in the assimilation cycles.

Acknowledgement

Authors thank the National Department of Civil Protection and Roberto Cremonini for providing radar volumes.

References

Aksoy, A., Dowell, D. C., and Snyder, C. (2009). A multicase comparative assessment of the ensemble kalman filter for assimilation of radar observations. part i: Storm-scale analyses. *Monthly Weather Review*, **137**(6), 1805–1824.

Bick, T., Simmer, C., Tromel, S., Wapler, K., Hendricks Franssen, H.-J., Stephan, K., Blahak, U., Schraff, C., Reich, H., Zeng, Y., and Potthast, R. (2016). Assimilation of 3d radar reflectivities with an ensemble kalman filter on the convective scale. *Quarterly Journal of the Royal Meteorological Society*, **142**(696), 1490–1504.

Desroziers, G., Berre, L., Chapnik, B., and Poli, P. (2005). Diagnosis of observation, background and analysis-error statistics in observation space. *Quarterly Journal of the Royal Meteorological Society*, **131**(613), 3385–3396.

Dong, J. and Xue, M. (2008). Assimilation of radial velocity and reflectivity data from coastal wsrâ88d radars using an ensemble kalman filter for the analysis and forecast of landfalling hurricane ike. *Quarterly Journal of the Royal Meteorological Society*, **139**(671), 467–487.

Dowell, D. C., Wicker, L. J., and Snyder, C. (2011). Ensemble kalman filter assimilation of radar observations of the 8 may 2003 oklahoma city supercell: Influences of reflectivity observations on storm-scale analyses. *Monthly Weather Review*, **139**(1), 272–294.

Gastaldo, T., Poli, V., Marsigli, C., Alberoni, P. P., and Paccagnella, T. (2018). Data assimilation of radar reflectivity volumes in a letkf scheme. *Nonlinear Processes in Geophysics Discussions (in review)*, **2018**, 1–21.

Hunt, B. R., Kostelich, E. J., and Szunyogh, I. (2007). Efficient data assimilation for spatiotemporal chaos: A local ensemble transform kalman filter. *Physica D: Nonlinear Phenomena*, **230**(1), 112 – 126. Data Assimilation.

Jones, C. D. and Macpherson, B. (2006). A latent heat nudging scheme for the assimilation of precipitation data into an operational mesoscale model. *Meteorological Applications*, **4**(3), 269–277.

Leuenberger, D. and Rossa, A. (2004). Revisiting the latent heat nudging scheme for the rainfall assimilation in convective system. In *Proc. of 3^{th} European Radar Conference on Radar Meteorology and Hydrology (ERAD)*, pages 162–167, Visby, Gotland, Sweden, 6–10 September 2004.

Leuenberger, D. and Rossa, A. (2007). Revisiting the latent heat nudging scheme for the rainfall assimilation of a simulated convective storm. *Meteorol. Atmos. Phys.*, **98**(3–4), 195–215.

Roberts, N. M. and Lean, H. W. (2008). Scale-selective verification of rainfall accumulations from high-resolution forecasts of convective events. *Monthly Weather Review*, **136**(1), 78–97.

Schraff, C., Reich, H., Rhodin, A., Schomburg, A., Stephan, K., Perianez, A., and Potthast, R. (2016). Kilometre-scale ensemble data assimilation for the cosmo model (kenda). *Quarterly Journal of the Royal Meteorological Society*, **142**(696), 1453–1472.

Stephan, K., Klink, S., and Schraff, C. (2008). Assimilation of radar-derived rain rates into the convective-scale model cosmo-de at dwd. *Quarterly Journal of the Royal Meteorological Society*, **134**(634), 1315–1326.

Wernli, H., Paulat, M., Hagen, M., and Frei, C. (2008). Salâa novel quality measure for the verification of quantitative precipitation forecasts. *Monthly Weather Review*, **136**(11), 4470–4487.

Severe weather and hail detection using the X band weather radar Tuscany network

Andrea Antonini[1] , Samantha Melani[1,2], Alberto Ortolani[1,2], Andrea Telleschi[3], Andrea Lombardi[3], Irene Giannini[3], Bernardo Gozzini[1]

[1]*LaMMA Consortium, Via Moadonna Del Piano 10, 50019 Sesto Fiorentino (FI), Italy*
[2]*CNR-IBIMET, Via Giovanni Caproni 8, 50145 Firenze, Italy*
[3]*ELDES s.r.l, Via di Porto 2/B, 50018 Scandicci (Firenze), Italy*

(Dated: 19 June 2018)

1 Introduction

In the last years, an occurrence increment of the weather patterns generating severe thunderstorms was observed for the Mediterranean area. This aspect has been particularly relevant in Tuscany (central Italy) where several heavy rains events leaded to river floods and landslides, especially in coastal areas. Indeed, the synergy of high sea surface temperatures and moist air-masses combined with deep troughs can produce very unstable environments that are favourable to the occurrence of such events.

For a better characterization of these phenomena and for limiting the related risks, a regional X-band weather radar network has been implemented in the Tuscany coastal areas. Three single-polarization weather radars, located in Livorno, Castiglione della Pescaia and Cima di Monte (Elba island), compose the regional network.

Firstly, this work describes the performances of such a network in the monitoring of some precipitation events, particularly intense. The radar composite has been compared with some ancillary data as satellites, raingauges, lightning observations and other radar systems operating in different frequencies (C and S band).

Severe weather systems are sometimes characterized by the presence of hail. Because of its spatial and temporal variability, an accurate detection of hail from ground measurements is very difficult, but an operational hail detection system could be useful for several objectives, from supporting risk management at urban scales to the assessment of damages in agriculture.

Few methods exist for automatic hail detection using single polarization radars, mainly based on the analysis of the vertical structure of reflectivity. Some methods use ancillary data, as the freezing level and the ground temperature, for a better characterization of the microphysics of the maximum vertical reflectivity cell, and consequently the presence of hail.

Two different algorithms, based on the Waldvogel approach and on the Vertically-Integrated Liquid Density (VIL-Density) product, have been tested and compared to assess the capability of such radar network in hail detection with the aim of developing a POH (Probability-of-Hail) index.

Some hail case studies, identified by the Tuscany meteorological office reports, have been analysed and preliminary results concerning the performances of these methods are shown.

2 Radar systems and methodo description

The X-band radar system used for the Tuscany network implementation is the WR10X produced by the ELDES s.r.l company (ELDES, 2018). Three systems constitute the network deployed along the coastal area (i.e., in Livorno, Elba island and Castiglione della Pescaia). At the maximum range of 108 km and with a range resolution of 450m, polar volumes scans are acquired every 15 minutes at ten elevations: from 0.5° to 5.0° at 0.5° steps. The radar systems are single polarization and non Doppler. Therefore, as well as a signal processing chain and 3D geolocation procedures, suitable filters for sea and land clutter removal have been implemented, as described in (Antonini, et al., 2017). A composite is available for integrating all the information in a single product for the observation of precipitation systems. A 2D composite is created assigning the highest reflectivity value in any overlapping points of the selected area. The maximum reflectivity values allow an immediate evaluation for each pixel of the intensity of the event, also used to activate early warning and preventive procedures.

The available products used for monitoring real time phenomena are the Horizontal and Vertical Maximum Intensity (HVMI), VMI, PPI, and the Range Height Indicator (RHI). These products allow a continuous monitoring of the 3D structure of the atmosphere for weather observation and nowcasting purposes.

During the intense weather phenomena the radar instruments can help the assessment of the microphysical structure of the meteorological eventss. The radars scan strategy is organized to operationally perform a RHI scan pointing towards the direction where the nucleus of higher reflectivity values is present. The RHI gives an immediate view of the vertical structure of the precipitation system. Heavy rain systems are very often characterized by an inner nucleus of reflectivity values higher than 45-50 dBZ, surrounded by lower values and generally decreasing in function of height. The localization and identification of these very high reflectivity nucleuses plays a crucial role for the processes of rainfall rate calibration,

mitigation of overestimation errors and hail detection (Smith, 1998). An extremely important source of error for heavy rainfall events is the significant influence of the elevation angle that cause an enhancement of reflectivity when sampling in the brightband. Additional complexity is introduced by the presence of hail.

In deeply convective thunderstorms the vertical development of the clouds consists of droplets (both liquid, water and ice crystals) distributed from the surface level to the top levels, up to 10 or more kilometers. Three main layers can be identified in the cloud vertical structure: the lower is a warm layer with temperatures above 0°C, where the droplets are in the liquid phase; an intermediate level is the supercooled, mixed, above the thermal zero (freezing level) at a temperature lower than 0°C where droplets are both in liquid and ice phase and finally the higher level is the cumulonimbus anvil, at a temperature lower than -40°C, with only ice crystal (Agency Suppression Hail).

Sometimes, in these conditions of strong vertical motions, liquid droplets can be pushed to heights with temperatures below 0°C and they come to thermodynamically instable supercooled condition. The hail formation processes are not completely understood, but some microphysical conditions are necessary for the hail precipitation formation: supercooled liquid water content in the cloud; hail embryos (Knight & Knight, 1970): small frozen raindrops growing by the effects of the surrounding thermodynamic instability of particles; and finally strong updraft motions.

The identification of the presence of hail is much simpler and more reliable using doppler and polarimetric radars and some algorithms exist allowing to define a probability that the storm is characterized by hail (POH – Probability Of Hail).

In the hailstorm some important features are present that have been used for the implementation of hail detection algorithms. The most important indicators are the presence of a reflectivity core of 50 dBZ or higher somewhere between 5 and 12 km altitude far above the freezing level, and the presence of radar echotops higher than 8 km.

Several algorithms exist for the detection of hail using single polarization weather radars, and some studies have been made for their comparison and their skill characterization (Holleman , 2001) also focusing on X-band systems (Capozzi, Picciotti, Mazzarella, Budillon, & Marzano, 2016).

In hail detection algorithms applied to single-polarization radars an analysis of the Vertical Profiles of Reflectivity (VPR) is implied, over the site of POH estimation. The estimation of the correct height relative to the measured reflectivity is strong affected by error due to signal propagation in the atmosphere, resulting in uncertainties in hail (Delobbe & Holleman, 2006). Fortunately the large number of elevations (10) collected at every timestamp by the X-band Tuscany radar network, very often allows the estimation of the VPR for hail detection purposes.

VIL is a nonlinear function of reflectivity and converts weather radar reflectivity data into estimates of equivalent liquid water content based on theoretical studies of drop size distributions and empirical studies of reflectivity factor and liquid water content (Greene & Clark, 1972). VIL is a radar-derived estimate of liquid water in the vertical atmospheric column. VIL density (VILD) is the VIL divided by the echo top height, and can be used to identify storms with high reflectivity values relative to their heights, that are very often characterized by hail (Amburn & Wolf, 1997). The increment of VILD is strongly correlated with the increment of hailstone size and quantity. Given the VILD in g m^{-3}, the probability of hail occurrence is defined as a cubic function. In this work we will adopt the coefficient derived in (Capozzi, Picciotti, Mazzarella, Budillon, & Marzano, 2016), resulting from the analysis of VILD measured for about fifty strong storms in the Gulf of Naples from 2012 to 2015:

$$POH(VILD) = 0.009344\,VILD^3 - 0.1106\,VILD^2 + 0.5057\,VILD + 0.05351 \qquad (2.1)$$

Most of methods used for the detection of severe weather are based on the maps of VMI, where for each pixel the maximum reflectivity values on the vertical column are represented. Reflectivity values exceeding 50dBZ very often indicate heavy rainfall (Auer Jr., 1994). A first indication of the hail presence is given by the vertical location of the higher reflectivity values. To permit the hail formation process the maximum reflectivity must be above the freezing level. Moreover the Waldvogel method for the detection of hail uses the maximum altitude at which a reflectivity of 45 dBZ is found (HZ45) in relation to the height of the freezing level (H_0) (Waldvogel, Federer, & Grimm, 1979). Given ΔH as the difference between HZ45 and H_0 (in km):

$$POH(\Delta H) = 0.319 + 0.133\,\Delta H \qquad (2.2)$$

The principal source of data for this study is an archive of volume scan reflectivity observations from the X-band Tuscany weather radars, but the analysis has been made also comparing those observations with all the other available data sources: data from other radar systems operating in different frequencies (C- and S-band), a dense raingauge network of more than 400 point measurement over the region, the lightnings occurrence information, satellite imagery. Finally the WRF NWP model is used to estimate the freezing level and to compute the vertical extension of the systems. Some severe weather and hailstorm cases will be presented and discussed in the next sections.

3 Case studies analysis

The Tuscany regional network is operational since 2012, when the first radar has been installed. During these years several precipitation events have been observed. A selection of recent heavy rain and hail events detected by the weather radars is presented and discussed.

3.1 Versilia strong rainfall event (2016-11-18,19)

This weather event originated from a perturbation on the Algerian and Tunisian coasts that activates a flow of mild and humid air over Tuscany. From the afternoon of 18th November and especially in the evening abundant precipitation occurred in the northern areas, in Lunigiana and Garfagnana. An intense perturbation, connected to a vast Atlantic trough, affected the central Mediterranean area. Heavy rains occurred between night and next morning. Maximum rainfall punctual values up to 200 mm (150-175 mm in 6 hours) in Lucca and 100 mm on the Apennines of Pistoia and Massa, where registered. This intense rainfall amount caused a flood wave of the Versilia River fortunately resolved without damage and without flooding. During the night the precipitation system propagates southerly.

Figure 1 presents a series of images collected from different weather radar systems (C, S, and X band) observing the precipitation phenomena.

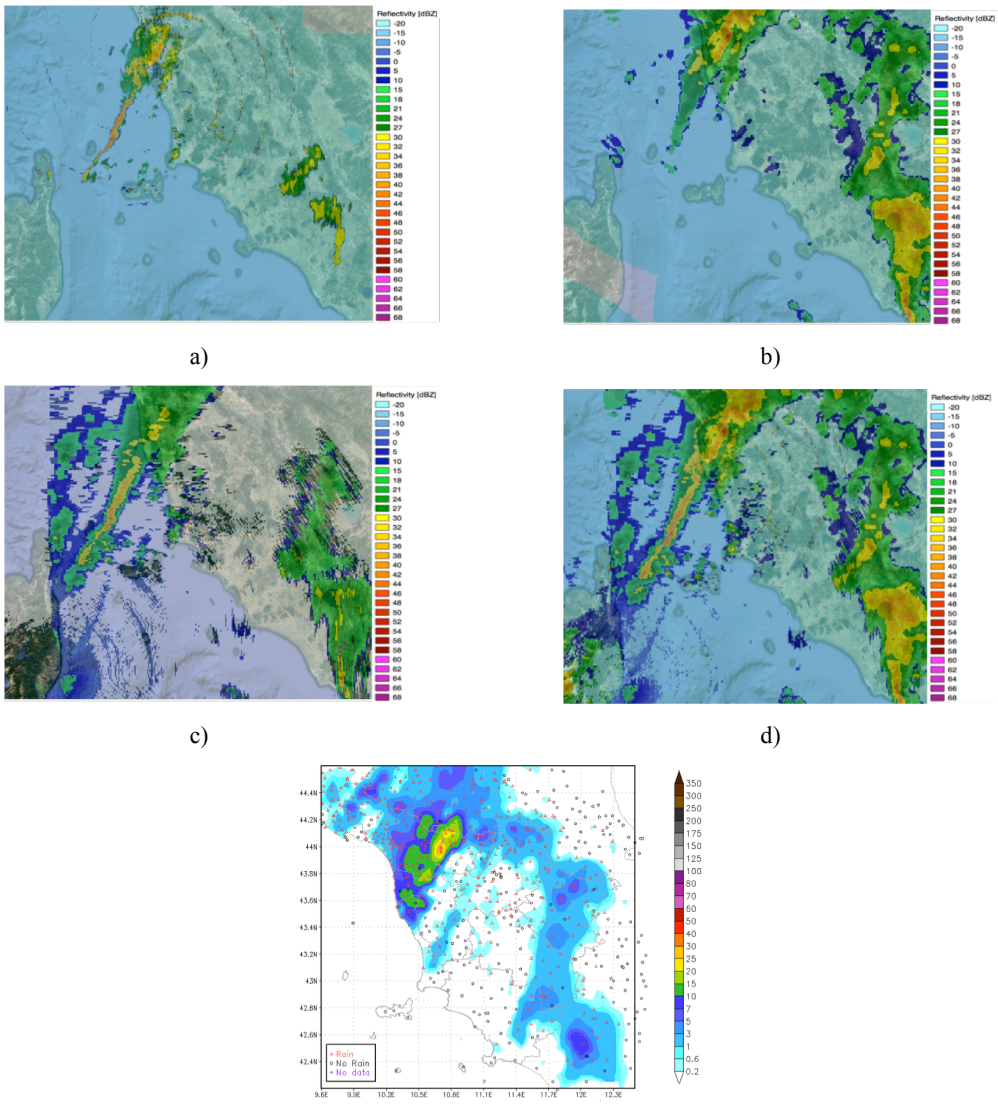
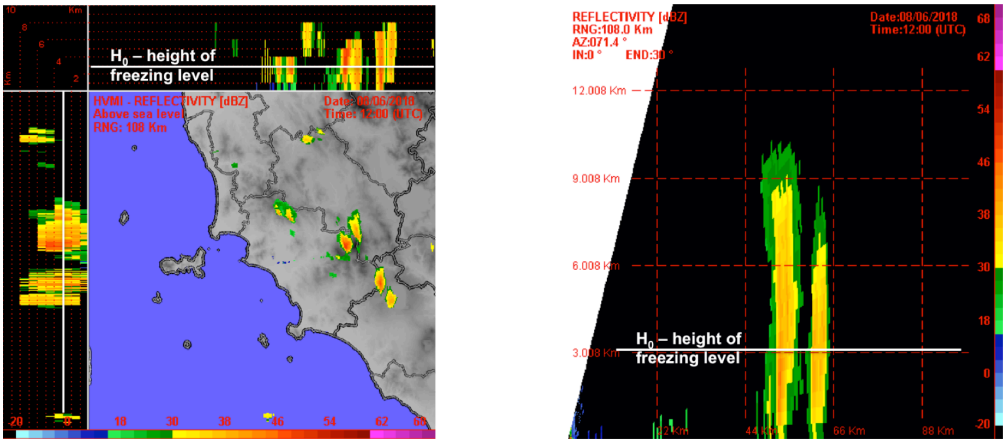


Figure 1: Radar observations of 19th November 2016. Time: 5:30 UTC. X-band Tuscany regional composite (a), C-band national composite (b), S-band Aleria radar systems (c), and all radar (X-C-S band) composite (d), interpolated raingauges rainfall map from 5:00 to 6:00 UTC (e)

As compared with raingauges observations the event is well detected by all the radar systems, also in the qualitative assessment of the intensity. The longitudinal section of the main precipitation system (the one to the north) is observed with high correlation, also over sea. Higher accordance is given by X and C band systems, with reflectivity values up to 50 dBZ. The longitudinal cells with very low intensity are not detected by C band national network, but are present in the X-band and S-band measurements. Finally the reflectivity intensity of the southern system seems quite high in C-band radars. The reflectivity fields resulting in the X-band mosaic are very clear of noise, and in some areas the precipitation is not detected. C and S band systems instead seem to overestimate the precipitation resulting in a minor detail, due to the lower resolution, as compared to X-band.

3.2 Arcidosso hail case study (2018-06-08)

On 8th June 2018, in the area of Arcidosso, a little municipality located in the weastern valley of the Amiata Mountain a violent storm has caused damage and several flooding and teams of firefighters had to act for some calls from some citizens. A strong hailstorm also fell, causing damage to gardens and crops. The most probable occurrence time of the hailstorm is around 12:00 UTC. The storm propagated in the southwest direction involving large areas. The Castiglione weather radar is located very near and has allowed observing and monitoring the evolution of the event. The images of the storm are presented in Figure 2, where the HVMI and the RHI products are shown.



a) b)

Figure 2: Radar observations of the hailstorm occurred in Tuscany on 8th june 2018, time 12:00 UTC. HVMI (a) and RHI (b) products are depicted

The HVMI shows the different precipitation cells, and the one with the greatest intensity is easily identifiable. RHI image is a section of the storm. Unfortunately this section is not exactly spatially coincident with the maximum values of reflectivity, but the vertical structure of the storm is well reconstructed, showing a very strong vertical development. During the event the freezing level (H_0) was quit height, as often happens during the summer season. No radiosoundings are located near the event, and for a better assessment of the microphysical structure of the cumulonimbus the freezing level value has been obtained from the WRF model output, providing the value H_0=3200m at the time of the storm occurrence.

The HVMI image shows the conical shape of the reconstructed scenario. This is due to the scan geometry. The maximum operational elevation is 5°, and is not sufficient to cover all the vertical extension of the storm. As the storm is located at about 45km from the radar site with an elevation angle of 5° the maximum height of a measured reflectivity cell (echotop) is about 5000m. This is about a half of the real storm echotop that is over 9000m, as suggested by the RHI image.

The estimation of the ΔH (Figure 3.b), with a threshold of 1.4km, as suggested in (Waldvogel, Federer, & Grimm, 1979), perfectly localizes the hailstorm. The extracted value is ΔH≅1.9km, which provides a POH(ΔH) ≅ 60%. The VILD (Figure 3.c) observed in a later moment (14:00 UTC) of the time series of the event, is about 2.4 g/m^3. The related POH(VILD) is 75%. The underestimation of the POH(ΔH) is due to the underestimation of the HZ45. By extrapolating the correct value from the RHI or the VPR, a plausible value of the HZ45 seems to be around 6500m, and the corresponding POH(ΔH) ≅ 75%.

The VPR also suggests a probable underestimation of the VILD in the related timestamp, due to an incomplete sampling of the vertical structure of the higher reflectivity nucleus.

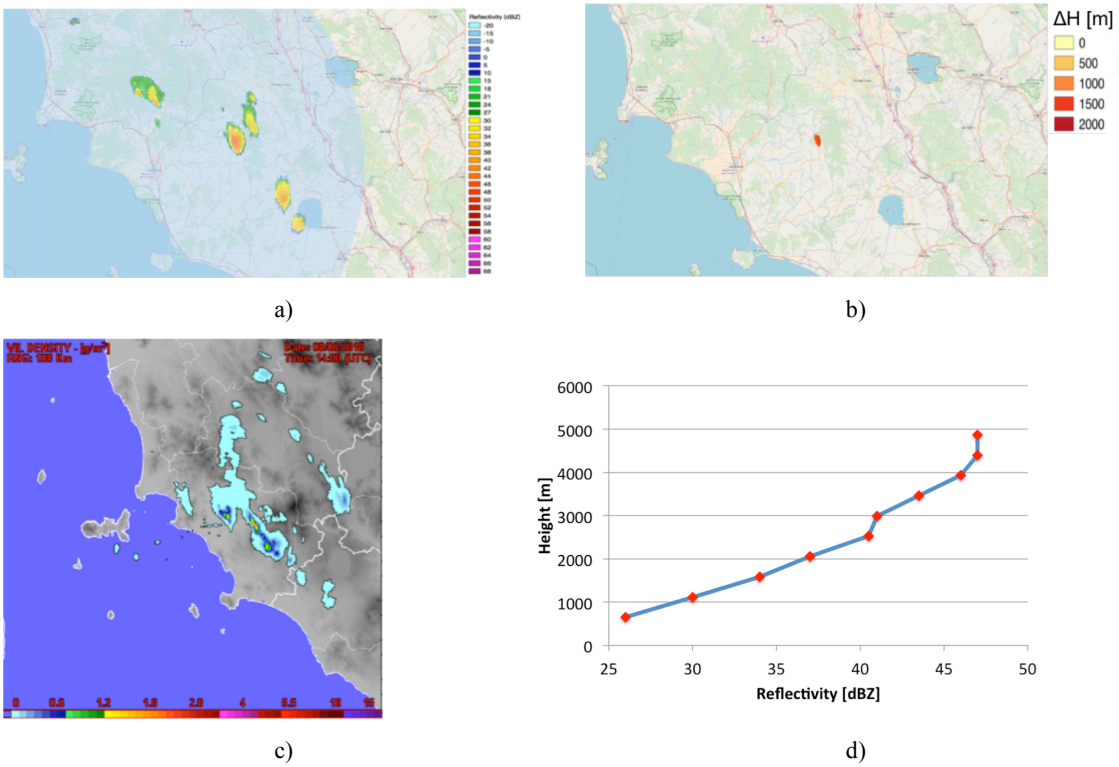


Figure 3: Radar observations of the hailstorm occurred in Tuscany on 8th june 2018. Network composite (a) Estimation of the ΔH (b) VILD estimation (c) Vertical Profile of Reflectivity

Finally it should be noted that it is not very clear the impact of high values of freezing level, combined with the liquid water in determining the hailstorms.

3.3 San Marcello Pistoiese hailstorm (2015-06-23)

This weather event is characterized by a transit of a fast perturbed system preceded by a mild and humid flow in the lower layers of the atmosphere, and several thunderstorms during the night with hailstorms and strong winds. The orographic triggering of convection and precipitation plays a crucial role.

Also in this case there is a strong vertical development of the precipitation system. Due to the distance from the observing radar systems the event is well reconstructed from reflectivity volumes and cross sectional observations (see Figure 4).

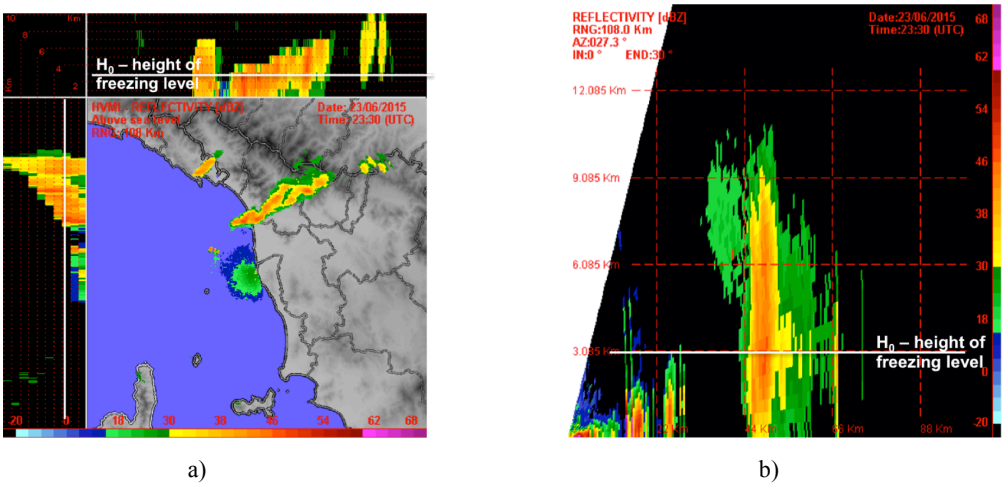
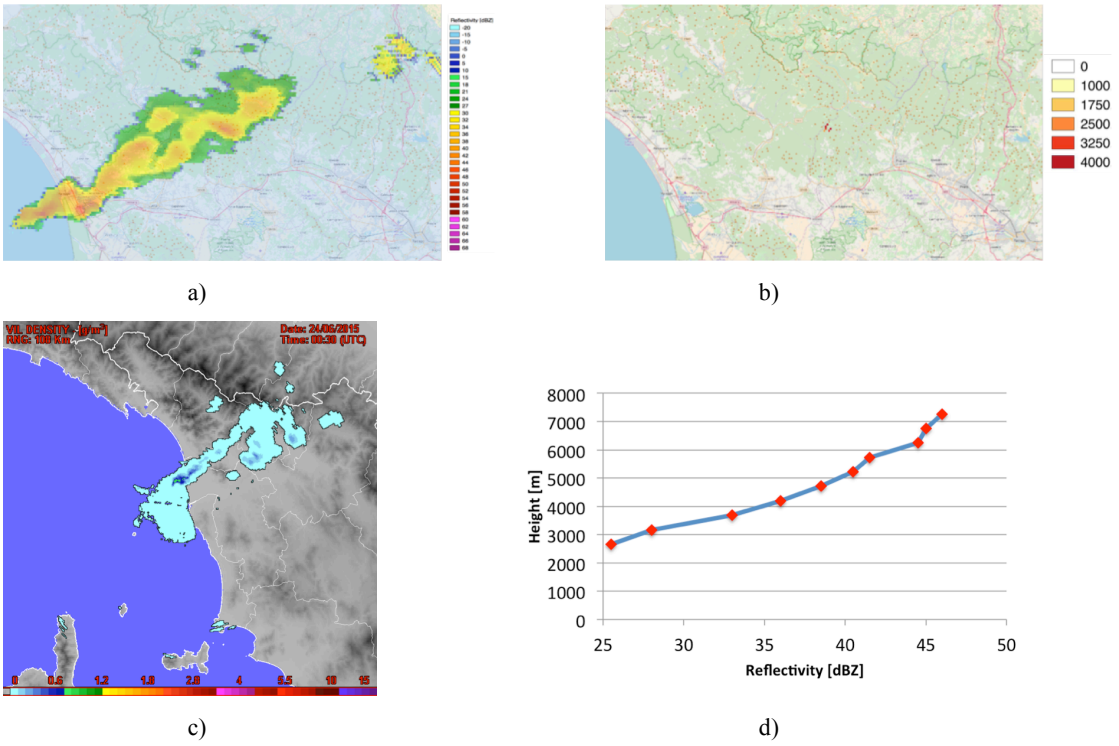


Figure 4: Radar observations of the hailstorm occurred in Tuscany on 23rd june 2015. HVMI (a) and RHI (b) products are depicted

The freezing level estimated from the WRF model is H_0=3000m. The cells imputed for hail occurence are very localized. The ΔH values are up to 4000m, with a POH(ΔH) ≅ 80%. In this case the VILD is about 1.2 g/m^3 and the POH(VILD) is 50%.



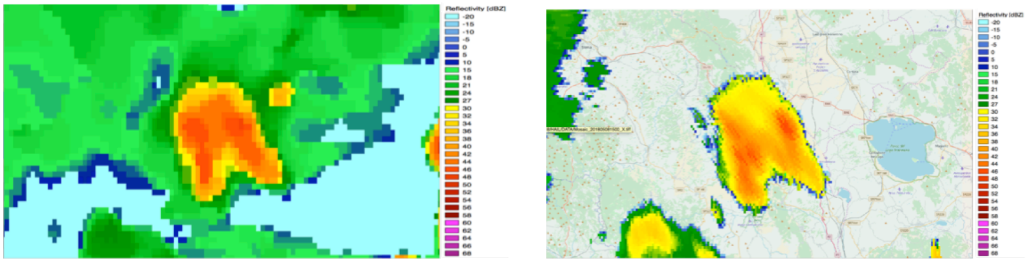
a) b) c) d)

Figure 5: Radar observations of the hailstorm occurred in Tuscany on 23rd june 2015. Network composite (a) Estimation of the ΔH (b) VILD estimation (c) Vertical Profile of Reflectivity

Also for this case the same considerations apply, as the reflectivity profile is strictly increasing up to 8000m and the height of the tower seems to be above 11km.

3.4 Torrita di Siena flood case sudy (2018-05-08)

Due to a structured weather system some intense and very localized precipitation phenomena affected the internal areas of the region, between Florence, Siena and more south. The precipitation caused several damages as torrents overflows flooding of roads, and block of the railways. The comparison of C and X-band radars (Figure 6) highlights some matching and some differences. A perfect accordance exists in the shape of the main precipitation cell.



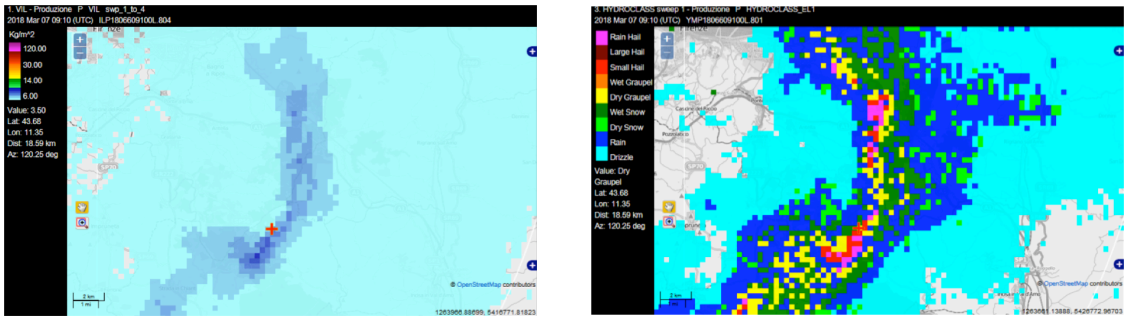
a) b)

Figure 6: Radar observations of an intense event occurred in Tuscany on 8th May 2018. Time 15:00 UTC. C-band national mosaic (a) and X-band Tuscany mosaic (b) are depicted

In this main cell C band radars images provide almost exclusively values around 50dBZ. However, the weather reports and the raingauges network observations show that the core of the system with greater intensity was rather localized. X-band radar observations provide values more differentiated within the cell, due to better spatial resolution, and the different intensities of precipitation are well identified. On the other hand the X band measurements lose the widespread rainfall fields, associated to lower reflectivity values (around 15dBZ), and corresponding light precipitation rates. This weak precipitation is not actually present in all the areas indicated in the C band composite, confirming a tendency to enlarge the patterns of light precipitation fields.

3.5 Impruneta hailstorm (2018-03-07)

A deep depression on the British islands trigger humid and unstable currents towards Europe and the Mediterranean. A frontal system transits in Italy with a mild south-western flow in the lower layers combined with the entrance of air gradually colder at high altitude. In this framework high instability is associated to the weather system, with some strong convection activities associated to intense hailstorms. Figure 7 shows the observations of the hailstorm using a X-band dual polarized weather radar.



a) b)

Figure 7:X-band polarimetric radar observations of a hailstorm occurred near Florence (Impruneta) on 7th March 2018. Time 9:10 UTC. VILD (a) and polarimetric observation of the precipitation type (b)

The polarimetric reconstruction of the precipitation type (Figure 7.b) localizes the area of hail occurrence, and is used for the visual validation of the VILD-based identification of hail. In this case the VILD is very high (values from 3.5 to 5 g/m^3) and the corresponding POH(VILD) spans from 70% to 85%. For this event, although occurred in a winter season the freezing level as obtained from the WF model is around H_0=1600 m.

4 Conclusions and remarks

This work describes some cases of very intense precipitation occurred in Tuscany as observed from the X band radar network. The usefulness of these systems for operational meteorological vigilance is corroborated from the results shown. Two algorithms for detecting hail in single polarization radar have been implemented and compared, one based on the cloud liquid water content, with respect to the echotop, and the other based on the vertical structure of the cloud tower, and in the height difference between high nucleus and freezing level. Both algorithms provide useful information for an early assessment of hail precipitation occurrence, with some related uncertainties.

To further explore the potentialities of such algorithms some further case studies, in a systematic analysis should be studied, by introducing a larger number of recorded hail cases. A big contribution could be given by using hail occurrence data as obtained by media communication, for a better space and time localization of phenomena.

As in some cases the radar volumes cannot cover all the 3D extension of the systems, the scan strategies should be modified to increment the possibility of observing the true vertical extension of the deep convection, elevations up to 10° should be included in the scan.

Moreover it is evident, also from literature that the probability of hail depends strongly on the height of the freezing level. When the freezing level is at lower height the probability of observing hail increases. However, many hail events occur in summer when the freezing level is typically above 2500 m. Some studies about the zonal climatology of such events should be conducted for a better assessment.

References

Agency Suppression Hail. (kein Datum). Von Agency Suppression Hail: http://www.weathermod-bg.eu/pages/obr_en.php abgerufen

Amburn, S., & Wolf, P. (1997). VIL Density as a Hail Indicator. *Weather And Forecasting* (12), 473-478.
Antonini, A., Melani, S., Corongiu, M., Romanelli, S., Mazza, A., Ortolani, A., et al. (2017). On the implementation of a regional X-band weather radar network. *Atmosphere* .
Auer Jr., A. (1994). Hail Recognition through the Combined Use of Radar Reflectivity and Cloud-Top Temperatures. *Monthly Weather Review* , 2218-2221.
Capozzi, V., Picciotti, E., Mazzarella, V., Budillon, G., & Marzano, F. (2016). Hail storm hazard in urban areas: identification and probability of occurrence by using a single-polarization X-band weather radar. *Hydrology and earth System Science Discussions* .
Delobbe, L., & Holleman, I. (2006). Uncertainties in radar echo top heights used for hail detection. *Journal Of Meteorological Applications* , 361-374.
Greene, D., & Clark, R. (1972). Vertically Integrated Liquid Water - A new analysis tool. *Monthly Weather Review* , 548-552.
Holleman , I. (2001). *Hail detection using single polarization radar.* KNMI.
Knight, C., & Knight, N. (1970). Hailstone Embryos. *Journal Of Atmospheric Science* , 659-666.
Smith, M. L. (1998). Rainfall Estimation by the WSR-88D for Heavy Rainfall Events. *Weather and Forecasting* (13), 416-436.
Waldvogel, A., Federer, B., & Grimm, P. (1979). Criteria for the Detection of Hail Cells. *Journal Of Applied Meteorology* , 1521-1525.

Multisource data verification of a weather radar surface precipitation type product

E. Casellas[1,2], J. Bech[2], R. Veciana[1], N. Pineda[1], T. Rigo[1], J. Moré[1], S. González[3], A. Paci[4]
[1]*Meteorological Service of Catalonia, Barcelona, Spain*
[2]*Department of Applied Physics – Meteorology, University of Barcelona, Spain*
[3]*Agencia Estatal de Meteorología – DT Catalunya, Barcelona, Spain*
[4]*CNRM/GMEI Météo-France, Toulouse, France*

(Dated: 22 June 2018)

1 Introduction

Forecasting and surveillance of snowfall events at low altitudes is critical in regions where these phenomena are not common, like in Southern Europe and the Mediterranean coastal regions. They can cause major problems of road safety and transport and damage communications infrastructures that are not prepared for snow conditions. Therefore, it is important to know the surface precipitation type to provide valuable information to decision-makers in surveillance tasks.

There are several meteorological instruments that offer a classification of hydrometeors, such as present weather sensors and disdrometers. A dense network of these kind of instruments would be ideal to monitor precisely snowfall events. However, if a country scale region must be surveilled, this becomes an expensive project, so different approaches to this problem must be considered. Dual-polarization radars can discern between different precipitation types like rain, snow, sleet and drizzle. The classification of these kind of radars is not necessarily the same as it would be in the surface, still it is an appropriate solution for large scale surveillance. One alternative approach, when dual-polarization radars are not available, is the combination of weather radar data and surface meteorological variables observations from which precipitation type can be estimated. A variety of precipitation type classification strategies are available and involve different meteorological variables such as the one proposed by Zhang et al. (2011) or by Koistinen and Saltikoff (1998).

The last strategy was the one followed by the Meteorological Service of Catalonia (SMC) to implement a surface precipitation type (SPT) product in 2006 (Bech et al. 2014). The aim of this study is to provide a verification of the SPT product in Catalonia (NE Iberian Peninsula) using manifold sources, for example METAR observations and Social Networks inputs. For specific events and for a location in the Pyrenees, Micro Rain Radar and disdrometric data has also been considered.

2 Data and methodology

2.1 Precipitation type discrimination strategies

Two methodologies to discriminate precipitation type have been considered in this study. On one hand, Koistinen and Saltikoff (1998) (KS) approach, which is the same of the current operational surface precipitation type product at the SMC. On the other hand, a methodology described in Zhang et al. 2011 as a part of the USA National Mosaic Multi-Sensor QPE System (NMQ). Both strategies are described below:

- KS: The methodology proposed by Koistinen and Saltikoff (1998) provides an empirical formula to calculate the probability of precipitation type using temperature and relative humidity observations. Formally, the formula calculates the probability of rain and two thresholds are set to discriminate between snow, sleet and rain. In our case, the equation is flipped, so probability of snow is determined by (1) which may be expressed as

$$p(snow) = 1 - \frac{1}{1 + e^{(22 - 2.7T - 0.2RH)}} \quad (1)$$

  where T corresponds to temperature in Celsius and RH to relative humidity in %. If p(snow) obtained values are below 0.33 precipitation is in form of rain, if they are between 0.33 and 0.66 in form of sleet and classified as snow if they are above 0.66.

- NMQ: A complete precipitation classification process is defined in the NMQ system (Zhang et al. 2011). However, a reduced version of it is considered in this study. If surface temperature is less than 2ºC and wet bulb temperature less than 0ºC, precipitation is in form of snow. Otherwise, the NMQ procedure classifies precipitation as hail, warm rain, stratiform rain or convective rain. However, in this study, distinct types of rain are not taken into account and precipitation not categorized as snow is labelled as rain.

2.2 Surface precipitation type (SPT) product

The current operational product in the SMC is obtained following three steps:

- The SMC manages a network of 181 automatic weather stations that provide the required magnitudes for the probability of snow calculation (1). An analysis of these variables is made to obtain a temperature and relative humidity fields through a multivariate regression considering altitude and distance from the coast.
- Precipitation type field for the whole territory is calculated through (1) using the above-mentioned air temperature and relative humidity fields.
- Then, SPT field is masked with weather radar data to obtain the SPT product.

2.3 Precipitation type observations

Various sources of precipitation type observations are available for the verification. On one hand, there is a small number of METAR and SYNOP observation sites. Despite they are in places where snow is a quite rare phenomena, the quality of data is undeniable. On the other hand, there are two volunteer citizen-scientist networks supported by the SMC, one consists of meteorological observers and the second one is related to surveillance tasks. The latter reports any meteorological event that occurs, such as snow events, storms or seldom phenomena like tornadoes. A nivo-meteorological manned station network located in the Pyrenees monitors the risk of avalanches during winter months. In addition, it provides, among other measurements, information about the present weather three times per day.

Apart from the above-mentioned sources, social networks have been introduced as complementary data to test them as a valid source for verification purposes. For this study, Twitter has been selected because it is used by many people and provides all required data for verification: any kind of information tweeted (precipitation type in this case), location and time. As snow episodes at low altitudes are not common in Catalonia, they are very commented on social networks. For example, during February and March 2018 episodes, snow related hashtags were trending topic and lots of tweets were gathered. However, one drawback of Twitter as data source is that there is a considerable number of tweets talking about snow, but those referred to rain or sleet are anecdotic. Furthermore, snow events in countries where people are used to them will not be as commented as it would be, for instance, in a big city such as Barcelona.

Table 1:Number of observations by precipitation type and by source.

Source	Period	Snow	Sleet	Rain
Observers network (SMC)	2010-2017	1337	238	20342
Surveillance network (SMC)	2010-2017	2916	426	2285
NIMET	2010-2014	900	31	244
METAR	2010-2017	180	52	12367
Twitter	2018	1234	33	24

2.4 SPT verification

Performance of the current SPT product is evaluated by skill scores (POD, FAR, CSI and ETS). Observations and estimates of precipitation type are contrasted following a fuzzy verification framework. A single observation is compared against its neighbourhood and a hit is considered if there is at least one estimation in the surrounding area that agrees with the same of the observation. Apart from considering several grids for the verification (1x1, 3x3, 5x5 and 7x7 pixels, where each pixel is ~1 km^2), a range of time of 15 minutes before and after the observation is considered. This period takes into account that the weather radar precipitation field may take some time to reach the surface and also the differences that may exist between the moment the meteorological phenomenon occurs and when it is reported.

2.5 The Cerdanya site

The Cerdanya is a large valley located in the eastern part of the Pyrenees of Catalonia (NE Iberian Peninsula) (Figure 1). It is a singular basin due to its orographic configuration which predisposes the formation of cold air pools, mountain gravity waves and enhanced precipitation (Trapero et al., 2013, Miró et al., 2018).

A Micro Rain Radar (MRR), a disdrometer and a microwave radiometer (MWR), among other instruments, were deployed in Das for the ATMOUNT campaign to study orographic precipitation, mountain waves and thermal inversions (Table 2). The data collected ranges from December 2016 to April 2017. Despite the campaign ended on April 2017, MRR is still installed and on February 2018 a second generation Parsivel disdrometer was deployed. In addition, several automatic weather stations (AWS) are placed in the valley floor (Das) and its surroundings at different altitudes (Malniu, Cadí Nord and La Molina) (Figure 1, Table 2). All of them include pluviometric and snow depth measurements.

2.5.1 MRR and Parsivel disdrometer

A Micro Rain Radar is a K-band (24.23 GHz) meteorological radar profiler from which estimates of radar reflectivity, Doppler vertical velocity and spectral width can be derived. Parsivel disdrometer provides information of precipitation type every minute, the same temporal sampling as MRR output. Since only one disdrometer is available for this study, MRR data is used to infer precipitation type in the other three AWS locations. First, melting layer height is derived from MRR data following a methodology based on Massmann et al. (2017) to discriminate between ice-initiated rain and warm rain. This method stablishes a melting layer height at a specific minute when three conditions meet: 1) during a 30 minutes period, 15 before and 15 after the studied minute, there is an accumulation of at least 0.5 mm of precipitation, 2) there is a vertical gradient of Doppler velocity greater than -1.65 m/s/210 m at the minute given and 3) this gradient is present at least 35% of the 30-minute period. Therefore, all MRR bins below the melting layer will be considered as rain and the rest of them as snow. If the melting layer detection algorithm output does not provide a melting layer height, precipitation type is classified by a vertical velocity threshold of 2.8 m/s (Yuter et al., 2006). If Doppler velocity is greater than 2.8 m/s precipitation is classified as rain, otherwise as snow. Finally, this classification is compared with the one made by the disdrometer.

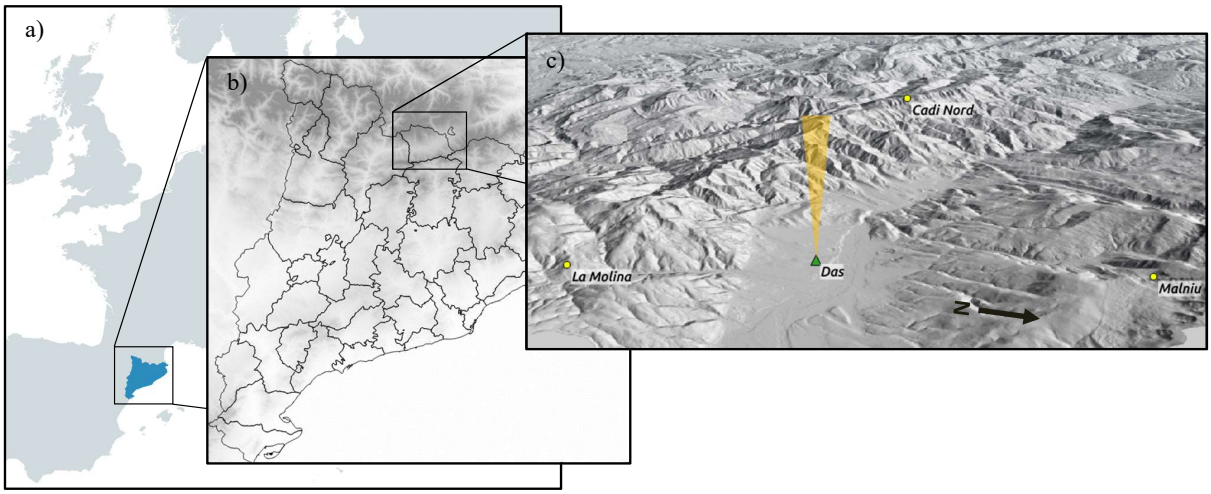


Figure 1: a) Catalonia in SW Europe. b) The Cerdanya Valley in Catalonia. c) Instrumentation installed in The Cerdanya Valley. Yellow circle: Automatic Weather Station; Green triangle: Automatic Weather Station, Parsivel disdrometer, Micro Rain Radar and Microwave Radiometer.

Table 2: Meteorological instruments in The Cerdanya Valley used in this study.

Instrument	Location	Altitude (m)	d* (km)	Temporal resolution (min)
Parsivel disdrometer	Das	1097	-	1
Micro Rain Radar	Das	1097	-	1
Radiometer (Météo-France)	Das	1097	-	2-3
AWS 1 (SMC)	Das	1097	-	30
AWS 2 (AEMET)	La Molina	1704	8	30**
AWS 3 (SMC)	Cadí Nord	2143	23	30
AWS 4 (SMC)	Malniu	2230	11	30

**distance from MRR*

***resampled from 10-minute measurements*

2.5.2 MRR and Automatic Weather Stations (AWS)

After the agreement between MRR derived precipitation type and Parsivel measurements is tested, MRR data is compared with the surrounding AWSs. The assumption here is that if the precipitation system above Das site is large enough and stratiform, may be the same one as in La Molina, Malniu and Cadí Nord. To evaluate this hypothesis, pluviometric and snow depth data from AWS is considered. AWS data is recorded every 30 minutes, if during this period any of the two above-mentioned measurements experience an increase, precipitation is considered in the AWS location. Then, if during the same time range the bins of MRR data at the height of the station contains any minute of reflectivity data, presence of precipitation

is also considered. Therefore, if both conditions are met, a hit between MRR and AWS data is stated. Skill scores are calculated to assess the concordance among MRR and AWS measurements.

2.5.3 KS and NMQ verification with Parsivel and MRR data

The AWS data selected for this study include air temperature and relative humidity measurements. KS and NMQ precipitation type has been calculated for each meteorological station for the selected episodes. Skill scores are calculated to compare precipitation type estimates with Parsivel and MRR data. As Parsivel and MRR temporal resolution is 1 minute, their data is resampled in groups of 30 minutes. The resampling implies that the precipitation type of each of these groups is the one that appears the most in the time range defined. In case of a draw, snow is selected. Micro Rain Radar designed algorithm (Section 2.5.1) only discriminates precipitation between rain and snow, but not sleet. For this reason, KS method is simplified and only one threshold is set, 0.5. This means that if p(snow) from (1) is bigger than 0.5, snow is considered, otherwise precipitation is classified as rain. In addition, only 30-minute groups of MRR data that coincides with precipitation in the AWS location (an increase of snow depth or pluviometric accumulation) is considered.

3 Results

3.1 General verification

In this section an example of SPT verification with precipitation type observations from different sources, such as citizen-scientists networks, is done. An episode on February 27th, 2016 has been chosen to illustrate the performance of the SPT product. 116 observations were gathered: 48 of snow, 56 of rain and 12 of sleet. Skill scores (Table 3) show a good performance of SPT product for snow and rain considering 3x3 grids. Regarding sleet results, the SPT product behaves poorly for this episode and for all grids considered.

Table 3: SPT product verification skill scores for a snowfall event and different grid sizes (in km).

Snow / No snow				Sleet / No sleet				Rain / No rain			
Grid	POD	FAR	ETS	Grid	POD	FAR	ETS	Grid	POD	FAR	ETS
1x1	0.46	0.26	0.21	1x1	0.00	1.00	-0.06	1x1	0.92	0.31	0.38
3x3	0.76	0.12	0.52	3x3	0.25	0.50	0.17	3x3	0.92	0.22	0.53
5x5	0.76	0.10	0.54	5x5	0.50	0.20	0.41	5x5	0.92	0.16	0.62
7x7	0.76	0.03	0.60	7x7	0.50	0.20	0.41	7x7	0.92	0.14	0.65

3.2 Twitter as data source

During the first months of 2018 five snowfall events at low altitudes occurred in Catalonia. These are the first episodes where precipitation type observations from Twitter were gathered. A total of 1291 tweets are available for verification, 1234 of snow, 33 of sleet and 24 of rain. The verification of these data is done against the SPT product, in this case only with snow

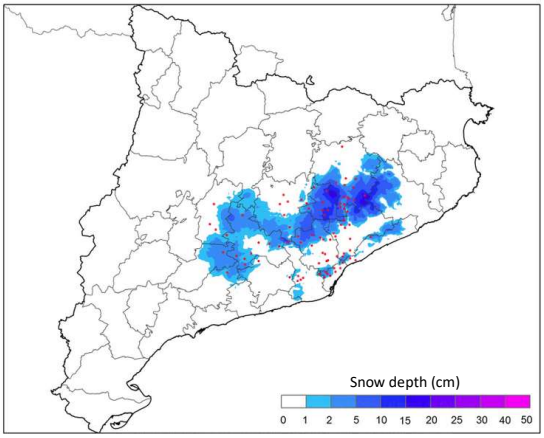


Figure 2: Snow depth and Twitter snow observations (red points) for February 12th, 2018 episode between 12 UT and 24 UT.

observations as there is a small amount of data from sleet and rain. 97% of tweets reporting snow coincide with weather radar precipitation field. In addition, when evaluated by precipitation type and compared to the smallest grid (1x1), POD score is 0.62, but it reaches 0.74 when an area of ~9 km^2 (3x3) is considered.

It can be seen from Figure 2 that there is an agreement between the area of snow depth built by meteorological observers and AWS data and the locations of tweets reporting snow.

3.3 Micro Rain Radar and disdrometric data

Agreement between Micro Rain Radar derived precipitation type and disdrometer present weather code has been tested. An evaluation in terms of POD, FAR, CSI and ETS is done. Before comparing precipitation type from both instruments, an analysis is done to check if MRR and Parsivel disdrometer detects precipitation identically. In this case, disdrometer data is considered as ground truth. Data from 15 days (episodes) is considered and represent 21286 minutes of data: 9460 with precipitation and 11826 without it (Table 4). Skill scores are presented in the first row of Table 5 and show a clear concordance between Parsivel and MRR data in terms of precipitation occurrence.

Table 4: Comparison between Parsivel disdrometer and MRR precipitation observations of 15 episodes at Das.

		Disdrometer		
		Precipitation	No precipitation	Total
MRR	Precipitation	8490	1479	9960
	No precipitation	970	10347	11317
	Total	9460	11826	

The same analysis is done to evaluate the algorithm proposed for MRR precipitation type discrimination. For this purpose, only MRR data that agrees with Parsivel disdrometer (ground truth) is considered. Results (Table 5) show that ETS score is the same for both analyses and that there is a higher POD for rain (0.88) category than for snow (0.78). The first three height levels of MRR measurements are discarded to avoid near-fields effects (Maahn and Kollias 2012). This may explain part of the lower POD score for snow than for rain, as snow at 300 m AGL may melt during its path to the surface. Therefore, Parsivel, which is placed at the surface, may detect different precipitation type than MRR proposed algorithm. In addition, the procedure to discriminate precipitation type from MRR measurements (Section 2.5.1) may be rearranged and a different velocity threshold considered.

3.4 Micro Rain Radar and AWS

In order to establish a horizontal range of consistency between the MRR measurements at Das site and precipitation in AWS locations around the Cerdanya Valley (Figure 1) a similar scheme of that of section 3.3 is followed. Similar results are obtained for the three stations considered and for the 15 episodes. Although POD and FAR are relatively high and low, respectively, the ETS is nearly 0.30 for the three AWS locations (Table 6). However, if data is analysed in an event scale some differences between AWS arise, specifically for those episodes where precipitation systems are small or convective rather than large and stratiform.

Table 5: Skill scores of Parsivel and MRR observations and precipitation type evaluation.

MRR vs Parsivel	POD	FAR	CSI	ETS
Precipitation/No precipitation	0.90	0.15	0.78	0.62
Snow/No snow	0.78	0.13	0.70	0.49
Rain/No rain	0.88	0.21	0.71	0.49

Table 6: Skill scores of MRR data against AWS pluviometric and snow depth observations.

MRR vs AWS	POD	FAR	CSI	ETS
La Molina (1705 m)	0.84	0.35	0.58	0.30
Cadí Nord (2143 m)	0.91	0.34	0.62	0.31
Malniu (2230 m)	0.88	0.27	0.66	0.33

3.5 Specific episodes at The Cerdanya Valley

Among the fifteen episodes studied in The Cerdanya Valley site, two of them where transitions between snow and rain occur are selected. The first two graphs of Figures 3 and 4 illustrate a) radar reflectivity and b) Doppler velocity, both from MRR

measurements. Then c) and d) show different precipitation type estimates and measurements. In Das and La Molina sites, MRR derived precipitation type is presented together with KS, NMQ and SPT product precipitation type estimates. Although SPT uses KS methodology to calculate probability of precipitation type, equation (1) is fed by temperature and relative humidity interpolated fields rather than AWS measurements, so KS and SPT estimates may differ. KS and NMQ representations are independent of precipitation, therefore they are represented continuously. On the contrary, SPT depends on the weather radar precipitation field and the precipitation type of the nearest pixel for each AWS location is selected. Particularly, Parsivel simplified present weather code (snow, sleet, rain) is also represented at Das site. e) shows three different SPT product frames.

The first episode selected took place on March 25th, 2017 (Figure 3). Focusing at the valley floor (Das), the event is characterized by two transitions. The first one is from rain to snow and occurs around 0800 UT. It is captured by the five precipitation type measurements and estimates presented. Parsivel data shows an abrupt transformation of precipitation type whereas KS calculations, both KS and SPT, show a gradual transition with a short period of sleet. At 13 UT, after the snowfall, disdrometric measurements exhibit a progressive change from snow to rain with more than one hour of sleet. This transition is represented also by SPT and KS estimates, but MRR and NMQ fail to get it correct as they report snow and rain continuously, respectively.

At La Molina location, at 600 m above Das site, there is a transition from rain to snow between 0200 UT and 0300 UT. It is the one that precedes the precipitation type change at Das at 0800 UT. In this case, SPT, KS and NMQ agree with the MRR derived precipitation class. Data from the other two AWS locations are not considered as no transition between precipitation types is observed.

The second episode took place on April 26th, 2017 and consisted of successive showers and a transition from rain to snow at the end of the event. The height where falling snow melts and transforms to rain is nearly the same of the freezing level height derived from microwave radiometer temperature profile. The melting layer remains relatively high during a great part of the event. However, it experiences a gradual fall from 1000 m AGL to 0 m AGL between 18 UT and 00 UT. This coincides when at Das and La Molina sites, precipitation in from of rain transforms to snow. Although at La Molina the four methodologies present the same behaviour, a difference between them arise at Das location. SPT at Das does not experience any precipitation type transition while the other four do. This may be due to temperature and relative humidity interpolation errors, as SPT estimates differ from those of KS from AWS Das measurements.

Results considering the 15 episodes together can be seen at Table 7. As mentioned in Section 2.5.3, data from MRR and Parsivel is resampled from 1 minute to 30 minutes to match AWS temporal resolution. 441 groups of 30 minutes of data are available for Das location and 229 for La Molina. Results show that for Das site, KS methodology behaves the best, both for MRR estimates and Parsivel (PAR) measurements. Although some skill scores for Rain/No rain are better for NMQ approach than KS, all ETS scores are higher for KS.

Regarding La Molina site, KS is better for Snow/No snow discrimination and NMQ for Rain/No rain. However, in terms of ETS scores, differences are very small.

Table 7: Skill scores of MRR and Parsivel disdrometer data against KS and NMQ estimates at Das and La Molina sites.

			POD	FAR	CSI	ETS
Das	Snow/No snow	MRR vs KS	0.82	0.14	0.72	0.54
		MRR vs NMQ	0.69	0.11	0.64	0.45
		PAR vs KS	0.92	0.10	0.83	0.70
		PAR vs NMQ	0.75	0.07	0.71	0.55
	Rain/No rain	MRR vs KS	0.88	0.15	0.76	0.54
		MRR vs NMQ	0.92	0.23	0.73	0.45
		PAR vs KS	0.91	0.07	0.85	0.70
		PAR vs NMQ	0.95	0.18	0.78	0.55
La Molina	Snow/No snow	MRR vs KS	0.94	0.23	0.73	0.44
		MRR vs NMQ	0.89	0.18	0.75	0.49
	Rain/No rain	MRR vs KS	0.66	0.10	0.62	0.44
		MRR vs NMQ	0.76	0.14	0.68	0.49

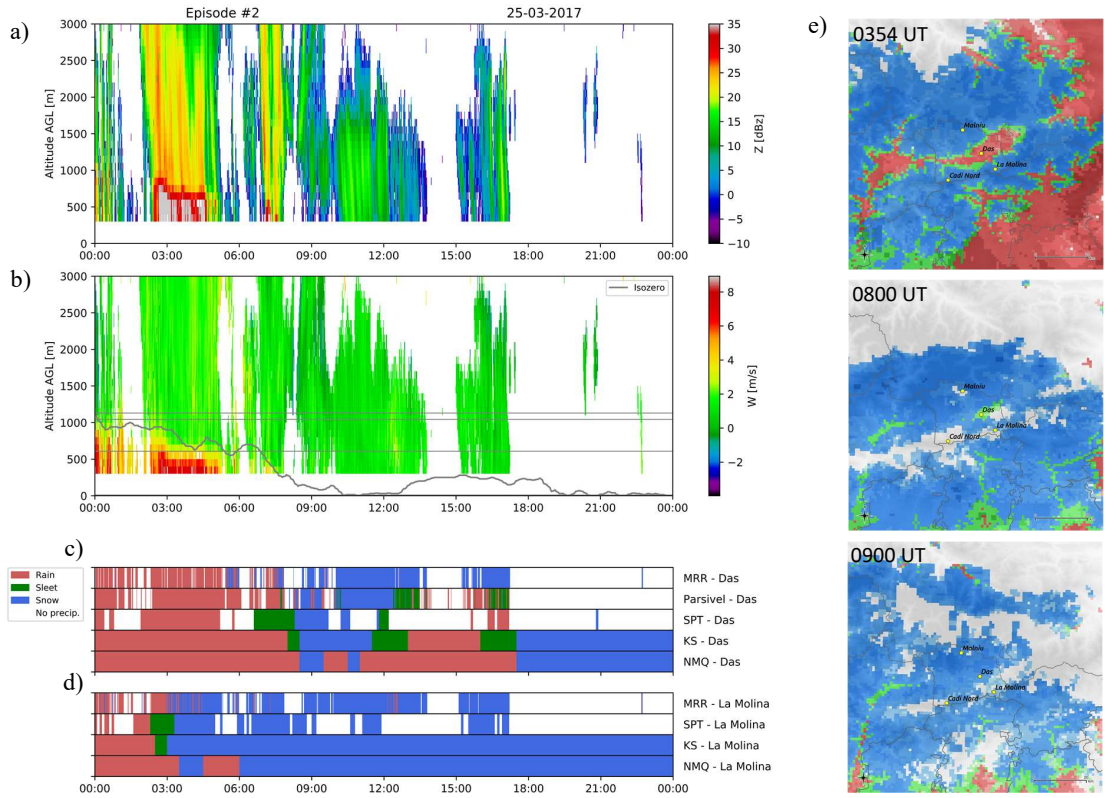


Figure 3: March 25th, 2017 episode. a) and b) are a time-height measurements of radar reflectivity and Doppler velocity from MRR, respectively. b) also includes melting layer height derived from MWR data. c) and d) include the representation of different precipitation type measurements (Parsivel, only for Das site) and estimates (MRR, KS, SPT and NMQ). KS and NMQ representations are independent of precipitation, therefore they are represented continuously. e) SPT product frames for The Cerdanya Valley area.

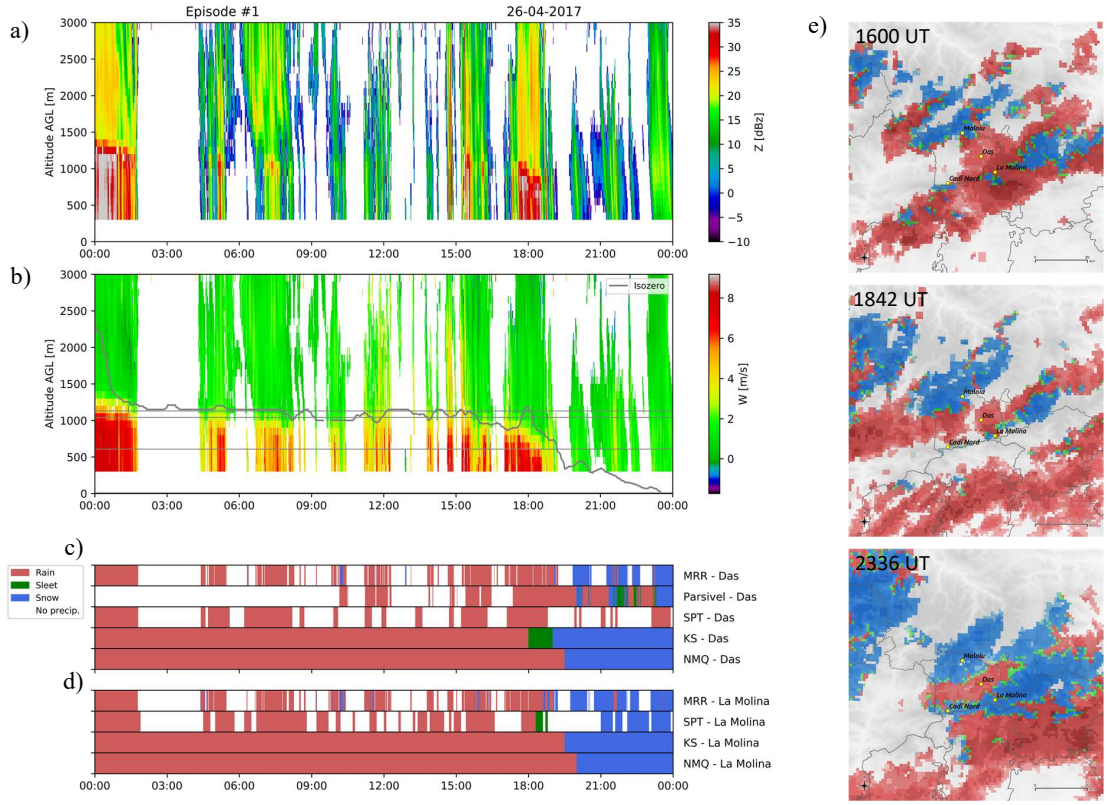


Figure 4: The same of Figure 1 for April 26th, 2017 episode.

4 Discussion

The Surface Precipitation Type (SPT) product, since it was operatively installed in 2006, has been used by meteorological observers and predictors of the SMC and transport authorities. It became an important and useful tool to monitor snow events at low altitudes in Catalonia.

Data gathered between 2010 and 2018 provides a great amount of precipitation type observations that allows to perform an extensive verification of the SPT product for the whole territory of Catalonia. Compared to other precipitation type verification studies, the amount of data available for the Catalan region is quite smaller. This may be explained through the lower frequency of snow events and a lack of an open application to report precipitation type such as mPing (Elmore et al., 2014). In this study, SPT product verification results are only presented for one episode. Skill scores in Table 3 show a quite good performance for rain and snow, which is the critical precipitation type to monitor. The study of precipitation type observations from social networks, such as Twitter, showed that they can be a valuable tool to monitor snowfall events at low altitudes. For the moment, all the gathered tweets will be used as complementary data to verify the SPT product. The verification itself will be performed by the sources mentioned in Table 1, except Twitter, and disdrometric data.

The instrumentation deployed in The Cerdanya Valley provides valuable information to evaluate, among other applications, the SPT product and precipitation type discrimination strategies. MRR precipitation type algorithm proposed shows similar results to those of Parsivel present weather measurements. This allowed to test precipitation type at MRR site surroundings which involve La Molina, Cadí Nord and Malniu AWS. The last two meteorological stations were discarded during the verification procedures. Both locations rarely exhibit any MRR precipitation type transition nor KS and NMQ for the episodes selected. In addition, they are a bit far from Das site where MRR is installed (11 and 28 km, respectively). For those reasons, only La Molina site was verified.

For the 15 episodes selected, results show that performance of KS methodology is better than NMQ in terms of snow detection. In addition, the possibility to discriminate between three precipitation types (snow, sleet and rain) rather than two (snow and rain), provides more information and more realistic snow to rain or rain to snow transitions. The brief study presented here opens up the possibility to verify SPT product and KS strategy with a larger disdrometric dataset and to check the precipitation type thresholds from equation (1). In addition, the differences observed between the SPT product precipitation type and the same reported by the KS formula (1) using data from AWS at Das site may be due to interpolation errors (Figure 4). For this reason, different interpolation strategies, such as clustering, will be considered to reduce problems not related to the formula itself. The next step once an extensive verification of the current operational SPT product finishes, is to lay the foundations for a nowcasting SPT product.

Acknowledgement

This study was made using data from the ATMOUNT Campaign (Météo-France, AEMET, CENMA, SMC, Universitat of Barcelona, Universitat Politècnica de Catalunya, Univeristat de les Illes Balears, University of Portsmouth, OWL University and Laboratoire d'Aerologie). This work was partly supported by projects CGL2015-65627-C3-2-R (MINECO/FEDER), CGL2016-81828-REDT (MINECO) and DI065/2017 (Industrial Doctorate Programme of the Government of Catalonia).

References

Bech, J., Vidal, V., Ortiz, J. A., Pineda, N., & Veciana, R. (2014). Real-time estimation of surface precipitation type merging weather radar and automated station observations. *17th International Weather Road Conference, Andorra*, 2–9.

Elmore, K. L., Flamig, Z. L., Lakshmanan, V., Kaney, B. T., Farmer, V., Reeves, H. D., & Rothfusz, L. P. (2014). MPING: Crowd-sourcing weather reports for research. *Bulletin of the American Meteorological Society*, *95*(9), 1335–1342. https://doi.org/10.1175/BAMS-D-13-00014.1

Koistinen, J., & Saltikoff, E. (1998). Experience of customer products of accumulated snow, sleet and rain. *Advanced Weather Radar Systems*, 397.

Maahn, M., & Kollias, P. (2012). Improved Micro Rain Radar snow measurements using Doppler spectra post-processing. *Atmospheric Measurement Techniques*, *5*(11), 2661–2673. https://doi.org/10.5194/amt-5-2661-2012

Massmann, A. K., Minder, J. R., Garreaud, R. D., Kingsmill, D. E., Valenzuela, R. A., Montecinos, A., … Snider, J. R. (2017). The Chilean Coastal Orographic Precipitation Experiment: Observing the Influence of Microphysical Rain Regimes on Coastal Orographic Precipitation. *Journal of Hydrometeorology*, *18*(10), 2723–2743. https://doi.org/10.1175/JHM-D-17-0005.1

Miró, J. R., Peña, J. C., Pepin, N., Sairouni, A., & Aran, M. (2018). Key features of cold-air pool episodes in the northeast of the Iberian Peninsula (Cerdanya, eastern Pyrenees). *International Journal of Climatology*, *38*(3), 1105–1115. https://doi.org/10.1002/joc.5236

Trapero, L., Bech, J., & Lorente, J. (2013). Numerical modelling of heavy precipitation events over Eastern Pyrenees: Analysis of orographic effects. *Atmospheric Research*, *123*, 368–383. https://doi.org/10.1016/j.atmosres.2012.09.014

Yuter, S. E., Kingsmill, D. E., Nance, L. B., & Löffler-Mang, M. (2006). Observations of precipitation size and fall speed characteristics within coexisting rain and wet snow. *Journal of Applied Meteorology and Climatology*, *45*(10), 1450–1464. https://doi.org/10.1175/JAM2406.1

Zhang, J., Howard, K., Langston, C., Vasiloff, S., Kaney, B., Arthur, A., … Dempsey, C. (2011). National mosaic and multi-sensor QPE (NMQ) system description, results, and future plans. *Bulletin of the American Meteorological Society*, *92*(10), 1321–1338. https://doi.org/10.1175/2011BAMS-D-11-00047.1

Comparison of clutter detection schemes for non-Doppler, non-polarimetric X band radars

Samantha Melani[1,2], Andrea Antonini[2], Francesca Caparrini[1], Andrea Telleschi[3], Andrea Lombardi[3], Alessandro Mazza[1,2] and Alberto Ortolani[1,2]

[1]*CNR-IBIMET, Via G. Caproni, 8 50145 Firenze, ITALY*
[2]*LaMMA Consortium, Via Madonna Del Piano, 10 50019 Sesto Fiorentino (FI), ITALY*
[3]*ELDES srl, via di Porto, 2/B 50018 Scandicci (FI), ITALY*

(Dated: 22 June 2018)

1 Introduction

Radar echoes of non-meteorological targets must be necessarily identified and removed as far as hydrology and precipitation estimates are concerned: relevant biases in the estimation of rainfall fields can be introduced with a negative impact on the performance of using such data for meteorological and hydrological nowcasting, applications.

Ground clutter and weather signals have different statistical properties, as the stability of reflectivity echoes relative to very close volumetric cells is much higher in case of clutter than of weather signals. More complex is the identification of sea clutter because it changes very rapidly in the horizontal direction, and presents a radial attenuation as the distance from the radar increases. In addition, sea clutter values decrease as a function of height, so vertical gradient signatures can be used in the clutter identification process.

Common used approaches, for non-doppler and non-polarimetric radar systems, identify clutter in the reflectivity data by creating a static map of areas where clutter is most prevalent. Another method is to make a more dynamic map that identifies clutter from image to image. Identification of clutter in reflectivity maps and the relative correction schemes has been extensively described in literature (Aoyagi, 1983), (Andrieu, 1997), (Creutin, 1997), (Grecu, 2000), (Steiner, 2002), (Siggia, 2004), (Berenguer, 2005), (Hubbert, 2009a), (Hubbert, 2009b).

In this work, two different algorithms for the removal of ground and sea clutter have been tested and discussed for two case studies, under different meteorological conditions. Preliminary results show a strong dependence of the analysed algorithms on the radar site: they must be necessarily customized to each radar location, because of the ground and sea clutter signatures strongly dependent on local orography and territory.

2 Data and methods

2.1 Radar systems

This study employs data gathered by the X-band radar systems located along the coastal areas of Tuscany region. The systems constitute aregional network: the first weather radar has been installed in Cima di Monte, a mountain height about 470 m in the western part of Elba Island. The second one has been placed in the Livorno's port, on the top of a silo at an altitude of about 72 m asl. Finally, the third system has been installed in Castiglione della Pescaia about 25km north of Grosseto, over the building of the local municipality at a height of about 15 m.

Table 1 shows the main characteristics of the non-Doppler and non-polarimetric systems (all of the same type: WR10X produced by ELDES srl, https://www.eldesradar.com/prodotto/wr-10x/). They have a gate resolution of 450 m and a maximum selectable range of 108km. A scan every 15 min and 10 elevations from 0.5° to 5.0° in steps of 0.5° were selected for the operational configurations of the X-band network.

Table 1. WR10X radar technical specifications.

Parameter	Value
Operating frequency	9.410 ± 0.03 GHz
Peak power	10 kW
Pulse width	0.6 μs
Pulse Repetition Frequency	800 Hz
Receiver dynamics	>90 dB, 8 bits codify
Sensitivity	10 dBZ @ 25 km

Noise figure	<4 dB
Minimum Detectable Signal	<–100 dB
Antenna type	Circular Pencil beam diameter 70 cm
Antenna 3 dB lobe	<3.2° in elevation and in azimuth
Antenna gain	35÷40 dB
Antenna speed	20°/s

2.2 Sea and ground clutter removal algorithms

In the next sections, two different algorithms for the removal of sea and ground clutter will be presented, one developed and implemented by ELDES (hereinafter named ALGO1), the other by LaMMA (Laboratory of Monitoring and Environmental Modelling for the sustainable development) Consortium (hereinafter named ALGO2).

2.2.1 ELDES's algorithm (ALGO1)

Data produced by a weather radar are commonly affected by ground clutter at lower elevations. Non-coherent radar, without Doppler capability, typically uses statistical clutter filters in order to detect and cancel the clutter echoes.

The ground clutter filter of WR-10X radar is applied at the lowest elevation sweep, and it is based on the following steps (Figure 1):

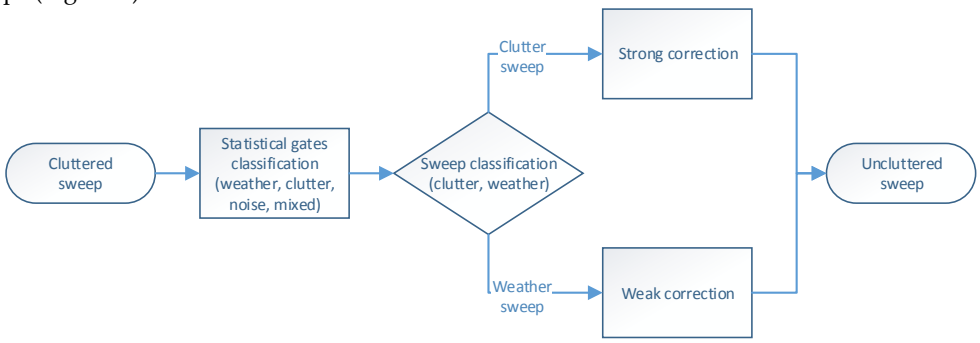


Figure 1: General scheme of the ELDES ground clutter algorithm.

For each gate, the classification is performed by analyzing the azimuth samples, available in the gate, of the power level at the output of the receiver channel (Figure 2).

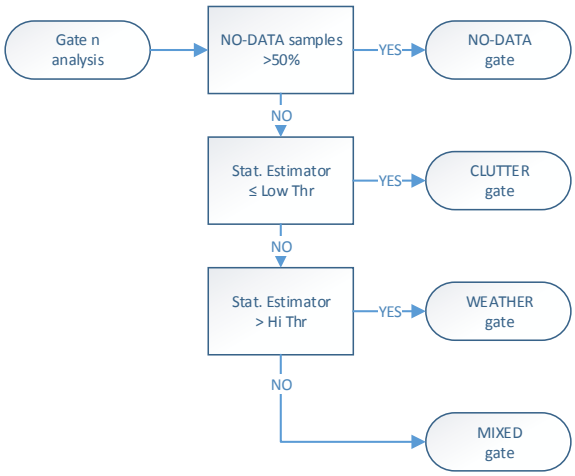


Figure 2: Scheme of the gate classification.

Two different configurable Statistical Estimators can be used in order to detect the texture's differences between clutter and weather: standard deviation and lag-1 correlation.

- ESTIMATOR 1: Standard deviation

The standard deviation is obtained by sampling on 14 bit the power level at the output of the receiver channel:

$$\sigma_{gate} = \frac{\sum_{n=1}^{L}(P_n - \overline{P_{gate}})}{L}, \quad (2.1)$$

where:

L = number of azimuth samples available in the gate;
P_n = nth sample of the log received power;
$\overline{P_{gate}}$ = average of azimuth samples available in the gate.

Generally, the clutter gates are characterized by low values of standard deviation but when the clutter is due to woodlands in presence of wind or snowy close mountain areas such values increase up to assume those corresponding to areas affected by weak or distant weather fronts.

- ESTIMATOR 2: Lag-1 correlation

The spatial correlation at lag-1 is obtained by sampling on 14 bit the power level at the output of the receiver channel:

$$R_{gate}(1) = \frac{\sum_{n=1}^{L-1} P_n * P_{n+1}}{\sum_{n=1}^{L-1} P_n * P_n}, \quad (2.2)$$

where:

L = number of azimuth samples available in the gate;
P_n = nth sample of the linear received power.

Such statistical index allows removing the clutter even when it is due to: woodland in presence of wind, snowy mountains or urban area subjected to multipath effects.

The classification of the sweep is performed by counting the number of clutter marked as "CLUTTER gate": if higher than a configurable threshold, it is classified as a "clutter sweep" (predominant clutter), otherwise it is considered a "weather sweep" (predominant weather). Two different correction filters are applied depending on the type of sweep.

The different management between clutter and weather sweeps has been implemented in order to avoid that, in absence of weather events, the radar map shows too many residues of the filtering in correspondence of ground clutter areas.

In presence of a clutter sweep (predominance of clutter), a strong correction is used. For a weather sweep, a week correction is applied, for a further classification of mixed gates.

- Strong correction (for "clutter sweep"): the sweep is compared with a static clutter map: each non-WEATHER gate is set to NO-DATA.
- Weak correction (for "weather sweep"): the sweep is compared with a static clutter map: each WEATHER gate is kept, and a correction is applied to the MIXED gates. The gate is classified based on the classification (WEATHER / CLUTTER) of the surrounding gates (square window neighborhood of configurable dimension).

The sea clutter removal algorithm is based on the difference of reflectivity along the vertical profile, which is a very good indicator of the presence of sea clutter. Generally, in rainy situations, the vertical reflectivity profile is smooth and regular while in presence of echoes returned from the sea, the vertical reflectivity profile appears uneven with a decrease/disappearance of the reflectivity values with the increasing of the antenna elevation angle because the sea clutter is a phenomenon that appears only at lowest elevations. The gates of these sweeps affected by sea clutter are compared with the gates of a reference sweep, acquired at the elevation considered the limit angle beyond it the PPI images do not show sea clutter. The estimation of the vertical gradient is performed considering the earth's curvature.

Considering that also the echo returned from weather targets can show abrupt changes in vertical reflectivity profile, when a gate is classified as sea clutter for the classification of the subsequent gates, the algorithm uses two different thresholds T3 and T4, by using the same logic. The T1 and T2 thresholds are reactivated as soon as the algorithm classifies a gate as not affected by sea clutter (Alberoni, 2001), (Capozzi, 2014).

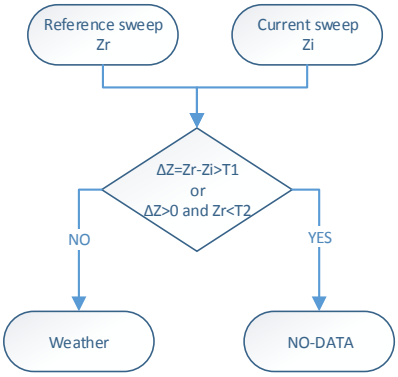


Figure 3: General scheme of the sea clutter algorithm.

2.2.1 LaMMA's algorithm (ALGO2)

The LaMMA's clutter algorithm consists of two schemes, one statistical for ground clutter and the other based on texture features for sea clutter. The main characteristics are here reported, referring to (Antonini, 2017) for more details.

The algorithm for ground clutter identification is based on the stability of radar signature when the radar beam intersects and is backscattered by mountain and reliefs (Andrieu, 1997). The implemented algorithm is based on (Sugier, 2002) and operates a statistical scheme based on the standard deviation of neighbor cells along azimuth. The basic idea is that the reflectivity cells affected by ground clutter that are contiguous in azimuth are very strongly correlated for the majority of cases because of the high spatio-temporal closeness of the observations; this does not occur in the case of two precipitation backscattering cells which are highly variable in space and time.

In summary, as shown in Figure 4, for each cell of the final product (1° in azimuth x 450 m of range resolution), the standard deviation of the 40 maximum available observations is used to discriminate the ground clutter from precipitation. The former is characterized by low standard deviations and not much fluctuating values while the latter has higher standard deviations and values that are more variable. The algorithm uses two thresholds (σ_{min}, σ_{max}) based on the specific characteristics of the area covered by radars and computed during clear air conditions (total absence of precipitation and cloudiness), once collected a sufficient number of scans (Figure 4a).

If the standard deviation is below the minimum threshold, the corresponding cell is classified as ground clutter, if it is above the maximum threshold it is classified as precipitation. Each ground cell with an intermediate standard deviation value is further processed by a module based on the KNMI operational clutter removal scheme (Wessels, 1992), (Holleman, 2004).

Figure 4b shows the flowchart of the decision tree algorithm and the threshold values for each test.

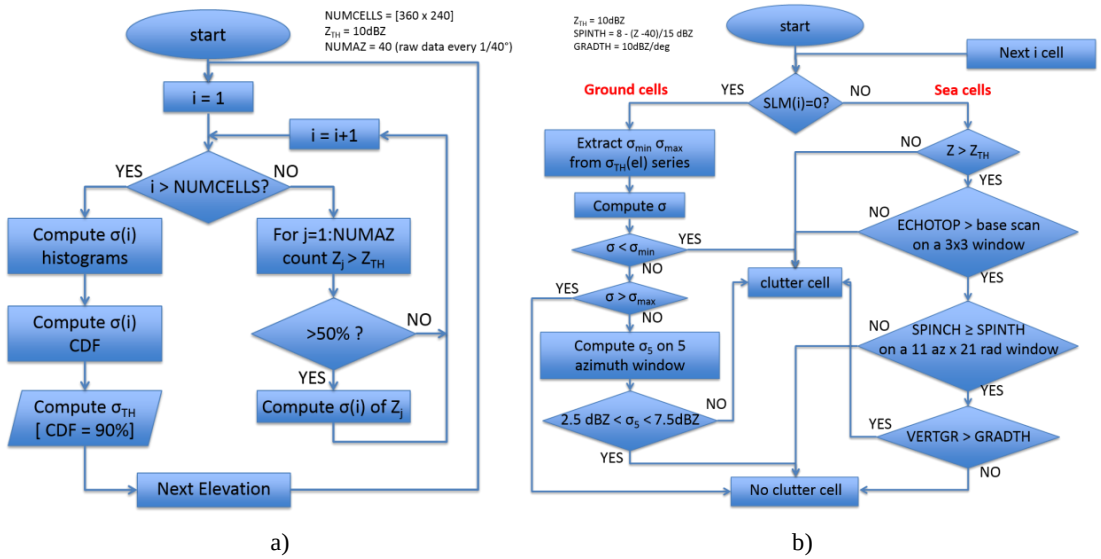


Figure 4: Flow chart of the clutter removal scheme: (a) Set-up in clear air conditions; (b) Operational sea and ground clutter identification algorithm.

For sea clutter removal, the (Steiner, 2002) algorithm was used (Figure 4b). It takes advantage of the 3D reflectivity structure and was built upon three key parameters: the vertical extent of radar echoes (ECHOTOP), the vertical gradient of reflectivity (VERTGR), and the spatial variability of the reflectivity fields (SPINCH). The clutter scheme is a decision-tree algorithm in which the selected features for clutter-identification are analysed according to a sequential logical chain by means of thresholds: each pixel of the polar base-scan is examined to determine if it should be kept, removed, or potentially replaced.

Basically, the key parameters exploit:

- ECHOtop test removes most of the sea clutter echoes that are separated from precipitation, because of a lack of vertical extent of those echoes.
- VERTGR test characterises the shallow extent of clutter, as even when rainfall affects meaningful clutter areas, the negative values of the vertical gradient of reflectivity tend to be high.
- SPINCH test grasps the spatial variability of clutter echoes, especially when embedded in precipitation, as reflectivity fields present higher spatial variability and more significant fluctuations with respect to rainfall echoes.

3 Results for some case studies

Two case studies for different meteorological conditions and clutter disturbances are shown, for Elba and Livorno radars. The evaluation of both the algorithms performance are made in rainy conditions, for precipitation embedded or not embedded in clutter echoes. Data from Castiglione della Pescaia are not available for these case studies.

3.1 06 may 2017

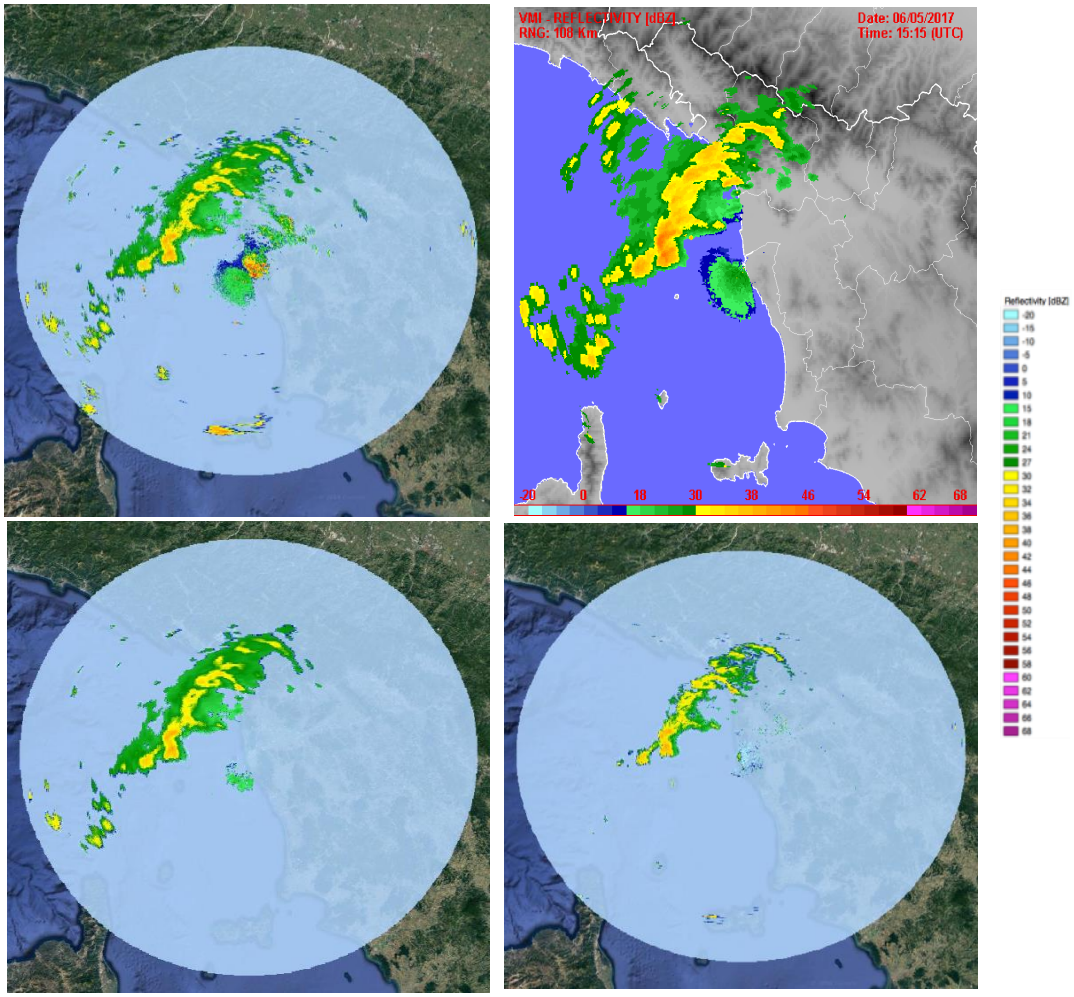
A depression zone is located on the upper Tyrrhenian Sea, causing in the late morning the generation of some convective weather systems over the sea that propagate easterly towards the northern and central areas of the region. In the afternoon, new precipitative events generate over sea between Corsica and Elba Island, causing thunderstorms especially in the Pisa and Lucca areas moving to the inner parts in the evening. Both radar systems detect the presence of the storms very well, especially in marine areas where ground raingauges measurements are not available.

An extensive area of clutter is present over sea around both radar sites (Figure 5a,b and Figure 6a,b), partially overlapped with precipitation for the Elba case study (see Figure 6a). Clutter disturbances around Elba and Livorno sites are generally more pronounced for the lower elevations, even if sea clutter around Livorno is often persistent also up to the highest elevations (i.e., 5.0°).

Both the clutter removal algorithms are really efficient in removing ground clutter on Corsica, Elba Island and in the central part of Tuscany, where the reliefs produce very reflective echoes that could be misinterpreted as precipitation if not correctly removed (Figure 5c,d).

Around Livorno site, some sea clutter features remain as the clutter echoes persist up to 5.0°; they are better resolved by the ALGO2 as it uses the combination of different features, not only the 3D reflectivity structure (as in ALGO1) that, in this case, is almost constant for all the elevations. On the other hand, ALGO2 presents the tendency to remove meteorological reflectivity echoes in a greater extent respect to ALGO1.

a) b)



c) d)

Figure 5. PPI radar scans for an elevation of 4.0° for 06 May 2017, 15:15 UTC for Livorno radar. a) Non-decluttered image, b) VMI product, c) Decluttered image using ALGO1, d) decluttered image using ALGO2.

In Figure 6 (a,b), disturbances due to ground clutter are evident along the mountains reliefs of Corsica and the northern and central Apennines in Tuscany. Such features are more pronounced for the lower elevations even if sea clutter around Elba site is persistent also up to the highest elevations (i.e., 2.5°).

The application of both the algorithms leads to a considerable reduction of sea and ground clutter while retaining the all the precipitative features embedded in clutter returns. The precipitation overlapped to sea clutter northern to the Elba Island is well retained by both the algorithms, even if ALGO2 seems to remove meteorological radar returns in a greater extent, especially in the northern part of the region where it filters out the echoes too much. Also, some ground disturbances remain on Elba island and along the coasts due to the application of ALGO2.

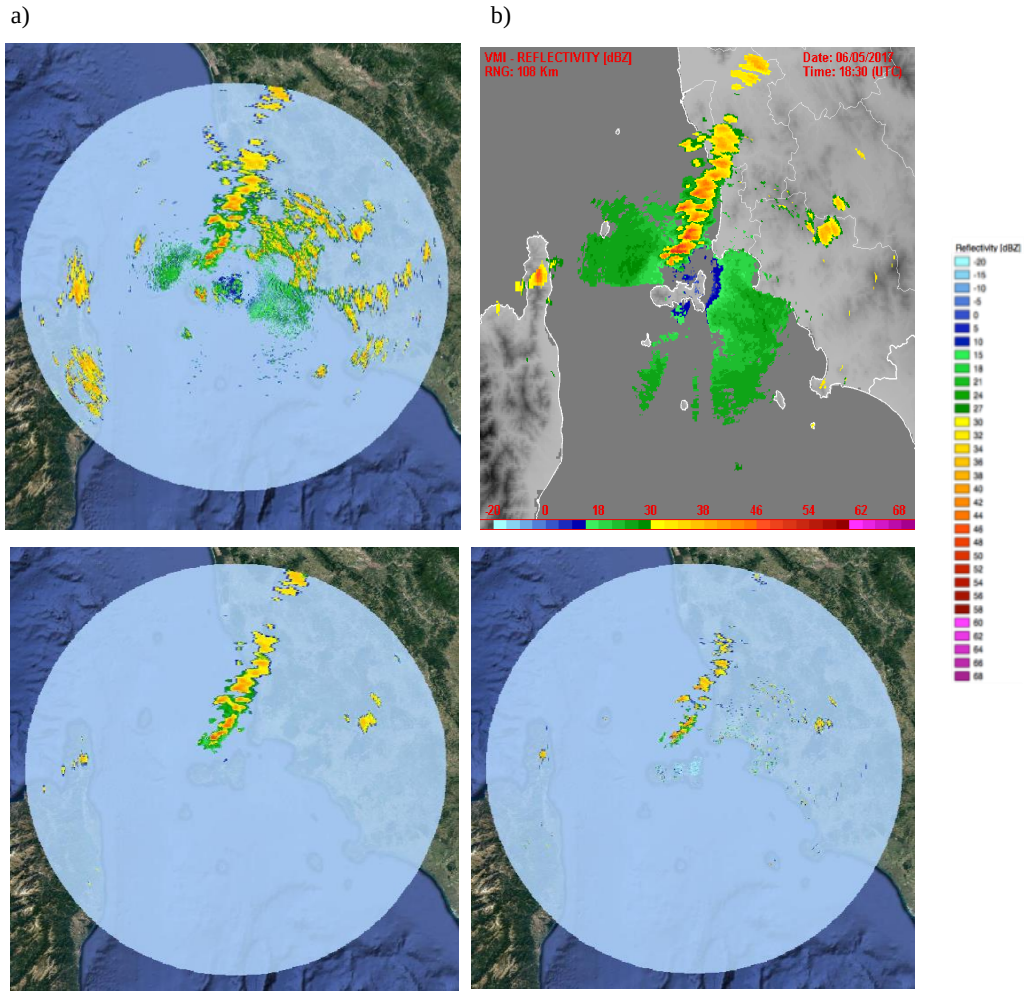
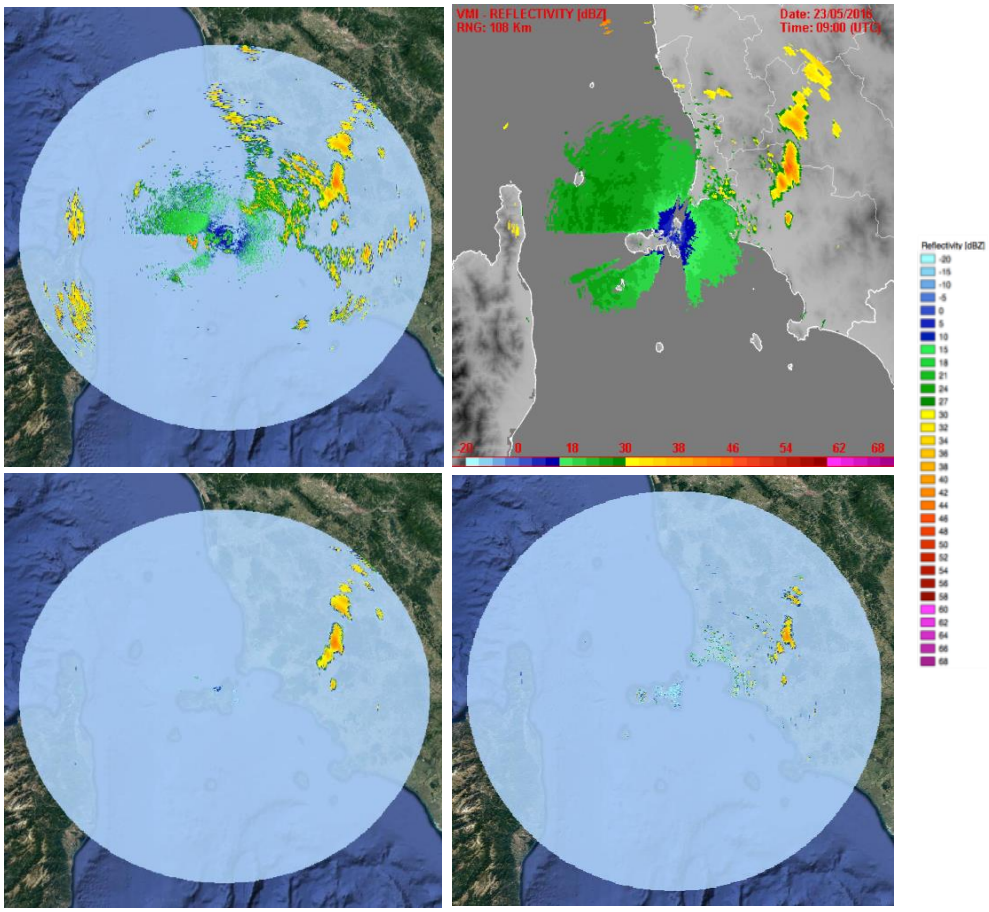


Figure 6: PPI radar scans for an elevation of 1.5° for 06 May 2017, 18:30 UTC for Elba radar: a) Non-decluttered image, b) VMI product, c) Decluttered image using ALGO1, d) decluttered image using ALGO2.

3.2 23 may 2016

This case study is characterized by a relevant presence of ground clutter echoes over Elba site, along the Tuscany coasts, over Corsica and in the inner areas of the southern part of the region (Figure 7a,b). Widespread sea clutter disturbances are also present around Elba site that persist up to the highest elevations (up to 5.0°, not shown). Some convective precipitative events also affected the study domain, starting along the coast early in the morning and reaching the south-estearn part later in the afternoon.

a) b)



c) d)

Figure 7: PPI radar scans for an elevation of 1.5° for 23 May 2016, 09:00 UTC for Elba radar: a) Non-decluttered image, b) VMI product, c) Decluttered image using ALGO1, d) decluttered image using ALGO2.

The decluttered images (Figure 7c,d) show the efficiency of both the algorithms in removing totally sea clutter around Elba island, while retaining the main meteorological reflectivity echoes although ALGO2 reduces them in a more consistent way. Some ground clutter noises remain over Elba Island and in the areas in front of it due to the application of ALGO2 while ALGO1 algorithm proves to give good results also at far distances from radar site.

4 Conclusions

The performance of two different algorithms for sea and ground clutter removal during rainy conditions have been analyzed, using data from two X-band, non-Doppler, non-polarimetric radars deployed along the Tuscany coasts.

Preliminary results show how both the algorithms have to be necessarily customized for each radar location, because ground and sea clutter signatures are highly dependent on local orography and territory. Future works will be devoted to enlarge the casuistry of the weather events in order to tune in a more customized way the thresholds used in the algorithms.

Both the algorithms efficiently remove ground clutter due to the massive presence of mountains in Tuscany, Coarse and Elba, which produces strong radar echoes that, if not correctly identified and removed, could produce high biases in rainfall fields estimations. Sea clutter is well removed for Elba radar, even if some clutter disturbances remain visible around Livorno site as clutter affects the higher elevations (up to 5°). In addition, precipitation features that are embedded in clutter echoes are well retained in their form and intensity. Qualitative comparisons between the two different algorithms show the tendency of the ALGO2 to retain the meteorological reflectivity echoes in a lesser extent, while leaving some ground clutter noises for the lower elevations. When sea clutter extends to the higher elevations, ALGO2 seems to be a little bit more efficient because of the use of additional features not present in ALGO1.

References

Alberoni, P. A. (2001). Use of the vertical reflectivity profile for identification of anomalous propagation. *Meteorol. Appl.*, 8, 257–266.

Andrieu, H. C.-D. (1997). Use of a weather radar for the hydrology of a mountainous area. Part I: Radar measurement interpretation. *J. Hydrol.*, 193, 1–25.

Antonini, A. M. (2017). On the Implementation of a Regional X-Band Weather Radar Network. *Atmosphere*, 8, 25.

Aoyagi, J. (1983). A study on the MTI weather radar system for rejecting ground clutter. *Papers in Meteor. and Geophy*, 33, 187–243.

Berenguer, M. S.-D. (2005). A fuzzy logic technique for identifying nonprecipitating echoes in radar scans. *J. Atmos. Oceanic Technol.*, 23, 1157–1180.

Capozzi, V. P. (2014). X-band weather radar monitoring of precipitation fields in Naples urban areas: data quality, comparison and analysis. *Proc. of ERAD 2014 - 8th European Conference on Radar in Meteorology and Hydrology, Garmisch-Partenkirchen, Germany*.

Creutin, J.-D. A. (1997). Use of a weather radar for the hydrology of a mountainous area. Part II: Radar measurement validation. *J. Hydrol.*, 193, 26–44.

Grecu, M. K. (2000). An Efficient Methodology for Detection of Anomalous Propagation Echoes in Radar Reflectivity Data Using Neural Networks. *J. Atmos. Oceanic Tech.*, 23, 121-129.

Holleman, I. B. (2004). Review of the KNMI Clutter Removal Scheme. In *Technical Report, KNMI TR-284.* Royal Netherlands Meteorological Institute (KNMI): De Bilt, The Netherlands.

Hubbert, M. D. (2009a). Weather Radar Ground Clutter. Part I: Identification, Modeling, and Simulation. *J. Atmos. Oceanic Tech.*, 26, 1165-1180.

Hubbert, M. D. (2009b). Weather Radar Ground Clutter. Part II: Real-Time Identification and Filtering. *J. Atmos. Oceanic Tech.*, 26, 1181-1197.

Siggia, A. D. (2004). Gaussian model adaptive processing (GMAP) for improved ground clutter cancellation and moment calculation. *Proc. ERAD 2004*, 2, 421–424.

Steiner, M. a. (2002). Use of three-dimensional reflectivity structure for automated detection and removal of non-precipitating echoes in radar data. *J. Atmos. Oceanic Technol.*, 19, 673–686.

Sugier, J. C. (2002). Detection and removal of clutter and anaprop in radar data using a statistical scheme based on echo fluctuation. *Proc. of the 2nd European Radar European Conference on Radar in Meteorology, ERAD 2002*, (S. 17-24). Delft, The Netherlands, 18–22 Nov.

Wessels, H. B. (1992). Automatic Suppression of Anomalous Propagation Clutter for Noncoherent Weather Radars. In *Scientific Report WR-92-06.* Royal Netherlands Meteorological Institute (KNMI): De Bilt, The Netherlands.

Operational Hydrological Modelling of Small Watershed using QPE from Dual-Pol Radar in Brazil

Cesar Beneti[1], Roberto V. Calheiros[1], Mino Sorribas[1], Camila Oliveira[1], Leonardo Calvetti[3], Jorge Ruviaro[1], and Reverton Neundorf[1]

[1]*SIMEPAR - Parana Meteorological Service, Brazil*
[2]*UFPR - Parana Federal University, Brazil*
[3]*UFPel - Federal University of Pelotas, Brazil*

(Dated: 22 June 2018)

Abstract: Among other applications, radar-rainfall (RR) and QPE (Quantitative Precipitation Estimation) based on radar reflectivity, dual polarization variables and multi-sensor information, provide important information for land surface hydrology, such as flood forecasting. The Marrecas River watershed (335 km^2) is a head-water catchment of the Iguazu river, located at southwest of Parana state, in southern Brazil. The watershed is predominantly covered by agriculture land, but it was severely channelized close to Francisco Beltrao City where significant flash floods occur during rainfall periods. Historical records indicate that once a year Francisco Beltrao has a flash flood after 5-6 hours of extreme rainfall. Therefore, SIMEPAR (Parana Meteorological Service) developed a flood alert system using rainfall-runoff model forced with RR and QPE, and tipping-bucket observations to forecast river water levels (using rating-curves). In this study, we used hourly dataset from a S-Band dual polarimetric radar with two tropical R(Z) relations based distrometer data, a polarimetric R(Z,ZDR) algorithm from the literature and a multi-sensor approach using radar, satellite and rain gauge. Two hydrological models (Sacramento Soil Moisture Accounting, SAC-SMA; Brazilian SMAP model) were used and calibrated with the Multiobjective Complex Evolution (MOCOM-UA) using observed discharge time-series. Although our previous studies indicated accurate RR-based simulations, in some cases floods were not detected when using catchment-lumped rainfall derived from multi-sensor QPE. In this study we advance further in this subject using improved R(Z,ZDR) relations and QPE for the period of 2016-2017 and flood event-based rainfall-runoff calibration. Thus, we focused model optimization and analyses for major flood events. The Marrecas River has two tributaries in the upper reaches, but all these catchments are ungauged. Hence, the development (and timing) of floods in the Marrecas River can be complex and strongly related to storms spatio-temporal distribution. To explore this aspect, we also perform a first analysis in using RR in rainfall-runoff model with a nested catchment discretization (i.e. semi-distributed), which will be presented in this conference.

1. Introduction

Improved rainfall estimates enhance the potential of radar for many applications such as flood forecasting and management of hydro power generation. In less than 5 years, in Brazil we increased our radar coverage, from 23 single polarization radars to 15 additional dual polarization radars, mainly S-Band, with a concentration in the southern region, an area prone to severe weather, usually related to mesoscale convective systems. This region is responsible for more than 35% of the national hydro power energy generation, directly dependent on precipitation distribution and water availability, and storm events result in disasters related to flood inundation. Polarimetric techniques, which undergo an ever-growing implementation, carry the promise of providing rainfall estimates which are significantly more accurate than those derived from single polarization measurements.

A better representation of rainfall spatial distribution and its uncertainties is crucial for accurate forecasts of river discharges and water levels. Radar estimations of QPE (Quantitative Precipitation Estimation) are very useful information for hydrological applications because of high spatial and temporal resolution improving runoff forecasts and reducing model dependence on unreliable parameter estimates of watershed characteristics. However, radar QPE depends on the calibration, good adjustment with rain gauges and distrometers, data filtering, distance from the radar, orography, signal propagation, among other factors. A multi-sensor integration approach of remote sensing precipitation estimation using meteorological satellites and weather radars with rain gauges improves the accuracy of hydrological models when compared to a model using gauge data only.

1.1. Study area

In this study, we have selected the Marrecas River catchment to evaluate the performance of quantitative precipitation estimates for in rainfall-runoff modeling. The Marrecas River flows in a mostly rural catchment until it enters the city of Francisco Beltrao where it is channelized. Figure 1 presents the area of the catchment in the region. Near the urbanized area, it also receives a major contribution from the Quatorze River, but there are no water level gauges installed in this tributary. The city of Francisco Beltrao grew up beside the Marrecas River and have suffered with occasional inundations due to its major floods.

Over the last 25 years, these floods caused almost 0.5 billion US Dollars in property and crop losses. Between 2013 and

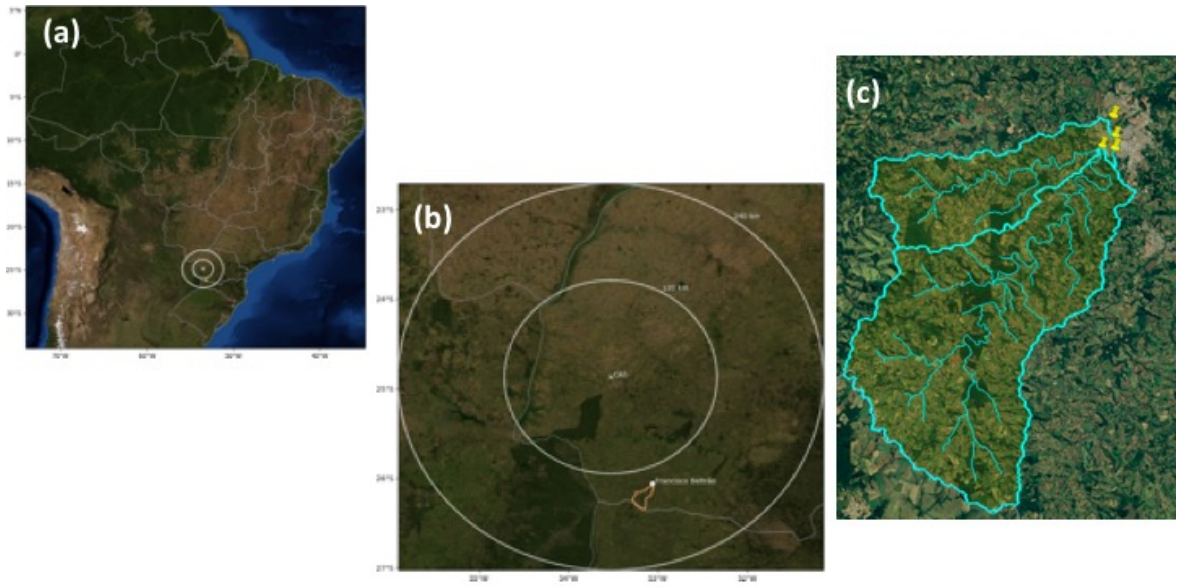


Figure 1: (a) Radar and basin location in South America; (b) Marrecas river basin in radar range and Francisco Beltrao city; (c) Marrecas river basin and rain gauges (yellow markers.



Figure 2: Flooding in Francisco Beltrao city in November, 2017.

2015, three events were recorded bringing great injuries to local properties. In recent years, river floods resulted in economic damages related to overbank inundation but also due to restrictions in the water supply operation during floods. In fact, a recent rainfall event during early November 2017 resulted in a flooding event with peak flow about 230 m^3/s (10 years return period) with a rising limb developing in 2 days (Figure 2).

The watershed area is 335 km^2 and the fast rainfall-runoff response time, between the rainfall and river flow peaks is between 12 to 24 hours. But, larger floods can have full development up to 2 – 5 days. The hydrological network is sparse in the region with rain gauges outside the catchment. Because of such characteristics, an early warning system is vital to prevent even bigger losses.

2. Methodology

In this study, we evaluate the use of rainfall estimates retrieved from radar, multisensor QPE product Calvetti et al. (2017) and tipping-bucket observations in the simulation of a rainfall-runoff at a 335 km^2 river catchment. We used a limited dataset from a S-Band dual polarimetric radar with tropical R(Z) relations based on distrometer data and a polarimetric R(Z,ZDR) and R(Z,KDP) algorithm, following Crisologo et al. (2014). Figures 3 and 4 present sample cases of precipitation estimation with the multisensor QPE product (SIPREC)as well as the polarimetric rainfall estimation obtained from the S-Band and also a distrometric relation for the region of the events. Those accumulations were integrated throughout 2 days during the period of study. The rainfall estimation from the polarimetric weather radar will be used to evaluate the impact of radar data in river basin in Brazil.

At present, various hydrological models have been developed and widely used in water resources planning and flood forecasting. Each model has its specific conceptual formulation, thus the capability to reproduce aspects of the real world depends

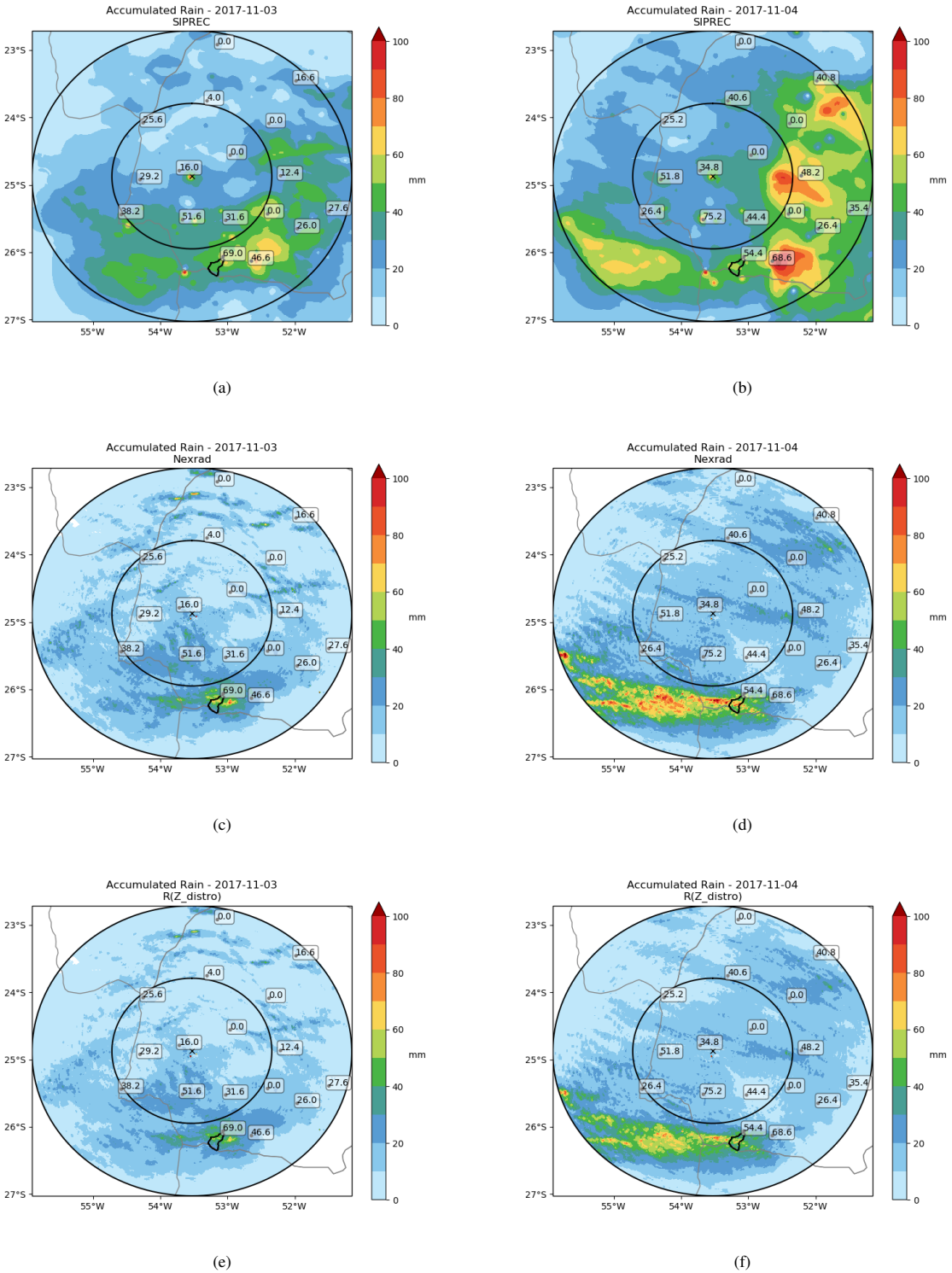
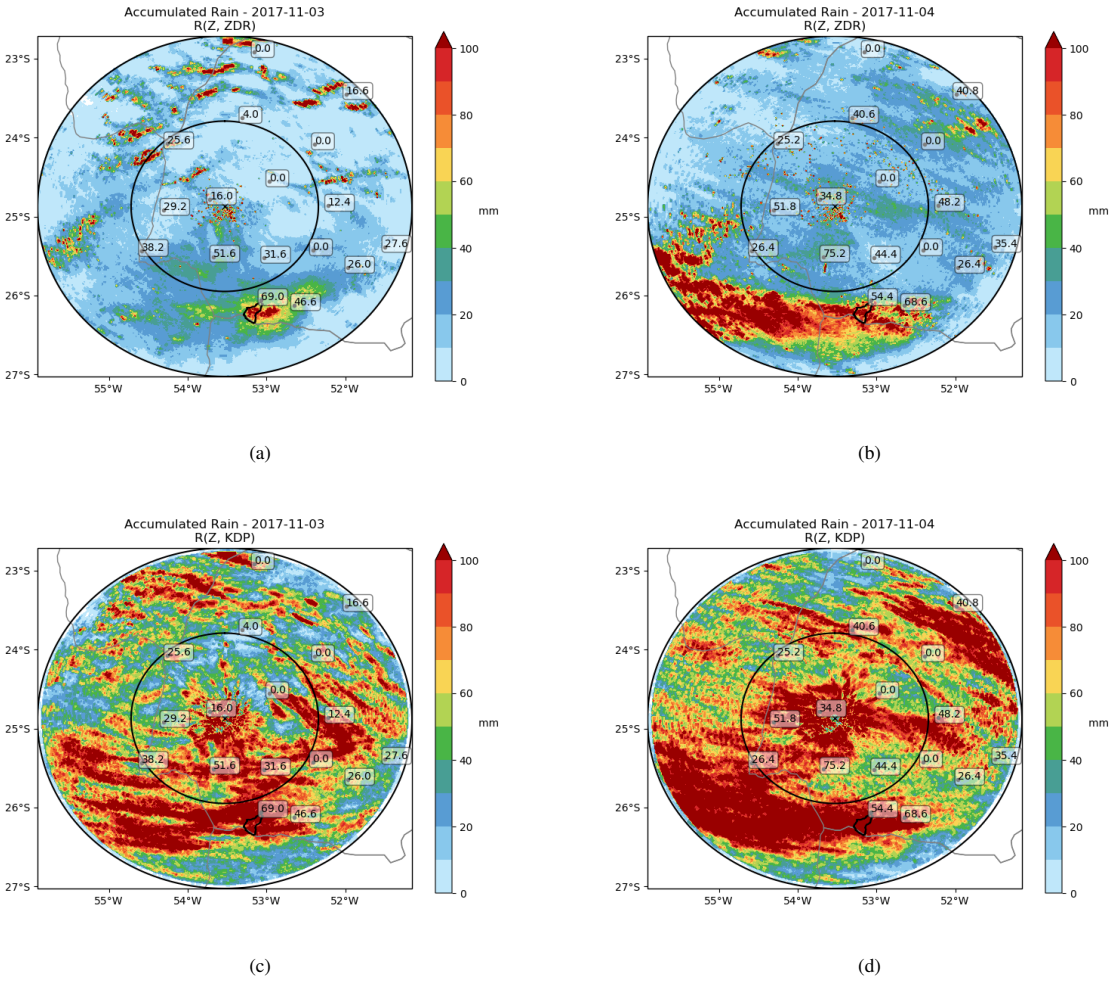


Figure 3: Precipitation estimation in the radar and basin area compared with raingauge daily rainfall accumulation. (a) and (b): Mulsisensor QPE (Calvetti etal 2017); (c) and (d): NEXRAD tropical Z–R; (e) and (f): Distrometric Z–R relationship (Calheiros et al 2018).



(a) (b)

(c) (d)

Figure 4: Precipitation estimation in the radar and basin area compared with raingauge daily rainfall accumulation. (a) and (b): Polarimetriz R(Z,ZDR); and c) and (d): Polarimetric R(Z,KDP).

on the underlying assumptions, but also in input and output measurements that sets model forcing, boundary and initial conditions. The areal precipitation is the dominant input for rainfall-runoff models and is often estimated from interpolation of rain gauge data, derived from remote sensors and radars.

Model performance was assessed for flood events in years 2016 and 2017 (verification and calibration). Hourly data of rainfall and streamflow were used for model calibration using the Multi-objective Complex Evolution (MOCOM-UA, Yapo et al. (1998)). In the multi-objective approach,parameter optimization was defined towards a trade-off between the KGE (Gupta et al. (2009)), logNS (Nash-Sutcliffe of log-transformed discharges) and (error in volume). Finally, other statistics such as Nash-Sutcliff (NS), pearson correlation and RMSE were also evaluated. In order to reduce the sensitivity to initial state variables a dry warm-up period was used and not considered in the model calibration.

Two hydrologic models were selected for this study including the Sacramento Soil Moisture-Accounting model (SAC-SMA, Burnash and McGuire (1973); Duan et al. (1992)) and the Brazilian SMAP (Soil-Moisture Accounting Procedure, (Lopes J.E.G (1982)). These are nonlinear, time-continuous and conceptual rainfall-runoff models, requiring inputs of precipitation and potential evapotranspiration (i.e. Penman-Monteith). The SMAP model is based on the USGS SCS TR-55 model accounting for water balance dynamics and uses tank models for catchment/river routing. The hydrologic models were forced with three different rainfall estimates retrieved from radar, tipping-bucket observations and multi-sensor QPE Calvetti et al. (2017). The SAC-SMA is known to be used operationally for flood forecasting by several weather services including the United States of America. At SIMEPAR, both SAC-SMA and SMAP are operational for flood warning and hydropower operation systems. Nevertheless, the ONS (Operador Nacional do Sistema Eletrico Brasileiro) uses the SMAP model (and adaptations) to support short-range energy planning in many brazilian watersheds.

3. Results

The rainfall-runoff model performance for SAC-SMA and SMAP for the flood events of nov/2017 are summarized in the Table 1. Hence, it was possible to reproduce the large floods with both hydrological models and the four different rainfall estimates. The correlations between observed and simulated discharges was high, in most cases larger than 0.75, and RMSE in the range of 15 and 35 m^3/s is low when compared to flood peaks of 200 m^3/s (return period of 5 years). For the SAC-SMA model simulations the KGE values were mostly between 0.50–0.82 with rainfall retrieved from radar; and 0.93 for the raingauge. In general, model performance was satisfactory for the SAC-SMA and best simulations with rain gauge, R(Z,ZDR) and SIPREC. The results for the SMAP model were also in good agreement with KGE between 0.75–0.94, however, KGE, NS and Pearson were in general larger for R(disdro) and SIPREC than for rain gauge.

Table 1: Rainfall-runoff model performance for SAC-SMA and SMAP - flood events in nov/2017

Forcing	Model	KGE	ΔV (*1e2%)	NS	logNS	PEARSON	RMSE
Raingauge	*SAC-SMA*	0.93	0.01	0.87	0.80	0.93	17.64
	SMAP	0.91	0.00	0.82	0.73	0.91	20.50
R(Z.ZDR)	*SAC-SMA*	0.82	0.02	0.66	0.68	0.82	28.68
	SMAP	0.75	0.01	0.51	0.66	0.75	34.08
R_{distro}	*SAC-SMA*	0.51	0.03	0.56	0.13	0.78	32.42
	SMAP	0.94	0.00	0.89	0.83	0.94	16.48
SIPREC	*SAC-SMA*	0.71	0.00	0.69	0.29	0.83	27.19
	SMAP	0.94	0.00	0.88	0.81	0.94	17.21

Figures 5 and 6 show the observed discharges and simulation results from SMAP and SAC-SMA model runs for a sequence of major flood events during oct-nov/2017. For the SAC-SMA model, it is also possible to verify a good agreement in simulations, although in this case R(Z,ZDR) and raingauge were more reliable. The SMAP was able to reproduce the peak of the two major flood events. It was also possible to see that R(disdro) and SIPREC were in better agreements with the smaller floods. The 100 m^3/s flood in the beginning of oct/16 clearly illustrates uncertainty related to different combinations of rainfall inputs and models.

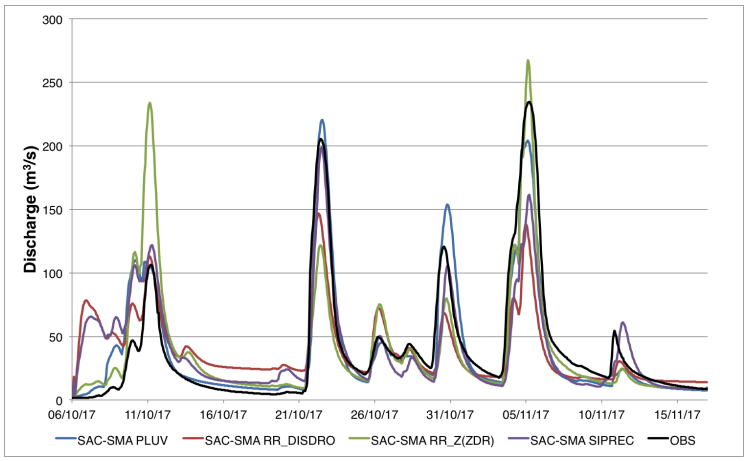


Figure 5: Simulated discharges for flood events in november 2017 with the SAC-SMA model and different QPE

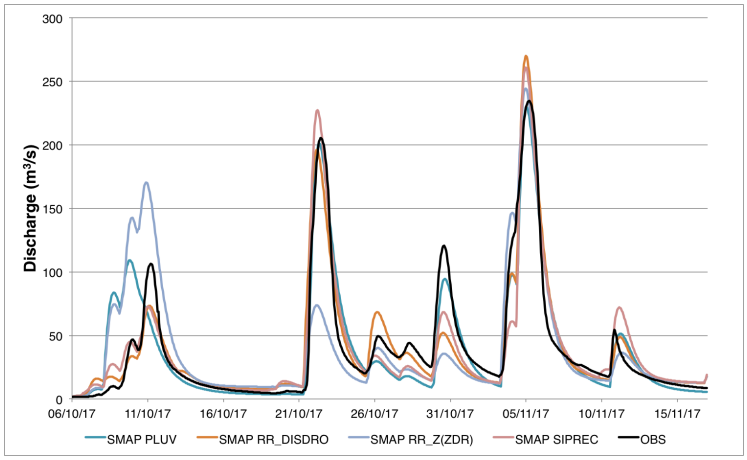


Figure 6: Simulated discharges for flood events in november 2017 with the SMAP model and different QPE

The rainfall-runoff model performance for SAC-SMA and SMAP for the flood events of oct/2017 are summarized in the Table 2. Correlations between observed and simulated discharges was high (>0.71) and RMSE in the range of 15–44 m^3/s, large in relation to the flood peak of 100 m^3/s. For this case, most of the statistics were not satisfactory for this event, as a result from overestimation of discharges. There is general trend in the formation of two convoluted floods in the first days of model runs, associated with rainfall estimates that did not result in real increase of the water level. However, SAC-SMA performed well for rain gauge and R(Z,ZDR) with KGE(NS) of 0.77(0.81). The SMAP model also showed a good agreement for R(Z,ZDR) with KGE(NS) value of 0.68(0.53). Figures 7 and 8 illustrates results for model runs for the oct/2016 flood events.

Table 2: Rainfall-runoff model performance for SAC-SMA and SMAP - flood event in oct/2016

Forcing	Model	KGE	ΔV (*1e2%)	NS	logNS	PEARSON	RMSE
Raingauge	*SAC-SMA*	0.77	0.11	0.59	0.75	0.81	11.97
	SMAP	-0.43	0.92	-1.49	0.44	0.93	21.69
R(Z,ZDR)	*SAC-SMA*	0.77	0.02	0.81	0.39	0.91	5.99
	SMAP	0.68	0.18	0.53	0.38	0.84	9.43
Rdisdro	*SAC-SMA*	-1.47	2.15	-7.06	-2.32	0.71	38.99
	SMAP	-0.20	0.90	-0.94	0.00	0.90	19.11
SIPREC	*SAC-SMA*	-1.92	2.19	-9.07	-1.78	0.87	43.61
	SMAP	-0.64	1.04	-2.14	0.39	0,94	24.35

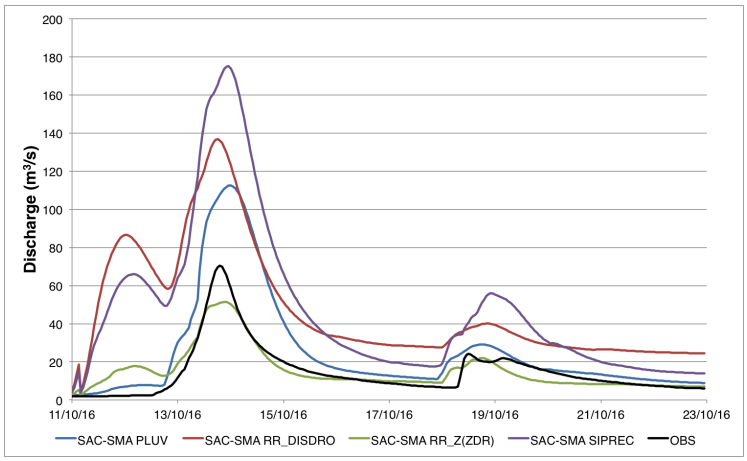


Figure 7: Simulated discharges for flood events in october 2016 with the SAC-SMA model and different QPE

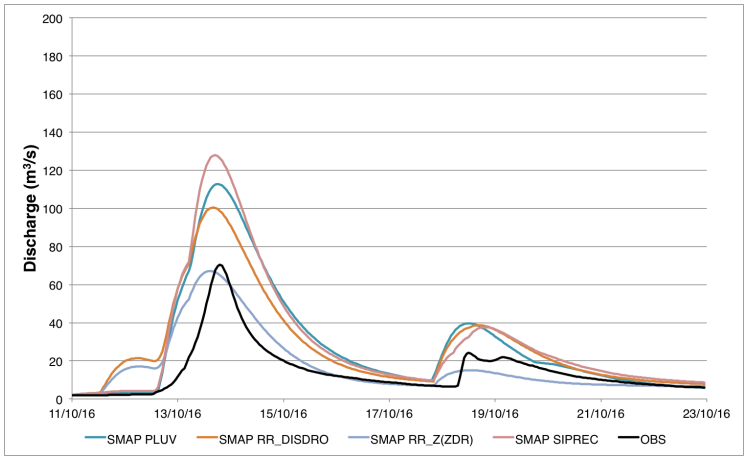


Figure 8: Simulated discharges for flood events in october 2016 with the SMAP model and different QPE

The hydrological processes in the SMAP conceptual model is less complex than the SAC-SMA and can explain, at least partially, the inter-model capabilities. The SMAP model tends to reproduce hydragragh flashiness in smaller catchments, but it is also more sensitive to initial conditions. Since the Marrecas River has peak flows much larger than the mean discharge (10 m^3/s), the multi-objective optimization provided a good balance for both high and low flows forecasts, reproducing the hydrograph variability.

Both SAC-SMA and SMAP simulated river discharges in a realistic manner, but with no clear better estimation in radar-derived rainfall. Even if R(Z,ZDR) showed good agreement in both periods of flood events (oct/2016 and nov/2017), a more conservative approach for flood forecast and alert in the Marrecas River should consider an ensemble of these models. The successful use of rainfall retrieved from radar for rainfall-runoff modeling stresses its potential use in providing reliable rainfall and flood estimates in less-well monitored areas within its range, such as the Quatorze river.

4. Conclusion

In this study we evaluated rainfall-runoff models forced with radar rainfall inputs for river flood prediction. In general, simulations with SAC-SMA and SMAP indicate that tipping-bucket and radar-derived rainfall were both capable to provide reliable to flood prediction in the Marrecas river. The rainfall derived from R(Z,ZDR) provided reliable simulations for the major flood events in oct/2016 and nov/2017. The prediction of catchment runoff in ungauged catchments in the region - such as the Quatorze River - is most likely to benefit from the radar information. Finally, besides the rainfall uncertainty, flood modeling and forecast also depends of the model structure and accuracy of rating curves at high flows.

References

F. R. Burnash, R.J.C. and R. McGuire, “A generalized streamflow simulation system conceptual modeling for digital computers,” Joint Federal-State River Forecast Center, Sacramento, CA, Tech. Rep., 1973.

L. Calvetti, C. Beneti, R. L. A. Neundorf, R. T. Inouye, T. N. dos Santos, A. M. Gomes, D. L. Herdies, and L. G. G. de Goncalves, "Quantitative precipitation estimation integrated by poissonâs equation using radar mosaic, satellite, and rain gauge network," *Journal of Hydrologic Engineering*, vol. 22, no. 5, p. E5016003, 2017.

I. Crisologo, G. Vulpiani, C. C. Abon, C. P. C. David, A. Bronstert, and M. Heistermann, "Polarimetric rainfall retrieval from a c-band weather radar in a tropical environment (the philippines)," *Asia-Pacific Journal of Atmospheric Sciences*, vol. 50, no. 1, pp. 595–607, 2014. [Online]. Available: https://doi.org/10.1007/s13143-014-0049-y

Q. Duan, S. Sorooshian, and V. Gupta, "Effective and efficient global optimization for conceptual rainfall-runoff models," *Water Resources Research*, vol. 28, no. 4, pp. 1015–1031, 1992.

H. V. Gupta, H. Kling, K. K. Yilmaz, and G. F. Martinez, "Decomposition of the mean squared error and nse performance criteria: Implications for improving hydrological modelling," *Journal of Hydrology*, vol. 377, no. 1, pp. 80 – 91, 2009. [Online]. Available: http://www.sciencedirect.com/science/article/pii/S0022169409004843

C. J. Lopes J.E.G, Braga B.P.F, "Smap - a simplified hydrological model," in *Applied Modelling in Catchment Hydrology ed. V.P.Singh, Water Resourses Publications.*, 1982.

P. O. Yapo, H. V. Gupta, and S. Sorooshian, "Multi-objective global optimization for hydrologic models," *Journal of Hydrology*, vol. 204, no. 1, pp. 83 – 97, 1998. [Online]. Available: http://www.sciencedirect.com/science/article/pii/S0022169497001078

Paired Distrometric Measurements in the South of Brazil: Wind Effects and Sampling Uncertainties

Roberto V. Calheiros [1], Cesar Beneti[1], Camila Oliveira[1,2], and Leonardo Calvetti[3]

[1]*SIMEPAR - Parana Meteorological Service, Brazil*
[2]*UFPR - Parana Federal University, Brazil*
[3]*UFPEL - Federal University of Pelotas, Brazil*

(Dated: 22 June 2018)

1. Introduction

Drop size distribution (DSD) is basic for the analysis of the microstructure of rainfall, which is of primary importance for the remote sensing of precipitation. As well, DSD plays an important role e.g. in precipitation physics, numerical weather and hydrological modeling, telecommunications, agricultural and soil sciences. Reliable measurements of DSD are basic to the understanding of the microstructure of rainfall at a more advanced level of analysis.

Measurements of DSD are usually performed at ground level using distrometers; the OTT Parsivel instrument is one of the distrometers most widely used in validation and comparison of weather radars, which is the application of interest in this study. In fact, when distrometer is used in radar calibration, errors in the measurements can have a significant impact, e.g. in the coefficient and exponent of the derived relationships between rain rate and radar variables. DSD measurements are affected by uncertainties resulting from both the natural variability of rainfall and the sampling fluctuations, a situation inherent to the measurement of any physical process.

At a more advanced level of an analysis, these uncertainties must be considered quantitatively. In this paper the approach of Jaffrain and Berne (2011) is followed to characterize and quantify the sampling uncertainties in the measurements from OTT Parsivel distrometers deployed in the State of Paraná, Brazil. These instruments are associated with the operations of two long-range S band radars (TXS: 25.5053^{o}S, 50.3613^{o}W and CAS: 24.8700^{o}S, 53.5293^{o}W) covering regions of high socio-economical relevance with outstanding agro-industrial activities and energy production. In fact, these radar survey an area where more than 33% of the hydro-power energy in the country is generated.

In a previous work (Calheiros et al., 2017) the compatibility of the distrometer measurements with those from the radars and collocated rain-gages was verified. In section 2 the instrumental measurement setting and data characterization are presented. Wind impact on the measurements is explored in section 3; while results are presented in sector 4. Section 5 closes the paper with a summary, ongoing work, and conclusions.

2. Instrumental Setup and Data Processing

For the present work, available data were from two paired OTT Parsivel distrometers (hereafter DR1 and DR2) which were disposed perpendicularly to each other, in the N-S and E-W directions, as shown schematically in Fig. 1.

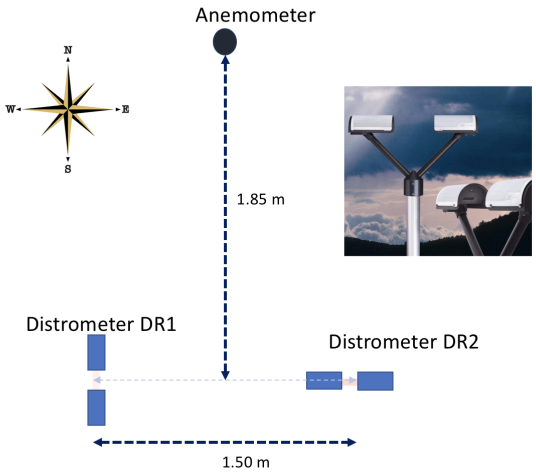
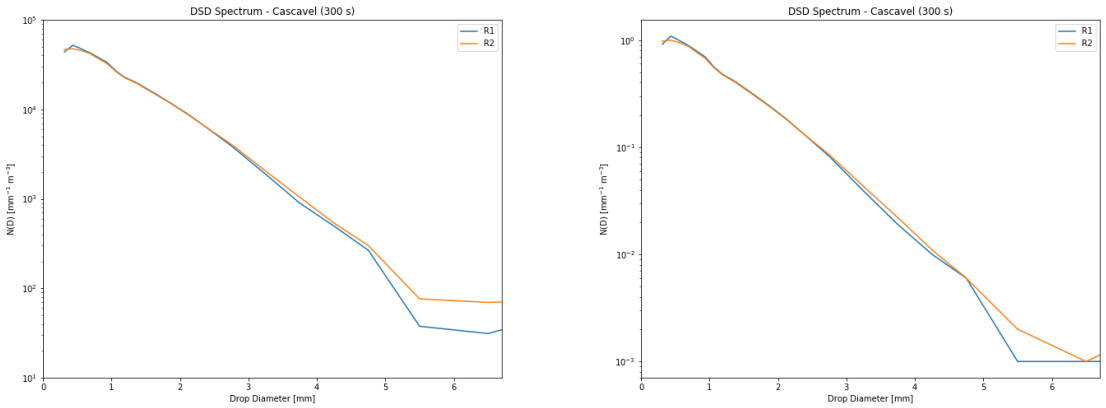


Figure 1: Schematic instrumental setup of the paired distrometers DR1 (N-S) and DR2 (E-W).



(a) (b)

Figure 2: DSD spectra from DR1 and DR2 measurements for a time resolution of 300s (a) over the dataset period and (b) as an average over the period (21 Feb 2014 to 07 Aug 2014).

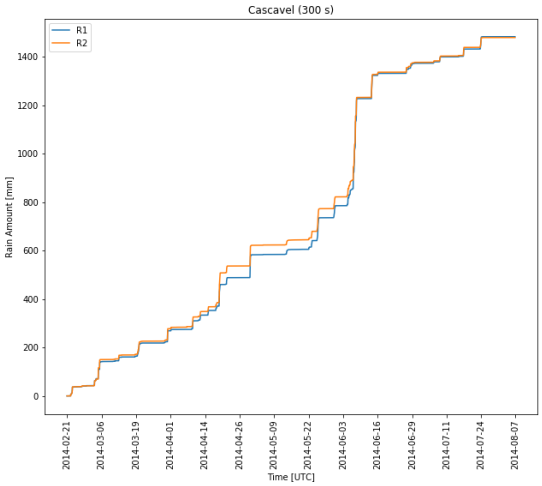


Figure 3: Rainfall from DR1 and DR2 at 300 s time resolution accumulated over the dataset period.

The instruments were collocated with the CAS radar. The dataset available from paired operations of the distrometers covered the period from 21 February 2014 to 07 August 2014 and data were recorded at a time resolution of 60 s in 32 diameter classes and 16 velocity classes. In Fig. 2 the DSD spectra measured by DR1 and DR2 at a time resolution of 300 s is shown.

DR1 spectrum shows a number concentration of drops slightly smaller than that from DR2, for a size diameter of about 2.5 mm and larger. Comparatively, the corresponding spectra from Jaffrain and Berne (2011) show the slight difference from a size diameter of 1.8 mm up to 5 mm). Fig. 3 present the rainfall accumulated by DR1 and DR2 during the dataset period, which amounts to approximately 1480 mm.

A comparison between the rain rates from DR1 and DR2 (R1 and R2 respectively) is presented in the scatterplot of Fig. 4.

In the previous work (Calheiros et al., 2017) before mentioned rain rates from DR1 covering a longer period at 900 s time resolution were compared to a collocated rain gage with comparable results. Time sequence of the differences R1-R2 covering the whole dataset period is presented in Fig. 5.

Characterization of the rainfall (Tokay et al., 2005) was performed based on seven major events selected from the study period and is presented in Table 1.

The scatterplot of the percent total difference of the rainfall accumulated by each distrometer (from RainTotal column in Table 1) in each event as a function of maximum rain rate is shown in Fig. 6.

There is indication of a possible trend, without considering event 6 which features an exceptional duration and extreme rainfall rate of 238 mm/h. It should be noted that Tokay et al. (2005), while working with a substantially higher number of

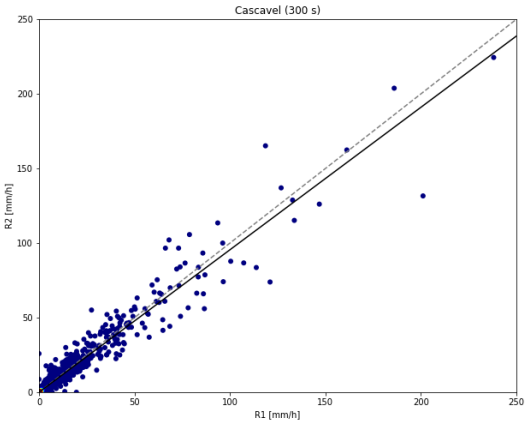


Figure 4: Dispersion diagram of rain rate R1 vs rain rate R2 at 300 s resolution, from measurements with DR1 and DR2, respectively.

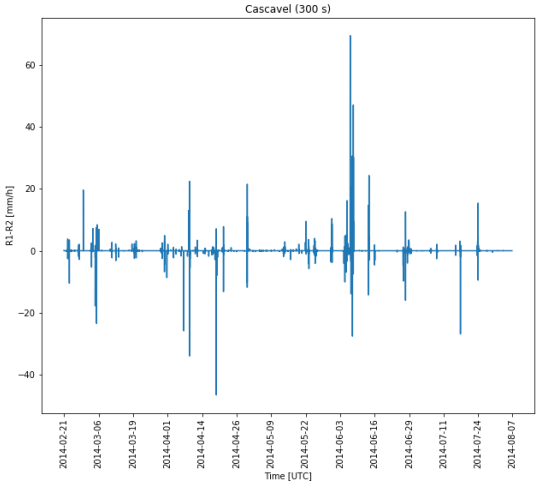


Figure 5: Temporal evolution of the difference between the 300 s resolution rain rates R1 and R2 covering the dataset period.

Table 1: Characterization of rainfall over DR1 and DR2 for seven major events during the dataset period.

Event	Date	Start Time (UTC)	End Time (UTC)	Rainy Minutes	Max Rain Rate (mm/h)	Rain Total (mm)	$\lvert\Delta R_{total}\rvert$
1	05/03/14	17:35	18:10	40 – 40	96.6	28.6 – 31.5	2.9
2	09/04/14	16:05	20:10	250 – 245	102.1	32.1 – 37.5	5.4
3	19/04/14	09:40	20:10	560 – 565	165.2	88.9 – 121.9	33.0
4	30/04/14 – 01/05/14	20:00	09:10	600 – 565	137	94 – 85.2	8.8
5	07–08/06/14	09:00	17:15	1400 – 1395	238.1	371.4 – 339.8	31.6
6	14/06/14	01:00	10:15	540 – 540	68.5	95.8 – 94.9	0.9
7	17-18/07/14	18:50	04:00	400 – 405	105.7	30.1 – 33.6	3.5

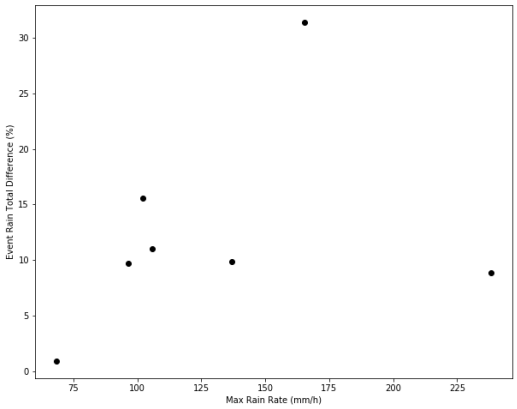
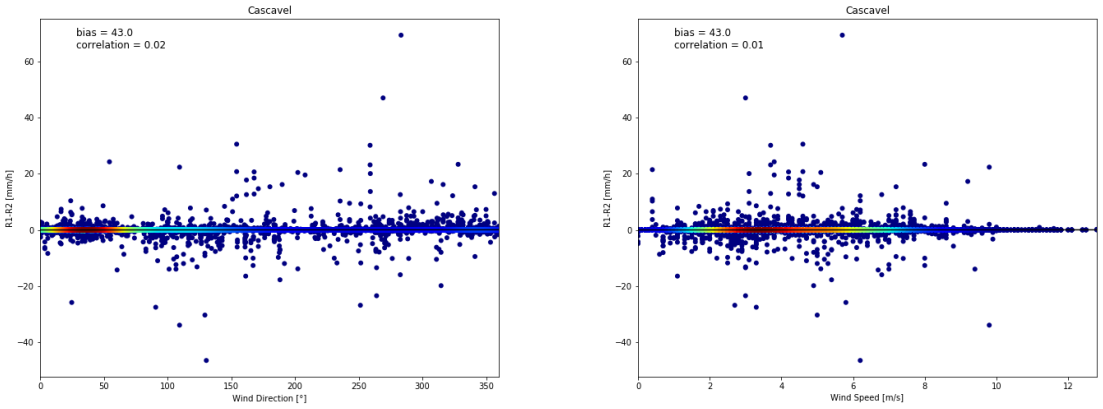


Figure 6: Scatterplot of percentual difference between the accumulated rainfall from DR1 and DR2 for the events in Table 1 as a function of maximum rain rate for the event.



(a) (b)

Figure 7: Difference between R1 and R2 (rain rates from DR1 and DR2, respectively) as a function of wind direction (a) and wind speed (b).

events, point out that "interestingly" such trend was not identified. Also, in comparisons with their work, it should be noted that they used a different kind of distrometer, i.e., the JW impact instrument.

3. Wind Effects

Scatterplots of R1-R2 vs wind direction and wind speed, as shown in Fig. 7 (a) and (b), were elaborated which have shown correlations coefficients of 0.02 and 0.01, respectively. These values are comparable to those of Jaffrain and Berne (2011) who obtained correlation coefficients of -0.05 and -0.08.

While, in general, these results do not indicate a significant influence of the wind on the difference between the measurements from the distrometers, the noticeable number of cases featuring substantial deviations prompted further investigation, in the context of this preliminary work. A first verification following the work of Tokay et al. (2005) considering whole events was performed by taking the events characterized in Table 1 and elaborating a scatterplot of the percent total differences of rainfall accumulated by DR1 and DR2 vs the mean wind speed for each event, as depicted in Fig. 8.

While impaired by the small number of events when compared with theirs, the percent differences obtained in the present work are compatible with those for most (80%) of their events. As shown in the scatterplot six of the seven events presented percent differences in the total accumulation under 20%; for the remaining event percent difference was 23%. A second verification was undertaken, now for individual cases of 300 s time resolution rain rates, i.e. R1 and R2, selected from the seven events of Table 1. Cases are characterized in Table 2. Only cases of high rain rates equal to or exceeding 90 mm/h and with a percent difference between R1 and R2 exceeding 10% were selected.

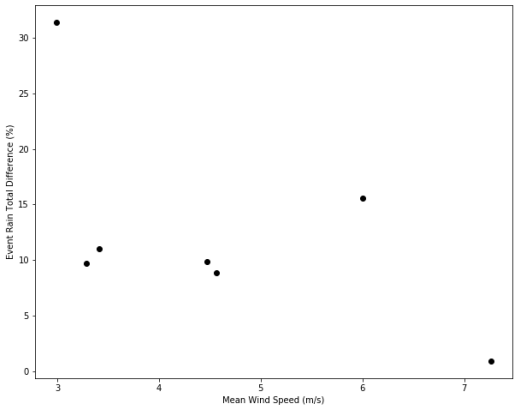
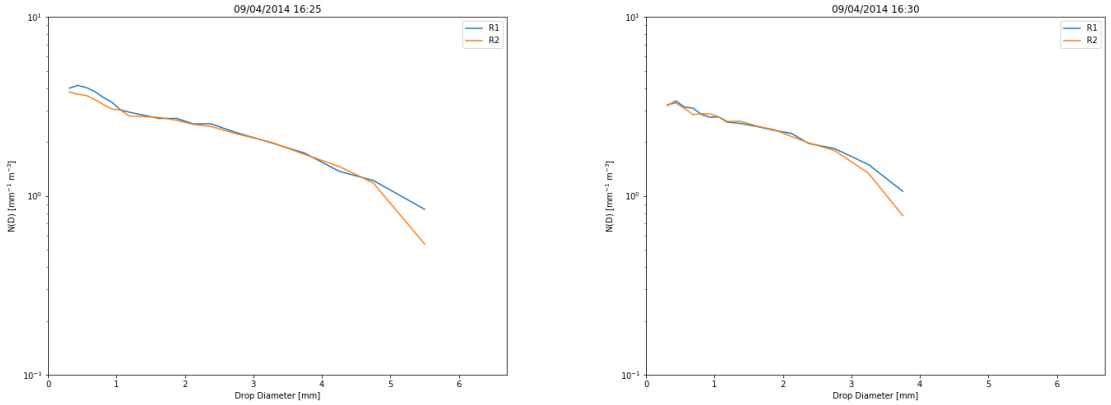


Figure 8: Scatterplot of percentual difference between the accumulated rainfall from DR1 and DR2 for the events in Table 1 as a function of mean wind speed for the event.

Table 2: Cases of rainfall at 300 s resolution from the seven major events in Table 1 when rain rate was equal to or bigger than 90 mm/h and percent difference between R1 and R2 exceeded 10%.

Case	Date	Rmax (mm/h)	Wind Direction (°)	Gust Wind (m/s)	|R1-R2| (%)
1	05/03/14 17:50	96.6	264.1	9.1	27.7
2	09/04/14 16:25	102.1	109.5	14.5	40.0
3	09/04/14 16:30	96.5	109.5	14.5	26.3
4	19/04/14 10:10	113.5	314.7	19.1	19.2
5	19/04/14 12:20	165.2	130.5	9.3	32.8
6	19/04/14 12:50	96.6	129.4	8.3	37.3
7	07/06/14 10:20	201.1	283.3	11.1	41.8
8	07/06/14 17:30	107.2	202.3	8.8	21.1
9	07/06/14 20:40	146.8	168.0	6.7	15.2
10	07/06/14 20:45	133.7	168.0	6.7	14.9
11	08/06/14 04:45	100.4	162.0	7.8	13.4
12	08/06/14 13:35	121.0	269.2	5.0	48.3
13	08/06/14 14:55	113.8	259.0	7.9	30.6
14	17/07/14 22:50	105.7	251.4	8.2	29.2



(a) (b)

Figure 9: DSD spectra for 300 s time resolution from DR1 and DR2 for (a) 09/04/2014 at 16:25 and (b) 16:30h LT (UTC).

Table 3: Relative sampling uncertainty σ_ϵ and σ_ω (relative) as defined in Jaffrain and Berne (2011) for the paired DR1 and DR2 (one collocated distrometer) as a function of time resolution for rain rate values in the interval [0.1, 2] mm/h.

Time Step	σ_ϵ	σ_ω
60	0.24	0.34
300	0.21	0.29
600	0.16	0.23
900	0.12	0.17

In 79% of the cases, the angle between the wind direction and the direction of the distrometer laser beam axis (N-S for DR1 and E-W for DR2) varied between 6°and 22°, i.e. the wind was nearly aligned with one the beams. In 71% of the cases, in which the percent difference |R1-R2| was varying between 19% and 41.8%, gust winds varied between 7.9 and 19.1 m/s. In their paper Friedrich et al. (2013) explore the influence of strong winds on the quality of Parsivel measurements, based inclusive on data from convective thunderstorms during the VORTEX2 experiment. They investigate an artifact characterized by a large concentration of raindrops with large diameter and unrealistic fall velocities, which is correlated to high wind speeds. Regarding the VORTEX2 data they report that in strong winds, i.e. > 7m/s large particles with size diameter > 6 mm are characteristic in the histograms. They comment that in addition to wind speed, the wind direction in relation to the laser beam axis orientation may also affect measurement. Also, they inform that the manufacturer recommends that the Parsivel be oriented with the laser beam axis perpendicular to the wind. In an early verification, in the context of the present study, a set of spectra from DR1 and DR2 from two cases in Table 2, e.g. 09/04/2014 at 16:25 h UTC and 16:30 h UTC, were generated. Mean wind speed was 9.8 m/s and wind gust was 14.5 m/s; percent differences between distrometer rain rates were 40% and 26.3% respectively. Spectra are shown in Fig. 9 (a) and (b); it is noted that larger raindrops size diameter goes from about 5.5 mm to about 3.8 mm and the number concentration decrease throughout the full range of size diameters as the maximum rain rate goes from 102.1 mm/h to 96.5 mm/h to 21.3 mm/h (not shown) and the wind speed goes from 9.8 m/s to 7.2 m/s (not shown) and wind gusts from 14.5 m/s to 11.0 m/s (not shown).

4. Sampling Uncertainty Results

For quantification of the sampling uncertainty the moments of DSD, i.e. rain rate R and ZH (radar reflectivity at horizontal polarization) were used (Tokay et al., 2002, 2005). ZH and ZDR were computed for S band. The methodology of Jaffrain and Berne (2011) was followed and, as in Tokay et al. (2005), it was considered that DR1 and DR2 sample the same population of droplets. The relative sampling uncertainty , as defined by the authors (see their Eq. 14), is calculated for R considering one collocated station (see their Fig. 9), which is the case in this study, for the same R interval as theirs, for different values of time resolution; results are presented on Table 3.

The computation of the relative sampling uncertainty is then extended to different classes of R up to 90 mm/h, covering most of existing values of rain rate. Results are presented as a set of curves of uncertainty as a function of class and time resolution. Class width was defined to include a minimum of 30 samples, considering a reliable quantification of the uncertainty. Since time resolution affects substantially the relative uncertainty several values were used from 60 s (as set in DR1 and DR2) to 2000 s. Because of assumptions of Gaussian distribution in the methodoly of Jaffrain and Berne (2011) a verification was performed using one class of R, for a specific time resolution, as shown in Fig. 10.

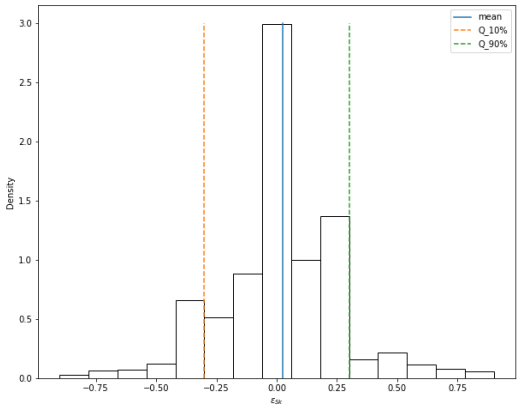


Figure 10: Rain rate value distribution for the interval [0.1, 2] mm/h at a time resolution of 60 s.

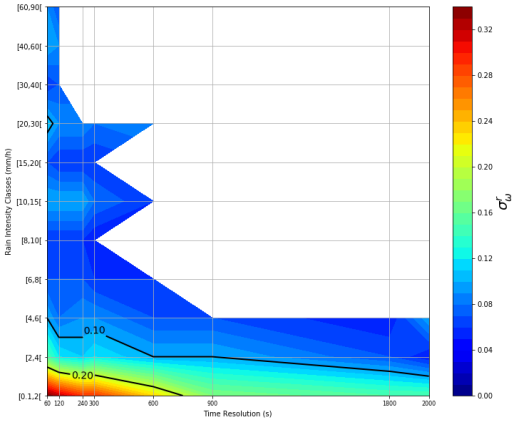


Figure 11: Relative sampling uncertainty for estimates of rain rate as a function of rain rate and time resolution.

Similarly to the finding of the authors, the assumption looks acceptable. The results for the sampling uncertainty on R estimates are shown in Fig. 11.

The relative sampling uncertainty varies between about 4% and 34%. In general, it increases with the increase of the order of the class and the increase of time step. There are three relatively small inhomogeneity areas in this general pattern for time resolution between 60s and 300s. The first is around the 15 mm/h level line where uncertainty rises to 10%, the second is around the 30 mm/h level where uncertainties exceeds 10%, and the third is around the 60 mm/h level line from time resolution of 60s to 120s where uncertainty is again 10%. For time step of 300s and lower the uncertainty is below about 10%-11% for all R values above approximately 5-6 mm/h and between about 10% and 34% from 5-6 mm/h down to the lowest rain rate. From time step of 300s and higher the general pattern of decreasing uncertainty with increasing rain rate and increasing time step is followed Fig. 12 shows the relative sampling uncertainty associated to the estimates of radar reflectivity at horizontal polarization (ZH), for the indicated classes of reflectivity (dBZ) and time resolution.

The sampling uncertainty isoline of 5% descends gradually from 25 dBZ to 20 dBZ, from time resolution of 60s to 120s. Uncertainty increases to about 19% at the 10 dBZ level line for all values of time resolution. Down from 10 dBZ to the 0 dBZ level line the uncertainty increases to about 50%-60% for all time resolution. Above about 10 dBZ, the general pattern shows a decrease of uncertainty from 19% to less than about 3%. There is a relatively small inhomogeneity in this pattern, in the upper portion of the map, from about 35 dBZ to 40 dBZ and from time resolution of 600s to 1800 s, where uncertainty increases to about 4%-5%.

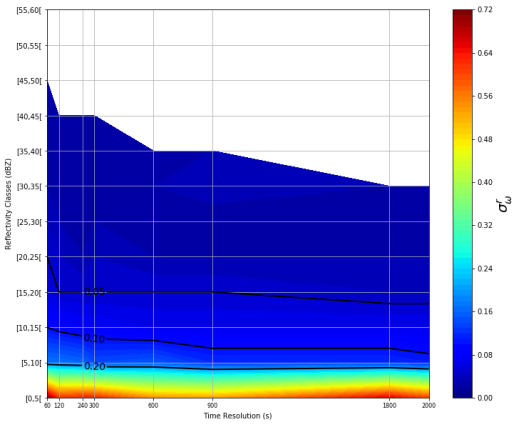


Figure 12: Relative sampling uncertainty for estimates of radar reflectivity ZH from **[DR1, DR2 > definir]** *at S band as a function of ZH and time resolution.*

5. Comments and conclusions

The Parsivel distrometer is one of the instruments for measurements of DSD at the ground level most widely used as a support to calibration of weather radars. Differences in the distrometer measurements affect the coefficient and exponent of the derived radar rainfall algorithms. The quantification of the variability of DSD measurements is of paramount importance for radar based precipitation estimation, among other environmental applications. The variability resulting from the sampling process of DSD measurement must be taken into account for a reliable quantification of the variability of DSD. This issue is dealt with in this study following Jaffrain and Berne (2011), is based on a dataset from a different climate and extends their work to heavy precipitation. Wind effects were considered and while in general influences were not significant, a noticeable number of cases with substantial differences led to further verification. Rainfall characterization was performed with major events and differences between distrometer measurements from the events as a function of mean wind speed were mostly within 20%, a result comparable to Tokay et al. (2005). Individual cases within the events, with high rain rates and significant differences between the measurements from the distrometers, were considered. In 71% of the cases the wind direction and the long axis of the distrometer were nearly aligned, and wind gusts were between 7.9 m/s and 19.1 m/s. DSD spectra for two selected sequential cases from the major events, featuring high wind speeds and differences between distrometer measurements were verified. It is noted that larger drops size diameter decreases from approximately 5.5 mm to 3.8 mm when rain rates and wind speeds decrease significantly. The relative sampling uncertainty related to the estimates of rain rate (R) and reflectivity at horizontal polarization (ZH) were quantified. For R the uncertainty ranged from approximately 4% to 32%; the general pattern is of decreasing uncertainty with increasing values of rain intensity and increasing time resolution. Uncertainty is below about 11% for a time resolution of 300 s and lower and for rain rate at or above 5 to 6 mm/h; for rain rates below 5 to 6 mm/h and 0.1 mm/h uncertainty is between 10% and 34% There are three inhomogeneity areas in the general pattern between time step of 60 s and 300 s, at around 15 mm/h with uncertainty of about 10%, at around 30 mm/h with uncertainty exceeding 10% and at around 60 mm/h from time step of 60 s and 120 s with uncertainty of 10%. For ZH the uncertainty varied between about 3% and 60%. The general pattern shows uncertainty gradually decreasing with increasing ZH and for all time steps, from 19% at the 10 dBZ level to about 3%. Between about 10 dBZ and 0 dBZ level lines uncertainty increases to about 50-60. There is a relatively small inhomogeneity in the uncertainty map within about 35-40 dBZ and 600–1800 s. The preliminary results regarding wind effects suggest that further investigation should be undertaken. The patterns of sampling uncertainty maps for R and ZH are, in general, comparable. The maps are, on the whole, compatible with the corresponding maps of Jaffrain and Berne (2011). The results related to the quantification of uncertainty suggest that the extension of their approach to the heavy rainfall in this study is valid. On going work includes exploring a larger number of events and cases for wind effects and quantification of uncertainty for ZDR and KDP.

References

R. V. Calheiros, C. Oliveira, C. Beneti, and L. Calvetti, "Distrometric Drop Size Distribution in South Brazil: Derived Z–R Relationships and Comparisons with Radar Measurements," in *38th Conference on Radar Meteorology*, 2017, p. Paper 1.1.

K. Friedrich, S. Higgins, F. J. Masters, and C. R. Lopez, "Articulating and stationary parsivel disdrometer measurements in conditions with strong winds and heavy rainfall," *Journal of Atmospheric and Oceanic Technology*, vol. 30, no. 9, pp. 2063–2080, 2013.

J. Jaffrain and A. Berne, "Experimental quantification of the sampling uncertainty associated with measurements from parsivel disdrometers," *Journal of Hydrometeorology*, vol. 12, pp. 352–370, 2011.

A. Tokay, A. Kruger, W. F. Krajewski, P. A. Kucera, and A. J. Pereira Filho, "Measurements of drop size distribution in the southwestern amazon basin," *Journal of Geophysical Research*, vol. 107, no. D20, 2002. [Online]. Available: https://doi.org/10.1029/2001jd000355

A. Tokay, P. G. Bashor, and K. R. Wolff, "Error characteristics of rainfall measurements by collocated joss waldvogel disdrometers," *Journal of Atmospheric and Oceanic Technology*, vol. 22, no. 5, pp. 513–527, 2005. [Online]. Available: https://doi.org/10.1175/JTECH1734.1

Tracking small unmanned aerial vehicles using weather radar

Krzysztof Orzeł[1], David Pepyne[1], Sean Turner[1], Jezabel Vilardell Sanchez[1], Apoorva Bajaj[1], Michael Zink[1], and Stephen Frasier[1]

[1]*University of Massachusetts, Amherst, MA 01003, USA*
(Dated: 22 June 2018)


Krzysztof Orzeł

1. Introduction

The Federal Aviation Administration (FAA) estimates that by 2021 as many as six million small Unmanned Aerial Vehicles (sUAVs) or micro-drones could be in U.S. skies. This trend has been driven by the ease of regulations, availability of low-cost micro-drones, capabilities such as aerial reconnaissance and maneuverability, innovative uses of these systems, such as inspections of pipelines and utility lines, law enforcement and package delivery. At the same time, however, micro-drones increasingly have been creating problems that jeopardize public safety, business continuity and privacy concerns. Drone safety incidents, including flying improperly, or getting too close to other aircraft, now average about 250 a month (Levin, 2017). A counter-drone industry has developed around drone surveillance, or the monitoring and tracking of non-cooperative sUAVs (Holland-Michel, 2018).

The Center for Collaborative Adaptive Sensing of the Atmosphere (CASA) at the University of Massachusetts, Amherst has pioneered the innovative use of X-band dual polarization weather radar to detect, classify and track sUAVs (Orzel et al., 2017). Since most sUAV parts are made of carbon fiber, plastic and styrofoam, this class of drones is characterized by a very small radar cross section (RCS) between -30dBsm and -10dBsm (Schroder et al., 2015)(Chenchen and Hao, 2016). SUAVs exhibit a characteristic micro-Doppler signature that can be used for detection and for discrimination from avian targets such as birds (Werth, 2016). Tracking drones or birds, either in software or visually on a display, also requires a very fast update rate on order of 5 seconds. This necessitates the use of next generation multi-function phased array radar (MPAR) (Stailey and Hondl, 2016) or low-power radar network (Adams, 2018).

The radar being used in this project is a Phase Spin Weather Radar (PSWR) (Orzel and Frasier, 2018), which is located on campus of the University of Massachusetts at Amherst. PSWR is a dual polarization, X-band, 1D phased array radar. Dual-polarization is a current standard in weather radar industry and can be used to improve target classification (Torvik et al., 2016). PSWR in its current configuration is able to perform simultaneously a full 360 degree mechanical scan in the azimuth and a 90 degree (ground to zenith) electronic scan in the elevation. Hence a complete coverage of airspace can be achieved and the site revisit time is significantly reduced. Due to the size of an antenna and the transmitter power weather radars are well equipped to detect small airborne targets. On the other hand range resolution on order of 50-150 meters impedes radar ability to operate in the multi-target scenario such as drone swarms.

The rest of this paper is organized as follows. Section 2 focuses on the detection and classification techniques used in this work. In section 3 the results from different drone flight tests will be presented and the performance of a tracking algorithm will be compared to the UAV GPS log. Section 4 presents conclusions and recommendations for future work.

2. Detection and classification

Mechanical vibrations or rotations of structures on a target introduce frequency modulation on the radar return known as the micro-Doppler phenomenon (Chen et al., 2006). It can be expected that the signature of a multi-rotor UAV is related to the signature of a helicopter. For a helicopter the spectral signature is composed of a strong but narrow main body (ie fuselage and hub) Doppler component, which corresponds to the velocity of the helicopter and a much wider, but weaker Doppler components contributed by the rotating blades. Chen (2011) provides formula for a maximum Doppler shift induced by a rotating blade:

$$\begin{aligned} V_{tip} &= 2\pi L\Omega \\ f_{D_{max}} &= (2V_{tip}/\lambda)cos\beta \end{aligned} \tag{2.1}$$

where the velocity of the blade tip V_{tip} is a product of blade length L and rotation rate Ω. The maximum Doppler shift $f_{D_{max}}$ is scaled by a radar wavelength λ and the elevation angle β. A popular commercial drone, that crashed on the grounds of the White House (Shear and Schmidt, 2015), has a blade radius of 12 cm and rotation rate between 100 (hover) and 150 (max speed) revolutions per second, which results in a maximum Doppler shift of 4.95 and 7.43 kHz respectively. Thus, the

Table 1: Pseudocode for I,Q signal processing.

1. Get I,Q samples for current dwell and apply pulse compression. For the experiments the PSWR was operated in an alternating dual-polarization mode, 128 pulses per dwell (64 at each polarization) were collected at a PRF of 3000 Hz (1500 Hz per polarization). Given the X-band transmit frequency, this gives a Doppler velocity range of $\pm 12 m/s$ per polarization.
2. Calculate the micro-Doppler spectrum for each polarization using the modified periodogram method with a Hann window.
3. Implement 1D CA-CFAR in range for each spectral coefficient. This gives a pattern of detections for each range gate that represents the locations of the peaks in the micro-Doppler spectrum.
4. Use the pattern of detections in each range gate to decide if a "drone signature" is present. One way to do this is simply to count the number of detections in a range gate and announce detection when the count exceeds a certain threshold. Due to folding we expect spectral components induced by rotating blades in each Doppler gate (subject to signal to noise ratio). This can effectively isolate drones from other targets like birds, clutter, planes, and cars which tend to give a pattern of detections with a very small count. We also note that this technique can to some degree detect slow moving drones in clutter when the blade signatures are visible to either side of the clutter spike.
5. Report target (range gate, azimuth, time and number of detections in a range gate) to a down stream tracker.

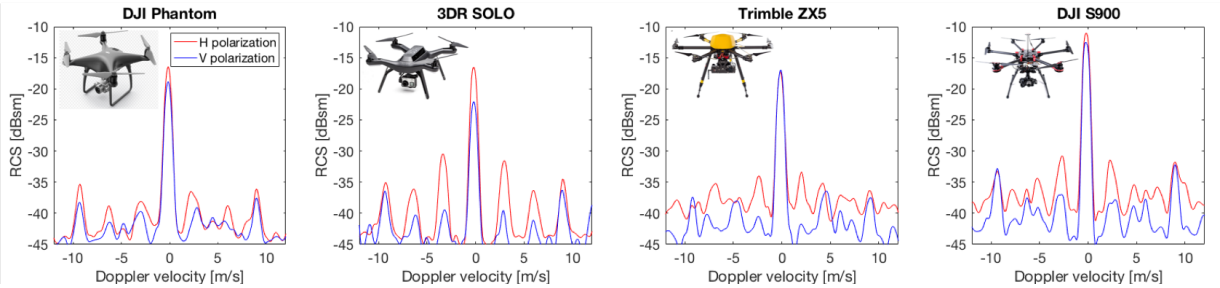


Figure 1: Micro-Doppler signatures of different UAV targets.

Nyquist sampling rate on order of 15 kHz is required. This is not feasible with the operational long-range weather radar and as a consequence folding in Doppler spectrum is expected.

In our study 4 different UAVs were examined: 2 quadcopters (DJI Phantom 4 and 3DR Solo) and 2 hexacopters (Trimble ZX5 and DJI S900). Each UAV micro-Doppler signature was aligned to the zero-Doppler velocity bin and then multiple measurements were accumulated in order to average out the RCS aspect angle dependence. The mean signatures are presented in Figure 1 and the key parameters are listed in Table 2. We note that horizontal polarization is preferable for drone detection. It provides higher measured main body RCS in 3 out of 4 cases. This was verified by Chenchen and Hao (2016) in their investigation of the dependence of RCS on polarization. They noted that the return strength from the battery pack has decreased, but the return strength from the drone motors have increased when horizontal- instead of vertical polarization was utilized. Ritchie et al. (2015) reported that significantly different RCS values (up to 30 dB in flashes at $f_c = 10GHz$) of rotating DJI blades can be expected for horizontal and vertical polarizations. The micro-Doppler signature is more prevalent in H-channel, although for DJI Phantom the difference is subtle to notice. All UAV signatures are symmetrical, while bird signature tends to be asymmetric (de Wit et al., 2014). The biggest UAV (ie DJI S900) exhibits the highest RCS as expected. The main body RCS is between -10 and -20 dBsm, which is in a good agreement with previously reported values. The micro-Doppler components in the spectrum are between -45 and -30 dBsm. In general, the micro-Doppler signature can be effectively used for target classification, if sufficient system sensitivity can be guaranteed.

Several researchers (Molchanov et al., 2013)(de Wit et al., 2014) proposed short time Fourier transform (STFT) based methods for UAV feature extraction. Oh et al. (2018) provides a thorough comparison of the state-of-the-art UAV classification

Table 2: Radar cross section of different commercial small UAVs measured by PSWR in horizontal and vertical polarization. All values present the mean over several (50+) measurements at different target aspect angles. Peak sidelobe level (PSL) indicates the peak spectral return related to the spinning blades. RCS indicates the peak spectral return related to the main body.

Parameter	DJI Phantom 4	3DR Solo	Trimble ZX5	DJI S900
$RCS_H[dBsm]$	-16.4	-16.6	-17.3	-11.1
$RCS_V[dBsm]$	-18.9	-22.1	-17	-12.5
$RCS_H - RCS_V[dB]$	2.5	5.5	-0.3	1.4
$PSL_H[dBsm]$	-35.3	-30.5	-33.4	-30.8
$PSL_V[dBsm]$	-37.5	-36.3	-36.4	-32.2

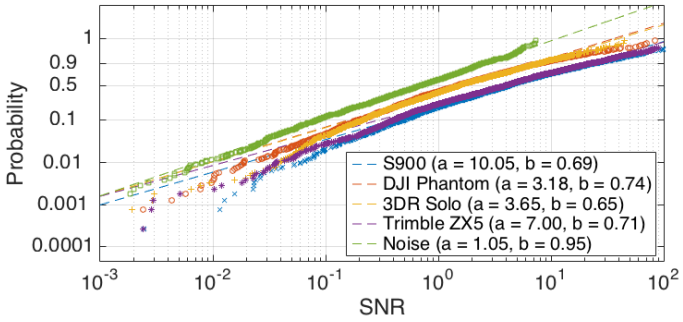


Figure 2: Weibull probability density function for different UAV targets and noise samples.

Table 3: PSWR tracking performance of DJI S900 target. The altitude is related to the UAV take off location, which was approximately 45 meters below radar site. The video of UAV tracking is available at: https://vimeo.com/275839325

Date	Mission	Altitude [m]	Range [m]	$\mu_r[m]$	σ_r	$\mu_{az}[^\circ]$	σ_{az}
2017/12/15	$Flight\#4$	80-110	1050-1200	2.46	3.43	-0.13	0.72
	$Flight\#5$	110	950-1250	0.7	5.17	-0.35	0.67
2018/04/24	$Flight\#1$	100	950-1200	-0.14	2.91	-0.28	0.94
	$Flight\#2$	100	900-1200	0	4.64	-0.17	0.87
	$Flight\#3$	120	950-1200	0.06	4.57	-0.32	0.96
2018/06/12	$Flight\#1$	90	1000-1500	-0.13	7.04	-0.08	1.67
	$Flight\#2$	50-100	950-1200	-0.75	4.39	0.64	1.3

methods. These techniques are effective if a long duration target observation or/and high pulse repetition frequency (PRF) can be implemented. The future multi-function radar systems will be able to implement these techniques to some extent, but PSWR in its current configuration is not capable to provide the required quality of data due to slow pedestal movement and limited PRF. For this paper, the detection scheme used involved a simple cell averaging constant false alarm rate (CA-CFAR) algorithm performed in range-Doppler domain followed by an extraction of targets which present a general micro-Doppler signature. The procedure is presented in Table 1.

The statistics of data used to generate mean micro-Doppler signatures are investigated using the Weibull distribution. The Doppler component of the main body is excluded from these computations. The probability density function (pdf) of a Weibull random variable is given by:

$$f(x|a,b) = \frac{b}{a}\left(\frac{x}{a}\right)^{b-1} e^{-(x/a)^b} \quad x \geq 0 \tag{2.2}$$

where a is scale parameter and b is a shape parameter. The larger the scale parameter, the more spread out the distribution. If the data in x has a Weibull distribution, then the data is located along the reference line defined by a shape parameter in pdf. Distributions other than Weibull will introduce curvature in the plot. The probability density functions for 4 UAVs are presented in Figure 2. Additionally, for a reference we add PSWR noise data (green line), which should be exponentially distributed (b=1). The shape parameter of b=0.95 and scale parameter of a=1.05 confirm that noise samples have a Weibull distribution. On the other hand UAV data fit exhibits slight curvature for SNR > 10. The shape parameter is in range 0.65 and 0.74. Furthermore, we observe a noticeable difference in scale parameters, which allows to visually separate quadcopters form hexacopters.

3. Tracking

The output of the detection algorithm in the previous section becomes the input to a tracker. A challenge with tracking drones is they can move fast, slow, hover, turn suddenly, move up and down rapidly, etc. It is thus hard to come up with motion models for drones. One way to deal with drones is via fast update rate, since all motion looks locally linear when viewed at a high enough sample rate. Since our system didn't have a particularly fast update rate (approximately 15 seconds per PPI sweep), the tracking algorithm is based on Global Nearest Neighbor (GNN) approach, which attempts to find and to propagate the single most likely hypothesis at each scan (Konstantinova et al., 2003). The first detection is placed in its own track e.g. Track 1. Then the next detection is compared to Track 1. If that new detection being compared is too far away based on a distance threshold it will be placed into a new track. Each detection is compared to the last point of all the created tracks and then assigned to the track which it is closest to. This method worked reliably due to low number of targets and fairly low speed of UAV (3-6 m/s).

During the project several field campaigns were conducted. PSWR based tracking performance is presented in Table 3. DJI S900 target was flown between between 1000 and 1500 meters from the radar at various altitudes. The height of the drone

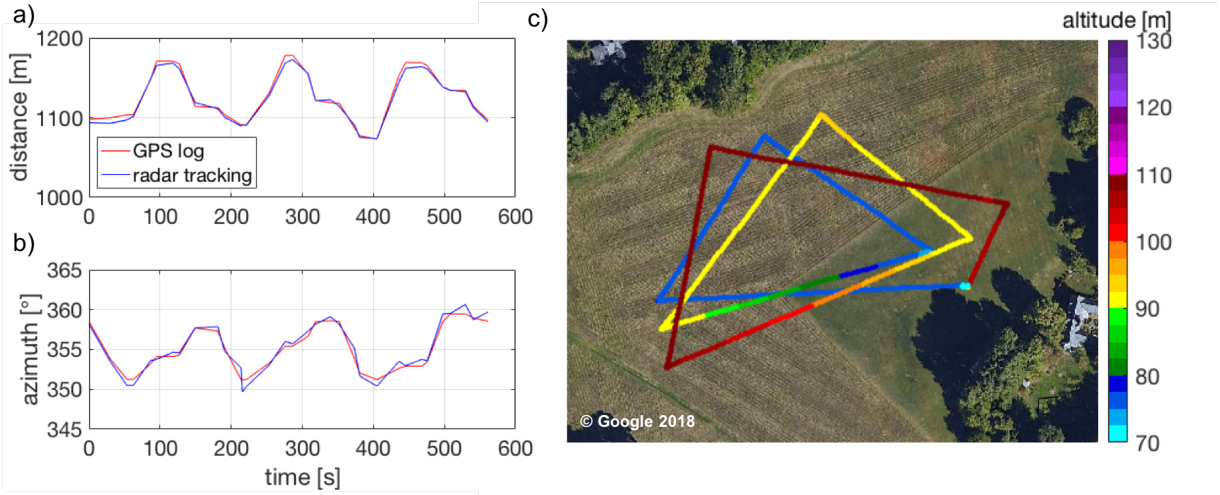


Figure 3: Flight #4 conducted on 2017/12/15: a) distance measured by radar- b) azimuth measured by radar compared with UAV GPS log. Panel c) presents the overlay of GPS track on a satellite picture. The drone ascended from 80 to 110 meters above ground level during the mission.

launch field was approximately 45 meters below the height of the radar site. In comparison to the GPS position data recorded on board of the drone, the mean error in range μ_r is in most cases below 1 m and the standard deviation of range estimation σ_r is smaller than 7m. The mean error in azimuth μ_{az} is smaller than 0.7° and the standard deviation of azimuth estimation σ_r is less smaller 1.7°.

This good tracking performance is illustrated in Figure 3 . For this mission the drone was hovering for 30 seconds in each corner and then progressing to the next one with a speed of 5m/s. The hover state is indicated by flat sections in Figure 3a and b. Hovering drone presents a clutter like target centered at zero-Doppler bin, but the micro-Doppler signature still allows for target detection. Our major issue was an aging mechanical pedestal, which prevented efficient tracking of high speed UAVs. Therefore, a phased array system with an electronic beam steering in azimuth or both azimuth and elevation would have been a better choice. It would then be possible to make the beam revisit the target location as frequently as needed.

4. Conclusions

This paper described the development of algorithms for the automated detection, classification, and tracking of sUAV with a low power, dual polarized, pulse doppler weather radar. Detection and classification was based on the identification of the micro-Doppler signature characteristic of copter-type targets. The algorithm was shown to work well for a variety of 4 rotor and 6 rotor drones. We observed that on average horizontal polarization promises higher chance of UAV detection. The tracker was based on a GNN approach. It worked well despite the low revisit time on order of 15 seconds, but needs to be modified to enable high speed UAV tracking. Future work is needed to explore detection and tracking of drone swarms (multiple close together drones that may or may not split and join during flight). Furthermore, detection in high urban clutter should be investigated. Use of electronic scanning is also preferable for an efficient clutter filtering as well as UAV and birds discrimination. We have demonstrated that functionality can be added to weather radar during "clear air" days when no severe weather is expected, and the radar can be used for micro-drone surveillance. This multi-function capability (weather and drone surveillance) could make such systems cost-effective for use in urban environments where these airborne hazards endanger lives and property.

Acknowledgment

The authors are grateful to the UAV pilots Silas Hughes, Daniel Myers and Ryan Wicks for the safe and smooth operations. We thank Eric Lyons for his help related to radar network communication. This work was supported by NSF Partnerships for Innovation - Accelerating Innovation Research Technology Transfer Award Number 1700967. Any opinions, findings, conclusions, or recommendations expressed in this material are those of the authors and do not necessarily reflect those of the NSF.

References

E. Adams, “Raytheon’s New Radar Could Bring Flying Cars and Drones to Our Cities,” 2018. [Online]. Available: https://www.wired.com/story/raytheon-radar-drones/

V. C. Chen, F. Li, S. S. Ho, and H. Wechsler, "Micro-Doppler effect in radar: phenomenon, model, and simulation study," *IEEE Transactions on Aerospace and Electronic Systems*, vol. 42, no. 1, pp. 2–21, Jan. 2006.

V. C. Chen, *The Micro-doppler Effect in Radar*. Artech House, 2011, google-Books-ID: eJ7eMHpxt30C.

J. L. Chenchen and L. Hao, "An Investigation on the Radar Signatures of Small Consumer Drones," *IEEE Antennas and Wireless Propagation Letters*, 2016.

J. de Wit, R. Harmanny, and P. Molchanov, "Radar micro-Doppler feature extraction using the Singular Value Decomposition," in *Radar Conference (Radar), 2014 International*, Oct. 2014, pp. 1–6.

A. Holland-Michel, *Counter Drone Systems*, Feb. 2018. [Online]. Available: http://dronecenter.bard.edu/files/2018/02/CSD-Counter-Drone-Systems-Report.pdf

P. Konstantinova, A. Udvarev, and T. Semerdjiev, "A Study of a Target Tracking Algorithm Using Global Nearest Neighbor Approach," in *Proceedings of the 4th International Conference Conference on Computer Systems and Technologies: E-Learning*, ser. CompSysTech '03. New York, NY, USA: ACM, 2003, pp. 290–295. [Online]. Available: http://doi.acm.org/10.1145/973620.973668

A. Levin, "Surge in Drone Safety Reports Prompts Emergency Action at FAA," *Bloomberg.com*, Oct. 2017. [Online]. Available: https://www.bloomberg.com/news/articles/2017-10-13/surge-in-drone-safety-reports-prompts-emergency-action-at-faa

P. Molchanov, K. Egiazarian, J. Astola, R. Harmanny, and J. de Wit, "Classification of small UAVs and birds by micro-Doppler signatures," in *Radar Conference (EuRAD), 2013 European*, Oct. 2013, pp. 172–175.

B. S. Oh, X. Guo, F. Wan, K. A. Toh, and Z. Lin, "Micro-Doppler Mini-UAV Classification Using Empirical-Mode Decomposition Features," *IEEE Geoscience and Remote Sensing Letters*, vol. 15, no. 2, pp. 227–231, Feb. 2018.

K. A. Orzel and S. J. Frasier, "Weather Observation by an Electronically Scanned Dual-Polarization Phase-Tilt Radar," *IEEE Transactions on Geoscience and Remote Sensing*, vol. 56, no. 5, pp. 2722–2734, May 2018. [Online]. Available: https://ieeexplore.ieee.org/document/8244253/

K. A. Orzel, S. Govindasamy, A. Bennett, D. Pepyne, and S. Frasier, "Detection and identification of the Remotely Piloted Aircraft System using a weather radar," *AMS 38th Conference on Radar Meteorology*, Aug. 2017. [Online]. Available: https://ams.confex.com/ams/38RADAR/meetingapp.cgi/Paper/321077

M. Ritchie, F. Fioranelli, and H. Griffiths, "Micro-Drone RCS Analysis," 2015.

A. Schroder, M. Renker, U. Aulenbacher, A. Murk, U. Boniger, R. Oechslin, and P. Wellig, "Numerical and experimental radar cross section analysis of the quadrocopter DJI Phantom 2," in *2015 IEEE Radar Conference*, Oct. 2015, pp. 463–468.

M. D. Shear and M. S. Schmidt, "White House Drone Crash Described as a U.S. Workers Drunken Lark," *The New York Times*, Jan. 2015. [Online]. Available: https://www.nytimes.com/2015/01/28/us/white-house-drone.html

J. E. Stailey and K. D. Hondl, "Multifunction Phased Array Radar for Aircraft and Weather Surveillance," *Proceedings of the IEEE*, vol. 104, no. 3, pp. 649–659, Mar. 2016.

B. Torvik, K. E. Olsen, and H. Griffiths, "Classification of Birds and UAVs Based on Radar Polarimetry," *IEEE Geoscience and Remote Sensing Letters*, vol. 13, no. 9, pp. 1305–1309, Sep. 2016.

S. Werth, "Evaluating features for broad species based classification of bird observations using dual-polarized doppler weather radar," *Masters Theses*, Jan. 2016. [Online]. Available: https://scholarworks.umass.edu/masters_theses_2/381

Airborne Implementation of PDPP Technique on The NRC W-band Radar

Cuong Nguyen[1], Alessandro Battaglia[2], Mengistu Wolde[1], Andrew Pazmany[3] and Anthony Illingworth[4]

[1] *National Research Council Canada*
[2] *University of Leicester, UK*
[3] *ProSensing Inc., Amherst, Massachusetts*
[4] *University of Reading, UK*

1 Introduction

The measurement of 3D atmospheric winds in the troposphere and in the boundary layer remains one of the great priorities of the next decade (The National Academies Press, 2017). Such measurements have the potential to shed light on a variety of processes ranging from cloud dynamics and convection to transport of aerosols, pollutants and gases (including water vapor). Additionally, they can be assimilated to improve the climate modelling.

A combination of active systems (radars and lidars) and passive radiometry is currently envisaged to be the best approach in order to provide global observations from satellites. Active sensors that exploit the Doppler effect and use either aerosol, gas molecules or cloud particles as tracers of the winds have the clear advantage of providing vertical profiles of winds but are more technologically challenging. The ESA Aeolus mission with its Doppler lidar (Stoffelen et al., 2005) and the ESA-JAXA Earth-CARE mission with its nadir-pointing Doppler W-band radar (Illingworth et al., 2015) will offer a first assessment of the potential of such instruments in mapping at least one component of the winds (the line of sight wind in clear air and thin ice clouds for Aelous, the vertical wind in clouds for EarthCARE). However, the implementation of Doppler radar has been a challenging concept to bring to a spaceborne platform due to the fast movement of the platform coupled with finite beamwidth of the radar's antenna inducing very short decorrelation times. To mitigate this problem, high sensitivity and narrow beamwidth W-band radars have been considered (Battaglia et al., 2013; Illingworth et al., 2018a). At short wavelength, Doppler retrieval becomes challenging due to the range-velocity dilemma. For horizontal winds measurement, the conventional pulse pair Doppler processing is not adequate. The polarization diversity pulse pair (PDPP) technique (Doviak and Sirmans, 1973) is proposed for wind-focused Doppler radar space missions.

In this paper, the implementation of PDPP technique on the National Research Council Canada W-band Doppler radar (NAW) (Wolde *et al.*, 2005) and the first-ever airborne PDPP Doppler measurements are presented. The PDPP pulses are interleaved with standard staggered pulse repetition time (PRT) pulses allows a better understanding of the strengths and drawbacks of the proposed method.

2 Implementation of PDPP on the NRC airborne W-band radar system (NAW)

2.1 PDPP Waveform

The default transmit pulsing scheme for the NRC W-band radar is pulse pair 10 (PP10) where the pulses are transmitted in a sequence of groups of 10 pulses. The pulse spacing and group spacing are selected adequately to meet the system duty cycle requirements. The PDPP waveform is implemented by modifying the existing PP10 mode. A sequence of H/V and V/H polarization diversity pulse pairs are interleaved with staggered PRT conventional H/H and V/V pulse pairs (Fig. 1). Thus, for this scheme, PDPP pulses are pulse # 4, 5, 6 and 7. The first two pulses are used for real-time display. In addition, pulse pair products such as staggered PRT velocity and LDRs are used to verify and analyze PDPP data. During the flights, the system displays H-polarization reflectivity and the mean Doppler velocity from the first two pulses of the PDPP sequence. The data system records the raw I/Q samples from the digital receiver for post processing. This PDPP implementation minimized the change required in hardware and real-time display software.

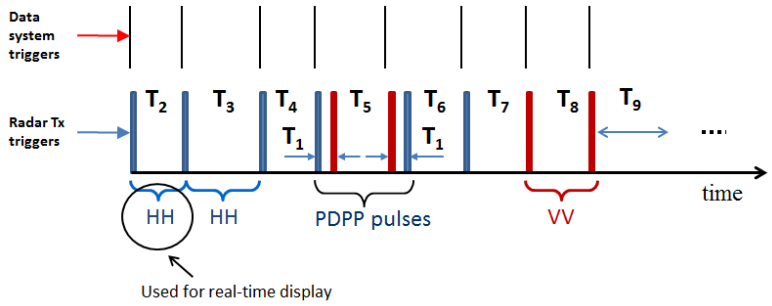


Figure 1: PDPP mode waveform implemented in the Convair W-band airborne radar.

2.2 Antenna Selection for PDPP

PDPP data was collected using the dual-polarization aft-looking antenna in combination with a reflector as well as the side dual-polarization antenna (Fig. 2). Both antennas were operated separately, as opposed to receiving/transmitting simultaneously. Radar beam incidence angles ranging from 0° to ~85° were achieved by performing various aircraft manoeuvers and/or changing the mirror orientation depending on the antenna being used. Details of antenna beam configurations and PDPP pulsing parameters options are provided in Table 1. The altitude of the aircraft during the manoeuvers ranged from 1.5 km to 7 km. The duration of each manoeuver ranged from 1 minute (e.g. for a 45 degree orbit) to several minutes (e.g. while performing roll sweeps). Each manoeuver was repeated for time periods of at least 30 minutes in length, while maintaining a constant altitude. PDPP data was collected at four different PDPP pulse-spacings (6, 12, 20 and 40 μs).

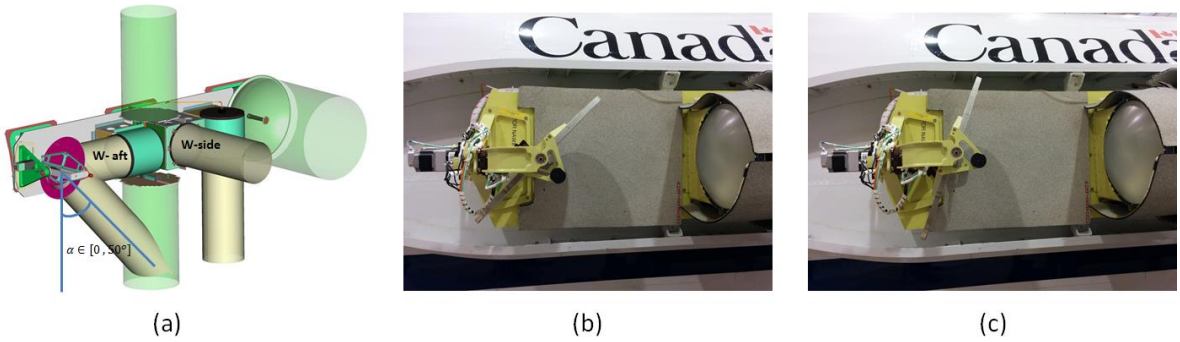


Figure 2: The NRC Airborne W- and X-band (NAWX) radar installation inside the starboard blister radome mounted on the Convair 580 (a). For PDPP, side and aft antennas are used. The aft antenna beam can be redirected from nadir (b) and up to 50° forward along the flight direction (c).

Table 1: The Airborne Manoeuvers and Antenna Selection Options for PDPP measurements

Aircraft Manoeuver	Antenna	Description	Incidence Angle (°)
Horizontal transects	Aft + reflector	Data collection at different beam angles obtained by changing the reflector position while the aircraft maintains a constant altitude.	0 to 50 Along the flight track
Orbits	Aft + reflector	Aft-looking beam is redirected to nadir view via the reflector. Change in aircraft roll angles from 0 to 45 degrees.	0 to 45 Across-track direction
	Side	Change in aircraft roll angles from 0 to 45 degrees.	45 to 90 Across-track direction

Roll sweeps	Aft + reflector	Aft-looking beam is redirected to nadir view via the reflector. Change in aircraft roll angles from -45 to 45 degrees.	0 to 45 Across-track direction

2.3 Reflectivity Calibration

In this work, the end-to-end calibration was done using backscattering properties of the water surface. Detailed description of this method can be found in e.g. Li et al. (2005); Tanelli et al. (2008). In summary, for 94 GHz radars at a 10° incidence angle, the mean value of measured σ_0 (in clear air condition) is 5.85 dB with a standard deviation of 0.6 dB (Li et al., 2005). Fig. 3 shows the water surface radar cross section (σ_0) as a function of incidence angle at different polarizations and with respect to different surface wind directions. It is shown that the horizontal and vertical polarization reflectivity agree very well and there is a crossover point around an incidence angle of 10°, with near-constant radar cross section regardless of wind direction.

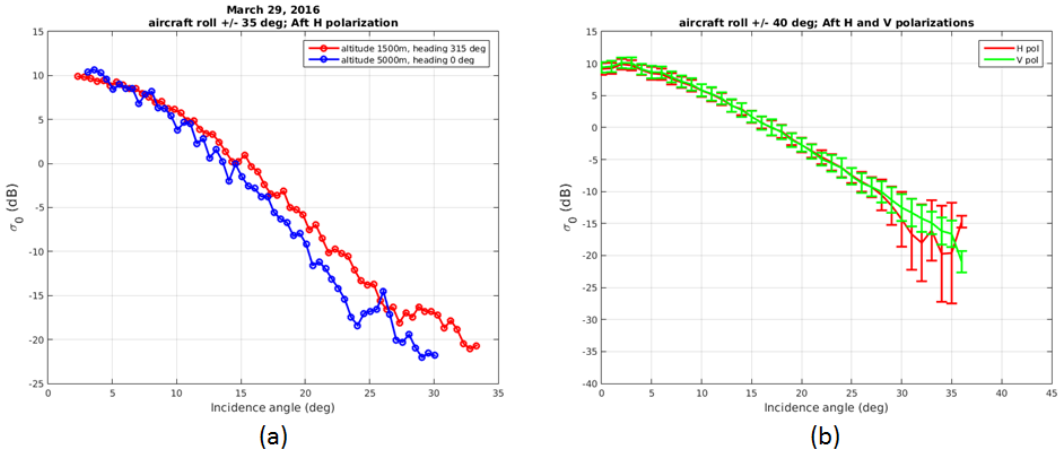


Figure 3: Radar cross section of the surface (σ_0) as a function of incidence angle: (a) measured σ_0 from H polarization over water surface with different wind directions on March 29, 2017 calibration flight. There is a cross point at incidence angle of around 10° incidence angle and σ_0 of 5.85 dB. (b) σ_0 for both horizontal and vertical polarizations for March 04, 2017 flight shows a good polarimetric calibration.

2.4 Antenna Beam Pointing Calibration

Because the measured radial Doppler velocity is affected by the motion of the platform, and the hydrometeors' motion relative to the earth, the platform motion component has to be removed in order to obtain the hydrometeors' motion. The accuracy of this correction is determined by the accuracy of the antenna beam pointing vector and the accuracy of the aircraft altitude and ground velocity measurements. In the Convair, the INS module (Honeywell) and the W-band radar are co-located. This, along with an INS-GPS real-time integrated data system, provides high resolution and accurate information on the platform's altitude and 3-D motion. The beam pointing vectors calibration procedure is done using a similar method described in (Haimov et al., 2013). The datasets used for this calibration were obtained via ground calibration flights performed on January and March 17 of 2017.The calibration flights were performed over calm weather, and over flat terrain.

For the side looking antenna, the antenna mount is rigid and no moving mechanism on the beam transmit path is involved the beam angle can be calibrated with a maximum root mean square error less than 0.1^o. The calibration of the beam vector of the W-band aft antenna, however, would not be as accurate as that of the nadir and side antennas. This is because the aft antenna beam is re-directed via a mirror (Fig. 2) whose coordinates also need to be estimated. Thus, instead of optimizing for three elements of the beam vector of the aft antenna, six parameters including the coordinates of the normal of the reflector need to be optimized. This complex optimization problem often provides unstable results. To simplify the problem, an assumption of the normal of the reflector to be in the vertical plane and perfectly perpendicular to the aircraft fuselage at its home position is made. The position of the reflector then can be simply computed from elevation and azimuth angles of the mirror's two stepper motors. The reflected beam of the aft antenna can be expressed as,

$$\vec{b}_r = \vec{b}_{aft} - 2(\vec{b}_{aft} \bullet \vec{n}_{mirror})\vec{n}_{mirror} \qquad (2.1)$$

where $\vec{b}_r$, $\vec{b}_{aft}$ and $\vec{n}_{mirror}$ are reflected beam vector, aft antenna beam pointing vector and the mirror's normal vector respectively and [•] is the dot operator. The optimization is setup with respect to $\vec{b}_r$ and then $\vec{b}_{aft}$ is solved from (2.1). This procedure provides an error less than 0.5^o in the estimation of the incidence angle of the aft antenna.

3 PDPP Velocity Processing

In order to compute the PDPP velocity, phases of the correlation estimates of the two HV and VH PDPP pairs are calculated.

$$\Phi_1 = angle(R_{HV}) = \Phi_{Vd} + \Phi_{dp} \quad (3.1)$$

$$\Phi_2 = angle(R_{VH}) = \Phi_{Vd} - \Phi_{dp} \quad (3.2)$$

For Equations 2-3, Φ_{Vd} is the phase shift due to the signal Doppler velocity during T_{hv} interval and Φ_{dp} is the differential phase between polarizations. It can be seen that PDPP velocity can be estimated from Φ_1 and Φ_2 after correcting for Φ_{dp}. The differential phase can be expressed as seen in Equation 4.

$$\Phi_{dp} = \Phi_0 + \Phi_p \quad (3.3)$$

Where Φ_0 is the system differential phase and Φ_p is the propagation differential phase due to the medium. The system differential phases of the NAWX antennas are intrinsic system parameters and need to be characterized. For the side antenna, $\Phi_o$should be a constant value. For the aft antenna, the reflector alters the system differential phase. It is observed that the system differential phase measured at the main bang (Tx pulse) before the reflector is approximately -65° while the value at the 1st range gate is different. In fact, the value of Φ_o can be expressed as a function of the reflector position. In PDPP configurations, the reflector was set to be at nadir position or was moved forward; therefore in this work, Φ_0 is characterized as a function of elevation motor angle. Figure 6 shows the estimated Φ_0 using the 20170325_145335 data file. It is shown that Φ_0 varies in a wide range depending on the reflector angle. In the PDPP processing algorithm, for a given reflector angle, the system differential phase is obtained using a lookup table. It is worth noting that the issue of a varying Φ_0 is only associated with the aft reflector and would not be a problem for a fixed antenna setup such as the side antenna.

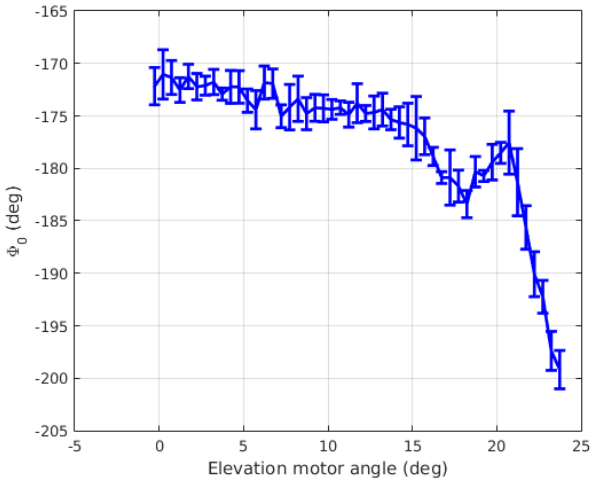


Figure 4: The system phase (Φ_0) of the aft antenna as a function of elevation motor angle. Data is shown for the 25-March-2017 dataset.

The estimation of the propagation differential phase at W-band frequency is not a trivial task and would require a thorough analysis that is beyond the scope of this report. Here, we propose a method to obtain the best estimates of PDPP velocities within the current NAW PDPP hardware configuration that accounts for the propagation differential phase. The algorithm being proposed can also be extended for use with other radar systems running the PDPP waveform. The algorithm is summarized below:

Step 1: Start at range gate 1, calculate the system differential phase (Φ_0) and remove it from Eq. 2&3. The resultant phases are used to estimate PDPP velocity:

$$\hat{\Phi}_{Vd}^1 = \hat{\Phi}_1 - \Phi_0 \quad (3.4)$$

$$\hat{\Phi}_{Vd}^2 = \hat{\Phi}_2 + \Phi_0 \quad (3.5)$$

$$\hat{v}_{pdpp}^1 = v_N^{pdpp} \hat{\Phi}_{Vd}^1 / 180 \quad (3.6)$$

$$\hat{v}_{pdpp}^2 = v_N^{pdpp}\hat{\Phi}_{Vd}^2/180 \quad (3.7)$$

Basically, we get two estimates of PDPP velocities which can be comparable or can be $\pm 2v_N^{pdpp}$ different. In addition, the aircraft motion contribution can be computed from the aircraft INS data and antenna beam vector. In general,

$$v_{pdpp} = v_{AC} + v_p \quad (3.8)$$

where v_{AC} is the aircraft motion contribution and v_p is the precipitation radial velocity.

The platform motion contribution can be small (nadir looking cases) or very large such as in cases of aft antenna looking forward or in the WIVERN conical scanning scheme. The velocity unfolding can be done either with measured PDPP velocity ($\hat{v}_{pdpp}$) or with v_p after removing platform motion. In this method, the measured PDPP velocity can be unfolded based on v_{AC}. Basically, from a set of three velocities ($\hat{v}_{pdpp}^1$, $\hat{v}_{pdpp}^2$, v_{AC}) one can easily find a "correct" velocity within the interval $[v_{AC} - v_N^{pdpp},\ v_{AC} + v_N^{pdpp}]$

Step 2: Once the velocities in Step 1 are unfolded, compute the phases Φ_1 and Φ_2 from unfolded velocity. Move to the next range gate. Since the difference in propagation phase within one range gate is small (order of degrees), the re-computed phases Φ_1 and Φ_2 from the previous gate are used to correct for Φ_1 and Φ_2 of the current gate.

Step 3: Compute velocity from two unfolded phases Φ_1 and Φ_2:

$$\hat{v}_{pdpp} = v_N^{pdpp} * 0.5(\hat{\Phi}_1 + \hat{\Phi}_2) \quad (3.9)$$

Step 4: Compute Φ_{dp} from two unfolded phases Φ_1 and Φ_2.

Step 5: Move to next range gate. Repeat Step 2.

Step 6: End at the last range gate.

Φ_{dp} is an accumulative function and in general, it is a monotonically increasing function. However, in oriented ice crystals this assumption may not hold. Thus, the algorithm would be more robust with additional steps to verify this situation. The method is tested with various set of data with different T_{hv} values and it appears to works well.

4 Field Campaign Case Study

4.1 Ghost echoes and impacts on PDPP velocity estimates: Case 10-Jan-2017

In this flight the Convair made extensive samplings of a frontal system over Lake Ontario and its surrounding regions in Ontario, Canada and the state of New York, USA. The NAW was run in PDPP mode for the last segment of flight duration, during which the aircraft sampled the tail of a winter storm over Lake Ontario. During the PDPP data collection, the aircraft first performed repeated roll sweep maneuvers by varying the roll angles ~ ±45°, and then performed an orbit maneuver using the side antenna. Winds at the flight level of ~5 km were NW at 30 m/s.

This case is selected to highlight the high incidence angle measurements with strong ground depolarization, and with significant SNR variations. The data shown in this section was from the side antenna whose incidence angle varied from 50° to 100°. The aircraft started in a 40° bank (right wing down) until 17:21:01 UTC, rolled wings level just before 17:21:05 UTC, after which the aircraft entered a shallow left bank. The measured reflectivities from the first two PDPP pulses (Z_{hh} and Z_{vh}) are depicted in Fig. 5. Note that the H- receiver must be turned off when the V-pulse is sent out, which corresponds to a blind layer in the left panel. There are a couple of interesting observations from this case. Firstly, at ground gates, the reflectivity, and the depolarization level varied significantly when the radar beam moved from the land to the water surface. At the start of the segment, the radar beam was pointing towards a large island (Fig. 5a). As the aircraft rolled level from 17:21:01 UTC to 17:21:05 UTC, the beam would have scanned the water surface between the island and the mainland in the upper right of Fig. 5a. The above is supported by the variation reflectivity observed in Fig. 5b and 5c, where a sharp change in the surface reflectivity is observed around 17:20:56 UTC. The effect of the aircraft roll can also be seen in these figures at the upward curve starting around 17:21:01 UTC, as the ground return moves farther away from the aircraft. Secondly, the linear depolarization ratio (LDR) of the water surface is much higher than that of the lands resulting in stronger ghost echoes as seen in Fig 5b and 5c. The ghost echoes presented at both H and V signals at different range gates.

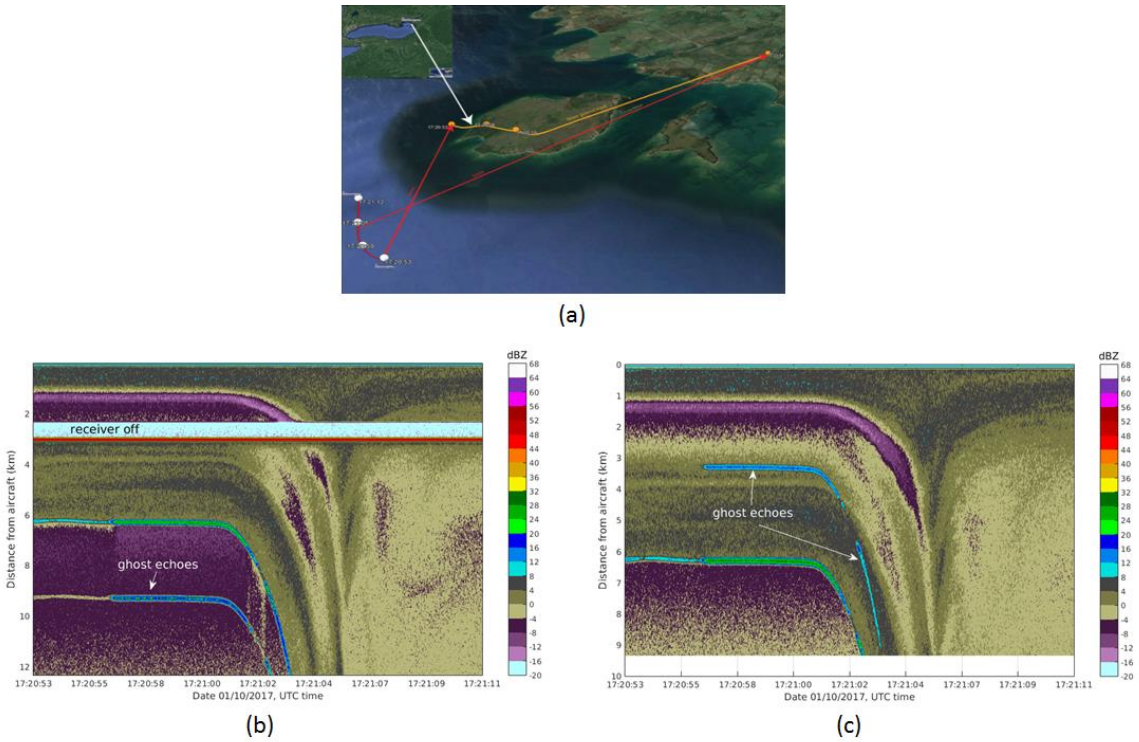


Figure 5: The case 10-Jan-2017: (a)flight path is in red and the side antenna beam projection on ground is in yellow; (b)reflectivity from the first PDPP pulse Z_{hh} and (c) reflectivity from the second PDPP pulse Z_{vh}.

Figure 6 shows a comparison of the Doppler velocities as measured via a PDPP sequence with $T_{hv} = 20\ \mu s$ ($v_a^{PDPP} = 39.8\ ms^{-1}$) and a conventional PP technique using two staggered PRFs ($v_a^{stg} = 26.5\ ms^{-1}$). For a better comparison, we used the same scale between -40 and 40 m/s for the Doppler velocities. The radar beam's transition from the big island to the water is seen as a sudden increase in the Doppler velocity around 17:20:56 UTC. In general, the two velocity measurements are comparable. The Doppler velocity derived from the staggered PRF appears to be less noisy than the one derived from the PDPP. At regions where ghost echoes are present and SNR drops significantly, PDPP estimates express very high standard deviations (Figs. 7).

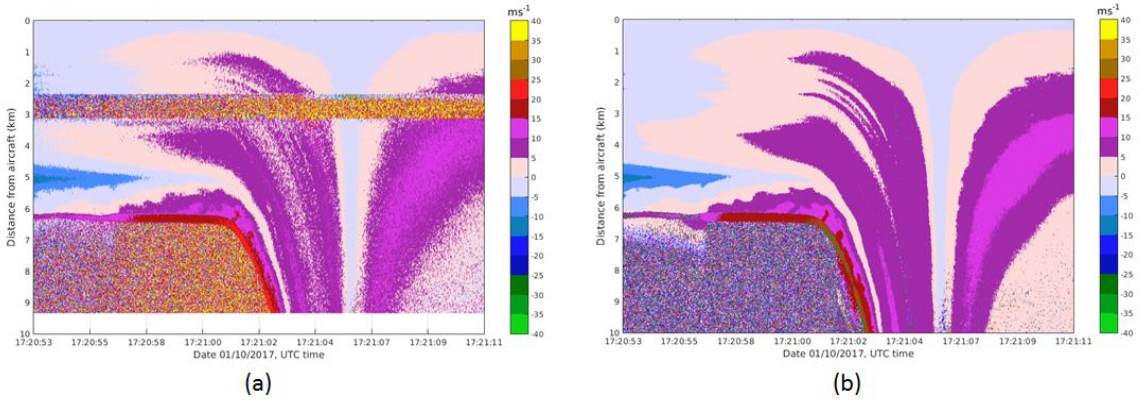


Figure 6: Doppler velocity measurements using PDPP (a) and staggered PRT (b) for the case 10-Jan-2017.

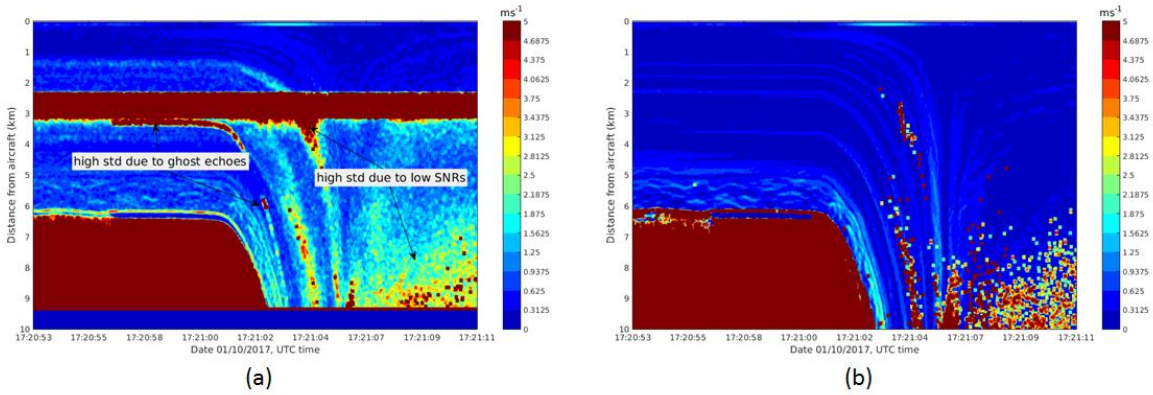


Figure 7: Standard deviation of Doppler velocity measurements in Fig. 6 which were computed using a 3x3 pixels window centered at each point (in time and space).

4.2 Very High Doppler Velocity Measurements: Case 25-Mar-2017

This extreme high Doppler observation was first reported in Wolde *et al.* (2018). For this case, we highlight instances of high V_d from the PDPP measurement inside a major winter storm on 25 March 2017. The Convair flew for over 5 hours sampling the winter storm over land near Buffalo, NY, over Lake Huron and Lake Ontario as the frontal system moved towards southern Ontario. The PDPP data was collected using the aft antenna and reflector combinations while the aircraft is performing a horizontal transect and descending from 5 to 4.4 km (Fig. 8). The use of the aft antenna in combination with the reflector provides a unique means to direct the antenna beam to a wide range of positions. By steering the aft antenna's beam to a large slant angle, the maximum Doppler velocity introduced by the aircraft motion can reach up to 100 m/s, which makes a good test for evaluating the PDPP method's high velocity retrieval capability. The beam position began at nadir, and was steered to the reflector limit (50◦ incidence angle) at which point the beam was then moved back to the nadir position with step decrements of 10°. The PDPP spacing (T_{hv}) for this case was set at 6 µs (900 m) which provides a maximum unambiguous Doppler of 132.9 m/s.

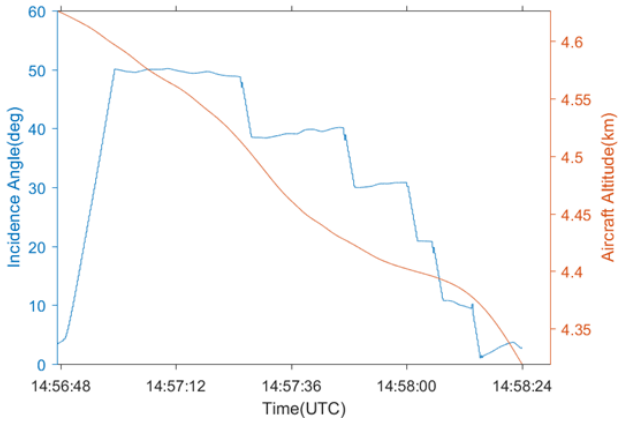


Figure 8: Aft-antenna beam incidence angle and aircraft altitude for case 25-Mar-2017.

Fig. 9 shows PDPP reflectivity fields (Z_{hh} and Z_{vh}) measured during this stepped change in the reflector's angle. There was a well-defined melting layer at around 2.5 km which can be seen at beginning of this segment when the antenna beam was at nadir position. As the antenna beam moved forward along the flight path, the ground and melting layers appear at different radar range. Similar to the case study in the previous section, ghost echoes associated with the ground and melting layer are observed in the PDPP reflectivity.

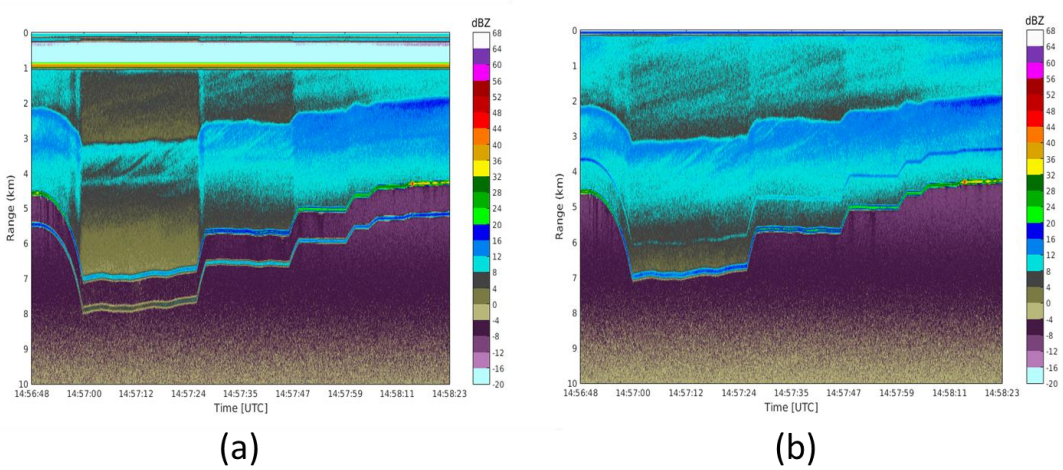


Figure 9: Similar to Fig. 5 but for flight 25-Mar-2017.

The measured PDPP Doppler properly retrieved using a method described in section 3 is depicted in Fig. 10a. The measured Doppler can be as high as 100 m/s in regions where the reflector was steered at ≈ 50◦ and reduced to a few m/s when the reflector moved back to nadir position. In all scenarios, PDPP technique works very well. There is almost no velocity folding even at weak signal regions (around 14:57:12 UTC and at 6 km altitude). In contrast, a comparison with the conventional staggered PRT techniques is shown in Fig. 10b. In that figure, estimated velocities at ground gates using PDPP, staggered PRT pulses and computed aircraft contribution are plotted. Due to a much narrower Nyquist range, staggered PRT velocity was folded many times. This case is a successful example of using PDPP technique to measure very high radial Doppler velocity in order to obtain accurate horizontal winds from the space.

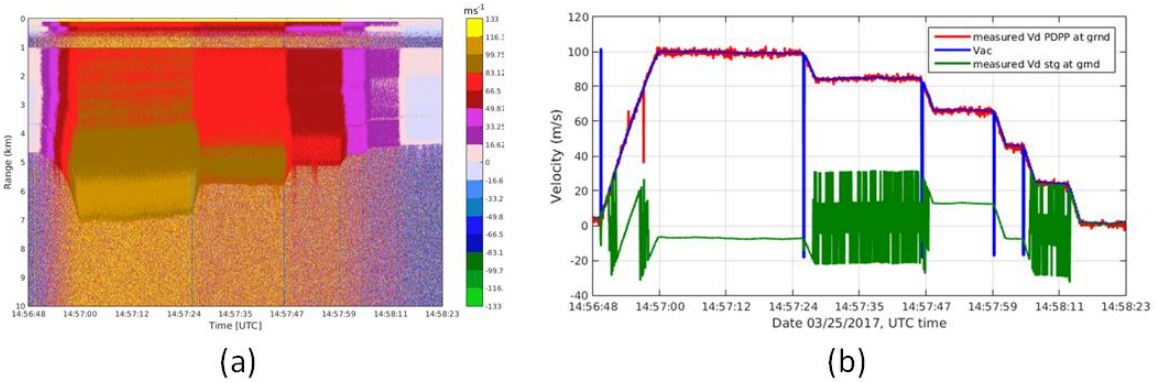


Figure 10: PDPP Doppler field (a) and Doppler measurements at ground gates (b) (the aircraft contribution computed from the aircraft INS data is the blue line).

5 Conclusion

This work describes the implementation of polarization diversity on the NRC Airborne W-band radar and the novel results collected during different flights conducted over North America in 2016 and 2017. This is the first time a PDPP mode has been implemented with a W-band radar on a moving platform. In this campaign, a comprehensive PDPP I/Q dataset has been collected, which allows characterizing PDPP-based Doppler velocity estimates in various environmental conditions. The polarization diversity technique allows much larger velocity to be measured unambiguously. Doppler velocities exceeding 100 m/s were measured during the field campaign when adopting a pulse pair separation T_{hv} equal 6 μs. Cross-talk between the two polarizations caused by depolarization at backscattering deteriorates the quality of the observations by introducing "ghost echoes" in the power signals and by increasing the noise level in the Doppler measurements. The regions affected by crosstalk are generally associated with the strongly depolarizing surface and hydrometeor returns.

Acknowledgement

This work was supported in part by the European Space Agency under the activity Doppler Wind Radar Demonstrator (ESA-ESTEC) under Contract 4000114108/15/NL/MP and in part by CEOI-UKSA under Contract RP10G0327E13. We acknowledge the support from the NRC staffs during the flight campaign.

References

Battaglia, A., Tanelli, S. and Kollias, P. Polarization diversity for millimeter space-borne Doppler radars: an answer for observing deep convection? J. Atmos. Ocean Technol., 2013, Vol. 30 (12) , pp. 2768– 2787.

Doviak, R. J., and Sirmans, D. Doppler radar with polarization diversity. J. Atmos. Sci., 1973, Vol. 30, pp. 737–738.

Illingworth, A. J., et al. The EarthCARE Satellite: the next step forward in global measurements of clouds, aerosols, precipitation and radiation. Bull. Amer. Met. Soc., 2015.

Illingworth, A. J., et al. Wivern: A new satellite concept to provide global in-cloud winds, precipitation and cloud properties. Bull. Amer. Met. Soc., in press, 2018.

Wolde, M. and Pazmany, A. NRC dual-frequency airborne radar for atmospheric research. 32nd Int. Conf. on Radar Meteorology, Albuquerque, NM, Amer. Meteor. Soc., 2005, P1R.9.

Wolde, M., Battaglia, A., Nguyen, C., Pazmany, A., and Illingworth, A. J. Implementation of Polarization Diversity Pulse Pair Technique using airborne W-band radar, *submitted to AMT, 2018*

The Decadal Survey, (Ed.). Thriving on Our Changing Planet: A Decadal Strategy for Earth Observation from Space. The National Academies Press, 2017.

Stoffelen, A., et al. The Atmospheric Dynamics Mission for Global Wind Field Measurement. Bull. Amer. Met. Soc., 2015, Vol. 86, pp. 73–87.

Bistatic Scattering from Bragg Turbulence at X-Band: A Potential Mechanism for Clear Air Sensing Using CASA-Type Radar Networks

David J. McLaughlin

Department of Electrical and Computer Engineering, University of Massachusetts, Amherst, MA 01864, USA
(Dated: 24 June 2018)

1 Introduction

Dense networks of low-power, short-range X-band radars are an emerging technology with the potential for superior lower-altitude observations compared to today's long-range C and S band weather radar networks [1]. Long-range radars are blocked from observing the lower troposphere owing to the earth's curvature. Since these radars are spaced 100 km or even several hundred km apart, national networks comprised of large radars are unable to provide comprehensive boundary layer coverage. Small "CASA-type" radar networks are comprised of "dense networks" of smaller radars, each with maximum range of ~30 km. The short radar range defeats the earth curvature blockage problem, and extended networks comprised of 10's, 100's, or even 1000's of radars offer the potential for gap-free coverage, from the boundary layer up to the tops of storms. X-Band radar networks are presently deployed in limited numbers in several nations either operationally (eg, in Japan [2] and France [3]) or for research in the USA, Italy and elsewhere. Although they are demonstrating capability in providing high resolution and low-altitude observations, there is concern that these radar networks have insufficient sensitivity to observe low-reflectivity weather, such as clear air.

Over limited regions (up to several 10's of km from the antenna) where current large, long-range radars do have boundary later visibility, these radars have sufficient sensitivity to measure boundary layer winds via insect echo and Bragg-scattering from refractive index fluctuations [4, slide 3]. The SENSR project in the USA, which aims to replace all national civil infrastructure radars with multifunction phased array radar, offers a preliminary specification of -18.5 dBZ for the detection of distributed air motion tracers [5, slide 113]. Because they operate with large power*aperture product, long-range radars are able to achieve such sensitivity levels. Small, short-range X-band radars operate with significantly lower power*aperture product, and as such they have insufficient sensitivity to measure clear air via Bragg-scattering.

The vast majority of radars deployed today operate in a monostatic configuration, in which the transmitter and receiver are co-located, typically sharing a common antenna. This paper considers the use of bistatic configurations in a network of low-power X-band radars. In a bistatic geometry, where the radar transmitter and receiver are separated from each other by tens of km, the radar volume resolution cell can be substantially larger then in the monostatic case. This can result in bistatic configurations having higher signal-to-noise ratio and hence enhanced weather detectability compared to the monostatic configuration. More interesting and potentially more impactful, the Bragg resonant wavelength in a bistatic geometry can be substantially larger than the corresponding Bragg wavelength for a monostatic radar. Theoretical calculations show that, when the atmospheric structure parameter, C_n^2 is high enough, the volume reflectivity can be large enough to allow low-power bistatic X-band radars to perform clear-air weather surveillance via enhanced scattering from Bragg-resonance. The theory being used here is not new, and multiple papers and textbooks (eg, [7], [8]) have described the bistatic scattering enhancement effect. When this enhancement is exploited in the context of a network of low-power X-band phased array radars – operating in a bistatic mode – the potential emerges for a new capability to comprehensively sense low-level boundary-layer winds in clear air. Indeed, *if* this phenomenology can be exploited and developed into a reliable measurement technique, it could be a "game changer" in the sense of providing a new means to comprehensively observe boundary layer winds during clear-air.

This paper is arranged as follows: section 2 compares the geometry and signal-to-noise performance of monostatic vs. bistatic short-range X-band radar networks observing Rayleigh-scattering from precipitation. Bistatic and monostatic scattering reflectivity levels from Rayleigh scatterers are identical, so this comparison illustrates the how increased volume resolution results in increased SNR for the bistatic case relative to the monostatic case. Section 3 considers the problem of clear-air (absent hydrometeors, lofted debris, and insects) in an X-band network. The source of clear-air echo is Bragg-resonant scatter from fluctuations in the index of refraction caused by atmospheric turbulence. These fluctuations are essentially undetectable by low power X-band microwave radars, but they are shown to "bloom" in a bistatic geometry, and the plots given in this section provide an indication of the potential to actually map clear

Table 1. X-Band Radar Specifications	
Peak Power	10 kW
Wavelength	3.2 cm
Antenna Gain	38 dB
Beamwidth	1.8 degrees
Pulse Width	1 uSEC
Bandwidth	1.5 MHz
Noise Figure	5.5 dB

air winds in a bistatic network.

2 Monostatic vs. Bistatic Weather Radar Networks

Figure 1 conceptually shows the geometry of monostatic and bistatic radars.

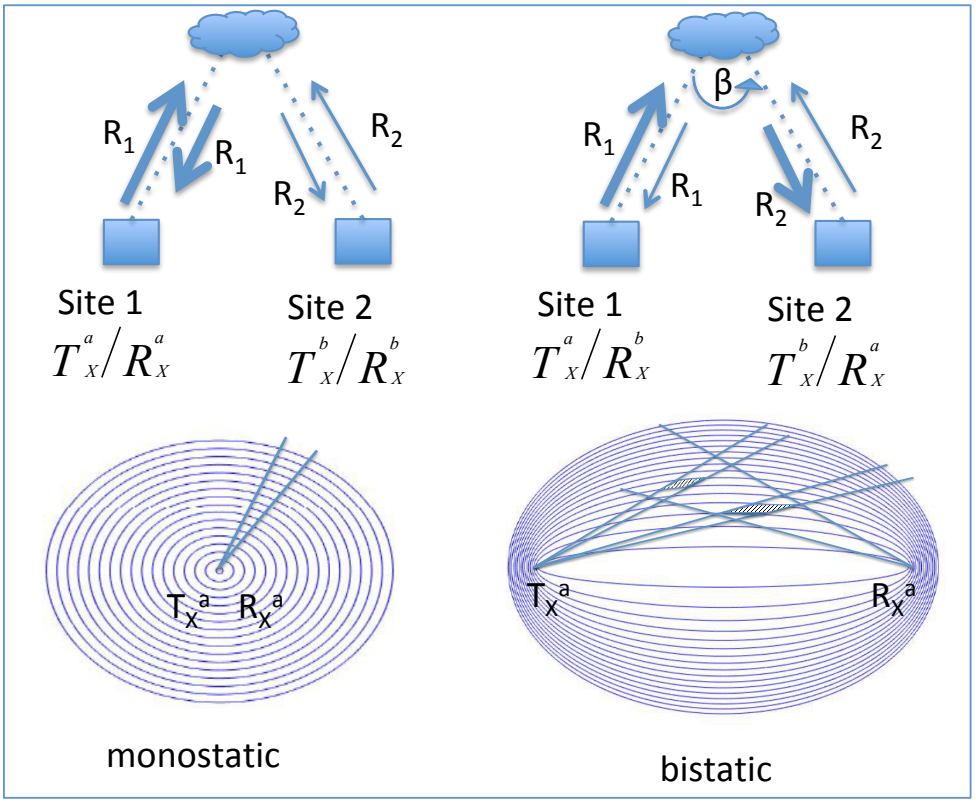


Figure 1. Schematic representation of monostatic and bistatic geometries

2.1 Monostatic Case

The signal-to-noise ratio for a monostatic weather radar viewing precipitation is given by

$$SNR_m = \frac{P_t G^2 \lambda^2 \eta V_m}{(4\pi)^3 R_t^4 k T B F_n} \quad (1)$$

where all variables will be familiar to radar meteorologists. Here, the backscattering cross section per unit volume is given by $\eta = \frac{\pi^5}{\lambda^4}|K_w|^2 Z_e$ where $|K_w| = 0.93$ for liquid water, and Z_e is the reflectivity of the hydrometeors being observed. The resolution volume of a monostatic radar, set by the transmitter pulse width, antenna beamwidth, and distance from the antenna, is given by $V_m = \frac{\pi}{4} R_t^2 \theta^2 \frac{c\tau}{2} \frac{1}{2\ln(2)}$ m^3. Table 1 lists the characteristics of a typical "CASA-type" X-band radar - meaning the radar is physically small and has low average power. The peak power of 10kW represents the power obtained from a relatively low cost magnetron transmitter; likewise, this peak power level could readily be achieved using a 100 W solid state transmitter utilizing a swept-frequency chirp pulse with pulse-compression gain of 20 dB. Fig. 1 shows the SNR for a single radar (left) and for a networked configuration of seven such radars spaced 30 km apart for three different values of reflectivity, Ze. In these and subsequent images, the horizontal and vertical span of each plot is 60 km. The color code and contours in these and subsequent plots represent single-pulse SNR in dB. Assuming 0 dB SNR is required for an adequate observation, regions having SNR > 0 dB (yellow, green color) can be considered to be observed, while regions having SNR < 0 dB (blue, violet) can be considered to be unobserved by the radar network.

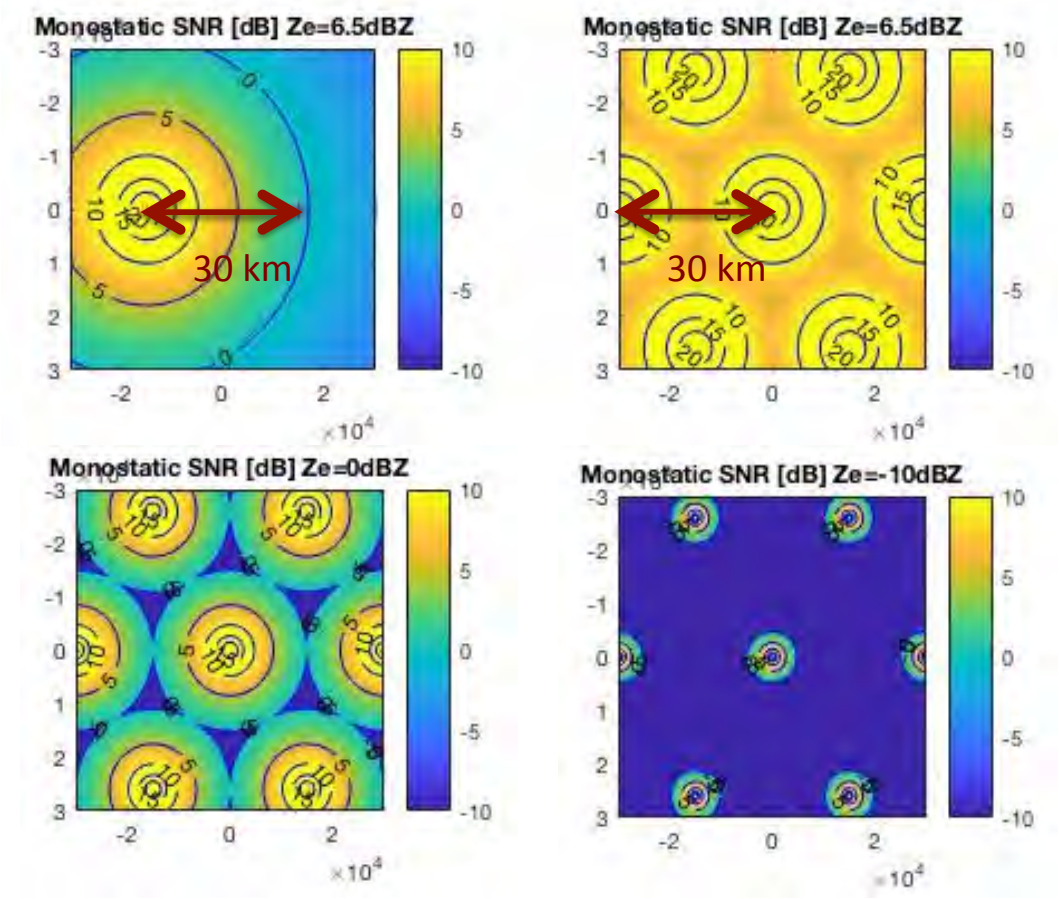


Figure 2. Monstatic SNR for single radar and 7-radar networks for different Ze values

The Z_e=6.5 dBZ reflectivity plot at the upper left (UL) of Fig. 2 shows that a single "CASA-type" radar achieves detectability out to 30 km range. Detectability of 6.5 dBZ precipitation is achieved *everywhere* when these radars are spaced 30 km apart as shown in the upper right figure (UR). Decreasing the reflectivity to 0 dBZ (lower left, LL) and -10 dBZ (lower right, LR) results in coverage gaps in between the radars. Indeed, the -10 dBZ case only provides detectability in the small region near each radar. A rule-of-thumb that can be taken from these figures is that a low-power X-band radar network has a sensitivity of ~6.5 dBZ.

2.2 Bistatic Case

The signal-to-noise ratio for a bistatic weather radar viewing precipitation is given by

$$SNR_b = \frac{P_t G^2 \lambda^2 \eta_b V_m}{(4\pi)^3 R_t^2 R_r^2 k T B F_n} \tag{2}$$

where the backscattering cross section per unit volume is given by $\eta_b = \frac{\pi^5}{\lambda^4}|K_w|^2 Z_e$. The resolution volume for a bistatic radar is, in general, a function of the transmitting and receiving antenna beamwidths and the intersection of these beams with the bistatic range-gate geometry, as illustrated in the lower half of Fig 1. In this work, we consider the special case where the receiving antenna beam is wide enough that only the transmitter antenna and the range gates define the volume resolution cell. An approximation for the resolution volume for this case, described by [6] and [9] gives the bistatic resolution volume as $V_b = \frac{\pi}{4} R_t^2 \theta^2 \frac{c\tau}{2} \frac{1}{2\ln(2)} \frac{1}{cos^2(\frac{\beta}{2})}$ m^3, where the bistatic angle, β is the angle included by the transmitter-to-scattering-volume and scattering-volume-to-receiver vectors (the monostatic case is $\beta = 0$,and the forward scatter case is $\beta = 180$ as illustrated in the next section.) The denominator in the expression for V_b expression accounts for the increase in bistatic resolution cell volume as β increases, this effect is illustrated by comparing the size of the two hatched regions in the lower right of Fig 1. The UL panel of Fig. 3 shows the SNR for a single bistatic radar having transmitter and receiver separated by a 30 km baseline. When compared with Fig. 2 UL, it is apparent that sensitivity in the bistatic geometry is shifted toward the receiving antenna site with less sensitivity near and to the left of the transmitter site. The bistatic sensitivity also exhibits a sideways tear-drop shaped lobe pattern. These behaviors result from the monostatic SNR being proportional to $1/R_t^2$ (inverse quadratic range-spreading with increasing distance from the transmitter) and the bistatic SNR being proportional to

$1/R_T^2 cos^2\left(\frac{\beta}{2}\right)$ (inverse quadratic range-spreading from both the transmitting and receiving sites, along with increasing quadratic volume resolution from the transmitter site, and the aforementioned cos term.

We are considering the situation where radars are placed in 30 km proximity to each other in a 2-dimensional network. Since each radar is equipped with a transmitter and a receiver, then bistatic operation can operate two-way across a baseline as shown in Fig. 3 UR. In subsequent plots, we will examine the bistatic SNR achieved when multiple 2-way baselines (two bistatic radars: one transmitter on left and receiver on right; and a second transmitter on right and second receiver on left side of the baseline) are deployed in 7 radar networks, analogous to the networks previously discussed in Fig. 2. For comparison between monostatic and bistatic cases, Fig. 3 LL shows the SNR for two monostatic radars separated from each other by 30 km, and Fig 3. LR shows the ratio between the 2 way bistatic SNR (UR) and the 2 radar monostatic SNR case (LL). The bistatic case has higher sensitivity by 2.5 to more than 10 dB, depending on location relative to the baseline. This results entirely from the increased size of the bistatic resolution cell, as discussed below.

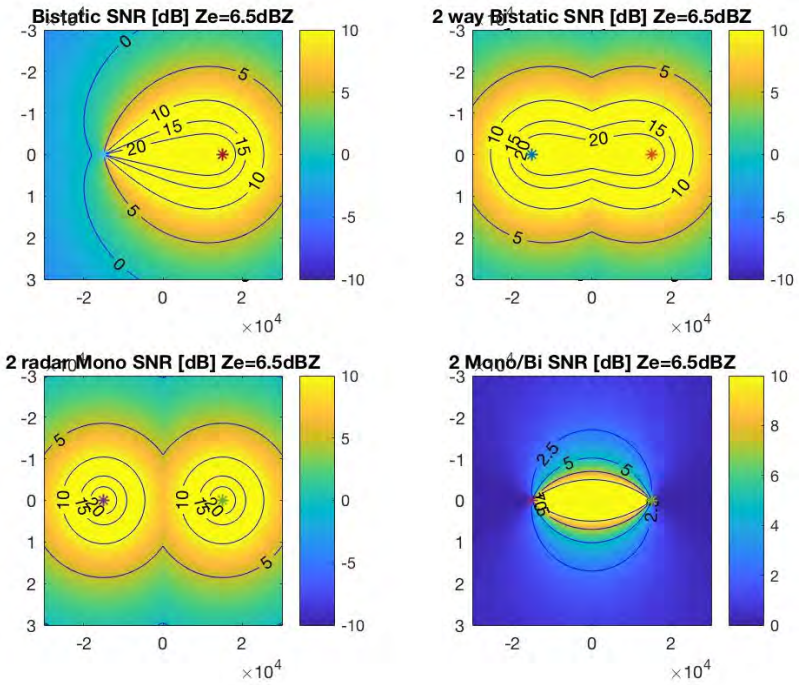


Figure 3. SNR for single bistatic radar (UL), two bistatic radars (UR), two monostatic radars (LL), and SNR ratio of 2 bistatic and 2 monostatic radar configurations (LR)

Figure 4. compares the geometry and resolution cell size for monostatic and bistatic cases and also, for comparison, lists representative values for the resolution cell size for NEXRAD, a long-range, high-power radar.

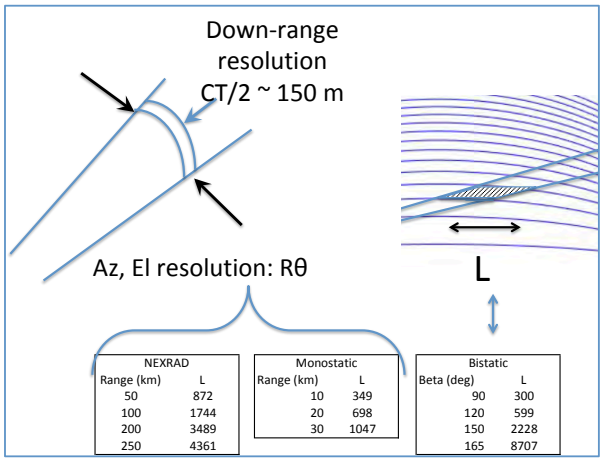


Figure 4. Resolution comparison of X-band monostatic and bistatic and NEXRAD radars

Monostatic radars have narrow down-range resolution, set by the transmitted pulse width to a typical value of 150 m. Spreading of the beam with increasing range results in significantly larger resolution cell size in the azimuth and elevation directions. X-band monostatic resolution is typically < 1 km in these dimensions. In contrast, the NEXRAD system, with 1 degree antenna beamwidth, has typical resolution of several km. The largest cell size in the bistatic case, set by the intersection of the transmitter beam and the range-gate geometry, varies with bistatic angle, and can grow to several km or more as the baseline is approached.

2.3 Bistatic/Monostatic SNR Comparison

Referring back to Fig. 1, a scenario involving two monostatic radars (left) and two bistatic radars (right) both viewing a volume of precipitation is given. The combined signal-to-noise ratio for the two cases is developed next to provide insight into the behavior of the network depictions to follow. When all constant terms in the SNR equations are lumped into a constant, A, the individual and combined SNR for the two monostatic radars is given by:

$SNR^a_{mono} = \frac{AR_1^2}{R_1^4} = \frac{A}{R_1^2}$ while $SNR^b_{mono} = \frac{AR_2^2}{R_2^4} = \frac{A}{R_2^2}$ and the SNR for the combination of the two radars is given by $SNR^{a+b}_{mono} = A(\frac{1}{R_2^2} + \frac{1}{R_2^2})$. Likewise, the SNR for the two bistatic radars is given by: $SNR^a_{bi} = \frac{AR_1^2}{R_1^2R_2^2cos^2(\beta/2)} = \frac{A}{R_2^2cos^2(\beta/2)}$ and $SNR^b_{bi} = \frac{AR_2^2}{R_1^2R_2^2cos^2(\beta/2)} = \frac{A}{R_1^2cos^2(\beta/2)}$ and the SNR for the combination of the two bistatic radars is given by $SNR^{a+b}_{bi} = \frac{A}{cos^2(\beta/2)}(\frac{1}{R_2^2} + \frac{1}{R_2^2})$. Given these equations, it is straightforward to see that $\frac{SNR^{a+b}_{bi}}{SNR^{a+b}_{mono}} = \frac{1}{cos^2(\beta/2)}$ which is simply the ratio of resolution volumes for bistatic and monostatic radars; this is the shape plotted in Fig. 3 LR.

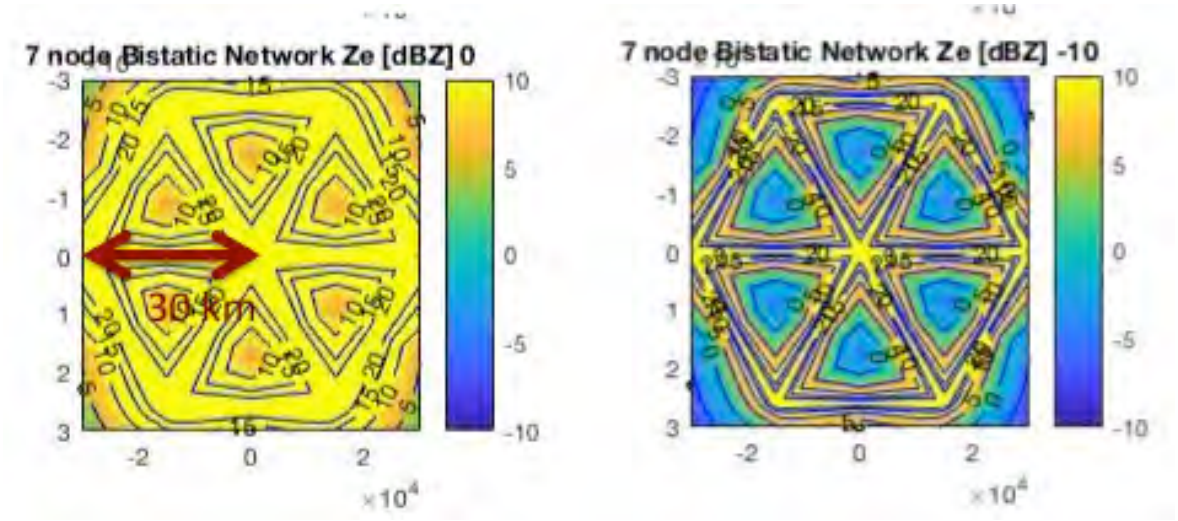


Figure 5. SNR for 7 node 2-way bistatic networks for Ze=0 dBZ (UL) and Ze=-10 dBZ(UR)

Figure 5 shows SNR for a 7 node network of bistatic radars for cases where Ze=0 dBZ (left) and Ze=-10 dBZ (right). When compared to Figure 2, the bistatic SNR exceeds the monostatic SNR everywhere; detectability is achieved everywhere in the 0 dBZ case as evidenced by SNR exceeding 0 dB all throughout the region. This is the result of the increased bistatic volume resolution, and higher SNR is achieved closest to the bistatic baselines, where resolution volume is highest. The bistatic -10 dBZ case achieves detectability in between the baselines but loses detectability in the center of the isosceles triangles defined by three baselines (blue-colored regions surrounded by the 0 dB SNR contours).

3 Bragg Scattering from Clear-Air Refractive Turbulence

We now turn our attention to the clear-air situation, where neither precipitation nor insects are available as sources of radar scatter. Bragg scattering from refractive turbulence fluctuations can provide a source of radar echo in this case. This topic has been covered in published papers and text books (eg, [7], [8]). We follow the derivation in [10]. The volume reflectivity for Bragg scattering is given by $\eta = \frac{128\pi^6}{\lambda^4}\psi(k)$ where λ is the radar wavelength and $\psi(k)$ is the spectral density of refractive index turbulence. Assuming the refractive index variations are in the inertial sub-range and the turbulence is statistically homogeneous and isotropic, $\psi(k) \sim 0.033C_n^2k^{-11/3}$ where k is the Bragg-resonant wavenumber, given by $k = 2\pi/L$ where L is the Bragg-resonant wavelength. Figure 6 illustrates how L can be determined in a bistatic geometry. (Note that this figure describes the scattering geometry using supplementary angles, the bistatic angle, β, and the forward scatter angle, θ_s. Both angles are used in the literature, but β is used here as it can provide a more intuitive understanding of the geometry, as this angle reduces to 0^0 for the monostatic, or backscatter case, and 180^0 for the forward scatter case). The Bragg-resonant condition requires that phase shift in the radar echo from two scatterers at different range be 2π or 360^0.

With reference to Fig 6, the excess travel path (shown in red) for the more distant scatterer, compared to the closer scatterer, is $2Lcos(\beta/2)$ and when set equal to λ results in the Bragg-resonance condition, $L = {}^{\lambda}/_{2\cos(\beta/2)}$ and the corresponding Bragg-resonant wavenumber is $k = {}^{2\pi}/_{L} = \frac{2\pi}{L/2}\cos({}^{\beta}/_{2})$. With this value of k used in $\psi(k)$ the resulting radar reflectivity per unit volume is given by $\eta = 0.38\lambda^{-1/3}C_n^2 cos^{-11/3}(\beta/2)$. The dependence on bistatic angle, which has been pointed out by numerous others (eg, [7]) means that bistatic echo can be substantially larger than the, normally weak, monostatic backscatter from turbulence. It is a common practice in radar meteorology to describe radar scattering in terms of an equivalent reflectivity, Ze, given by $Z_e = \frac{\lambda^4\eta}{\pi^5|K_w|^2}$. When the bistatic value for η is substituted into this expression, we have the following expression for the equivalent radar reflectivity for Bragg-scattering from turbulence in the bistatic case: $Z_e = 1.335 \cdot 10^{15} C_n^2 \lambda^{11/3} cos^{-11/3}(\beta/2)$.

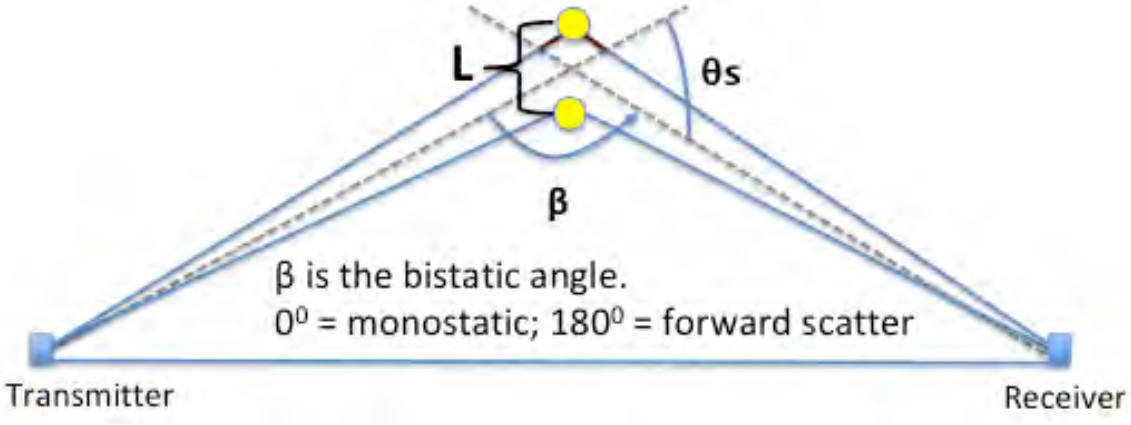


Figure 6. Bistatic Geometry for Bragg Scattering

Table 2 provides example values of Z_e in dBZ for different values of Cn2 and different bistatic angles. Looking back at Fig 1. For all monostatic cases (bistatic angle = 0) Ze is small enough to render the turbulence undetectable except in a very small region.

Table 2. Example Ze values

	BIstatic Angle (degrees)		
Cn2	**0**	**90**	**150**
1.00E-11	-13.6	-8.0	7.9
1.00E-12	-23.6	-18.0	-2.1
1.00E-13	-33.6	-28.0	-12.1
1.00E-14	-43.6	-38.0	-22.1

Monostatic detectability for the first two rows of Table 2 (ie, Ze= -13.6 dB and -23.6 dB) is depicted in Figure 7 for 2-radar configurations. Not surprisingly, detectability is limited only to very small regions near the radars, indicating that low-power X-band monostatic networks are unable to practically sense clear air turbulence.

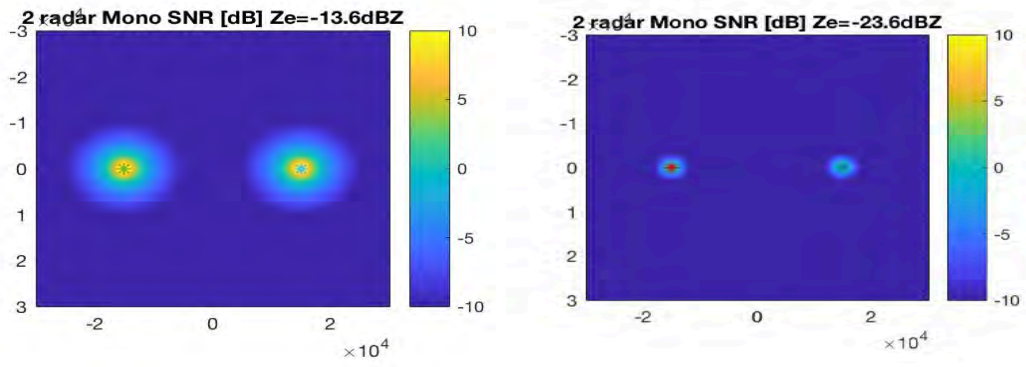


Figure 7. SNR maps for 2 monostatic configurations for clear air Bragg Scattering for Cn2=10e-11 (L) and Cn2=10e-12 (R)

Before examining the bistatic SNR for clear air, we first examine the characteristics of the bistatic Ze equation developed above, for insights. Figure 8 shows a two-way bistatic baseline configuration revealing how the bistatic angle, β, (UL), Bragg resonant scale, L, (UR), Ze in dBZ (LL) and SNR (LR) vary with spatial position for the case where Cn2=10^{-11}. In the region where the bistatic angle exceeds ~ 100 degrees, the bistatic reflectivity Ze ranges from -5 dBZ to more than 20 dBZ, in marked contrast to the -13.6 dBZ monostatic value for this turbulence condition; this results in detectability (SNR> 0 dB) throughout these regions. The bistatic SNR (LR) ranges from 0 to more than 10 dB in this region, contrasted with < 10 dB SNR over much the region depicted in the monostatic case of Fig 6 (L). The increased SNR results from >9 dB increase in bistatic Ze and > 5 dB increase due to increased volume resolution cell size.

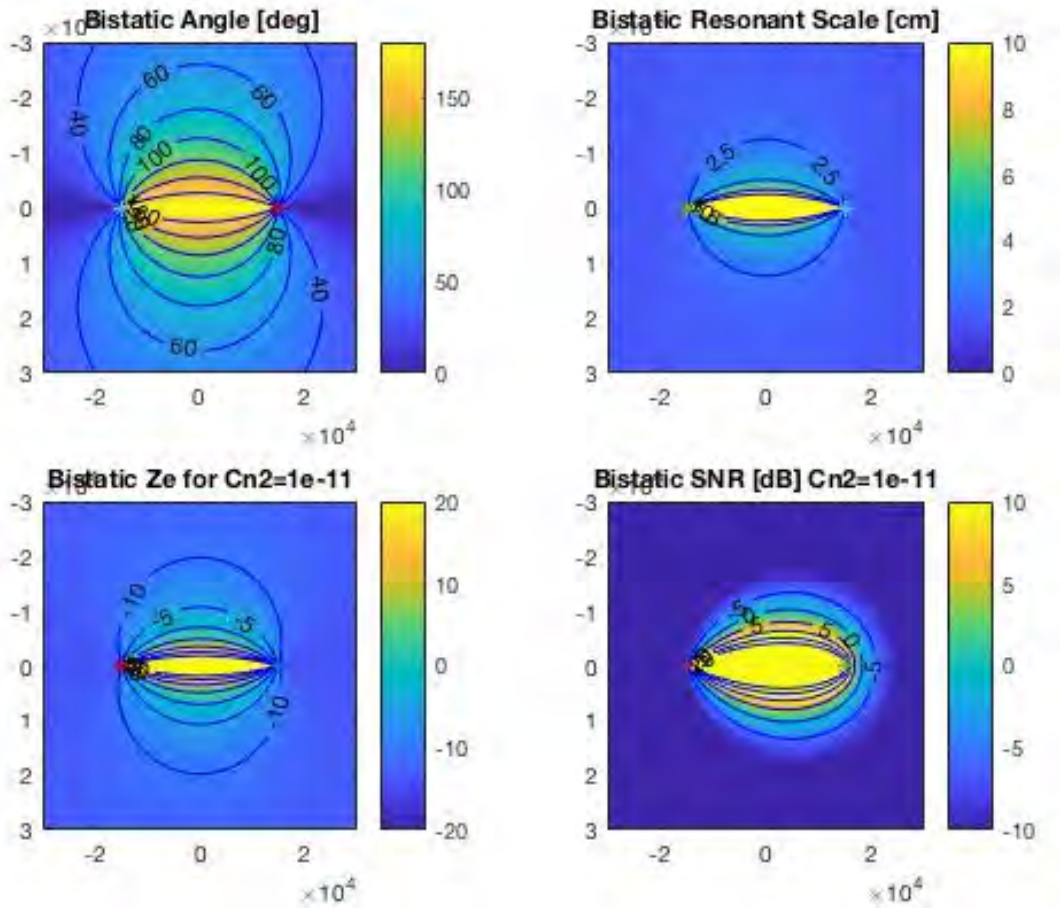


Figure 8. Bistatic Scattering Variables

Figure 8 depicts the bistatic SNR for a 7 radar, 2-way bistatic network viewing clear air for four different values of Cn2. The enhanced SNR relative to the monostatic case results in an ability to detect clear-air at different regions throughout the measurement area. For the Cn2=10^{-11} case, detectability is complete, without gaps. Lower values of Cn2 result in coverage gaps at regions of the bistatic baselines.

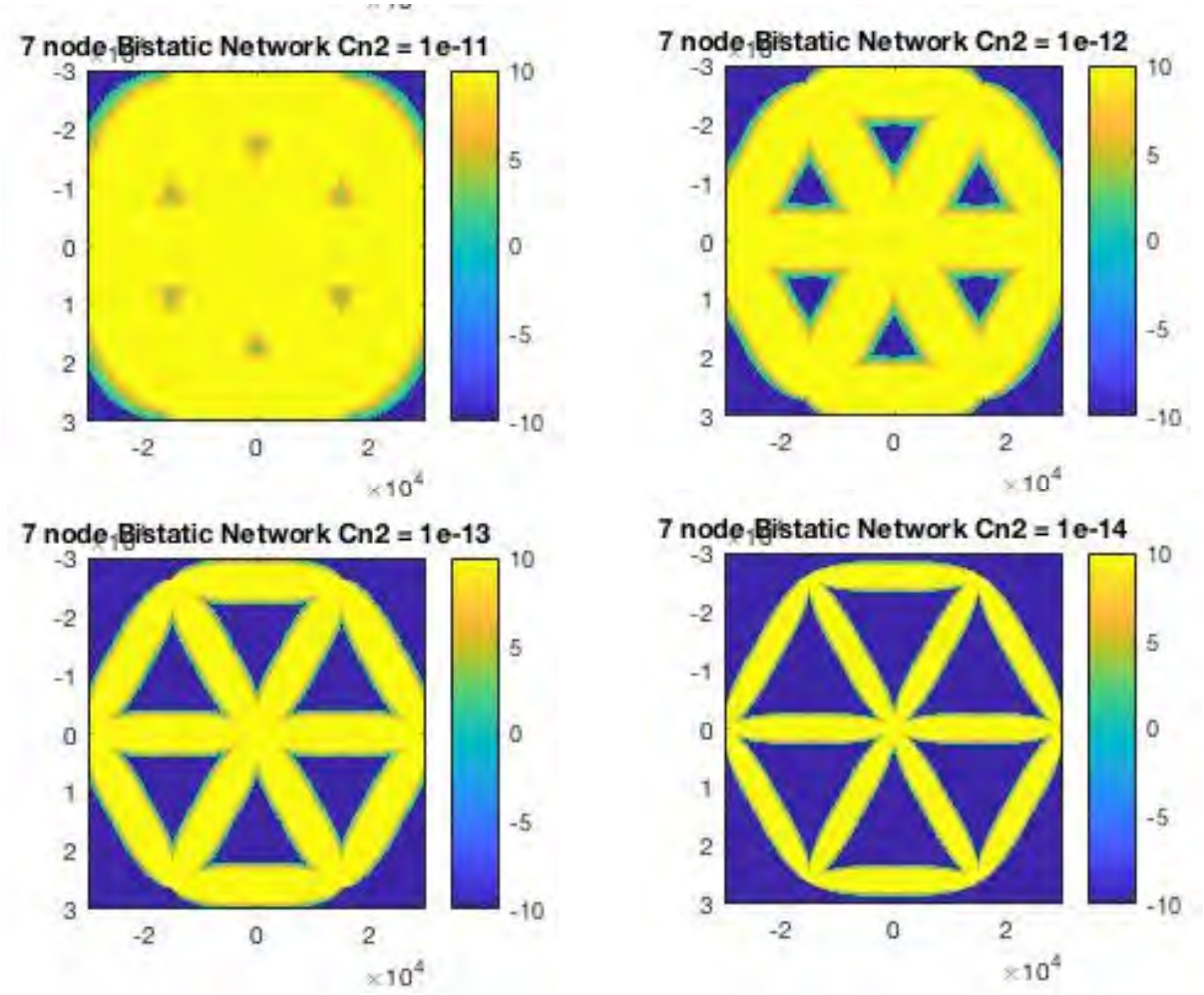


Figure 9. SNR for 7 node, 2-way bistatic configuraions for 4 Cn2 values

A primary use of weather radar is the detection of wind speed, and a key advantage of a dense network having overlapping coverage is the ability to map the wind vector field. Detailed analysis of this application is beyond the scope of this paper, however we take a preliminary look in Figure 10. This figure reproduces the SNR plots from Fig. 9, while masking out those regions where $\beta < 40^0$ or $\beta > 150^0$. This numbers are from [6] where it was demonstrated, using both analysis and observational data, that a wind vector retrieval is most effective when data from this range of β angles is used. This Figure shows the potential for mapping the wind vector field over most regions for Cn2=10^{-11}, some regions for Cn2=1e-12. Below Cn2=10^{-12}, SNR is inadequate to map winds over much of the region.

4. Discussion

The plots shown in this paper indicate that dense networks of low power radars, when operating in a bistatic mode, can achieve significantly higher sensitivity and detectability than the monostatic mode. The bistatic mode trades resolution for sensitivity (larger resolution cell size ~ higher SNR) and provides the ability for comprehensive low-altitude mapping when Ze < 0 dBZ. Absent precipitation and insects, the bistatic mode can exploit bistatic enhanced scattering from Bragg-scale turbulence, and the plots indicate these low-power networks can actually map the clear air in the boundary layer. Masking out regions where $\beta > 150^0$ significantly limits the regions where this enhancement can be exploited for full wind-vector measurement, however.

It seems to be conventional wisdom that high-power, long-range S and C-band radars can map weak-echo boundary layer winds, while low-power, short-range X band radars lack sensitivity for such measurements. A geometric fact about any long-range radar is that earth curvature prevents the radar from viewing the boundary later over much of the coverage region. Short-range radar networks do not suffer this earth coverage problem, and the plots shown here indicate these networks have some potential to map boundary later winds, without earth curvature blockage, when Cn2 is high enough.

Additional work is necessary to take these ideas into implementation. Among the many issues to be investigated further are:

Network laydown geometry and wind field retrieval. This paper assumes a specific radar network topology, namely one in which the radars deployed in equilateral triangles spaced 30 km apart. Other topologies may prove to be better able to exploit the bistatic scattering effects discussed here to retrieve wind fields.

Receiving antenna beamwidth, beam-synchronization, and pulse-chasing. We assumed use of receiving antenna beam wider than the transmitter beam, so that the resolution volume is only determined by the range gate spacing and antenna beamwidth. Incorporating a narrower receiving antenna beam would decrease the resolution cell volume, which may desirable in some cases. Narrow transmitter and receiver beams would only overlap at small spatial volumes, and this would complicate the volume coverage pattern and beam scanning strategy. Conducting full volume scans would require a sweep of the receiving antenna beam down through the various range gates *for each beam position* of the transmitter antenna (in contrast, echoes from all range gates are received for each pulse-repetition interval and beam position with a monostatic radar.) Whereas this might be impractical when mechanically-scanned radars are used, phased array radars are able to rapidly perform such a sweep using "pulse chasing" [11].

Transmitted waveform. This analysis assumed use of a fixed duration transmitter pulse and fixed receiver beamwidth and only considered single-pulse SNR. In practice, waveform design will need to take into consideration the use of batches of received pulse echoes to achieve measurement precision; moreover, the design will need to consider the range-Doppler dilemma and potentially the use of variable-duration pulse width and receiver bandwidth as a function of range from the transmitter and receiver antenna sites.

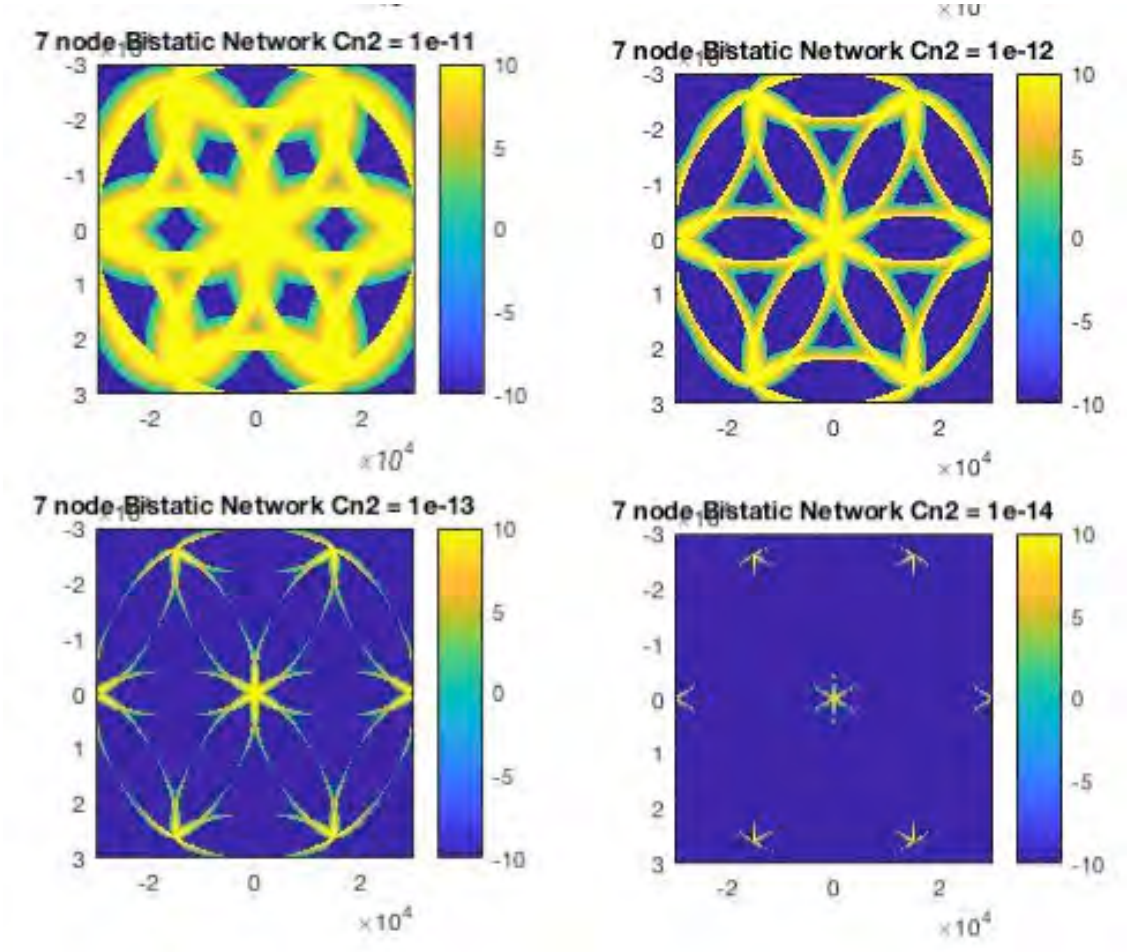


Figure 10. Bistatic SNR for 7 node, 2 way network with beta regions <40 and >150 degrees masked out

Acknowledgement

The theory presented here is not new, and the work of the authors listed in the references is appreciated, as that work enabled the system calculations to be performed here. The author is aware of the length of this extended conference abstract. Paraphrasing Mark Twain, "If I had more time, I would have written a shorter paper."

References

[1] McLaughlin D, Pepyne, D, et al, "Short Wavelength Technology and the Potential for Distributed Networks of Small Radar Systems, Bulletin American Meteorological Society, December 2009.

[2] Hirano, K., Maki, M., et al, "Composite Rainfall Map from C-band Conventional and X-Band Dual-Polarimetric Radars for the Whole of Japan, " ERAD 2014

[3] Cremonini, R., Tabary, P., et al, "Evaluation of X-Band Radar Technologies Within Opera 3 Project," ERAD 2012.

[4] Weber, M. and Istok, M.,"Weather Radar Fundamentals", SENSR Industry Week Workshop, 28 March, 2018, https://faaco.faa.gov/index.cfm/announcement/view/30396

[5] Pica, J., "Spectrum Efficient National Surveillance Radar (SENSR) Program – NOAA Coverage Volumes: Overview", SENSR Industry Week Workshop, 26 March 2018, https://faaco.faa.gov/index.cfm/announcement/view/30396

[6] Satoh, S. and Wurman, J., "Accuracy of Wind Fields Observed by a Bistatic Doppler Radar Network," Journal Atmospheric and Oceanic Technology, Vol. 20, August 2003.

[7] Atlas, D., Naito, K., and Carbone, R., "Bistatic Microwave Probing of a Refractively Perturbed Clear Atmosphere", Journal of the Atmospheric Sciences, Vol. 25, March 1968.

[8] Doviak, R. and Zrnic, D., Doppler Radar & Weather Observations, 2nd Ed., Elsevier, 1993.

[9] De Elia, R. and Zawadzki, I., "Optimal Layout of a Bistatic Radar Network," Journal Atmospheric and Oceanic Technology, Vol. 18, July, 2001.

[10] Tulu, Z., Frasier, S., Janaswamy, R, and McLaughlin, D., "Considerations for Bistatic Probing of Clear-Air Winds in the Atmospheric Boundary Layer," Radio Science, Vol, 41, 2006.

[11] Willis, N., Bistatic Radar, Artech House, 1991

Operational monitoring of T/R-Limiter degradation based on close range ground clutter

Tiemo Mathijssen[1], Stan Broere[1], Hans Beekhuis[1], and Hidde Leijnse[1]

[1]*Royal Netherlands Meteorological Institute, Utrechtseweg 297, 3731 GA De Bilt, the Netherlands*

(Dated: 25 June 2018)

1. Introduction

T/R limiters are widely employed as receiver protection equipment in operational weather radars. Typically the lifespan of a weather radar exceeds that of such limiters, resulting in a need to replace them. When replaced on a corrective basis, the radar downtime can occur at inconvenient moments during severe weather. Also the radioactive substances often present in these limiters poses strict regulation and administration of these components, which can be a nuisance during unscheduled repair. Moreover, T/R limiter failure typically leads to the frontend breaking too. It is usually preceded by degradation, which can affect data for an extended time before the failure. Preventive replacement is undesired, due to the very large variation in lifespan of these components. Ideally, a warning message is generated specifying that component degradation has commenced. T/R limiters typically show an increased recovery time before failing, which can be exploited to monitor component degradation. Large recovery times will show up in produced data by reduced ground clutter at close range to the radar site. Monitoring the close-range ground clutter could give an indication of the state of the limiter (Beekhuis and Leijnse, 2012). This study presents further results to which extent monitoring of ground clutter can be used to identify T/R limiter degradation and other sources of measurement error.

2. Radar data

Up to 2016, KNMI has operated two Selex Meteor 360AC single polarization radars, located in De Bilt (5.17834E, 52.10168N) and in Den Helder (4.790767E, 52.95271N) overlooking the sea. Details of these radars and its scanning schedule is described by Beekhuis and Holleman (2008). In 2016, these have been replaced by two Selex Meteor 735CDP10 dual polarization weather radars in Herwijnen (5.138056E, 51.83694N) and at the same location in Den Helder (4.790767E, 52.95271N). Also a new scanning schedule is introduced with the radar installation, which is displayed in table 1. Every five minutes the antenna moves downwards twice in a staggered way to allow the production of a pseudo CAPPI every 2.5 minute based on different elevations. The lowest elevation is repeated a total of three times, of which two times with a single PRF with the purpose to maximize the signal-to-noise ratio, and once with dual PRF to obtain accurate velocity data.

no	elevation [°]	high PRF [Hz]	low PRF [Hz]	pulsewidth [μs]	rangebin size [m]
1	90	1600	2400	0.50	75
2	12	2000	1200	0.60	90
3	8.0	2000	1200	0.60	90
4	4.5	1200	800	1.00	150
5	2.0	800	600	1.50	225
6	0.8	800	600	1.50	225
7	0.3	450	-	2.67	399
8	25	2000	1200	0.60	90
9	20	2000	1200	0.60	90
10	15	2000	1200	0.60	90
11	10	2000	1200	0.60	90
12	6.0	1200	800	1.00	150
13	2.8	800	600	1.50	225
14	1.2	800	600	1.50	225
15	0.3	800	600	1.50	225
16	0.3	450	-	2.67	399

Table 1: KNMI Scanning strategy

3. Method

In order to monitor degradation of the T/R limiter, the recovery time of the component can be exploited. The T/R limiter prevents the transmitted signal to enter the receiver without attenuation. Shortly after the transmitted pulse has passed, the T/R limiter should recover to its low attenuation state. A well-known degradation process of such devices shows the increase of the recovery time. Whenever the recovery time increases beyond the time that reflected signals would pass into the receiver, the reflected ground clutter will be attenuated close to the radar. With a further increasing recovery time, also data further away from the radar will be affected.

It is thus possible to obtain a diagnostic of T/R limiter functioning by observing the long-term stability of near-radar ground clutter from resulting uncorrected reflectivity data. Low elevations produce a ground clutter return that on average should be approximately constant in time, although day-to-day changes and an annual trend can be expected. Any reduction in close range clutter power could indicate degradation of the T/R limiter. This would be visible by a decreasing ground clutter level for the closest rangebin. Later in time, the increased recovery time will not only affect the first rangebin, but also the second. Even later, the third rangebin, etc. A small rangebin size will thus lead to an early detection of T/R limiter failure.
The algorithm evaluates the uncorrected reflectivity close to the radar. For data reduction reasons and for statistical reasons, the azimuthal average for each range bin is calculated every radar cycle, which is repeated every 5 minutes at KNMI. This is done for a selected amount of elevations. Once per day, the time average is consequently calculated for each range bin, leading to a day-and-azimuthal-averaged value as a function of the range or rangebin number. The resulting daily values are then be visualised for a selected number of rangebins to observe if any reduction in reflectivity has taken place, indicating possible T/R limiter degradation.

4. Results

Results of two different cases are presented. One is a historic case from 2009, in which the T/R limiter degradation of the De Bilt radar had gone unnoticed for several months. Section 4.1 elaborates on this case, which shows the capability of the tool to identify T/R limiter degradation. Section 4.2 shows the current operational data for the Herwijnen radar and Den Helder radar. Although no T/R limiter degradation is observed in the recent time, it shows the value of the tool for general data quality monitoring purposes.

4.1. De Bilt T/R limiter degradation case

As a sample case a degradation T/R limiter from the De Bilt radar is taken from 2009, that clearly shows the extent of unnoticed T/R limiter degradation. The device had been steadily degrading from August 2009, but was only discovered in December. An overview of the reflectivity at 0.3° elevation near the radar is displayed for the correct functioning T/R limiter in figure 1 and for the degraded T/R limiter in figure 2. This shows the impact degradation can have on the radar data. The resulting averaged daily clutter power for the 0.3° elevation is shown in figure 3, visualising the trend of individual rangebins and in figure 4 in a contour plot. An average of the ground clutter is taken for each rangebin from the 1st of August 2008 until the 31st of July 2009, which is subtracted from the daily values with the purpose to normalize the data. From August 2009, the increased T/R limiter recovery time is affecting the first rangebin, from mid-August the second. This continued to affect rangebins further from the radar until the degradation of the T/R limiter was noticed and the device was exchanged early December 2009. Monitoring would have resulted in a much earlier detection, avoiding data to be corrupted by the faulty component.

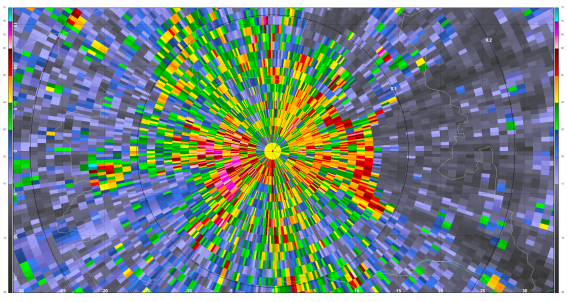


Figure 1: Reflectivity at 0.3° elevation near radar De Bilt, taken at the 7th of August 2009 at 1:55 UTC. The T/R limiter is still functioning correctly and ground clutter is visible close to the radar.

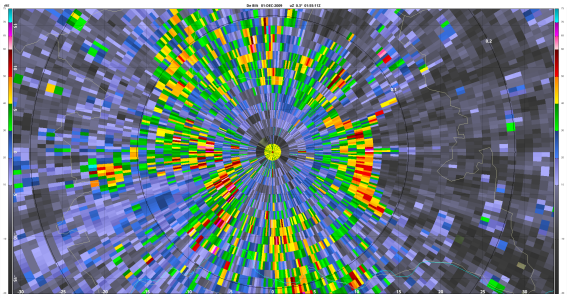


Figure 2: Reflectivity at 0.3° elevation near radar De Bilt, taken at the 1st of December 2009 at 1:55 UTC. The T/R limiter is degraded and ground clutter is nearly absent close to the radar.

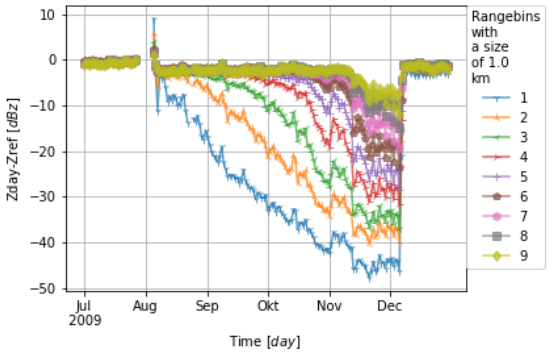


Figure 3: Normalized daily azimuth average ground clutter per rangebin of the 0.3° elevation of De Bilt radar. Normalisation is done based on a reference period from 1st of August 2008 until the 31st of July 2009. Consecutive reduction of ground clutter is visible for increasing rangebins, indicating degradation of the T/R limiter.

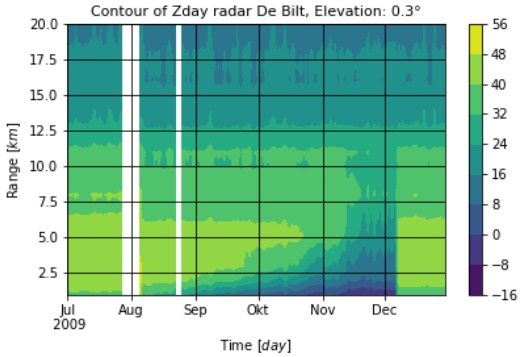


Figure 4: Contourplot of the normalized daily azimuth average ground clutter of the 0.3° elevation of De Bilt radar as a function of range. Normalisation is done based on a reference period from 1st of August 2008 until the 31st of July 2009. Consecutive reduction of ground clutter is visible for increasing rangebins, indicating degradation of the T/R limiter.

4.2. Operational monitoring of radar Herwijnen and Den Helder

The monitoring is applied on an operational basis by analysing every volume scan, which KNMI generates every 5 minutes. Scans 1, 7 and 15 are selected in the KNMI case, but others can be selected easily in the developed tool. Scan 1 provides the smallest rangebin size, such that an early detection of T/R limiter degradation should be noticeable. Adversely, the 90° elevation results in a very limited amount of ground clutter. Scan no. 7 and no. 15 both feature sufficient amount of ground clutter, since these are at only 0.3° elevation. Scan no. 7 features the highest signal-to-noise ratio, while scan no. 15 uses a smaller rangebin size. Every 5 minutes, an azimuth average for each rangebin of the selected elevations is made, and once per day a time average is created and displayed on an internal website in an automated fashion. The script is written such that it is easily transportable to different radar data in the Opera data and information model (ODIM) format.

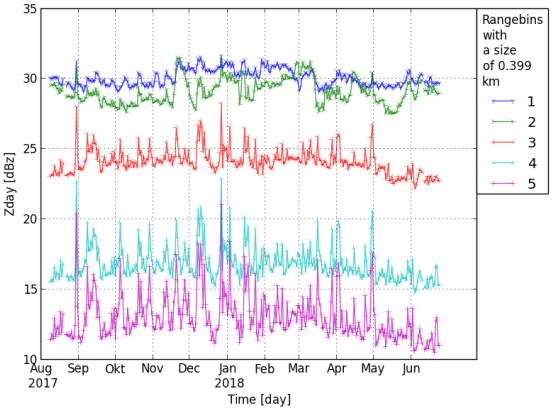


Figure 5: Daily azimuth average ground clutter per rangebin of the horizontal channel scan 7 at 0.3° elevation of radar Den Helder. The step change in August 2017 is caused by a change in signal processor settings.

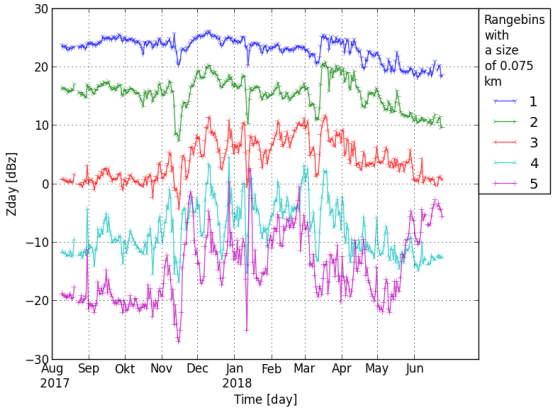


Figure 6: Daily azimuth average ground clutter per rangebin of the horizontal channel of the birdbath scan radar Den Helder. The step change in August 2017 is caused by a change in signal processor settings. The step in the first rangebin in February 2018 and the upward trend are not yet clarified.

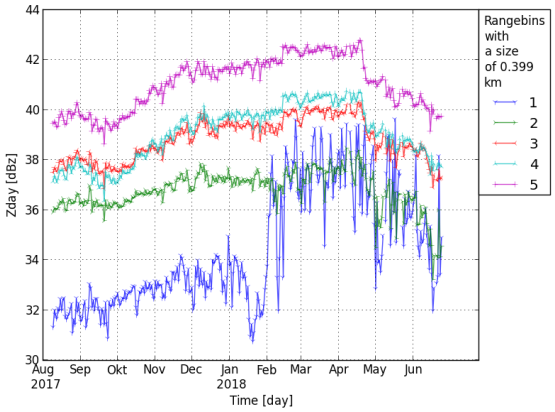


Figure 7: Daily azimuth average ground clutter per range-bin of vertical channel of radar Herwijnen. The step change in August 2017 is caused by a change in signal processor settings.

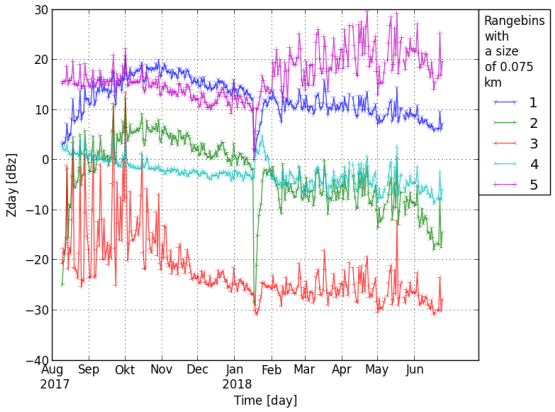


Figure 8: Daily azimuth average ground clutter per range-bin of vertical channel of radar Herwijnen. The step change in August 2017 is caused by a change in signal processor settings. The step in the first rangebin in February 2018 and the upward trend are not yet clarified.

The trend of the last 16 months of daily average clutter reflectivity of the horizontal channel of radar Den Helder is displayed for the 0.3° elevation of scan no. 7 in figure 5 and for the 90° elevation of scan no. 1 in figure 6. The rangebins further from the radar are affected by sea clutter, leading to large variations in daily values. As expected, the birdbath scan features a much lower clutter power as it is directed 90° upward, reducing the amount of ground clutter to a minimum and meteorological signals to be more prominent. The very small rangebin size of 75 meter should lead to a very rapid identification in case of T/R limiter degradation, however the noise could obscure this effect.

The operational monitoring for the vertical channel of the Herwijnen radar is displayed in figure 7 for the 0.3° elevation of scan no. 7, while for the 90° birdbath scan the result is visualised in figure 8. An upwards trend is visible up to April 2018 for the low elevation, while the trend seems downwards for the birdbath scan. The reason for the drift is still unclear. It is unlikely that is can be attributed to the T/R limiter, since it is visible in all rangebins at the same time, and is in opposite directions for different elevations. Another unexplained feature is the step change in the first rangebin of the 0.3° elevation, and the dip in the birdbath scan in February 2018. Even though these phenomena are still unexplained, they show that the monitoring tool does not only monitor T/R limiter degradation, but many other phenomena. This makes it an appropiate tool, not only for T/R limiter monitoring, but for overall radar data quality monitoring.

5. Conclusion

A tool is developed for early detection of T/R limiter degradation based on automated monitoring of close-range clutter. A historic case of T/R limiter degradation in radar De Bilt over the course of several month shows that the method can be used for early detection of degradation. Also, the tool is applied to present current operational data near real-time. The analysis and visualisation is done automatically and presented on an internal website automatically. Results show that T/R limiter degradation has not been observed recently. However, some unexplained fluctuations in close-range ground clutter are identified. This proves that the tool can also be used as general data quality monitor. Furthermore, the tool is easily transported to other weather radars that create volume data based on the ODIM format.

References

H. Beekhuis and I. Holleman, “From pulse to product,” in *5th European conference on radar in meteorology and hydrology*, 2008.

H. Beekhuis and H. Leijnse, “An operational radar monitoring tool,” in *7th European conference on radar in meteorology and hydrology*, 2012.

From Pulse to Product,
Highlights of the upgrade project of the Dutch national weather radar network

Hans Beekhuis, Tiemo Mathijssen
KNMI, Utrechtseweg 297, 3731 GA, De Bilt, The Netherlands
(Dated: 22 June 2018)
Extended Abstract to Poster 408

1 Introduction

In 2015 KNMI has successfully finished the upgrade of the Dutch weather radar network. The main results of this upgrade are replacement of the two weather radar sensors of the KNMI Weather Radar Network and enhancements in the subsequent product processing in order to fully deploy capabilities found in the modern weather radar equipment.

During the European tender carried out in this project SELEX SI (formerly known as Gematronik) was awarded a contract to perform the replacement of both KNMI weather radars. Part of this contract is the integral maintenance of the radars, including all repairs and spares on a flat fee basis. KNMI itself however is taking care of the monitoring and configuration of the radars. KNMI in this way stays in control over its radar production.



Figure 1: The radar site Herwijnen at 5.1379E 51.8370N Low 25 meter tower, but far better radar horizon.



Figure 2: The retired radar on the 45meter tower at the KNMI premises in De Bilt .

In the course of his project KNMI took the opportunity to relocate the radar that for historical reasons was situated on the main premises of KNMI in De Bilt to a new location near the village of Herwijnen. Main reason for this relocation stems from the detoriation of the radar horizon of De Bilt, due to the vertical expansion of the city of Utrecht. KNMI acquired access to the tower of the former ATC radar situated in Herwijnen.

The radar product processing, in our central computer facilities, was updated as well. The Rainbow based Radar Product Processor is offering ‘off the shelf’ data processing, but is extended with KNMI maintained input and output filters, in order to create flexibility in the conversion to and from formats used by KNMI.

Some of the main design considerations are stated in this abstract, for the purpose of sharing this information

1.1 Workhorse approach

KNMI strived to deploy a rugged design with a strong focus on cost effectiveness and reliable operational use. This is reflected by KNMI's choice to stick on the classical receiver under elevation design. By placing the receiver in a well acclimatized room and providing hard wired connections to the signal processor, problems related with reliability often found in Receiver over Elevation (ROEL) setups are avoided. By restricting dual polarization operation modes to Simultaneous Transmit and Receive (STAR) mode only, problems that can occur with the switching elements in the waveguide are absent too. To keep the price of the radar low KNMI choose to install magnetron driven radars. Although klystron based transmitters show better performance characteristics when it comes to phase and power stability, much of the shortcomings of a magnetron driven transmitter can be corrected for by a capable signal processor.

1.2 Constant duty scan

Modern modulator equipment design does not rely on a pulse forming network to deliver power to its magnetron. In the classic pulse forming modulator design one could only chose from few discrete pulse lengths, but the modulators in the KNMI radars allow for choosing any pulse length between 0.5 and 3.5 microseconds. By carefully choosing pulse repetition rates and pulse lengths for each elevation it is possible to operate the magnetron close to its maximum power for each individual elevation in the volume scan. In this way the volume is probed with the maximum available energy, which thus optimizes the amount of information that can be derived from the atmosphere. As an extra the operating frequency of the magnetron is more frequency stable, because of the continuous load reduces temperature variations in the operating temperature of the magnetron.

1.3 Calibration on the fly

The (receive) path calibration of the radar is monitored by performing a single point calibration during every volume scan. For this purpose two high power wide ban noise sources are mounted in the receive path, one for each polarization. The noise sources are activated by the volume scan scheduler such that data sampled is not of meteorological interest as it will be beyond the atmosphere. In a similar way zero checks are performed several times during a volume scan. The results obtained are monitored on stability and trends. KNMI does not let the installations automatically adjust the calibration, but is warned by the radar monitor software when deviations in the calibration are detected by the built in test equipment.

1.4 Maintenance by the manufacturer

KNMI has decided not to perform maintenance of the radars itself, but to outsource it to the manufacturer. In former days KNMI employed its own radar technicians, but when they grew into retirement, their functions were not replaced. The main driver for this is that the maintenance of radar equipment is greatly reduced from radar generation to radar generation. Early nineties KNMI still scheduled yearly some 60 workdays on checks and maintenance of the two radars, while the current setup is serviced with an ample 6 days yearly. This made it more and more difficult for KNMI staff to keep up their skills on the desired level of operationality. On the other hand these skills are necessarily available by a manufacturer that designs and builds the radar equipment. So the KNMI management decided that the integral maintenance should be part of the tender, and that this should be acquired against fixed yearly costs. In this way the trust of the manufacturer in its own equipment is translated in yearly costs and covered by a service level agreement. As a result the total cost of ownership for the radars has not risen during this tender, whilst the risks on costly repairs are not put on the KNMI administration. It is mentioned here that radome maintenance is part of this settlement as well, as it is foreseen that the radome coating shall be renewed each five years.

1.5 Monitoring and configuration by KNMI

Knowledge on radar hardware and software configuration is important for KNMI in order to make an optimal use of the equipment. KNMI decided that this function should stay with KNMI. New young staff has been trained during the upgrade project and is now responsible for the configuration of the radar. Skilled staff is also important as interface to the manufacturer, reporting and commenting on errors and specifying enhancements needed by KNMI. Also monitoring of the equipment is a duty that KNMI performs. By automating procedures the level of monitoring is brought both to a higher level and a less time consuming task.

2 Radar Sensor Layout and Characteristics

KNMI operates two identical Meteor METEOR 735CDP10 Magnetron based C-band Dual polarization weather radars from SELEX, located in Herwijnen (5.1379E 51.8370N, WSG-84) and at a naval base in Den Helder (4.78997E 52.9533N, WSG-84). A brief overview of the main components in the radar processing chain is detailed below:

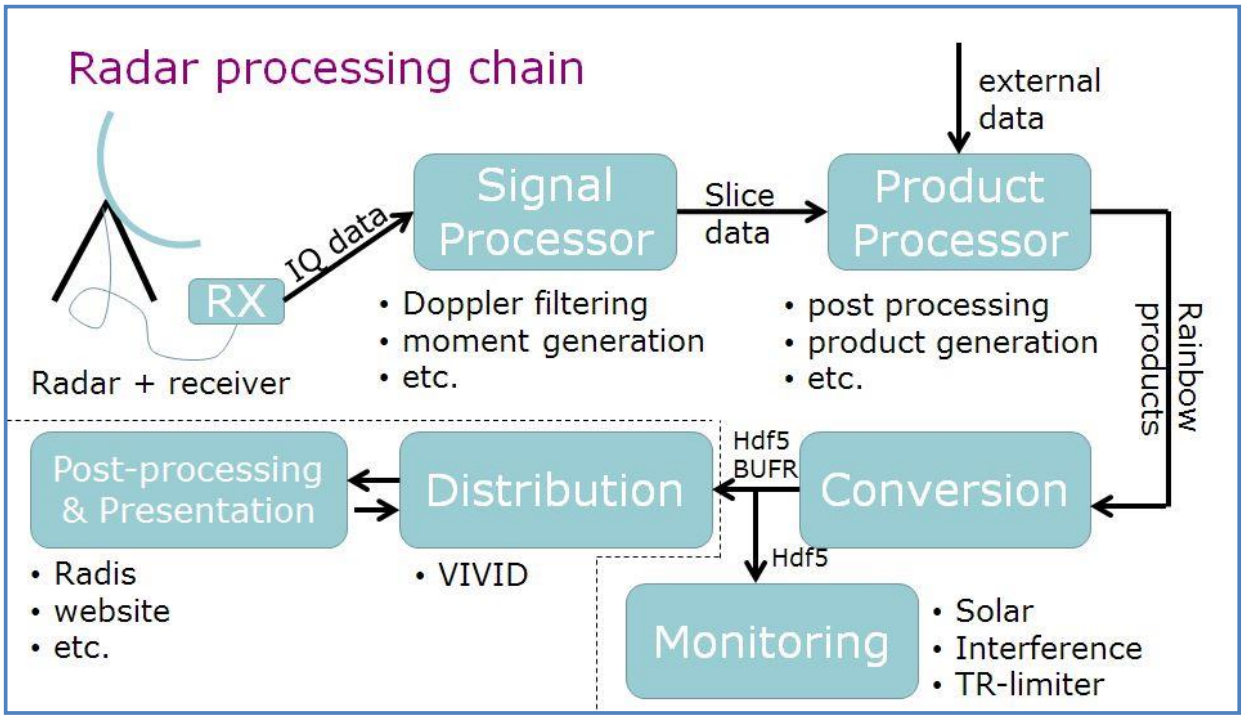


Figure 3: The radar processing chain..

2.1 Antenna and Mover

The 4.3 meter antenna is offering a one degree beam width and a 45 dB gain. The brushless drives and built in servos allow for a compact design of the radar cabinets as the servo racks are now integrated in the pedestal. The mover positions the antenna with high accuracy and can move 180 degrees over its horizontal axis.

2.2 Transmitter

The KNMI radars use magnetron based C-band transmitters offering a nominal peak power of 500 kW/peak. As setups require nowadays that spurious out of band emissions are greatly reduced a harmonic filter is placed in the waveguide. This filter is filled with SF6 gas to avoid arcing, which could occur in the filter due to the complex geometrical shapes needed to perform the filtering. The RF pulse is split in an horizontal and vertical channel after it passed the filter of equal power. As already stated the modulator setup can accommodate pulse lengths anywhere between 0.5 and 3.5 microseconds. The transmitter allows for Pulse Repetition Frequencies up to 2400 Hz.

2.3 Receiver

The returned echo signals in H and V are captured by two analog frontends that allows for a 120 dB dynamical range, and a 2 dB noise figure. Each frontend uses two separate receivers that have a gain offset of 20 dB. The most sensitive receiver is used to process low and intermediate signals but before the receiver reaches the nonlinear region of is sensitivity curve the less sensitive receiver takes over to handle the higher signal levels. By combining these signals a 120 dB dynamical range is reached. The receiver downmixes the received signals to an Intermediate Frequency (IF) of 60 MHz. The analog IF signals are digitized in the GDRX digital receiver directly, using 80 MHz ADCs. The GDRX receiver takes in the attenuated HF pulse generated by the magnetron too. This TX-sample is used to generate In-phase and Quadrature-phase (I & Q) signals, and to monitor the transmitted power.

2.4 Signal Processor

The signal processor is a capable industrial linux machine. Processing power and storage make it possible to retrieve and process all the moments in at the same time. KNMI retrieves the moments Zh, Zv, uZh, uZV, Vh Vv, W Wv, ZDR , cCor cCorv SQI SQIV CPA CPAv uPhiDp PhiDp, KdP, RhoHv. The signal processor is capable of processing all moments simultaneously. From the Signal Processor data are sent to the central Product Processor on a per PPI basis thus minimizing lag times due to transmission. The signal processor has a 3 terabyte storage buffer that can be used as a ring buffer to record continuously IQ data on the fly, thus allowing for replay and analysis of recorded events.

2.5 Control Processor

The radar control processor runs on standard industrial hardware, and is responsible for controlling all the radar hardware. Of course the antenna is the most "active" element to be controlled. But the control processer handles all bite messages and health and safety checks of the radar equipment too. It is the control processor too that controls the various interlock circuitry and software so to safeguard human exposure to dangerous voltages, radiation and physical risks.

2.6 Product Processor

The Linux based Radar Product Processor is using Rainbow5 application software for the product generation and configuration control of the radars. All single radar products are generated on this platform. In addition it performs compositing of local and European radar data. The Product Processor is extended with user maintainable input and output converters. As a result it is able to process BUFR data delivered by the GTS, as well as the sensor data coming in from the radar sensors. Output of the system is fed into the central KNMI distribution systems.

2.7 Distribution and display

KNMI uses an open (HDF5 based) data model for distributing radar data. This model is used for internal and external users alike. Applications within KNMI use this format to post-process radar data. One of these postprocessors is the web based display called RADIS available for all computers within KNMI, which has been developed in house using java.

New in house developments are underway in the form of a web based meteorological workstation called GEOWEB is now running for test.

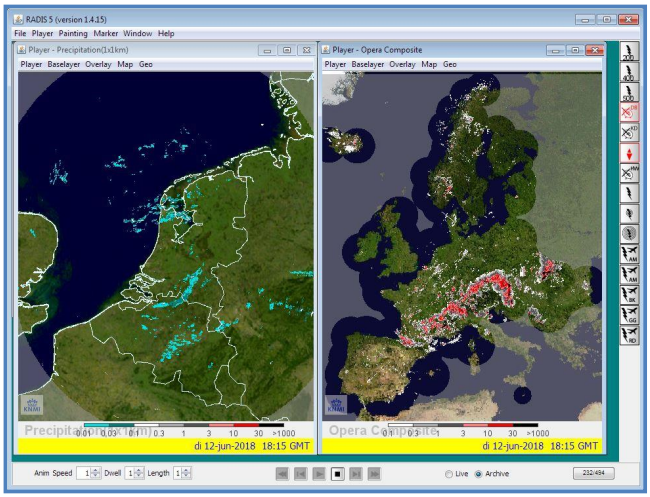


Figure 4: KNMI Radis display showing NL and ODC composite

3 Radar in operation: Scan schedule

The operational scanning of the KNMI weather radars generates a 16-elevation volume every 5 minutes. For all elevations in this volume scan, parameters can be chosen independently.

no.	elevation [deg]	high PRF [Hz]	low PRF [Hz]	pulsewidth [µs]	Time start	Time end
1	90	2400	-	0.5	0:00	0:12
2	12	2000	1200	0.6	0:12	0:27
3	8.0	2000	1200	0.6	0:27	0:39
4	4.5	1200	800	1	0:39	0:54
5	2.0	800	600	1.5	0:54	1:10
6	0.8	800	600	1.5	1:10	1:27
7	0.3	450	-	2.67	1:27	1:59
8	25	2000	1200	0.6	1:59	2:12
9	20	2000	1200	0.6	2:12	2:24
10	15	2000	1200	0.6	2:24	2:36
11	10	2000	1200	0.6	2:36	2:48
12	6.0	1200	800	1	2:48	3:03
13	2.8	800	600	1.5	3:03	3:19
14	1.2	800	600	1.5	3:19	3:36
15	0.3	800	600	1.5	3:36	3:59
16	0.3	450	-	2.67	3:59	4:30

Table 1: The main parameters of the volume scan.

The KNMI volume scan is semi interlaced, and allows for generating two pseudo cappi products from the same volume that are using nearly the same elevations but are time separated by 2.5 minutes. This intermediate pseudo cappi is currently running under test. By top down scanning the lowest elevation that is covering most of the area in pseudo cappi products is captured just before the production starts, so most of the visual content of the products distributed is scanned just a minute before. The lowest elevation is repeated a total of 3 times: twice at single PRF for the generation of the pseudo cappi and another time using dual PRF to obtain unambiguous velocity data.Also a 90degree elevation scan (birdbath) is part of the schedule. This scan is added for the purpose of monitoring Zdr stability. What is new here is that monitoring parameters (noise level, single point calibration and Zdr stability are integral part of the volume scan, so these parameters can be acquired with a minimal overhead, and are available in every volume scan.

4 Corrections applied on Volume Data

4.1 Clutter Processing

The KNMI ground clutter processing scheme based upon statistical filtering has been abandoned. This method has been used from 1992 to 2016, with a last update introduced in 2007. Research by Iwan Holleman shows that dualpol radars offer far better opportunities to reduce clutter in addition to the DFT-filtering with spectral reconstruction which is now applied on all elevations. Aart Overeem is currently working on the operational implementation of these clutter filters.

4.2 Occultation correction

Even in a country as flat as the Netherlands the radar beam can be obstructed, be it mostly by man made objects that mostly block only small sectors. The applied occultation correction reconstructs blocked sectors on a per elevation basis by performing a linear weighted averaging of data found close to the edges of the blockage.

5 Quality Monitoring, Looking at the sun and more

The sun emitting in its spectrum weak radar signals offers the possibility to check the radar sensors against an external source. By offline processing of received volume sets KNMI is monitoring the sun passages during sunrise and sunset. The output of this tool offers a day to day record of the sun power compared to the DRAO standard. It shows that our installations follow DROA observations in good agreement thus offering a valuable monitoring tool for the sustained low power sensitivity of our receivers. In a similar way deviations in the pointing of the antenna as small as 0.05 degree are easily detected. Although these procedures were first developed around 2005, this suite of solar monitoring procedures has shown gradual growth in the products that can be monitored, as well as in the number of radars it is applied to. Latest innovations are application of this type of monitoring on the Opera Odyssey volume data hub providing a cross European monitoring, and work in progress to have similar procedures applied on the Nextrad network.

Other parameters will be added to the monitoring suite. Lately TR-limiter failure that can be seen in the range dependant degradation of return close to the radar is implemented. As an example of its output see figure 4 below, in which indeed no deviations are seen. For more examples see the extended abstract by Tiemo Mathijssen on operational monitoring of TR-limiter degradation. (This ERAD2018 conference ID 407)

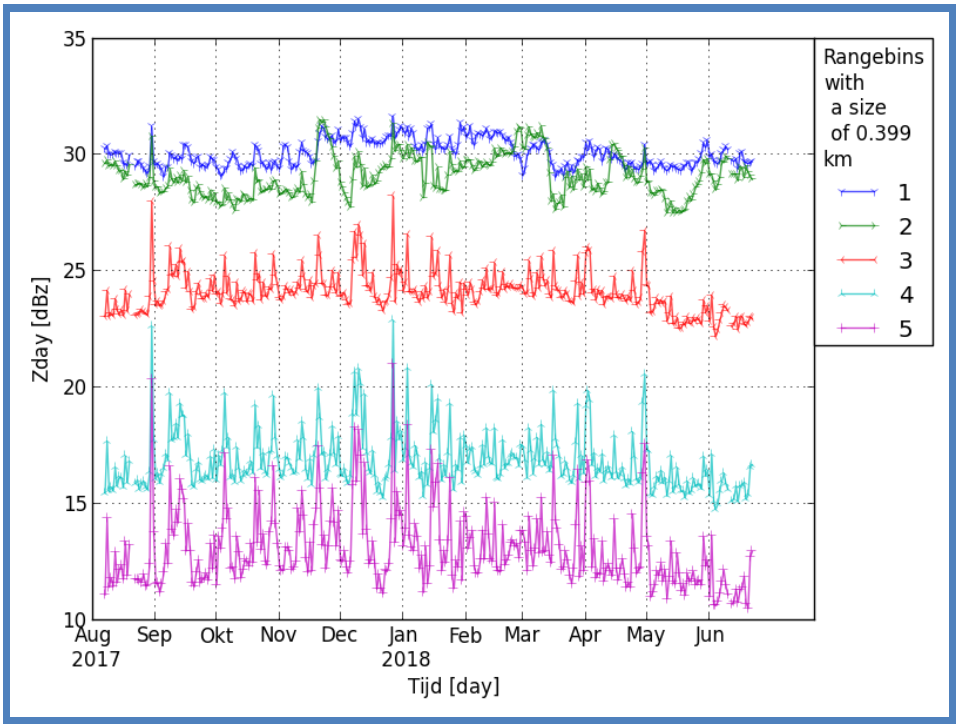


Figure 5: Monitoring Tr-limiter degradation, nothing to worry here.

Other offline monitors are currently under development. These include Zdr stability statistics (WLAN) interference alerting and monitoring of the total transmitted power by analyzing nearby ground echo return.

6 Data Model

The KNMI internal standard for operational radar products and volume data is based on HDF5. KNMI uses a proprietary (although freely available) data model. One of the advantages of the hierarchical structure of HDF5 is the way metadata can be stored along with the data.
The KNMI data model and the Opera data model are close, as they evolved from shared ideas originally promoted by Baltrad. KNMI is now experimenting with a hybrid form of HDF based volume data. In the volumes two meta data sets are available, being in the form prescribed by ODIM as well as in the form the KNMI model requests. So software expecting ODIM or KNMI style metadata will be able to read these volumes. As KNMI uses an open data policy all radar data is distributed freely, which can be read from the KNMI Data Center (KDC). Professional end-users are offered enhanced delivery services against additional costs.

7 Product generation

In order to be able to fulfill high availability KNMI distributes preferably products based upon multiple radar inputs, E.g. composites, to its professional external users:

7.1 Reflectivity Composites

Reflectivity composites at low altitude (1500 meter above msl) for Netherlands and Western Europe. These main radar products are showing the temporal and spatial evolution of precipitation patterns. KNMI uses an adopted form of range weighted compositing that suppresses close to the radar echo return (and thus ground echo's).

7.2 Accumulated Precipitation

Precipitation is accumulated over 3 hour and 24 hour periods. The accumulations are based on the reflectivity composite and are adjusted with rain gauge observations.

7.3 Echotop Height Composites

The echotop height composites show the observed maximum height of the radar echoes. They are of special interest for aviation purposes.

7.4 Hail Warning Product

Large hail is detected using the height difference between the 45 dBZ echotops and a fixed height of 2500m, which is assumed the average freezing level over the Netherlands in summer conditions. model.

7.5 Single radar products

But when requested KNMI distributes single radar products to other post processing institutions, such as the opera data centre Odyssey, the E-profile data hub, or bilateral exchange partners as IRM, or the DWD. Preferable these products are ODIM based volumes, but other products are available as well.

=<+>=

Republication of Zawadzki, I. (1984)



Conference Volume: 22nd Conference On Radar Meteorology, 10-13 Sept. 1984, Zurich, Switzerland. Published By The Amer. Meteorological Society, Boston, Mass. USA

9.1

FACTORS AFFECTING THE PRECISION OF RADAR MEASUREMENTS OF RAIN

I. Zawadzki
Département de Physique, Université du Québec à Montréal
Canada H3C 3P8

1 Introduction

A number of factors introduce discrepancies between radar measurements of rain rate and the actual rain rate at ground. Some of these factors cause random errors; others produce systematic bias, and several depend on the distance between the radar and the point at which the measurement is made. Let us list these factors in three groups:

a) Sources of random errors

1) Variability of drop-size distribution at ground, from storm to storm.
2) Variability of drop-size distribution at ground within each storm.
3) Time-space variability of precipitation under cloud base.
4) Advection of precipitation.
5) Variations in the radar calibration.
6) Residual signal fluctuations

b) Sources of systematic errors

1) Change in the drop-size distribution from the heigh of radar measurement to ground (coalescence, break-up and evaporation).
2) Attenuation.
3) Wet radome.
4) Time sampling by the radar

c) Sources of range dependent errors

1) Size of the radar sample volume coupled with the non-uniformity of the field of reflectivity.
2) Increase in height with range of the sample volume.
3) Minimum detectable signal
4) Propagation, shadows.

This classification is not unique since some of the factors could be placed in two or the three groups (for example, shadows will introduce systematic errors) In this work a quantitative evaluation of some of the above factors is given in view of assessing their relative importance.

2. Variability of drop-size distribution

Fig. 1 shows a scattergram obtained from disdrometer data by Richards and Crozier (1982). Data were taken from three rain seasons comprising over 15000 minutes of observation. No separation by rain type has been made: cold-front, warm-front, convective and stratiform precipitation is included. Thus Fig. 1 shows the effect of drop spectra variability from storm to storm, within each storm, etc. What it all amounts to is a standard deviation of ~ 33% in the rain rate estimation. Joss et al. (1970), using a vertically pointed antenna, have shown that this error can further be reduced by a choice of one of three drop-size distributions for convective rain, stratiform rain and drizzle.

At the same time as the data of Fig. 1 were taken, a well calibrated radar located at 36 km from the disdrometer was measuring the back-

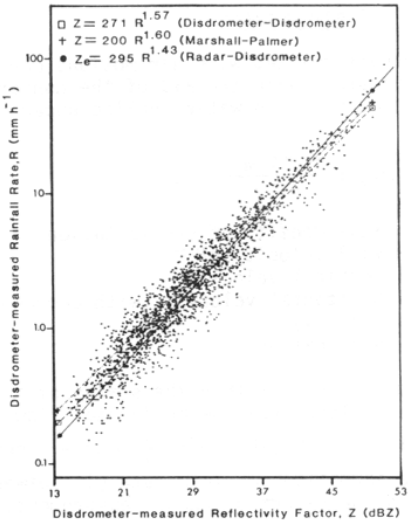


Fig. 1. Scattergram of disdrometer derived values of Z and R for data in the Toronto, Ont. region taken during 1977/78/79 summer seasons (from Richards and Crozier, 1983) Each point represent a 7 min. sample.

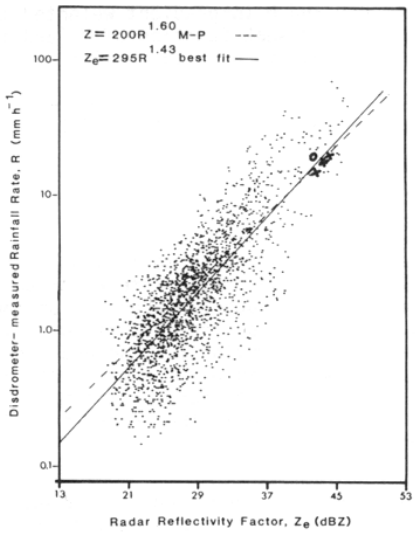


Fig. 2. Scattergram of radar measured Z and disdrometer derived R for the same events as in Fig. 1 (from Richards and Crozier)

scattered power from rain just above the disdrometer (the center of the radar beam was at 360 m above ground). A direct comparison of the radar measured Z and disdrometer measured R is shown in Fig. 2. The uncertainly in R tripled (to a ~100% standard deviation) and this in spite of the particularly favorable situation of the radar measu-

rements! We know that radar estimations of rain rate degrade fast with range.

We must conclude that the variability of the drop-size distribution is a relatively minor factor affecting the precision of radar estimates of rain rate.

3. Effect of air motions

The errors related with air motions can be better understood with the aid of the conservation equation for rain water applied under cloud base:

$$\frac{\partial M}{\partial t} + \vec{\nabla}_H \quad M\vec{V}_H + \frac{\partial (M[V+w])}{\partial z} = E \qquad (1)$$

Where M = mass density of precipitation
V = fall velocity of M
w = vertical velocity
$\vec{V}_H$ = horizontal velocity (with components u and v)
E = evaporation

We will suppose that within the scales of interest (a few kilometers) the horizontal flow is slab symetrical with v=0 (thus $\frac{\partial u}{\partial x} = -\frac{\partial w}{\partial z}$) and $\frac{\partial M}{\partial x}$ constant. With these asumptions we integrate (1) between z=0 and z=h the height of radar measurement:

$$\frac{\partial}{\partial t} M_T + \bar{u}h \frac{\partial M}{\partial x} + M_h V_h - M_o V_o + \tilde{w}(M_h - M_o) = E_T$$

where the subscripts T, h and o represent the total in the column, the value at z=h and the value at z=0 respectively; $\bar{u}$ is the mean of u in the column and $\tilde{w}$ represents a value of w somewhere between ground and h ($\tilde{w}$=gradient weighted mean). Since V is a very weak function of M (and thus of z) we may consider $V_h \simeq V_o$ to obtain:

$$\frac{M_h - M_o}{M_o} = \left[\frac{1}{R_o}\left(E_T - \frac{\partial M_T}{\partial t} + h\frac{\bar{u}}{|\bar{V}|}\frac{\partial \ln M}{\partial x}\right)\left(1 - \frac{\tilde{w}}{|\bar{V}|}\right)^{-1}\right]$$
$$\simeq \frac{R_h - R_o}{R_o} \qquad (2)$$

We notice that vertical motions will introduce a difference between rain rate at ground and at height h only through the presence of the other factors in the square brackets of (2). In this sense vertical motion is a second order effect. Furthermore, since V ≃ 5 m/s vertical motion has a minor effect: for $\tilde{w} \simeq \pm 1$ m/s it represents 20% of change in the errors introduced by the other factors.

On the other hand, horizontal gradients of reflectivity have a mean value between 5 and 10 dBZ/km (Torlaschi and Humphries, 1983), therefore $\frac{\partial \ln M}{\partial x} \simeq \frac{1}{km}$ (for 8 dBZ/km and a M-P distributions). For h = 1 km and $\bar{u} \simeq 5$ m/s the horizontal advection introduces an error of 100%! Areal averages will tend to diminish this effect. The average over the entire cell of precipitation will yield a nil net advection of M; however, the average over the entire cell of the term

$$\left(h\frac{\bar{u}}{|\bar{V}|}\frac{\partial \ln M}{\partial x}\right)\left(1 - \frac{\tilde{w}}{|\bar{V}|}\right)^{-1}$$

will vanish only if $\bar{u}$ and $\tilde{w}$ are independent which is not likely to be true. We should expect different effects of horizontal advection during the growing and the decaying stages of precipitation ($\tilde{w} > 0$ and $\tilde{w} < 0$ respectively).

4. Collision, break-up and evaporation

Let us consider now the effect on rainrate measurements of the changes in drop-diameter distribution between cloud base and ground.

A theoretical study of collision, break-up and evaporation of drops under cloud base has been done by Carrieres (1981) In this study, collision was simulated by the stochastic equation, break-up modeled after Brazier-Smith et al. (1973) and evaporation was calculated according to the diffusion equation. For our discussion we will reproduce some of Carrieres' results.

First, let us consider the interaction between drops and neglect evaporation. Fig. 3 shows the changes in Z and R (with respect to the values at cloud base) as a drop-size distribution is modified with distance fallen from an initially exponential form. The curves correspond to rates of 3.29 (1), 10.8 (2) and 21.6 mmh^{-1} (3). As expected R changes very little: its variation is due to changes in drops fall speed of the slightly modified distribution. The reflectivity factor is modified by 15% to 25%. Thus if a Z-R relationship obtained from drop spectra at ground is used, systematic underestimation of the order of 9 to 16% will be introduced in R.

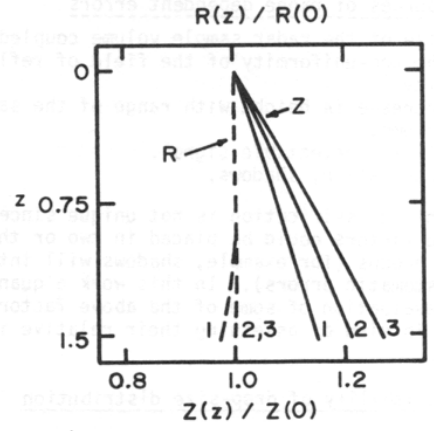


Fig. 3. Changes in Z and R due to collision and break-up for an initially exponential DSD with R(0) = 3.3, 10.8 and 21.6 mmh^{-1}

Let us now add evaporation effects to the drop spectrum in its fall from cloud base to ground. Fig. 4 shows the changes with height of Z and R, from the initial values of 43.1 dBZ and 21.6 mmh^{-1} at cloud base, as the rain falls through air in which the relative humidity changes linearly with height from 100% at cloud base to 45% (1), 70% (2) and 90% (3) at ground. Thus, from a single pair (Z,R) we have obtained through drop interaction and evaporation the points (43.1 dBZ; 16 mmh^{-1}), (43.6; 18) (44; 20). In Fig. 2 the original point (circle) and the three point at ground (crosses) are shown. Some of the scatter in Figs 1 and 2 is due to this effect.

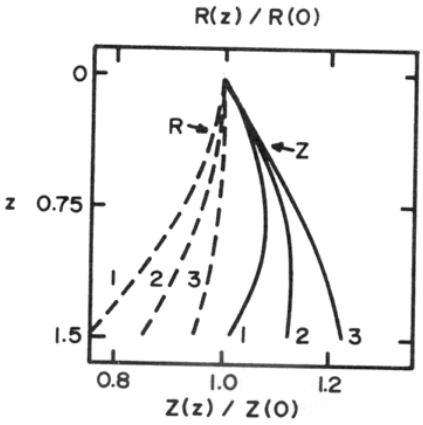


Fig. 4. As Fig. 3 including evaporation for $R(n=0) = 21.6\ mmh^{-1}$; humidity at ground is 45% 70, and 90% for the curves 1, 2, 3 respectively.

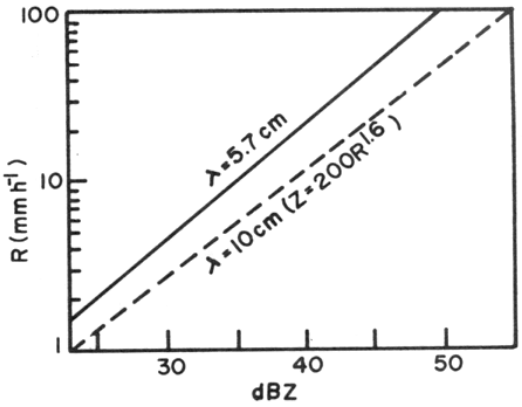


Fig. 5. Average R-Z_e relationship for a C-band radar suffering attenuation by rain. The dashed line shows the relationship for an S band radar ($Z = 200R^{1.6}$).

For a R-Z relationship obtained from drop-size distributions at ground the consequences of these effects on the rain rate estimation are: an underestimation (more severe with less evaporation, surprisingly) and a relatively small random error which quite likely is already included in the Z-R relationship derived from drop-size distribution. Calculations as those of Fig. 4 could be made for a variety of conditions in order to develope correction factors to be applied opperationaly.

5. Attenuation

For S band radars attenuation by precipitation is negligible. However, dry air reduces the signal strength at a rate of 6.5×10^{-3} dBZ/km (for 20°C and a wavelength of 10 cm) which represents a systematic error of ~25% in rain rate at 100 km. Given the ease with which a correction for attenuation by atmospheric gases can be made there is no reason for not having it incorporated in every system once and for all

Due to an appreciably lower cost C band radars are in use around the world. In addition to atmospheric gases precipitation introduces appreciable attenuation for 5 cm radars. To get a quantitative idea of the severity of the problem the following calculations were performed; the time scale of a 10 years record of a single rain-gage record was transformed into a space scale using the 70 kPa wind (for details concerning the data, the method of analysis and its rationale the reader is reffered to Drufuca and Zawadzki, 1975). These synthetic space records were transformed from R to Z using $Z = 200\ R^{1.6}$. Attenuation as a function of distance was then calculated using the expression $y = 0.003\ R$ (where y is the specific attenuation in dB/km and the constant in the relationship was taken from Wexler and Atlas, 1963) for a hypothetical 5 cm radar located at various points within each synthetic storm. In this way the attenuated reflectivity was obtained for a large number of points for which the actual rainrate was known. Over 500 storms and a large number of radar locations within each storm where considered. From a regression analysis it was then possible to obtain the average relationship between rain rate and the attenuated reflectivity shown in Fig. 5. As can be seen the systematic error is quite large: 50% for $R = 2\ mmh^{-1}$, 80% for $R = 10\ mmh^{-1}$. Of course, the error will be range dependent. Furthermore, superimposed on this bias, attenuation introduces an appreciable random error - standard deviation of ~20%.

6. Smoothing of gradients

A simple example will illustrate this effect: consider a uniform precipitation, in which $Z = A\ R^{1.56}$ filling one half of the beam and no precipitation in the other half. The average rainrate over the beam-width equals one half of the rate in the precipitating region. The measured Z will also be one half of the reflectivity in the precipitation region. Clearly this pair (Z,R) does not satisfy our Z-R relationship. Let us go a step further: assume now that the drop diameter distribution within the precipitation is exponential, that is $N_D = N_0 \exp(-\lambda D)$, and the terminal fall velocity is proportional to $D^{\frac{1}{2}}$. In this case

$$Z = N_0^{-0.56}\ CR^{1.56}$$

where C is a numerical constant. In our example the half filled beam will "see" N_0 divided by two; thus, the relationship between measured reflectivity and rainrate (interpreted as the average value over the beam-width, as usually) will have a new coefficient and the same exponent.

The half-filled beam is a particular case of non-uniformity. To study this effect for a combination of actual non-uniformities, drop diameter distribution from 80 storms (part of the data used by Richards and Crozier to obtain Fig. 1) comprising a total of over 5000 minutes of observation were smoothed by a running window of a width Δt. Points with $R < 0.1\ mmh^{-1}$ were rejected.

The results show that the exponent in the power-law changed very little with Δt, as expected. The coefficient, however decreased appreciably with increasing width of the window .

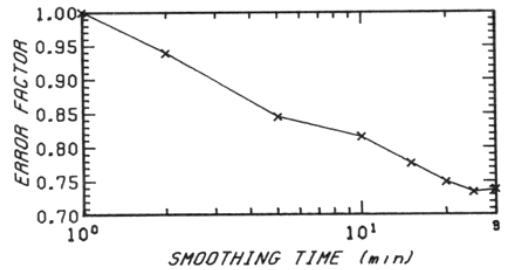


Fig. 6. Changes in the coefficient of the R-Z relationship with the amount of smoothing (relative to 1-min smoothing)

Fig. 6 shows the coefficient normalised to the value for Δt=1min ("error factor") as a function of Δt. Thus, if a Z-R relationship determined from 1 min-distributions is applied to measurements where the precipitation was integrated over 10 min (or its equivalent in space) R will be determined with an error factor of 75. Fig. 6 illustrates the effect of smoothing a non-uniform precipitation field on the rainrate inferred from measured reflectivity. It is easy to see that this effect is related to the non linearity of the R-Z relationship. In effect, in our example of the half filled beam, where both Z and R are simply divided by two, a simple proportionality between the two would have not been affected by the beam smoothing. On the other hand, the various stages leading to a radar measurement contain other non-linearities: the radar beam does a non-linear weighting of the illuminated volume; the post-detection integration on a logarithmic scale adds another non-linearity. Consequently the actual problem is appreciably more complex than suggested above.

The combined effects of these non-linearities on the radar measurements of non-uniform fields of precipitation have been discussed in some detail previously (Zawadzki, 1982). Let us consider here a simple situation: a precipitation pattern with a constant gradient G (in dBZ/km) in one direction and uniform in the other two. Furthermore, we will assume that the rain drop-diameter distribution is a one parameter function so that the same R-Z relationship is valid at every point of the pattern (say $Z = 200R^{1.6}$) Consider a Gaussian beam scanning this precipitation and a post-detection integration after a logarithmic detector performed over an area D x D ("measurement cell"). Thus the reflectivity level and the rain rate along the x-axis can be represented by

$$Z = Z(0)\exp(Gx/m) \text{ and } R = R(0)\exp(aGx/m) \quad (3)$$

where m = 10 log e, Z(0) is the reflectivity factor at the center of the measurement cell, $R(0) \propto Z(0)^a$ and $a = 1/1.6$.

The actual average rainrate $\overline{R}$ over the measurement cell is obtained by integration of (3) over D x D:

$$\frac{\overline{R}}{R(0)} = \frac{2m}{DaG}\sinh\left(\frac{aGD}{2m}\right) \quad (4)$$

The radar measures a reflectivity factor Z_{oo} resulting from, first a Gaussian-beam weighted

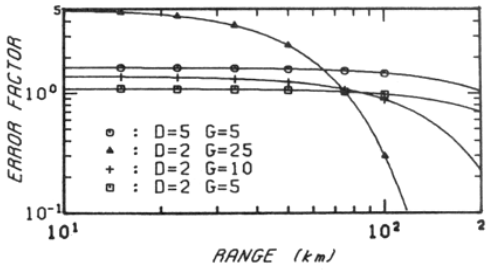


Fig. 7. Biases in the rain rate measurement by radar within a region of constant gradient G dBZ and for a measurement cell of D x D.

average of Z and second, by integration over an area D x D. If the gradient G is in the cross-range direction these two operations lead to

$$\frac{Z_{oo}}{Z(0)} = \exp\left[\left(\frac{\alpha G}{2m}\right)^2\right] \quad (5)$$

where $\alpha^2 = \frac{r^2\theta_o^2}{8\ln 2}$ and θ_o the one way 3 dB beamwidth. Thus, the radar derived rainrate is $R_{oo} = k\, Z_{oo}^a$, usually interpreted as the average rate over D x D. The error factor, that is, the ratio $\overline{R}/R_{oo}$ is

$$F = \frac{2m}{aDG}\exp\left[-a\left(\frac{\alpha G}{2m}\right)^2\right]\sinh\left(\frac{aGD}{2m}\right) \quad (6)$$

In (6) the exponential factor represents the effect of beam smoothing and the sinh factor results from the interpretation of the measurement as a mean over the measurement cell

Statistics of gradients obtained from radar measurements show an exponential distribution of G with a mean value (extropolated to zero range) between 5 and 10 dBZ/km (Torlaschi and Humphries, 1983). In Fig. 7 the error factor is shown as a function of range. Thus, if a radar is calibrated with a gage located 10 km away while the detected rain has a cross-range gradient of 10 dBZ/km the same rain at 100 km will be underestimated by 40% (for a measurement cell of 2 km cross-range). For 25 dBZ/km the underestimation factor under the same conditions will be 0.06! This extreme example shows the erratic nature of this error and the danger of calibrating the radar with a gage in real time.

7 Height of the beam above cloud base

With increasing range larger portions of the radar beam "illuminate" precipitation located further up from cloud base. Since, on the average the amount of precipitation increases with fallen distance for a given precipitation at ground the detected reflectivity will decrease with range. Therefore, on the average the actual rainrate at ground will be underestimated. On the other hand, vertical and horizontal advection of precipitation within clouds introduces a strong random component in the relationship between rainrate aloft and at ground. In addition to this there is a time lag between the detection of a given precipitation aloft and the time this precipitation will fall at the ground, increasing the errors in the estimates of near instantaneous rainrate.

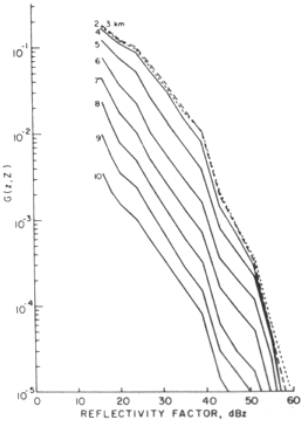


Fig. 8a. Probability of reflectivity values exeeding the indicated values for various heights (from Rogers and Yau, 1982)

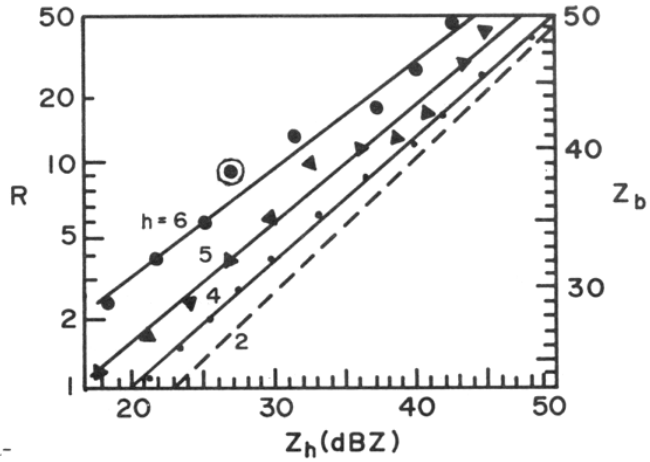


Fig. 8b. Relationship between reflectivity factor at height h and at h = 2 km obtained from Fig. 8 by comparison in probability.

The effects of the height of the radar beam will become particularly severe at ranges beyond 100 km. To evaluate these effects we will simplify the complexity of the problem by establishing relationships of the reflectivity at cloud base to the reflectivity at various heights by comparison in probability. This concept is based on the idea that if Z_b (reflectivity factor at cloud base) and Z_h (reflectivity factor at height h) occur with the same frequency then such pairs (Z_b, Z_h) define Z_b-Z_h relationship. It is clear that this relationship will transform the probability of Z_h into the probability of Z_b assuming that a physical relationship exist between Z_h and Z_b. Thus, a relationship established by comparison in probability permits a correct estimation of averages (and all the moments of the distribution) of a large number of measurements. A range dependent Z_e-R relationship by comparison in probability between measured Z at various ranges and raingage statistics was obtained by Calheiros and Zawadzki (1983). Fig. 8a shows the fraction of area covered by various radar measured reflectivity factors at different heights. These curves, obtained from an entire rain season of data, can be interpreted as cummulative frequencies of occurrence of Z_h (conditional to the occurrence of echo on the lower height, 2 km CAPPI). From these curves the relationships between Z_b and Z_h (for different heights) shown in Fig. 8b were obtained. For example, in Fig. 8a reflectivity exeeding ~39 dBZ at h = 2 km occur with the same frequency as those exeeding 27 dBZ at h = 6 km; this is the circled point in the corresponding curve in Fig. 8b. On Fig. 8b a scale of R was added using $Z = 200R^{1.6}$. Assuming that the precipitation is observed at a 1^o elevation of the beam, the various heights correspond roughly to ranges 150, 180 and 200 km for h = 4; 5 and 6 km respectively. Thus, 30 dBZ measured at r = 150 km corresponds (on the average) to 4 mmh^{-1} while at r = 200 km the correct estimate would be 10 mmh^{-1}, that is, if the height effect is the only one present and all the power is concentrated at a given height. In reality the distributed beam power will be weighting a rapidly decreasing profile of Z in the upper half of the beam and a more gently increasing values of Z in the lower half. Fig. 8b was prepared to illustrate the effect of the beam height rather than to give a set of curves to be used in opperational situation.

It should be noticed that the comparison in probability takes into account changes in water phase, bright band included. By this method, however, we can only evaluate the systematic effects of the beam height.

8. Minimum detectable signal

In Fig. 9 the contribution to total rainfall by rates lower than indicated is shown. The curve was obtained from 10 years of tipping bucket raingage located in the Montreal area. 70% of the rain comes from R < 8 mmh^{-1} Thus, if the MDS is such that rain rates below say 1 mmh^{-1} are not detected at a given range, rain accumulations will be underestimated by 18%. Such error will be caused by two effects: first, because the minimum detectable Z increases with range and second, because a given measured Z corresponds to larger R at increasing ranges due to the previously discussed effects.

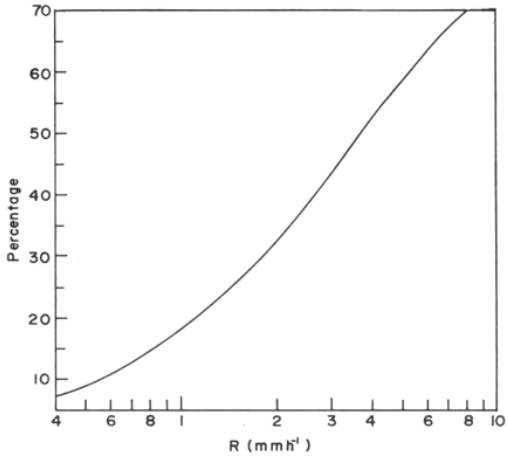


Fig. 9. Percent of contribution to total amount of rates below the indicated value obtained from 10 years of a raingage measurement in the Montreal area.

As an example consider a radar for which rainrate is measured on a one degree PPI display. Let us suppose that the only factor introducing errors is the height of the radar beam. In this case the set of curves on our Fig. 8b represents the climatological average relationships between the measured Z and rainrate at ground for the ranges of 150; 180 and 200 km. With the help of Figs 9 and 8b we will determine now the fraction of rainfall which will be missed at various ranges due to the MDS and due to the combined effect of MDS and the beam height, for a radar for which the MDS is 23 dBZ at 100 km. Without the height effect Fig. 9 indicates that 15% would be missed at r = 180 km since at this range the MDS (=25.5 dBZ) corresponds to 0.8 mmh^{-1} if we measure Z under cloud base. However, since at this range the beam height is 5 km the measured Z corresponds (on the average) to 3 mmh^{-1}; Fig. 9 indicates that the rainfall is underestimated by 43%. Fig. 10 shows the underestimation factor as a function of range obtained in this way for a radar for which this effect was particularly severe. Attenuation tends to accentuate the trend shown in Fig. 10 while the gradient effect acts in the opposite direction.

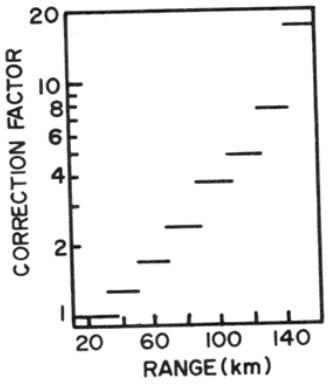


Fig. 10. Range correction factor obtained from statistics of radar echo and statistics of raingage data for an actual radar (from Calheiros and Zawadzki, 1983)

9 Discussion

A great deal of effort has been made to account for the variability of the drop-size spectra: real time calibration with one (or more gages), dual wavelength, polarization diversity and a great care in deriving Z-R relationships from drop spectra measured at ground.

The analysis presented here shows that, from the point of view of precipitation measurements at ground, the variability of drop-size spectra introduces one of many errors and not the most severe at that. Even if some of the above mentioned techniques succeed in determining precisely the drop-size distribution within the "illuminated volume" the improvement in rain measurements at ground is not likely to be great.

Real time calibration of the radar with a raingage, although an atractive idea in principle, may introduce as many problems as solutions: if the calibration is made in regions where biases due to non uniformity of the precipitation field are severe the whole rain rate pattern will be estimated with additional (and severe) errors. The same effect will be introduced by horizontal advection and by attenuation (whenever present). Calibrating with a gage may have the effect of uncalibrating the radar entirely, particularly in cellular rain patterns.

Reflectivity-rainrage relationships obtained by radar-raingage comparison (in probability or by regression) will compensate on the average all the errors if enough data are used in the comparison. Range effects can be compensated for by statistics of reflectivity as a function of range such as described by Calheiros and Zawadzki (1983). However, these techniques will not eliminate the large scatter of individual measurements of rain rate. The accuracy of radar estimates of precipitation at ground will only be improved by addressing the various sources of error in a painstaking and a meticulous manner. The combination of hardware and software made available by the technology of today permits a complexity of radar data processing which should be helpfull in reducing the errors discussed here.

Acknowledgments. The author is grateful to Dr. C. Crozier of the Atmospheric Environment Service of Canada, who kindly provided the disdrometer data used for calculations leading to Fig. 6. J.-P. Samson performed the calculations for Fig. 5.

REFERENCES

Brazier-Smith, P.R., S.G. Jennings and J. Latham, 1973. Raindrop interactions and rainfall rates within clouds. Quart. J. Roy. Met. Soc., 99, 260-272.

Calheiros, R.V. and I. Zawadzki, 1983. Reflectivity-rain data relationship for radar hydrology in Brazil Proc. 21st Conf. on Radar Meteor. Boston, Mass., 687-692.

Carrieres, T., 1981. Evaporation and drop interaction in a rainshaft. Ms. Sc. Thesis, McGill University, Montreal, Canada, pp 67.

Drufuca, G. and I. Zawadzki, 1975. Statistics of raingage data. J. Appl. Met., 14, 1419-1429.

Joss, J., K. Schram, J.C. Thaus and A. Waldvogel, 1970. On the quantitative determination of precipitation by radar. Eidgenössischen Kommission Zum Studium der Hagelbildung und der Hagelabwehr, Nr. 63, Locarno-Monti Switzerland, pp 38.

Richards, W. and C. Crozier, 1983. Precipitation measurements with a C-band radar in Southern Ontario. Atmos.-Ocean., 21, 125-137.

Rogers, R.R. and M.K. Yau, 1982. Areal extent and vertical structure of radar weather echoes at Montreal. PAGEOPH, 120, 273-285.

Torlaschi, E. and R. Humphries, 1983. Statistics of reflectivity gradients. Proc. 21st Radar Met. Conf., Boston, Mass., 173-175.

Wexler, R. and D. Atlas, 1963. Radar reflectivity and attenuation of rain. J. Appl. Met., 2, 276-280.

Zawadzki, I., 1982. The quantitative interpretation of weather radar measurements. Atmos.-Ocean, 20, 158-180.

Author Index

ÖZTÜRK, 397
ÇUBUK, 397

ABEL, 260
ADACHI, 128, 354, 837
ADAM, 298
ADIROSI, 44, 46, 78, 274
AHN, 76, 272
ALBERONI, 99, 110, 210, 440, 851, 883
ALBO, 220
ALCOBA, 39, 286
ALDA, 278, 558
ALDERLIESTE, 193
ALESSANDRO, 937
ALPERT, 284
ALTUBE, 111, 160, 261, 687
ALVES, 462
AMENT, 416
ANAGNOSTOU, 187, 199, 219, 830
ANDRIEU, 39
ANTONINI, 156, 214, 274, 363, 615, 889, 906
ARÚS, 111
ARAI, 128, 342
ARANDA, 248, 278, 558, 566
ARGEÍ, 261
ARGEMÍ, 160
ARMON, 171
ARTHUR, 145
ARULRAJ, 449
ATENCIA, 320
AUGROS, 125, 133, 400
AUSTIN, 246
AYZEL, 326, 336

BÖEHME, 280
BÁRDOSSY, 456
BACH, 330
BAEK, 91
BAELEN, 448, 633
BAJAJ, 148, 463, 932
BALDINI, 44, 46, 78, 99, 274, 352, 357
BALTAS, 219, 830
BANG, 76, 91, 438
BARBIERI, 159, 654
BARDOSSY, 183
BARGAOUI, 276
BARRAGAN, 267
BARRAS, 141
BARROS, 449
BARTON, 141
BASTARD, 133, 400
BATTAGLIA, 48, 49, 62, 251, 348, 353, 378, 937
BAUER (H.S.), 437
BAUER (S.), 462
BAUER-PFUNDSTEIN, 372
BAUERNSCHUBERT, 211, 330
BAZLOVA, 337, 442, 870
BECH, 111, 261, 288, 367, 687, 786, 897
BECHINI, 110, 135, 237
BECKER, 152, 154, 486
BECKMANN, 132
BEEK, 439
BEEKHUIS, 166, 259, 956, 960
BEER, 279
BELACHSEN, 171
BELL (A.), 322
BELL (M.M.), 86, 150, 304
BENEDETTI, 214, 615

BENETI, 80, 175, 287, 436, 810, 817, 915, 923
BENNETT, 68
BERENGUER, 147, 178, 189, 198, 399, 412
BERIZZI, 357
BERNDSEN, 66, 67
BERNE, 42, 43, 50, 53, 70, 76, 77, 85, 87, 272, 407, 780
BESIC, 70, 85, 87, 141, 407
BEST, 96, 260, 454, 505
BEUSCH, 315
BHARADWAJ, 283, 371, 377, 386
BHAVANI SHANKAR, 374, 477
BILJIĆ, 129, 662
BLAHAK, 211, 330, 332
BLIŽŇÁK, 226
BLUESTEIN, 101
BLYTH, 68, 90, 260, 454
BOCHARNIKOV, 337, 442, 870
BOER, 345
BOETTCHER, 306
BOGUNOVIĆ, 129, 662
BONADONNA, 460
BOODOO, 395, 822
BOOS, 462, 466
BORDERIES, 204
BOROWSKA, 297
BOSCACCI, 141
BOUDEVILLAIN, 50, 276, 400
BOUVIER, 286
BRABANT, 462, 466
BRACCI, 78
BRAUER, 177, 198
BRINGI, 42, 43, 58, 524
BROERE, 259, 956
BRUIN, 201
BUDILLON, 206, 269
BUKOVCIC, 494
BUNN, 322
BURLANDO, 182, 190

CALHEIROS, 80, 175, 810, 915, 923
CALPINI, 141
CALVETTI, 80, 175, 287, 436, 810, 817, 915, 923
CAMP, 263
CAMPANA, 110
CAMPISTROM, 163
CAO, 157
CAPARRINI, 363, 906
CAPECCHI, 214, 615
CAPOZZI, 206, 269
CAPPELLIN, 231
CARANTI, 167
CARDOSO, 436, 810
CARLIN, 221
CARON, 208, 747
CASELLAS, 288, 897
CASSARDO, 135
CASSIRAGA, 399
CASTÁN, 111
CAUMONT, 125, 204, 402
CAZENAVE, 286, 400, 455
CELANO, 110
CHAHINIAN, 286
CHAN, 722
CHANDRASEKAR, 148, 237, 302, 324, 325, 797
CHANG, 76, 223
CHAPMAN, 462
CHASE, 60, 62, 115, 586
CHATELET, 365, 756
CHAUMONT, 165
CHAVEZ, 116
CHEN (G.), 93
CHEN (H.), 148
CHEONG, 409
CHEVALLEY, 407
CHO, 76, 91
CHOI, 146
CHUNG, 225, 875
CHWALA, 265
CIACH, 462
CIARDINI, 78
CIPOLLONE, 159, 654
CLEMENS, 416
CLEMENTI, 141
COCCIA, 357
COCKS, 145, 398
COELHO, 287, 436, 810, 817
COFFIN, 246
COLLIS, 63, 65, 112, 115, 153, 203,

261, 270, 687
COMES, 167
COOPER, 145
CORRAL, 178, 189
COUTURE, 395, 822
CREMONI, 681
CREMONINI, 110, 135, 138, 151, 237
CRISOLOGO, 241
CRISTIANO, 180
CROPP, 411
CROSIER, 260
CRUZ, 335
CUCCOLI, 357
CURTIS, 306, 322

D′ADDERIO, 349
D′AMICO, 357
DADDERIO, 285
DARLINGTON, 252, 394
DARRIN, 370
DAWSON, 267
DEJANOVIC, 158, 601
DELANOË, 204, 244
DELOBBE, 143, 188, 263, 277, 335, 467, 491
DELRIEU, 276, 400, 434, 455, 765
DEMARGNE, 172
DEMARIA, 411
DEN HEUVEL, 53
DESHPANDE, 380
DESMET, 462
DHAVALE, 82
DIDSZUN, 239
DIETRICH, 269, 285, 349
DIXON, 231, 235, 304
DOKTER, 462
DOLAN, 60, 586
DONALDSON, 395, 822
DONOHUE, 132
DOO, 310
DORSEY, 260
DUCROCQ, 204
DUFOURNET, 340, 469
DUFTON, 68, 72, 249, 605
DUPONT, 244
DURAN-ALARCON, 50

EERTWEGH, 195
EGAÑA, 122, 123, 545, 552
EGUIARA, 278, 558
EHRET, 437
EINFALT, 185, 193, 417, 429
ELLIS, 220, 256
ENDO, 112, 270
ENZEL, 171
EROSHKINA, 305, 846
EVARISTO, 114
EWALD, 51

FABIO, 159, 460, 654
FABRY, 150, 215, 218, 360, 366, 704
FACHERIS, 274
FALCONI, 54, 861
FARDON, 165
FATICHI, 182, 190
FAURE, 358, 400, 434, 765
FEGER, 330, 332, 341
FEIGE, 330
FENG, 86, 150, 360
FENNIG, 417
FERNANDEZ, 367, 786
FERRETTI, 99, 206
FIBBI, 214, 615
FIGUERAS, 141
FILLION, 208, 747
FINE, 172
FINLON, 60, 586
FOLEGANI, 440, 851
FORESTI, 85, 141, 315, 318, 323, 335, 407, 738
FORNASIERO, 440, 851
FORTESCUE, 260, 310
FOUCHIER, 172
FRANK, 444
FRASIER, 264, 267, 298, 361, 463, 514, 932
FRECH, 234, 236, 594
FREDJ, 446
FRERK, 417, 429
FRIDLIND, 63
FRIEDRICH, 154, 486
FU, 271
FUJIWARA, 128, 342
FULTON, 295

GÓMEZ-HERNÁNDEZ, 399
GÓRSKA, 462
GABELLA, 53, 85, 141, 233, 407, 780
GAO, 221
GARANDEAU, 172
GARCIA-BENADÍ, 367, 786
GASTALDO, 210, 883
GATLIN, 58, 346, 524
GAUSSIAT, 132, 133, 165, 358, 375, 400, 402, 408, 434, 765
GAZTELUMENDI, 122, 123, 278, 545, 552, 558
GEHRING, 70, 87, 272, 407
GENG, 95, 103, 184
GENTHON, 50
GENTILE, 99
GEORGE, 302
GERBER, 85
GERHARDS, 308
GERMANN, 85, 121, 141, 315, 316, 318, 323, 407, 738
GHARANJIK, 374, 477
GIANGRANDE, 283, 377
GIANNETTI, 274
GIANNINI, 156, 889
GIESEN, 180
GILL, 234, 594
GIORDANO, 110
GIRES, 266
GOKDERE, 200
GOLDBERGER, 283
GONZÁLEZ (S.), 367, 786, 897
GOODRICH, 411
GORGUCCI, 44, 78, 352
GOSSET, 39, 286
GOTTAS, 191
GOUDENHOOFDT, 188
GOURLEY, 145, 389
GOZZINI, 156, 214, 615, 889
GRAZIOLI, 141, 258, 282
GRECU, 346
GRIFFIN, 61
GRIGIONI, 78
GROSS, 51
GULBRANDSEN, 131
GUYOT, 41
HAASE, 143, 234, 249, 462, 491, 594, 605
HABERLANDT, 339
HACHANI, 276
HADVÁRI, 257
HAEFELE, 465, 620
HAEFFELIN, 244
HAFER, 152
HAGEN, 51
HAMANN, 141, 316
HAMPTON, 90
HAN, 75, 164
HANADO, 313
HANDWERKER, 106, 415, 447, 579
HANSEN, 208, 747
HARASTI, 216
HARDIN, 283, 345, 377
HAREN, 212
HARRINGTON, 64, 65, 73
HARRISON, 96, 260, 454, 505
HAZENBERG, 411
HEBERLING, 298
HEISTERMANN, 241, 326, 336, 390, 392
HEIZENREDER, 334
HELMERT, 162
HELMUS, 261, 687
HENGSTEBECK, 162, 280, 334
HERDIES, 436, 810
HERING, 121, 141, 316
HERNANDEZ, 278, 558
HEROLD, 280
HEUVEL, 141, 233, 780
HEUVELINK, 198, 201
HICKMAN, 84, 151, 681
HINSKEN, 185
HIRAKUCHI, 354, 837
HOFF, 330
HOGG, 360
HOHTI, 234, 319, 594, 772
HOLLEMAN, 232, 234, 594
HOLLMANN, 154, 486
HOLTSLAG, 212
HOMEYER, 115
HONDL, 293
HOOGEBOOM, 243

HOUCHENS, 377
HOUZE, 377
HOWARD, 145, 398
HU, 130
HUANG, 68, 130
HUBBERT, 220, 231, 235, 236
HUDAK, 395, 822
HUSNOO, 252
HUUSKONEN, 232, 234, 594

ICHIBA, 266
IGUCHI, 344
ILLINGWORTH, 252, 348, 353, 421, 937
IMBERT, 133
INGARAMO, 167
INOUE, 128, 342
ISHITSU, 128, 342
ISOM, 283, 307, 371, 386
IVIĆ, 303
IWANAMI, 309

JACKSON, 63, 112, 115, 153, 270
JACQUES, 208, 747
JAMES, 370
JAVELLE, 172
JENSEN, 64, 65
JESSEN, 429
JHA, 380
JOE, 334
JOHNSON, 249, 605
JOO, 387
JUNG (E.), 379
JUNG (S.), 75, 146, 169, 254, 458
JUNGHÄNEL, 152
JUNK, 330
JUNYENT, 148
JURAŠEK, 405, 672
JURCZYK, 328, 427
JØRGENSEN, 231

KAŇÁK, 405, 672
KAŠPAR, 226
KALAPUREDDY, 82, 384
KALOGIROS, 187, 219, 830
KALTHOFF, 415, 447, 579
KANG, 83, 192, 425
KANN, 320
KARABAYIR, 397
KARBOU, 402
KARNIELI, 446
KARSISTO, 329
KATSAFADOS, 219, 830
KATSUMATA, 95, 103, 184
KAUTZ, 411
KAWAMOTO, 344
KAWAMURA, 313
KAWASAKI, 309
KE, 225, 875
KENNEDY, 43
KHAIN, 224
KHANAL, 400, 455
KIJAZI, 108
KIKUCHI, 292, 364
KILAMBI, 218, 366
KIM (D.), 75, 146, 164
KIM (H.), 83, 169, 254
KIM (J.), 146, 164
KIM (K.), 76, 91, 163, 169
KIM (M.), 163
KIM (N.), 76
KIM (W.), 164
KIM (Y.), 209
KIRSCH, 416
KIRSTETTER, 350, 358, 389, 426
KITCUBE TEAM, 415
KNEIFEL, 62, 378, 382
KNIGHT, 157
KOBAYASHI, 354, 443, 837
KOISTINEN, 428
KOLLIAS, 270, 378
KONG, 104, 722
KOOPMANS, 212
KOSIBA, 100, 101, 301
KOUKETSU, 313
KRAJEWSKI, 393
KREITZ, 133
KREMER, 455
KRISHNAMOORTHY, 218
KUK, 164
KUMAR, 88
KUMJIAN, 56, 64, 65, 73, 203, 804
KUNSTMANN, 265

KURRI, 234, 255, 542, 594
KUSTERS, 308
KUSUNOKI, 128, 342
KWON, 163
KYZNAROVÁ, 124, 126

LADD, 260, 310
LAFLEUR, 264, 514
LANG, 115, 270
LANGSTON, 145
LE BASTARD, 402
LEBSOCK, 60, 586
LEE (C.), 76, 91, 356
LEE (D.), 76, 83, 91, 117, 438
LEE (G.), 75, 91, 209, 272, 321, 356, 379, 387, 438
LEE (J.), 117, 146, 254
LEE (S.), 75, 146, 164, 169, 254, 458
LEE (W.), 93, 304
LEE (Y.), 209
LEHMANN, 465, 620
LEHNING, 85
LEIBIUK, 161
LEIJNSE, 143, 177, 195, 234, 259, 300, 391, 401, 412, 422, 444, 445, 451, 462, 491, 594, 956
LEINONEN, 60, 62, 385, 586
LENDERINK, 412
LENGFELD, 152
LERBER, 36, 54, 60, 329, 385, 428, 586, 861
LETH, 445, 451
LEUENBERGER, 272
LEYSER, 280
LI (H.), 381, 864
LI (Q.), 51, 161
LI (X.), 118
LIALIUSHKIN, 442, 870
LIECHTI, 462
LIER-WALQUI, 63–65, 203
LIMAN, 255, 542
LIN, 112, 270
LINDENMAIER, 307
LINDFORS, 227, 646
LIOU, 137, 169, 223, 473
LIPZIG, 50
LISCHI, 357
LLASAT, 98, 695
LOMBARDI, 156, 363, 889, 906
LOUF, 112
LOZAR, 211, 330
LUKACH, 72, 466, 467
LUMB, 260
LUPIDI, 357
LUSSANA, 131
LYONS, 148, 394
LYU, 321, 438

MÜHLBAUER, 115, 241, 279, 390, 392
MÜLLER (M.), 226
MÜLLER (S.), 240, 713
MÉRI, 405, 672
MAIELLO, 99, 206
MANCINI, 242
MARGARYAN, 431
MARKS, 350, 426
MARRA (A.C.), 269, 285, 349
MARRA (F.), 171, 182, 190, 197, 199
MARSIGLI, 210, 883
MARTET, 133, 165
MARTINA, 167
MARTINAITIS, 145
MARTINKUS, 203
MARURI, 122, 123, 248, 278, 465, 545, 552, 558, 566, 620
MARZANO, 54, 99, 159, 460, 654, 861
MATHIJSSEN, 166, 259, 956, 960
MATROSOV, 191, 345
MATTHEWS, 283
MAWANDHA, 406, 733
MAYER, 51
MAZZA, 363, 906
MAZZARELLA, 206, 269
MCFARQUHAR, 38, 494
MCLAUGHLIN, 299, 946
MEGA, 292, 364
MEI, 283
MEIER, 320
MEIRINK, 412
MELANI, 156, 214, 274, 363, 615, 889, 906
MELNIKOV, 294, 627

MELO, 76
MENZ, 462
MEREU, 460
MERTENS, 308
MESSER, 284
MESSERI, 214, 615
MEUNIER, 218
MEYMARIS, 235
MICHELSON, 208, 234, 395, 594, 747, 822
MILANI, 357
MILLA, 40
MILLET, 165
MIN, 209
MINAROVA, 89
MING, 118
MIRKOVIC, 311
MISHRA, 374, 477
MITCHELL, 411
MIZUTANI, 181, 292, 640
MOISSEEV, 36, 52, 54, 60, 138, 151, 381, 385, 586, 681, 861, 864
MOLNAR, 182, 190
MONTAMAT, 167
MONTANGON, 125
MONTANYÀ, 111
MONTOPOLI, 44, 46, 78, 159, 269, 460, 654
MORÉ, 288, 897
MORAL, 98, 695
MORALES, 452
MORDELT, 193
MORGAN, 322
MORI, 95, 103
MORIN, 171, 182, 197, 199
MORRISON, 64, 65, 203
MOTT, 132, 162
MOYA, 229
MRINAL, 370
MROZ, 48, 49, 62, 251
MURPHY, 38, 494
MYAGKOV, 92, 410

NA, 192, 425
NAGUMO, 354, 837
NAI, 306
NAVARRO, 452
NEEF, 330
NEELY III, 72, 90, 260, 454
NEMETH, 257
NERINI, 85, 141, 315, 318, 323, 738
NESBITT, 62, 115
NEUNDORF, 175, 915
NEUPER, 106, 437
NGUYEN, 348, 937
NICOL, 246
NIEMELÄ, 227, 646
NIJHUIS, 340, 469
NILSSON, 462
NISHII, 453, 534
NISI, 121, 141, 316
NOMURA, 354, 443, 837
NOTT, 260
NOVÁK, 124, 126, 143, 491

O′SHEA, 260
OŚRÓDKA, 328, 427
OH, 458
OHTA, 313
OISHI, 406, 733
OKI, 344
OKON, 405, 672
OLENEV, 442, 870
OLIVEIRA, 80, 175, 915, 923
ONOMURA, 128
ORGANDE, 172
ORI, 36, 54, 382, 861
ORIOLARGEMÍ, 687
ORTOLANI, 156, 214, 274, 363, 615, 889, 906
ORZEŁ, 463, 932
OTTERSTEN, 374, 477
OTTO, 340, 469
OUDEJANS, 243
OUE, 270
OVEREEM, 177, 300, 391, 412, 422, 445, 451, 457

PACCAGNELLA, 210, 883
PACI, 897
PALACIO, 122, 123, 545, 552
PALMER, 295
PANDITHURAI, 380
PANEGROSSI, 269, 285, 349

PANZIERA, 141
PAPADOPOULOS, 219, 830
PARK, 147, 321, 412, 438
PASCHALIS, 190
PASETTI, 440, 851
PASI, 214, 615
PATRA, 82, 384
PAULAT, 330
PAULITSCH, 109, 273
PAUWELS, 41
PAVLYUKOV, 305, 846
PAZ, 266
PAZMANY, 348, 937
PEGRAM, 183
PEI, 423
PEJCIC, 279
PELEG, 171, 182, 190, 199
PEPYNE, 463, 932
PERTTULA, 227, 319, 646, 772
PETERSEN, 58, 76, 346, 350, 358, 411, 426, 524
PETROLINO, 274
PEURA, 319, 772
PEZZOLI, 135
PFAFFENZELLER, 165
PFISTER, 193
PHILIPS, 148
PICCIOTTI, 99, 159, 460, 654
PICEL, 63
PICKERING, 454
PINEDA, 111, 261, 288, 687, 897
PIPPITT, 350, 426
PLAGGENMARS, 193
PLAS, 412
POELMAN, 277
POFFO, 167
POLETTI, 178, 189
POLI, 210, 883
PORCÙ, 78, 349, 440, 851
POSADA, 330, 332, 341
POSIO, 255, 542
POSSELT, 65
POST, 138, 450
POTTHAST, 330
POTVIN, 270
PRADO, 409
PRAKASH, 41
PRAT, 64, 65, 203
PRAZ, 70, 76, 77, 87
PRINCIPE, 122, 123, 545, 552
PROBERT, 234, 594
PROTAT, 41, 112
PSCHEIDT, 105
PUCA, 285
PUDASHINE, 41
PULKKINEN, 324, 329, 428, 797

QUADRO, 436, 810
QUIBUS, 467

RÝVA, 127
RABRENOVIC, 136
RAHU, 450
RAICH, 284
RATHMANN, 162
RAUPACH, 42, 43, 77, 300
REBORA, 178, 189
REED, 260
REID, 395, 822
REIMEL, 65
REINOSO-RONDINEL, 419
REMILLARD, 65
REMPEL, 330, 332
REVERDIN, 77
REYNIERS, 335, 466
REZACOVA, 120
RICO-RAMIREZ, 71, 420
RIEMEL, 64
RIGO, 98, 111, 160, 261, 288, 687, 695, 897
RILLING, 256
RIOS GAONA, 300
ROBERTO, 44, 46, 78, 99, 269
ROBERTS, 108
ROCADENBOSCH, 264, 267, 361, 514
RODRÍGUEZ (A.), 167
RODRIGUEZ (O.), 111
RODRIGUEZ (P.), 395, 462, 822
RODRIGUEZ GONZALEZ, 167
ROMATSCHKE, 231, 256
RONDA, 212
ROSE, 92, 410

ROSSI, 159, 654
ROVAI, 214, 615
ROVERSI, 440, 851
ROZIN, 287, 817
RUSSCHENBERG, 66, 67, 243, 244, 373, 419
RUTLEDGE, 302
RUVIARO, 175, 915
RUZANSKI, 325
RYU, 321, 356
RYZHKOV, 38, 61, 84, 221, 224, 338, 393, 398, 414, 438, 494, 574

SÜSSER-RECHBERGER, 273
SAAVEDRA, 229, 279, 409
SAFFE, 167
SAKKA, 239
SALAZAR, 242, 278, 295, 558
SALTIKOFF, 143, 154, 227, 329, 486, 491, 646
SANCHEZ, 932
SANCHEZ-RIVAS, 71
SANO′, 285, 349
SAPIR, 462
SARTORI, 141
SASSA, 69, 453, 534
SATOH, 292
SCARCHILLI, 78
SCHAUWECKER, 258
SCHEIBEL, 176, 185, 193
SCHERTZER, 117, 266
SCHLEISS, 174
SCHMID, 240, 462, 466, 713
SCHMIDT, 338, 414, 574
SCHNEEBELI, 272
SCHRIER, 412
SCHROM, 56, 64, 65, 73, 804
SCHULTZE, 330, 332, 341
SCHUUR, 61
SCHVARTZMAN, 306, 312
SCHWIERZ, 121
SCIPION, 40, 88, 409
SCOLLO, 460
SCOVELL, 132
SEAGER, 444
SECK, 448, 633
SEED, 41, 322
SEIFERT, 211, 330
SEMPERE, 198
SEMPERE-TORRES, 147, 178, 189, 399, 412
SEO, 393
SHAMOUN-BARANES, 462
SHARMA, 182
SHEHU, 339
SHERMAN, 115, 153
SHIROOKA, 95, 103
SHUPE, 377
SIDERIS, 141, 315, 318, 407, 738
SIDSELRUD, 131
SIGMARSSON, 295
SILVA, 40, 88, 116, 229, 409, 436, 810
SILVER, 446
SILVESTRO, 178, 189
SIMMER, 84, 114, 279, 338, 414, 574
SIMPSON, 132
SINISALO, 428
SKOURI-PLAKALI, 266
SKRIPNIKOVA, 120
SMIATEK, 265
SMITH, 171, 180
SNYDER, 221, 224
SODERHOLM, 486
SOHN, 164
SOKOL, 89
SOLAZZO, 135
SOLONIN, 442, 870
SONNA, 167
SORRIBAS, 175, 915
SOUVERIJNS, 50
SOUZA, 336
STECHMAN, 115
STEDRONSKY, 157
STEENEVELD, 212
STEIB, 257
STEINERT, 162, 281
STEPANIAN, 462
STEPANOV, 340, 469
STEPHAN, 211
STEVANOVIĆ, 129, 662
STOCKER, 278, 558
STOJANOVIC, 395, 822
SUGIMOTO, 354, 443, 837

SUH, 83
SUK, 458
SULMONI, 258, 282
SUN (J.), 137, 220, 223, 473
SUN (L.), 271
SUTHERLAND-STACEY, 246
SUZUKI, 128, 342
SWICK, 350
SY, 60, 586
SZTURC, 328, 427

TAHANOUT, 365, 756
TAI, 137, 473
TAKAHASHI, 181, 292, 309, 640
TAKIZAWA, 364
TANAMACHI, 119, 264, 267, 361, 514
TANELLI, 60, 62, 586
TANG, 145, 398
TANI, 109, 273
TAPIADOR, 76, 272
TASSONE, 154, 486
TAYLOR, 253
TCHIGUIRINSKAIA, 117, 266
TELLESCHI, 156, 363, 889, 906
TERINK, 195
TESCHL, 109, 273
TESTIK, 423
THEEUWES, 212
THOMPSON, 252, 421
THURAI, 42, 43, 58, 524
TIIRA, 36, 52, 151, 681
TOKAY, 44, 346, 350, 426
TOLEDO, 244
TORRES, 293, 306, 312, 369, 394
TOUSSAINT, 308
TRÖMEL, 84, 105, 114, 279, 338, 414, 574
TRACKSDORF, 162
TRAVOV, 305, 846
TREFALT, 121, 141
TREIS, 193
TRETHEWEY, 310
TRIDON, 62, 251
TSAI, 256
TURK, 62
TURKO, 286
TURNER, 267, 463, 932
TWINTERRATH, 152
TYYNELÄ, 385

UÇURUM, 397
UEKI, 95, 103
UIJLENHOET, 41, 177, 195, 198, 201, 212, 300, 391, 422, 444, 445, 451, 457
UNAL, 66, 67, 94, 243, 373, 419
URBAN, 154, 486
USHIO, 181, 292, 364, 640

VACCARONO, 237
VALDIVIA, 40, 88, 409
VANHOENACKER, 467
VARLAS, 219, 830
VASIĆ, 129, 662
VECIANA, 288, 897
VEERKAMP, 308
VELDHUIS, 180
VENTURA, 85, 258, 282
VERLINDEN, 462
VIGNON, 70
VILARDELL-SANCHEZ, 463
VINOGRADOV, 337
VIVEKANANDAN, 256
VOGELMANN, 112, 270
VOGT, 165
VOORMANSIK, 138, 450
VOS, 391
VRANIC, 158, 601
VUCINIC, 158, 601
VULPIANI, 110, 249, 285, 605

WADA, 292
WADOUX, 201
WAINWRIGHT, 462
WALDEN, 260, 310
WALDINGER, 264, 267, 514
WALKER, 41
WANG (M.), 271
WANG (R.), 271
WANG (Y.), 113, 118, 320
WANIHA, 108
WAPLER, 162, 330, 332, 334, 341
WARDE, 369, 394

WARREN, 241
WATLET, 263
WATTERS, 251
WECKWERTH, 220
WEIGL, 152
WEIPERT, 239
WEISSHAUPT, 462, 465, 620
WELLPOTT, 260
WELZBACHER, 211, 330
WERNER, 162, 330–332, 341, 355
WESTBROOK, 260
WHITE, 191
WILFERT, 263
WILLEMS, 188
WILLIAMS, 246, 377
WILSON, 108
WINGO, 58, 524
WINTERRATH, 326
WOLDE, 348, 937
WOLFF, 346, 350, 358, 426, 457
WOLSIEFFER, 298
WOOD, 283
WRIGHT, 180
WU, 137, 473
WULFMEYER, 437
WURMAN, 100, 101, 301

XIA, 271
XUE, 118, 222

YAGMUR, 187
YAKIMAINEN, 442, 870
YAN, 456
YAO, 130
YAPI, 286
YE, 387
YEARY, 295
YEOM, 76, 91
YIN, 243, 244, 373
YOKOI, 95, 103
YOO, 192, 425
YOSHIKAWA, 364
YOSHIMI, 181, 640
YOSHIMURA, 69
YOUNG, 161
YU, 375, 400, 408

ZACHAROV, 226
ZAMORIN, 337
ZAURI, 159, 654
ZEHTINDJIEV, 462
ZHANG (G.), 93, 297
ZHANG (J.), 145, 389, 398
ZHANG (P.), 398, 494
ZHAO, 93, 118, 222
ZHENG, 447, 579
ZHU, 222
ZINK, 463, 932
ZINNER, 51
ZRNIC, 291, 297, 311
ZWAN, 243